Wave motion in finite and infinite media using the Thin-Layer Method

by
Joonsang Park

Bachelor of Science in Civil Engineering
Yonsei University, Seoul, Korea, 1993

Master of Science in Civil Engineering
Yonsei University, Seoul, Korea, 1996

Master of Science in Civil and Environmental Engineering
MIT, Cambridge, MA, USA, 1998

Submitted to the Department of Civil and Environmental Engineering
in partial fulfillment of the requirements for the degree of Doctor of Science
in Structures and Materials
at the
MASSACHUSETTS INSTITUTE OF TECHNOLOGY

February, 2002

Author .....
Department of Civil and Environmental Engineering
February, 2002

Certified by .....
Eduardo Kausel, Professor of Civil and Environmental Engineering
Department of Civil and Environmental Engineering

Accepted by .....
.....
Oral Buyukozturk, Chairman
Departmental Committee on Graduate Studies

Wave motion in finite and infinite media using the Thin-Layer Method

by
Joonsang Park

Submitted to the Department of Civil and Environmental Engineering
On January 31, 2002 in partial fulfillment of the requirements for the
Degree of Doctor of Science in Structures and Materials

Abstract

The Thin-Layer Method (TLM) is a semi-analytical technique that is efficient for wave propagation problems involving partially heterogeneous media. While the method has been used widely for horizontally stratified media, e.g. dynamic response of foundations over layered soils, there remain many unexplored aspects. These include a thorough evaluation of the TLM's accuracy and range of applicability as well as its extension to semi-infinite and infinite media. Based on these considerations, we have three main goals to pursue in this study. The first one is to explore and improve the accuracy and convergence of the TLM associated with finite media. The second one is to extend the applicability of the TLM to model and analyze semi-infinite and infinite multilayered media. The third one is to develop two novel TLM's that are useful in analyzing wave motions in cylindrically or spherically laminated solids and shells. We proceed our study by separating it into the following three parts.

In the first part, we begin by characterizing numerical dispersion phenomena in the TLM by means of general solutions and frequency spectra for discrete homogeneous full-spaces, which are obtained in closed-form with the aid of a finite difference scheme. Then, we determine the optimal combination of the consistent and lumped mass matrices by introducing tuning factors into the discrete system of equations. As a result, we improve the accuracy of not only the eigenvalues associated with free-vibration problems, but also the modal responses to external dynamic loads. To assess the accuracy and convergence of the modal solutions, we compute both the displacements and internal stresses for some canonical examples and then compare with the associated exact analytical solutions. From this exploration, we discover various aspects of the TLM modal solutions in connection with the spatial-temporal characteristics of sources and receivers. We consider both the linear and quadratic expansion TLM's. Finally, we determine the reasonable numbers of thin-layers per wavelength needed to calculate accurate responses with the TLM. In addition, we find out that the quadratic expansion TLM is more accurate and efficient than the linear expansion TLM.

In the second part, we utilize the substructure method and the paraxial approximation for the purpose of analyzing the semi-infinite and infinite multilayered media by means of the TLM. The substructure method is applied to the TLM formulation in the time-domain, while the paraxial approximation is used for the TLM formulation in the frequency-domain. In addition, for the application of the substructure method, we derive new closed-form Green's functions in the wavenumber-time domain for a homogeneous half-space by means of contour integration. We extensively investigate the characteristics of the both formulations to improve their stability and accuracy. For stable and effective calculation, we propose the use of an artificial buffer layer and an adaptive buffer layer for the time-domain and frequency-domain formulations, respectively. Furthermore, we also derive the exact analytical Green's functions in the space-frequency domain

for a layered half-space subjected to *SH* wave motion and a homogeneous half-space subjected to *SV-P* wave motion by means of contour integration. We compare the numerical results obtained with the TLM against the exact analytical Green's functions to assess the accuracy of the TLM combined with a hybrid system of the paraxial approximation and the adaptive buffer layer.

In the third part, we develop two new TLM's formulated in the cylindrical and spherical coordinate systems, respectively. The one is called the Cylindrical Thin-Layer Method (CTLM) and the other is called the Spherical Thin-Layer Method (STLM). These two are formulated in both the linear and quadratic expansion. To verify the two developed TLM's, we compute the propagation modes for a homogeneous cylindrical/spherical solid and shell, and compare these with the associated exact analytical solutions. For this purpose, we also derive the exact analytical solutions for the continuous models of interest.

Thesis supervisor: Eduardo Kausel
Title: Professor of Civil and Environmental Engineering

Acknowledgments

My working with my advisor, Professor Eduardo Kausel, during last four and half years was one of the happiest times in my life. I am deeply grateful for his support, encouragement and guidance that I have received from him. Also, I would like to express my gratitude to my two other committees, Professor Connor and Professor Wooh, Professor Mei, Professor Büyüköztürk, and Professor Ulm in the department. What I have learned from all of them will be a solid foundation for my future works in civil engineering fields. I am also grateful to Cynthia Stewart for her great helps. I always remember my first day at MIT when she gave me a good impression about MIT. Thank you so much, Cynthia.

I am grateful to all the colleagues and Professor Savidis at the Technical University in Berlin. Working together with them was always fun and productive, and their advises about my thesis and research were very helpful. Also, I would like to thank people at Earth Resources Laboratory of MIT for thinking about problems together and providing good suggestions as well. Specially, I would like to express my gratitude to Professor Toksöz, Dr. Burns, and Dr. Rao.

I deeply thank the Washington Sanitary Suburban Commission for financially supporting my study and research.

I am thankful to all my dear friends in Room 1-050, Daniel, David, Dominic & George, Jesse, Louis, Karen & Martin, Michael, Monica, Pong, Vince, and Yijun. Studying together with them at the basement office for last four and half years was always enjoyable, and also sharing our knowledge was good experience and very helpful.

Also, I would like to express my thankfulness to all Korean students and their families in the department, and all Yonsei university alumni families at MIT. I wish that all of them could achieve what they want from studying at MIT during their young life periods, and also contribute their useful knowledge for the world development at the end.

I am deeply thankful to Jinwoo, Yeonjoo, Jeeseong's family, Taeshin's family, Younghoon's family at D.C, and Yongki's family. Their love, concerns and helping me out were always supportive and encouraging me a lot during last few years. Also, the moments spending together will be my wonderful reminiscence ever.

I deeply appreciate endless love and support from my family. Their help and concerns made my study well done. My elder brother, Joonhong, always gave me precious advises, although he also was busy and tired of his own study. My sister-in-law, Seongjean, always encouraged me with tenderness. Also, talking with her is always making myself feel so good and recover from tiredness. My mother and father, Youngsook and Taekwon, helped and encouraged me a lot. They always trust me, which is always a good motivation for me to continue my job with having great confidence. Thank you so much for every thing and I love you all.

Table of contents

Chapter 1 Introduction

1.1 Motivations and scope

The Thin-Layer Method (TLM) is a semi-analytical technique used to solve wave propagation problems involving partially heterogeneous media. The method is based on a finite-element discretization of the media in the direction in which the material properties are heterogeneous, and using analytical methods for the remaining coordinate directions. While the method has been used widely in the context of horizontally stratified media, such as traffic loads on pavements, the dynamic response of foundations over layered soils, and non-destructive techniques for laminated composite materials, there remain many unexplored aspects. These include a thorough evaluation of the TLM's accuracy and range of applicability as well as its extension to semi-infinite and infinite media. Based on these considerations, we proceed our study by separating it into the following three parts.

In the first part, i.e. in chapters 2, 3 and 4, we begin by characterizing numerical dispersion phenomena in the TLM discrete models by means of general solutions and frequency spectra for isotropic homogeneous discrete full-spaces subjected to plane waves. The general solutions and frequency spectra are obtained in closed-form with the aid of a finite difference scheme. Then, we determine an optimal combination of consistent and lumped mass matrices by introducing tuning factors into the discrete system of equations. As a result, we improve the accuracy of not only the eigenvalues associated with free-vibration problems, but also the TLM modal responses to external dynamic loads. To assess the accuracy and convergence of the TLM modal solutions, we compute both the displacements and internal stresses for some canonical examples and then compare these with the associated exact analytical solutions. From this exploration, we discover various aspects of the TLM modal solutions in connection with possible numerical errors that can occur in real analyses. For this purpose, we also derive and present the exact analytical solutions in the form of modal superposition solutions as well as by means of the image source method. We consider both the linear and quadratic expansion TLM's. Finally, we determine a recommended numbers of thin-layers per wavelength needed to calculate accurate modal responses with the TLM. In addition, we observe that the quadratic expansion TLM is more accurate and efficient than the linear expansion TLM.

In the second part, i.e. in chapters 5 and 6, we utilize the substructure method and the paraxial approximation for the purpose of analyzing semi-infinite and infinite multilayered media with the TLM. The substructure method is applied to the TLM formulation in the time-domain, while the paraxial approximation is used for the TLM formulation in the frequency-domain. In addition, for the application of the substructure method, we derive new closed-form Green's functions in the wavenumber-time domain for a homogeneous half-space by means of the contour integration method. We extensively investigate the characteristics of the both the time-domain and frequency-domain formulations, as a result of which we improve their stability and accuracy. For stable and effective calculation, we propose the use of an artificial buffer layer and an adaptive buffer layer for the time-domain and frequency-domain formulations, respectively. Furthermore, we also derive exact analytical Green's functions in the space-frequency domain for a layered half-space subjected to *SH* wave motion and a homogeneous half-space subjected to *SV-P* wave motion by means of the contour integration method. We compare the numerical results obtained with the TLM against the exact analytical Green's functions to assess the accuracy of the TLM combined with a hybrid system of the paraxial approximation and the adaptive buffer layer.

In the third part, i.e. in chapters 7 and 8, we develop two new TLM formulations in the cylindrical and spherical coordinate systems, respectively. These are the Cylindrical Thin-Layer Method (CTLM) and the Spherical Thin-Layer Method (STLM). Both of these two are formulated not only in linear expansion, but also in quadratic expansion. Also, we present the modal solutions for displacement responses in the time-domain. To verify the validation of the two developed TLM's, we first compare them with the TLM for flat layers, based on the fact that a hollow cylinder and sphere with a large radius relative to its thickness behaves like an infinite plate. Then, we compute the propagation modes (or eigenvalues) for a homogeneous cylindrical/spherical solid and shell, and compare these with the associated exact analytical solutions. For this purpose, we also derive the exact analytical solutions for the continuous models of interest.

1.2 Historical background

Since its inception in the 1970's, the TLM has evolved into an efficient technique for the analysis of wave motion in layered soils and other laminated media. Because the TLM is based on a partial-discretization technique, it requires relatively small computational efforts in comparison with other full-discretization methods such as the finite difference method and the finite element method. In addition, the TLM can easily couple with standard finite element methods for such practical purposes as soil-structure interaction problems or irregular-shaped layered systems. Finally, the TLM can provide various Green's functions for arbitrarily multilayered media without any added difficulty, which are very useful indeed when combined with the boundary element methods.

From the historical point of view, the origin of the TLM can be traced to the work of Lysmer [1970] where he formulated the characteristic equations for the analysis of generalized Rayleigh wave in isotropic layered media by means of a limiting process to finite elements of linear expansion. He also calculated the dispersion characteristics and group velocities on the basis of Rayleigh's quotient. A few years later, Waas [1972] and Lysmer and Waas [1972] derived the characteristic equations directly from the principle of virtual work without performing a limiting process from finite elements. Waas [1972] extensively analyzed the Rayleigh and Love wave motions in plane and axisymmetric problems. In addition, they obtained transmitting boundaries for finite element representations of irregular soil media.

At the same period, Nelson et al. [1971], Dong and Nelson [1972], Nelson and Dong [1973] developed essentially the same method, which they called the extended Ritz technique in their papers, for studying the free vibrations of laminated orthotropic plates and circular cylinders. In their studies, a quadratic interpolation function is employed to approximate displacement fields in the layering direction and Hamilton's principle is used to arrive at the free vibration equations. Furthermore, Datta et al. [1988] used cubic Hermite polynomials and obtained a characteristic equation of fourth order in the horizontal wavenumber for the case of plane strain. Alekseyev and Mikhaylenko [1976] developed a technique for analyzing vertically inhomogeneous elastic half-spaces on the basis of an extension of the method of partial separation of the variables using the finite difference method instead of the finite element method. Rukos [1978] treated, with complete generality, the partial discretization of the boundary value problem of elastostatics, and illustrated the accuracy of the method for domains of bounded, semi-infinite, and infinite extent.

Drake [1972a, 1972b, 1980] applied the transmitting boundaries of Waas [1972] and Lysmer and Waas [1972] to analyze Love and Rayleigh waves in irregular layered media. At the same time,

Kausel [1974] formulated the transmitting boundaries in cylindrical coordinates to analyze the vibration behavior of circular foundations. Kausel and Roësset [1977] developed the semi-analytical hyper-element for the analysis of layered soils of finite and infinite domains. Kausel and Roësset [1981] derived the stiffness matrices for layered soils in the form of both the exact and discrete solutions, and also presented their advantages over the Haskell-Thompson transfer matrix method. Tassoulas and Kausel [1983] obtained semi-discrete particular solutions satisfying inhomogeneous boundary conditions to assess the dynamic behavior of circular and annular foundations.

Kausel [1981] provided the most general framework for the calculation of the Green's functions for isotropic layered media by means of the TLM. In his study, he considered various dynamic loads with arbitrary spatial-temporal characteristics via Fourier and Hankel transformations, and derived in closed-form the consistent stresses as well as displacements. Based on this work, Kausel and Peek [1982a] presented the Green's functions for dynamic loads of various types such as disk loads, ring loads, point loads, seismic single and double couples, and etc. A similar technique was also developed independently by Tajimi [1980] to investigate the dynamic stiffness of surface foundations. Olson and Orcutt [1984] formulated the discrete wavenumber/finite element method by utilizing discrete wavenumber decomposition for the horizontal dependence of the wave motion in terms of a Fourier-Bessel series. In their study, the vertical-direction and time dependence of the wave motion is obtained as the solution to a system of partial differential equations, which are solved numerically by a combination of finite element and finite difference methods.

Kausel [1986] extended the TLM to allow the modeling of wave propagation in fully anisotropic, layered systems. In addition, Kausel [1993,1994] formulated the TLM in the time domain to compute the Green's functions for fully anisotropic layered systems. At the same time, Touhei [1994] formulated a discrete wavenumber and normal mode superposition method, which turned out to be quite similar to the work by Kausel [1994]. Geller and Ohminato [1994] and Geller and Hatori [1995] analyzed laterally heterogeneous media by means of the so-called direct solution method. Cummins [1994] and Cummins et al. [1994] formulated complete seismograms by means of the direct solution method of linear expansion for *SH* and *SV-P* spherically symmetric case. Park [1998] formulated the TLM in cylindrical coordinate system, called the cylindrical thin layer method (CTLM), to obtain the Green's functions for cylindrically laminated anisotropic elastic media. Kausel [1998] presented the Green's functions for laminated media subjected to a class of dynamic point sources such as force dipoles, blast loads and bimoments (moment dipoles). In addition, Han et al. [2001a,b] analyzed transient waves in functionally graded materials excited by impact loads.

The modeling of layered media over elastic half-spaces or within full-spaces was developed with the application of the paraxial approximation [Seale 1985; Kausel and Seale 1987; Seale and Kausel 1989]. As a result, the applicability of the Green's functions was extended from layered systems of finite depth to layered systems on semi-infinite and infinite media. Maeda and Kausel [1991] and Kausel [1992] extensively investigated the accuracy and stability of the paraxial approximation in the context of analyses for layered half-spaces and full-spaces.

Kausel and Peek [1982b] applied the Green's functions obtained with the TLM to the boundary element method to study laminates with irregularities such as cavities and inclusions. Prosper [2001] developed the traction boundary element method based on the Green's functions calculated by means of the TLM and applied it to the detection of delaminations in laminated plates. Schepers [2001] optimized the TLM to calculate more accurate Green's functions for near

fields in the context of the boundary element method and studied the behavior of foundations on elastic half-spaces.

Tan [1989] formulated a finite element method for layered solid-fluid media by means of the formulation for solid media, taking the shear modulus in the fluid domain as zero. Ghibril [1992] illustrated the capabilities of the TLM for the problem of waves scattering due to finite interfacial cracks. In addition, he analyzed fluid-solid coupled stratified systems by means of the TLM, where he imposed continuity conditions between solid and fluid media in a rigorous manner instead of using a zero shear modulus for the fluid. Liu and Achenbach [1994, 1995] formulated a so-called strip element method and investigated wave scattering by cracks in anisotropic laminated plates. It should be noted that the strip element method of Liu and Achenbach is virtually the same as the TLM and the semi-analytical hyper-elements formulated by Kausel and Roësset [1977], Kausel [1981], and Tassoulas and Kausel [1983]. Xi et al. [2000a] applied the strip-element method to the analysis of wave scattering by a crack in an immersed axisymmetric laminated cylinder.

1.3 Thin-layer method in Cartesian coordinates

In this section, we introduce and review the TLM formulation in a Cartesian coordinate system of (x, y, z), where the z coordinate corresponds to the depth or layering direction of multi-layered media of interest. We consider two kinds of the TLM formulations: the one is formulated in the frequency domain, and the other is formulated in the time domain. Herein, we call the first one the ω-TLM and the second one the t-TLM for short. In particular, we present the response functions (or Green's functions) associated with only *SH* and *SV-P* line loads in this section. For furthermore response functions such as Green's functions for point loads, disk loads, ring loads, etc., the readers can refer to the studies by Kausel [1981, 1994] and Kausel and Peek [1982a].

This section is composed of seven subsections 1.3.1-1.3.7. In section 1.3.1, we obtain the wave equation in matrix form for the most general anisotropic material in a Cartesian coordinate system, and also set up the necessary boundary conditions. In section 1.3.2, we formulate the TLM by means of the principle of virtual work and the discretization of the wave equation along the z direction, after which we end up with a discrete wave equation. In section 1.3.3, we transform the discrete wave equation by means of a Fourier transformation with respect to the spatial (x, y) and temporal (t) variables. As a result, we obtain a purely algebraic expression for the dynamic systems of interest, which could be solved in various ways such as inversion of the dynamic stiffness matrix or by spectral decomposition. In sections 1.3.4 and 5, we obtain the modal superposition solutions (or Green's functions) for *SH* and *SV-P* harmonic line loads, by means of eigenvalue problems in the wavenumber variable. In sections 1.3.6 and 7, we obtain the modal superposition solutions (or Green's functions) for *SH* and *SV-P* transient line loads, by means of eigenvalue problems in the frequency variable. We present in closed-form the responses for displacement components, consistent stress components, and nodal load components.

1.3.1 Wave equation in Cartesian coordinates

Consider a horizontally stratified, locally homogeneous and anisotropic, linearly elastic medium of infinite lateral extent whose motion is acted upon by dynamic loads at some location. At any arbitrary point in the medium, the dynamic equilibrium equation, the stress-strain relation, and the strain-displacement relation are given by

$$\rho\ddot{\mathbf{u}} - \mathbf{L}^T\boldsymbol{\sigma} = \mathbf{b} \tag{1.3.1}$$

$$\boldsymbol{\sigma} = \mathbf{D}\boldsymbol{\varepsilon} \tag{1.3.2}$$

$$\boldsymbol{\varepsilon} = \mathbf{L}\mathbf{u} \tag{1.3.3}$$

In these equations,

$$\rho = \rho(x, y, z) \quad \text{(the mass density)} \tag{1.3.4a}$$

$$\mathbf{u} = \mathbf{u}(x, y, z, t) = \begin{bmatrix} u_x & u_y & u_z \end{bmatrix}^T \quad \text{(the displacement vector)} \tag{1.3.4b}$$

$$\mathbf{b} = \mathbf{b}(x, y, z, t) = \begin{bmatrix} b_x & b_y & b_z \end{bmatrix}^T \quad \text{(the body load vector)} \tag{1.3.4c}$$

$$\boldsymbol{\sigma} = \boldsymbol{\sigma}(x, y, z, t) = \begin{bmatrix} \sigma_x & \sigma_y & \sigma_z & \tau_{yz} & \tau_{xz} & \tau_{xy} \end{bmatrix}^T \quad \text{(the stress tensor)} \tag{1.3.4d}$$

$$\boldsymbol{\varepsilon} = \boldsymbol{\varepsilon}(x, y, z, t) = \begin{bmatrix} \varepsilon_x & \varepsilon_y & \varepsilon_z & \gamma_{yz} & \gamma_{xz} & \gamma_{xy} \end{bmatrix}^T \quad \text{(the strain tensor)} \tag{1.3.4e}$$

$$\mathbf{D} = \mathbf{D}(x, y, z) = \{d_{ij}\} \quad i, j = 1, 2, ..., 6 \quad \text{(the constitutive matrix, symmetric)} \tag{1.3.4f}$$

$$\mathbf{L}^T = \begin{Bmatrix} \frac{\partial}{\partial x} & \cdot & \cdot & \cdot & \frac{\partial}{\partial z} & \frac{\partial}{\partial y} \\ \cdot & \frac{\partial}{\partial y} & \cdot & \frac{\partial}{\partial z} & \cdot & \frac{\partial}{\partial x} \\ \cdot & \cdot & \frac{\partial}{\partial z} & \frac{\partial}{\partial y} & \frac{\partial}{\partial x} & \cdot \end{Bmatrix} \quad \text{(a differential operator)} \tag{1.3.4g}$$

The superscript T in these equations denotes a transposed vector or matrix, and the double dot indicates the second derivative with respect to time t. Substituting equations (1.3.2 and 3) into equation (1.3.1), we are led to the wave equation in Cartesian coordinates:

$$\rho\ddot{\mathbf{u}} - \mathbf{L}^T\mathbf{D}\mathbf{L}\mathbf{u} = \mathbf{b} \tag{1.3.5}$$

On the other hand, the differential operation $\mathbf{L}$ can be rewritten as

$$\mathbf{L} = \mathbf{L}_x\frac{\partial}{\partial x} + \mathbf{L}_y\frac{\partial}{\partial y} + \mathbf{L}_z\frac{\partial}{\partial z} \tag{1.3.6}$$

where

$$\mathbf{L}_x = \begin{Bmatrix} 1 & \cdot & \cdot \\ \cdot & \cdot & \cdot \\ \cdot & \cdot & \cdot \\ \cdot & \cdot & \cdot \\ \cdot & \cdot & 1 \\ \cdot & 1 & \cdot \end{Bmatrix}, \quad \mathbf{L}_y = \begin{Bmatrix} \cdot & \cdot & \cdot \\ \cdot & 1 & \cdot \\ \cdot & \cdot & \cdot \\ \cdot & \cdot & 1 \\ \cdot & \cdot & \cdot \\ 1 & \cdot & \cdot \end{Bmatrix}, \quad \mathbf{L}_z = \begin{Bmatrix} \cdot & \cdot & \cdot \\ \cdot & \cdot & \cdot \\ \cdot & \cdot & 1 \\ \cdot & 1 & \cdot \\ 1 & \cdot & \cdot \\ \cdot & \cdot & \cdot \end{Bmatrix}$$

It follows that the expansion of the product $\mathbf{L}^T\mathbf{D}\mathbf{L}$ is of the form

$$\begin{aligned} \mathbf{L}^T\mathbf{D}\mathbf{L} = {} & \mathbf{D}_{xx}\frac{\partial^2}{\partial x^2} + \mathbf{D}_{yy}\frac{\partial^2}{\partial y^2} + \mathbf{D}_{zz}\frac{\partial^2}{\partial z^2} \\ & (\mathbf{D}_{xy} + \mathbf{D}_{yx})\frac{\partial^2}{\partial x\partial y} + (\mathbf{D}_{xz} + \mathbf{D}_{zx})\frac{\partial^2}{\partial x\partial z} + (\mathbf{D}_{yz} + \mathbf{D}_{zy})\frac{\partial^2}{\partial y\partial z} \end{aligned} \tag{1.3.7}$$

with material matrices $\mathbf{D}_{\alpha\beta}$ defined by

$$\mathbf{D}_{\alpha\beta} = \mathbf{L}_\alpha^T\mathbf{D}\mathbf{L}_\beta, \quad \alpha, \beta = x, y, z \tag{1.3.8}$$

These matrices depend only on the material parameters, and can be readily evaluated for any anisotropic medium. Substituting equations (1.3.7 and 8) into equation (1.3.5), we obtain the general wave equation for an anisotropic solid in Cartesian coordinates.

On the other hand, the vector of internal stresses in any horizontal plane can be written as

$$\mathbf{s} = \mathbf{L}_z^T \boldsymbol{\sigma} = \mathbf{L}_z^T \mathbf{D} \mathbf{L} \mathbf{u} \tag{1.3.9}$$

whose components are

$$\mathbf{s} = \begin{bmatrix} \tau_{zx} & \tau_{zy} & \sigma_z \end{bmatrix}^T \tag{1.3.10}$$

Finally, the boundary conditions at regions where the external tractions $\mathbf{t}$ are prescribed are of the form

$$\mathbf{t} - \mathbf{s}_\nu = \mathbf{0} \tag{1.3.11}$$

with $\mathbf{s}_\nu$ being the vector of internal stresses at the boundary with normal $\boldsymbol{\nu}$. For an upper horizontal boundary $\mathbf{s}_\nu = \mathbf{s}$, while for a lower horizontal boundary $\mathbf{s}_\nu = -\mathbf{s}$, with $\mathbf{s}$ given in either case by equations (1.3.9 and 10).

1.3.2 Formulation of the TLM

To solve the wave equation, we begin by dividing the physical domain into layers that are thin in the finite element sense. Each of these thin-layers may in turn be composed of sub-layers; the number of sub-layers, if any, will depend on the interpolation order m chosen for the thin-layer formulation, as will be seen. We proceed next to cut out an individual thin-layer, and then label the sub-layers with indices, l, l+1,...,l+m (from the top down). We preserve the equilibrium of each thin-layer by applying tractions $\mathbf{t}_l$, $\mathbf{t}_{l+m}$ on the two exposed surfaces such that they match the internal stresses there. We approximate the displacement field within the thin-layer by means of an interpolation as

$$\mathbf{u} = \mathbf{N} \mathbf{U} \tag{1.3.12}$$

with $\mathbf{N} = \mathbf{N}(z)$ being a matrix containing the interpolation polynomials, and $\mathbf{U} = \mathbf{U}(x, y, t)$ a column vector composed of the interface displacement vectors

$$\mathbf{U} = \begin{bmatrix} \mathbf{u}_l^T & \mathbf{u}_{l+1}^T & \cdots & \mathbf{u}_{l+m}^T \end{bmatrix}^T \tag{1.3.13}$$

For example, for the linear (m=1) and quadratic (m=2) interpolation, the matrix $\mathbf{N}$ is given as

$$\mathbf{N} = \begin{bmatrix} \zeta \mathbf{I} & (1-\zeta)\mathbf{I} \end{bmatrix} \qquad (\text{for } m=1) \tag{1.3.14a}$$

$$\mathbf{N} = \begin{bmatrix} \zeta(2\zeta-1)\mathbf{I} & 4\zeta(1-\zeta)\mathbf{I} & (1-\zeta)(1-2\zeta)\mathbf{I} \end{bmatrix} \qquad (\text{for } m=2) \tag{1.3.14b}$$

where $\mathbf{I}$ is the 3×3 identity matrix, and $\zeta = z/h$, with h being the thickness of the thin-layer.

Clearly, equation (1.3.12) represents a partial discretization of the displacement field, namely only in the direction of layering. Thus, when we substitute the displacement expansion (1.3.12) into both of the wave equation (1.3.5) and the boundary conditions (1.3.11), we find that these equations are not satisfied identically, but exhibit instead residual body forces $\mathbf{r} = \mathbf{r}(x, y, z, t)$ and residual boundary tractions $\mathbf{q} = \mathbf{q}(x, y, z, t)$, i.e.

$$\mathbf{b} - \rho \ddot{\mathbf{u}} + \mathbf{L}^T \mathbf{D} \mathbf{L} \mathbf{u} = \mathbf{r} \tag{1.3.15a}$$

$$\mathbf{t} - \mathbf{s}_\nu = \mathbf{q} \tag{1.3.15b}$$

To derive the discrete equations of motion and dispose of these unbalanced forces $\mathbf{r}$ and $\mathbf{q}$, we apply the method of weighted residuals to the thin-layer, and require the virtual work done by the residual forces throughout an elementary volume of the thin-layer (of width dx, depth dy, and height h) to be zeros:

$$\left[\delta\mathbf{u}_l^T\mathbf{q}_l+\delta\mathbf{u}_{l+m}^T\mathbf{q}_{l+m}+\int_0^h\delta\mathbf{u}^T\mathbf{r}dz\right]dxdy=0 \tag{1.3.16}$$

The first two terms represent the virtual work performed by the residual tractions at the upper and lower boundaries of the thin-layer, while the third term corresponds to the virtual work done by the residual body forces. Substituting equations (1.3.12 and 15) into equation (1.3.16) and discarding the product $dxdy$, we obtain

$$\begin{aligned}&\delta\mathbf{u}_l^T\mathbf{t}_l+\delta\mathbf{u}_{l+m}^T\mathbf{t}_{l+m}+\delta\mathbf{U}^T\int_0^h\mathbf{N}^T\mathbf{b}\,dz\\&=\delta\mathbf{U}^T\left\{\int_0^h\rho\mathbf{N}^T\mathbf{N}dz\right\}\ddot{\mathbf{U}}+\delta\mathbf{u}_l^T\mathbf{s}_l-\delta\mathbf{u}_{l+m}^T\mathbf{s}_{l+m}-\delta\mathbf{U}^T\left\{\int_0^h\mathbf{N}^T\mathbf{L}^T\mathbf{DLN}dz\right\}\mathbf{U}\end{aligned} \tag{1.3.17}$$

When we require this expression to be valid for arbitrary variation $\delta\mathbf{U}$, we obtain the dynamic equilibrium equation for the thin-layer as

$$\begin{bmatrix}\mathbf{p}_l\\\mathbf{p}_{l+1}\\\vdots\\\mathbf{p}_{l+m}\end{bmatrix}=\left\{\int_0^h\rho\mathbf{N}^T\mathbf{N}dz\right\}\begin{bmatrix}\ddot{\mathbf{u}}_l\\\ddot{\mathbf{u}}_{l+1}\\\vdots\\\ddot{\mathbf{u}}_{l+m}\end{bmatrix}+\begin{bmatrix}\mathbf{L}_z^T\mathbf{DLu}|_{z=h}\\\mathbf{0}\\\vdots\\-\mathbf{L}_z^T\mathbf{DLu}|_{z=0}\end{bmatrix}-\left\{\int_0^h\mathbf{N}^T\mathbf{L}^T\mathbf{DLN}dz\right\}\begin{bmatrix}\mathbf{u}_l\\\mathbf{u}_{l+1}\\\vdots\\\mathbf{u}_{l+m}\end{bmatrix} \tag{1.3.18}$$

The left-hand side contains the consistent external tractions $\mathbf{p}$ acting on the sub-layer interfaces which result from the interface tractions $\mathbf{t}$ and body loads $\mathbf{b}$. The right-hand side, on the other hand, contains the internal loads as well as the elastic loads of deformation. Evaluation of this expression for a given interpolation order and material constitution requires tedious algebra manipulation and finally provides an equation of the form

$$\mathbf{P}=\mathbf{M}\ddot{\mathbf{U}}-\mathbf{A}_{xx}\frac{\partial^2\mathbf{U}}{\partial x^2}-\mathbf{A}_{xy}\frac{\partial^2\mathbf{U}}{\partial x\partial y}-\mathbf{A}_{yy}\frac{\partial^2\mathbf{U}}{\partial y^2}-\mathbf{B}_x\frac{\partial\mathbf{U}}{\partial x}-\mathbf{B}_y\frac{\partial\mathbf{U}}{\partial y}+\mathbf{GU} \tag{1.3.19}$$

where

$$\mathbf{M}=\left\{\int_0^h\rho\mathbf{N}^T\mathbf{N}dz\right\} \tag{1.3.20}$$

$$\mathbf{A}_{\alpha\alpha}=\left\{\int_0^h\mathbf{N}^T\mathbf{D}_{\alpha\alpha}\mathbf{N}dz\right\},\quad\alpha=x,y \tag{1.3.21a}$$

$$\mathbf{A}_{xy}=\left\{\int_0^h\mathbf{N}^T(\mathbf{D}_{xy}+\mathbf{D}_{yx})\mathbf{N}dz\right\} \tag{1.3.21b}$$

$$\mathbf{B}_\alpha=\left\{\int_0^h\mathbf{N}^T\mathbf{D}_{\alpha z}\mathbf{N}'dz\right\}-\left\{\int_0^h\mathbf{N}'^T\mathbf{D}_{z\alpha}\mathbf{N}dz\right\},\quad\alpha=x,y \tag{1.3.22}$$

$$\mathbf{G}=\left\{\int_0^h\mathbf{N}'^T\mathbf{D}_{zz}\mathbf{N}'dz\right\} \tag{1.3.23}$$

In equations (1.3.22) and (1.3.23), $\mathbf{N}'$ denotes the first derivative of the interpolation matrix with respect to z. Notice that the $\mathbf{M}$, $\mathbf{A}_{\alpha\alpha}$, and $\mathbf{G}$ matrices are symmetric, while the $\mathbf{B}_\alpha$ matrices are skew-symmetric. These matrices are listed in Appendix 1A.

At this stage, we proceed to overlap the results for a single thin-layer with those of all other thin-layers, like the element stiffness matrices in a finite element formulation, so as to generate the system matrix. Since the overlapping process is straightforward and the resulting system of equations has the same form as equation (1.3.19), we need not introduce additional symbols for this purpose. Instead, equation (1.3.19) can be understood as representing the complete system of layers, relating the consistent interface tractions $\mathbf{P}=\mathbf{P}(x,y,t)$ applied at the layer interfaces with the displacements $\mathbf{U}=\mathbf{U}(x,y,t)$ observed there. Such a system is narrowly banded and has a total of $3N$ degrees of freedom, with N being the number of active interfaces (which depends on the

number of layers, the expansion order m and the boundary conditions at the top and bottom surfaces).

1.3.3 Transformation of the discrete wave equation

As can be seen in equation (1.3.19), the partial discretization of the wave equation in the direction of layering eliminates the functional dependence on the vertical coordinate z, and yields a system of partial differential equations in the two horizontal coordinates (x, y) and time (t). To solve this equation, we begin by performing Fourier transformations with respect to the two horizontal coordinates (x, y) and time (t). The Fourier transformations and their inverses of the displacements and the consistent interface tractions are

$$\bar{\mathbf{U}}(k_x,k_y,\omega)=\int_{-\infty}^{\infty}dt\int_{-\infty}^{\infty}dx\int_{-\infty}^{\infty}dy\mathbf{U}(x,y,t)e^{-\mathrm{i}(\omega t-k_x x-k_y y)} \tag{1.3.24a}$$

$$\bar{\mathbf{P}}(k_x,k_y,\omega)=\int_{-\infty}^{\infty}dt\int_{-\infty}^{\infty}dx\int_{-\infty}^{\infty}dy\mathbf{P}(x,y,t)e^{-\mathrm{i}(\omega t-k_x x-k_y y)} \tag{1.3.24b}$$

$$\mathbf{U}(x,y,t)=\frac{1}{(2\pi)^3}\int_{-\infty}^{\infty}d\omega\int_{-\infty}^{\infty}dk_x\int_{-\infty}^{\infty}dk_y\bar{\mathbf{U}}(x,y,t)e^{\mathrm{i}(\omega t-k_x x-k_y y)} \tag{1.3.24c}$$

$$\mathbf{P}(x,y,t)=\frac{1}{(2\pi)^3}\int_{-\infty}^{\infty}d\omega\int_{-\infty}^{\infty}dk_x\int_{-\infty}^{\infty}dk_y\bar{\mathbf{P}}(x,y,t)e^{\mathrm{i}(\omega t-k_x x-k_y y)} \tag{1.3.24d}$$

where ω is the angular frequency, k_x and k_y are the wavenumbers in x and y directions, respectively, and $\mathrm{i}=\sqrt{-1}$. Applying equations (1.3.34c and d) to equation (1.3.19), we obtain the wave equation in the wavenumber-frequency domain of the form.

$$\bar{\mathbf{P}}=\bar{\mathbf{K}}_{dyn}\bar{\mathbf{U}} \tag{1.3.25}$$

with the dynamic stiffness matrix $\bar{\mathbf{K}}_{dyn}$ being given by

$$\bar{\mathbf{K}}_{dyn}=k_x^2\mathbf{A}_{xx}+k_xk_y\mathbf{A}_{xy}+k_y^2\mathbf{A}_{yy}+\mathrm{i}(k_x\mathbf{B}_x+k_y\mathbf{B}_y)+\mathbf{G}-\omega^2\mathbf{M} \tag{1.3.26}$$

While it is possible to solve the above problem in equation (1.3.25) without any difficulty, we choose instead to restrict our attention to a more special class of problems, namely those systems that have a (symmetric, positive-definite) constitutive matrix of the form

$$\mathbf{D}=\begin{Bmatrix} d_{11} & d_{12} & d_{13} & \cdot & \cdot & d_{16} \\ d_{21} & d_{22} & d_{23} & \cdot & \cdot & d_{26} \\ d_{31} & d_{32} & d_{33} & \cdot & \cdot & d_{36} \\ \cdot & \cdot & \cdot & d_{44} & d_{45} & \cdot \\ \cdot & \cdot & \cdot & d_{54} & d_{55} & \cdot \\ d_{61} & d_{62} & d_{63} & \cdot & \cdot & d_{66} \end{Bmatrix} \tag{1.3.27}$$

This constitutive matrix corresponds to a medium that is somewhat more general than an orthotropic material. When this condition is satisfied, it is possible to reduce equation (1.3.25) to a fully real and symmetric form. This simply requires modifying the vertical (z-direction) components of both the load and displacement vectors by a factor of $\mathrm{i}=\sqrt{-1}$, which changes the problem into

$$\bar{\mathbf{P}}=\hat{\mathbf{K}}_{dyn}\bar{\mathbf{U}} \tag{1.3.28}$$

with

$$\bar{\mathbf{P}} = \left[\bar{p}_x^1 \quad \bar{p}_y^1 \quad \mathrm{i}\bar{p}_z^1 \quad \bar{p}_x^2 \quad \cdots \quad \mathrm{i}\bar{p}_z^N \right]^T \tag{1.3.29a}$$

$$\bar{\mathbf{U}} = \left[\bar{u}_x^1 \quad \bar{u}_y^1 \quad \mathrm{i}\bar{u}_z^1 \quad \bar{u}_x^2 \quad \cdots \quad \mathrm{i}\bar{u}_z^N \right]^T \tag{1.3.29b}$$

$$\hat{\mathbf{K}}_{dyn} = k_x^2 \mathbf{A}_{xx} + k_x k_y \mathbf{A}_{xy} + k_y^2 \mathbf{A}_{yy} + k_x \hat{\mathbf{B}}_x + k_y \hat{\mathbf{B}}_y + \mathbf{G} - \omega^2 \mathbf{M} \tag{1.3.29c}$$

These modifications are accomplished in equation (1.3.25) by multiplying every third row by i and every third column by $-\mathrm{i}$. Inspection of the structure of all the matrices involved (see Appendix 1A) reveals that this modification affects only the $\mathrm{i}\mathbf{B}_\alpha$ terms, which become both real and symmetric. The modified matrices $\hat{\mathbf{B}}_\alpha$ are obtained from the $\mathbf{B}_\alpha$ by simply changing the sign of every third row.

For a prescribed loading vector, $\bar{\mathbf{P}}$, the displacement vector $\bar{\mathbf{U}}$ is calculated by formal inversion of the dynamic stiffness matrix:

$$\bar{\mathbf{U}} = \hat{\mathbf{K}}_{dyn}^{-1} \bar{\mathbf{P}} \tag{1.3.30}$$

In practice, this inversion is not necessary, since either a Gaussian reduction would be performed, or the spectral decomposition formulated in the following four sections could be used. Once obtaining $\bar{\mathbf{U}}$, we can calculate the responses in the space-time domain with the aid of equation (1.3.24c).

1.3.4 Responses due to *SH* harmonic line loads

Here, we consider the modal superposition responses to an *SH* harmonic line load of excitation frequency ω in an isotropic elastic medium. The associated discrete wave equation in the wavenumber-frequency domain is given as

$$\left[\mathbf{A} k^2 + \mathbf{G} - \omega^2 \mathbf{M} \right] \bar{\mathbf{U}}_y = \bar{\mathbf{P}}_y \tag{1.3.31}$$

where the following transformations relating the space and wavenumber domains are imposed.

$$\bar{\mathbf{U}}_y = \bar{\mathbf{U}}_y(k,\omega) = \int_{-\infty}^{\infty} \tilde{\mathbf{U}}_y(x,\omega) e^{\mathrm{i}kx} dx \tag{1.3.32a}$$

$$\bar{\mathbf{P}}_y = \bar{\mathbf{P}}_y(k,\omega) = \int_{-\infty}^{\infty} \tilde{\mathbf{P}}_y(x,\omega) e^{\mathrm{i}kx} dx \tag{1.3.32b}$$

Also, the matrices **A**, **G**, and **M** in equation (1.3.31) are obtained from $\mathbf{A}_{xx}$, **G**, **M** in equation (1.3.19) by collecting the anti-plane elements that are associated with only the y-direction components. We assume that an *SH* harmonic line load is applied at x=0 and at an n-th elevation (or interface) in the discrete medium of interest. Then, we can express the load in the space-frequency domain as

$$\tilde{\mathbf{P}}_y(x,\omega) = \delta(x)\boldsymbol{\delta}(n) \tag{1.3.33a}$$

where $\boldsymbol{\delta}(n)$ is a Dirac-delta vector with only the n-th entry being 1 and all the others being zeros. Then, the Fourier transform of $\tilde{\mathbf{P}}_y$ is obtained by means of equation (1.3.32b), and is given as

$$\bar{\mathbf{P}}_y(k,\omega) = \boldsymbol{\delta}(n) \tag{1.3.33b}$$

(A) Displacements due to an *SH* line load

First, we consider the displacement responses. In the TLM, we use the spectral decomposition to solve the above given system of equations by means of modal expansions. The reader may refer

to an MIT research report by Kausel [1981] for more detail. The propagation modes of the system analyzed are obtained from the eigenvalue problem that results from setting the load vector in equation (1.3.31) equal to zero:

$$\left[\mathbf{A}k_j^2+\mathbf{C}\right]\phi_j=\mathbf{0},\quad j=1,\ldots,M \tag{1.3.34a}$$

or equivalently

$$\left[\mathbf{A}\Phi\mathbf{K}_L^2+\mathbf{C}\Phi\right]=\mathbf{O} \tag{1.3.34b}$$

where k_j is the eigenvalue, ϕ_j is the mode shapes, M is the total number of modes, $\mathbf{C}=\mathbf{G}-\omega^2\mathbf{M}$, $\Phi=\{\phi_j\}$, and $\mathbf{K}_L=diag\{k_j\}$. In addition, it is assumed that the mode shapes satisfy the following ortho-normal conditions.

$$\Phi\mathbf{A}\Phi^T=\mathbf{I} \tag{1.3.35a}$$

$$\Phi\mathbf{C}\Phi^T=-\mathbf{K}_L^2 \tag{1.3.35b}$$

To obtain the modal expansion for $\bar{\mathbf{U}}_y$, we assume the response of the form

$$\bar{\mathbf{U}}_y=\Phi\bar{\mathbf{f}} \tag{1.3.36}$$

where $\bar{\mathbf{f}}=\bar{\mathbf{f}}(k,\omega)$ is the modal component vector in the wavenumber-frequency domain. Substituting equation (1.3.36) into equation (1.3.31) and then pre-multiplying by Φ^T, we obtain

$$\bar{\mathbf{f}}=\left[\mathbf{I}k^2-\mathbf{K}_L^2\right]^{-1}\Phi^T\bar{\mathbf{P}}_y=\left[\mathbf{I}k^2-\mathbf{K}_L^2\right]^{-1}\Phi^T\delta(n)=\left[\mathbf{I}k^2-\mathbf{K}_L^2\right]^{-1}\Gamma_y \tag{1.3.37}$$

where Γ_y is the participation factor vector due to the *SH* line load in equation (1.3.33b). Hence, the displacement in the wavenumber-frequency domain is given as

$$\bar{\mathbf{U}}_y=\Phi\left[\mathbf{I}k^2-\mathbf{K}_L^2\right]^{-1}\Gamma_y \tag{1.3.38}$$

To obtain the responses in the space-frequency domain, we need to perform an inverse Fourier transformation with respect to k as

$$\tilde{\mathbf{U}}_y(x,\omega)=\frac{1}{2\pi}\int_{-\infty}^{\infty}\bar{\mathbf{U}}_y(k,\omega)e^{-ikx}dk \tag{1.3.39}$$

Finally, we can obtain the closed-form displacements in the space-frequency domain as

$$\tilde{\mathbf{U}}_y=\frac{1}{2\mathrm{i}}\Phi\mathbf{E}_{|x|}^L\mathbf{K}_L^{-1}\Phi^T\delta(n)=\frac{1}{2\mathrm{i}}\Phi\mathbf{E}_{|x|}^L\mathbf{K}_L^{-1}\Gamma_y \tag{1.3.40}$$

where $\mathbf{E}_{|x|}^L=diag\left\{e^{-ik_j|x|}\right\}$. For the practical purpose, we express equation (1.3.40) in summation form as

$$\tilde{u}_y^{mn}=\sum_{j=1}^{M}\phi_j^m\tilde{f}_j=\sum_{j=1}^{M}\phi_j^m\phi_j^n\frac{e^{-\mathrm{i}k_j|x|}}{2\mathrm{i}k_j} \tag{1.3.41}$$

where m is the elevation index for the response points and $\tilde{f}_j$ the modal component in the space-frequency domain.

(B) Nodal loads on a vertical plane due to an *SH* line load

Next, we consider the stresses in a vertical plane. The associated strain is given in vector form as:

$$\tilde{\Gamma}_{xy}=\frac{\partial\tilde{U}_y}{\partial x}=\frac{\partial}{\partial x}\left[\frac{1}{2\mathrm{i}}\Phi\mathbf{E}_{|x|}^L\mathbf{K}_L^{-1}\Gamma_y\right]=\mp\frac{1}{2}\Phi\mathbf{E}_{|x|}^L\Gamma_y \tag{1.3.42}$$

with the negative sign being associated with positive x and vice versa. We notice that the strains (and stresses) are discontinuous at x=0. If the domain to the right of the section x considered is

removed, it becomes then necessary to apply consistent antiplane line loads to the section to the left in order to preserve equilibrium with the internal stresses. The consistent nodal loads $\tilde{\mathbf{q}}_l$ applied at the nodes defined by the intersection of the interfaces and the vertical plane considered can be obtained as follows. The strain $\tilde{\gamma}$ within an l-th thin layer is expresses as

$$\tilde{\gamma} = \mathbf{N}_m \tilde{\boldsymbol{\gamma}}_l \tag{1.3.43}$$

where $\mathbf{N}_m = \mathbf{N}_m(\zeta)$ is the interpolation function with expansion order m, $\zeta = z/h_l$, and $\tilde{\boldsymbol{\gamma}}_l = [\tilde{\gamma}_l \quad \tilde{\gamma}_{l+1} \quad \cdots \quad \tilde{\gamma}_{l+m}]^T$. The consistent nodal loads $\tilde{\mathbf{q}}_l$ in equilibrium with the stresses $\tilde{\tau}_{xy} = G_l \tilde{\gamma}_{xy}$ are then

$$\tilde{\mathbf{q}}_l = \begin{bmatrix} \tilde{q}_l \\ \tilde{q}_{l+1} \\ \vdots \\ \tilde{q}_{l+m} \end{bmatrix} = G_l h_l \int_0^1 \mathbf{N}_m^T \mathbf{N}_m \tilde{\boldsymbol{\gamma}}_l d\zeta = \mathbf{A}_l \tilde{\boldsymbol{\gamma}}_l \tag{1.3.44}$$

which constitutes the contribution of the l-th layer to the consistent nodal loads. If all the layers to the right of section x are removed, then the consistent nodal loads are obtained overlapping the contributions of all the layers. This implies overlapping $\mathbf{A}_l$. The result is

$$\begin{aligned} \tilde{\mathbf{Q}}_y = \mathbf{A}\Gamma_{xy} &= \mp\frac{1}{2}\mathbf{A}\boldsymbol{\Phi}\mathbf{E}_{|x|}^L\boldsymbol{\Phi}^T\boldsymbol{\delta}(n) \\ &= \mp \mathrm{i}\mathbf{A}\boldsymbol{\Phi}\mathbf{K}_L\boldsymbol{\Phi}^{-1}\frac{1}{2\mathrm{i}}\boldsymbol{\Phi}\mathbf{K}_L^{-1}\mathbf{E}_{|x|}^L\boldsymbol{\Phi}^T\boldsymbol{\delta}(n) \\ &= \mp \mathrm{i}\mathbf{A}\boldsymbol{\Phi}\mathbf{K}_L\boldsymbol{\Phi}^{-1}\tilde{\mathbf{U}}_y = \mp\mathbf{R}\tilde{\mathbf{U}}_y \end{aligned} \tag{1.3.45}$$

The matrix $\mathbf{R} = \mathrm{i}\mathbf{A}\boldsymbol{\Phi}\mathbf{K}_L\boldsymbol{\Phi}^{-1}$ is the Waas-Lysmer anti-plane transmitting boundary (the dynamic stiffness matrix of the domain removed).

(C) Stresses in a horizontal plane due to an *SH* line load

Now, we consider the stresses on the horizontal plane. For this, we substitute equation (1.3.38) into equation (1.3.31), and then perform the inverse Fourier transformation over the wavenumber k, which provides the stresses on the horizontal plane in the space-frequency domain. Finally, on the horizontal planes at the l-th layer, we obtain a stress vector of the form

$$\tilde{\boldsymbol{\tau}}_{zy}^l = \frac{1}{2\mathrm{i}}\sum_{j=1}^{M}\mathbf{K}_j^l\boldsymbol{\phi}_j^l\gamma_{y,j}\frac{e^{-\mathrm{i}k_j|x|}}{k_j} + \delta(x)\mathbf{A}^l\sum_{j=1}^{M}\boldsymbol{\phi}_j^l\gamma_{y,j} \tag{1.3.46}$$

where

$$\tilde{\boldsymbol{\tau}}_{zy} = \left[\tilde{\tau}_{zy}^l \quad 0 \quad \cdots \quad 0 \quad \tilde{\tau}_{zy}^{l+m}\right]^T \tag{1.3.47}$$

$$\mathbf{K}_j^l = \mathbf{A}_l k_j^2 + \mathbf{G}_l - \omega^2\mathbf{M}_l \tag{1.3.48}$$

$$\gamma_{y,j} = \text{ the participation factor in equation (1.3.37)} \tag{1.3.49}$$

In the equations above, m is the order of the interpolation function used, and the matrices $\mathbf{A}_l$, $\mathbf{G}_l$, and $\mathbf{M}_l$ are the layer matrices for the l-th layer. For the more detail derivation, the reader may refer to an MIT research report by Kausel [1981].

1.3.5 Responses due to *SV-P* harmonic line loads

We next consider the modal superposition responses to an *SV-P* harmonic line load of excitation frequency ω in an isotropic elastic medium. The associated discrete wave equation in the wavenumber-frequency domain is given as:

$$\left[\mathbf{A}k^2 + \mathbf{B}k + \mathbf{G} - \omega^2\mathbf{M}\right]\bar{\mathbf{U}} = \bar{\mathbf{P}} \tag{1.3.50a}$$

where

$$\bar{\mathbf{U}} = \left[\bar{\mathbf{U}}_x \quad \mathrm{i}\bar{\mathbf{U}}_z\right]^T \tag{1.3.50b}$$

$$\bar{\mathbf{P}} = \left[\bar{\mathbf{P}}_x \quad \mathrm{i}\bar{\mathbf{P}}_z\right]^T \tag{1.3.50c}$$

The matrices **A**, **B**, **G**, and **M** above are obtained from $\mathbf{A}_{xx}$, $\hat{\mathbf{B}}_x$, **G**, **M** in equations (1.3.19 and 29c) by collecting the in-plane elements that are associated with only the x- and z-direction components. For the simple manipulation in the following, we ignore the factor $\mathrm{i}\left(=\sqrt{-1}\right)$ in equations (1.3.50b and c). Also, the following transformations relating the space and wavenumber domains are imposed.

$$\bar{\mathbf{U}} = \bar{\mathbf{U}}(k,\omega) = \int_{-\infty}^{\infty} \tilde{\mathbf{U}}(x,\omega)e^{\mathrm{i}kx}dx \tag{1.3.51a}$$

$$\bar{\mathbf{P}} = \bar{\mathbf{P}}(k,\omega) = \int_{-\infty}^{\infty} \tilde{\mathbf{P}}(x,\omega)e^{\mathrm{i}kx}dx \tag{1.3.51b}$$

We assume that the *SV-P* harmonic line load is applied at x=0 and at an n-th elevation in the discrete medium. So, we can express the load in the space-frequency domain as

$$\tilde{\mathbf{P}}(x,\omega) = \left[\delta(x)\delta(n) \quad \mathbf{0}\right]^T \qquad \text{(horizontal line load)} \tag{1.3.52a}$$

$$\tilde{\mathbf{P}}(x,\omega) = \left[\mathbf{0} \quad \delta(x)\delta(n)\right]^T \qquad \text{(vertical line load)} \tag{1.3.52b}$$

where $\delta(n)$ is a Dirac-delta vector defined such that only the n-th entry is 1 and all others are zeros. The Fourier transform $\bar{\mathbf{P}}$ of the load is then obtained by means of equation (1.3.51b) as

$$\bar{\mathbf{P}}(k,\omega) = \left[\delta(n) \quad \mathbf{0}\right]^T \qquad \text{(horizontal line load)} \tag{1.3.52c}$$

$$\bar{\mathbf{P}}(k,\omega) = \left[\mathbf{0} \quad \delta(n)\right]^T \qquad \text{(vertical line load)} \tag{1.3.52d}$$

(A) Displacements due to an *SV-P* line load

First, we calculate the displacement response by means of modal expansion. So, we begin with the spectral decomposition of the system of equations in matrix form. The reader may refer to an MIT research report by Kausel [1981] for more details. The natural modes of wave propagation in the system are obtained from the eigenvalue problem that follows from setting the load vector in equation (1.3.50a) equal to zero:

$$\left[\mathbf{A}k_j^2 + \mathbf{B}k_j + \mathbf{C}\right]\phi_j = \mathbf{0}, \quad j = 1,\ldots,M \tag{1.3.53}$$

where k_j is the eigenvalue, ϕ_j is the mode shapes, M is the total number of modes, and $\mathbf{C}=\mathbf{G}-\omega^2\mathbf{M}$. To solve this eigenvalue problem, we begin by rearranging rows and columns by degrees of freedom rather than by interface (i.e., grouping first all the horizontal degrees of freedom, and then all the vertical degrees of freedom). The resulting eigenvalue problem is then given as:

$$\begin{Bmatrix} \mathbf{A}_x k_j^2 + \mathbf{C}_x & \mathbf{B}_{xz}k_j \\ \mathbf{B}_{xz}^T k_j & \mathbf{A}_z k_j^2 + \mathbf{C}_z \end{Bmatrix} \begin{Bmatrix} \phi_{xj} \\ \phi_{zj} \end{Bmatrix} = \begin{Bmatrix} \mathbf{0} \\ \mathbf{0} \end{Bmatrix} \tag{1.3.54a}$$

where the subscripts x and z represent the direction of the associated degrees of freedom. This eigenvalue problem may be furthermore transformed into

$$\begin{Bmatrix} \mathbf{A}_x k_j^2 + \mathbf{C}_x & \mathbf{B}_{xz} \\ \mathbf{B}_{xz}^T k_j^2 & \mathbf{A}_z k_j^2 + \mathbf{C}_z \end{Bmatrix} \begin{Bmatrix} \phi_{xj} \\ k_j \phi_{zj} \end{Bmatrix} = \begin{Bmatrix} \mathbf{0} \\ \mathbf{0} \end{Bmatrix} \tag{1.3.54b}$$

which is a linear (although non-symmetric) eigenvalue problem in k_j. An alternative linear eigenvalue problem is also

$$\begin{Bmatrix} \mathbf{A}_x k_j^2 + \mathbf{C}_x & \mathbf{B}_{xz} k_j^2 \\ \mathbf{B}_{xz}^T & \mathbf{A}_z k_j^2 + \mathbf{C}_z \end{Bmatrix} \begin{Bmatrix} k_j \phi_{xj} \\ \phi_{zj} \end{Bmatrix} = \begin{Bmatrix} \mathbf{0} \\ \mathbf{0} \end{Bmatrix} \tag{1.3.54c}$$

having a characteristic matrix which is the transpose of that in equation (1.3.54b). Both of these eigenvalue problems yield the same eigenvalues and have the associated "*left*" and "*right*" eigenvectors $\mathbf{y}_j$ and $\mathbf{z}_j$ as:

$$\mathbf{y}_j = \begin{Bmatrix} k_j \phi_{xj} \\ \phi_{zj} \end{Bmatrix} \quad \text{and} \quad \mathbf{z}_j = \begin{Bmatrix} \phi_{xj} \\ k_j \phi_{zj} \end{Bmatrix} \tag{1.3.55a,b}$$

that are also mutually orthogonal with respect to the characteristic equation as will be shown in equations (1.3.57a and b). The eigenvalue problem may be written as

$$\bar{\mathbf{A}} \mathbf{z}_j k_j^2 + \bar{\mathbf{C}} \mathbf{z}_j = \mathbf{0} \qquad \text{or} \qquad \bar{\mathbf{A}} \mathbf{Z} \mathbf{K}_R + \bar{\mathbf{C}} \mathbf{Z} = \mathbf{O} \tag{1.3.56a,b}$$

and

$$\bar{\mathbf{A}}^T \mathbf{y}_j k_j^2 + \bar{\mathbf{C}}^T \mathbf{y}_j = \mathbf{0} \qquad \text{or} \qquad \bar{\mathbf{A}}^T \mathbf{Y} \mathbf{K}_R + \bar{\mathbf{C}}^T \mathbf{Y} = \mathbf{O} \tag{1.3.56c,d}$$

which satisfy the ortho-normal conditions

$$\mathbf{Y}^T \bar{\mathbf{A}} \mathbf{Z} = \mathbf{K}_R \quad \text{and} \quad \mathbf{Y}^T \bar{\mathbf{C}} \mathbf{Z} = -\mathbf{K}_R^3 \tag{1.3.57a,b}$$

In the equations above, we use matrices defined as

$$\bar{\mathbf{A}} = \begin{Bmatrix} \mathbf{A}_x & \cdot \\ \mathbf{B}_{xz}^T & \mathbf{A}_z \end{Bmatrix} \qquad \bar{\mathbf{C}} = \begin{Bmatrix} \mathbf{C}_x & \mathbf{B}_{xz} \\ \cdot & \mathbf{C}_z \end{Bmatrix}$$

$$\mathbf{Y} = \{\mathbf{y}_j\} \qquad \mathbf{Z} = \{\mathbf{z}_j\} \qquad \mathbf{K}_R = diag\{k_j\} \tag{1.3.58a-e}$$

The equilibrium equation related to equations (1.3.56a,b) is given as

$$\left[\bar{\mathbf{A}} k^2 + \bar{\mathbf{C}}\right] \bar{\mathbf{U}}_r = \bar{\mathbf{P}}_r \tag{1.3.59}$$

with the subscript r representing the quantities associated with the *right* eigenvector,

$$\bar{\mathbf{U}}_r = \begin{Bmatrix} \bar{\mathbf{U}}_x \\ k \bar{\mathbf{U}}_z \end{Bmatrix} \quad \text{and} \quad \bar{\mathbf{P}}_r = \begin{Bmatrix} \bar{\mathbf{P}}_x \\ k \bar{\mathbf{P}}_z \end{Bmatrix} \tag{1.3.60a,b}$$

To obtain the modal solutions, we assume displacements of the form

$$\bar{\mathbf{U}}_r = \mathbf{Z} \bar{\mathbf{f}} \tag{1.3.61}$$

where $\bar{\mathbf{f}} = \bar{\mathbf{f}}(k, \omega)$ is the modal component vector in the wavenumber-frequency domain. Substituting equation (1.3.61) into equation (1.3.59) and then pre-multiplying by $\mathbf{Y}^T$, we obtain

$$\bar{\mathbf{f}} = \mathbf{K}_R^{-1} \left[\mathbf{I} k^2 - \mathbf{K}_R^2\right]^{-1} \mathbf{Y}^T \bar{\mathbf{P}} = \mathbf{K}_R^{-1} \left[\mathbf{I} k^2 - \mathbf{K}_R^2\right]^{-1} \Gamma_l \tag{1.3.62}$$

where Γ_l is the participation factor vector associated with the "*left*" eigenvector due to the *SV-P* line load. Concerning the case of line loads, notice also that this Γ_l could be either $\Gamma_{l,x}$ or $\Gamma_{l,z}$ defined as

$$\Gamma_{l,x} = \mathbf{Y}^T \bar{\mathbf{P}} = \mathbf{Y}^T \begin{Bmatrix} \delta(n) \\ \mathbf{0} \end{Bmatrix} \qquad \text{(horizontal line load)} \tag{1.3.63a}$$

$$\Gamma_{l,z} = \mathbf{Y}^T \bar{\mathbf{P}} = \mathbf{Y}^T \begin{Bmatrix} \mathbf{0} \\ \delta(n) \end{Bmatrix} \qquad \text{(vertical line load)} \tag{1.3.63b}$$

Hence, the displacement in the wavenumber-frequency domain is given as:

$$\bar{\mathbf{U}}_r = \mathbf{Z}\mathbf{K}_R^{-1}\left[\mathbf{I}k^2 - \mathbf{K}_R^2\right]^{-1}\mathbf{Y}^T\bar{\mathbf{P}} = \mathbf{Z}\mathbf{K}_R^{-1}\left[\mathbf{I}k^2 - \mathbf{K}_R^2\right]^{-1}\Gamma_l \tag{1.3.64}$$

Transforming back to $\bar{\mathbf{U}}$ from $\bar{\mathbf{U}}_r$, we obtain the expressions for the displacements in the wavenumber-frequency domain as

$$\begin{aligned}\bar{\mathbf{U}} = \begin{Bmatrix} \bar{\mathbf{U}}_x \\ \bar{\mathbf{U}}_z \end{Bmatrix} &= \begin{bmatrix} \Phi_x[\mathbf{I}k^2 - \mathbf{K}_R^2]^{-1}\Phi_x^T & k\Phi_x\mathbf{K}_R^{-1}[\mathbf{I}k^2 - \mathbf{K}_R^2]^{-1}\Phi_z^T \\ k\Phi_z[\mathbf{I}k^2 - \mathbf{K}_R^2]^{-1}\mathbf{K}_R^{-1}\Phi_x^T & \Phi_z[\mathbf{I}k^2 - \mathbf{K}_R^2]^{-1}\Phi_z^T \end{bmatrix}\begin{Bmatrix} \bar{\mathbf{P}}_x \\ \bar{\mathbf{P}}_z \end{Bmatrix} \\ &= \begin{bmatrix} \Phi_x[\mathbf{I}k^2 - \mathbf{K}_R^2]^{-1}\Gamma_x & k\Phi_x\mathbf{K}_R^{-1}[\mathbf{I}k^2 - \mathbf{K}_R^2]^{-1}\Gamma_z \\ k\Phi_z[\mathbf{I}k^2 - \mathbf{K}_R^2]^{-1}\mathbf{K}_R^{-1}\Gamma_x & \Phi_x[\mathbf{I}k^2 - \mathbf{K}_R^2]^{-1}\Gamma_z \end{bmatrix}\end{aligned} \tag{1.3.65}$$

where

$$\Gamma_x = \Phi^T\bar{\mathbf{P}} = \Phi^T\begin{Bmatrix} \delta(n) \\ \mathbf{0} \end{Bmatrix} \qquad \text{(horizontal line load)} \tag{1.3.66a}$$

$$\Gamma_z = \Phi^T\bar{\mathbf{P}} = \Phi^T\begin{Bmatrix} \mathbf{0} \\ \delta(n) \end{Bmatrix} \qquad \text{(vertical line load)} \tag{1.3.66b}$$

To obtain the responses in the space-frequency domain, we perform the inverse Fourier transformation with respect to k as

$$\tilde{\mathbf{U}}(x,\omega) = \frac{1}{2\pi}\int_{-\infty}^{\infty}\bar{\mathbf{U}}(k,\omega)e^{-ikx}dk \tag{1.3.67}$$

Finally, we obtain in closed-form the displacements due to *SV-P* line loads in the space-frequency domain as

$$\tilde{\mathbf{U}} = \begin{Bmatrix} \tilde{\mathbf{U}}_x \\ \tilde{\mathbf{U}}_z \end{Bmatrix} = \frac{1}{2\mathrm{i}}\begin{bmatrix} \Phi_x\mathbf{E}_{|x|}^R\mathbf{K}_R^{-1}\Gamma_x & \pm\Phi_x\mathbf{E}_{|x|}^R\mathbf{K}_R^{-1}\Gamma_z \\ \pm\Phi_z\mathbf{K}_R^{-1}\mathbf{E}_{|x|}^R\Gamma_x & \Phi_x\mathbf{E}_{|x|}^R\mathbf{K}_R^{-1}\Gamma_z \end{bmatrix} \tag{1.3.68}$$

where $\mathbf{E}_{|x|}^R = diag\left\{e^{-\mathrm{i}k_j|x|}\right\}$, and the positive and negative signs in the off-diagonal terms are for the positive and negative x, respectively. For the practical purposes, we can express equation (1.3.68) for $0<x$ in summation form

$$\tilde{u}_{\alpha\beta}^{mn} = \sum_{j=1}^{M}\phi_{\alpha j}^m\tilde{f}_{\beta j} = \sum_{j=1}^{M}\phi_{\alpha j}^m\phi_{\beta j}^n\frac{e^{-\mathrm{i}k_j x}}{2\mathrm{i}k_j} \tag{1.3.69}$$

where m and n are the elevation indices for the receiver and source points, respectively, α and β the indices for the direction of the receiver and source, i.e., x or z, and $\tilde{f}_{\beta j}$ the modal component in the space-frequency domain.

(B) Nodal loads in vertical planes due to an *SV-P* line load

Next, we consider the nodal loads in a vertical plane. In continuum mechanics, the stresses in a vertical plane are expresses as

$$\begin{Bmatrix} \tilde{\sigma}_x \\ \tilde{\tau}_{xz} \end{Bmatrix} = \left[\begin{bmatrix} \lambda+2G & \cdot \\ \cdot & G \end{bmatrix}\frac{\partial}{\partial x} + \begin{bmatrix} \cdot & \lambda \\ G & \cdot \end{bmatrix}\frac{\partial}{\partial z}\right]\begin{Bmatrix} \tilde{u}_x \\ \tilde{u}_z \end{Bmatrix} \tag{1.3.70}$$

Since we apply an interpolation function of certain type for the displacement field in the discrete model, we can express the displacement within a thin-layer as

$$\tilde{\mathbf{u}}_l = \begin{bmatrix} \tilde{u}_x & \tilde{u}_z \end{bmatrix}^T = \mathbf{N}_m \tilde{\mathbf{U}}_l \tag{1.3.71}$$

where $\mathbf{N}_m = \mathbf{N}_m(\zeta)$ is the interpolation function of expansion order m, $\zeta = z/h_l$, and $\tilde{\mathbf{U}}_l = \begin{bmatrix} \tilde{u}_x^l & \tilde{u}_z^l & \tilde{u}_x^{l+1} & \tilde{u}_z^{l+1} & \cdots & \tilde{u}_x^{l+m} & \tilde{u}_z^{l+m} \end{bmatrix}^T$. The consistent nodal loads in equilibrium with the stresses of $\tilde{\sigma}_x$ and $\tilde{\tau}_{zx}$ are then

$$\tilde{\mathbf{q}}_l = \begin{bmatrix} \tilde{q}_{x,l} \\ \tilde{q}_{z,l} \\ \vdots \\ \tilde{q}_{z,l+m} \end{bmatrix} = h_l \int_0^1 \mathbf{N}_m^T \begin{Bmatrix} \tilde{\sigma}_x \\ \tilde{\tau}_{xz} \end{Bmatrix} d\zeta \tag{1.3.72}$$

Substitution of equation (1.3.71) into equation (1.3.70) followed by performing integration in equation (1.3.72) yields the consistent nodal loads for the l-th thin-layer as

$$\begin{aligned} \tilde{\mathbf{q}}_l &= h_l \left[\int_0^1 \left(\mathbf{N}_m^T \begin{Bmatrix} \lambda+2G & \cdot \\ \cdot & G \end{Bmatrix} \mathbf{N}_m \frac{\partial}{\partial x} + \frac{1}{h_l} \mathbf{N}_m^T \begin{Bmatrix} \cdot & \lambda \\ G & \cdot \end{Bmatrix} \frac{\partial \mathbf{N}_m}{\partial \zeta} \right) d\zeta \right] \tilde{\mathbf{U}}_l \\ &= \left[\mathbf{A}_l \frac{\partial}{\partial x} + \mathbf{D}_l \right] \tilde{\mathbf{U}}_l \end{aligned} \tag{1.3.72'}$$

which constitutes the contribution of the l-th layer to the consistent nodal loads. The matrix $\mathbf{D}_l$ is obtained by collecting only x and z components from $g_{ij}\mathbf{D}_{xz}$ in Appendix 1A. If all the layers to the right of section x are removed, then the consistent nodal loads are obtained overlapping the contributions of all the layers. This implies overlapping $\mathbf{A}_l$ and $\mathbf{D}_l$. Inserting the factor $\mathrm{i}\left(=\sqrt{-1}\right)$ ignored in equation (1.3.50b,c), we obtain the actual displacements and modified modal shapes as

$$\tilde{\mathbf{U}} = \frac{1}{2\mathrm{i}} \boldsymbol{\Phi} \mathbf{E}_{|x|}^R \mathbf{K}_R^{-1} \tilde{\boldsymbol{\Phi}}^T \qquad \text{for } 0 < x \tag{1.3.73a}$$

$$\tilde{\mathbf{U}} = \frac{1}{2\mathrm{i}} \tilde{\boldsymbol{\Phi}} \mathbf{E}_{|x|}^R \mathbf{K}_R^{-1} \boldsymbol{\Phi}^T \qquad \text{for } x < 0 \tag{1.3.73b}$$

$$\boldsymbol{\Phi} = \begin{Bmatrix} \boldsymbol{\Phi}_x \\ -i\boldsymbol{\Phi}_z \end{Bmatrix} \quad \text{and} \quad \tilde{\boldsymbol{\Phi}} = \begin{Bmatrix} \boldsymbol{\Phi}_x \\ i\boldsymbol{\Phi}_z \end{Bmatrix} \tag{1.3.74a,b}$$

The resulting consistent nodal load vectors are then given as

$$\begin{aligned} \tilde{\mathbf{Q}} &= \frac{1}{2\mathrm{i}} \left[-\mathrm{i}\mathbf{A}\boldsymbol{\Phi} \mathbf{E}_{|x|}^R \tilde{\boldsymbol{\Phi}}^T + \mathbf{D}\boldsymbol{\Phi} \mathbf{E}_{|x|}^R \mathbf{K}_R^{-1} \tilde{\boldsymbol{\Phi}}^T \right] \\ &= -\frac{1}{2\mathrm{i}} \left[\mathrm{i}\mathbf{A}\boldsymbol{\Phi}\mathbf{K}_R\boldsymbol{\Phi}^{-1} - \mathbf{D} \right] \boldsymbol{\Phi} \mathbf{K}_R^{-1} \mathbf{E}_{|x|}^R \tilde{\boldsymbol{\Phi}}^T \quad \text{for } 0 < x \\ &= -\mathbf{R}\tilde{\mathbf{U}} \end{aligned} \tag{1.3.75a}$$

$$\begin{aligned} \tilde{\mathbf{Q}} &= \frac{1}{2\mathrm{i}} \left[\mathrm{i}\mathbf{A}\tilde{\boldsymbol{\Phi}}\mathbf{K}_R\tilde{\boldsymbol{\Phi}}^{-1} + \mathbf{D} \right] \tilde{\boldsymbol{\Phi}} \mathbf{K}_R^{-1} \mathbf{E}_{|x|}^R \boldsymbol{\Phi}^T \\ &= \mathbf{L}\tilde{\mathbf{U}} \end{aligned} \qquad \text{for } x < 0 \tag{1.3.75b}$$

The matrix $\mathbf{R} = \mathrm{i}\mathbf{A}\boldsymbol{\Phi}\mathbf{K}_R\boldsymbol{\Phi}^{-1} - \mathbf{D}$ and $\mathbf{L} = \mathrm{i}\mathbf{A}\tilde{\boldsymbol{\Phi}}\mathbf{K}_R\tilde{\boldsymbol{\Phi}}^{-1} + \mathbf{D}$ are the Waas-Lysmer in-plane transmitting boundary (the dynamic stiffness matrix of the domain removed) corresponding to the right and left layered regions that stretch for $0 < x < \infty$ and $-\infty < x < 0$, respectively.

(C) Stresses in horizontal planes due to an *SV-P* line load

Now, we consider the stresses in a horizontal plane. For this, we substitute equation (1.3.65) into equation (1.3.50a), and then perform the inverse Fourier transformation over the wavenumber k, which provides the stresses in a horizontal plane in the space-frequency domain. Finally, in the horizontal planes at the l-th layer, we obtain a stress vector of the form

$$\tilde{\boldsymbol{\tau}}_l = \frac{1}{2\mathrm{i}} \sum_{j=1}^{M} \mathbf{K}_j^l \boldsymbol{\phi}_j^l \gamma_{\alpha,j} \frac{e^{-\mathrm{i}k_j|x|}}{k_j} + \delta(x)\mathbf{A}^l \sum_{j=1}^{M} \widehat{\boldsymbol{\phi}}_{\alpha,j}^l \gamma_{\alpha,j}, \qquad \alpha = x, z \tag{1.3.76}$$

where

$$\tilde{\boldsymbol{\tau}}_l = \left[\tilde{\tau}_{xz}^l \quad \tilde{\sigma}_z^l \quad 0 \quad 0 \quad \cdots \quad -\tilde{\tau}_{xz}^{l+m} \quad -\tilde{\sigma}_z^{l+m} \right]^T \tag{1.3.77a}$$

$$\mathbf{K}_j^l = \mathbf{A}_l k_j^2 + \mathbf{B}_l k_j + \mathbf{G}_l - \omega^2 \mathbf{M}_l \tag{1.3.77b}$$

$\gamma_{\alpha,j}$ = participation factor in equation (1.3.63a or b) (1.3.77c)

$$\widehat{\boldsymbol{\phi}}_{x,j}^l = \left[\phi_{x,j}^l \quad 0 \quad \phi_{x,j}^{l+1} \quad 0 \quad \cdots \quad \phi_{x,j}^{l+m} \quad 0 \right]^T \tag{1.3.77d}$$

$$\widehat{\boldsymbol{\phi}}_{z,j}^l = \left[0 \quad \phi_{z,j}^l \quad 0 \quad \phi_{z,j}^{l+1} \quad \cdots \quad 0 \quad \phi_{z,j}^{l+m} \right]^T \tag{1.3.77e}$$

In the equations above, m is the order of the interpolation function used, and the matrices $\mathbf{A}_l$, $\mathbf{B}_l$, $\mathbf{G}_l$, and $\mathbf{M}_l$ are the layer matrices for the l-th layer. For the more detail derivation, the reader may refer to an MIT research report by Kausel [1981].

1.3.6 Response due to *SH* transient line loads

Here, we consider wave motion in an isotropic elastic medium subjected to an *SH* transient line load. The discrete wave equation is given in the wavenumber-frequency domain as:

$$\left[\mathbf{A}k^2 + \mathbf{G} - \omega^2 \mathbf{M} \right] \bar{\mathbf{U}}_y = \bar{\mathbf{P}}_y \tag{1.3.78}$$

which is exactly the same as equation (1.3.31). Note that the following transformation relations between the frequency and time domains are imposed,

$$\bar{\mathbf{U}}_y = \bar{\mathbf{U}}_y(k,\omega) = \int_{-\infty}^{\infty} \hat{\mathbf{U}}_y(k,t) e^{-\mathrm{i}\omega t} dt \tag{1.3.79a}$$

$$\bar{\mathbf{P}}_y = \bar{\mathbf{P}}_y(k,\omega) = \int_{-\infty}^{\infty} \hat{\mathbf{P}}_y(k,t) e^{-\mathrm{i}\omega t} dt \tag{1.3.79b}$$

We assume that the *SH* transient line load is applied at x=0 and elevation n in the discrete medium. So, we can express the load in the wavenumber-time domain as:

$$\hat{\mathbf{P}}_y(k,t) = \boldsymbol{\delta}(n)\delta(t) \tag{1.3.80a}$$

where $\boldsymbol{\delta}(n)$ is a Dirac-delta vector with only the nth entry being 1 and all others being zeros. The Fourier transform of $\hat{\mathbf{P}}_y$ is obtained by means of equation (1.3.79b) as

$$\bar{\mathbf{P}}_y(k,\omega) = \boldsymbol{\delta}(n) \tag{1.3.80b}$$

(A) Displacements due to an *SH* line load

First, we calculate the displacement responses in terms of modal expansion. For this, we use the spectral decomposition. The reader may refer to a paper by Kausel [1994] for more detail. The natural modes of wave propagation in the system are obtained from the eigenvalue problem that follows from setting the load vector in equation (1.3.78) equal to zero:

$$\left[\mathbf{A}k^2+\mathbf{G}-\mathbf{M}\omega_j^2\right]\boldsymbol{\phi}_j=\mathbf{0},\quad j=1,\ldots,M \tag{1.3.81a}$$

or equivalently

$$\left[\mathbf{K}_{sta}\boldsymbol{\Phi}-\mathbf{M}\boldsymbol{\Phi}\boldsymbol{\Omega}^2\right]=\mathbf{O} \tag{1.3.81b}$$

where ω_j is the eigenvalue, $\boldsymbol{\phi}_j$ is the mode shapes, M is the total number of modes, $\mathbf{K}_{sta}=\mathbf{A}k^2+\mathbf{G}$, $\boldsymbol{\Phi}=\{\boldsymbol{\phi}_j\}$, and $\boldsymbol{\Omega}=diag\{\omega_j\}$. In addition, the mode shapes satisfy the following ortho-normal conditions

$$\boldsymbol{\Phi}\mathbf{M}\boldsymbol{\Phi}^T=\mathbf{I} \tag{1.3.82a}$$

$$\boldsymbol{\Phi}\mathbf{K}_{sta}\boldsymbol{\Phi}^T=-\boldsymbol{\Omega}^2 \tag{1.3.82b}$$

To obtain the modal solutions, we assume the response of the form

$$\bar{\mathbf{U}}_y=\boldsymbol{\Phi}\bar{\mathbf{q}} \tag{1.3.83}$$

where $\bar{\mathbf{q}}=\bar{\mathbf{q}}(k,\omega)$ is the modal component vector in the wavenumber-frequency domain. Substituting equation (1.3.83) into equation (1.3.78), and then pre-multiplying by $\boldsymbol{\Phi}^T$, we obtain

$$\bar{\mathbf{q}}=\left[\boldsymbol{\Omega}^2-\mathbf{I}\omega^2\right]^{-1}\boldsymbol{\Phi}^T\bar{\mathbf{P}}_y=\left[\boldsymbol{\Omega}^2-\mathbf{I}\omega^2\right]^{-1}\boldsymbol{\Phi}^T\boldsymbol{\delta}(n)=\left[\boldsymbol{\Omega}^2-\mathbf{I}\omega^2\right]^{-1}\boldsymbol{\Gamma}_y \tag{1.3.84}$$

where $\boldsymbol{\Gamma}_y$ is the participation factor vector due to an *SH* line load. Hence, the displacement in the wavenumber-frequency domain is given as

$$\bar{\mathbf{U}}_y=\boldsymbol{\Phi}\left[\boldsymbol{\Omega}^2-\mathbf{I}\omega^2\right]^{-1}\boldsymbol{\Phi}^T\bar{\mathbf{P}}_y=\boldsymbol{\Phi}\left[\boldsymbol{\Omega}^2-\mathbf{I}\omega^2\right]^{-1}\boldsymbol{\Gamma}_y \tag{1.3.85}$$

To obtain the responses in the wavenumber-time domain, we perform an inverse Fourier transformation with respect to ω in the form

$$\hat{\mathbf{U}}_y(k,t)=\frac{1}{2\pi}\int_{-\infty}^{\infty}\bar{\mathbf{U}}_y(k,\omega)e^{i\omega t}d\omega \tag{1.3.86}$$

Finally, we obtain the closed-form displacements in the wavenumber-time domain as

$$\hat{\mathbf{U}}_y(k,t)=\boldsymbol{\Phi}\mathbf{H}_t\boldsymbol{\Phi}^T\mathbf{e}(n)=\boldsymbol{\Phi}\mathbf{H}_t\boldsymbol{\Gamma}_y \tag{1.3.87}$$

where $\mathbf{H}_t=diag\left\{\sin\omega_j t/\omega_j\right\}$ whose elements are well known as the impulse response functions of the mode j. For practical purpose, we express equation (1.3.87) in the modal summation form

$$\hat{u}_y^{mn}=\sum_{j=1}^{M}\phi_j^m\hat{q}_j=\sum_{j=1}^{M}\phi_j^m\phi_j^n\frac{\sin\omega_j t}{\omega_j} \tag{1.3.88}$$

where m is the elevation index for the response points and $\hat{q}_j$ the modal component in the wavenumber-time domain.

(B) Nodal loads in vertical planes due to an *SH* line load

Next, we consider the stresses in vertical planes. The associated strain is given in vector form as:

$$\boldsymbol{\Gamma}_{xy}=\frac{\partial\hat{\mathbf{U}}_y}{\partial x}=\frac{\partial}{\partial x}\left[\boldsymbol{\Phi}\mathbf{H}_t\boldsymbol{\Gamma}_y\right]=-ik\boldsymbol{\Phi}\mathbf{H}_t\boldsymbol{\Gamma}_y \tag{1.3.89}$$

where it is implicitly implied that $\partial/\partial x=-ik$. If the domain to the right of the section x considered is removed, it becomes necessary to apply consistent antiplane line loads to the section to the left in order to preserve equilibrium with the internal stresses. The consistent nodal loads applied at the nodes defined by the intersection of the interfaces and the vertical plane considered can be obtained as follows. The strain γ within an l-th thin-layer is expresses as

$$\gamma=\mathbf{N}_m\boldsymbol{\gamma}_l \tag{1.3.90}$$

where $\mathbf{N}_m=\mathbf{N}_m(\zeta)$ is the interpolation function of order m, $\zeta=z/h_l$, and $\gamma_l=[\gamma_l \quad \gamma_{l+1} \quad \cdots \quad \gamma_{l+m}]^T$. The consistent nodal loads in equilibrium with the internal stresses $\tau=G_l\gamma$ are then given as:

$$\mathbf{q}_l=\begin{bmatrix} q_l \\ q_{l+1} \\ \vdots \\ q_{l+m} \end{bmatrix}=G_l h_l \int_0^1 \mathbf{N}_m^T \mathbf{N}_m \gamma_l d\zeta = \mathbf{A}_l \gamma_l \tag{1.3.91}$$

which constitutes the contribution of the l-th layer to the consistent nodal loads. If all the layers to the right of section x are removed, then the consistent nodal loads are obtained by overlapping the contributions of all the layers. This implies overlapping $\mathbf{A}_l$ for all the thin-layers. The result is

$$\mathbf{Q}_y=\mathbf{A}\Gamma_{xy}=-\mathrm{i}k\mathbf{A}\Phi\mathbf{H}_t\Phi^T\delta(n) \tag{1.3.92}$$

(C) Stresses in horizontal planes due to an *SH* line load

Now, we consider the stresses in horizontal planes. Substituting equation (1.3.85) into equation (1.3.78), and then performing an inverse Fourier transformation over the frequency ω, we can obtain the stresses in a horizontal plane in the wavenumber-time domain. Finally, we have the stress vector at the l-th layer of the form

$$\hat{\tau}_{yz}^l=\left[\sum_{j=1}^{M}\mathbf{K}_j^l\phi_j^l\phi_j^T\delta(n)\frac{\sin\omega_j t}{\omega_j}+\delta(t)\mathbf{M}^l\sum_{j=1}^{M}\phi_j^l\phi_j^T\delta(n)\right] \tag{1.3.93}$$

where

$$\hat{\tau}_{yz}=\left[\hat{\tau}_{yz}^l \quad 0 \quad \cdots \quad 0 \quad \hat{\tau}_{yz}^{l+m}\right]^T \tag{1.3.94}$$

$$\mathbf{K}_j^l=\mathbf{A}^l k^2+\mathbf{G}^l-\omega_j^2\mathbf{M}^l \tag{1.3.95}$$

In the equations above, m is the order of the interpolation function used, and the matrices $\mathbf{A}_l$, $\mathbf{G}_l$, and $\mathbf{M}_l$ are the layer matrices for the l-th layer.

1.3.7 Responses due to *SV-P* transient line loads

Here, we consider wave motion in an isotropic elastic medium subjected to an *SV-P* transient line load. The discrete wave equation is given in the wavenumber-frequency domain as:

$$\left[\mathbf{A}k^2+\mathbf{B}k+\mathbf{G}-\omega^2\mathbf{M}\right]\bar{\mathbf{U}}=\bar{\mathbf{P}} \tag{1.3.96a}$$

where

$$\bar{\mathbf{U}}=\left[\bar{\mathbf{U}}_x \quad \mathrm{i}\bar{\mathbf{U}}_z\right]^T \tag{1.3.96b}$$

$$\bar{\mathbf{P}}=\left[\bar{\mathbf{P}}_x \quad \mathrm{i}\bar{\mathbf{P}}_z\right]^T \tag{1.3.96c}$$

The matrices **A**, **B**, **G**, and **M** above are obtained from $\mathbf{A}_{xx}$, $\hat{\mathbf{B}}_x$, **G**, **M** in equations (1.3.19 and 29c) by collecting the in-plane elements that are associated with only the x- and z-direction components. For the simple manipulation in the following, we ignore the factor $\mathrm{i}\left(=\sqrt{-1}\right)$ in equations (1.3.96c and d). Imposing the transformation relations between time and frequency domains,

$$\bar{\mathbf{U}}=\bar{\mathbf{U}}(k,\omega)=\int_{-\infty}^{\infty}\hat{\mathbf{U}}(k,t)e^{-\mathrm{i}\omega t}dt \tag{1.3.97a}$$

$$\bar{\mathbf{P}} = \bar{\mathbf{P}}(k,\omega) = \int_{-\infty}^{\infty} \hat{\mathbf{P}}(k,t) e^{-i\omega t} dt \tag{1.3.97b}$$

We assume that the *SV-P* line load is applied at x=0 and elevation n in the discrete medium. So, we can express the load in the wavenumber-time domain as

$$\hat{\mathbf{P}}(k,t) = [\delta(n)\delta(t) \quad \mathbf{0}]^T \qquad \text{(horizontal line load)} \tag{1.3.98a}$$

$$\hat{\mathbf{P}}(k,t) = [\mathbf{0} \quad \delta(n)\delta(t)]^T \qquad \text{(vertical line load)} \tag{1.3.98b}$$

where $\boldsymbol{\delta}(n)$ is a Dirac-delta vector defined such that only the n-th entry is 1 and all others are zeros. The Fourier transform, $\bar{\mathbf{P}}$, is obtained by means of equation (1.3.97b) as

$$\bar{\mathbf{P}}(k,\omega) = [\boldsymbol{\delta}(n) \quad \mathbf{0}]^T \qquad \text{(horizontal line load)} \tag{1.3.98c}$$

$$\bar{\mathbf{P}}(k,\omega) = [\mathbf{0} \quad \boldsymbol{\delta}(n)]^T \qquad \text{(vertical line load)} \tag{1.3.98d}$$

(A) Displacements due to an *SV-P* line load

First, we calculate the displacement responses by means of the modal superposition. For this, we use the spectral decomposition. The reader may refer to a paper by Kausel [1994] for more details. The natural modes of wave propagation in the system are obtained from the eigenvalue problem that follows from setting the load vector in equation (1.3.97a) equal to zero:

$$\left[\mathbf{A}k^2 + \mathbf{B}k + \mathbf{G} - \mathbf{M}\omega_j^2\right]\boldsymbol{\phi}_j = \mathbf{0}, \quad j = 1,\ldots,M \tag{1.3.99a}$$

or equivalently

$$\left[\mathbf{K}_{sta}\boldsymbol{\Phi} - \mathbf{M}\boldsymbol{\Phi}\boldsymbol{\Omega}^2\right] = \mathbf{O} \tag{1.3.99b}$$

where ω_j is the eigenvalue, $\boldsymbol{\phi}_j$ is the mode shapes, M is the total number of modes, $\mathbf{K}_{sta}=\mathbf{A}k^2 + \mathbf{B}k + \boldsymbol{G}$, $\boldsymbol{\Phi}=\{\boldsymbol{\phi}_j\}$, and $\boldsymbol{\Omega}=diag\{\omega_j\}$. In addition, the mode shapes satisfy the following ortho-normal conditions

$$\boldsymbol{\Phi}\mathbf{M}\boldsymbol{\Phi}^T = \mathbf{I} \tag{1.3.100a}$$

$$\boldsymbol{\Phi}\mathbf{K}_{sta}\boldsymbol{\Phi}^T = -\boldsymbol{\Omega}^2 \tag{1.3.100b}$$

To obtain the modal solutions, we assume the displacement responses of the form

$$\bar{\mathbf{U}}_y = \boldsymbol{\Phi}\bar{\mathbf{q}} \tag{1.3.101}$$

where $\bar{\mathbf{q}} = \bar{\mathbf{q}}(k,\omega)$ is the modal component vector in the wavenumber-frequency domain. Substituting equation (1.3.101) into equation (1.3.97a) and then pre-multiplying by $\boldsymbol{\Phi}^T$, we obtain

$$\bar{\mathbf{q}} = \left[\boldsymbol{\Omega}^2 - \mathbf{I}\omega^2\right]^{-1}\boldsymbol{\Phi}^T\bar{\mathbf{P}} = \left[\boldsymbol{\Omega}^2 - \mathbf{I}\omega^2\right]^{-1}\boldsymbol{\Gamma} \tag{1.3.102}$$

where $\boldsymbol{\Gamma}$ is the participation factor vector due to the *SV-P* line load. Concerning the case of line loads, it is also noticed that this $\boldsymbol{\Gamma}$ could be either $\boldsymbol{\Gamma}_x$ or $\boldsymbol{\Gamma}_z$ defined as:

$$\boldsymbol{\Gamma}_x = \boldsymbol{\Phi}^T\bar{\mathbf{P}} = \boldsymbol{\Phi}^T\begin{Bmatrix}\boldsymbol{\delta}(n)\\ \mathbf{0}\end{Bmatrix} \quad \text{(horizontal line load)} \tag{1.3.103a}$$

$$\boldsymbol{\Gamma}_z = \boldsymbol{\Phi}^T\bar{\mathbf{P}} = \boldsymbol{\Phi}^T\begin{Bmatrix}\mathbf{0}\\ \boldsymbol{\delta}(n)\end{Bmatrix} \quad \text{(vertical line load)} \tag{1.3.103b}$$

Hence, the displacement in the wavenumber-frequency domain is given

$$\bar{\mathbf{U}} = \boldsymbol{\Phi}\left[\boldsymbol{\Omega}^2 - \mathbf{I}\omega^2\right]^{-1}\boldsymbol{\Phi}^T\bar{\mathbf{P}} = \boldsymbol{\Phi}\left[\boldsymbol{\Omega}^2 - \mathbf{I}\omega^2\right]^{-1}\boldsymbol{\Gamma} \tag{1.3.104}$$

To obtain the responses in the wavenumber-time domain, we perform the inverse Fourier transformation with respect to ω as

$$\hat{\mathbf{U}}(k,t)=\frac{1}{2\pi}\int_{-\infty}^{\infty}\bar{\mathbf{U}}(k,\omega)e^{i\omega t}d\omega \tag{1.3.105}$$

Finally, we obtain the closed-form displacements in wavenumber-time domain as

$$\hat{\mathbf{U}}(k,t)=\begin{Bmatrix}\hat{\mathbf{U}}_x\\ \hat{\mathbf{U}}_z\end{Bmatrix}=\begin{Bmatrix}\boldsymbol{\Phi}_x\mathbf{H}_t\boldsymbol{\Gamma}_x & \boldsymbol{\Phi}_x\mathbf{H}_t\boldsymbol{\Gamma}_z\\ \boldsymbol{\Phi}_z\mathbf{H}_t\boldsymbol{\Gamma}_x & \boldsymbol{\Phi}_z\mathbf{H}_t\boldsymbol{\Gamma}_z\end{Bmatrix} \tag{1.3.106}$$

where $\mathbf{H}_t=diag\left\{\sin\omega_j t/\omega_j\right\}$ whose elements are well known as the impulse response function of the mode j. For practical purpose, we express equation (1.3.106) in modal summation form

$$\hat{u}_{\alpha\beta}^{mn}=\sum_{j=1}^{M}\phi_{\alpha j}^{m}\hat{q}_{\beta j}=\sum_{j=1}^{M}\phi_{\alpha j}^{m}\phi_{\beta j}^{n}\frac{\sin\omega_j t}{\omega_j} \tag{1.3.107}$$

where m and n are the elevation indices for the receiver and source points, respectively, α and β the indices for the direction of the receiver and source, i.e., x or z, and $\hat{q}_{\beta j}$ the modal component in the wavenumber-time domain.

(B) Nodal loads in vertical planes due to *SV-P* line load

Next, we consider the stresses in a vertical plane. In continuum mechanics, the stresses in vertical planes are expresses as

$$\begin{Bmatrix}\hat{\sigma}_x\\ \hat{\tau}_{xz}\end{Bmatrix}=\left[\begin{bmatrix}\lambda+2G & \cdot\\ \cdot & G\end{bmatrix}\frac{\partial}{\partial x}+\begin{bmatrix}\cdot & \lambda\\ G & \cdot\end{bmatrix}\frac{\partial}{\partial z}\right]\begin{Bmatrix}\hat{u}_x\\ \hat{u}_z\end{Bmatrix} \tag{1.3.108}$$

Since we apply an interpolation function of certain type for the displacement field in the discrete model, we can express the displacement within a thin-layer as:

$$\hat{\mathbf{u}}_l=\begin{bmatrix}\hat{u}_x & \hat{u}_z\end{bmatrix}^T=\mathbf{N}_m\hat{\mathbf{U}}_l \tag{1.3.109}$$

where $\mathbf{N}_m=\mathbf{N}_m(\zeta)$ is the interpolation function of order m, $\zeta=z/h_l$, and $\hat{\mathbf{U}}_l=\begin{bmatrix}\hat{u}_x^l & \hat{u}_z^l & \hat{u}_x^{l+1} & \hat{u}_z^{l+1} & \cdots & \hat{u}_x^{l+m} & \hat{u}_z^{l+m}\end{bmatrix}^T$. The consistent nodal loads in equilibrium with the stresses of $\hat{\sigma}_x$ and $\hat{\tau}_{zx}$ are then

$$\hat{\mathbf{q}}_l=\begin{bmatrix}\hat{q}_{x,l}\\ \hat{q}_{z,l}\\ \vdots\\ \hat{q}_{z,l+m}\end{bmatrix}=h_l\int_0^1\mathbf{N}_m^T\begin{Bmatrix}\hat{\sigma}_x\\ \hat{\tau}_{xz}\end{Bmatrix}d\zeta \tag{1.3.110a}$$

Substitution of equation (1.3.109) into equation (1.3.108) followed by integration of equation (1.3.110a) yields the consistent nodal loads for the l-th thin-layer as:

$$\begin{aligned}\hat{\mathbf{q}}_l&=h_l\left[\int_0^1\left(\mathbf{N}_m^T\begin{bmatrix}\lambda+2G & \cdot\\ \cdot & G\end{bmatrix}\mathbf{N}_m(-ik)+\frac{1}{h_l}\mathbf{N}_m^T\begin{bmatrix}\cdot & \lambda\\ G & \cdot\end{bmatrix}\frac{\partial\mathbf{N}_m}{\partial\zeta}\right)d\zeta\right]\hat{\mathbf{U}}_l\\&=\left[\mathbf{A}_l(-ik)+\mathbf{D}_l\right]\hat{\mathbf{U}}_l\end{aligned} \tag{1.3.110b}$$

which constitutes the contribution of the l-th thin-layer to the consistent nodal loads. The matrix $\mathbf{D}_l$ is obtained by collecting only x and z components from $g_{ij}\mathbf{D}_{xz}$ in Appendix 1A. It should also be noticed that $\partial\hat{\mathbf{U}}/\partial x=-ik\hat{\mathbf{U}}$ in equation (1.3.110b). If all the thin-layers to the right or left of section x are removed, then the consistent nodal loads are obtained by overlapping the contributions of all the layers. This implies overlapping $\mathbf{A}_l$ and $\mathbf{D}_l$. The resulting consistent nodal load vectors are then given as

$$\hat{\mathbf{Q}} = [\mathbf{A}(-ik) + \mathbf{D}]\hat{\mathbf{U}} \tag{1.3.111}$$

(C) Stresses in horizontal planes due to an *SV-P* line load

Now, we consider the stresses in a horizontal plane. Substituting equation (1.3.104) into equation (1.3.96a), and then performing an inverse Fourier transformation over the frequency ω, we obtain the stresses on the horizontal plane in the wavenumber-time domain. Finally, we have a stress vector at the l-th layer of the form

$$\hat{\boldsymbol{\tau}}_l = \sum_{j=1}^{M} \mathbf{K}_j^l \boldsymbol{\phi}_j^l \gamma_{\alpha,j} \frac{\sin \omega_j t}{\omega_j} + \delta(t)\mathbf{M}^l \sum_{j=1}^{M} \hat{\boldsymbol{\phi}}_{\alpha,j}^l \gamma_{\alpha,j}, \qquad \alpha = x, z \tag{1.3.112}$$

where

$$\hat{\boldsymbol{\tau}}_l = \left[\hat{\tau}_{xz}^l \quad \hat{\sigma}_z^l \quad 0 \quad 0 \quad \cdots \quad -\hat{\tau}_{xz}^{l+m} \quad -\hat{\sigma}_z^{l+m} \right]^T \tag{1.3.113a}$$

$$\mathbf{K}_j^l = \mathbf{A}_l k^2 + \mathbf{B}_l k + \mathbf{G}_l - \omega_j^2 \mathbf{M}_l \tag{1.3.113b}$$

$\gamma_{\alpha,j}$ = participation factor in equation (1.3.103a or b) (1.3.113c)

$$\hat{\boldsymbol{\phi}}_{x,j}^l = \left[\phi_{x,j}^l \quad 0 \quad \phi_{x,j}^{l+1} \quad 0 \quad \cdots \quad \phi_{x,j}^{l+m} \quad 0 \right]^T \tag{1.3.113d}$$

$$\hat{\boldsymbol{\phi}}_{z,j}^l = \left[0 \quad \phi_{z,j}^l \quad 0 \quad \phi_{z,j}^{l+1} \quad \cdots \quad 0 \quad \phi_{z,j}^{l+m} \right]^T \tag{1.3.113e}$$

In the equations above, m is the order of the interpolation function used, and the matrices $\mathbf{A}_l$, $\mathbf{B}_l$, $\mathbf{G}_l$, and $\mathbf{M}_l$ are the layer matrices for the l-th thin-layer.

Appendix 1A

All the layer matrices, except the $\mathbf{B}_\alpha$, are of the form.

$$\text{Layer matrix} = \begin{Bmatrix} g_{11}\mathbf{H} & g_{12}\mathbf{H} & \cdots \\ g_{21}\mathbf{H} & \ddots & \\ \vdots & & g_{m+1,m+1}\mathbf{H} \end{Bmatrix} = \{g_{ij}\mathbf{H}\}$$

Table 1. Matrices $\mathbf{H}$ and coefficients g_{ij} for different layer matrices.

H		
	Anisotropic	Isotropic
M	$h\begin{Bmatrix} 1 & \cdot & \cdot \\ \cdot & 1 & \cdot \\ \cdot & \cdot & 1 \end{Bmatrix}$	$h\begin{Bmatrix} 1 & \cdot & \cdot \\ \cdot & 1 & \cdot \\ \cdot & \cdot & 1 \end{Bmatrix}$
$\mathbf{A}_{xx}$	$h\begin{Bmatrix} d_{11} & d_{16} & d_{15} \\ & d_{66} & d_{56} \\ sym & & d_{55} \end{Bmatrix}$	$h\begin{Bmatrix} \lambda+2G & \cdot & \cdot \\ \cdot & G & \cdot \\ \cdot & \cdot & G \end{Bmatrix}$
$\mathbf{A}_{xy}$	$h\begin{Bmatrix} 2d_{16} & d_{12}+d_{66} & d_{14}+d_{56} \\ & 2d_{26} & d_{25}+d_{46} \\ sym & & 2d_{45} \end{Bmatrix}$	$h\begin{Bmatrix} \cdot & \lambda+G & \cdot \\ \lambda+G & \cdot & \cdot \\ \cdot & \cdot & \cdot \end{Bmatrix}$
$\mathbf{A}_{yy}$	$h\begin{Bmatrix} d_{66} & d_{26} & d_{46} \\ & d_{22} & d_{24} \\ sym & & d_{44} \end{Bmatrix}$	$h\begin{Bmatrix} G & \cdot & \cdot \\ \cdot & \lambda+2G & \cdot \\ \cdot & \cdot & G \end{Bmatrix}$
G	$\frac{1}{h}\begin{Bmatrix} d_{55} & d_{45} & d_{35} \\ & d_{44} & d_{34} \\ sym & & d_{33} \end{Bmatrix}$	$\frac{1}{h}\begin{Bmatrix} G & \cdot & \cdot \\ \cdot & G & \cdot \\ \cdot & \cdot & \lambda+2G \end{Bmatrix}$
g_{ij}		
	Linear Expansion	Quadratic Expansion
$\mathbf{M}, \mathbf{A}_{\alpha\beta}$	$\frac{1}{6}\begin{Bmatrix} 2 & 1 \\ 1 & 2 \end{Bmatrix}$	$\frac{1}{30}\begin{Bmatrix} 4 & 2 & -1 \\ 2 & 16 & 2 \\ -1 & 2 & 4 \end{Bmatrix}$
G	$\begin{Bmatrix} 1 & -1 \\ -1 & 1 \end{Bmatrix}$	$\frac{1}{3}\begin{Bmatrix} 7 & -8 & 1 \\ -8 & 16 & -8 \\ 1 & -8 & 7 \end{Bmatrix}$

Table 2. Matrices $\mathbf{D}$ and coefficients g_{ij} for the layer matrix $\mathbf{B}_\alpha$

$\mathbf{D}$		
	Anisotropic	Isotropic
$\mathbf{D}_{xz}$	$\begin{Bmatrix} d_{51} & d_{41} & d_{31} \\ d_{56} & d_{46} & d_{36} \\ d_{55} & d_{45} & d_{35} \end{Bmatrix}$	$\begin{Bmatrix} \cdot & \cdot & \lambda \\ \cdot & \cdot & \cdot \\ G & \cdot & \cdot \end{Bmatrix}$
$\mathbf{D}_{yz}$	$\begin{Bmatrix} d_{56} & d_{46} & d_{36} \\ d_{52} & d_{42} & d_{32} \\ d_{54} & d_{44} & d_{34} \end{Bmatrix}$	$\begin{Bmatrix} \cdot & \cdot & \cdot \\ \cdot & \cdot & \lambda \\ \cdot & G & \cdot \end{Bmatrix}$
g_{ij}		
	Linear Expansion	Quadratic Expansion
$\mathbf{B}_\alpha$	$\frac{1}{2}\begin{Bmatrix} 1 & -1 \\ 1 & -1 \end{Bmatrix}$	$\frac{1}{6}\begin{Bmatrix} 3 & -4 & 1 \\ 4 & 0 & -4 \\ -1 & 4 & -3 \end{Bmatrix}$

Chapter 2 Numerical dispersion in the TLM

2.1 Introduction

When an elastic continuous medium subjected to propagating waves is modeled with the TLM (or with finite elements), the discretization process introduces numerical dispersion (or error) that represents a discrepancy between the solutions for the discrete and continuous models. Inasmuch as this numerical artifact generally degrades the accuracy of wave fields obtained with discrete models, it behooves to minimize this degradation to the extent possible. With this objective in mind, we characterize here the numerical dispersion of discrete systems modeled with the linear and quadratic expansion TLM's and compare these characteristics with those of analytical exact solutions. On the basis of this characterization, we develop *optimal tuning factors* for the dynamic stiffness matrices in the TLM, with the aid of which the numerical dispersion can be minimized and the discrete solutions improved. These factors also help in reducing any spurious reflections and transmissions of waves that can take place at the interfaces of the discrete layers, even (or perhaps most importantly) when the layers have identical material properties.

The following deductive reasoning is the motivation of developing the tuning factors. It is well known that the formulation of dynamic problems by means of discrete methods generally leads to consistent mass matrices that have the same bandwidth as the stiffness matrices. For computational efficiency, it is often convenient to replace these with diagonal lumped mass matrices, which can be derived from the consistent mass matrices by simple addition of the off-diagonal terms to the diagonal terms. In the context of free vibration problems, the consistent mass matrix generally produces eigenvalues that exceed the exact eigenvalues of the continuous model (i.e. natural frequencies), as can be demonstrated by recourse to the enclosure theorem and Rayleigh's quotient. By contrast, the lumped mass matrix generally produces eigenvalues that are smaller than those of the continuous model. These two observations suggest that a hybrid between the consistent and lumped mass matrices could conceivably lead to improved and more accurate results, and this is indeed the case. As will be shown in this chapter, it is not only possible to optimally tune the mass matrices, but also the stiffness matrices, which can be adjusted so as to further improve the computed discrete eigenvalues, especially for anti-plane problems.

This chapter is composed of four sections, each of which is concerned with anti-plane waves modeled by the linear expansion TLM, in-plane waves modeled by the linear expansion TLM, anti-plane waves modeled by the quadratic expansion TLM, and in-plane waves modeled by the quadratic expansion TLM, respectively. All the sections are built up in a similar fashion, which is briefly described in the following two paragraphs.

In the first part of each section, we first find the general solution and the wavenumber spectrum for isotropic homogeneous full-spaces via a finite difference scheme. Thereafter, we qualitatively estimate the numerical dispersion errors in the TLM in terms of wavenumber-frequency spectra. As a result, we find a limiting relationship between wavelength and discretization size. Then, we proceed to analyze the free-vibration problems of ideal structures or media whose exact analytical solutions (i.e. eigenvalues) are known in closed form. Examples are homogeneous plates (e.g. plates with free-free or mixed boundary conditions), homogeneous strata, and so on. In addition, we obtain solutions for infinite or semi-infinite domain problems modeled with the TLM which, because of the infinite number of discrete equations, are strictly unsolvable in the classical finite

element sense. Formally using the general solutions, however, we find the solutions to those problems.

In the second part of each section, we quantitatively estimate the numerical dispersion in the TLM in terms of frequencies and phase velocities. As a result, we find the optimal values for the tuning factors, which are valid only for a certain range of dimensionless wavenumber in discretization direction (ξ_z). In addition, we propose a lower bound for the number of thin layers per wavelength (N_λ) that is dependent on the range of ξ_z in consideration. Then, we numerically solve the free-vibration problems of interest by changing the tuning factors, to show the best improvement in eigenvalues due to the optimal tuning factors. In addition, we observe how many modes among all computed modes are accurate with the application of the optimal tuning factors.

Figure 2.1.1 shows the two uncoupled *SH* and *SV-P* harmonic plane waves propagating at an angle θ in the x-z plane. The analytical, exact spectrum equations of these harmonic waves in continuum mechanics are given by

$$SH \text{ wave} \quad : \omega_S = C_S k = C_S \sqrt{k_x^2 + k_z^2} \tag{2.1.1}$$

$$SV\text{-}P \text{ wave} : \omega_S = C_S k = C_S \sqrt{k_x^2 + k_z^2} \text{ and } \omega_P = C_P k = C_P \sqrt{k_x^2 + k_z^2} \tag{2.1.2}$$

where ω's are the frequencies, C's the phase velocities, and k's the wavenumbers in each direction. In general, the wavenumbers k's can be purely real, purely imaginary, or complex numbers. The discrete TLM model has its own spectrum equations that we shall introduce later on in this chapter. We shall explore the numerical dispersions in the TLM by comparing the spectrum equations of the discrete and continuous models in terms of frequencies and phase velocities.

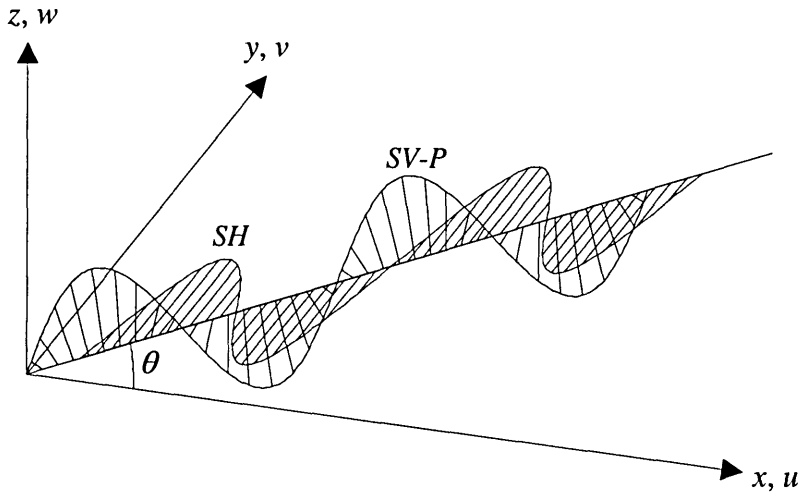

Figure 2.1.1 Two uncoupled *SH* and *SV-P* harmonic waves propagating at an angle θ

2.2 Anti-plane (*SH*) waves with linear expansion TLM

We first consider the propagation of *SH* waves modeled by the TLM that is based on a linear expansion, or TLM1 for short. In the first part of this section, we obtain the general solution and the frequency-wavenumber spectrum for the discrete *SH* wave equation modeled with the TLM1. By means of a qualitative investigation of this spectrum, we find a reference frame for judging the dimensionless wavenumbers in discrete models. We also formulate and solve three guided wave problems whose exact solutions for the continuous model are known in closed form.

In the second part, we continue to characterize the numerical dispersion as a function of vertical direction wavenumber (ξ_z) and direction of propagation (θ) by estimating frequencies and phase velocities. Through these characterizations, we obtain the optimal tuning factors that are valid only for a certain range of vertical direction wavenumber (ξ_z). Based on the range of ξ_z, we also propose a lower bound for the number of thin layers per wavelength. We then consider two numerical examples of finite and semi-infinite domains. In these two examples, we compare the TLM1 solution with the exact analytical solutions in order to verify the optimality of the tuning factors. As an additional result, we can also judge the extent to which the optimal tuning factors improve the accuracy of the eigenvalues computed with the TLM1.

2.2.1 Discrete solutions for anti-plane problems

Consider a single TLM1 thin layer that is subjected to *SH* wave motion as shown in figure 2.2.1. Notice that a degree of freedom, v, is involved at each node or interface. The governing equation is given by

$$\mathbf{P}_l = \mathbf{K}\mathbf{U}_l \tag{2.2.1}$$

where

$$\mathbf{P}_l = \{p_l \quad p_{l-1}\}^T \quad : \text{consistent external traction vector} \tag{2.2.2a}$$

$$\mathbf{U}_l = \{v_l \quad v_{l-1}\}^T \quad : \text{displacement vector} \tag{2.2.2b}$$

$$\mathbf{K} = \mathbf{A}k_x^2 + \mathbf{G} - \omega^2\mathbf{M} \quad : \text{dynamic stiffness matrix} \tag{2.2.2c}$$

$$\mathbf{A} = (1-\beta)\mathbf{A}_L + \beta\mathbf{A}_C: \quad \mathbf{A}_C = \frac{Gh}{6}\begin{bmatrix} 2 & 1 \\ 1 & 2 \end{bmatrix}, \qquad \mathbf{A}_L = \frac{Gh}{6}\begin{bmatrix} 3 & \cdot \\ \cdot & 3 \end{bmatrix} \tag{2.2.3abc}$$

$$\mathbf{G} = \frac{G}{h}\begin{bmatrix} 1 & -1 \\ -1 & 1 \end{bmatrix} \tag{2.2.3d}$$

$$\mathbf{M} = (1-\mu)\mathbf{M}_L + \mu\mathbf{M}_C: \mathbf{M}_C = \frac{\rho h}{6}\begin{bmatrix} 2 & 1 \\ 1 & 2 \end{bmatrix}, \qquad \mathbf{M}_L = \frac{\rho h}{6}\begin{bmatrix} 3 & \cdot \\ \cdot & 3 \end{bmatrix} \tag{2.2.3efg}$$

In the above expressions, k_x is the horizontal wavenumber, the subscripts L and C identify the lumped and consistent matrices, and β and μ are the tuning factors for the matrices **A** and **M**, respectively. Also, ρ is the mass density, G is the shear modulus, and h is the thickness of each thin layer.

For convenience and generality in future analysis, we define two auxiliary parameters and three dimensionless variables for wavenumbers and frequency, namely

$$a = \beta\xi_x^2 - 6 - \mu\Omega^2,$$

$$b=(3-\beta)\xi_x^2+6-(3-\mu)\Omega^2,$$

$$\xi_x=k_x h, \qquad \xi_z=k_z h, \qquad \text{and} \qquad \Omega=\frac{\omega h}{C_S}.$$

If we were to model a full-space with the TLM1, that would entail the assembly of an infinite number of layers to establish the discrete wave equation, requiring the overlapping of identical system equations such as equation (2.2.1). In the neighborhood of any particular interface l, this system would be compactly written with recourse to the above auxiliary parameters as

$$p_l=\frac{G}{6h}[av_{l+1}+2bv_l+av_{l-1}] \tag{2.2.4a}$$

This equation (2.2.4a) is a finite differences equation which models the discrete *SH* wave problem in the frequency-wavenumber domain. In the case of a semi-infinite medium, the presence of the top surface requires an additional equation (or boundary condition), namely

$$p_0=\frac{G}{6h}[bv_0+av_{-1}] \tag{2.2.4b}$$

Consider a stress-free wave motion in a homogeneous full-space (so-called body wave), which is obtained by setting the external traction vector to zero, that is, $p_l = 0$ in equation (2.2.4a). This yields a homogeneous set of finite differences equations, whose solution is the general solution to the homogeneous full-space. Also, involved is an associated eigenvalue problem that yields the wavenumber-frequency spectrum for the body wave. To obtain the general solution and the spectrum, assume a trial solution of the form

$$v_l=AZ^l \tag{2.2.5}$$

Substituting this trial solution into equation (2.2.4a) and dividing by Z^l, we obtain the spectrum equation.

$$aY+b=0 \tag{2.2.6}$$

where $Y=\frac{1}{2}(Z+Z^{-1})$. It should be realized that equation (2.2.6) is a condition for the existence of non-trivial solutions for equation (2.2.4a). The two solutions of the above quadratic equation for Z are then

$$Z_{1,2}=Y\pm\sqrt{Y^2-1} \tag{2.2.7}$$

which can be expressed as

$$Z_{1,2}=e^{\pm i\xi_z}=\cos\xi_z\pm i\sin\xi_z \tag{2.2.8}$$

One of the two roots represents a wave propagating in the positive z-direction, and the other a wave propagating in the negative z-direction. Also, it is noted that the two roots have a complex conjugate (or reciprocal) relationship. The general solution is then of the form

$$v_l=AZ^l+BZ^{-l} \tag{2.2.9a}$$

or equivalently

$$v_l=\bar{A}\cos\xi_z l+\bar{B}\sin\xi_z l \tag{2.2.9b}$$

in which A and B (or $\bar{A}$ and $\bar{B}$) are unknown constants. Substitution of equation (2.2.8) into equation (2.2.6) yields the spectrum equation in explicit form as

$$\left(3-2\beta\sin^2\frac{\xi_z}{2}\right)\xi_x^2+12\sin^2\frac{\xi_z}{2}-\left(3-2\mu\sin^2\frac{\xi_z}{2}\right)\Omega^2=0 \tag{2.2.10}$$

where

$$\xi_x=k_x h=kh\cos\theta=\frac{2\pi h\cos\theta}{\lambda}=\frac{2\pi h\cot\theta}{\lambda_z} \tag{2.2.11a}$$

$$\xi_z = k_z h = kh\sin\theta = \frac{2\pi h \sin\theta}{\lambda} = \frac{2\pi h}{\lambda_z} \qquad (2.2.11b)$$

In equations (2.2.11a and b), k and λ represent the wavenumber and wavelength along the wave propagation direction defined by the angle θ in figure 2.1.1. It can be shown that for very low wavenumbers (or very long wavelengths) in the z direction, the spectrum equation (2.2.10) approaches the exact spectrum for a continuous medium, i.e. $\omega = C_S k = C_S\sqrt{k_x^2 + k_z^2}$, or equivalently $\Omega = \sqrt{\xi_x^2 + \xi_z^2}$.

Having found the relationship between frequency and wavenumbers in equation (2.2.10), we can calculate the apparent phase velocities as

$$V = \frac{\omega}{k} \qquad \text{phase velocity in the propagation direction} \qquad (2.2.12a)$$

$$V_x = \frac{\omega}{k_x} \qquad x \text{ component of phase velocity} \qquad (2.2.12b)$$

$$V_z = \frac{\omega}{k_z} \qquad z \text{ component of phase velocity} \qquad (2.2.12c)$$

Figures 2.2.2 and 2.2.3 present a qualitative comparison of the frequency-wavenumber spectrum obtained with the discrete model (dashed line) against the exact analytical spectrum (solid line). The first figure shows the numerical dispersion for a fixed horizontal wavenumber (ξ_x= 0.5π and ξ_x=π) as a function of vertical wavenumber ξ_z, while the second shows the numerical dispersion for a fixed vertical wavenumber (ξ_z=0.5π and ξ_z=π) as a function of horizontal wavenumber ξ_x. In either case, the discrete model is computed for fully consistent matrices, that is, the tuning factors used are β=μ=1.0.

As seen in figure 2.2.2, the numerical dispersion takes place mostly in the high vertical wavenumber region, and *complex* branches exist in the discrete model that do not exist in the continuum. Also, it should be recognized from equation (2.2.10) that the discrete model possesses periodicity as well as branches whose associated group velocity is *negative* while the phase velocity is *positive*. These properties introduce not only numerical error, but also an ambiguity to the propagation direction of energy. In order to avoid this ambiguity, we adopt the following convention for the wavenumber ξ_z (or equivalently wavelength λ_z):

$$0 < \mathrm{Re}\,\xi_z \left(= \mathrm{Re}\,k_z h = \mathrm{Re}\frac{2\pi}{\lambda_z} h\right) < \pi \text{ or equivalently } 0 < \mathrm{Re}\frac{2h}{\lambda_z} < 1.0 \qquad (2.2.13)$$

This convention states that the wavelength along the discretization direction, λ_z, must be longer than twice the discretization size h. The same convention will hold for the *SV-P* waves modeled by the TLM1 to be considered later on.

It is observed in figure 2.2.3 that high horizontal wavenumbers produce smaller errors than the low horizontal wavenumbers for a given vertical wavenumber. The reason is that the high horizontal wavenumbers involve waves that propagate nearly horizontally. Inasmuch as this is a direction in which the TLM does *not* discretize, little error can be expected to occur. Indeed, when the waves propagates fully in the horizontal direction, no error at all takes place in the TLM.

We next determine the spectrum equations for three canonical problems: (1) a discrete homogeneous stratum, (2) a discrete homogenous plate, and (3) Love waves in a layer underlain by a half space modeled with the TLM1. In section 2.2.2, we numerically compare the eigenvalues obtained from the discrete and exact analytical solutions for only the second and third problems and seek to improve the discrete solutions with the aid of the optimal tuning factors β and μ.

(1) Homogeneous stratum

Consider a discrete homogeneous stratum of total depth H that is composed of N TLM1 thin layers. The two boundary conditions for this problem are a) zero stress at the top surface (i.e. l=0) and b) zero displacement at the bottom (l=–N). These conditions are

$$p_0 = 0 \qquad \text{at } l=0 \tag{2.2.14a}$$

$$v_{-N} = 0 \qquad \text{at } l=-N \tag{2.2.14b}$$

We substitute equation (2.2.9b) into equations (2.2.14) and obtain the resulting boundary condition in matrix form as

$$\begin{Bmatrix} b+a\cos\xi_z & -a\sin\xi_z \\ \cos\xi_z N & -\sin\xi_z N \end{Bmatrix} \begin{Bmatrix} \bar{A} \\ \bar{B} \end{Bmatrix} = \begin{Bmatrix} 0 \\ 0 \end{Bmatrix} \tag{2.2.14c}$$

Solving the associated eigenvalue problem, we obtain the spectrum equation as

$$\Omega = \frac{\omega h}{C_S} = \sqrt{\frac{1}{\left(3-2\mu\sin^2\dfrac{\xi_{zj}}{2}\right)}\left[\left(3-2\beta\sin^2\frac{\xi_{zj}}{2}\right)\xi_x^2 + 12\sin^2\frac{\xi_{zj}}{2}\right]} \tag{2.2.15a}$$

where

$$h = \frac{H}{N},\ \xi_{zj} = \frac{(j-\frac{1}{2})\pi}{N}, \qquad j=1,2,\ldots,N$$

For comparison, the exact analytical solution to this eigenvalue problem is introduced of the dimensionless form

$$\Omega = \frac{\omega h}{C_S} = \sqrt{\xi_x^2 + \left((j-\tfrac{1}{2})\frac{\pi h}{H}\right)^2} \qquad j=1,2,\ldots,\infty \tag{2.2.15b}$$

First, it is noticed that only N distinct eigenvalues (or modes) are available in the TLM model of interest, while the infinite number of eigenvalues is obtained from the exact analytical solutions. Secondly, it is noted that for very small ξ_{zj} the two equations (2.2.15a and b) become identical regardless of the values of tuning factors β and μ in use. This identification can be easily verified by expanding equation (2.2.15a) in Taylor series with respect to ξ_{zj}=0. Therefore, it follows that by applying sufficiently large number of thin layers (N), the exact values for first few eigenvalues can always be obtained from the TLM1.

(2) Homogeneous plate

Consider next a discrete homogenous plate of thickness H, composed of N TLM1 thin layers. The boundary conditions are now the traction-free surfaces at l=0 and l=–N, which are expressed as

$$p_0 = 0 \qquad \text{at } l=0 \tag{2.2.16a}$$

$$p_{-N} = 0 \qquad \text{at } l=-N \tag{2.2.16b}$$

Substituting equation (2.2.9b) into equations (2.2.16), we obtain the homogeneous matrix equation

$$\begin{Bmatrix} b+a\cos\xi_z & -a\sin\xi_z \\ a\cos\xi_z(N-1)+b\cos\xi_z N & -a\sin\xi_z(N-1)+b\sin\xi_z N \end{Bmatrix} \begin{Bmatrix} \bar{A} \\ \bar{B} \end{Bmatrix} = \begin{Bmatrix} 0 \\ 0 \end{Bmatrix} \tag{2.2.16c}$$

Solving the associated eigenvalue problem, we obtain the spectrum equation in closed form as

$$\Omega = \frac{\omega h}{C_S} = \sqrt{\frac{1}{\left(3-2\mu\sin^2\frac{\xi_{zj}}{2}\right)}\left[\left(3-2\beta\sin^2\frac{\xi_{zj}}{2}\right)\xi_x^2 + 12\sin^2\frac{\xi_{zj}}{2}\right]} \tag{2.2.17a}$$

where

$$h=\frac{H}{N}\ , \qquad \xi_{zj}=\frac{j\pi}{N}, \qquad j=0,1,2,\ldots,N$$

It is noticed that only N+1 distinct eigenvalues (or modes) are obtained from the TLM1 model of interest. For comparison, the exact analytical solution to this eigenvalue problem is introduced of the dimensionless form

$$\Omega = \frac{\omega h}{C_S} = \sqrt{\xi_x^2 + \left(j\frac{\pi h}{H}\right)^2} \qquad j=0,1,2,\ldots \tag{2.2.17b}$$

In section 2.2.2, we numerically calculate the eigenvalues of this discrete plate with specified values for C_S, H, and N and compare them with the exact analytical solution by means of the dispersion curves. Also, we consider four combinations of tuning factors and show the best improvement in eigenvalues with the help of the optimal tuning factors to be determined in section 2.2.2.

(3) Love waves

We consider the guided waves in a discrete homogenous layer over a discrete elastic half space, i.e. so-called Love waves in the continuum. The upper layer is composed of N TLM1 thin layers whose total thickness is H. The wave speed of the upper layer is slower than that of the half-space. The discrete half space is composed of an infinitely large number of thin layers. The x-axis is taken to coincide with the interface between the layer and the half-space. This example is more complicated than the previous two, because we now have two displacement fields, one for the upper layer and another for the half space. The general solutions are now

$$v_{L,l} = \bar{A}_L \cos\xi_{zL} l + \bar{B}_L \sin\xi_{zL} l \tag{2.2.18a}$$

$$v_{H,l} = A_H Z_H^l \tag{2.2.18b}$$

in which the subscripts L and H identify the upper layer and the half space, respectively. Equation (2.2.18b) contains only one term, because $v_{H,l}$ must satisfy the radiation condition, i.e. $|Z_H| > 1$ for $l < 0$. The boundary conditions are now a stress-free surface and two continuity conditions for displacements and stresses at the interface. These are given by

1) stress-free condition at $z = H$, ($l = N$) : $p_{L,N} = 0$ (2.2.19a)

2) displacement continuity at $z = 0$, ($l = 0$) : $v_{L,0} - v_{H,0} = 0$ (2.2.19b)

3) stress continuity at $z = 0$, ($l = 0$) : $p_{L,0} + p_{H,0} = 0$ (2.2.19c)

Substitute equations (2.2.18) into the above boundary conditions, we obtain the homogeneous matrix equation

$$\begin{Bmatrix} b_L\cos\xi_z N + a_L\cos\xi_z(N-1) & b_L\sin\xi_z N - a_L\sin\xi_z(N-1) & \cdot \\ 1 & \cdot & -1 \\ [a_L\cos\xi_{zL} + b_L] & a_L\sin\xi_{zL} & \kappa[b_H + a_H Z_H^{-1}] \end{Bmatrix} \begin{Bmatrix} \bar{A}_L \\ \bar{B}_L \\ A_H \end{Bmatrix} = \begin{Bmatrix} 0 \\ 0 \\ 0 \end{Bmatrix} \tag{2.2.19d}$$

where $\kappa = \frac{G_H}{G_L}\frac{h_L}{h_H}$. Solving the system of equations (2.2.19d) for nontrivial solutions for $\bar{A}_L$, $\bar{B}_L$, and A_H, we obtain the Love wave modes for the discrete model. However, since the elements of the matrix contain transcendental functions, we shall not be able to obtain the eigenvalues in closed form. Instead, numerical search techniques are necessary to find the modes.

In section 2.2.2, we perform numerical analysis to calculate the N eigenvalues of this discrete layered half-space with specified values for G_H, G_L, h_L, H, and N and compare them with the associated exact solution by means of the dispersion curves. Also, we consider three combinations of tuning factors and show the best improvement in eigenvalues with the help of the optimal tuning factors to be determined in section 2.2.2.

2.2.2 Numerical dispersion and tuning factors

In this section, we characterize the numerical dispersion of *SH* waves modeled with the TLM based on a linear expansion, or TLM1 for short, by means of the canonical problems formulated in the previous section. The problems are (1) body waves propagating vertically, (2) body waves propagating at an angle to the horizontal axis, (3) a homogeneous plate, and (4) Love waves in a layer underlain by a half space. From the first two examples, we determine the optimal tuning factors of β and μ and propose a lower bound for the number of thin layers per wavelength. Thereafter, we apply these factors to the last two problems to verify that the optimal tuning factors improve best the propagation modes computed from the TLM1.

(1) Body waves propagating vertically : tuning factor μ

Here, we consider the *SH* waves propagating only vertically, so there is no harmonic variation in the horizontal direction, i.e. ξ_x=0. This problem is formally identical to the 1-D problem of *SH* waves in an infinitely long shear beam discretized with finite elements. Setting ξ_x=0 in equation (2.2.4a), we obtain the modified governing equation.

$$p_l = \frac{G}{6h}\left[\bar{a}v_{l+1} + 2\bar{b}v_l + \bar{a}v_{l-1}\right] \tag{2.2.20}$$

where $\bar{a} = -6 - \mu\Omega^2$, and $\bar{b} = 6 - (3-\mu)\Omega^2$. This equation (2.2.20) contains only one tuning factor, namely μ, so finding its optimal value is a straightforward task. With the help of equations (2.2.10) and (2.2.12c), the phase velocity is calculated as

$$V_z = \frac{\omega}{k_z} = \frac{2C_S}{\xi_z}\frac{\sin\frac{\xi_z}{2}}{\sqrt{\left(1 - \frac{2}{3}\mu\sin^2\frac{\xi_z}{2}\right)}}. \tag{2.2.21}$$

To explore the numerical dispersion characteristics of this wave, the apparent phase velocity V_z in equation (2.2.21) is computed for four different values of μ=0, 1/3, 2/3, and 1. Figure 2.2.4

displays the ratio of V_z to $C_z(=C_S)$ as a function of vertical wavenumber ξ_z and the tuning factor μ, in which C_z is the true vertical phase velocity. It is shown that an optimal factor μ must exist whose value lies between 1/3 and 2/3 and will be valid only for $0<\xi_z/\pi<1/2$. For $\xi_z/\pi>1/2$, on the other hand, the numerical dispersion increases significantly regardless of the tuning factor μ. This was expected, because high values of ξ_z correspond to waves whose wavelength is short in comparison to the thickness of the discrete layers, so they cannot be modeled (or propagated) faithfully. Therefore, we will focus only on the range of $0<\xi_z/\pi<1/2$ to determine the optimal value for μ. More interestingly, the condition of $0<\xi_z/\pi<1/2$ provides a lower bound for the number of TLM1 thin layers per wavelength $N_\lambda=\lambda_z/h$ such that N_λ must be no less than 4, i.e. $N_\lambda \geq 4$. Determining N_λ is importantly and directly related to the accuracy of the TLM, which will be discussed in more detail in chapter 4.

To estimate the error caused by the numerical dispersion in the present example, we define an error function ε as

$$\varepsilon = \int_0^{\pi/2} d\varepsilon = \int_0^{\pi/2} \left(\frac{V_z(\xi_z,\mu)}{C_z} - 1 \right)^2 d\xi_z \qquad (2.2.22)$$

which provides the integrated squared error over the significant range of vertical wavenumbers (i.e. for wavelengths that are long compared to the discretization). Figure 2.2.5 shows the error function in terms of the tuning factor μ. As can be seen, ε is zero at $\mu=0.55$, while it is greater than zero for all other values of μ. Hence, the optimal tuning factor is $\mu=0.55$.

(2) Body waves propagating at an angle to the horizontal axis : tuning factor β

Next, we consider the more general problem in which the *SH* wave propagates at an arbitrary angle with respect to positive horizontal axis (i.e. ξ_x is non-zero in equation 2.2.4a). Thus, it is now necessary to consider tuning factors for both matrices **A** and **M**, namely β and μ, respectively, and evaluate their effect on the numerical dispersion as functions of both the propagation angle and the vertical wavenumber. As in the case of vertically propagating waves, we evaluate both the ratio of phase velocities *V/C* and the associated error function ε defined by equation (2.2.22); these are shown in figures 2.2.6 and 2.2.7, respectively.

Figure 2.2.6 shows the variation of *V/C* with respect to the vertical wavenumber ξ_z for the propagation angles θ of 15, 30, 45, 60, 75, and 90°. In each case, this ratio is evaluated for $\beta=1$, and $\mu=0$, 0.55 and 1.0 (i.e. $\mathbf{A_C}+\mathbf{M_L}$, $\mathbf{A_C}+\mathbf{M_T}$ and $\mathbf{A_C}+\mathbf{M_C}$ respectively). It is noticed that the discrete results for $\mathbf{A_C}+\mathbf{M_L}$ and $\mathbf{A_C}+\mathbf{M_C}$ are slower and faster, respectively, than the exact results, while the discrete results for $\mathbf{A_C}+\mathbf{M_T}$ are nearly exact for $\xi_z/\pi < 1/2$. This observation shows that an optimal value for μ exists for arbitrary angles of propagation θ, including 90 degrees, and that it is likely to be 0.55.

To find the optimal values for β and μ, we again make use of equation (2.2.22), replacing V_z by V and C_z by C, where C is the phase velocity of waves propagating at an angle θ in the continuous model. In this example, however, the error function ε is a function of not only μ, but also β, i.e. $\varepsilon=\varepsilon(\beta,\mu)$ for a given propagation angle θ. Figure 2.2.7 shows the variation of this error function for various propagation angles in terms of a standard surface plot. It is now clear that the use of $\beta=0.55$ and $\mu=0.55$ constitute the best choice for both of the tuning factors, and that these factors are independent of the propagation angle θ. The identical values for β and μ may be understood from the fact that the two matrices **A** and **M** are proportional to each other in the case of a discrete, homogeneous full space.

(3) Homogeneous plate

We now consider the free vibration of a homogeneous plate of thickness H=1.0 and shear velocity C_S=1.0. For a discrete model, the plate of interest is discretized into 10 thin layers, i.e. N=10, and so only 11 distinct eigenvalues (or modes) exist in the present discrete model. This problem is a practical example that can be solved by the general procedures of the TLM formulated in chapter 1. Because of simplicity of this problem, however, we may also obtain the solution in closed form by means of a finite difference scheme as shown in equation (2.2.17a). Through this example, we assess the effect of the tuning factors β and μ on eigenvalue problems for finite domain systems. For this purpose, we consider the following four combinations of the tuning factors: (i) β=1.00 and μ=1.00 ($\mathbf{A}_C$+$\mathbf{M}_C$); (ii) β=1.00 and μ=0.00 ($\mathbf{A}_C$+$\mathbf{M}_L$); (iii) β=1.00 and μ=0.55 ($\mathbf{A}_C$+$\mathbf{M}_T$); (iv) β=μ=0.55 ($\mathbf{A}_T$+$\mathbf{M}_T$).

Figure 2.2.8 compares the frequency-wavenumber dispersion of the discrete solutions (dashed lines) with the exact analytical solutions (solid lines). The discrete solutions are computed for the above four combinations of tuning factors. It is noted that there are shown only 11 branches in each plot, although the infinite number of modes (or branches) exists in the exact analytical solution as shown in equation (2.2.17b). As is apparent, the use of the optimal tuning factors, i.e. β=μ=0.55, provides the best agreement with the exact solutions. It is also noted that the use of β=1.00 and μ=0.55 also gives good results for small horizontal wavenumbers, i.e. $\xi_x<\pi/4$, but not for high horizontal wavenumbers. Therefore, we conclude that the tuning factors β=μ=0.55 are indeed the optimal choice for anti-plane problems modeled with the TLM1.

It is also observed from figure 2.2.8 that only the 5 or 6 modes of the 11 modes in the discrete solution are accurate despite the application of optimal tuning factors. The reason is related to the range of vertical wavenumber ξ_z over which the numerical error $\varepsilon(\beta,\mu)$ in equation (2.2.22) is estimated to determine the optimal tuning factors. Remember that the optimal tuning factors are determined only for the significant range of vertical wavenumber, i.e. $0<\xi_z/\pi<0.5$. In fact, the 5 or 6 modes are the first half of the set of modes, which can be easily verified by accounting the index j or ξ_{zj} in equation (2.2.17a) in the present problem. In addition, inspecting equation (2.2.17a) reveals that ξ_{zj}/π for the accurate first half modes is no greater than 0.5. Finally, it is concluded that with the application of optimal tuning factors only the first half of the set of all computed modes (or equivalently the modes with $0<\xi_{zj}/\pi<0.5$) is accurate as far as the dispersion relation is concerned.

(4) Love waves

We consider the last example in this section: a layer underlain by a half-space, i.e. the so-called Love wave problem. The thickness and shear velocity of the layer is H=1.0 and C_L =1.0, respectively. The shear velocity of the half space is C_H=2.0. The mass density ρ for both is 1.0. Therefore, the shear moduli for the layer and half-space are $G_L(=\rho C_L^2)$=1.0 and $G_H(=\rho C_H^2)$=4.0, respectively. For a discrete model, the layer is composed of 20 TLM1 thin layers (N=20), so that the thickness $h_L(=H/N)$ of each thin layer is 0.05(=1/20) and the total number of degrees of freedom (or interfaces) is 21. Taking into consideration the wave-velocity contrast between the two materials, the thickness of thin layers for the half space (h_H) is set to be 0.10. In the discrete model of interest, the first twenty propagation modes are the only valid modes. So, we compare these twenty modes with the exact analytical solution to assess the effect of the tuning factors β and μ on eigenvalue problems for layered semi-infinite systems. For this purpose, we consider the

following three combinations of tuning factors: (i) β=1.00 and μ=1.00 ($\mathbf{A}_C$+$\mathbf{M}_C$); (ii) β=1.00 and μ=0.00 ($\mathbf{A}_C$+$\mathbf{M}_L$); (iii) β=μ=0.55 ($\mathbf{A}_T$+$\mathbf{M}_T$). It is noted that the combination of β=1.00 and μ=0.55 ($\mathbf{A}_C$+$\mathbf{M}_T$) is excluded, because the homogenous plate problem has already revealed that the tuning factors of β=1.00 and μ=0.55 produce significant numerical errors for high wavenumbers ξ_x.

Figure 2.2.9 compares the frequency-wavenumber dispersion of the discrete solutions (dashed lines) with the exact analytical solutions (solid lines) for the three combinations of tuning factors. First of all, it is observed that the optimal tuning factors of β=μ=0.55 improves the accuracy of eigenvalues to the significant extent. Secondly, only the first half (or 10 in this example) of the set of 20 modes are shown to be accurate. Therefore, it is proved that the tuning factors β=μ=0.55 are indeed the optimal choice for *SH* wave problems of semi-infinite domain as well as finite domain. In addition, it is verified that as long as using the optimal tuning factors, we can calculate accurately the first half of the set of modes obtained from the TLM1 not only for a homogeneous layer, but also for two-layered systems (or even multilayered systems).

2.2.3 Summary

In this section, we have obtained the general solution and the frequency-wavenumber spectrum for the discrete *SH* wave formulated by means of the TLM1. On the basis of a qualitative investigation of the spectrum, we have found that the wavelengths along the discretization direction (λ_z) must be no shorter than twice the discretization size (h), i.e. $\lambda_z \geq 2h$. Then, three wave propagation problems in finite and semi-infinite discrete media have been solved formally and successfully. The comprehensive characterization of the numerical dispersion in the discrete homogenous full-space has yielded the optimal tuning factors of β=μ=0.55 that are valid only for $0<\xi_z/\pi<1/2$. Also, it has been found that the number of thin layers per wavelength N_λ ($=\lambda_z/h$) must be no less than 4, i.e. $N_\lambda \geq 4$ for the range of ξ_z in consideration. From the free vibration problems of an *SH* plate and a layer on a half-space, it is verified that the use of optimal tuning factors really provides the best agreement with the exact analytical solutions in terms of eigenvalues. More importantly, it is observed that the first half computed modes are very close to those of the exact analytical solution, provided that the optimal tuning factors are used.

2.3 In-plane (*SV-P*) waves with linear expansion TLM

We here consider the *SV-P* wave propagation modeled with the TLM1. In the first part of this section 2.3, we obtain the general solution and the frequency-wavenumber spectrum for the *SV-P* wave equation modeled with the TLM1. Through a qualitative investigation of the spectrum, we confirm the convention for the wavelength along the discretization direction and the discretization size, i.e. $\lambda_z \geq 2h$. Then, we solve formally two guided wave problems by means of the obtained general solutions. The two problems are a discrete homogeneous plate with mixed boundary conditions and the Rayleigh surface waves on a discrete homogeneous half-space.

In the second part, we first extensively characterize the numerical dispersion of body waves for five different Poisson's ratios as a function of vertical direction wavenumber (ξ_z) and the propagation angle (θ). As a result, we confirm that the same range of ξ_z as the case of *SH* wave is only useful as determining the optimal tuning factors. Then, with the calculation of the error functions, we determine the optimal tuning factors. By analyzing two free-vibration problems of finite domain, we verify that the optimal tuning factors indeed improve the accuracy of the

eigenvalues in the context of the TLM. In addition, we find out how many modes are accurate among a set of all computed modes with the application of the optimal tuning factors. In the last problem, we consider the problem of Rayleigh surface wave to show the effect of the tuning factors on the accuracy of the TLM1 analysis for (semi-) infinite media.

2.3.1 Discrete solution for in-plane problems

Consider a single TLM1 thin layer subjected to *SV-P* wave motion as shown in figure 2.3.1. Since *SV-P* wave motion is involved, the two degrees of freedom, u and w, are assigned at each node or interface. The governing equation for the thin layer is then expressed as

$$\mathbf{P}_l = \mathbf{K}\,\mathbf{U}_l \tag{2.3.1}$$

$$\mathbf{P}_l = \{\mathbf{p}_l \quad \mathbf{p}_{l-1}\}^T = \{p_{x,l} \quad p_{z,l} \quad p_{x,l-1} \quad p_{z,l-1}\}^T \quad : \text{consistent traction vector} \tag{2.3.2a}$$

$$\mathbf{U}_l = \{\mathbf{u}_l \quad \mathbf{u}_{l-1}\}^T = \{u_l \quad w_l \quad u_{l-1} \quad w_{l-1}\}^T \quad : \text{displacement vector} \tag{2.3.2b}$$

$$\mathbf{K} = \mathbf{A}k_x^2 + \mathbf{B}k_x + \mathbf{G} - \omega^2\mathbf{M} \quad : \text{stiffness matrix} \tag{2.3.2c}$$

where

$$\mathbf{A} = \frac{h}{6}\begin{Bmatrix} (3-\alpha)(\lambda+2G) & \cdot & \alpha(\lambda+2G) & \cdot \\ \cdot & (3-\beta)G & \cdot & \beta\,G \\ \alpha(\lambda+2G) & \cdot & (3-\alpha)(\lambda+2G) & \cdot \\ \cdot & \beta\,G & \cdot & (3-\beta)G \end{Bmatrix} \tag{2.3.3a}$$

$$\mathbf{B} = \frac{1}{2}\begin{Bmatrix} \cdot & \lambda-G & \cdot & -(\lambda+G) \\ \lambda-G & \cdot & \lambda+G & \cdot \\ \cdot & \lambda+G & \cdot & -(\lambda-G) \\ -(\lambda+G) & \cdot & -(\lambda-G) & \cdot \end{Bmatrix} \tag{2.3.3b}$$

$$\mathbf{G} = \frac{1}{h}\begin{Bmatrix} G & \cdot & -G & \cdot \\ \cdot & \lambda+2G & \cdot & -(\lambda+2G) \\ -G & \cdot & G & \cdot \\ \cdot & -(\lambda+2G) & \cdot & \lambda+2G \end{Bmatrix} \tag{2.3.3c}$$

$$\mathbf{M} = (1-\mu)\mathbf{M}_L + \mu\mathbf{M}_C = \frac{\rho h}{6}\begin{Bmatrix} 3-\mu & \cdot & \mu & \cdot \\ \cdot & 3-\mu & \cdot & \mu \\ \mu & \cdot & 3-\mu & \cdot \\ \cdot & \mu & \cdot & 3-\mu \end{Bmatrix} \tag{2.3.3d}$$

where α, β and μ are the tuning factors for the matrices **A** and **M**, and the subscripts L and C represent the lumped and consistent matrices. Note that the matrix **A** has two tuning factors α and β. The reason is that the matrix **A** has two wave components, i.e. *P* and *S* waves. The elements having the factor λ+2G are related to the *P* wave component, and the elements having the factor G are related to the *S* wave component. Therefore, the *P* and *S* wave components are individually tuned by means of α and β, respectively. Also, k_x is the horizontal wavenumber, ρ is the mass density, λ is the Lamé constant, G is the shear modulus, and h is the thickness of the thin layer.

For the sake of future convenience, we introduce the three auxiliary matrices and four dimensionless parameters defined as

$$\mathbf{a}=\begin{Bmatrix} a_{11} & a_{12} \\ a_{21} & a_{22} \end{Bmatrix}$$

$$=\begin{Bmatrix} \alpha r & \cdot \\ \cdot & \beta \end{Bmatrix}\xi_x^2+3(r-1)\begin{Bmatrix} \cdot & -1 \\ 1 & \cdot \end{Bmatrix}\xi_x+6\begin{Bmatrix} -1 & \cdot \\ \cdot & -r \end{Bmatrix}-\mu\begin{Bmatrix} 1 & \cdot \\ \cdot & 1 \end{Bmatrix}\Omega^2$$

$$\mathbf{b}=\begin{Bmatrix} b_{11} & \cdot \\ \cdot & b_{22} \end{Bmatrix}$$

$$=\begin{Bmatrix} (3-\alpha)r & \cdot \\ \cdot & (3-\beta) \end{Bmatrix}\xi_x^2+6\begin{Bmatrix} 1 & \cdot \\ \cdot & r \end{Bmatrix}-(3-\mu)\begin{Bmatrix} 1 & \cdot \\ \cdot & 1 \end{Bmatrix}\Omega^2$$

$$\mathbf{b}_0=\begin{Bmatrix} b_{11} & b_{12} \\ b_{21} & b_{22} \end{Bmatrix}$$

$$=\begin{Bmatrix} (3-\alpha)r & \cdot \\ \cdot & (3-\beta) \end{Bmatrix}\xi_x^2+3(r-3)\begin{Bmatrix} \cdot & 1 \\ 1 & \cdot \end{Bmatrix}\xi_x+6\begin{Bmatrix} 1 & \cdot \\ \cdot & r \end{Bmatrix}-(3-\mu)\begin{Bmatrix} 1 & \cdot \\ \cdot & 1 \end{Bmatrix}\Omega^2$$

$$\xi_x=k_x h, \qquad \xi_z=k_z h, \qquad \Omega=\frac{\omega h}{C_S}, \text{ and } \quad r=\frac{\lambda+2G}{G}=\frac{C_P^2}{C_S^2}=\frac{2-2\nu}{1-2\nu}$$

To describe the wave motion in a homogenous full space composed of infinitely many identical thin layers, we write the recursive equation of motion at the l^{th} interface as

$$\mathbf{p}_l=\frac{G}{6h}\left[\mathbf{a}^T\mathbf{u}_{l+1}+2\mathbf{b}\mathbf{u}_l+\mathbf{a}\mathbf{u}_{l-1}\right] \tag{2.3.4a}$$

In the special case of a half-space, the top surface (i.e. z=0 or l=0), which is associated with boundary conditions, obeys instead the equation

$$\mathbf{p}_0=\frac{G}{6h}\left[\mathbf{b}_0\mathbf{u}_0+\mathbf{a}\mathbf{u}_{-1}\right] \tag{2.3.4b}$$

In a particular case of vertically propagating waves, i.e. k_x = 0.0, the discrete equation of motion of equation (2.3.4a) separates into two uncoupled scalar equations, each of which involves only the horizontal (u) or vertical (w) component. In this case, the u component results solely from S waves (as in a shear beam), while the w component arises purely from P waves (as in a rod).

To determine the general solutions, we assume a solution in the form.

$$\mathbf{u}_l=Z^l\boldsymbol{\phi} \tag{2.3.5}$$

in which $\boldsymbol{\phi}=\{\phi_x \quad \phi_z\}^T$ is the eigenvector, whose direction cosine determines the direction of particle motion or the polarization. Substituting equation (2.3.5) into equation (2.3.4a) and setting $\mathbf{p}_l=\mathbf{0}$, we obtain the following homogeneous equation in the matrix form.

$$\left[\mathbf{a}^T Z+2\mathbf{b}+\mathbf{a}Z^{-1}\right]\boldsymbol{\phi}=\mathbf{0} \tag{2.3.6a}$$

or

$$\begin{Bmatrix} 2a_{11}Y+2b_{11} & -2a_{12}\bar{Y} \\ 2a_{12}\bar{Y} & 2a_{22}Y+2b_{22} \end{Bmatrix}\begin{Bmatrix} \phi_x \\ \phi_z \end{Bmatrix}=\begin{Bmatrix} 0 \\ 0 \end{Bmatrix} \tag{2.3.6b}$$

or

$$\left[\begin{Bmatrix} r[6+2\alpha(Y-1)] & \cdot \\ \cdot & 6+2\beta(Y-1) \end{Bmatrix}\xi_x^2+\begin{Bmatrix} \cdot & 6\bar{Y}(r-1) \\ -6\bar{Y}(r-1) & \cdot \end{Bmatrix}\xi_x+\right.$$

$$+\begin{Bmatrix} 12(1-Y) & \cdot \\ \cdot & 12r(1-Y) \end{Bmatrix} - \begin{Bmatrix} 6+2\mu(Y-1) & \cdot \\ \cdot & 6+2\mu(Y-1) \end{Bmatrix} \Omega^2 \Bigg] \begin{Bmatrix} \phi_x \\ \phi_z \end{Bmatrix} = \begin{Bmatrix} 0 \\ 0 \end{Bmatrix} \tag{2.3.6c}$$

where the two variables Y and $\bar{Y}$ are defined as

$$Y = \tfrac{1}{2}(Z + Z^{-1}), \qquad \bar{Y} = \tfrac{1}{2}(Z - Z^{-1}), \qquad \text{and} \qquad \bar{Y}^2 = Y^2 - 1.$$

A nontrivial solution exists only if the determinant of the coefficient matrix in equation (2.3.6c) vanish. After additional manipulation for the determinant, we obtain the following spectrum equation for Y.

$$Y^2 - 2\alpha_1 Y + \alpha_2 = 0 \tag{2.3.7}$$

where

$$\alpha_1 = -\frac{1}{2}\frac{a_{11}b_{22} + a_{22}b_{11}}{a_{11}a_{22} + a_{12}^2} \quad \text{and} \quad \alpha_2 = \frac{b_{11}b_{22} - a_{12}^2}{a_{11}a_{22} + a_{12}^2}$$

The two roots Y's that correspond to P and S wave components are, respectively

$$Y_i = \alpha_1 \pm \sqrt{\alpha_1^2 - \alpha_2} \qquad \text{with } i = P, S \tag{2.3.8}$$

Additionally, the directions of particle motion for each component (Θ), the so-called polarization, can be obtained from the eigenvectors of equation (2.3.6c) in the form.

$$\Theta_i = \tan^{-1}\left[\frac{\phi_{z,i}}{\phi_{x,i}}\right] = \tan^{-1}\left[-\gamma_i - \sqrt{\gamma_i^2 - 1}\right] \tag{2.3.9a}$$

where

$$\gamma_i = \frac{\{r[3+\alpha(Y_i-1)] - [3+\beta(Y_i-1)]\}\xi_x^2 + 6(r-1)(Y_i-1)}{6(r-1)\bar{Y}\xi_x}, \tag{2.3.9b}$$

It is clear that these two directions are perpendicular to each other because of the orthogonality of the two eigenvectors in equation (2.3.6c). Also, it can be easily recognized from equation (2.3.9b) that the polarization is independent of the tuning factor μ. Furthermore, if α=β, the polarization is independent of Poisson's ratio ν. However, it can not be easily confirmed whether the polarization of this discrete model either coincides with the direction of propagation (P waves), or does it lie in a plane perpendicular to that direction (S waves), as is the case for homogeneous P and S waves in a continuous space. We numerically demonstrate these characteristics in section 2.3.2.

The two Z's for each Y in equation (2.3.8) can be written as

$$Z_{i1,2} = Y_i \pm \sqrt{Y_i^2 - 1} \qquad \text{or} \qquad Z_{i1,2} = e^{\pm i\xi_{zi}} = \cos\xi_{zi} \pm i\sin\xi_{zi} \tag{2.3.10}$$

The corresponding eigenvectors are then given by

$$\phi_{i1} = \begin{Bmatrix} a_{12}\bar{Y}_{i1} \\ a_{11}Y_{i1} + b_{11} \end{Bmatrix} = \begin{Bmatrix} a_{12}\bar{Y}_i \\ a_{11}Y_i + b_{11} \end{Bmatrix} = \begin{Bmatrix} \phi_{ix} \\ \phi_{iz} \end{Bmatrix} \tag{2.3.11a}$$

$$\phi_{i2} = \begin{Bmatrix} a_{12}\bar{Y}_{i2} \\ a_{11}Y_{i2} + b_{11} \end{Bmatrix} = \begin{Bmatrix} a_{12}(-\bar{Y}_i) \\ a_{11}Y_i + b_{11} \end{Bmatrix} = \begin{Bmatrix} -\phi_{ix} \\ \phi_{iz} \end{Bmatrix} \tag{2.3.11b}$$

Finally, the general solution is of the form.

$$\mathbf{u}_l = AZ_P^l\phi_{P1} + BZ_P^{-l}\phi_{P2} + CZ_S^l\phi_{S1} + DZ_S^{-l}\phi_{S2} \tag{2.3.12a}$$

or equivalently

$$\mathbf{u}_l = \begin{Bmatrix} \cos\xi_{zP}l\ \phi_{Px} \\ -i\sin\xi_{zP}l\ \phi_{Pz} \end{Bmatrix}\bar{A} + \begin{Bmatrix} -i\sin\xi_{zP}l\ \phi_{Px} \\ \cos\xi_{zP}l\ \phi_{Pz} \end{Bmatrix}\bar{B} + \begin{Bmatrix} \cos\xi_{zS}l\ \phi_{Sx} \\ -i\sin\xi_{zS}l\ \phi_{Sz} \end{Bmatrix}\bar{C} + \begin{Bmatrix} -i\sin\xi_{zS}l\ \phi_{Sx} \\ \cos\xi_{zS}l\ \phi_{Sz} \end{Bmatrix}\bar{D} \tag{2.3.12b}$$

where A, B, C, and D (or $\bar{A}$, $\bar{B}$, $\bar{C}$, and $\bar{D}$) are unknown constants. Substitution of equation (2.3.10) into equation (2.3.6c) yields the spectrum equation in more explicit form as

$$\left|\begin{Bmatrix} r[6-4\alpha\sin^2\frac{\xi_z}{2}] & \cdot \\ \cdot & 6-4\beta\sin^2\frac{\xi_z}{2} \end{Bmatrix}\xi_x^2 + \begin{Bmatrix} \cdot & 6(r-1)\mathrm{i}\sin\xi_z \\ -6(r-1)\mathrm{i}\sin\xi_z & \cdot \end{Bmatrix}\xi_x + \right.$$

$$\left. + \begin{Bmatrix} 24\sin^2\frac{\xi_z}{2} & \cdot \\ \cdot & 24r\sin^2\frac{\xi_z}{2} \end{Bmatrix} - \begin{Bmatrix} 6-4\mu\sin^2\frac{\xi_z}{2} & \cdot \\ \cdot & 6-4\mu\sin^2\frac{\xi_z}{2} \end{Bmatrix}\Omega^2 \right| = 0 \qquad (2.3.13)$$

in which

$$\xi_x = k_x h = kh\cos\theta = \frac{2\pi h\cos\theta}{\lambda} = \frac{2\pi h\cot\theta}{\lambda_z} \qquad (2.3.14a)$$

$$\xi_z = k_z h = kh\sin\theta = \frac{2\pi h\sin\theta}{\lambda} = \frac{2\pi h}{\lambda_z} \qquad (2.3.14b)$$

with k and λ being the wavenumber and wavelength along the wave propagation direction θ. It can be shown that for a very lower wavenumber (or a very long wavelength) in z direction, the spectrum equation (2.3.13) approaches the exact analytical spectrum equations given in dimensionless form as $\Omega_P = \sqrt{r(\xi_{xP}^2 + \xi_{zP}^2)}$ and $\Omega_S = \sqrt{\xi_{xS}^2 + \xi_{zS}^2}$.

Having found the relationship between frequency and wavenumbers from equation (2.3.13), we can obtain the apparent phase velocities as follows.

$$V_P = \frac{\omega_P}{k} \quad : P \text{ wave phase velocity in the propagation direction} \qquad (2.3.15a)$$

$$V_S = \frac{\omega_S}{k} \quad : S \text{ wave phase velocity in the propagation direction} \qquad (2.3.15b)$$

$$V_{Px} = \frac{\omega_P}{k_x} \quad : P \text{ wave phase velocity in the } x \text{ direction} \qquad (2.3.15c)$$

$$V_{Sx} = \frac{\omega_S}{k_x} \quad : S \text{ wave phase velocity in the } x \text{ direction} \qquad (2.3.15d)$$

$$V_{Pz} = \frac{\omega_P}{k_z} \quad : P \text{ wave phase velocity in the } z \text{ direction} \qquad (2.3.15e)$$

$$V_{Sz} = \frac{\omega_S}{k_z} \quad : S \text{ wave phase velocity in the } z \text{ direction} \qquad (2.3.15f)$$

Figures 2.3.2 and 2.3.3 make a qualitative comparison of the frequency-wavenumber spectrum obtained with the TLM1 (dashed line) against the exact analytical spectrum (solid line) for a particular case of Poisson's ratio ν=0.30. Since the *SV-P* wave is associated in this section, two branches exist in the spectrum: one is for *S* wave and the other is for *P* wave. Figure 2.3.2 shows the numerical dispersion for a fixed horizontal wavenumber (ξ_x=0.5π and ξ_x=π) as a function of vertical wavenumber ξ_z. Figure 2.3.3, on the other hand, shows the numerical dispersion for a fixed vertical wavenumber (ξ_z=0.25π and ξ_z=0.75π) as a function of horizontal wavenumber ξ_x. In either case, the discrete model is computed for fully consistent matrices, that is, the tuning factors used are α=β=μ=1.0.

As clearly shown in figure 2.3.2, the similar characteristics are observed to those seen in figure 1.2.3, such as significant numerical error in the high vertical wavenumber region, existence of complex branches, periodicity of branches, possibility of negative group velocity, and so on. Therefore, we adopt the same convention for the vertical wavenumber ξ_z (or the wavelength along the discretization direction λ_z) as the TLM1 for *SH* wave in section 2.2, which states that λ_z must be longer than twice the discretization thickness h.

The first plot in figure 2.3.3 shows that high horizontal wavenumbers produce smaller errors than the low horizontal wavenumbers for a given vertical wavenumber ξ_z=0.25π. The reason is the same as the *SH* wave problem in section 2.2, i.e. that the high horizontal wavenumbers involve waves that propagate nearly horizontally. On the other hand, it is observed in the second plot for ξ_z=0.75π that the significant numerical errors occur in the whole range of ξ_x considered, which is not seen in the problem of *SH* waves of section 2.2. Therefore, it is expected that concerning its accuracy, the TLM1 for *SV-P* wave could produce less accurate results (e.g. eigenvalues or eigenvectors) than the TLM1 for *SH* wave, especially for the high vertical wavenumbers, e.g. ξ_z=0.75π.

We proceed to derive formally the spectrum equations for two guided wave examples: (1) a discrete homogeneous plate with mixed boundary conditions; and (2) Rayleigh surface waves on a discrete homogeneous half-space. Concerning the first example, the solutions are obtained in fully analytical form due to the simplicity of the problem. By contrast, the solution for the second example is obtained in an implicit form, which requires numerical search techniques. In section 2.3.2, we compare the discrete solutions with the associated exact analytical solutions for the two examples and seek to improve the discrete solutions with the help of obtained optimal tuning factors α, β, and μ.

(1) Homogeneous plate with mixed boundary conditions

Consider a discrete homogeneous plate of thickness H that is composed of N (even integer) thin layers of the TLM1. The mixed boundary conditions of interest are that the vertical displacement and the horizontal stress are both zero at the top (l=N/2) and bottom (l=–N/2) surfaces, namely

$$w_l = 0 \tag{2.3.16a}$$

$$p_{xl} = 0 \tag{2.3.16b}$$

Under these boundary conditions, it is possible to uncouple the wave motion in the plate into the symmetric and anti-symmetric modes. The symmetric mode is associated with the wave motion whose vertical displacement (w_l) and horizontal stress (p_{xl}) are both zero at the middle (l=0) of the thickness. On the other hand, the anti-symmetric mode is associated with the wave motion whose horizontal displacement (u_l) and vertical stress (p_{zl}) are both zero at the middle (l=0) of the thickness.

Consider first the symmetric mode, of which the displacement fields are of the form.

$$\mathbf{u}_l = \begin{Bmatrix} \cos\xi_{zP} l\ \phi_{Px} \\ -\mathrm{i}\sin\xi_{zP}\, l\, \phi_{Pz} \end{Bmatrix} \bar{A} + \begin{Bmatrix} \cos\xi_{zS} l\ \phi_{Sx} \\ -\mathrm{i}\sin\xi_{zS} l\ \phi_{Sz} \end{Bmatrix} \bar{C} \tag{2.3.17}$$

Substitution of equation (2.3.17) into equations (2.3.16a and b) yields

$$\begin{Bmatrix} w_{\bar{N}} \\ p_{x\bar{N}} \end{Bmatrix} = \begin{bmatrix} -\mathrm{i}(a_{11}\cos\xi_{zP} + b_{11})\sin\xi_{zP}\bar{N} & -\mathrm{i}(a_{11}\cos\xi_{zS} + b_{11})\sin\xi_{zS}\bar{N} \\ -\mathrm{i}a_{12}(a_{11} + b_{11}\cos\xi_{zP})\sin\xi_{zP}\bar{N} & -\mathrm{i}a_{12}(a_{11} + b_{11}\cos\xi_{zS})\sin\xi_{zS}\bar{N} \end{bmatrix} \begin{Bmatrix} \bar{A} \\ \bar{C} \end{Bmatrix} = \begin{Bmatrix} 0 \\ 0 \end{Bmatrix} \tag{2.3.18}$$

where $\bar{N} = N/2$. For nontrivial solutions to be present, the determinant of the coefficient matrix must vanish. The associated spectrum equation is then given by

$$f(\xi_x, \Omega) = a_{12} \sin \xi_{zP} \bar{N} \sin \xi_{zS} \bar{N} \cdot \cdot [(a_{11} \cos \xi_{zP} + b_{11})(a_{11} + b_{11} \cos \xi_{zS}) - (a_{11} \cos \xi_{zS} + b_{11})(a_{11} + b_{11} \cos \xi_{zP})] = 0 \tag{2.3.19}$$

From equation (2.3.19), it is seen that the symmetric mode can be separated into two independent modes such as P and S wave components. This perfect separation implies an important physics that there is no mode conversion phenomenon between P and S waves when the waves in the plate reflect at the surface. Finally, the two independent modes are given in the form.

$$\xi_{zPj} = \frac{j\pi}{\bar{N}}, \quad j = 0,1,\cdots,\bar{N}-1 \tag{2.3.20a}$$

$$\xi_{zSj} = \frac{j\pi}{\bar{N}}, \quad j = 1,2,\cdots,\bar{N} \tag{2.3.20b}$$

Insert of equations (2.3.20a and b) into equation (2.3.13) can provide the spectrum equation in terms of the frequency, the horizontal wavenumber, and the modal index j, which is not shown in explicit form herein. For purpose of comparison, the two independent modes of the exact analytical solutions are introduced in the form without any detail derivation.

$$\xi_{zPj} = \frac{j\pi}{\bar{N}}, \quad j = 0,1,\cdots,\infty \tag{2.3.20c}$$

$$\xi_{zSj} = \frac{j\pi}{\bar{N}}, \quad j = 1,2,\cdots,\infty \tag{2.3.20d}$$

Next, consider the anti-symmetric mode, whose displacement fields are given in the form.

$$\mathbf{u}_l = \begin{Bmatrix} -i \sin \xi_{zP} l \ \phi_{Px} \\ \cos \xi_{zP} l \ \phi_{Pz} \end{Bmatrix} \bar{B} + \begin{Bmatrix} -i \sin \xi_{zS} l \ \phi_{Sx} \\ \cos \xi_{zS} l \ \phi_{Sz} \end{Bmatrix} \bar{D} \tag{2.3.21}$$

Substitution of equation (2.3.21) into equations (2.3.16a and b) yields

$$\begin{Bmatrix} w_{\bar{N}} \\ p_{x\bar{N}} \end{Bmatrix} = \begin{Bmatrix} (a_{11} \cos \xi_{zP} + b_{11}) \cos \xi_{zP} \bar{N} & (a_{11} \cos \xi_{zS} + b_{11}) \cos \xi_{zS} \bar{N} \\ a_{12}(a_{11} + b_{11} \cos \xi_{zP}) \cos \xi_{zP} \bar{N} & a_{12}(a_{11} + b_{11} \cos \xi_{zS}) \cos \xi_{zS} \bar{N} \end{Bmatrix} \begin{Bmatrix} \bar{B} \\ \bar{D} \end{Bmatrix} = \begin{Bmatrix} 0 \\ 0 \end{Bmatrix} \tag{2.3.22}$$

The associated spectrum equation is then given of the form.

$$f(\xi_x, \Omega) = a_{12} \cos \xi_{zP} \bar{N} \cos \xi_{zS} \bar{N} \cdot \cdot [(a_{11} \cos \xi_{zP} + b_{11})(a_{11} + b_{11} \cos \xi_{zS}) - (a_{11} \cos \xi_{zS} + b_{11})(a_{11} + b_{11} \cos \xi_{zP})] = 0 \tag{2.3.23}$$

Equation (2.3.23) again shows that the P and S wave components are independent of each other. Therefore, we have two independent modes in the form.

$$\xi_{zPj} = \frac{(j - \frac{1}{2})\pi}{\bar{N}}, \quad j = 1,2,\cdots,\bar{N} \tag{2.3.24a}$$

$$\xi_{zSj} = \frac{(j - \frac{1}{2})\pi}{\bar{N}}, \quad j = 1,2,\cdots,\bar{N} \tag{2.3.24b}$$

Insert of equations (2.3.24a and b) into equation (2.3.13) can yield the spectrum equation in terms of the frequency, the horizontal wavenumber, and the modal index j, which is not shown in explicit form herein. For reference, the two independent modes of the exact analytical solutions for the anti-symmetric modes are introduced in the form without any detail derivation.

$$\xi_{zPj} = \frac{(j - \frac{1}{2})\pi}{\bar{N}}, \quad j = 1,2,\cdots,\infty \tag{2.3.24c}$$

$$\xi_{zSj} = \frac{(j-\frac{1}{2})\pi}{\bar{N}}, \qquad j = 1,2,\cdots,\infty \tag{2.3.24d}$$

In one example of section 2.3.2, the eigenvalues for the plate of interest are numerically calculated for specified values of ρ, C_S, ν, H, and N, and then compared with the exact analytical solutions by means of the dispersion curves. In addition, three different combinations of tuning factors are applied to the TLM1 solutions in order to verify the best improvement in eigenvalues by virtue of the optimal values of tuning factors.

(2) Rayleigh surface waves on a half space

We next determine the spectrum equation for the Rayleigh surface wave on a discrete homogeneous half-space ($l \leq 0$). For this purpose, we need to remove two terms in equation (2.3.12a) that violate the radiation condition at $z = -\infty$, leading to the following displacement field.

$$\mathbf{u}_l = (AZ_P^l \boldsymbol{\phi}_P + CZ_S^l \boldsymbol{\phi}_S) e^{\mathrm{i}(\omega t - k_x x)}, \; l = 0, -1, -2, \ldots \tag{2.3.25}$$

where A and C are determined from the boundary conditions of interest, and the Z's are chosen such that $|Z| > 1.0$. In this particular problem, we have to apply the stress-free boundary condition at the surface, which by means of equation (2.3.4b) results in

$$\mathbf{0} = \mathbf{b}_0 \mathbf{u}_0 + \mathbf{a}\mathbf{u}_{-1} \tag{2.3.26}$$

Inserting (2.3.25) into (2.3.26), we obtain the following equation.

$$\begin{Bmatrix} 0 \\ 0 \end{Bmatrix} = \begin{bmatrix} C_{11} & C_{12} \\ C_{21} & C_{22} \end{bmatrix} \begin{Bmatrix} A \\ C \end{Bmatrix} \tag{2.3.27}$$

in which

$$C_{11} = b_{11}\phi_{Px} + b_{12}\phi_{Pz} + Z_P^{-1}(a_{11}\phi_{Px} + a_{12}\phi_{Pz})$$
$$C_{12} = b_{11}\phi_{Sx} + b_{12}\phi_{Sz} + Z_S^{-1}(a_{11}\phi_{Sx} + a_{12}\phi_{Sz})$$
$$C_{21} = b_{21}\phi_{Px} + b_{22}\phi_{Pz} + Z_P^{-1}(a_{21}\phi_{Px} + a_{22}\phi_{Pz})$$
$$C_{22} = b_{21}\phi_{Sx} + b_{22}\phi_{Sz} + Z_S^{-1}(a_{21}\phi_{Sx} + a_{22}\phi_{Sz})$$

A nontrivial solution to equation (2.3.27) exists only if the determinant of the coefficient matrix vanishes, leading to the following condition

$$\begin{vmatrix} C_{11} & C_{12} \\ C_{21} & C_{22} \end{vmatrix} = 0 \tag{2.3.28}$$

Equation (2.3.28) is the spectrum equation for the Rayleigh surface wave modeled with the TLM1. While the Rayleigh surface waves are *non-dispersive* in the continuum, they are *dispersive* in the TLM1 model, as will be seen in section 2.3.2. In section 2.3.2, three different combinations of tuning factors are again applied in order to investigate the effect of the tuning factors on the accuracy of eigenvalues obtained with the TLM1.

2.3.2 Numerical dispersion and tuning factors

In this section, we characterize the numerical dispersion of *SV-P* waves modeled with the TLM1 by means of the problems formulated in section 2.3.1 and an additional problem of Mindlin plate. To begin with, we explore the features of numerical dispersion of the body waves in a discrete homogeneous full-space. Then, we try to determine the optimal values for tuning factors in a similar fashion to section 2.2. Thereafter, to verify the improvement in eigenvalues achieved by

virtue of the optimal tuning factors, we solve three free-vibration problems such as a homogeneous plate with mixed boundary conditions, the Mindlin plate with stress-free boundary conditions, and the Rayleigh surface wave on a homogeneous half-space.

(1) Body waves

Here, we characterize the numerical dispersion of body waves in a discrete homogeneous full-space modeled with the TLM1 that is subjected to *SV-P* wave motion. For this goal, we compare the phase velocities V_S and V_P in equations (2.3.15a and b) and the polarization Θ in equation (2.3.9a) obtained with the TLM1 against those obtained from the continuum. Since the problem of interest is now in a plane-strain state, the Poisson's ratio ν possibly influences the numerical dispersion phenomena in the TLM1 model. Therefore, five Poisson's ratios of ν=0.0, 0.1, 0.2, 0.3, and 0.4 are considered. In addition, to show the effect of tuning factors on the numerical dispersion, the TLM1 model is calculated for three different mass matrices of fully lumped $\mathbf{M}_L$ (μ=0), tuned $\mathbf{M}_T$ (μ=0.55), and fully consistent $\mathbf{M}_C$ (μ=1) as setting α=β=1.0 for the matrix **A**.

Figures 2.3.4–8 show the numerical results for ν=0.0, 0.1, 0.2, 0.3, and 0.4, respectively. In each figure, the three quantities of V_S/C_S, V_P/C_P, and θ–Θ are shown as a function of the vertical wavenumber ξ_z and the propagation angle θ. The angles considered are θ=15, 30, 45, 60, and 75. To show the effect of tuning factors, all the results for the fully lumped mass matrix $\mathbf{M}_L$ (μ=0), the tuned mass matrix $\mathbf{M}_T$ (μ=0.55), and the fully consistent mass matrix $\mathbf{M}_C$ (μ=1) are shown together in each plot. The dashed, solid, and dotted lines represent the results for $\mathbf{M}_L$, $\mathbf{M}_T$ and $\mathbf{M}_C$, respectively.

It is observed in all the figures 2.3.4–8 that the TLM1 model for *SV-P* waves has the numerical dispersion that is dependent on the vertical wavenumber ξ_z and the propagation angle θ. Also, it is seen that the degree of the numerical dispersion is larger and larger as the two parameters of ξ_z and θ become larger and larger. As to the Poisson's ratio effect, it is shown that the dependency of the numerical dispersion on the Poisson's ratio exists, but is not significant. With regard to the polarization, confirmed are the two facts that are considered in section 2.3.1: (1) the polarization is independent of the mass tuning factor μ and (2) when setting α=β, the polarization is independent of the Poisson's ratio. In addition, it is noticed that the results computed for the tuned mass matrix with μ=0.55 ($\mathbf{M}_T$) are much better than those calculated for the fully lumped and consistent mass matrices, which is true especially for $\xi_z/\pi(=2h/\lambda_z) \leq 0.5$. By contrast, for $\xi_z/\pi > 0.5$, the degree of the numerical dispersion is significant regardless of the considered values of μ. This observation is identical to that for the TLM1 for *SH* wave in section 2.2. Therefore, the same range of ξ_z as the TLM1 for *SH* wave, i.e. $0<\xi_z/\pi<1/2$, is applied to determine the optimal tuning factors for the TLM1 for *SV-P* wave. Furthermore, the condition of $\xi_z/\pi<1/2$ again provides a lower bound for the number of thin layers per wavelength $N_\lambda(=\lambda_z/h)$ such that $N_\lambda \geq 4$.

(2) Tuning factors

We begin with the tuning factor μ for the mass matrix. We can argue that its optimal value must be 0.55 that is the optimal value of μ for the *SH* wave problems. The reason is as follows. When waves propagate only in the vertical direction (i.e. the horizontal wavenumber ξ_x is zero), the wave motion uncouples completely into two components of *SV* and *P* waves and the system behaves like a shear beam and a rod, respectively. Remember from section 2.2 that with setting ξ_x=0, the equation of motion for *SH* waves is identical to a shear beam, where the tuning factor μ is only involved. Inasmuch as the equations of motion for the shear beam and the rod obey the

same classical wave equation (even if they have different propagation speeds), it follows that the optimal value for μ for *SV-P* waves must be the same as that for *SH* waves. Also, it is already seen in figures 2.3.4–8 that the value of μ=0.55 indeed provides the smallest error among three cases of μ=0.00, 0.55, and 1.00. Therefore, in this section 2.3, we seek the optimal values for only the remaining tuning factors α and β in conjunction with a fixed, optimal value μ=0.55.

Next, we attempt to determine the optimal values for α and β in the matrix **A**. For this goal, we start with defining two error functions ε_S and ε_P for *S* and *P* waves, respectively, as

$$\varepsilon_S = \varepsilon_S(\alpha,\beta,\nu) = \int_0^{\pi/2}\left(\frac{V_S}{C_S}-1\right)^2 d\xi_z \tag{2.3.29a}$$

$$\varepsilon_P = \varepsilon_P(\alpha,\beta,\nu) = \int_0^{\pi/2}\left(\frac{V_P}{C_P}-1\right)^2 d\xi_z \tag{2.3.29b}$$

which provide the integrated squared errors over the significant range of ξ_z, $0 \le \xi_z/\pi (=2h/\lambda_z) \le 1/2$. Recognize that the error functions are now a function of not only α and β with a fixed value of μ=0.55, but also the Poisson's ration, because the problem of interest is in a plane-strain state.

Figures 2.3.9a–13b show the variation of the error functions ε_S and ε_P for the five different Poisson's ratios such as ν=0.0, 0.1, 0.2, 0.3, and 0.4 in terms of a standard surface plot. In each figure, considered are six different propagation angles of θ=15, 30, 45, 60, 75, and 90°. It is obvious that for each Poisson's ratio, there exists *no* optimal combination of α and β that can minimize both the error functions ε_S and ε_P regardless of the propagation angle θ. Meanwhile, it is noticed that for each Poisson's ratio, the variation of ε_S is in general more sensitive than the variation of ε_P with respect to α and β. This observation suggests that we may try to minimize the numerical dispersion error by means of only the *S* wave component rather than both the *S* and *P* wave components. It is shown in all the surface plots of ε_S that regardless of the propagation angle θ, the integrated squared error ε_S has its minimum value at the point of α=1.0 and β=1.0, even though there are some exceptions for small angles of θ=15 and/or 30°. Finally, we choose a set of α=1.0 and β=1.0 as the optimal tuning factors, which is nothing but the case of the fully consistent matrix **A**.

(3) Plate with mixed boundary conditions

Consider next the free-vibration of the homogeneous plate with mixed boundary conditions that is formulated in section 2.3.1. By solving this problem, we estimate the effect of the tuning factors on the accuracy of the eigenvalues computed from the TLM1. The geometry and material properties of the plate are given such that the thickness H=1.0, the mass density ρ=1.0, the shear velocity C_S=1.0, and the Poisson's ratio ν=0.31. In addition, for a discrete model, the plate is discretized into 12 thin layers, i.e. N=12, which produces 24 distinct eigenvalues (or modes) for the problem of interest. We also consider three combinations of tuning factors such as (i) α=β=1, μ=0 ($\mathbf{A}_C$+$\mathbf{M}_L$); (ii) α=β=1, μ=0.55 ($\mathbf{A}_C$+$\mathbf{M}_T$); and (iii) α=β=1, μ=1 ($\mathbf{A}_C$+$\mathbf{M}_C$). Then, we compare each of three with the exact analytical solutions.

Figures 2.3.14a, b, and c present the frequency-wavenumber dispersion of the TLM1 solutions (dashed lines) computed for (i) α=β=1, μ=0 ($\mathbf{A}_C$+$\mathbf{M}_L$); (ii) α=β=1, μ=0.55 ($\mathbf{A}_C$+$\mathbf{M}_T$); and (iii) α=β=1, μ=1 ($\mathbf{A}_C$+$\mathbf{M}_C$), respectively, in comparison with the exact analytical solution (solid lines). In each figure, the symmetric and anti-symmetric modes are plotted separately. It is observed that the use of the optimal values of α=β=1, μ=0.55 ($\mathbf{A}_C$+$\mathbf{M}_T$) produces the best agreement with the

exact analytical solution. So, it is proved that the optimal tuning factors improve the accuracy of the eigenvalues computed from the TLM1. In addition, it must be noticed that this improvement is achieved only for 8 or 10 modes, not for all the 24 computed modes. Remember that some similar results are observed for the *SH* wave problem in section 2.2 in which it is seen that only the first half of the set of all computed modes are accurate with the help of the optimal tuning factors. Similarly, it is concluded for this problem of *SV-P* wave that only the one-third (=8/24) of the set of all computed modes are accurate with the application of the optimal tuning factors.

(4) Mindlin plate

Here, we consider an additional problem that is not formulated in section 2.3.1. The problem is the free-vibration of the homogeneous plate with stress-free conditions at the both top and bottom surfaces whose exact analytical solutions are derived and presented in chapter 4. By solving this problem, we again estimate the effect of the tuning factors on the accuracy of the eigenvalues computed from the TLM1. The geometry and material properties of the homogeneous plate are the exactly same as those of the plate with mixed boundary conditions, i.e. $\rho=C_S=H=1.0$ and $\nu=0.31$. For a discrete model, the plate is discretized again into 12 thin layers, i.e. $N=12$, which produces 26 distinct eigenvalues (or modes) for the problem of interest. We again consider three combinations of tuning factors such as (i) $\alpha=\beta=1$, $\mu=0$ ($\mathbf{A}_C+\mathbf{M}_L$); (ii) $\alpha=\beta=1$, $\mu=0.55$ ($\mathbf{A}_C+\mathbf{M}_T$); and (iii) $\alpha=\beta=1$, $\mu=1$ ($\mathbf{A}_C+\mathbf{M}_C$). Then, we compare each of three with the exact analytical solutions.

Figures 2.3.15a, b, and c present the frequency-wavenumber dispersion of the TLM1 solutions (dashed lines) computed for (i) $\alpha=\beta=1$, $\mu=0$ ($\mathbf{A}_C+\mathbf{M}_L$); (ii) $\alpha=\beta=1$, $\mu=0.55$ ($\mathbf{A}_C+\mathbf{M}_T$); and (iii) $\alpha=\beta=1$, $\mu=1$ ($\mathbf{A}_C+\mathbf{M}_C$), respectively, in comparison with the exact analytical solution (solid lines). In each figure, the symmetric and anti-symmetric modes are plotted separately for convenience in comparison. It is confirmed that the use of the optimal values of $\alpha=\beta=1$, $\mu=0.55$ ($\mathbf{A}_C+\mathbf{M}_T$) indeed produces the best agreement with the exact analytical solution. So, it is verified once again that the optimal tuning factors improve the accuracy of the eigenvalues computed from the TLM1 for *SV-P* wave problems. Also, note that this improvement is achieved only for about 10 modes. Therefore, it is again concluded that for the *SV-P* wave problem only about the one-third of the set of all computed modes are accurate with the application of the optimal tuning factors.

(5) Rayleigh surface waves in a homogeneous half-space.

We consider the problem of Rayleigh surface wave on a discrete homogeneous half-space that is formulated by means of the TLM1 in section 2.3.1. As numerically solving this problem of semi-infinite domain, we explore the influence of the optimal tuning factors on the accuracy of the TLM1 in terms of eigenvalues. The material properties of the homogeneous half-space are given such that the mass density ρ and the shear velocity C_S are both 1.0 and the Poisson's ratio ν is 0.31. We consider three combinations of tuning factors such as (i) $\alpha=\beta=1$, $\mu=0$ ($\mathbf{A}_C+\mathbf{M}_L$); (ii) $\alpha=\beta=1$, $\mu=0.55$ ($\mathbf{A}_C+\mathbf{M}_T$); and (iii) $\alpha=\beta=1$, $\mu=1$ ($\mathbf{A}_C+\mathbf{M}_C$) and compute the apparent phase velocity of the Rayleigh surface wave V_R for each combination. Then, we compare them with the true exact phase velocity C_R that is 0.9289 in the present problem.

Figure 2.3.16 presents the variation of V_R/C_R as a function of the horizontal wavenumber ξ_x for all the three combinations of tuning factors: (i) $\alpha=\beta=1$, $\mu=0$ ($\mathbf{A}_C+\mathbf{M}_L$, dotted line); (ii) $\alpha=\beta=1$, $\mu=0.55$ ($\mathbf{A}_C+\mathbf{M}_T$, solid line); and (iii) $\alpha=\beta=1$, $\mu=1$ ($\mathbf{A}_C+\mathbf{M}_C$, dashed line). Notice first that the apparent phase velocity for the Rayleigh surface wave V_R is dispersive, i.e. a function of ξ_x, while

the true phase velocity C_R is non-dispersive in the continuum. Next, it is seen that the combination of $\alpha=\beta=1$, $\mu=0$ ($\mathbf{A}_C+\mathbf{M}_L$, dotted line) shows the best agreement with the exact solution for the range of the horizontal wavenumber ξ_x of interest. Therefore, it is revealed that the optimal tuning factors of $\alpha=\beta=1$ and $\mu=0.55$ do not improve to the best degree the accuracy of the TLM1 concerned with the semi-infinite media of interest. However, it should be realized that the degree of the numerical dispersion errors for all the three combinations is quite small. The reason is that the Rayleigh surface wave propagates only in the horizontal direction in which the TLM does not discretize.

2.3.3 Summary

In the first part of this section 2.3, the general solution and the frequency-wavenumber spectrum are obtained for the discrete *SV-P* wave equation modeled with the TLM1. The qualitative investigation of the spectrum has provided the convention for the wavelength along the discretization direction λ_z and the discretization size h, i.e. $\lambda_z \geq 2h$, which is exactly the same as *SH* wave modeled with the TLM1. In addition, it is observed that for the high vertical wavenumbers, e.g. $\xi_z=0.75\pi$, the TLM1 for *SV-P* wave possibly produce less accurate results than the TLM1 for *SH* wave. Then, two guided wave problems are solved formally and perfectly by means of the obtained general solutions.

In the second part, extensive characterization of the *SV-P* body waves is performed for five Poisson's ratios of $\nu=0.0$, 0.1, 0.2, 0.3, and 0.4. It is confirmed that for the TLM1 model, the range of $0<\xi_z/\pi<1/2$ is only useful as determining the optimal tuning factors, and furthermore provides a lower bound for the number of thin layers per wavelength $N_\lambda(=\lambda_z/h)$ such that $N_\lambda \geq 4$. Then, the calculation of the error functions $\varepsilon_S(\alpha,\beta)$ and $\varepsilon_P(\alpha,\beta)$ has determined the optimal tuning factors as $\alpha=\beta=1$ and $\mu=0.55$. By analyzing two free-vibration problems of finite domain, it is verified that the optimal tuning factors indeed improve the accuracy of the eigenvalues in the context of the TLM. In addition, it is found that for *SV-P* wave problems, only the one-third of the set of all computed modes are accurate with the application of the optimal tuning factors. In the last problem, the Rayleigh surface wave is considered. Interestingly, it is observed that the optimal tuning factors of $\alpha=\beta=1$ and $\mu=0.55$ do not improve to the best degree the accuracy of the TLM1. Instead, the tuning factors of $\alpha=\beta=1$ and $\mu=0$ (the case of fully lumped mass matrix) shows the best agreement with the exact solution concerned with the semi-infinite media of interest.

2.4 Anti-plane (*SH*) waves with quadratic expansion TLM

In this section, we consider the propagation of *SH* waves modeled with the TLM that is based on a quadratic expansion, or TLM2 for short. In the first part of this section, we obtain the general solution and the frequency-wavenumber spectrum for the discrete *SH* wave equation modeled with the TLM2. It is revealed that there are two independent branches in the TLM2 model such as *acoustical* and *optical* branches. Thereafter, by means of a qualitative investigation of this spectrum, we find a reference frame for judging the dimensionless wavenumbers in discrete models. Then, we formulate and solve three guided wave problems in close form whose exact analytical solutions are known in closed form for the continuum.

In the second part, we characterize the numerical dispersion as a function of vertical direction wavenumber (ξ_z) and direction of propagation (θ) by estimating frequencies and phase velocities. Through these characterizations, we obtain the optimal tuning factors that are valid only for a certain range of vertical direction wavenumber (ξ_z). Based on the range of ξ_z, we also propose a lower bound for the number of TLM2 thin layers per wavelength. We then consider two numerical examples of finite and semi-infinite domains. In these two examples, we compare the TLM2 solution with the exact analytical solutions in order to confirm the validity of the optimal tuning factors. As an additional result, we can also judge the extent to which the optimal tuning factors improve the accuracy of the eigenvalues computed with the TLM2.

2.4.1 Discrete solutions for anti-plane problems

Consider a single TLM2 thin layer subjected to *SH* wave motion as depicted in figure 2.4.1. It is noted that there exists an internal node indicated by v_l' that does not exist in the TLM1. The discrete governing equation for this single layer is obtained in the following.

$$\mathbf{P}_l = \mathbf{K}\mathbf{U}_l \tag{2.4.1}$$

where

$$\mathbf{P}_l = \{p_l \quad p'_l \quad p_{l-1}\}^T \qquad \text{: consistent external traction vector} \tag{2.4.2a}$$

$$\mathbf{U}_l = \{v_l \quad v'_l \quad v_{l-1}\}^T \qquad \text{: displacement vector} \tag{2.4.2b}$$

$$\mathbf{K} = \mathbf{A}k_x^2 + \mathbf{G} - \omega^2\mathbf{M} \qquad \text{: stiffness matrix} \tag{2.4.2c}$$

$$\mathbf{A} = (1-\beta)\mathbf{A}_C + \beta\mathbf{A}_L \tag{2.4.3a}$$

$$\mathbf{A}_C = \frac{Gh}{30}\begin{Bmatrix} 4 & 2 & -1 \\ 2 & 16 & 2 \\ -1 & 2 & 4 \end{Bmatrix}, \qquad \mathbf{A}_L = \frac{Gh}{30}\begin{Bmatrix} 5 & \cdot & \cdot \\ \cdot & 20 & \cdot \\ \cdot & \cdot & 5 \end{Bmatrix} \tag{2.4.3bc}$$

$$\mathbf{G} = \frac{G}{3h}\begin{Bmatrix} 7 & -8 & 1 \\ -8 & 16 & -8 \\ 1 & -8 & 7 \end{Bmatrix} \tag{2.4.3d}$$

$$\mathbf{M} = (1-\mu)\mathbf{M}_L + \mu\mathbf{M}_C \tag{2.4.3e}$$

$$\mathbf{M}_C = \frac{\rho h\omega^2}{30}\begin{Bmatrix} 4 & 2 & -1 \\ 2 & 16 & 2 \\ -1 & 2 & 4 \end{Bmatrix}, \qquad \mathbf{M}_L = \frac{\rho h\omega^2}{30}\begin{Bmatrix} 5 & \cdot & \cdot \\ \cdot & 20 & \cdot \\ \cdot & \cdot & 5 \end{Bmatrix} \tag{2.4.3fg}$$

In the above expressions, p'_l and v'_l are the traction and displacement at the internal node. The other notations and subscripts have the same meanings as those in section 2.2. Also, four auxiliary parameters and three dimensionless variables are introduced as follows.

$$a = -\beta\xi_x^2 + 10 + \mu\Omega^2$$
$$a' = 2\beta\xi_x^2 - 80 - 2\mu\Omega^2$$
$$b = (5-\beta)\xi_x^2 + 70 - (5-\mu)\Omega^2$$
$$b' = 2(5-\beta)\xi_x^2 + 80 - 2(5-\mu)\Omega^2$$
$$\xi_x = k_x h, \qquad \xi_z = k_z h, \qquad \text{and} \qquad \Omega = \frac{\omega h}{C_S}.$$

Assembling identical governing equations such as equation (2.4.1) with recourse to the above auxiliary parameters, we obtain the discrete *SH* wave equation modeled with the TLM2 as

$$\mathbf{P}_l = \begin{Bmatrix} p_l \\ p'_l \end{Bmatrix} = \frac{G}{30h} \begin{Bmatrix} av_{l+1} + a'v'_{l+1} + 2bv_l + a'v'_l + av_{l-1} \\ a'v_l + 2b'v'_l + a'v_{l-1} \end{Bmatrix} \tag{2.4.4a}$$

In the case of semi-infinite media, we need to apply the boundary condition at the top surface l=0 as

$$p_0 = \frac{G}{30h}\{bv_0 + a'v'_0 + av_{-1}\} \tag{2.4.4b}$$

To obtain the general solution to the discrete *SH* wave equation in equation (2.4.4a), we set $\mathbf{P}_l$=**0** and assume the displacement field of v_l and v'_l in the form.

$$v_l = AZ^{2l} \quad \text{and} \quad v'_l = A'Z^{2l-1} \tag{2.4.5ab}$$

Substituting equations (2.4.5a and b) into equation (2.4.4a) and dividing the first and second rows by Z^{2l} and Z^{2l-1}, respectively, we obtain the following equation.

$$\begin{Bmatrix} a(Z^2 + Z^{-2}) + 2b & a'(Z + Z^{-1}) \\ a'(Z + Z^{-1}) & 2b' \end{Bmatrix} \begin{Bmatrix} A \\ A' \end{Bmatrix} = \begin{Bmatrix} 0 \\ 0 \end{Bmatrix} \tag{2.4.6a}$$

or

$$\begin{Bmatrix} 4aY^2 - 2(a-b) & 2a'Y \\ 2a'Y & 2b' \end{Bmatrix} \begin{Bmatrix} A \\ A' \end{Bmatrix} = \begin{Bmatrix} 0 \\ 0 \end{Bmatrix} \tag{2.4.6b}$$

or

$$\left[\begin{Bmatrix} 10 - 4\beta Y^2 & 4\beta Y \\ 4\beta Y & 4(5-\beta) \end{Bmatrix} \xi_x^2 + \begin{Bmatrix} 120 + 40Y^2 & -160Y \\ -160Y & 160 \end{Bmatrix} - \begin{Bmatrix} 10 - 4\mu Y^2 & 4\mu Y \\ 4\mu Y & 4(5-\mu) \end{Bmatrix} \Omega^2 \right] \begin{Bmatrix} A \\ A' \end{Bmatrix} = \begin{Bmatrix} 0 \\ 0 \end{Bmatrix} \tag{2.4.6c}$$

where $Y = \frac{1}{2}(Z + Z^{-1})$. This homogeneous set of equations has a non-trivial solution only if its determinant of the coefficient matrix vanishes. From this condition, the two eigenvalues and eigenvectors are obtained of the form

$$Y_{\text{aco,opt}} = \pm\sqrt{\frac{(a-b)b'}{(2ab' - a'^2)}} \tag{2.4.7a}$$

$$\begin{Bmatrix} A \\ A' \end{Bmatrix}_{\text{aco,opt}} = \begin{Bmatrix} 1 \\ -\dfrac{a'}{b'} Y_{\text{aco,opt}} \end{Bmatrix} = \begin{Bmatrix} 1 \\ c_{\text{aco,opt}} \end{Bmatrix} \tag{2.4.7b}$$

As shown in equations (2.4.7a and b), there exist two solutions, i.e. Y_{aco} and $Y_{opt}(=-Y_{aco})$. The one is the acoustical branch, i.e. sgn $c_{aco} = 1$, and the other is the optical branch, i.e. sgn $c_{opt} = -1$. As already discussed in the case of the TLM1, each solution has two components $Z_{1,2}$ that propagate in opposite directions, and are given by

$$Z_{aco\,1,2} = Y_{aco} \pm \sqrt{Y_{aco}^2 - 1} \tag{2.4.8a}$$

$$Z_{opt\,1,2} = Y_{opt} \pm \sqrt{Y_{opt}^2 - 1} \tag{2.4.8b}$$

or

$$Z_{aco1,2} = e^{\pm i\frac{\xi_{z,aco}}{2}} = \cos\frac{\xi_{z,aco}}{2} \pm i\sin\frac{\xi_{z,aco}}{2} \tag{2.4.9a}$$

$$Z_{opt1,2} = e^{\pm i\frac{\xi_{z,aco}}{2}} = \cos\frac{\xi_{z,aco}}{2} \pm i\sin\frac{\xi_{z,aco}}{2} \tag{2.4.9b}$$

Therefore, the general solution is expressed in the form.

$$v_l = A_{aco}Z_{aco}^{2l} + B_{aco}Z_{aco}^{-2l} + A_{opt}Z_{opt}^{2l} + B_{opt}Z_{otp}^{-2l} \tag{2.4.10a}$$

$$v'_l = c_{aco}[A_{aco}Z_{aco}^{2l-1} + B_{aco}Z_{aco}^{-2l+1}] + c_{opt}[A_{opt}Z_{opt}^{2l-1} + B_{opt}Z_{opt}^{-2l+1}] \tag{2.4.10b}$$

Also, it can be deduced from equation (2.4.7a) that these acoustical and optical solutions have a relationship of $Z_{opt}=-1/Z_{aco}$, i.e. complex conjugate relationship. Then, equations (2.4.10a and b) can be expressed in terms of only the acoustical component as follows.

$$v_l = (A_{aco} + B_{opt})Z_{aco}^{2l} + (B_{aco} + A_{opt})Z_{aco}^{-2l} \tag{2.4.11a}$$

$$v'_l = c_{aco}[(A_{aco} + B_{opt})Z_{aco}^{2l-1} + (B_{aco} + A_{opt})Z_{aco}^{-2l+1}] \tag{2.4.11b}$$

Finally, we may obtain the general solution of the form

$$v_l = AZ_{aco}^{2l} + BZ_{aco}^{-2l} \tag{2.4.12a}$$

$$v'_l = c_{aco}[AZ_{aco}^{2l-1} + BZ_{aco}^{-2l+1}] \tag{2.4.12b}$$

or equivalently

$$v_l = \bar{A}\cos l\xi_{z,aco} + i\bar{B}\sin l\xi_{z,aco} \tag{2.4.13a}$$

$$v'_l = c_{aco}[\bar{A}\cos\frac{(2l-1)}{2}\xi_{z,aco} + i\bar{B}\sin\frac{(2l-1)}{2}\xi_{z,aco}] \tag{2.4.13b}$$

in which A and B (or $\bar{A}$ and $\bar{B}$) are the unknown constants to be determined from the boundary conditions of interest. Substitution of equations (2.4.13a and b) into equation (2.4.4) produces after tedious manipulations the frequency-wavenumber spectrum in more explicit form

$$\left|\begin{Bmatrix} 10-4\beta Y_{aco}^2 & 4\beta Y_{aco} \\ 4\beta Y_{aco} & 4(5-\beta) \end{Bmatrix}\xi_x^2 + \begin{Bmatrix} 120+40Y_{aco}^2 & -160Y_{aco} \\ -160Y_{aco} & 160 \end{Bmatrix} - \begin{Bmatrix} 10-4\mu Y_{aco}^2 & 4\mu Y_{aco} \\ 4\mu Y_{aco} & 4(5-\mu) \end{Bmatrix}\Omega^2\right| = 0 \tag{2.4.14}$$

in which

$$Y_{aco} = \frac{1}{2}(Z_{aco,1} + Z_{aco,2}) = \cos\frac{\xi_{z,aco}}{2} \tag{2.4.15a}$$

$$\xi_x = k_x h = kh\cos\theta = \frac{2\pi h\cos\theta}{\lambda} = \frac{2\pi h\cot\theta}{\lambda_z} \tag{2.4.15b}$$

$$\xi_z = k_z h = kh\sin\theta = \frac{2\pi h\sin\theta}{\lambda} = \frac{2\pi h}{\lambda_z} \tag{2.4.15c}$$

with k and λ being the wavenumber and wavelength along the wave propagation direction θ. It can be shown that for very low wavenumbers (or very long wavelengths) in the z direction, the spectrum equation (2.4.14) approaches the exact one for a continuous medium, i.e. $\omega = C_S k = C_S\sqrt{k_x^2 + k_z^2}$ or equivalently $\Omega = \sqrt{\xi_x^2 + \xi_z^2}$. Having found the relationship between frequency and wavenumbers from equation (2.4.14), we can obtain the apparent phase velocities as

$$V = \frac{\omega}{k} \quad : \text{phase velocity in the propagation direction} \tag{2.4.16a}$$

$$V_x = \frac{\omega}{k_x} \quad : x \text{ component of phase velocity} \tag{2.4.16b}$$

$$V_z = \frac{\omega}{k_z} \quad : z \text{ component of phase velocity} \tag{2.4.16c}$$

Figures 2.4.2 and 2.4.3 present a qualitative comparison of the frequency-wavenumber spectrum obtained with the TLM2 against the exact analytical spectrum. Note in each figure that a dashed and dot-dashed line represents the acoustical and optical branches, respectively, and a solid line represents the exact analytical spectrum. The first figure shows the numerical dispersion for a fixed horizontal wavenumber (ξ_x=0.5π and ξ_x=π) as a function of vertical wavenumber ξ_z, while the second shows the numerical dispersion for a fixed vertical wavenumber (ξ_z=0.5π and ξ_z=1.5π) as a function of horizontal wavenumber ξ_x. In either case, the TLM2 model is computed for fully consistent matrices, that is, the tuning factors used are β=μ=1.0.

In figure 2.4.2, observe first that the acoustical and optical branches cross each other at ξ_z/π=1 with respect to which there is symmetry between the two branches. This observation can be deduced from equation (2.4.7a) as well. In addition, at the cross point, i.e. ξ_z/π=1, exists a short complex branch that corresponds to the so-called stopping band region in Ω where no harmonic wave motion (or no propagation mode) exists at all in the TLM2 model. Along the acoustical branches, it is shown that the numerical dispersion occurs mostly in the high vertical wavenumber region as seen in the TLM1 in sections 2.2 and 2.3. Also, observed are some ambiguous phenomena such as the regions of negative group velocity and the periodicity as the case of the TLM1. In order to avoid this ambiguity, we adopt the convention for the wavenumber ξ_z or equivalently wavelength λ_z in the TLM2

$$0 < \mathrm{Re}\,\xi_z (= \mathrm{Re}\,k_z h = \mathrm{Re}\frac{2\pi}{\lambda_z} h) < 2.0\pi \text{ or equivalently } 0 < \mathrm{Re}\frac{2h}{\lambda_z} < 2.0 \tag{2.4.17}$$

This convention states that the wavelength along the discretization direction, λ_z, must be longer than the discretization size h. The same convention will be valid for the *SV-P* waves modeled with the TLM2.

It is recognized in figure 2.4.3 that the acoustical and optical branches exist together, but they do not cross each other as the case of figure 2.4.2. Then, notice in the left plot that the acoustical branch is remarkably identical to the exact analytical branch. It is also observed that high horizontal wavenumbers produce smaller numerical dispersion than the low horizontal wavenumbers for a given vertical wavenumber. The reason is that the high horizontal wavenumbers involve waves that propagate nearly horizontally as already explained in sections 2.2 and 2.3.

We next determine the spectrum equations for three canonical problems: (1) a discrete homogeneous stratum, (2) a discrete homogenous plate, and (3) Love waves in a layer underlain by a half space by means of the TLM2 model. In section 2.4.2, we numerically compare the eigenvalues obtained from the discrete and exact analytical solutions for only the second and third problems and seek to improve the discrete solutions with the aid of the optimal tuning factors β and μ.

(1) Homogeneous stratum

Consider a discrete homogeneous stratum of total depth H that consists of N TLM2 thin layers. The associated boundary conditions such as zero stress at the top surface (l=0) and zero displacement at the bottom (l=-N) are expressed as

$$p_0 = 0 \qquad \text{at } l=0 \tag{2.4.18a}$$

$$v_{-N} = 0 \qquad \text{at } l=N \tag{2.4.18b}$$

We substitute equations (2.4.12) into equations (2.4.18) to obtain the following condition in matrix form.

$$\begin{Bmatrix} b + a'c_{aco}\cos\frac{\xi_z}{2} + a\cos\xi_z & a'c_{aco}\sin\frac{\xi_z}{2} + a\sin\xi_z \\ \cos N\xi_z & \sin N\xi_z \end{Bmatrix} \begin{Bmatrix} \bar{A} \\ -i\bar{B} \end{Bmatrix} = \begin{Bmatrix} 0 \\ 0 \end{Bmatrix} \tag{2.4.19}$$

Solving the associated eigenvalue problem, we obtain the spectrum equation in closed form as

$$\left| \begin{Bmatrix} 10-4\beta Y_j^2 & 4\beta Y_j \\ 4\beta Y_j & 4(5-\beta) \end{Bmatrix} \xi_x^2 + \begin{Bmatrix} 120+40Y_j^2 & -160Y_j \\ -160Y_j & 160 \end{Bmatrix} - \begin{Bmatrix} 10-4\mu Y_j^2 & 4\mu Y_j \\ 4\mu Y_j & 4(5-\mu) \end{Bmatrix} \Omega^2 \right| = 0 \tag{2.4.20a}$$

in which

$$Y_j = \cos\frac{\xi_{z,j}}{2}, \quad h = \frac{H}{N}, \quad \xi_{zj} = \frac{(j-\frac{1}{2})\pi}{N}, \quad j = 1,2,\ldots,2N$$

For comparison, we present the exact analytical solution to the continuous homogeneous stratum in dimensionless form.

$$\Omega = \frac{\omega h}{C_S} = \sqrt{\xi_x^2 + \left((j-\tfrac{1}{2})\frac{\pi h}{H}\right)^2} \qquad j = 0,1,2,\cdots \tag{2.4.20b}$$

Notice that $2N$ distinct eigenvalues (or modes) are available in the TLM2 model of interest, while N distinct eigenvalues are achieved from the TLM1 model in section 2.2.2. It is also noted that for very small ξ_{zj} the two equations (2.4.20a and b) become identical regardless of the values of tuning factors β and μ in use. Therefore, it is concluded that the use of sufficiently large N can produce the exact values for first few eigenvalues of interest.

(2) Homogeneous plate

Consider next a discrete homogenous plate of thickness H, composed of N TLM2 thin layers. The two boundary conditions of traction-free surfaces are given as

$$p_0 = 0 \qquad \text{at } l=0 \tag{2.4.21a}$$

$$p_{-N} = 0 \qquad \text{at } l=-N \tag{2.4.21b}$$

We substitute equations (2.4.12) into equations (2.4.21) and obtain the next condition in matrix form.

$$\begin{Bmatrix} b+a'c_{aco}\cos\frac{\xi_z}{2}+a\cos\xi_z & a'c_{aco}\sin\frac{\xi_z}{2}+a\sin\xi_z \\ a\cos(N-1)\xi_z+a'c_{aco}\cos(2N-1)\frac{\xi_z}{2}+b\cos N\xi_z & a\sin(N-1)\xi_z+a'c_{aco}\sin(2N-1)\frac{\xi_z}{2}+b\sin N\xi_z \end{Bmatrix} \begin{Bmatrix} \bar{A} \\ -i\bar{B} \end{Bmatrix} = \begin{Bmatrix} 0 \\ 0 \end{Bmatrix} \tag{2.4.22}$$

The associated eigenvalue problem yields the spectrum equation in closed form as

$$\left| \begin{bmatrix} 10-4\beta Y_j^2 & 4\beta Y_j \\ 4\beta Y_j & 4(5-\beta) \end{bmatrix} \xi_x^2 + \begin{bmatrix} 120+40Y_j^2 & -160Y_j \\ -160Y_j & 160 \end{bmatrix} - \begin{bmatrix} 10-4\mu Y_j^2 & 4\mu Y_j \\ 4\mu Y_j & 4(5-\mu) \end{bmatrix} \Omega^2 \right| = 0 \tag{2.4.23a}$$

in which

$$Y_j = \cos\frac{\xi_{z,j}}{2}, \quad h=\frac{H}{N}, \quad \xi_{zj}=\frac{j\pi}{N}, \quad j=0,1,\ldots,2N$$

It is noticed that only $2N+1$ distinct eigenvalues (or modes) are obtained from the TLM2 model of interest. For comparison, we introduce the exact analytical solution to the continuous homogeneous plate in dimensionless form

$$\Omega=\frac{\omega h}{C_S}=\sqrt{\xi_x^2+\left(j\frac{\pi h}{H}\right)^2} \qquad j=0,1,2,\cdots \tag{2.4.23b}$$

In section 2.4.2, we numerically calculate the $2N+1$ distinct eigenvalues of this discrete plate with specified values for C_S, H, and N and compare them with the exact analytical solution by means of the dispersion curves. In addition, we consider four combinations of tuning factors and prove the best improvement in eigenvalues with the help of the optimal tuning factors.

(3) Love waves

We consider the guided waves in a discrete homogenous layer over a discrete elastic half space, i.e. so-called Love wave problem in the continuum. The upper layer has total thickness H and is composed of N TLM2 thin layers. The wave speed of the upper layer is slower than that of the half-space. The discrete half space is composed of an infinite number of TLM2 thin layers, and the interface coincides with the x-axis. This example is more complicated than the two previous ones, because two displacement fields are now involved, namely v_L for the upper layer and v_H for the half space. The relevant expressions for the general solutions are now

$$v_{Ll}=\bar{A}_L\cos l\xi_{zL}+\mathrm{i}\bar{B}_L\sin l\xi_{zL} \tag{2.4.24a}$$

$$v'_{Ll}=c_{acoL}[\bar{A}_L\cos\frac{(2l-1)}{2}\xi_{zL}+\mathrm{i}\bar{B}_L\sin\frac{(2l-1)}{2}\xi_{zL}] \tag{2.4.24b}$$

$$v_{Hl}=A_H Z_H^{2l} \tag{2.4.24c}$$

$$v'_{Hl}=c_{acoH}A_H Z_H^{2l-1} \tag{2.4.24d}$$

The subscripts L and H identify the upper layer and the half space, respectively. Equations (2.4.24cd) contain only one term, because $v_{H,l}$ and $v'_{H,l}$ must satisfy the radiation condition, i.e. $|Z_H| > 1$ for $l < 0$. The boundary conditions are a stress-free condition at the top surface and two continuity conditions for the displacement and stress at the interface given by

1) stress-free condition at $z = H$, $(l = N)$: $p_{LN} = 0$ (2.4.25a)

2) displacement continuity at $z = 0$, $(l = 0)$: $v_{L0} - v_{H0} = 0$ (2.4.25b)

3) stress continuity at $z = 0$, $(l = 0)$: $p_{L0} + p_{H0} = 0$ (2.4.25c)

We substitute equations (2.4.24) into the above boundary conditions and obtain the next condition in matrix form.

$$\begin{Bmatrix} C_{11} & C_{12} & C_{13} \\ C_{21} & C_{22} & C_{23} \\ C_{31} & C_{32} & C_{33} \end{Bmatrix} \begin{Bmatrix} \bar{A}_L \\ \mathrm{i}\bar{B}_L \\ A_H \end{Bmatrix} = \begin{Bmatrix} 0 \\ 0 \\ 0 \end{Bmatrix} \tag{2.4.25d}$$

where

$$C_{11} = b_L \cos N\xi_{zL} + a'_L c_{acoL} \cos(2N-1)\frac{\xi_{zL}}{2} + a_L \cos(N-1)\xi_{zL}$$

$$C_{12} = b_L \sin N\xi_{zL} + a'_L c_{acoL} \sin(2N-1)\frac{\xi_{zL}}{2} + a_L \sin(N-1)\xi_{zL}$$

$$C_{31} = a_L \cos\xi_{zL} + a'_L c_{acoL} \cos\frac{\xi_{zL}}{2} + b_L$$

$$C_{32} = a_L \sin\xi_{zL} + a'_L c_{acoL} \sin\frac{\xi_{zL}}{2}$$

$$C_{33} = \kappa\left[a_H Z_H^{-2} + a'_H c_{acoH} Z_H^{-1} + b_H\right]$$

$$C_{21} = -C_{23} = 1$$

$$C_{13} = C_{22} = 0$$

$$\kappa = \frac{G_H}{G_L}\frac{h_L}{h_H}$$

Solving a system of equation (2.4.25d) for nontrivial solutions for $\bar{A}_L$, $\bar{B}_L$, and A_H, we obtain the Love wave modes for the discrete system. The eigenvalues in this problem cannot, however, be obtained in closed form, so a numerical search technique is required to find out the propagation modes.

In section 2.4.2, we perform numerical analysis to calculate the $2N$ eigenvalues (or branches) of this discrete layered half-space with specified values for G_H, G_L, h_L, H, and N and compare them with the associated exact solution by means of the dispersion curves. Also, we consider three combinations of tuning factors and verify the best improvement in eigenvalues with the help of the optimal tuning factors to be determined in section 2.4.2.

2.4.2 Numerical dispersion and tuning factors

In this section, we characterize the numerical dispersion of *SH* waves modeled with the TLM2 by means of the canonical problems formulated in section 2.4.1. The problems are (1) body waves propagating vertically, (2) body waves propagating at an angle to the horizontal axis, (3) a homogeneous plate, and (4) Love waves in a layer underlain by a half space. From the first two

examples, we determine the optimal tuning factors of β and μ and propose a lower bound for the number of thin layers per wavelength N_λ. Thereafter, we apply the optimal tuning factors to the last two problems to verify that the optimal tuning factors improve best the propagation modes computed from the TLM2.

(1) Body waves propagating vertically: tuning factor μ

Here, we again consider a particular *SH* wave that propagates only in the vertical direction. So, it follows that there is no variation in the horizontal direction, i.e. ξ_x=0. Setting ξ_x=0 in equation (2.4.14) and formally solving the associated eigenvalue problem, we obtain the spectrum equation for Ω.

$$\left[5-\mu\left(3-2\sin^2\frac{\xi_z}{2}\right)\right]\Omega^4-2\left[60-2(5+3\mu)\sin^2\frac{\xi_z}{2}\right]\Omega^2+480\sin^2\frac{\xi_z}{2}=0 \qquad (2.4.26a)$$

or simply

$$A\Omega^4-2B\Omega^2+C=0 \qquad (2.4.26b)$$

Notice that equation (2.4.26a or b) contains only one tuning factor, namely μ. Then, the apparent phase velocity V_z is then calculated as follows.

$$V_z=\frac{\omega}{k_z}=\frac{\Omega}{\xi_z} \qquad (2.4.27)$$

To explore the numerical dispersion characteristics of this wave, the apparent phase velocity V_z in equation (2.4.27) is computed for four different values of μ=0, 1/3, 2/3, and 1. Figure 2.4.4 displays the ratio of V_z to C_z(=C_S) as a function of wavenumber ξ_z and the tuning factor μ. Note that C_z is the true phase velocity of the exact analytical solution. It is seen that there is a discontinuity at ξ_z=1.0π where the stopping band exists. As a result, significant numerical dispersion can occur around ξ_z=1.0π. It is also anticipated that an optimal value for μ is about 1/3 and will be effective only for the range of $0\le\xi_z\le(4/5)\pi$. In other words, the optimal tuning factor μ will not improve the accuracy of *SH* waves that are involved with the range of $\xi_z\ge(4/5)\pi$. Remember that some similar observation has been discussed in section 2.2. In addition, this condition of $0\le\xi_z\le(4/5)\pi$ gives a lower bound for the number of TLM2 thin layers per wavelength $N_\lambda(=\lambda_z/h)$ such that $N_\lambda\ge5/2$.

To estimate the error caused by the numerical dispersion in the present example, we define an error function ε as

$$\varepsilon=\int_0^{(4/5)\pi}d\varepsilon=\int_0^{(4/5)\pi}\left(\frac{V_z(\xi_z,\mu)}{C_z}-1\right)^2 d\xi_z \qquad (2.4.28)$$

which estimates the integrated squared error for $0\le\xi_z\le(4/5)\pi$. Figure 2.4.5 shows the error function ε versus the tuning factor μ. As can be seen, ε is zero at μ =0.33 (or 1/3), while it is greater than zero for all other values of μ. Hence, it is concluded that the optimal tuning factor is μ=0.33.

(2) Body waves propagating at an angle to the horizontal axis: tuning factor β

Next, we consider a more general *SH* wave that propagates at an arbitrary angle with respect to positive horizontal axis, i.e. $\xi_x\neq0$. Thus, it is now necessary to consider both the tuning factors β and μ, and evaluate their effect on the numerical dispersion as functions of both the vertical wavenumber ξ_z and the propagation angle θ. For this purpose, we calculate the ratio of phase

velocities V/C and the associated error function ε in equation (2.4.28). The results are shown in figures 2.4.6 and 2.4.7, respectively.

Figure 2.4.6 shows the variation of V/C with respect to the vertical wavenumber ξ_z for the propagation angles θ of 15, 30, 45, 60, 75, and 90°. In each case, this ratio is evaluated for β=1, and μ=0, 0.33 and 1.0 (i.e. $\mathbf{A}_C+\mathbf{M}_L$, $\mathbf{A}_C+\mathbf{M}_T$ and $\mathbf{A}_C+\mathbf{M}_C$ respectively). It is observed that the results obtained from $\mathbf{A}_C+\mathbf{M}_T$ are much more accurate than those obtained from $\mathbf{A}_C+\mathbf{M}_L$ and $\mathbf{A}_C+\mathbf{M}_C$, except the case of angle θ=15°. In addition it should be emphasized that this observation is true only for the range of $0\leq\xi_z\leq(4/5)\pi$. Therefore, it is expected that an optimal value for μ indeed exists for any arbitrary angle of propagation θ, and that it is in all probability to be 0.33.

To find the optimal values for both β and μ, we again utilize equation (2.4.28) with replacement of V_z by V and C_z by C. Here, C is the true phase velocity of waves propagating at an angle θ in the continuum. In addition, the error function ε is a function of not only μ, but also β, i.e. $\varepsilon=\varepsilon(\beta,\mu)$ for a given propagation angle θ. Figure 2.4.7 shows the variation of this error function for various propagation angles in terms of a standard surface plot. Notice that the degree of error of the TLM2 of interest is relatively very small in comparison with the degree of error of the TLM1 in section 2.2. It is now clear that the use of $\beta=\mu$=0.33 is the best choice for both of the tuning factors, and that these factors are independent of the propagation angle θ. The identical values for β and μ is understood again from the fact that the two matrices $\mathbf{A}$ and $\mathbf{M}$ are proportional to each other as the case of the TLM1 in section 2.2.

(3) Homogeneous plate

We now consider the free vibration of a homogeneous plate of thickness H=1.0 and shear velocity C_S=1.0. For a discrete model, the homogeneous plate is discretized into 5 TLM2 thin layers, i.e. N=5, and so only 11(=2N+1) distinct eigenvalues (or modes) exist in the present discrete model. Because of simplicity of this problem, the closed form solution is available as shown in equation (2.4.23a). Through this example, we assess the effect of the tuning factors β and μ on eigenvalue problems for finite domain systems. For this purpose, we consider the following four combinations of the tuning factors: (i) β=1.00 and μ=1.00 ($\mathbf{A}_C+\mathbf{M}_C$); (ii) β=1.00 and μ=0.00 ($\mathbf{A}_C+\mathbf{M}_L$); (iii) β=1.00 and μ=0.33 ($\mathbf{A}_C+\mathbf{M}_T$); (iv) $\beta=\mu$=0.33 ($\mathbf{A}_T+\mathbf{M}_T$).

Figure 2.4.8 compares the frequency-wavenumber dispersion of the discrete solutions (dashed lines) with the exact analytical solutions (solid lines). The discrete solutions are computed for the above four combinations of tuning factors. It is noted that there are shown only 11 branches in each plot, although the infinite number of modes (or branches) exists in the exact analytical solution as shown in equation (2.4.23b). As is apparent, the use of the optimal tuning factors of $\beta=\mu$=0.33 presents the best agreement with the exact solutions. It is also noted that the use of β=1.00 and μ=0.33 also gives good results for small horizontal wavenumbers, i.e. $\xi_x/\pi<1/2$, but not for high horizontal wavenumbers. Therefore, we conclude that the tuning factors $\beta=\mu$=0.33 are indeed the optimal choice for anti-plane problems modeled with the TLM2.

It is also observed from figure 2.4.8 that only the 5 modes of the 11 modes in the discrete solution are accurate despite the application of optimal tuning factors. The reason is related to the range of vertical wavenumber ξ_z over which the numerical error $\varepsilon(\beta,\mu)$ in equation (2.4.28) is estimated to determine the optimal tuning factors. Remember that the optimal tuning factors are determined only for the significant range of vertical wavenumber, i.e. $0<\xi_z/\pi<4/5$. In fact, the modal indices j of the 5 modes are 0, 1, 2, 3, and 4, respectively, which can be easily verified by accounting the

index j or ξ_{zj} in equation (2.4.23a). Finally, it is concluded that with the application of optimal tuning factors only the first two-fifth of the set of all computed modes (or equivalently the modes with $0<\xi_{zj}/\pi<4/5$) is accurate as far as the dispersion relation is concerned.

(4) Love waves

In this last example, we consider a homogeneous layer underlain by a homogeneous half-space, i.e. the so-called Love wave problem. The thickness and shear velocity of the layer is H=1.0 and C_L =1.0, respectively. The shear velocity of the half space is C_H=2.0. The mass density ρ for both is 1.0. It follows that the shear moduli for the layer and half-space are $G_L(=\rho C_L^2)$=1.0 and $G_H(=\rho C_H^2)$=4.0, respectively. For a discrete model, the layer is composed of 10 TLM2 thin layers (N=20), so that the thickness $h_L(=H/N)$ of each thin layer is 0.1(=1/10) and the total number of degrees of freedom (or interfaces) is 21. Taking into consideration the wave-velocity contrast between the two materials, the thickness of thin layers for the half space (h_H) is set to be 0.2. In the discrete model of interest, the first twenty propagation modes are the only valid modes. So, we compare these twenty modes with the exact analytical solution to assess the effect of the tuning factors β and μ on eigenvalue problems for layered semi-infinite systems. For this purpose, we consider the following three combinations of tuning factors: (i) β=1.00 and μ=1.00 ($\mathbf{A}_C$+$\mathbf{M}_C$); (ii) β=1.00 and μ=0.00 ($\mathbf{A}_C$+$\mathbf{M}_L$); (iii) β=μ=0.33 ($\mathbf{A}_T$+$\mathbf{M}_T$).

Figure 2.4.9 compares the frequency-wavenumber dispersion of the discrete solutions (dashed lines) with the exact analytical solutions (solid lines) for the three combinations of tuning factors. First of all, it is observed that the optimal tuning factors of β=μ=0.33 improves to the great extent the accuracy of eigenvalues. Secondly, only the first two-fifth (or 8 modes in this example) of the set of 20 computed modes are shown to be quite accurate. Therefore, it is proved that the tuning factors β=μ=0.33 are indeed the optimal choice for *SH* wave problems of semi-infinite domain as well as finite domain. In addition, it is verified that as long as using the optimal tuning factors, we can calculate accurately the first two-fifth of the set of modes obtained from the TLM2 not only for a homogeneous layer, but also for two-layered systems (or even multilayered systems).

2.4.3 Summary

In this section, the general solution and the frequency-wavenumber spectrum are obtained for the discrete *SH* wave formulated by means of the TLM2. The qualitative investigation of the spectrum has discovered that the wavelengths along the discretization direction (λ_z) must be no shorter than the discretization size (h), i.e. $\lambda_z \geq h$. In addition, it is observed that the stopping band region exists at $\xi_z=\pi$ at which significant numerical dispersion can take place. Then, three wave propagation problems in finite and semi-infinite discrete media have been solved formally and successfully. The comprehensive characterization of the numerical dispersion in the discrete homogenous full-space has yielded the optimal tuning factors of β=μ=0.33 that are valid only for $0<\xi_z/\pi<4/5$. Also, it is found that the number of TLM2 thin layers per wavelength N_λ ($=\lambda_z/h$) must be no less than 5/2, i.e. $N_\lambda \geq 5/2$ for the range of ξ_z in consideration. From the free vibration problems of a homogeneous plate and a layer on a homogeneous half-space, it is verified that the use of optimal tuning factors really provides the best agreement with the exact analytical solutions in terms of eigenvalues. More importantly, it is observed that the first two-fifth computed modes are very close to those of the exact analytical solution, provided that the optimal tuning factors are applied.

2.5. In-Plane (*SV-P*) waves with quadratic expansion TLM

In this section, we consider the *SV-P* wave propagation modeled with the TLM2. In the first part of this section 2.5, we obtain the general solution and the frequency-wavenumber spectrum for the *SV-P* wave equation modeled with the TLM2. It is revealed that there are four independent branches such as *S*-, *P*-acoustical branches, and *S*-, *P*-optical branches. Through a qualitative investigation of the spectrum, we confirm the convention for the wavelength along the discretization direction and the discretization size, i.e. $\lambda_z \geq h$. Then, we solve formally two guided wave problems by means of the obtained general solutions. The two problems are a discrete homogeneous plate with mixed boundary conditions and the Rayleigh surface waves on a discrete homogeneous half-space.

In the second part, we first extensively characterize the numerical dispersion of body waves for five different Poisson's ratios as a function of vertical direction wavenumber (ξ_z) and the propagation angle (θ). As a result, we confirm that the same range of ξ_z as the case of *SH* wave is only useful as determining the optimal tuning factors. Then, with the calculation of the error functions, we determine the optimal tuning factors. By analyzing two free-vibration problems of finite domain, we verify that the optimal tuning factors indeed improve the accuracy of the eigenvalues in the context of the TLM. In addition, we find out how many modes are accurate among a set of all computed modes with the application of the optimal tuning factors. In the last problem, we consider the problem of Rayleigh surface wave to show the effect of the tuning factors on the accuracy of the TLM1 analysis for (semi-) infinite media.

2.5.1 Discrete solutions for in-plane problems

Consider a single TLM2 thin layer subjected to *SV-P* wave motion as shown in figure 2.5.1. It is noticed that since *SV-P* wave motion is involved, the two degrees of freedom u and w are involved at each external and internal node. The governing equation is then expressed as

$$\mathbf{P}_l = \mathbf{K}\mathbf{u}_l \tag{2.5.1}$$

where

$$\mathbf{P}_l = \{\tau_l \quad \sigma_l \quad \tau'_l \quad \sigma'_l \quad \tau_{l-1} \quad \sigma_{l-1}\}^T \tag{2.5.2a}$$

$$\mathbf{u}_l = \{u_l \quad w_l \quad u'_l \quad w'_l \quad u_{l-1} \quad w_{l-1}\}^T \tag{2.5.2b}$$

$$\mathbf{K} = \mathbf{A}k_x^2 + \mathbf{B}k_x + \mathbf{G} - \omega^2\mathbf{M} \tag{2.5.2c}$$

In the above expressions, the matrices **A**, **B**, **G**, and **K** are defined in the appendix to this chapter. Also, τ'_l, σ'_l, u'_l, and w'_l are the traction and displacement components at the internal node. For the sake of future convenience, we also introduce the five auxiliary matrices and four dimensionless parameters as follows

$$\mathbf{a} = \begin{Bmatrix} a_{11} & a_{12} \\ a_{21} & a_{22} \end{Bmatrix}$$

$$= \begin{Bmatrix} -\alpha r & \cdot \\ \cdot & -\beta \end{Bmatrix}\xi_x^2 + \begin{Bmatrix} \cdot & 5(r-1) \\ -5(r-1) & \cdot \end{Bmatrix}\xi_x + \begin{Bmatrix} 10 & \cdot \\ \cdot & 10r \end{Bmatrix} - \begin{Bmatrix} -\mu & \cdot \\ \cdot & -\mu \end{Bmatrix}\Omega^2$$

$$\mathbf{a}' = \begin{Bmatrix} a'_{11} & a'_{12} \\ a'_{21} & a'_{22} \end{Bmatrix}$$
$$= \begin{Bmatrix} 2\alpha r & \cdot \\ \cdot & 2\beta \end{Bmatrix}\xi_x^2 + \begin{Bmatrix} \cdot & -20(r-1) \\ 20(r-1) & \cdot \end{Bmatrix}\xi_x + \begin{Bmatrix} -80 & \cdot \\ \cdot & -80r \end{Bmatrix} - \begin{Bmatrix} 2\mu & \cdot \\ \cdot & 2\mu \end{Bmatrix}\Omega^2$$
$$\mathbf{b} = \begin{Bmatrix} b_{11} & b_{12} \\ b_{21} & b_{22} \end{Bmatrix}$$
$$= \begin{Bmatrix} (5-\alpha)r & \cdot \\ \cdot & (5-\beta) \end{Bmatrix}\xi_x^2 + \begin{Bmatrix} 70 & \cdot \\ \cdot & 70r \end{Bmatrix} - \begin{Bmatrix} (5-\mu) & \cdot \\ \cdot & (5-\mu) \end{Bmatrix}\Omega^2$$
$$\mathbf{b}' = \begin{Bmatrix} b'_{11} & b'_{12} \\ b'_{21} & b'_{22} \end{Bmatrix}$$
$$= \begin{Bmatrix} 2(5-\alpha)r & \cdot \\ \cdot & 2(5-\beta) \end{Bmatrix}\xi_x^2 + \begin{Bmatrix} 80 & \cdot \\ \cdot & 80r \end{Bmatrix} - \begin{Bmatrix} 2(5-\mu) & \cdot \\ \cdot & 2(5-\mu) \end{Bmatrix}\Omega^2$$
$$\mathbf{b}_0 = \begin{Bmatrix} b_{11} & b_{12} \\ b_{21} & b_{22} \end{Bmatrix}$$
$$= \begin{Bmatrix} (5-\alpha)r & \cdot \\ \cdot & (5-\beta) \end{Bmatrix}\xi_x^2 + \begin{Bmatrix} \cdot & 15(r-3) \\ 15(r-3) & \cdot \end{Bmatrix}\xi_x + \begin{Bmatrix} 70 & \cdot \\ \cdot & 70r \end{Bmatrix} - \begin{Bmatrix} (5-\mu) & \cdot \\ \cdot & (5-\mu) \end{Bmatrix}\Omega^2$$

$$\xi_x = k_x h, \qquad \xi_z = k_z h, \qquad \Omega = \frac{\omega h}{C_S}, \text{ and } \quad r = \frac{\lambda + 2G}{G} = \frac{C_P^2}{C_S^2} = \frac{2-2\nu}{1-2\nu}$$

To describe the wave motion in a homogenous full space consisting of the identical TLM2 thin layers, we write the recursive equation of motion at the l^{th} interface as

$$\mathbf{P}_l = \begin{Bmatrix} \mathbf{p}_l \\ \mathbf{p}'_l \end{Bmatrix} = \frac{G}{30h}\begin{Bmatrix} \mathbf{a}^T\mathbf{u}_{l+1} + \mathbf{a}'^T\mathbf{u}'_{l+1} + 2\mathbf{b}\mathbf{u}_l + \mathbf{a}'\mathbf{u}'_l + \mathbf{a}\mathbf{u}_{l-1} \\ \mathbf{a}'^T\mathbf{u}_l + 2\mathbf{b}'\mathbf{u}'_l + \mathbf{a}'\mathbf{u}_{l-1} \end{Bmatrix} \tag{2.5.3a}$$

In the particular case of a homogeneous half-space, the top surface (i.e. z=0), which is associated with boundary conditions, obeys instead the equation

$$\mathbf{p}_0 = \frac{G}{30h}\{\mathbf{b}_0\mathbf{u}_l + \mathbf{a}'\mathbf{u}'_l + \mathbf{a}\mathbf{u}_{l-1}\} \tag{2.5.3b}$$

To derive the general solution, we begin with assuming a trial solution in the form.

$$\mathbf{u}_l = Z^{2l}\boldsymbol{\phi} \text{ and } \mathbf{u}'_l = Z^{2l-1}\boldsymbol{\phi}' \tag{2.5.4ab}$$

in which $\boldsymbol{\phi} = \{\phi_x \quad \phi_z\}^T$ and $\boldsymbol{\phi}' = \{\phi'_x \quad \phi'_z\}^T$ are, respectively, the eigenvectors for the external and internal nodes. Substituting equations (2.5.4a and b) into equation (2.5.3a) and dividing the first two rows and last two rows by Z^{2l} and Z^{2l-1}, respectively, we obtain the following equation for free vibration problem, i.e. $\mathbf{P}_l = \mathbf{0}$.

$$\begin{Bmatrix} \mathbf{a}^T Z^2 + \mathbf{a}Z^{-2} + 2\mathbf{b} & \mathbf{a}'^T Z + \mathbf{a}'Z^{-1} \\ \mathbf{a}'^T Z + \mathbf{a}'Z^{-1} & 2\mathbf{b}' \end{Bmatrix}\begin{Bmatrix} \boldsymbol{\phi} \\ \boldsymbol{\phi}' \end{Bmatrix} = \begin{Bmatrix} \mathbf{0} \\ \mathbf{0} \end{Bmatrix} \tag{2.5.5a}$$

or

$$\begin{Bmatrix} a_{11}(4Y^2-2)+2b_{11} & -4a_{12}Y\bar{Y} & 2a'_{11}Y & -2a'_{12}\bar{Y} \\ 4a_{12}Y\bar{Y} & a_{22}(4Y^2-2)+2b_{22} & 2a'_{12}\bar{Y} & 2a'_{22}Y \\ 2a'_{11}Y & -2a'_{12}\bar{Y} & 2b'_{11} & \cdot \\ 2a'_{12}\bar{Y} & 2a'_{22}Y & \cdot & 2b'_{22} \end{Bmatrix} \begin{Bmatrix} \phi_x \\ \phi_z \\ \phi'_x \\ \phi'_z \end{Bmatrix} = \mathbf{0} \tag{2.5.5b}$$

or

$$\left[\bar{\mathbf{A}}\xi_x^2 + \bar{\mathbf{B}}\xi_x + \bar{\mathbf{G}} - \bar{\mathbf{M}}\Omega^2\right]\Phi = \mathbf{0} \tag{2.5.5c}$$

where $Y = \frac{1}{2}(Z + Z^{-1})$, $\bar{Y} = \frac{1}{2}(Z - Z^{-1})$, $\bar{Y}^2 = Y^2 - 1$, $\Phi = \left\{\phi^T \quad \phi'^T\right\}^T$ and the matrices $\bar{\mathbf{A}}$, $\bar{\mathbf{B}}$, $\bar{\mathbf{G}}$, and $\bar{\mathbf{M}}$ are listed in the appendix to this chapter. For simplicity in the following derivation, we can express equation (2.5.5a) simply as follows.

$$\begin{Bmatrix} \mathbf{C}_{11} & \mathbf{C}_{12} \\ \mathbf{C}_{21} & \mathbf{C}_{22} \end{Bmatrix} \begin{Bmatrix} \phi \\ \phi' \end{Bmatrix} = \mathbf{0} \tag{2.5.5d}$$

A nontrivial solution exists only if the determinant of the coefficient matrix in equation (2.5.5d) must vanish. This condition can be given by the following equations.

$$\phi' = -\mathbf{C}_{22}^{-1}\mathbf{C}_{21}\phi \tag{2.5.6a}$$

$$\left[\mathbf{C}_{11} - \mathbf{C}_{12}\mathbf{C}_{22}^{-1}\mathbf{C}_{21}\right]\phi = \mathbf{0} \tag{2.5.6b}$$

where

$$\mathbf{C}_{22}^{-1}\mathbf{C}_{21} = \frac{1}{b'_{11}b'_{22}} \begin{Bmatrix} a'_{11}b'_{22}Y & -a'_{12}b'_{22}\bar{Y} \\ a'_{12}b'_{11}\bar{Y} & a'_{22}b'_{11}Y \end{Bmatrix}$$

$$\mathbf{C}_{11} - \mathbf{C}_{12}\mathbf{C}_{22}^{-1}\mathbf{C}_{21} = \begin{Bmatrix} a_{11}(4Y^2-2)+2b_{11} & a'_{12}Y\bar{Y} \\ -a'_{12}Y\bar{Y} & a_{22}(4Y^2-2)+2b_{22} \end{Bmatrix}$$

$$-2\begin{Bmatrix} a'^2_{11}/b'_{11}Y^2 - a'^2_{12}/b'_{22}\bar{Y}^2 & -a'_{12}(a'_{11}/b'_{11} + a'_{22}/b'_{22})Y\bar{Y} \\ a'_{12}(a'_{11}/b'_{11} + a'_{22}/b'_{22})Y\bar{Y} & a'^2_{22}/b'_{22}Y^2 - a'^2_{12}/b'_{11}\bar{Y}^2 \end{Bmatrix}$$

With additional manipulations of equation (2.5.6b), we obtain the spectrum equation for Y as

$$\alpha_0\tilde{Y}^2 - 2\alpha_1\tilde{Y} + \alpha_2 = 0 \tag{2.5.7}$$

where

$$\tilde{Y} = Y^2$$

$$\alpha_0 = 16(a_{12}^2 + a_{11}a_{22})$$
$$+\frac{1}{b'_{11}}(64a_{12}^2a'_{11} + 128a_{11}a_{12}^2 - 8a_{22}a'^2_{11})$$
$$+\frac{1}{b'_{22}}(64a_{12}^2a'_{22} - 8a_{11}a'^2_{22} + 128a_{12}^2a_{22})$$
$$+\frac{1}{b'_{11}b'_{22}}(4a'^2_{11}a'^2_{22} + 128a_{12}^2a'_{11}a'_{22} + 1024a_{12}^4)$$

$$\alpha_1 = 8(a_{12}^2 + a_{11}a_{22}) - 4(a_{22}b_{11} + a_{11}b_{22})$$
$$+\frac{1}{b_{11}'}(32a_{12}^2a_{11}' + 96a_{11}a_{12}^2 - 2a_{22}a_{11}'^2 - 32a_{12}^2b_{11} + 2b_{22}a_{11}'^2)$$
$$+\frac{1}{b_{22}'}(32a_{12}^2a_{22}' - 2a_{11}a_{22}'^2 + 96a_{12}^2a_{22} + 2b_{11}a_{22}'^2 - 32a_{12}^2b_{22})$$
$$+\frac{1}{b_{11}'b_{22}'}(64a_{12}^2a_{11}'a_{22}' + 1024a_{12}^4)$$
$$\alpha_2 = 4\left[16\frac{a_{12}^2}{b_{11}'} + (a_{22} - b_{22})\right]\left[16\frac{a_{12}^2}{b_{22}'} + (a_{11} - b_{11})\right]$$

Then, we obtain the two $\tilde{Y}$'s that correspond to P and S wave components, respectively.

$$\tilde{Y}_i = \frac{1}{\alpha_0}\left(\alpha_1 \pm \sqrt{\alpha_1^2 - \alpha_2}\right), \tag{2.5.8a}$$

$$Y_{ij} = \pm\sqrt{\tilde{Y}_i}, \tag{2.5.8b}$$

where i= P or S for P and S wave components, respectively, and j=aco or opt for acoustical and optical branches, respectively. It should be noticed that equation (2.5.8b) implies the following relationship.

$$Y_{i\,\mathrm{opt}} = -Y_{i\,\mathrm{aco}} \tag{2.5.8c}$$

or equivalently

$$Z_{i\,\mathrm{opt}} = -1/Z_{i\,\mathrm{aco}} \tag{2.5.8d}$$

Additionally, the directions of particle motion for each component at both the external and internal nodes can be written in terms of the eigenvectors.

$$\Theta_{ij} = \tan^{-1}\left[\frac{\phi_z}{\phi_x}\right]_{ij} \qquad \text{at the external node} \tag{2.5.9a}$$

$$\Theta_{ij}' = \tan^{-1}\left[\frac{\phi_z'}{\phi_x'}\right]_{ij} \qquad \text{at the internal node} \tag{2.5.9b}$$

We have the two Z's for each Y_{ij} in equations (2.5.8b) as follows.

$$Z_{ijk} = Y_{ij} \pm \sqrt{Y_{ij}^2 - 1} \qquad \text{or} \quad Z_{ijk} = e^{\pm i\frac{\xi_{ijk}}{2}} = \cos\frac{\xi_{ijk}}{2} \pm i\sin\frac{\xi_{ijk}}{2} \tag{2.5.10}$$

where k(=1,2) represents the direction of propagation, i.e. positive or negative in the z-direction and the other indices i and j represent the same meaning as above. The corresponding eigenvectors at the external and internal nodes are then given in the form.

$$\boldsymbol{\phi}_{ijk} = \begin{Bmatrix}\phi_{xijk}\\ \phi_{zijk}\end{Bmatrix} = \begin{Bmatrix}[4a_{12} - 2a_{12}(a_{11}'/b_{11}' + a_{22}'/b_{22}')]Y_{ijk}\bar{Y}_{ijk}\\ (4a_{11} - 2a_{11}'^2/b_{11}')Y_{ijk}^2 + 2a_{12}'^2/b_{22}'\bar{Y}_{ijk}^2 - 2(a_{11} - b_{11})\end{Bmatrix} \tag{2.5.11a}$$

$$\boldsymbol{\phi}_{ijk}' = \begin{Bmatrix}\phi_{xijk}'\\ \phi_{zijk}'\end{Bmatrix} = -\frac{1}{b_{11}'b_{22}'}\begin{Bmatrix}a_{11}'b_{22}'Y_{ij} & -a_{12}'b_{22}'\bar{Y}_{ij}\\ a_{12}'b_{11}'\bar{Y}_{ij} & a_{22}'b_{11}'Y_{ij}\end{Bmatrix}\begin{Bmatrix}\phi_{xijk}\\ \phi_{zijk}\end{Bmatrix} \tag{2.5.11b}$$

Finally, the general solution is obtained in explicit form

$$\mathbf{u}_l = A_{\mathrm{aco}}Z_{P\mathrm{aco}1}^{2l}\boldsymbol{\phi}_{P\mathrm{aco}1} + B_{\mathrm{aco}}Z_{P\mathrm{aco}2}^{2l}\boldsymbol{\phi}_{P\mathrm{aco}2} + A_{\mathrm{opt}}Z_{P\mathrm{opt}1}^{2l}\boldsymbol{\phi}_{P\mathrm{opt}1} + B_{\mathrm{opt}}Z_{P\mathrm{opt}2}^{2l}\boldsymbol{\phi}_{P\mathrm{opt}2}$$
$$+ C_{\mathrm{aco}}Z_{S\mathrm{aco}1}^{2l}\boldsymbol{\phi}_{S\mathrm{aco}1} + D_{\mathrm{aco}}Z_{S\mathrm{aco}2}^{2l}\boldsymbol{\phi}_{S\mathrm{aco}2} + C_{\mathrm{opt}}Z_{S\mathrm{opt}1}^{2l}\boldsymbol{\phi}_{S\mathrm{opt}1} + D_{\mathrm{opt}}Z_{S\mathrm{opt}2}^{2l}\boldsymbol{\phi}_{S\mathrm{opt}2} \tag{2.5.12a}$$

$$\mathbf{u}_l' = A_{aco} Z_{Paco1}^{2l-1} \boldsymbol{\phi}_{Paco1}' + B_{aco} Z_{Paco2}^{2l-1} \boldsymbol{\phi}_{Paco2}' + A_{opt} Z_{Popt1}^{2l-1} \boldsymbol{\phi}_{Popt1}' + B_{opt} Z_{Popt2}^{2l-1} \boldsymbol{\phi}_{Popt2}'$$
$$+ C_{aco} Z_{Saco1}^{2l-1} \boldsymbol{\phi}_{Saco1}' + D_{aco} Z_{Saco2}^{2l-1} \boldsymbol{\phi}_{Saco2}' + C_{opt} Z_{Sopt1}^{2l-1} \boldsymbol{\phi}_{Sopt1}' + D_{opt} Z_{Sopt2}^{2l-1} \boldsymbol{\phi}_{Sopt2}' \quad (2.5.12b)$$

With the help of equation (2.5.8d), this can be simplified to be of the form.

$$\mathbf{u}_l = A Z_{P1}^{2l} \boldsymbol{\phi}_{P1} + B Z_{P2}^{2l} \boldsymbol{\phi}_{P2} + C Z_{S1}^{2l} \boldsymbol{\phi}_{S1} + D Z_{S2}^{2l} \boldsymbol{\phi}_{S2} \quad (2.5.13a)$$

$$\mathbf{u}_l' = A Z_{P1}^{2l-1} \boldsymbol{\phi}_{P1}' + B Z_{P2}^{2l-1} \boldsymbol{\phi}_{P2}' + C Z_{S1}^{2l-1} \boldsymbol{\phi}_{S1}' + D Z_{S2}^{2l-1} \boldsymbol{\phi}_{S2}' \quad (2.5.13b)$$

where we omit the index identifying the acoustical branches for the sake of simple expression. We deduce the following relationships between the eigenvectors from equations (2.5.11a and b).

$$\boldsymbol{\phi}_{i1} = \begin{Bmatrix} \phi_{ix} \\ \phi_{iz} \end{Bmatrix} \text{ and } \boldsymbol{\phi}_{i2} = \begin{Bmatrix} -\phi_{ix} \\ \phi_{iz} \end{Bmatrix} \quad (2.5.14a)$$

$$\boldsymbol{\phi}_{i1}' = \begin{Bmatrix} \phi_{ix}' \\ \phi_{iz}' \end{Bmatrix} \text{ and } \boldsymbol{\phi}_{i2}' = \begin{Bmatrix} -\phi_{ix}' \\ \phi_{iz}' \end{Bmatrix} \quad (2.5.14b)$$

Inserting equation (2.5.10) into equations (2.5.13a and b) and making use of equations (2.5.14a and b), we obtain the following equivalent expression of the general solution for *SV-P* wave problems modeled with the TLM2.

$$\mathbf{u}_l = \begin{Bmatrix} \cos\xi_{zP}(2l)\,\phi_{Px} \\ -i\sin\xi_{zP}(2l)\,\phi_{Pz} \end{Bmatrix} \bar{A} + \begin{Bmatrix} -i\sin\xi_{zP}(2l)\,\phi_{Px} \\ \cos\xi_{zP}(2l)\,\phi_{Pz} \end{Bmatrix} \bar{B}$$
$$+ \begin{Bmatrix} \cos\xi_{zS}(2l)\,\phi_{Sx} \\ -i\sin\xi_{zS}(2l)\,\phi_{Sz} \end{Bmatrix} \bar{C} + \begin{Bmatrix} -i\sin\xi_{zS}(2l)\,\phi_{Sx} \\ \cos\xi_{zS}(2l)\,\phi_{Sz} \end{Bmatrix} \bar{D} \quad (2.5.15a)$$

$$\mathbf{u}_l' = \begin{Bmatrix} \cos\xi_{zP}(2l-1)\,\phi_{Px}' \\ -i\sin\xi_{zP}(2l-1)\,\phi_{Pz}' \end{Bmatrix} \bar{A} + \begin{Bmatrix} -i\sin\xi_{zP}(2l-1)\,\phi_{Px}' \\ \cos\xi_{zP}(2l-1)\,\phi_{Pz}' \end{Bmatrix} \bar{B}$$
$$+ \begin{Bmatrix} \cos\xi_{zS}(2l-1)\,\phi_{Sx}' \\ -i\sin\xi_{zS}(2l-1)\,\phi_{Sz}' \end{Bmatrix} \bar{C} + \begin{Bmatrix} -i\sin\xi_{zS}(2l-1)\,\phi_{Sx}' \\ \cos\xi_{zS}(2l-1)\,\phi_{Sz}' \end{Bmatrix} \bar{D} \quad (2.5.15b)$$

Substitution of equation (2.5.10) into equation (2.5.5c) with replacement of $(Y, \bar{Y})$ by $(Y_{ij}, \bar{Y}_{ij})$ yields the spectrum equation for wavenumber ξ_x and Ω as follows

$$\left| \bar{\mathbf{A}}_{ij} \xi_x^2 + \bar{\mathbf{B}}_{ij} \xi_x + \bar{\mathbf{G}}_{ij} - \bar{\mathbf{M}}_{ij} \Omega^2 \right| = 0 \quad (2.5.16)$$

where the subscripts i and j represent the replacement of $(Y, \bar{Y})$ by $(Y_{ij}, \bar{Y}_{ij})$. It can be shown that for very small vertical wavenumbers (i.e. a very long wavelengths in the z direction), the spectrum equation (2.5.16) approaches the analytical exact spectrum equations in dimensionless form given by $\Omega_P = \sqrt{r(\xi_{xP}^2 + \xi_{zP}^2)}$ and $\Omega_S = \sqrt{\xi_{xS}^2 + \xi_{zS}^2}$.

Having found the relationship between frequency and wavenumbers from equation (2.5.16), we can obtain the apparent phase velocities as follows.

$V_P = \dfrac{\omega_P}{k}$: P wave phase velocity in the propagation direction (2.5.17a)

$V_S = \dfrac{\omega_S}{k}$: S wave phase velocity in the propagation direction (2.5.17b)

$V_{Px} = \dfrac{\omega_P}{k_x}$: P wave phase velocity in the x direction (2.5.17c)

$V_{Sx} = \dfrac{\omega_S}{k_x}$: S wave phase velocity in the x direction (2.5.17d)

$$V_{Pz} = \frac{\omega_P}{k_z} \quad : P \text{ wave phase velocity in the } z \text{ direction} \tag{2.5.17e}$$

$$V_{Sz} = \frac{\omega_S}{k_z} \quad : S \text{ wave phase velocity in the } z \text{ direction} \tag{2.5.17f}$$

Figures 2.5.2 and 2.5.3 present a qualitative comparison of the frequency-wavenumber spectrum obtained from equation (2.5.16) against the exact analytical spectrum for a particular case of Poisson's ratio ν=0.30. Note in each figure that the dashed and dot-dashed lines represent the *S*- and *P*-acoustical branches and the *S*- and *P*-optical branches, respectively, and a solid line represents the exact analytical spectrum. The first figure shows the numerical dispersion for a fixed horizontal wavenumber (ξ_x=0.5π and ξ_x=π) as a function of vertical wavenumber ξ_z, while the second shows the numerical dispersion for a fixed vertical wavenumber (ξ_z=0.5π and ξ_z=1.5π) as a function of horizontal wavenumber ξ_x. In either case, the TLM2 model is computed for fully consistent matrices, that is, the tuning factors used are α=β=μ=1.0.

In figure 2.5.2, recognize first that each of the *S*- and *P*-acoustical branches (dashed lines) intersects with both of the *S*- and *P*-optical branches (dot-dashed lines) at certain points. As a result, there exist four cross points where four short complex branches exist. As discussed in section 2.4, these complex branches correspond to the stopping band regions. Next, it is observed along the *S*- and *P*-acoustical branches that the numerical dispersion error occurs mostly in the high vertical wavenumber region. Also, some ambiguities are shown: such as the regions of negative group velocity and the periodicity. These two observations are similar to those already seen in section 2.4. Therefore, it behooves to adopt the same convention as the TLM2 for *SH* wave in section 2.4 for the vertical wavenumber ξ_z (or the wavelength along the discretization direction λ_z), which states that λ_z must be longer than the discretization thickness *h*.

It is recognized in figure 2.5.3 that the acoustical and optical branches coexist, and there is a intersection between *P*-acoustical and *S*-optical branches, or *S*-acoustical and *P*-optical branches. Then, notice in the left plot (ξ_z=0.5π) that the *S*- and *P*-acoustical branches are remarkably identical to the exact analytical branches for the range of ξ_x of interest. It is also observed that high horizontal wavenumbers produce smaller numerical dispersion than the low horizontal wavenumbers, which is seen more clearly in the right plot (ξ_z=1.5π) than in the left plot (ξ_z=0.5π). The reason is that the high horizontal wavenumbers involve waves that propagate nearly horizontally as already explained in previous sections 2.2–4.

We continue to derive formally the spectrum equations for two guided wave examples: (1) a discrete homogeneous plate with mixed boundary conditions; and (2) Rayleigh surface waves on a discrete homogeneous half-space. Concerning the first example, the solutions are obtained in fully analytical form due to the simplicity of the problem. On the other hand, the solution for the second example is obtained in an implicit form, which requires numerical search techniques. In section 2.5.2, we compare the discrete solutions with the associated exact analytical solutions for the two examples and seek to improve the discrete solutions with the help of obtained optimal tuning factors α, β, and μ.

(1) Homogenous plate with mixed boundary conditions

Consider a discrete homogeneous plate of thickness *H* that is composed of *N* (even integer) TLM2 thin-layers. The mixed boundary conditions of interest are that the vertical displacement and the horizontal stress are both zero at the top (l=N/2) and bottom (l=–N/2) surfaces, namely

$$w_l = 0 \tag{2.5.17a}$$

$$p_{xl} = 0 \tag{2.5.17b}$$

Under these boundary conditions, it is possible to uncouple the wave motion in the plate into the symmetric and anti-symmetric modes, as discussed in section 2.3.

Consider first the symmetric mode, of which the displacement fields are of the form.

$$\mathbf{u}_l = \begin{Bmatrix} \cos\xi_{zP}(2l)\,\phi_{Px} \\ -i\sin\xi_{zP}(2l)\,\phi_{Pz} \end{Bmatrix} \bar{A} + \begin{Bmatrix} \cos\xi_{zS}(2l)\,\phi_{Sx} \\ -i\sin\xi_{zS}(2l)\,\phi_{Sz} \end{Bmatrix} \bar{C} \tag{2.5.18a}$$

$$\mathbf{u}_l' = \begin{Bmatrix} \cos\xi_{zP}(2l-1)\,\phi_{Px}' \\ -i\sin\xi_{zP}(2l-1)\,\phi_{Pz}' \end{Bmatrix} \bar{A} + \begin{Bmatrix} \cos\xi_{zS}(2l-1)\,\phi_{Sx}' \\ -i\sin\xi_{zS}(2l-1)\,\phi_{Sz}' \end{Bmatrix} \bar{C} \tag{2.5.18b}$$

Substitution of equations (2.5.18a and b) into equations (2.5.17a and b) yields

$$\begin{Bmatrix} w_{\bar{N}} \\ p_{x\bar{N}} \end{Bmatrix} = \begin{Bmatrix} C_{u\alpha}\sin 2\bar{N}\xi_{zP} & C_{u\beta}\sin 2\bar{N}\xi_{zS} \\ C_{w\alpha}\sin 2\bar{N}\xi_{zP} & C_{w\beta}\sin 2\bar{N}\xi_{zS} \end{Bmatrix} \begin{Bmatrix} \bar{A} \\ \bar{C} \end{Bmatrix} = \begin{Bmatrix} 0 \\ 0 \end{Bmatrix} \tag{2.5.19}$$

where $\bar{N} = N/2$,

$$C_{u\alpha} = -ib_{12}[2b_{11} + 2a_{11}\cos 2\alpha - 2a_{11}'^2/b_{11}'\cos^2\alpha - 2a_{12}'^2/b_{22}'\sin^2\alpha]$$

$$\begin{aligned} C_{w\alpha} = C_{u\alpha} + ia_{12}'\{&[a_{11}/2 + b_{11}/2\cos 2\alpha \\ &+ [2a_{22}'/b_{22}'(a_{11}+b_{11}) - a_{11}'^2/b_{11}'(1/2 + 2a_{22}'/b_{22}')]\cos^2\alpha \\ &+ [2a_{11}'/b_{11}'(a_{11}-b_{11}) + a_{12}'/b_{22}'(1/2 + 2a_{11}'/b_{11}')]\sin^2\alpha\} \end{aligned}$$

$$C_{u\beta} = -ib_{12}[2b_{11} + 2a_{11}\cos 2\beta - 2a_{11}'^2/b_{11}'\cos^2\beta - 2a_{12}'^2/b_{22}'\sin^2\beta]$$

$$\begin{aligned} C_{w\beta} = C_{u\beta} + ia_{12}'\{&[a_{11}/2 + b_{11}/2\cos 2\beta \\ &+ [2a_{22}'/b_{22}'(a_{11}+b_{11}) - a_{11}'^2/b_{11}'(1/2 + 2a_{22}'/b_{22}')]\cos^2\beta \\ &+ [2a_{11}'/b_{11}'(a_{11}-b_{11}) + a_{12}'/b_{22}'(1/2 + 2a_{11}'/b_{11}')]\sin^2\beta\} \end{aligned}$$

For nontrivial solutions to exist, the determinant of the coefficient matrix must vanish. Thus, the associated spectrum equation is given by

$$f(\xi_x, \Omega) = \sin 2\bar{N}\xi_{zP}\sin 2\bar{N}\xi_{zS}(C_{u\alpha}C_{w\beta} - C_{u\alpha}C_{w\beta}) = 0 \tag{2.5.20}$$

From equation (2.5.20), it is seen that the symmetric mode can be separated into two independent modes such as P and S wave components. This perfect separation implies an important physics that there is no mode conversion phenomenon between P and S waves when the waves in the plate reflect at the surface. Finally, the two independent modes are given of the form.

$$\xi_{zPj} = \frac{j\pi}{2\bar{N}}, \qquad j = 0,1,\cdots,2\bar{N}-1 \tag{2.5.21a}$$

$$\xi_{zSj} = \frac{j\pi}{2\bar{N}}, \qquad j = 1,2,\cdots,2\bar{N} \tag{2.5.21b}$$

Insert of equations (2.5.21a and b) into equation (2.5.16) can provide the spectrum equation in terms of the frequency, the horizontal wavenumber, and the modal index j, which is not shown in explicit form herein. For the purpose of comparison, the two independent modes of the exact analytical solutions are introduced without any detail derivation in the form.

$$\xi_{zPj} = \frac{j\pi}{2\bar{N}}, \qquad j = 0,1,\cdots,\infty \tag{2.5.21c}$$

$$\xi_{zSj} = \frac{j\pi}{2\bar{N}}, \qquad j = 1,2,\cdots,\infty \tag{2.5.21d}$$

Next, consider the anti-symmetric mode, whose displacement fields are given in the form.

$$\mathbf{u}_l = \begin{Bmatrix} -i\sin\xi_{zP}(2l)\,\phi_{Px} \\ \cos\xi_{zP}(2l)\,\phi_{Pz} \end{Bmatrix} \bar{B} + \begin{Bmatrix} -i\sin\xi_{zS}(2l)\,\phi_{Sx} \\ \cos\xi_{zS}(2l)\,\phi_{Sz} \end{Bmatrix} \bar{D} \tag{2.5.22a}$$

$$\mathbf{u}_l' = \begin{Bmatrix} -i\sin\xi_{zP}(2l-1)\,\phi_{Px}' \\ \cos\xi_{zP}(2l-1)\,\phi_{Pz}' \end{Bmatrix} \bar{B} + \begin{Bmatrix} -i\sin\xi_{zS}(2l-1)\,\phi_{Sx}' \\ \cos\xi_{zS}(2l-1)\,\phi_{Sz}' \end{Bmatrix} \bar{D} \tag{2.5.22b}$$

Substitution of equations (2.5.22a and b) into equations (2.5.17a and b) yields

$$\begin{Bmatrix} w_{\bar{N}} \\ p_{x\bar{N}} \end{Bmatrix} = \begin{bmatrix} C_{u\alpha}\cos 2\bar{N}\xi_{zP} & C_{u\beta}\cos 2\bar{N}\xi_{zS} \\ C_{w\alpha}\cos 2\bar{N}\xi_{zP} & C_{w\beta}\cos 2\bar{N}\xi_{zS} \end{bmatrix} \begin{Bmatrix} \bar{A} \\ \bar{C} \end{Bmatrix} = \begin{Bmatrix} 0 \\ 0 \end{Bmatrix} \tag{2.5.23}$$

where $\bar{N} = N/2$,

$$\begin{aligned}
C_{u\alpha} &= b_{12}[2b_{11} + 2a_{11}\cos 2\alpha - 2a_{11}'^2/b_{11}'\cos^2\alpha - 2a_{12}'^2/b_{22}'\sin^2\alpha] \\
C_{w\alpha} &= C_{u\alpha} - a_{12}'\{[a_{11}/2 + b_{11}/2\cos 2\alpha \\
&\quad + [2a_{22}'/b_{22}'(a_{11}+b_{11}) - a_{11}'^2/b_{11}'(1/2 + 2a_{22}'/b_{22}')]\cos^2\alpha \\
&\quad + [2a_{11}'/b_{11}'(a_{11}-b_{11}) + a_{12}'/b_{22}'(1/2 + 2a_{11}'/b_{11}')]\sin^2\alpha\} \\
C_{u\beta} &= b_{12}[2b_{11} + 2a_{11}\cos 2\beta - 2a_{11}'^2/b_{11}'\cos^2\beta - 2a_{12}'^2/b_{22}'\sin^2\beta] \\
C_{w\beta} &= C_{u\beta} - a_{12}'\{[a_{11}/2 + b_{11}/2\cos 2\beta \\
&\quad + [2a_{22}'/b_{22}'(a_{11}+b_{11}) - a_{11}'^2/b_{11}'(1/2 + 2a_{22}'/b_{22}')]\cos^2\beta \\
&\quad + [2a_{11}'/b_{11}'(a_{11}-b_{11}) + a_{12}'/b_{22}'(1/2 + 2a_{11}'/b_{11}')]\sin^2\beta\}
\end{aligned}$$

Then, the associated spectrum equation is given by

$$f(\xi_x, \Omega) = \cos 2\bar{N}\xi_{zP}\cos 2\bar{N}\xi_{zS}(C_{u\alpha}C_{w\beta} - C_{u\alpha}C_{w\beta}) = 0 \tag{2.5.24}$$

Equation (2.5.24) again shows that the *P* and *S* wave components are independent of each other. Therefore, we have two independent modes of the form.

$$\xi_{zPj} = \frac{(j-\frac{1}{2})\pi}{2\bar{N}}, \qquad j = 1,2,\cdots,2\bar{N} \tag{2.5.25a}$$

$$\xi_{zSj} = \frac{(j-\frac{1}{2})\pi}{2\bar{N}}, \qquad j = 1,2,\cdots,2\bar{N} \tag{2.5.25b}$$

Insert of equations (2.5.25a and b) into equation (2.5.16) can provide the spectrum equation in terms of the frequency, the horizontal wavenumber, and the modal index *j*, which is not shown in explicit form herein. For the purpose of comparison, the two independent modes of the exact analytical solutions are introduced as follows.

$$\xi_{zPj} = \frac{(j-\frac{1}{2})\pi}{2\bar{N}}, \qquad j = 1,2,\cdots,\infty \tag{2.5.25c}$$

$$\xi_{zSj} = \frac{(j-\frac{1}{2})\pi}{2\bar{N}}, \qquad j = 1,2,\cdots,\infty \tag{2.5.25d}$$

In one example of section 2.5.2, the eigenvalues for the plate of interest are numerically calculated for specified values of ρ, C_S, ν, H, and N, and then compared with the exact analytical solutions by means of the dispersion curves. In addition, three different combinations of tuning factors are applied to the TLM2 solutions in order to verify the best improvement in eigenvalues by virtue of the optimal values of tuning factors.

(2) Rayleigh surface waves on a half space

We next determine the spectrum equation for the Rayleigh surface wave on a discrete homogeneous half-space ($l \le 0$) modeled with the TLM2. For this purpose, we need to remove two terms in equations (2.5.13a and b) that violate the radiation condition at $z = -\infty$, leading to the following displacement field.

$$\mathbf{u}_l = AZ_{P1}^{2l}\boldsymbol{\phi}_{P1} + CZ_{S1}^{2l}\boldsymbol{\phi}_{S1} \tag{2.5.26a}$$

$$\mathbf{u}_l' = AZ_{P1}^{2l-1}\boldsymbol{\phi}_{P1}' + CZ_{S1}^{2l-1}\boldsymbol{\phi}_{S1}' \tag{2.5.26b}$$

where A and C are determined from the boundary conditions, and the Z's are properly chosen i.e. $|Z|>1.0$ so that the radiation condition must be satisfied at $z=-\infty$. In this problem, we have to apply the stress-free boundary condition at the surface, which results in

$$\frac{G}{30h}\{\mathbf{b}_0\mathbf{u}_l + \mathbf{a}'\mathbf{u}_l' + \mathbf{a}\mathbf{u}_{l-1}\} = \mathbf{0} \tag{2.5.27}$$

Inserting equations (2.5.26a and b) into equation (2.5.27), we obtain the characteristic equation

$$\begin{Bmatrix} 0 \\ 0 \end{Bmatrix} = \begin{bmatrix} C_{11} & C_{12} \\ C_{21} & C_{22} \end{bmatrix} \begin{Bmatrix} A \\ C \end{Bmatrix} \tag{2.5.28}$$

in which

$$C_{11} = b_{11}\phi_{Px} + b_{12}\phi_{Pz} + Z_P^{-1}(a_{11}'\phi_{Px}' + a_{12}'\phi_{Pz}') + Z_P^{-2}(a_{11}\phi_{Px} + a_{12}\phi_{Pz})$$

$$C_{12} = b_{11}\phi_{Sx} + b_{12}\phi_{Sz} + Z_S^{-1}(a_{11}'\phi_{Sx}' + a_{12}'\phi_{Sz}') + Z_S^{-2}(a_{11}\phi_{Sx} + a_{12}\phi_{Sz})$$

$$C_{21} = b_{21}\phi_{Px} + b_{22}\phi_{Pz} + Z_P^{-1}(a_{21}'\phi_{Px}' + a_{22}'\phi_{Pz}') + Z_P^{-2}(a_{21}\phi_{Px} + a_{22}\phi_{Pz})$$

$$C_{22} = b_{21}\phi_{Sx} + b_{22}\phi_{Sz} + Z_S^{-1}(a_{21}'\phi_{Sx}' + a_{22}'\phi_{Sz}') + Z_S^{-2}(a_{21}\phi_{Sx} + a_{22}\phi_{Sz})$$

The existence of a nontrivial solution to equation (2.5.28) requires the vanishing of the determinant of the matrix in equation (2.5.28). Hence, the following must be satisfied.

$$\begin{vmatrix} C_{11} & C_{12} \\ C_{21} & C_{22} \end{vmatrix} = 0 \tag{2.5.29}$$

Equation (2.5.29) provides the spectrum equation for the Rayleigh surface wave modeled with the TLM2. While the Rayleigh surface wave is *non-dispersive* in the continuum, it is *dispersive* in the TLM2 model, as will be seen in section 2.5.2. In section 2.5.2, three different combinations of tuning factors are again applied in order to investigate the effect of the tuning factors on the accuracy of eigenvalues obtained with the TLM2.

2.5.2 Numerical dispersion and tuning factors

In this section, we characterize the numerical dispersion of *SV-P* waves modeled with the TLM2 by means of the problems formulated in section 2.5.1 and an additional problem of the Mindlin plate. To begin with, we explore the features of numerical dispersion of the body waves in a discrete homogeneous full-space. Then, we try to determine the optimal values for tuning factors. Thereafter, to verify the improvement in eigenvalues achieved by virtue of the optimal tuning factors, we solve three free-vibration problems such as a homogeneous plate with mixed boundary conditions, the Mindlin plate with stress-free boundary conditions, and the Rayleigh surface wave on a homogeneous half-space.

(1) Body waves

We here characterize the numerical dispersion of body waves in a homogeneous full-space modeled with the TLM2, being subjected to *SV-P* wave motion. For this purpose, we compute not only the phase velocities V_S and V_P in equations (2.5.17a and b), but also the polarization at both external and internal nodes, i.e. Θ and Θ' in equation (2.5.9a and b). Then, we compare them with those obtained from the continuum. Since the present problem is in a plane-strain state, the Poisson's ratio ν possibly has its effect on the numerical dispersion phenomena in the TLM2 model. Therefore, five Poisson's ratios of ν=0.0, 0.1, 0.2, 0.3, and 0.4 are considered. In addition, to show the effect of tuning factors on the numerical dispersion, the TLM2 model is calculated for three different mass matrices of fully lumped $\mathbf{M}_L$ (μ=0), tuned $\mathbf{M}_T$ (μ=0.33), and fully consistent $\mathbf{M}_C$ (μ=1) as setting α=β=1.0 for the matrix $\mathbf{A}$.

Figures 2.5.4a,b–8a,b display the numerical results for ν=0.0, 0.1, 0.2, 0.3, and 0.4, respectively. In each figure a, the two quantities of V_S/C_S and V_P/C_P are shown as a function of the vertical wavenumber ξ_z and the propagation angle θ. On the other hand, in each figure b, the other two quantities of θ–Θ and θ–Θ' are shown as a function of ξ_z and θ. The angles considered are θ=15, 30, 45, 60, and 75. To show the effect of tuning factors, all the results for the fully lumped mass matrix $\mathbf{M}_L$ (μ=0), the tuned mass matrix $\mathbf{M}_T$ (μ=0.55), and the fully consistent mass matrix $\mathbf{M}_C$ (μ=1) are shown together in each plot. The dashed, solid, and dotted lines represent the results obtained by means of $\mathbf{M}_L$, $\mathbf{M}_T$ and $\mathbf{M}_C$, respectively. Also, it is noted that several discontinuities exist due to the stopping bands as seen in figure 2.5.2.

It is observed in all the figures 2.5.4a,b–8a,b that the TLM2 model for *SV-P* waves has the numerical dispersion that is dependent on both of ξ_z and θ. Concerning the ratios of V_S/C_S and V_P/C_P in each figure a, it is seen that the degree of the numerical dispersion is larger and larger as the vertical wavenumber ξ_z becomes larger. It is also shown that the dependency of the numerical dispersion on the Poisson's ratio exists, but is not significant. With regard to the polarization in each figure b, the two facts are to be noticed: (1) the polarization is dependent of the mass tuning factor μ and (2) when setting α=β, the polarization is dependent of the Poisson's ratio. Remember that the exact opposite observations are achieved in section 2.3 for the TLM1. In addition, it is noticed that the results computed for the tuned mass matrix with μ=0.33 ($\mathbf{M}_T$) are a little bit better than those calculated for the fully lumped and consistent mass matrices, which is true particularly for approximately $\xi_z/\pi(=2h/\lambda_z)\leq 4/5$. By contrast, for $\xi_z/\pi>4/5$, the degree of the numerical dispersion is significant regardless of the considered values of μ. This observation is identical to that for the TLM2 for *SV-P* wave in section 2.4. Therefore, the same range of ξ_z as the TLM2 for *SH* wave, i.e. $0<\xi_z/\pi<4/5$, is applied to determine the optimal tuning factors for the TLM2 for *SV-P* wave. Furthermore, the condition of $\xi_z/\pi<4/5$ again provides a lower bound for the number of thin layers per wavelength $N_\lambda(=\lambda_z/h)$ such that $N_\lambda \geq 5/2$.

(2) Tuning factors

We begin with determining an optimal value for the tuning factor μ. As following the same reasoning as the case of the TLM1 in section 2.3, we simply decide the optimal value for μ as 0.33. Also, remember that figures 2.5.4a–8a already show that the use of μ=0.33 provides the smallest error among the three cases of μ=0.00, 0.33, and 1.00. Therefore, in this section, we shall seek optimal values for the remaining tuning factors α and β in conjunction with a fixed, optimal value μ=0.33.

Next, we try to determine the optimal values for α and β in the matrix **A**. For this goal, we start with defining two error functions ε_S and ε_P for *S* and *P* waves, respectively, as

$$\varepsilon_S = \varepsilon_S(\alpha,\beta) = \int_0^{(4/5)\pi}\left(\frac{V_S}{C_S}-1\right)^2 d\xi_z \tag{2.5.30a}$$

$$\varepsilon_P = \varepsilon_P(\alpha,\beta) = \int_0^{(4/5)\pi}\left(\frac{V_P}{C_P}-1\right)^2 d\xi_z \tag{2.5.30b}$$

which provide the integrated squared errors over the significant range of ξ_z, $0\le\xi_z/\pi(=2h/\lambda_z)\le 4/5$. Recognize that the error functions are now a function of not only α and β with a fixed value of μ=0.33, but also the Poisson's ration, because the problem of interest is in a plane-strain state.

Figures 2.5.9a,b–13a,b show the variation of the error functions ε_S and ε_P for the five different Poisson's ratios such as ν=0.0, 0.1, 0.2, 0.3, and 0.4, respectively, in terms of a standard surface plot. In each figure, considered are six different propagation angles of θ=15, 30, 45, 60, 75, and 90°. It is obvious that for each Poisson's ratio, there is *no* optimal combination of α and β that can ideally minimize both the error functions ε_S and ε_P regardless of the propagation angle θ. Also, notice that the degree of error of the TLM2 of interest is relatively very small in comparison with the degree of error of the TLM1 in section 2.3. This observation induces an important fact that as long as the optimal value of μ=0.33 is applied, the numerical dispersion error in the TLM2 for *SV-P* wave is not only negligible but also almost invariant with respect to the two tuning factors α and β. Finally, we simply choose a set of α=1.0 and β=1.0 as the optimal tuning factors, which is nothing but the case of the conventional TLM, i.e. the fully consistent matrix **A**.

(3) Plate with mixed boundary conditions

Consider next the free-vibration of the homogeneous plate with mixed boundary conditions that is formulated in section 2.5.1. By solving this problem, we estimate the effect of the tuning factors on the accuracy of the eigenvalues computed from the TLM2. The geometry and material properties of the plate are given such that the thickness H=1.0, the mass density ρ=1.0, the shear velocity C_S=1.0, and the Poisson's ratio ν=0.31. In addition, for a discrete model, the plate is discretized into 6 TLM2 thin-layers, i.e. N=6, which produces 24 distinct eigenvalues (or modes) for the problem of interest. We also consider three combinations of tuning factors such as (i) α=β=1, μ=0 ($\mathbf{A}_C$+$\mathbf{M}_L$); (ii) α=β=1, μ=0.33 ($\mathbf{A}_C$+$\mathbf{M}_T$); and (iii) α=β=1, μ=1 ($\mathbf{A}_C$+$\mathbf{M}_C$). Then, we compare each of three with the exact analytical solutions.

Figures 2.5.14a, b, and c present the frequency-wavenumber dispersion of the TLM2 solutions (dashed lines) computed for (i) α=β=1, μ=0 ($\mathbf{A}_C$+$\mathbf{M}_L$); (ii) α=β=1, μ=0.33 ($\mathbf{A}_C$+$\mathbf{M}_T$); and (iii) α=β=1, μ=1 ($\mathbf{A}_C$+$\mathbf{M}_C$), respectively, in comparison with the exact analytical solution (solid lines). In each figure, the symmetric and anti-symmetric modes are plotted separately. It is observed that the use of the optimal values of α=β=1, μ=0.33 ($\mathbf{A}_C$+$\mathbf{M}_T$) produces the best agreement with the exact analytical solution. So, it is proved that the optimal tuning factors improve the accuracy of the eigenvalues computed from the TLM2. In addition, it must be noticed that this improvement is achieved only for 8 or 9 modes, not for all the 24 computed modes. Remember that some similar results are observed for the *SH* wave problem in section 2.4 in which it is seen that only the first two-fifth of the set of all computed modes are accurate with the help of the optimal tuning factors. Similarly, it is concluded for this problem of *SV-P* wave that only the one-third (=8/24) of the set of all computed modes are accurate with the application of the optimal tuning factors.

(4) Mindlin plate

Here, we consider the Mindlin plate as an additional problem. The problem is the free-vibration of the homogeneous plate with stress-free conditions at the both top and bottom surfaces whose exact analytical solutions are derived and presented in chapter 4. By solving this problem, we again estimate the effect of the tuning factors on the accuracy of the eigenvalues computed from the TLM2. The geometry and material properties of the homogeneous plate are the exactly same as those of the plate with mixed boundary conditions, i.e. $\rho=C_S=H=1.0$ and $\nu=0.31$. For a discrete model, the plate is discretized again into 6 TLM2 thin-layers, i.e. $N=6$, which produces 26 distinct eigenvalues (or modes) for the problem of interest. We again consider three combinations of tuning factors such as (i) $\alpha=\beta=1$, $\mu=0$ ($\mathbf{A}_C+\mathbf{M}_L$); (ii) $\alpha=\beta=1$, $\mu=0.33$ ($\mathbf{A}_C+\mathbf{M}_T$); and (iii) $\alpha=\beta=1$, $\mu=1$ ($\mathbf{A}_C+\mathbf{M}_C$). Then, we compare each of three with the exact analytical solutions.

Figures 2.5.15a, b, and c present the frequency-wavenumber dispersion of the TLM1 solutions (dashed lines) computed for (i) $\alpha=\beta=1$, $\mu=0$ ($\mathbf{A}_C+\mathbf{M}_L$); (ii) $\alpha=\beta=1$, $\mu=0.33$ ($\mathbf{A}_C+\mathbf{M}_T$); and (iii) $\alpha=\beta=1$, $\mu=1$ ($\mathbf{A}_C+\mathbf{M}_C$), respectively, in comparison with the exact analytical solution (solid lines). In each figure, the symmetric and anti-symmetric modes are plotted separately for convenience in comparison. It is confirmed that the use of the optimal values of $\alpha=\beta=1$, $\mu=0.33$ ($\mathbf{A}_C+\mathbf{M}_T$) indeed produces the best agreement with the exact analytical solution. So, it is verified once again that the optimal tuning factors improve the accuracy of the eigenvalues computed from the TLM2 for *SV-P* wave problems. Also, note that this improvement is achieved only for about 8 or 9 modes. Therefore, it is again concluded that for the *SV-P* wave problem only about the one-third of the set of all computed modes are accurate with the application of the optimal tuning factors.

(5) Rayleigh surface waves in a homogenous half space.

We consider the problem of Rayleigh surface wave on a discrete homogeneous half-space that is formulated by means of the TLM2 in section 2.5.1. As numerically solving this problem of semi-infinite domain, we explore the influence of the optimal tuning factors on the accuracy of the TLM2 in terms of eigenvalues. The material properties of the homogeneous half-space are given such that the mass density ρ and the shear velocity C_S are both 1.0 and the Poisson's ratio ν is 0.31. We consider three combinations of tuning factors such as (i) $\alpha=\beta=1$, $\mu=0$ ($\mathbf{A}_C+\mathbf{M}_L$); (ii) $\alpha=\beta=1$, $\mu=0.33$ ($\mathbf{A}_C+\mathbf{M}_T$); and (iii) $\alpha=\beta=1$, $\mu=1$ ($\mathbf{A}_C+\mathbf{M}_C$) and compute the apparent phase velocity of the Rayleigh surface wave V_R for each combination. Then, we compare them with the true exact phase velocity C_R that is 0.9289 in the present problem.

Figure 2.5.16 presents the variation of V_R/C_R as a function of the horizontal wavenumber ξ_x for all the three combinations of tuning factors: (i) $\alpha=\beta=1$, $\mu=0$ ($\mathbf{A}_C+\mathbf{M}_L$, dotted line); (ii) $\alpha=\beta=1$, $\mu=0.33$ ($\mathbf{A}_C+\mathbf{M}_T$, solid line); and (iii) $\alpha=\beta=1$, $\mu=1$ ($\mathbf{A}_C+\mathbf{M}_C$, dashed line). Notice first that the apparent phase velocity for the Rayleigh surface wave V_R is dispersive, i.e. a function of ξ_x, while the true phase velocity C_R is non-dispersive in the continuum. Next, it is seen that the combination of $\alpha=\beta=1$, $\mu=0$ ($\mathbf{A}_C+\mathbf{M}_L$, dotted line) shows the best agreement with the exact solution for the range of the horizontal wavenumber ξ_x of interest. Therefore, it is revealed that the optimal tuning factors of $\alpha=\beta=1$ and $\mu=0.33$ do not improve to the best degree the accuracy of the TLM2 concerned with the semi-infinite media of interest. However, it should be realized that the degree of the numerical dispersion errors for all the three combinations is quite small. The reason is that the Rayleigh surface wave propagates only in the horizontal direction in which the TLM does not discretize.

2.5.3 Summary

In the first part of this section 2.5, the general solution and the frequency-wavenumber spectrum are obtained for the discrete *SV-P* wave equation modeled with the TLM2. The qualitative investigation of the spectrum has provided the convention for the wavelength along the discretization direction λ_z and the discretization size h, i.e. $\lambda_z \geq h$, which is exactly the same as *SH* wave modeled with the TLM2. In addition, it is observed that there exist four stopping band regions at which significant numerical dispersion can take place. Then, two guided wave problems are solved formally and perfectly by means of the obtained general solutions.

In the second part, extensive characterization of the *SV-P* body waves is performed for five Poisson's ratios of ν=0.0, 0.1, 0.2, 0.3, and 0.4. It is confirmed that for the TLM2 model, the range of $0<\xi_z/\pi<4/5$ is only useful as determining the optimal tuning factors, and furthermore provides a lower bound for the number of thin layers per wavelength $N_\lambda(=\lambda_z/h)$ such that $N_\lambda \geq 5/2$. Then, the calculation of the error functions $\varepsilon_S(\alpha,\beta)$ and $\varepsilon_P(\alpha,\beta)$ has determined the optimal tuning factors as $\alpha=\beta=1$ and $\mu=0.33$. By analyzing two free-vibration problems of finite domain, it is verified that the optimal tuning factors indeed improve the accuracy of the eigenvalues in the context of the TLM. In addition, it is found that for *SV-P* wave problems, only the one-third of the set of all computed modes are accurate with the application of the optimal tuning factors. In the last problem, the Rayleigh surface wave is considered. Interestingly, it is observed that the optimal tuning factors of $\alpha=\beta=1$ and $\mu=0.33$ do not improve to the best degree the accuracy of the TLM1. Instead, the tuning factors of $\alpha=\beta=1$ and $\mu=0$ (the case of fully lumped mass matrix) shows the best agreement with the exact solution concerned with the semi-infinite media of interest.

APPENDIX FOR SECTION 2.5

The matrices **A**, **B**, **G**, and **M** in equation (2.5.2c) are listed below.

$$\mathbf{A}=\frac{h}{30}\begin{Bmatrix}(5-\alpha)(\lambda+2G) & \cdot & 2\alpha(\lambda+2G) & \cdot & -\alpha(\lambda+2G) & \cdot \\ \cdot & (5-\beta)G & \cdot & 2\beta G & \cdot & -\beta G \\ 2\alpha(\lambda+2G) & \cdot & 4(5-\alpha)(\lambda+2G) & \cdot & 2\alpha(\lambda+2G) & \cdot \\ \cdot & 2\beta G & \cdot & 4(5-\beta)G & \cdot & 2\beta G \\ -\alpha(\lambda+2G) & \cdot & 2\alpha(\lambda+2G) & \cdot & (5-\alpha)(\lambda+2G) & \cdot \\ \cdot & -\beta G & \cdot & 2\beta G & \cdot & (5-\beta)G \end{Bmatrix}$$

$$\mathbf{B}=\frac{1}{6}\begin{Bmatrix}\cdot & 3(\lambda-G) & \cdot & -4(\lambda+G) & \cdot & (\lambda+G) \\ 3(\lambda-G) & \cdot & 4(\lambda+G) & \cdot & -(\lambda+G) & \cdot \\ \cdot & 4(\lambda+G) & \cdot & \cdot & \cdot & -4(\lambda+G) \\ -4(\lambda+G) & \cdot & \cdot & \cdot & 4(\lambda+G) & \cdot \\ \cdot & -(\lambda+G) & \cdot & 4(\lambda+G) & \cdot & -3(\lambda-G) \\ (\lambda+G) & \cdot & -4(\lambda+G) & \cdot & -3(\lambda-G) & \cdot \end{Bmatrix}$$

$$\mathbf{G}=\frac{1}{3h}\begin{Bmatrix}7(\lambda+2G) & \cdot & -8(\lambda+2G) & \cdot & (\lambda+2G) & \cdot \\ \cdot & 7G & \cdot & -8G & \cdot & G \\ -8(\lambda+2G) & \cdot & 16(\lambda+2G) & \cdot & -8(\lambda+2G) & \cdot \\ \cdot & -8G & \cdot & 16G & \cdot & -8G \\ (\lambda+2G) & \cdot & -8(\lambda+2G) & \cdot & 7(\lambda+2G) & \cdot \\ \cdot & G & \cdot & -8G & \cdot & 7G \end{Bmatrix}$$

$$\mathbf{M}=\frac{\rho h}{30}\begin{Bmatrix}(5-\mu) & \cdot & 2\mu & \cdot & -\mu & \cdot \\ \cdot & (5-\mu) & \cdot & 2\mu & \cdot & -\mu \\ 2\mu & \cdot & 4(5-\mu) & \cdot & 2\mu & \cdot \\ \cdot & 2\mu & \cdot & 4(5-\mu) & \cdot & 2\mu \\ -\mu & \cdot & 2\mu & \cdot & (5-\mu) & \cdot \\ \cdot & -\mu & \cdot & 2\mu & \cdot & (5-\mu) \end{Bmatrix}$$

The matrices $\bar{\mathbf{A}}$, $\bar{\mathbf{B}}$, $\bar{\mathbf{G}}$, and $\bar{\mathbf{M}}$ in equation (2.5.5c) are listed below.

$$\bar{\mathbf{A}} = \begin{Bmatrix} r(10-4\alpha Y^2) & \cdot & 4r\alpha Y & \cdot \\ \cdot & (10-4\beta Y^2) & \cdot & 4\beta Y \\ 4r\alpha Y & \cdot & 4r(5-\alpha) & \cdot \\ \cdot & 4\beta Y & \cdot & 4(5-\beta) \end{Bmatrix}$$

$$\bar{\mathbf{B}} = \begin{Bmatrix} \cdot & 20(r-1)Y\bar{Y} & \cdot & -80(r-1)\bar{Y} \\ 20(r-1)Y\bar{Y} & \cdot & -80(r-1)\bar{Y} & \cdot \\ \cdot & -80(r-1)\bar{Y} & \cdot & \cdot \\ -80(r-1)\bar{Y} & \cdot & \cdot & \cdot \end{Bmatrix}$$

$$\bar{\mathbf{G}} = \begin{Bmatrix} 120+40Y^2 & \cdot & -160Y & \cdot \\ \cdot & r(120+40Y^2) & \cdot & -160rY \\ -160Y & \cdot & 160 & \cdot \\ \cdot & -160rY & \cdot & 160r \end{Bmatrix}$$

$$\bar{\mathbf{M}} = \begin{Bmatrix} 10-4\mu Y^2 & \cdot & 4\mu Y & \cdot \\ \cdot & 10-4\mu Y^2 & \cdot & 4\mu Y \\ 4\mu Y & \cdot & 4(5-\mu) & \cdot \\ \cdot & 4\mu Y & \cdot & 4(5-\mu) \end{Bmatrix}$$

Figures for section 2.2

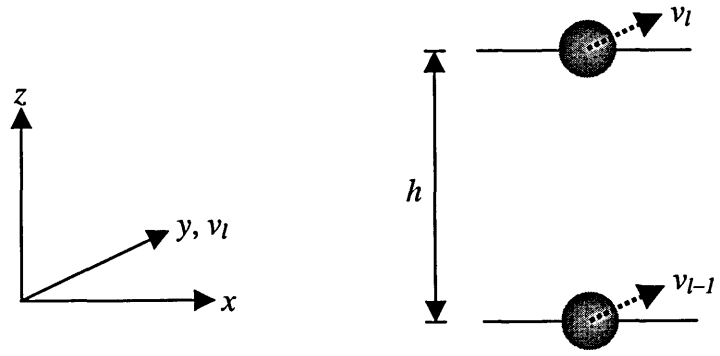

Figure 2.2.1 Coordinate system and a TLM1 thin-layer subjected to *SH* wave motion

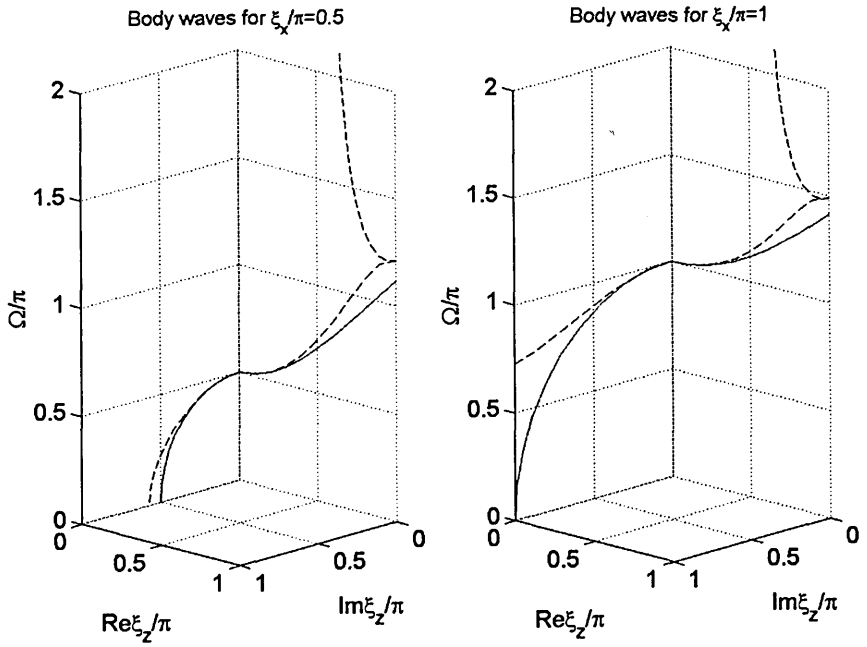

Figure 2.2.2 Dispersion of *SH* body waves as function of vertical wavenumber for fixed horizontal wavenumber: Left for ξ_x=0.5π, Right for ξ_x=1.0π (dashed line for TLM1, solid line for Exact)

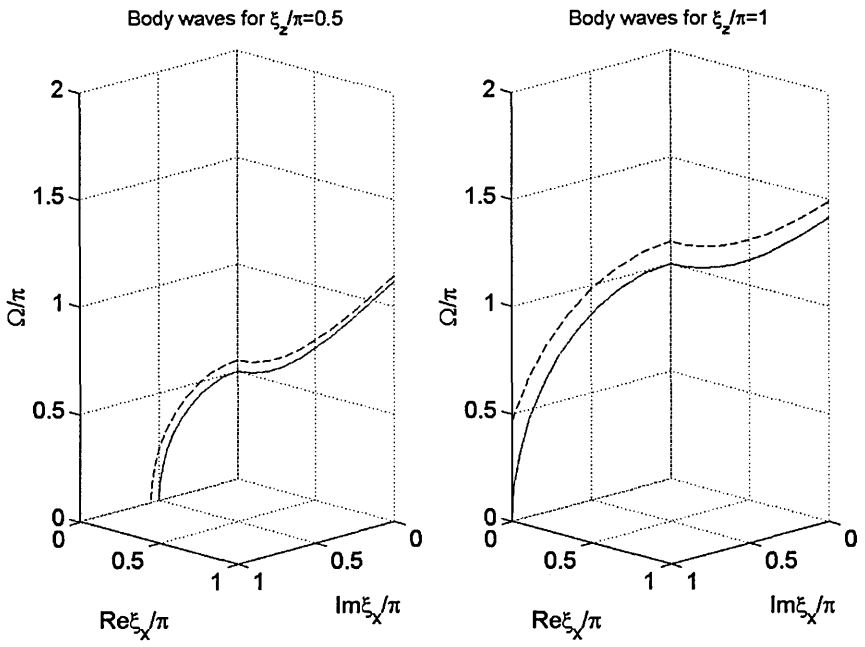

Figure 2.2.3 Dispersion of *SH* body waves as function of horizontal wavenumber for fixed vertical wavenumber: Left for $\xi_z=0.5\pi$, Right for $\xi_z=1.0\pi$ (dashed line for TLM1, solid line for Exact)

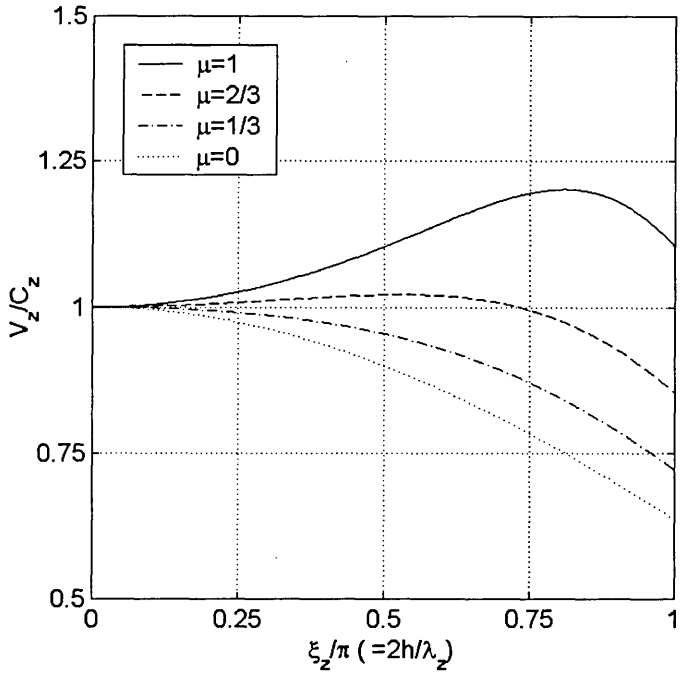

Figure 2.2.4 Numerical dispersion of an infinite shear beam modeled with TLM1 in terms of ratio of apparent vertical phase velocity to true vertical phase velocity (V_z/C_z)

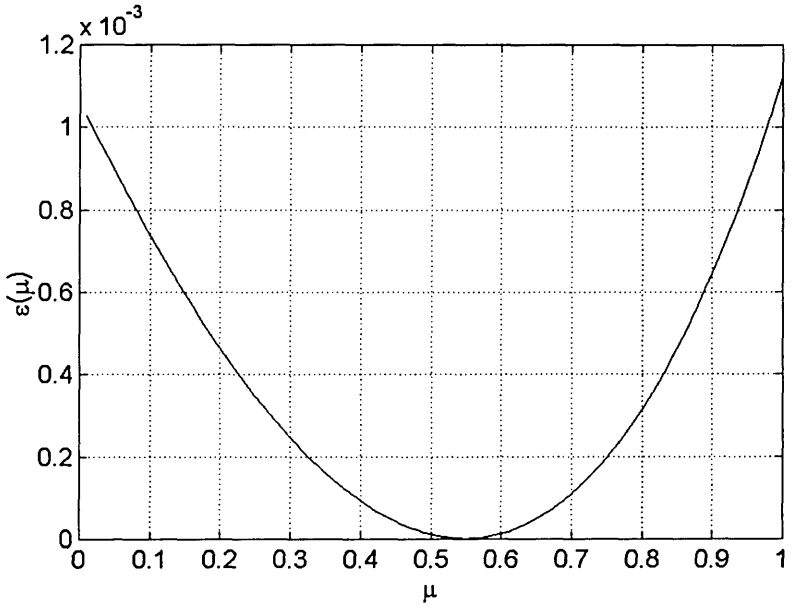

Figure 2.2.5 Integrated squared error ε for an infinite shear beam modeled with TLM1

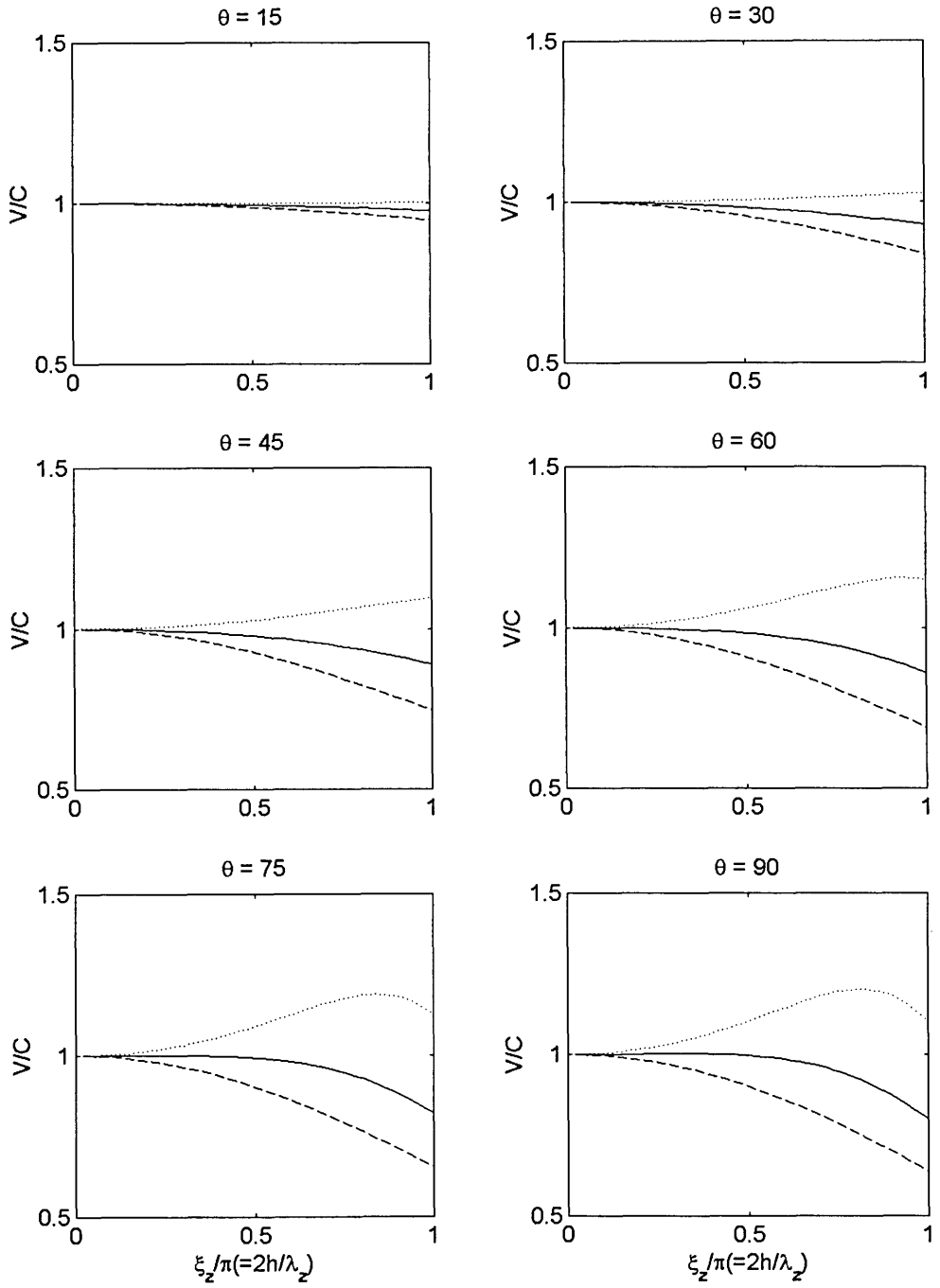

Figure 2.2.6 Numerical dispersion of a homogeneous full-space modeled with TLM1 in terms of ratio of apparent phase velocity to true phase velocity (V/C): β=1.0, μ=0.0 (dashed); β=1.0, μ=0.55 (solid); β=1.0, μ=1.0 (dotted)

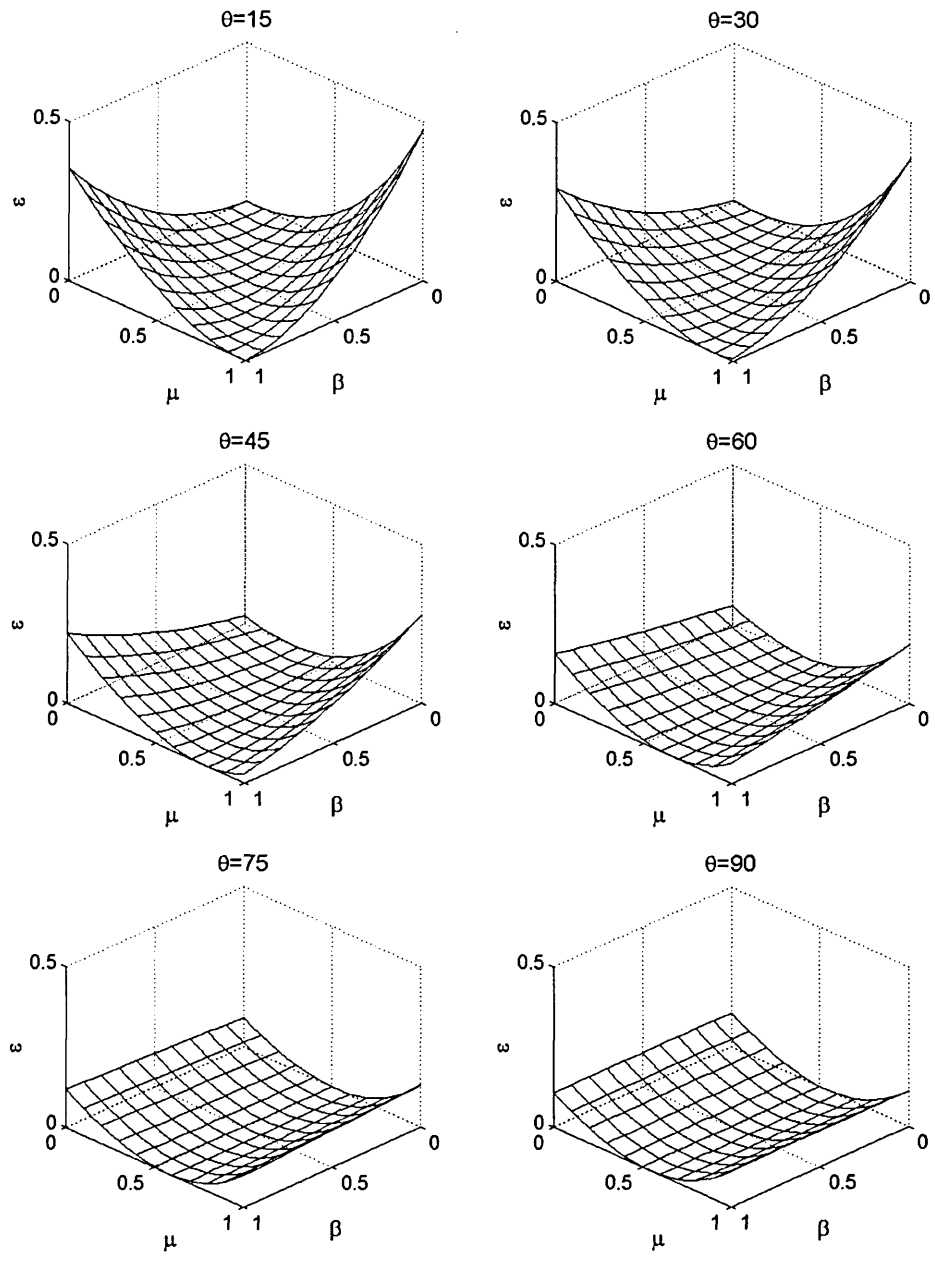

Figure 2.2.7 Integrated squared error ε for a homogeneous full-space modeled with TLM1 for θ=15, 30, 45, 60, 75, 90°

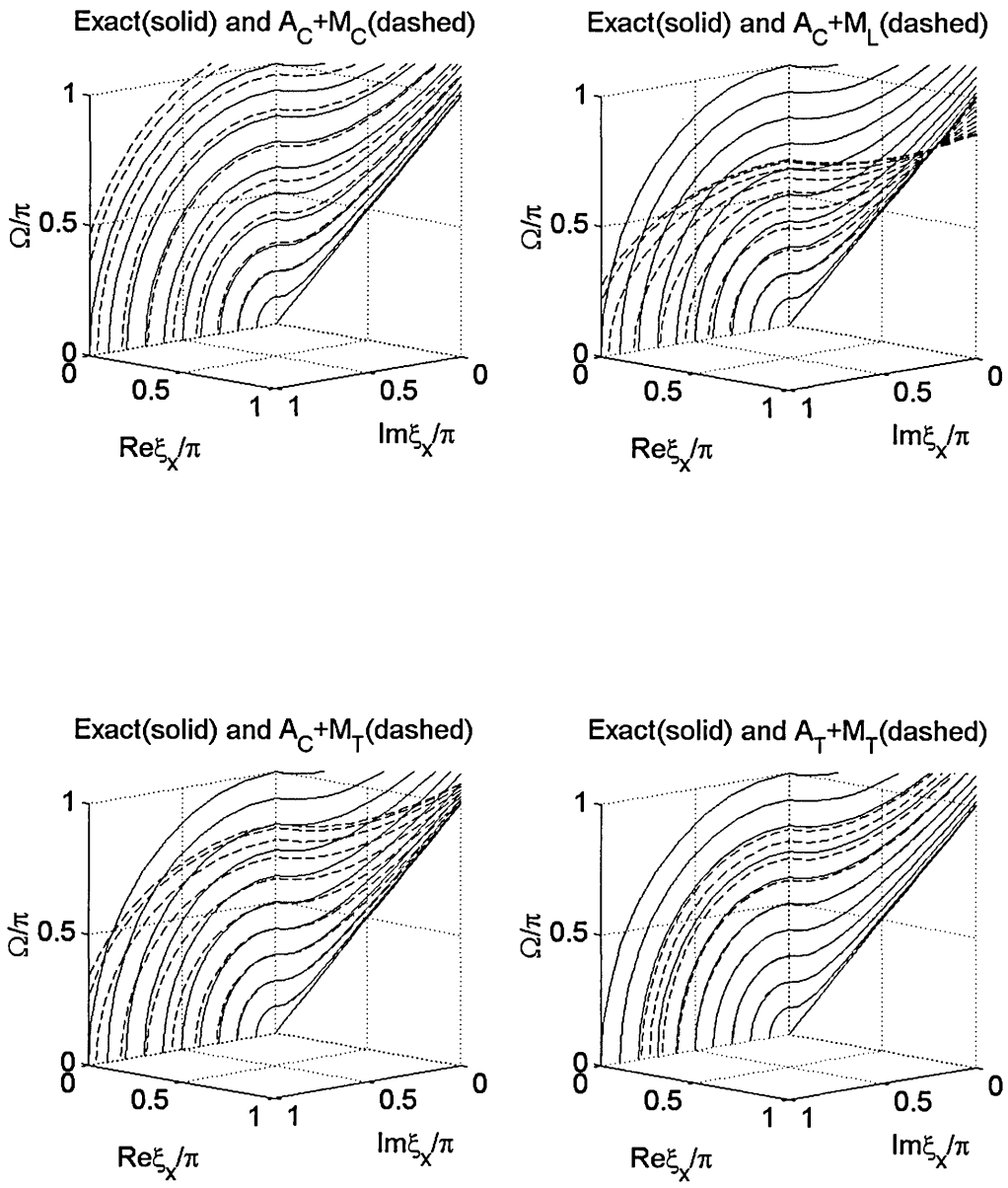

Figure 2.2.8 Dispersion curves of an *SH* homogeneous plate modeled with TLM1 for β=μ=1.0; β=1.0, μ=0.0; β=1.0, μ=0.55; and β=μ=0.55 (dashed line for TLM1, solid line for Exact)

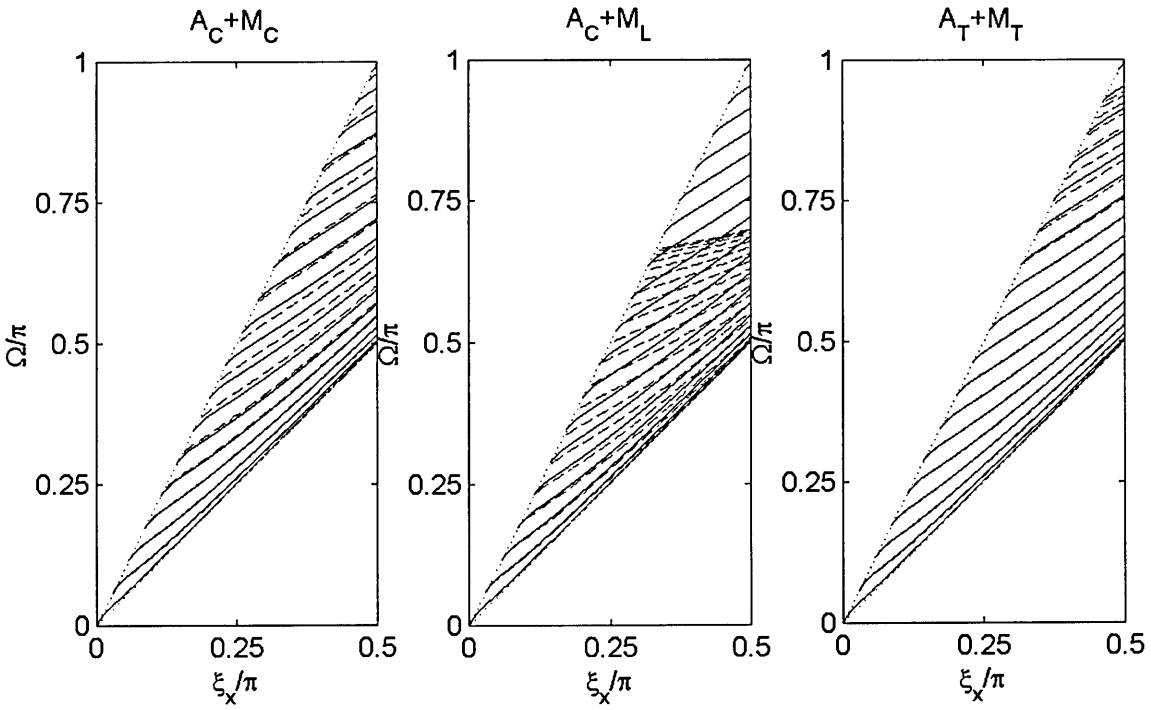

Figure 2.2.9 Dispersion curves of Love waves modeled with TLM1
for $\beta=\mu=1.0$; $\beta=1.0$, $\mu=0.0$; and $\beta=\mu=0.55$ (dashed line for TLM1, solid line for Exact)

Figures for section 2.3

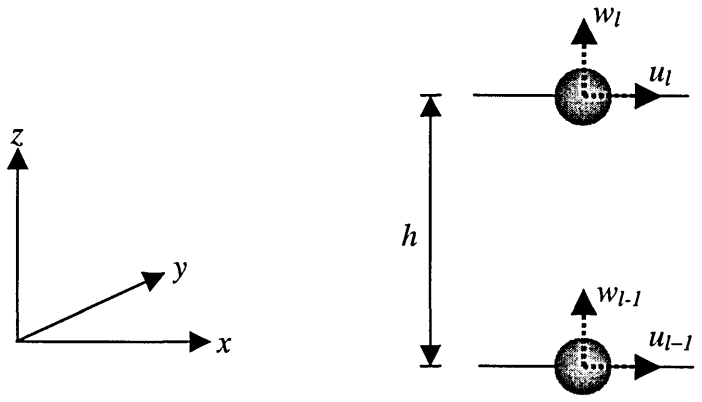

Figure 2.3.1 Coordinate system and a TLM1 thin-layer subjected to *SV-P* wave motion

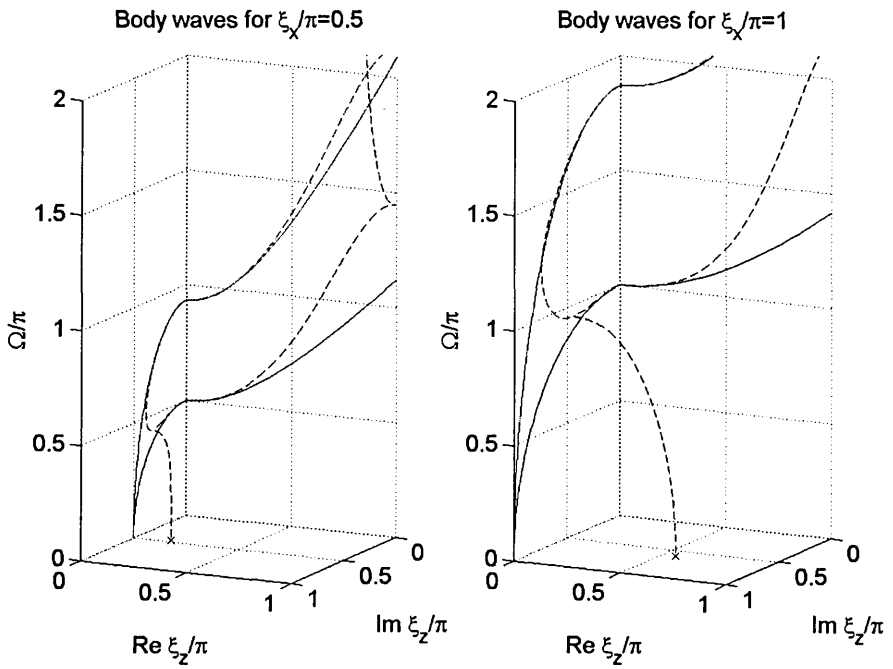

Figure 2.3.2 Dispersion of *SV-P* body waves (ν=0.30) as function of vertical wavenumber for fixed horizontal wavenumber: Left for ξ_x=0.5π, Right for ξ_x=1.0π (dashed line for TLM1, solid line for Exact)

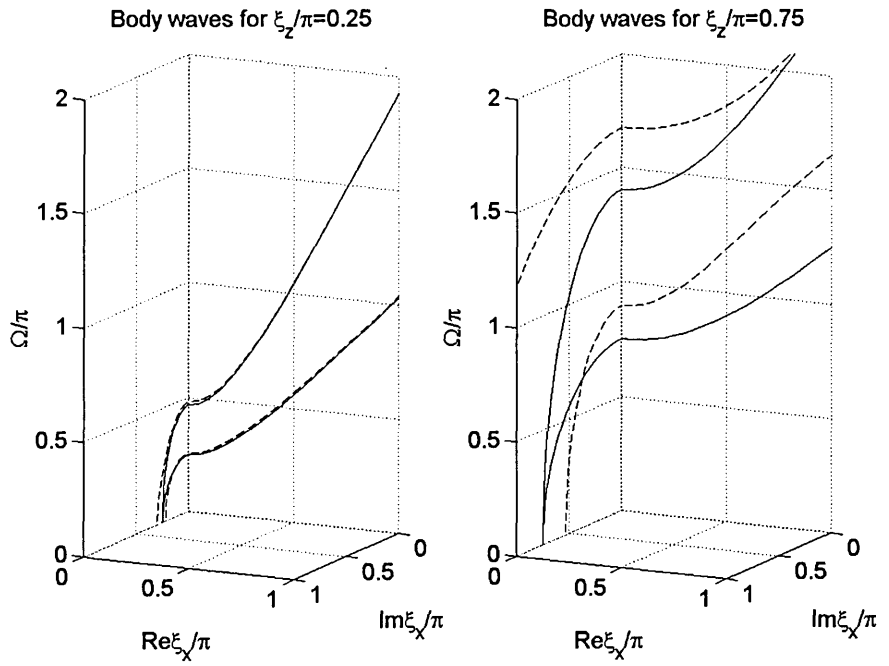

Figure 2.3.3 Dispersion of *SV-P* body waves (ν=0.30) as function of vertical wavenumber for fixed horizontal wavenumber: Left for ξ_x=0.25π, Right for ξ_x=0.75π (dashed line for TLM1, solid line for Exact)

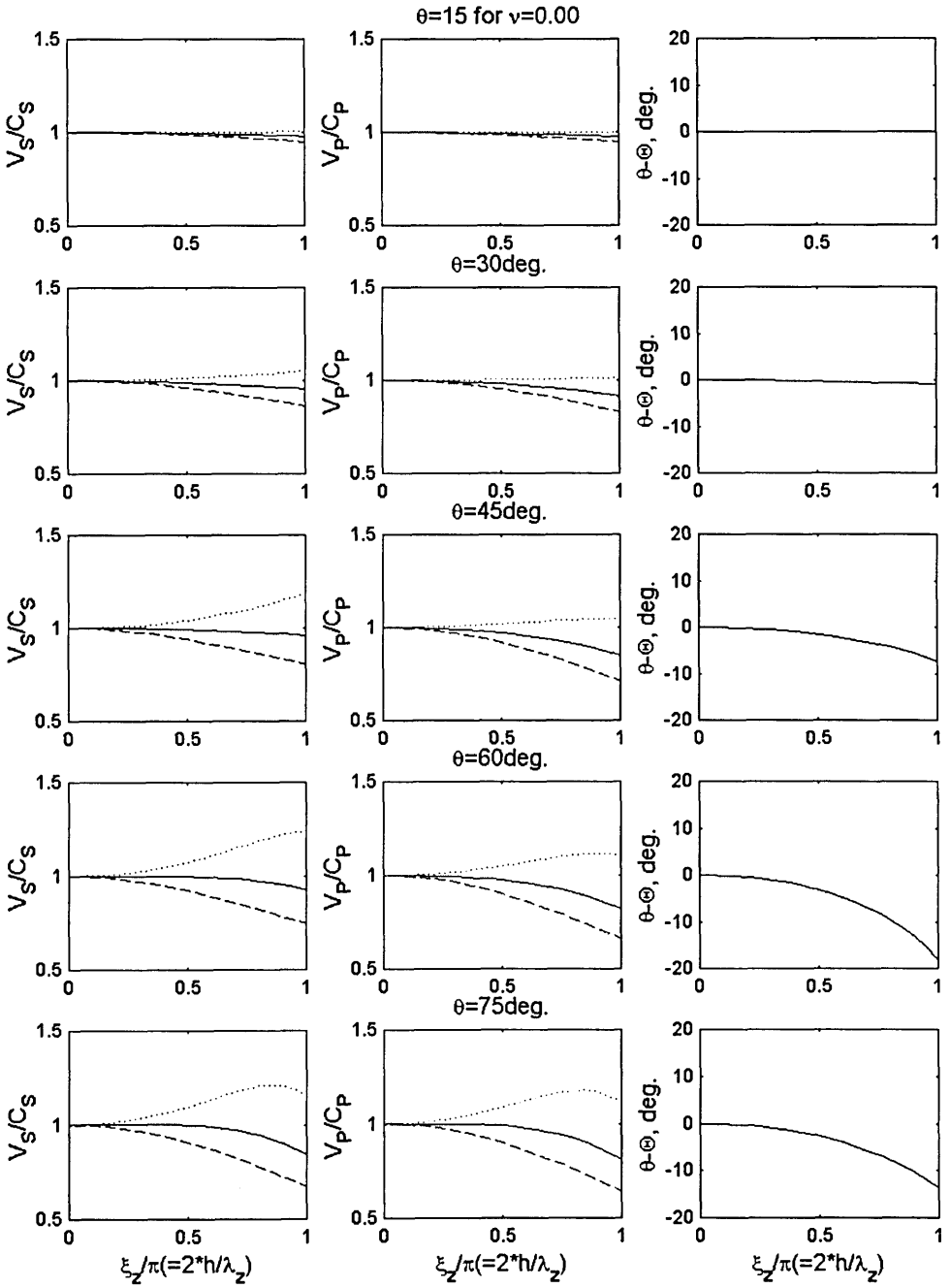

Figure 2.3.4 Numerical dispersion of a homogeneous full-space (ν=0.0) modeled with TLM1 in terms of ratios of apparent phase velocity to true phase velocity (V_S/C_S, V_P/C_P) and differences between propagation and polarity angles (θ−Θ): α=β=1.0, μ=0.0 (dashed); α=β=1.0, μ=0.55 (solid); α=β=1.0, μ=1.0 (dotted)

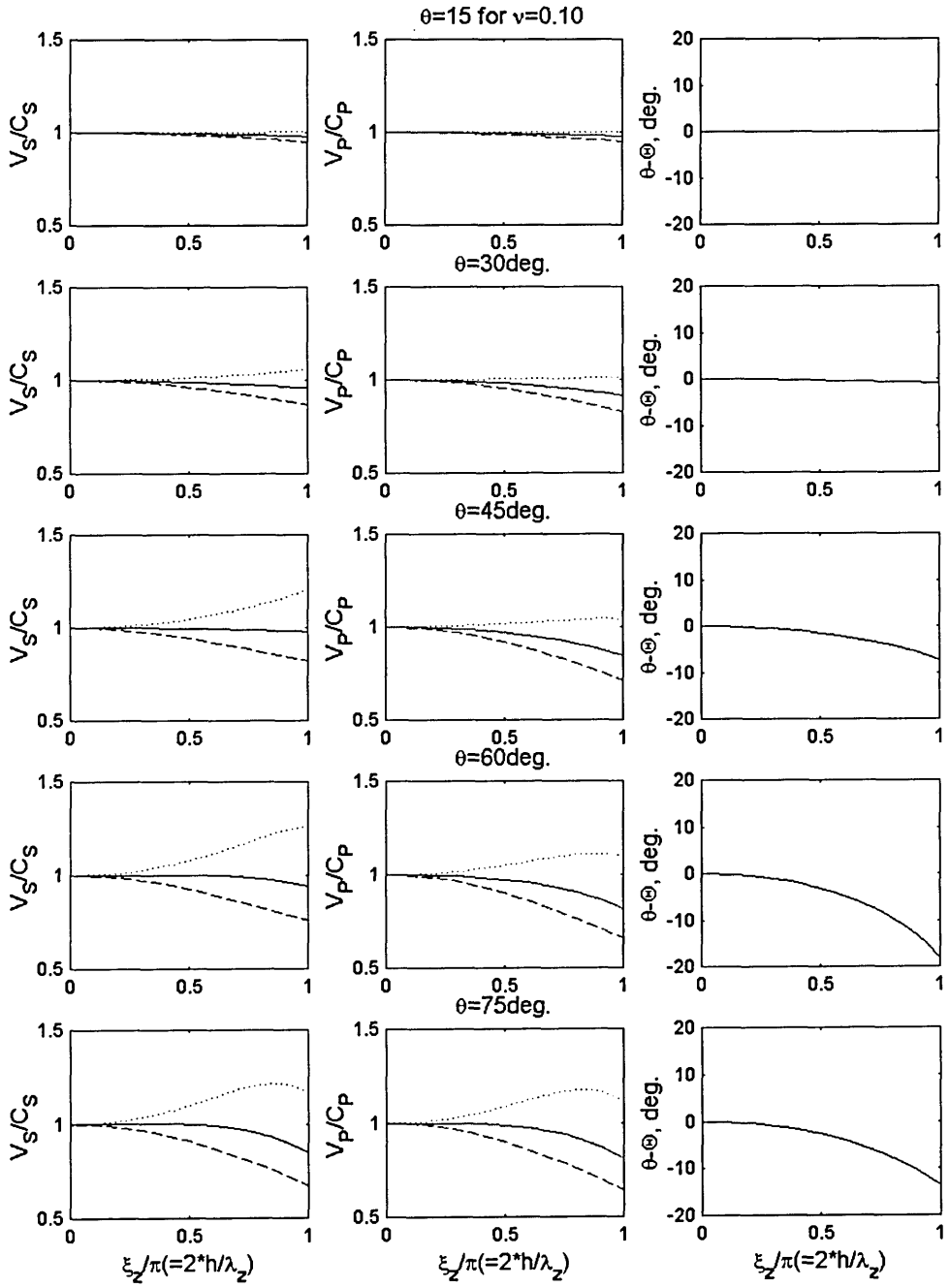

Figure 2.3.5 Numerical dispersion of a homogeneous full-space (ν=0.1) modeled with TLM1 in terms of ratios of apparent phase velocity to true phase velocity (V_S/C_S, V_P/C_P) and differences between propagation and polarity angles (θ–Θ):
α=β=1.0, μ=0.0 (dashed); α=β=1.0, μ=0.55 (solid); α=β=1.0, μ=1.0 (dotted)

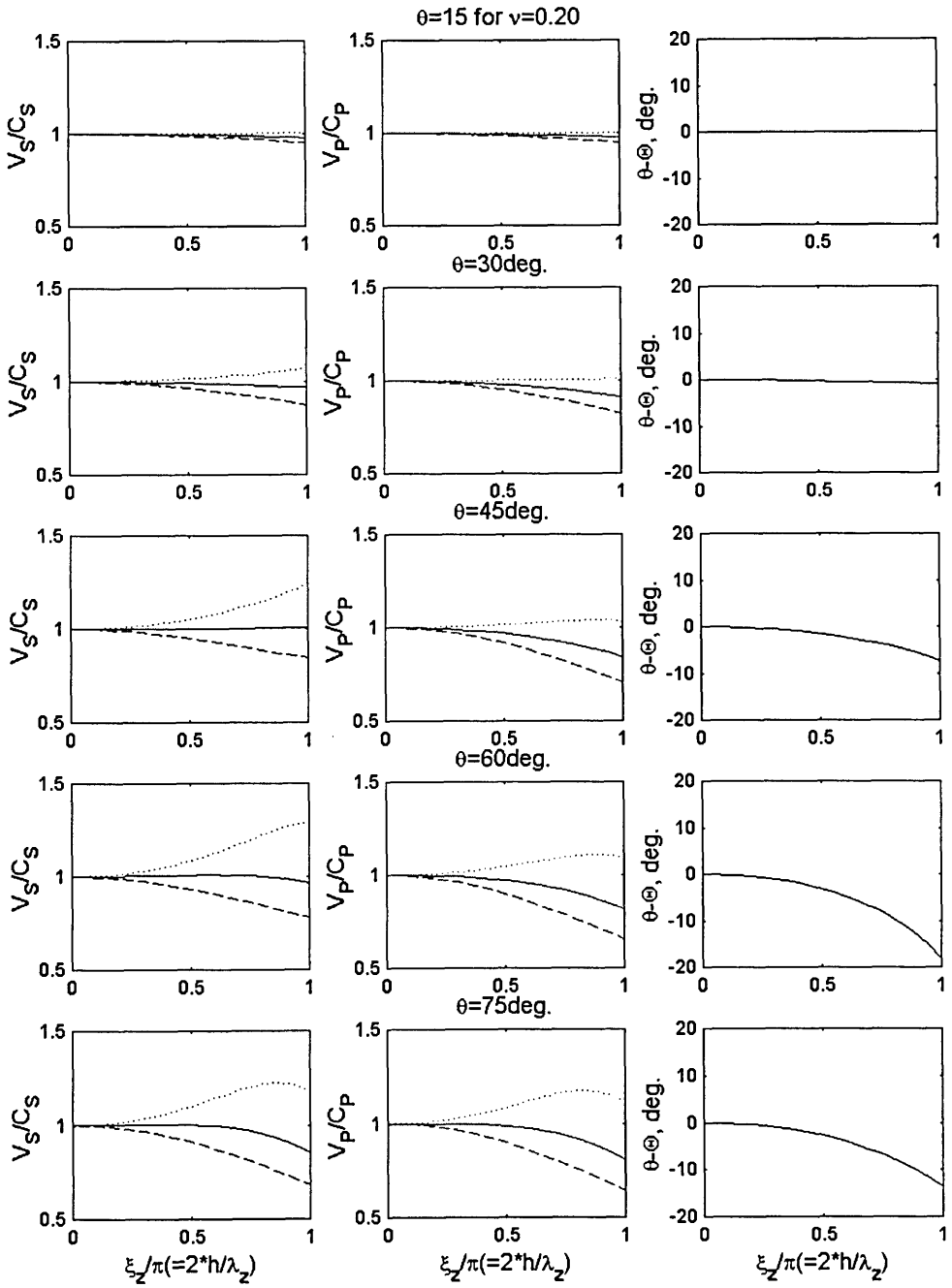

Figure 2.3.6 Numerical dispersion of a homogeneous full-space (ν=0.2) modeled with TLM1 in terms of ratios of apparent phase velocity to true phase velocity (V_S/C_S, V_P/C_P) and differences between propagation and polarity angles ($\theta-\Theta$):
$\alpha=\beta$=1.0, μ=0.0 (dashed); $\alpha=\beta$=1.0, μ=0.55 (solid); $\alpha=\beta$=1.0, μ=1.0 (dotted)

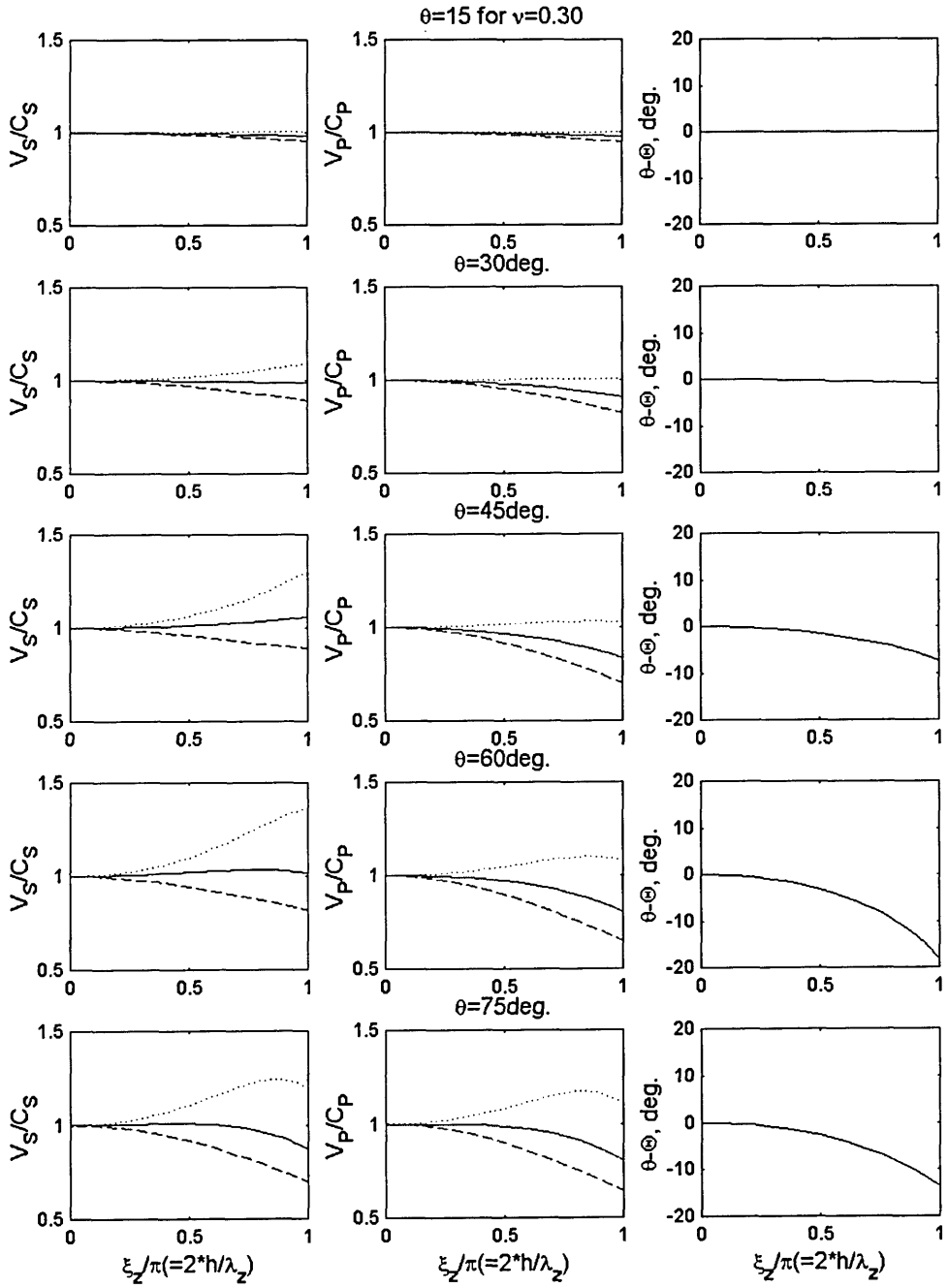

Figure 2.3.7 Numerical dispersion of a homogeneous full-space (ν=0.3) modeled with TLM1 in terms of ratios of apparent phase velocity to true phase velocity (V_S/C_S, V_P/C_P) and differences between propagation and polarity angles (θ–Θ): α=β=1.0, μ=0.0 (dashed); α=β=1.0, μ=0.55 (solid); α=β=1.0, μ=1.0 (dotted)

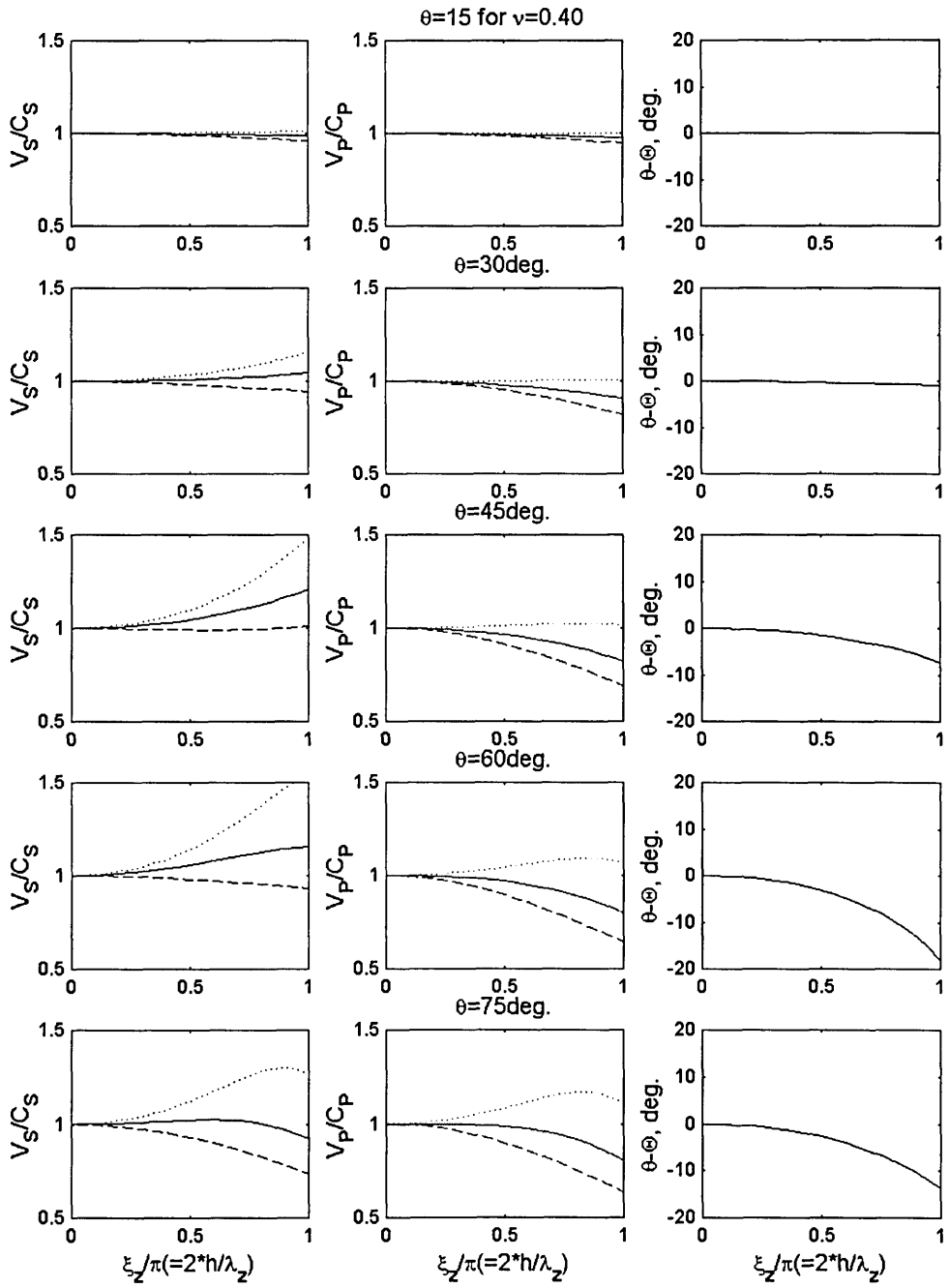

Figure 2.3.8 Numerical dispersion of a homogeneous full-space (ν=0.4) modeled with TLM1 in terms of ratios of apparent phase velocity to true phase velocity (V_S/C_S, V_P/C_P) and differences between propagation and polarity angles (θ–Θ): α=β=1.0, μ=0.0 (dashed); α=β=1.0, μ=0.55 (solid); α=β=1.0, μ=1.0 (dotted)

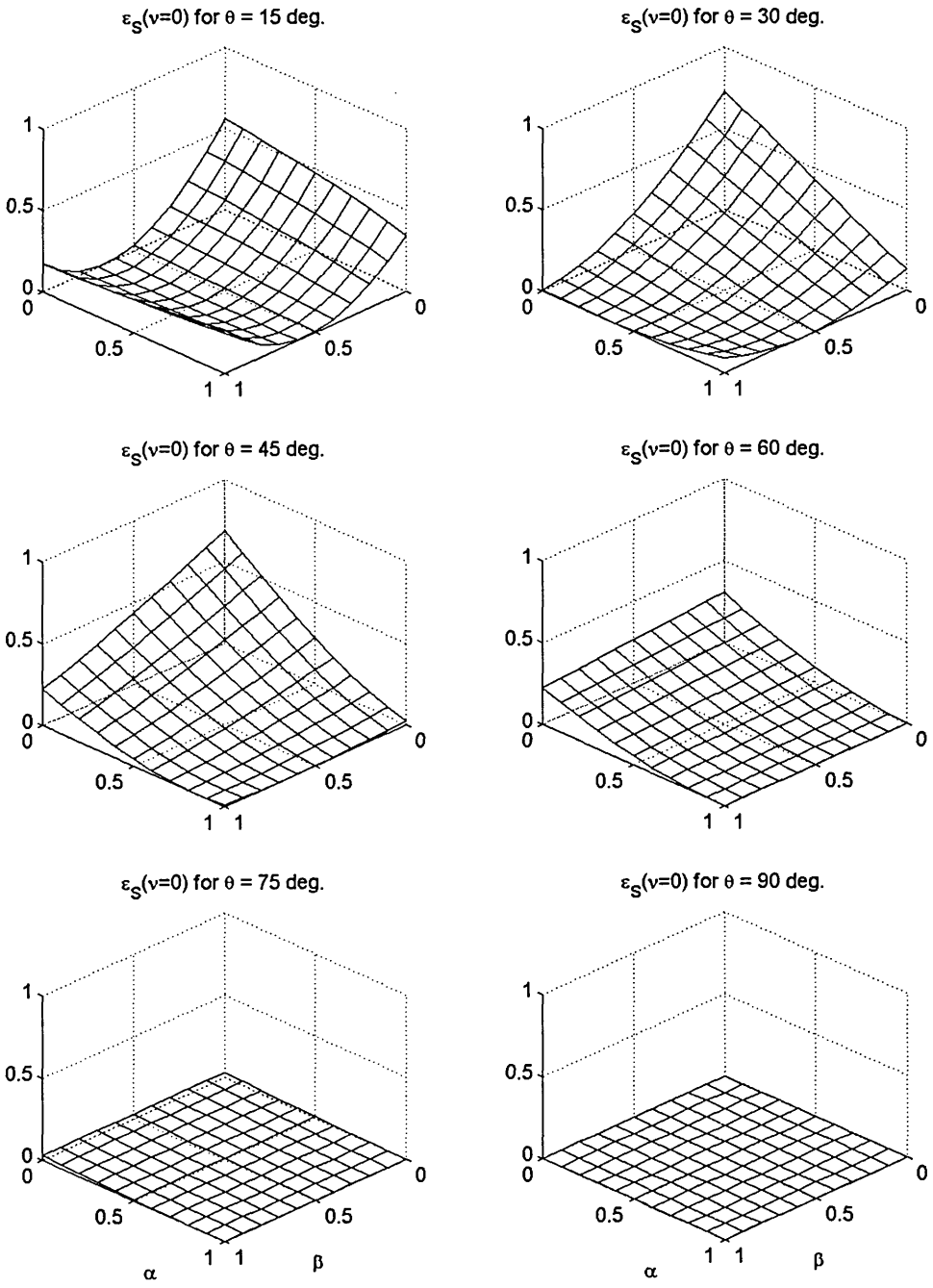

Figure 2.3.9a Integrated squared error ε_S for a full-space (ν=0.0) modeled with TLM1 for θ=15, 30, 45, 60, 75, 90°

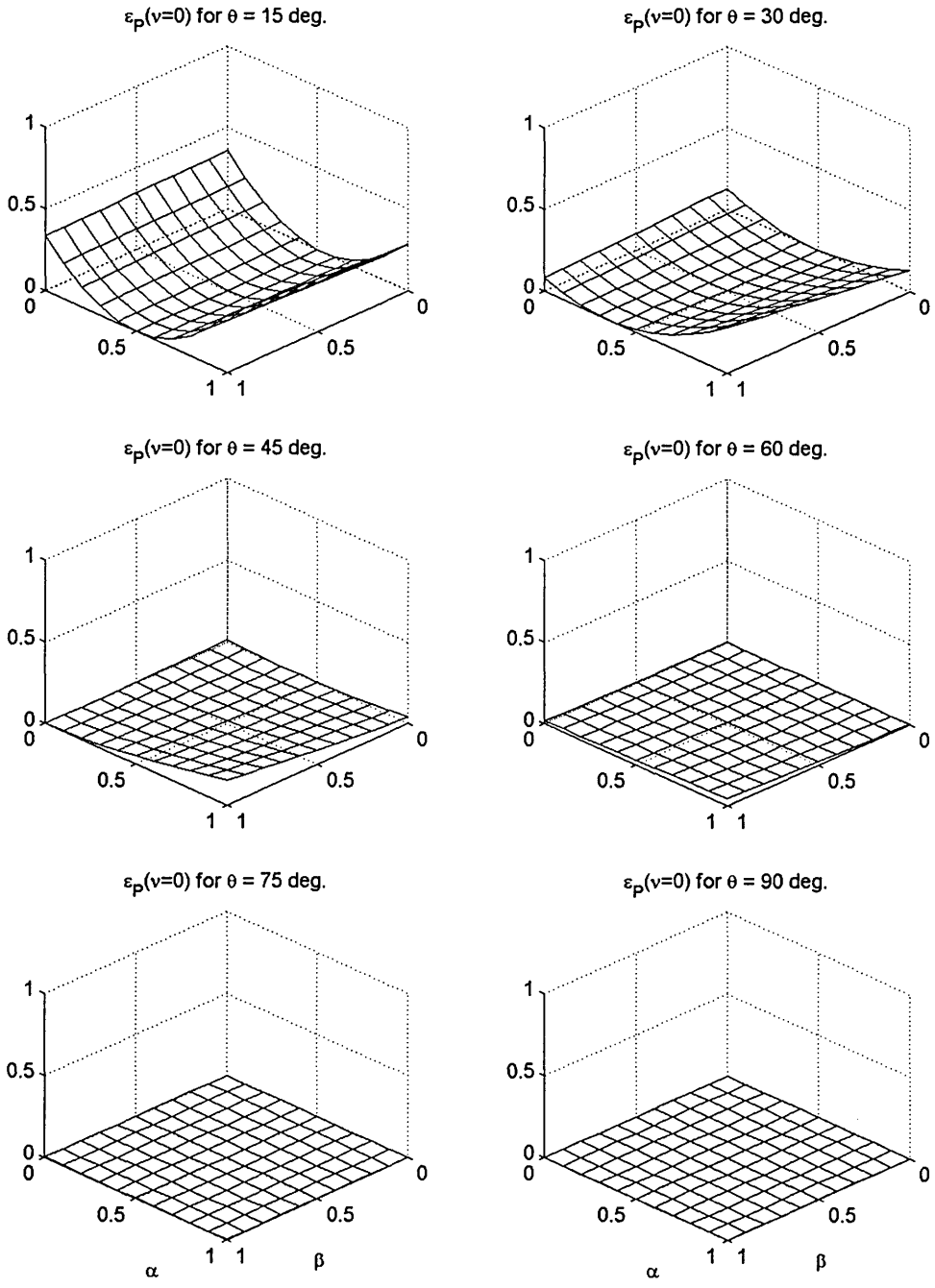

Figure 2.3.9b Integrated squared error ε_P for a full-space (ν=0.0) modeled with TLM1 for θ=15, 30, 45, 60, 75, 90°

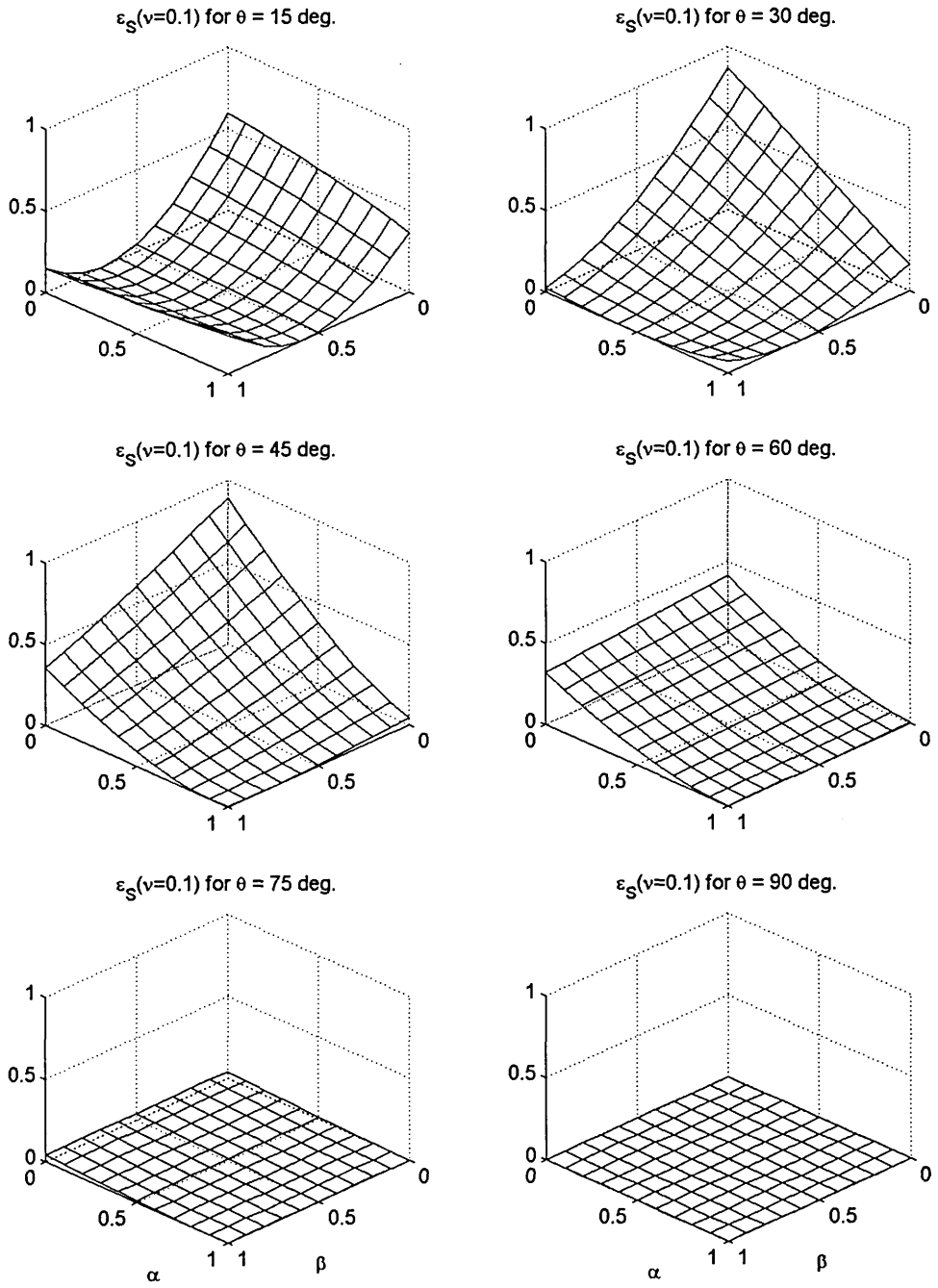

Figure 2.3.10a Integrated squared error ε_S for a full-space (ν=0.1) modeled with TLM1 for θ=15, 30, 45, 60, 75, 90°

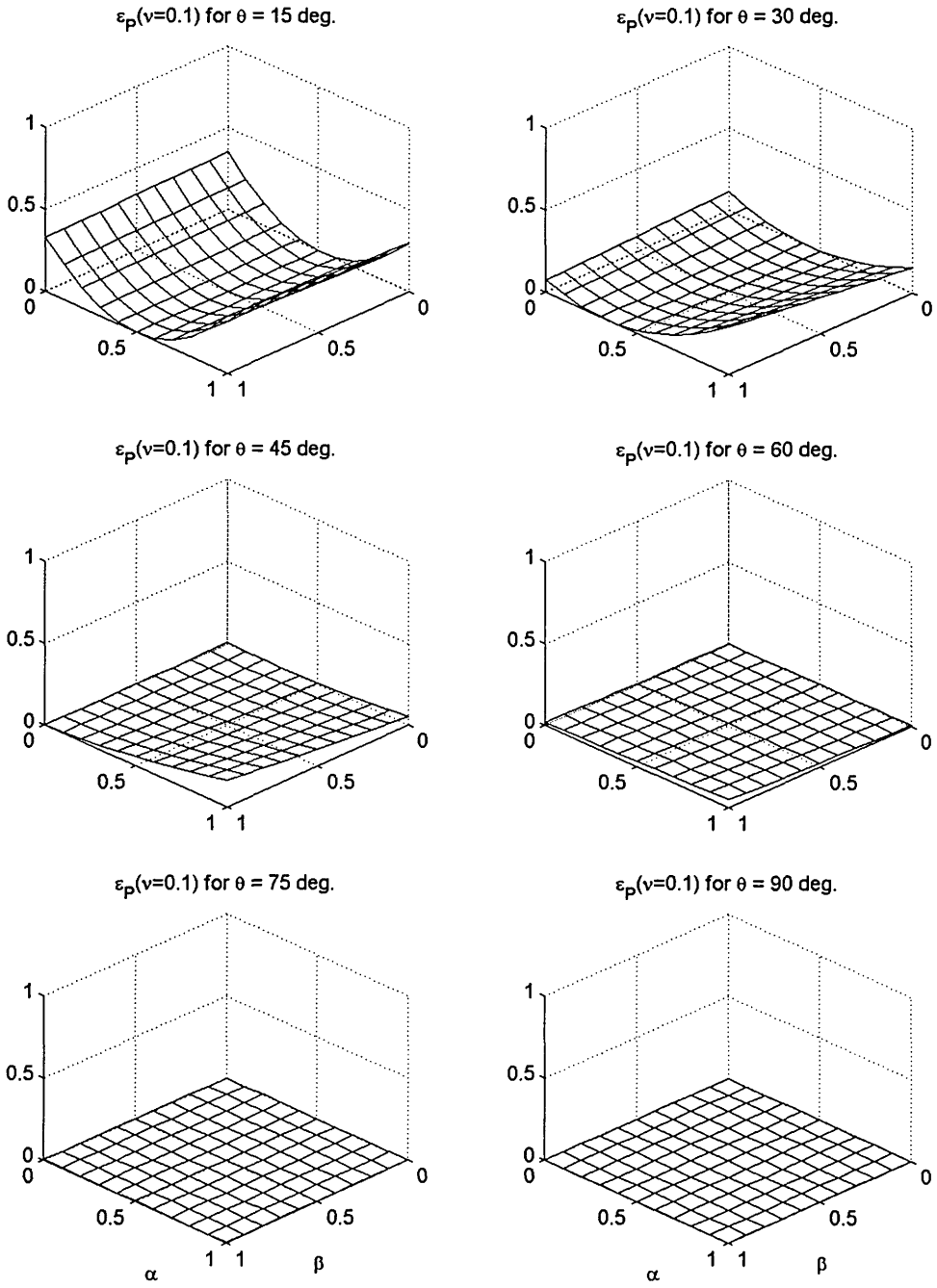

Figure 2.3.10b Integrated squared error ε_P for a full-space (ν=0.1) modeled with TLM1 for θ=15, 30, 45, 60, 75, 90°

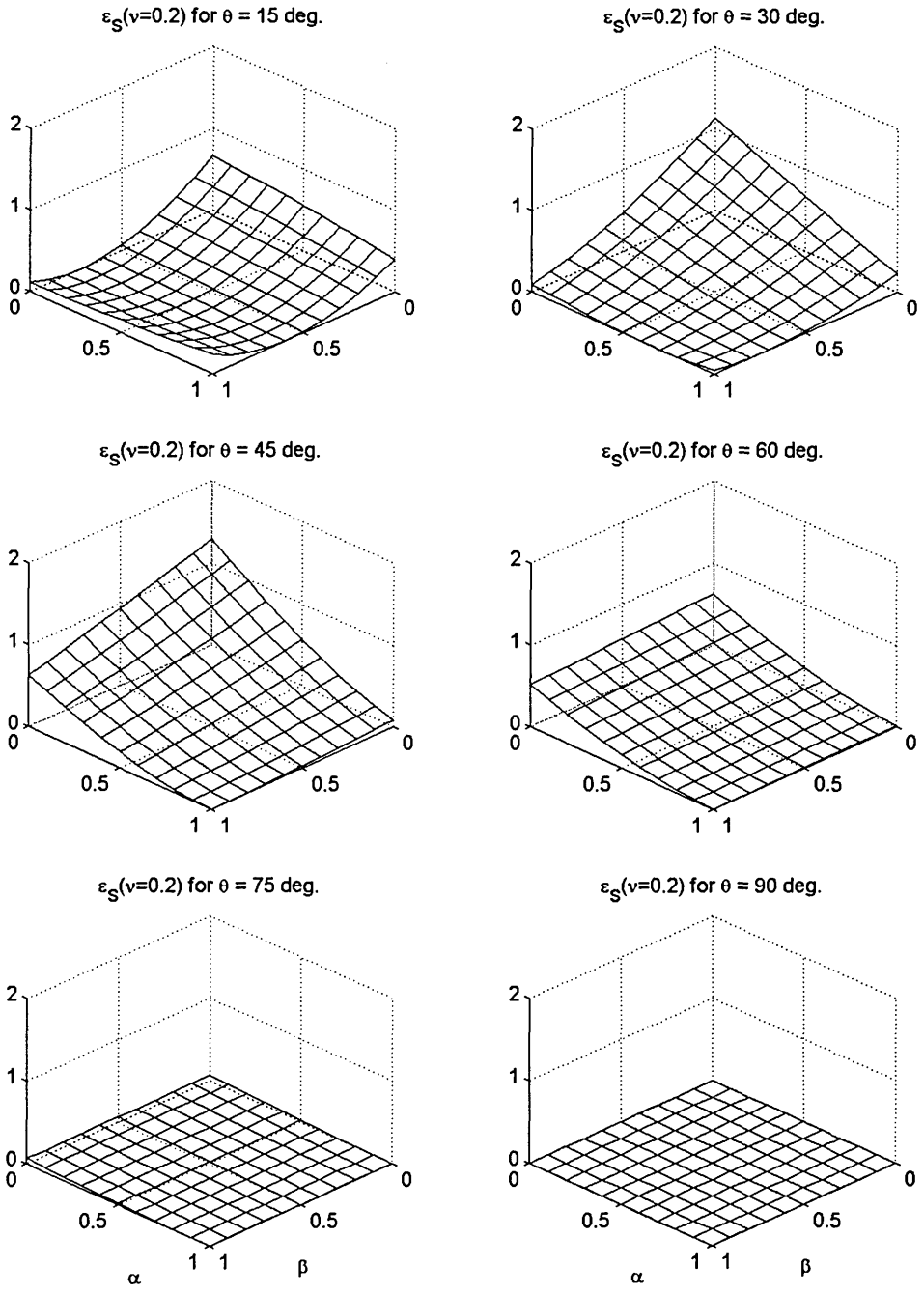

Figure 2.3.11a Integrated squared error ε_S for a full-space (ν=0.2) modeled with TLM1 for θ=15, 30, 45, 60, 75, 90°

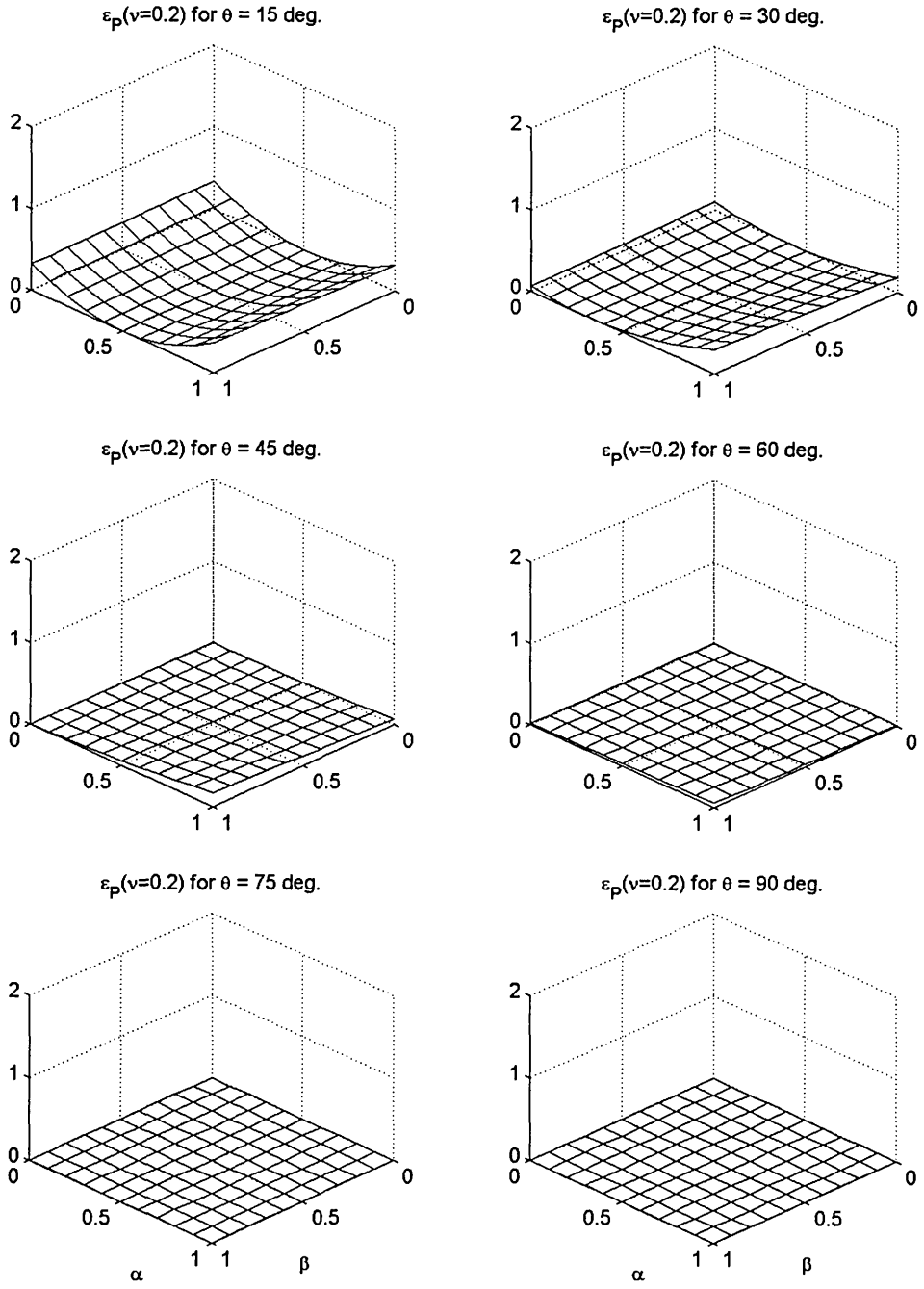

Figure 2.3.11b Integrated squared error ε_P for a full-space (ν=0.2) modeled with TLM1 for θ=15, 30, 45, 60, 75, 90°

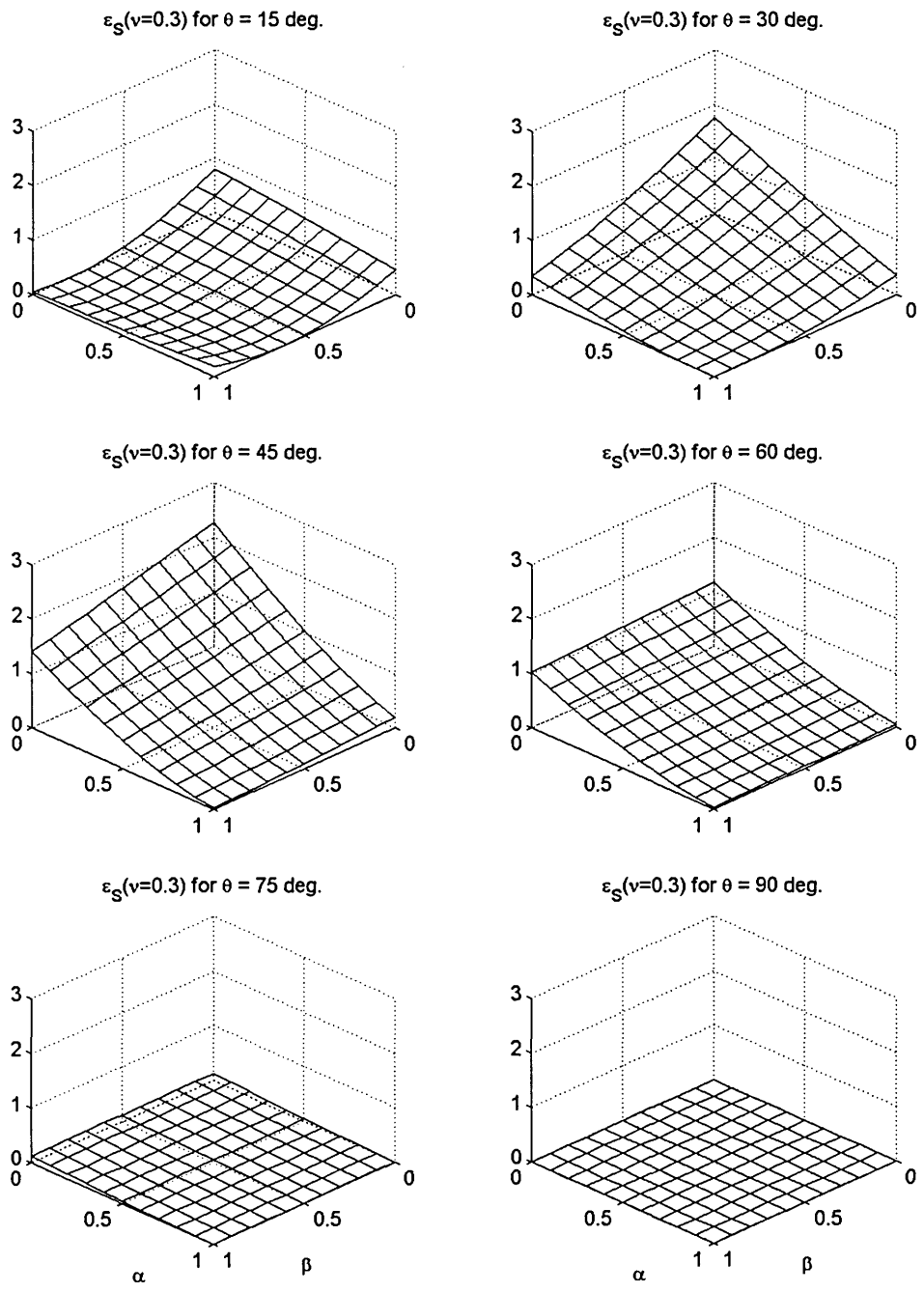

Figure 2.3.12a Integrated squared error ε_S for a full-space (ν=0.3) modeled with TLM1 for θ=15, 30, 45, 60, 75, 90°

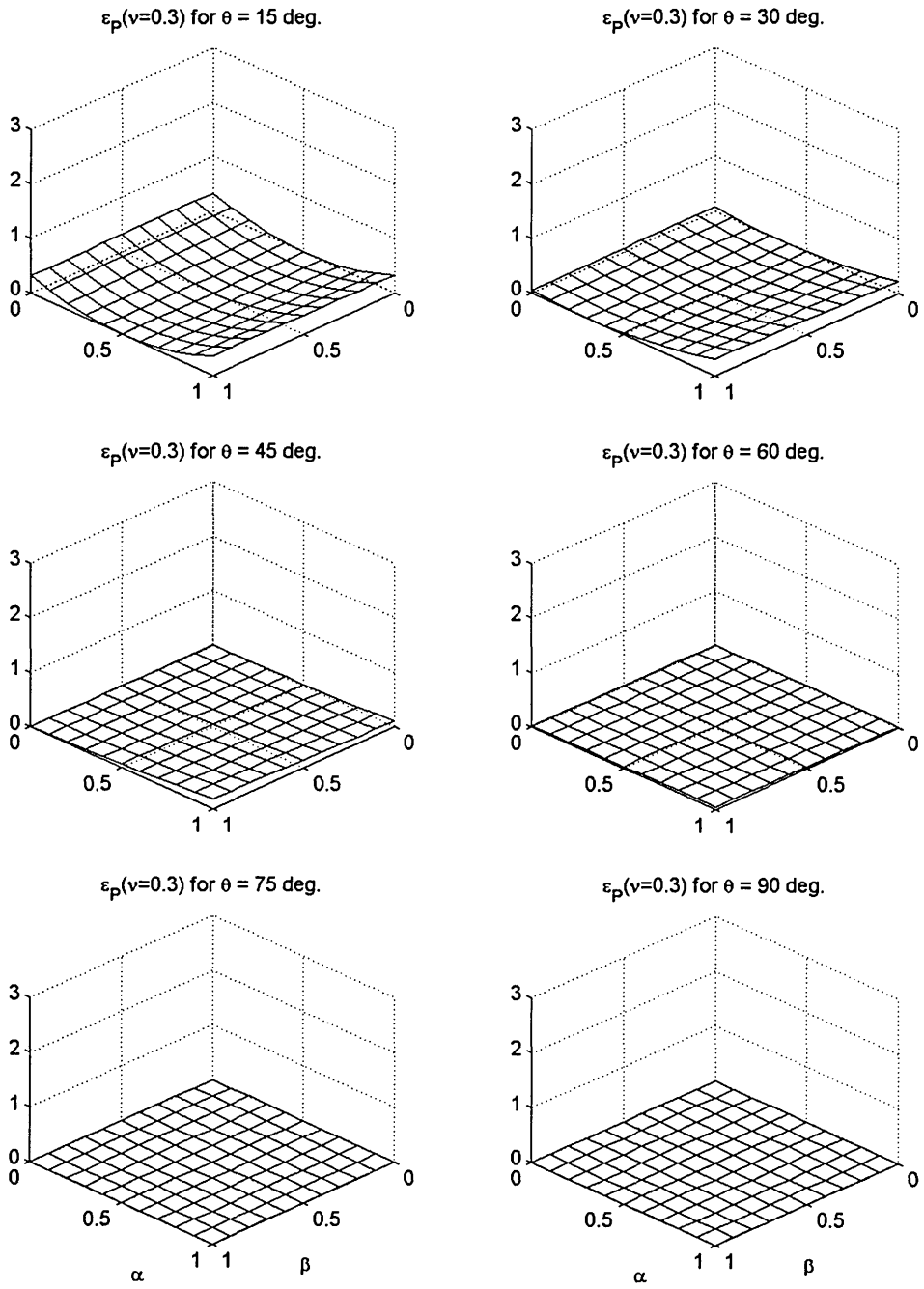

Figure 2.3.12b Integrated squared error ε_P for a full-space (ν=0.3) modeled with TLM1 for θ=15, 30, 45, 60, 75, 90°

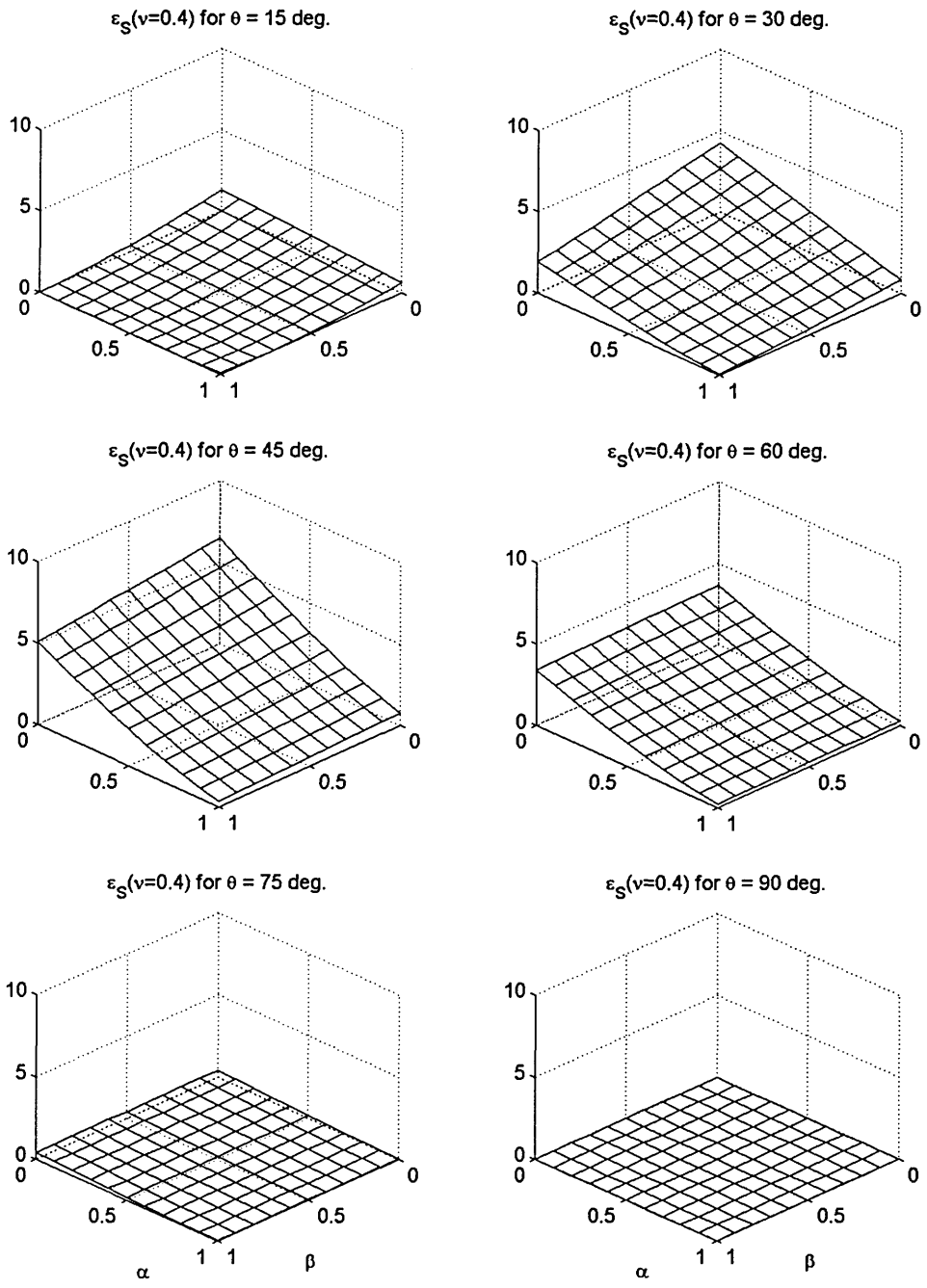

Figure 2.3.13a Integrated squared error ε_S for a full-space (ν=0.4) modeled with TLM1 for θ=15, 30, 45, 60, 75, 90°

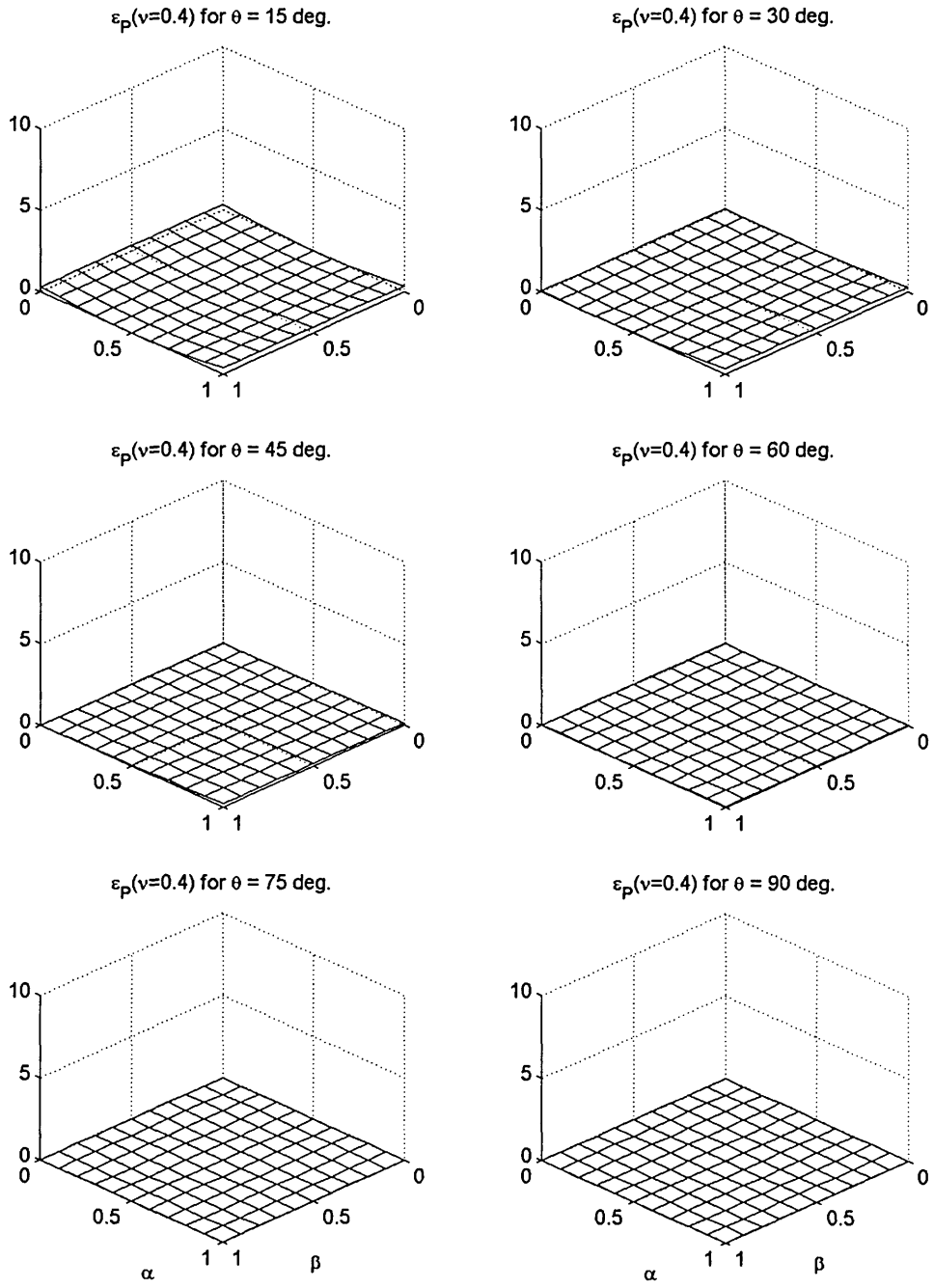

Figure 2.3.13b Integrated squared error ε_P for a full-space (ν=0.4) modeled with TLM1 for θ=15, 30, 45, 60, 75, 90°

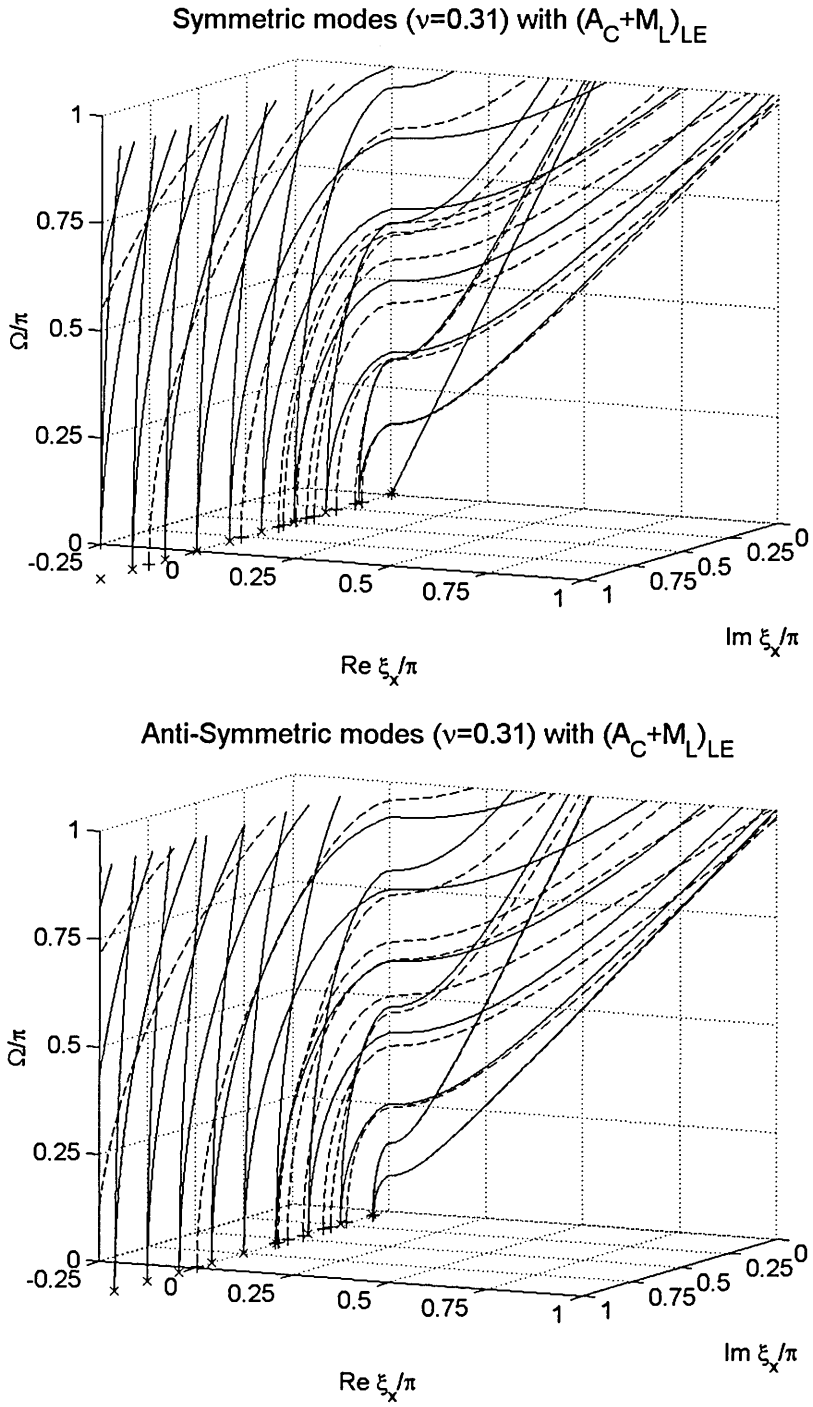

Figure 2.3.14a Dispersion curves of a mixed BC plate (ν=0.31) modeled with TLM1 for α=β=1.0, μ=0.0 (dashed line for TLM1, solid line for Exact)

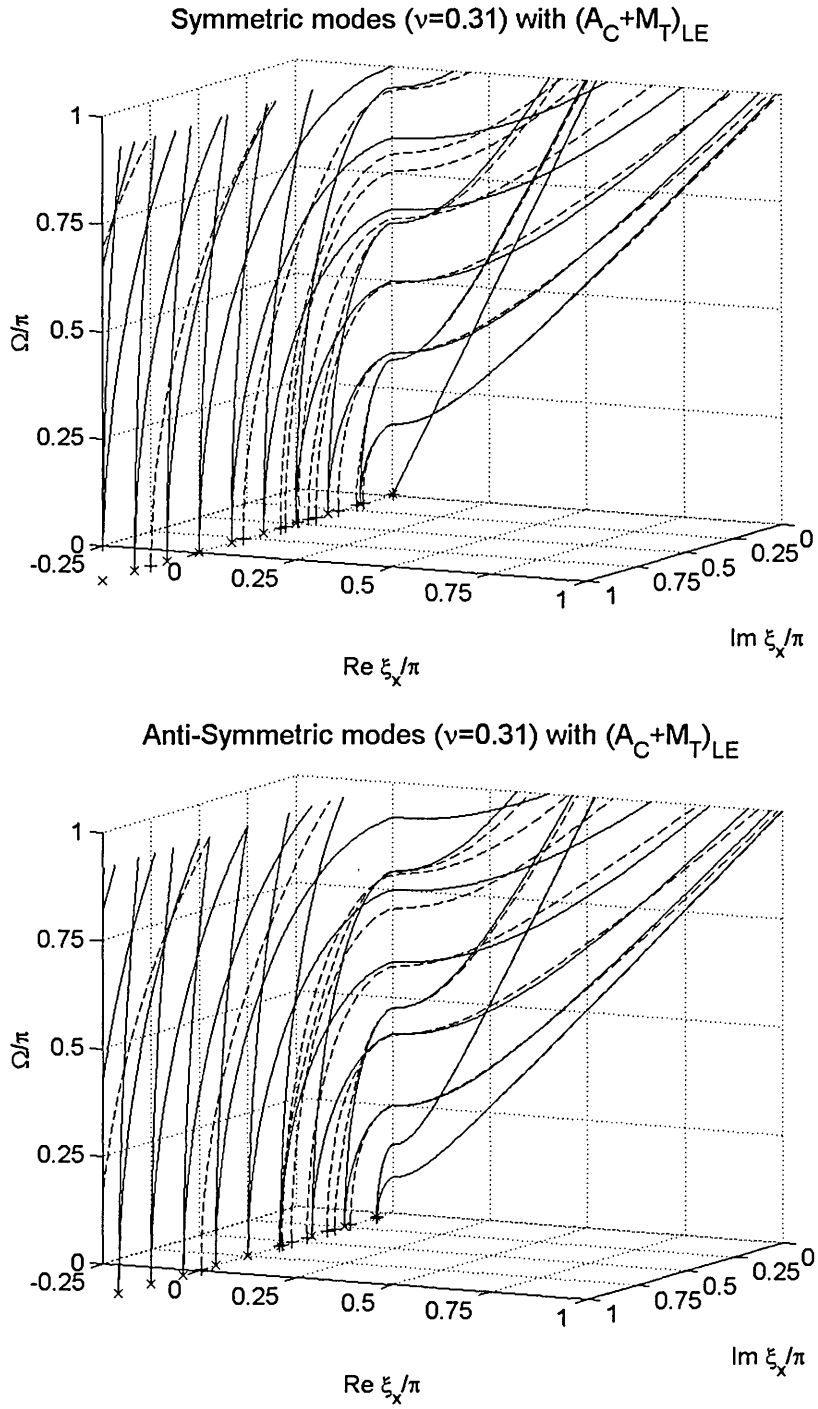

Figure 2.3.14b Dispersion curves of a mixed BC plate (ν=0.31) modeled with TLM1 for α=β=1.0, μ=0.55 (dashed line for TLM1, solid line for Exact)

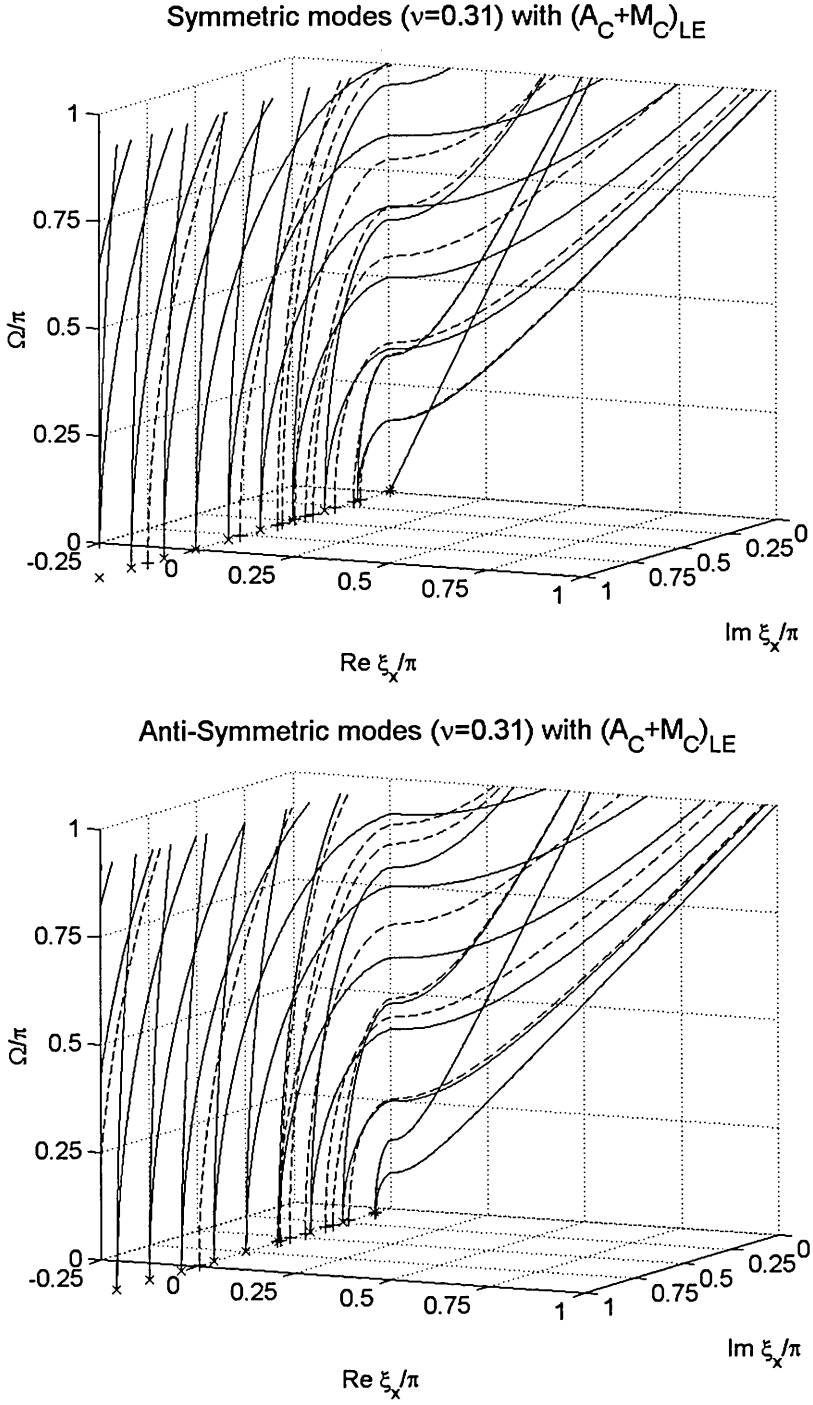

Figure 2.3.14c Dispersion curves of a mixed BC plate (ν=0.31) modeled with TLM1 for α=β=1.0, μ=1.0 (dashed line for TLM1, solid line for Exact)

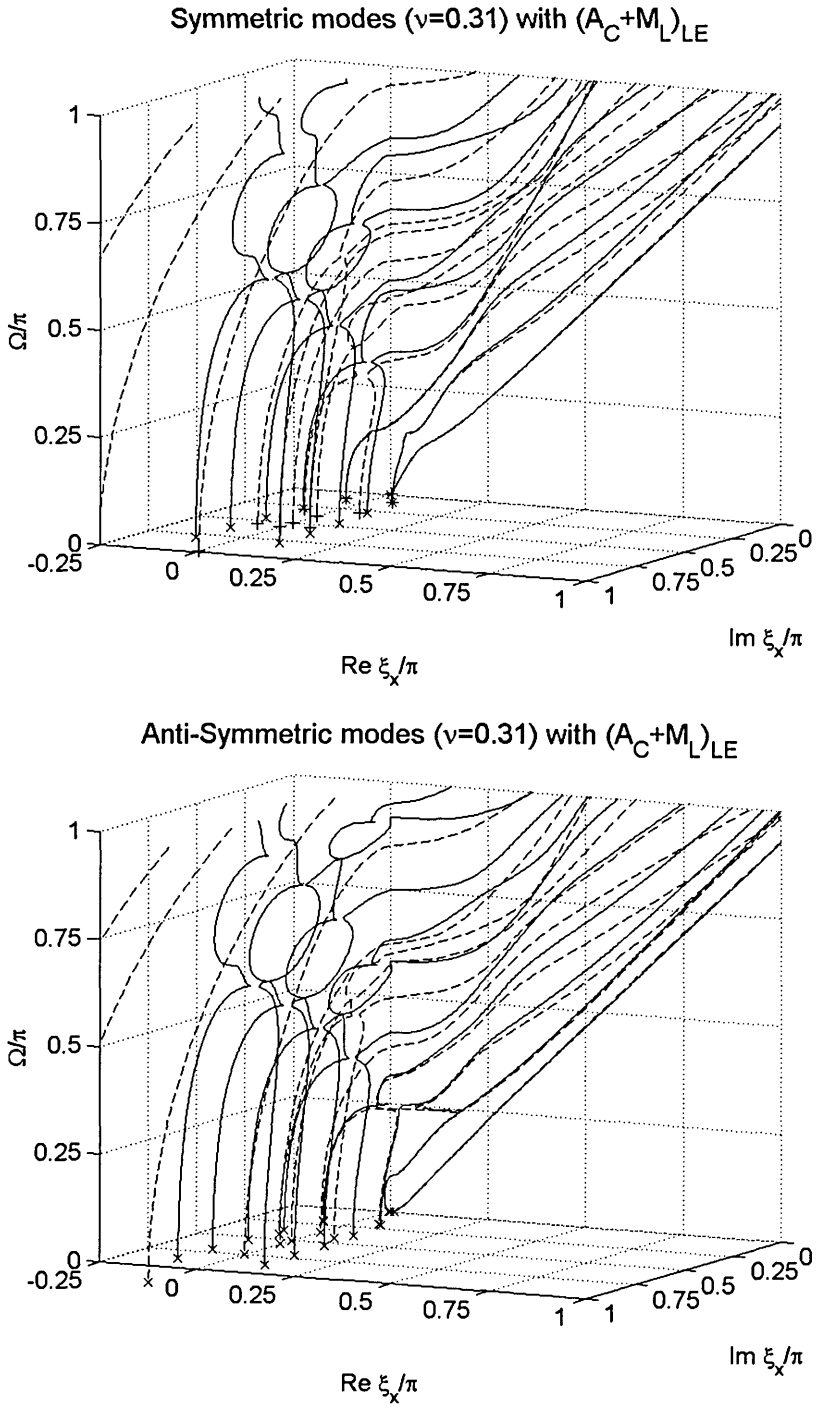

Figure 2.3.15a Dispersion curves of Mindlin plate (ν=0.31) modeled with TLM1 for α=β=1.0, μ=0.0 (dashed line for TLM1, solid line for Exact)

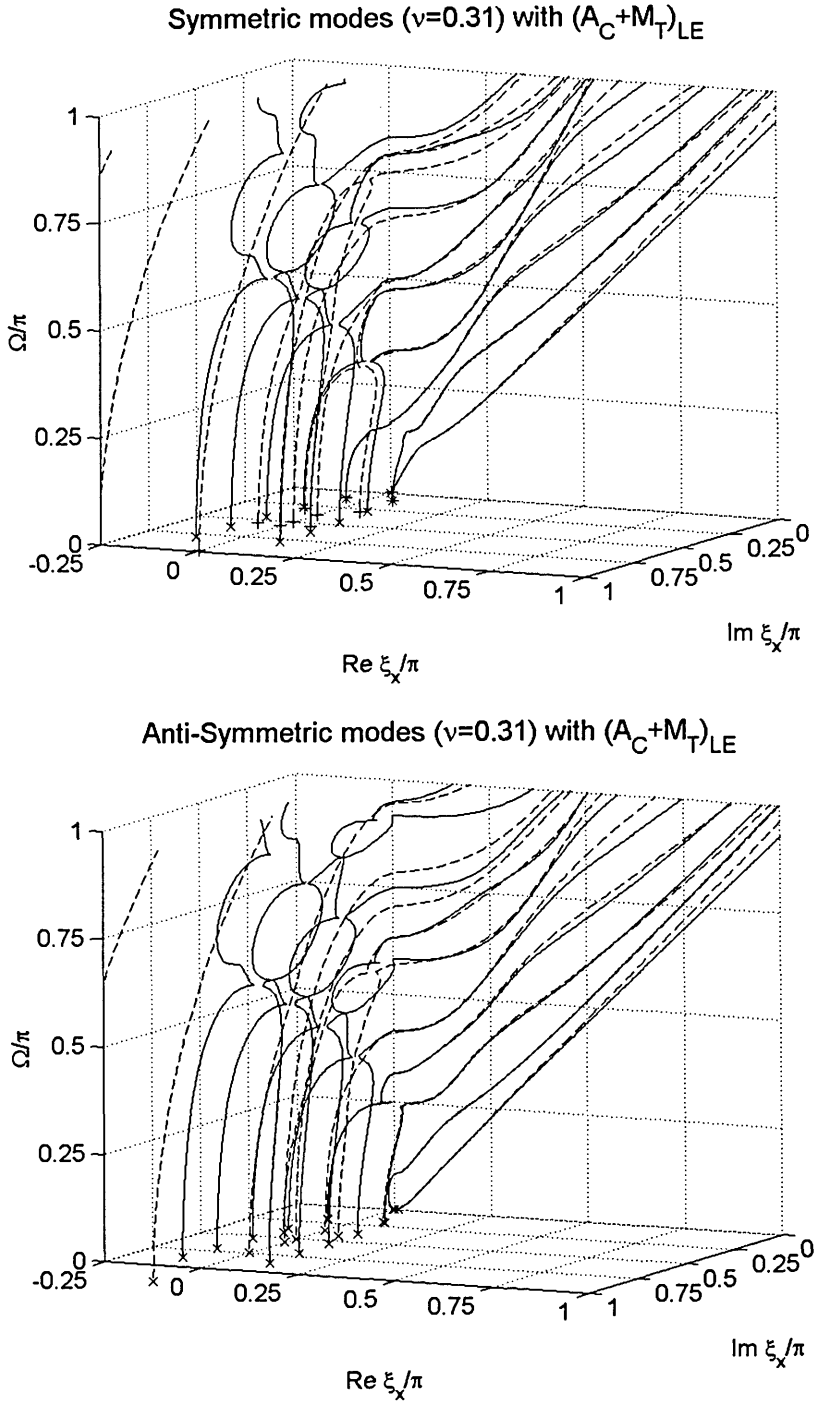

Figure 2.3.15b Dispersion curves of Mindlin plate (ν=0.31) modeled with TLM1 for α=β=1.0, μ=0.55 (dashed line for TLM1, solid line for Exact)

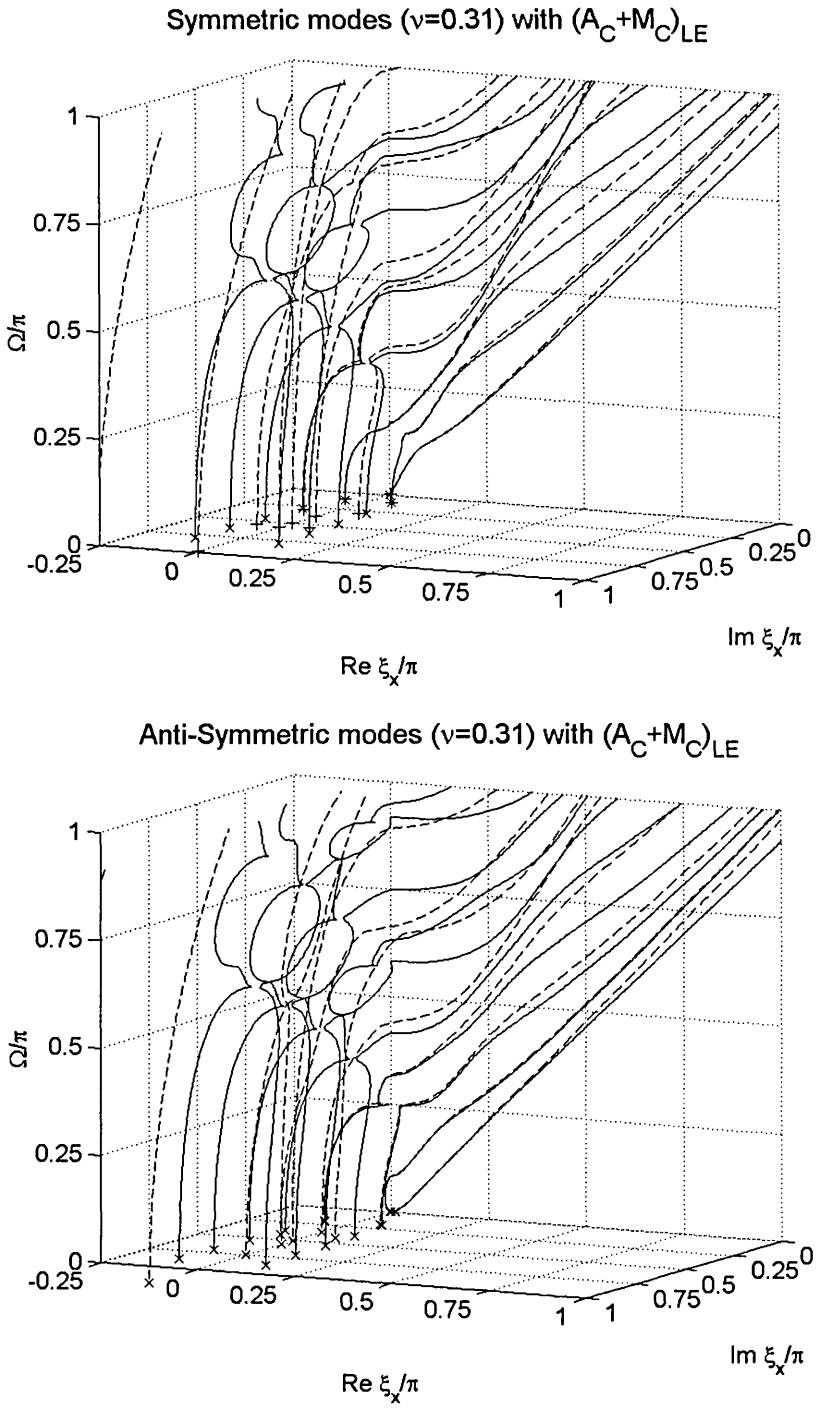

Figure 2.3.15c Dispersion curves of Mindlin plate (ν=0.31) modeled with TLM1 for α=β=1.0, μ=1.0 (dashed line for TLM1, solid line for Exact)

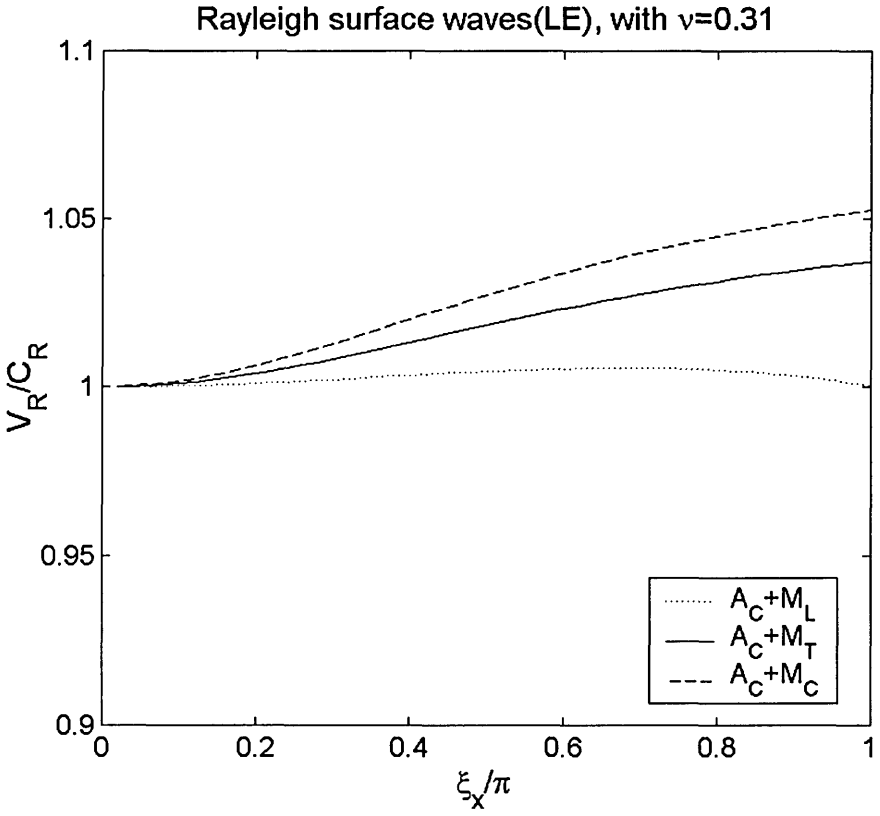

Figure 2.3.16 Numerical dispersion of Rayleigh surface waves (ν=0.31) modeled with TLM1 in terms of ratio of apparent Rayleigh surface wave to true Rayleigh surface wave V_R/C_R: α=β=1.0, μ=0.0 (dot-dashed line); α=β=1.0, μ=0.55 (solid line); α=β=1.0, μ=1.0 (dashed line)

Figures for section 2.4

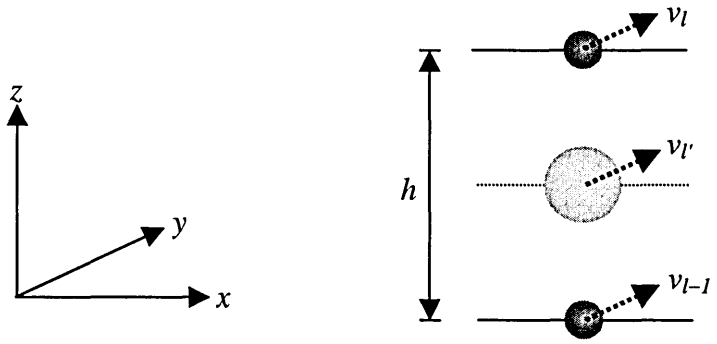

Figure 2.4.1. Coordinate system and a TLM2 thin-layer subjected to *SH* wave motion

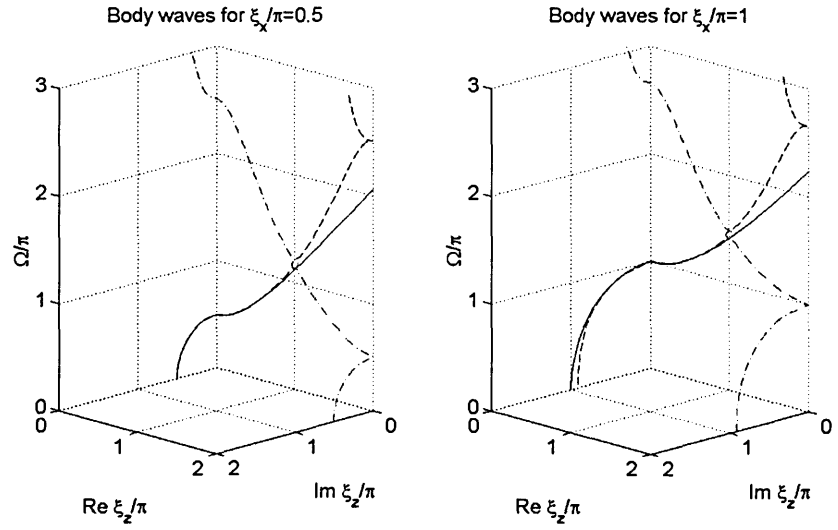

Figure 2.4.2 Dispersion of *SH* body waves as function of vertical wavenumber for fixed horizontal wavenumber: Left for ξ_x=0.5π, Right for ξ_x=1.0π (dashed line for acoustical branch, dot-dashed line for optical branch, solid line for Exact)

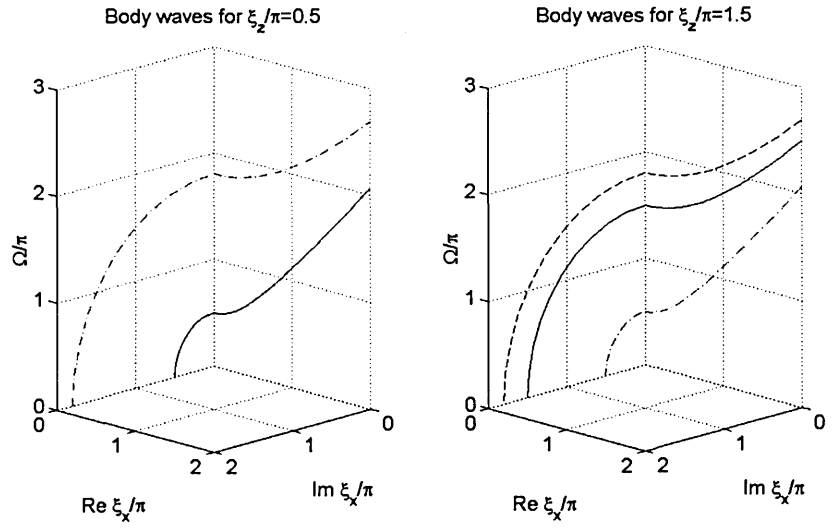

Figure 2.4.3 Dispersion of *SH* body waves as function of horizontal wavenumber for fixed vertical wavenumber: Left for $\xi_z=0.5\pi$, Right for $\xi_z=1.5\pi$ (dashed line for acoustical branch, dot-dashed line for optical branch, solid line for Exact)

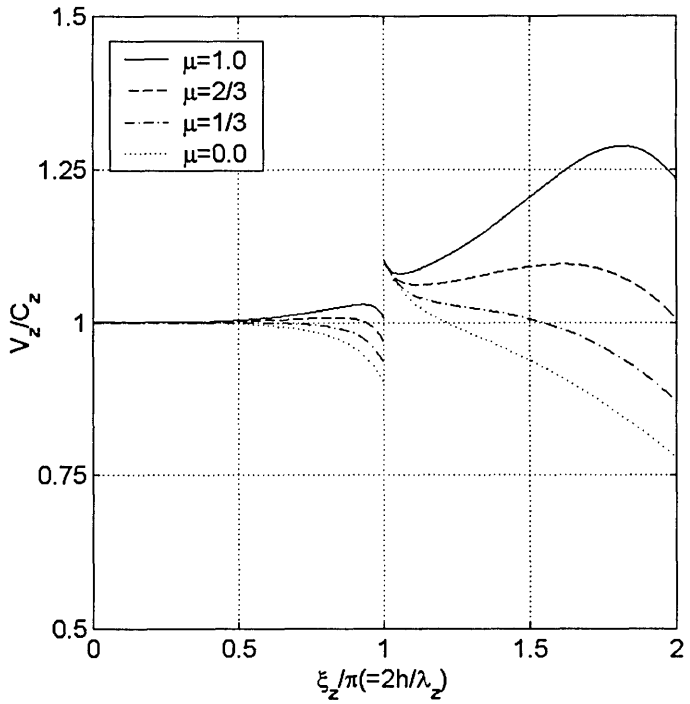

Figure 2.4.4 Numerical dispersion of an infinite shear beam modeled with TLM2 in terms of ratio of apparent vertical phase velocity to true vertical phase velocity (V_z/C_z)

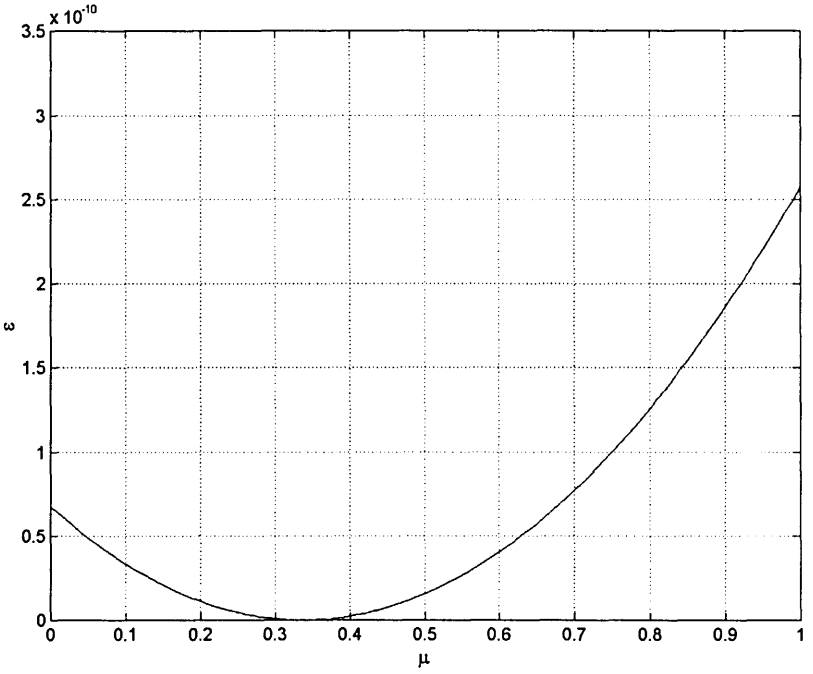

Figure 2.4.5 Integrated squared error ε for an infinite shear beam modeled with TLM2

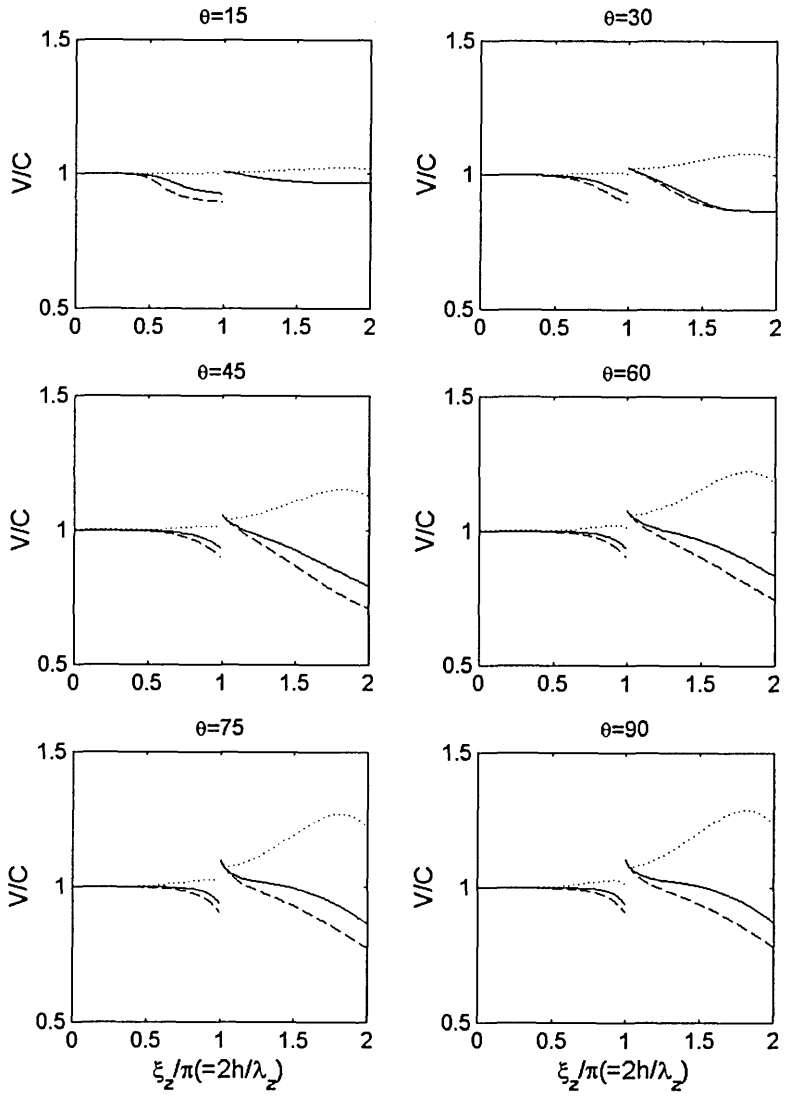

Figure 2.4.6 Numerical dispersion of a homogeneous full-space modeled with TLM2 in terms of ratio of apparent phase velocity to true phase velocity (*V/C*): β=1.0, μ=0.0 (dashed); β=1.0, μ=0.33 (solid); β=1.0, μ=1.0 (dotted)

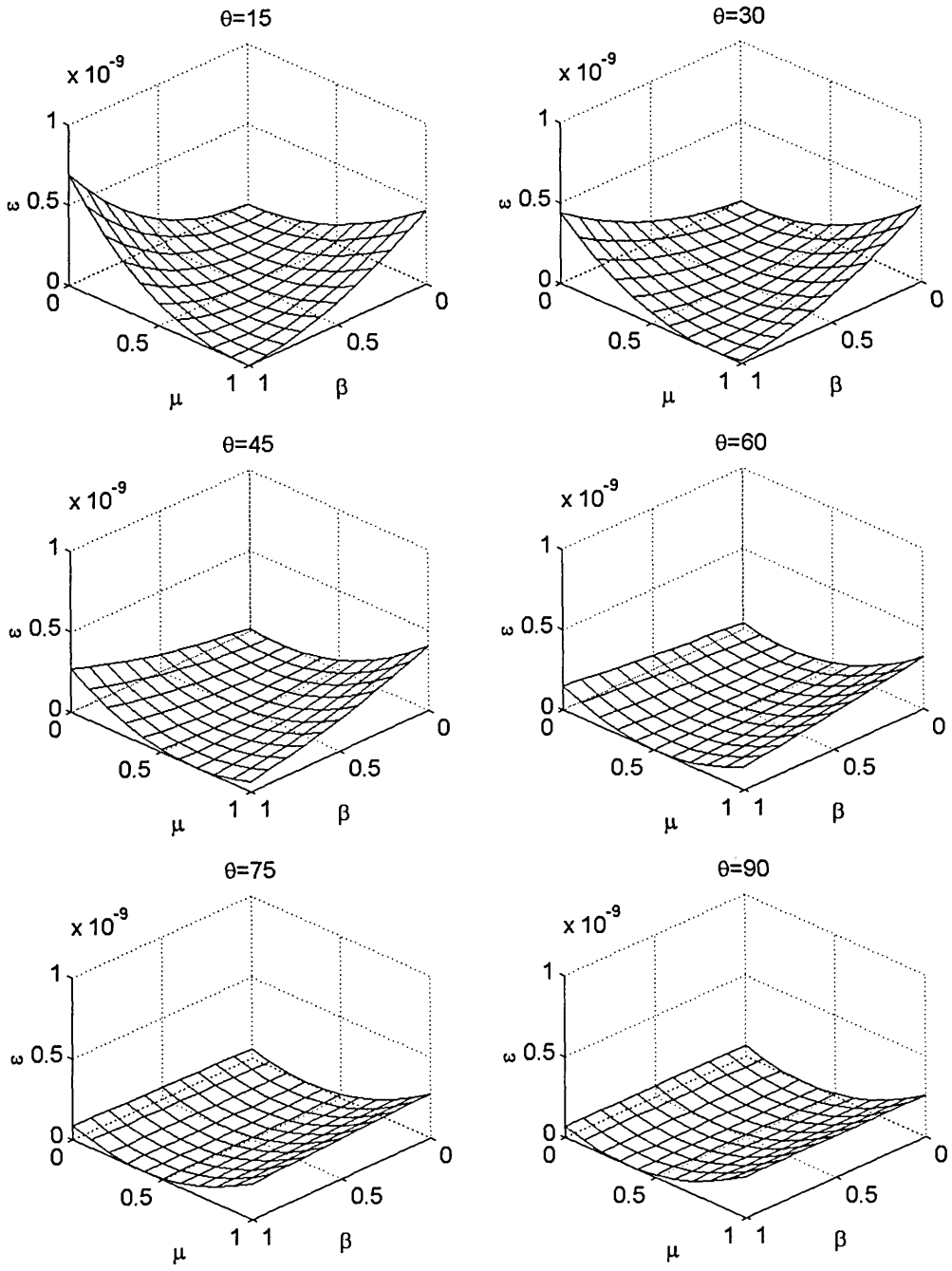

Figure 2.4.7 Integrated squared error ε for a homogeneous full-space modeled with TLM2 for θ=15, 30, 45, 60, 75, 90°

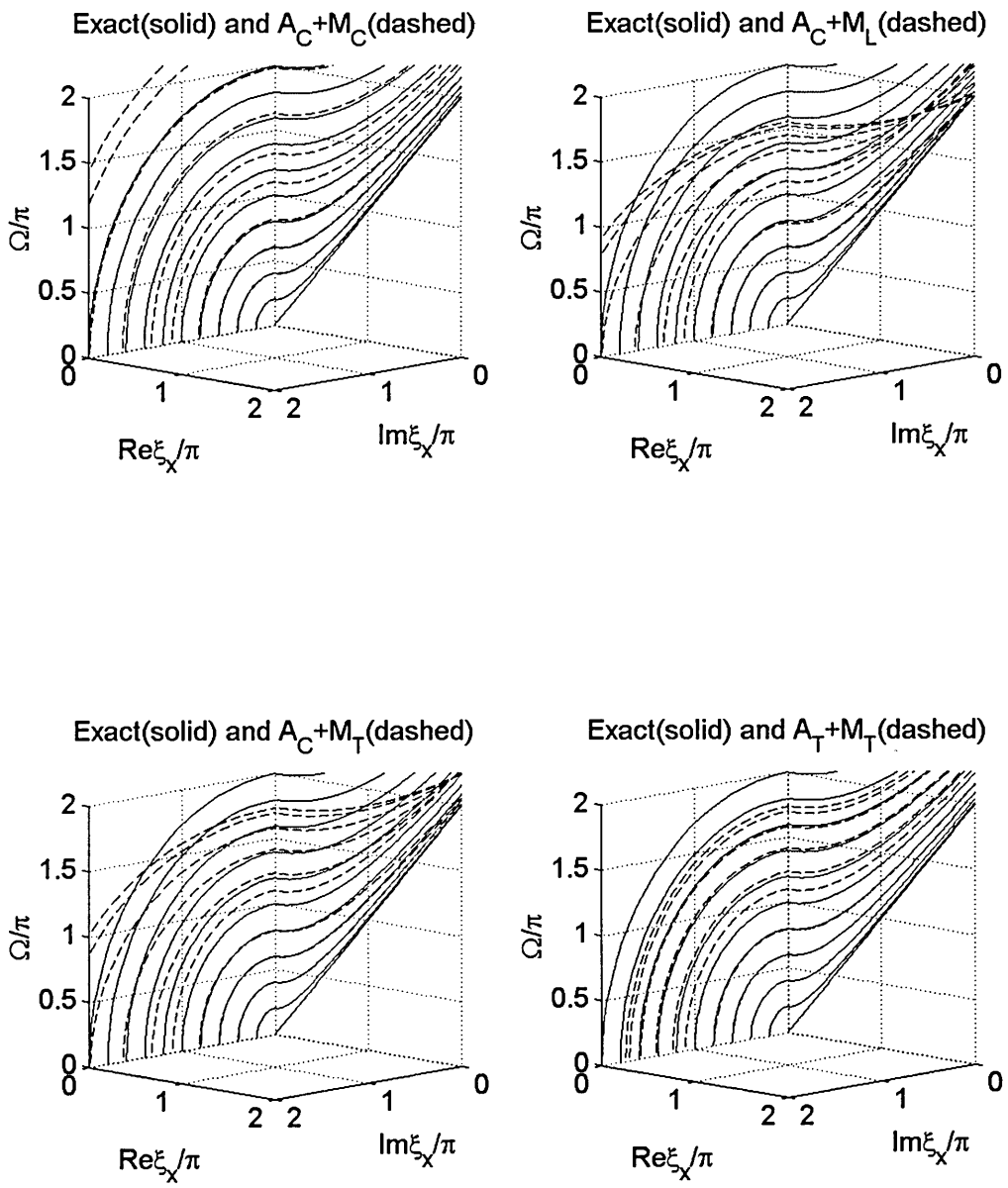

Figure 2.4.8 Dispersion curves of an *SH* homogeneous plate modeled with TLM2 for β=μ=1.0; β=1.0, μ=0.0; β=1.0, μ=0.33; and β=μ=0.33 (dashed line for TLM2, solid line for Exact)

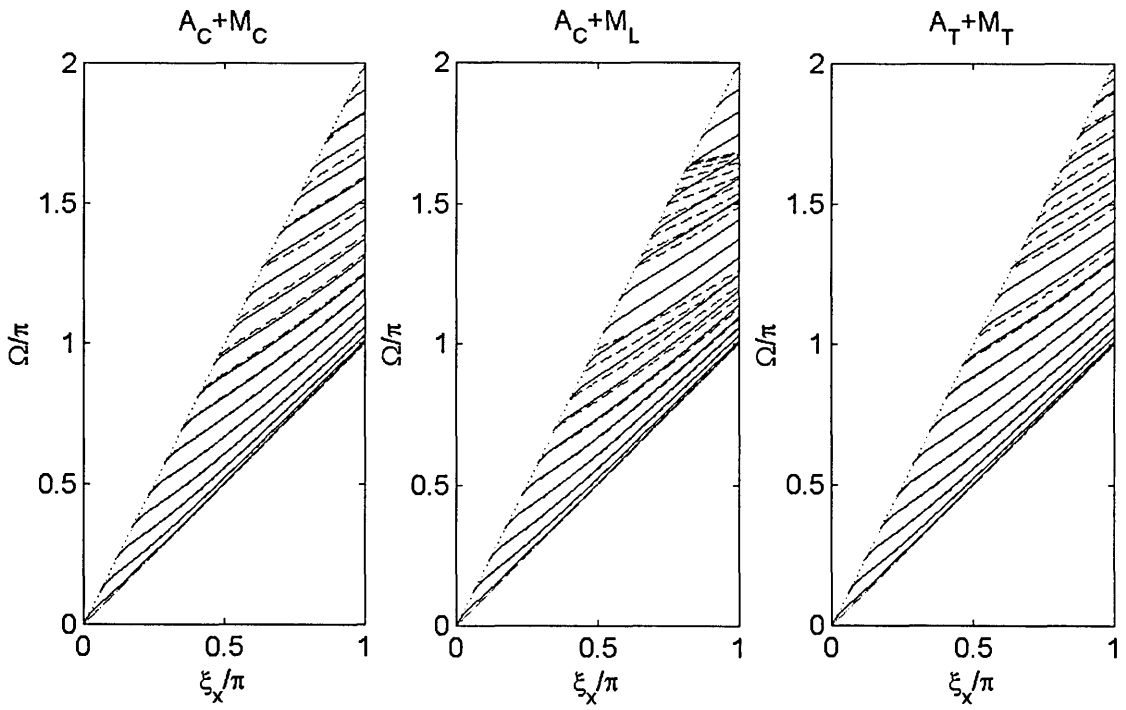

Figure 2.4.9 Dispersion curves of Love waves modeled with TLM2
for $\beta=\mu=1.0$; $\beta=1.0$, $\mu=0.0$; and $\beta=\mu=0.33$ (dashed line for TLM2, solid line for Exact)

Figures for section 2.5

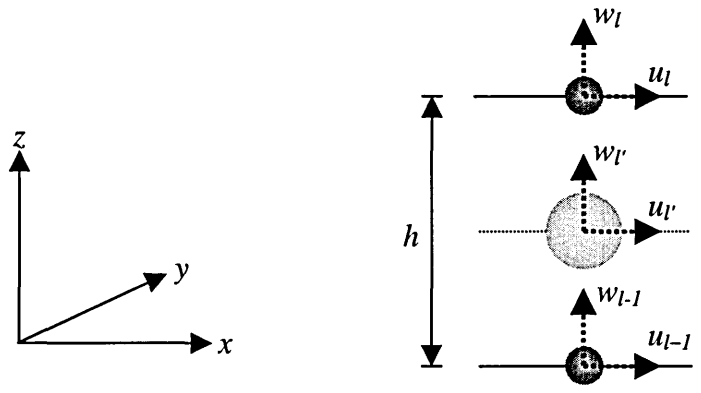

Figure 2.5.1 Coordinate system and a TLM2 thin-layer subjected to *SV-P* wave motion

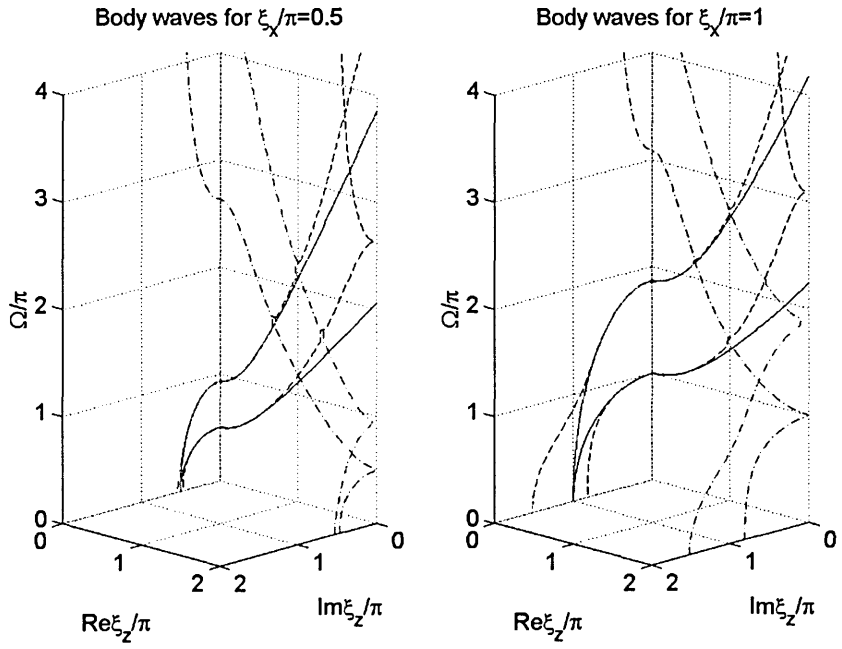

Figure 2.5.2 Dispersion of *SV-P* body waves (ν=0.30) as function of vertical wavenumber for fixed horizontal wavenumber: Left for ξ_x=0.5π, Right for ξ_x=1.0π
(solid line: exact *P* and *S*, dashed line: acoustical *P* and *S*, dashed-dotted line: optical *P* and *S*)

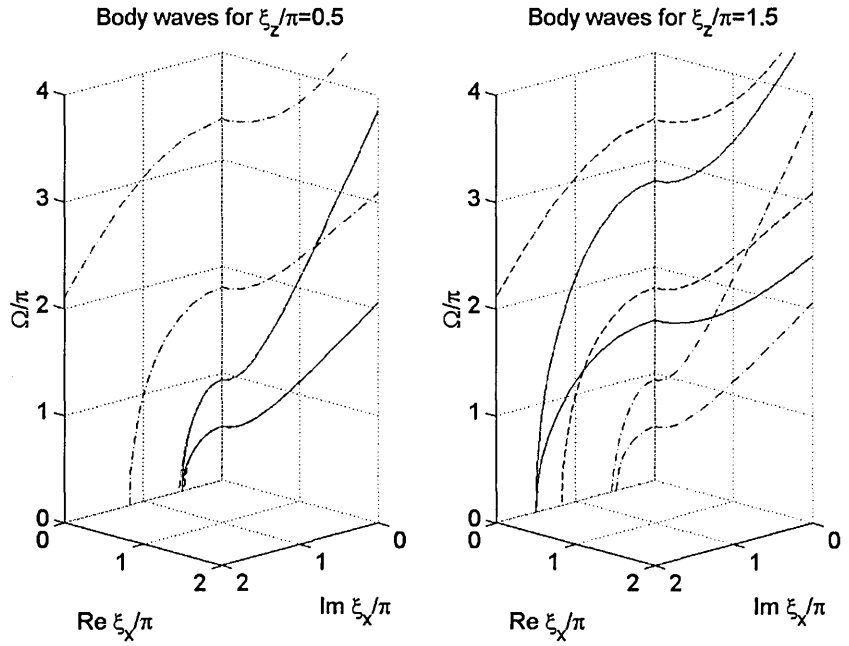

Figure 2.5.3 Dispersion of *SV-P* body waves (ν=0.30) as function of horizontal wavenumber for fixed vertical wavenumber: Left for ξ_z=0.5π, Right for ξ_z=1.5π
(solid line: exact *P* and *S*, dashed line: acoustical *P* and *S*, dashed-dotted line: optical *P* and *S*)

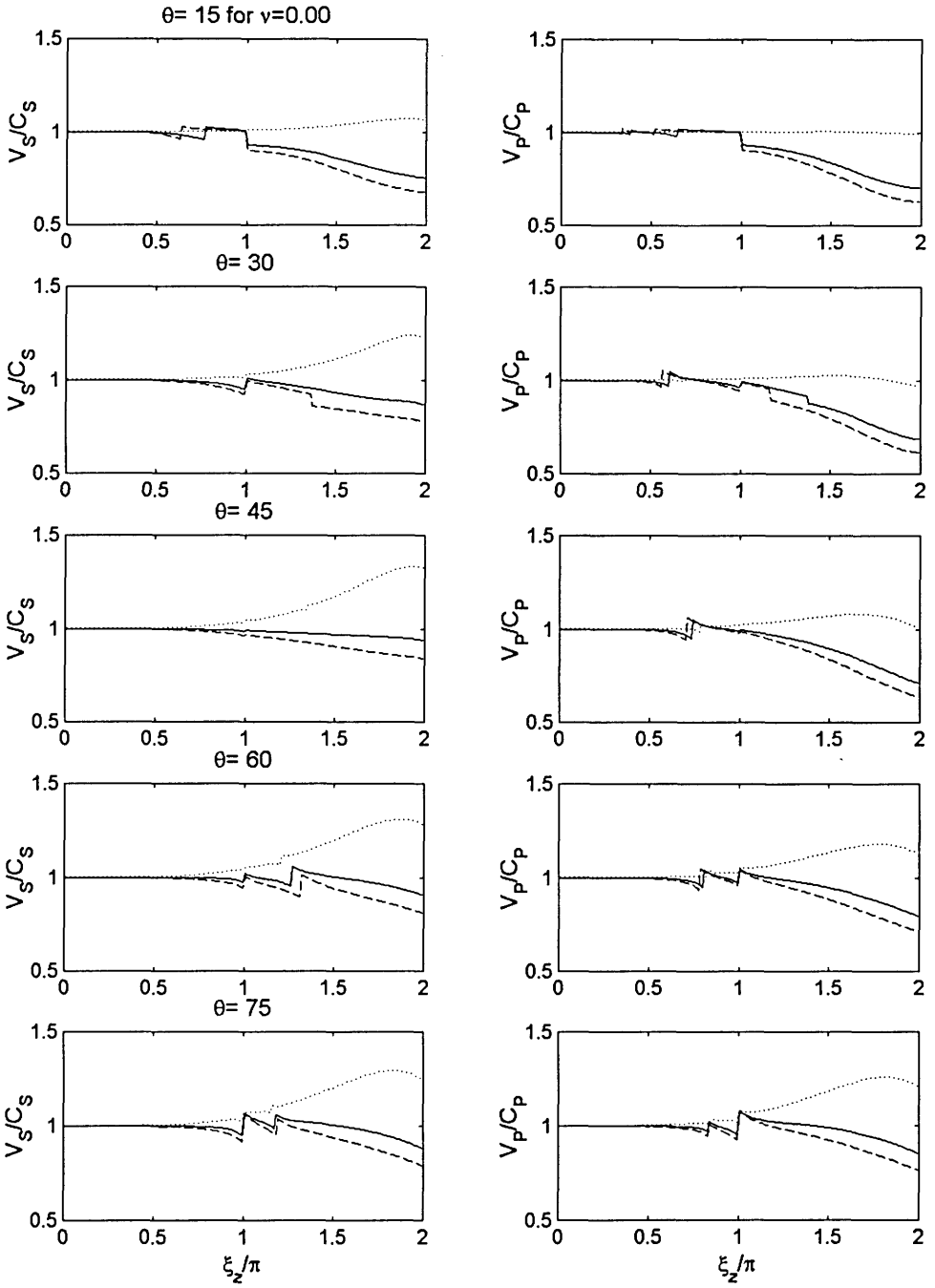

Figure 2.5.4a Numerical dispersion of a homogeneous full-space (ν=0.0) modeled with TLM2 in terms of Ratios of apparent phase velocity to true phase velocity (V_S/C_S, V_P/C_P): α=β=1.0, μ=0.0 (dashed); α=β=1.0, μ=0.33 (solid); α=β=1.0, μ=1.0 (dotted)

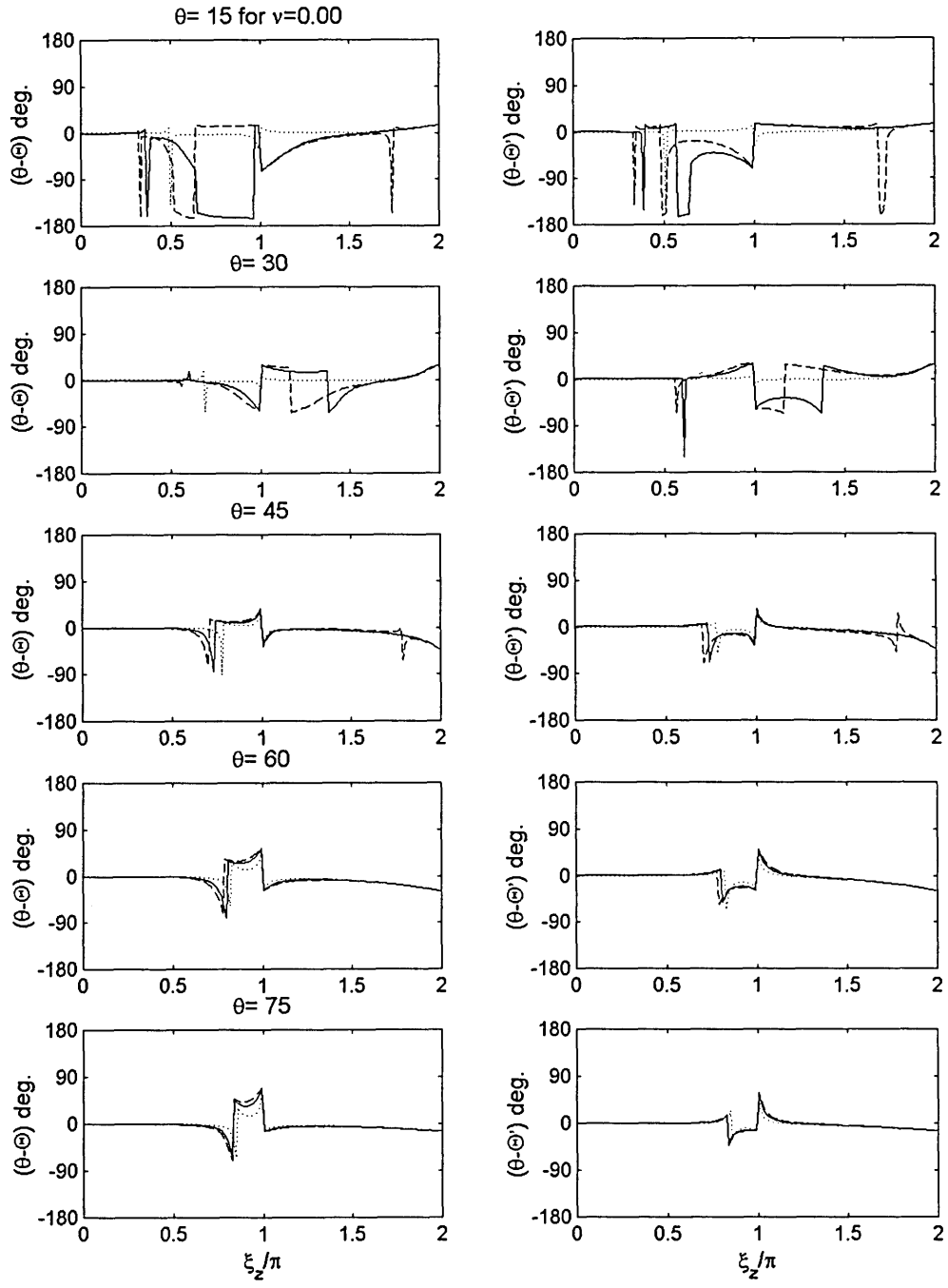

Figure 2.5.4b Numerical dispersion of a homogeneous full-space (ν=0.0) modeled with TLM2 in terms of differences between propagation and polarity angles (θ−Θ,θ−Θ'): α=β=1.0, μ=0.0 (dashed); α=β=1.0, μ=0.33 (solid); α=β=1.0, μ=1.0 (dotted)

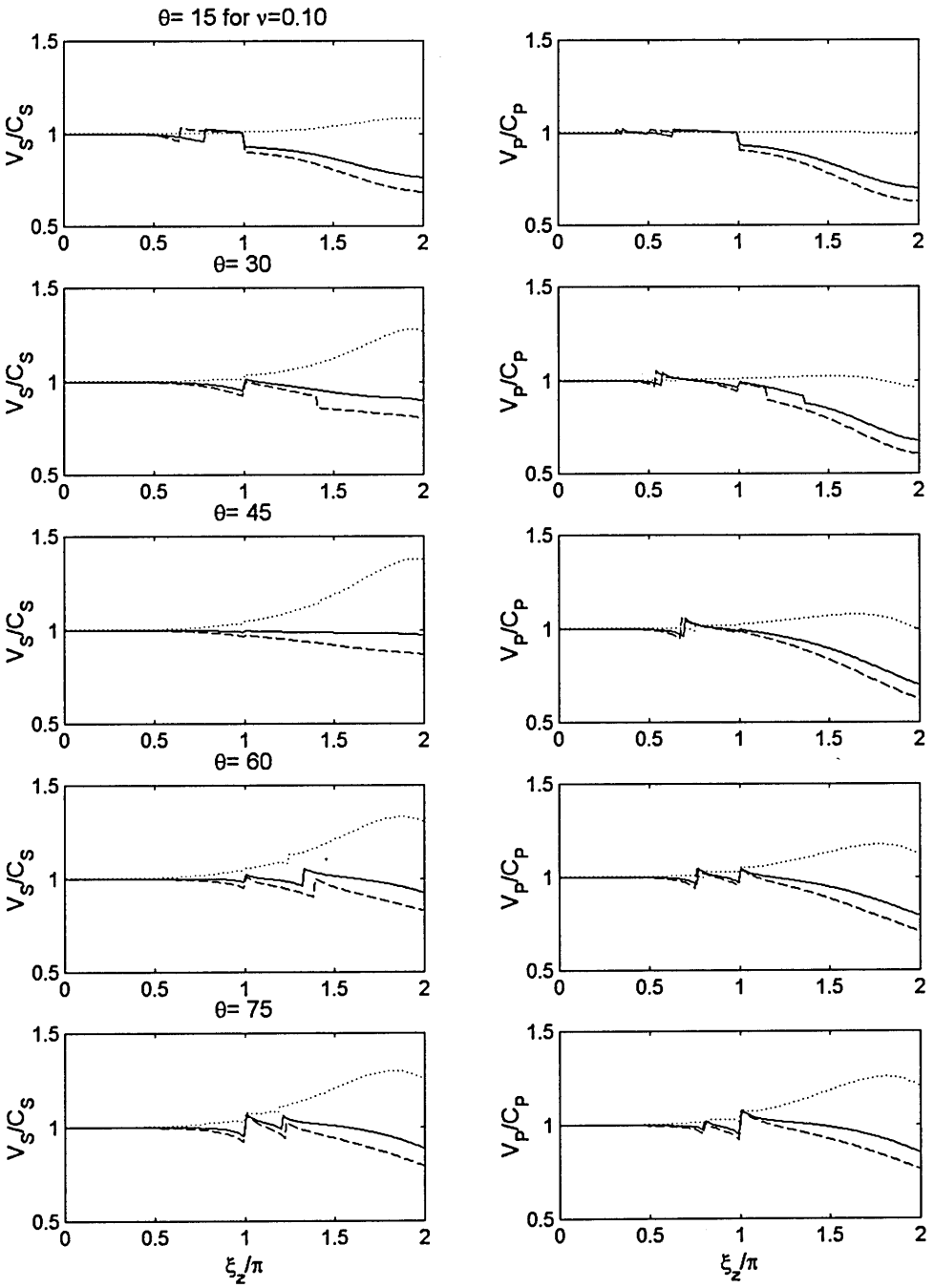

Figure 2.5.5a Numerical dispersion of a homogeneous full-space (ν=0.1) modeled with TLM2 in terms of ratios of apparent phase velocity to true phase velocity (V_S/C_S, V_P/C_P): α=β=1.0, μ=0.0 (dashed); α=β=1.0, μ=0.33 (solid); α=β=1.0, μ=1.0 (dotted)

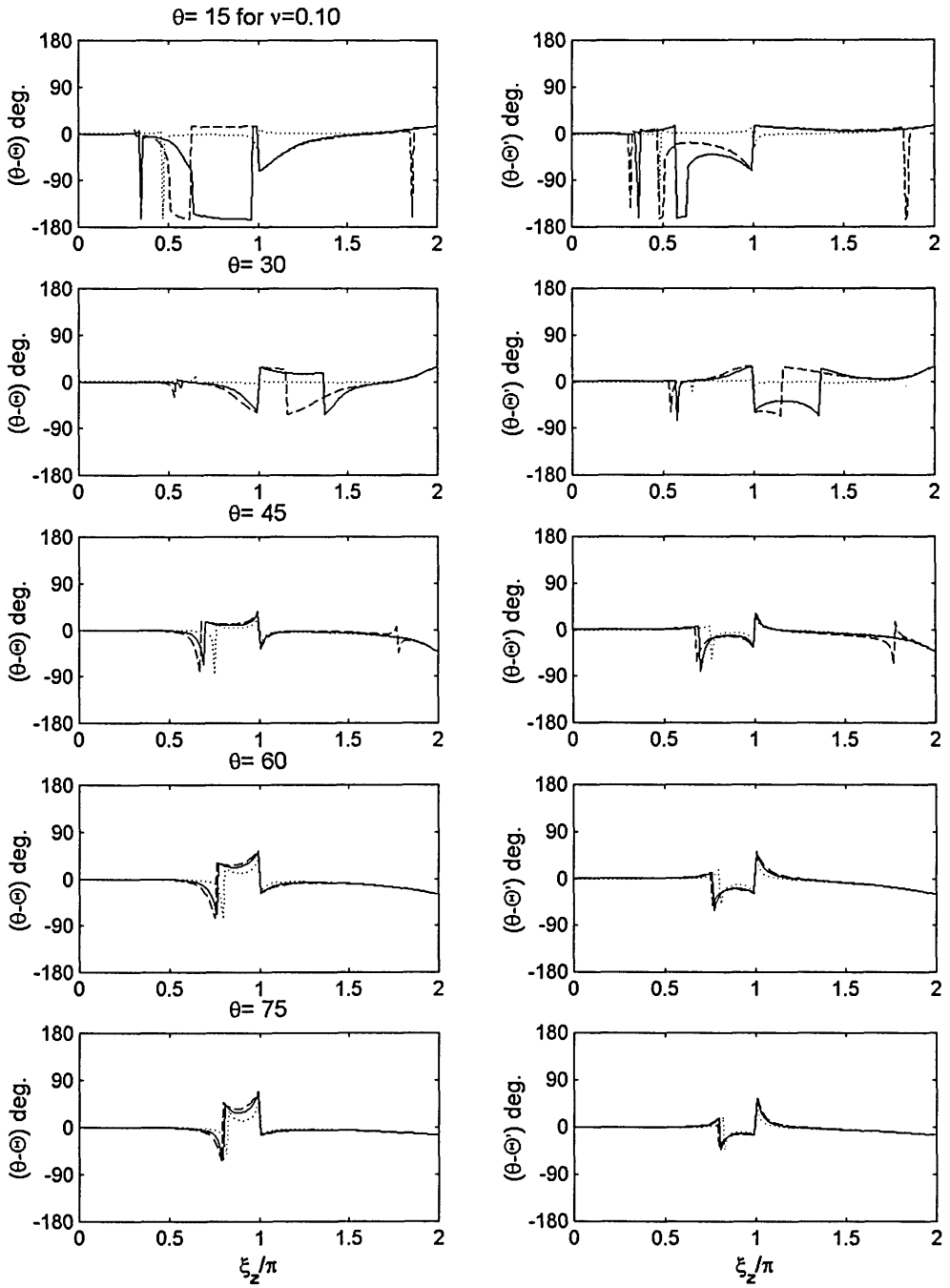

Figure 2.5.5b Numerical dispersion of a homogeneous full-space (ν=0.1) modeled with TLM2 in terms of differences between propagation and polarity angles (θ−Θ,θ−Θ'): α=β=1.0, μ=0.0 (dashed); α=β=1.0, μ=0.33 (solid); α=β=1.0, μ=1.0 (dotted)

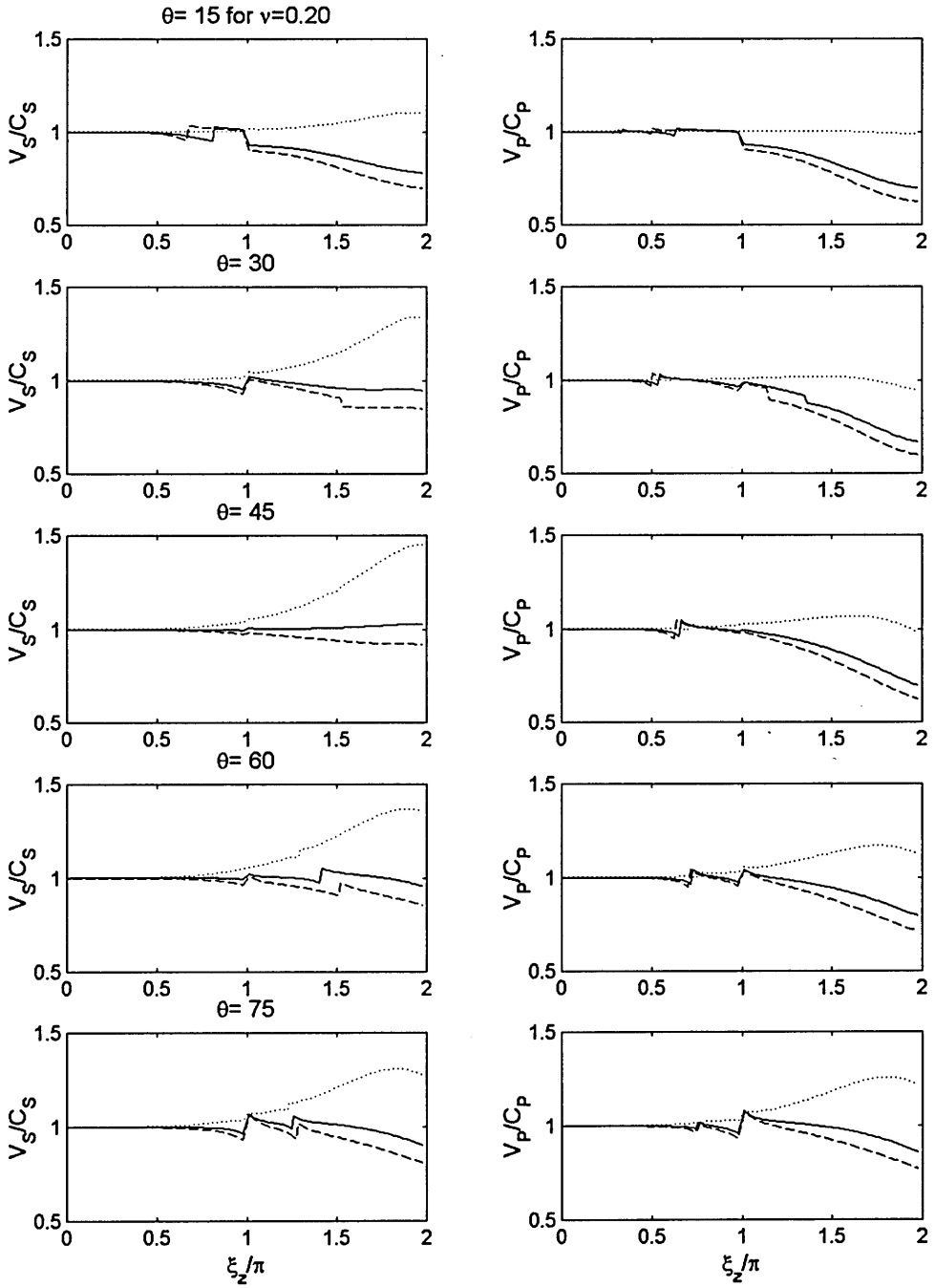

Figure 2.5.6a Numerical dispersion of a homogeneous full-space (ν=0.2) modeled with TLM2 in terms of ratios of apparent phase velocity to true phase velocity (V_S/C_S, V_P/C_P): α=β=1.0, μ=0.0 (dashed); α=β=1.0, μ=0.33 (solid); α=β=1.0, μ=1.0 (dotted)

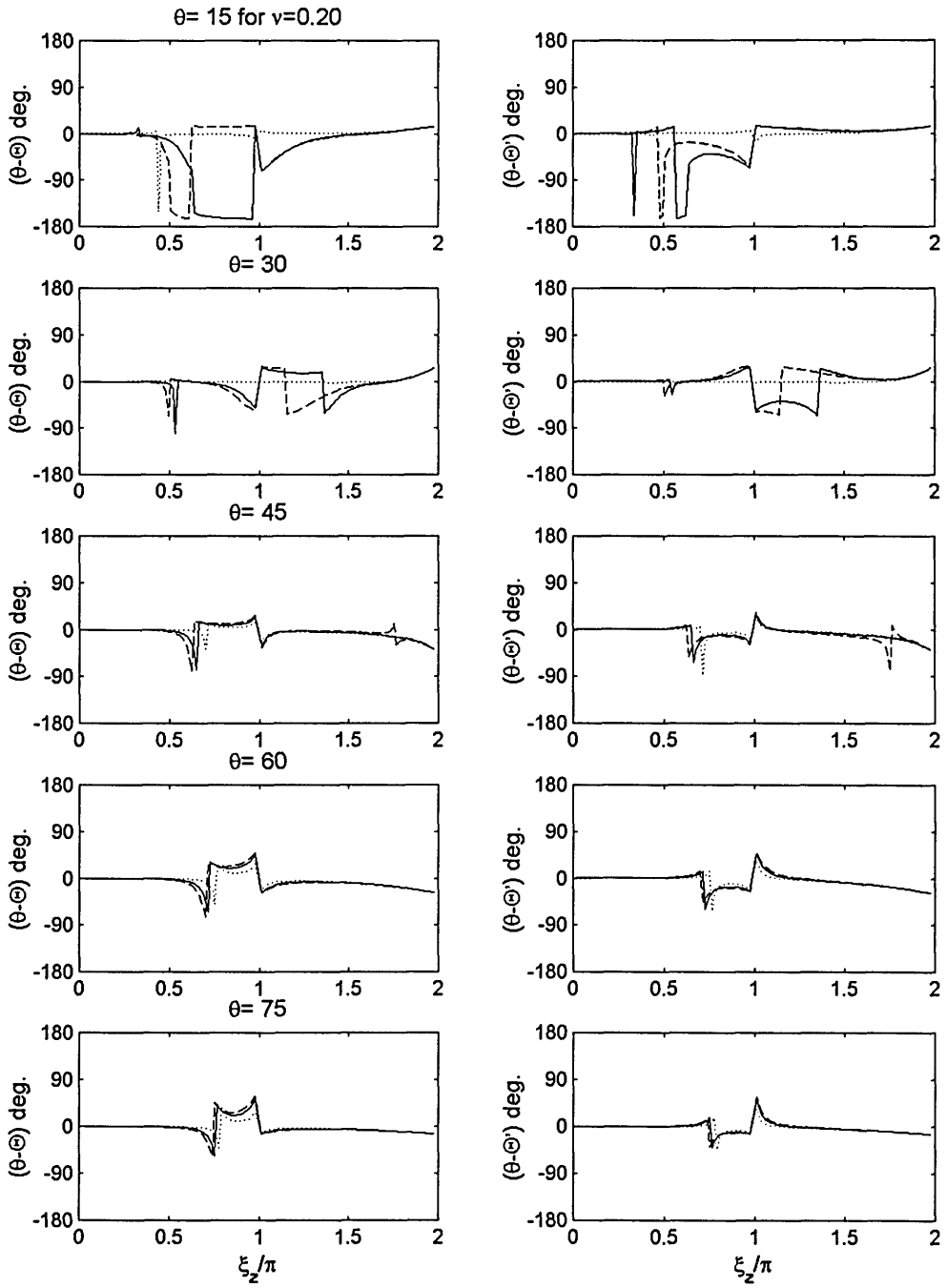

Figure 2.5.6b Numerical dispersion of a homogeneous full-space (ν=0.2) modeled with TLM2 in terms of Differences between propagation and polarity angles (θ−Θ,θ−Θ'): α=β=1.0, μ=0.0 (dashed); α=β=1.0, μ=0.33 (solid); α=β=1.0, μ=1.0 (dotted)

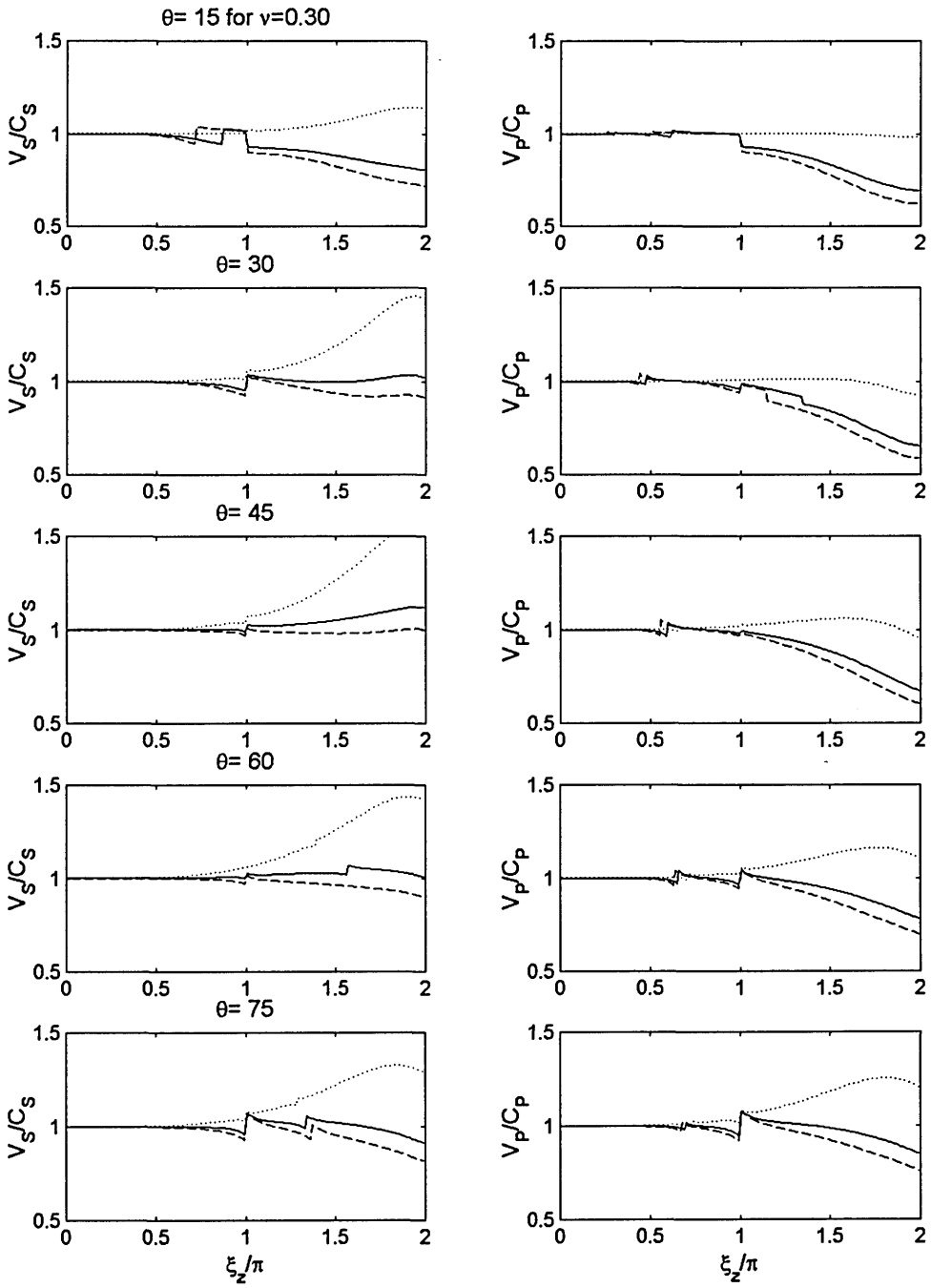

Figure 2.5.7a Numerical dispersion of a homogeneous full-space (ν=0.3) modeled with TLM2 in terms of ratios of apparent phase velocity to true phase velocity (V_S/C_S, V_P/C_P): α=β=1.0, μ=0.0 (dashed); α=β=1.0, μ=0.33 (solid); α=β=1.0, μ=1.0 (dotted)

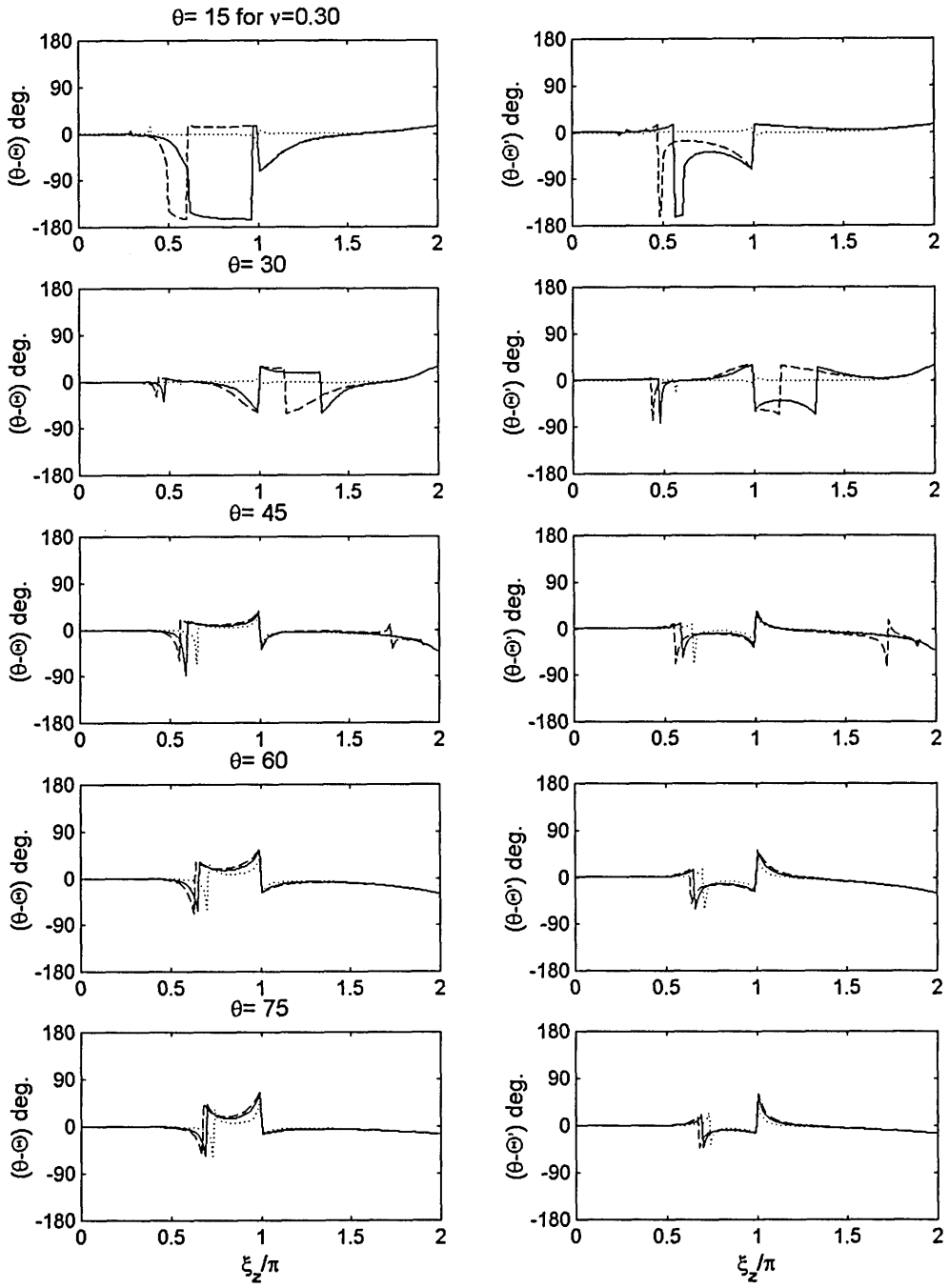

Figure 2.5.7b Numerical dispersion of a homogeneous full-space (ν=0.3) modeled with TLM2 in terms of differences between propagation and polarity angles (θ–Θ,θ–Θ'): α=β=1.0, μ=0.0 (dashed); α=β=1.0, μ=0.33 (solid); α=β=1.0, μ=1.0 (dotted)

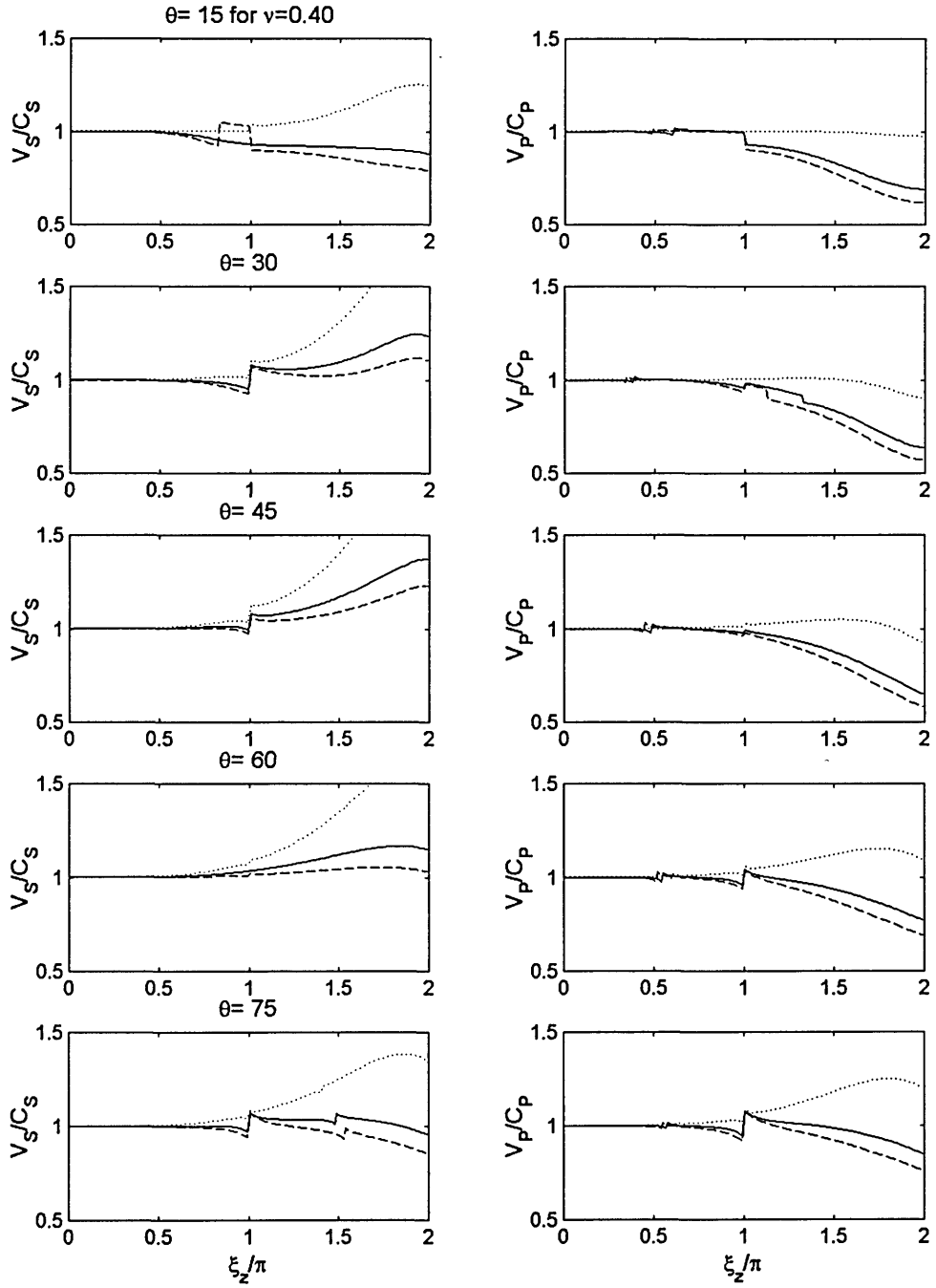

Figure 2.5.8a Numerical dispersion of a homogeneous full-space (ν=0.4) modeled with TLM2 in terms of ratios of apparent phase velocity to true phase velocity (V_S/C_S, V_P/C_P): α=β=1.0, μ=0.0 (dashed); α=β=1.0, μ=0.33 (solid); α=β=1.0, μ=1.0 (dotted)

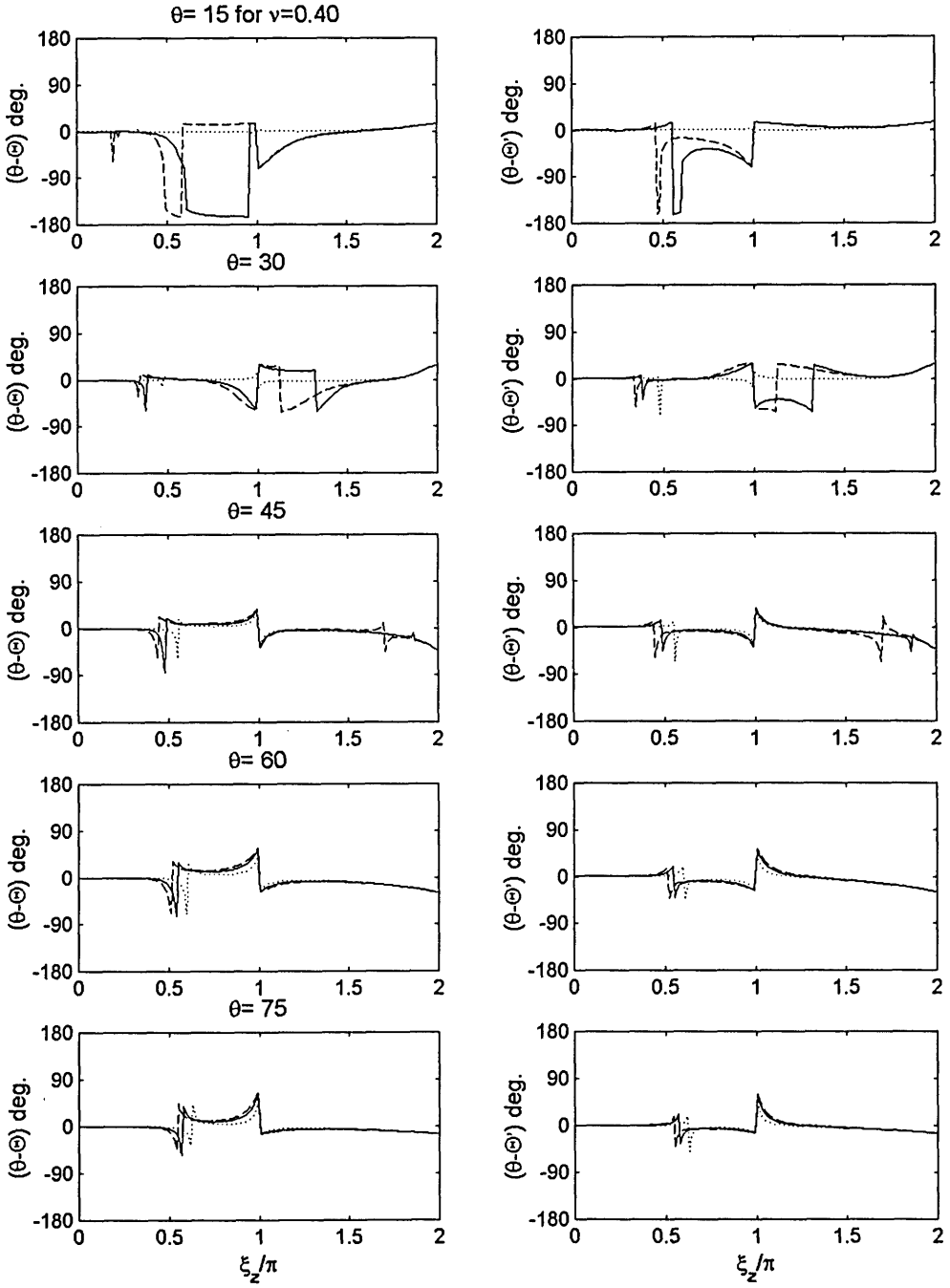

Figure 2.5.8b Numerical dispersion of a homogeneous full-space (ν=0.4) modeled with TLM2 in terms of differences between propagation and polarity angles (θ−Θ,θ−Θ'): α=β=1.0, μ=0.0 (dashed); α=β=1.0, μ=0.33 (solid); α=β=1.0, μ=1.0 (dotted)

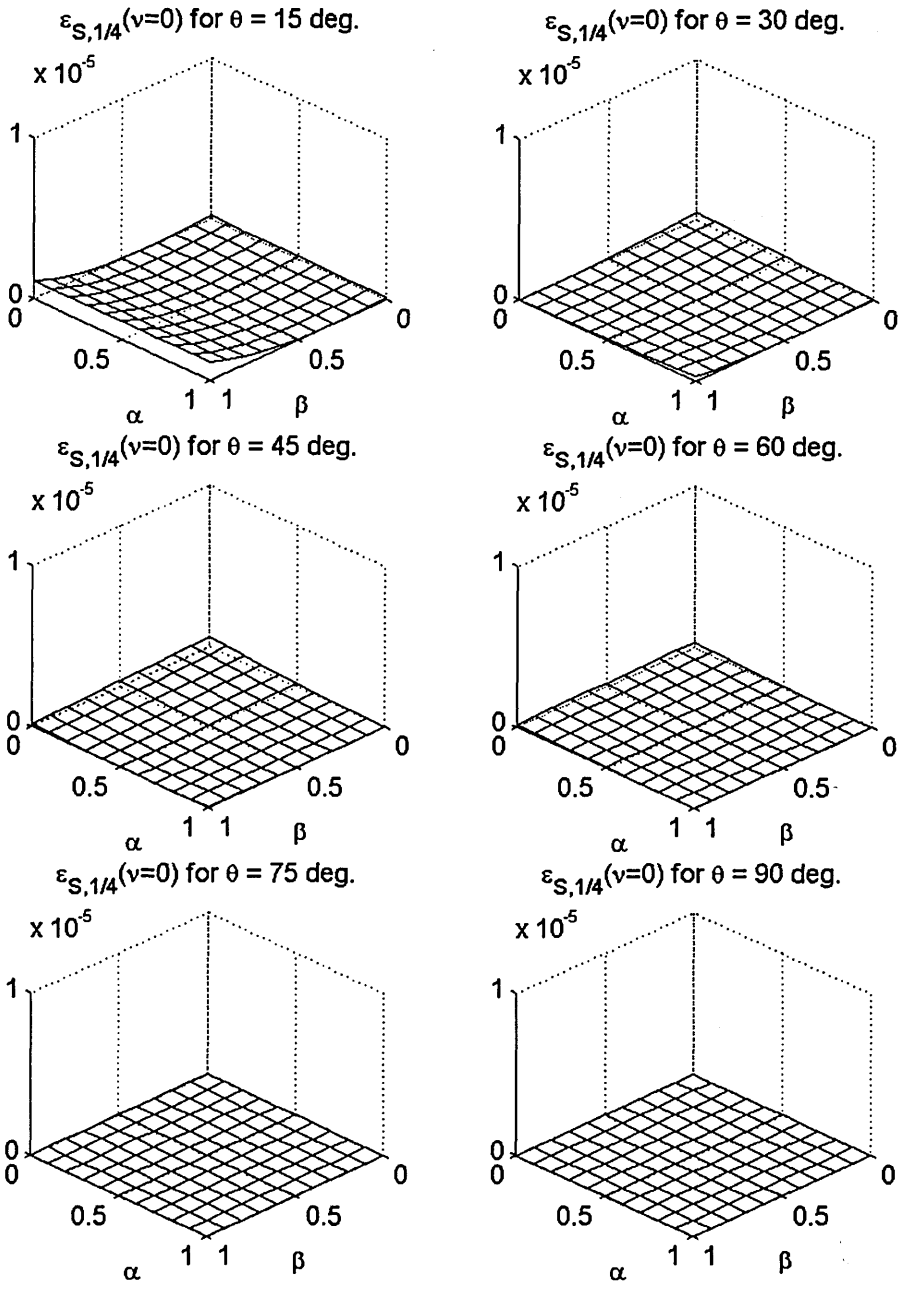

Figure 2.5.9a Integrated squared error ε_S for a homogeneous (ν=0.0) modeled with TLM2 for θ=15, 30, 45, 60, 75, 90°

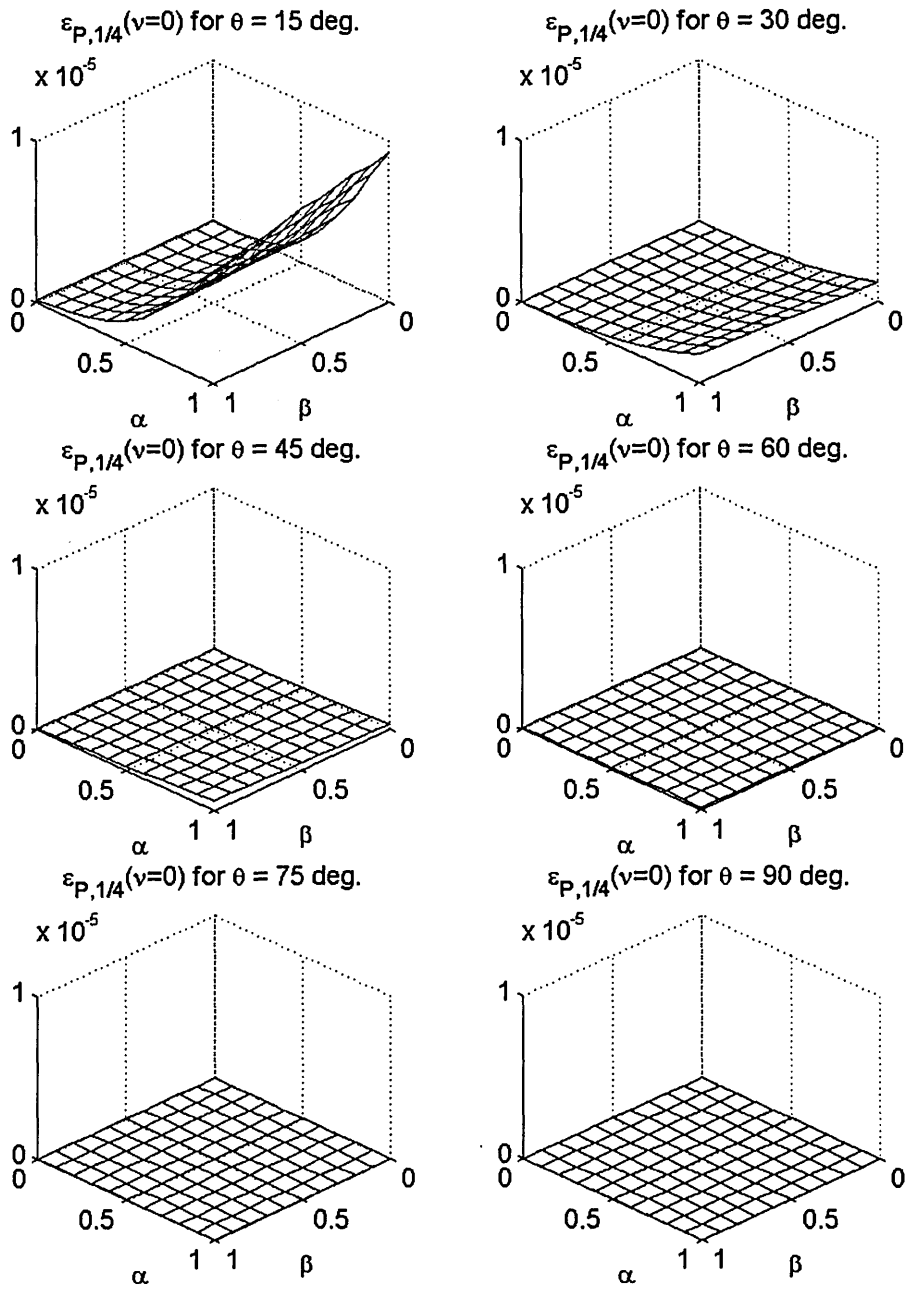

Figure 2.5.9b Integrated squared error ε_P for a homogeneous (ν=0.0) modeled with TLM2 for θ=15, 30, 45, 60, 75, 90°

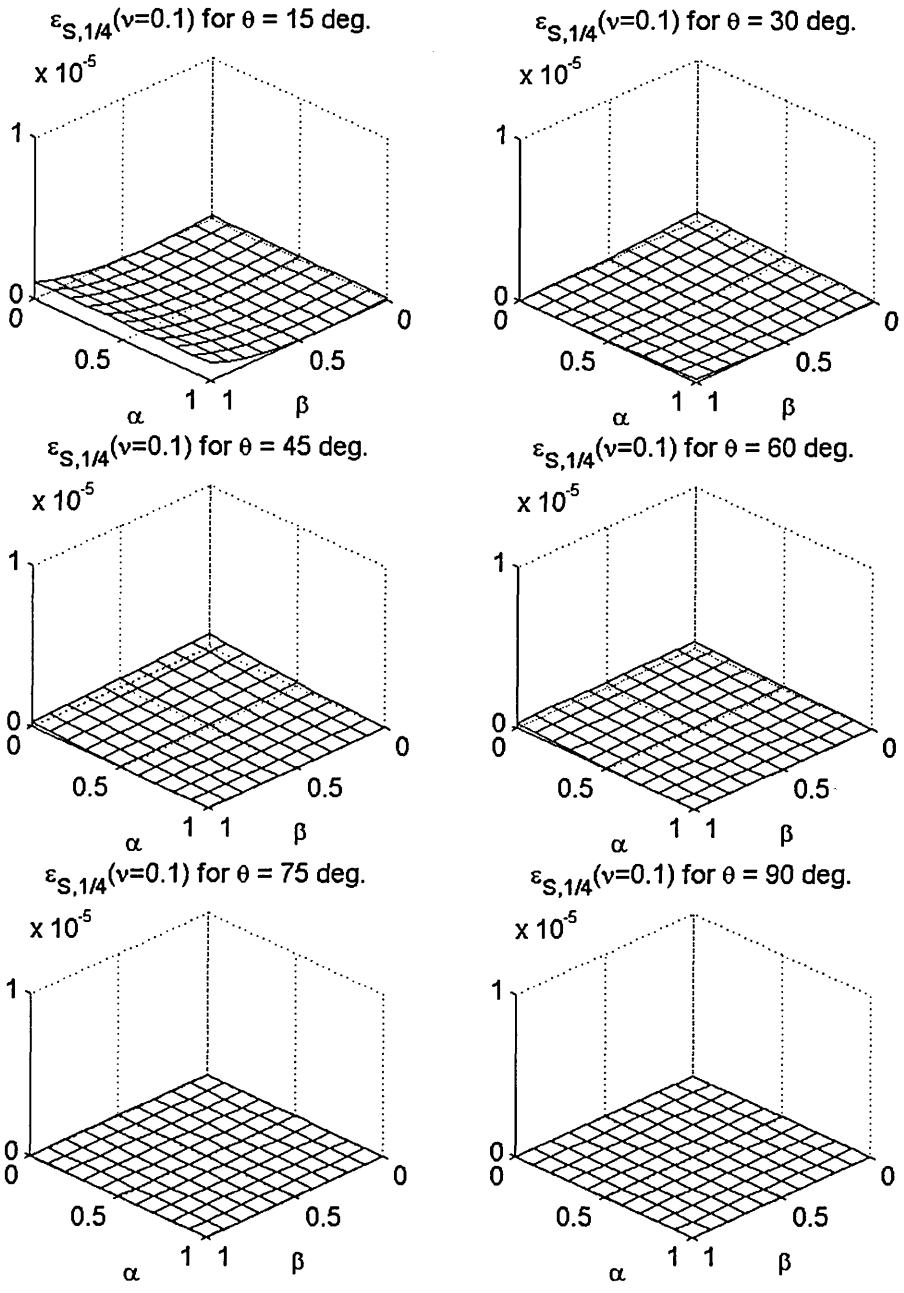

Figure 2.5.10a Integrated squared error ε_S for a homogeneous (ν=0.1) modeled with TLM2 for θ=15, 30, 45, 60, 75, 90°

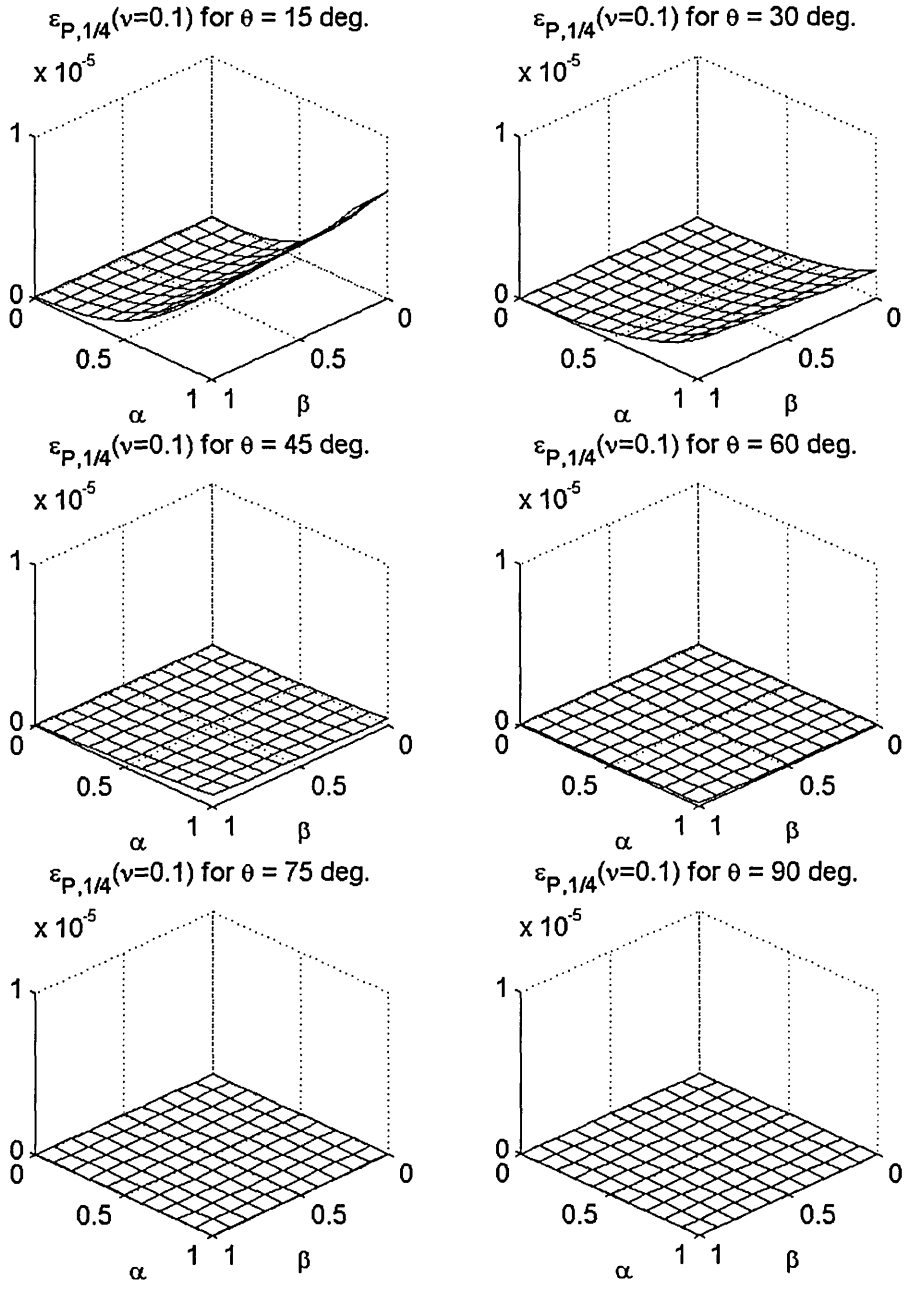

Figure 2.5.10b Integrated squared error ε_P for a homogeneous (ν=0.1) modeled with TLM2 for θ=15, 30, 45, 60, 75, 90°

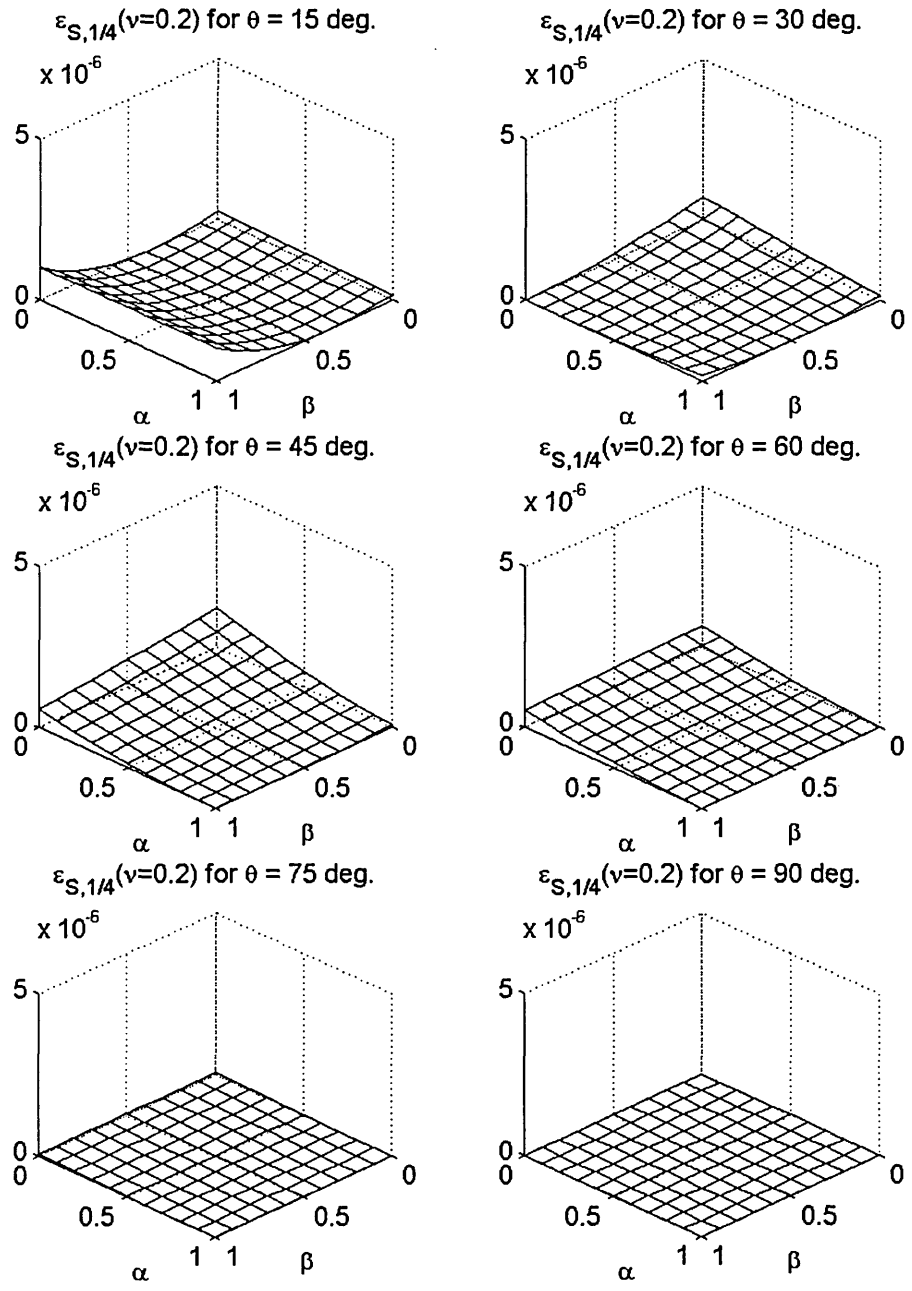

Figure 2.5.11a Integrated squared error ε_S for a homogeneous (ν=0.2) modeled with TLM2 for θ=15, 30, 45, 60, 75, 90°

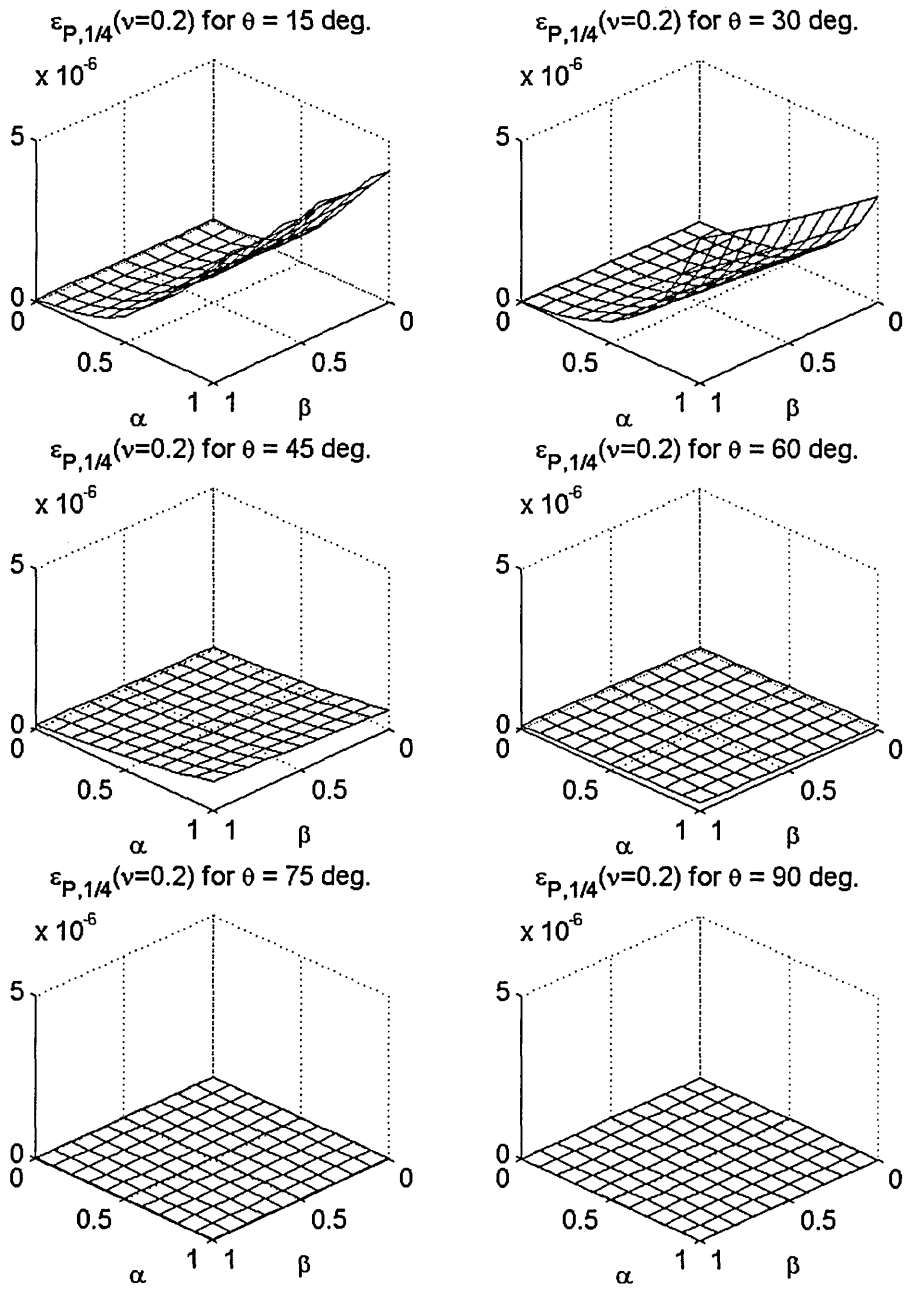

Figure 2.5.11b Integrated squared error ε_P for a homogeneous (ν=0.2) modeled with TLM2 for θ=15, 30, 45, 60, 75, 90°

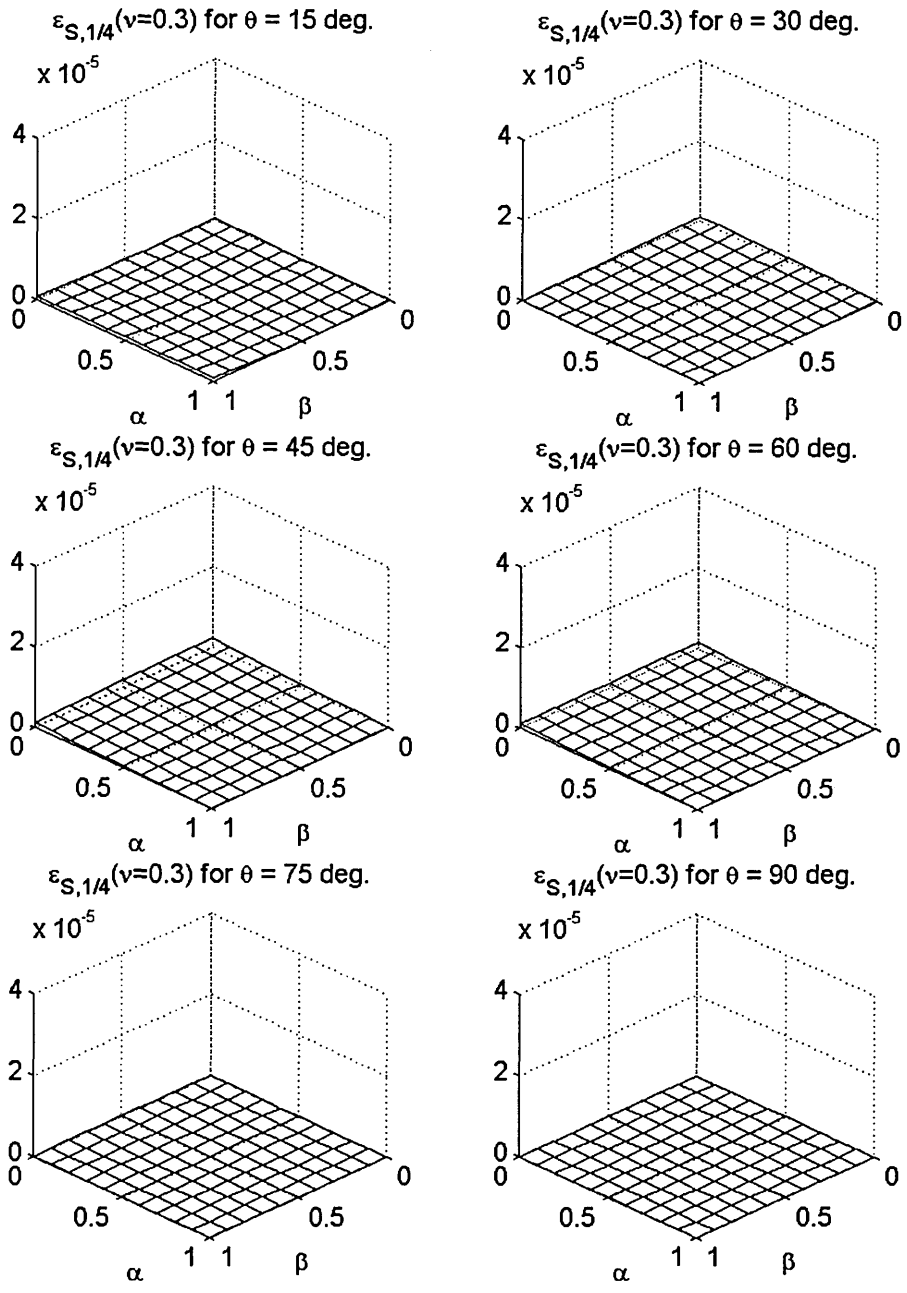

Figure 2.5.12a Integrated squared error ε_S for a homogeneous (ν=0.3) modeled with TLM2 for θ=15, 30, 45, 60, 75, 90°

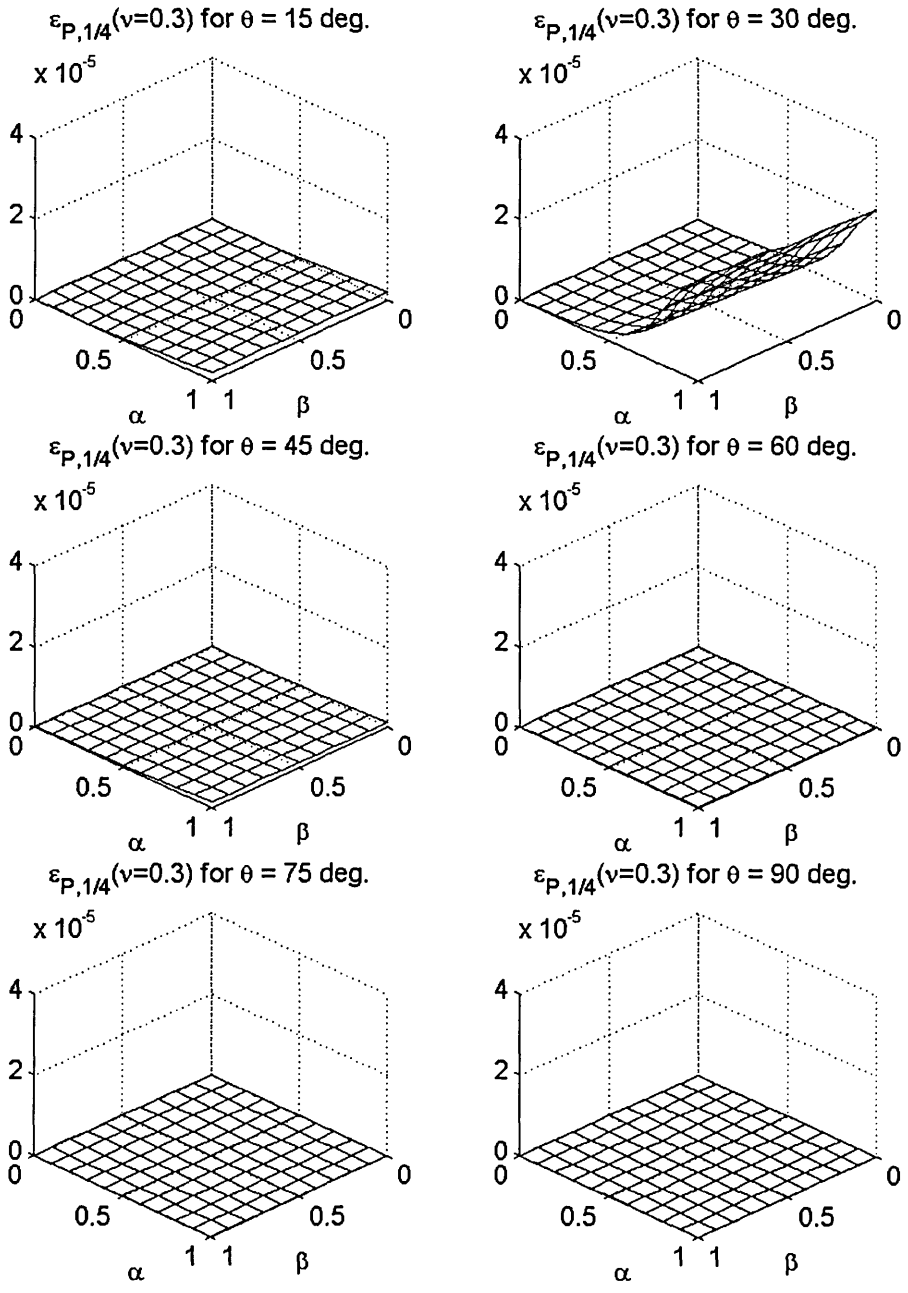

Figure 2.5.12b Integrated squared error ε_P for a homogeneous (ν=0.3) modeled with TLM2 for θ=15, 30, 45, 60, 75, 90°

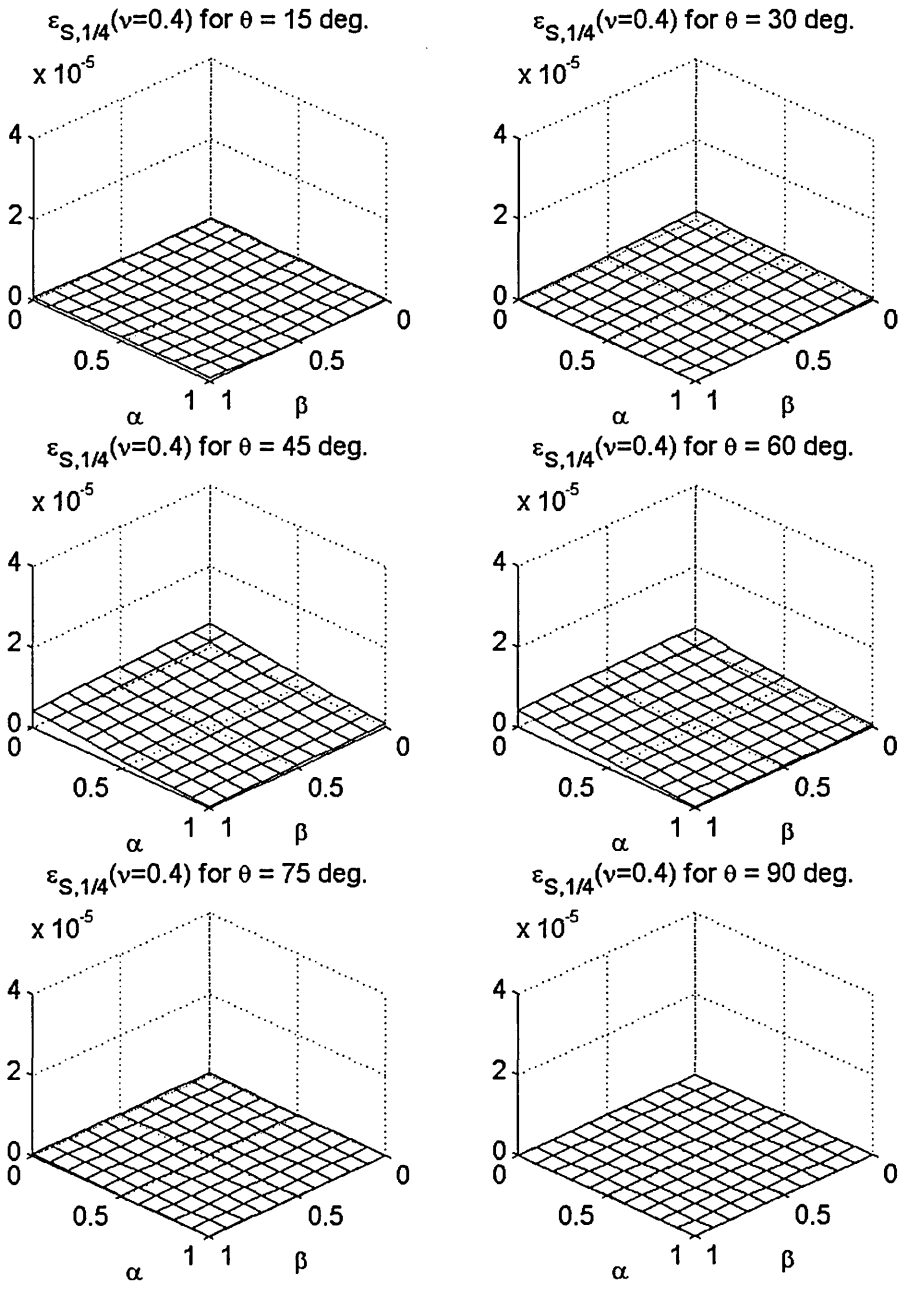

Figure 2.5.13a Integrated squared error ε_S for a homogeneous (ν=0.4) modeled with TLM2 for θ=15, 30, 45, 60, 75, 90°

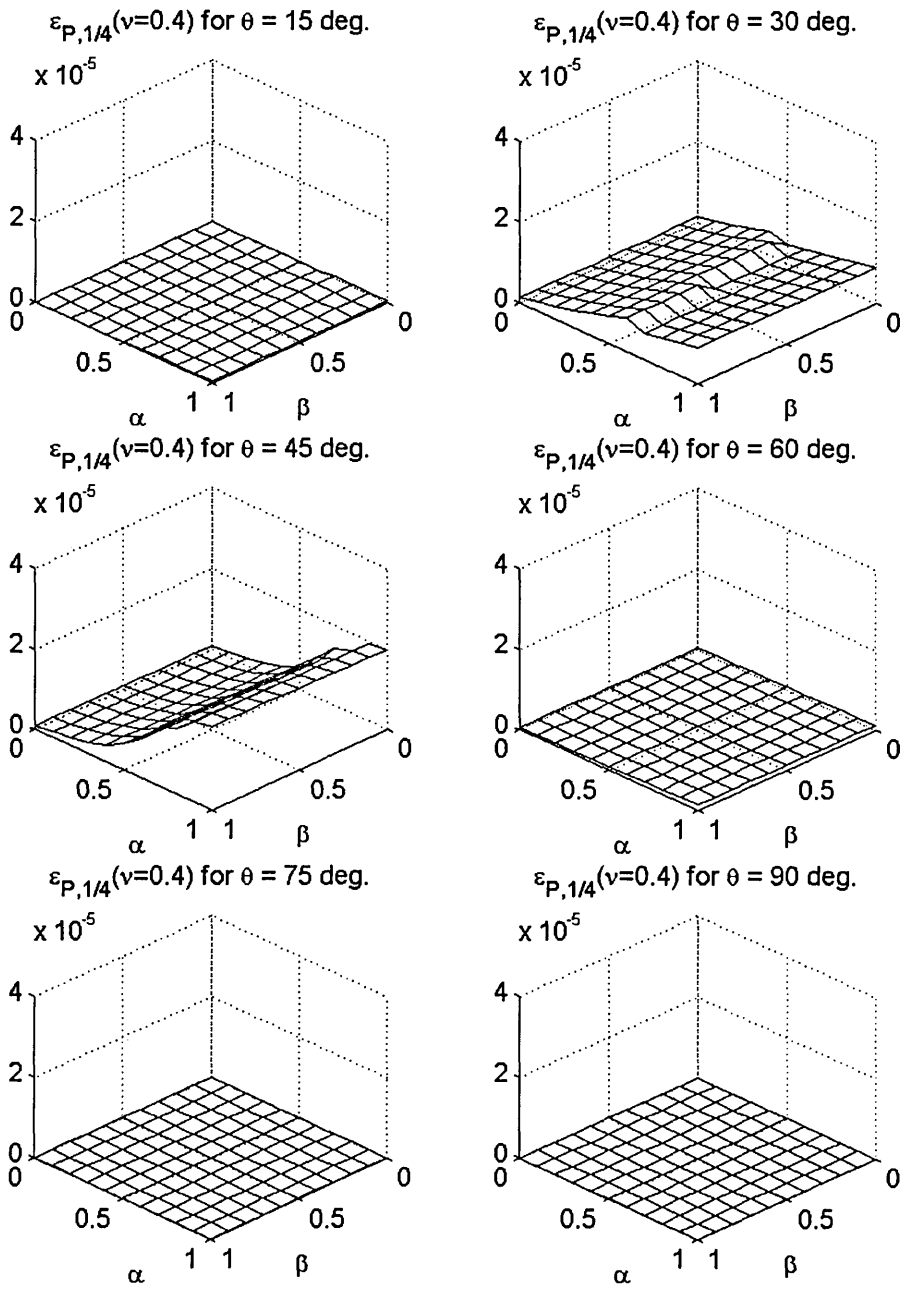

Figure 2.5.13b Integrated squared error ε_P for a homogeneous (ν=0.4) modeled with TLM2 for θ=15, 30, 45, 60, 75, 90°

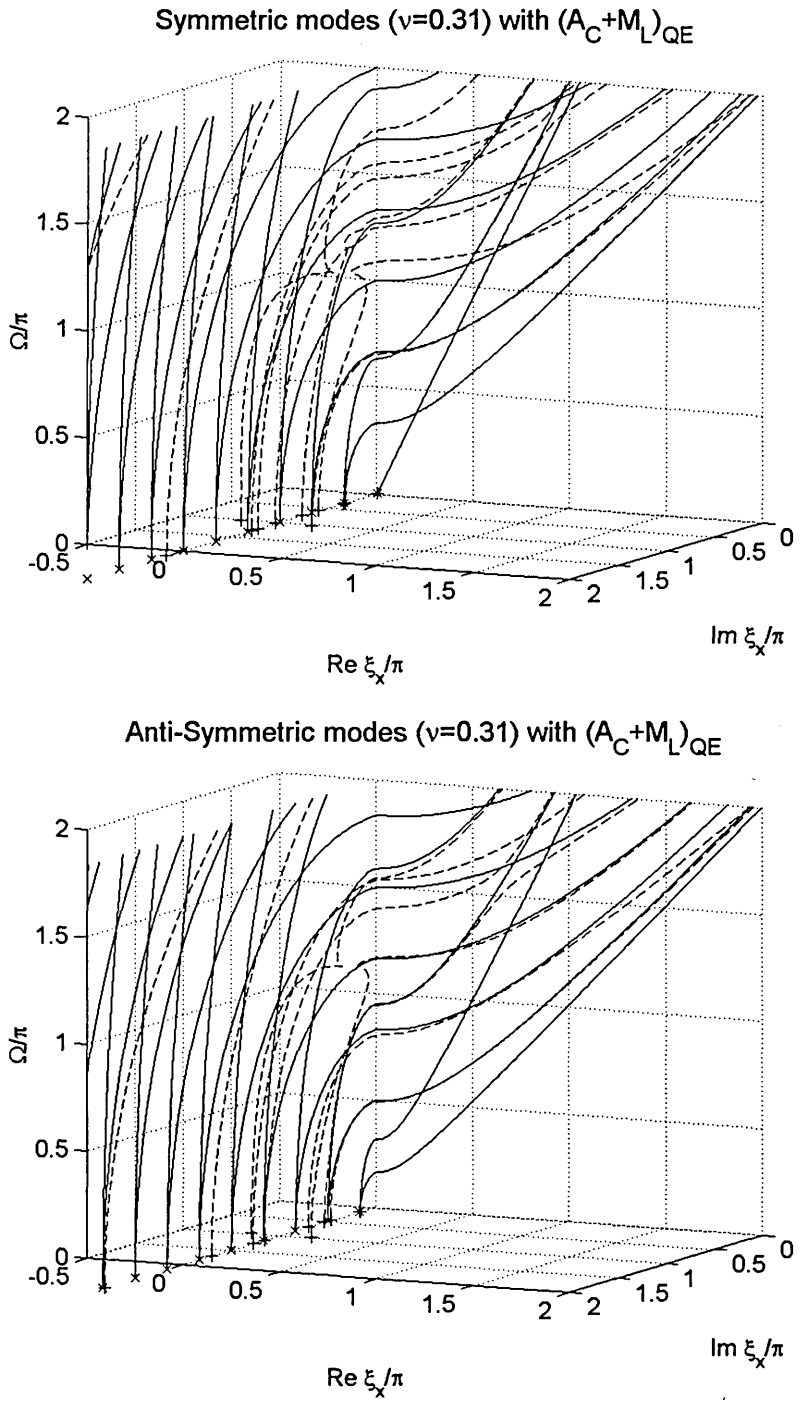

Figure 2.5.14a Dispersion curves of a BC plate (ν=0.31) modeled with TLM2 for α=β=1.0, μ=0.0 (dashed line for TLM2, solid line for Exact)

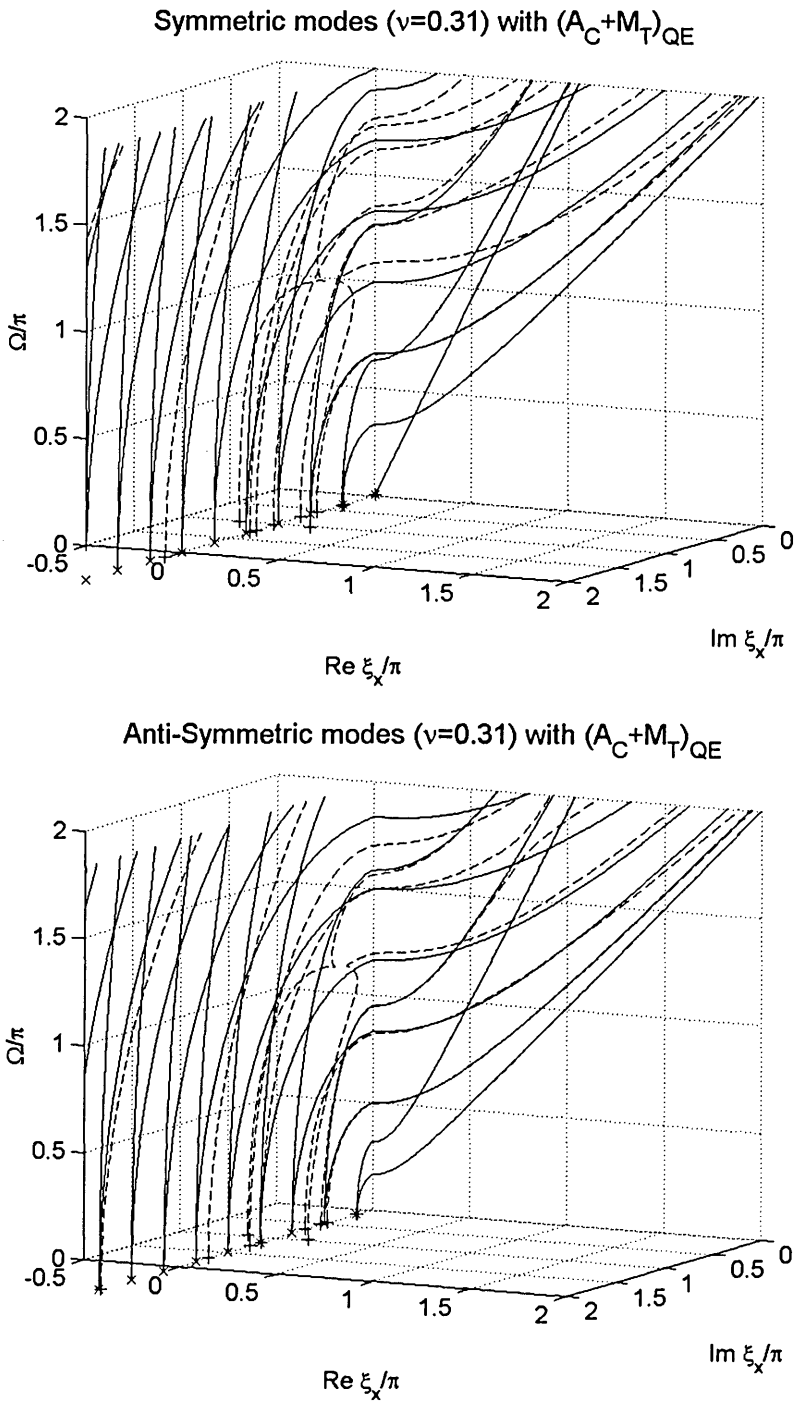

Figure 2.5.14b Dispersion curves of a BC plate (ν=0.31) modeled with TLM2 for α=β=1.0, μ=0.33 (dashed line for TLM2, solid line for Exact)

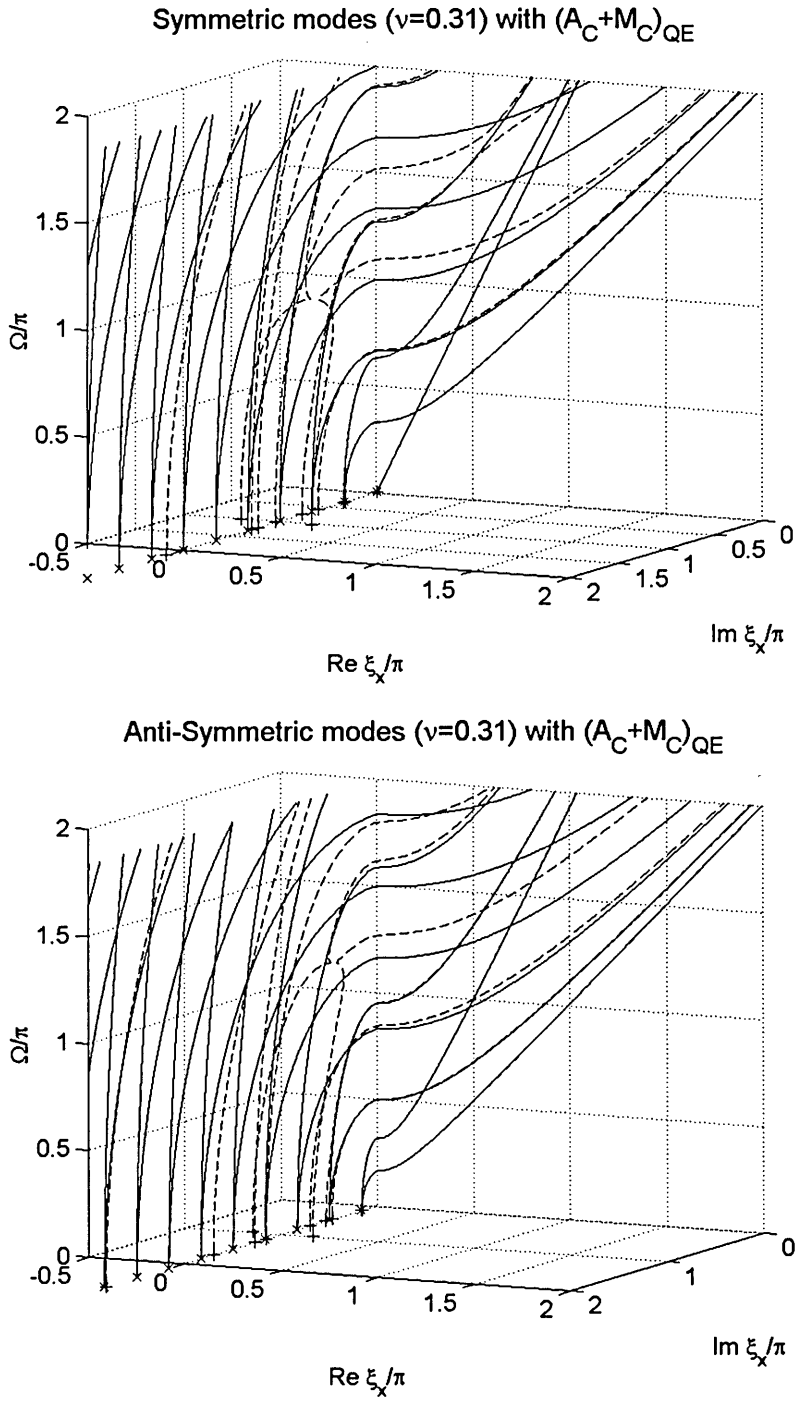

Figure 2.5.14c Dispersion curves of a BC plate (ν=0.31) modeled with TLM2 for α=β=1.0, μ=1.0 (dashed line for TLM2, solid line for Exact)

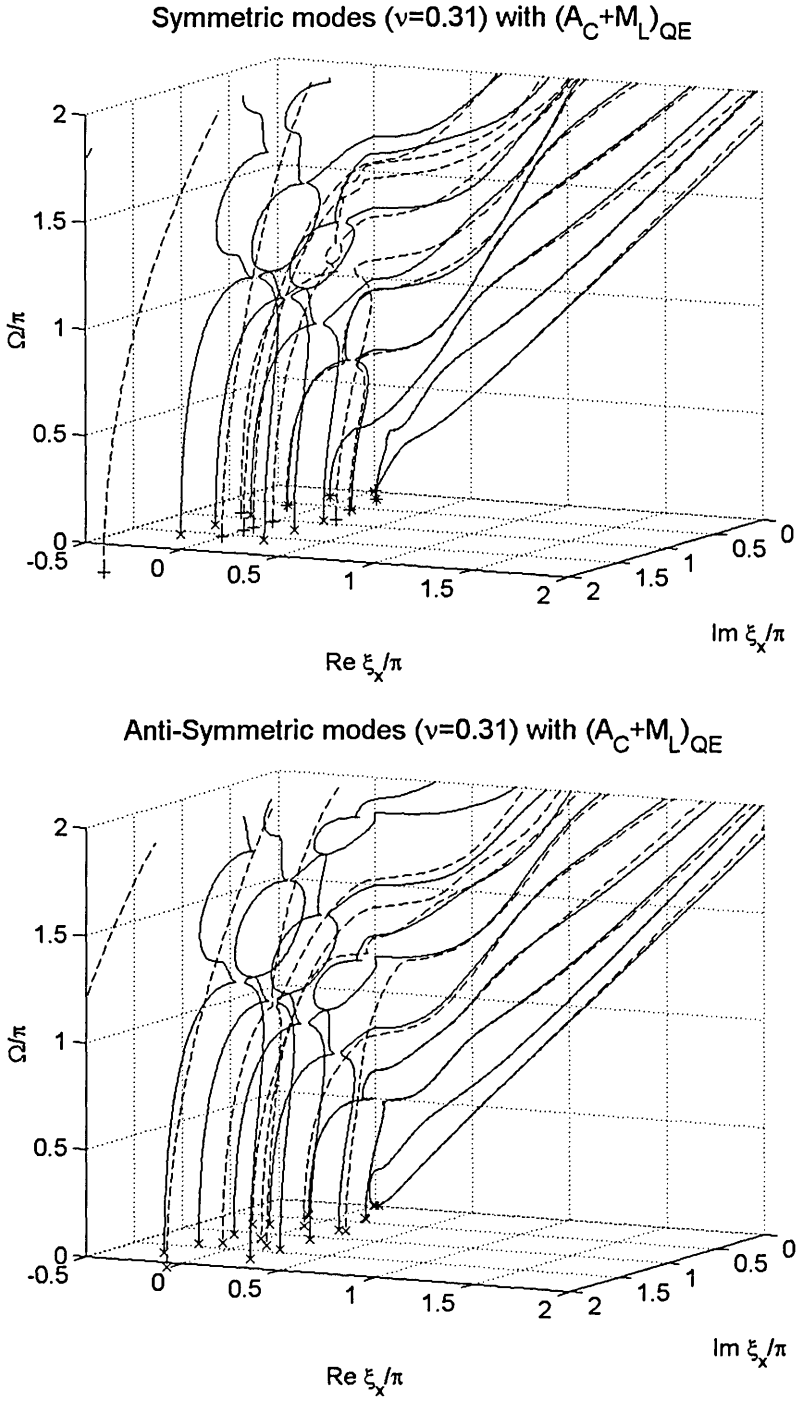

Figure 2.5.15a Dispersion curves of Mindlin plate (ν=0.31) modeled with TLM2 for α=β=1.0, μ=0.0 (dashed line for TLM2, solid line for Exact)

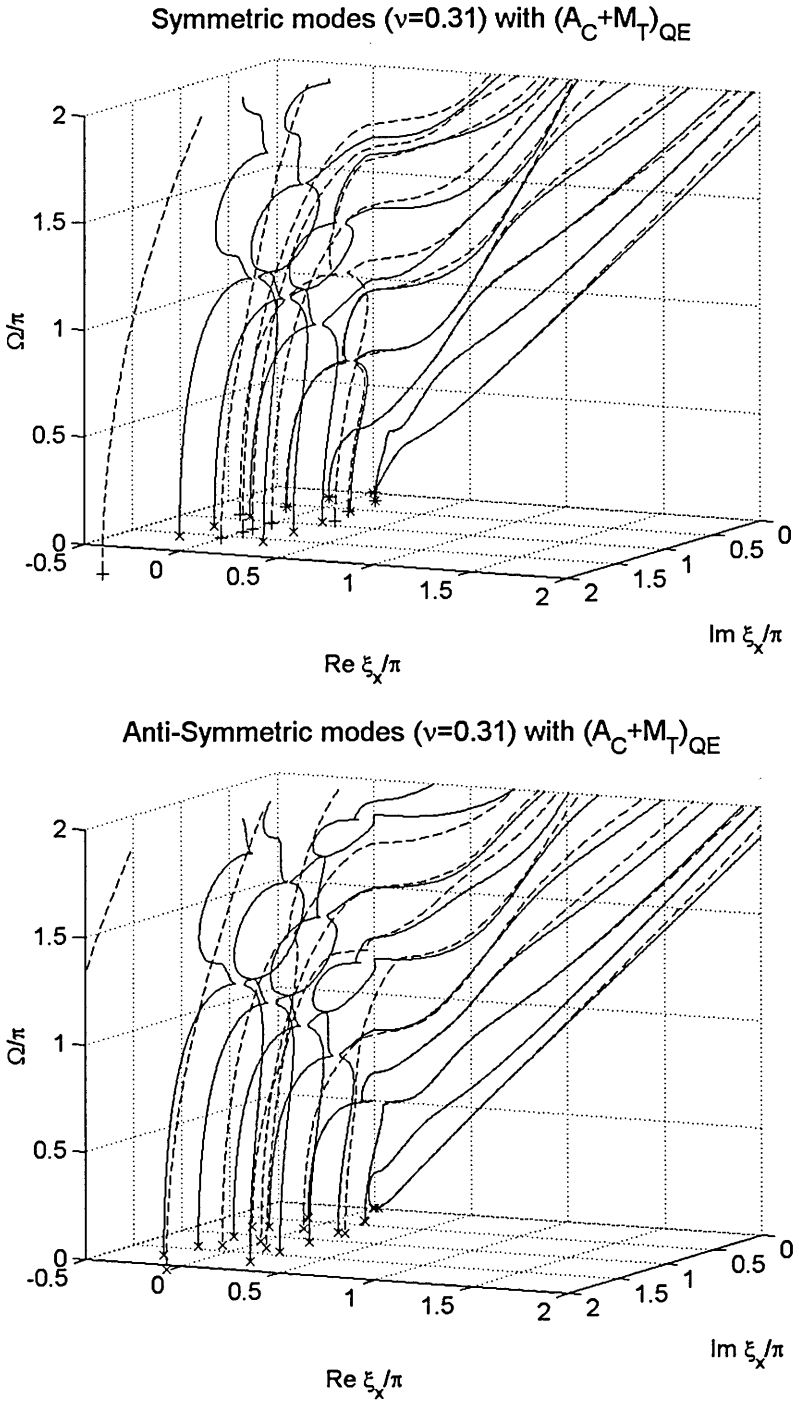

Figure 2.5.15b Dispersion curves of Mindlin plate (ν=0.31) modeled with TLM2 for α=β=1.0, μ=0.33 (dashed line for TLM2, solid line for Exact)

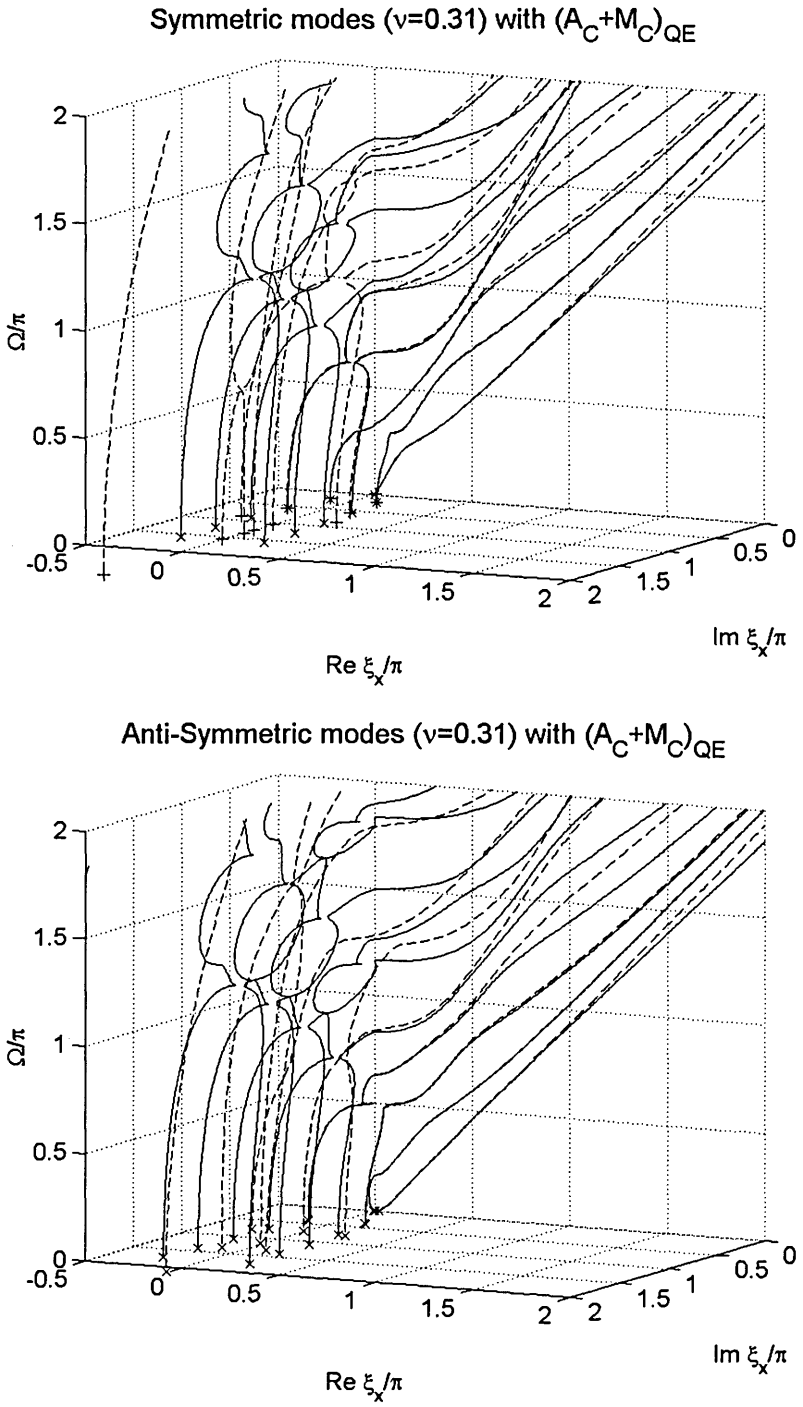

Figure 2.5.15c Dispersion curves of Mindlin plate (ν=0.31) modeled with TLM2 for α=β=1.0, μ=1.0 (dashed line for TLM2, solid line for Exact)

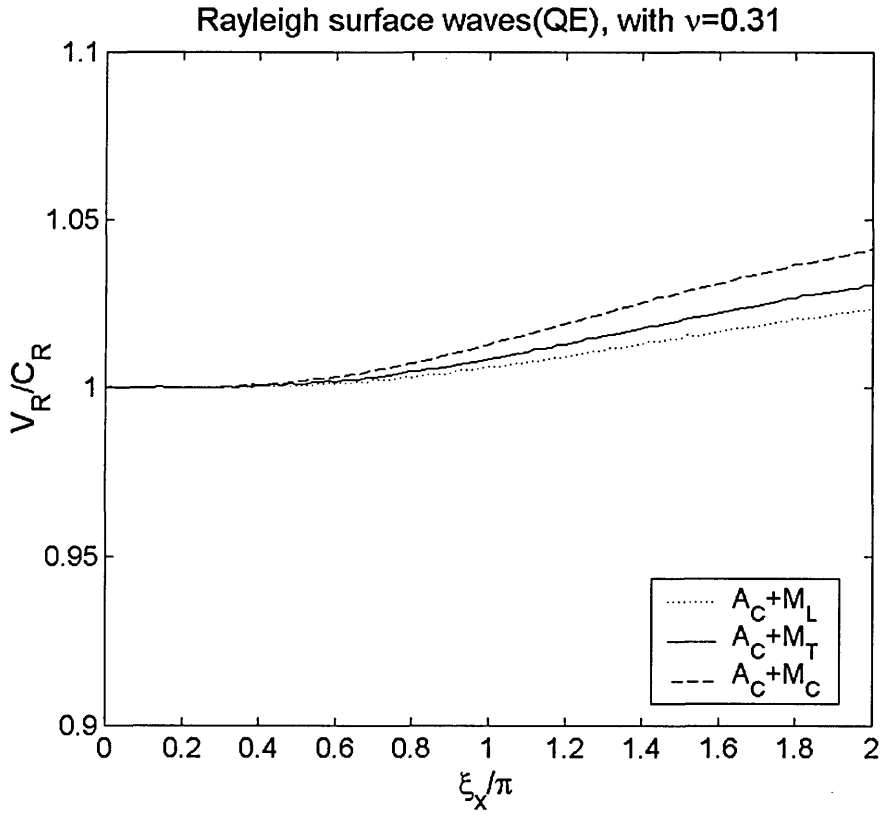

Figure 2.5.16 Numerical dispersion of Rayleigh surface waves (ν=0.31) modeled with TLM2 in terms of ratio of apparent Rayleigh surface wave to true Rayleigh surface wave V_R/C_R: α=β=1.0, μ=0.0 (dot-dashed line); α=β=1.0, μ=0.33 (solid line); α=β=1.0, μ=1.0 (dashed line)

Chapter 3 Effect of the tuning factors on the modal solutions

3.1 Introduction

In this short chapter, we investigate the effect that the tuning factors have on the accuracy of the modal solutions obtained with the TLM. Through this investigation, we verify that the responses are most accurate when the optimal tuning factors determined in chapter 2 are used. The reason is that the optimal tuning factors provide the most accurate mode shapes as well as the most accurate eigenvalues. We consider the modal solutions of both the TLM1 and TLM2, and compare their accuracy and efficiency. As a result, we propose to use the TLM2 rather than the TLM1 in consideration of the accuracy and computational cost in analysis.

For the above purpose, we compute the modal solutions of an example structure for three or four combinations of the tuning factors and then compare them with the associated exact analytical solutions. The example structure of interest is a homogeneous plate with stress-free boundary conditions at the both top and bottom surfaces, subjected to an *SH* or *SV-P* line load. The exact analytical solutions due to the *SH* and *SV-P* line loads are derived and presented in appendices 4B and 4C, respectively, of chapter 4. Particularly, in this chapter we are interested in only the displacement responses of the homogeneous plate. The investigation for the accuracy of internal stress components is performed in chapter 4.

In section 3.2, we assess the effect of the tuning factors on the accuracy of the ω-TLM modal solutions, by computing the displacement responses of the homogeneous plate due to an *SH* and *SV-P* harmonic line load with a single excitation frequency f_{ex}. In section 3.3, we explore the effect of the tuning factors on the accuracy of the t-TLM modal solutions, by calculating the displacement seismograms of the homogeneous plate due to an *SH* and *SV-P* transient line load.

3.2 ω-TLM modal solutions with the tuning factors

In this section, we explore the effect of the tuning factors on the accuracy of the ω-TLM modal solutions. For this purpose, we compute the modal solutions of an example structure for three or four combinations of the tuning factors and then compare them with the associated exact analytical solutions. The example structure is a homogeneous plate with stress-free boundary conditions at both the top and bottom surfaces, subjected to a *SH* or *SV-P* harmonic line load. The line load is applied at the top surface and has a single excitation frequency f_{ex}. In particular, we are interested in only the displacement responses of the homogeneous plate.

3.2.1 Plate subjected to an *SH* harmonic line load

We first explore the effect of the tuning factors on the accuracy of the ω-TLM modal solutions as for *SH* wave motions. For this purpose, we calculate the harmonic responses (displacements) in a homogeneous plate subjected to an *SH* harmonic line load. Concerning the material properties and geometry of the plate, the mass density (ρ), the shear velocity (C_S), and the thickness (H) are all chosen to be 1.0. The *SH* harmonic line load is applied at the top surface of the plate and its excitation frequency f_{ex} is 2.75.

To estimate the effect of the tuning factors β and μ on the accuracy of the ω-TLM modal responses, the motion of this plate is analyzed with changing the tuning factors. The results are then compared with the exact analytical solution that is derived in appendix 3B. The following four combinations of β and μ are considered. For the TLM1 models, four combinations are applied such that β=1.0 and μ=0.0 ($\mathbf{A_C}$+$\mathbf{M_L}$); β=1.0 and μ=1.0 ($\mathbf{A_C}$+$\mathbf{M_C}$); β=1.0 and μ=0.55 ($\mathbf{A_C}$+$\mathbf{M_T}$); β=μ=0.55 ($\mathbf{A_T}$+$\mathbf{M_T}$). On the other hand, for the TLM2 models, four combinations are applied such that β=1.0 and μ=0.0 ($\mathbf{A_C}$+$\mathbf{M_L}$); β=1.0 and μ=1.0 ($\mathbf{A_C}$+$\mathbf{M_C}$); β=1.0 and μ=0.33 ($\mathbf{A_C}$+$\mathbf{M_T}$); β=μ=0.33 ($\mathbf{A_T}$+$\mathbf{M_T}$). Concerning the discretization, the number of thin-layers per wavelength N_λ is chosen such that N_λ=4 is used for the TLM1 and N_λ=2 is used for the TLM2. Remember that N_λ=4 for the TLM1 and N_λ=2 for the TLM2 are the lower bounds for the number of thin-layers per wavelength that is proposed in chapter 2. Therefore, the validity of the proposed N_λ in chapter 2 can be verified through the present problem as well.

Figures 3.2.1–4 show the numerical results obtained with the TLM1 of $\mathbf{A_C}$+$\mathbf{M_L}$, $\mathbf{A_C}$+$\mathbf{M_C}$, $\mathbf{A_C}$+$\mathbf{M_T}$, and $\mathbf{A_T}$+$\mathbf{M_T}$, respectively. The first plot in each figure displays the eigenvalues obtained with the TLM1 (×) in comparison with the exact analytical eigenvalue (o) on the complex wavenumber plane. The second and third plots compare the real and imaginary parts of the displacement v, i.e. Re v and Im v, at the top surface obtained with the TLM1 (solid line) against the exact analytical solutions (dashed line) for $0.0<x<4.0$. It is clearly shown that the application of β=μ=0.55 ($\mathbf{A_T}$+$\mathbf{M_T}$) really provides the best agreement with the exact analytical solutions in terms of not only the eigenvalues, but also the modal solutions. Therefore, it is verified that the optimal tuning factors obtained in chapter 2 improve the accuracy of the modal responses obtained with the TLM1 as well as the eigenvalues. In addition, this best accuracy achieved with the optimal tuning factors confirms the validity of the condition of $N_\lambda \geq 4$ that is proposed for the TLM1 in chapter 2. In figure 3.2.3, it should also be noticed that the use of β=1.0 and μ=0.55 ($\mathbf{A_C}$+$\mathbf{M_T}$) improves the accuracy of the modal solution only for small x (e.g. $x<0.5$), but not for large x. The inaccuracy associated with large x results from the numerical dispersion error in the high propagation modes such as the 3rd, 4th, 5th and 6th modes, not the non-propagation modes, as shown in figure 3.2.3. The degree of this numerical error can be easily estimated by comparing the 3rd, 4th, 5th and 6th eigenvalues k_j in the two figures 3.2.3 and 3.2.4. More detail discussion about this error is provided in chapter 4.

Figures 3.2.5–8 show the numerical results obtained with the TLM2 of $\mathbf{A_C}$+$\mathbf{M_L}$, $\mathbf{A_C}$+$\mathbf{M_C}$, $\mathbf{A_C}$+$\mathbf{M_T}$, and $\mathbf{A_T}$+$\mathbf{M_T}$, respectively, in comparison with the exact analytical solutions. The first plot in each figure compares the eigenvalue obtained with the TLM2 (×) against the exact analytical eigenvalue (o). The second and third plots compare the real and imaginary parts of the displacement, i.e. Re v and Im v, at the top surface obtained with the TLM2 (solid line) against the exact analytical solutions (dashed line) for $0.0<x<4.0$. It is again clearly shown that the application of the optimal tuning factors of β=μ=0.33 ($\mathbf{A_T}$+$\mathbf{M_T}$) really provides the best agreement with the exact analytical solutions in terms of not only the eigenvalues, but also the modal solutions. Therefore, it is proved that the optimal tuning factors improve to the best degree the accuracy of the modal responses as well as the eigenvalues, computed with the TLM2. In addition, this best accuracy achieved with the optimal tuning factors confirms the validity of the condition of $N_\lambda \geq 2$ that is proposed for the TLM2 in chapter 2. In figure 3.2.7, it should be noticed that the use of β=1.0 and μ=0.33 ($\mathbf{A_C}$+$\mathbf{M_T}$) improves the accuracy of the modal solution only for small x (e.g. $x<0.7$), but not for large x. This inaccuracy for large x is caused by the numerical dispersion error in the high propagation modes such as the 5th and 6th modes, not the non-

propagation modes, as shown in figure 3.2.7. The degree of this numerical error can be easily estimated by comparing the associated 5th and 6th eigenvalues k_j in the two figures 3.2.7 and 3.2.8.

In application of β=1.0, and μ=0.55 (for the TLM1) or 0.33 (for the TLM2), both indicated by $\mathbf{A_C}$+$\mathbf{M_T}$, the errors in the modal solutions discussed above can be reduced simply by increasing N_λ. In the present problem, N_λ=4 is used for the TLM1, and N_λ=2 is used for the TLM2. As increasing N_λ, however, we can obtain more accurate high propagation modes, and then can calculate the more accurate modal solutions as well. This is the case of Schepers [2001], in which as for calculating the accurate modal solutions to *SH* wave problems, he has proposed the use of N_λ=10 for the TLM1 with the application of β=1.0 and μ=0.55 ($\mathbf{A_C}$+$\mathbf{M_T}$).

3.2.2 Plate subjected to an *SV-P* harmonic line load

We next investigate the effect of the tuning factors on the accuracy of the ω-TLM modal solutions concerned with *SV-P* wave motions. For this purpose, we calculate the harmonic responses (displacements) in a homogeneous plate subjected to an *SV-P* harmonic line load. Concerning the material properties and geometry of the plate, the mass density (ρ), the shear velocity (C_S), and the thickness (H) are all chosen to be 1.0, and the Poisson's ratio ν is 0.31. In addition, the damping ratio used is 0.1%. The *SV-P* harmonic line load is applied at the top surface in the vertical ($z-$) direction and its excitation frequency f_{ex} is 2.5.

To estimate the effect of the tuning factors α, β and μ on the accuracy of the ω-TLM modal responses, the harmonic motion of this plate is analyzed with fixing α=β=1.0, but changing μ. The results are then compared with the exact analytical solution that is derived in appendix 3C. The following three values for μ are considered. For the TLM1 models, the three values are such that μ=0.0 ($\mathbf{A_C}$+$\mathbf{M_L}$); μ=1.0 ($\mathbf{A_C}$+$\mathbf{M_C}$); μ=0.55 ($\mathbf{A_C}$+$\mathbf{M_T}$). On the other hand, for the TLM2, the three values are such that μ=0.0 ($\mathbf{A_C}$+$\mathbf{M_L}$); μ=1.0 ($\mathbf{A_C}$+$\mathbf{M_C}$); μ=0.33 ($\mathbf{A_C}$+$\mathbf{M_T}$). Concerning the discretization, the number of thin-layers per wavelength N_λ is chosen such that N_λ=8 is applied for the TLM1 model and N_λ=4 is applied for the TLM2 model, both of which are twice the lower bound for N_λ proposed in chapter 2. Therefore, it is expected that the accuracy of the present discrete models is better than that of the discrete models in section 3.2.1 where the lower bounds for the proposed N_λ are used in analysis.

Figures 3.2.9–11 show the numerical results obtained with the TLM1 of $\mathbf{A_C}$+$\mathbf{M_L}$, $\mathbf{A_C}$+$\mathbf{M_C}$, and $\mathbf{A_C}$+$\mathbf{M_T}$, respectively. The first plot in each figure displays the eigenvalue obtained with the TLM1 (×) in comparison with the exact analytical eigenvalue (o) on the complex wavenumber plane. The second and third plots compare the real and imaginary parts of the horizontal displacement u_{xz}, i.e. Re u_{xz} and Im u_{xz}, at the top surface obtained with the TLM1 (solid line) against the exact analytical solutions (dashed line) for 0.0<x<2.0. The variable u_{ij} represents a displacement in the i-direction due a load in the j-direction. The fourth and fifth plots compare the real and imaginary parts of the vertical displacement u_{zz}, i.e. Re u_{zz} and Im u_{zz}, at the top surface obtained with the TLM1 (solid line) against the exact analytical solutions (dashed line) for 0.0<x<2.0. It is clearly shown that the application of α=β=1.0 and μ=0.55 ($\mathbf{A_C}$+$\mathbf{M_T}$) really provides the best agreement with the exact analytical solutions in terms of not only the eigenvalues, but also the modal solutions. Therefore, it is verified that the optimal tuning factors obtained in chapter 2 improve best the accuracy of the modal solutions as well as the eigenvalues obtained with the TLM1. In addition, the comparison of figures 3.2.9-11 with figures 3.2.1-3

reveals that the modal solution obtained with N_λ=8 is more accurate than that obtained with N_λ=4. Therefore, it is confirmed that the larger N_λ is used, the more accurate results are obtained.

Figures 3.2.12–14 show the numerical results obtained with the TLM2 of $\mathbf{A_C}$+$\mathbf{M_L}$, $\mathbf{A_C}$+$\mathbf{M_C}$, and $\mathbf{A_C}$+$\mathbf{M_T}$, respectively. The first plot in each figure displays the eigenvalue obtained with the TLM2 (×) in comparison with the exact analytical eigenvalue (o) on the complex wavenumber plane. The second and third plots compare the real and imaginary parts of the horizontal displacement u_{xz}, i.e. Re u_{xz} and Im u_{xz}, at the top surface obtained with the TLM2 (solid line) against the exact analytical solutions (dashed line) for 0.0<x<2.0. The variable u_{ij} represents a displacement in the i-direction due a load in the j-direction. The fourth and fifth plots compare the real and imaginary parts of the vertical displacement u_{zz}, i.e. Re u_{zz} and Im u_{zz}, at the top surface obtained with the TLM2 (solid line) against the exact analytical solutions (dashed line) for 0.0<x<2.0. It is clearly shown that the application of α=β=1.0 and μ=0.33 ($\mathbf{A_C}$+$\mathbf{M_T}$) really provides the best agreement with the exact analytical solutions in terms of not only the eigenvalues, but also the modal solutions. Therefore, it is verified that the optimal tuning factors obtained in chapter 2 improve the accuracy of the modal responses as well as the eigenvalues computed with the TLM2. In addition, the comparison of figures 3.2.12-14 with figures 3.2.5-7 reveals that the modal solution obtained with N_λ=4 is much more accurate than that obtained with N_λ=2. Therefore, it is again confirmed that the larger N_λ is used, the more accurate results are obtained.

In addition, it should be recognized that the modal solutions obtained with the TLM2 are much more accurate than those obtained with the TLM1. This can be easily observed by comparing the two results in figures 3.2.11 and 3.2.14, both of which are calculated with application of the optimal tuning factors. Since N_λ=8 is used for the TLM1 model and N_λ=4 is used for the TLM2 model, the total number of the degrees of freedom involved is identical for both the models. It follows that the computational cost of both the models is quite comparable. Finally, in consideration of both the accuracy and computational cost in analysis, we propose to use the TLM2 rather than the TLM1.

3.3 *t*-TLM modal solutions with the tuning factors

In this section, we explore the effect of the tuning factors on the accuracy of the *t*-TLM modal solutions. For this purpose, we compute the modal solutions of an example structure for three or four combinations of the tuning factors and then compare them with the associated exact analytical solutions. The example structure is a homogeneous plate with stress-free boundary conditions at the top and bottom surfaces, subjected to a *SH* or *SV-P* transient line load. The transient line load is applied at the top surface and is a *bell-shaped* function in both x and t. More details about this *bell-shaped* function are explained in chapter 4. In particular, we are interested in the seismograms of the homogeneous plate, only in terms of displacements.

3.3.1 Plate subjected to an *SH* transient line load

We first explore the effect of the tuning factors on the accuracy of the *t*-TLM modal solutions as for *SH* wave motions. For this purpose, we synthesize the displacement seismogram v in a homogeneous plate subjected to an *SH* transient line load. Concerning the material properties and geometry of the plate, the mass density (ρ), the shear velocity (C_S), and the thickness (H) are all

chosen to be 1.0. The *SH* transient line load is applied at the top surface of the plate and is a bell-shaped function with $a=t_d=0.2$ where a and t_d are half the width in the x-direction and the time-duration, respectively, of the line load

To estimate the effect of the tuning factors β and μ on the accuracy of the t-TLM modal responses, the motion of this plate is analyzed with changing the tuning factors. The results are then compared with the exact analytical solution that is derived in appendix 3B. The following four combinations of β and μ are considered. For the TLM1 models, four combinations are used such that β=1.0 and μ=0.0 ($\mathbf{A_C}$+$\mathbf{M_L}$); β=1.0 and μ=1.0 ($\mathbf{A_C}$+$\mathbf{M_C}$); β=1.0 and μ=0.55 ($\mathbf{A_C}$+$\mathbf{M_T}$); $\beta=\mu$=0.55 ($\mathbf{A_T}$+$\mathbf{M_T}$). On the other hand, for the TLM2 models, four combinations are used such that β=1.0 and μ=0.0 ($\mathbf{A_C}$+$\mathbf{M_L}$); β=1.0 and μ=1.0 ($\mathbf{A_C}$+$\mathbf{M_C}$); β=1.0 and μ=0.33 ($\mathbf{A_C}$+$\mathbf{M_T}$); $\beta=\mu$=0.33 ($\mathbf{A_T}$+$\mathbf{M_T}$). Concerning the discretization, the number of thin-layers per wavelength N_λ is chosen such that N_λ=4 is used for the TLM1 and N_λ=2 is used for the TLM2. Remember that N_λ=4 for the TLM1 and N_λ=2 for the TLM2 are the lower bounds for the proposed number of thin-layers per wavelength proposed in chapter 2. Therefore, the validity of the proposed N_λ in chapter 2 can also be verified through the present problem.

Figure 3.3.1 shows four displacement seismograms obtained with the TLM1 (solid line) of $\mathbf{A_C}$+$\mathbf{M_L}$, $\mathbf{A_C}$+$\mathbf{M_C}$, $\mathbf{A_C}$+$\mathbf{M_T}$, and $\mathbf{A_T}$+$\mathbf{M_T}$, respectively, in comparison with the exact analytical solution (dashed line). The dot-dashed line in each plot displays the difference between the exact analytical solution and the TLM1 modal solution. The displacement seismogram v is recorded at x=1 on the top surface of the plate and for $0<t<4$. It is observed that the combination of $\beta=\mu$=0.55 ($\mathbf{A_T}$+$\mathbf{M_T}$) provides the almost perfect agreement with the exact analytical solution. Therefore, it is concluded that the combination of $\beta=\mu$=0.55 ($\mathbf{A_T}$+$\mathbf{M_T}$) is the optimal choice for improving to the best extent the accuracy of the TLM1 modal solution. In addition, this best accuracy achieved in the modal solution verifies the validity of the condition of $N_\lambda \geq 4$ that is determined for the TLM1 in chapter 2.

Figure 3.3.2 shows four displacement seismograms obtained with the TLM2 (solid line) of $\mathbf{A_C}$+$\mathbf{M_L}$, $\mathbf{A_C}$+$\mathbf{M_C}$, $\mathbf{A_C}$+$\mathbf{M_T}$, and $\mathbf{A_T}$+$\mathbf{M_T}$, respectively, in comparison with the exact analytical solution (dashed line). The dot-dashed line in each plot represents the difference between the exact analytical solution and the TLM2 modal solution. The displacement seismogram v is recorded at x=1 on the top surface of the plate and for $0<t<4$. It is seen that the combination of $\beta=\mu$=0.33 ($\mathbf{A_T}$+$\mathbf{M_T}$) provides the almost perfect agreement with the exact analytical solution. Therefore, it is concluded that the combination of $\beta=\mu$=0.33 ($\mathbf{A_T}$+$\mathbf{M_T}$) is the optimal choice for improving to the best extent the accuracy of the TLM2 modal solution. In addition, this best accuracy achieved in the modal solution verifies the validity of the condition of $N_\lambda \geq 2$ that is determined for the TLM2 in chapter 2.

3.3.2 Plate subjected to an *SV-P* transient line load

We continue to explore the effect of the tuning factors on the accuracy of the t-TLM modal solutions concerned with *SV-P* wave motions. For this purpose, we synthesize the displacement seismograms of u_{xz} and u_{zz} in a homogeneous plate subjected to an *SV-P* transient line load applied in the vertical (z-) direction. Note that u_{xz} and u_{zz} are the displacements in the x- and z-direction, respectively, due to a load in the z-direction. Concerning the material properties and geometry of the plate, the mass density (ρ), the shear velocity (C_S), and the thickness (H) are all chosen to be 1.0, and the Poisson's ratio ν is 0.31. The *SV-P* transient line load is applied at the

top surface in the vertical ($z-$) direction and is a bell-shaped function with $a=t_d=0.2$ where a and t_d are half the width in the x-direction and the time-duration, respectively, of the line load.

To estimate the effect of the tuning factors α, β and μ on the accuracy of the t-TLM modal responses, the time-dependent motion of this plate is analyzed with fixing $\alpha=\beta=1.0$, but changing μ. The results are then compared with the exact analytical solution that is derived in appendix 3C. The following three values for μ are considered. For the TLM1 models, the three values are such that $\mu=0.0$ ($\mathbf{A_C}+\mathbf{M_L}$); $\mu=1.0$ ($\mathbf{A_C}+\mathbf{M_C}$); $\mu=0.55$ ($\mathbf{A_C}+\mathbf{M_T}$). On the other hand, for the TLM2, the three values are such that $\mu=0.0$ ($\mathbf{A_C}+\mathbf{M_L}$); $\mu=1.0$ ($\mathbf{A_C}+\mathbf{M_C}$); $\mu=0.33$ ($\mathbf{A_C}+\mathbf{M_T}$). Concerning the discretization, the number of thin-layers per wavelength N_λ is chosen such that $N_\lambda=8$ is applied for the TLM1 model and $N_\lambda=4$ is applied for the TLM2 model, both of which are twice the lower bound for N_λ proposed in chapter 2. Therefore, it would be interesting to see if the accuracy of the present discrete models is better than that of the discrete models in section 3.3.1 where the lower bound for the proposed N_λ is used in analysis.

Figures 3.3.3-5 show the displacement seismograms obtained with the TLM1 (solid line) of $\mathbf{A_C}+\mathbf{M_L}$, $\mathbf{A_C}+\mathbf{M_C}$, and $\mathbf{A_C}+\mathbf{M_T}$, respectively, in comparison with the exact analytical solution (dashed line). The displacement seismograms of u_{xz} and u_{zz} are recorded at $x=1$ on the top surface of the plate and for $0<t<4$. It is observed that the combination of $\alpha=\beta=1$ and $\mu=0.55$ ($\mathbf{A_C}+\mathbf{M_T}$) provides the best agreement with the exact analytical solution. Therefore, it is concluded that the combination of $\alpha=\beta=1$ and $\mu=0.55$ ($\mathbf{A_C}+\mathbf{M_T}$) is the optimal choice for improving to the best extent the accuracy of the TLM1 modal solution. In addition, this achieved accuracy in the modal solution verifies the validity of the condition of $N_\lambda\geq 4$ that is determined for the TLM1 in chapter 2.

Figures 3.3.6-8 show the displacement seismograms obtained with the TLM2 (solid line) of $\mathbf{A_C}+\mathbf{M_L}$, $\mathbf{A_C}+\mathbf{M_C}$, and $\mathbf{A_C}+\mathbf{M_T}$, respectively, in comparison with the exact analytical solution (dashed line). The displacement seismograms of u_{xz} and u_{zz} are recorded at $x=1$ on the top surface of the plate and for $0<t<4$. It is observed that the combination of $\alpha=\beta=1$ and $\mu=0.33$ ($\mathbf{A_C}+\mathbf{M_T}$) provides the best agreement with the exact analytical solution. Therefore, it is concluded that the combination of $\alpha=\beta=1$ and $\mu=0.33$ ($\mathbf{A_C}+\mathbf{M_T}$) is the optimal choice for improving to the best extent the accuracy of the TLM2 modal solution. In addition, this achieved accuracy in the modal solution verifies the validity of the condition of $N_\lambda\geq 2$ that is determined for the TLM2 in chapter 2.

In addition, it should be noticed that the modal solutions obtained with the TLM2 are more accurate than those obtained with the TLM1. This can be easily observed by comparing the two results in figures 3.3.5 and 3.3.8, both of which are calculated with application of the optimal tuning factors. Since $N_\lambda=8$ is used for the TLM1 model and $N_\lambda=4$ is used for the TLM2 model, the total number of the degrees of freedom involved is identical for both the models. It follows that the computational cost of both the models is quite comparable. Finally, in consideration of both the accuracy and computational cost in analysis, we propose to use the TLM2 rather than the TLM1.

Figures for section 3.2

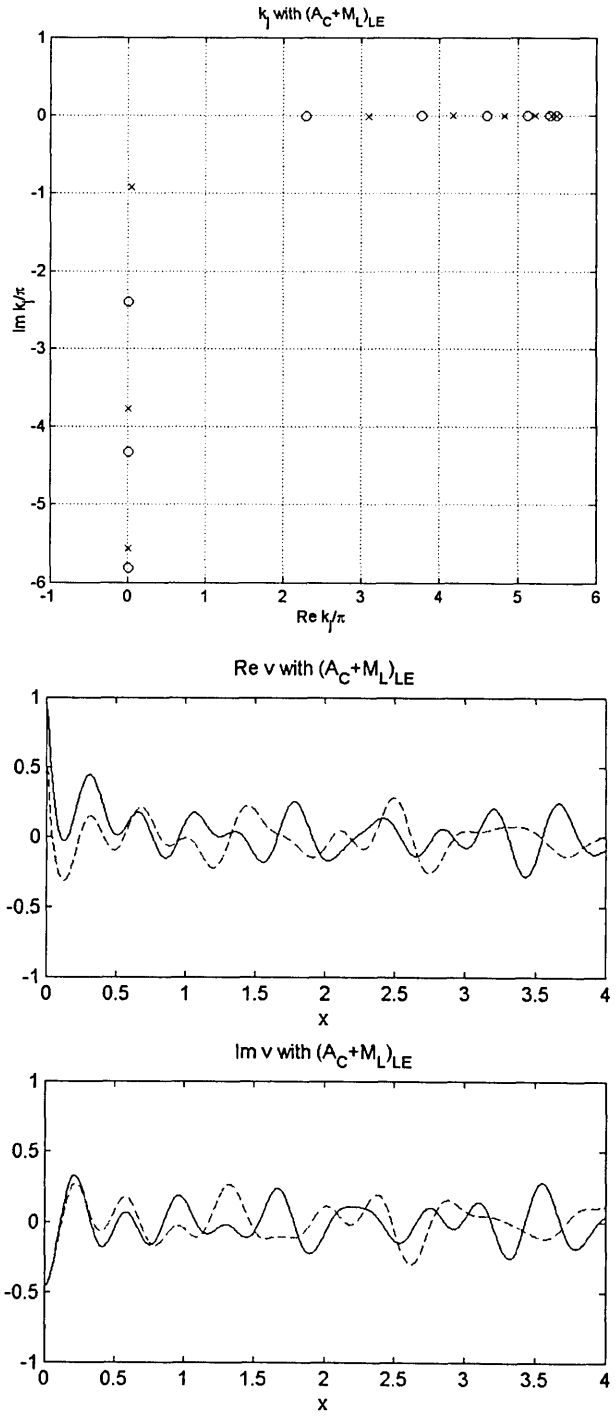

Figure 3.2.1 Harmonic wave motion obtained with TLM1 of β=1, μ=0 ($\mathbf{A_C}$+$\mathbf{M_L}$):
eigenvalues k_j and surface displacements v
for homogeneous plate subjected to *SH* surface line load of f_{ex}=2.75
(×:TLM1 k_j; o: Exact k_j; solid curve: TLM1 v; dashed curve: Exact v)

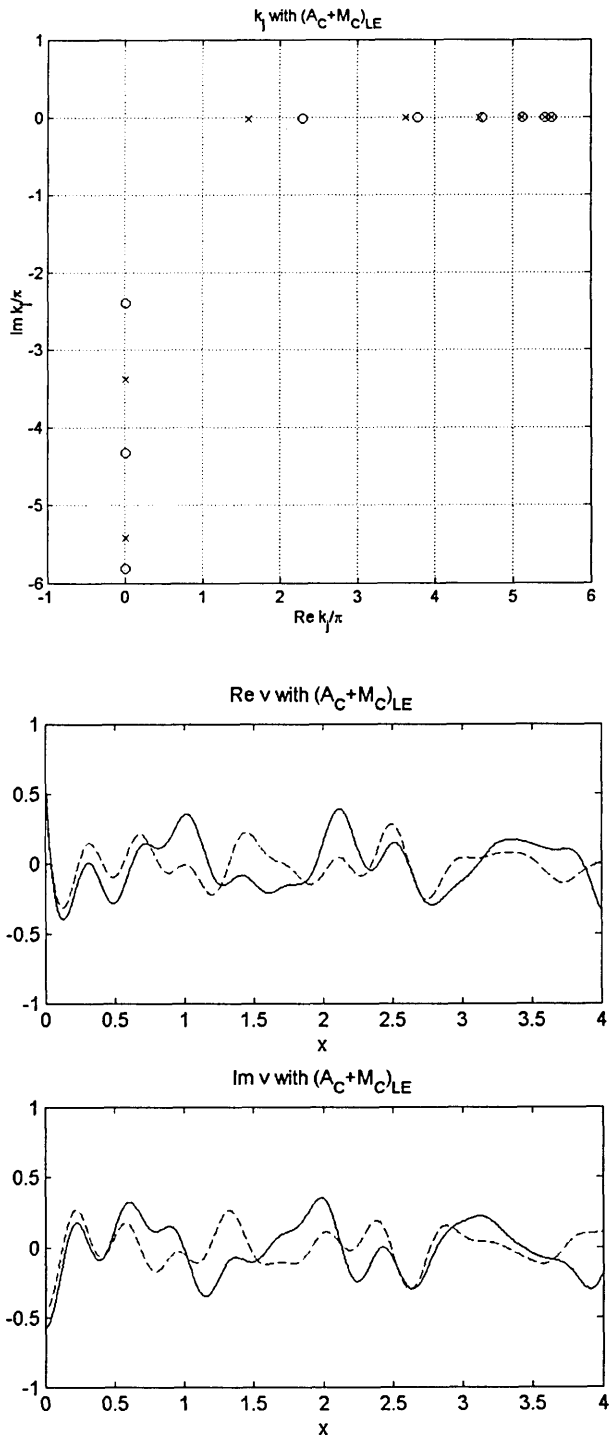

Figure 3.2.2 Harmonic wave motion obtained with TLM1 of $\beta=\mu=1$ ($\mathbf{A_C}+\mathbf{M_C}$): eigenvalues k_j and surface displacements v for homogeneous plate subjected to *SH* surface line load of $f_{ex}=2.75$ (×:TLM1 k_j; o: Exact k_j; solid curve: TLM1 v; dashed curve: Exact v)

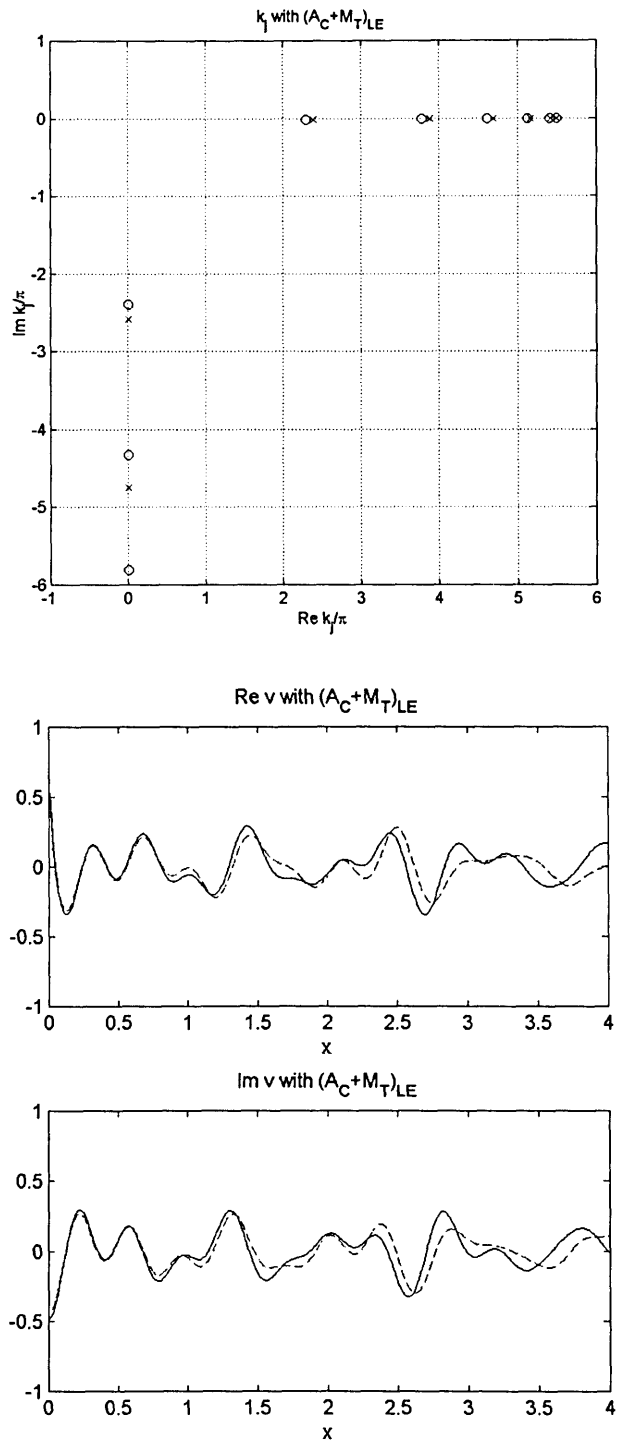

Figure 3.2.3 Harmonic wave motion obtained with TLM1 of β=1, μ=0.55 ($\mathbf{A}_C$+$\mathbf{M}_T$):
eigenvalues k_j and surface displacements v
for homogeneous plate subjected to *SH* surface line load of f_{ex}=2.75
(×:TLM1 k_j; o: Exact k_j; solid curve: TLM1 v; dashed curve: Exact v)

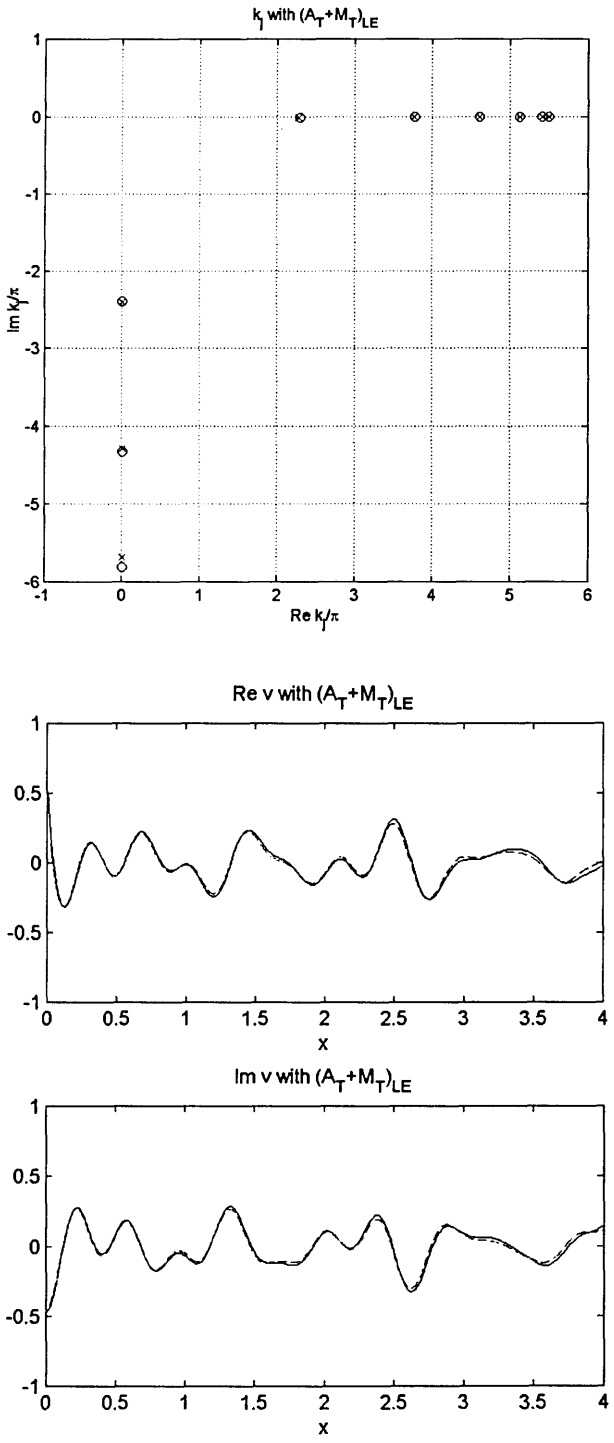

Figure 3.2.4 Harmonic wave motion obtained with TLM1 of β=μ=0.55 ($\mathbf{A_T}$+$\mathbf{M_T}$): eigenvalues k_j and surface displacements v for homogeneous plate subjected to *SH* surface line load of f_{ex}=2.75 (×:TLM1 k_j; o: Exact k_j; solid curve: TLM1 v; dashed curve: Exact v)

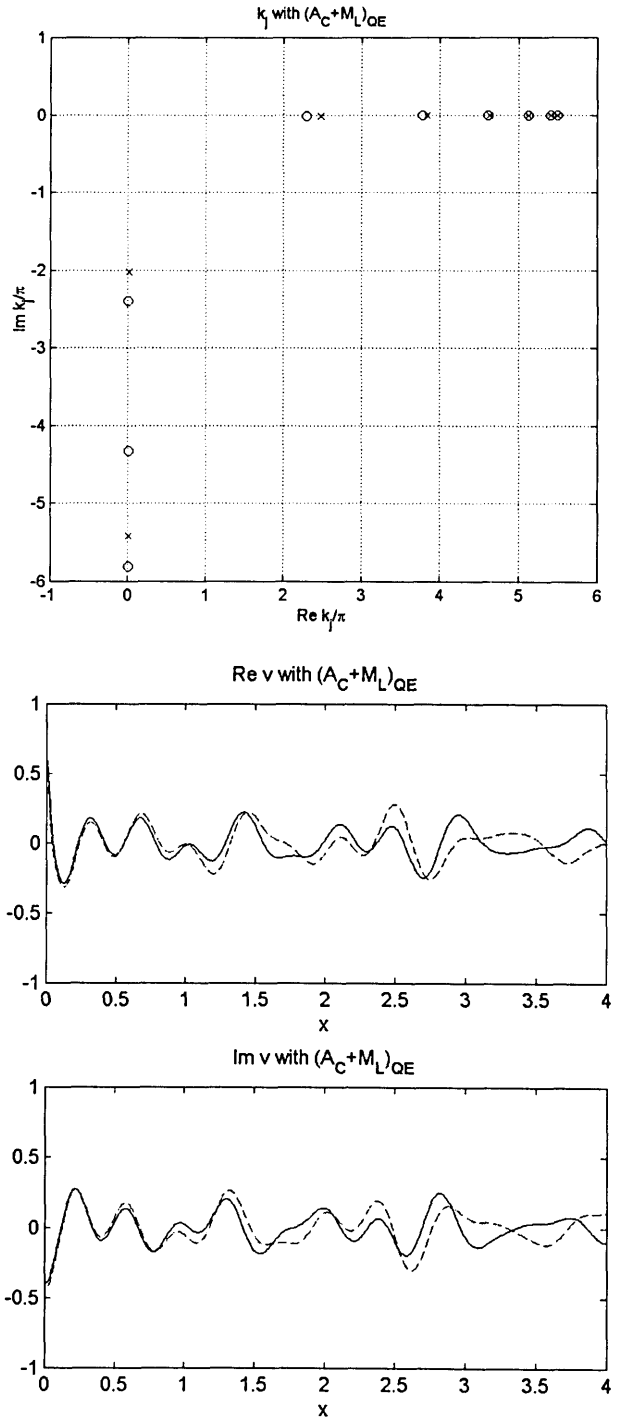

Figure 3.2.5 Harmonic wave motion obtained with TLM2 of β=1, μ=0 ($\mathbf{A_C}$+$\mathbf{M_L}$): eigenvalues k_j and surface displacements v for homogeneous plate subjected to *SH* surface line load of f_{ex}=2.75 (×:TLM2 k_j; o: Exact k_j; solid curve: TLM2 v; dashed curve: Exact v)

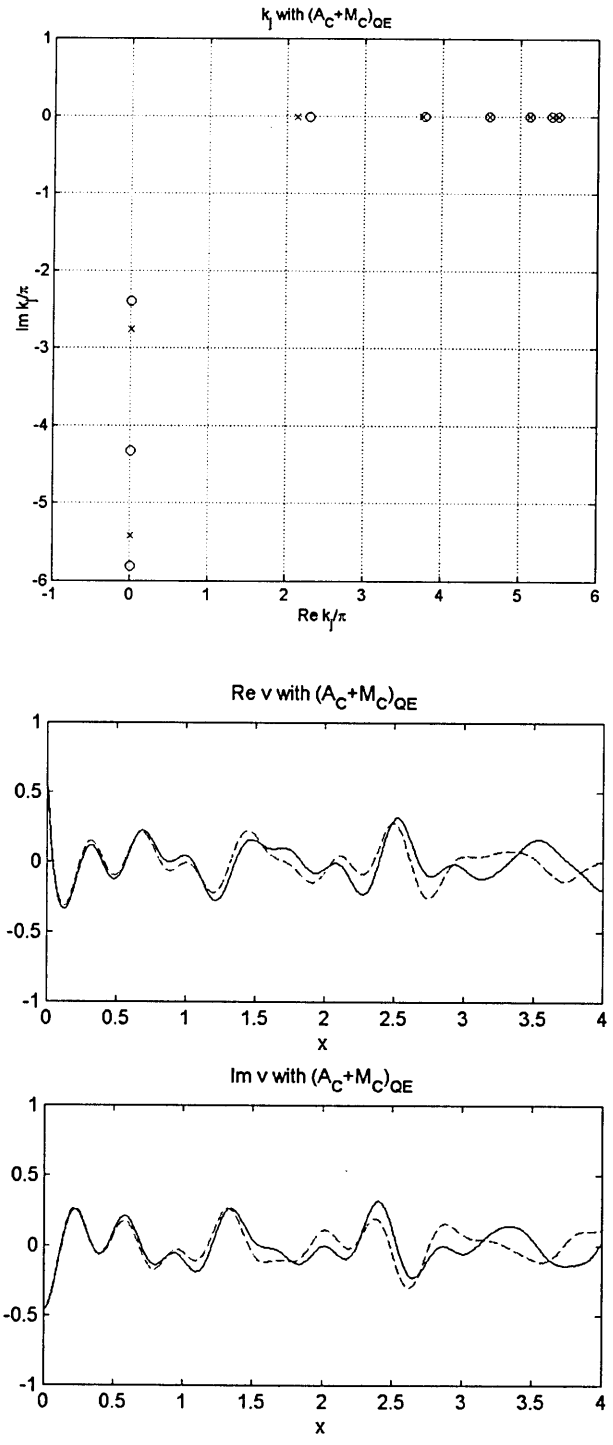

Figure 3.2.6 Harmonic wave motion obtained with TLM2 of $\beta=\mu=1$ ($\mathbf{A_C+M_C}$): eigenvalues k_j and surface displacements v for homogeneous plate subjected to *SH* surface line load of $f_{ex}=2.75$ (×:TLM2 k_j; o: Exact k_j; solid curve: TLM2 v; dashed curve: Exact v)

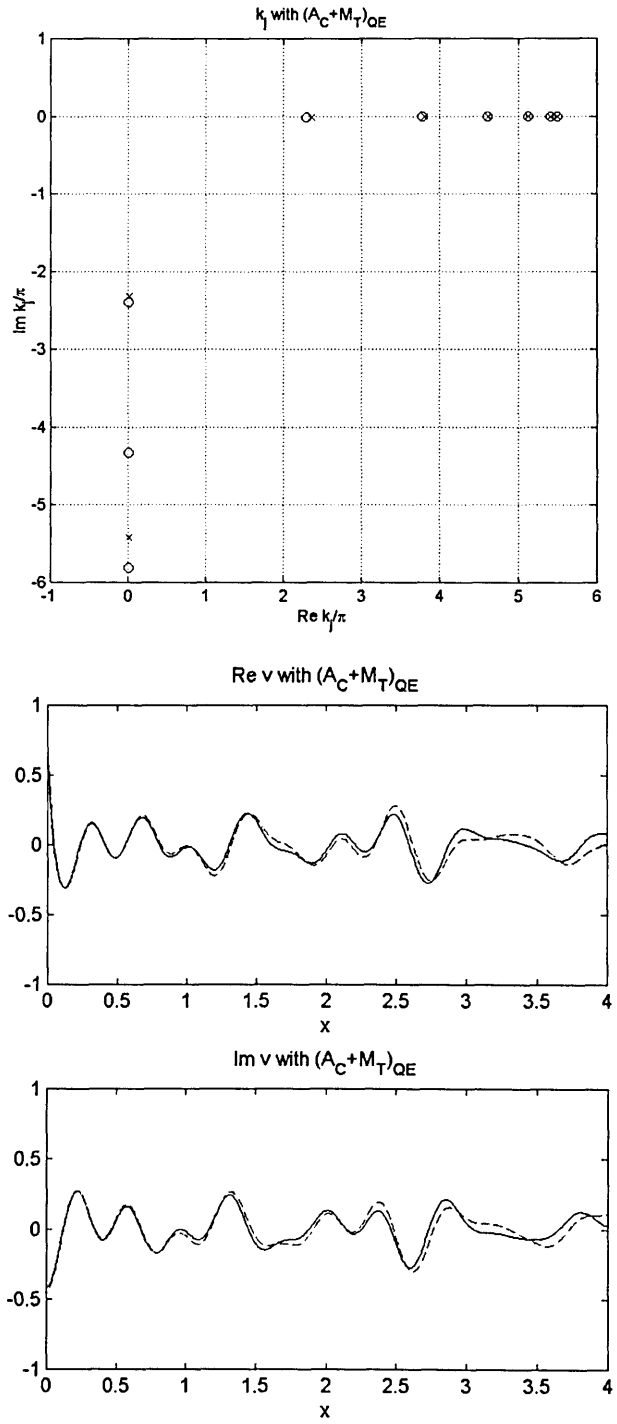

Figure 3.2.7 Harmonic wave motion obtained with TLM2 of β=1, μ=0.33 ($\mathbf{A_C}$+$\mathbf{M_T}$): eigenvalues k_j and surface displacements v for homogeneous plate subjected to *SH* surface line load of f_{ex}=2.75 (×:TLM2 k_j; o: Exact k_j; solid curve: TLM2 v; dashed curve: Exact v)

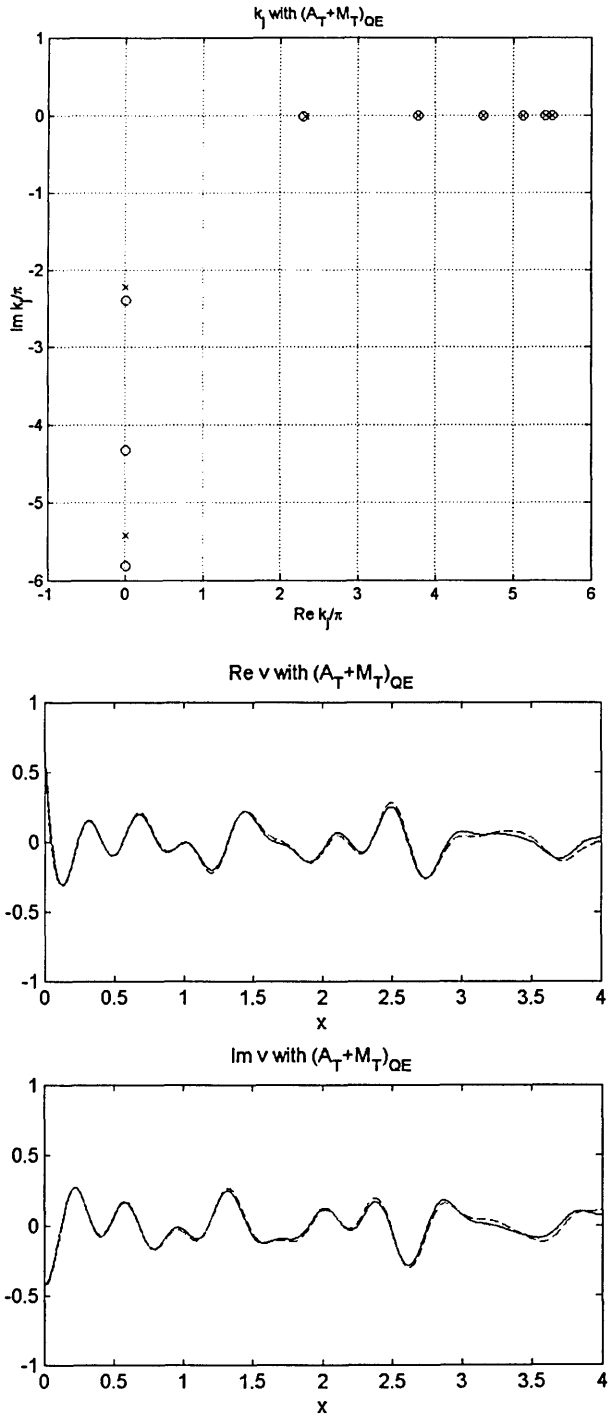

Figure 3.2.8 Harmonic wave motion obtained with TLM2 of $\beta=\mu=0.33$ (A_T+M_T): eigenvalues k_j and surface displacements v for homogeneous plate subjected to *SH* surface line load of $f_{ex}=2.75$ (×:TLM2 k_j; o: Exact k_j; solid curve: TLM2 v; dashed curve: Exact v)

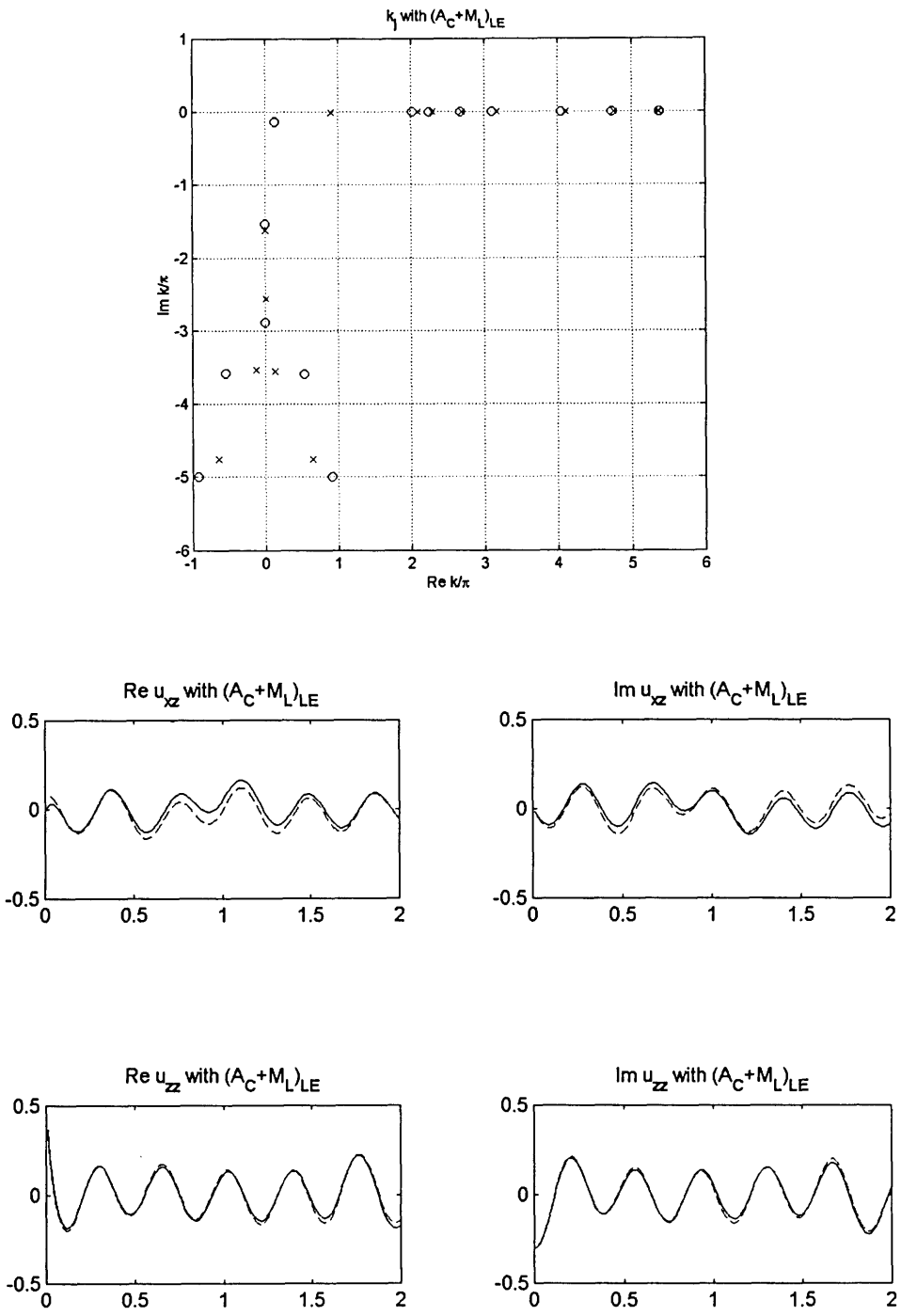

Figure 3.2.9 Harmonic wave motion obtained with TLM1 of α=β=1, μ=0 ($\mathbf{A_C}$+$\mathbf{M_L}$): eigenvalues k_j and surface displacements u_{xz}, u_{zz} for homogeneous plate subjected to *SV-P* surface line load of f_{ex}=2.50 in vertical direction (×:TLM1 k_j; o: Exact k_j; solid curve: TLM1 u_{xz}, u_{zz}; dashed curve: Exact u_{xz}, u_{zz})

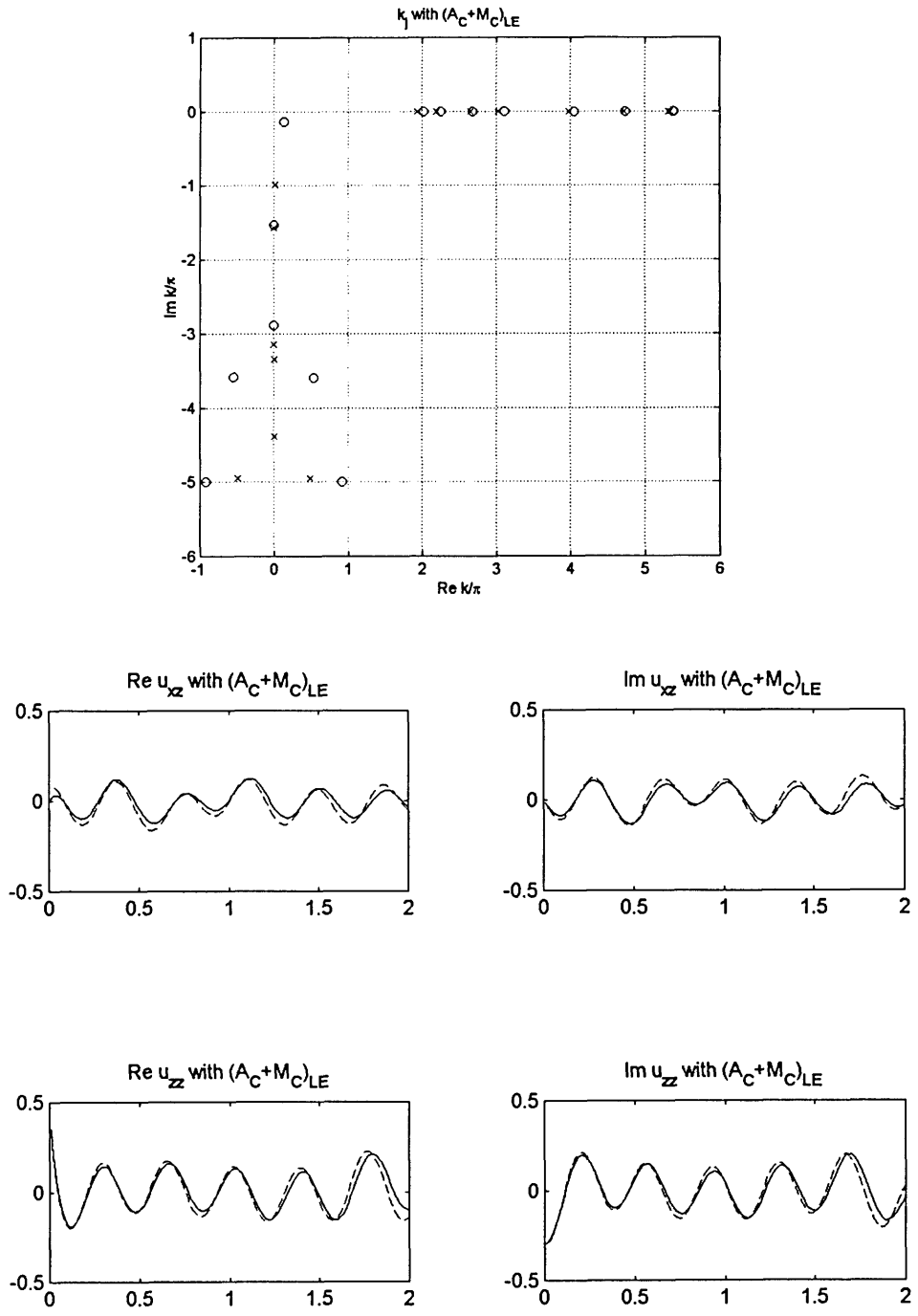

Figure 3.2.10 Harmonic wave motion obtained with TLM1 of $\alpha=\beta=\mu=1$ ($\mathbf{A}_C+\mathbf{M}_C$): eigenvalues k_j and surface displacements u_{xz}, u_{zz} for homogeneous plate subjected to *SV-P* surface line load of $f_{ex}=2.50$ in vertical direction (×:TLM1 k_j; o: Exact k_j; solid curve: TLM1 u_{xz}, u_{zz}; dashed curve: Exact u_{xz}, u_{zz})

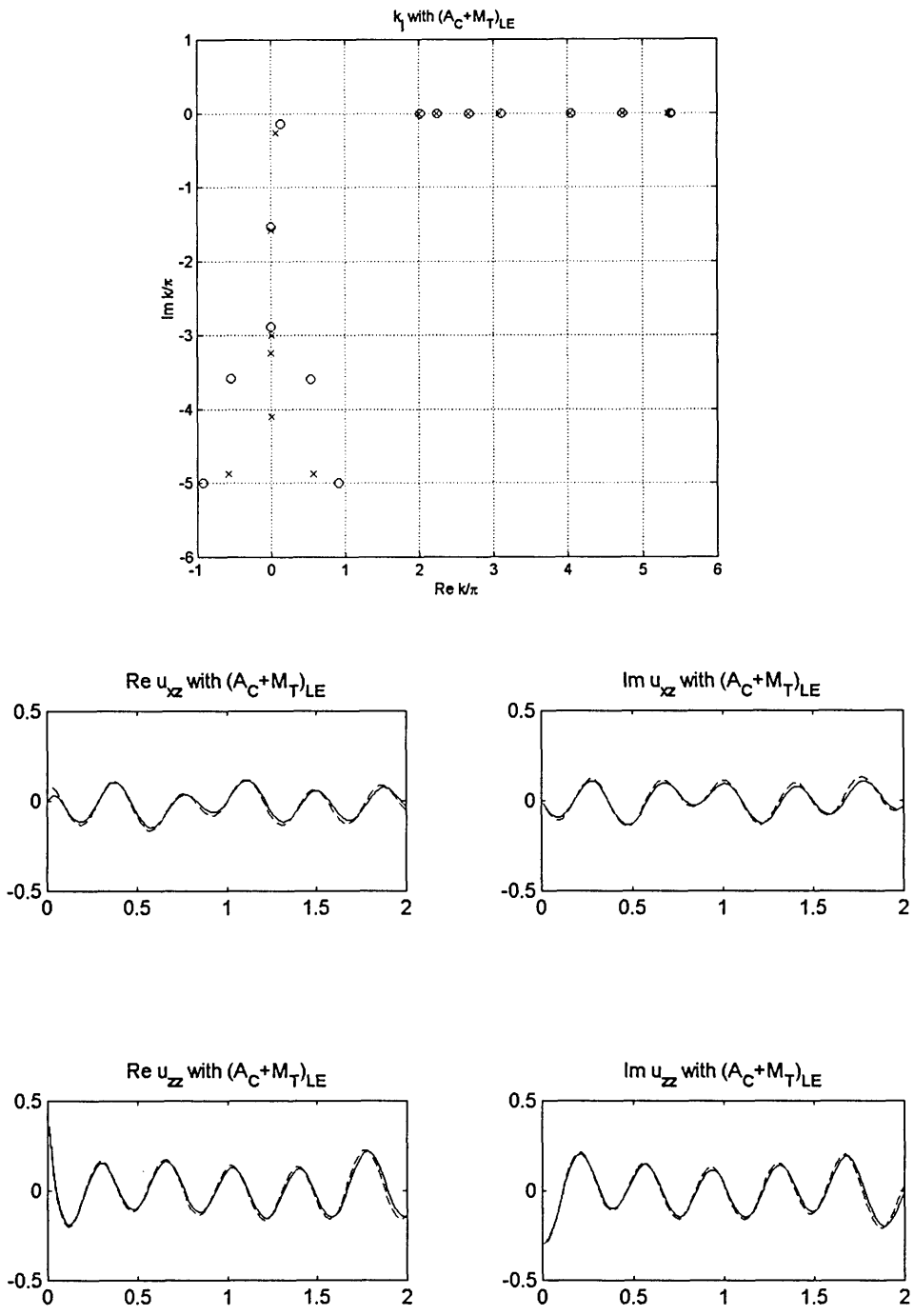

Figure 3.2.11 Harmonic wave motion obtained with TLM1 of α=β=1, μ=0.55 ($\mathbf{A_C}$+$\mathbf{M_T}$): eigenvalues k_j and surface displacements u_{xz}, u_{zz} for homogeneous plate subjected to *SV-P* surface line load of f_{ex}=2.50 in vertical direction (×:TLM1 k_j; o: Exact k_j; solid curve: TLM1 u_{xz}, u_{zz}; dashed curve: Exact u_{xz}, u_{zz})

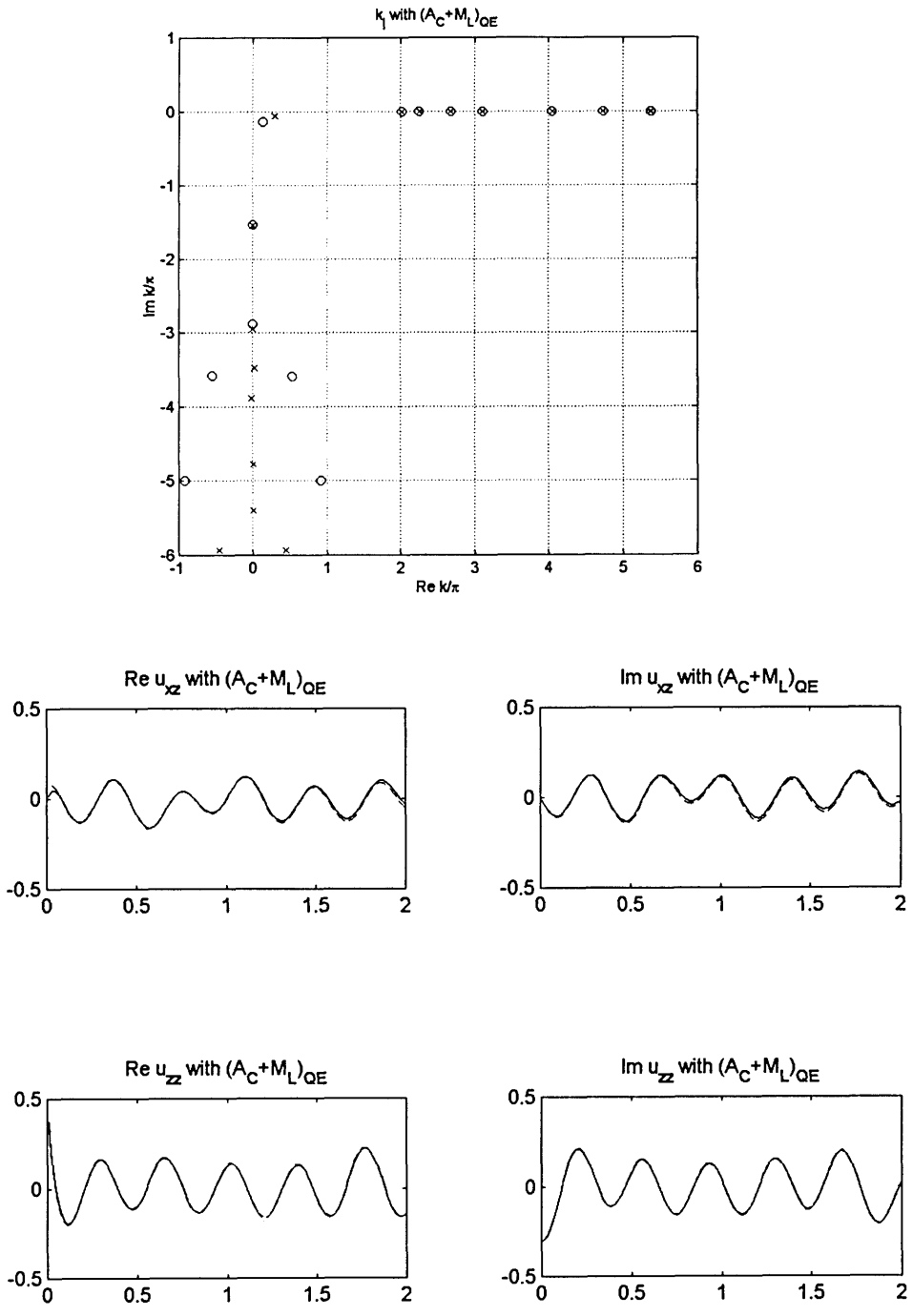

Figure 3.2.12 Harmonic wave motion obtained with TLM2 of α=β=1, μ=0 ($\mathbf{A_C}$+$\mathbf{M_L}$): eigenvalues k_j and surface displacements u_{xz}, u_{zz} for homogeneous plate subjected to *SV-P* surface line load of f_{ex}=2.50 in vertical direction (×:TLM2 k_j; o: Exact k_j; solid curve: TLM2 u_{xz}, u_{zz}; dashed curve: Exact u_{xz}, u_{zz})

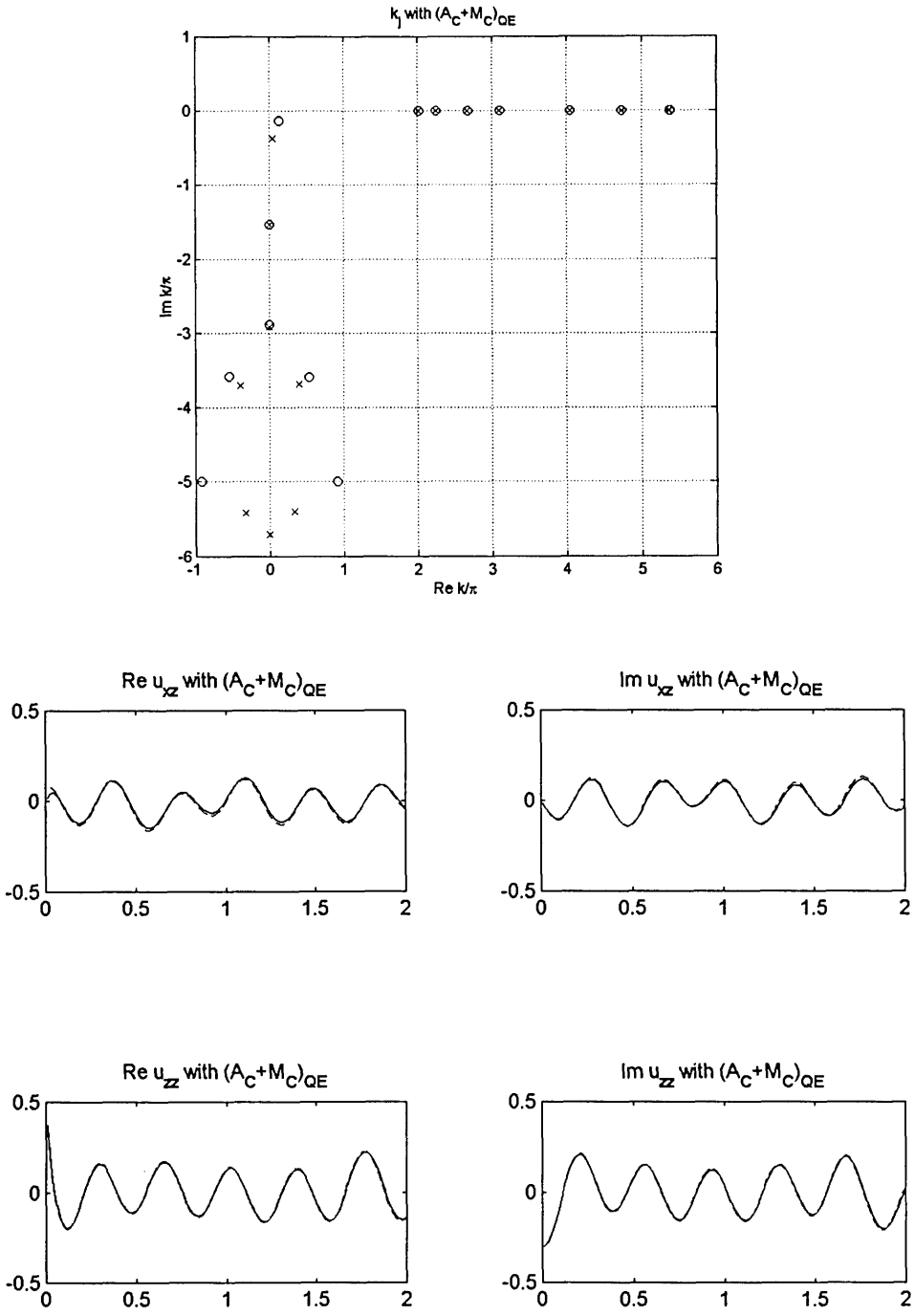

Figure 3.2.13 Harmonic wave motion obtained with TLM2 of $\alpha=\beta=\mu=1$ (A_C+M_C): eigenvalues k_j and surface displacements u_{xz}, u_{zz} for homogeneous plate subjected to *SV-P* surface line load of $f_{ex}=2.50$ in vertical direction (×:TLM2 k_j; o: Exact k_j; solid curve: TLM2 u_{xz}, u_{zz}; dashed curve: Exact u_{xz}, u_{zz})

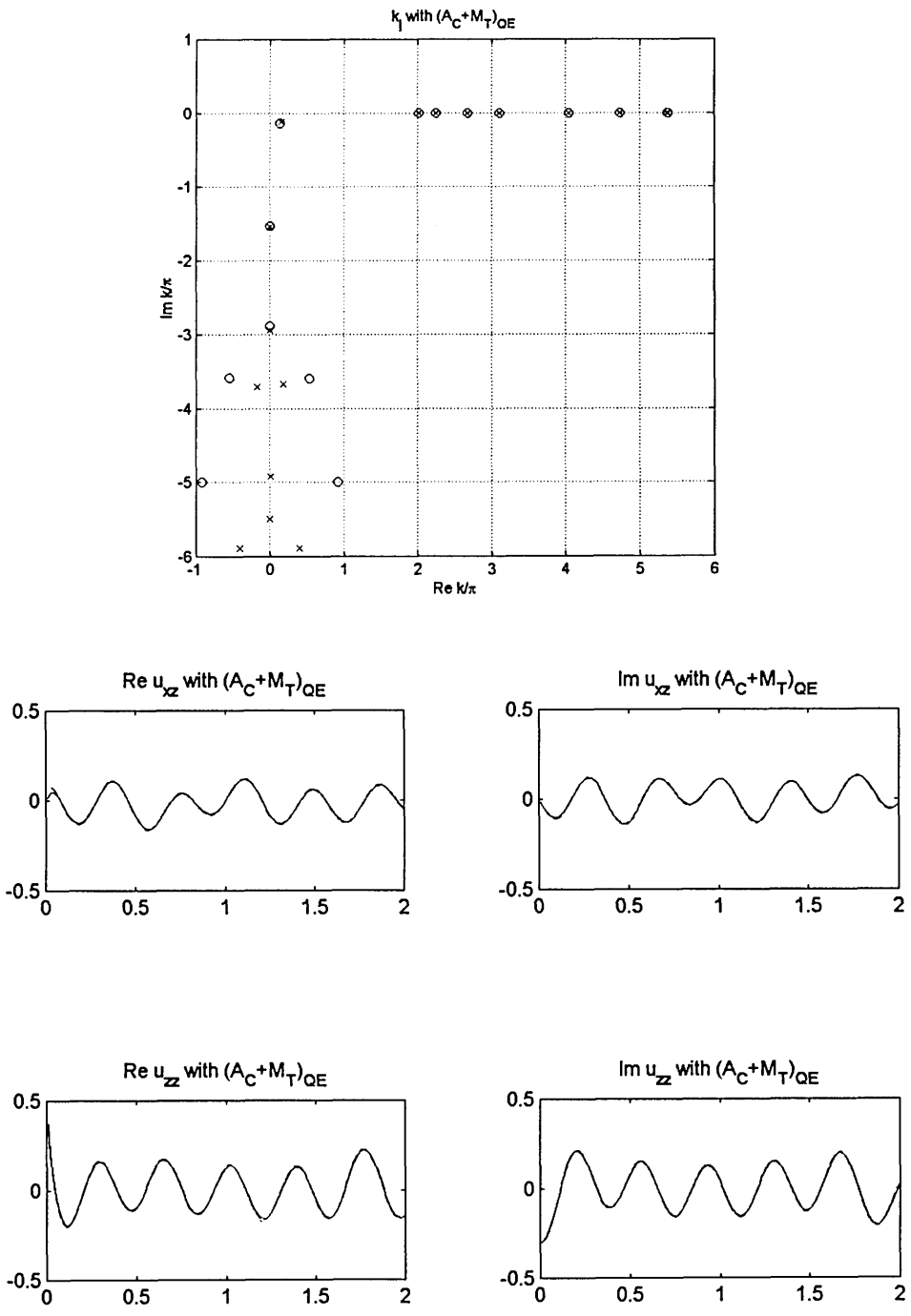

Figure 3.2.14 Harmonic wave motion obtained with TLM2 of α=β=1, μ=0.33 ($\mathbf{A_C}$+$\mathbf{M_T}$): eigenvalues k_j and surface displacements u_{xz}, u_{zz} for homogeneous plate subjected to *SV-P* surface line load of f_{ex}=2.50 in vertical direction (×:TLM2 k_j; o: Exact k_j; solid curve: TLM2 u_{xz}, u_{zz}; dashed curve: Exact u_{xz}, u_{zz})

Figures for section 3.3

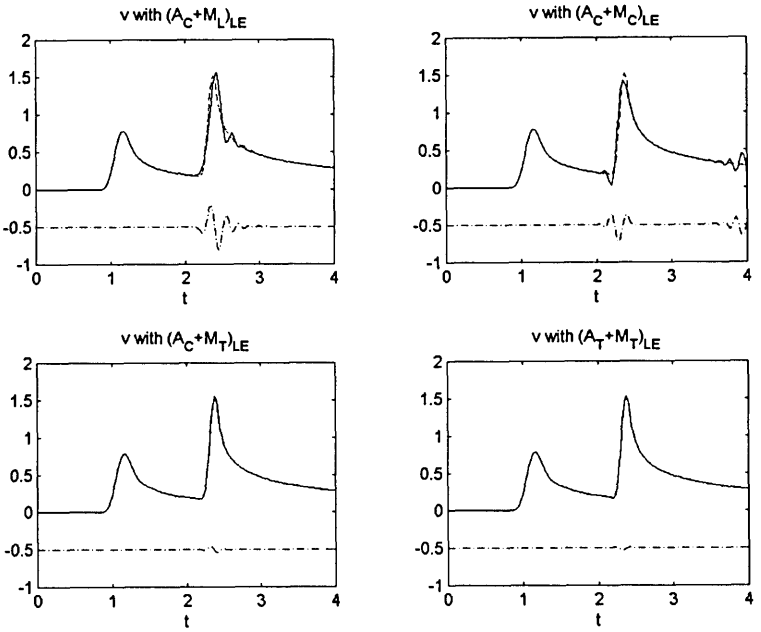

Figure 3.3.1 Surface seismograms of v at x=1.0 in homogeneous plate obtained with TLM1 of β=1, μ=0 ($\mathbf{A_C+M_L}$); β=1, μ=1 ($\mathbf{A_C+M_C}$); β=1, μ=0.55 ($\mathbf{A_C+M_T}$); β=0.55, μ=0.55 ($\mathbf{A_T+M_T}$), for *SH* surface line load of $a=t_d$=0.2. (solid curve: TLM1 v; dashed curve: Exact v)

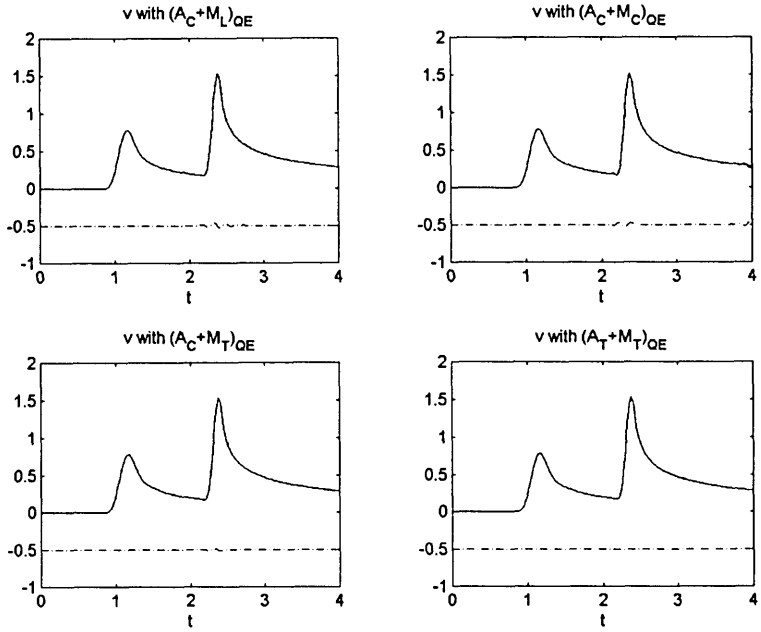

Figure 3.3.2 Surface seismograms of v at x=1.0 in homogeneous plate obtained with TLM2 of β=1, μ=0 ($\mathbf{A_C+M_L}$); β=1, μ=1 ($\mathbf{A_C+M_C}$); β=1, μ=0.33 ($\mathbf{A_C+M_T}$); β=0.33, μ=0.33 ($\mathbf{A_T+M_T}$), for *SH* surface line load of $a=t_d$=0.2. (solid curve: TLM2 v; dashed curve: Exact v)

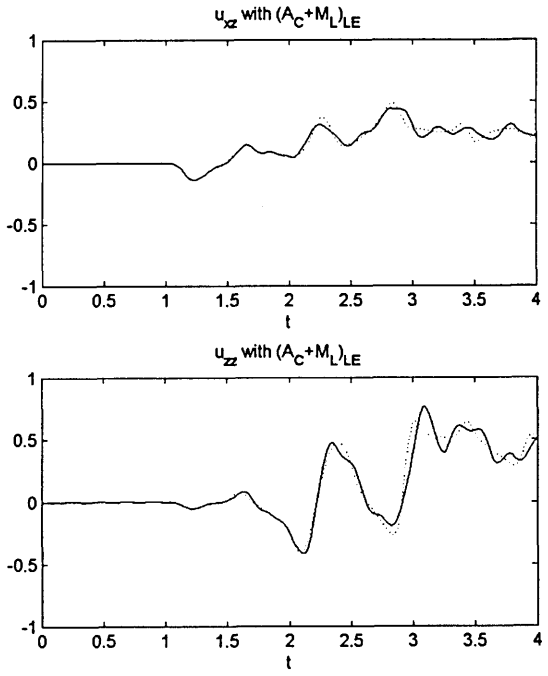

Figure 3.3.3 Surface seismograms of u_{xz}, u_{zz} at x=1.0 in homogeneous plate obtained with TLM1 of α=β=1, μ=0 ($\mathbf{A_C}$+$\mathbf{M_L}$), for *SV-P* surface line load of a=t_d=0.2 in vertical direction. (solid curve: TLM1 u_{xz}, u_{zz}; dashed curve: Exact u_{xz}, u_{zz})

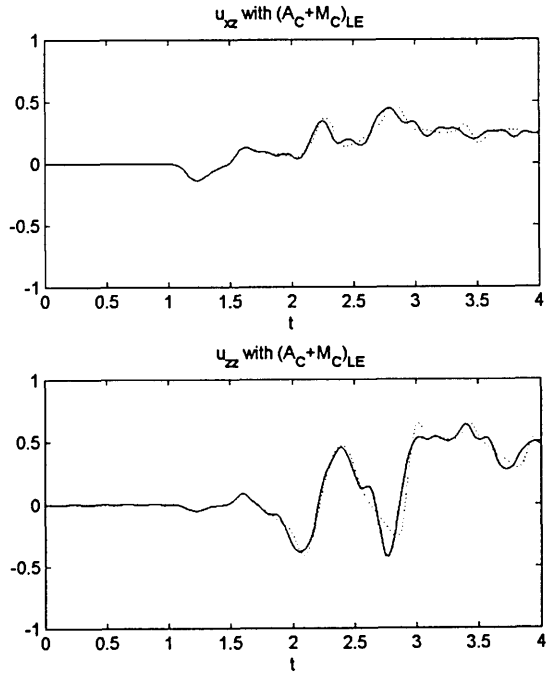

Figure 3.3.4 Surface seismograms of u_{xz}, u_{zz} at x=1.0 in homogeneous plate obtained with TLM1 of α=β=1, μ=1 ($\mathbf{A_C}$+$\mathbf{M_C}$) , for *SV-P* surface line load of a=t_d=0.2 in vertical direction. (solid curve: TLM1 u_{xz}, u_{zz}; dashed curve: Exact u_{xz}, u_{zz})

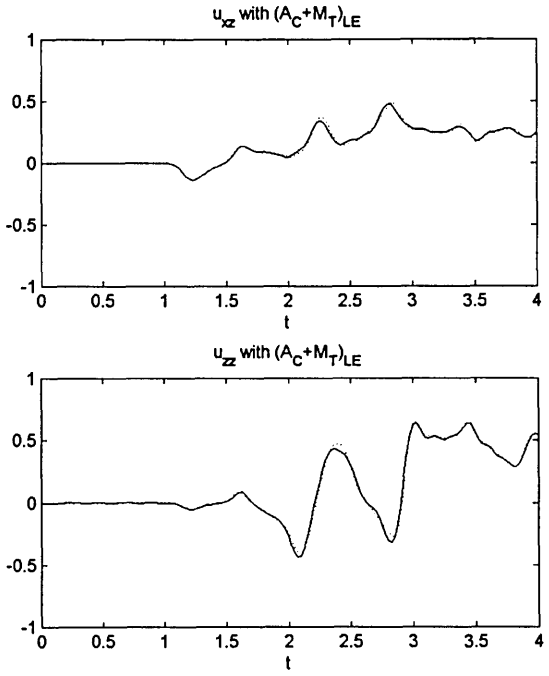

Figure 3.3.5 Surface seismograms of u_{xz}, u_{zz} at x=1.0 in homogeneous plate obtained with TLM1 of α=β=1, μ=0.55 ($\mathbf{A_C}$+$\mathbf{M_T}$) , for *SV-P* surface line load of a=t_d=0.2 in vertical direction. (solid curve: TLM1 u_{xz}, u_{zz}; dashed curve: Exact u_{xz}, u_{zz})

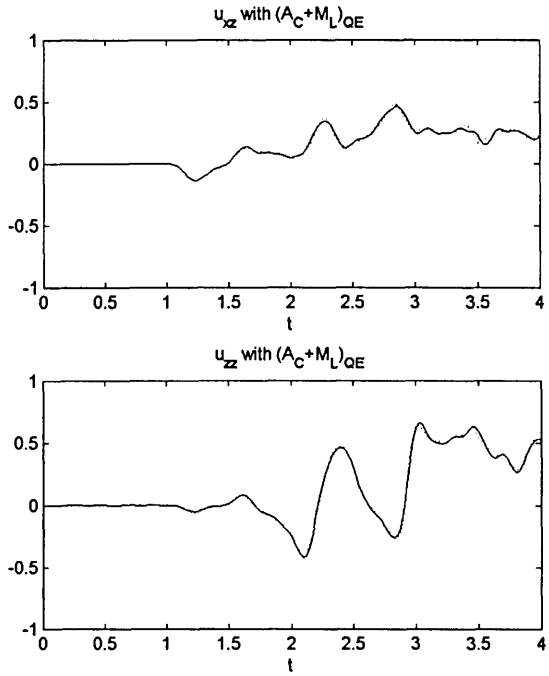

Figure 3.3.6 Surface seismograms of u_{xz}, u_{zz} at x=1.0 in homogeneous plate obtained with TLM2 of α=β=1, μ=0 ($\mathbf{A_C}$+$\mathbf{M_L}$), for *SV-P* surface line load of a=t_d=0.2 in vertical direction. (solid curve: TLM2 u_{xz}, u_{zz}; dashed curve: Exact u_{xz}, u_{zz})

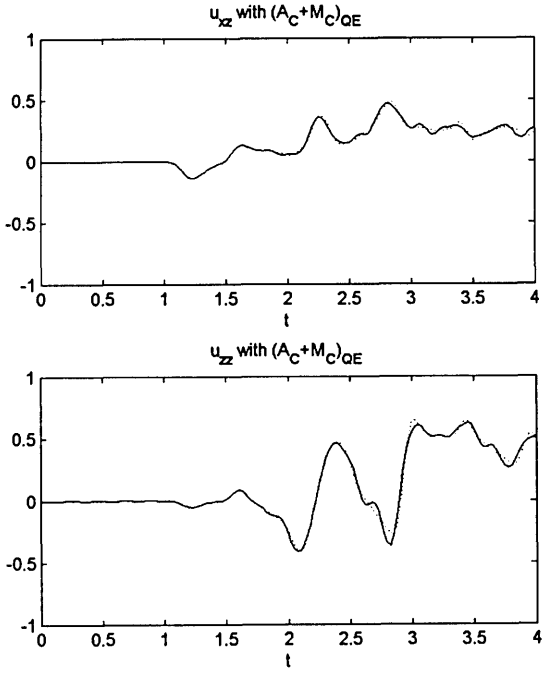

Figure 3.3.7 Surface seismograms of u_{xz}, u_{zz} at x=1.0 in homogeneous plate obtained with TLM2 of α=β=1, μ=1 ($\mathbf{A_C}$+$\mathbf{M_C}$), for *SV-P* surface line load of a=t_d=0.2 in vertical direction. (solid curve: TLM2 u_{xz}, u_{zz}; dashed curve: Exact u_{xz}, u_{zz})

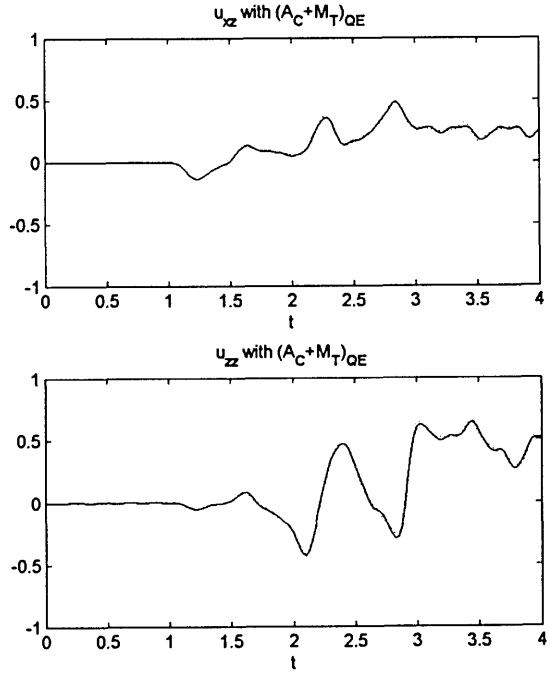

Figure 3.3.8 Surface seismograms of u_{xz}, u_{zz} at x=1.0 in homogeneous plate obtained with TLM2 of α=β=1, μ=0.33 ($\mathbf{A_C}$+$\mathbf{M_T}$) , for *SV-P* surface line load of a=t_d=0.2 in vertical direction. (solid curve: TLM2 u_{xz}, u_{zz}; dashed curve: Exact u_{xz}, u_{zz})

Chapter 4 Convergence and accuracy of the modal solutions

In this chapter, we study the convergence and accuracy of the modal solutions obtained with the TLM. A converged modal solution means a solution that describes wave motion of systems of interest by means of a sufficient number of modes, without any loss of input energy generated by external sources. The accuracy of the TLM modal solutions can be estimated by comparison with known exact analytical solutions. Since the TLM is a semi-discrete numerical technique, its convergence and accuracy are intimately related to the discretization scheme, i.e. the number of thin-layers, which is also directly associated with the number of modes included into modal summations. Ideally, the infinite number of thin-layers could yield the converged and accurate responses. From the practical point of view, however, we need a reasonable discretization scheme so as to calculate numerical solutions both accurately and efficiently.

To assess the convergence and accuracy of the TLM modal solutions, we choose relatively simple examples whose exact analytical solutions are known in closed form and/or in terms of exact modal superposition. The examples are isotropic homogenous plates and strata subjected to *SH* and *SV-P* wave motion. Their exact analytical solutions are derived and illustrated in the appendices 4A, 4B, and 4C.

As shown in chapter 1, there are two formulations of the TLM's, i.e., the TLM formulated in the frequency domain, and the TLM formulated in the time domain. For short, we call herein the former as the ω-TLM and the latter as the t-TLM. These two formulations have different calculation procedures, i.e. different types of eigenvalue problems, and so are the features of their modal solutions. However, there are some common aspects between the two formulations as well. So, in section 4.1, we explore the common aspects of the two formulations by briefly overviewing the TLM analysis procedure of calculating the modal solutions. In section 4.2, we characterize and assess in more detail the convergence and accuracy of the ω-TLM modal solutions. First, we investigate various aspects of the ω-TLM modal solutions in terms of the displacement response of a homogeneous stratum subjected to *SH* harmonic line loads. Secondly, we assess the accuracy of the ω-TLM in terms of both the displacement and stress response by analyzing three simple examples such as a homogeneous stratum and plate subjected to *SH* and *SV-P* harmonic line loads. In section 4.3, we characterize and assess in more detail the convergence and accuracy of the t-TLM modal solutions. First, we investigate various aspects of the t-TLM modal solutions in terms of the displacement response of a homogeneous plate subjected to *SH* transient line loads. Secondly, we assess the accuracy of the t-TLM in terms of both the displacement and stress response by analyzing three simple examples such as a homogeneous stratum and plate subjected to *SH* and *SV-P* transient line loads.

4.1 Overview of TLM modal solutions

We briefly overview here the TLM analysis procedure of calculating the modal solutions, which is composed of four steps, as will be shown in the following four paragraphs. Based on this overview, we point out two aspects of convergence and accuracy of the TLM modal solution, which are basically related to the spatial and temporal characteristics of external sources and receivers. The two aspects can be easily observed just by examining the analysis procedure and the TLM modal solutions.

The first step in the TLM analysis is to determine the spatial and temporal characteristics of a given source $\mathbf{P}(x,z,t)$ by means of its spectra in both the wavenumber (k) and frequency (ω) domain. Inspection of the source spectrum in the wavenumber domain reveals the significant wavenumber range of $k_{min} \le k \le k_{max}$ that contributes the most to the modal solutions. As a consequence, the lower and upper limits of the wavenumber integration in the t-TLM can be taken as k_{min} and k_{max}, respectively, instead of $-\infty$ and $+\infty$. On the other hand, inspection of the source spectrum in the frequency domain provides the significant range of ω, i.e. $\omega_{min} \le \omega \le \omega_{max}$ whose spectral components have major contribution to the modal solutions. According to ω_{max}, the minimum wavelength λ_{min} is then given as $2\pi C/\omega_{max}$ or C/f_{max} where C is the shear wave speed of each layer, and f_{max} is the maximum frequency (in Hz) having a relationship with the maximum angular frequency as $\omega_{max}=2\pi f_{max}$.

The second step consists in determining the discretization size h for each layer and constructing the dynamics stiffness matrix $\mathbf{K}_{dyn}$ for a whole system of interest. The discretization size h for each layer is determined of the form.

$$h \le \frac{\lambda_{min}}{N_\lambda} \tag{4.1.1}$$

where N_λ is the number of thin-layers per wavelength. Remember that the proposed N_λ in chapter 2 is

$$N_\lambda = 4 \qquad \text{for the TLM1} \tag{4.1.2}$$

$$N_\lambda = 2 \qquad \text{for the TLM2} \tag{4.1.3}$$

However, it should be noted that proper N_λ must be chosen according to required accuracy and problems of interest.

The third step is to solve eigenvalue problems for the constructed dynamic stiffness matrix $\mathbf{K}_{dyn}$ to obtain the propagation modes in terms of eigenvalues (k_j or ω_j) and mode shapes (ϕ_j).

The fourth step that is the final step is to calculate the modal solutions in the following form of modal expansion or series.

$$\tilde{\mathbf{U}}(x,\omega) = \sum_{j=1}^{M} \phi_j \tilde{f}_j(x,\omega) \qquad \text{for the } \omega\text{-TLM} \tag{4.1.4}$$

$$\mathbf{U}(x,t) = \frac{1}{2\pi}\int_{k_{min}}^{k_{max}} \hat{\mathbf{U}}(k,t)e^{-ikx}dk = \frac{1}{2\pi}\int_{k_{min}}^{k_{max}} \left[\sum_{j=1}^{M} \phi_j \hat{q}_j(k,t)\right] e^{-ikx}dk \qquad \text{for the } t\text{-TLM} \tag{4.1.5}$$

where $\tilde{\mathbf{U}} = \tilde{\mathbf{U}}(x,\omega)$ and $\hat{\mathbf{U}} = \hat{\mathbf{U}}(k,t)$ are the displacement vectors in the ω-TLM and the t-TLM, respectively, M is the total number of the modes involved in the modal superposition, and $\tilde{f}_j(x,\omega)$ and $\hat{q}_j(k,t)$ are the modal components or participation factors in the ω-TLM and the t-TLM, respectively.

We consider first the convergence of the TLM modal solution associated with temporal characteristics of external sources. In general, a modal solution to a source of high-frequency content converges more slowly than a modal solution to a source of low-frequency content. The reason is that to calculate accurate responses to high-frequency excitations, it is necessary to include correspondingly high modes into the modal solutions. In other words, the parameter M in equations (4.1.4 and 5) becomes larger. In addition, the computational cost of solving the associated eigenvalue problems increases together with the frequency content. The reason is that as the excitation frequency becomes higher, the corresponding wavelength shortens, which in

turns requires a finer discretization of the media, see equation (4.1.1). Thus, the dynamic stiffness matrix to be solved increases in size.

Next, we briefly consider the convergence and accuracy concerned with both of the spatial and temporal characteristics of receivers. In general, the convergence and accuracy associated with receivers are related to singularities and discontinuities in wave motion. Since the responses in the TLM are provided in series form (i.e. modal superposition), the convergence near the singularities and discontinuities is very slow and the accuracy is very sensitive as well. In the ω-TLM, the singularities occur simply near to sources, i.e. $x \approx 0$. So, the convergence and accuracy of the ω-TLM are dependent on only the spatial characteristic of the receivers. On the other hand, the singularities are complicated in the t-TLM, because the singularities exist near the wave fronts as well as in the vicinity of sources. Therefore, the convergence and accuracy of the t-TLM depend on both the spatial and temporal characteristics of the receivers.

In sections 4.2 and 4.3, we discuss in more detail not only the above two aspects, but also other features, by means of numerical and practical examples. In addition, we determine the required number of thin-layers per wavelength N_λ needed to calculate accurately modal solutions not only for displacements, but also for nodal stresses and loads.

4.2 TLM in the ω-domain: ω-TLM

We characterize and assess here in more detail the convergence and accuracy of the ω-TLM modal solutions. For this purpose, we begin by investigating various aspects of displacement responses of a homogeneous stratum subjected to *SH* line loads. From this investigation, we determine the number of thin-layers per wavelength N_λ needed to accurately calculate the modal responses with the ω-TLM. Thereafter, we assess the accuracy of the ω-TLM in terms of both the displacement and stress responses by analyzing three simple examples for a homogeneous stratum and plate subjected to *SH* and *SV-P* harmonic line loads.

We consider both the TLM1 and TLM2 in this section. Concerning the tuning factors, we apply the optimal values determined in chapter 2. A summary of the optimal values is as follows:

the TLM1 for *SH* wave problems : $\beta=\mu=0.55$
the TLM2 for *SH* wave problems : $\beta=\mu=0.33$
the TLM1 for *SV-P* wave problems : $\alpha=\beta=1.0$ and $\mu=0.55$
the TLM2 for *SV-P* wave problems : $\alpha=\beta=1.0$ and $\mu=0.33$

4.2.1 Characterization of the modal solution

We estimate the convergence and accuracy of the modal solutions in the ω-TLM by means of a simple problem involving *SH* waves. In a nutshell, we investigate the convergence and accuracy in terms of the spatial and temporal characteristics of the sources, the spatial and temporal characteristics of the receivers, and the dispersion characteristics found in chapter 2. From this investigation, we reveal a variety of important aspects of the modal solutions in the ω-TLM.

The simple problem analyzed here concerns the response of a homogeneous stratum subjected to an *SH* surface line load as shown in figure 4.2.1. The mass density, the shear velocity, and the

thickness (or depth) of the stratum are all taken as unity, i.e. $\rho=C_S=H=1$, while the damping ratio ξ_d is 0.001. The *SH* line load p is given of the form

$$p = p_y(x,z,t) = \delta(x)\delta(z)e^{i\omega_{ex}t} \tag{4.2.1}$$

where ω_{ex} is the excitation frequency representing temporal characteristics of the external source p. Following the four analysis steps explained in section 4.1, we solve an eigenvalue problem of the form.

$$\mathbf{K}_{dyn}\boldsymbol{\phi}_j = \left[\mathbf{A}k_j^2 + \mathbf{G} - \mathbf{M}\omega_{ex}^2\right]\boldsymbol{\phi}_j = \mathbf{0} \tag{4.2.2}$$

The displacement response in the x-ω domain is then given as

$$\tilde{v}^{mn}(x,\omega_{in}) = \sum_{j=1}^{M}\phi_j^m\tilde{f}_j = \sum_{j=1}^{M}\phi_j^m\phi_j^n\frac{e^{-ik_j|x|}}{2ik_j} \tag{4.2.3}$$

where $\tilde{v}^{mn}$ is the displacement at elevation m due to a load at elevation n, and M is the total number of modes involved in the modal superposition. If all computed modes are included in the calculation, then M is given for the present problem as

$$M = N \qquad \text{for the TLM1} \tag{4.2.4}$$

$$M = 2N \qquad \text{for the TLM2} \tag{4.2.5}$$

where N is the total number of thin-layers used in analysis. In general, however, it is not necessary to include all the computed modes into the modal solution because the evanescent modes with imaginary and complex eigenvalues k_j do not contribute significantly to the final results in the far-field, as will be seen in this section.

To determine the convergence and accuracy characteristics, we compare the modal solutions of the ω-TLM with the exact analytical solutions. The exact analytical solutions to this stratum are presented in appendices 4A and 4B of this chapter, where they are derived by means of the image source method and the continuous modal solution, respectively. Figure 4.2.2 displays the dispersion curves of this stratum obtained with the exact analytical eigenvalue problem.

(A) Sources

Here, we consider the effect of the characteristics of sources on the convergence and accuracy of the modal solutions in the ω-TLM. First of all, we consider the effect of temporal characteristics of sources on convergence. Secondly, we consider the effect of temporal characteristics of sources on accuracy. Thirdly, we consider the effects of spatial characteristics of sources on convergence. Finally, we estimate the accuracy of the modal solutions in connection with the temporal characteristics of sources and the number of thin-layers per wavelength.

We begin with the effect of temporal characteristics of sources, i.e. ω_{ex}, on the convergence of the ω-TLM modal solutions. As we have already observed in section 4.1, the modal solution to a source of high-frequency content converges more slowly than the modal solution to a source of low-frequency content. For example, consider a stratum excited at two different frequencies ω_1 and ω_2 where $\omega_1>\omega_2$. To calculate the responses to the high-frequency excitation, it is necessary to include the corresponding high propagation modes into the modal solutions. Therefore, the modal solution due to the high frequency ω_1 converges more slowly than the modal solution due to the low frequency ω_2.

Next, we consider the effect of temporal characteristics of sources, i.e. ω_{ex}, on the accuracy of the ω-TLM modal solutions. At some frequencies of excitation, there exists a very special mode

whose eigenvalue k_o is nearly zero in absolute value, i.e. $|k_o| \approx 0$. This special mode occurs only when the excitation frequency ω_{ex} is close to the *resonant* (or cutoff) frequency ω_R at which the wave associated with this k_o propagates nearly vertically (i.e. in the direction of the layers). As can be easily recognized in equation (4.2.3), the factor $1/k_o$ then becomes very large in value, so this mode dominates strongly in the modal summation, even when k_o is not the eigenvalue of the first mode of the stratum. Therefore, in the case when $\omega_{ex} \approx \omega_R$, the accuracy of the modal solution is mostly controlled by the accuracy of this o-th mode. Hence, it is necessary to calculate the o-th mode with high accuracy. In addition, if k_o is exactly zero, which constitutes a *double pole*, then equation (4.2.3) is no longer valid. In that case, it is necessary to use $\tilde{v}_o^{mn} = \phi_o^m \phi_o^n x$ instead, the amplitude of which grows linearly with x. This contradiction can be avoided by assuming that the stratum has certain amount of damping, i.e. $\xi_a \neq 0$. Then, theoretically, the associated eigenvalue problem never produces zero eigenvalues.

Next, consider the effects of spatial characteristics of sources on the convergence of the modal solutions. The line load in equation (4.2.1) is a special type whose distribution in space x is that of a δ function, and for which the associated response function in equation (4.2.3) is referred to as a Green's function. There are many practical applications in which the convergence of the response functions to the actual loads may be faster than that for line loads. Since the system of interest is of linear elasticity, superposition of multiple-load effects is always possible by utilizing the modal solution in equation (4.2.3). Therefore, we can calculate the responses due to any load arbitrarily distributed in the x direction by means of superposition, or equivalently, by integration. Consider, for example, a strip load of unit amplitude applied over a certain range $-a<x<a$ where a is half the width of the strip load. The response (for $x>a$) can be obtained by integrating the modal solution in equation (4.2.3) via convolution over the strip load as follows.

$$\tilde{v}_{strip}^{mn} = \int_{-a}^{a} \tilde{v}^{mn}(x-\xi) p_{strip}(\xi) d\xi = \int_{-a}^{a} \sum_{j=1}^{M} \phi_j^m \phi_j^n \frac{e^{-ik_j|x-\xi|}}{2ik_j} d\xi$$

$$= \sum_{j=1}^{M} \phi_j^m \phi_j^n \int_{-a}^{a} \frac{e^{-ik_j|x-\xi|}}{2ik_j} d\xi = \sum_{j=1}^{M} \phi_j^m \phi_j^n \frac{e^{-ik_j x}}{-2k_j^2} [e^{ik_j a} - e^{ik_j(-a)}]$$

$$= \sum_{j=1}^{M} \phi_j^m \phi_j^n \frac{e^{-ik_j x}}{ik_j^2} \sin k_j a \qquad (4.2.6)$$

Observe that the convergence is now faster than for line loads, because the solution contains the factor $1/k_j^2$ rather than $1/k_j$ as in equation (4.2.3).

Next, we estimate the accuracy of the modal solutions in connection with not only the temporal characteristics of the sources ω_{ex}, but also the number of thin-layers per wavelength N_λ. For this purpose, we calculate the displacement at a point $(x,z) = (1, 0)$ due to a line load applied on the surface while changing both ω_{ex} and N_λ. We obtain the numerical results by means of both of the ω-TLM and the exact analytical modal solution and then compare the two results. From this analysis, we propose the proper N_λ with which the accurate modal solutions can be obtained.

Figures 4.2.3a,b display the logarithm of the amplitudes and the phase angles Θ (in radians) of the displacements obtained with the TLM1 and the TLM2, respectively. Each of the sharp peaks in the plots for displacements corresponds to the resonant frequencies. Four different N_λ's are considered for the analysis, namely N_λ=2,4,8,12 for the TLM1 and N_λ=1,2,4,6 for the TLM2. In addition, for each N_λ, the displacement is calculated in the range of frequencies f_{ex} from 0 to 2 Hz. In each plot the result of the ω-TLM (solid line) is compared with that of the exact analytical

modal solution (dashed line). To avoid the singularity at the resonant frequency, a damping ratio ξ_d=0.001 is used in analysis.

Figure 4.2.3a shows the results obtained with the TLM1. The TLM1 with N_λ=2 yields acceptable results only for relatively low frequencies, i.e. f_{ex}<0.5, while with N_λ=4, it provides acceptable results for all the frequencies of interest. The TLM1 with N_λ=8 produces essentially the exact results, although some discrepancies still persist at the resonant frequencies. Finally, the TLM1 with N_λ=12 shows perfect agreement with the exact analytical solution, even at the resonant frequencies. In the light of these results, we propose the discretization criterion N_λ=12 to calculate accurate displacements with the TLM1.

Figure 4.2.3b shows the results obtained with the TLM2. The TLM2 with N_λ=1 yields the correct results only for relatively low frequencies, i.e. f_{ex}<0.6, while N_λ=2 provides acceptable results for all the frequencies of interest. The TLM2 with N_λ=4 yields virtually perfect results, so that an additional refinement to N_λ =6 doesn't reveal any further improvements. Thus, we propose the use of N_λ=4 to calculate accurate displacements with the TLM2.

(B) Receivers

Here, we consider the effect of the characteristics of receivers on the convergence and accuracy of the modal solutions in the ω-TLM. Since we are concerned with the ω-TLM, we consider only the spatial characteristics of receivers. Then, we distinguish between propagating and non-propagating modes depending on the type of eigenvalue k_j. Finally, we establish a criterion to distinguish the near- and far-field solutions for a given evanescent mode of the form k_j=$-i\eta_j$.

As discussed in section 4.1, the spatial characteristics of receivers have significant effect on the convergence and accuracy of the modal solutions with the ω-TLM. In other words, the convergence and accuracy of the modal solutions in the ω-TLM are dependent on the distance between the external sources and the receivers, namely the near-field and far-field solutions. In general, the near-field solution converges slowly. The reason is that the high evanescent (i.e. non-propagating) modes in equation (4.2.3) contribute strongly to the wave field in the immediate vicinity of the source, so a large number of modes is necessary. It follows that the accuracy of the near-field solution is sensitive to the degree of numerical error of these non-propagating modes. On the other hand, the far-field solution converges relatively fast, because only the propagating modes (which for any given frequency are finite in number) have major contribution to the modal solutions, and in addition no singularities are involved in the wave motion. Therefore, the accuracy of the far-field solution depends only on the accuracy of the propagating modes, and is nearly independent of any numerical error in the evanescent modes.

Consider an example to illustrate the effect of the spatial characteristics of receivers on the convergence and accuracy of the modal solutions in the ω-TLM. The example involves the displacement on the surface of a stratum in the range 0<x<1 caused by a line load with f_{ex}=4.5 Hz applied on the surface. The associated propagating modes are the first 9 modes shown in the dispersion curves of figure 4.2.2. The displacement is obtained with both of the TLM1 with N_λ=12 and the TLM2 with N_λ=4. In both the cases, the total number of thin-layers N is 54, and the total number of computed modes is also 54. In addition, the modal solutions are calculated for various M (=the number of modes included in modal summation), namely 8, 9, 10, and 54.

Figures 4.2.4a and b display the numerical results (solid line) obtained with the TLM1 and the TLM2, respectively, in comparison with the exact analytical solutions (dashed line) obtained with the image source method. As can be seen, the far-field solutions for $0.3<x$ converge with just 9 or 10 propagation modes, i.e. M=9 or 10, while the near-field solutions for $x<0.3$ converge more slowly, and require a larger number of modes. Notice in the two figures that the responses show sharp variation near the source point, which causes the slow convergence in the near-field solutions.

The propagating and non-propagating modes referred to previously can be distinguished according to the type of eigenvalue k_j. As seen in figure 4.2.2, the eigenvalues k_j can be purely real, purely imaginary, or complex numbers. Therefore, and without any loss of generality, k_j can be expressed as $\xi_j - i\eta_j$ with $0 \le \eta_j$. It follows that the factor $\exp(-ik_j x)/2ik_j$ in equation (4.2.3) for $0 \le x$ can be expressed in one of the following three forms:

$$\text{(A)} \quad \frac{e^{-ik_j x}}{2ik_j} = \frac{e^{-i\xi_j x}}{2i\xi_j} \qquad \text{when } \xi_j \neq 0, \eta_j = 0 \tag{4.2.7}$$

$$\text{(B)} \quad \frac{e^{-ik_j x}}{2ik_j} = \frac{e^{-\eta_j x}}{2\eta_j} \qquad \text{when } \xi_j = 0, \eta_j \neq 0 \tag{4.2.8}$$

$$\text{(C)} \quad \frac{e^{-ik_j x}}{2ik_j} = \frac{e^{-\eta_j x} e^{-i\xi_j x}}{2(\eta_j + i\xi_j)} \qquad \text{when } \xi_j \neq 0, \eta_j \neq 0 \tag{4.2.9}$$

Case (A) corresponds to a propagating mode, because equation (4.2.7) represents harmonic wave motion in the x direction. Case (B) corresponds to a non-propagating mode, because equation (4.2.8) represents exponentially decaying amplitudes in the x direction. Case (C) corresponds to either a propagating mode or a non-propagating mode, depending on the magnitude of η_j. In the case of a stratum in antiplane motion as being considered herein, these complex eigenvalues arise only when the material has damping, i.e. $\xi_d \neq 0.0$.

Next, we establish a criterion to distinguish the near- and far-field solutions for a given evanescent mode of the form $k_j = -i\eta_j$. First, we assume that the amplitude of all the mode shapes is order of 1, and choose a parameter ε such that $e^{-\varepsilon} \ll 1$. For example, $e^{-3} \approx 0.05$ and $e^{-5} \approx 0.007$. Then, the contributions of all the evanescent modes can be determined according to equation (4.2.8). Disregarding the factor 2 in the denominator, we formulate the following relationship.

$$\frac{e^{-\eta_j x}}{\eta_j} < e^{-\varepsilon} \tag{4.2.10}$$

where $e^{-\varepsilon}$ on the right hand side defines the tolerance. It follows that any mode, say the j^{th}, that satisfies equation (4.2.10) will have very small contribution to the final results. Hence, if these modes are ordered by the magnitude of the imaginary part, it follows that the contribution to the response of all modes higher than the j^{th} is negligible. From equation (4.2.10) and adding a subscript j to x, we arrive at the following criterion.

$$\frac{\varepsilon - \log \eta_j}{\eta_j} < x_j \tag{4.2.11}$$

In this expression, x_j denotes the critical distance that corresponds to η_j. In other words, for a given η_j, we can consider the region $x<x_j$ as the near-field, and $x_j<x$ as the far-field. It also follows that the mode of $k_j = -i\eta_j$ has significant contribution to the former, but negligible contribution to the latter.

(C) Numerical dispersion

In chapter 2, we evaluated the numerical dispersion in the TLM, and found the optimal tuning factors needed for the dynamic stiffness matrix $\mathbf{K}_{dyn}$. With the help of these factors, we were able to minimize the numerical error in the eigenvalues and mode shapes obtained with discrete models. However, despite the tuning factors, some small errors still persist. Here, we explore the effect of these inaccuracies on the final modal responses. For this purpose, a couple of examples are considered, and a remedy is proposed to ameliorate the remaining error.

First, we consider the effect of the dispersion error on the far-field solution. Let $k_{E,j}$ and $k_{D,j}$ be the j-th eigenvalues obtained with the exact and the discrete solutions, respectively. Assume that these two eigenvalues have a small discrepancy ε. Then, we can express $k_{D,j}$ as

$$k_{D,j} = k_{E,j} \pm \varepsilon \tag{4.2.12}$$

If we now substitute $k_{E,j}$ and $k_{D,j}$ into equation (4.2.3) we can write the last factor there as

$$\frac{e^{-ik_{E,j}x}}{2ik_{E,j}} \tag{4.2.13}$$

$$\frac{e^{-ik_{D,j}x}}{2ik_{D,j}} = \frac{e^{-i(k_{E,j}\pm\varepsilon)x}}{2i(k_{E,j}\pm\varepsilon)} = \frac{e^{-ik_{E,j}x}}{2i(k_{E,j}\pm\varepsilon)} e^{\mp i\varepsilon x} \approx \frac{e^{-ik_{E,j}x}}{2ik_{E,j}} e^{\mp i\varepsilon x} \tag{4.2.14}$$

Equation (4.2.14) shows that the amplitude of the discrete solution converges to the exact solution, because $|e^{i\varepsilon x}| \approx 1.0$. However, if x is large, then the factor $e^{i\varepsilon x}$ could lead to significant discrepancies in the phase angles Θ. To demonstrate this observation more explicitly, we consider the same example as figure 4.2.4, except that we now calculate the displacement in the far field, i.e. for $0<x<4.0$. Figures 4.2.5a and b show the numerical results in terms of the amplitude and the phase angle obtained with the TLM1 and the TLM2 (solid line), respectively, and with the exact analytical solution (dashed line). As can be seen, the numerical error in the phase angles increases for larger x. It is also observed that the error of the TLM2 is much smaller than that of the TLM1.

In subsection (A), we considered a special eigenvalue k_o and discussed its significant contribution to the final modal solutions. Since this eigenvalue plays such an important role, any small error associated with k_o deteriorates the final results not only the far-field, but also in the near-field. To overcome this problem, we propose a hybrid method as follows.

Instead of using eigenvalues in the vicinity of k_o such as k_{o-1} and k_o, or k_o and k_{o+1} obtained with the ω-TLM, we make use instead of the exact eigenvalues. For this purpose, a new routine is required that searches for the exact eigenvalues with the continuous model. The associated computational effort is small, because we start the search with the eigenvalues obtained with the ω-TLM as initial guesses, and use the mode shapes obtained with the ω-TLM.

To verify this proposed hybrid method, we consider again the stratum with an excitation frequency f_{in}=4.25 Hz, which coincides with the 9-th resonant frequency. Figures 4.2.6a and b show the results from the conventional TLM1 and TLM2 (solid line), respectively, in comparison with the exact modal superposition (dashed line). It is seen that there are significant errors for both the TLM1 and the TLM2. Figures 4.2.7a and b show the results obtained with the hybrid method (solid line) in comparison with the exact modal superposition (dashed line). It is proved that the proposed hybrid method significantly improves the final results.

4.2.2 *SH* wave problem

We now assess the accuracy of the ω-TLM in the computation of stresses as well as displacements elicited by *SH* waves. For this purpose, we evaluate the consistent nodal loads in vertical planes and the consistent stresses in horizontal planes. For practical purposes, we analyze two simple examples involving a homogeneous stratum and a homogeneous plate subjected to harmonic *SH* line loads. The associated exact analytical solutions are derived and presented in appendix 4B. We compute the responses by means of both the TLM1 and TLM2 with N_λ proposed in section 4.2.1, and then compare them with the exact analytical solutions.

(A) Homogeneous stratum

We explore here the accuracy of the ω-TLM by analyzing a homogeneous stratum subjected to an *SH* line load. The material properties and geometry of the stratum, namely the mass density, the shear wave velocity, and the thickness, are all taken as unity, i.e. $\rho=C_S=H=1.0$. The line load is applied at the top surface and its excitation frequency is $f_{ex}=2.50$, which corresponds to a wavelength $\lambda=C_S/f_{ex}=0.4$. Using the ω-TLM, we compute the displacement $v(x,z,\omega)$, the consistent stress in a horizontal plane $\tau_{zy}(x,z,\omega)$, and the consistent nodal load on a vertical plane $q_y(x,z,\omega)$ for the whole stratum, and compare these with the exact analytical solutions. For this purpose, the consistent nodal load q_y is calculated by means of equation (1.3.45) for both the ω-TLM and the exact analytical solution.

We begin by investigating the accuracy of the TLM1. For the discrete model, we analyze the stratum by means of the TLM1 with $N_\lambda=12$, as proposed in section 4.2.1. Thus, it follows that the total number of thin-layers $N(=H/h=HN_\lambda/\lambda)$ is 30, so the total number of degrees of freedom for the discrete model is 30. Figure 4.2.8 shows the numerical results obtained with the TLM1 (solid line) in comparison with the exact analytical solutions (dashed line). The two plots on the first row present the real and imaginary part of the displacement v. The two plots on the second row present the real and imaginary part of the consistent stress τ_{zy}. The two plots on the third row present the real and imaginary part of the consistent nodal load q_y. Each line in the six plots represents the variation of the responses at interface $i=1,3,5,\ldots,29$ (counted from the top down) and for $0\le x\le 2$. It is observed from figure 4.2.8 that all the three components of v, τ_{zy}, and q_y obtained with the TLM1 using $N_\lambda=12$ are in good agreement with the exact analytical solutions, for the whole domain considered. Therefore, it is proved that the TLM1 with $N_\lambda=12$ provides quite good accuracy for not only the displacement component, but also the internal stress components.

Next, we assess the accuracy of the TLM2. For the discrete model, we analyze the stratum by means of the TLM2 with $N_\lambda=4$ as proposed in section 4.2.1. So, it follows that the total number of thin-layers $N(=H/h=HN_\lambda/\lambda)$ is 10 and the total number of degrees of freedom for the discrete model is 20. Figure 4.2.9 shows the numerical results obtained with the TLM2 (solid line) in comparison with the exact analytical solutions (dashed line). The two plots on the first row present the real and imaginary part of the displacement v. The two plots on the second row present the real and imaginary part of the consistent stress τ_{zy}. The two plots on the third row present the real and imaginary part of the consistent nodal load q_y. Each line in the six plots represents the variation of the responses at interface $i=1,2,3,\ldots,10$ (from the top) and for $0\le x\le 2$. It is observed in figure 4.2.9 that all three fields v, τ_{zy}, and q_y obtained with the TLM2 using $N_\lambda=4$

are in good agreement with the exact analytical solutions throughout the domain of interest. Therefore, it is again verified that the TLM2 with N_λ=4 provides quite good accuracy for not only the displacement component, but also the internal stress components.

(B) Homogeneous plate

Next, we explore the accuracy of the ω-TLM by analyzing a homogeneous plate subjected to an *SH* line load. The material properties and geometry of the stratum are the same as those for the stratum considered previously, i.e. ρ=C_S=H=1.0. An *SH* line load is applied at the top surface with an excitation frequency f_{ex} = 2.25, for which the associated wavelength is λ=C_S/f_{ex} = 0.4445. Using the ω-TLM, we compute the displacement $v(x,z,\omega)$, the consistent stress on horizontal planes $\tau_{zy}(x,z,\omega)$, and the consistent nodal load on vertical planes $q_y(x,z,\omega)$ throughout the plate, and compare these with the exact analytical solutions. It should be noted again that the consistent nodal load q_y is calculated by means of equation (1.3.45).

We begin by investigating the accuracy of the TLM1. For the discrete model, we analyze the plate by means of the TLM1 with N_λ=12 as proposed in section 4.2.1. So, it follows that the total recommended number of thin-layers N(=H/h= HN_λ/λ) is 27. However, we choose N=30 instead to match the stratum case. Then the total number of degrees of freedom for the discrete model is 30 . Figure 4.2.10 shows the numerical results obtained with the TLM1 (solid line) in comparison with the exact analytical solutions (dashed line). The two plots on the first row present the real and imaginary part of the displacement v. The two plots on the second row present the real and imaginary part of the consistent stress τ_{zy}. The two plots on the third row present the real and imaginary part of the consistent nodal load q_y. Each line in the six plots represents the variation of the responses at interfaces i=1,3,5,...,31 (from the top) and for 0≤x≤2. It is observed from figure 4.2.10 that all three field quantities v, τ_{zy}, and q_y obtained with the TLM1 using N_λ=12 are in good agreement with the exact analytical solutions, for the whole domain of interest. Therefore, it is confirmed that the TLM1 with N_λ=12 provides quite good accuracy for not only the displacements, but also for the internal stresses.

Next, we assess the accuracy of the TLM2. For the discrete model, we analyze the plate by means of the TLM2 with N_λ=4 as proposed in section 4.2.1, for which the total recommended number of thin-layers is N=H/h= HN_λ/λ=9. However, N=10 is used for actual calculation, so that the total number of degrees of freedom for the discrete model is 21. Figure 4.2.11 shows the numerical results obtained with the TLM2 (solid line) in comparison with the exact analytical solutions (dashed line). The two plots on the first row present the real and imaginary part of the displacement v. The two plots on the second row present the real and imaginary part of the consistent stress τ_{zy}. The two plots on the third row present the real and imaginary part of the consistent nodal load q_y. Note that each line in the six plots represents the variation of the responses at interface i=1,2,3,...,11 (from the top) and for 0≤x≤2. It is observed in figure 4.2.9 that all the three field quantities v, τ_{zy}, and q_y obtained with the TLM2 using N_λ=4 are in good agreement with the exact analytical solutions, for the whole domain of interest. Therefore, it is confirmed that the TLM2 with N_λ=4 provides quite good accuracy for not only the displacement component, but also the internal stress components.

4.2.3 *SV-P* wave problem

We assess here the accuracy of the ω-TLM for *SV-P* wave problems in terms of both the displacement and stress responses. For practical purposes, we analyze again a homogeneous plate, but this time subjected to *SV-P* harmonic line loads. The associated exact analytical solutions are derived and presented in appendix 4C. The material properties and geometry of the stratum, namely the mass density, the shear wave velocity, and the thickness, are all taken as unity, i.e. $\rho=C_S=H=1.0$. In addition, Poisson's ratio used is $\nu=0.31$ (as in the classical Mindlin plate), and the damping ratio imposed is 0.1%. An *SV-P* line load is applied at the top surface in the vertical direction with an excitation frequency $f_{ex}=2.25$, for which the associated wavelength is $\lambda=C_S/f_{ex}=0.4445$. We are interested in the horizontal and vertical displacements, u and w, the consistent stresses on horizontal planes, τ_{zx} and σ_z, and the consistent nodal loads on vertical planes, q_x and q_z. We compute all responses by means of both the TLM1 and TLM2 with N_λ as proposed in section 4.2.1, and then compare these with the exact analytical solutions. It should be noted that the consistent nodal loads, q_x and q_z, are calculated by means of equation (1.3.75) for both the ω-TLM and the exact analytical solution.

We start by exploring the accuracy of the TLM1 for *SV-P* wave problems. For the discrete model, we analyze the plate by means of the TLM1 with $N_\lambda=12$ as proposed in section 4.2.1, which implies a total number of thin-layers $N=H/h= HN_\lambda/\lambda=27$. For the actual analysis, however, N is chosen to be 30, so the total number of degrees of freedom for the discrete model is 62. Figure 4.2.12a,b show the numerical results obtained with the TLM1 (solid line) in comparison with the exact analytical solutions (dashed line). Figure 4.2.12a display the real and imaginary parts of u, w, τ_{zx}, and figure 4.2.12b show the real and imaginary parts of σ_z, q_x, q_z. Note that each line in the twelve plots represents the variation of the responses at interface $i=1,3,5,\ldots,29$ (from the top) and for $0\le x\le 2$. It is observed from figures 4.2.12a,b that all the six response quantities u, w, τ_{zx}, σ_z, q_x and q_z obtained with the TLM1 using $N_\lambda=12$ are in good agreement with the exact analytical solutions throughout the domain considered. Therefore, it is seen that the TLM1 with $N_\lambda=12$ provides quite good accuracy for the displacement components and the internal stress components, not only for *SH* wave problems, but also for *SV-P* wave problems.

We next assess the accuracy of the TLM2 for *SV-P* wave problems. For the discrete model, we analyze the plate by means of the TLM2 with $N_\lambda=4$ as proposed in section 4.2.1, for which the total number of thin-layers is $N=H/h= HN_\lambda/\lambda=9$. For the actual analysis, however, N is chosen to be 10, so that the total number of degrees of freedom for the discrete model of the plate is 42. Figure 4.2.13a,b show the numerical results obtained with the TLM2 (solid line) in comparison with the exact analytical solutions (dashed line). Figure 4.2.13a display the real and imaginary parts of u, w, τ_{zx}, and figure 4.2.13b shows the real and imaginary parts of σ_z, q_x, q_z. Each line in the twelve plots represents the variation of the responses at interface $i=1,3,5,\ldots,11$ (from the top) and for $0\le x\le 2$. It is observed from figures 4.2.13a,b that all the six components of u, w, τ_{zx}, σ_z, q_x, q_z obtained with the TLM2 using $N_\lambda=4$ are in good agreement with the exact analytical solutions throughout the domain considered. Therefore, it is verified that the TLM2 with $N_\lambda=4$ provides quite good accuracy for the displacement components and the internal stress components, not only for *SH* wave problems, but also for *SV-P* wave problems.

4.3 TLM in the time domain: *t*-TLM

In this section, we characterize and assess in more detail the convergence and accuracy of the *t*-TLM modal solutions. For this purpose, we begin by investigating various aspects of displacement responses of a homogeneous plate subjected to *SH* transient line loads. From this investigation, we determine the number of thin-layers per wavelength N_λ needed to obtain accurate modal responses with the *t*-TLM. Thereafter, we assess the accuracy of the *t*-TLM in terms of both the displacement and stress responses by analyzing three simple examples, namely a homogeneous stratum and plate subjected to *SH* and *SV-P* transient line loads.

We consider both the TLM1 and TLM2 in this section. Concerning the tuning factors, we apply the optimal values determined in chapter 2. A summary of the optimal values is as follows:

TLM1 for *SH* wave problems : $\beta=\mu=0.55$
TLM2 for *SH* wave problems : $\beta=\mu=0.33$
TLM1 for *SV-P* wave problems : $\alpha=\beta=1.0$ and $\mu=0.55$
TLM2 for *SV-P* wave problems : $\alpha=\beta=1.0$ and $\mu=0.33$

4.3.1 Characterization of the modal solution

We assess the convergence and accuracy of the modal solutions in the *t*-TLM by means of a homogeneous plate with shear wave velocity $C_S=1.0$ and thickness $H=1.0$, subjected to *SH* wave motion as shown in figure 4.3.1. This plate problem is one of the simplest examples, through which we investigate the dependence of convergence and accuracy on the spatial and temporal characteristics of sources, the spatial and temporal characteristics of receivers, and the numerical dispersion of the TLM found in chapter 2. From this investigation, we reveal a number of characteristics in the modal solutions with the *t*-TLM.

We calculate displacement responses due to an *SH* line load given as

$$p = p_y(x,z,t) = f(x)\delta(z)h(t) \tag{4.3.1}$$

where $f(x)$ and $h(t)$ are the spatial and temporal variation of the line load, respectively. In particular, the bell-shaped variation in both the space x and time t, so-called *Hanning window*, is considered here, for which $f(x)$ and $h(t)$ are of the form.

$$f(x)=\begin{cases}\dfrac{1}{a}\cos^2\dfrac{\pi}{2a}x & |x|\le a\\ 0 & |x|>a\end{cases} \tag{4.3.2}$$

$$h(t)=\begin{cases}\dfrac{2}{t_d}\sin^2\dfrac{\pi}{t_d}t & 0\le t\le t_d\\ 0 & t<0,\ t_d<t\end{cases} \tag{4.3.3}$$

where a is the half width of the load and t_d is the loading duration.

Following the four analysis steps described in section 4.1, we begin by determining the spatial and temporal characteristics of the applied source p. Based on this characterization, we decide on the thickness of the discrete layers and the practical integration range needed to invert the Fourier transform over wavenumbers k. The Fourier transforms of $f(x)$ and $h(t)$ in equations (4.3.2 and 3) are of the form

$$\hat{f}(k)=\int_{-\infty}^{\infty} f(x)e^{ikx}dx=\frac{\sin ka}{ka[1-(ka/\pi)^2]} \tag{4.3.4}$$

$$\tilde{h}(\omega)=\int_{-\infty}^{\infty} h(t)e^{-i\omega t}dt=\frac{\sin \omega t_d/2}{\omega t_d/2\left[1-\left(\omega t_d/2\pi\right)^2\right]}e^{-i\omega t_d/2} \tag{4.3.5}$$

Figure 4.3.2 shows the spectra of these two functions as well as the dispersion curve of the plate obtained with the exact analytical solution. Clearly, the amplitudes of the loading function are negligible beyond the wavenumber $k_{max}=2\pi/a$ and frequency $\omega_{max}=4\pi/t_d$ (i.e. $f_{max}=2/t_d$). This implies that the load spectrum-components beyond k_{max} and ω_{max} have negligible contribution to the wave motion. Through this section 4.3.1, we set $a=t_d=0.2$ and so $k_{max}=10\pi$ and $\omega_{max}=20\pi$. Then, we assemble the dynamic stiffness matrix $\mathbf{K}_{dyn}$ and solve the associated eigenvalue problem of the form

$$\mathbf{K}_{dyn}\boldsymbol{\phi}_j=\left[\mathbf{A}k^2+\mathbf{G}-\mathbf{M}\omega_j^2\right]\boldsymbol{\phi}_j=\mathbf{0} \tag{4.3.6}$$

The displacement in the k-t domain is then obtained by means of the modal summation

$$\hat{v}^{mn}(k,t)=\sum_{j=1}^{M}\phi_j^m\hat{q}_j=\sum_{j=1}^{M}\phi_j^m\phi_j^n\frac{\sin\omega_j t}{\omega_j} \tag{4.3.7}$$

where $\hat{v}^{mn}$ is the displacement at elevation m due to a load at elevation n, and M is the total number of modes included in the modal summations. In the present problem, M does not exceed

$$M=N+1 \qquad \text{for the TLM1} \tag{4.3.8}$$

$$M=2N+1 \qquad \text{for the TLM2} \tag{4.3.9}$$

where $N=H/h=HN_\lambda/\lambda_{min}$ is the total number of thin-layers. For practical purposes, it is not necessary to include all the computed modes in the modal solution, because in general the high modes do not contribute much to the final results in the far-field, as was the case in the ω-TLM.

In order to obtain the solution in the x-t domain, we perform the inverse Fourier transformation as

$$v^{mn}(x,t)=\frac{1}{2\pi}\int_{-\infty}^{\infty}\hat{v}^{mn}(k,t)e^{-ikx}dk \tag{4.3.10}$$

As shown in the spectra of figure 4.3.2, the amplitudes of the load in the wavenumber domain beyond k_{max} are small enough that they can be ignored. Hence, we replace the preceding integration by

$$v^{mn}(x,t)=\frac{1}{\pi}\int_0^{k_{max}}\hat{v}^{mn}(k,t)\cos kx\,dk \tag{4.3.11}$$

where the inverse Fourier cosine transformation is applied because of the symmetry of the function $\hat{v}^{mn}$ in the present problem. If the function $\hat{v}^{mn}$ were anti-symmetry with respect to k, the inverse Fourier sine transformation would be performed instead,. i.e.

$$v^{mn}(x,t)=\frac{1}{\pi}\int_0^{k_{max}}\hat{v}^{mn}(k,t)\sin kx\,dk \tag{4.3.12}$$

Practically, the wavenumber integration in equations (4.3.10-12) is performed by means of a finite discrete summation, not by an analytical integration (or even the FFT). For instance, instead of calculating equation (4.3.11), we calculate a summation with an interval Δk,

$$v^{mn}(x,t)=\frac{\Delta k}{\pi}\left[\frac{1}{2}\hat{v}^{mn}(k_0,t)+\sum_{i=1}^{M_k}\hat{v}^{mn}(k_i,t)\cos(k_i x)\right] \tag{4.3.13}$$

where $k_i=i\Delta k$ and $M_k=k_{max}/\Delta k$. Kausel [1994] points out that when choosing Δk, it is necessary to avoid the influence of the spatial periodicity of the discrete Fourier series in equation (4.3.13). So, he suggests the use of a criterion of the form

$$\Delta k \le \frac{2\pi}{L} = \frac{2\pi}{x_{max} + C_{max} t_{max} + a} \tag{4.3.14}$$

where x_{max}, C_{max}, t_{max} are the farthest distance, the fastest wave speed, the longest time in calculation, respectively, and L is the spatial periodicity of the load due to the discrete summation.

To estimate the convergence and accuracy, we compare the modal solutions obtained with the discrete t-TLM with the exact analytical solutions, which are derived and presented in appendices 4A and 4B using the image source method and the continuous modal solution, respectively. Figure 4.3.2 displays the dispersion curves of the plate and the spectra of the loading function in equations (4.3.2 and 3).

(A) Sources

Here, we consider the effect of the characteristics of sources on the convergence and accuracy of the modal solutions in the t-TLM, namely the effect of the spatial and temporal characteristics of the sources. Thereafter, we estimate the accuracy of the modal solutions in connection with both the temporal characteristics of the sources and the number of thin-layers per wavelength.

First, we consider the effect of the spatial characteristics of the sources on the convergence of the t-TLM modal solutions. As discussed in section 4.1, the spatial characterization of sources provides the significant wavenumber range k, i.e. $k_{min} \le k \le k_{max}$ that contributes to the modal solutions. Also, it is observed from equation (4.3.13) that a large k_{max} requires a large M_k for discrete summations, because $M_k = k_{max}/\Delta k$ for a fixed Δk. Therefore, the convergence of equation (4.3.13) clearly depends on k_{max}. Hence, it follows from the definition of the function $f(x)$ in equation (4.3.2) that the smaller the load half-width a is, the slower the convergence, because $k_{max} = 2\pi/a$ and $M_k = k_{max}/\Delta k$.

Next, consider the effect of the temporal characteristics of the sources on the convergence of the t-TLM modal solutions. As already pointed out in section 4.1, a modal solution to a source of high-frequency content converges more slowly than a modal solution to a source of low-frequency content. Hence, in connection with the function $h(t)$ in equation (4.3.3), it is inferred that a modal solution associated with smaller t_d converges more slowly than that associated with larger t_d, because of $\omega_{max} = 4\pi/t_d$.

Finally, we consider the accuracy of the t-TLM modal solution as a function of the number of thin-layers per wavelength N_λ. Recall from section 4.1 that this N_λ plays an important role in determining the discretization size in connection with the temporal characteristics of external sources, i.e. ω_{max} as shown in equation (4.1.1). For this purpose, we calculate the displacement seismogram v of the plate at $(x,z)=(1,0)$ due to a transient line load with $a=t_d=0.2$ as a function of N_λ. We perform the numerical analysis by means of both of the t-TLM and the exact analytical modal solution and then compare the two results. From this analysis, we propose the proper N_λ with which accurate modal solutions can be obtained.

Figures 4.3.3 displays the displacement seismogram v of the plate at $(x,z)=(1,0)$ for $0 \le t \le 5$, obtained with the TLM1 on the left column, and the TLM2 on the right column. Each sharp peak in the plots corresponds to the arrival of a wave-front . For the analyses with the TLM1 and TLM2, four different N_λ's are considered, namely $N_\lambda=2,4,8,12$ and $N_\lambda=1,2,4,6$, respectively. In

each plot that, the result of the t-TLM (solid line) is compared with that of the exact analytical modal solution (dashed line).

As can be seen in figure 4.3.3, the use of N_λ=2 for the TLM1 and N_λ=1 for the TLM2 produces significant errors in the seismograms, except for the direct wave arrivals involving no reflection. In the case of N_λ=4 for the TLM1 and N_λ=2 for the TLM2, the results are acceptable and exhibit little error. The inaccuracies can be seen near the arrivals of the second and third peaks corresponding to wave fronts for multiply reflected waves. It is believed that this error is caused by the numerical dispersion of the higher modes in the discrete models, as will be seen in subsection (C). On the other hand, the use of N_λ=8 for the TLM1 and N_λ=4 for the TLM2 shows an almost perfect agreement with the exact analytical solution. In addition, notice that the results obtained with N_λ=12 for the TLM1 and N_λ=6 for the TLM2 are virtually identical to those obtained with N_λ=8 for the TLM1 and N_λ=4 for the TLM2. Hence, we propose the use of N_λ=8 for the TLM1 and N_λ=4 for the TLM2 for calculating accurate displacement with the t-TLM.

(B) Receivers

The convergence and accuracy of the t-TLM are considered in connection with the spatial and temporal characteristics of the receivers. As discussed in section 4.1, the convergence and accuracy of the modal solutions depend on the existence of singularities in wave motion of interest. Since the final response of the t-TLM is provided in the x-t domain, there are two types of singularities, i.e. spatial and temporal singularities. The former occurs only near to the source point, as was the case of the ω-TLM, while the latter takes place at the arrivals of multi-reflection waves. The two singularities require the inclusion of many high modes in the modal summations, as a result of which the convergence is very slow. In addition, it is expected that the numerical dispersion error involved in the high modes computed with the t-TLM deteriorates the accuracy of the final response.

First, we investigate the convergence with the spatial characteristics of the receivers. For this purpose, we calculate displacement snap-shots at t=1.85 along the surface ($0 \le x \le 4.0$) due to a surface line load with $a=t_d$=0.2, and vary the number of modes included into modal summations, namely M=8, 12, 16, and 20. The results are then compared with the exact analytical modal solution using a sufficient number of modes. For the discrete models, N_λ=8 and N_λ=4 are used for the TLM1 and the TLM2, respectively.

Figure 4.3.4 shows the convergence of the modal solutions obtained with the TLM1 and TLM2 (solid line) in comparison with the converged solution obtained with the exact analytical modal superposition (dashed line). As can be seen, the near field solutions converge slowly, while the far field solutions converge very fast with even only 8 modes being included. Therefore, it is confirmed that the singularity near the source point decreases the speed in convergence.

Next, we consider the convergence with the temporal characteristics of the receivers. For this purpose, we again calculate the seismograms at (x,z)=(1.0,0.0) due to a surface line load with $a=t_d$=0.2 for $0 \le t \le 5$, and M=8, 12, 16, and 20. The results are then compared with the converged solution obtained with the exact analytical modal superposition. For the discrete models, N_λ=8 and N_λ=4 are applied for the TLM1 and the TLM2, respectively.

Figure 4.3.5 displays the convergence of the seismograms at (x,z)=(1,0) calculated by means of the TLM1 with N_λ=8 and the TLM2 with N_λ=4 (solid line) in comparison with the converged

solution obtained with the exact analytical modal superposition (dashed line). It is clearly seen that the convergence is slow near the second and third sharp peaks that correspond to the wavefronts of the reflected waves. In addition, the third peak converges more slowly than the second one. The reason is that the third peak experiences more reflections along its propagation path than the second one. Therefore, the third peak requires a large number of modes in its modal summation. It is confirmed that the arrivals of reflected waves cause a sharp variation in the responses, and that the modal solutions at the corresponding times converge slowly.

(C) Numerical Dispersion

We now consider the effect of the numerical dispersion on the accuracy of the t-TLM modal solution. In chapter 2, it was seen that the optimal tuning factors improve the accuracy of computed eigenvalues of only the low modes, not the high modes. So, it is expected that the numerical error associated with the high modes deteriorates the accuracy of the t-TLM modal solutions. To investigate this feature, we consider first the phase difference between the t-TLM modal solution and the exact analytical solution. Then, we consider a numerical example to confirm practically the effect of the numerical dispersion of the high modes on the accuracy. Finally, we propose a strategy to decrease this numerical dispersion effect.

First, consider the phase difference between the t-TLM modal solution and the exact analytical solution, which is produced by the numerical dispersion in the t-TLM. Let $\omega_{E,j}$ and $\omega_{D,j}$ be the j-th eigenvalues of the exact analytical solution and the t-TLM, respectively. Then, $\omega_{D,j}$ can be expressed in terms of $\omega_{E,j}$ as

$$\omega_{D,j} = \omega_{E,j} \pm \varepsilon \tag{4.3.15}$$

where ε represents the error in eigenvalues between the t-TLM and the exact modal solution. Consider the last term in equation (4.3.7), i.e. $\sin\omega_j t/\omega_j$, which is actually the impulse response function for each mode j and is a function of time t. Compare the two impulse response functions of the exact analytical solution and the t-TLM as

$$\frac{\sin\omega_{E,j}t}{\omega_{E,j}} = \mathrm{Im}\frac{e^{i\omega_{E,j}t}}{\omega_{E,j}} \tag{4.3.16}$$

$$\frac{\sin\omega_{D,j}t}{\omega_{D,j}} = \mathrm{Im}\frac{e^{i\omega_{D,j}t}}{\omega_{D,j}} = \mathrm{Im}\frac{e^{i(\omega_{E,j}\pm\varepsilon)t}}{\omega_{E,j}\pm\varepsilon} \approx \mathrm{Im}\frac{e^{i\omega_{E,j}t}e^{\pm i\varepsilon t}}{\omega_{E,j}} \tag{4.3.17}$$

It is expected that the component $e^{\pm i\varepsilon t}$ in equation (4.3.17) can produce a significant phase difference for large t, even for a very small ε. Notice also that the seismograms for large t at a given receiver involves multiply reflected waves, as can be seen in figures 4.3.6a,b.

Next, we consider a numerical example to show the numerical error caused by the numerical dispersion in the high modes. In this example, we once more calculate the seismogram of the plate at $(x,z)=(1.0,0.0)$ due to a surface line load with $a=t_d=0.2$, but now we consider the interval $0\le t\le 10$. The reason of considering such a long time window is to include a larger number of multiply reflected waves in the seismograms. Notice that these multiple reflections are associated with high modes rather than low modes, as previously discussed in subsection (B). For the discrete models, $N_\lambda=8$ and $N_\lambda=4$ are used for the TLM1 and the TLM2, respectively. Then, the total number of computed modes in this example is 81. In particular, we calculate two kinds of seismograms in this example using $M=81$ and $M=41$. The two results are then compared with the two exact analytical solutions that are also calculated with the 81 and 41 exact modes, respectively.

Figure 4.3.6a displays the numerical results obtained with M=81. The two plots in the first row compare the seismograms obtained with the TLM1 and the TLM2 (solid line) against the exact analytical solution (dashed line). The two plots in the second row display, respectively, the difference between each of the two discrete models (i.e. TLM1 and TLM2) and the exact analytical solution. Recall that the seismograms obtained with the t-TLM include all the computed modes, i.e. M=81. It is observed that the waves having a higher multiple reflections exhibit more numerical error, which is caused by the numerical dispersion of the high modes. Therefore, it is confirmed that the numerical dispersion in the high modes deteriorates the final responses.

Figure 4.3.6b presents the numerical results obtained with M=41 in the same fashion as figure 4.3.6a. It is observed that the difference between the t-TLM and the exact analytical solution is reduced. The reason for this reduced error is that by truncating the high modes, we avoid the numerical dispersion effect associated with those high modes. In other words, we include only the accurate eigenvalues and modal shapes into the modal superposition. In addition, the elimination of incorrect high modes improves to the great extent the convergence of the modal solutions. Therefore, we conclude that the truncation of incorrect high modes obtained with the t-TLM is necessary, because the truncation not only improves the accuracy of the modal solutions, but also reduces remarkably the computational time.

4.3.2 *SH* wave problems

We now assess the accuracy of the t-TLM for *SH* wave problems for the computation of stresses as well as displacements. To this effect, we consider both of the consistent nodal load on vertical planes and the consistent stresses on horizontal planes. For practical purposes, we analyze two simple examples, namely a homogeneous stratum and a homogeneous plate subjected to *SH* transient line loads. The associated exact analytical solutions are derived and presented in appendix 4B. We compute the responses by means of both the TLM1 and TLM2 with N_λ as proposed in section 4.3.1, and then compare them with the exact analytical solutions.

(A) Homogeneous stratum

We explore here the accuracy of the t-TLM by analyzing a homogeneous stratum subjected to an *SH* line load whose variations in x and t are both bell-shaped, as defined in equations (4.3.1 to 3). The material properties and geometry of the stratum, namely the mass density, the shear wave velocity, and the thickness, are all taken as unity, i.e. ρ=C_S=H=1.0. The *SH* transient line load is applied at the top surface. Also, its half width a and its loading duration t_d are both 0.2. Hence, the associated minimum wavelength is $\lambda_{min}=C_S/f_{max}$ =0.1, and the maximum wavenumber k_{max} is 10π. We compute by means of the t-TLM the displacement $v(x,z,t)$, the consistent stresses on horizontal planes $\tau_{zy}(x,z,t)$, and the consistent nodal load on vertical planes $q_y(x,z,t)$, and then compare these with the exact analytical solutions. It should be noted that the consistent nodal load q_y is calculated by means of equation (1.3.92) for both the t-TLM and the exact analytical solution.

We begin by investigating the accuracy of the TLM1. For the discrete model, we analyze the stratum by means of the TLM1 with N_λ=8 as proposed in section 4.3.1. So, it follows that the

total number of thin-layers is $N=H/h=HN_\lambda/\lambda=80$ and the total number of degrees of freedom is 80. Figure 4.3.7 shows the numerical results obtained with the TLM1 (solid line) in comparison with the exact analytical solutions (dashed line). The three plots present the displacement v, the consistent stress τ_{zy}, and the consistent nodal load q_y, respectively, for snap-shots at t=3.0. Each line in the three plots represents the variation of the responses at interfaces i=1,9,17,...,73 (from the top) and for $0\leq x\leq 4$. It is observed from figure 4.3.7 that all the three response variables v, τ_{zy}, and q_y obtained with the TLM1 using N_λ=8 are in good agreement with the exact analytical solutions throughout the domain considered. Therefore, it is seen that the TLM1 with N_λ=8 provides quite good accuracy not only for the displacements, but also the internal stresses.

Next, we assess the accuracy of the TLM2. For the discrete model, we analyze the stratum using N_λ=4 as proposed in section 4.3.1, implying a total number of thin-layers is $N=H/h=HN_\lambda/\lambda=40$, and a total number of degrees of freedom of 80. Figure 4.3.8 shows the numerical results obtained with the TLM2 (solid line) in comparison with the exact analytical solutions (dashed line). The three plots present the displacement v, the consistent stress τ_{zy}, and the consistent nodal load q_y, respectively, in terms of snap-shots at t=3.0. Each line in the three plots represents the variation of the responses at interfaces i=1,5,9,...,37 (from the top) and for $0\leq x\leq 4$. It is observed from figure 4.3.8 that all the three components of v, τ_{zy}, and q_y obtained with the TLM2 using N_λ=4 are in good agreement with the exact analytical solutions throughout the domain considered. Therefore, the TLM2 with N_λ=4 provides quite good accuracy for both the displacement and the internal stresses.

(B) Homogeneous plate

Next, we explore the accuracy of the t-TLM by analyzing a homogeneous plate subjected to an *SH* line load whose variations in x and t are both bell-shaped as defined in equations (4.3.1 to 3). The material properties and geometry of the stratum are identical to those of the stratum just considered, i.e. $\rho=C_S=H$=1.0. The *SH* transient line load is applied at the top surface, and its half width a and duration t_d are both 0.2. Thus, the associated minimum wavelength is $\lambda_{min}=C_S/f_{max}$=0.1 and the maximum wavenumber is $k_{max}=10\pi$. We then compute by means of the t-TLM the displacement $v(x,z,t)$, the consistent stress on horizontal planes $\tau_{zy}(x,z,t)$, and the consistent nodal load on vertical planes $q_y(x,z,t)$, and then compare these with the exact analytical solutions.

We begin by investigating the accuracy of the TLM1. For the discrete model, we analyze the plate by means of the TLM1 with N_λ=8 as proposed in section 4.3.1. So, it follows that the total number of thin-layers is $N=H/h=HN_\lambda/\lambda=80$ and the total number of degrees of freedom is 81. Figure 4.3.9 shows the numerical results obtained with the TLM1 (solid line) in comparison with the exact analytical solutions (dashed line). The three plots present the displacement v, the consistent stress τ_{zy}, and the consistent nodal load q_y, respectively, in terms of snap-shots taken at t=3.0. Each line in the three plots represents the variation of the responses at interfaces i=1,9,17,...,81 (from the top) and for $0\leq x\leq 4$. It is observed from figure 4.3.9 that all the three components, namely v, τ_{zy}, and q_y are in good agreement with the exact analytical solutions throughout the domain of interest. Therefore, the TLM1 with N_λ=8 provides quite good accuracy not only for the displacements, but also the internal stresses.

We next assess the accuracy of the TLM2. For the discrete model, we analyze the plate by means of the TLM2 with N_λ=4 as proposed in section 4.3.1. So, it follows that the total number of thin-layers is $N=H/h=HN_\lambda/\lambda$=40 and the total number of degrees of freedom for the discrete model is 81. Figure 4.3.10 shows the numerical results obtained with the TLM2 (solid line) in comparison with the exact analytical solutions (dashed line). The three plots present the displacement v, the consistent stress τ_{zy}, and the consistent nodal load q_y, respectively, in terms of snap-shots at t=3.0. Note that each line in the three plots represents the variation of the responses at interfaces i=1,5,9,...,41 (from the top) and for $0\leq x\leq 4$. It is observed from figure 4.3.10 that all the three of v, τ_{zy}, and q_y obtained with the TLM2 using N_λ=4 are in good agreement with the exact analytical solutions. Thus, it is confirmed that the TLM2 with N_λ=4 provides quite good accuracy for not only the displacement component, but also the internal stress components.

4.3.3 *SV-P* wave problems

We assess here the accuracy of the t-TLM for *SV-P* wave problems in terms of both the displacement and stress responses. For practical purposes, we analyze a homogeneous plate subjected to an *SV-P* transient line load whose variation in x and t is bell-shaped, as defined in equations (4.3.1 to 3). The associated exact analytical solutions are derived and presented in appendix 4C. The material properties and geometry of the stratum, namely the mass density, the shear wave velocity, and the thickness are all unity, i.e. $\rho=C_S=H$=1.0. Also, Poisson's ratio ν is taken as 0.31 (as in the Mindlin plate). The *SV-P* line load is applied at the top surface in the vertical direction. Also, its half width a and duration t_d are both 0.2. Then, the associated minimum wavelength is $\lambda_{min}=C_S/f_{max}$=0.1, and the maximum wavenumber is $k_{max}=10\pi$. We are interested in the horizontal and vertical displacements, u and w, the consistent stresses in horizontal planes, τ_{zx} and σ_z, and the consistent nodal loads on the vertical plane, q_x and q_z. We compute the responses by means of both the TLM1 and TLM2 with N_λ as proposed in section 4.3.1, and then compare these with the exact analytical solutions. It should be noted that the consistent nodal loads, q_x and q_z, are calculated by means of equation (1.3.111) for both the t-TLM and the exact analytical solution.

We start by exploring the accuracy of the TLM1 for *SV-P* wave problems. For the discrete model, we analyze the plate by means of the TLM1 with N_λ=8, as proposed in section 4.3.1. It follows that the total number of thin-layers is $N=H/h=HN_\lambda/\lambda$=80 and then the total number of degrees of freedom in the discrete model is 162. Figure 4.3.11a,b show the numerical results obtained with the TLM1 (solid line) in comparison with the exact analytical solutions (dashed line). Figure 4.3.11a displays snap-shots at t=3.0 for u, w, and τ_{zx}, while figure 4.3.11b shows snap-shots at t=3.0 for σ_z, q_x, and q_z. Each line in the six plots represents the variation of the responses at interfaces i=1,9,17,...,81 (from the top) and for $0\leq x\leq 4$. It is observed from figures 4.3.11a,b that all the six filed quantities u, w, τ_{zx}, σ_z, q_x and q_z obtained with the TLM1 using N_λ=8 are in good agreement with the exact analytical solutions. Therefore, the TLM1 with N_λ=8 provides quite good accuracy for the displacement components and the internal stress components, not only for *SH* wave problems, but also for *SV-P* wave problems.

Next, we investigate the accuracy of the TLM2 for *SV-P* wave problems. For the discrete model, we analyze the plate by means of the TLM2 with N_λ=4, so that the total number of thin-layers is $N=H/h=HN_\lambda/\lambda$=40 and the total number of degrees of freedom in the discrete model is 162. Figures 4.3.12a,b show the numerical results obtained with the TLM2 (solid line) in comparison with the exact analytical solutions (dashed line). Figure 4.3.12a displays snap-shots at t=3.0 of u,

w, and τ_{zx}, while figure 4.3.11b shows snap-shots at t=3.0 of σ_z, q_x, and q_z. Each line in the six plots represents the variation of the responses at interfaces i=1,5,9,...,41 (from the top) and for $0 \le x \le 4$. It is observed from figures 4.3.12a,b that all the six of u, w, τ_{zx}, σ_z, q_x and q_z obtained with the TLM2 using N_λ=4 are everywhere in good agreement with the exact analytical solutions. Thus, the TLM2 with N_λ=4 provides quite good accuracy for both the displacements and internal stresses, not only for *SH* wave problems, but also for *SV-P* wave problems.

Figures for section 4.2

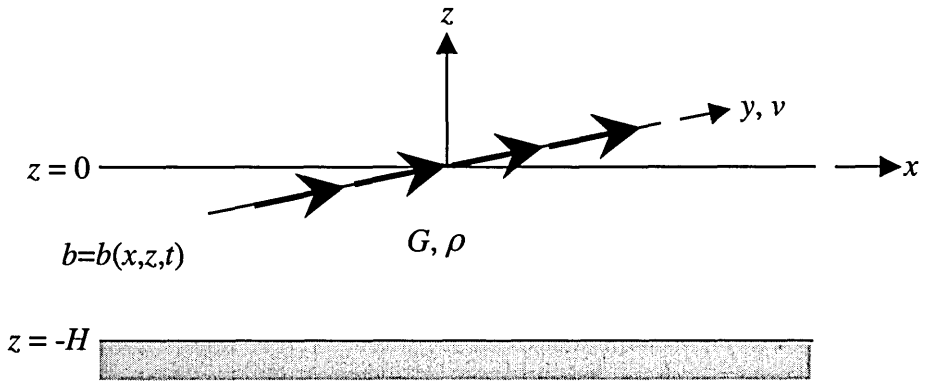

Figure 4.2.1 Homogeneous stratum of thickness H subjected to an SH line load b

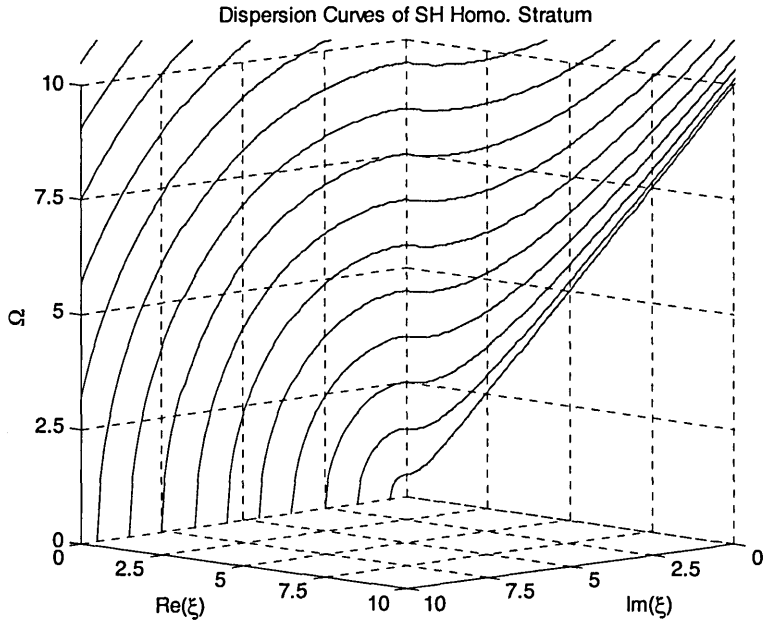

Figure 4.2.2 Dispersion curves for SH homogeneous stratum of thickness H
SH waves ($\Omega=\omega H/\pi C_S$, and $\xi=kH/\pi$)

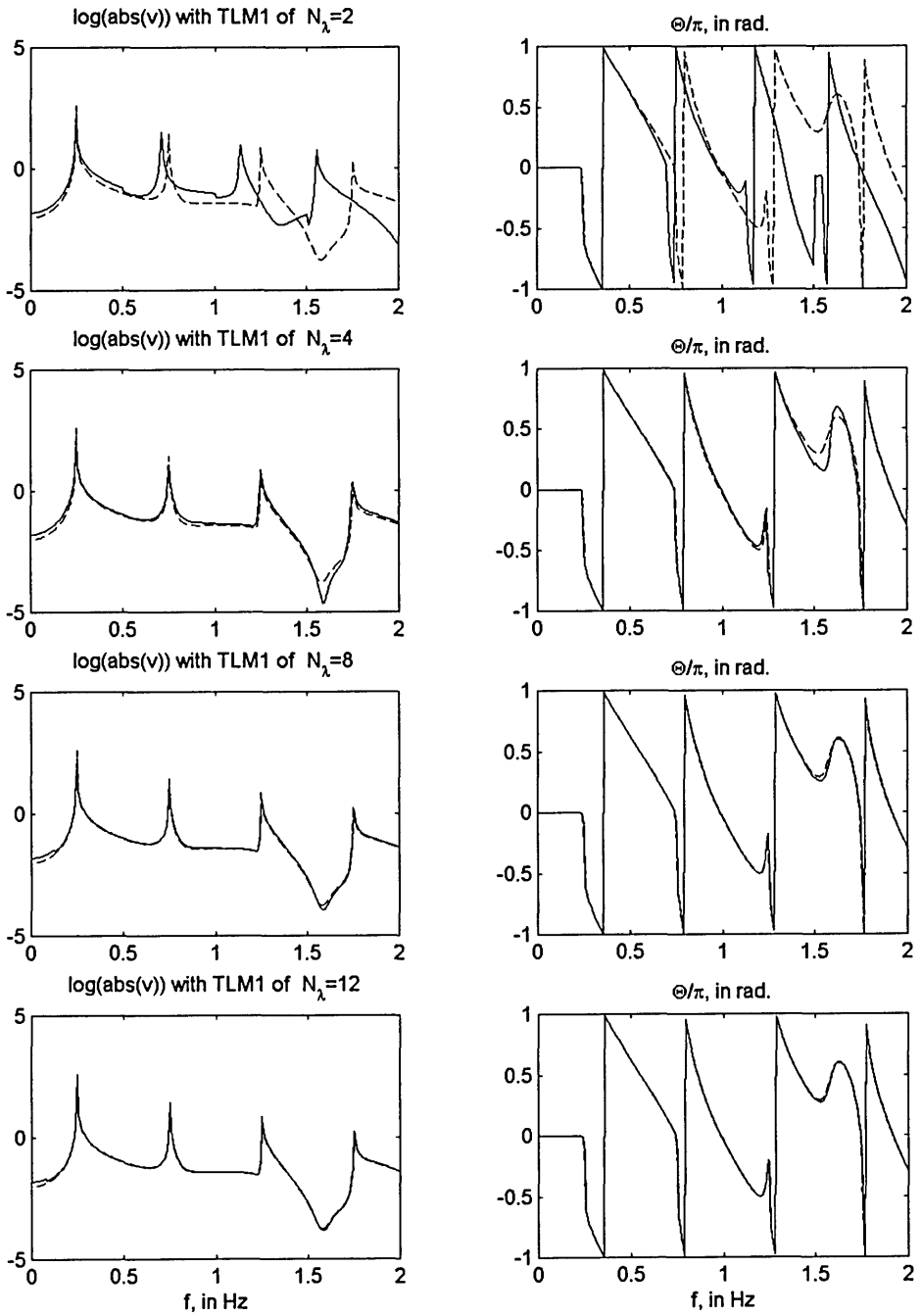

Figure 4.2.3a Accuracy of TLM1 modal solutions as function of f_{ex} and N_λ
in terms of logarithmic amplitudes and phase angles in radian of displacement v at $(x,z)=(1.0,0.0)$
due to *SH* surface line load (solid for TLM1, dash for Exact modal superposition)

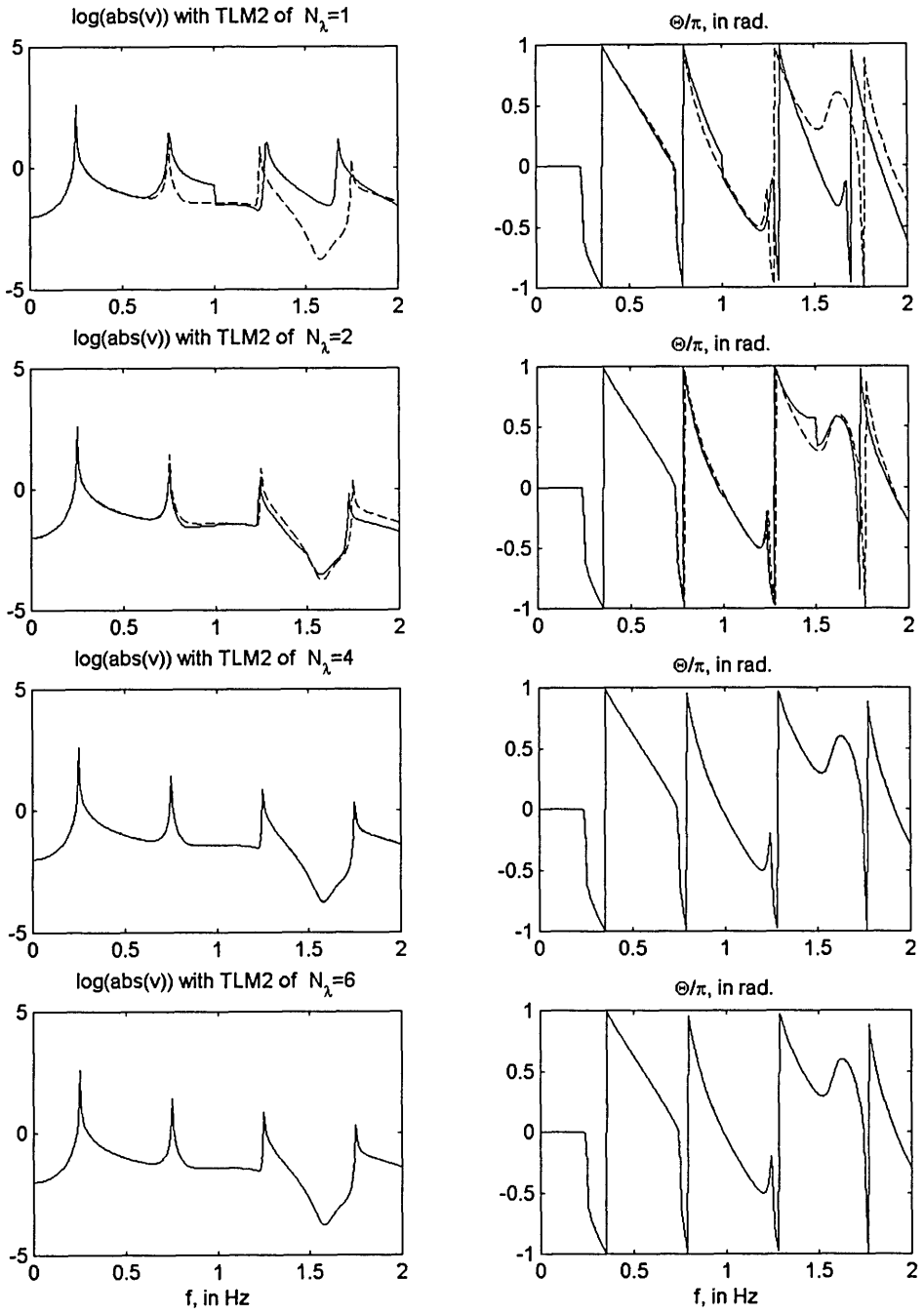

Figure 4.2.3b Accuracy of TLM2 modal solutions as function of f_{ex} and N_λ
in terms of logarithmic amplitudes and phase angles in radian of displacement v at $(x,z)=(1.0,0.0)$
due to *SH* surface line load (solid for TLM2, dash for Exact modal superposition)

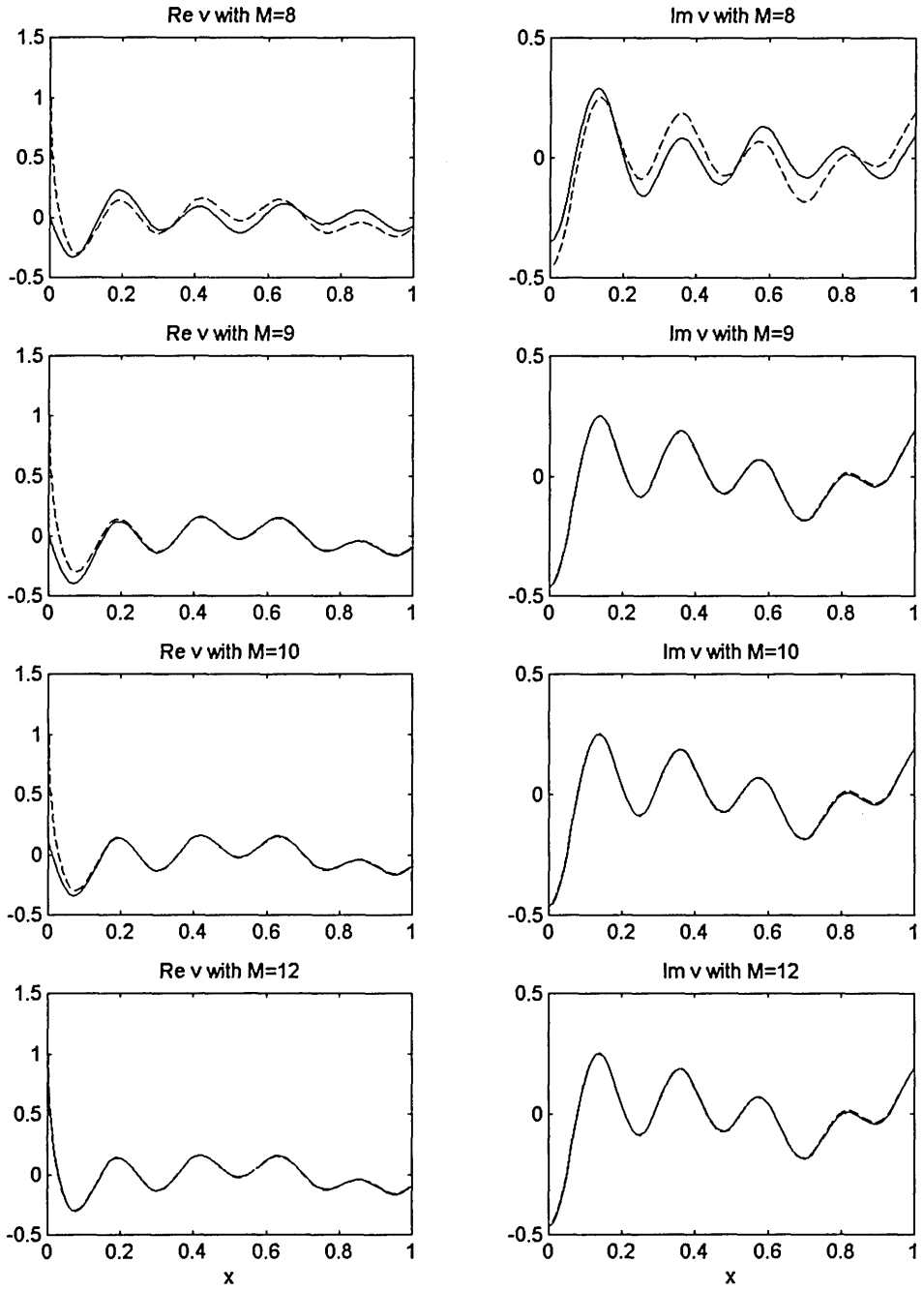

Figure 4.2.4a Convergence of TLM1 modal solutions with N_λ=12
in terms of surface displacement v due to SH surface line load of f_{ex}=4.50
(solid for TLM1, dash for Image source method)

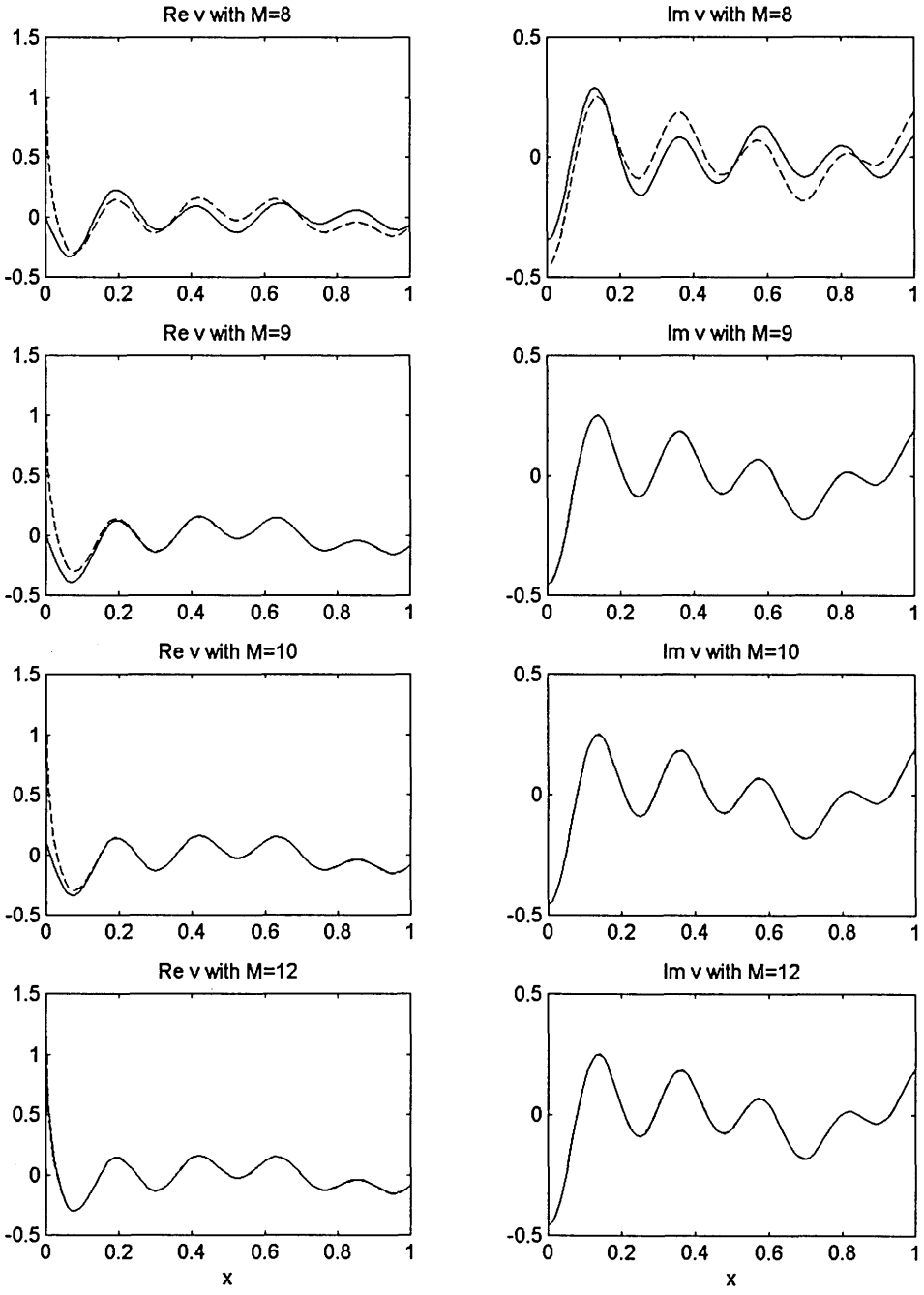

Figure 4.2.4b Convergence of TLM2 modal solutions with N_λ=4
in terms of surface displacement v due to SH surface line load of f_{ex}=4.50
(solid for TLM2, dash for Image source method)

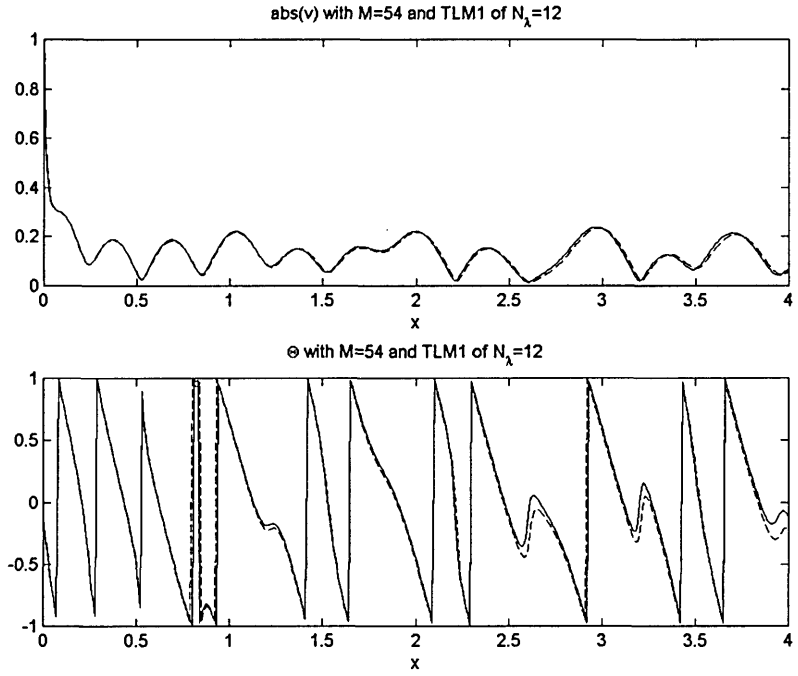

Figure 4.2.5a Effect of numerical dispersion on far-field solutions of TLM1 of N_λ=12 in terms of amplitude and phase angle in radian of surface displacement v due to *SH* surface line load of f_{ex}=4.50 (solid for TLM1, dash for Image source method)

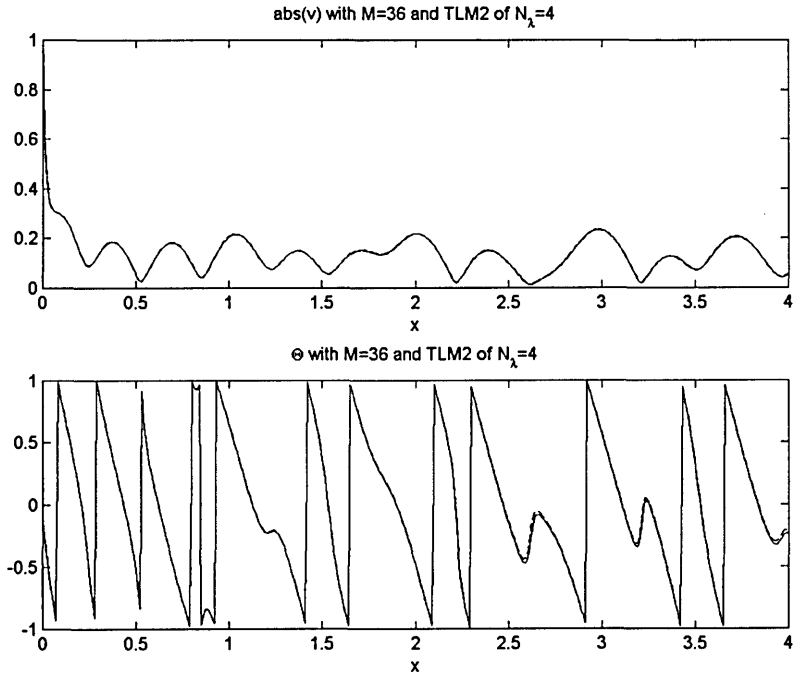

Figure 4.2.5b Effect of numerical dispersion on far-field solutions of TLM2 of N_λ=4 in terms of amplitude and phase angle in radian of surface displacement v due to *SH* surface line load of f_{ex}=4.50 (solid for TLM2, dash for Image source method)

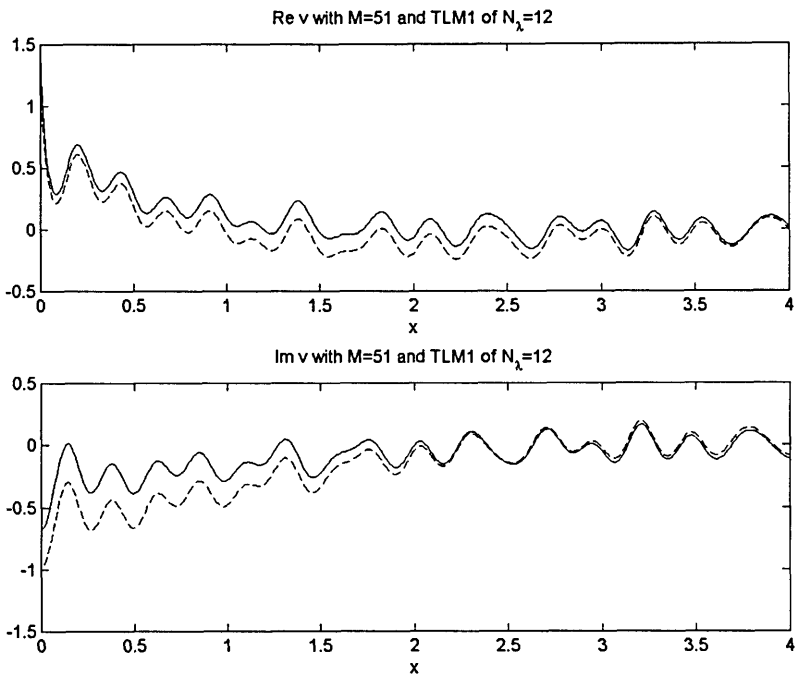

Figure 4.2.6a Effect of numerical dispersion on near-field solutions of TLM1 of N_λ=12 in terms of surface displacement v due to *SH* surface line load of f_{ex}=4.25 (solid for TLM1, dash for Image source method)

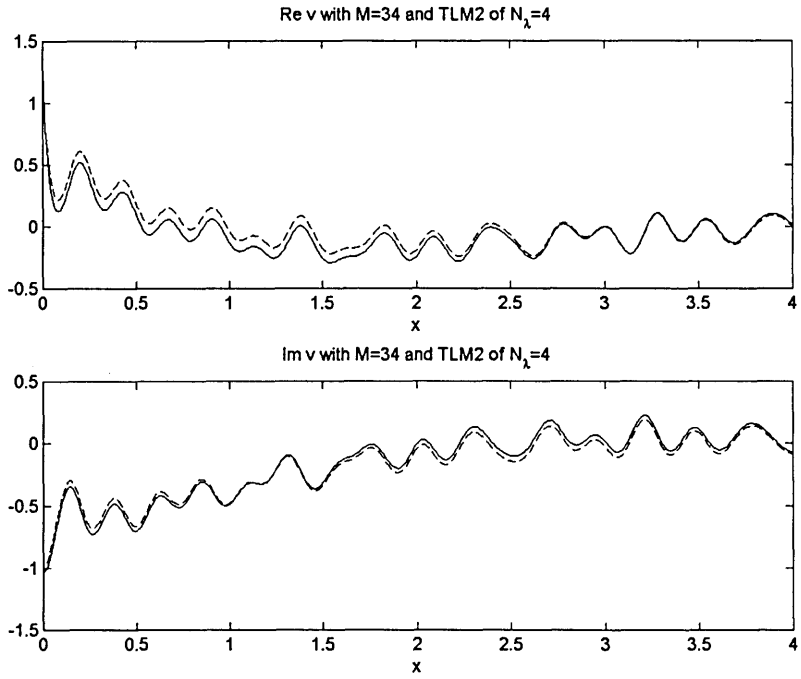

Figure 4.2.6b Effect of numerical dispersion on near-field solutions of TLM2 of N_λ=4 in terms of surface displacement v due to *SH* surface line load of f_{ex}=4.25 (solid for TLM2, dash for Image source method)

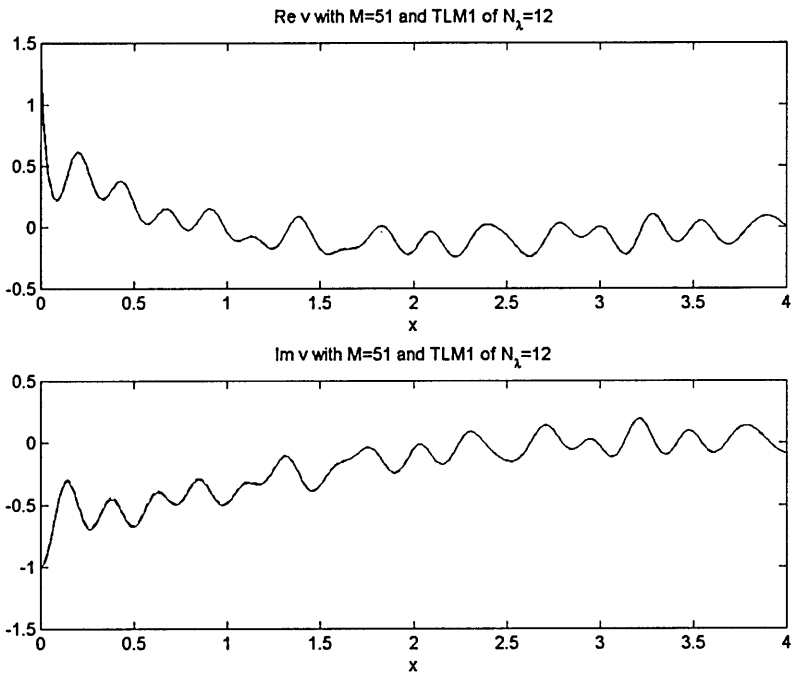

Figure 4.2.7a Near-field solutions improved by the hybrid method: TLM1 of N_λ=12 in terms of surface displacement v due to SH surface line load of f_{ex}=4.25 (solid for TLM1, dash for Image source method)

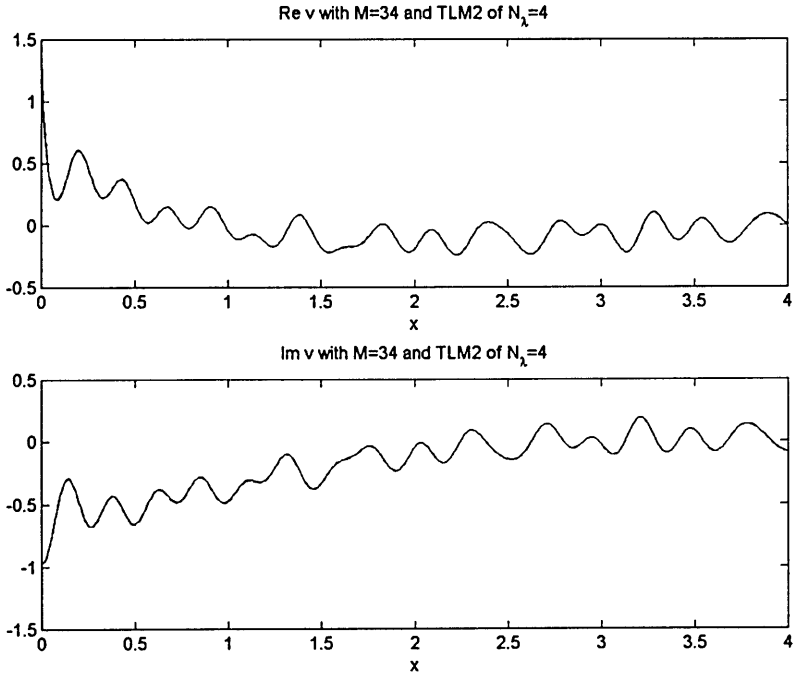

Figure 4.2.7b Near-field solutions improved by the hybrid method: TLM2 of N_λ=4 in terms of surface displacement v due to SH surface line load of f_{ex}=4.25 (solid for TLM2, dash for Image source method)

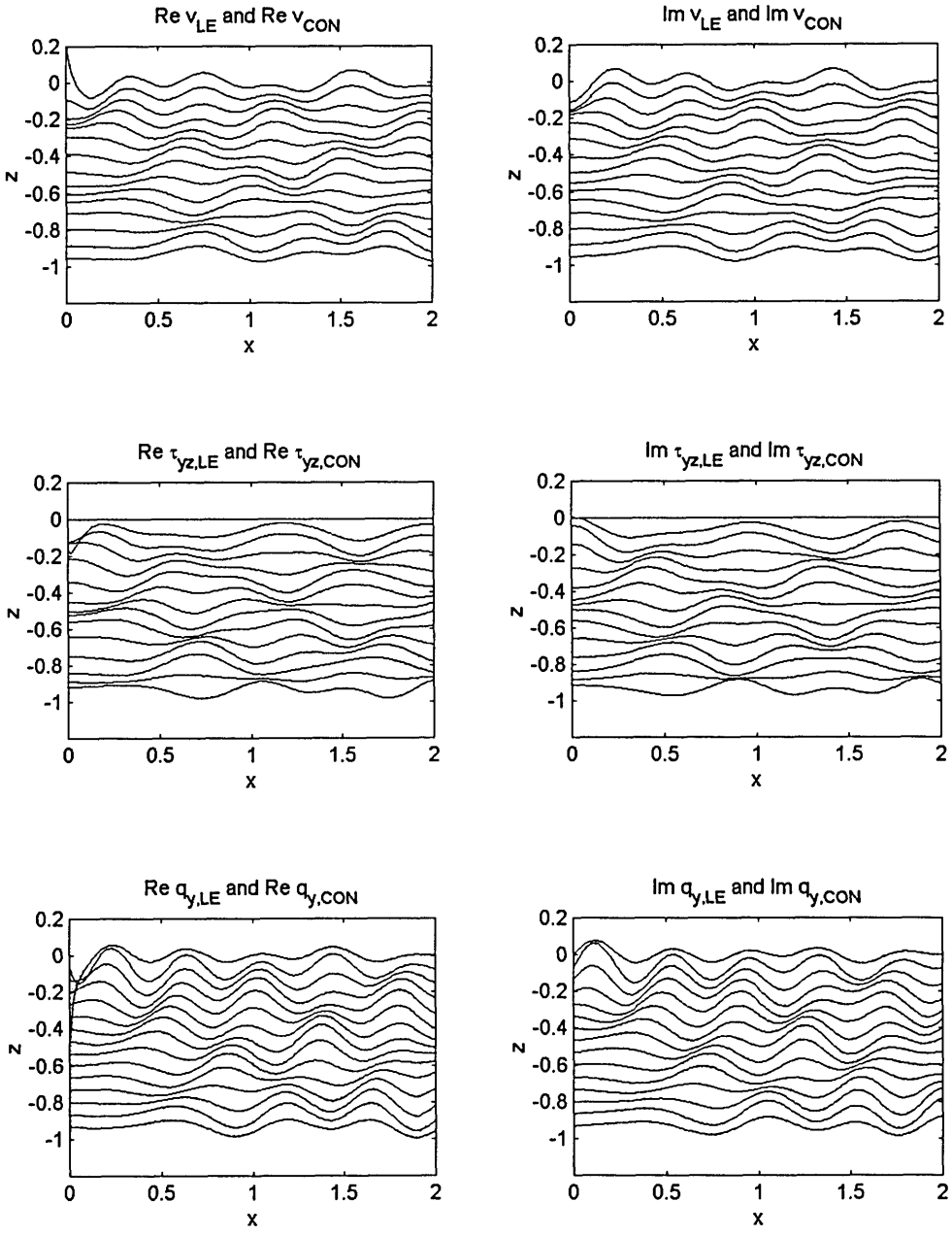

Figure 4.2.8 Harmonic responses v, τ_{zy}, q_y of homogeneous stratum obtained with TLM1 due to *SH* surface line load of f_{ex}=2.50
(solid for TLM1 N_λ=12; dashed for Exact analytical solution)

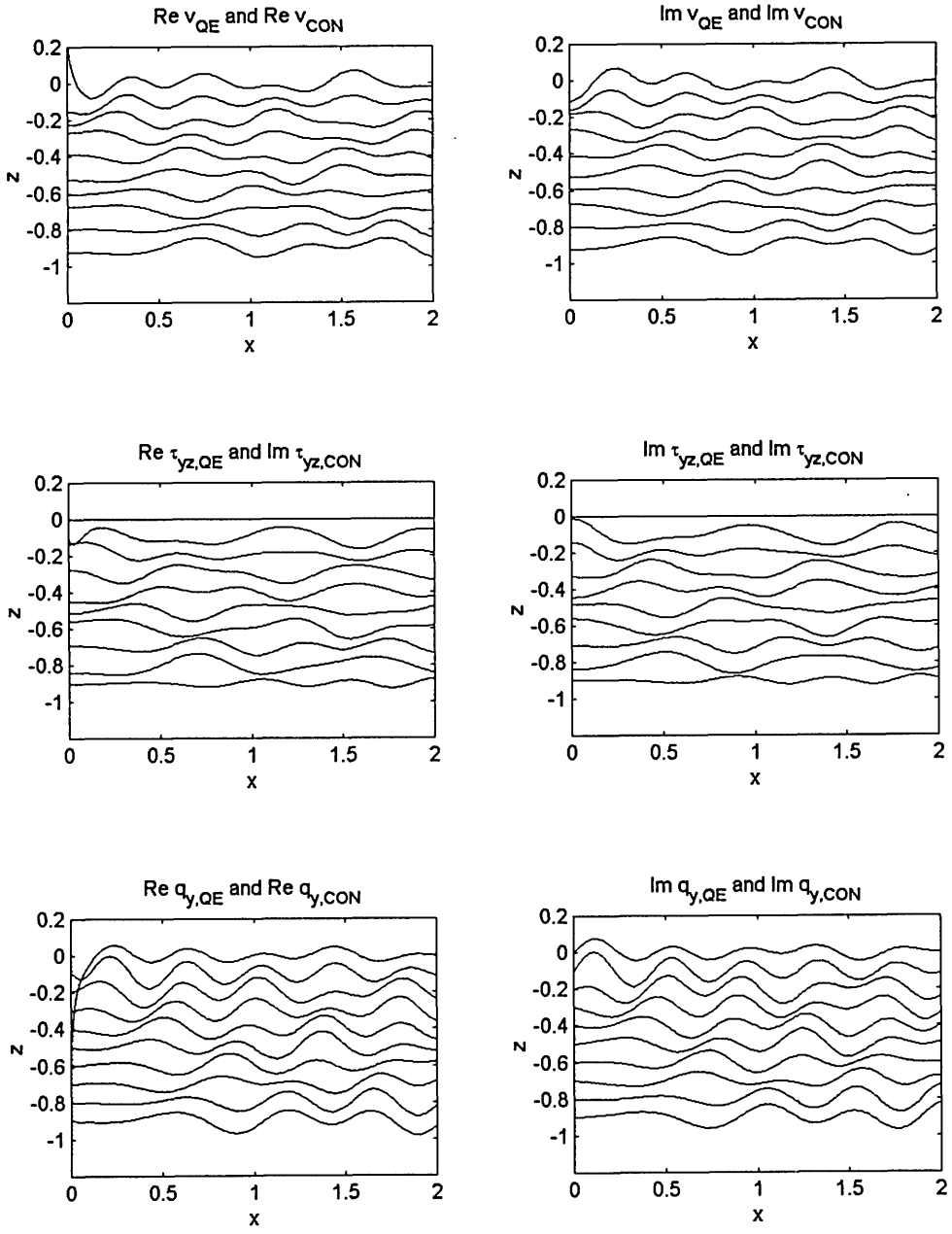

Figure 4.2.9 Harmonic responses v, τ_{zy}, q_y of homogeneous stratum obtained with TLM2 due to *SH* surface line load of f_{ex}=2.50
(solid for TLM2 N_λ=4; dashed for Exact analytical solution)

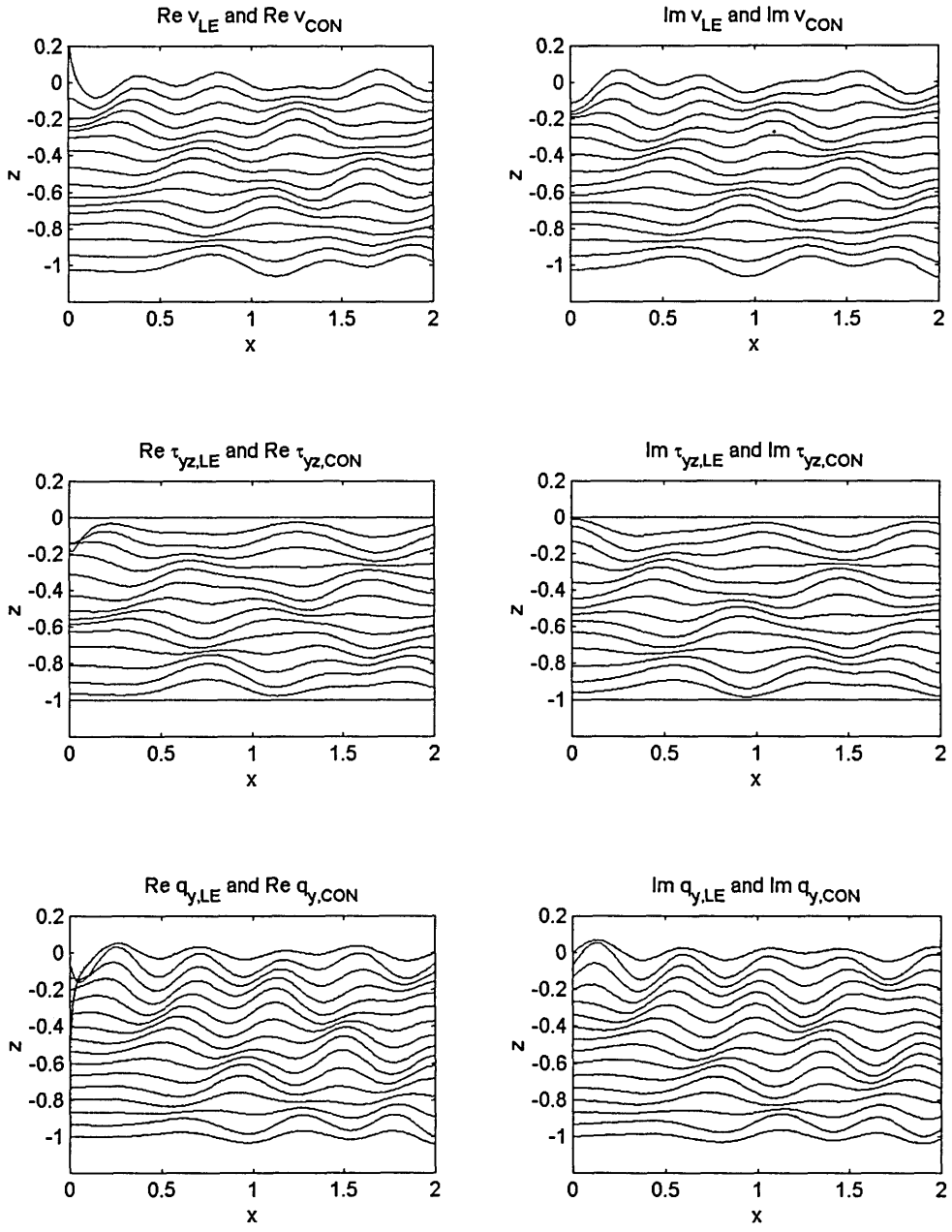

Figure 4.2.10 Harmonic responses v, τ_{zy}, q_y of homogeneous plate obtained with TLM1 due to *SH* surface line load of f_{ex}=2.25
(solid for TLM1 N_λ=12; dashed for Exact analytical solution)

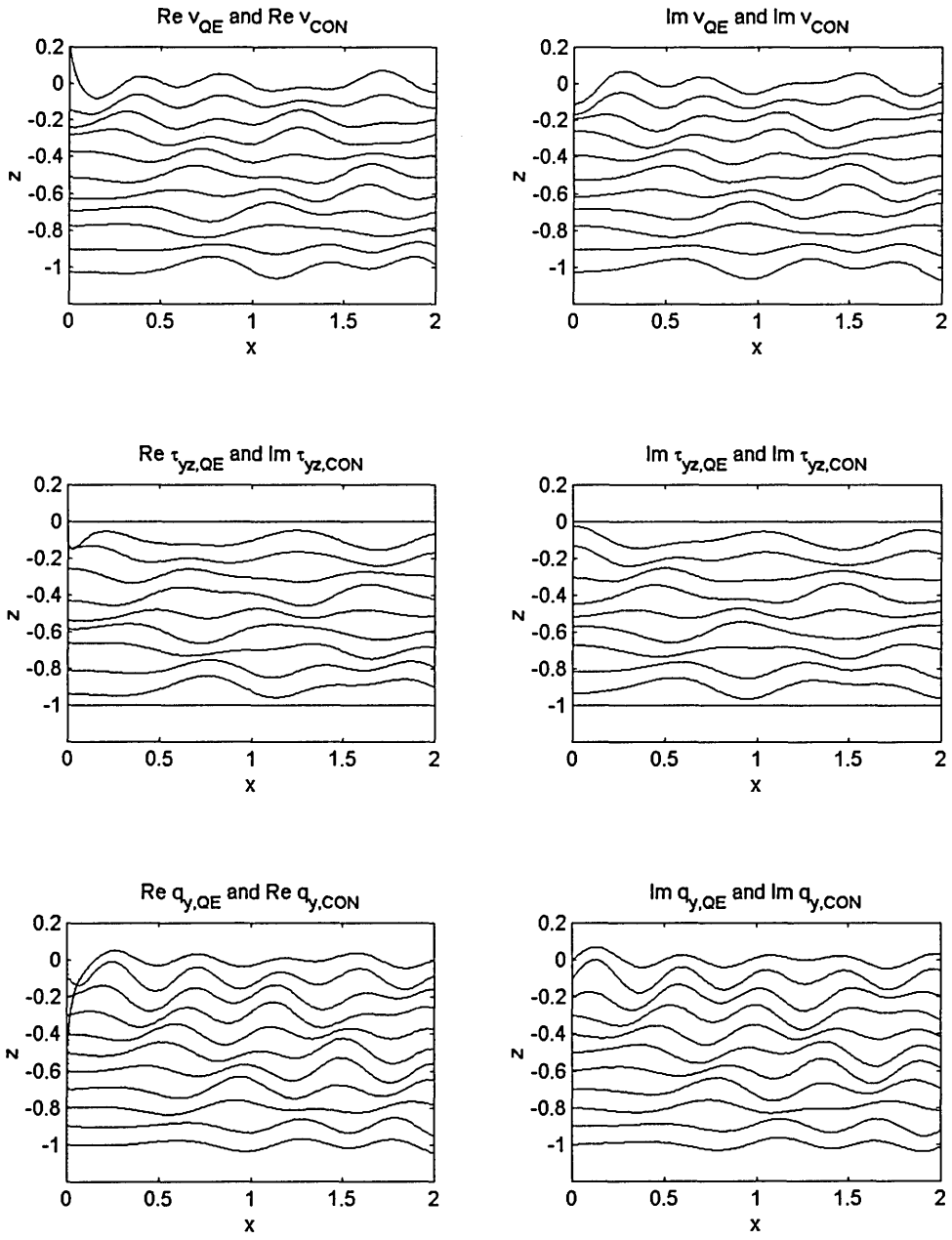

Figure 4.2.11 Harmonic responses v, τ_{zy}, q_y of homogeneous plate obtained with TLM2 due to *SH* surface line load of f_{ex}=2.25
(solid for TLM2 N_λ=4; dashed for Exact analytical solution)

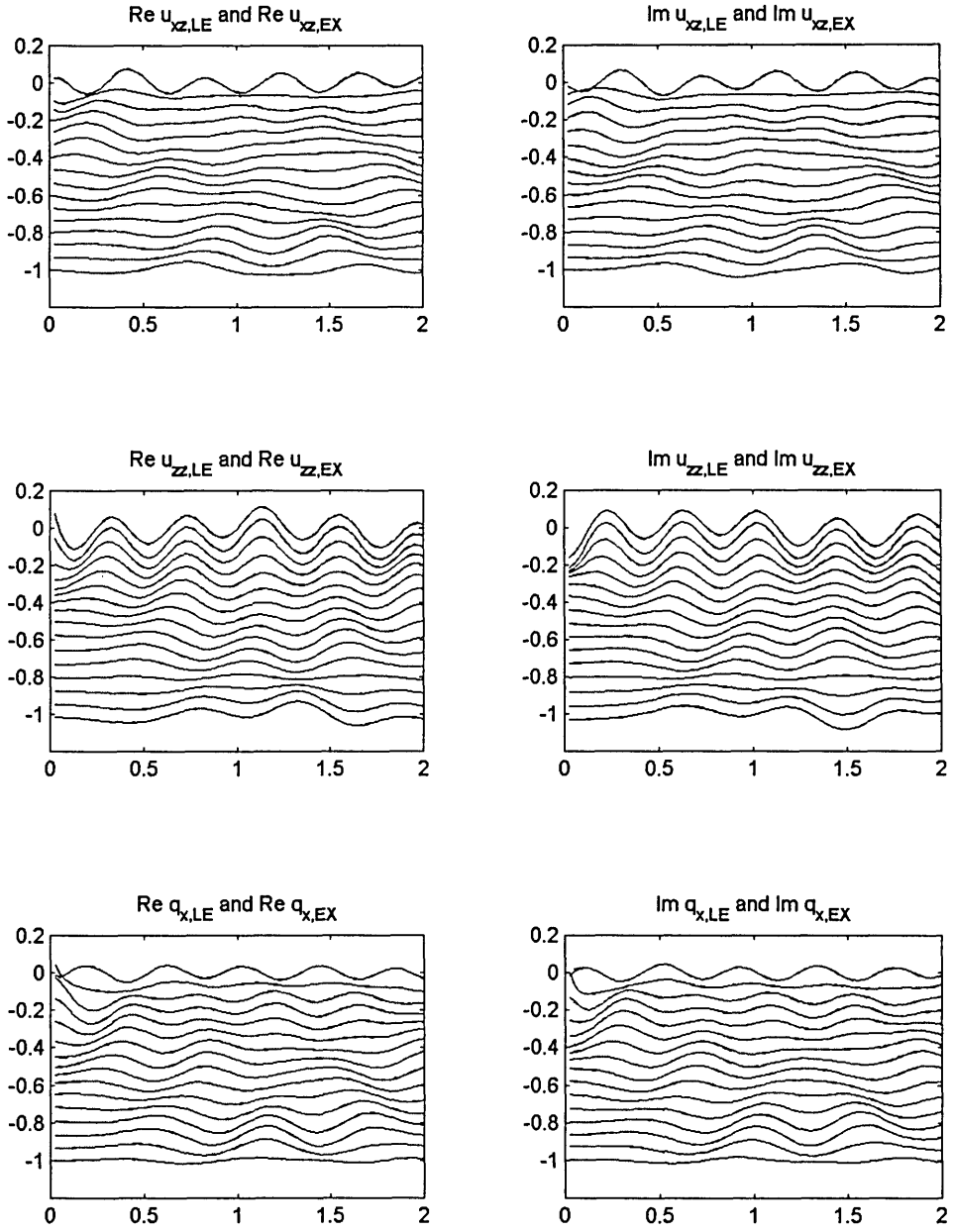

Figure 4.2.12a Harmonic responses u_{xz}, u_{zz}, q_x of homogeneous plate obtained with TLM1 due to *SV-P* vertical line load of f_{ex}=2.25 applied at the top surface (solid for TLM1 N_λ=12; dashed for Exact analytical solution)

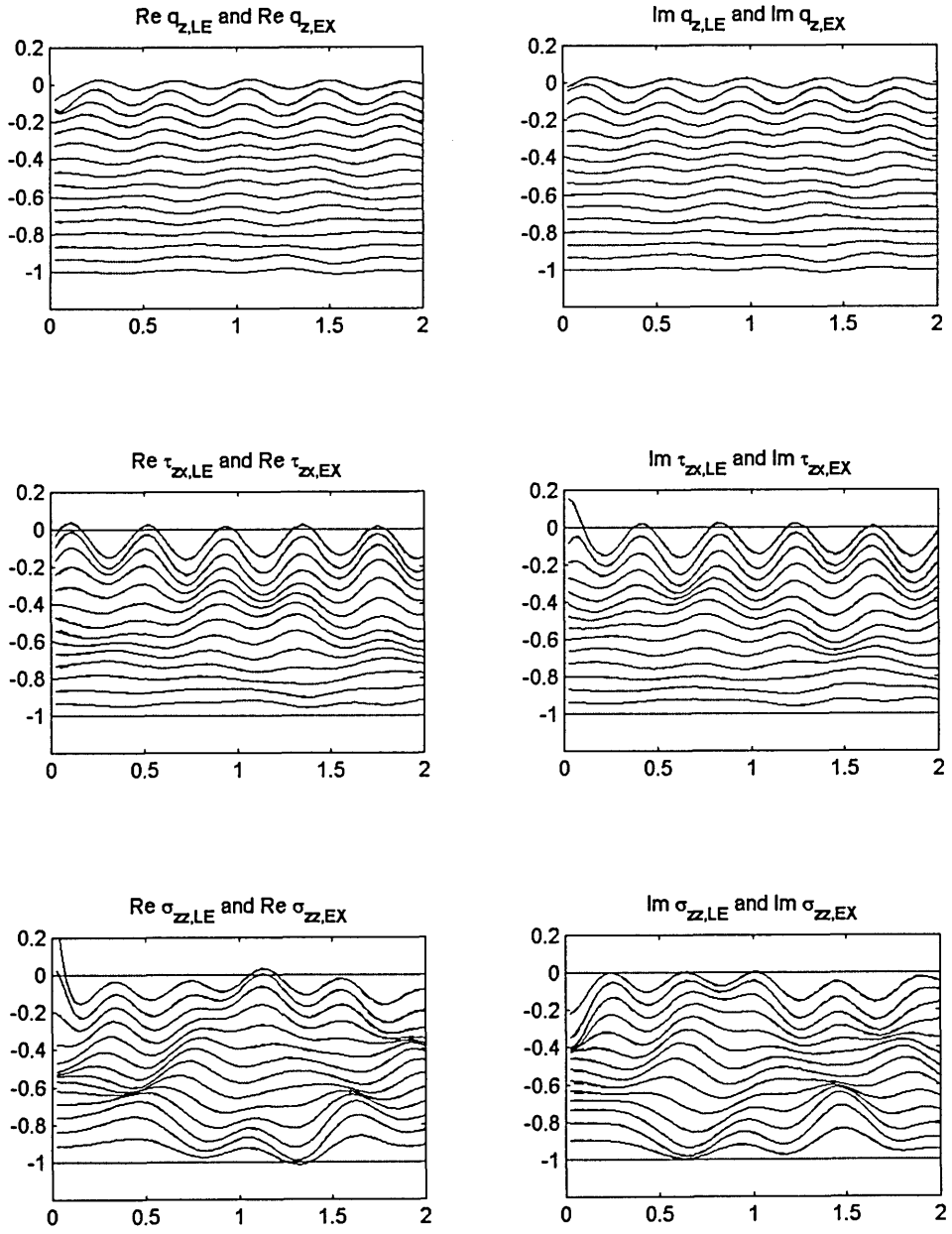

Figure 4.2.12b Harmonic responses q_z, τ_{zx}, σ_{zz} of homogeneous plate obtained with TLM1 due to *SV-P* vertical line load of f_{ex}=2.25 applied at the top surface (solid for TLM1 N_λ=12; dashed for Exact analytical solution)

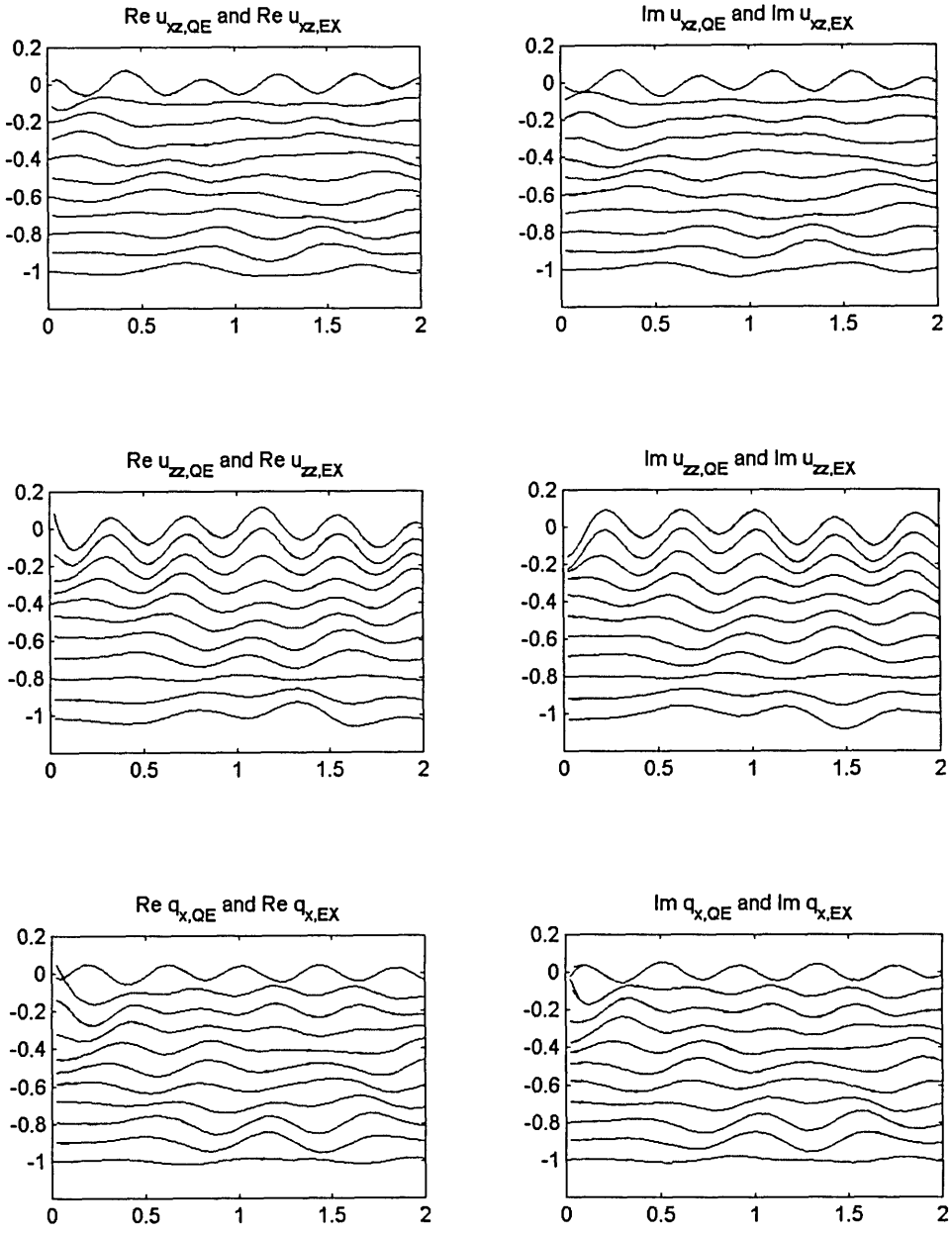

Figure 4.2.13a Harmonic responses u_{xz}, u_{zz}, q_x of homogeneous plate obtained with TLM2 due to *SV-P* vertical line load of f_{ex}=2.25 applied at the top surface (solid for TLM2 N_λ=4; dashed for Exact analytical solution)

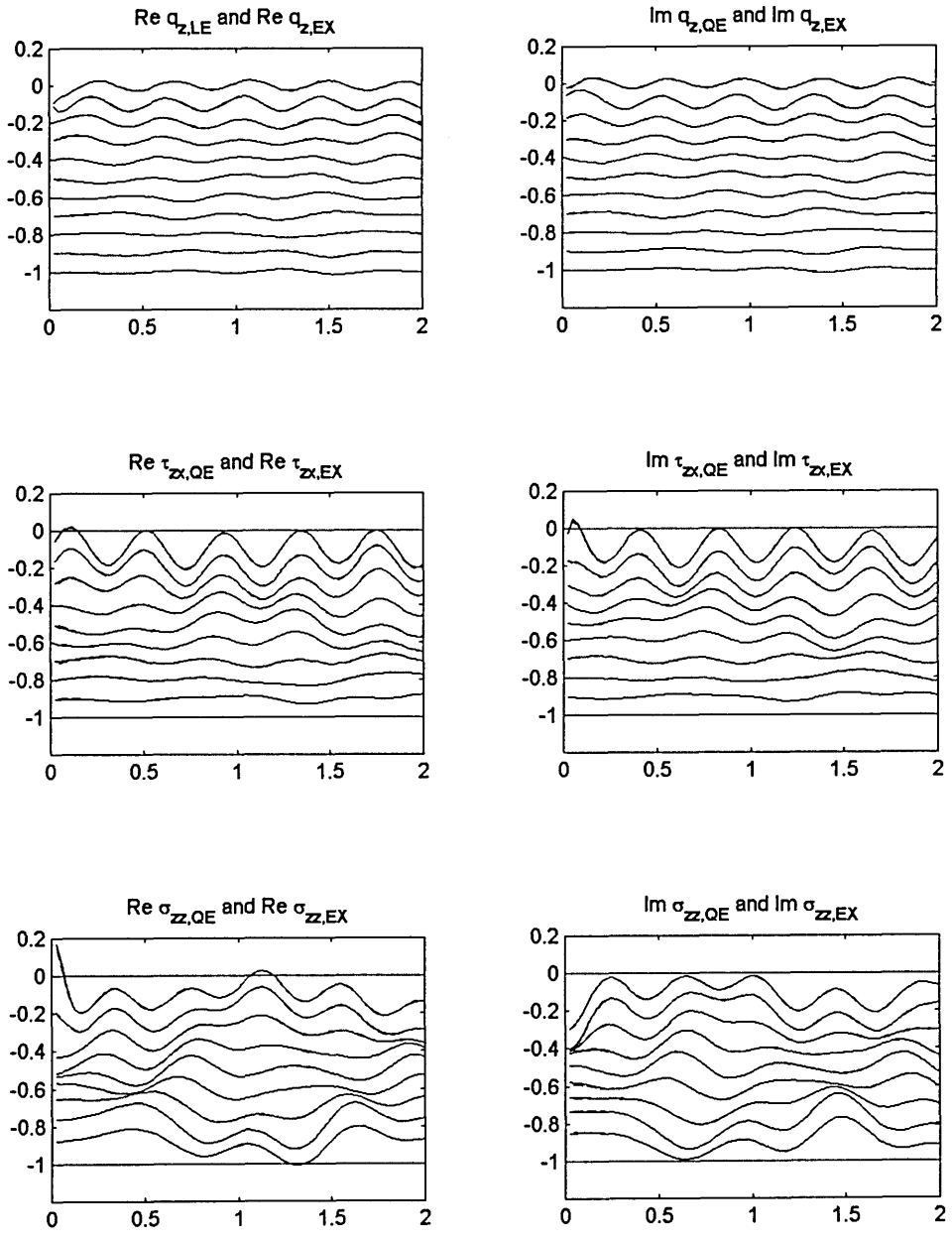

Figure 4.2.13b Harmonic responses q_z, τ_{zx}, σ_{zz} of homogeneous plate obtained with TLM2 due to *SV-P* vertical line load of f_{ex}=2.25 applied at the top surface (solid for TLM2 N_λ=4; dashed for Exact analytical solution)

Figures for section 4.3

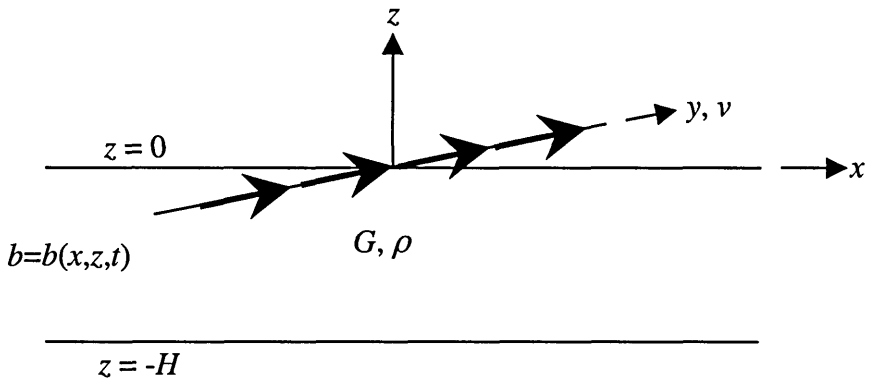

Figure 4.3.1 Homogeneous plate of thickness H subjected to an SH line load b

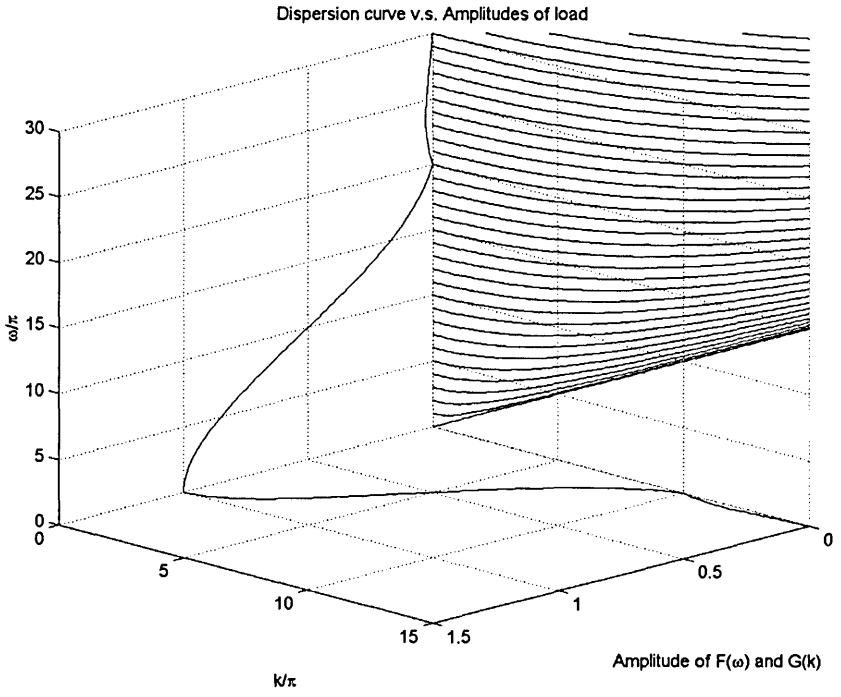

Figure 4.3.2 Dispersion curves of SH homogeneous plate of thickness H and spectra of the loading function (*Hanning* window) in wavenumber-frequency domain

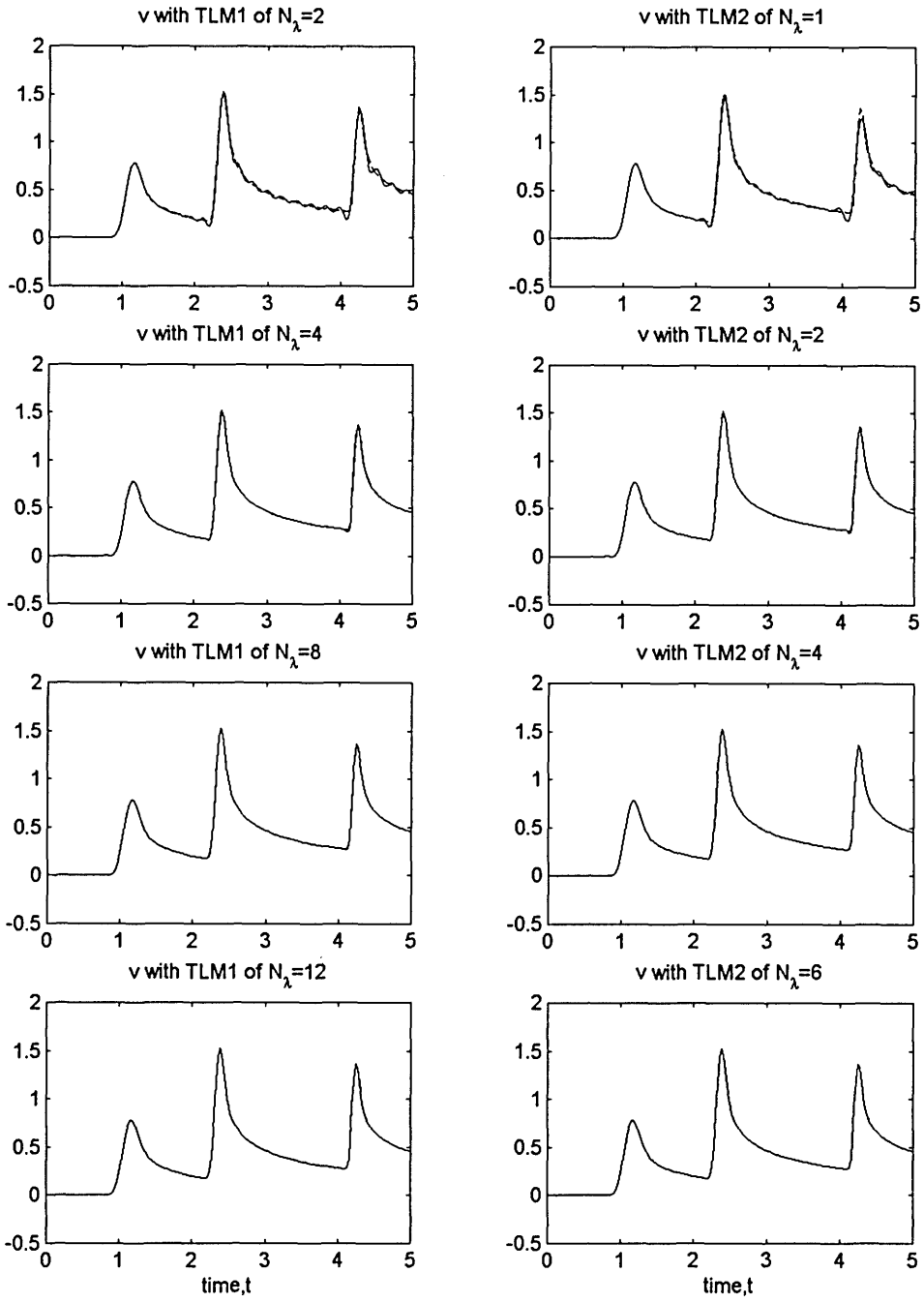

Figure 4.3.3 Accuracy of t-TLM modal solutions as function of N_λ
seismograms of v at (x=1, z=0) in homogeneous plate subjected to *SH* surface line load with $a=t_d$=0.2: the left column obtained with TLM1 and the right column obtained with TLM2 (solid for TLM, dashed for Exact modal superposition)

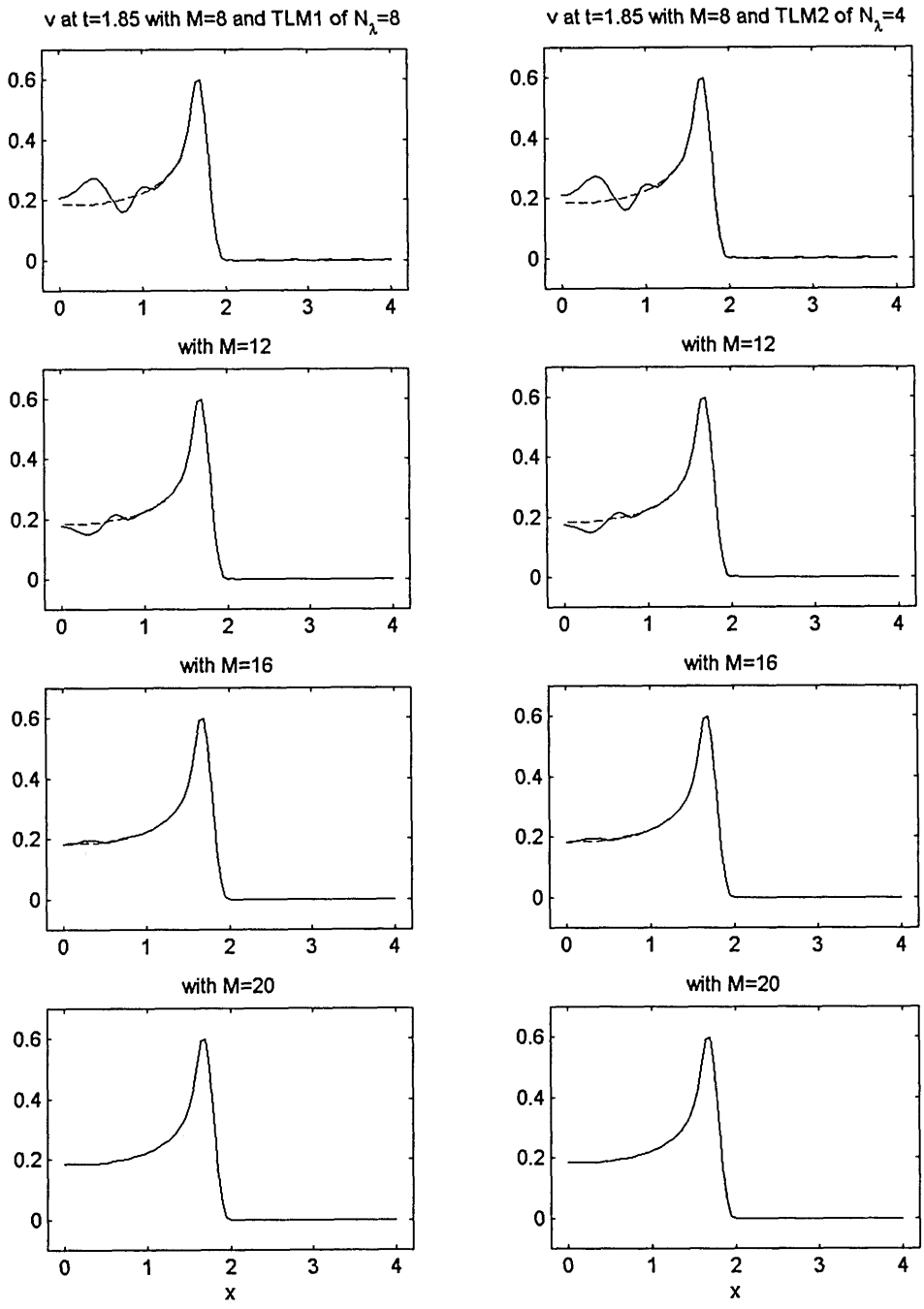

Figure 4.3.4 Convergence of t-TLM modal solutions as function of x and M snapshots of surface v for t=1.85 of homogeneous plate subjected to *SH* surface line load with a=t_d=0.2: the left column obtained with TLM1 and the right column obtained with TLM2 (solid for TLM, dashed for Exact modal superposition)

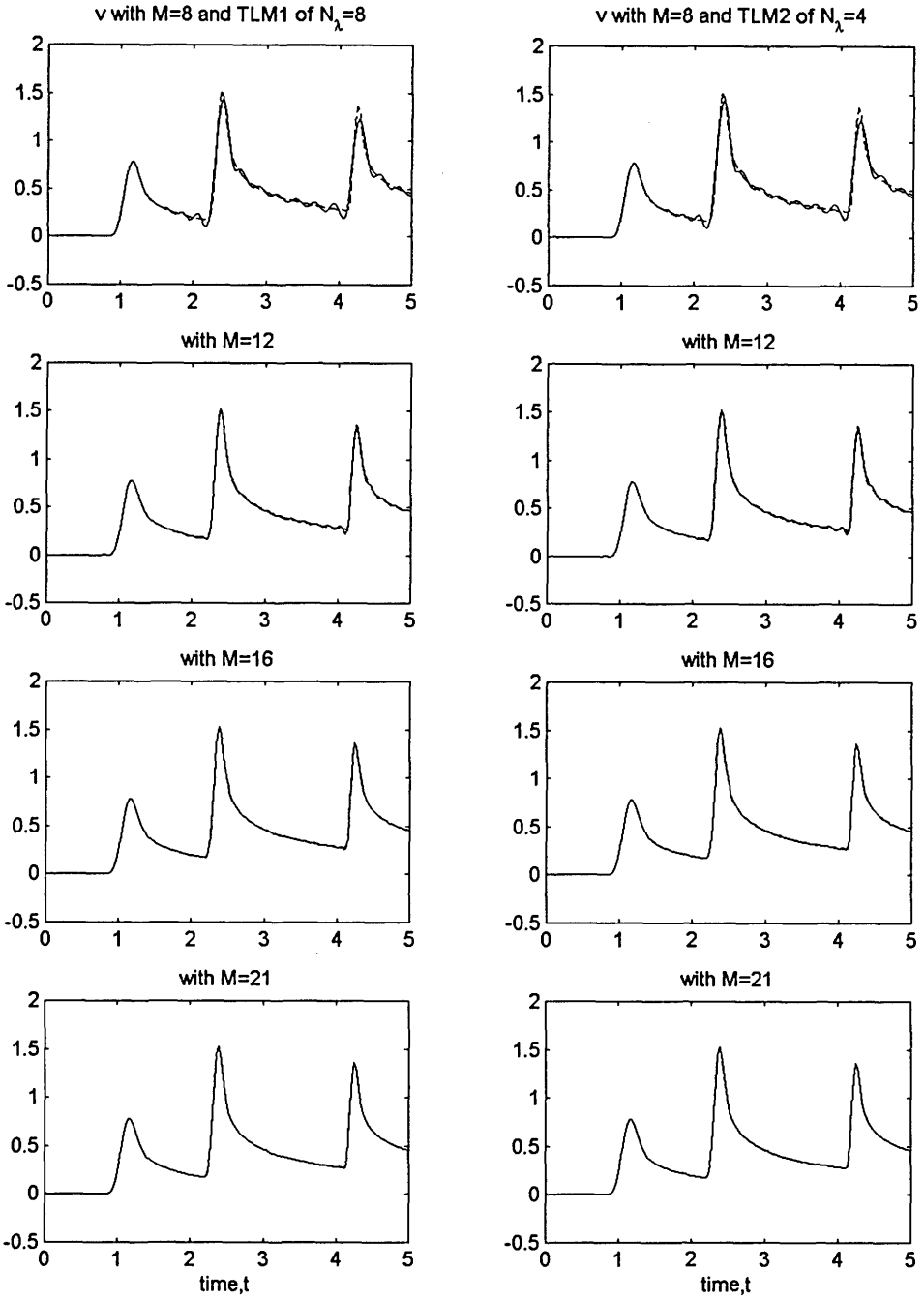

Figure 4.3.5 Convergence of *t*-TLM modal solutions as function of t and M seismograms v at (x=1, z=0) in homogeneous plate subjected to *SH* surface line load with $a=t_d$=0.2: the left column obtained with TLM1 and the right column obtained with TLM2 (solid for TLM, dashed for Exact modal superposition)

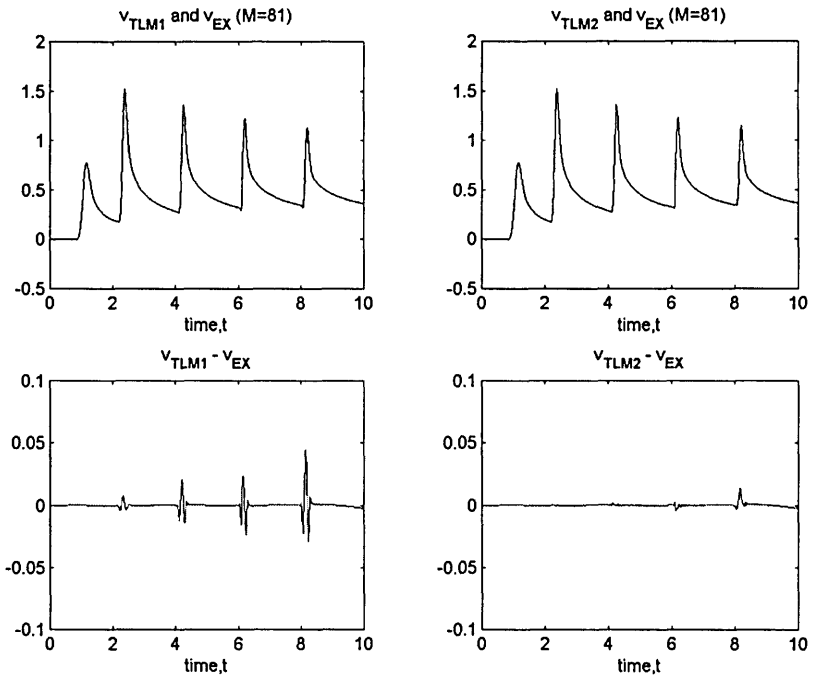

Figure 4.3.6a Errors due to numerical dispersion of high computed modes for surface displacement v of homogeneous plate subjected to *SH* surface line load: the left column obtained with TLM1 and the right column obtained with TLM2 (solid for TLM, dashed for Exact modal superposition)

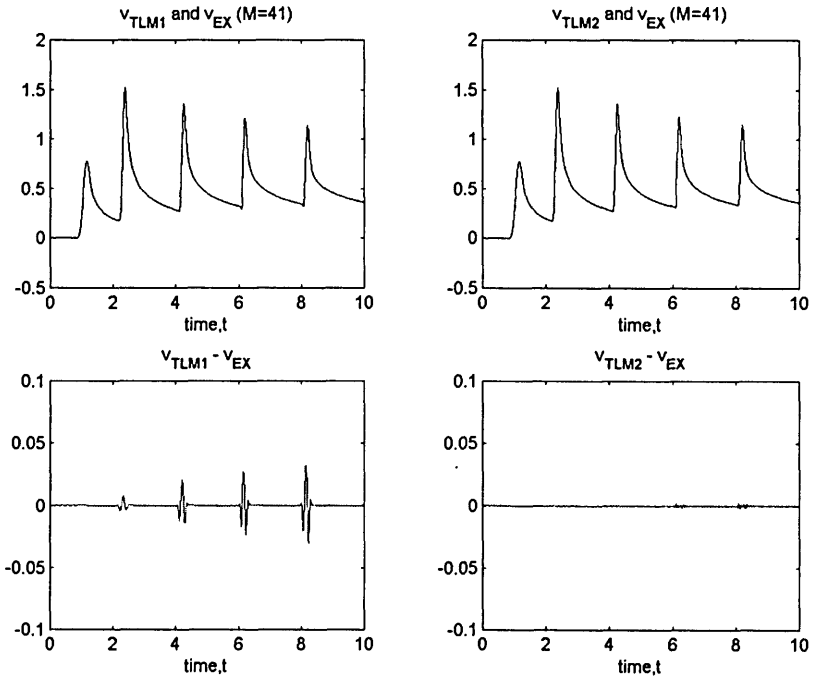

Figure 4.3.6b Improvement achieved by truncation of high computed modes for surface displacement v of homogeneous plate subjected to *SH* surface line load: the left column obtained with TLM1 and the right column obtained with TLM2 (solid for TLM, dashed for Exact modal superposition)

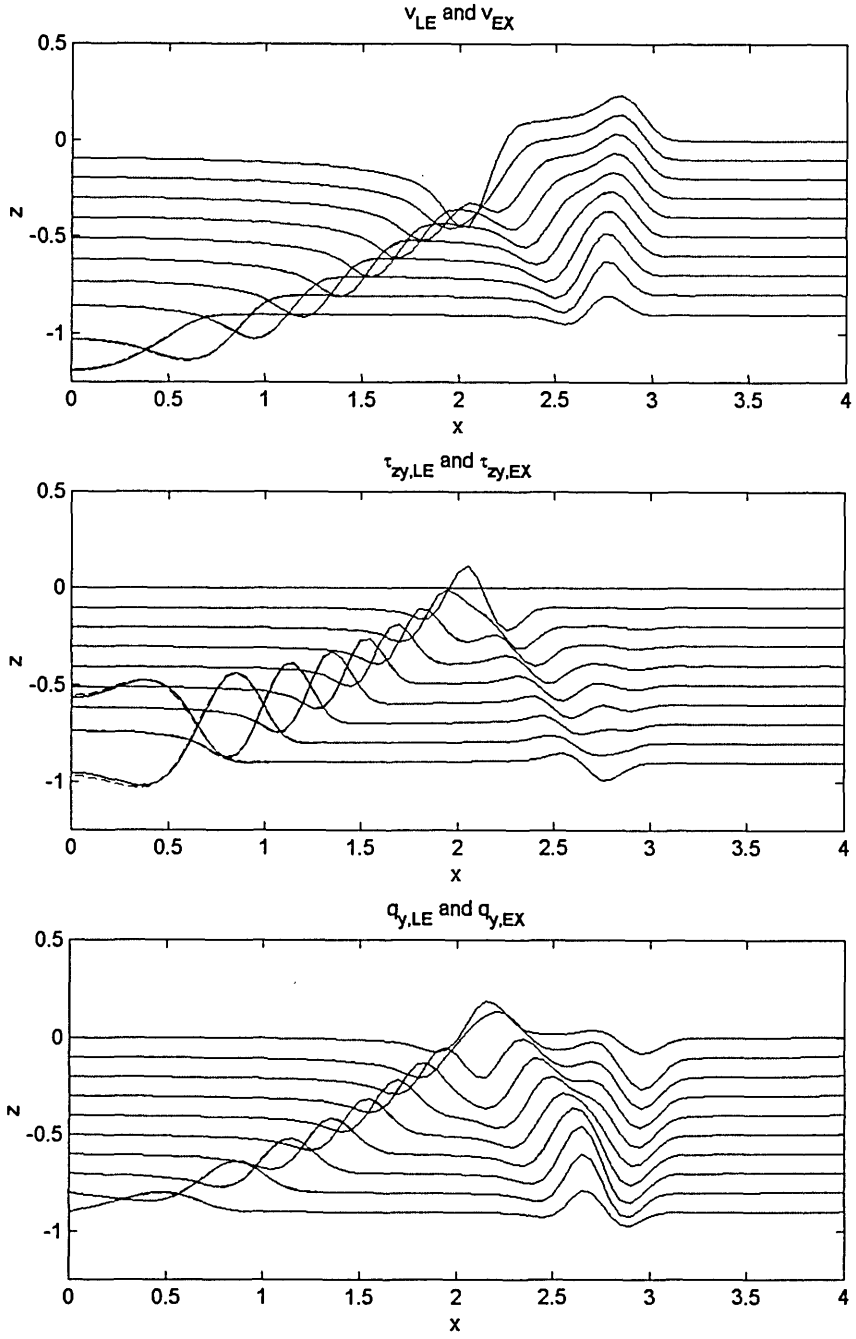

Figure 4.3.7 Snapshots of v, t_{zy}, q_y of homogeneous stratum obtained with TLM1 of N_λ=8 due to *SH* surface line load with a=t_d=0.2
(solid for TLM1; dashed for Exact analytical modal solution)

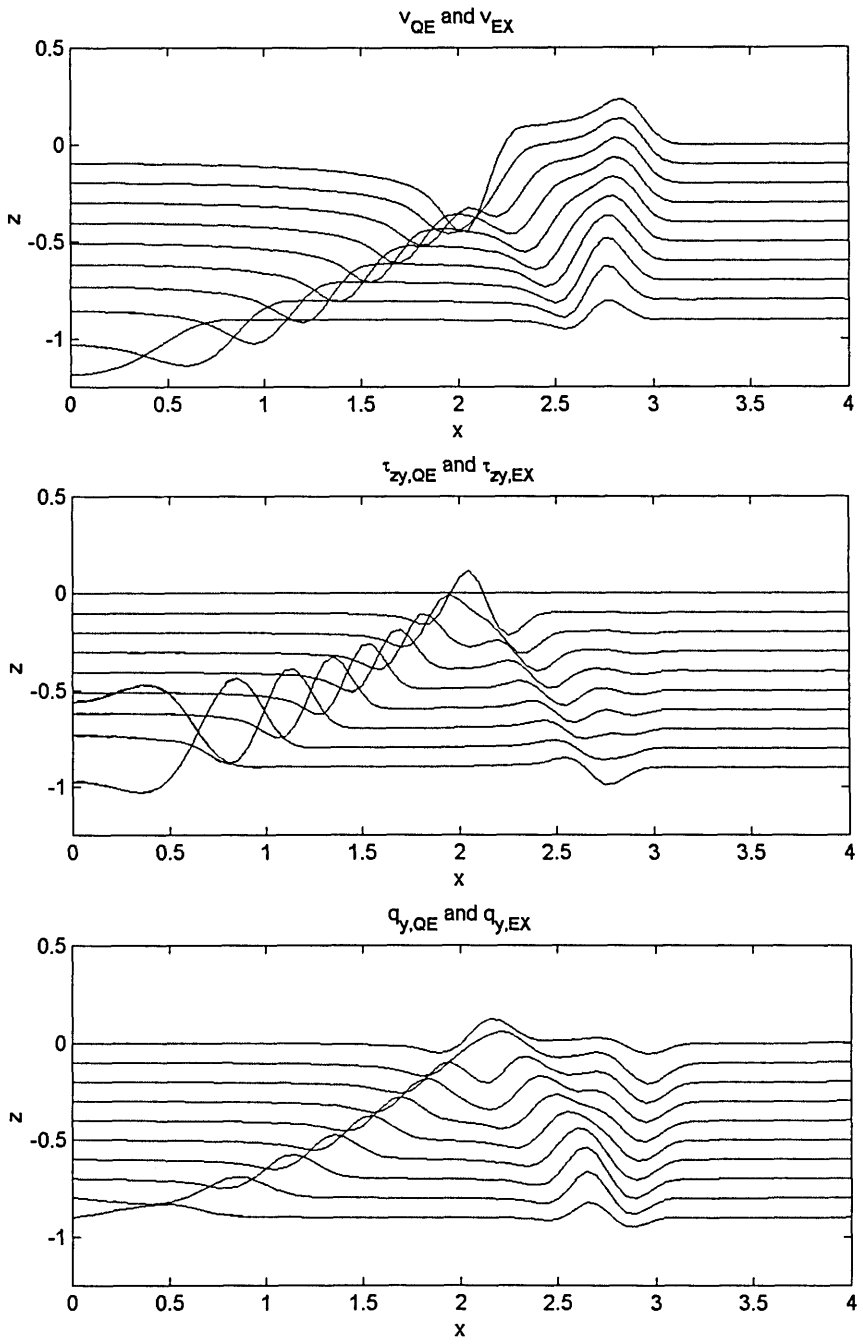

Figure 4.3.8 Snapshots of v, t_{zy}, q_y of homogeneous stratum obtained with TLM2 of N_λ=4 due to *SH* surface line load with a=t_d=0.2
(solid for TLM2; dashed for Exact analytical modal solution)

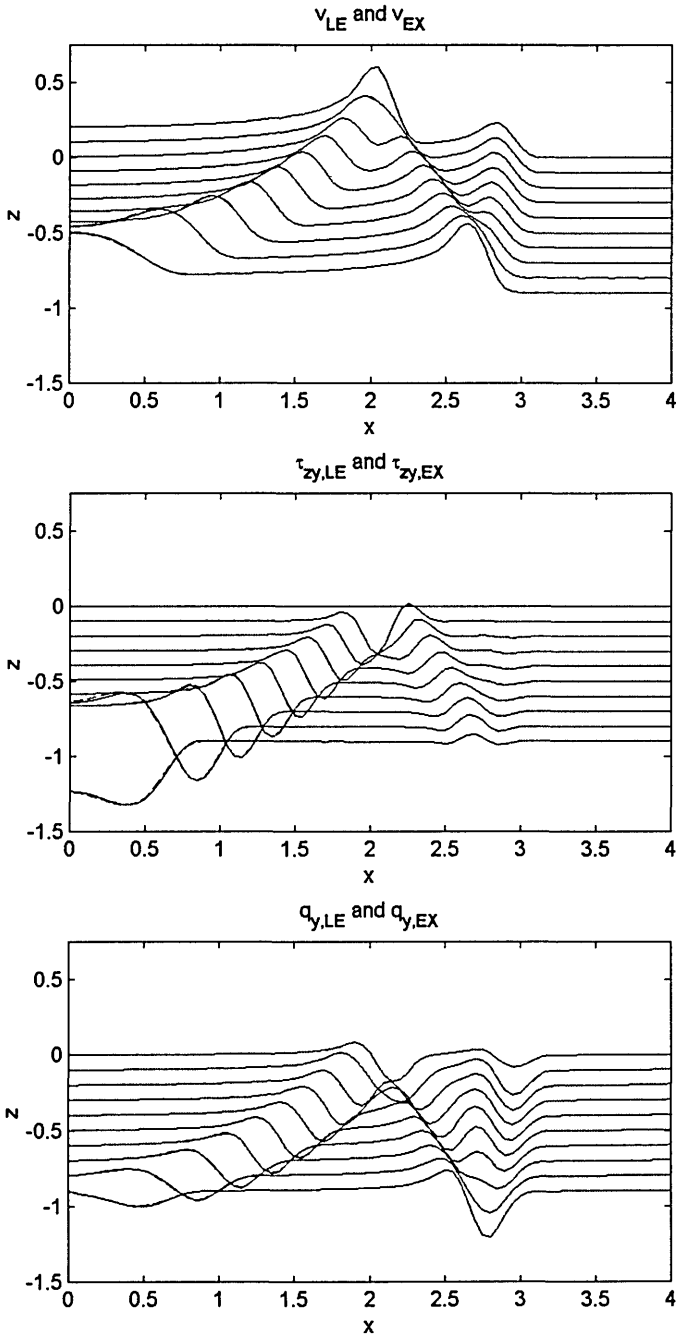

Figure 4.3.9 Snapshots of v, t_{zy}, q_y of homogeneous plate obtained with TLM1 of N_λ=8 due to *SH* surface line load with a=t_d=0.2
(solid for TLM1; dashed for Exact analytical modal solution)

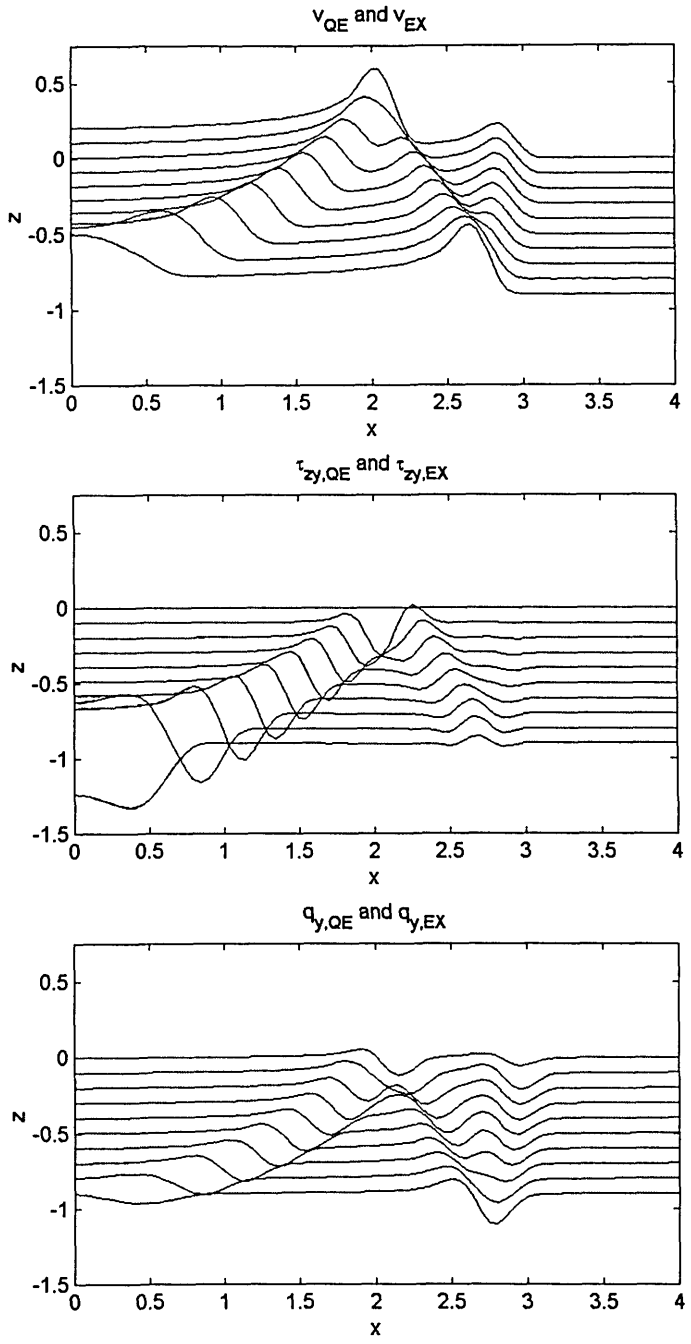

Figure 4.3.10 Snapshots of v, t_{zy}, q_y of homogeneous plate obtained with TLM2 of N_λ=4 due to *SH* surface line load with a=t_d=0.2
(solid for TLM2; dashed for Exact analytical modal solution)

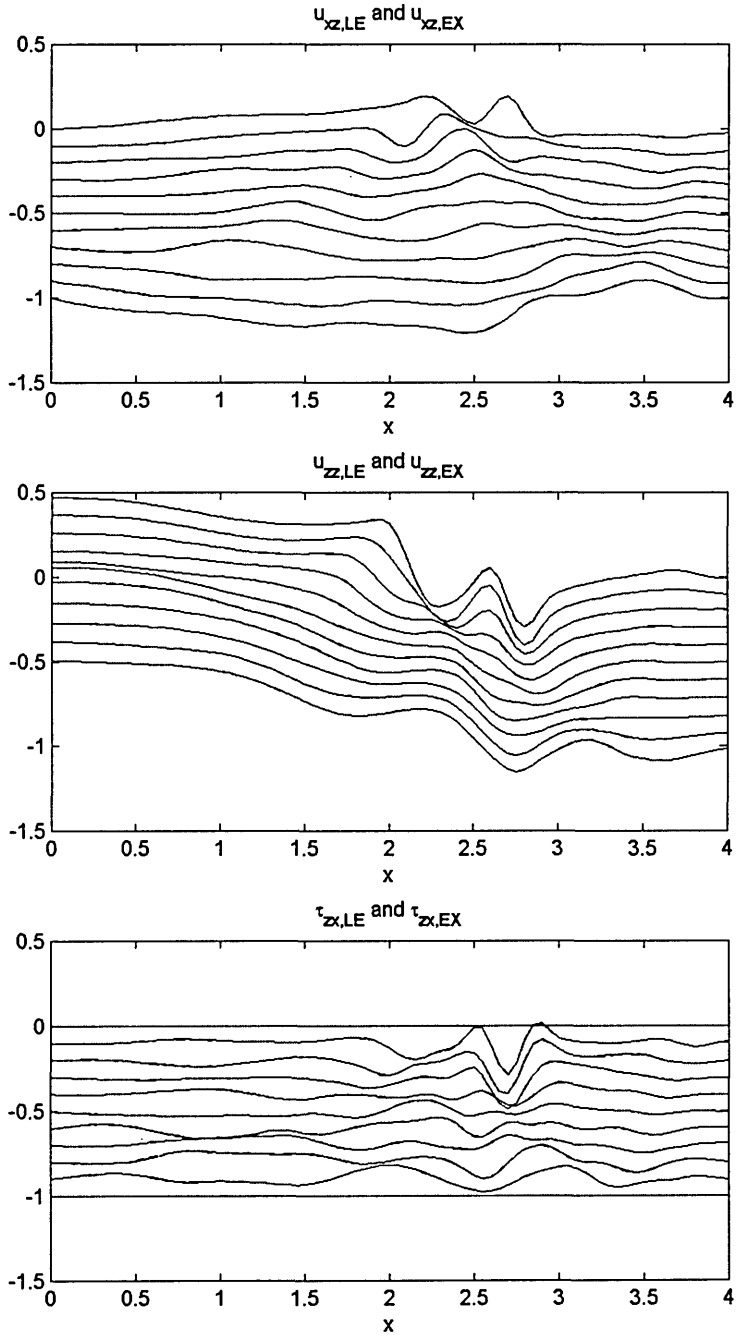

Figure 4.3.11a Snapshots of u_{xz}, u_{zz}, τ_{zx} of homogeneous plate obtained with TLM1 of N_λ=8 due to *SV-P* surface line load in vertical direction with $a=t_d$=0.2
(solid for TLM1; dashed for Exact analytical modal solution)

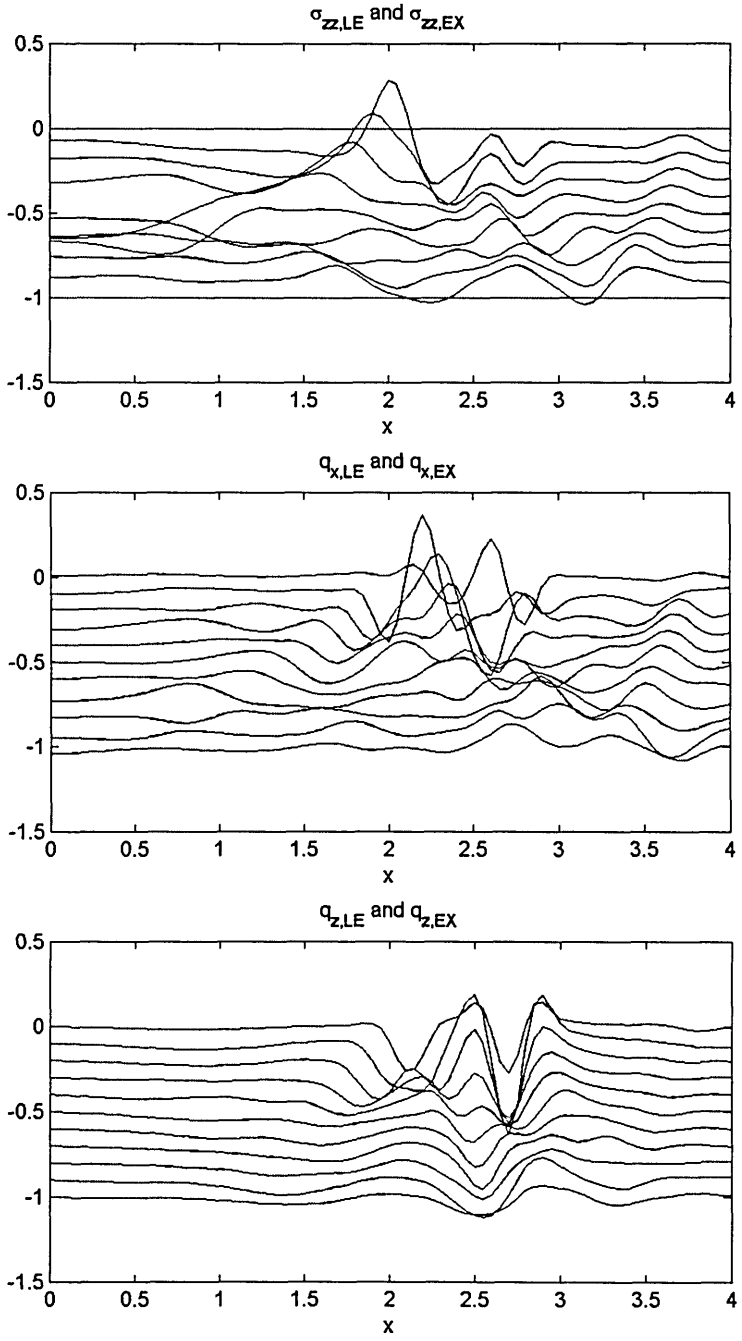

Figure 4.3.11b Snapshots of σ_{zz}, q_x, q_z of homogeneous plate obtained with TLM1 of N_λ=8 due to *SV-P* surface line load in vertical direction with $a=t_d$=0.2 (solid for TLM1; dashed for Exact analytical modal solution)

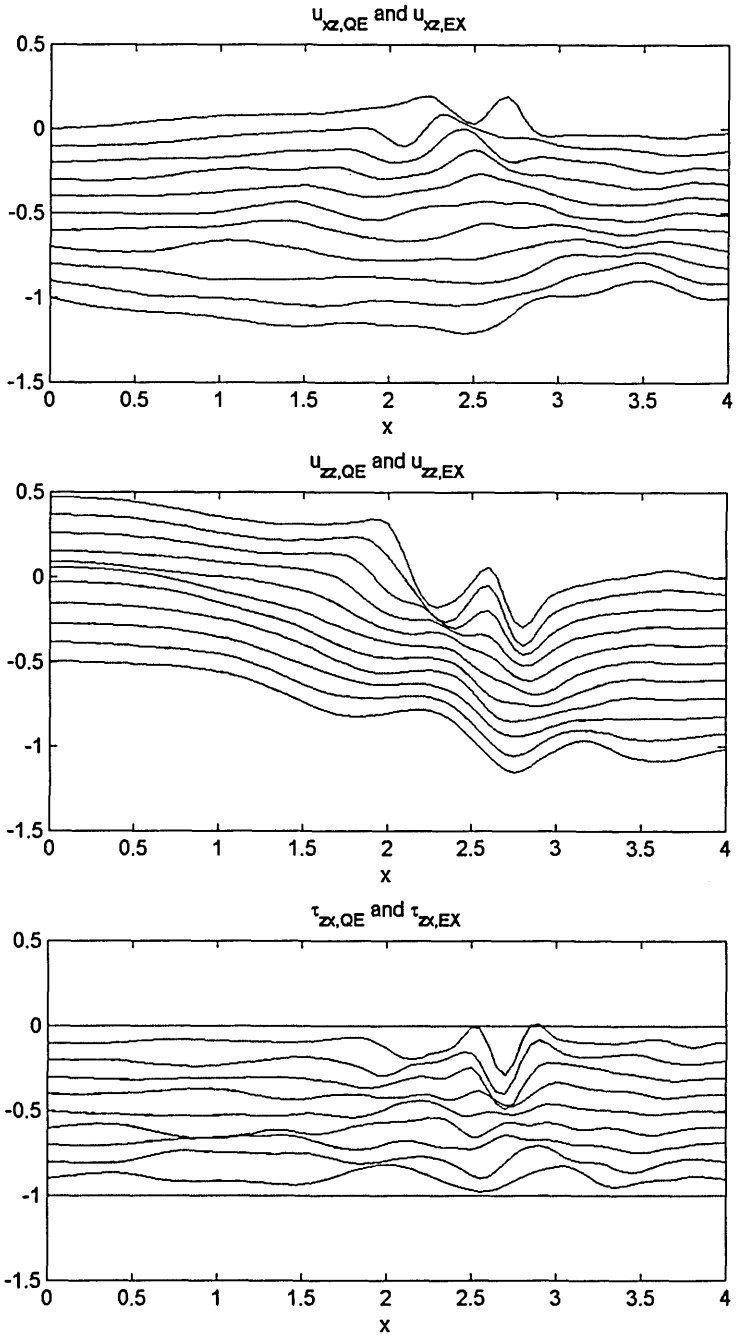

Figure 4.3.12a Snapshots of u_{xz}, u_{zz}, τ_{zx} of homogeneous plate obtained with TLM2 of N_λ=4 due to *SV-P* surface line load in vertical direction with $a=t_d$=0.2 (solid for TLM2; dashed for Exact analytical modal solution)

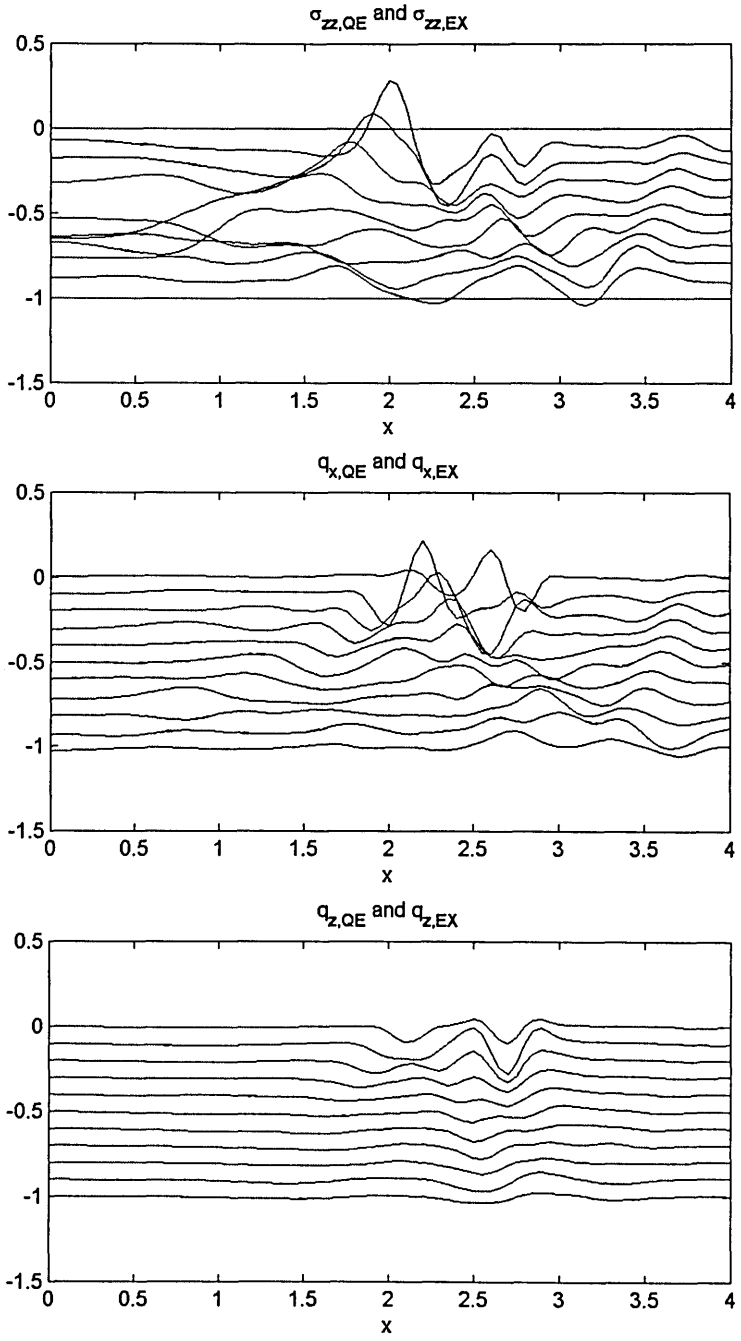

Figure 4.3.12b Snapshots of σ_{zz}, q_x, q_z of homogeneous plate obtained with TLM2 of N_λ=4 due to *SV-P* surface line load in vertical direction with a=t_d=0.2 (solid for TLM2; dashed for Exact analytical modal solution)

Appendix 4A: Image Source Method for *SH* wave problems

Here, we formulate the image source method for a homogeneous layer of thickness H subjected to *SH* line loads. Three types of boundary conditions are considered, namely "*free-free*", "*free-fixed*", and "*fixed-fixed*", where "*free*" and "*fixed*" refer to a boundary for stress-free and displacement-fixed conditions, respectively. We first obtain the solutions in the space-time domain, or x-t domain for short, by utilizing the Green function of a homogeneous full-space. Then, we obtain the solutions for both the space-frequency (x-ω) and wavenumber-time (k-t) domains simply by performing the Fourier transformations.

To formulate the image source method for the present problem, we first consider the ray paths of the multiply-reflected waves within the domain of interest as shown in figure 4A.1, where we apply a line load $p=\delta(x)\delta(z-z_s)\delta(t)$ and look at the response v at (x_m, z_m). The solid lines represent the paths of waves generated by the real source within the layer. On the other hand, the dashed lines express the paths of waves resulting from the associated image sources $S_{\pm i}$. For analysis, we have to determine two important factors which are the locations $z_{\pm i}$ and the polarization $f_{\pm i}$ of the image sources $S_{\pm i}$. From figure 4A.1, we can derive the following relationships for the locations of the image sources.

$$z_{\pm i} = z_s \pm 2[(m \pm n)U + mL] \tag{4A.1}$$

$$2m \pm n = i \tag{4A.2}$$

where i=1,2,3,..., m=0,1,2,... and n=0 or 1. In equation (4A.1), z_{+i} and z_{-i} are the coordinates of the i-th image source $S_{\pm i}$ along the positive and negative z-axes, respectively. According to equation (4A.2), the integers m and n can be uniquely determined for a given i. For example, for i=1, we obtain $z_{+1}= z_s+2[(0+1)U+0L]= z_s+2U$ with a set of m=0 and n=1, and $z_{-1}= z_s-2[(1-1)U+1L]= z_s-2L$ with a set of m=1 and n=1. The coefficients of $(m\pm n)$ and m in front of U and L represent the total number of reflections at the upper and lower boundary, respectively, along the associated ray paths within the layer. Therefore, we can determine the polarization according to these coefficients. In addition, since the sign of wave polarization reverses only if the boundary condition is "fixed", we can determine the polarization factor $f_{\pm i}$ as

$$f_{\pm i} = (1)^{m\pm n}(1)^m \qquad \text{for "}\textit{free-free}\text{"} \tag{4A.3a}$$

$$f_{\pm i} = (1)^{m\pm n}(-1)^m \qquad \text{for "}\textit{free-fixed}\text{"} \tag{4A.3b}$$

$$f_{\pm i} = (-1)^{m\pm n}(-1)^m \qquad \text{for "}\textit{fixed-fixed}\text{"} \tag{4A.3c}$$

Hence, we can write the image sources $S_{\pm i}$ of the form

$$S_{\pm i} = f_{\pm i}\delta(x)\delta(z - z_{\pm i})\delta(t) \tag{4A.4}$$

The exact Green function G_{yy} for a homogeneous full-space subjected to the line load $\delta(x)\delta(z)\delta(t)$ is well known, which is

$$G_{yy} = \frac{1}{2\pi}\frac{1}{\rho C_S^2}\frac{H(t-\tau)}{\sqrt{t^2-\tau^2}} \tag{4A.5a}$$

$$\tau = \frac{\sqrt{x^2+z^2}}{C_S} \tag{4A.5b}$$

where ρ and C_S are the mass density and shear wave speed, and H is Heaviside's unit step function. As shown in figure 4A.1, the solutions can be obtained by superimposing the responses due to both the real and associated image sources. So, we can express v in the x-t domain of the form

$$v(x,z,t)=\frac{1}{2\pi}\frac{1}{\rho C_S^2}\left[\frac{H(t-\tau_s)}{\sqrt{t^2-\tau_s^2}}+\sum_{i=1}^{\infty}f_{\pm i}\frac{H(t-\tau_{\pm i})}{\sqrt{t^2-\tau_{\pm i}^2}}\right] \tag{4A.6a}$$

$$\tau_s=\frac{r_s}{C_S}=\frac{\sqrt{x^2+(z-z_s)^2}}{C_S} \tag{4A.6b}$$

$$\tau_{\pm i}=\frac{r_{\pm i}}{C_S}=\frac{\sqrt{x^2+(z-z_{\pm i})^2}}{C_S} \tag{4A.6c}$$

where the first term in the bracket represents the response due to the real source, and the summation term due to the associated image sources $S_{\pm i}$.

Performing the following Fourier transformations, we obtain the responses in the x-ω and k-t domains, respectively, as

$$\begin{aligned}\tilde{v}(x,z,\omega)&=\int_{-\infty}^{\infty}v(x,z,t)e^{-i\omega t}dt\\&=-\frac{i}{4\rho C_S^2}\left[H_0^{(2)}\left(k_\beta r_s\right)+\sum_{i=1}^{\infty}f_{\pm i}H_0^{(2)}\left(k_\beta r_{\pm i}\right)\right]\end{aligned} \tag{4A.7a}$$

$$\begin{aligned}\hat{v}(k,z,t)&=\int_{-\infty}^{\infty}v(x,z,t)e^{ikx}dx\\&=\frac{1}{2\rho C_S}\left[J_0\left(kC_S\sqrt{t^2-\tau_{z,s}^2}\right)H(t-\tau_{z,s})+\sum_{i=1}^{\infty}f_{\pm i}J_0\left(kC_S\sqrt{t^2-\tau_{z,\pm i}^2}\right)H(t-\tau_{z,\pm i})\right]\end{aligned} \tag{4A.7b}$$

where $H_0^{(2)}$ is the second Hankel function of order 0, J_0 the first Bessel function of order 0, $k_\beta=\omega/C_S$, $\tau_{z,s}=(z-z_s)/C_S$, and $\tau_{z,\pm i}=(z-z_{\pm i})/C_S$.

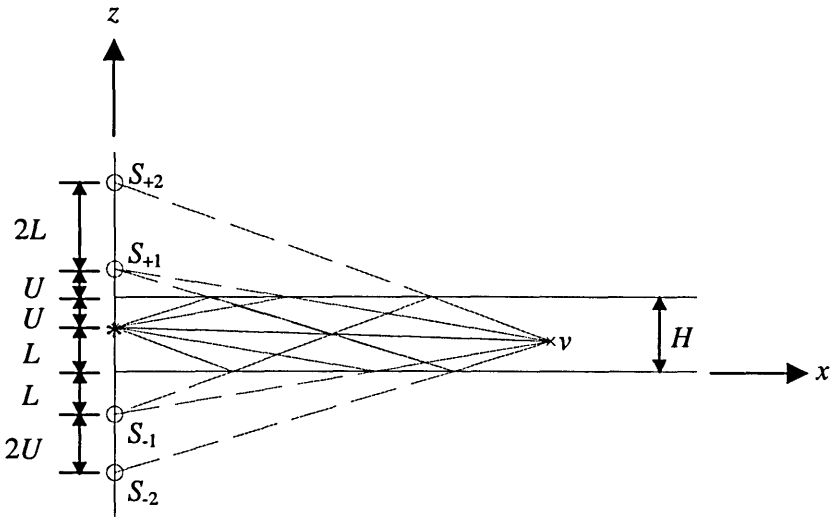

Figure 4A.1 Real and image sources, and associated ray paths

Appendix 4B: Homogeneous Plate subjected to *SH* Line Loads

We analyze a homogeneous plate subjected to *SH* line loads by means of the continuous modal superposition method. Through this example we explore the characteristics of TLM as well as the modal superposition method itself, because most of the involved procedures are similar in both of these methods. The plate model considered here can easily be changed into a homogenous stratum subjected to *SH* line loads, the formulas for which will be given later without any detailed derivation. We consider the formulations in both the frequency and time domains.

Consider a homogeneous plate of thickness H, subjected to a time-dependent excitation $b=b(x,z,t)$ (body force) shown in figure 4B.1. The equation of motion and the associated boundary conditions are

$$\rho\frac{\partial^2 v}{\partial t^2}-G\left[\frac{\partial^2 v}{\partial x^2}+\frac{\partial^2 v}{\partial z^2}\right]=b(x,z,t) \tag{4B.1a}$$

$$\tau_{yz}=0 \qquad \text{at } z=0,\text{-}H \tag{4B.1b}$$

Also,

$$v(x,z,t)=y \text{ direction displacement} \tag{4B.2a}$$

$$\tau_{yz}=G\gamma_{yz}=G\frac{\partial v}{\partial z}=\text{stress in horizontal planes} \tag{4B.2b}$$

$$\tau_{xy}=G\gamma_{xy}=G\frac{\partial v}{\partial x}=\text{stress in vertical planes} \tag{4B.2c}$$

In general, we may *assume* a solution of the form

$$v(x,z,t)=\frac{1}{(2\pi)^2}\int_{-\infty}^{\infty}d\omega\int_{-\infty}^{\infty}dk\ \ \bar{v}(k,z,\omega)e^{\mathrm{i}(\omega t-kx)} \tag{4B.3a}$$

$$\bar{v}(k,z,\omega)=\int_{-\infty}^{\infty}dt\int_{-\infty}^{\infty}dx\ \ v(x,z,t)e^{-\mathrm{i}(\omega t-kx)} \tag{4B.3b}$$

where we apply the dual Fourier transform to the time and spatial variable t and x. When we perform the inverse Fourier transform in eq. (4B.3a), however, we have difficulties due to infinite number of poles that produce singularities in the integral in eq. (4B.3a). To overcome this difficulty, we analyze this special plate by means of the modal superposition method. For this purpose, we need to analyze the homogeneous wave equation i.e., b=0 so as to obtain the normal modes of wave propagation.

$$\rho\frac{\partial^2 v}{\partial t^2}-G\left[\frac{\partial^2 v}{\partial x^2}+\frac{\partial^2 v}{\partial z^2}\right]=0 \tag{4B.4a}$$

with the boundary conditions

$$\tau_{yz}=0, \qquad \text{at } z=0 \text{ and } \text{-}H \tag{4B.4b}$$

As in the TLM, we have two choices to formulate the modal analysis: 1) *frequency domain* formulation and 2) *time domain* formulation. Each formulation has its own features, and we consider the response functions (displacements, v, and stresses, τ_{yz} and τ_{xy}) in both domains. Figure 4B.2 shows the dispersion curve for this plate. As seen in figure 4B.2, the dispersion curve has real and imaginary branches. The real branch represents the propagating modes, while the imaginary branch represents the non-propagating or *evanescent* modes.

(1) Modal superposition in the frequency domain for a plate

Assume a modal solution of the form

$$v = \phi_j(z) e^{i(\omega t - k_j x)} \tag{4B.5}$$

in which j is the modal index. In the frequency formulation, ω is the parameter and k_j is the eigenvalue. Substituting this assumed solution into eq. (4B.4a), we obtain

$$\phi_j'' + \beta_j^2 \phi_j = 0 \tag{4B.6}$$

with

$$\beta_j^2 = (\omega / C_S)^2 - k_j^2, \qquad C_S = \sqrt{\frac{G}{\rho}} \tag{4B.7ab}$$

Eq. (4B.6) has a general solution of the form

$$\phi_j(z) = A \cos \beta_j z + B \sin \beta_j z \tag{4B.8}$$

From the stress-free boundary conditions at the top and bottom, i.e., z=0, and $-H$, equation (4B.1b), we obtain

$$\phi'(0) = 0 \quad \Rightarrow \quad B = 0 \tag{4B.9a}$$

$$\phi'(-H) = 0 \quad \Rightarrow \quad \beta_j H = j\pi, \quad j = 0,1,2,\cdots \tag{4B.9b}$$

It follows that the eigenvalues is

$$k_j = \sqrt{(\omega / C_S)^2 - (j\pi / H)^2} \tag{4B.10}$$

The dispersion curve in figure 2 is based on eq. (4B.10) by means of the dimensionless frequency Ω and wavenumber ξ. The mode shapes are then

$$\phi_j(z) = \cos \frac{j\pi z}{H} \tag{4B.11}$$

This mode shape is not yet normalized, which will be accomplished after obtaining the modal equation in the next section.

Consider next a plate subjected to a line load with a given frequency ω at x=0, z=z_0. The equation of motion is now

$$\rho \frac{\partial^2 \tilde{v}}{\partial t^2} - G\left[\frac{\partial^2 \tilde{v}}{\partial x^2} + \frac{\partial^2 \tilde{v}}{\partial z^2}\right] = P(\omega)\delta(x)\delta(z - z_0) \tag{4B.12}$$

For this harmonic load, assume a solution of the form

$$\tilde{v}(x, z, \omega) = \sum_{j=0}^{\infty} \phi_j(z) f_j(x) e^{i\omega t} \tag{4B.13}$$

where we include the factor $e^{i\omega t}$ so as to carry out the differential operators with respect to t without any ambiguity. Introducing equation (4B.13) into equation (4B.12), we obtain

$$\sum_{j=0}^{\infty} \left[(-\rho\omega^2 + G\beta_j^2) f - G f_j''\right] \phi_j = P(\omega)\delta(z - z_0) \tag{4B.14}$$

We next pre-multiply by an arbitrary mode $\phi_l(z)$, and integrate with respect to z so as to take advantage of the orthogonality of the modes. On the left-hand side, this involves the integral

$$\int_{-H}^{0} \phi_l(z)\phi_j(z) dz = \begin{Bmatrix} 0 & j \neq l \\ H/2 & j = l \neq 0 \\ H & j = l = 0 \end{Bmatrix} \tag{4B.15}$$

while on the right-hand side, we have

$$\int_{-H}^{0} \phi_j(z)\delta(z-z_0)dz = \phi_j(z_0) \tag{4B.16}$$

Hence, the summation uncouples into

$$-GH(f_0'' + k_0^2 f_0) = P(\omega)\delta(x) \qquad \text{for } j=0 \tag{4B.17a}$$

$$-\frac{GH}{2}(f_j'' + k_j^2 f_j) = P(\omega)\delta(x)\phi_j(z_0) \qquad \text{for } j>0 \tag{4B.17b}$$

Equations (4B.17) are the modal equations. To solve these equations, we carry out a Fourier transform into the wavenumber domain. For $j>0$, we have

$$\frac{GH}{2}(k^2 - k_j^2)\bar{f}_j(k,z,\omega) = P(\omega)\phi_j(z_0) \tag{4B.18}$$

so that

$$\bar{f}_j(k) = \frac{2P(\omega)}{GH}\frac{1}{k^2-k_j^2}\phi_j(z_0) \tag{4B.19}$$

where we apply the Fourier transform of the form

$$f_j(x) = \frac{1}{2\pi}\int_{-\infty}^{\infty} dk\, e^{-ikx}\int_{-\infty}^{\infty} f_j(\xi)e^{ik\xi}d\xi$$

We invert this back into the spatial domain by means of the inverse Fourier transform

$$f_j(x) = \frac{1}{2\pi}\int_{-\infty}^{\infty}\bar{f}_j(k)e^{-ikx}dk = \frac{P(\omega)\phi_j(z_0)}{GH\pi}\int_{-\infty}^{\infty}\frac{1}{k^2-k_j^2}e^{-ikx}dk \tag{4B.20}$$

which evaluates to

$$f_j(x) = \frac{P(\omega)\phi_j(z_0)}{GH}\frac{e^{-ik_j|x|}}{ik_j} \qquad \text{Im}(k_j) < 0 \tag{4B.21}$$

A similar result holds for $j=0$, except for a factor ½. Finally, the modal solution is

$$\begin{aligned}\tilde{v}(x,z,\omega) &= \frac{P(\omega)}{iGH}\left[\frac{e^{-ik_0|x|}}{2k_0} + \sum_{j=1}^{\infty}\phi_j(z)\phi_j(z_0)\frac{e^{-ik_j|x|}}{k_j}\right] \\ &= \frac{P(\omega)}{iGH}\left[\frac{e^{-ik_0|x|}}{2k_0} + \sum_{j=1}^{\infty}\cos\frac{j\pi z}{H}\cos\frac{j\pi z_0}{H}\frac{e^{-ik_j|x|}}{k_j}\right]\end{aligned} \tag{4B.22}$$

In equation (4B.22), we omit the factor $e^{i\omega t}$. Notice that $iGk_0H = i\rho\omega C_s H$ can be interpreted as the impedance of a viscous dashpot. The stress components are expressed in the form

$$\begin{aligned}\tilde{\tau}_{yz}(x,z,\omega) = G\tilde{\gamma}_{yz} = G\frac{\partial\tilde{v}}{\partial z} &= \frac{P(\omega)}{iH}\left[\sum_{j=1}^{\infty}\frac{d\phi_j(z)}{dz}\phi_j(z_0)\frac{e^{-ik_j|x|}}{k_j}\right] \\ &= -\frac{P(\omega)}{iH}\left[\sum_{j=1}^{\infty}\frac{j\pi}{H}\sin\frac{j\pi z}{H}\cos\frac{j\pi z_0}{H}\frac{e^{-ik_j|x|}}{k_j}\right]\end{aligned} \tag{4B.23}$$

$$\begin{aligned}\tilde{\tau}_{xy}(x,z,\omega) = G\tilde{\gamma}_{xy} = G\frac{\partial\tilde{v}}{\partial x} &= \mp\frac{P(\omega)}{H}\left[\frac{1}{2}e^{-ik_0|x|} + \sum_{j=1}^{\infty}\phi_j(z)\phi_j(z_0)e^{-ik_j|x|}\right] \\ &= \mp\frac{P(\omega)}{H}\left[\frac{1}{2}e^{-ik_0|x|} + \sum_{j=1}^{\infty}\cos\frac{j\pi z}{H}\cos\frac{j\pi z_0}{H}e^{-ik_j|x|}\right]\end{aligned} \tag{4B.24}$$

(2) Modal superposition in the frequency domain for a stratum

A homogeneous stratum subjected to an *SH* line load has boundary conditions

$$\tau_{yz} = 0 \qquad \text{at } z=0 \tag{4B.25a}$$

$$v = 0 \qquad \text{at } z=-H \tag{4B.25b}$$

In conjunction with the differential equation, these boundary conditions produce eigenvalues eigenvectors (mode shapes) that differ from those of the plate, although the details are similar. For this reason, we omit the derivation here and just display the final results:

Eigenvalues k_j:

$$k_j = \sqrt{(\omega/C_S)^2 - [(j-1/2)\pi/H]^2}\,, \qquad j=1,2,3,\ldots \tag{4B.26a}$$

Eigenvector (mode shape) :

$$\phi_j(z) = \cos\frac{(j-1/2)\pi}{H}z \tag{4B.26b}$$

Displacements :

$$\tilde{v}(x,z,\omega) = \frac{P(\omega)}{\mathrm{i}GH}\sum_{j=1}^{\infty}\cos\frac{(j-1/2)\pi z}{H}\cos\frac{(j-1/2)\pi z_0}{H}\frac{e^{-\mathrm{i}k_j|x|}}{k_j} \tag{4B.27}$$

Stresses :

$$\tilde{\tau}_{yz}(x,z,\omega) = -\frac{P(\omega)}{\mathrm{i}H}\left[\sum_{j=1}^{\infty}\frac{(j-1/2)\pi}{H}\sin\frac{(j-1/2)\pi z}{H}\cos\frac{(j-1/2)\pi z_0}{H}\frac{e^{-\mathrm{i}k_j|x|}}{k_j}\right] \tag{4B.28}$$

$$\tilde{\tau}_{xy}(x,z,\omega) = \mp\frac{P(\omega)}{H}\left[\sum_{j=1}^{\infty}\cos\frac{(j-1/2)\pi z}{H}\cos\frac{(j-1/2)\pi z_0}{H}e^{-\mathrm{i}k_j|x|}\right] \tag{4B.29}$$

(3) Modal superposition in the time domain for a plate

Assume a modal solution of the form

$$v = \phi_j(z)e^{\mathrm{i}(\omega_j t - kx)} \tag{4B.30}$$

in which j is the modal index. In the frequency formulation, k is the parameter and ω_j is the eigenvalue. Substituting this assumed solution into eq. (4B.4a), we obtain

$$\phi_j'' + \beta_j^2\phi_j = 0 \tag{4B.31}$$

with

$$\beta_j^2 = (\omega_j/C_S)^2 - k^2, \qquad C_S = \sqrt{\frac{G}{\rho}} \tag{4B.32ab}$$

Eq. (4B.31) has a general solution of the form

$$\phi_j(z) = A\cos\beta_j z + B\sin\beta_j z \tag{4B.33}$$

From the stress-free boundary conditions at the top and bottom, i.e., z=0, and $-H$, we obtain

$$\phi'(0) = 0 \quad \Rightarrow \quad B = 0 \tag{4B.34a}$$

$$\phi'(-H) = 0 \quad \Rightarrow \quad \beta_j H = j\pi, \quad j = 0,1,2,\cdots \tag{4B.34b}$$

It follows that

$$\omega_j = C_S\sqrt{k^2 + (j\pi/H)^2} \tag{4B.35}$$

The dispersion curve in figure 2 is based on equation (4B.35) by means of the dimensionless frequency Ω and wavenumber ξ. The modal shapes are then

$$\phi_j(z) = \cos\frac{j\pi z}{H} \tag{4B.36}$$

This mode shape is not yet normalized, which will be done after finding the modal equation in the next section.

Consider next a plate subjected to a line load with a given wavenumber k at x=0, z=z_0. The equation of motion is now

$$\rho\frac{\partial^2\hat{v}}{\partial t^2} - G\left[\frac{\partial^2\hat{v}}{\partial x^2} + \frac{\partial^2\hat{v}}{\partial z^2}\right] = P(k)\delta(z-z_0)\delta(t) \tag{4B.37}$$

For this harmonic load, assume a solution of the form

$$\hat{v}(k,z,t) = \sum_{j=0}^{\infty}\phi_j(z)q_j(t)e^{-ikx} \tag{4B.38}$$

where we include the factor e^{-ikx} in order to carry out the differential operators with respect to x without any ambiguity. Introducing equation (4B.38) into equation (4B.37), we obtain

$$\sum_{j=0}^{\infty}\left[\rho\ddot{q}_j + G(\beta_j^2 + k^2)q\right]\phi_j = P(k)\delta(z-z_0)\delta(t) \tag{4B.39}$$

$$\sum_{j=0}^{\infty}\rho[\ddot{q}_j + \omega_j^2 q_j]\phi_j = P(k)\delta(z-z_0)\delta(t) \tag{4B.39'}$$

We pre-multiply by an arbitrary mode $\phi_l(z)$, and integrate with respect to z so as to take advantage of orthogonality of the modes. On the left-hand side, this involves the integral

$$\int_{-H}^{0}\phi_l(z)\phi_j(z)dz = \begin{Bmatrix} 0 & j\neq l \\ H/2 & j=l\neq 0 \\ H & j=l=0 \end{Bmatrix} \tag{4B.40}$$

while on the right-hand side, we have

$$\int_{-H}^{0}\phi_j(z)\delta(z-z_0)dz = \phi_j(z_0) \tag{4B.41}$$

Hence, the summation uncouples into

$$-\rho H(\ddot{q}_0 + \omega_0^2 q_0) = P(k)\delta(t) \qquad \text{for } j=0 \tag{4B.42a}$$

$$-\frac{\rho H}{2}(\ddot{q}_j + \omega_j^2 q_j) = P(k)\delta(t)\phi_j(z_0) \qquad \text{for } j>0 \tag{4B.42b}$$

Equations (4B.42) are the modal equations. To solve these equations, we carry out a Fourier transform into the frequency domain. For $j > 0$, we have

$$\frac{\rho H}{2}(\omega_j^2 - \omega^2)\bar{q}_j(\omega) = P(k)\phi_j(z_0) \tag{4B.43}$$

so that

$$\bar{q}_j(\omega) = \frac{2P(k)}{\rho H}\frac{1}{\omega_j^2 - \omega^2}\phi_j(z_0) \tag{4B.44}$$

where we apply the Fourier transform of the form

$$q_j(t) = \frac{1}{2\pi}\int_{-\infty}^{\infty}d\omega e^{i\omega t}\int_{-\infty}^{\infty}q_j(\tau)e^{-i\omega\tau}d\tau$$

We invert this back into the time domain by means of the inverse Fourier transform

$$q_j(t)=\frac{1}{2\pi}\int_{-\infty}^{\infty}\bar{q}_j(k,z,\omega)e^{i\omega t}d\omega=\frac{P(k)\phi_j(z_0)}{\rho H\pi}\int_{-\infty}^{\infty}\frac{1}{\omega_j^2-\omega^2}e^{i\omega t}d\omega \tag{4B.45}$$

which evaluates to

$$q_j(t)=\frac{2P(k)\phi_j(z_0)}{\rho H}\frac{\sin\omega_j t}{\omega_j} \tag{4B.46}$$

A similar result holds for $j = 0$, except for a factor ½. Finally, the modal solution is

$$\begin{aligned}\hat{v}(k,z,t)&=\frac{2P(k)}{\rho H}\left[\frac{1}{2}\frac{\sin\omega_0 t}{\omega_0}+\sum_{j=1}^{\infty}\phi_j(z)\phi_j(z_0)\frac{\sin\omega_j t}{\omega_j}\right]\\&=\frac{2P(k)}{\rho H}\left[\frac{1}{2}\frac{\sin\omega_0 t}{\omega_0}+\sum_{j=1}^{\infty}\cos\frac{j\pi z}{H}\cos\frac{j\pi z_0}{H}\frac{\sin\omega_j t}{\omega_j}\right]\end{aligned} \tag{4B.47}$$

In equation (4B.47), we omit the factor e^{-ikx}. The stress components are expressed of the form

$$\begin{aligned}\hat{\tau}_{yz}(k,z,t)=G\hat{\gamma}_{yz}=G\frac{\partial\hat{v}}{\partial z}&=\frac{2GP(k)}{\rho H}\left[\sum_{j=1}^{\infty}\frac{d\phi_j(z)}{dz}\phi_j(z_0)\frac{\sin\omega_j t}{\omega_j}\right]\\&=-\frac{2GP(k)}{\rho H}\left[\sum_{j=1}^{\infty}\frac{j\pi}{H}\sin\frac{j\pi z}{H}\cos\frac{j\pi z_0}{H}\frac{\sin\omega_j t}{\omega_j}\right]\end{aligned} \tag{4B.48}$$

$$\begin{aligned}\hat{\tau}_{xy}(k,z,t)=G\hat{\gamma}_{xy}=G\frac{\partial\hat{v}}{\partial x}&=-ik\frac{2GP(k)}{\rho H}\left[\frac{1}{2}\frac{\sin\omega_0 t}{\omega_0}+\sum_{j=1}^{\infty}\phi_j(z)\phi_j(z_0)\frac{\sin\omega_j t}{\omega_j}\right]\\&=-ik\frac{2GP(k)}{\rho H}\left[\frac{1}{2}\frac{\sin\omega_0 t}{\omega_0}+\sum_{j=1}^{\infty}\cos\frac{j\pi z}{H}\cos\frac{j\pi z_0}{H}\frac{\sin\omega_j t}{\omega_j}\right]\end{aligned} \tag{4B.49}$$

The final step in this formulation is to invert the quantities from the wavenumber domain into the spatial domain. For example, the displacement v is obtained by

$$v(x,z,t)=\frac{1}{2\pi}\int_{-\infty}^{\infty}\hat{v}(k,z,t)e^{-ikx}dk \tag{4B.50}$$

(4) Modal superposition in the time domain for a stratum

A homogeneous stratum subjected to an *SH* line load has boundary conditions

$\tau_{yz}=0$ at z=0 (4B.51a)

$v=0$ at z=-H (4B.51b)

Because of the similarity with the plate case, we omit a detailed derivation here and just display the final results, i.e. eigenvalues, mode shapes, displacement and stresses:

Eigenvalues ω_j:

$$\omega_j=C_S\sqrt{k^2+[(j-1/2)\pi/H]^2}\,, \qquad j=1,2,3,\ldots \tag{4B.52a}$$

Eigenvector (mode shape) :

$$\phi_j(z)=\cos\frac{(j-1/2)\pi}{H}z \tag{4B.52b}$$

Displacements :

$$\hat{v}(k,z,t)=\frac{2P(k)}{\rho H}\sum_{j=1}^{\infty}\cos\frac{(j-1/2)\pi z}{H}\cos\frac{(j-1/2)\pi z_0}{H}\frac{\sin\omega_j t}{\omega_j} \tag{4B.53}$$

Stresses :

$$\hat{\tau}_{yz}(k,z,t)=-\frac{2GP(k)}{\rho H}\sum_{j=1}^{\infty}\frac{(j-1/2)\pi}{H}\sin\frac{(j-1/2)\pi z}{H}\cos\frac{(j-1/2)\pi z_0}{H}\frac{\sin\omega_j t}{\omega_j} \tag{4B.54}$$

$$\hat{\tau}_{xy}(k,z,t)=-\mathrm{i}k\frac{2GP(k)}{\rho H}\sum_{j=1}^{\infty}\cos\frac{(j-1/2)\pi z}{H}\cos\frac{(j-1/2)\pi z_0}{H}\frac{\sin\omega_j t}{\omega_j} \tag{4B.55}$$

Figures for appendix 4B

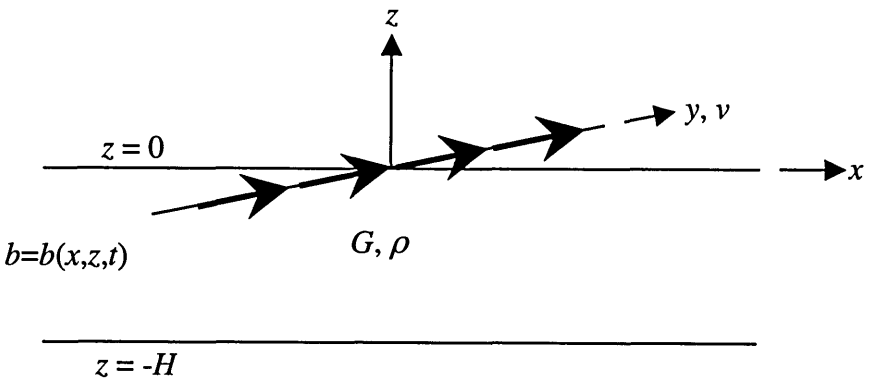

Figure 4B.1 Homogeneous plate of thickness H subjected to SH source b

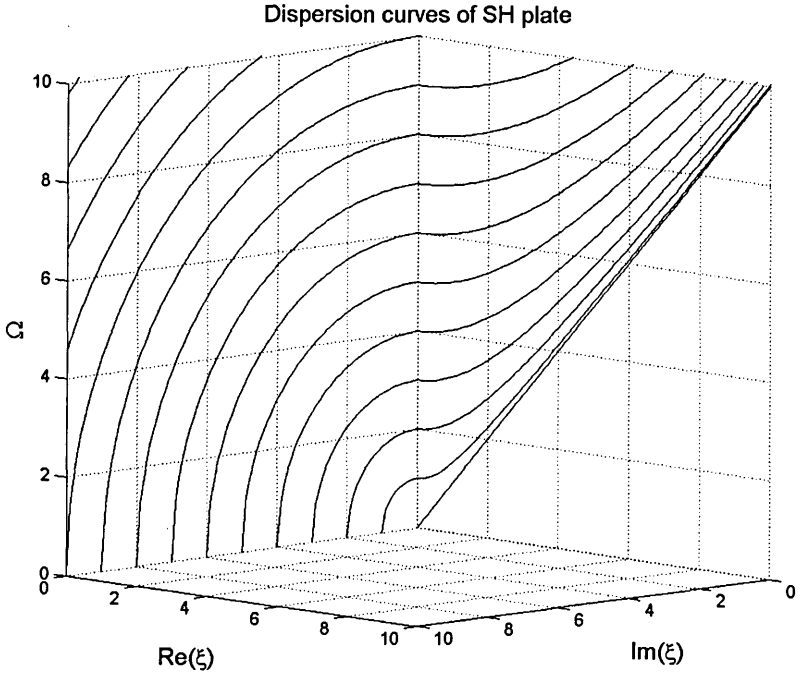

Figure 4B.2 Dispersion curve of SH homogeneous plate
($\Omega \equiv \omega H/C_S\pi$, $\xi \equiv kH/\pi$)

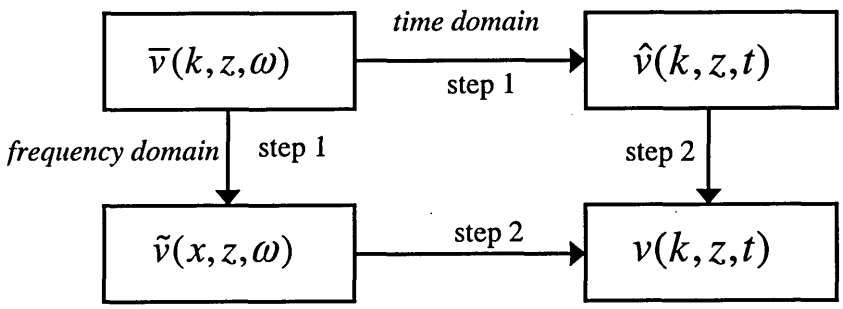

Figure 4B.3 Analysis procedures of frequency- and time-domain formulations

Appendix 4C: Homogeneous Plate subjected to *SV-P* Line Loads

We consider a homogeneous plate subjected to *SV-P* line loads as shown in figure 4C.1. We seek the associated modal solutions formulated in both the x-ω and k-t domains. The equation of motion and boundary conditions are given by

$$\rho\ddot{\mathbf{u}} - \mathbf{L}^T\mathbf{D}\mathbf{L}\mathbf{u} = \mathbf{b} \qquad \text{in } -\infty < x < \infty \text{ and } -b \le z \le b \tag{4C.1a}$$

$$\tau_{xz} = \sigma_z = 0 \qquad \text{at } z = \pm b \tag{4C.1b}$$

where ρ is the mass density, the superscript dot represents the partial derivative with respect to time t,

$$\mathbf{u} = \{u \quad w\}^T \qquad \text{(displacement vector)} \tag{4C.1c}$$

$$\mathbf{b} = \{b_x \quad b_z\}^T \qquad \text{(body force vector: line loads in this study)} \tag{4C.1d}$$

$$\mathbf{D} = \begin{Bmatrix} \lambda+2G & \lambda & \cdot \\ \lambda & \lambda+2G & \cdot \\ \cdot & \cdot & G \end{Bmatrix} \qquad \text{(constitutive matrix, symmetric)} \tag{4C.1e}$$

$$\mathbf{L} = \mathbf{L}_x\frac{\partial}{\partial x} + \mathbf{L}_z\frac{\partial}{\partial z} \qquad \text{(differential operator)} \tag{4C.1f}$$

$$\mathbf{L}_x = \begin{Bmatrix} 1 & \cdot & \cdot \\ \cdot & \cdot & 1 \end{Bmatrix}^T, \text{ and } \mathbf{L}_z = \begin{Bmatrix} \cdot & \cdot & 1 \\ \cdot & 1 & \cdot \end{Bmatrix}^T \tag{4C.1g,h}$$

We expand equation (4C.1a) and equation (4C.1b) in more explicit form to obtain

$$\mathbf{M}\ddot{\mathbf{u}} - \left[\mathbf{D}_{xx}\frac{\partial^2}{\partial x^2} + (\mathbf{D}_{xz}+\mathbf{D}_{zx})\frac{\partial^2}{\partial x\partial z} + \mathbf{D}_{zz}\frac{\partial^2}{\partial z^2}\right]\mathbf{u} = \mathbf{b} \tag{4C.2a}$$

$$\begin{Bmatrix} \tau_{xz} \\ \sigma_z \end{Bmatrix} = \left[\mathbf{D}_{zx}\frac{\partial}{\partial x} + \mathbf{D}_{zz}\frac{\partial}{\partial z}\right]\mathbf{u} \tag{4C.2b}$$

where

$$\mathbf{M} = \begin{Bmatrix} \rho & \cdot \\ \cdot & \rho \end{Bmatrix}, \quad \mathbf{D}_{xx} = \begin{Bmatrix} \lambda+2G & \cdot \\ \cdot & G \end{Bmatrix}, \quad \mathbf{D}_{xz} = \mathbf{D}_{zx}^T = \begin{Bmatrix} \cdot & \lambda \\ G & \cdot \end{Bmatrix}, \quad \mathbf{D}_{zz} = \begin{Bmatrix} G & \cdot \\ \cdot & \lambda+2G \end{Bmatrix} \tag{4C.2e-f}$$

The constants λ and G are referred to as the *Lamé*'s constants. Also, the associated (reduced) from the three dimensional problem) constitutive law and infinitesimal strains are given of the form

$$\boldsymbol{\sigma} = \mathbf{D}\boldsymbol{\varepsilon} \tag{4C.3a}$$

$$\boldsymbol{\varepsilon} = \mathbf{L}\mathbf{u} \tag{4C.3b}$$

where $\boldsymbol{\sigma} = \{\sigma_x \quad \sigma_z \quad \tau_{zx}\}^T$ and $\boldsymbol{\varepsilon} = \{\varepsilon_x \quad \varepsilon_z \quad \gamma_{zx}\}^T$ are the stress vector and the strain vector, respectively.

(1) General solutions in the *k*-ω domain

Since we seek the free vibration modes in the plate, we set **b=0** in equation (4C.1a) or equation (4C.2a) and assume the general solution to be of the form

$$\mathbf{u} = \begin{Bmatrix} \bar{u}(z) \\ \bar{w}(z) \end{Bmatrix} e^{\mathrm{i}(\omega t - kx)} \tag{4C.4}$$

Substitution of equation (4C.4) into equations (4C.2ab) provides

$$\left[k^2 \mathbf{D}_{xx} + \mathrm{i}k\left(\mathbf{D}_{xz} + \mathbf{D}_{zx}\right)\frac{d}{dz} - \mathbf{D}_{zz}\frac{d^2}{dz^2} - \omega^2 \mathbf{M} \right] \bar{\mathbf{u}} = \mathbf{0} \tag{4C.5a}$$

$$\begin{Bmatrix} \bar{\tau}_{xz} \\ \bar{\sigma}_z \end{Bmatrix} = \left[\mathbf{D}_{zx}(-\mathrm{i}k) + \mathbf{D}_{zz}\frac{d}{dz} \right] \mathbf{u} \tag{4C.5b}$$

Since the general solution for this problem is well known, it is presented here without any detailed derivation.

For non-zero frequency ($\omega \neq 0$):

$$\bar{u}(z) = A\cos\alpha z + B\sin\alpha z + C\cos\beta z + D\sin\beta z \tag{4C.6a}$$

$$\mathrm{i}\bar{w}(z) = \frac{\alpha}{k}[A\sin\alpha z - B\cos\alpha z] + \frac{k}{\beta}[-C\sin\beta z + D\cos\beta z] \tag{4C.6b}$$

$$\mathrm{i}\bar{\sigma}_x = (k + \beta^2/k - 2\alpha^2/k)G[A\cos\alpha z + B\sin\alpha z] + 2kG[C\cos\beta z + D\sin\beta z] \tag{4C.6c}$$

$$\mathrm{i}\bar{\sigma}_z = -\left(k - \beta^2/k\right)G[A\cos\alpha z + B\sin\alpha z] - 2kG[C\cos\beta z + D\sin\beta z] \tag{4C.6d}$$

$$\bar{\tau}_{xz} = 2\alpha G[-A\sin\alpha z + B\cos\alpha z] + \left(\beta - k^2/\beta\right)G[-C\sin\beta z + D\cos\beta z] \tag{4C.6e}$$

For zero frequency ($\omega = 0$):

$$\bar{u}(z) = A\cosh kz + B\sinh kz + Cz\sinh kz + Dz\cosh kz \tag{4C.7a}$$

$$\mathrm{i}\bar{w}(z) = -A\sinh kz - B\cosh kz + C[\kappa/k\sinh kz - z\cosh kz] + D[\kappa/k\cosh kz - z\sinh kz] \tag{4C.7b}$$

$$\mathrm{i}\bar{\sigma}_x = 2kG[A\cosh kz + B\sinh kz] + C[2Gkz\sinh kz + \lambda(\kappa-1)\cosh kz] + D[2Gkz\cosh kz + \lambda(\kappa-1)\sinh kz] \tag{4C.7c}$$

$$\mathrm{i}\bar{\sigma}_z = -2kG[A\cosh kz + B\sinh kz] + C[(\lambda+2G)(\kappa-1)\cosh kz - 2Gkz\sinh kz] + D[(\lambda+2G)(\kappa-1)\sinh kz - 2Gkz\cosh kz] \tag{4C.7d}$$

$$\bar{\tau}_{xz} = 2kG[A\sinh kz + B\cosh kz] + C[-(\kappa-1)\sinh kz + 2kz\cosh kz] + D[-(\kappa-1)\cosh kz + 2kz\sinh kz] \tag{4C.7e}$$

where A, B, C, D are the unknown constants, $\alpha = \sqrt{(\omega/C_P)^2 - k^2}$, $\beta = \sqrt{(\omega/C_S)^2 - k^2}$, and $\kappa = 3 - 4\nu$.

For simplicity in our analysis, we distinguish between symmetric and anti-symmetric modes. Equations (4C.6) for the non-zero frequency are thus separated into the following:

Symmetric mode ($\omega \neq 0$):

$$\bar{u}(z) = A\cos\alpha z + C\cos\beta z \tag{4C.8a}$$

$$\bar{w}(z) = -\mathrm{i}\left(A\frac{\alpha}{k}\sin\alpha z - C\frac{k}{\beta}\sin\beta z \right) \tag{4C.8b}$$

Anti-Symmetric mode ($\omega \neq 0$):

$$\bar{u}(z) = B\sin\alpha z + D\sin\beta z \tag{4C.9a}$$

$$\bar{w}(z) = \mathrm{i}\left(B\frac{\alpha}{k}\cos\alpha z - D\frac{k}{\beta}\cos\beta z\right) \tag{4C.9b}$$

We can write the corresponding expressions for the zero frequency case as

Symmetric mode ($\omega = 0$):

$$\bar{u}(z) = A\cosh kz + Cz\sinh kz \tag{4C.10a}$$

$$\bar{w}(z) = \mathrm{i}\left(A\sinh kz - C[\kappa/k\sinh kz - z\cosh kz]\right) \tag{4C.10b}$$

Anti-Symmetric mode ($\omega = 0$):

$$\bar{u}(z) = B\sinh kz + Dz\cosh kz \tag{4C.11a}$$

$$\bar{w}(z) = \mathrm{i}\left(B\cosh kz - D[\kappa/k\cosh kz - z\sinh kz]\right) \tag{4C.11b}$$

Substitution of equations (4C.8-11) into the boundary conditions in equation (4C.1b) or equation (4C.2b) yields the spectrum equations F's and the associated mode shapes φ as follows:

Symmetric mode ($\omega \neq 0$):

$$F(k,\omega) = 4k\alpha\sin\alpha b\cos\beta b - (k^2-\beta^2)(\beta/k - k/\beta)\cos\alpha b\sin\beta b = 0 \tag{4C.12a}$$

$$\varphi = \begin{Bmatrix}\varphi_x\\ \varphi_z\end{Bmatrix} = \begin{Bmatrix}\cos\alpha z + R\cos\beta z\\ -\mathrm{i}\left(\frac{\alpha}{k}\sin\alpha z - R\frac{k}{\beta}\sin\beta z\right)\end{Bmatrix} \tag{4C.12b}$$

$$R = \frac{C}{A} = -\frac{2\alpha\sin\alpha b}{(\beta - k^2/\beta)\sin\beta b} = \frac{(\beta^2/k - k)\cos\alpha b}{2k\cos\beta b} \tag{4C.12c}$$

Anti-Symmetric mode ($\omega \neq 0$):

$$F(k,\omega) = -4k\alpha\cos\alpha b\sin\beta b + (k^2-\beta^2)(\beta/k - k/\beta)\sin\alpha b\cos\beta b = 0 \tag{4C.13a}$$

$$\varphi = \begin{Bmatrix}\varphi_x\\ \varphi_z\end{Bmatrix} = \begin{Bmatrix}\sin\alpha z + R\sin\beta z\\ \mathrm{i}\left(\frac{\alpha}{k}\cos\alpha z - R\frac{k}{\beta}\cos\beta z\right)\end{Bmatrix} \tag{4C.13b}$$

$$R = \frac{D}{B} = -\frac{2\alpha\cos\alpha b}{(\beta - k^2/\beta)\cos\beta b} = \frac{(\beta^2/k - k)\sin\alpha b}{2k\sin\beta b} \tag{4C.13c}$$

Symmetric mode ($\omega = 0$):

$$F(k) = 2\sinh kb\cosh kb + 2kb = 0 \tag{4C.14a}$$

$$\varphi = \begin{Bmatrix}\varphi_x\\ \varphi_z\end{Bmatrix} = \begin{Bmatrix}\cosh kz + Rz\sinh kz\\ \mathrm{i}\left(\sinh kz - R(\frac{\kappa}{k}\sinh kz - z\cosh kz)\right)\end{Bmatrix} \tag{4C.14b}$$

$$R = \frac{C}{A} = -\frac{2k\sinh kb}{(1-\kappa)\sinh kb + 2kb\cosh kb} \tag{4C.14c}$$

Anti-Symmetric mode (ω=0):

$$F(k) = 2\sinh kb\cosh kb - 2kb = 0 \tag{4C.15a}$$

$$\varphi = \begin{Bmatrix} \varphi_x \\ \varphi_z \end{Bmatrix} = \begin{Bmatrix} \sinh kz + Rz\cosh kz \\ \mathrm{i}\left(\cosh kz - R(\frac{\kappa}{k}\cosh kz - z\sinh kz)] \right) \end{Bmatrix} \tag{4C.15b}$$

$$R = \frac{D}{B} = -\frac{2k\cosh kb}{(1-\kappa)\cosh kb + 2kb\sinh kb} \tag{4C.15c}$$

There is an interesting observation, perhaps not known yet, that the *eigenvalues* for the above spectrum equations for zero frequency are *independent* of Poisson's ratio ν. Hence, once we solve equations (4C.14a) and (4C.15a), we can apply the found eigenvalues to a material with any arbitrary ν. However, the associated mode shapes in equations (4C.14bc) and (4C.15bc) do depend on Poisson's ratio, so the final response is indeed a function of this ratio.

The 3-D plots in figures 4C.2a and C.2b display the dispersion curves for the symmetric modes and the anti-symmetric modes, respectively, for a plate with ρ=1.0, C_S=1.0, ν=0.31, and H=1.0.

(2) Modal superposition in the *x*-ω domain

We begin with three orthogonality conditions that are essential in determining the participation factors in our modal superposition. For this purpose, we first write the expressions for the field equation and the boundary conditions in terms of the eigenvalues and eigenvectors as

$$k_j^2\mathbf{D}_{xx}\boldsymbol{\phi}_j + \mathrm{i}k_j\left(\mathbf{D}_{xz} + \mathbf{D}_{zx}\right)\boldsymbol{\phi}_j' - \mathbf{D}_{zz}\boldsymbol{\phi}_j'' - \omega^2\mathbf{M}\boldsymbol{\phi}_j = \mathbf{0} \tag{4C.16a}$$

$$\left[-\mathrm{i}k_j\mathbf{D}_{zx}\boldsymbol{\phi}_j + \mathbf{D}_{zz}\boldsymbol{\phi}_j'\right]_{z=\pm b} = \mathbf{0} \tag{4C.16b}$$

where primes denote derivatives with respect to z, and $\boldsymbol{\phi}_j$ is the normalized eigenvector that is proportional to $\boldsymbol{\varphi}_j$ in equations (4C.12-15) by the j-th normalization constant. Also, the equations associated with the adjoined vector $\tilde{\boldsymbol{\phi}}_i = \{-\phi_{ix} \quad \phi_{iz}\}^T$ are

$$\tilde{\boldsymbol{\phi}}_i^T k_i^2\mathbf{D}_{xx} - \mathrm{i}k_i\tilde{\boldsymbol{\phi}}_i'^T\left(\mathbf{D}_{zx} + \mathbf{D}_{xz}\right) - \tilde{\boldsymbol{\phi}}_i''^T\mathbf{D}_{zz} - \tilde{\boldsymbol{\phi}}_i^T\omega^2\mathbf{M} = \mathbf{0} \tag{4C.17a}$$

$$\left[\mathrm{i}k_i\tilde{\boldsymbol{\phi}}_i^T\mathbf{D}_{xz} + \tilde{\boldsymbol{\phi}}_i'^T\mathbf{D}_{zz}\right]_{z=\pm b} = \mathbf{0} \tag{4C.17b}$$

with $\mathbf{D}_{zx} = \mathbf{D}_{xz}^T$.

We attempt to obtain the 1st orthogonality condition. For this purpose, divide equations (4C.16a) and (4C.17a) by the eigenvalues k_j and k_i, respectively, and multiply equation (4C.16a) by $\tilde{\boldsymbol{\phi}}_i^T$ from the left and equation (4C.17a) by $\boldsymbol{\phi}_j$ from the right. Next, integrate them over z to obtain

$$\int_{-b}^{+b}\tilde{\boldsymbol{\phi}}_i^T\left[k_j\mathbf{D}_{xx}\boldsymbol{\phi}_j + \mathrm{i}\left(\mathbf{D}_{xz} + \mathbf{D}_{zx}\right)\boldsymbol{\phi}_j' - \frac{1}{k_j}\mathbf{D}_{zz}\boldsymbol{\phi}_j'' - \frac{1}{k_j}\omega^2\mathbf{M}\boldsymbol{\phi}_j\right]dz = 0 \tag{4C.18}$$

$$\int_{-b}^{+b}\left[k_i\tilde{\boldsymbol{\phi}}_i^T\mathbf{D}_{xx} - \mathrm{i}\tilde{\boldsymbol{\phi}}_i'^T\left(\mathbf{D}_{zx} + \mathbf{D}_{xz}\right) - \frac{1}{k_i}\tilde{\boldsymbol{\phi}}_i''^T\mathbf{D}_{zz} - \frac{\omega^2}{k_i}\tilde{\boldsymbol{\phi}}_i^T\mathbf{M}\right]\boldsymbol{\phi}_j dz = 0 \tag{4C.19}$$

Subtraction of equation (4C.19) from equation (4C.18) followed by integration by parts and applying the boundary conditions provides the 1st orthogonality condition of the form.

$$\frac{(k_j-k_i)}{k_jk_i}\int_{-b}^{+b}\left[k_jk_i\tilde{\boldsymbol{\phi}}_i^T\mathbf{D}_{xx}\boldsymbol{\phi}_j-\tilde{\boldsymbol{\phi}}_i'^T\mathbf{D}_{zz}\boldsymbol{\phi}_i'+\omega^2\tilde{\boldsymbol{\phi}}_i^T\mathbf{M}\boldsymbol{\phi}_i\right]dz=0 \tag{4C.20}$$

Also, the associated normalization constant is determined from the following relationship.

$$\int_{-b}^{+b}\left[k_jk_i\tilde{\boldsymbol{\phi}}_i^T\mathbf{D}_{xx}\boldsymbol{\phi}_j-\tilde{\boldsymbol{\phi}}_i'^T\mathbf{D}_{zz}\boldsymbol{\phi}_i'+\omega^2\tilde{\boldsymbol{\phi}}_i^T\mathbf{M}\boldsymbol{\phi}_i\right]dz=2k_jk_i\delta_{ij} \tag{4C.21}$$

which is consistent with the TLM convention.

Next, we achieve the 2nd orthogonality condition as follows. Without dividing by eigenvalues, we follow the same procedures as the 1st orthogonality condition as follows. Multiply equation (4C.16a) by $\tilde{\boldsymbol{\phi}}_i^T$ from the left and equation (4C.17a) by $\boldsymbol{\phi}_j$ from the right. Next, integrate them over z to finally obtain

$$\int_{-b}^{+b}\tilde{\boldsymbol{\phi}}_i^T\left[k_j^2\mathbf{D}_{xx}\boldsymbol{\phi}_j+\mathrm{i}k_j\left(\mathbf{D}_{xz}+\mathbf{D}_{zx}\right)\boldsymbol{\phi}_j'-\mathbf{D}_{zz}\boldsymbol{\phi}_j''-\omega^2\mathbf{M}\boldsymbol{\phi}_j\right]dz=0 \tag{4C.22}$$

$$\int_{-b}^{+b}\left[\tilde{\boldsymbol{\phi}}_i^Tk_i^2\mathbf{D}_{xx}-\mathrm{i}k_i\tilde{\boldsymbol{\phi}}_i'^T\left(\mathbf{D}_{zx}+\mathbf{D}_{xz}\right)-\tilde{\boldsymbol{\phi}}_i''^T\mathbf{D}_{zz}-\tilde{\boldsymbol{\phi}}_i^T\omega^2\mathbf{M}\right]\boldsymbol{\phi}_j dz=0 \tag{4C.23}$$

Subtraction of equation (4C.23) from equation (4C.22) followed by integration by parts and applying the boundary conditions provides the 2nd orthogonality condition of the form

$$(k_j-k_i)\int_{-b}^{+b}\left[(k_j+k_i)\tilde{\boldsymbol{\phi}}_i^T\mathbf{D}_{xx}\boldsymbol{\phi}_j+\mathrm{i}\left(\tilde{\boldsymbol{\phi}}_i^T\mathbf{D}_{xz}\boldsymbol{\phi}_j'-\tilde{\boldsymbol{\phi}}_i'^T\mathbf{D}_{zx}\boldsymbol{\phi}_j\right)\right]dz=0 \tag{4C.24}$$

Then, the normalization constant for this second orthogonality condition is determined from

$$\int_{-b}^{+b}\left[(k_j+k_i)\tilde{\boldsymbol{\phi}}_i^T\mathbf{D}_{xx}\boldsymbol{\phi}_j+\mathrm{i}\left(\tilde{\boldsymbol{\phi}}_i^T\mathbf{D}_{xz}\boldsymbol{\phi}_j'-\tilde{\boldsymbol{\phi}}_i'^T\mathbf{D}_{zx}\boldsymbol{\phi}_j\right)\right]dz=(k_j+k_i)\delta_{ij} \tag{4C.25}$$

We now consider a 3rd orthogonality condition that is associated with using the right and left eigenvectors defined as $\mathbf{z}_j=\left\{\phi_{jx}\quad \mathrm{i}k_j\phi_{jz}\right\}^T$ and $\mathbf{y}_j=\left\{k_j\phi_{jx}\quad \mathrm{i}\phi_{jz}\right\}^T$, respectively. We need to develop the associated governing equations and boundary conditions as:

For a right eigenvector with k_j:

$$\left[\vec{\mathbf{A}}_Rk_j^2+\vec{\mathbf{C}}_R\right]\mathbf{z}_j=\begin{Bmatrix}0\\0\end{Bmatrix} \tag{4C.26a}$$

$$\begin{Bmatrix}\bar{\tau}_{xz}\\ \mathrm{i}k_j\bar{\sigma}_z\end{Bmatrix}=\left[\begin{Bmatrix}G & \cdot\\ \cdot & \lambda+2G\end{Bmatrix}\frac{\vec{d}}{dz}+\begin{Bmatrix}\cdot & -G\\ \lambda k_j^2 & \cdot\end{Bmatrix}\right]\mathbf{z}_j=\begin{Bmatrix}0\\0\end{Bmatrix}\qquad \text{at } z=\pm b. \tag{4C.26b}$$

For a left eigenvector with k_i:

$$\mathbf{y}_i^T\left[\tilde{\mathbf{A}}_Lk_i^2+\tilde{\mathbf{C}}_L\right]=\{0\quad 0\} \tag{4C.27a}$$

$$\{k_i\bar{\tau}_{xz}\quad \mathrm{i}\bar{\sigma}_z\}=\mathbf{y}_i^T\left[\begin{Bmatrix}G & \cdot\\ \cdot & \lambda+2G\end{Bmatrix}\frac{\vec{d}}{dz}+\begin{Bmatrix}\cdot & -\lambda\\ Gk_i^2 & \cdot\end{Bmatrix}\right]=\{0\quad 0\}\qquad \text{at } z=\pm b. \tag{4C.27b}$$

where $(\vec{\ })$ and $(\overleftarrow{\ })$ represent the direction of the derivatives operation and

$$\vec{\mathbf{A}}_R=\begin{Bmatrix}\lambda+2G & \cdot\\ -(\lambda+G)\dfrac{\vec{d}}{dz} & G\end{Bmatrix},\qquad \vec{\mathbf{C}}_R=\begin{Bmatrix}-G\dfrac{\vec{d}^2}{dz^2}-\rho\omega^2 & (\lambda+G)\dfrac{\vec{d}}{dz}\\ \cdot & -(\lambda+2G)\dfrac{\vec{d}^2}{dz^2}-\rho\omega^2\end{Bmatrix} \tag{4C.28ab}$$

$$\tilde{\mathbf{A}}_L = \begin{Bmatrix} \lambda+2G & \cdot \\ (\lambda+G)\dfrac{\tilde{d}}{dz} & G \end{Bmatrix}, \qquad \tilde{\mathbf{C}}_L = \begin{Bmatrix} -G\dfrac{\tilde{d}^2}{dz^2} - \rho\omega^2 & -(\lambda+G)\dfrac{\tilde{d}}{dz} \\ \cdot & -(\lambda+2G)\dfrac{\tilde{d}^2}{dz^2} - \rho\omega^2 \end{Bmatrix} \quad \text{(4C.28cd)}$$

In order to find out the orthogonality condition, we need to perform the following integration.

$$\int_{-b}^{+b} \left(\mathbf{y}_i^{\,T} \left[\tilde{\mathbf{A}}_R k_j^2 + \tilde{\mathbf{C}}_R \right] \mathbf{z}_j - \mathbf{y}_i^{\,T} \left[\tilde{\mathbf{A}}_L k_i^2 + \tilde{\mathbf{C}}_L \right] \mathbf{z}_j \right) dz = 0 \quad \text{(4C.29)}$$

We expand in more explicit form to obtain

$$\begin{aligned} \int_{-b}^{+b} \Bigg[& \mathbf{y}_i^{\,T} \left(\mathbf{D}_{xx} \mathbf{z}_j k_j^2 + \begin{Bmatrix} \cdot & \lambda \\ -Gk_j^2 & \cdot \end{Bmatrix} \mathbf{z}_j' + \begin{Bmatrix} \cdot & G \\ -\lambda k_j^2 & \cdot \end{Bmatrix} \mathbf{z}_j' - \mathbf{D}_{zz} \mathbf{z}_j'' \right) \\ & - \left(\mathbf{y}_i^{\,T} \mathbf{D}_{xx} k_i^2 + \mathbf{y}_i'^{T} \begin{Bmatrix} \cdot & -\lambda \\ Gk_i^2 & \cdot \end{Bmatrix} + \mathbf{y}_i'^{T} \begin{Bmatrix} \cdot & -G \\ \lambda k_i^2 & \cdot \end{Bmatrix} - \mathbf{y}_i''^{T} \mathbf{D}_{zz} \right) \mathbf{z}_j \Bigg] dz = 0 \end{aligned} \quad \text{(4C.30)}$$

where the terms of mass are canceled by each other. Application of integration by parts (to the third and fourth terms in the first line, and the second and fourth terms in the second line) followed by the boundary conditions provides

$$\begin{aligned} & \int_{-b}^{+b} (k_j^2 - k_i^2) \mathbf{y}_i^{\,T} \mathbf{D}_{xx} \mathbf{z}_j dz + \int_{-b}^{+b} \mathbf{y}_i^{\,T} \begin{Bmatrix} \cdot & \lambda \\ -Gk_j^2 & \cdot \end{Bmatrix} \mathbf{z}_j' dz - \int_{-b}^{+b} \mathbf{y}_i'^{T} \begin{Bmatrix} \cdot & G \\ -\lambda k_j^2 & \cdot \end{Bmatrix} \mathbf{z}_j dz \\ & - \int_{-b}^{+b} \mathbf{y}_i'^{T} \begin{Bmatrix} \cdot & -G \\ \lambda k_i^2 & \cdot \end{Bmatrix} \mathbf{z}_j dz + \int_{-b}^{+b} \mathbf{y}_i^{\,T} \begin{Bmatrix} \cdot & -\lambda \\ Gk_i^2 & \cdot \end{Bmatrix} \mathbf{z}_j' dz = 0 \end{aligned} \quad \text{(4C.31)}$$

Finally, we can obtain the 3rd orthogonality condition as

$$(k_j^2 - k_i^2) \left[\int_{-b}^{+b} \mathbf{y}_i^{\,T} \mathbf{D}_{xx} \mathbf{z}_j dz - \int_{-b}^{+b} \mathbf{y}_i^{\,T} \begin{Bmatrix} \cdot & \cdot \\ G & \cdot \end{Bmatrix} \mathbf{z}_j' dz + \int_{-b}^{+b} \mathbf{y}_i'^{T} \begin{Bmatrix} \cdot & \cdot \\ \lambda & \cdot \end{Bmatrix} \mathbf{z}_j dz \right] = 0 \quad \text{(4C.32a)}$$

or

$$(k_j^2 - k_i^2) \left[\int_{-b}^{+b} \mathbf{y}_i^{\,T} \tilde{\mathbf{A}}_R \mathbf{z}_j dz + \mathbf{y}_i^{\,T} \begin{Bmatrix} \cdot & \cdot \\ \lambda & \cdot \end{Bmatrix} \mathbf{z}_j \Big|_{-b}^{+b} \right] = 0 \quad \text{(4C.32b)}$$

For practical purposes, this condition is best written in scalar form.

$$(\lambda+2G) k_i \int_{-b}^{+b} u_i u_j dz - G k_j \int_{-b}^{+b} w_i w_j dz + \mathrm{i}\lambda \int_{-b}^{+b} w_i' u_j dz - \mathrm{i}G \int_{-b}^{+b} w_i u_j' dz = A_j \delta_{ij} \quad \text{(4C.33a)}$$

where A_j is a yet to be determined normalization constant, and u and w replace ϕ_x and ϕ_z, respectively. Interchanging i and j, we obtain the alternate form

$$(\lambda+2G) k_j \int_{-b}^{+b} u_i u_j dz - G k_i \int_{-b}^{+b} w_i w_j dz + \mathrm{i}\lambda \int_{-b}^{+b} w_j' u_i dz - \mathrm{i}G \int_{-b}^{+b} w_j u_i' dz = A_i \delta_{ij} \quad \text{(4C.33b)}$$

Adding these two forms, we obtain the *second* orthogonality condition, whose normalization constant we already know. Hence

$$\begin{aligned} & (k_i + k_j) \left[(\lambda+2G) \int_{-b}^{+b} u_i u_j dz - G \int_{-b}^{+b} w_i w_j dz \right] \\ & + \mathrm{i}\lambda \int_{-b}^{+b} \left(u_i w_j' + w_i' u_j \right) dz - \mathrm{i}G \int_{-b}^{+b} \left(u_i' w_j + w_i u_j' \right) dz = (A_i + A_j) \delta_{ij} = 2k_j \delta_{ij} \end{aligned} \quad \text{(4C.34)}$$

Finally, it follows that $A_j = k_j$.

We next obtain the modal solutions for the Mindlin plate subjected to *SV-P* line loads with application of the transmitting boundary conditions on the vertical plane that are given as

$$\begin{Bmatrix}\sigma_{xx}\\ \tau_{xz}\end{Bmatrix}=\left[\begin{bmatrix}\lambda+2G & \cdot\\ \cdot & G\end{bmatrix}\frac{\partial}{\partial x}+\begin{bmatrix}\cdot & \lambda\\ G & \cdot\end{bmatrix}\frac{\partial}{\partial z}\right]\begin{Bmatrix}u\\ w\end{Bmatrix} \tag{4C.35a}$$

or briefly

$$\mathbf{s}=\left[\mathbf{D}_{xx}\frac{\partial}{\partial x}+\mathbf{D}_{xz}\frac{\partial}{\partial z}\right]\mathbf{u} \tag{4C.35b}$$

Equilibrium of a thin vertical section extending from 0^- to 0^+ requires

$$\boxed{\mathbf{s}^- - \mathbf{s}^+ = \mathbf{p}} \tag{4C.36}$$

a) Horizontal load

Using the modal expansion, the displacements are

$$\mathbf{u}^+ = \sum_{j=0}^{\infty}\gamma_j\boldsymbol{\phi}_j e^{-ik_j x} \qquad x>0 \tag{4C.37a}$$

$$\mathbf{u}^- = \sum_{j=0}^{\infty}\gamma_j\tilde{\boldsymbol{\phi}}_j e^{ik_j x} \qquad x<0 \tag{4C.37b}$$

where the participation factor γ_j is the only unknown that is determined as follows.
At x=0, we must have continuity of displacements. Hence

$$\mathbf{u}^+ = \mathbf{u}^- \qquad \Rightarrow \qquad \sum_{j=0}^{\infty}\gamma_j\left(\boldsymbol{\phi}_j - \tilde{\boldsymbol{\phi}}_j\right)=\mathbf{0} \tag{4C.38}$$

which implies

$$\boxed{\sum_{j=0}^{\infty}\gamma_j w_j = 0} \quad \text{and thus also} \quad \boxed{\sum_{j=0}^{\infty}\gamma_j w_j' = 0} \tag{4C.39ab}$$

Also, from the modal expansion, the stresses near the load are

$$\mathbf{s}^+ = \sum_{j=0}^{\infty}\gamma_j\left[-ik_j\mathbf{D}_{xx}\boldsymbol{\phi}_j + \mathbf{D}_{xz}^T\boldsymbol{\phi}_j'\right] \tag{4C.40a}$$

$$\mathbf{s}^- = \sum_{j=0}^{\infty}\gamma_j\left[ik_j\mathbf{D}_{xx}\tilde{\boldsymbol{\phi}}_j + \mathbf{D}_{xz}^T\tilde{\boldsymbol{\phi}}_j'\right] \tag{4C.40b}$$

Hence, the equilibrium condition requires that

$$\mathbf{s}^- - \mathbf{s}^+ = \sum_{j=0}^{\infty}\gamma_j\left[ik_j\mathbf{D}_{xx}\left(\tilde{\boldsymbol{\phi}}_j + \boldsymbol{\phi}_j\right) + \mathbf{D}_{xz}^T\left(\tilde{\boldsymbol{\phi}}_j' - \boldsymbol{\phi}_j'\right)\right] = \mathbf{p} \tag{4C.41}$$

In terms of the components, the second equation in equation (4C.41) yields the identity 0=0, which is not interesting. The first component, on the other hand, leads to

$$2\sum_{j=0}^{\infty}\gamma_j\left[ik_j(\lambda+2G)u_j - \lambda w_j'\right] = \delta(z-z_0) \tag{4C.42}$$

But from equations (4C.39ab), we can see that the second term in the equilibrium equation cancels. Hence

$$(\lambda+2G)\sum_{j=0}^{\infty}\gamma_j k_j u_j = \frac{1}{2i}\delta(z-z_0) \tag{4C.43}$$

Multiplying by u_i and integrating over the height, we obtain

$$(\lambda+2G)\sum_{j=0}^{\infty}\gamma_j k_j \int_{-b}^{+b} u_i\, u_j\, dz = \frac{1}{2\mathrm{i}} u_i(z_0) \tag{4C.44}$$

We will show next that because of orthogonality, the LHS reduces to

$$(\lambda+2G)\sum_{j=0}^{\infty}\gamma_j k_j \int_{-b}^{+b} u_i\, u_j\, dz = \gamma_i\, A_i \tag{4C.45}$$

in which

$$\boxed{A_j = k_j\left[(\lambda+2G)\int_{-b}^{+b} u_j^2\, dz - G\int_{-b}^{+b} w_j^2\, dz\right] + \mathrm{i}\lambda\int_{-b}^{+b} u_j w_j'\, dz - \mathrm{i}G\int_{-b}^{+b} u_j' w_j\, dz} \tag{4C.46}$$

so that

$$\boxed{\gamma_j = \frac{u_j(z_0)}{2\mathrm{i}\, A_j}} \tag{4C.47}$$

From the third orthogonality condition, we have

$$(\lambda+2G)k_j\int_{-b}^{+b} u_i u_j\, dz - G k_i \int_{-b}^{+b} w_i w_j\, dz + \mathrm{i}\lambda\int_{-b}^{+b} u_i w_j'\, dz - \mathrm{i}G\int_{-b}^{+b} u_i' w_j\, dz = A_i\delta_{ij} \tag{4C.48}$$

where A_i is simply the result of the left-hand side (LHS) when $i=j$. Multiplying by the participation factor and adding up over all modes, we obtain

$$\begin{aligned}&(\lambda+2G)\sum_{j=0}^{\infty}\gamma_j k_j \int_{-b}^{+b} u_i u_j\, dz - G k_i \int_{-b}^{+b} w_i\left[\sum_{j=0}^{\infty}\gamma_j w_j\right] dz \\ &+\mathrm{i}\lambda\int_{-b}^{+b} u_i\left[\sum_{j=0}^{\infty}\gamma_j w_j'\right]_j dz - \mathrm{i}G\int_{-b}^{+b} u_i'\left[\sum_{j=0}^{\infty}\gamma_j w_j\right] dz = \sum_{j=0}^{\infty}\gamma_j A_i\,\delta_{ij} = \gamma_i A_i\end{aligned} \tag{4C.49}$$

Because of equations (4C.39ab), the last three summations in brackets on the LHS are automatically zero. Hence, it follows that

$$(\lambda+2G)\sum_{j=0}^{\infty}\gamma_j k_j \int_{-b}^{+b} u_i u_j\, dz = \gamma_i\, A_i \tag{4C.50}$$

which proves the condition used to solve for the participation factors for a horizontal load.

b) Vertical load

Using the modal expansion, the displacements are now

$$\mathbf{u} = \sum_{j=0}^{\infty}\gamma_j \boldsymbol{\phi}_j e^{-\mathrm{i}k_j x} \qquad x>0 \tag{4C.51a}$$

$$\mathbf{u} = -\sum_{j=0}^{\infty}\gamma_j \tilde{\boldsymbol{\phi}}_j e^{\mathrm{i}k_j x} \qquad x<0 \tag{4C.51b}$$

where the participation factor γ_j is only the unknown that is determined as follows.
Notice the minus sign in the second equation, which differs from the horizontal case. At $x=0$, we must have again continuity of displacements. Hence

$$\mathbf{u}^+ = \mathbf{u}^- \qquad \Rightarrow \qquad \sum_{j=0}^{\infty}\gamma_j\left(\boldsymbol{\phi}_j + \tilde{\boldsymbol{\phi}}_j\right) = \mathbf{0} \tag{4C.52}$$

which implies

$$\boxed{\sum_{j=0}^{\infty}\gamma_j u_j = 0} \quad \text{and thus also} \quad \boxed{\sum_{j=0}^{\infty}\gamma_j u_j' = 0} \tag{4C.53ab}$$

Also, from the modal expansion, the stresses near the load are

$$\mathbf{s}^{+} = \sum_{j=0}^{\infty} \gamma_j \left[-\mathrm{i} k_j \mathbf{D}_{xx} \boldsymbol{\phi}_j + \mathbf{D}_{xz}^T \boldsymbol{\phi}_j' \right] \tag{4C.54a}$$

$$\mathbf{s}^{-} = -\sum_{j=0}^{\infty} \gamma_j \left[\mathrm{i} k_j \mathbf{D}_{xx} \tilde{\boldsymbol{\phi}}_j + \mathbf{D}_{xz}^T \tilde{\boldsymbol{\phi}}_j' \right] \tag{4C.54b}$$

Hence, the equilibrium condition requires that

$$\mathbf{s}^{-} - \mathbf{s}^{+} = \sum_{j=0}^{\infty} \gamma_j \left[\mathrm{i} k_j \mathbf{D}_{xx} \left(\boldsymbol{\phi}_j - \tilde{\boldsymbol{\phi}}_j \right) - \mathbf{D}_{xz}^T \left(\boldsymbol{\phi}_j' + \tilde{\boldsymbol{\phi}}_j' \right) \right] = \mathbf{p} \tag{4C.55}$$

In terms of the components, the first equation yields the identity 0=0, which is not interesting. The second component, on the other hand, leads to

$$2G \sum_{j=0}^{\infty} \gamma_j \left[\mathrm{i} k_j w_j - u_j' \right] = \delta(z - z_0) \tag{4C.56}$$

But from equations (4C.53ab), we can see that the second term in the equilibrium equation cancels. Hence

$$G \sum_{j=0}^{\infty} \gamma_j k_j w_j = \frac{1}{2\mathrm{i}} \delta(z - z_0) \tag{4C.57}$$

Multiplying by w_i and integrating over the height, we obtain

$$G \sum_{j=0}^{\infty} \gamma_j k_j \int_{-b}^{+b} w_i \, w_j \, dz = \frac{1}{2\mathrm{i}} w_i(z_0) \tag{4C.58}$$

Again because of orthogonality, the above summation reduces to

$$\gamma_i \, A_i = -G \sum_{j=0}^{\infty} \gamma_j k_j \int_{-b}^{+b} w_i \, w_j \, dz \tag{4C.59}$$

in which A_j is as before, so that

$$\boxed{\gamma_j = -\frac{w_j(z_0)}{2\mathrm{i} A_j}} \tag{4C.60}$$

Once more, from the third orthogonality condition (but observe that we exchanged i and j), we have for $i \neq j$

$$(\lambda + 2G) k_i \int_{-b}^{+b} u_i u_j \, dz - G k_j \int_{-b}^{+b} w_i w_j \, dz + \mathrm{i}\lambda \int_{-b}^{+b} w_i' u_j \, dz - \mathrm{i} G \int_{-b}^{+b} w_i u_j' \, dz = A_i \delta_{ij} \tag{4C.61}$$

Multiplying by the participation factor and adding up over all modes, we obtain

$$\begin{aligned} &(\lambda + 2G) k_i \int_{-b}^{+b} u_i \left[\sum_{j=0}^{\infty} \gamma_j u_j \right] dz - G \sum_{j=0}^{\infty} \gamma_j k_j \int_{-b}^{+b} w_i w_j \, dz \\ &+ \mathrm{i}\lambda \int_{-b}^{+b} w_i' \left[\sum_{j=0}^{\infty} \gamma_j u_j \right] dz - \mathrm{i} G \int_{-b}^{+b} w_i \left[\sum_{j=0}^{\infty} \gamma_j u_j' \right] dz = \sum_{j=0}^{\infty} \gamma_j \, A_i \, \delta_{ij} = \gamma_i \, A_i \end{aligned} \tag{4C.62}$$

Because of equations (4C.53ab), the first summation in brackets as well as the last two are automatically zero. Hence, it follows that

$$-G \sum_{j=0}^{\infty} \gamma_j \, k_j \int_{-b}^{+b} w_i w_j \, dz = \gamma_i A_i \tag{4C.63}$$

which completes the proof.

(3) Modal superposition in the *k-t* domain

We again begin with the orthogonality condition. For this purpose, we write the field equation and the boundary conditions in terms of an eigenvalue and an eigenvector for a j-th mode as

$$k^2\mathbf{D}_{xx}\phi_j + ik\left(\mathbf{D}_{xz}+\mathbf{D}_{zx}\right)\phi_j' - \mathbf{D}_{zz}\phi_j'' - \omega_j^2\mathbf{M}\phi_j = \mathbf{0} \tag{4C.64a}$$

$$\left[-ik\mathbf{D}_{zx}\phi_j + \mathbf{D}_{zz}\phi_j'\right]_{z=\pm b} = \mathbf{0} \tag{4C.64b}$$

where primes represent the derivative with respect to z, and ϕ_j is the normalized eigenvector that is proportional to φ_j in equations (4C.12-15) by the j-th normalization constant.
Also, we may have the equations associated with a normalized eigenvector ϕ_i of the form.

$$k^2\mathbf{D}_{xx}\phi_i + ik\left(\mathbf{D}_{xz}+\mathbf{D}_{zx}\right)\phi_i' - \mathbf{D}_{zz}\phi_i'' - \omega_i^2\mathbf{M}\phi_i = \mathbf{0} \tag{4C.65a}$$

$$\left[-ik\mathbf{D}_{zx}\phi_i + \mathbf{D}_{zz}\phi_i'\right]_{z=\pm b} = \mathbf{0} \tag{4C.65b}$$

Next, we multiply equation (4C.64a) by ϕ_i^T from the left and equation (4C.65a) by ϕ_j^T from the left. Next, integrate them over z to obtain

$$\int_{-b}^{+b}\phi_i^T\left[k^2\mathbf{D}_{xx}\phi_j + ik\left(\mathbf{D}_{xz}+\mathbf{D}_{zx}\right)\phi_j' - \mathbf{D}_{zz}\phi_j'' - \omega_j^2\mathbf{M}\phi_j\right]dz = 0 \tag{4C.66}$$

$$\int_{-b}^{+b}\phi_j^T\left[k^2\mathbf{D}_{xx}\phi_i + ik\left(\mathbf{D}_{xz}+\mathbf{D}_{zx}\right)\phi_i' - \mathbf{D}_{zz}\phi_i'' - \omega_i^2\mathbf{M}\phi_i\right]dz = 0 \tag{4C.67}$$

Subtraction of equation (4C.67) from equation (4C.66) followed by integration by parts and applying the boundary conditions provides the orthogonality condition of the form.

$$\rho(\omega_i^2-\omega_j^2)\int_{-b}^{+b}\phi_j^T\phi_i\,dz = 0 \tag{4C.68}$$

Also, the associated normalization constant is determined from the following relationship:

$$\rho\int_{-b}^{+b}\phi_j^T\phi_i\,dz = \delta_{ij} \tag{4C.69}$$

which is consistent with the TLM convention.

Now, we move on to find out the modal solutions that is our final goal. For this purpose, we first assume the modal solution of the form.

$$\hat{\mathbf{u}}(k,z,t) = \sum_{j=0}^{\infty}\gamma_j(t)\phi_j(z)e^{-ikx} \tag{4C.70}$$

where the participation factor γ_j is the only unknown and $\hat{\mathbf{u}}$ is a harmonic function in x with k.
In order to calculate the participation factor, we consider the governing equation

$$\mathbf{M}\ddot{\hat{\mathbf{u}}} - \left[\mathbf{D}_{xx}\frac{\partial^2}{\partial x^2} + \left(\mathbf{D}_{xz}+\mathbf{D}_{zx}\right)\frac{\partial^2}{\partial x\partial z} + \mathbf{D}_{zz}\frac{\partial^2}{\partial z^2}\right]\hat{\mathbf{u}} = e^{-ikx}\delta(z-z_0)\delta(t)\mathbf{p} \tag{4C.71}$$

where $\mathbf{p}$ is a vector of $[1 \quad 0]^T$ for a horizontal load or $[0 \quad 1]^T$ for a horizontal load.
Inserting equation (4C.70) into equation (4C.71) and pre-multiplication of ϕ_i^T followed by integration over the thickness provides

$$\int_{-b}^{+b}\left\{\phi_i^T\left[\mathbf{M}\frac{\partial^2}{\partial t^2} - \mathbf{D}_{xx}\frac{\partial^2}{\partial x^2} - \left(\mathbf{D}_{xz}+\mathbf{D}_{zx}\right)\frac{\partial^2}{\partial x\partial z} - \mathbf{D}_{zz}\frac{\partial^2}{\partial z^2}\right]\sum_{j=0}^{\infty}\gamma_j\phi_j e^{-ikx}\right\}dz = \int_{-b}^{+b}\phi_i^T\left[e^{-ikx}\delta(z-z_0)\delta(t)\mathbf{p}\right]dz \tag{4C.72}$$

With the help of equations (4C.64, 68, and 69), equation (4C.72) attain the form.

$$\left(\frac{d^2}{dt^2}+\omega_i^2\right)\gamma_i = \delta(t)\phi_i^T(z_0)\mathbf{p} \tag{4C.73}$$

in which we omit the term of e^{-ikx} on both the sides.
Apply the Fourier transformation to γ_i over time t as

$$\tilde{\gamma}_i(\omega) = \int_{-\infty}^{\infty}\gamma_i(t)e^{i\omega t}dt \qquad \text{and} \qquad \gamma_i(t) = \frac{1}{2\pi}\int_{-\infty}^{\infty}\tilde{\gamma}_i(\omega)e^{-i\omega t}dt \tag{4C.74a,b}$$

Then, we can obtain the participation factor in the ω-domain as

$$\left(\omega_i^2-\omega^2\right)\tilde{\gamma}_i = \phi_i^T(z_0)\mathbf{p} = p_i \tag{4C.75a}$$

or

$$\tilde{\gamma}_i = \frac{p_i}{\omega_i^2-\omega^2} \tag{4C.75b}$$

Inversion of Fourier transformation yields for mode i:

$$\gamma_i = \frac{\sin\omega_i t}{\omega_i}p_i \tag{4C.76}$$

Finally, we can express the modal superposition of the form.

$$\hat{\mathbf{u}}(k,z,t) = \sum_{j=0}^{\infty}\frac{\sin\omega_j t}{\omega_j}p_j\phi_j e^{-ikx} \tag{4C.77}$$

To complete our analysis, we have to perform the inverse Fourier transformation over the wavenumber k to obtain the solutions in the x-t domain as

$$\mathbf{u}(x,z,t) = \frac{1}{2\pi}\int_{-\infty}^{+\infty}\hat{\mathbf{u}}(k,z,t)dk = \frac{1}{2\pi}\int_{-\infty}^{+\infty}\left[\sum_{j=0}^{\infty}\frac{\sin\omega_j t}{\omega_j}p_j\phi_j e^{-ikx}\right]dk \tag{4C.78}$$

Figures for appendix 4C

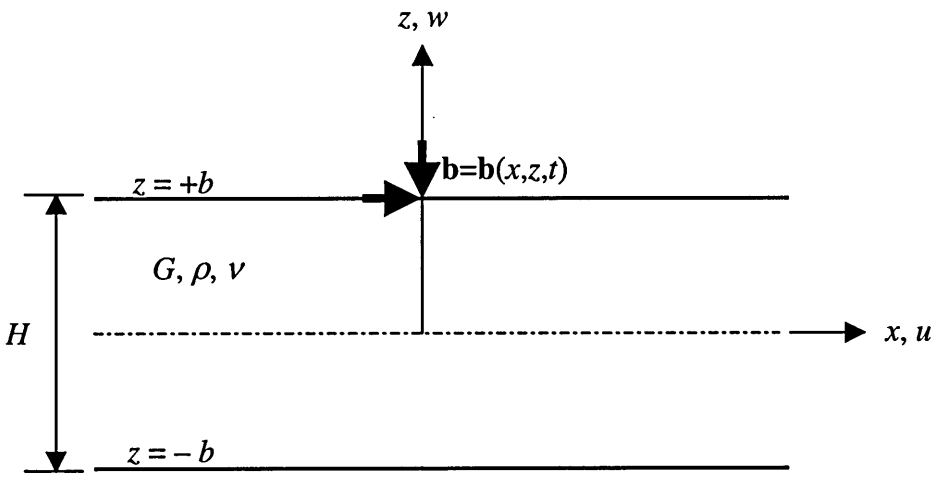

Figure 4C.1. Homogeneous plate subjected to *SV-P* line loads **b**

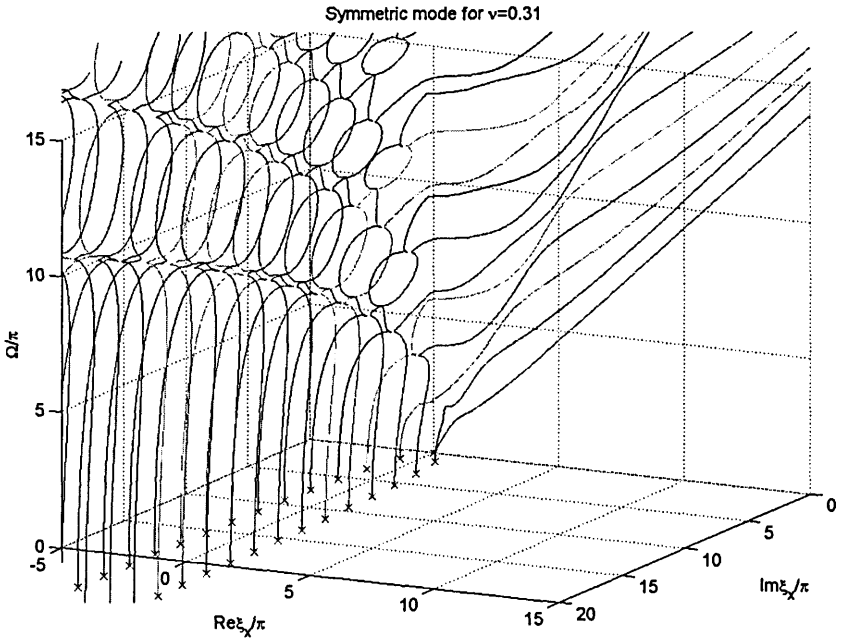

Figure 4C.2a Dispersion curves of Mindlin plate (ν=0.31) for the symmetric modes ($\Omega=\omega H/C_S$ and $\xi_x=kH$)

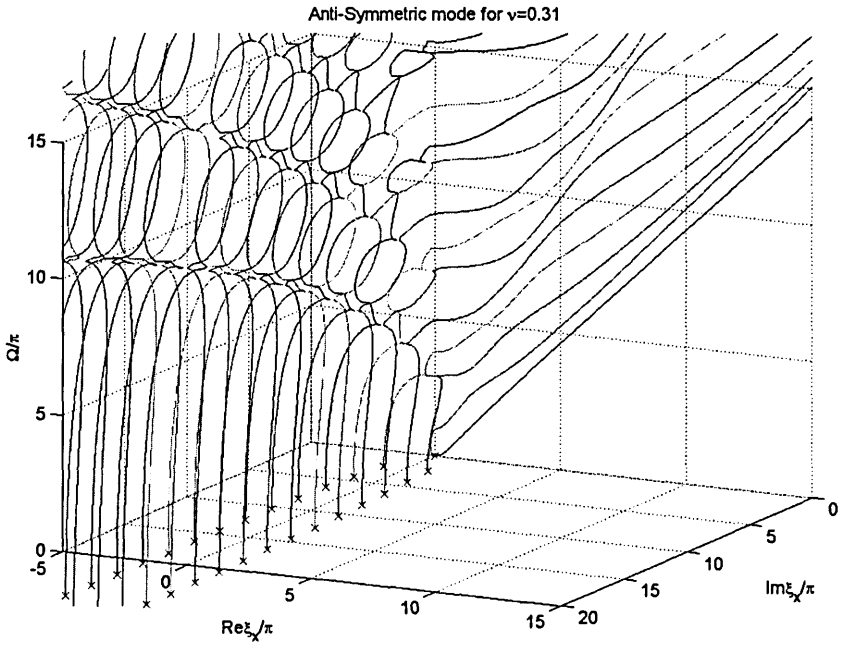

Figure 4C.2b Dispersion curves of Mindlin plate (ν=0.31) for the anti-symmetric modes ($\Omega=\omega H/C_S$ and $\xi_x=kH$)

Chapter 5 Infinite media modeling with the *t*-TLM

5.1 Introduction

We develop herein a hybrid method, by which we extend the *t*-TLM method from finite media to (semi-) infinite media. As shown in chapter 4, the *t*-TLM provides very accurate responses for finite-depth domains subjected to dynamics loads. However, due to its inherent origin in the finite element method, the *t*-TLM is unable to analyze media that extend to infinity in the direction of layering, i.e. that are unbounded in the depth (z-) direction, because that would entail infinite matrices. To overcome this important shortcoming, we make use of the substructure method and combine the *t*-TLM modal solution with the exact analytical Green functions for a homogeneous half-space formulated in the wavenumber and time domain, or *k-t* domain for short. The exact analytical Green functions needed for this purpose are derived and presented in section 5.3, and constitute the key component of the substructure method developed in this chapter.

The substructure method is a technique by which the analysis of a complex structure is performed in various steps, separating the structure into simpler substructures which are more efficiently (or easily) handled than the complete system in one single step. The analysis of each substructure is then followed by synthesis, to ensure compatibility and equilibrium across the interfaces separating the various structures. The technique is based on the principle of superposition, so that it is restricted to linear systems.

The presentation in this chapter is as follows. In section 5.2, we develop the substructure method by combining the *t*-TLM modal solution with the exact analytical Green functions for a homogeneous half-space in the *k-t* domain, and then investigate its stability and accuracy. From here, we decide on the proper time step Δt needed for the numerical solution of the convolution equations, and also find out the number of accurate high modes needed for the modal solutions. Furthermore, we propose the use of a buffer layer that stabilizes the final responses, especially for a system composed of significantly dissimilar materials. In section 5.3, we derive and present the exact analytical Green functions for a homogeneous half-space in the *k-t* domain, which is a key element in the substructure method being considered. In section 5.4, we apply the technique to various examples of multilayered half-spaces so as to validate the developed method. Also, we investigate the wave motions elicited by sources within complicated multilayered half-spaces.

5.2 Substructure method and stability

5.2.1 Substructure method

We begin by defining the problem involved in the application of the substructure method. Our goal is to obtain the dynamic response of a semi-infinite, layered half-plane due to a line source $\mathbf{p}(x,z,t)$ applied at $z=z_n(\geq 0)$, as shown in figure 5.2.1. The semi-infinite medium consists of an upper layered domain ($z>0$) of thickness H and a lower homogeneous half-space ($z\leq 0$). The horizontal x-axis is defined at the interface between the upper layered domain and the lower half-space. In addition, ρ_{I} and ρ_{II} are the mass densities of the upper layered domain and the lower half-space, respectively, and $C_{S,\mathrm{I}}$ and $C_{S,\mathrm{II}}$ the shear wave velocities, and ν_{I} and ν_{II} the Poisson's

ratios. For the upper layered domain, i.e. $0 \le z \le H$, the material properties ρ_I, $C_{S,I}$, and ν_I are functions of z, while for the half-space of $z<0$, ρ_{II}, $C_{S,II}$, and ν_{II} are assumed constant. In general, it is not trivial to calculate the dynamic response in the space-time domain $\mathbf{u}(x,z,t)$ for these kinds of multi-layered systems.

In the following, we formulate a powerful and efficient technique for the calculation of the dynamic response $\mathbf{u}(x,z,t)$ in the semi-infinite multi-layered medium shown in figure 5.2.1. For this purpose, the substructure method is applied in the wavenumber-time domain, or *k-t* domain for short, with the aid of two known Green functions that are both obtained in closed form with the *t*-TLM and the contour integral method, respectively. The Green function obtained with the *t*-TLM is a semi-analytical solution in the *k-t* domain for a finite multi-layered medium, while the Green function obtained with the contour integral method is an exact analytical solution in the *k-t* domain for a homogeneous half-space subjected to a surface line load. The latter is a new Green's function that is derived in this study. By virtue of the two Green functions, the analysis of the semi-infinite multi-layered medium of interest can be performed in separate steps, dividing the whole medium into two relatively simple substructures for the upper layered medium ($0 \le z \le H$) and the homogeneous half-space ($z \le 0$). The analysis of each substructure is then followed by synthesis, to ensure the two conditions of compatibility and equilibrium across the interface between the two substructures.

Figure 5.2.2 shows the complete medium separated into two substructure, namely the upper layered system and the lower homogeneous half-space. When an external line load $\hat{\mathbf{p}}^n$ is applied load at $z=z_n$, dynamic internal stresses $\hat{\boldsymbol{\tau}}^0$ develop at the interface between the upper layered system and the half-space, i.e. $z=0$. In general, $\hat{\boldsymbol{\tau}}^0$ is unknown until the problem of interest is completely solved. For general 3D problems, $\hat{\boldsymbol{\tau}}^0$ is of the form.

$$\hat{\boldsymbol{\tau}}^0 = \begin{bmatrix} \hat{\tau}^0_{zx} & \hat{\tau}^0_{zy} & \hat{\sigma}^0_{zz} \end{bmatrix}^T \tag{5.2.1}$$

The first and third elements of $\hat{\boldsymbol{\tau}}^0$ in equation (5.2.1) are associated with *SV-P* wave motion, while the second element is associated with *SH* wave motion. Before the whole system is separated, $\hat{\boldsymbol{\tau}}^0$ is the internal stress vector, as shown in the left of figure 5.2.2. On the other hand, after separation, $\hat{\boldsymbol{\tau}}^0$ becomes the boundary condition for both the two substructures, that is

$$\hat{\mathbf{s}}_I = -\hat{\boldsymbol{\tau}}^0 \qquad \text{for the upper layered system} \tag{5.2.2}$$

$$\hat{\mathbf{s}}_{II} = +\hat{\boldsymbol{\tau}}^0 \qquad \text{for the half-space} \tag{5.2.3}$$

where $\hat{\mathbf{s}}_I$ and $\hat{\mathbf{s}}_{II}$ are the traction vectors at the interface for the upper layered system and the lower half-space, respectively, and satisfy the equilibrium conditions at the interface, simply because $\hat{\mathbf{s}}_I + \hat{\mathbf{s}}_{II} = \mathbf{0}$.

By virtue of the superposition theorem for linear elastic systems, the displacement responses in the *k-t* domain for each substructure can be expressed as

$$\hat{\mathbf{u}}^{mn}_I(k,t) = \hat{\mathbf{G}}^{mn}_I * \hat{\mathbf{p}}^n + \hat{\mathbf{G}}^{m0}_I * \hat{\mathbf{s}}_I = \hat{\mathbf{G}}^{mn}_I * \hat{\mathbf{p}}^n - \hat{\mathbf{G}}^{m0}_I * \hat{\boldsymbol{\tau}}^0 \tag{5.2.4}$$

$$\hat{\mathbf{u}}^{m0}_{II}(k,t) = \hat{\mathbf{G}}^{m0}_{II} * \hat{\mathbf{s}}_{II} = \hat{\mathbf{G}}^{m0}_{II} * \hat{\boldsymbol{\tau}}^0 \tag{5.2.5}$$

where

$$\hat{\mathbf{u}}^{mn}_I(k,t) = \begin{bmatrix} \hat{u}^{mn}_I & \hat{v}^{mn}_I & \hat{w}^{mn}_I \end{bmatrix}^T \qquad \text{(=the displacement vector for } 0 \le z \le H\text{)} \tag{5.2.6}$$

$$\hat{\mathbf{u}}^{mn}_{II}(k,t) = \begin{bmatrix} \hat{u}^{mn}_{II} & \hat{v}^{mn}_{II} & \hat{w}^{mn}_{II} \end{bmatrix}^T \qquad \text{(=the displacement vector for } z \le 0\text{)} \tag{5.2.7}$$

$$\hat{\mathbf{G}}^{mn}_I(k,t) = \left\{ \hat{G}^{mn}_{I,ij} \right\} \qquad \text{(=the Green function matrix for } 0 \le z \le H\text{, with } i,j=x,\, y,\, z\text{)} \tag{5.2.8}$$

$$\hat{\mathbf{G}}_{\mathrm{II}}^{mn}(k,t)=\left\{\hat{G}_{\mathrm{II},ij}^{mn}\right\} \qquad (=\text{the Green function matrix for } z\le 0, \text{ with } i,j=x,\ y,\ z) \qquad (5.2.9)$$

In equations (5.2.4-9), the superscripts m and n represent the elevations of the field (or receiver) and the source points, respectively, and the subscripts i and j the directions of the displacements and the unit line loads, respectively. Notice that $\hat{\mathbf{G}}_{\mathrm{I}}^{mn}$ and $\hat{\mathbf{G}}_{\mathrm{II}}^{mn}$ are calculated in closed form with the t-TLM and the contour integral method, respectively. Furthermore, $\hat{\mathbf{G}}_{\mathrm{I}}^{mn}$ and $\hat{\mathbf{G}}_{\mathrm{II}}^{mn}$ have the following structure for the most general 3D problems.

$$\hat{\mathbf{G}}^{mn}=\begin{Bmatrix}\hat{G}_{xx}^{mn} & \hat{G}_{xy}^{mn} & \hat{G}_{xz}^{mn}\\ \hat{G}_{yx}^{mn} & \hat{G}_{yy}^{mn} & \hat{G}_{yz}^{mn}\\ \hat{G}_{zx}^{mn} & \hat{G}_{zy}^{mn} & \hat{G}_{zz}^{mn}\end{Bmatrix} \qquad (5.2.10)$$

For the line load problem, however, $\hat{\mathbf{G}}^{mn}$ becomes of the form

$$\hat{\mathbf{G}}^{mn}=\begin{Bmatrix}\hat{G}_{xx}^{mn} & \cdot & \hat{G}_{xz}^{mn}\\ \cdot & \hat{G}_{yy}^{mn} & \cdot\\ \hat{G}_{zx}^{mn} & \cdot & \hat{G}_{zz}^{mn}\end{Bmatrix} \qquad (5.2.11)$$

Practically, equation (5.2.11) can be uncoupled into two independent wave motions of *SV-P* and *SH* waves as

SV-P wave: $$\hat{\mathbf{G}}^{mn}=\begin{Bmatrix}\hat{G}_{xx}^{mn} & \hat{G}_{xz}^{mn}\\ \hat{G}_{zx}^{mn} & \hat{G}_{zz}^{mn}\end{Bmatrix} \qquad (2\times 2 \text{ matrix}) \qquad (5.2.12)$$

SH wave: $$\hat{\mathbf{G}}^{mn}=\hat{G}_{yy}^{mn} \qquad (1\times 1 \text{ matrix, i.e. scalar}) \qquad (5.2.13)$$

It is convenient to consider simultaneously the *SV-P* and *SH* wave motion cases, so we continue to use the 3×3 matrix form of equation (5.2.11). For practical computations, however, equations (5.2.12 and 13) should be calculated individually for each wave motion.

Next, we calculate the unknown $\hat{\boldsymbol{\tau}}^0$ in equation (5.2.4 and 5) by make use of the displacement continuity condition at the interface (z_m=0 with m=0), which is given in the form

$$\hat{\mathbf{u}}_{\mathrm{II}}^{00}=\hat{\mathbf{u}}_{\mathrm{I}}^{0n} \qquad (5.2.14)$$

or more explicitly

$$\hat{\mathbf{G}}_{\mathrm{II}}^{00}*\hat{\boldsymbol{\tau}}^0=\hat{\mathbf{G}}_{\mathrm{I}}^{0n}*\hat{\mathbf{p}}^n-\hat{\mathbf{G}}_{\mathrm{I}}^{00}*\hat{\boldsymbol{\tau}}^0 \qquad (5.2.15)$$

Collecting the terms associated with $\hat{\boldsymbol{\tau}}^0$ on the left hand side, we obtain the equation

$$\left(\hat{\mathbf{G}}_{\mathrm{II}}^{00}+\hat{\mathbf{G}}_{\mathrm{I}}^{00}\right)*\hat{\boldsymbol{\tau}}^0=\hat{\mathbf{G}}_{\mathrm{I}}^{0n}*\hat{\mathbf{p}}^n \qquad (5.2.16)$$

For simplicity in ensuing manipulations, we express equation (5.2.16) as

$$\hat{\mathbf{F}}*\hat{\boldsymbol{\tau}}=\hat{\mathbf{H}}*\hat{\mathbf{p}} \qquad (5.2.17)$$

where

$$\hat{\boldsymbol{\tau}}=\hat{\boldsymbol{\tau}}^0 \qquad (5.2.18)$$

$$\hat{\mathbf{p}}=\hat{\mathbf{p}}^n \qquad (5.2.19)$$

$$\hat{\mathbf{F}}=\hat{\mathbf{G}}_{\mathrm{II}}^{00}+\hat{\mathbf{G}}_{\mathrm{I}}^{00} \qquad (5.2.20)$$

$$\hat{\mathbf{H}}=\hat{\mathbf{G}}_{\mathrm{I}}^{0n} \qquad (5.2.21)$$

Notice that $\hat{\boldsymbol{\tau}}$ is only the unknown in equation (5.2.17). For continuous functions in time t, equation (5.2.17) is expressed in integral equation form

$$\int_0^t \hat{\mathbf{F}}(t-\tau)\hat{\boldsymbol{\tau}}(\tau)d\tau = \int_0^t \hat{\mathbf{H}}(t-\tau)\hat{\mathbf{p}}(\tau)d\tau \tag{5.2.22}$$

This type of integral equation is referred to as the first-kind Volterra equation [Arfken, 1985]. Since we are solving our present problem numerically, i.e. in discrete-time series, we solve instead the following difference equation at each time step

$$\sum_{j=0}^{i}\left[\hat{\mathbf{F}}(t_i-\tau_j)\hat{\boldsymbol{\tau}}(\tau_j)\right]\Delta t = \sum_{j=0}^{i}\left[\hat{\mathbf{H}}(t_i-\tau_j)\hat{\mathbf{p}}(\tau_j)\right]\Delta t \quad \text{with } i=0,1,2,\ldots,N_t \tag{5.2.23}$$

where $t_i=i\Delta t$, $\tau_j=j\Delta t$, $\Delta t(=T/N_t)$, and T is the total time in calculation. Equation (5.2.23) can be rewritten in more compact form

$$\sum_{j=0}^{i}\left[\hat{\mathbf{F}}_{i-j}\hat{\boldsymbol{\tau}}_j\right] = \sum_{j=0}^{i}\left[\hat{\mathbf{H}}_{i-j}\hat{\mathbf{p}}_j\right] \tag{5.2.24}$$

Furthermore, expanding equation (5.2.24) for each time step t_i, we obtain the system of equations

$$\begin{aligned}
\hat{\mathbf{F}}_0\hat{\boldsymbol{\tau}}_0 &= \hat{\mathbf{H}}_0\hat{\mathbf{p}}_0 &&, \quad i=0\\
\hat{\mathbf{F}}_1\hat{\boldsymbol{\tau}}_0+\hat{\mathbf{F}}_0\hat{\boldsymbol{\tau}}_1 &= \hat{\mathbf{H}}_1\hat{\mathbf{p}}_0+\hat{\mathbf{H}}_0\hat{\mathbf{p}}_1 &&, \quad i=1\\
\hat{\mathbf{F}}_2\hat{\boldsymbol{\tau}}_0+\hat{\mathbf{F}}_1\hat{\boldsymbol{\tau}}_1+\hat{\mathbf{F}}_0\hat{\boldsymbol{\tau}}_2 &= \hat{\mathbf{H}}_2\hat{\mathbf{p}}_0+\hat{\mathbf{H}}_1\hat{\mathbf{p}}_1+\hat{\mathbf{H}}_0\hat{\mathbf{p}}_2 &&, \quad i=2\\
&\vdots &&, \quad \vdots\\
\hat{\mathbf{F}}_{N_t}\hat{\boldsymbol{\tau}}_0+\hat{\mathbf{F}}_{i-1}\hat{\boldsymbol{\tau}}_1+\cdots+\hat{\mathbf{F}}_1\hat{\boldsymbol{\tau}}_{N_t-1}+\hat{\mathbf{F}}_0\hat{\boldsymbol{\tau}}_{N_t} &= \hat{\mathbf{H}}_{N_t}\hat{\mathbf{p}}_0+\hat{\mathbf{H}}_{N_t-1}\hat{\mathbf{p}}_1+\cdots+\hat{\mathbf{H}}_1\hat{\mathbf{p}}_{N_t-1}+\hat{\mathbf{H}}_0\hat{\mathbf{p}}_{N_t} &&, \quad i=N_t
\end{aligned} \tag{5.2.25}$$

The unknown traction vector $\hat{\boldsymbol{\tau}}_i$ for each time step i can then be determined iteratively for increasing i from 0 to N_t in the form

$$\begin{aligned}
\hat{\boldsymbol{\tau}}_0 &= \hat{\mathbf{F}}_0^{-1}\left[\hat{\mathbf{H}}_0\hat{\mathbf{p}}_0\right] &&, \quad i=0\\
\hat{\boldsymbol{\tau}}_1 &= \hat{\mathbf{F}}_0^{-1}\left[\hat{\mathbf{H}}_1\hat{\mathbf{p}}_0+\hat{\mathbf{H}}_0\hat{\mathbf{p}}_1-\hat{\mathbf{F}}_1\hat{\boldsymbol{\tau}}_0\right] &&, \quad i=1\\
\hat{\boldsymbol{\tau}}_2 &= \hat{\mathbf{F}}_0^{-1}\left[\hat{\mathbf{H}}_2\hat{\mathbf{p}}_0+\hat{\mathbf{H}}_1\hat{\mathbf{p}}_1+\hat{\mathbf{H}}_0\hat{\mathbf{p}}_2-\left(\hat{\mathbf{F}}_2\hat{\boldsymbol{\tau}}_0+\hat{\mathbf{F}}_1\hat{\boldsymbol{\tau}}_1\right)\right] &&, \quad i=2\\
&\vdots &&, \quad \vdots\\
\hat{\boldsymbol{\tau}}_{N_t} &= \hat{\mathbf{F}}_0^{-1}\left[\hat{\mathbf{H}}_{N_t}\hat{\mathbf{p}}_0+\hat{\mathbf{H}}_{N_t-1}\hat{\mathbf{p}}_1+\cdots+\hat{\mathbf{H}}_1\hat{\mathbf{p}}_{N_t-1}+\hat{\mathbf{H}}_0\hat{\mathbf{p}}_{N_t}-\left(\hat{\mathbf{F}}_{N_t}\hat{\boldsymbol{\tau}}_0+\hat{\mathbf{F}}_{i-1}\hat{\boldsymbol{\tau}}_1+\cdots+\hat{\mathbf{F}}_1\hat{\boldsymbol{\tau}}_{N_t-1}\right)\right] &&, \quad i=N_t
\end{aligned} \tag{5.2.26}$$

Substituting the determined $\hat{\boldsymbol{\tau}}_i(=\hat{\boldsymbol{\tau}}_i^0)$ into equations (5.2.4 and 5), we can calculate the responses in the k-t domain at any elevation $z=z_m$ in both of the upper layered system and the half-space. In order to obtain the final responses in the x-t domain, we perform an inverse Fourier transformations in k as

$$\mathbf{u}_{\mathrm{I}}^{mn}(x,t) = \frac{1}{2\pi}\int_{-\infty}^{\infty}\hat{\mathbf{u}}_{\mathrm{I}}^{mn}(k,t)e^{-\mathrm{i}kx}dk \qquad (\text{for } 0\le z\le H) \tag{5.2.27}$$

$$\mathbf{u}_{\mathrm{II}}^{mn}(x,t) = \frac{1}{2\pi}\int_{-\infty}^{\infty}\hat{\mathbf{u}}_{\mathrm{II}}^{mn}(k,t)e^{-\mathrm{i}kx}dk \qquad (\text{for } z\le 0) \tag{5.2.28}$$

Next, we consider the responses due to axisymmetric loads such as point loads in the same semi-infinite medium as figure 5.2.1, which is generally formulated in a cylindrical coordinate system, i.e. in (r, θ, z). As is shown by Kausel [1981], the responses of axisymmetric problems, i.e. u_r, u_θ, u_z, can be expressed in terms of those of the plain strain problem in equation (5.2.6 or 7). Also, the Hankel transformation in 3D space substitutes the Fourier transformation in 2D space. Finally, the displacement in the space-time domain is obtained as

$$\mathbf{u}^{mn}(r,\theta,t)=\sum_{\mu=0}^{\infty}\mathbf{T}_{\mu}\int_{0}^{\infty}k\mathbf{C}_{\mu}\hat{\mathbf{u}}^{mn}(k,\theta,t)dk \tag{5.2.29}$$

where

$$\mathbf{u}^{mn}(r,\theta,t)=\left[u_r^{mn}\quad u_\theta^{mn}\quad u_z^{mn}\right]^T \tag{5.2.30}$$

$$\hat{\mathbf{u}}^{mn}(k,\theta,t)=\left[\hat{u}^{mn}\quad \hat{v}^{mn}\quad \hat{w}^{mn}\right]^T \qquad \text{equal to equation (5.2.6 or 7)} \tag{5.2.31}$$

$$\mathbf{T}_{\mu}=\begin{Bmatrix}\cos\mu\theta & \cdot & \cdot\\ \cdot & -\sin\mu\theta & \cdot\\ \cdot & \cdot & \cos\mu\theta\end{Bmatrix} \tag{5.2.32}$$

$$\mathbf{C}_{\mu}=\begin{Bmatrix}\dfrac{d}{d(kr)}J_{\mu} & \dfrac{\mu}{kr}J_{\mu} & \cdot\\ \dfrac{\mu}{kr}J_{\mu} & \dfrac{d}{d(kr)}J_{\mu} & \cdot\\ \cdot & \cdot & -J_{\mu}\end{Bmatrix} \tag{5.2.33}$$

In the above, $J_{\mu}=J_{\mu}(kr)$ are the Bessel functions of the first kind and μ-th order, k is the wavenumber in the radial direction, and μ = wavenumber in the azimuthal direction: μ=1 for a horizontal point load, and μ=0 for a vertical point load.

5.2.2 Stability and Accuracy

We consider next the stability and accuracy of the substructure method formulated in section 5.2.1. For this purpose, we discuss four issues in subsections (A), (B), (C), and (D), namely the stability, accuracy, Poisson's ratio effect, and application of a buffer layer. The stability of the technique is intimately related to the time step Δt in equation (5.2.23), because we numerically solve the associated integral equations in the form of equation (5.2.23). In subsection (A), we propose a criterion for the proper Δt through some numerical experiments, so as to obtain stable responses with the substructure method. The accuracy of this substructure method is associated with two parameters, which are the number of thin-layers per wavelength N_λ and the maximum frequency involved with the t-TLM modal solutions f_M. In subsection (B), the proper values for the two parameters are determined through some numerical examples. In subsection (C), we consider the effect of the Poisson's ratio on the response stability in *SV-P* wave problems. Finally, in subsection (D), we propose the use of a buffer layer of some minimum thickness H_B for more efficient calculation.

We proceed with the discussion of the above issues by solving a test example of a layer ($0\le z\le H$, H=1) overlain by a homogeneous half-space ($z\le 0$) subjected to a surface line load **p**. The material properties of the layer and the half-space will be specified in each subsection. Meanwhile, the applied surface line load is defined as

$$p_i(x,z,t)=f(x)\delta(z-H)h(t) \quad \text{with } i=x,\ y,\ \text{or } z \tag{5.2.34}$$

where $f(x)$ and $h(t)$ are given in the form.

$$f(x)=\begin{cases}\dfrac{1}{a}\cos^2\dfrac{\pi}{2a}x & |x|\le a\\ 0 & |x|>a\end{cases} \qquad \text{with } a \text{ being half the width of the load} \tag{5.2.35}$$

$$h(t)=\begin{cases}\dfrac{2}{t_d}\sin^2\dfrac{\pi}{t_d}t & 0\le t\le t_d \\ 0 & t<0,\ t_d<t\end{cases} \quad \text{with } t_d \text{ being the loading duration} \tag{5.2.36}$$

The line load has a bell-shaped variation in both the space x and time t, so-called *Hanning window*. The Fourier Transform of $f(x)$ and $h(t)$ are of the form.

$$\hat{f}(k)=\int_{-\infty}^{\infty} f(x)e^{ikx}dx=\frac{\sin ka}{ka[1-(ka/\pi)^2]} \tag{5.2.37}$$

$$\tilde{h}(\omega)=\int_{-\infty}^{\infty} h(t)e^{-i\omega t}dt=\frac{\sin \omega t_d/2}{\omega t_d/2\left[1-\left(\omega t_d/2\pi\right)^2\right]}e^{-i\omega t_d/2} \tag{5.2.38}$$

As shown in chapter 4, the amplitude of the given load function in the wavenumber and frequency domain becomes negligible beyond the wavenumber $k_{max}=2\pi/a$ and frequency $\omega_{max}=4\pi/t_d$, which means that the spectral components beyond k_{max} and ω_{max} are insignificant. Through this section, we set $a=t_d=0.2$, which implies $k_{max}=10\pi$ and $f_{max}=\omega_{max}/2\pi=10.0$.

(A) Stability

The first task is to decide the criterion for the proper time step Δt so as to obtain stable responses with the substructure method. Note that $\hat{\mathbf{F}}(t)$ and $\hat{\mathbf{H}}(t)$ in equations (5.2.22) are the syntheses of a certain number M of modal components whose maximum frequency f_M is to be no less than the maximum frequency of the applied load f_{max}, as discussed in chapter 4. Therefore, in order to express precisely $\hat{\mathbf{F}}(t)$ and $\hat{\mathbf{H}}(t)$ in discrete time step Δt, the following condition must be satisfied:

$$f_{max}\le f_M\le f_{\Delta t,Nyq}=1/(2\Delta t) \qquad \text{or} \qquad \Delta t\le\frac{1}{2f_M}\le\frac{1}{2f_{max}} \tag{5.2.39}$$

where $f_{\Delta t,Nyq}$ is the so-called Nyquist frequency associated with a time step Δt up to which the useful frequency range extends in the spectra defined via the Discrete Fourier Transform (DFT) or the Fast Fourier Transform (FFT). Notice that the condition in equation (5.2.39) is sufficient only for precisely expressing $\hat{\mathbf{F}}(t)$ and $\hat{\mathbf{H}}(t)$ in discrete time-series, but not for solving equation (5.2.23) in discrete time-series.

Now, we determine the criterion for the proper time step Δt by analyzing numerically the test example, where an *SH* line load p_y in equation (5.2.34) is applied and the material properties and geometry of the upper layer and the homogeneous half-space are given as $\rho_I=\rho_{II}=C_{S,I}=C_{S,II}=H=1$ and Poisson's ratio is $\nu_I=\nu_{II}=0.30$. Since the material properties of both the upper layer and the lower half-space are identical, the behavior of the whole system is exactly the same as that of a homogeneous half-space whose exact analytical solution is given in section 4.3. By means of the substructure method, we calculate the displacement response $v(x,z,t)$ at $(x,z)=(1,1)$ for $0\le t\le 5$ with changing time step Δt such that $\Delta t=1/(2f_M)$, $1/(4f_M)$, and $1/(8f_M)$ where $f_M=f_{max}$ is used. For the calculation of the Green function for the upper layer, we apply the TLM1 with $N_\lambda=8$.

The three plots in figure 5.2.3 compare the response obtained with the substructure method (solid line) against the exact analytical solution (dashed line) for $\Delta t=1/(2f_M)$, $1/(4f_M)$, and $1/(8f_M)$, respectively, with $f_M=f_{max}$ in this case. It is observed that the use of $\Delta t=1/(2f_M)$ provides a totally unstable result, while the use of $\Delta t=1/(4f_M)$ and $1/(8f_M)$ provides stable responses. In fact, the

agreement between the substructure method and the exact analytical solution is almost perfect for $\Delta t=1/(4f_M)$ and $1/(8f_M)$. Therefore, we propose the following criterion for the proper time step Δt to obtain the stable result from the substructure method.

$$\Delta t \le \frac{1}{4f_M} \tag{5.2.40}$$

However, it should be recognized that even though the results are stable with application of $\Delta t \le 1/(4f_M)$, some small errors are detected around at $t=2.24$ in the second and third plots. These small errors seem to be caused by weak spurious reflections at the interface between the upper layer and the lower half-space, which is not supposed to happen. So, our second task is to find out the causes of these spurious reflections and how to avoid them.

(B) Accuracy

As shown in the second and third plots of figure 5.2.3, there exist spurious reflections, which deteriorate the final results. There are two reasons for these spurious reflections: 1) Numerical dispersion error in the high modes computed with the *t*-TLM, and 2) Non-converged *t*-TLM modal solutions in the *k-t* domain. The first reason is obvious, because as discussed in chapters 2 and 4, the *t*-TLM provides incorrect eigenvalues and mode shapes for the highest modes. On the other hand, the second reason is not directly understandable, because we have obtained the converged and accurate results with the TLM1 using the discretization $N_\lambda=8$ recommended in chapter 4.

The explanation for this incomplete convergence of the modal solution in the *k-t* domain is as follows. All modal solutions in the *k-t* domain must be considered to be near-field responses, because in the *k-t* domain the spatially harmonic loads are distributed from $-\infty$ to $+\infty$ in the *x*-direction, so the responses are periodic as well. Thus, there are no far-field responses in the *k-t* domain. Therefore, to obtain the converged and accurate modal solutions in the *k-t* domain, an additional number of accurate high modes is necessary in the modal summation. The reason is the same as that argued in chapter 4 for near-field solutions in the *x-t* domain. Consequently, it is necessary to increase the number of thin-layers per wavelength N_λ, and include an additional number of accurate high modes having sufficiently high frequency content $f_M(>f_{max})$ in the modal solutions. In addition, the extra high modes require the adjustment of Δt according to equation (5.2.40). Otherwise, the solutions become unstable, because those high modes increase the involved maximum frequency f_M, i.e. $f_{max}<f_M$ where f_{max} is the maximum frequency of the load.

We now determine the proper values for N_λ and f_M so as to calculate accurate responses with the substructure method. For this purpose, we analyze the same test example as subsection (A) while changing N_λ and f_M for both the TLM1 and the TLM2. We consider the following six models.

Model 1: TLM1 with $N_\lambda=8$ and $f_M=f_{max}$
Model 2: TLM1 with $N_\lambda=8$ and $f_M=2f_{max}$
Model 3: TLM1 with $N_\lambda=12$ and $f_M=2f_{max}$
Model 4: TLM2 with $N_\lambda=4$ and $f_M=f_{max}$
Model 5: TLM2 with $N_\lambda=4$ and $f_M=2f_{max}$
Model 6: TLM2 with $N_\lambda=6$ and $f_M=2f_{max}$.

Figure 5.2.4 shows the displacement snap-shots at $t=1.4$ for all the six models listed above. The two snap-shots for Model 1 (TLM1 with $N_\lambda=8$ and $f_M=f_{max}$) and Model 4 (TLM2 with $N_\lambda=4$ and

$f_M=f_{max}$) confirm that weak spurious reflections take place at the interface and then propagate toward the top surface. Next, we observe that Model 2 (TLM1 with $N_\lambda=8$ and $f_M=2f_{max}$) and Model 5 (TLM2 with $N_\lambda=4$ and $f_M=2f_{max}$) decrease the degree of spurious reflection effect, but not completely, which implies that the incorrect high modes still affect the final responses. Therefore, it is concluded that accurate high modes ought to be included into the modal solutions, which can be achieved only by increasing the number of thin-layers per wavelength N_λ. Finally, it is shown form the two snap-shots in the last row of figure 5.2.4 that Model 3 (TLM1 with $N_\lambda=12$ and $f_M=2f_{max}$) and Model 6 (TLM1 with $N_\lambda=12$ and $f_M=2f_{max}$) avoid almost perfectly the effect of spurious reflection. In addition, it is noticed that the result of Model 6 is better than that of Model 3, which implies that the TLM2 provides more accurate results than the TLM1 when the same number of degree of freedoms are used, as seen in chapter 4. Finally, concerning the accuracy of the substructure method, we propose the use of

$$N_\lambda \geq 12 \qquad \text{for the TLM1} \tag{5.2.41}$$

$$N_\lambda \geq 6 \qquad \text{for the TLM2} \tag{5.2.42}$$

$$f_M \geq 2f_{max} \tag{5.2.43}$$

To complete our discussion in this subsection (B), we solve a test example in which the above homogeneous half-space is now subjected to an *SV-P* surface vertical line load p_z as given in equation (5.2.34). We apply the TLM2 with $N_\lambda=6$, $f_M=2.f_{max}$ and $\Delta t=1/(4f_M)$. Figures 5.2.5 and 6 show the snap-shots at $t=0.5$, 1.0, 1.5, and 2.0 for the horizontal(u_{zx}) and vertical(u_{zz}) displacements, respectively. It is verified that no spurious reflections take place with application of the proposed model with the TLM2 of $N_\lambda=6$, $f_M=2.f_{max}$ and $\Delta t=f_M/4$. In addition, it is observed that the Rayleigh wave motion is confined near the surface and carries most of the energy from the applied source. On the other hand, most of the energy associated with *S* and *P* waves penetrates into the half-space at the beginning and only a very small portion propagates along the surface.

Finally, it is concluded that the proposed substructure method models the wave motion within the semi-infinite (or infinite) domain with very good accuracy. In addition, the proposed technique synthesizes precisely the involved physical phenomena. Therefore, with the aid of the substructure method, we can study and explore even more complicated problems such as wave propagation in multilayered half-spaces.

(C) Poisson's ratio effect

Here, we consider the effect of Poisson's ratio ν on the stability of the substructure method, which will in turn modify the criterion for the proper time step Δt in equation (5.2.40), especially for *SV-P* wave problems with $\nu \approx 0.5$. We discuss this issue again with the test example of a homogeneous layer on a homogeneous half-space subjected to an *SV-P* surface vertical line load p_z as given in equation (5.2.34), where $\rho_I=\rho_{II}=C_{S,I}=C_{S,II}=H=1$.

In terms of Poisson' ratio ν, the ratio of *S* wave velocity to *P* wave velocity C_S/C_P is given by

$$\frac{C_P}{C_S}=\sqrt{\frac{2-2\nu}{1-2\nu}} \tag{5.2.44}$$

It is inferred from equation (5.2.44) that as $\nu \to 0.5$, the ratio tends to infinity. This significant difference between the two wave velocities can cause additional instability when the criterion in equation (5.2.40) is used. The reason is that the significant dissimilarity of the two wave

velocities produces more complicated wave motions at the interface where mode conversions are involved between S and P waves. Therefore, it is necessary to decrease the time step Δt, i.e. apply finer Δt, so as to describe more precisely the complicated wave motion.

We analyze the test example for a high Poisson's ratio ν=0.49 by means of the substructure method. We calculate the horizontal (u_{zx}) and vertical (u_{zz}) displacements with the use of the TLM2 with $N_{\lambda,QE}$=6, f_M=2.$f_{\max}$ and Δt=1/(4f_M), 1/(8f_M). It turns out that the use of Δt=f_M/4 produces unstable numerical results as the case of the first plot in figure 5.2.3 demonstrates, while the use of Δt=f_M/8 provides the stable numerical results. Figures 5.2.7 and 8 show the snap-shots at t=0.5, 1.0, 1.5, and 2.0 for the horizontal (u_{zx}) and vertical (u_{zz}) displacements, respectively. Hence, it is concluded that in *SV-P* wave problems, the time step Δt must be adjusted by taking into account the Poisson's ratio ν.

(D) Application of the buffer layer

We consider the stability of the substructure method in case that two significant dissimilar materials are contacted at the interface between the upper layered medium and the lower homogeneous half-space in figure 5.2.1. As the case of ν=0.5 in subsection (C), this significant difference in material properties can produce complicated wave motion at the interface such as mode conversion, reflection, and refraction. It follows that a much finer time step Δt is necessary for calculating stable responses. As a result, the computational cost may increase significantly.

To avoid this inefficiency, we here propose the use of a buffer layer of certain thickness H_B whose material properties are identical to the lower homogeneous half-space. This buffer layer is located between the upper layered medium and the lower homogeneous half-space, which is basically equivalent to shifting down the interface by H_B at which equations (5.2.23-25) are established and solved. This shifted interface is now an artificial one, because it is located between two identical materials. For practical purpose, we also propose the thickness of the buffer layer H_{BL} in the form.

$$H_{\mathrm{BL}} \geq \lambda_{\min} \tag{5.2.45}$$

where $\lambda_{\min}$ is the minimum wavelength in analysis.

For practical verification of the proposed buffer layer, we solve the test example of a homogeneous layer (ρ_{I}=$C_{S,\mathrm{I}}$=1.0, H=1.0, 0≤z≤H) overlain by a homogeneous half-space (ρ_{II}=1, $C_{S,\mathrm{II}}$=3.0, z≤0) subjected to an *SH* surface line load p_y in equation (5.2.34). We analyze this example by means of the TLM2 of N_λ=6, f_M=2.0f_{max}. Also, we consider three models: (1) Δt=1/(4f_M) without a buffer layer, (2) Δt=1/(8f_M) without a buffer layer, and (3) Δt=1/(4f_M) with a buffer layer of H_B=$\lambda_{\min}$ as suggested in equation (5.2.45). In this present example, $\lambda_{\min}$(=$C_{S,\mathrm{II}}$/$f_{\max}$)=3/10=0.3.

It turns out that the first model of Δt=1/(4f_M) without a buffer layer produces unstable result, as seen in the first plot of figure 5.2.3. On the other hand, the second and third models with Δt=1/(8f_M) without a buffer layer, and Δt=1/(4f_M) with a buffer layer of H_B=$\lambda_{\min}$ produce both stable results. Figure 5.2.9 presents the displacement snap-shots at t=0.5, 1.0, 1.5, and 2.0 obtained with Δt=1/(8f_M) without a buffer layer. Figure 5.2.10 displays the displacement snap-shots at t=0.5, 1.0, 1.5, and 2.0 obtained with Δt=1/(4f_M) with a buffer layer of H_B=$\lambda_{\min}$=0.3. Notice that the agreement between the two figures is remarkable. Finally, it is proved that the

application of a buffer layer of $H_B=\lambda_{min}$ improves the responses obtained with the substructure method from the point of view of both its efficiency and accuracy.

5.3 Green's functions in *k-t* domain on a homogeneous half-space

We derive here the Green functions in the *k-t* domain for a homogeneous half-space ($z\leq 0$) subjected to *SH* and *SV-P* surface line loads. For the case of an *SH* line load, the Green function is obtained in a completely closed form. On the other hand, for *SV-P* line loads, the Green functions are obtained by contour integration in the complex frequency plane and expressed in terms of the summation of the residues associated with the poles (i.e. free vibration terms) and branch-cut integrals without singularities.

5.3.1 Green's function for *SH* surface line loads

We start by deriving the Green function for *SH* surface line loads. First, consider a homogeneous half-space ($z\leq 0$) subjected to an *SH* surface line load, whose governing equation is established in the form

$$\rho\frac{\partial^2 v}{\partial t^2}-G\left[\frac{\partial^2 v}{\partial z^2}+\frac{\partial^2 v}{\partial z^2}\right]=p_y=\delta(x)\delta(z)\delta(t) \tag{5.3.1}$$

where $v=v(x,z,t)$ is the displacement in the y-direction expressed in the x-t domain, δ is the Dirac delta function, ρ is the mass density, and G is the shear modulus. Applying a double Fourier transformations to $v(x,z,t)$ with respect to x and t, we obtain the general solution for $z\leq 0$ in the k-ω domain in the absence of external force p_y as

$$\bar{v}(k,z,\omega)=Ae^{ksz} \tag{5.3.2}$$

where A is an unknown constant, $s=\sqrt{1-(\omega/kC_S)^2}$, and $C_S=\sqrt{G/\rho}$ (=shear velocity). Applying the traction boundary condition at the top surface, we can determine the unknown constant A and finally obtain the Green function $\bar{G}_{yy}$ in the k-ω domain as

$$\bar{G}_{yy}(k,z,\omega)=\frac{1}{Gks}e^{ksz} \tag{5.3.3}$$

In order to obtain the Green function in the *k-t* domain, we perform an inverse Fourier transform in ω as

$$\hat{G}_{yy}(k,z,t)=\frac{1}{2\pi}\int_{-\infty}^{\infty}\bar{G}_{yy}(k,z,\omega)e^{i\omega t}d\omega=\frac{1}{2\pi}\int_{-\infty}^{\infty}\frac{1}{Gks}e^{ksz}e^{i\omega t}d\omega \tag{5.3.4}$$

This inverse Fourier transformation has an exact solution, as given in the mathematical handbook by Spiegel [1968]. The final result is then

$$\hat{G}_{yy}(k,z,t)=\begin{cases}\dfrac{1}{\rho C_S}J_0\left(kC_S\sqrt{t^2-z^2/C_S^2}\right) & , \quad z/C_S\leq t \\ 0 & , \quad z/C_S>t\end{cases} \tag{5.3.5}$$

where J_0 is the Bessel function of the first kind and 0-th order.

5.3.2 Green's functions for *SV-P* surface line loads

Next, we derive the Green functions for *SV-P* surface line loads. First, consider a homogeneous half-space ($z \le 0$) subjected to *SV-P* surface line loads, for which the governing equation is given in matrix form as

$$\rho \ddot{\mathbf{u}} - \mathbf{L}^T \mathbf{D} \mathbf{L} \mathbf{u} = \mathbf{p} \tag{5.3.6}$$

where ρ is the mass density, the superscript dot represents the partial derivative with respect to time t,

$$\mathbf{u}(x,z,t) = \{u \quad w\}^T \qquad \text{(the displacement vector)} \tag{5.3.7a}$$

$$\mathbf{p}(x,z,t) = \{p_x \quad p_z\}^T \qquad \text{(the applied line load vector)} \tag{5.3.7b}$$

$$\mathbf{D} = \begin{bmatrix} \lambda+2G & \lambda & \cdot \\ \lambda & \lambda+2G & \cdot \\ \cdot & \cdot & G \end{bmatrix} \qquad \text{(the constitutive matrix)} \tag{5.3.7c}$$

$$\mathbf{L} = \mathbf{L}_x \frac{\partial}{\partial x} + \mathbf{L}_z \frac{\partial}{\partial z} \qquad \text{(the differential operator)} \tag{5.3.7d}$$

$$\mathbf{L}_x = \begin{bmatrix} 1 & \cdot & \cdot \\ \cdot & \cdot & 1 \end{bmatrix}^T, \text{ and } \mathbf{L}_z = \begin{bmatrix} \cdot & \cdot & 1 \\ \cdot & 1 & \cdot \end{bmatrix}^T \tag{5.3.7e,f}$$

In the constitutive matrix $\mathbf{D}$, the constants λ and G are referred to as the *Lamé*'s constants. Applying the double Fourier transformations to $\mathbf{u}(x,z,t)$ with respect to x and t, we obtain the general solution in the k-ω domain in the absence of external force $\mathbf{p}$ as

$$\bar{\mathbf{u}}(k,z,\omega) = \begin{Bmatrix} \bar{u} \\ \bar{w} \end{Bmatrix} = \begin{bmatrix} e^{krz} & e^{ksz} \\ \mathrm{i}re^{krz} & \mathrm{i}/s\, e^{ksz} \end{bmatrix} \begin{Bmatrix} A \\ B \end{Bmatrix} \tag{5.3.8}$$

where A, B are unknown constants, $r = \sqrt{1-(\omega/kC_P)^2}$, $s = \sqrt{1-(\omega/kC_S)^2}$, $C_P = \sqrt{(\lambda+2G)/\rho}$, and $C_S = \sqrt{G/\rho}$. Combining the traction conditions at the top surface with equation (5.3.8), we end up with the Green functions $\bar{G}_{ij}(k,z,\omega)$ in the k-ω domain as

$$\bar{G}_{xx}(k,z,\omega) = \frac{1}{4kG\Delta}\left[2se^{krz} - s(1+s^2)e^{ksz}\right] \tag{5.3.9a}$$

$$\bar{G}_{zx}(k,z,\omega) = \frac{\mathrm{i}}{4kG\Delta}\left[2rse^{krz} - (1+s^2)e^{ksz}\right] \tag{5.3.9b}$$

$$\bar{G}_{xz}(k,z,\omega) = \frac{\mathrm{i}}{4kG\Delta}\left[(1+s^2)e^{krz} - 2rse^{ksz}\right] \tag{5.3.9c}$$

$$\bar{G}_{zz}(k,z,\omega) = \frac{1}{4kG\Delta}\left[-r(1+s^2)e^{krz} + 2se^{ksz}\right] \tag{5.3.9d}$$

where

$$\Delta = -\frac{1}{4}(1+s^2)^2 + rs \tag{5.3.10}$$

Equation (5.3.10) is the well known Rayleigh surface wave equation that provides a non-dispersive *SV-P* propagation mode. A very close solution to this equation is

$$\omega_R = kC_R \tag{5.3.11a}$$

$$C_R = C_S(-0.0276\nu^3 - 0.056\nu^2 + 0.197\nu + 0.874) \tag{5.3.11b}$$

where C_R is the phase velocity of Rayleigh wave, and ν is the Poisson's ratio of the half-space of interest.

To obtain the Green functions in the *k-t* domain, we have to perform the inverse Fourier transform over ω in the form.

$$\hat{G}_{ij}(k,z,t)=\frac{1}{2\pi}\int_{-\infty}^{\infty}\bar{G}_{ij}(k,z,\omega)e^{i\omega t}d\omega \tag{5.3.12}$$

We begin by defining the parameters needed in the derivation that follows:

$$\Omega=\frac{\omega}{kC_S} \qquad \text{(dimensionless frequency)} \tag{5.3.13a}$$

$$\tau=kC_S t \qquad \text{(dimensionless time)} \tag{5.3.13b}$$

$$a=\frac{C_S}{C_P}=\sqrt{\frac{1-2\nu}{2-2\nu}} \qquad \text{(ratio of wave speeds)} \tag{5.3.13c}$$

$$r=\sqrt{1-(\omega/kC_P)^2}=\sqrt{1-a^2\Omega^2}=i\alpha \tag{5.3.13d}$$

$$s=\sqrt{1-(\omega/kC_S)^2}=\sqrt{1-\Omega^2}=i\beta \tag{5.3.13e}$$

$$\Delta_1=-\frac{1}{4}(1-\beta^2)^2-\alpha\beta \tag{5.3.13f}$$

$$\Delta_2=-\frac{1}{4}(1-\beta^2)^2+ir\beta \tag{5.3.13g}$$

$$\Delta_2^*=-\frac{1}{4}(1-\beta^2)^2-ir\beta=conj(\Delta_2) \tag{5.3.13h}$$

$$\Omega_S=\frac{\omega_S}{kC_S}=\frac{kC_S}{kC_S}=1 \qquad \text{(dimensionless branch-point for } S \text{ wave)} \tag{5.3.13i}$$

$$\Omega_P=\frac{\omega_P}{kC_S}=\frac{kC_P}{kC_S}=\frac{1}{a} \qquad \text{(dimensionless branch-point for } P \text{ wave)} \tag{5.3.13j}$$

$$\Omega_R=\frac{\omega_R}{kC_S} \qquad \text{(dimensionless Rayleigh pole)} \tag{5.3.13k}$$

$$r_R=r(\Omega=\Omega_R) \tag{5.3.13l}$$

$$s_R=s(\Omega=\Omega_R) \tag{5.3.13m}$$

$$D_R=\left.\frac{d\Delta}{d\Omega}\right|_{\Omega=\Omega_R}=\Omega_R\left[2-\Omega_R^2-\frac{r_R}{s_R}-a^2\frac{s_R}{r_R}\right] \tag{5.3.13n}$$

With the dimensionless parameters defined above, equation (5.3.12) can be expresses as

$$\begin{aligned}\hat{G}_{xx}(k,z,t)&=\frac{1}{8\pi\rho C_S}\int_{-\infty}^{\infty}\frac{1}{\Delta}\left[2se^{krz}-s(1+s^2)e^{ksz}\right]e^{i\Omega\tau}d\Omega\\&=\frac{1}{8\pi\rho C_S}\int_{-\infty}^{\infty}K_{xx}(s,r,\Delta)e^{i\Omega\tau}d\Omega\\&=\frac{1}{8\pi\rho C_S}I_{xx}\end{aligned} \tag{5.3.14a}$$

$$\hat{G}_{zx}(k,z,t) = \frac{\mathrm{i}}{8\pi\rho C_S}\int_{\infty}^{\infty}\frac{1}{\Delta}\left[2rse^{krz} - (1+s^2)e^{ksz}\right]e^{\mathrm{i}\Omega\tau}d\Omega$$

$$= \frac{\mathrm{i}}{8\pi\rho C_S}\int_{\infty}^{\infty}K_{zx}(s,r,\Delta)e^{\mathrm{i}\Omega\tau}d\Omega \qquad (5.3.14b)$$

$$= \frac{\mathrm{i}}{8\pi\rho C_S}I_{zx}$$

$$\hat{G}_{xz}(k,z,t) = \frac{\mathrm{i}}{8\pi\rho C_S}\int_{\infty}^{\infty}\frac{1}{\Delta}\left[(1+s^2)e^{krz} - 2rse^{ksz}\right]e^{\mathrm{i}\Omega\tau}d\Omega$$

$$= \frac{\mathrm{i}}{8\pi\rho C_S}\int_{\infty}^{\infty}K_{xz}(s,r,\Delta)e^{\mathrm{i}\Omega\tau}d\Omega \qquad (5.3.14c)$$

$$= \frac{\mathrm{i}}{8\pi\rho C_S}I_{xz}$$

$$\hat{G}_{zz}(k,z,t) = \frac{1}{8\pi\rho C_S}\int_{\infty}^{\infty}\frac{1}{\Delta}\left[-r(1+s^2)e^{krz} + 2se^{ksz}\right]e^{\mathrm{i}\Omega\tau}d\Omega$$

$$= \frac{1}{8\pi\rho C_S}\int_{\infty}^{\infty}K_{zz}(s,r,\Delta)e^{\mathrm{i}\Omega\tau}d\Omega \qquad (5.3.14d)$$

$$= \frac{1}{8\pi\rho C_S}I_{zz}$$

where K_{ij} are the kernels for each integral and shown to be the functions of s, r, Δ.

We proceed to calculate the four integrals I_{xx}, I_{zx}, I_{xz}, and I_{zz} defined in equations (5.3.14a-d). Instead of performing integration along the real Ω-axis as in equations (5.3.14a-d), we deform the integration path in the upper complex Ω-plane, or Ω_C-plane, as shown in figure 5.3.1. The use of $e^{\mathrm{i}\Omega\tau}$ in equations (5.3.14a-d) requires the upper Ω_C-plane. Since the integrands in each integral are odd functions of both of s and r, the branch-cuts around both of $\Omega = \pm\Omega_S (= \pm 1)$ and $\Omega = \pm\Omega_P (= \pm 1/a)$ are made along both of $\mathrm{Re}\, s = 0$ and $\mathrm{Re}\, r = 0$. The resulting contour integral has the form.

$$\begin{aligned}\oint dI_{ij} &= I_{ij} + \int_{\infty}^{1/a} dI_{ij} + \int_{1/a}^{1} dI_{ij} + \int_{1}^{1/a} dI_{ij} + \int_{1/a}^{\infty} dI_{ij} \\ &+ \int_{C_\infty} dI_{ij} + \int_{-\infty}^{-1/a} dI_{ij} + \int_{-1/a}^{-1} dI_{ij} + \int_{-1}^{-1/a} dI_{ij} + \int_{-1/a}^{\infty} dI_{ij} \\ &= 2\pi\mathrm{i}\sum \mathrm{Residues}\end{aligned} \qquad (5.3.15)$$

where $i,j=x,z$. All the integrands vanish on C_∞, so equation (5.3.15) can be expresses as

$$I_{ij} = 2\pi\mathrm{i}\sum(\mathrm{Residues})_{ij} - \int_{Branch-cut} dI_{ij} \qquad (5.3.16a)$$

$$\begin{aligned}\int_{Branch-cut} dI_{ij} &= \int_{\infty}^{1/a} dI_{ij} + \int_{1/a}^{1} dI_{ij} + \int_{1}^{1/a} dI_{ij} + \int_{1/a}^{\infty} dI_{ij} \\ &+ \int_{-\infty}^{-1/a} dI_{ij} + \int_{-1/a}^{1} dI_{ij} + \int_{-1}^{-1/a} dI_{ij} + \int_{-1/a}^{\infty} dI_{ij}\end{aligned} \qquad (5.3.16b)$$

For the proper contour integrals, we have to identify the correct phase of complex r and s along the deformed integration paths. We first inspect s and then apply the same reasoning to r. For this purpose, we shift down the frequency axis by $\mathrm{i}\eta$, as shown in figure 5.3.2. Then, s^2 is given as

$$
\begin{aligned}
s^2(\Omega_C) &= 1-(\Omega_C - \mathrm{i}\eta)^2 \\
&= 1-(\Omega + \mathrm{i}\zeta - \mathrm{i}\eta)^2 \\
&= 1-\Omega^2 + (\zeta-\eta)^2 + 2\mathrm{i}\Omega(\eta-\zeta)
\end{aligned}
\tag{5.3.17}
$$

By examining the signs of $\mathrm{Re}\, s^2$ and $\mathrm{Im}\, s^2$, we decide on which of the four quadrants the function s^2 lies; these quadrants (labeled by four small letters of i, ii, iii, iv) are shown in figure 5.3.2. Based on this, we can decide on which of the four quadrants (labeled by four large letters of I, II, III, IV) the function s is located, again as shown in figure 5.3.2. The Branch-cut integrals are then expressed as

$$
\begin{aligned}
\int_{Branch-cut} dI_{ij} = & \int_{1/a}^{1} K_{ij}(\mathrm{i}\beta, r, \Delta_2) e^{\mathrm{i}\Omega\tau} d\Omega + \int_{1}^{1/a} K_{ij}(-\mathrm{i}\beta, r, \Delta_2^*) e^{\mathrm{i}\Omega\tau} d\Omega \\
& + \int_{-1/a}^{-1} K_{ij}(\mathrm{i}\beta, r, \Delta_2) e^{\mathrm{i}\Omega\tau} d\Omega + \int_{-1}^{-1/a} K_{ij}(-\mathrm{i}\beta, r, \Delta_2^*) e^{\mathrm{i}\Omega\tau} d\Omega \\
& + \int_{\infty}^{1/a} K_{ij}(\mathrm{i}\beta, \mathrm{i}\alpha, \Delta_1) e^{\mathrm{i}\Omega\tau} d\Omega + \int_{1/a}^{\infty} K_{ij}(-\mathrm{i}\beta, -\mathrm{i}\alpha, \Delta_1) e^{\mathrm{i}\Omega\tau} d\Omega \\
& + \int_{-\infty}^{-1/a} K_{ij}(\mathrm{i}\beta, \mathrm{i}\alpha, \Delta_1) e^{\mathrm{i}\Omega\tau} d\Omega + \int_{-1/a}^{-\infty} K_{ij}(-\mathrm{i}\beta, -\mathrm{i}\alpha, \Delta_1) e^{\mathrm{i}\Omega\tau} d\Omega
\end{aligned}
\tag{5.3.18}
$$

where K_{ij} are the kernels in each integrand as defined in equations (5.3.14). Changing the integration direction so as to increase the absolute value of Ω along the path, we obtain

$$
\begin{aligned}
\int_{Branch-cut} dI_{ij} = & -\int_{1}^{1/a} K_{ij}(\mathrm{i}\beta, r, \Delta_2) e^{\mathrm{i}\Omega\tau} d\Omega + \int_{1}^{1/a} K_{ij}(-\mathrm{i}\beta, r, \Delta_2^*) e^{\mathrm{i}\Omega\tau} d\Omega \\
& - \int_{-1}^{-1/a} K_{ij}(\mathrm{i}\beta, r, \Delta_2) e^{\mathrm{i}\Omega\tau} d\Omega + \int_{-1}^{-1/a} K_{ij}(-\mathrm{i}\beta, r, \Delta_2^*) e^{\mathrm{i}\Omega\tau} d\Omega \\
& - \int_{1/a}^{\infty} K_{ij}(\mathrm{i}\beta, \mathrm{i}\alpha, \Delta_1) e^{\mathrm{i}\Omega\tau} d\Omega + \int_{1/a}^{\infty} K_{ij}(-\mathrm{i}\beta, -\mathrm{i}\alpha, \Delta_1) e^{\mathrm{i}\Omega\tau} d\Omega \\
& - \int_{-1/a}^{-\infty} K_{ij}(\mathrm{i}\beta, \mathrm{i}\alpha, \Delta_1) e^{\mathrm{i}\Omega\tau} d\Omega + \int_{-1/a}^{-\infty} K_{ij}(-\mathrm{i}\beta, -\mathrm{i}\alpha, \Delta_1) e^{\mathrm{i}\Omega\tau} d\Omega
\end{aligned}
\tag{5.3.19}
$$

Since the kernels in each row of equation (5.3.19) are conjugate to each other, the expression simplifies into

$$
\begin{aligned}
\int_{Branch-cut} dI_{ij} = & \int_{1}^{1/a} 2\mathrm{i}\,\mathrm{Im}\left[K_{ij}(-\mathrm{i}\beta, r, \Delta_2^*)\right] e^{\mathrm{i}\Omega\tau} d\Omega \\
& + \int_{1}^{1/a} 2\mathrm{i}\,\mathrm{Im}\left[K_{ij}(-\mathrm{i}\beta, r, \Delta_2^*)\right] e^{\mathrm{i}\Omega\tau} d\Omega \\
& + \int_{1/a}^{\infty} 2\mathrm{i}\,\mathrm{Im}\left[K_{ij}(-\mathrm{i}\beta, -\mathrm{i}\alpha, \Delta_1)\right] e^{\mathrm{i}\Omega\tau} d\Omega \\
& + \int_{-1/a}^{-\infty} 2\mathrm{i}\,\mathrm{Im}\left[K_{ij}(-\mathrm{i}\beta, -\mathrm{i}\alpha, \Delta_1)\right] e^{\mathrm{i}\Omega\tau} d\Omega
\end{aligned}
\tag{5.3.20}
$$

Additionally, replacing Ω by $-\Omega$ in the second and fourth integrals and considering the conjugate relationship between $e^{\mathrm{i}\Omega\tau}$ and $e^{-\mathrm{i}\Omega\tau}$, we can simplify the branch-cut integrals in equation (5.3.20) as

$$
\begin{aligned}
\int_{Branch-cut} dI_{ij} = & -4\int_{1}^{1/a} \mathrm{Im}\left[K_{ij}(-\mathrm{i}\beta, r, \Delta_2^*)\right] \sin\Omega\tau d\Omega \\
& -4\int_{1/a}^{\infty} \mathrm{Im}\left[K_{ij}(-\mathrm{i}\beta, -\mathrm{i}\alpha, \Delta_1)\right] \sin\Omega\tau d\Omega
\end{aligned}
\tag{5.3.21}
$$

Next, we consider the residues at $\Omega=\pm\Omega_R$. The residues of I_{ij} can be obtained as follows.

$$\sum(\text{Residues})_{ij} = \lim_{\Omega\to-\Omega_R}(\Omega+\Omega_R)K_{ij}e^{i\Omega\tau} + \lim_{\Omega\to\Omega_R}(\Omega-\Omega_R)K_{ij}e^{i\Omega\tau}$$

$$= \lim_{\Omega\to-\Omega_R}(\Omega+\Omega_R)\frac{N_{ij}}{\Delta}e^{i\Omega\tau} + \lim_{\Omega\to\Omega_R}(\Omega-\Omega_R)\frac{N_{ij}}{\Delta}e^{i\Omega\tau} \tag{5.3.22}$$

$$= \frac{N_{ij}(-\Omega_R)}{\left.\frac{d\Delta}{d\Omega}\right|_{\Omega=-\Omega_R}}e^{-i\Omega_R\tau} + \frac{N_{ij}(\Omega_R)}{\left.\frac{d\Delta}{d\Omega}\right|_{\Omega=\Omega_R}}e^{i\Omega_R\tau}$$

where $N_{ij}= N_{ij}(\Omega)$ represent only the numerator parts in the kernels in equations (5.3.14). Also, it can easily be observed that $N_{ij}(-\Omega_R)= N_{ij}(\Omega_R)$ and $d\Delta/d\Omega|_{\Omega=-\Omega R}=-d\Delta/d\Omega|_{\Omega=\Omega R}$. Due to the conjugate property of the two terms, only the imaginary parts survive and the result is then given in the form

$$\sum(\text{Residues})_{ij} = 2i\,\text{Im}\left[\frac{N_{ij}(\Omega_R)}{D_R}e^{i\Omega_R\tau}\right] = 2i\frac{N_{ij}(\Omega_R)}{D_R}\sin\Omega_R\tau \tag{5.3.23}$$

Then, substitution of equations (5.3.21) and (5.3.23) into equation (5.3.16a) yields

$$I_{ij} = -4\pi\frac{N_{ij}(\Omega_R)}{D_R}\sin\Omega_R\tau$$
$$+4\int_1^{1/a}\text{Im}\left[K_{ij}(-i\beta,r,\Delta_2^*)\right]\sin\Omega\tau d\Omega \tag{5.3.24}$$
$$+4\int_{1/a}^{\infty}\text{Im}\left[K_{ij}(-i\beta,-i\alpha,\Delta_1)\right]\sin\Omega\tau d\Omega$$

The final expressions for the Green functions in *k-t* domain are in the compact form

$$\hat{G}_{ij}(k,z,t) = \frac{e_{ij}}{8\pi\rho C_S}I_{ij}$$

$$= \frac{e_{ij}}{2\pi\rho C_S}\left\{-\pi\frac{N_{ij}(\Omega_R)}{D_R}\sin\Omega_R\tau + \int_1^{1/a}\text{Im}\left[K_{ij}(-i\beta,r,\Delta_2^*)\right]\sin\Omega\tau d\Omega\right. \tag{5.3.25}$$
$$\left. + \int_{1/a}^{\infty}\text{Im}\left[K_{ij}(-i\beta,-i\alpha,\Delta_1)\right]\sin\Omega\tau d\Omega\right\}$$

where $e_{xx}=e_{zz}=1$and $e_{zx}=e_{xz}=i$. To efficiently calculate the above branch-cut integrals, we apply Hermite interpolations to the kernels. We display the four Green functions in the following explicit form.

$$\hat{G}_{xx} = \frac{1}{2\pi\rho C_S}\left\{\frac{-\pi\left[2s_Re^{kr_Rz} - s_R(1+s_R^2)e^{ks_Rz}\right]}{D_R}\sin\Omega_R\tau\right.$$
$$-\int_{1/a}^{\infty}\frac{2\beta\cos k\alpha z - \beta(1-\beta^2)\cos k\beta z}{\Delta_1}\sin\Omega\tau d\Omega \tag{5.3.26a}$$
$$\left.-\int_1^{1/a}\frac{2\beta e^{krz}\,\text{Re}[\Delta_2] - \beta(1-\beta^2)\,\text{Re}\left[e^{-ik\beta z}\Delta_2\right]}{\Delta_2\Delta_2^*}\sin\Omega\tau d\Omega\right\}$$

$$\hat{G}_{zx}=\frac{\mathrm{i}}{2\pi\rho C_S}\left\{\frac{\pi\left[-2r_R s_R e^{kr_R z}+(1+s_R^2)e^{ks_R z}\right]}{D_R}\sin\Omega_R\tau\right.$$
$$-\int_{1/a}^{\infty}\frac{-2\alpha\beta\sin k\alpha z-(1-\beta^2)\sin k\beta z}{\Delta_1}\sin\Omega\tau d\Omega \qquad (5.3.26b)$$
$$\left.-\int_1^{1/a}\frac{2r\beta e^{krz}\,\mathrm{Re}[\Delta_2]+(1-\beta^2)\,\mathrm{Im}\left[e^{-\mathrm{i}k\beta z}\Delta_2\right]}{\Delta_2\Delta_2^*}\sin\Omega\tau d\Omega\right\}$$

$$\hat{G}_{xz}=\frac{\mathrm{i}}{2\pi\rho C_S}\left\{\frac{\pi\left[-(1+s_R^2)e^{kr_R z}+2r_R s_R e^{ks_R z}\right]}{D_R}\sin\Omega_R\tau\right.$$
$$-\int_{1/a}^{\infty}\frac{(1-\beta^2)\sin k\alpha z+2\alpha\beta\sin k\beta z}{\Delta_1}\sin\Omega\tau d\Omega \qquad (5.3.26c)$$
$$\left.-\int_1^{1/a}\frac{-(1-\beta^2)e^{krz}\,\mathrm{Im}[\Delta_2]-2r\beta\,\mathrm{Re}\left[e^{-\mathrm{i}k\beta z}\Delta_2\right]}{\Delta_2\Delta_2^*}\sin\Omega\tau d\Omega\right\}$$

$$\hat{G}_{zz}=\frac{1}{2\pi\rho C_S}\left\{\frac{\pi\left[r_R(1+s_R^2)e^{kr_R z}-2r_R e^{ks_R z}\right]}{D_R}\sin\Omega_R\tau\right.$$
$$-\int_{1/a}^{\infty}\frac{-\alpha(1-\beta^2)\cos k\alpha z+2\alpha\cos k\beta z}{\Delta_1}\sin\Omega\tau d\Omega \qquad (5.3.26d)$$
$$\left.-\int_1^{1/a}\frac{r(1-\beta^2)e^{krz}\,\mathrm{Im}[\Delta_2]-2r\,\mathrm{Im}\left[e^{-\mathrm{i}k\beta z}\Delta_2\right]}{\Delta_2\Delta_2^*}\sin\Omega\tau d\Omega\right\}$$

To complete our formulation, we present the Green functions for the case of k=0, which can be obtained in closed form as follows:

$$\hat{G}_{xx}=\begin{cases}\dfrac{1}{\rho C_S} & ,\ z/C_S\le t\\ 0 & ,\ z/C_S>t\end{cases} \qquad (5.3.27a)$$

$$\hat{G}_{zx}=0 \qquad (5.3.27b)$$

$$\hat{G}_{xz}=0 \qquad (5.3.27c)$$

$$\hat{G}_{zz}=\begin{cases}\dfrac{1}{\rho C_P} & ,\ z/C_P\le t\\ 0 & ,\ z/C_P>t\end{cases} \qquad (5.3.27d)$$

5.4 Applications to multilayered half-spaces

5.4.1 Anti-plane problems

Here, we analyze two numerical examples of multilayered half-spaces subjected to an *SH* transient line load, by means of the substructure method developed. The two examples are 1) a one-layered system on a homogeneous half-space, and 2) a two-layered system on a homogeneous half-space. Through these analyses, we illustrate wave motions within the upper layered domains in terms of displacement snapshots. The wave motions observed here are much more complicated than in the case of a homogeneous half-space. The reason is that due to the dissimilarity of material properties, the phenomena of reflection and transmission (or refraction) occur at the interfaces between the layers. In addition, head waves propagate through the media as well.

Consider the first example: a one-layered system ($0 \le z \le H$) on a homogeneous half-space ($z \le 0$) subjected to an *SH* transient line load. The mass density, the shear wave velocity, and the thickness of the upper layer are $\rho_1 = C_{S,1} = H = 1.0$, while the mass density and the shear wave velocity of the lower half-space are $\rho_2 = 1.0$ and $C_{S,2} = 2.0$. The *SH* line load is applied at the top-surface, i.e. $z = H(=1)$, and its variations in both x and t are defined by a bell-shaped function, i.e. so-called *Hanning* window, with $a = t_d = 0.2$, as defined in equations (4.2.35 and 36). Then, the associated maximum wavenumber $k_{\max}$ and maximum frequency $f_{\max}$ are 10π and 10. For discrete models, we apply the TLM2 with $N_\lambda = 8$, $\Delta t = 1/(4f_M)$, and a buffer layer of $H_{BL} = \lambda_{\min}$. Since $\lambda_{\min}(=C_{S,2}/f_{\max})$ is 0.2 in the present example, H_{BL} is chosen as 0.2.

Figure 5.4.1 shows the displacement snapshots at $t = 1$, 2, 3, and 4 for the upper one-layered system ($0 \le z \le 1$) in terms of a standard surface plot. The first snapshot for $t = 1$ shows that only the direct wave propagates with circular wavefronts through the medium, which is exactly identical to the case of a homogeneous half-space whose material properties are the same as the upper layer. The second snapshot for $t = 2$ displays the direct wave propagating still in the same fashion as the case of a homogeneous half-space, and the first reflection at the interface of $z = 0$ propagating upward and forming elliptical wavefronts. Notice that the polarization of this first reflection wave is opposite to the direct wave, because the half-space is stiffer than the upper layer, i.e. $C_{S,1} < C_{S,2}$. The third snapshot for $t = 3$ illustrates the direct wave propagating nearly vertically, and the first reflection at the top-surface at $z = 1$ propagating downward with elliptical wavefronts and without change in polarization. In addition, as can be seen in the third snapshot, a weak head wave propagates ahead of the direct wave. Finally, it is observed in the fourth snapshot for $t = 4$ that because most of the energy generated by the external source leaks into the half-space during multiple reflections, the amplitudes of all the reflected waves become progressively smaller. On the other hand, the direct wave propagates continues with significant amplitude.

Now, consider the second example: a two-layered system ($0 \le z \le H$, with $H = H_1 + H_2$) on a homogeneous half-space ($z \le 0$) subjected to an *SH* transient line load. The mass densities, the shear wave velocities, and the thickness' of the two upper layers are $\rho_1 = C_{S,1} = H_1 = 1.0$, and $\rho_2 = H_2 = 1.0$, $C_{S,2} = 2$, respectively, while the mass density and the shear wave velocity of the lower half-space are $\rho_3 = 1.0$ and $C_{S,3} = 3.0$, respectively. The *SH* line load is applied at the top-surface, i.e. $z = H(=H_1 + H_2 = 2)$, and its variations in both x and t are defined by a bell-shaped function, i.e. a Hanning window with $a = t_d = 0.2$, as defined in equations (4.2.35 and 36). Then, the associated

maximum wavenumber k_{max} and maximum frequency f_{max} are 10π and 10. For discrete models, we apply the TLM2 with N_λ=8, Δt=1/(4f_M), and a buffer layer H_{BL}=λ_{min}. Since λ_{min}(=$C_{S,3}/f_{max}$) is 0.3 in the present example, H_{BL} is chosen as 0.3.

Figure 5.4.2 displays the displacement snapshots at t=1, 2, 3, and 4 for the upper two-layered system ($0 \le z \le 2$) in terms of a standard surface plot. In each plot, the dotted line at z=1 represents the interface between the first ($1 \le z \le 2$) and second ($0 \le z \le 1$) upper layer. The first snapshot for t=1 shows that only the direct wave propagates with circular wavefronts through the medium, which is exactly identical to the case of a homogeneous half-space whose material properties are equal to those of the first upper layer ($1 \le z \le 2$). Next, it is observed in the second snapshot for t=2 that the wave motion in the first layer ($1 \le z \le 2$) is identical to the snapshot for t=2 of figure 5.4.1. In addition, it is shown that the first transmitted wave from the first layer ($1 \le z \le 2$) to the second layer ($0 \le z \le 1$) refracts and propagates through the second layer, and the first reflection wave at the interface at z=0 propagates with relatively weak amplitude. The weak amplitude of the reflection wave implies that most energy from the source has already leaked into the half-space. The third snapshot for t=3 shows again the similarity to the third snapshot in figure 5.4.1 for the first layer ($1 \le z \le 2$). However, there is a difference as well, that is, the first transmitted wave from the second layer ($0 \le z \le 1$) to the first layer ($1 \le z \le 2$) propagates through the first layer with weak amplitude. This transmitted wave results from the first reflection at the interface at z=0. In addition, two head waves are observed in the third snapshot for t=3, because not only the second layer is stiffer than the first layer, but also the half-space is stiffer than the second layer. One propagates through the first layer ahead of the direct wave generated by the source, and the other propagates through the both first and second layers ahead of both the direct wave and first transmitted wave from the first layer to the second layer. Finally, the fourth snapshot for t=4 illustrates that the wave motion in the first layer is similar to the fourth snapshot in figure 5.4.1, except the effect of the reflection waves at z=0. Also, notice that since most energy from the external source to the second layer leaks into the half-space during multiple reflections, the amplitudes of all the waves in the second layer become very small.

5.4.2 In-plane problems

Next, we analyze two numerical examples of multilayered half-spaces subjected to an *SV-P* vertical line load, by means of the substructure method developed. The two examples are 1) a one-layered system on a homogeneous half-space, and 2) a two-layered system on a homogeneous half-space. Through these analyses, we illustrate wave motions within the upper layered domains of interest in terms of snapshots for both the horizontal and vertical displacements u and w. The wave motions involved here are much more complicated than in the case of a homogeneous half-space. The reason is that because of the dissimilarity of material properties, the phenomena of reflection, transmission, refraction, and head waves occur at the interfaces between the layers. In addition, since both of *S* and *P* wave components are involved, the mode conversions between the two components also take place at each interface.

Consider the first example: a one-layered system ($0 \le z \le H$) on a homogeneous half-space ($z \le 0$) subjected to an *SV-P* vertical line load. The mass density, the shear wave velocity, the thickness, and the Poisson's ratio of the upper layer are ρ_1=$C_{S,1}$=H=1.0 and ν=0.25, respectively, while the mass density, the shear wave velocity, and the Poisson's ratio of the lower half-space are ρ_2=1.0, $C_{S,2}$=2.0, and ν=0.25, respectively. Then, it follows that dilation (*P*) wave velocities for the upper layer and the half-space are $C_{P,1}$=1.732 and $C_{P,2}$=3.464, respectively, and the Rayleigh surface wave velocity for the upper is $C_{R,1}$=0.9193. The *SV-P* transient line load p_z is applied at the top-

surface, i.e. $z=H(=1)$, and its variation in both x and t is defined by a Hanning window, with $a=t_d=0.2$, as defined in equations (4.2.35 and 36). Then, the associated maximum wavenumber k_{max} and maximum frequency f_{max} are 10π and 10. For discrete models, we apply the TLM2 with $N_\lambda=8$, $\Delta t=1/(4f_M)$, and a buffer layer of $H_{BL}=\lambda_{min}$. Since $\lambda_{min}(=C_{S,2}/f_{max})$ is 0.2 in the present example, H_{BL} is chosen as 0.2.

Figure 5.4.3 shows the displacement snapshots for u and w at t=0.5, 1.0, 1.5, and 2.0 for the upper one-layered system ($0\le z\le 1$) in terms of a standard surface plot. It is observed in the first two snapshots for t=0.5 that the P and S wave components propagate separately through the upper layer in the same fashion as the case of a homogeneous half-space. Observe also that near the top-surface, the amplitude of P wave components is much smaller than that of S wave component, while within the upper layer and below the top-surface, the amplitude of P wave components is comparable to that of S wave components. This confirms that a P wave cannot properly propagate along stress-free surfaces without an external source to sustain it. Also, notice that the Rayleigh surface wave propagates together with S wave along the top-surface at time t=0.5. The two snapshots for t=1.0 on the second row display that two weak reflected waves resulting from the incident direct P wave at the interface of z=0 propagate upward through the upper layer. The reason that two reflection waves propagate is the mode conversion from an incident P wave into two reflected S and P waves at the interface. Also, notice that the Rayleigh surface wave propagates along the top-surface and is clearly separated from the S wave components, and its amplitude is significant as well. The snapshots on the third and fourth rows illustrate the wave motions for t=1.5 and t=2.0, respectively. As shown in the four surface plots, the wave motions involved are extremely complicated, because of the multiple reflections, the head wave effects, and the mode conversion between P and S wave components at both the interface and top-surface. In addition, due to the multiple reflections and energy leakage into the half-space, the amplitudes of waves decrease to the great degree, which makes it more difficult to identify the involved waves and interpret the wave motions. However, it can be seen that the Rayleigh surface wave propagates in the almost same fashion as the case of a homogeneous half-space. This observation implies that in the present example, the depth of the upper layer (H=1) is large enough to prevent the Rayleigh surface wave from "touching" the interface between the upper layer and the half-space.

Next, consider the second example: a two-layered system ($0\le z\le H$, with $H=H_1+H_2$) on a homogeneous half-space ($z\le 0$) subjected to an *SV-P* vertical line load. The mass densities, the shear wave velocities, the thickness', and the Poisson's ratios of the two upper layers are $\rho_1=\rho_2=1$, $C_{S,1}=1$, $C_{S,2}=2$, $H_1=H_2=1.0$ and $\nu_1=\nu_2=0.25$, respectively, while the mass density, the shear wave velocity, and the Poisson's ratio of the lower half-space are $\rho_3=1.0$, $C_{S,3}=3.0$, and $\nu_3=0.25$, respectively. Then, it follows that dilation (P) wave velocities for the two upper layer and the half-space are $C_{P,1}=1.732$, $C_{P,2}=3.464$, and $C_{P,3}=5.196$, respectively, and the Rayleigh surface wave velocity for the upper is $C_{R,1}=0.9193$. The *SV-P* transient line load p_z is applied at the top-surface, i.e. $z=H(=2)$, and its variation in both x and t is defined by a Hanning window, with $a=t_d=0.2$, as defined in equations (4.2.35 and 36). Then, the associated maximum wavenumber k_{max} and maximum frequency f_{max} are 10π and 10. For discrete models, we apply the TLM2 with $N_\lambda=8$, $\Delta t=1/(4f_M)$, and a buffer layer of $H_{BL}=\lambda_{min}$. Since $\lambda_{min}(=C_{S,3}/f_{max})$ is 0.3 in the present example, H_{BL} is chosen as 0.3.

Figure 5.4.4 shows the displacement snapshots for u and w at t=0.5, 1.0, 1.5, and 2.0 for the upper two-layered system ($0\le z\le 2$) in terms of a standard surface plot. In each plot, the dotted line at z=1 represents the interface between the first ($1\le z\le 2$) and second ($0\le z\le 1$) upper layer. We begin by interpreting the wave motions in the first layer ($1\le z\le 2$), in comparison with the wave motions in

the upper layer ($0 \le z \le 1$) in figure 5.4.3. It is observed in the first ($t=0.5$) and second ($t=1.0$) snapshots that the wave motions in the first layer ($1 \le z \le 2$) are exactly identical to those in the upper layer ($0 \le z \le 1$) in figure 5.4.3. The reason is that at time $t=0.5$ and 1.0, the waves reflecting at the interface at $z=0$ have not yet arrived at the first layer. On the other hand, it is seen in the snapshots in the third (for $t=1.5$) and fourth (for $t=2.0$) rows that the reflection waves from the interface at $z=0$ have transmitted into the first layer ($1 \le z \le 2$). Hence, the wave motions in the first layer are now different from those in the upper layer ($0 \le z \le 1$) in figure 5.4.3. However, notice that the degree of difference is insignificant. The reason for this little difference is that when the reflection occurs at the interface of $z=0$, most energy leaks into the half-space and only small portion bounces up. Consequently, the waves transmitting from the second layer to the first layer are too weak to influence significantly the wave motions in the first layer ($1 \le z \le 2$). Also, notice that the Rayleigh surface wave motion propagates without any interruption resulting from the transmitted waves in the present problem for the whole time of interest.

Finally, we consider the wave motions in the second layer ($0 \le z \le 1$). The snapshots for $t=0.5$ in the first row show that the second layer is quiescent, because no wave has yet arrived from the source. The snapshots for $t=1.0$ display complicated interference phenomena where the P wave transmitted from the first layer ($1 \le z \le 2$) has already propagated upward after reflecting at the interface of $z=0$, while the transmitted S wave propagated downward. However, due to the complicated interference, the associated wavefronts are not clearly distinguished in the snapshots. The snapshots for $t=1.5$ and 2.0 illustrate even more complicated wave motions. The reasons for this extreme complication are that multiple reflections, head wave effects, and mode conversion between P and S wave components have taken place at the interfaces $z=0$ and $z=1$. In addition, due to the multiple reflections/transmissions and the associated energy leakage into the half-space, the amplitudes of waves decrease significantly, which makes it more complicated to identify the involved waves and interpret the wave motions.

Figures for section 5.2

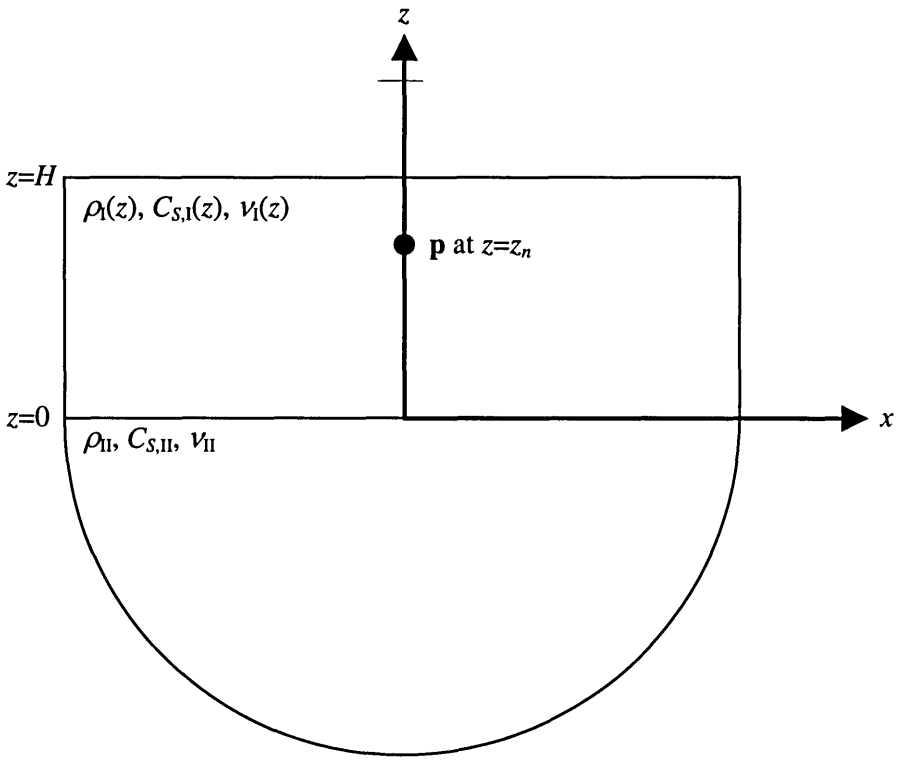

Figure 5.2.1 Semi-infinite medium subjected to a line load vector $\mathbf{p}(x,y,z,t)$ at $z=z_n$ and the coordinate system used

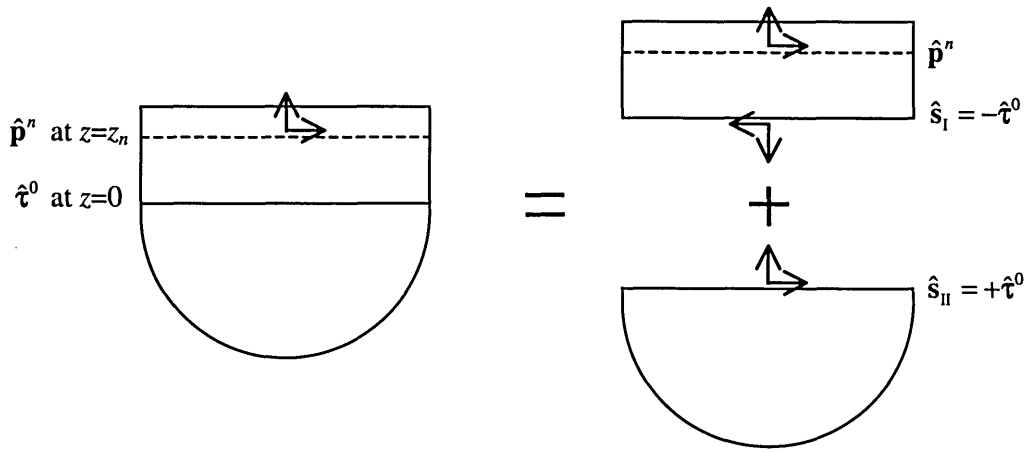

Figure 5.2.2 Substructuring of the semi-infinite medium into an upper layered system of $0\leq z\leq H$ and a homogeneous half-space of $z\leq 0$, by imposing the traction boundary conditions $\hat{\mathbf{s}}_{\mathrm{I}}$, $\hat{\mathbf{s}}_{\mathrm{II}}$ at the interface of $z=0$

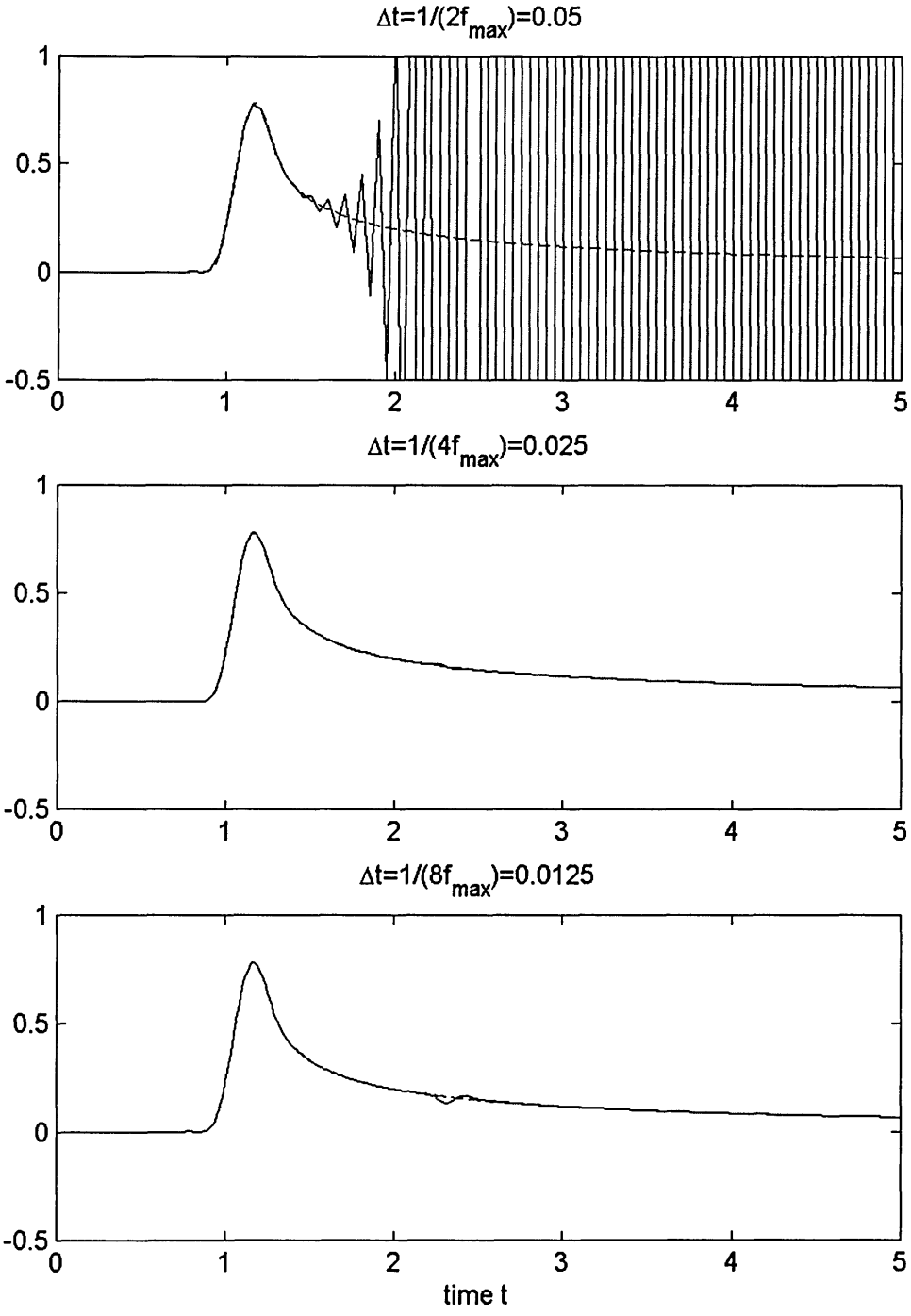

Figure 5.2.3 Stability of substructure method as function of Δt:
seismograms of surface v at x=1 in a homogeneous half-space (ρ=C_S=1)
subjected to *SH* surface line load of a=t_d=0.2, obtained with the TLM1 of N_λ=8,
and Δt=1/(2f_M), 1/(4f_M), and 1/(8f_M), f_M=f_{max}=10 (solid line for TLM1; dashed line for Exact)

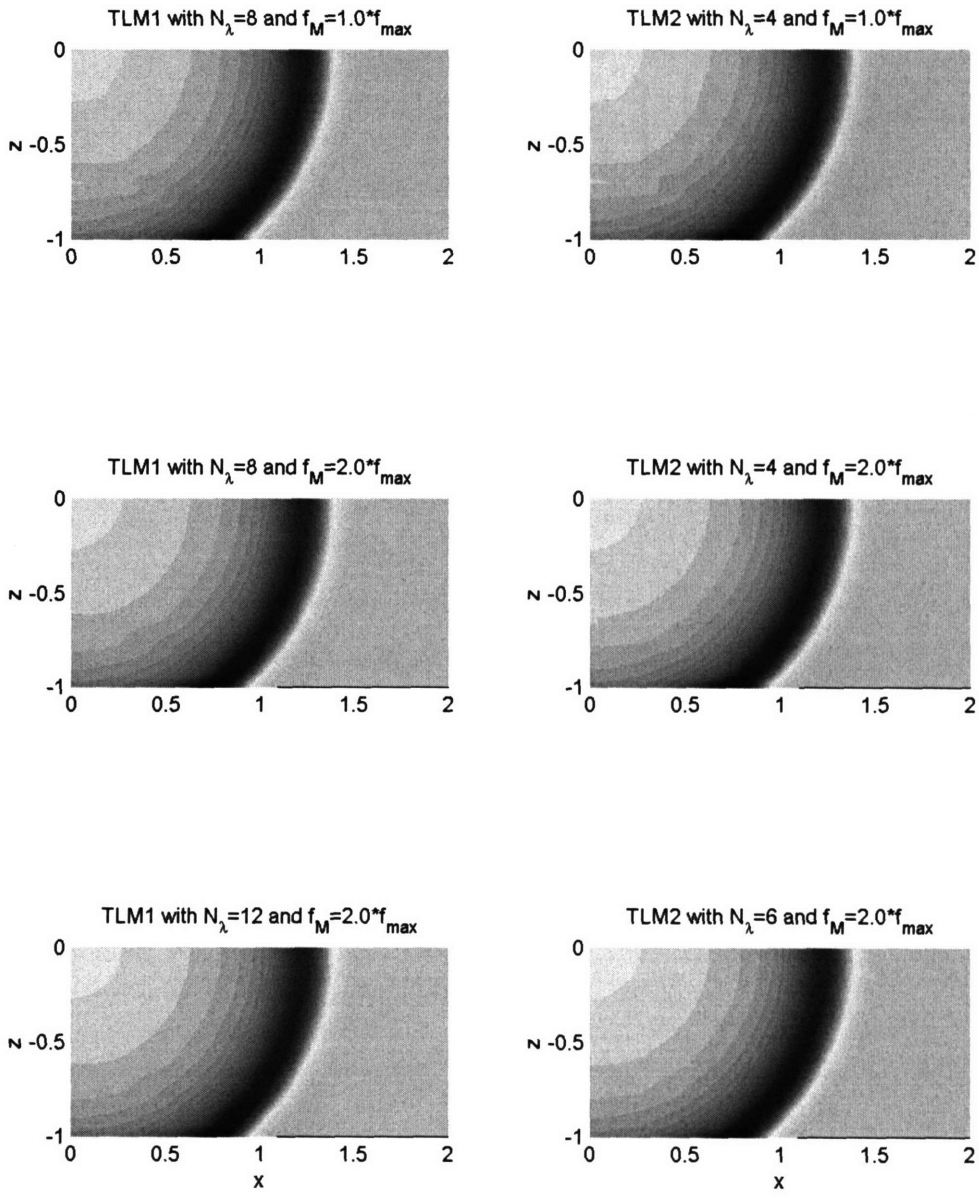

Figure 5.2.4 Accuracy of substructure method as function of N_λ and f_M:
snapshots of v at t=1.4 in a homogeneous half-space (ρ=C_S=1)
due to *SH* surface line load of a=t_d=0.2

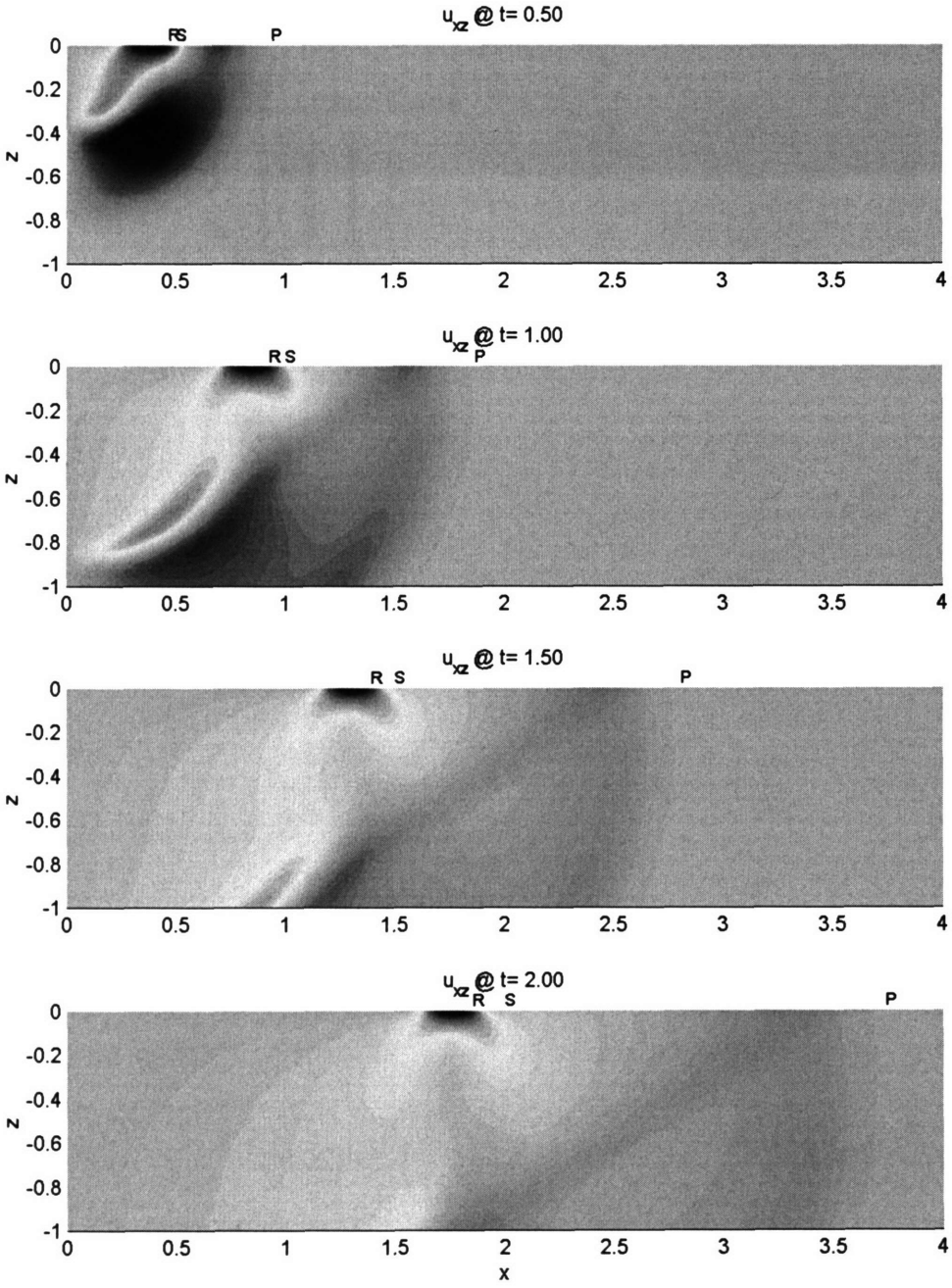

Figure 5.2.5 Snapshots of u_{xz} in a homogeneous half-space (ρ=C_S=1, ν=0.30) subjected to a vertical surface line load of a=t_d=0.2, calculated with TLM2 with N_λ=6

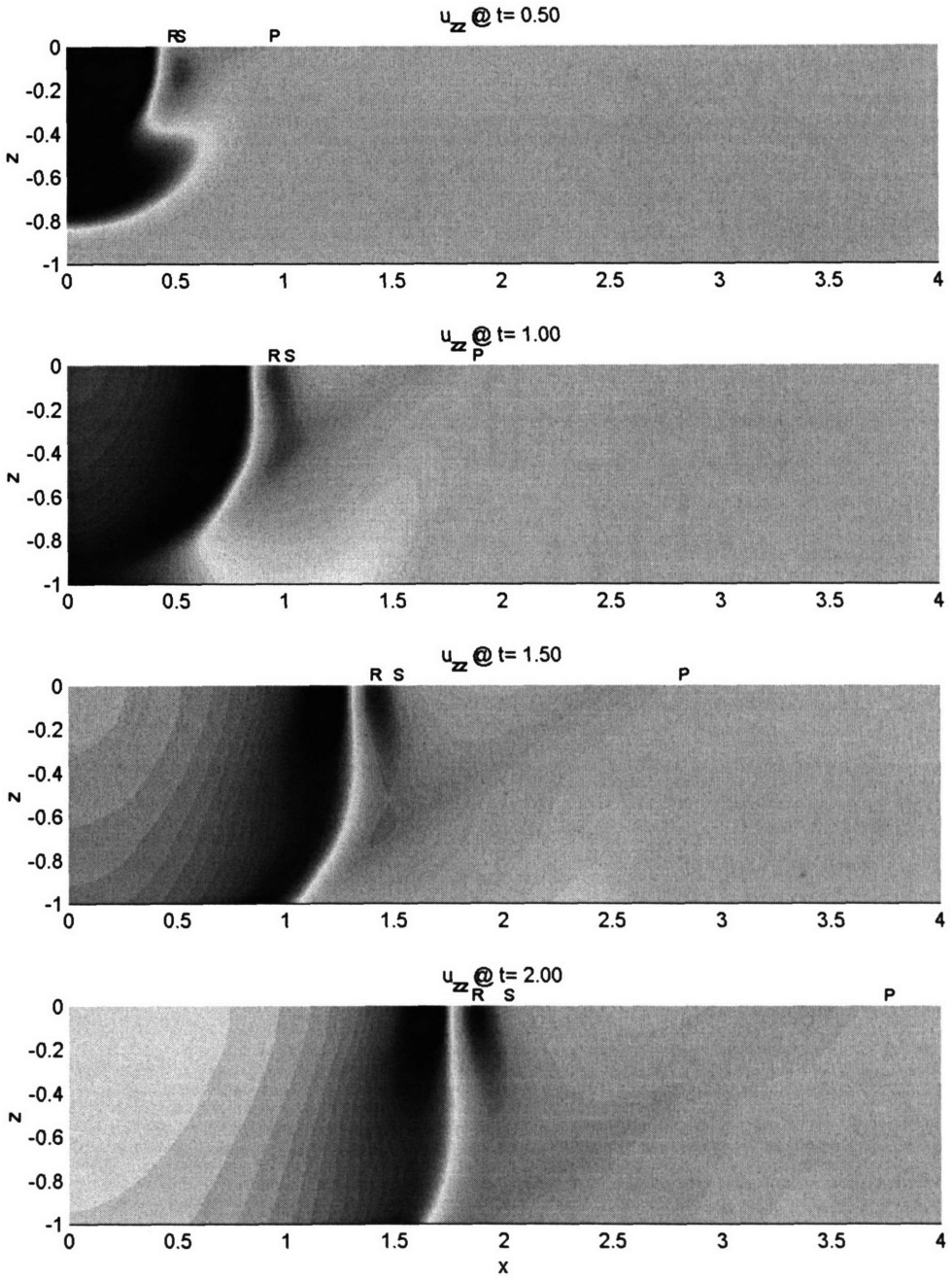

Figure 5.2.6 Snapshots of u_{zz} in a homogeneous half-space (ρ=C_S=1, ν=0.30) subjected to a vertical surface line load of a=t_d=0.2, calculated with TLM2 with N_λ=6

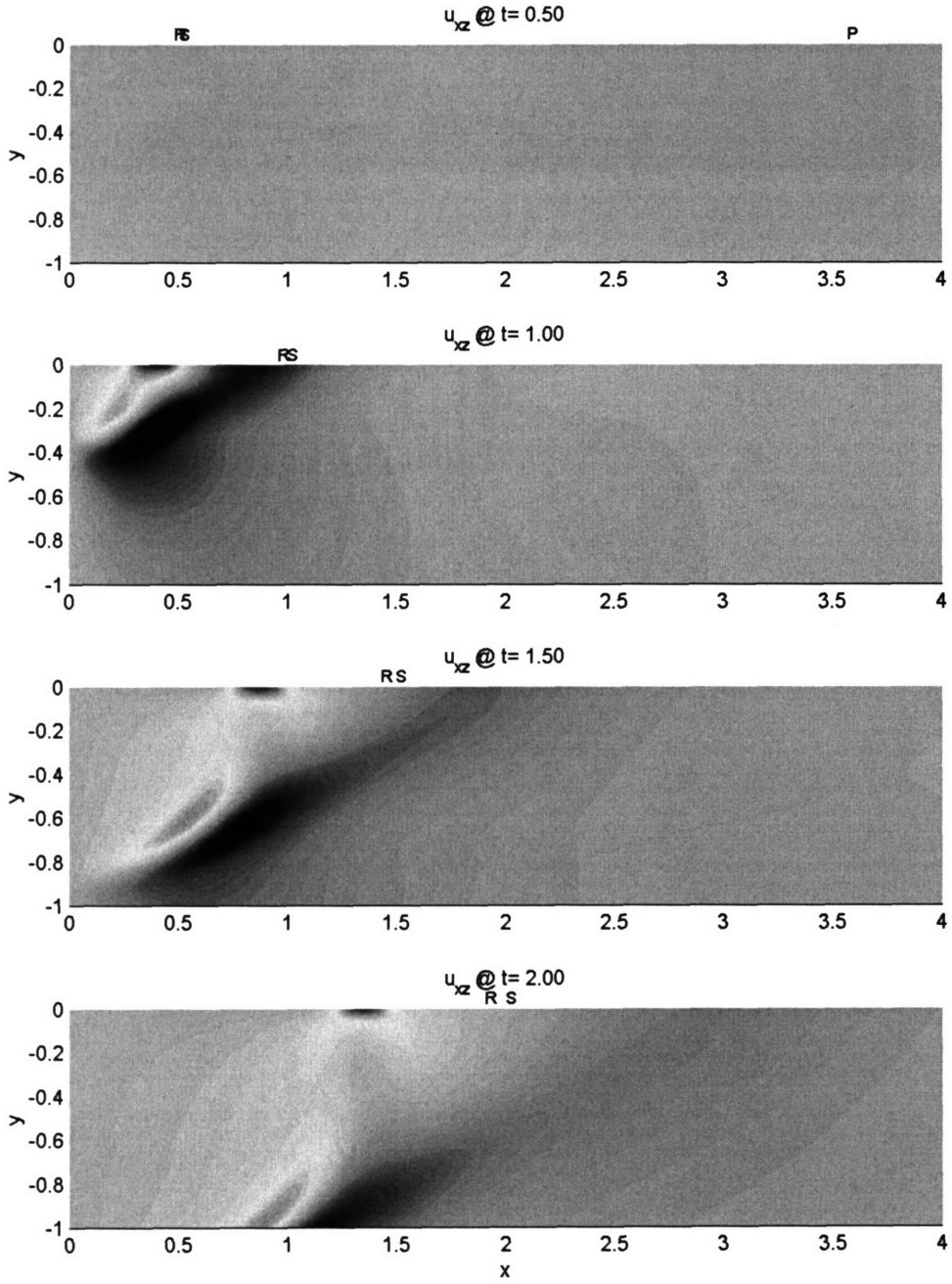

Figure 5.2.7 Snapshots of u_{xz} in a homogeneous half-space (ρ=C_S=1, ν=0.49) subjected to a vertical surface line load of a=t_d=0.2, calculated with TLM2 with N_λ=6

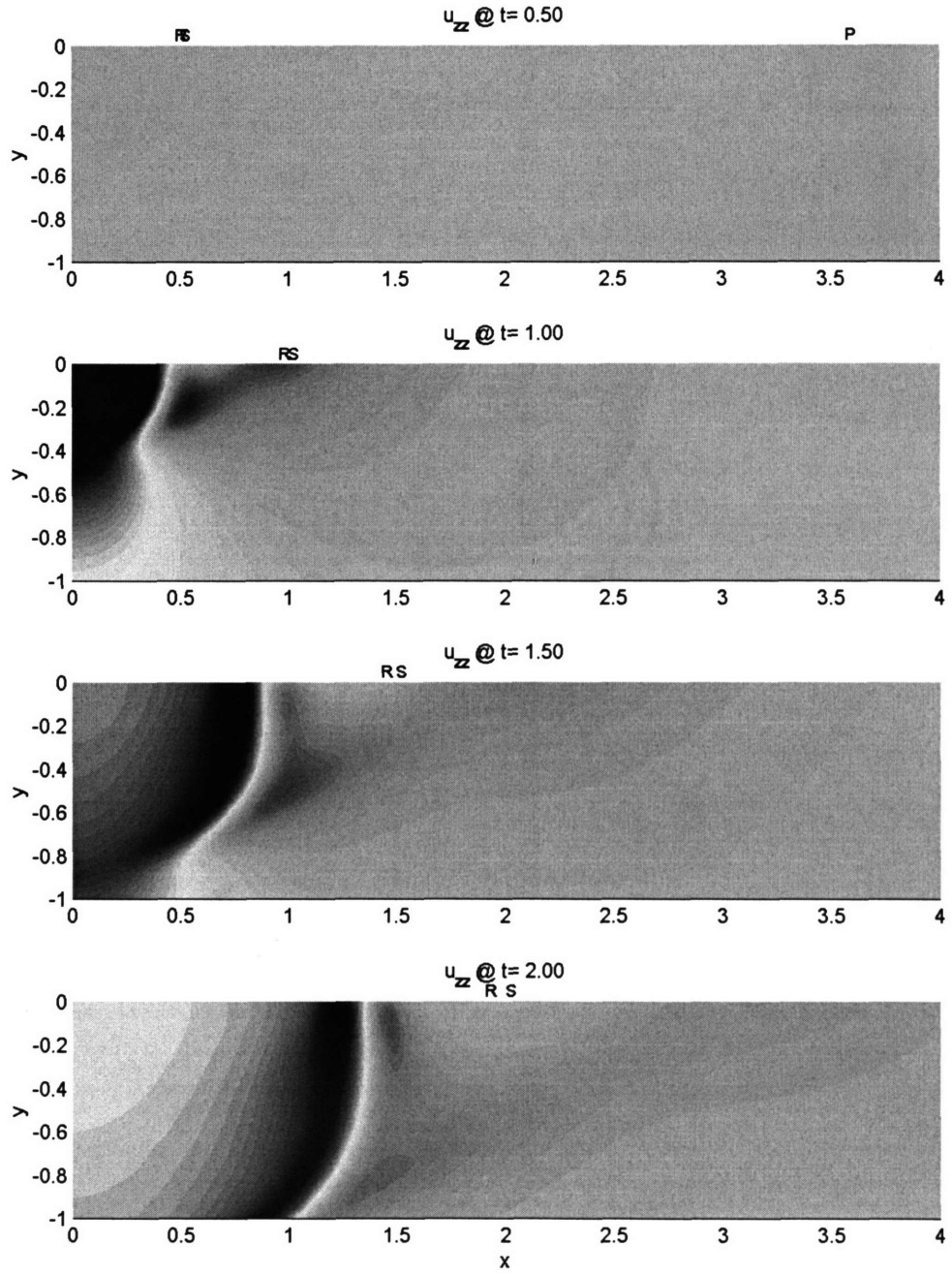

Figure 5.2.8 Snapshots of u_{zz} in a homogeneous half-space (ρ=C_S=1, ν=0.49) subjected to a vertical surface line load of a=t_d=0.2, calculated with TLM2 with N_λ=6

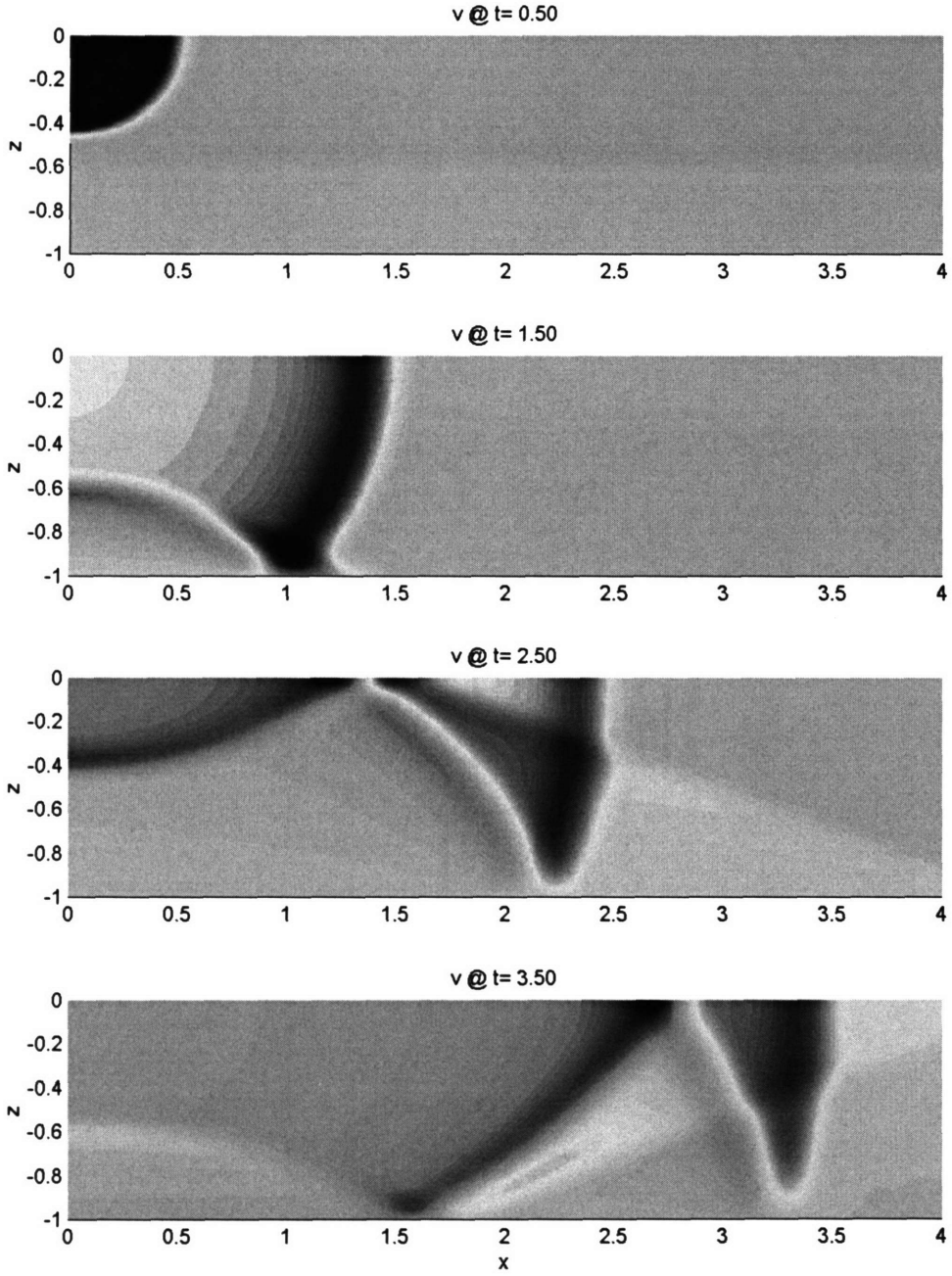

Figure 5.2.9 Snapshots of v without a buffer layer and with $\Delta t=1/(8f_M)$ in a layer ($\rho_{\mathrm{I}}=C_{S,\mathrm{I}}=H=1$) on a half-space ($\rho_{\mathrm{II}}=1, C_{S,\mathrm{II}}=3$) subjected to *SH* surface line load of $a=t_d=0.2$, obtained with TLM2 of $N_\lambda=6$

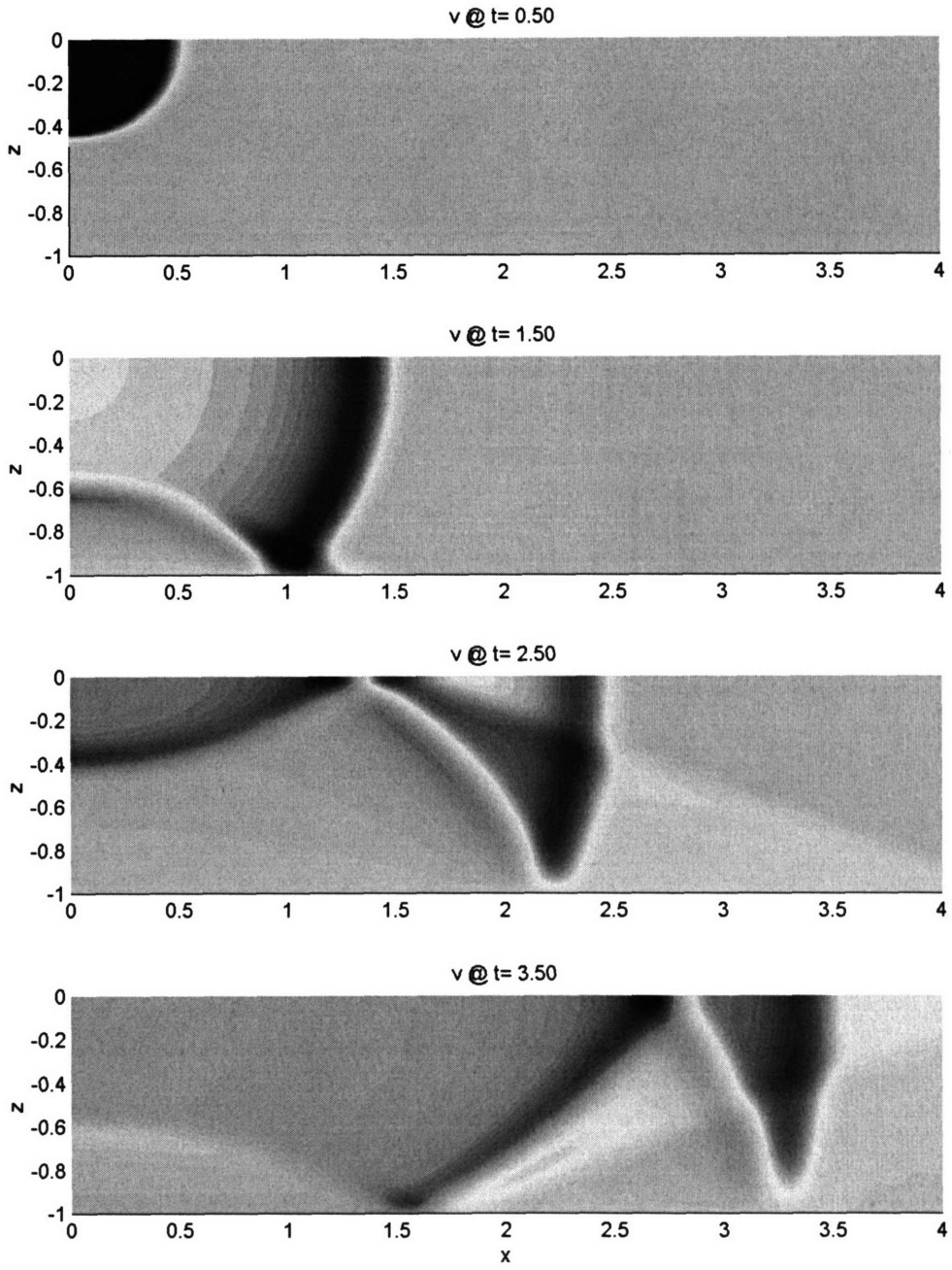

Figure 5.2.10 Snapshots of v with a buffer layer of $H_{BL}=\lambda_{min}$ and with $\Delta t=1/(4f_M)$ in a layer ($\rho_I=C_{S,I}=H=1$) on a half-space ($\rho_{II}=1, C_{S,II}=3$) subjected to SH surface line load of $a=t_d=0.2$, obtained with TLM2 of $N_\lambda=6$

Figures for section 5.3

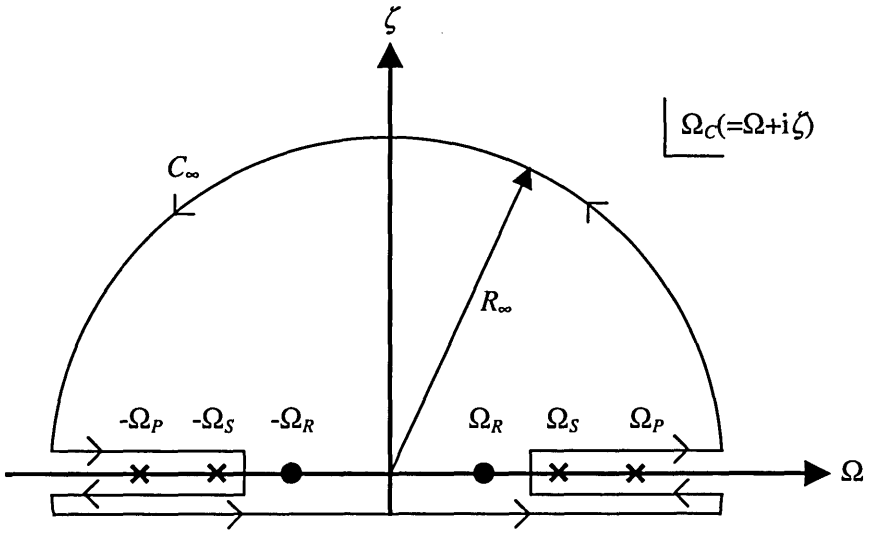

Figure 5.3.1 Contour integral paths, branch-points (×), and poles (•): Rayleigh wave problem

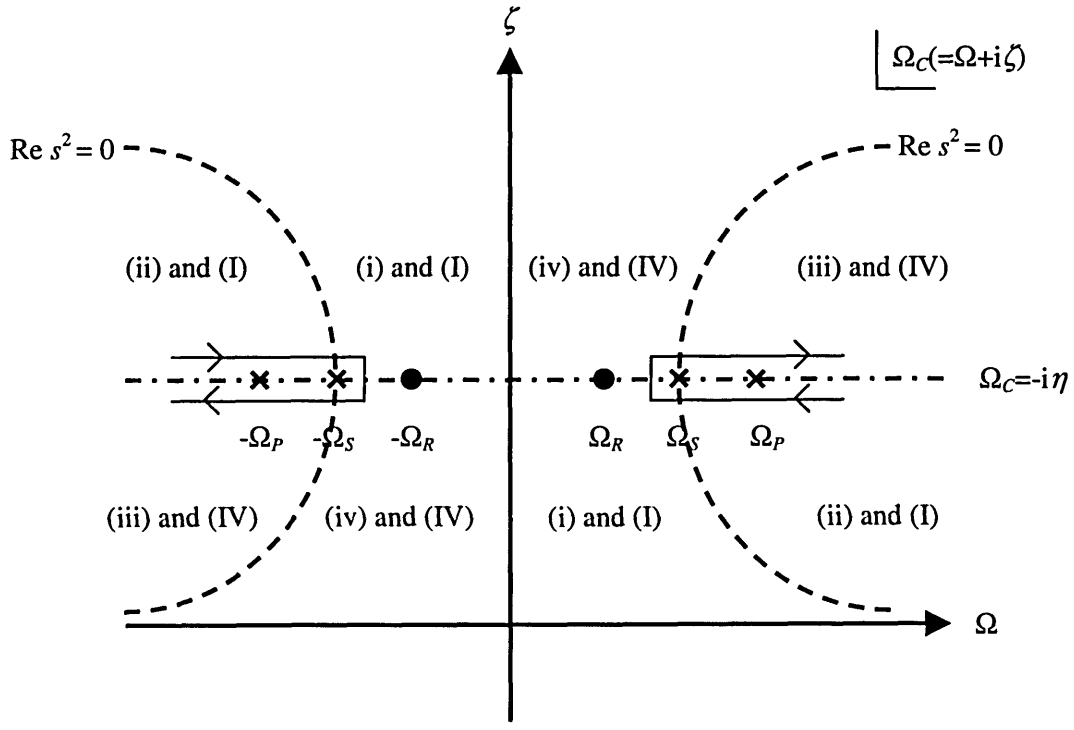

Figure 5.3.2 Identification of the branch-cuts and the quadrants for s^2 (i-iv) and s (I-IV).

Figures for section 5.4

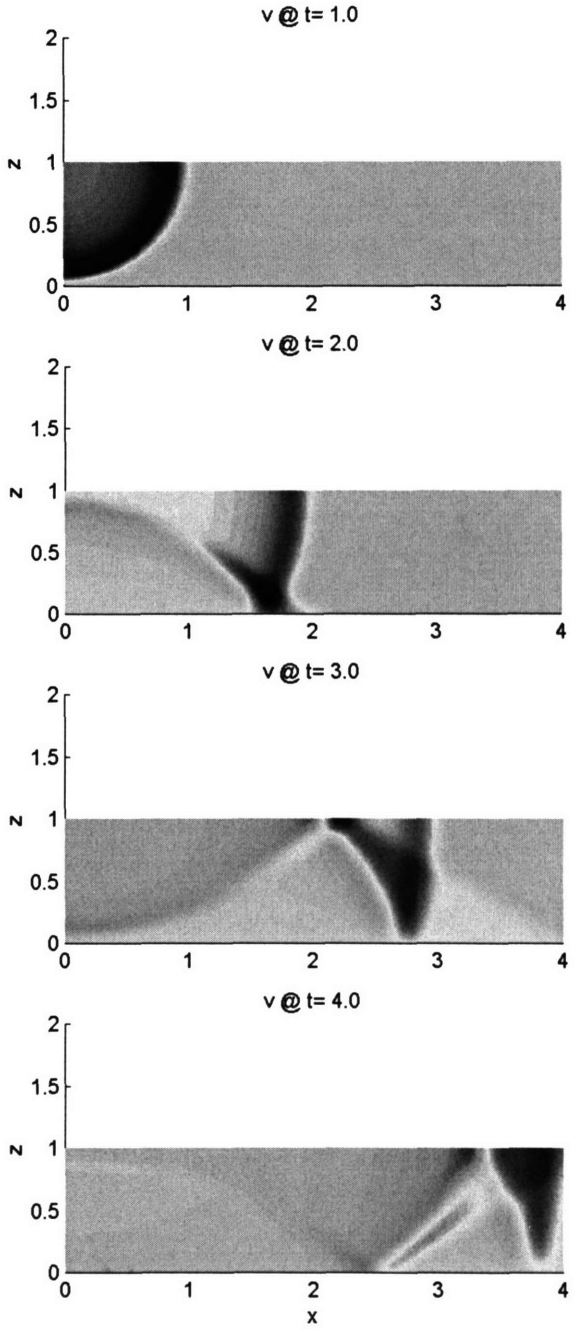

Figure 5.4.1 Snapshots of v in a one-layered half-space
(ρ_1=$C_{S,1}$=H=1; ρ_2=1, $C_{S,2}$=2)
subjected to SH surface line load of a=t_d=0.2,
obtained with TLM2 of N_λ=6, Δt=1/(4f_M) and with a buffer layer of H_{BL}=λ_{min}

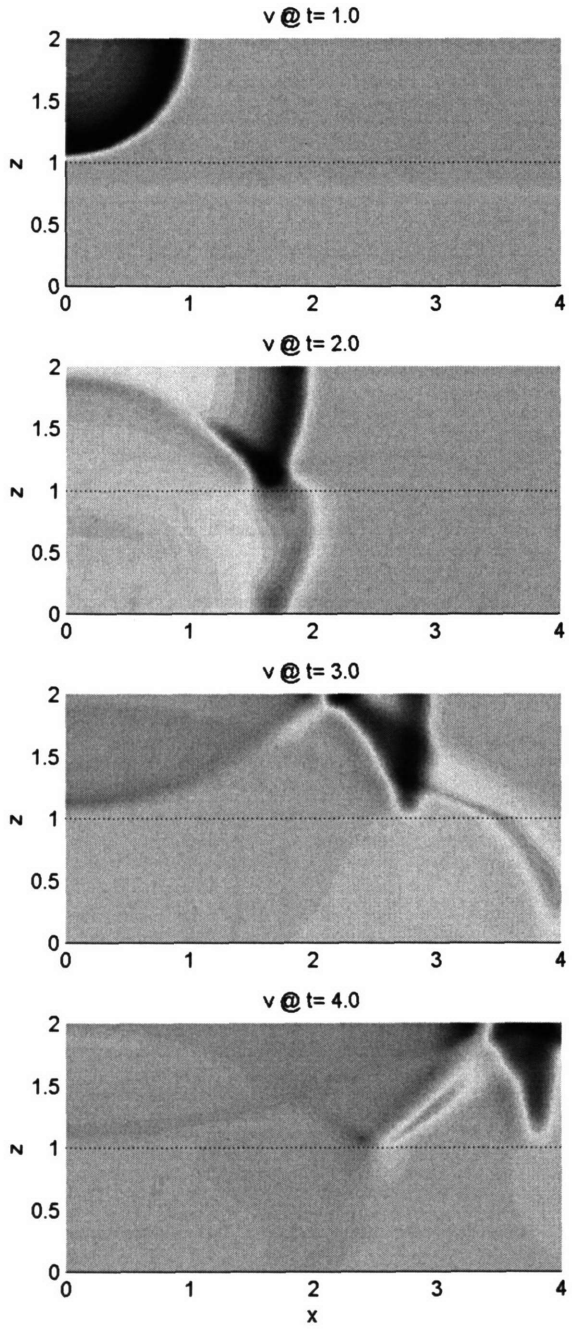

Figure 5.4.2 Snapshots of v in a two-layered half-space
(ρ_1=$C_{S,1}$=H_1=1; ρ_2=H_2=1.0, $C_{S,2}$=2; ρ_3=1, $C_{S,3}$=3)
subjected to *SH* surface line load of a=t_d=0.2,
obtained with TLM2 of N_λ=6, Δt=1/(4f_M) and with a buffer layer of H_{BL}=λ_{min}

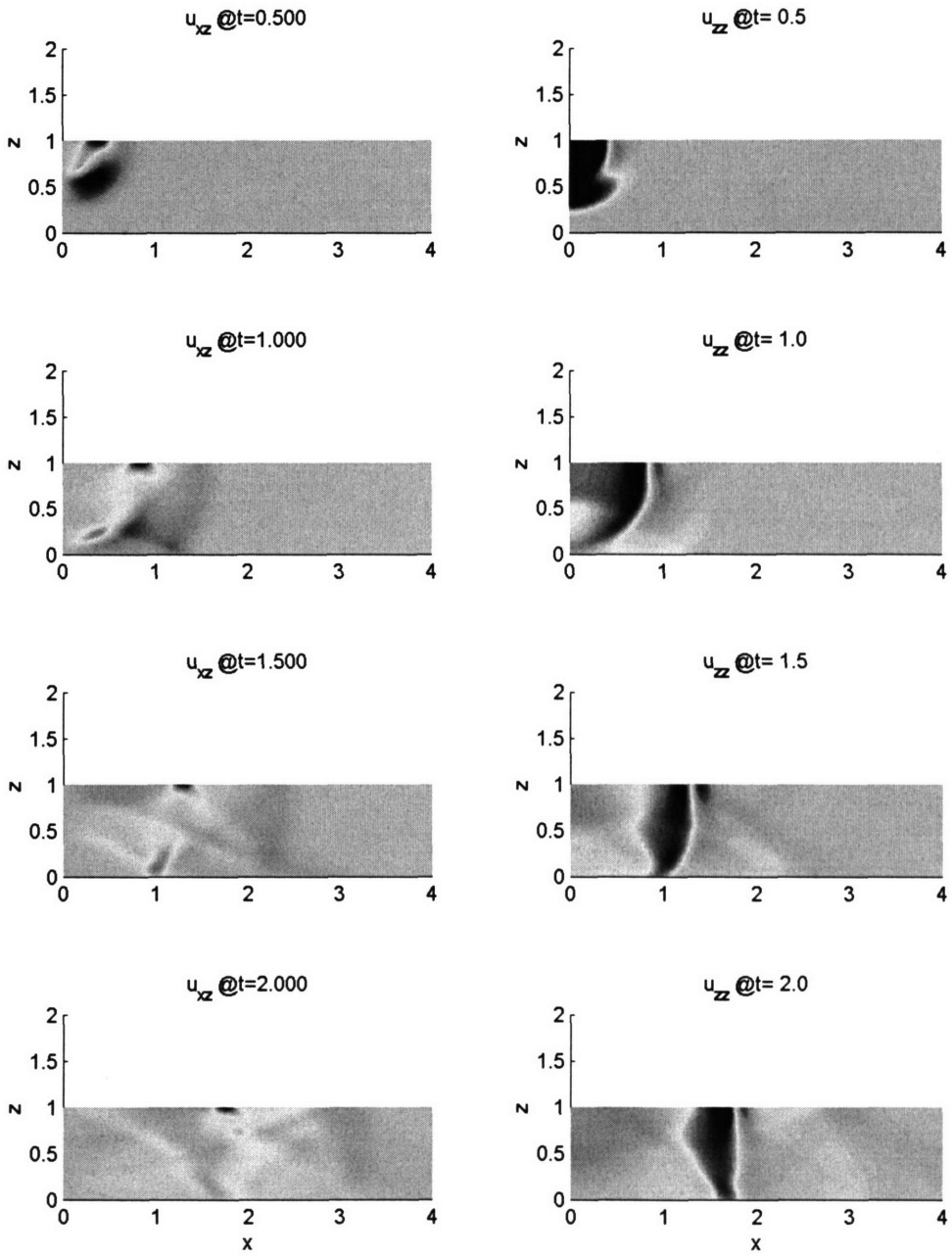

Figure 5.4.3 Snapshots of u_{xz},u_{zz} in a one-layered half-space
(ρ_1=$C_{S,1}$=H=1, ν_1=0.25; ρ_2=1, $C_{S,2}$=2, ν_2=0.25)
subjected to a vertical surface line load of a=t_d=0.2,
obtained with TLM2 of N_λ=6, Δt=1/(4f_M) and with a buffer layer of H_{BL}=λ_{min}

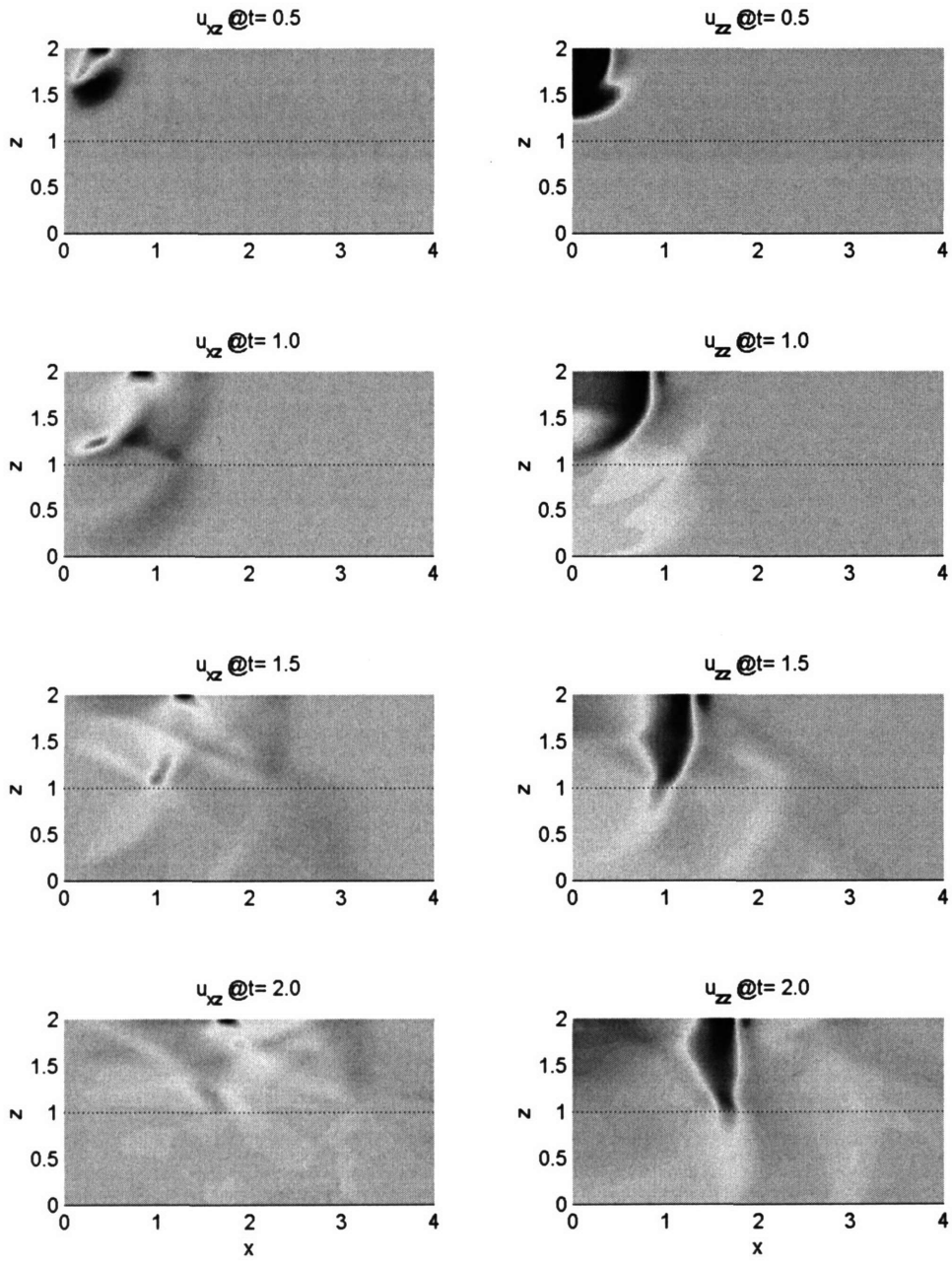

Figure 5.4.4 Snapshots of u_{xz},u_{zz} in a two-layered half-space
(ρ_1=$C_{S,1}$=H_1=1, ν_1=0.25; ρ_2=H_2=1, $C_{S,2}$=2, ν_2=0.25; ρ_3=1, $C_{S,3}$=3, ν_3=0.25)
subjected to a vertical surface line load of a=t_d=0.2,
obtained with TLM2 of N_λ=6, Δt=1/(4f_M) and with a buffer layer of H_{BL}=λ_{min}

Chapter 6 Infinite media modeling with the ω-TLM

6.1 Introduction

In this chapter, we explore the characteristics of (semi-) infinite media modeling with the ω-TLM, which is basically based on the application of a paraxial approximation and a buffer layer of appropriate thickness, see the papers of Maeda and Kausel [1991], Kausel [1992], Clayton and Engquist [1977]. We first review the preceding studies on the subject and get to understand the known features of the paraxial approximation and the buffer layer. Then, based on this review, we modify the paraxial approximation, particularly for *SV-P* wave problems, in order to improve the stability of calculated results. In addition, we propose the use of an adaptive buffer layer that is very efficient in the calculation of seismograms by means of the ω-TLM.

In section 6.2, we investigate the characteristics of the paraxial approximation and the buffer layer for both *SH* and *SV-P* wave problems. Through this investigation, we consider the stability of the paraxial approximation not only in the wavenumber domain, but also in the space domain. As a result, we determine a critical epicentral distance X_I closely related to the thickness of the buffer layer H_{BL}, which is especially important for *SH* wave problems. Also, we modify the paraxial approximation for *SV-P* wave problems and illustrate the achieved improvements through numerical examples. In section 6.3, we briefly discuss the hybrid method where we combine the mode shapes obtained with the ω-TLM and the exact eigenvalues to calculate responses in a more efficient way. The efficiency and validation of this strategy were already discussed and practically proved in chapter 4. Then, we propose the use of an adaptive buffer layer, which is very useful in seismogram calculations. In section 6.4, we analyze various examples of multilayered half-spaces to validate the (semi-) infinite media modeling with the ω-TLM combined with the paraxial approximation and the adaptive buffer layer. In addition, we get to understand the physics involved in these complicated systems. In appendix 6A, we derive the Green's functions in the x-ω domain for an *SH* one-layered half-space and an *SV-P* homogeneous half-spaces subjected to surface harmonic line loads. These Green functions are useful for gauging the accuracy of numerical results obtained with the ω-TLM combined with the paraxial approximation and the buffer layer.

6.2 Paraxial Approximation

The paraxial approximation $\mathbf{K}_{PA}$ for the boundary impedance can be obtained by expanding the exact impedance matrix $\mathbf{K}_{EX}$ of Kausel and Roësset [1981] in Taylor series in the wavenumber k, and retaining only first three terms as follows:

$$\mathbf{K}_{PA}(k) = \mathbf{K}_{EX}\Big|_{k=0} + \frac{k}{1!}\frac{d\mathbf{K}_{EX}}{dk}\Big|_{k=0} + \frac{k^2}{2!}\frac{d^2\mathbf{K}_{EX}}{dk^2}\Big|_{k=0} \tag{6.2.1}$$

where

$$\mathbf{K}_{EX} = ksG \qquad \text{for } SH \text{ waves} \tag{6.2.2a}$$

$$\mathbf{K}_{EX} = 2kG\left[\frac{1-s^2}{2(1-rs)}\begin{Bmatrix} r & 1 \\ 1 & s \end{Bmatrix} + \begin{Bmatrix} \cdot & -1 \\ -1 & \cdot \end{Bmatrix}\right] \qquad \text{for } SV\text{-}P \text{ waves} \tag{6.2.2b}$$

$$r = \sqrt{1 - \left(\frac{\omega}{kC_P}\right)^2} \tag{6.2.2c}$$

$$s = \sqrt{1 - \left(\frac{\omega}{kC_S}\right)^2} \tag{6.2.2d}$$

and C_S, C_P, G are the S-, P-wave speeds, shear modulus, respectively. Note that $\mathbf{K}_{EX}$ in equation (6.2.2b) is valid for a half-space $z \leq 0$. For a half-space $z \geq 0$, the signs of the off-diagonal terms in equation (6.2.2b) must be reversed. Figure 6.2.1 shows a layered system overlain by a homogeneous half-space and the coordinate system used in this chapter. The paraxial approximation in equation (6.2.1) represents the mechanical behavior of the homogeneous half-space of $z \leq 0$ in the mathematical sense.

6.2.1 Paraxial Approximation for *SH* wave Problems

Equation (6.2.1) provides the paraxial approximation $\mathbf{K}_{PA}$ for *SH* wave problems of the form

$$\mathbf{K}_{PA} = iG\left(k_S - \frac{1}{2}\frac{k^2}{k_S}\right) = i\omega\rho C_S\left(1 - \frac{1}{2}\frac{k^2}{k_S^2}\right) \tag{6.2.3}$$

where $k_S = \omega/C_S$.

First, we explore the characteristics of $\mathbf{K}_{PA}$ in equation (6.2.3) as a function of the wavenumber k. For this purpose, we compare $\mathbf{K}_{PA}$ in equation (6.2.3) with $\mathbf{K}_{EX}$ in equation (6.2.2a) for some range of wavenumbers k/k_S. Figure 6.2.2 compares the amplitude and phase angle of $\mathbf{K}_{PA}$ (dashed line) with those of $\mathbf{K}_{EX}$ (solid line). It is observed that $\mathbf{K}_{PA}$ shows a good agreement with $\mathbf{K}_{EX}$ only for small wavenumber k, i.e. $k \leq 0.6k_S$. This comparison predicts that $\mathbf{K}_{PA}$ can accurately model waves impinging on the paraxial boundary with incidence angle of $\theta \leq 45°$.

Similar observations were also found by Maeda and Kausel [1991], which are briefly summarized in this paragraph. They characterized $\mathbf{K}_{PA}$ by means of two important features: 1) the reflection coefficients between two identical and/or dissimilar semi-infinite media in contact modeled with $\mathbf{K}_{EX}$ and $\mathbf{K}_{PA}$; 2) the energy transmission in one cycle of harmonic motion. With these two characteristics, they explain in detail a spurious reflection phenomenon that can take place at the paraxial boundary, which can lead to unstable reverberation phenomena. Also, to overcome the instability problem, they propose a hybrid system consisting of the paraxial approximation $\mathbf{K}_{PA}$ and a buffer layer. The thickness of the buffer layer must be no less than half of the shear wavelength to calculate accurate responses, while it must be no less than a quarter of the shear wavelength to calculate acceptable responses. The important function of the buffer layer is to avoid the strong spurious reflection at the paraxial boundary related to inhomogeneous waves that decay exponentially within the buffer layer; hence, the waves do not feel the existence of the paraxial approximation.

We now characterize the behavior of the hybrid system composed of $\mathbf{K}_{PA}$ and the buffer layer as a function of its thickness and wavenumber k in comparison with $\mathbf{K}_{EX}$. We denote the hybrid system, the thickness of the buffer layer, the shear wavelength, and the ratio of the thickness to the shear wavelength as $\mathbf{K}_{PB}$, H_{BL}, λ_S, and $R_S = H_{BL}/\lambda_S$, respectively. We compare the amplitude and phase angle of $\mathbf{K}_{PB}$ against those of $\mathbf{K}_{EX}$. Figure 6.2.3 shows the comparisons of $\mathbf{K}_{PB}$ (dashed line) with $\mathbf{K}_{EX}$ (solid line) for R_S=0.25, 0.50, 0.75, 1.00. To avoid the influence of numerical errors from the TLM model, we model the buffer layer with the exact stiffness matrix (Kausel

and Roësset [1981]). It is observed that $\mathbf{K}_{PB}$ with $R_S \geq 0.5$ is really in a good agreement with $\mathbf{K}_{EX}$ for large k as well as for small k, which confirms the recommendation for the thickness of the buffer layer proposed by Maeda and Kausel [1991].

We now consider the accuracy and stability of the hybrid system $\mathbf{K}_{PB}$ associated with the near-field and far-field responses. It is observed in figure 6.2.3 that the behavior of $\mathbf{K}_{PB}$ with $R_S \geq 0.5$ is almost the same as that of $\mathbf{K}_{EX}$ for all wavenumbers of interest, which is true for the near-field responses, but not so for the far-field responses. The reason is that whenever propagating waves due to external sources impinge on the paraxial boundary with an incidence angle $\theta > 45°$, the waves feel the existence of the paraxial boundary and spurious reflections take place. This phenomenon affects and deteriorates the far-field responses, but not the near-field responses, as will be discussed in the next paragraph.

For illustration purposes, we proceed by considering a canonical example of a homogenous half-space subjected to an *SH* surface line load of a certain excitation frequency f_{ex}. The half-space is modeled with a hybrid system $\mathbf{K}_{PB}$ composed of an upper buffer layer of thickness $H_{BL}(=R_S\lambda_S)$ and a paraxial boundary impedance where $\lambda_S = C_S/f_{ex}$. Figure 6.2.4 depicts this example and displays two particular ray paths A and B originating from the surface source at $z_n=0$. The wave along path A is almost completely absorbed by the paraxial boundary impedance, because the wave impinges on the boundary with an angle $\theta < 45°$. On the other hand, the wave along path B is partly absorbed (solid line) and partly reflected (dashed line) by the paraxial boundary, because the wave impinges on the boundary with an angle $\theta > 45°$. As a result, a spurious reflection associated with path B deteriorates the response in the far field and contributes to non-physical reverberations in the system. In the light of this observation, we divide the whole system into the two domains I and II according to the stability and accuracy of the responses shown in figure 6.2.4. Domain I is a region (or near-field) where the response is stable and accurate. On the other hand, Domain II is a region (or far-field) where an unstable response may result from spurious reflections. In figure 6.2.4, the thick dotted line represents the border between the two domains I and II, and X_I is the epicentral distance or range, measured from the source to the border on the surface that is $2H_{BL}$ in the present example. It can be easily inferred that X_I is a function of the z coordinate of the source, i.e. $z_n(\leq 0)$ and the thickness of the buffer layer H_{BL}, which is given in the form.

$$X_I = (2H_{BL} + z_n)\tan 45° = 2H_{BL} + z_n \tag{6.2.4}$$

At this stage, we propose that a proper R_S must be chosen such that we can calculate a stable and accurate response within the whole region of interest. It follows that the larger the X_I required, the thicker H_{BL} must be.

In order to generalize the above observation, we consider a more complicated system composed of L dissimilar layers over a paraxial boundary subjected to an external source at z_n. Figure 6.2.5 shows a particular case with $L=4$. The piece-wise thick dotted lines represent the border between domains I and II. All incidence/refraction angles θ's are determined via Snell's law as

$$\frac{\sin\theta_1}{C_1} = \frac{\sin\theta_2}{C_2} = \cdots = \frac{\sin\theta_{L-1}}{C_{L-1}} = \frac{\sin\theta_L}{C_L} \tag{6.2.5}$$

where θ_L is always 45°, because this is the largest acceptable value for the angle associated with the paraxial boundary. For simplicity in the discussion, we assume that all angles θ are smaller than the critical angle θ_{cr} for each layer, so there is no total reflection at any interface. If a total reflection were to occur, the paraxial boundary would never feel the wave arrivals from the source, and would thus have no effect on the computed results. Once the θ's for each layer have

been obtained with the aid of equation (6.2.5), we can obtain the maximum range X_I for domain I by a generalization of equation (6.2.4) in the following form

$$X_I = (H_n - d)\tan\theta_n + \sum_{l=n+1}^{L} H_l \tan\theta_l + \sum_{l=1}^{L} H_l \tan\theta_l \qquad (6.2.6)$$

where d is the distance between the external source and the top surface, n is the index for the layer that contains the external source, and the H's are the thickness of each layer.

For practical verification of the above issues, we solve two numerical examples: 1) a homogeneous half-space and 2) a layered half-space (so-called Love wave problem). Both of these systems are subjected to an *SH* surface line load with frequency f_{ex}=2.5. We calculate the displacement responses by means of the ω-TLM with application of the hybrid system with $\mathbf{K}_{PB}$. The exact analytical solutions for both examples are derived by means of contour integrals in appendix 5A of this chapter. We compare the responses obtained with the ω-TLM against the exact analytical solutions.

For the first example, we choose the following material properties for the TLM2 discrete model: ρ=C_S=1.0 and N_λ=8. We consider three different buffer layers, R_S=0.50,0.75,1.0 to show the dependence of X_I on R_S. We choose N_λ=8 instead of the recommended N_λ=4 of previous chapters, to avoid numerical dispersion to the extent possible. Since the excitation frequency f_{ex} is 2.5 and the shear velocity C_S is 1.0, the shear wavelength λ_S is 0.4 and so H_{BL}=$R_S\lambda_S$=0.2, 0.3, 0.4. Consequently, the maximum ranges X_I's are estimated to be 0.4, 0.6, and 0.8, respectively, according to equation (6.2.4).

The numerical results are shown in figures 6.2.6a,b, 6.2.7a,b and 6.2.8a,b for H_{BL}(=$R_S\lambda_S$)=0.2, 0.3, and 0.4, respectively. Figures 6.2.6a, 6.2.7a, and 6.2.8a show the found eigenvalues k_j in the complex wavenumber plane (indicated by "×"). Figures 6.2.6b, 6.2.7b, and 6.2.8b illustrate the displacement responses by means of a standard surface plot in which the color intensities represent relative amplitudes of displacements. The eigenvalues here are purely spurious modes, because the homogeneous half-space being considered does not have any true free vibration modes, as shown in the appendix of this chapter. Interestingly, however, all these spurious eigenvalues are located near the branch-cut integral paths of the exact contour integral solutions. This observation implies that the modal superposition solutions with the spurious eigenvalues play an equivalent role to the branch-cut integrals in the exact contour integral solutions. Furthermore, it is observed from figures 6.2.6a-8b that as R_S increases, the spurious eigenvalues converge to the branch-cut integral paths and additionally, the stable domain I is extended farther. It is also remarkable in the two plots at the bottom of figures 6.2.6b, 6.2.7b, and 6.2.8b (which show the difference between the ω-TLM and the exact analytical solution) that the two domains I and II are clearly distinguished by the dotted lines whose intersections with the surface almost exactly coincide with X_I's estimated by equation (6.2.4) or (6.2.6).

Next, we consider the second example. We choose the following material properties for a TLM2 discrete model: for the upper layer ($0\le z\le 1$), ρ=C_S=1, H_1=1, N_λ=8; for the buffer layer ($-H_{BL}\le z\le 0$), ρ_R=1, C_R=2, N_λ=8, R_S=0.50,0.75,1.0. Since f_{ex} is 2.5 and C_R(>C_S) is 2.0, the shear wavelength λ_S of the buffer layer is 0.8 and so H_{BL}(=$R_S\lambda_S$)=0.4, 0.6, 0.8. According to the Snell's law in equation (6.2.5), θ_1 is 20.70°. Hence, the maximum ranges X_I's predicted with equation (6.2.6) are 1.55, 1.95, and 2.35.

Figures 6.2.9a,b to 6.2.11a,b display the numerical results for H_{BL}(=$R_S\lambda_S$)=0.4, 0.6, and 0.8, respectively. As shown in figures 6.2.9a, 6.2.10a, and 6.2.11a, the eigenvalues k_j obtained with

the ω-TLM (indicated by "×") are found not only along the branch-cut integral paths, which are purely spurious modes, but also found beyond the branch-point, i.e. k_f/k_S>1.0, on the real wavenumber axis. These eigenvalues with k_f/k_S>1.0 correspond to the true propagation modes or true poles in the Love wave problem. It is shown in the appendix that the true modes are associated with the residue summation in the exact contour integral solutions. As can be seen in the zoomed plots on the right in figures 6.2.9a, 6.2.10a, and 6.2.11a, the propagation modes from the TLM are almost identical to those of the exact solution (indicated by "o"). Therefore, it is concluded that the ω-TLM with application of the hybrid system $\mathbf{K}_{PB}$ provides a modal solution that is equivalent to the branch-cut integrals and the residue summations of the exact analytical solutions. It is also shown that as a larger R_S is used, the spurious eigenvalues approach the branch-cut integral paths. As a result, the stable domain I is extended farther. It is confirmed in the last two surface plots of each figure (which show the difference between the ω-TLM and the exact analytical solution) that the two domains of I and II are clearly distinguished as indicated by the dotted line, and the predicted X_I's from equation (6.2.6) are virtually identical to the numerical results.

Note (A): Layer over a homogeneous half-space

The above system of a homogeneous layer overlain by a homogeneous half-space, so-called *Love* wave problem, has interesting aspects that are intimately related to the propagation modes of the plate and of the stratum of the same material property and geometry as the layer, but with different boundary conditions. In a plate, the boundary conditions are free-free while for the stratum they are free-fixed. When the stiffness of the half-space approaches zero, the system becomes a plate. On the other hand, when the stiffness of the half-space is taken infinitely large, then the system becomes a stratum. Therefore, it could be argued that the behavior of the Love wave problem must lie somewhere in the middle of these two extreme cases, but this is not quite the case.

Figure 6.2.12 shows all the dispersion curves of the Love wave problem (solid curves), the plate (dashed curves), and the stratum (dotted-dashed curves). All of these dispersion curves are obtained from the exact analytical solutions. At zero-frequency, the branches of both the plate and the stratum start as purely imaginary branches (assuming no damping), and then turn real at cut-off frequencies that coincide with the resonant frequencies of the plate or stratum. On the other hand, the branches of the Love waves are purely real and appear suddenly at the intersection of the branches for the half-space $\omega=C_R k$ (the steeper straight line in figure 6.2.12) and the branches of the plate. In the high frequency range that follows, the branches for Love waves steadily approach the branches for the stratum. Thus, all propagation modes for Love waves with no damping are only real, and there exist no imaginary or complex branches. In addition, there is only the finite number of propagation modes for a given frequency or a given wavenumber, as shown in the dispersion curves. Thus, Love modes are seemingly not quite an intermediate step between a stratum and a plate, because the imaginary branches only appear quite suddenly when the stiffness of the half-space is either exactly zero or infinitely large.

Now, the wavenumber spectra for the plate, stratum or layer over elastic half-space emanate from a transcendental eigenvalue problem that follows from setting a characteristic determinant to zero. When the value of this determinant is evaluated for the case of the layer over elastic half-space for arbitrary combinations of frequency and wavenumber and the result is presented as a surface color plot where small values of the determinant lead to dark gray and zero values to black, then "tubes" are observed surrounding each of the branches in the wavenumber spectrum.

In addition, interesting and very revealing complex-valued tubes can be observed that emanate from the starting points of the real branches. Within these tubes, the determinant is not zero, but is small, which implies that the "axes" of the tubes represent near (but not exact) solutions for free evanescent waves. As the stiffness of the half-space then approaches either zero or infinity, the tubes approach the imaginary branches for the plate or stratum, respectively. This demonstrates that the Love wave problem is indeed an intermediate situation between the plate and the stratum.

The previous considerations are taken up next in the context of a solution to the Love wave problem using modal superposition. Now, we know that a finite number of real modes is not enough to represent the response to the Love wave problem in the near-field, a situation that we explore next. We begin our exploration by considering the behavior of the kernel K_I in equation (5A.3a) of appendix 5A. Figures 6.2.13a,b show the wavenumber spectra of the absolute values of K_I evaluated at the surface for two frequencies of f_{ex}=1.0 and 2.0, respectively. It can be seen that there exist the *infinite* number of the maximums of *finite* amplitude and a *finite* number of maximums of *infinite* amplitude. All the maximums are indicated by an "o". The maximums of *infinite* amplitude correspond to the true propagation modes of the Love wave problem. The maximums of *finite* amplitude appear only along the branch-cut and are believed to produce the significant contribution to the branch-cut integrals in the exact analytical solutions. Since they are not true poles, we call them *pseudo* poles. We then search for the branches of these *pseudo* poles in a certain frequency range by means of a numerical technique. The results are plotted by means of dots in figure 6.2.12 for a discrete sampling of frequencies. Remarkably, the branches of the *pseudo* poles (or *pseudo* branches) are almost identical to the branches of the stratum until they approach the branch of the half-space (ω=$C_R k$). Thereafter, the *pseudo* branches deviate upward from the stratum branches and move onto the half-space branch. As they pass the intersections between the half-space branch and the nearest high branches of the plate, these *pseudo* branches become the true propagation branches (solid curves). Thus, it is found that each branch or maximum of the Love wave problem starts as a *pseudo* branch that follows a stratum branch for low frequencies and then evolves into a true branch for high frequencies. More precisely, the j^{th} branch of the Love wave problem first follows the j^{th} stratum branch (j=1,2... for the stratum), crosses the j^{th} branch of the plate (j=0,1,2... for the plate) and finally approaches asymptotically to the $(j+1)^{th}$ stratum branch for high frequencies. At this stage, it should be remembered that the branch-cut integrals in the exact solutions have major contribution to the calculation of the near-field solutions as discussed in appendix 5A. Hence, it is concluded that the *pseudo* branches (i.e. evanescent pseudo-modes) play an important role in the near-field solutions. Finally, it follows that the deficiency of the modal solutions in the near field due to the finite number of propagation modes is compensated by the branch-cut integrals.

It is observed in figures 6.2.9b, 10b, and 11b that the spurious modes of the ω-TLM with $\mathbf{K}_{PB}$ are found near the branch-cut integral paths for the Love wave problems. In addition, there is a more interesting relationship between the true and spurious modes from the TLM with $\mathbf{K}_{PB}$ and the true and *pseudo* modes from the exact continuous models, which is discussed here. For this purpose, we compare the dispersion curves obtained from both the TLM with $\mathbf{K}_{PB}$ (dashed curves) and the exact solutions (solid curves), including the *pseudo* pole branches (dots) in figures 6.2.14a,b for H_{BL}=0.0 and 0.4, respectively. The same discrete model used above is considered, i.e. the TLM2 with N_λ=8. As can be seen, there are some remarkable coincidences in the imaginary components of k_j between the spurious modes of the discrete model and the *pseudo* modes of the exact analytical solution. This observation implies that the spurious modes provide a good equivalence to the branch-cut integrals in the exact analytical solutions. We recall that the *pseudo* modes have major contributions to the branch-cut integrals. Also, comparison of figures 6.2.14a,b shows that with the help of the buffer layer, the accuracy of the true propagation modes of the TLM with $\mathbf{K}_{PB}$

is significantly improved. Finally, we conclude that with the help of $\mathbf{K}_{PB}$, the ω-TLM can provide efficient and accurate solutions to the layered half-space problem, which is supported by the following two observations: (1) the spurious modes of the discrete model are almost identical to the *pseudo* modes of the exact analytical solution; (2) the true propagation modes are obtained with great accuracy.

6.2.2 Paraxial Approximation for *SV-P* wave Problems

Equation (6.2.1) provides the paraxial approximation $\mathbf{K}_{PA}$ for *SV-P* wave problems of the form

$$\mathbf{K}_{PA}=\omega\rho C_P\left[\mathrm{i}\begin{Bmatrix}\alpha & \cdot\\ \cdot & 1\end{Bmatrix}+\begin{Bmatrix}\cdot & 1-2\alpha\\ 1-2\alpha & \cdot\end{Bmatrix}\frac{k}{k_S}+\frac{\mathrm{i}}{2}\begin{Bmatrix}\alpha-2 & \cdot\\ \cdot & (1-2\alpha)/\alpha^2\end{Bmatrix}\left(\frac{k}{k_S}\right)^2\right] \tag{6.2.7}$$

where ρ=mass density, $\alpha=C_S/C_P$, and $k_S=\omega/C_S$.

We start by exploring the features of $\mathbf{K}_{PA}$ in equation (6.2.7) as a function of wavenumber k. For this purpose, we compare $\mathbf{K}_{PA}$ in equation (6.2.7) with $\mathbf{K}_{EX}$ in equation (6.2.2b) in terms of amplitude and phase angle. Figures 6.2.15a-d show the comparison of $\mathbf{K}_{EX}$ (dashed line) and $\mathbf{K}_{PA}$ (solid line) for Poisson's ratio ν=0.1, 0.2, 0.3, and 0.4, respectively. It is seen that $\mathbf{K}_{PA}$ is in a good agreement with $\mathbf{K}_{EX}$ for only small k, namely $k<(0.2\sim0.3)k_S$. The corresponding incidence angle θ for S wave is 11°~18°. As in the case of *SH* wave problems of section 6.2.1, it is expected that spurious reflections take place for waves with incidence angle $\theta>11°\sim18°$.

The above observation again suggests the use of a hybrid system $\mathbf{K}_{PB}$ composed of $\mathbf{K}_{PA}$ and a buffer layer for obtaining accurate results. It should be noticed that the thickness of the buffer layer is now a function of the wavelength for P waves λ_P, because $\lambda_P>\lambda_S$. So, we make use of $H_{BL}=R_P\lambda_P$. To verify the effect of the buffer layer of thickness H_{BL} on the accuracy of the hybrid system $\mathbf{K}_{PB}$, we compare the amplitude and phase angle of $\mathbf{K}_{PB}$ and $\mathbf{K}_{EX}$ with changing R_P. Figures 6.2.16a-d compare $\mathbf{K}_{PB}$ with R_P=0.25 (dashed line) and $\mathbf{K}_{EX}$ (solid line) for Poisson's ratio ν=0.1, 0.2, 0.3, and 0.4, respectively. Figures 6.2.17a-d compare $\mathbf{K}_{PB}$ with R_P=0.50 (dashed line) and $\mathbf{K}_{EX}$ (solid line) for Poisson's ratio ν=0.1, 0.2, 0.3, and 0.4, respectively. To avoid the influence of numerical errors stemming from the TLM, the exact stiffness matrix (Kausel and Roësset [1981]) is used in modeling the buffer layer. It is observed that the use of $R_P=H_{BL}/\lambda_P\geq0.50$ provides quite good approximation to $\mathbf{K}_{EX}$.

Next, we consider an alternative for assessing the behavior of $\mathbf{K}_{PA}$ in equation (6.2.7). The alternative is to consider the dispersion relation of S and P body waves taken up by Clayton and Engquist [1977]. These writers derived a paraxial approximation A2, which is identical to $\mathbf{K}_{PA}$ in equation (6.2.7) as proved by Kausel [1992]. In addition, Kausel pointed out a sign error in matrix $\mathbf{C}_2$ in the study by Clayton and Engquist. In this paragraph, we briefly elaborate on Clayton and Engquist's dispersion relation, and then assess its behavior in the context of numerical examples. Clayton and Engquist's paraxial approximation A2 is:

$$\frac{\partial^2\mathbf{u}}{\partial t\partial z}+\mathbf{C}_1\frac{\partial^2\mathbf{u}}{\partial t^2}+\mathbf{C}_2\frac{\partial^2\mathbf{u}}{\partial t\partial x}+\mathbf{C}_3\frac{\partial^2\mathbf{u}}{\partial x^2}=\mathbf{0} \tag{6.2.8}$$

where

$$\mathbf{u}=\begin{bmatrix}u & w\end{bmatrix}^T \qquad \text{(=the displacement vector)} \tag{6.2.9}$$

$$\mathbf{C}_1=\begin{Bmatrix}1/C_S & \cdot\\ \cdot & 1/C_P\end{Bmatrix} \tag{6.2.10}$$

$$\mathbf{C}_2 = (C_P - C_S)\begin{Bmatrix} \cdot & 1/C_S \\ 1/C_P & \cdot \end{Bmatrix} \qquad \text{(reversed sign!)} \tag{6.2.11}$$

$$\mathbf{C}_3 = \frac{1}{2}\begin{Bmatrix} C_S - 2C_P & \cdot \\ \cdot & C_P - 2C_S \end{Bmatrix} \tag{6.2.12}$$

Application of a Fourier transformation to equation (6.2.8) gives

$$\mathbf{u}(x,z,t) = \left(\frac{1}{2\pi}\right)^3 \int_{-\infty}^{\infty}\int_{-\infty}^{\infty}\int_{-\infty}^{\infty} \bar{\mathbf{u}}(k_x,k_z,\omega) e^{i(\omega t - k_x x - k_z z)} dk_x dk_z d\omega \tag{6.2.13}$$

which leads to the equation in the wavenumber-frequency domain

$$\left[\mathbf{I}K_z - \mathbf{C}_1 + \mathbf{C}_2 K_x - \mathbf{C}_3 K_x^2\right]\bar{\mathbf{u}} = \mathbf{0} \tag{6.2.14}$$

where $\mathbf{I}$ is the 2×2 identify matrix, and k_x, k_z, ω are the horizontal wavenumber, the vertical wavenumber, the angular frequency, respectively, and $K_z=k_z/\omega$, $K_x=k_x/\omega$. The dispersion relation sought is obtained by setting the determinant of the coefficient matrix in equation (6.2.14) equal to zero, namely

$$\det\left(\mathbf{I}K_z - \mathbf{C}_1 + \mathbf{C}_2 K_x - \mathbf{C}_3 K_x^2\right) = 0 \tag{6.2.15}$$

Figure 6.2.18 shows the dispersion curves (solid line) for *S* and *P* body waves obtained with the paraxial approximation A2 for Poisson's ratio ν=0.0, 0.1, 0.2, 0.3, 0.33, 0.40, 0.45, and 0.49, in comparison with the exact analytical solutions (dashed line). Note that in each figure, the upper solid line and the large dashed circle correspond to *S* waves, while the lower solid line and the small dashed circle correspond to *P* waves. It is observed that the paraxial approximation A2 shows good agreement with the exact analytical solution only for very small *k*. It is also noticed that the discrepancy in shear waves becomes very large for $\nu \geq 0.33(=1/3)$, when the sign of the second diagonal element in the matrix $\mathbf{C}_3$ reverses, i.e. $\frac{1}{2}(C_P-2C_S)$. This second diagonal element is directly related to the second diagonal element of the third matrix in equation (6.2.7), which can be easily proven from the paper by Kausel [1992]. Physically, this large discrepancy introduces significant evanescent wave motion, especially for *S* waves, which can in turn produce strong spurious reflections at the paraxial boundary. Interestingly, the discrepancy can be diminished by setting this second diagonal element in the matrix $\mathbf{C}_3$ to be zero when $\nu \geq 0.33$. The improvement associated with ν=0.40, 0.45, and 0.49 is shown in figure 6.2.19, where the results for ν=0.0, 0.1, 0.2, 0.3 and 0.33 are identical to those of figure 6.2.18. Also, notice that a significant improvement is achieved in *S* waves. So, we propose here a modified paraxial approximation A2 such that

$$\mathbf{C}_3 = \frac{1}{2}\begin{Bmatrix} C_S - 2C_P & \cdot \\ \cdot & C_P - 2C_S \end{Bmatrix} \qquad \text{for } \nu \leq 0.33 \tag{6.2.16}$$

$$\mathbf{C}_3 = \frac{1}{2}\begin{Bmatrix} C_S - 2C_P & \cdot \\ \cdot & \cdot \end{Bmatrix} \qquad \text{for } \nu \geq 0.33 \tag{6.2.17}$$

Then, $\mathbf{K}_{PA}$ in equation (6.2.7) modifies into

$$\mathbf{K}_{PA} = \omega\rho C_P\left[\mathrm{i}\begin{Bmatrix}\alpha & \cdot \\ \cdot & 1\end{Bmatrix} + \begin{Bmatrix} \cdot & 1-2\alpha \\ 1-2\alpha & \cdot \end{Bmatrix}\frac{k}{k_S} + \frac{\mathrm{i}}{2}\begin{Bmatrix}\alpha-2 & \cdot \\ \cdot & (1-2\alpha)/\alpha^2\end{Bmatrix}\left(\frac{k}{k_S}\right)^2\right]$$

$$\text{for } \nu \leq 0.33 \tag{6.2.18}$$

$$\mathbf{K}_{PA} = \omega\rho C_P\left[\mathrm{i}\begin{Bmatrix}\alpha & \cdot \\ \cdot & 1\end{Bmatrix} + \begin{Bmatrix} \cdot & 1-2\alpha \\ 1-2\alpha & \cdot \end{Bmatrix}\frac{k}{k_S} + \frac{\mathrm{i}}{2}\begin{Bmatrix}\alpha-2 & \cdot \\ \cdot & \cdot\end{Bmatrix}\left(\frac{k}{k_S}\right)^2\right]$$

$$\text{for } \nu \geq 0.33 \tag{6.2.19}$$

The accuracy and stability of the propagation modes in a dynamic systems are important in the context of the TLM. So, we now explore the characteristics of the dynamic stiffness matrix combined with $\mathbf{K}_{PA}$ from the point of view of the eigenvalue problems. Consider two perfectly-bonded half-spaces modeled with $\mathbf{K}_{EX}$ in equation (6.2.2b) for $z>0$ and $\mathbf{K}_{PA}$ in equation (6.2.7 or 19) for $z<0$. The shear velocities are C_{S+} for $z>0$ and C_{S-} for $z<0$, while the mass density and Poisson's ratios in both half-spaces are taken to be identical. It should be recognized that the signs of the off-diagonal elements in equation (6.2.2b) must be reversed in this problem, because now $\mathbf{K}_{EX}$ represents an upper half-space. Then, the eigenvalue problem for $\Omega=k_S/k=(\omega/kC_S)$ is provided in the form of $\det(\mathbf{K}_{EX}+\mathbf{K}_{PA})=0$. The eigenvalue Ω is calculated as a function of Poisson's ratio ν.

First, we consider the case $C_{S+}= C_{S-}$ (i.e. a homogeneous space) and solve the eigenvalue problem with application of equation (6.2.7). Figure 6.2.20 shows the obtained dispersion curve for Ω versus Poisson's ratio ν. It is shown that for $\nu>1/3$, there exist negative imaginary roots which are unstable roots, as pointed out by Kausel [1992]. On the other hand, positive imaginary roots are found for $\nu<1/3$. The application of equation (6.2.19) instead of equation (6.2.7) for $\nu>1/3$ can avoid the unstable negative imaginary roots. To verify this, we now consider the case $C_{S+}=2C_{S-}$. In this case, we solve the eigenvalue problem with application of equation (6.2.7), and then equations (6.2.18,19). Figures 6.2.21a,b display the dispersion curves obtained with application of equations (6.2.7) and (6.2.18,19), respectively. It is seen that the use of equation (6.2.7) provides an unstable negative imaginary branch for $\nu>1/3$, while the use of equation (6.2.18,19) produces only stable branches belonging to the 1st and 2nd quadrants for all ν. So, it follows that the modified $\mathbf{K}_{PA}$ in equation (6.2.18,19) really stabilizes the dynamic system represented by $\mathbf{K}_{EX}+\mathbf{K}_{PA}$. Furthermore, it is expected that well-conditioned dynamic systems can be constructed by combining the modified $\mathbf{K}_{PA}$ with a buffer layer. Some related examples are shown later in this section.

We continue with a discussion on the stability and accuracy of response calculations obtained with a hybrid system using $\mathbf{K}_{PB}$. For this purpose, we consider an example of a homogeneous half-space subjected to the surface line load in the positive z-direction whose exact analytical solution is derived and presented in appendix 5A. We choose material properties and excitation frequency $\rho=1.0$, $C_S=1.0$, $\nu=0.30$, and $f_{ex}=2.5$. Therefore, the P and Rayleigh surface wave speeds are $C_P=1.87$ and $C_R=0.93$, respectively. Then, the maximum and minimum wavelengths are $\lambda_P = C_P/f_{ex} = 1.87/2.5 = 0.75$ (≈ 0.80), $\lambda_R = C_R/f_{ex} = 0.93/2.5 = 0.37$ ($\approx \lambda_P/2$). We calculate displacement responses for five different buffer layers $H_{BL}=0.20$, 0.40, 0.60, 0.80, 1.00, each of which corresponds approximately to the case $R_P=0.25$, 0.50, 0.75, 1.00, and 1.25, respectively. For discrete models, we apply the TLM2 with $N_\lambda=8$. To estimate the accuracy, we compare the results obtained with $\mathbf{K}_{PB}$ against the exact analytical solution.

Figures 6.2.22a-c through 6.2.26a-c show the numerical results in comparison with the exact analytical solutions for $H_{BL}=0.20$, 0.40, 0.60, 0.80, and 1.00, respectively. Figures 6.2.22a, 6.2.23a, 6.2.24a, 6.2.25a, and 6.2.26a display the found eigenvalues k_j (indicated by "×") and the exact Rayleigh pole $k_R=\omega/C_R$ (indicated by "o") in the complex wavenumber plane. It is observed that as H_{BL} (or R_P) becomes larger, the Rayleigh pole obtained with $\mathbf{K}_{PB}$ becomes more accurate and the other spurious eigenvalues k_j are more densely distributed near and along the branch-cut. So, it is inferred that the $\mathbf{K}_{PB}$ with larger R_P produces the more correct modal solutions that play an equivalent role to the residue summations and the branch-cut integrals of the exact analytical solutions. Figures 6.2.22bc, 6.2.23bc, 6.2.24bc, 6.2.25bc, and 6.2.26bc compare the results of $\mathbf{K}_{PB}$ with the exact analytical solution in terms of the horizontal and vertical displacements. It is

shown that R_P must be no less than 0.50~0.75, or approximately $H_{BL} \geq 1.0\lambda_R \sim 1.5\lambda_R$, which implies the important fact that the thickness of the buffer layer must be deep enough to prevent the Rayleigh surface wave from touching the paraxial boundary. It is well known that the Rayleigh surface wave carries most of the energy from external sources along the top surface. So, if the buffer layer is not thick enough, the TLM combined with the paraxial boundary produces significant errors, as seen in figure 6.2.22b. Unlike the *SH* wave problem, a clear separation between two domains I and II according to the accuracy is not observed in the present problem. The reason is that most of the energy propagated along the surface by the Rayleigh surface wave, and this is modeled quite accurately with the TLM. So, little energy in the form of body waves penetrates the medium and touches the lower boundary. Therefore, the wave motion arriving at the paraxial boundary is too small to produce strong spurious reflections. Therefore, with the satisfaction of $H_{BL} \geq 1.0\lambda_R \sim 1.5\lambda_R$, the accuracy of the responses is nearly independent of the space coordinate.

To generalize the above discussion on the effect of Rayleigh surface waves, we consider also Stoneley interface waves. The Stoneley interface wave is also known to be a non-dispersive propagation mode that propagates along the interface between two dissimilar semi-infinite media [Cagniard, 1962]. Stoneley interface waves can also propagate at any interface of multilayered systems of semi-finite (and even finite) domains for very high wavenumbers or very high frequencies. Therefore, in application of the hybrid system $\mathbf{K}_{PB}$, the proper thickness of the buffer layer H_{BL} must be determined according to the wavelength of either the Rayleigh surface wave or the Stoneley interface wave, depending on the problems being considered.

Next, we verify the improvement achieved with the help of the modified $\mathbf{K}_{PA}$ in equations (6.2.18 and 19), in terms of displacement responses. For this purpose, we solve a homogeneous full-space subjected to a vertical line load of f_{ex}=2.5. The exact analytical solution for this problem is known in closed form [Dominguez and Abascal, 1984]. We use material properties ρ=1.0, C_S=1.0, and ν=0.25, 0.45. Then, the corresponding C_P's are 1.73 for ν=0.25 and 3.32 for ν=0.45, and the associated wavelengths λ_P's are 0.69 and 1.33, respectively. So, we set $H_{BL}(=R_P\lambda_P)$=1.0 which is sufficient for both of ν=0.25, 0.45. The buffer layer is modeled with a TLM2 model satisfying N_λ=8. Since we consider the homogeneous full-space domain, we must combine two identical hybrid systems of $\mathbf{K}_{PB}$ with H_{BL}=1 that represent the upper half-space and lower half-space, respectively.

First, we calculate the displacement responses by means of equation (6.2.7) for both of ν=0.25 and 0.45. Figures 6.2.27a,b and 6.2.28a,b show the numerical results for ν=0.25 and 0.45, respectively, in comparison with the exact analytical solution by means of a standard surface plot. It is seen that the use of equation (6.2.7) provides the quite good results for ν=0.25, but not for ν=0.45. The reason is that the responses for ν=0.45 obtained with equation (6.2.7) deteriorated because of the strong spurious reflections, as expected.

Secondly, we apply the modified $\mathbf{K}_{PA}$ of equation (6.2.18) instead of equation (6.2.7) to the case of ν=0.45. Figures 6.2.29a,b show the numerical results in comparison with the exact analytical solutions. It is observed that the use of the modified $\mathbf{K}_{PA}$ in equation (6.2.19) shows a good agreement with the exact analytical solutions. Finally, it is verified from the present numerical example that well-conditioned dynamic systems are achieved by combining the modified $\mathbf{K}_{PA}$ with a buffer layer.

6.3 Application to the TLM

6.3.1 Hybrid of the ω-TLM and the exact eigenvalues

Here, we apply the hybrid technique proposed in chapter 4 to the modeling of (semi-) infinite domains. The basic idea of the hybrid technique is to calculate the modal solutions by combining the mode shapes computed with the ω-TLM and the exact eigenvalues obtained with the exact continuous models. In addition, the exact eigenvalues are calculated without any significant additional effort in computation by means of numerical searching based on the eigenvalues obtained from the ω-TLM. In chapter 4, it was observed that the hybrid technique improves to the great extent the accuracy of the modal solutions for a stratum subjected to an *SH* line load excited at a resonant frequency. In general, the numerical dispersion error associated with the resonant frequencies considerably deteriorates the modal solutions, as shown in figure 4.2.6a, b. Also, it is recalled that even small errors in eigenvalues can produce significant numerical errors to the far-field solutions, but not the near-field solutions, as seen in figures 4.2.5a and b.

The hybrid technique is quite useful in connection with wave analyses of (semi-) infinite multi-layered media whose continuous models in general have only *finite* number of true propagation modes with either purely real eigenvalues k_j or complex eigenvalues with small imaginary part, Im $k_j \approx 0$. It is shown in section 6.2 that the ω-TLM combined with the paraxial approximation and the buffer layer, i.e. $\mathbf{K}_{PB}$, provides quite accurate, but not exact, eigenvalues for true propagation modes. Therefore, the computational effort in the numerical search for a finite number of exact k_j's for the true propagation modes on the basis of the excellent approximations k_j's obtained with the ω-TLM, is very small indeed.

We now consider a simple example where a homogeneous half-space of $\rho=C_S=1.0$ and $\nu=0.30$ is subjected to an *SV-P* vertical line load of $f_{ex}=2.5$ applied at the top surface. For this homogeneous half-space, there is only one true propagation mode, namely the non-dispersive Rayleigh surface wave pole k_R. The exact Rayleigh surface wave velocity C_R is 0.9273, and the associated wavelength $\lambda_R(=C_R/f_{ex})$ is 0.37. To verify the usefulness of the hybrid technique, we compute the displacement responses by means of both the conventional ω-TLM combined with $\mathbf{K}_{PB}$ of $H_{BL}=0.5(>\lambda_R=0.37)$ and the hybrid technique. For the conventional ω-TLM, the TLM2 with $N_\lambda=4$ and 8 are applied, while for the hybrid technique, the TLM2 with $N_\lambda=4$ are applied. Then, we compare these with the exact analytical solution.

Figures 6.3.1a,b,c show the numerical results (solid line) obtained with the conventional TLM2 with $N_\lambda=4$, the conventional TLM2 with $N_\lambda=8$, and the hybrid technique using TLM2 with $N_\lambda=4$, respectively, in comparison with the exact analytical solution (dashed line). It is observed in figure 6.3.1a that the far-field solutions are deteriorated by the numerical error associated with k_R obtained with the conventional TLM2 of $N_\lambda=4$. It is shown in figure 6.3.1b that this numerical error is reduced by using $N_\lambda=8$ instead of $N_\lambda=4$. Finally, figure 6.3.c shows that the numerical results obtained with the hybrid technique with $N_\lambda=4$ are in a good agreement with the exact analytical solution, and its accuracy is even better than that of the conventional ω-TLM with $N_\lambda=8$. Therefore, it is verified that the hybrid technique provides quite accurate and more efficient solutions than the conventional ω-TLM combined with $\mathbf{K}_{PB}$.

6.3.2 Adaptive buffer layer for seismogram calculation

Next, we discuss the application of the hybrid system $\mathbf{K}_{PB}$ to seismogram calculation, i.e. time-domain response syntheses. Then, for efficient calculation, we propose the use of an adaptive buffer layer whose physical thickness is a function of frequency f and whose mathematical dimension is a function of the ratio of thickness of a buffer layer to wavelength R_S and the number of thin-layers per wavelength N_λ. Then, we verify the efficiency of the proposed adaptive buffer layer by means of numerical examples and determine the proper values of R_S and N_λ for the adaptive buffer layer in connection with the seismogram calculation.

To calculate seismograms by means of the ω-TLM combined with $\mathbf{K}_{PB}$, there are several parameters to be considered in advance. First of all, concerning the use of $\mathbf{K}_{PB}$, we have to determine the maximum range x_{max} of receivers to be considered in the seismogram analyses. It is recalled from section 6.2 that the distance X_I between an external source and the border of domains I and II in figures 6.2.4 and 5 is a function of the buffer-layer thickness $H_{BL}(=R\lambda)$, which is important especially for anti-plane problems. Therefore, H_{BL} must be chosen such that $x_{max} \leq X_I$.

Secondly, regarding the inverse Discrete Fourier transformation or the inverse Fast Fourier transformation from the frequency-domain to the time-domain, we need to determine the maximum frequency and the sampling frequency to be considered. The maximum frequency f_{max} can be determined from the temporal characteristics of excitation sources, i.e. the frequency spectra of excitation sources. The sampling frequency Δf should be no greater than $1/t_{max}$ where t_{max} is the maximum time in the seismograms of interest. Then, the minimum frequency f_{min} is generally equal to Δf or $(\frac{1}{2})\Delta f$.

Once the range of frequency f_{min} and f_{max} has been decided, we need to determine the thickness H_{BL} of the buffer layer and its discretization size h_{BL}. Following the conventional ω-TLM, we usually set $H_{BL}=R\lambda_{max}=RC_S/f_{min}$ and $h_{BL}=\lambda_{min}/N_\lambda=C_S/(f_{max}N_\lambda)$. Notice that the thickness $H_{BL}=RC_S/f_{min}$ is too large for f_{max}, while $h_{BL}=C_S/(f_{max}N_\lambda)$ is too small for f_{min}. Therefore, the number of thin-layers for the buffer layer $N_{BL}(=H_{BL}/h_{BL})$ is given as $RN_\lambda f_{max}/f_{min}$, which require quite a large system of equations, and hence, a considerable computational expense. To avoid this inefficiency, we propose an adaptive buffer layer as follows.

The idea is to apply a buffer layer of just the "necessary" thickness for each frequency f such as $H_{BL}=R_S\lambda_S(=R_SC_S/f)$, and to discretize this buffer layer according to $N_\lambda=\lambda_S/h_{BL}$. Remember from chapter 4 that N_λ can be determined according to the required accuracy. Then, it follows that the total number of thin-layers N_{BL} for the buffer layer is given in the form.

$$N_{BL} = H_{BL} / h_{BL} = R_S\lambda_S / h_{BL} = R_S N_\lambda \tag{6.3.1}$$

Equation (6.3.1) indicates that the size of the system of equations for the buffer layer is now a function of only R_S and N_λ. Therefore, the physical thickness of the adaptive buffer layer is a function of f, satisfying the condition $H_{BL} \geq R_SC_S/f$. On the other hand, for the two fixed parameter R_S and N_λ, the mathematical size of the system of equations is invariant for all frequencies f of interest, namely independent of f. Therefore, when combined with the ω-TLM for seismogram calculation, the adaptive buffer layer proposed here is much more efficient than the conventional buffer layer that uses $H_{BL}=RC_S/f_{min}$ and $h_{BL}=C_S/(f_{max}N_\lambda)$.

Next, we combine the two systems of equations for the paraxial approximation $\mathbf{K}_{PA}$ and the adaptive buffer layer $\mathbf{K}_{BL}$, so as to finally express the combined system in the form of a product

of a parameter and a matrix, which can be directly and efficiently applied to seismogram calculations. It will be shown that the parameter is dependent on the frequency f, while the matrix is independent of f.

To begin with, we express k_S in equations (6.2.3 and 7) in terms of h_{BL} and N_λ as

$$k_S = \frac{\omega}{C_S} = \frac{2\pi f}{C_S} = \frac{2\pi}{\lambda_S} = \frac{1}{h_{BL}} \frac{2\pi}{N_\lambda} \tag{6.3.2}$$

Substituting equation (6.3.2) into equations (6.2.3 and 7), we obtain $\mathbf{K}_{PA}$ in the form.

$$\mathbf{K}_{PA} = \frac{1}{h_{BL}} \left[\bar{\mathbf{A}}_{PA} K^2 + \bar{\mathbf{B}}_{PA} K + \bar{\mathbf{G}}_{PA} \right] \tag{6.3.3}$$

where $K(=kh_{BL})$ is the dimensionless wavenumber, h_{BL} is given as $C_S/(N_\lambda f)$, and the three matrices are as follows:

For *SH* waves,

$$\bar{\mathbf{A}}_{PA} = -\mathrm{i} \frac{G}{2} \frac{N_\lambda}{2\pi} \tag{6.3.4a}$$

$$\bar{\mathbf{B}}_{PA} = 0 \tag{6.3.4b}$$

$$\bar{\mathbf{G}}_{PA} = \mathrm{i}G \frac{2\pi}{N_\lambda} \tag{6.3.4c}$$

For *SV-P* waves,

$$\bar{\mathbf{A}}_{PA} = \mathrm{i} \frac{G}{2} \frac{N_\lambda}{2\pi} \begin{Bmatrix} 1-2/\alpha & \cdot \\ \cdot & (1-2\alpha)/\alpha^3 \end{Bmatrix} \tag{6.3.5a}$$

$$\bar{\mathbf{B}}_{PA} = G \begin{Bmatrix} \cdot & 1/\alpha - 2 \\ 1/\alpha - 2 & \cdot \end{Bmatrix} \tag{6.3.5b}$$

$$\bar{\mathbf{G}}_{PA} = \mathrm{i}G \frac{2\pi}{N_\lambda} \begin{Bmatrix} 1 & \cdot \\ \cdot & 1/\alpha \end{Bmatrix} \tag{6.3.5c}$$

Notice that the terms in bracket in equation (6.3.3) are all independent of the frequency f, and only the factor $1/h_{BL}$ is a function of f such that $N_\lambda f/C_S$. Similarly, the dynamic stiffness matrices for the adaptive buffer layer can be expressed as

$$\mathbf{K}_{BL} = \left[\mathbf{A}_{BL} k^2 + \mathbf{B}_{BL} k + \mathbf{G}_{BL} - \omega^2 \mathbf{M}_{BL} \right] = \frac{1}{h_{BL}} \left[\bar{\mathbf{A}}_{BL} K^2 + \bar{\mathbf{B}}_{BL} K + \bar{\mathbf{G}}_{BL} - \Omega^2 \bar{\mathbf{M}}_{BL} \right] \tag{6.3.6}$$

where $\mathbf{A}_{BL}$, $\mathbf{B}_{BL}$, $\mathbf{G}_{BL}$, and $\mathbf{M}_{BL}$ are the material matrices of the conventional TLM, and $\bar{\mathbf{A}}_{BL}$, $\bar{\mathbf{B}}_{BL}$, $\bar{\mathbf{G}}_{BL}$, and $\bar{\mathbf{M}}_{BL}$ are the modified ones for the adaptive buffer layer defined as

$$\bar{\mathbf{A}}_{BL} = \mathbf{A}_{BL} h_{BL}^{-1} \tag{6.3.7a}$$

$$\bar{\mathbf{B}}_{BL} = \mathbf{B}_{BL} \tag{6.3.7b}$$

$$\bar{\mathbf{G}}_{BL} = \mathbf{G}_{BL} h_{BL} \tag{6.3.7c}$$

$$\bar{\mathbf{M}}_{BL} = \mathbf{M}_{BL} h_{BL}^{-1} \tag{6.3.7d}$$

$$\Omega = \omega h_{BL} = C_S \frac{2\pi}{N_\lambda} \tag{6.3.7e}$$

Notice again that the terms in bracket in equation (6.3.6) are all independent of the frequency f, and only the factor $1/h_{BL}$ is a function of f such that $N_\lambda f/C_S$. Combining equations (6.3.3 and 6) provides the adaptive dynamic systems for $\mathbf{K}_{PB}$, which can be expressed symbolically as

$$\mathbf{K}_{PB} = \frac{1}{h_{BL}} \left[\bar{\mathbf{A}}_{PB} K^2 + \bar{\mathbf{B}}_{PB} K + \bar{\mathbf{G}}_{PB} - \Omega^2 \bar{\mathbf{M}}_{PB} \right] \tag{6.3.8}$$

where ($\bar{\mathbf{A}}_{PB}$, $\bar{\mathbf{B}}_{PB}$, $\bar{\mathbf{G}}_{PB}$, $\bar{\mathbf{M}}_{PB}$) are obtained by assembling ($\bar{\mathbf{A}}_{BL}$, $\bar{\mathbf{B}}_{BL}$, $\bar{\mathbf{G}}_{BL}$, $\bar{\mathbf{M}}_{BL}$) and ($\bar{\mathbf{A}}_{PA}$, $\bar{\mathbf{B}}_{PA}$, $\bar{\mathbf{G}}_{PA}$, $\bar{\mathbf{M}}_{PA}$). It is noticed in equation (6.3.8) that all the terms in brackets are independent of f, and only h_{BL} is a function of f such that $h_{BL}=\lambda_S/N_\lambda=C_S/(fN_\lambda)$. Hence, the constructed adaptive system $\mathbf{K}_{PB}$ has a physical thickness that is a function of f and a mathematical size that is invariant with f. Finally, the assemblage of equations (6.3.8) with the dynamic stiffness matrices for the upper layers in figure 6.2.1 supplies the total system of equations to be solved. The associated examples are considered not only later in this section 6.3, but also in section 6.4.

Furthermore, there is an additional great application of the adaptive system $\mathbf{K}_{PB}$ in the form of equation (6.3.8). We can calculate in an extremely efficient way the epicentral seismograms for a homogeneous half-space subjected to surface line loads as follows. First, from equation (6.3.8), we solve the eigenvalue problem for the dimensionless wavenumber K in stead of k in the following form.

$$\left[\bar{\mathbf{A}}_{PB}K_j^2+\bar{\mathbf{B}}_{PB}K_j+\bar{\mathbf{G}}_{PB}-\Omega^2\bar{\mathbf{M}}_{PB}\right]\phi_j=\mathbf{0} \tag{6.3.9}$$

where the eigenvalue K_j and the mode shape ϕ_j are both independent of the frequency f. Once K_j have been found, the results for each f can be obtained by re-scaling as

$$k_j=\frac{K_j}{h_{BL}}=\frac{K_j}{\lambda_S/N_\lambda}=\frac{K_jN_\lambda}{C_S}f \tag{6.3.10}$$

Therefore, by solving only once the eigenvalue problem in equation (6.3.9), we can calculate the responses for any arbitrary frequency f by re-scaling the eigenvalues as shown in equation (6.3.10). After applying the orthogonal conditions to the mode shapes as in the conventional TLM, the modal solutions for any f (or ω) can be given as

$$\tilde{u}^{11}_{\alpha\beta}(x,\omega)=\frac{1}{h_{BL}}\sum_{j=1}^{M}\phi^1_{\alpha j}\phi^1_{\beta j}\frac{e^{-ik_j|x|}}{2ik_j}=\sum_{j=1}^{M}\phi^1_{\alpha j}\phi^1_{\beta j}\frac{e^{-ik_j|x|}}{2iK_j} \tag{6.3.11}$$

where the two 1's in the superscript represent the elevations of the surface receiver and source, respectively, and the subscripts $\alpha,\beta(=x, y, z)$ are the directions of receiver and source, respectively. It should be noticed that a factor sgn(x) must be added to equation (6.3.11) when $\alpha\neq\beta$. Performing the inverse DFT or inverse FFT with the modal solutions $\tilde{u}^{11}_{\alpha\beta}(x,\omega)$ in equation (6.3.11), we can obtain the seismograms in the time domain, i.e. $u^{11}_{\alpha\beta}(x,t)$ by solving only once the associated eigenvalue problem in equation (6.3.9).

To validate the adaptive buffer layer proposed above, we calculate the seismograms for $u^{11}_{yy}(x,t)$ and $u^{11}_{zz}(x,t)$ in a homogeneous half-space ($z\leq 0$) with $\rho=C_S=1.0$ and $\nu=0.30$, subjected to a surface line load of the form

$$p_i=\delta(x)\delta(z)h(t) \qquad \text{with } i=x, y, \text{ or } z \tag{6.3.12}$$

where

$$h(t)=\begin{cases}\dfrac{2}{t_d}\sin^2\dfrac{\pi}{t_d}t & , \quad 0\leq t\leq t_d \\ 0 & , \quad t<0, t_d<t\end{cases} \tag{6.3.13}$$

In equation (6.3.13), t_d is the time duration of loading and the associated maximum frequency f_{max} is $2/t_d$ as shown in chapter 4. We choose t_d=0.2 for the present problem, and so f_{max}=10 in the following numerical calculations. We calculate the seismograms by means of both equation (6.3.11) and the exact analytical solutions derived in appendix 5A, and compare these to verify the validity of the adaptive buffer layer proposed here. For discrete models, we use the TLM2 with N_λ=8.

First, we calculate the seismograms u_{yy}^{11} at 8 epicentral points x=0.25, 0.50,..., 2.0 by means of the adaptive $\mathbf{K}_{PB}$ with R_S=1.0, 2.0, 3.0. Figures 6.3.2, 3, 4 show the results (dashed line) for $u_{yy}^{11}(x,t)$ with R=1.0, 2.0, 3.0, respectively, in comparison with the exact solutions (solid line) for $0<t<4$. The corresponding minimum range $X_I(=2H_{BL})$ is 0.2, 0.4, 0.6, respectively, because λ_{min} is 0.1 in the present problem. It is observed that the use of R_S=1.0 and R_S=2.0 introduces numerical errors resulting from the strong spurious reflections at the paraxial boundary. On the other hand, the use of R_S=3.0 shows very good agreement with the exact solutions without any spurious reflections within the region of interest, i.e., x=0.25~2.0. Based on the observations in section 6.2, we should have expected strong spurious reflections just beyond the corresponding minimum X_I of 0.2, 0.4, 0.6 for R_S=1.0, 2.0, 3.0, respectively, in domain II. For example, in figure 6.3.4, the responses for $x\geq$0.6 should have been deteriorated by the spurious reflections from the paraxial boundary. However, no reflection appears in the seismograms. The reason is that the applied source in equation (6.3.12) transmits very weak body wave energy into the system at the high frequencies. Consequently, the associated spurious reflections at the paraxial boundary are too small to deteriorate the seismograms to any significant degree.

Next, we calculate the seismograms of u_{zz}^{11} at 8 epicentral points x=0.25, 0.50,..., 2.0 by means of the adaptive $\mathbf{K}_{PB}$ with R_S=1.0 and 2.0. Figures 6.3.5 and 6 display the responses for $u_{zz}^{11}(x,t)$ with R_S=1.0 and 2.0, respectively, where the relationship $R_S=H_{BL}/\lambda_S$ is used instead of $R_P=H_{BL}/\lambda_P$, by which we can easily compare the above results for u_{yy}^{11} that are due to an *SH* line load. It is seen in figure 6.3.5 that the responses with R_S=1.0 are not contaminated by the spurious reflections at the paraxial boundary, and even look very similar to those with R_S=2.0 in figure 6.3.6. The reason is that most of the energy from the source propagates along the surface in the form of Rayleigh waves, without penetrating into the buffer layer, as was already observed in section 6.2. Therefore, it is concluded that the adaptive buffer layer is more effective for *SV-P* wave problems than for *SH* wave problems.

Concerning the application of $\mathbf{K}_{PB}$ of equation (6.3.8) to a (semi-) infinite system such as the one in figure 6.2.1, a problem arises in determining a proper number of thin-layers per wavelength $N_{\lambda,BL}$ for the adaptive buffer layer that can be used for all the frequencies. In general, the total number of thin-layers N for the upper layered system in figure 6.2.1 can be chosen according to the maximum frequency f_{max} and N_λ. Then, it follows that, for any $f(<f_{max})$, the number of thin-layers per wavelength, which can be referred to as $N_{\lambda,f}$ for convenience, is greater than N_λ. Therefore, the adaptive buffer layer with a fixed $N_{\lambda,BL}$ could be inconsistent with the upper layer system with $N_{\lambda,f}$. This kind of inconsistency can produce numerical spurious reflections at the interface between the upper layer system and the adaptive buffer layer. Therefore, it is necessary to determine a proper and reasonable $N_{\lambda,BL}$ for the adaptive buffer layer that might be greater than N_λ so as to decrease the spurious reflections to the extent possible.

We try to determine here a proper and reasonable $N_{\lambda,BL}$ for the adaptive buffer layer by solving a numerical example. We consider again one of our canonical examples: a homogeneous half-space with $\rho=C_S$=1.0, subjected to an *SH* surface line load p_y defined by equations (6.3.12 and 13). We compute the displacement responses of this homogeneous half-space by modeling it as a system composed of a homogeneous layer ($0\leq z\leq H$, with H=1) and a homogeneous half-space ($z\leq 0$). The layer and the half-space have identical material properties. Clearly, the interface z=0 between the layer and the half-space is an artificial one, because the two media have identical material properties. We model the upper layer by means of the TLM2 with N_λ=4, and model the adaptive buffer layer R_S=4.0 with the TLM2 using four different $N_{\lambda,BL}$. We try four choices $N_{\lambda,BL}$=4, 8, 12,

and 16 for the adaptive buffer layer. Figures 6.3.7, 8, 9, and 10 display the corresponding snapshots of the displacements at t=0.3, 0.6,..., 1.8, in terms of a standard surface plot. It is shown that the adaptive buffer layers with $N_{\lambda,BL}$=4 and 8 provide numerical spurious reflections, while the adaptive buffers layer with $N_{\lambda,BL}\geq$12 produce no significant spurious reflections. It can be easily inferred that the model of $N_{\lambda,BL}$=12 corresponds to $N_{\lambda f}$ for f/f_{max}=1/3. This reasoning implies that in order to avoid significant spurious reflections, $N_{\lambda,BL}$ must be no less than $N_{\lambda f}$ for f/f_{max}=1/3.

6.4 Analyses of multilayered half-spaces

6.4.1 Anti-plane problems

Here, we analyze two numerical examples of multilayered half-spaces subjected to *SH* transient line loads, by means of the ω-TLM combined with the adaptive hybrid system $\mathbf{K}_{PB}$. The adaptive hybrid system $\mathbf{K}_{PB}$ consists of a combination of a paraxial approximation and an adaptive buffer layer, as proposed in section 6.3. The two examples are 1) a one-layered system on a homogeneous half-space, and 2) a two-layered system on a homogeneous half-space, which are exactly identical to those in section 4.4.1. Through these analyses, we illustrate wave motions within the upper layered domains in terms of displacement snapshots. In addition, we validate the use of the ω-TLM combined with the adaptive hybrid system $\mathbf{K}_{PB}$ in calculating seismograms, and compare with the results of section 4.4.1 obtained by means of the substructure method. As seen in section 4.4.1, the wave motions associated with the two layered cases are much more complicated than the case of a homogeneous half-space. The reason is that due to the dissimilarity of material properties, the phenomena of reflection, transmission (or refraction), and head waves occur at the interfaces between the layers.

The *SH* line load considered in this section 6.4.1 is given as

$$p_y = \delta(x)\delta(z-H)h(t) \tag{6.4.1}$$

where H is the thickness of the upper layered system (H=1 for the first example, and H=2 for the second example), and $h(t)$ is a Hanning window function with t_d=0.2, given as

$$h(t)=\begin{cases}\dfrac{2}{t_d}\sin^2\dfrac{\pi}{t_d}t & , \quad 0\leq t\leq t_d \\ 0 & , \quad t<0,\ t_d<t\end{cases} \tag{6.4.2}$$

Then, it follows that the associated maximum frequency f_{max}(=$2/t_d$) is 10. Note that the line load in equation (6.4.1) has the same temporal variation as that of the two examples in section 4.4.1. On the other hand, the spatial variation is taken as $\delta(x)$, instead of a Hanning window of half-width a, which was used for the corresponding examples in section 4.4.1. However, since a small half-width was used in section 4.4.1, i.e. a=0.2, it is expected that the wave motions in this section 6.4.1 should be quite similar to those in section 4.4.1.

Consider the first example: a one-layered system ($0\leq z\leq H$) on a homogeneous half-space ($z\leq 0$) subjected to the *SH* transient line load p_y of equation (6.4.1). The mass density, the shear wave velocity, and the thickness of the upper layer are ρ_1=$C_{S,1}$=H=1.0, respectively, while the mass density and the shear wave velocity of the lower half-space are ρ_2=1.0 and $C_{S,2}$=2.0, respectively. For discrete models, we apply the TLM2 with N_λ=4 and the adaptive hybrid system $\mathbf{K}_{PB}$ of $N_{\lambda,BL}$=12 and R_S(=H_{BL}/λ_S)=4.0 as proposed in section 6.3.2.

Figure 6.4.1 shows the displacement snapshots at t=1, 2, 3, and 4 for the upper layer ($0 \le z \le 1$) by means of a standard surface plot. First of all, in comparison with figure 4.4.1, it is verified that the ω-TLM combined with the adaptive hybrid system $\mathbf{K}_{PB}$ of $N_{\lambda,BL}$=12 and R_S=4.0 successfully provides accurate results without any spurious reflection effect for *SH* wave problems. The wave motions in this problem are very similar to those in figure 4.4.1, as pointed out previously. The first snapshot for t=1 shows that only the direct wave propagates with circular wavefronts through the medium, which is exactly identical to the case of a homogeneous half-space whose material properties are the same as the upper layer. The second snapshot for t=2 displays a direct wave propagating in the same fashion as in the case of a homogeneous half-space, and a first reflection at the interface of z=0 propagating upwards with an elliptical wave front. Notice that the polarization of this first reflection wave is opposite to that of the direct wave, because the half-space is stiffer than the upper layer, i.e. $C_{S,1}<C_{S,2}$. The third snapshot for t=3 shows a direct wave propagating almost as a vertical plane wave, and the first wave reflected at the top-surface z=1 propagating downwards with elliptical wave front and without change in polarization. In addition, it is seen in the third snapshot that a first head wave of weak amplitude propagates ahead of the direct wave. Finally, it is observed in the fourth snapshot for t=4 that since most energy generated by the external source leaks into the half-space during multiple reflections, the amplitudes of all the reflected waves become smaller and smaller. On the other hand, the direct wave propagates still with significant amplitude.

Next, consider the second example: a two-layered system ($0 \le z \le H$, with $H=H_1+H_2$) on a homogeneous half-space ($z \le 0$) subjected to the *SH* line load p_y in equation (6.4.1). The mass densities, shear wave velocities and thicknesses of the two upper layers are $\rho_1=C_{S,1}=H_1=1.0$, and $\rho_2=H_2=1.0$, $C_{S,2}=2$, respectively, while the mass density and the shear wave velocity of the lower half-space are $\rho_3=1.0$ and $C_{S,3}=3.0$, respectively. It follows that the total thickness of the upper layered system is now $H(=H_1+H_2)=2$. For discrete models, we apply the TLM2 with N_λ=4 and the adaptive hybrid system $\mathbf{K}_{PB}$ of $N_{\lambda,BL}$=12 and $R_S(=H_{BL}/\lambda_S)$=4.0 as proposed in section 6.3.2.

Figure 6.4.2 displays the displacement snapshots at t=1, 2, 3, and 4 for the upper two-layered system ($0 \le z \le 2$) by means of a standard surface plot. In each plot, the dotted line at z=1 represents the interface between the first ($1 \le z \le 2$) and second ($0 \le z \le 1$) upper layer. First of all, in comparison with figure 4.4.2, it is again verified that the ω-TLM combined with the adaptive hybrid system $\mathbf{K}_{PB}$ of $N_{\lambda,BL}$=12 and R_S=4.0 successfully provides accurate results without any spurious reflection effect for *SH* wave problems. The wave motions in this problem are very similar to those in figure 4.4.2, as pointed out above. The first snapshot for t=1 shows that only the direct wave propagates with circular wave fronts through the medium, which is exactly identical to the case of a homogeneous half-space whose material properties are equal to those of the first upper layer ($1 \le z \le 2$). Next, it is observed in the second snapshot for t=2 that the wave motion in the first layer ($1 \le z \le 2$) is identical to the snapshot for t=2 of figure 6.4.1. In addition, it is shown that the first transmitted wave from the first layer ($1 \le z \le 2$) to the second layer ($0 \le z \le 1$) refracts and propagates through the second layer, and the first reflection wave at the interface at z=0 propagates with relatively weak amplitude. The weak amplitude of the reflected wave implies that most of the energy from the source has already leaked into the half-space. The third snapshot for t=3 shows again the similarity to the third snapshot in figure 6.4.1 for the first layer ($1 \le z \le 2$). However, there is a difference as well, that is, the first transmitted wave from the second layer ($0 \le z \le 1$) to the first layer ($1 \le z \le 2$) propagates through the first layer with weak amplitude. This transmitted wave results from the first reflection at the interface at z=0. In addition, two head waves are observed in the third snapshot for t=3, because not only the second layer is stiffer than the first layer, but also

the half-space is stiffer than the second layer. One propagates through the first layer ahead of the direct wave generated by the source, and the other propagates through both the first and second layers ahead of the direct wave and first transmitted wave from the first layer to the second layer. Finally, the fourth snapshot for t=4 illustrates that the wave motion in the firs layer is similar to the fourth snapshot in figure 6.4.1, except the effect of the reflection waves at z=0. Also, notice that because most of the energy from the external source to the second layer leaks into the half-space during multiple reflections, the amplitudes of all the waves in the second layer become very small.

6.4.2 In-plane problems

Next, we analyze two numerical examples of multilayered half-spaces subjected to *SV-P* vertical line loads, by means of the ω-TLM combined with the adaptive hybrid system $\mathbf{K}_{PB}$. The two examples are 1) a one-layered system on a homogeneous half-space, and 2) a two-layered system on a homogeneous half-space, which are exactly identical to those in section 4.4.2. Through these analyses, we illustrate wave motions within the upper layered domains of interest in terms of snapshots for the both horizontal and vertical displacements u and w. In addition, we validate the ω-TLM combined with the adaptive hybrid system $\mathbf{K}_{PB}$ for calculating seismograms through comparison with the results of section 4.4.2 obtained with the substructure method. As seen in section 4.4.2, the wave motions involved here are much more complicated than the case of a homogeneous half-space. The reason is that due to the dissimilarity of material properties, the phenomena of reflection, transmission (or refraction), and head waves occur at the interfaces between the layers. In addition, since both of *S* and *P* wave components are involved, the mode conversions between the two components also take place at each interface.

The *SV-P* line load p_z considered in this section 6.4.2 is given as

$$p_z = \delta(x)\delta(z-H)h(t) \tag{6.4.3}$$

where H is the thickness of the upper layer system (H=1 for the first example, and H=2 for the second example), and $h(t)$ is given in equation (6.4.2). So, the associated maximum frequency $f_{max}(=2/t_d)$ is again 10. Note that the line load in equation (6.4.3) has the same temporal variation as the corresponding two examples in section 4.4.2. On the other hand, its spatial variation is given as $\delta(x)$, instead of the Hanning window with a half-width a, which is used for the corresponding examples in section 4.4.2. However, as the case of section 6.4.1 and for the same reason, it is expected that the wave motions in this section are quite similar to those in section 4.4.2.

Consider the first example: a one-layered system ($0 \le z \le H$) on a homogeneous half-space ($z \le 0$) subjected to the *SV-P* vertical line load p_z of equation (6.4.3). The mass density, the shear wave velocity, the thickness, and the Poisson's ratio of the upper layer are ρ_1=$C_{S,1}$=H=1.0 and ν=0.25, respectively, while the mass density, the shear wave velocity, and the Poisson's ratio of the lower half-space are ρ_2=1.0, $C_{S,2}$=2.0, and ν=0.25, respectively. Then, it follows that dilation (*P*) wave velocities for the upper layer and the half-space are $C_{P,1}$=1.732 and $C_{P,2}$=3.464, respectively, and the Rayleigh surface wave velocity for the upper is $C_{R,1}$=0.9193. For discrete models, we apply the TLM2 with N_λ=4 and the adaptive hybrid system $\mathbf{K}_{PB}$ with $N_{\lambda,BL}$=12 and $R_S(=H_{BL}/\lambda_S)$=2.0 as proposed in section 6.3.2.

Figure 6.4.3 shows the displacement snapshots for u and w at t=0.5, 1.0, 1.5, and 2.0 for the upper one-layered system ($0 \le z \le 1$) by means of a standard surface plot. First of all, in comparison with figure 4.4.3, it is verified that the ω-TLM combined with the adaptive hybrid system $\mathbf{K}_{PB}$ of

$N_{\lambda,BL}$=12 and R_S=2.0 successfully provides accurate results without any spurious reflection effect for *SV-P* wave problems. The wave motions in this problem are very similar to those in figure 4.4.3, as pointed out previously. It is observed in the two snapshots for t=0.5 that the *P* and *S* wave components propagate separately through the upper layer in the same fashion as the case of a homogeneous half-space. It should also be recognized that near the top-surface, the amplitude of *P* wave components is much smaller than that of *S* wave component, while within the upper layer and below the top-surface, the amplitude of *P* wave components is comparable to that of *S* wave components. This confirms the fact that *P* waves can not properly propagate along stress-free surfaces without an external source. Also, notice that the Rayleigh surface wave propagates closely behind the *S* wave along the top-surface at time t=0.5. Next, the two snapshots for t=1.0 on the second row display two weak reflected waves resulting from the incident direct *P* wave at the interface of z=0 propagating upward through the upper layer. The reason that these two reflection waves exist is the mode conversion from an incident *P* wave to two reflected *S* and *P* waves at the interface. Also, notice that the Rayleigh surface wave propagating along the top-surface is clearly separated from the *S* wave components, and its amplitude is significant as well. The snapshots on the third and fourth rows illustrate the wave motions for t=1.5 and t=2.0, respectively. As shown in the four surface plots, the wave motions involved are extremely complicated, because of the multiple reflections, the head wave effects, and the mode conversion between *P* and *S* wave components at both the interface and top-surface. In addition, due to the multiple reflections and energy leakage into the half-space, the amplitudes of waves decrease to a great degree, which makes it more difficult to identify the involved waves and interpret the wave motions. However, it is seen that the Rayleigh surface wave propagates in the almost same fashion as for a homogeneous half-space. This observation implies that in the present example, the depth of the upper layer (H=1) is large enough to prevent the Rayleigh surface wave from touching the interface between the upper layer and the half-space.

Next, consider the second example: a two-layered system ($0 \le z \le H$, with $H=H_1+H_2$) on a homogeneous half-space ($z \le 0$) subjected to the *SV-P* vertical line load p_z of equation (6.4.3). The mass densities, the shear wave velocities, the thickness', and the Poisson's ratios of the two upper layers are $\rho_1=\rho_2=1$, $C_{S,1}=1$, $C_{S,2}=2$, $H_1=H_2=1.0$ and $\nu_1=\nu_2=0.25$, respectively, while the mass density, the shear wave velocity, and the Poisson's ratio of the lower half-space are $\rho_3=1.0$, $C_{S,3}=3.0$, and $\nu_3=0.25$, respectively. Then, it follows that dilation (*P*) wave velocities for the two upper layer and the half-space are $C_{P,1}=1.732$, $C_{P,2}=3.464$, and $C_{P,3}=5.196$, respectively, and the Rayleigh surface wave velocity for the upper layer is $C_{R,1}=0.9193$. For discrete models, we apply the TLM2 with N_λ=4 and the adaptive hybrid system $\mathbf{K}_{PB}$ of $N_{\lambda,BL}$=12 and $R_S(=H_{BL}/\lambda_S)$=2.0 as proposed in section 6.3.2.

Figure 6.4.4 shows the displacement snapshots of u and w at t=0.5, 1.0, 1.5, and 2.0 for the upper two-layered system ($0 \le z \le 2$) by means of a standard surface plot. In each plot, the dotted line at z=1 represents the interface between the first ($1 \le z \le 2$) and second ($0 \le z \le 1$) upper layer. First of all, in comparison with figure 4.4.4, it is verified that the ω-TLM combined with the adaptive hybrid system $\mathbf{K}_{PB}$ of $N_{\lambda,BL}$=12 and R_S=2.0 successfully provides accurate results without any spurious reflection effect for *SV-P* wave problems. The wave motions in this problem are much similar to those in figure 4.4.4, as pointed out above.

We begin by interpreting the wave motions in the first layer ($1 \le z \le 2$), in comparison with the wave motions in the upper layer ($0 \le z \le 1$) in figure 6.4.3. It is observed in the snapshots on the first (for t=0.5) and second (for t=1.0) rows that the wave motions in the first layer ($1 \le z \le 2$) are exactly identical to those in the upper layer ($0 \le z \le 1$) in figure 6.4.3. The reason is that at time t=0.5 and 1.0, the waves reflecting at the interface at z=0 have not yet arrived at the first layer. On

the other hand, it is seen in the snapshots on the third (for t=1.5) and fourth (for t=2.0) rows that the reflection waves from the interface at z=0 transmit into the first layer ($1 \le z \le 2$). Hence, the wave motions in the first layer are now different from those in the upper layer ($0 \le z \le 1$) in figure 6.4.3. However, notice that the degree of difference is insignificant. The reason for this small difference is that when a reflection occurs at the interface of z=0, most of the energy leaks into the half-space and only small fraction bounces up. Consequently, the waves transmitting from the second layer into the first layer are too weak to significantly influence the wave motions in the first layer ($1 \le z \le 2$). Also, notice that the Rayleigh surface wave motion propagates without any interruption resulting from the transmitted waves in the present problem for the whole time of interest.

We now consider the wave motions in the second layer ($0 \le z \le 1$). The snapshots for t=0.5 on the first row show that the second layer is quiescent, because no wave have yet arrived from the source. The snapshots for t=1.0 display complicated interference phenomena caused by P waves transmitted from the first layer ($1 \le z \le 2$) already propagating upward after reflecting at the interface of z=0, while transmitted S waves propagate downward. However, due to the complicated interference, the associated wavefronts cannot clearly be distinguished in the snapshots. The snapshots for t=1.5 and 2.0 illustrate even more complicated wave motions. The reasons for this extreme complication are that the multiple reflections, the head wave effects, and the mode conversion between P and S wave components occur associated with both the interfaces of z=0 and z=1. In addition, due to the multiple reflections/transmissions and the associated energy leakage into the half-space, the amplitudes of the involved waves decrease to the great degree, which makes it more difficult to identify the involved waves and interpret the wave motions.

Figures for section 6.2

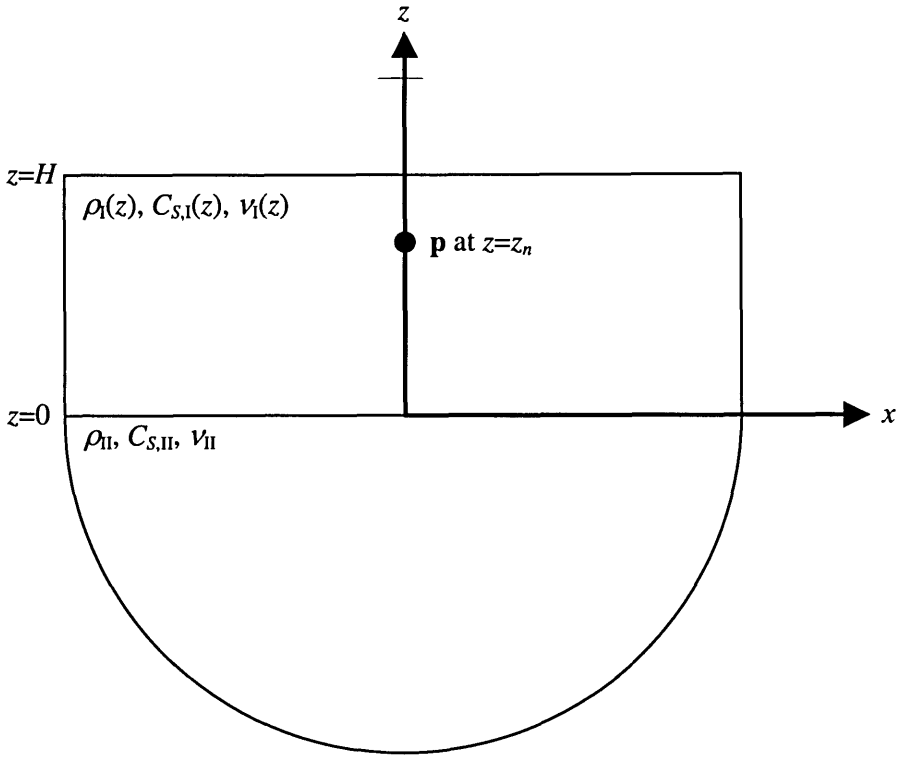

Figure 6.2.1 Semi-infinite medium subjected to a line load vector $\mathbf{p}(x,y,z,\omega)$ at $z=z_n$ and the coordinate system used.

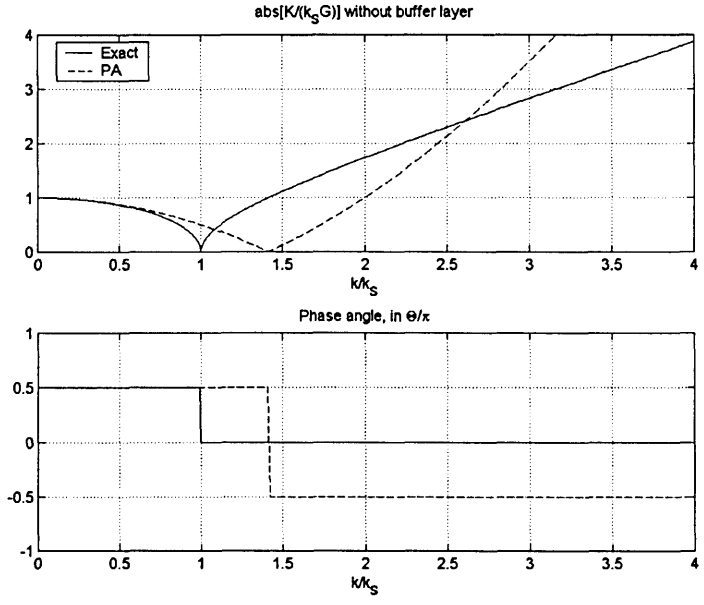

Figure 6.2.2 Comparison of $\mathbf{K}_{EX}$ and $\mathbf{K}_{PA}$ without the buffer layer for *SH* waves (solid line: $\mathbf{K}_{EX}$; dashed line: $\mathbf{K}_{PA}$)

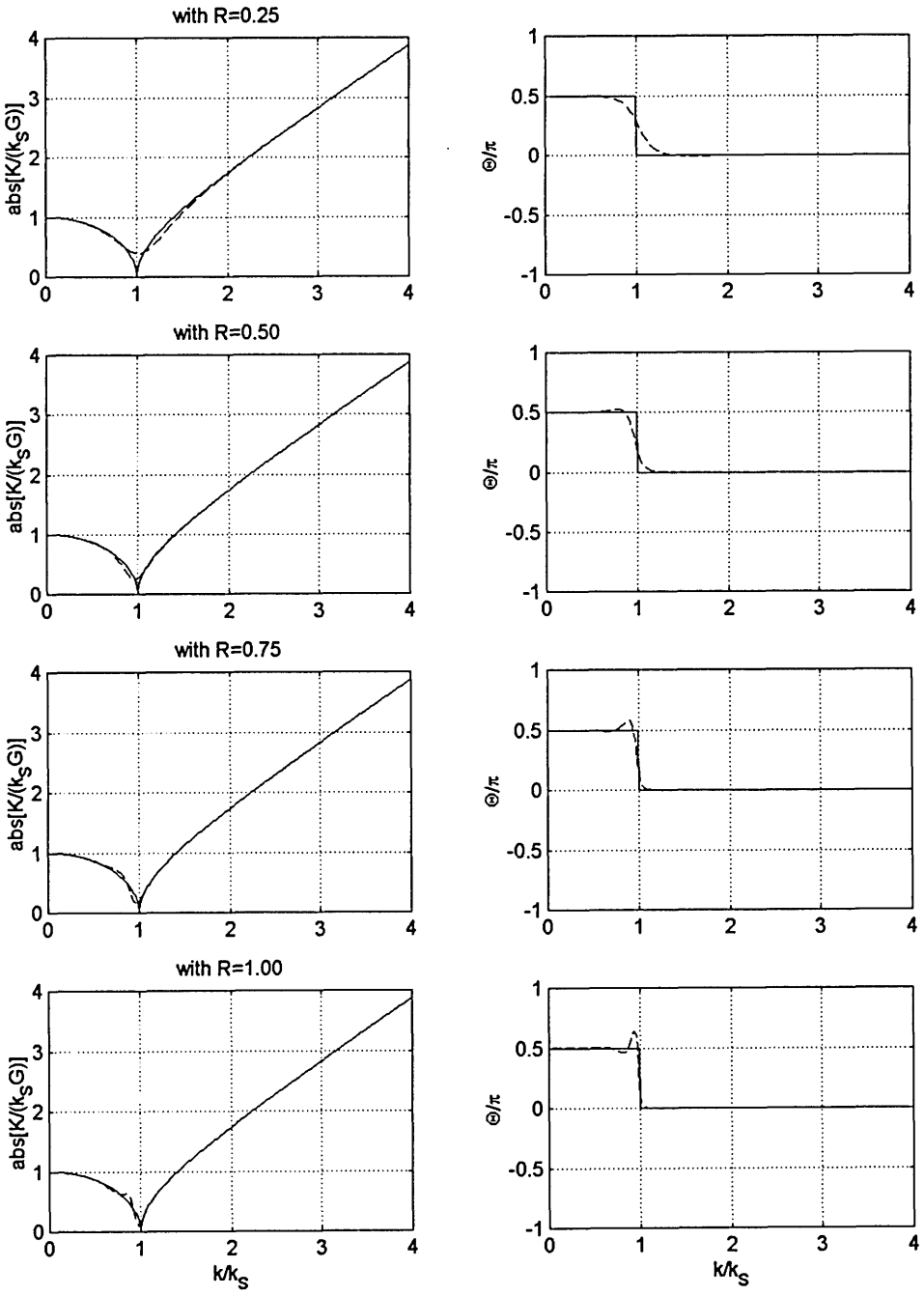

Figure 6.2.3 Comparison of $\mathbf{K}_{EX}$ and $\mathbf{K}_{PB}$ with the buffer layer for *SH* waves (solid line: $\mathbf{K}_{EX}$; dashed line: $\mathbf{K}_{PB}$)

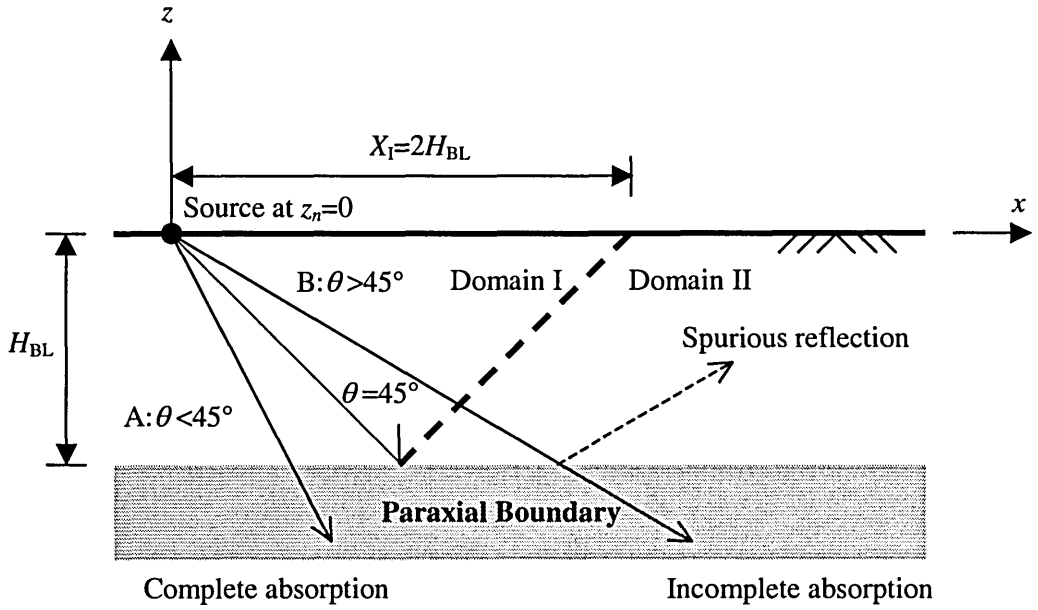

Figure 6.2.4 Stability of the hybrid system $\mathbf{K}_{PB}$ for *SH* waves:
wave A: completely absorbed; wave B: incompletely absorbed
domain I: stable; domain II: unstable

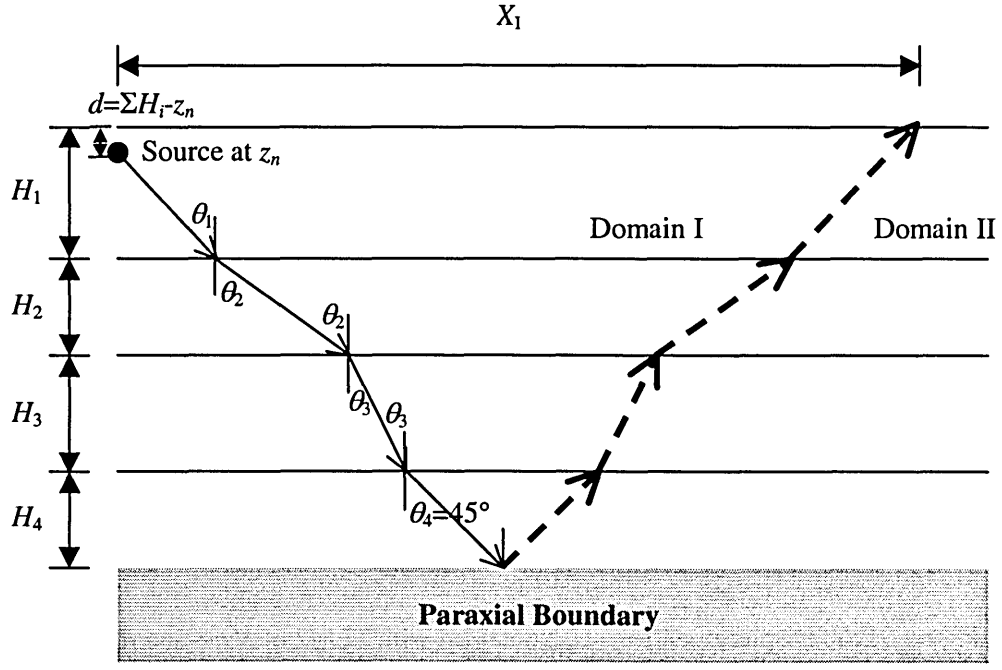

Figure 6.2.5 Theoretical ray paths distinguishing domains I and II,
for an example system composed of 4 layers over the paraxial boundary impedance (*SH* waves)

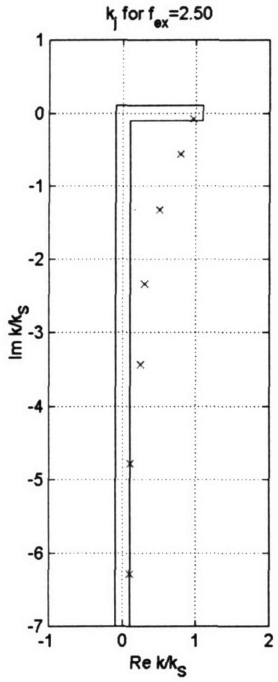

Figure 6.2.6a Eigenvalues k_j (×) obtained with TLM2 of N_λ=8 and R_S=0.5 for a homogeneous half-space (ρ=C_S=1) for f_{ex}=2.5

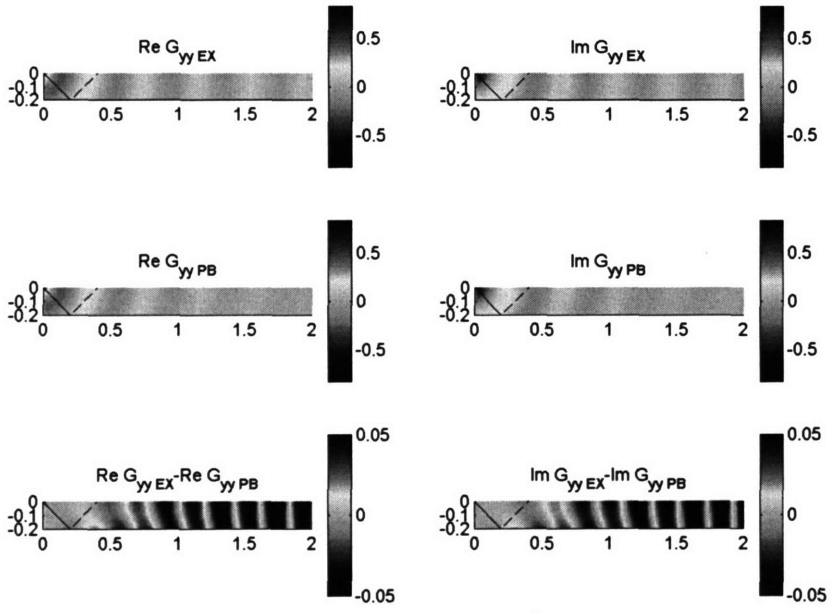

Figure 6.2.6b Displacements v(=G_{yy}) obtained with TLM2 of N_λ=8 and R_S=0.5 in a homogeneous half-space (ρ=C_S=1) subjected to *SH* harmonic surface line load of f_{ex}=2.5 ($G_{yy\,PB}$: TLM2 of N_λ=8 and R_S=0.5; $G_{yy\,EX}$: Exact solution)

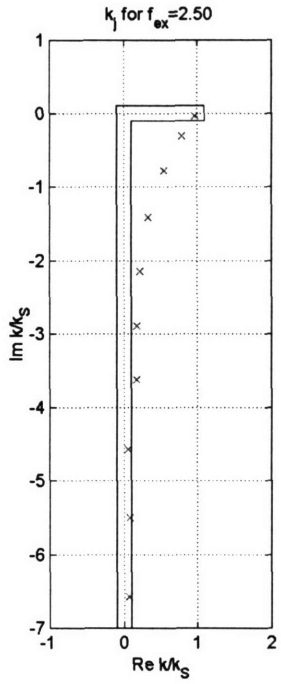

Figure 6.2.7a Eigenvalues k_j (×) obtained with TLM2 of N_λ=8 and R_S=0.75 for a homogeneous half-space (ρ=C_S=1) for f_{ex}=2.5

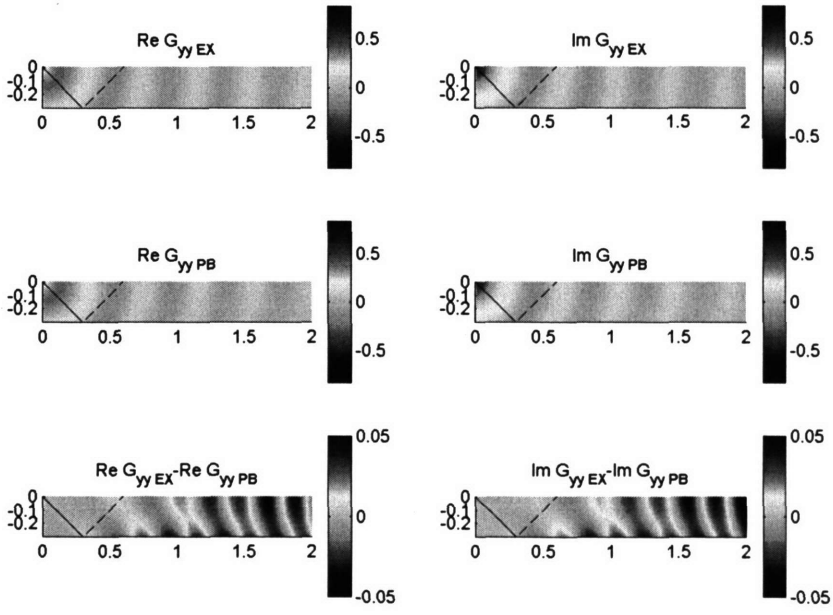

Figure 6.2.7b Displacements v(=G_{yy}) obtained with TLM2 of N_λ=8 and R_S=0.75 in a homogeneous half-space (ρ=C_S=1) subjected to *SH* harmonic surface line load of f_{ex}=2.5 ($G_{yy\,PB}$: TLM2 of N_λ=8 and R_S=0.75; $G_{yy\,EX}$: Exact solution)

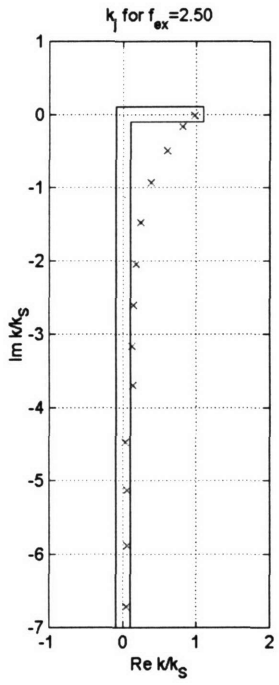

Figure 6.2.8a Eigenvalues k_j (×) obtained with TLM2 of N_λ=8 and R_S=1.0 for a homogeneous half-space (ρ=C_S=1) for f_{ex}=2.5

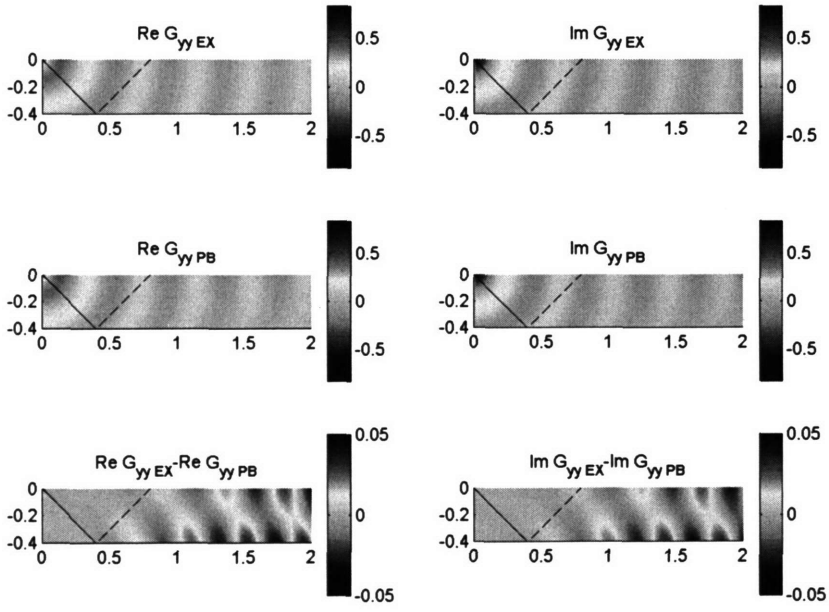

Figure 6.2.8b Displacements v(=G_{yy}) obtained with TLM2 of N_λ=8 and R_S=1.0 in a homogeneous half-space (ρ=C_S=1) subjected to *SH* harmonic surface line load of f_{ex}=2.5 ($G_{yy\,PB}$: TLM2 of N_λ=8 and R_S=1.0; $G_{yy\,EX}$: Exact solution)

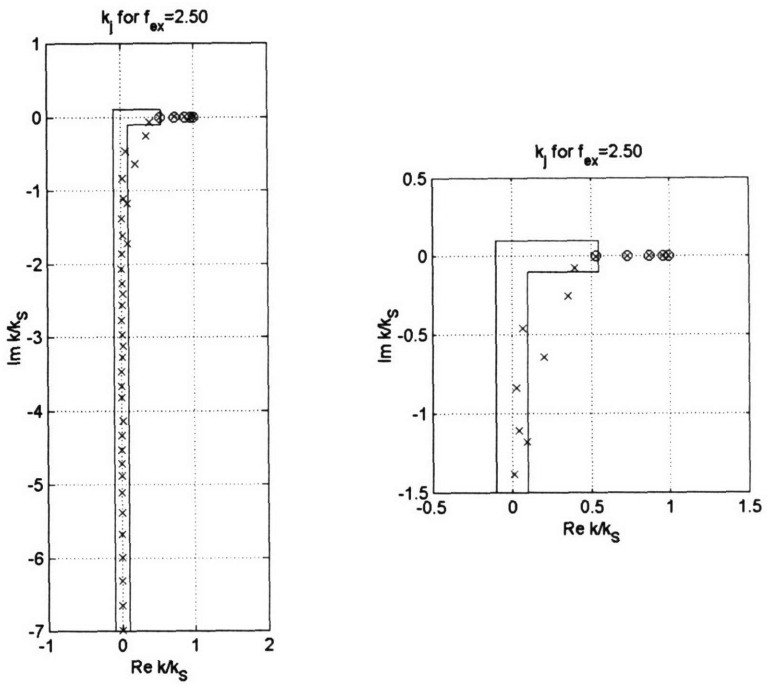

Figure 6.2.9a Eigenvalues k_j (×) obtained with TLM2 of N_λ=8 and R_S=0.50 for a one-layered homogeneous half-space (ρ=C_S=1, H_1=1; ρ_R=1, C_R=2) for f_{ex}=2.5, (o: Exact true propagation mode)

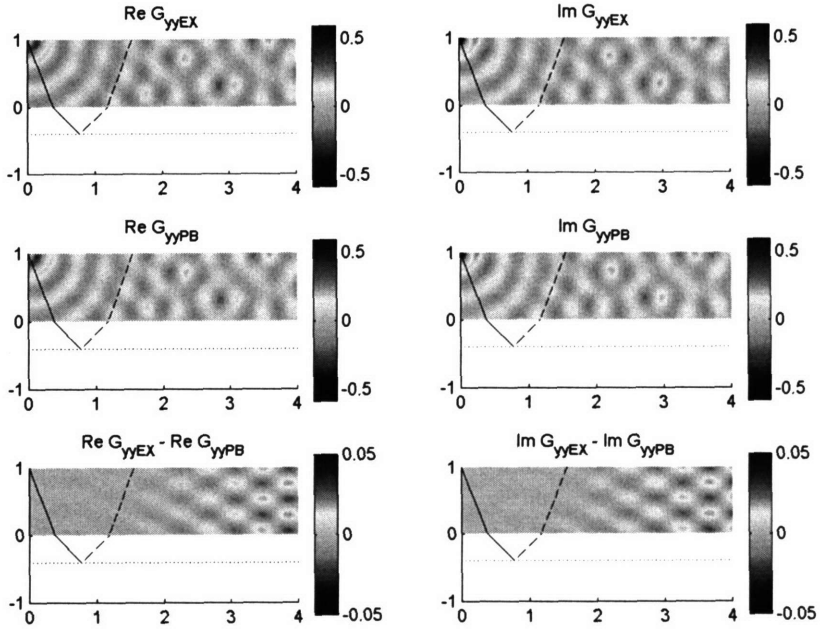

Figure 6.2.9b Displacements v(=G_{yy}) obtained with TLM2 of N_λ=8 and R_S=0.50 in a one-layered homogeneous half-space (ρ=C_S=1, H_1=1; ρ_R=1, C_R=2) subjected to *SH* harmonic surface line load of f_{ex}=2.5 ($G_{yy\,PB}$: TLM2 of N_λ=8 and R_S=0.5; $G_{yy\,EX}$: Exact solution)

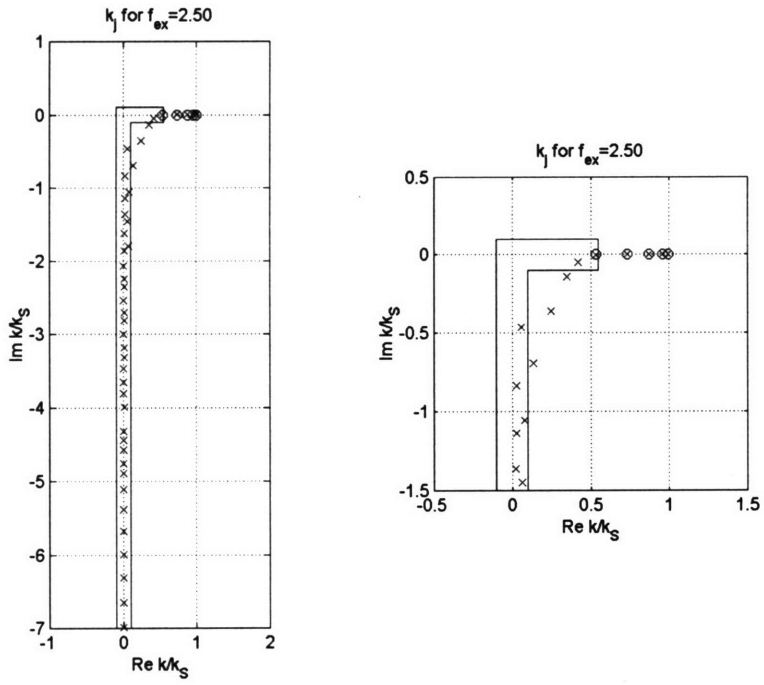

Figure 6.2.10a Eigenvalues k_j (×) obtained with TLM2 of N_λ=8 and R_S=0.75 for a one-layered homogeneous half-space (ρ=C_S=1, H_1=1; ρ_R=1, C_R=2) for f_{ex}=2.5, (o: Exact true propagation mode)

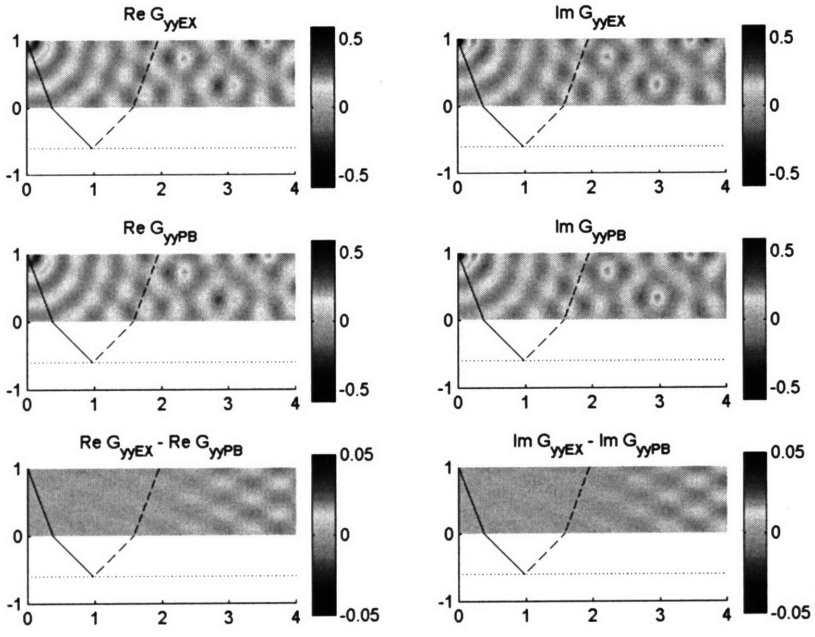

Figure 6.2.10b Displacements v(=G_{yy}) obtained with TLM2 of N_λ=8 and R_S=0.75 in a one-layered homogeneous half-space (ρ=C_S=1, H_1=1; ρ_R=1, C_R=2) subjected to *SH* harmonic surface line load of f_{ex}=2.5 ($G_{yy\,PB}$: TLM2 of N_λ=8 and R_S=0.75; $G_{yy\,EX}$: Exact solution)

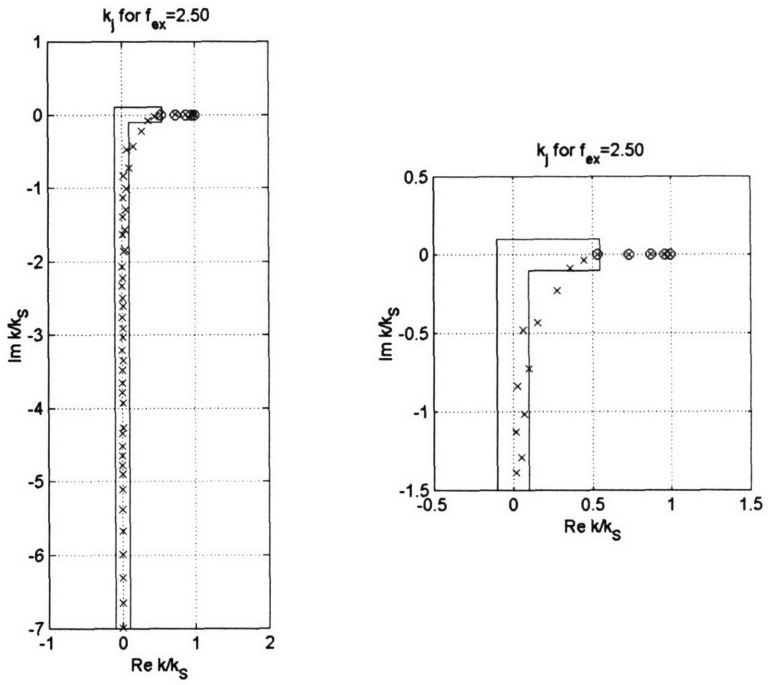

Figure 6.2.11a Eigenvalues k_j (×) obtained with TLM2 of N_λ=8 and R_S=1.0 for a one-layered homogeneous half-space (ρ=C_S=1, H_1=1; ρ_R=1, C_R=2) for f_{ex}=2.5, (o: Exact true propagation mode)

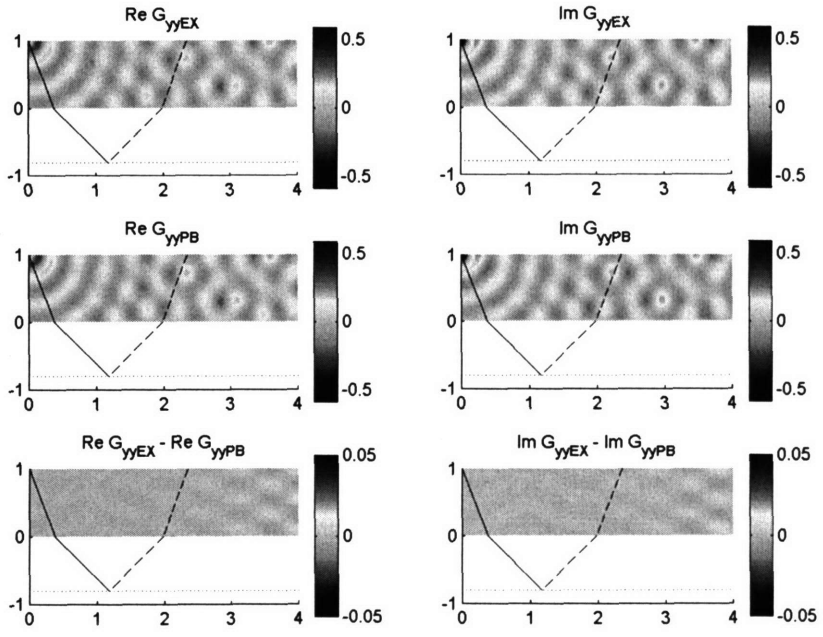

Figure 6.2.11b Displacements v(=G_{yy}) obtained with TLM2 of N_λ=8 and R_S=1.0 in a one-layered homogeneous half-space (ρ=C_S=1, H_1=1; ρ_R=1, C_R=2) subjected to *SH* harmonic surface line load of f_{ex}=2.5 ($G_{yy\,PB}$: TLM2 of N_λ=8 and R_S=1.0; $G_{yy\,EX}$: Exact solution)

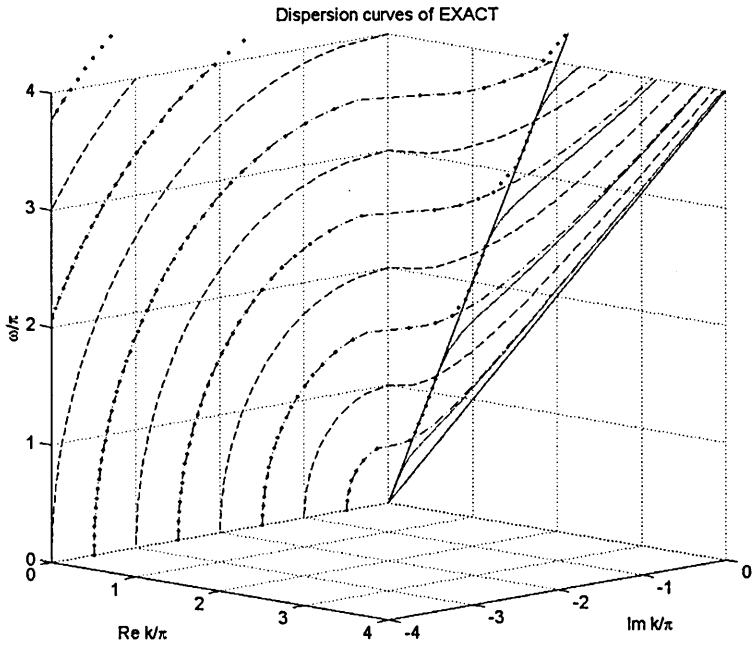

Figure 6.2.12 Dispersion curves of three different problems:
the *Love* wave problem (solid curves), the plate (dashed curves), and the stratum (dotted-dashed curves) and the *pseudo* branches (dots) (all obtained with the exact continuous model)

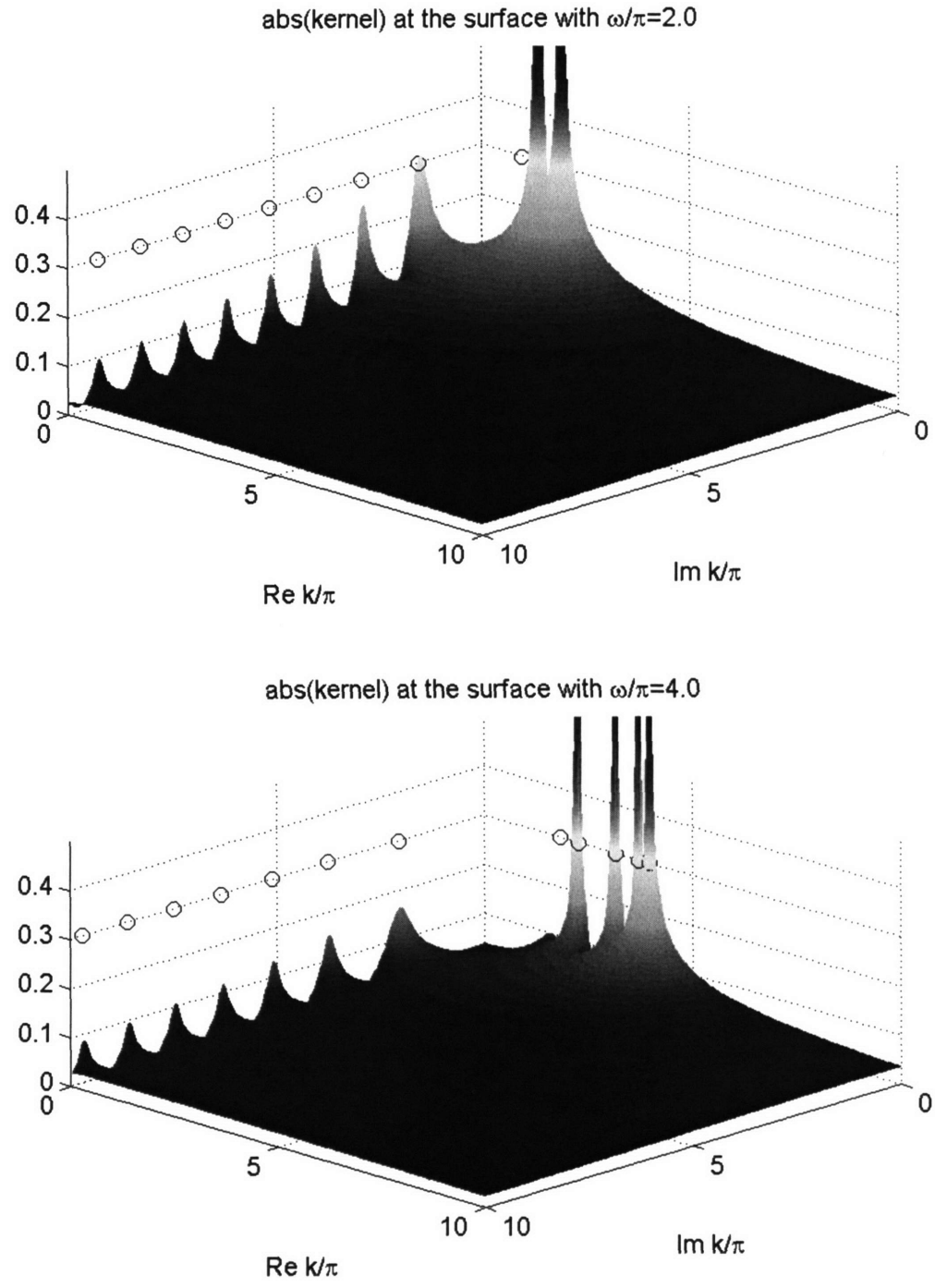

Figure 6.2.13a,b Wavenumber spectra of the absolute values of kernel K_1 in equation (5A.3a) for two frequencies of $\omega=2\pi$, 4π (o: finite and infinite maximum points)

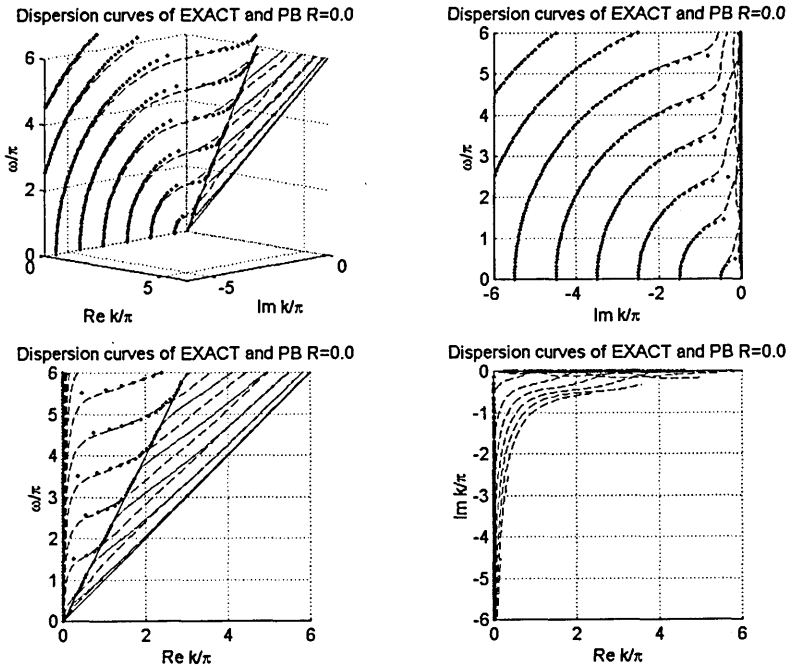

Figure 6.2.14a Dispersion curves for the *Love* wave problem using H_{BL}=0.0
from four different view points
(dashed curves: TLM2 with $\mathbf{K}_{PB}$; solid curves: Exact solutions; dots: *pseudo* pole branches)

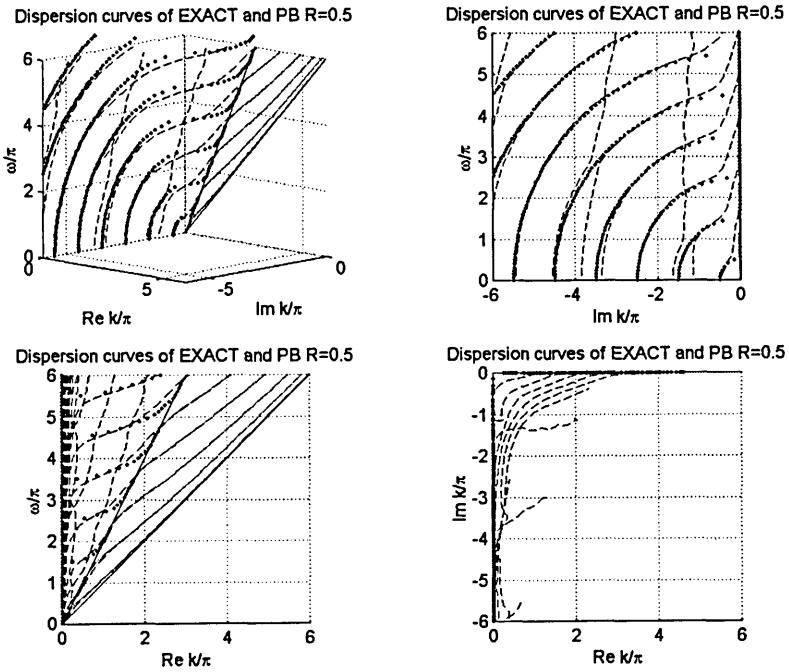

Figure 6.2.14b Dispersion curves for the *Love* wave problem using H_{BL}=0.4
from four different view points
(dashed curves: TLM2 with $\mathbf{K}_{PB}$; solid curves: Exact solutions; dots: *pseudo* pole branches)

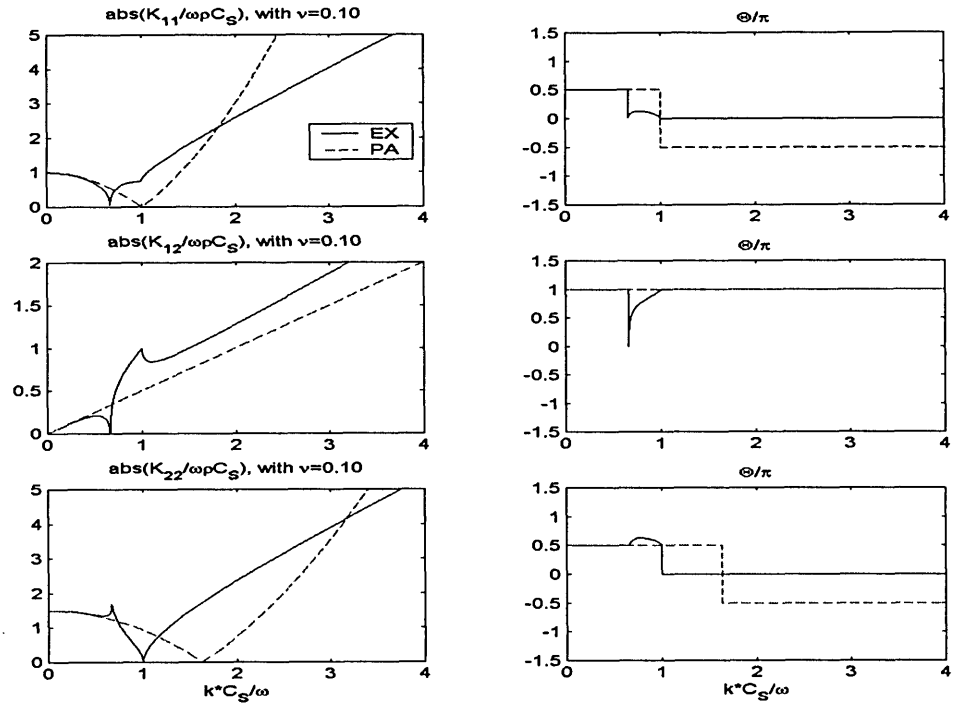

Figure 6.2.15a Comparison of $\mathbf{K}_{EX}$ and $\mathbf{K}_{PA}$ for *SV-P* waves (ν=0.1)
(solid line: $\mathbf{K}_{EX}$; dashed line: $\mathbf{K}_{PA}$)

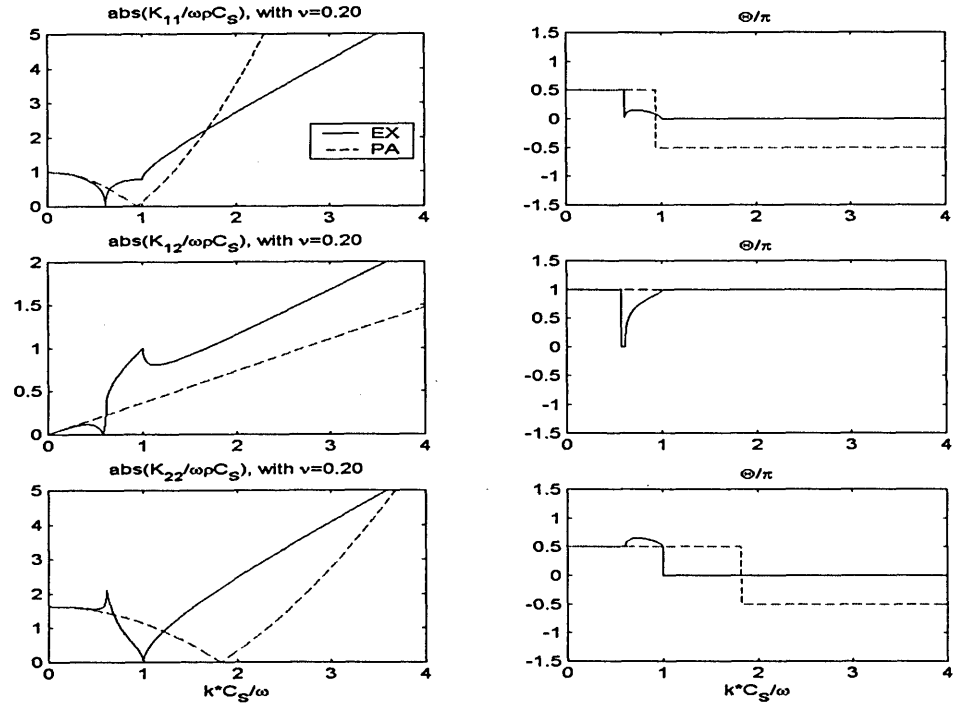

Figure 6.2.15b Comparison of $\mathbf{K}_{EX}$ and $\mathbf{K}_{PA}$ for *SV-P* waves (ν=0.2)
(solid line: $\mathbf{K}_{EX}$; dashed line: $\mathbf{K}_{PA}$)

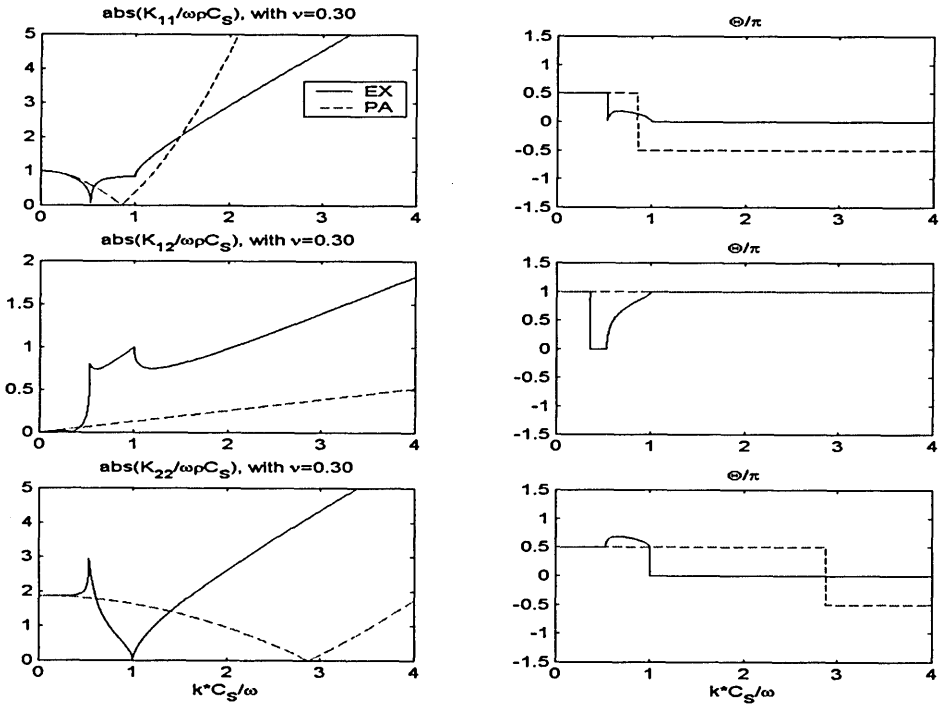

Figure 6.2.15c Comparison of $\mathbf{K}_{EX}$ and $\mathbf{K}_{PA}$ for *SV-P* waves (ν=0.3)
(solid line: $\mathbf{K}_{EX}$; dashed line: $\mathbf{K}_{PA}$)

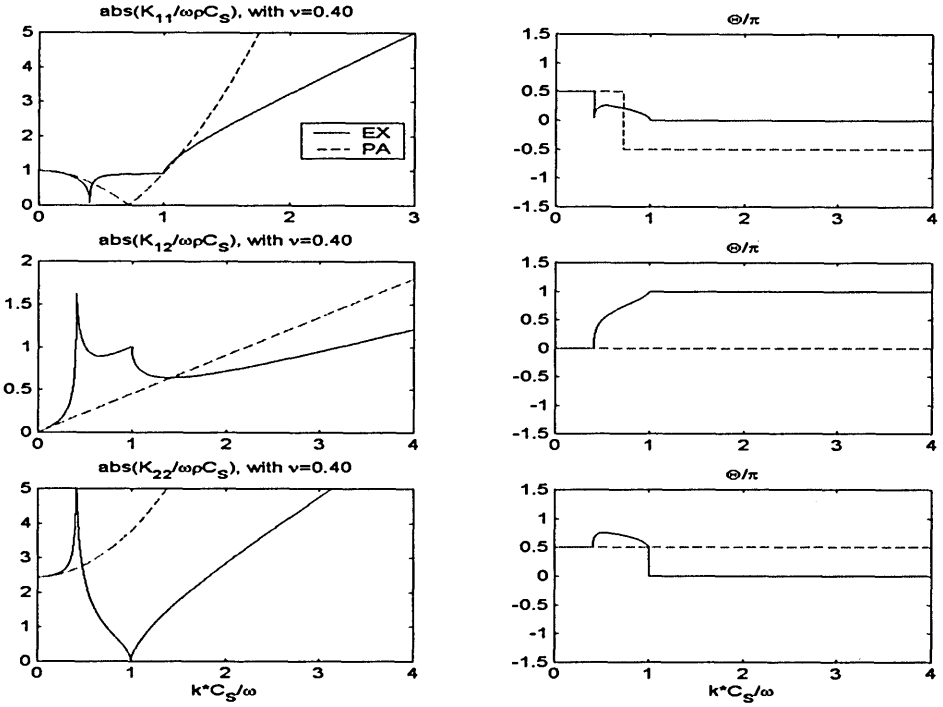

Figure 6.2.15d Comparison of $\mathbf{K}_{EX}$ and $\mathbf{K}_{PA}$ for *SV-P* waves (ν=0.4)
(solid line: $\mathbf{K}_{EX}$; dashed line: $\mathbf{K}_{PA}$)

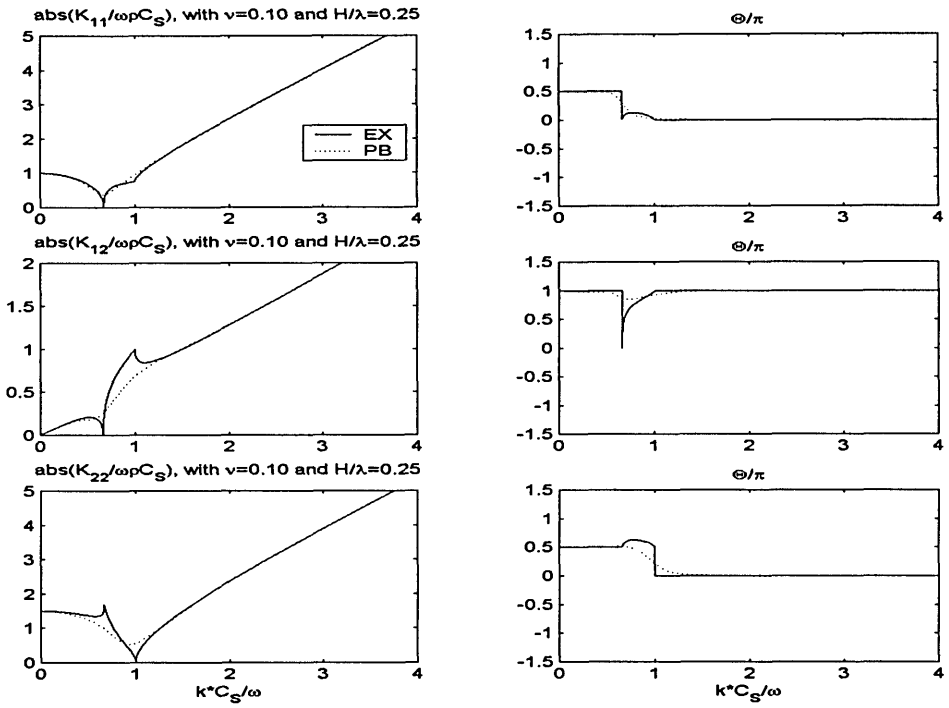

Figure 6.2.16a Comparison of $\mathbf{K}_{EX}$ and $\mathbf{K}_{PB}$ with R_P=0.25 for *SV-P* waves (ν=0.1) (solid line: $\mathbf{K}_{EX}$; dashed line: $\mathbf{K}_{PA}$)

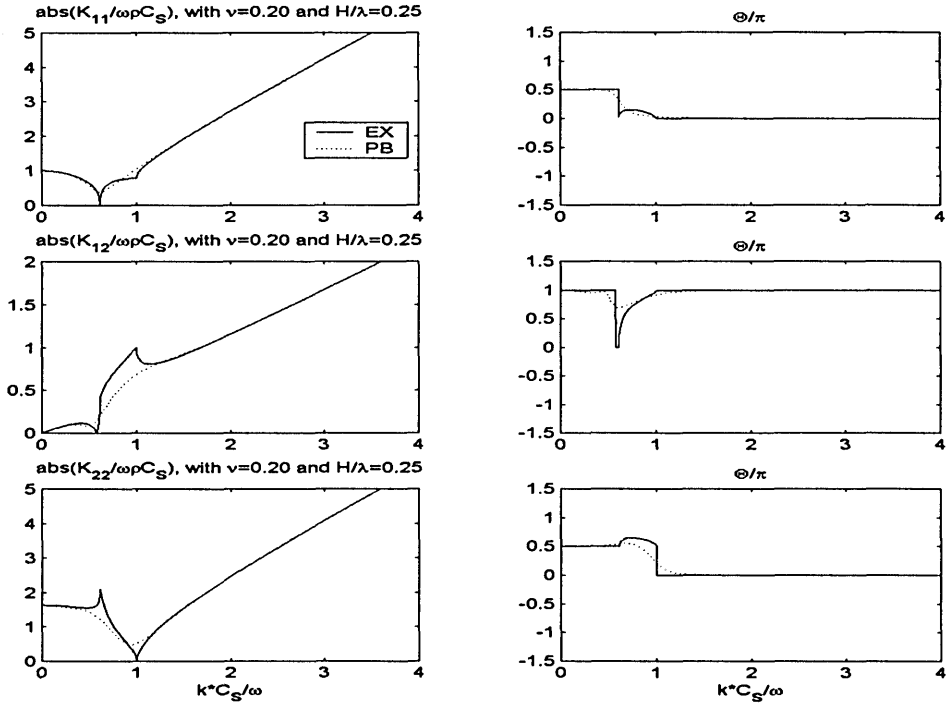

Figure 6.2.16b Comparison of $\mathbf{K}_{EX}$ and $\mathbf{K}_{PB}$ with R_P=0.25 for *SV-P* waves (ν=0.2) (solid line: $\mathbf{K}_{EX}$; dashed line: $\mathbf{K}_{PA}$)

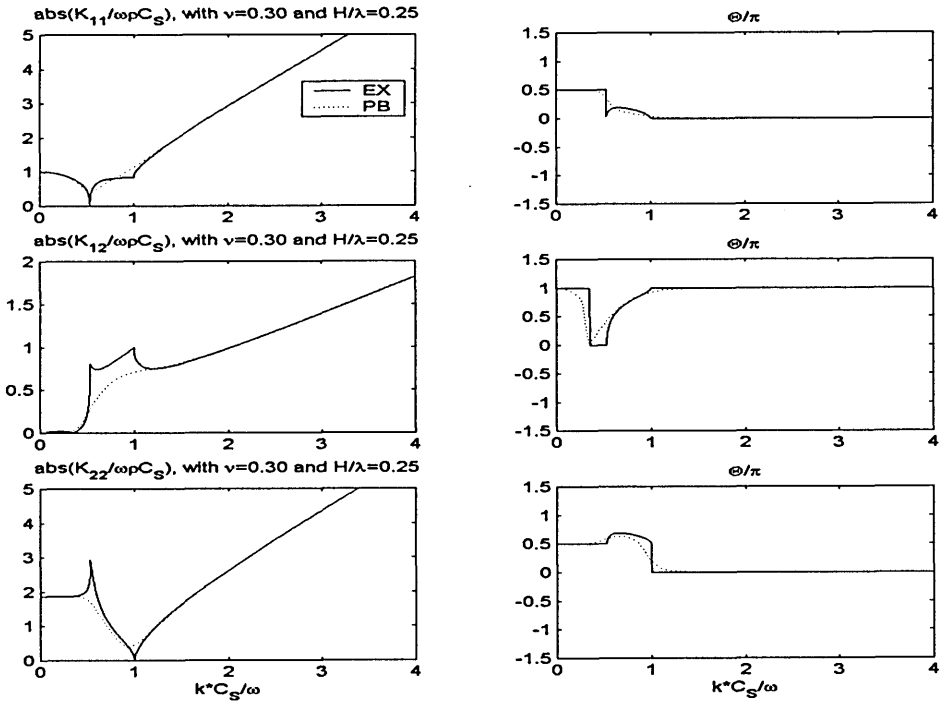

Figure 6.2.16c Comparison of $\mathbf{K}_{EX}$ and $\mathbf{K}_{PB}$ with R_P=0.25 for *SV-P* waves (ν=0.3) (solid line: $\mathbf{K}_{EX}$; dashed line: $\mathbf{K}_{PA}$)

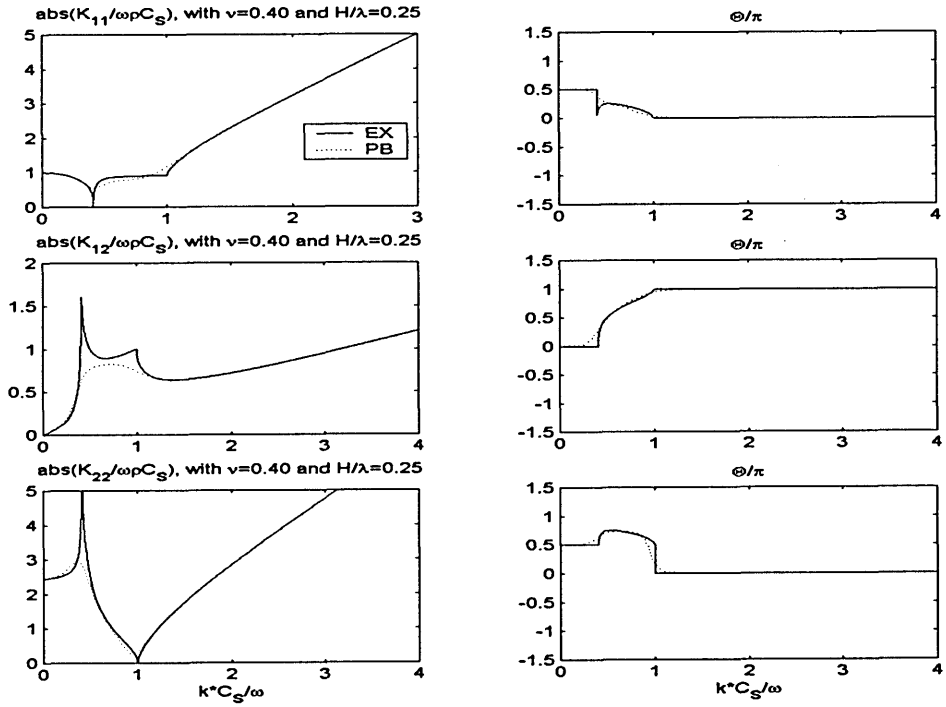

Figure 6.2.16d Comparison of $\mathbf{K}_{EX}$ and $\mathbf{K}_{PB}$ with R_P=0.25 for *SV-P* waves (ν=0.4) (solid line: $\mathbf{K}_{EX}$; dashed line: $\mathbf{K}_{PA}$)

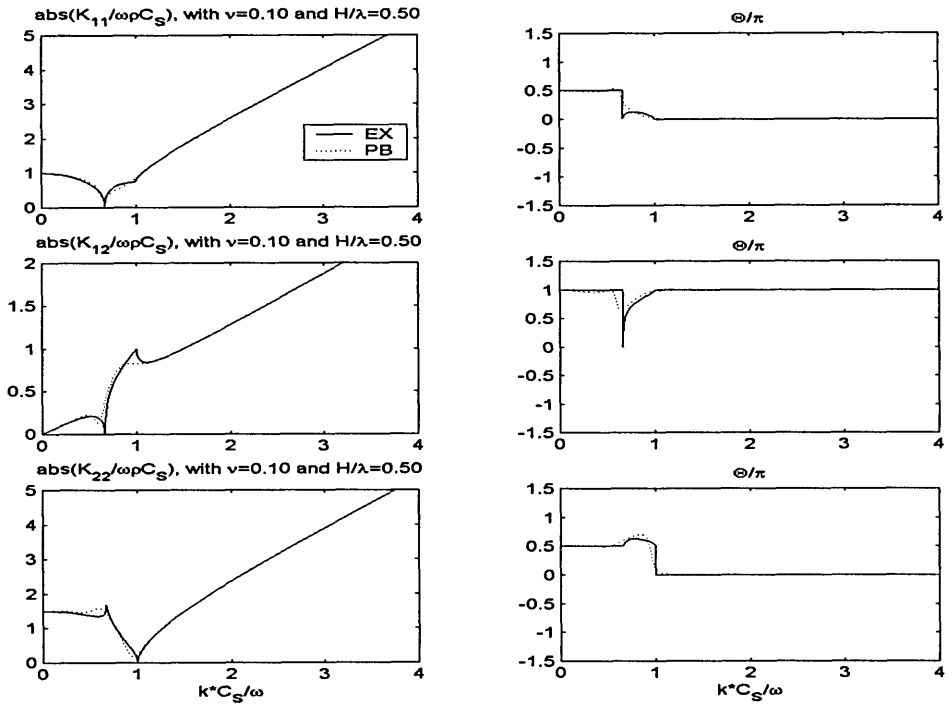

Figure 6.2.17a Comparison of $\mathbf{K}_{EX}$ and $\mathbf{K}_{PB}$ with R_P=0.50 for *SV-P* waves (ν=0.1) (solid line: $\mathbf{K}_{EX}$; dashed line: $\mathbf{K}_{PA}$)

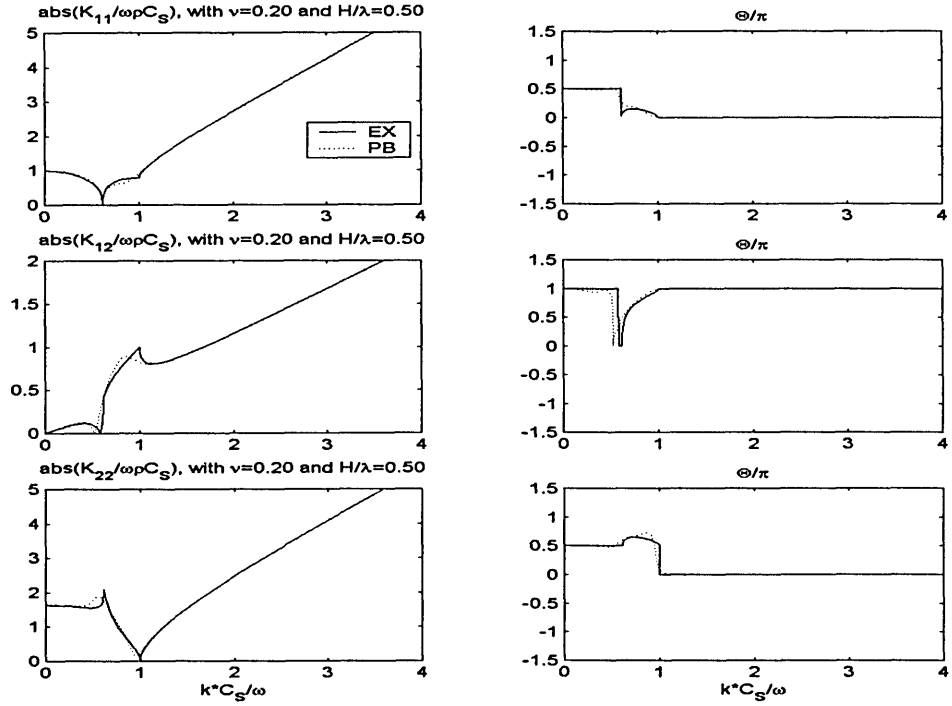

Figure 6.2.17b Comparison of $\mathbf{K}_{EX}$ and $\mathbf{K}_{PB}$ with R_P=0.50 for *SV-P* waves (ν=0.2) (solid line: $\mathbf{K}_{EX}$; dashed line: $\mathbf{K}_{PA}$)

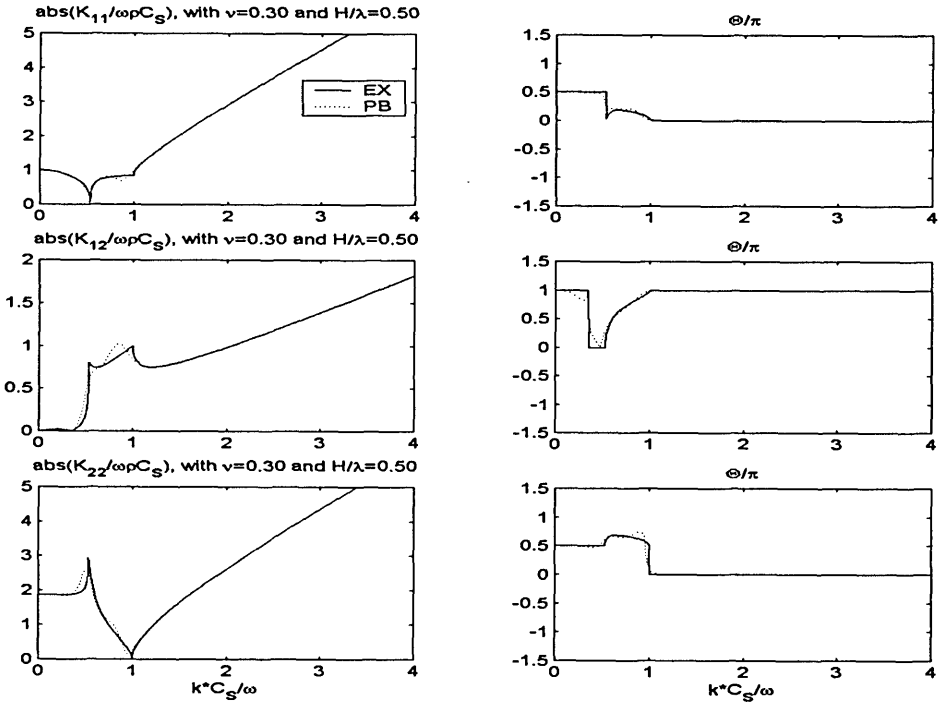

Figure 6.2.17c Comparison of $\mathbf{K}_{EX}$ and $\mathbf{K}_{PB}$ with R_P=0.50 for *SV-P* waves (ν=0.3) (solid line: $\mathbf{K}_{EX}$; dashed line: $\mathbf{K}_{PA}$)

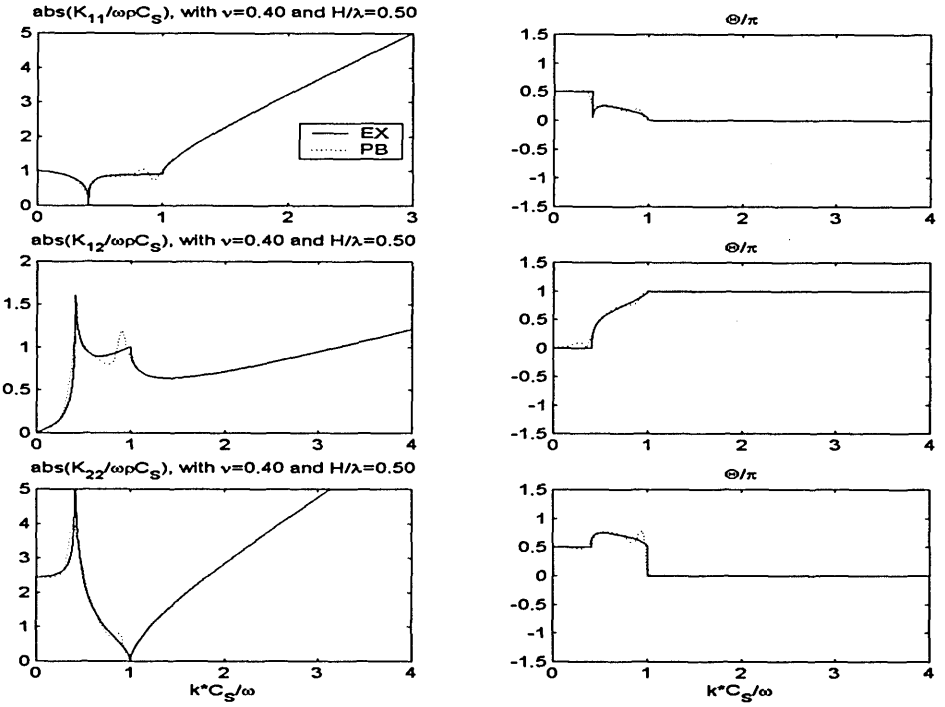

Figure 6.2.17d Comparison of $\mathbf{K}_{EX}$ and $\mathbf{K}_{PB}$ with R_P=0.50 for *SV-P* waves (ν=0.4) (solid line: $\mathbf{K}_{EX}$; dashed line: $\mathbf{K}_{PA}$)

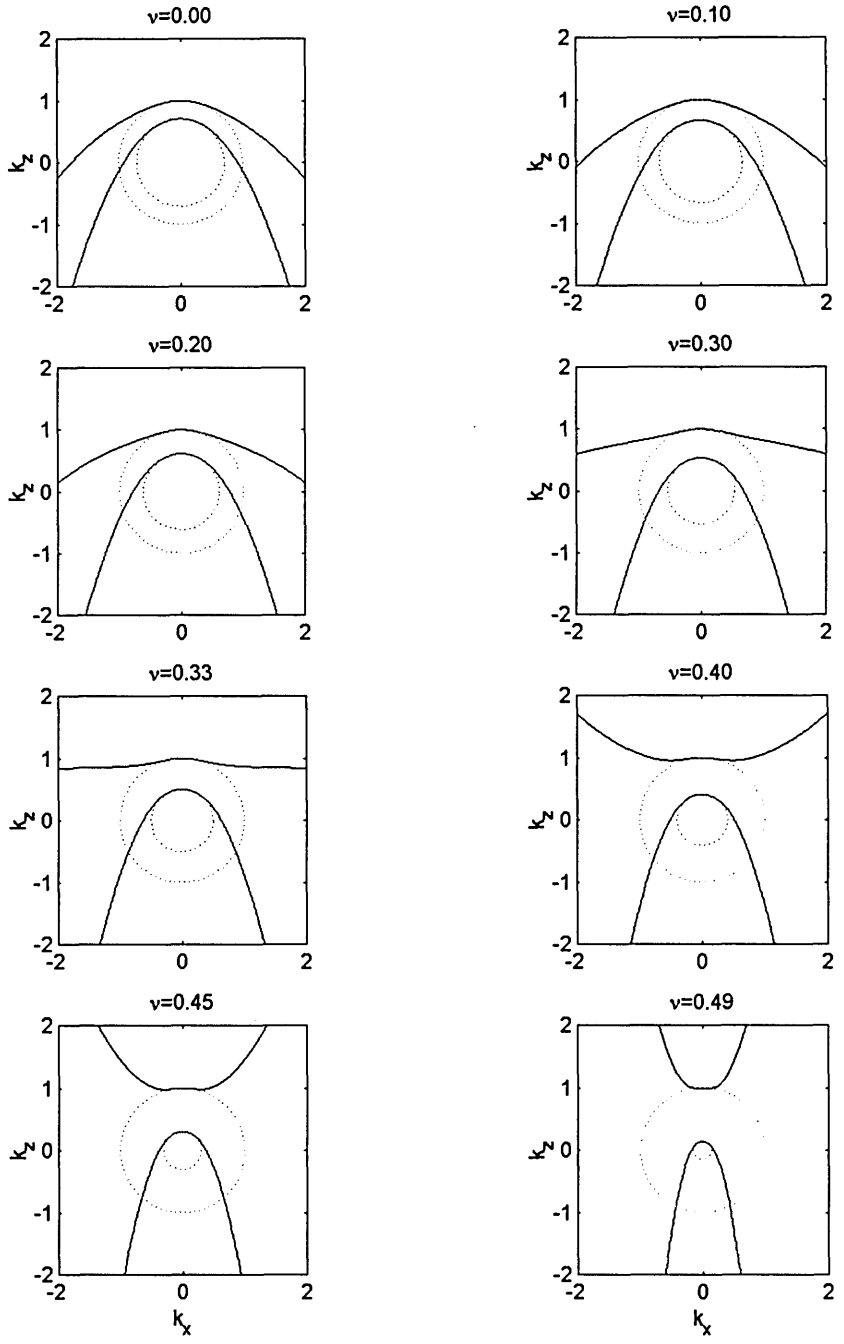

Figure 6.2.18 Dispersion curves of *S* and *P* body waves with original $\mathbf{K}_{PA}$ (solid lines: original $\mathbf{K}_{PA}$; dashed lines: Exact solutions)

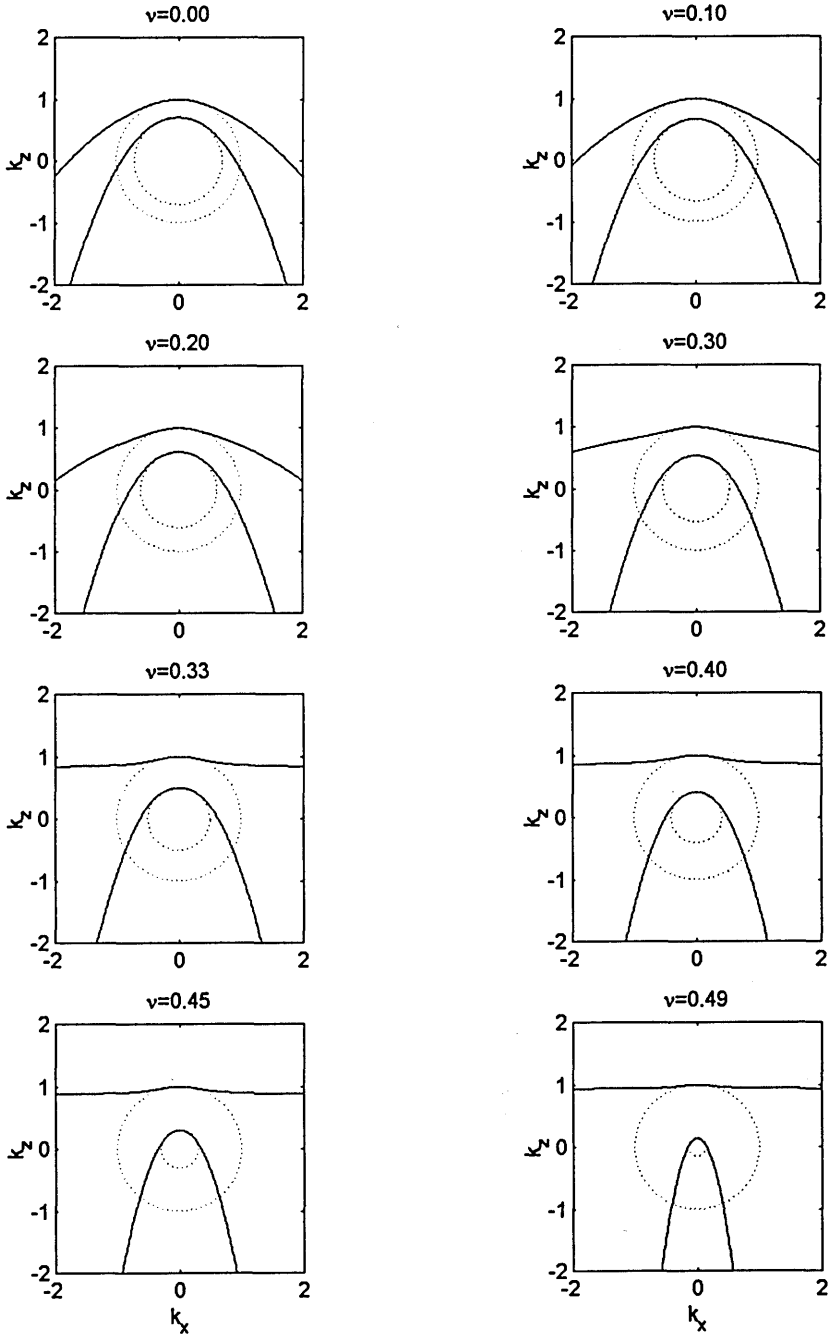

Figure 6.2.19 Dispersion curves of *S* and *P* body waves with modified $\mathbf{K}_{PA}$ (solid lines: modified $\mathbf{K}_{PA}$; dashed lines: Exact solutions)

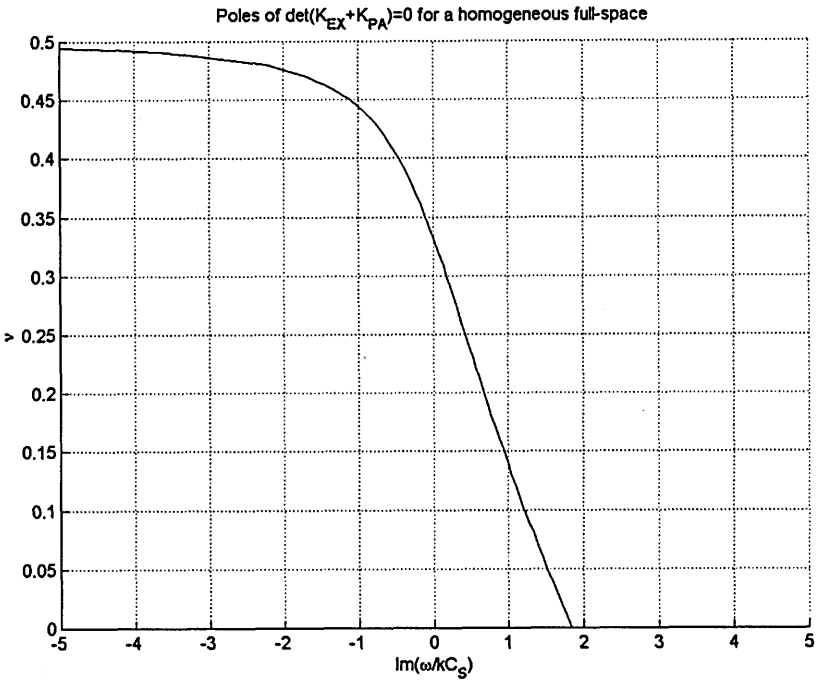

Figure 6.2.20 Root of det($\mathbf{K}_{EX}$+$\mathbf{K}_{PA}$)=0 (C_{S+}= C_{S-}) using original $\mathbf{K}_{PA}$

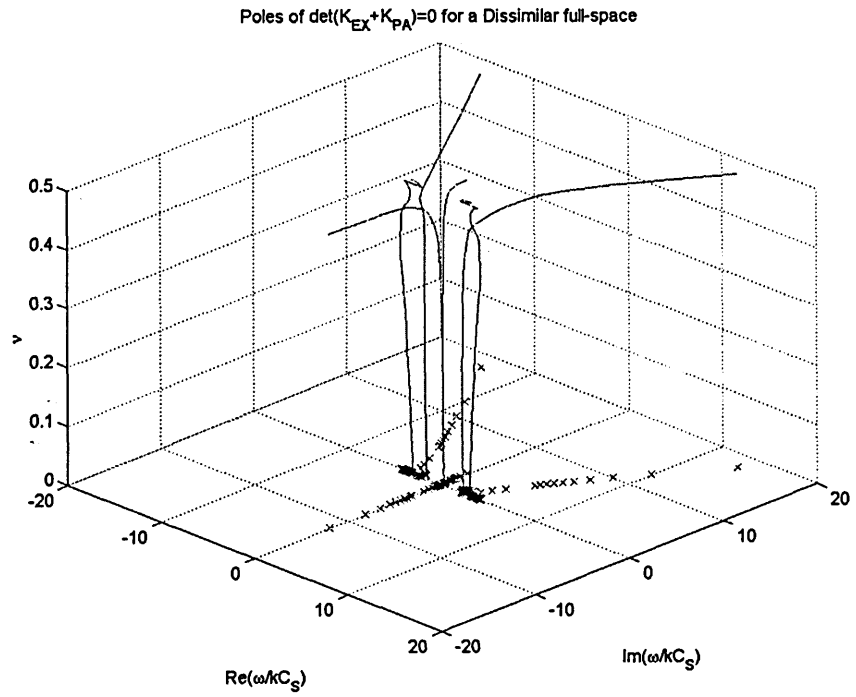

Figure 6.2.21a Propagation modes of det($\mathbf{K}_{EX}$+$\mathbf{K}_{PA}$)=0 (C_{S+}=2C_{S-}) using original $\mathbf{K}_{PA}$

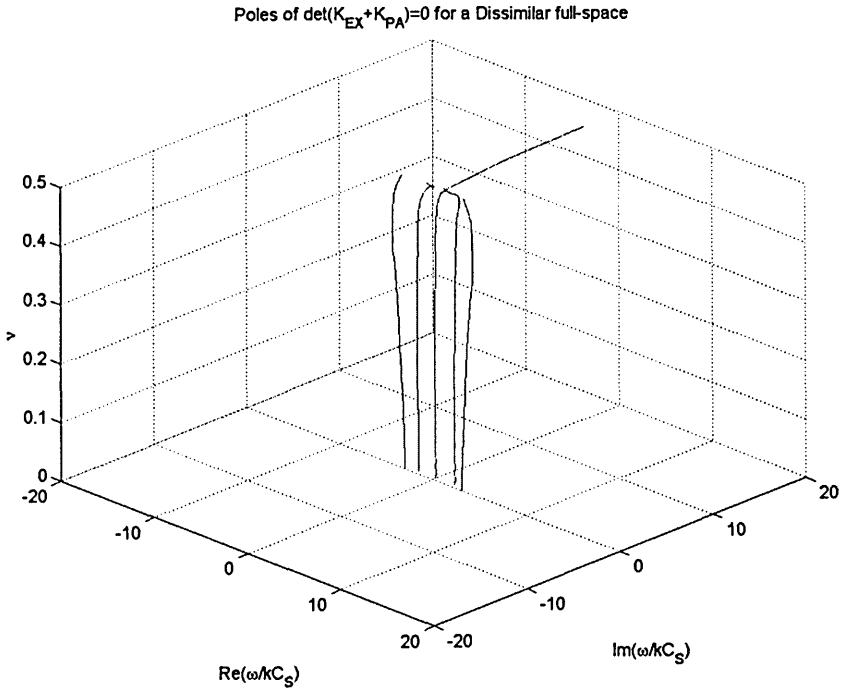

Figure 6.2.21b Propagation modes of det($\mathbf{K}_{EX}$+$\mathbf{K}_{PA}$)=0 (C_{S+}=2C_{S-}) using modified $\mathbf{K}_{PA}$

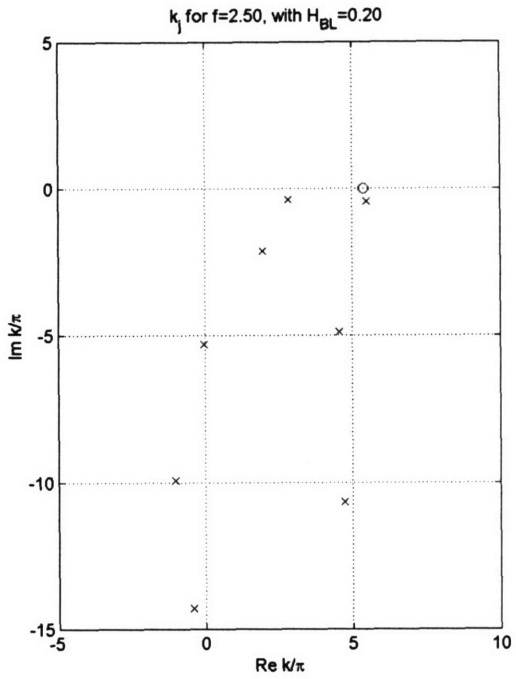

Figure 6.2.22a Eigenvalues k_j (×) obtained with TLM2 of N_λ=8 and R_P=0.25
for a homogeneous half-space (ρ=C_S=1, ν=0.3) for f_{ex}=2.5, (o: Exact Rayleigh pole k_R)

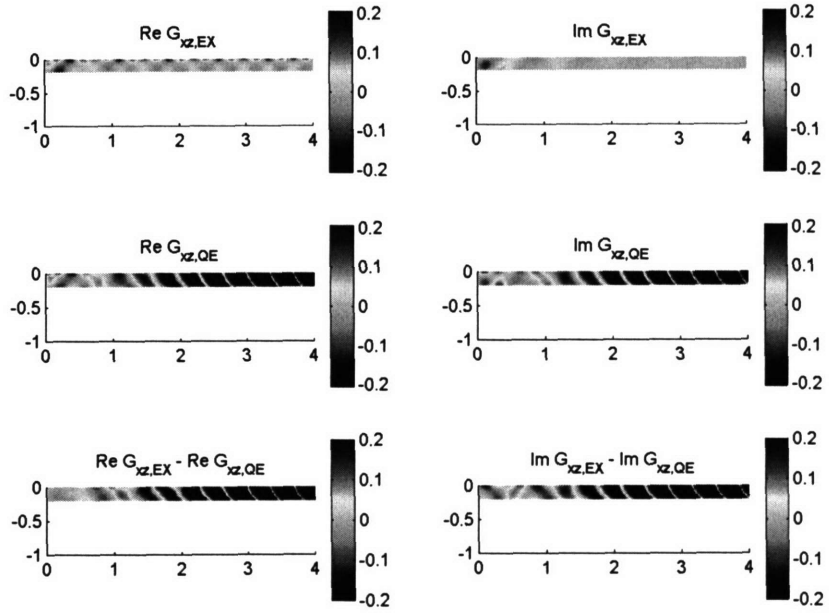

Figure 6.2.22b Displacements u_{xz}(=G_{xz}) obtained with TLM2 of N_λ=8 and R_P=0.25
in a homogeneous half-space (ρ=C_S=1, ν=0.3)
subjected to harmonic vertical line load of f_{ex}=2.5 applied at the top surface
($G_{xz\ QE}$: TLM2 of N_λ=8 and R_P=0.25; $G_{xz\ EX}$: Exact solution)

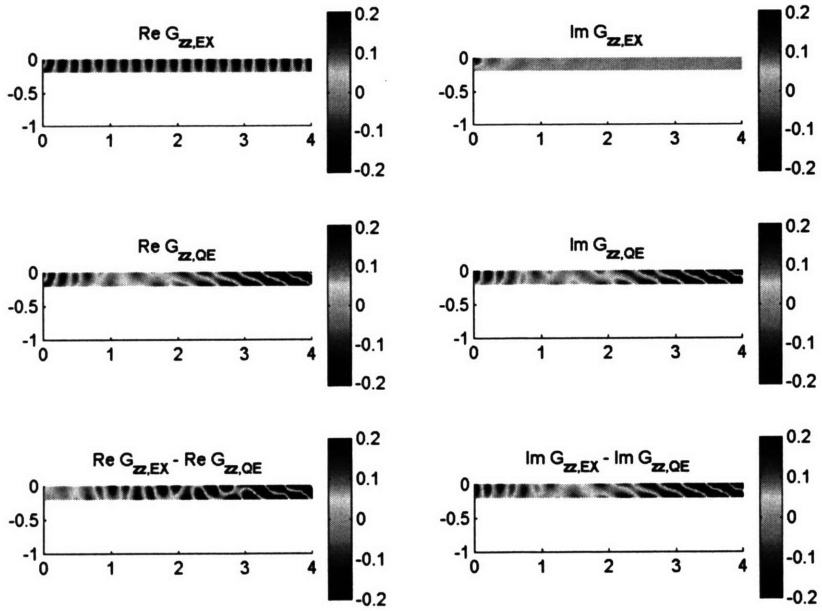

Figure 6.2.22c Displacements $u_{zz}(=G_{zz})$ obtained with TLM2 of N_λ=8 and R_P=0.25 in a homogeneous half-space (ρ=C_S=1, ν=0.3) subjected to harmonic vertical line load of f_{ex}=2.5 applied at the top surface ($G_{xz\,QE}$: TLM2 of N_λ=8 and R_P=0.25; $G_{xz\,EX}$: Exact solution)

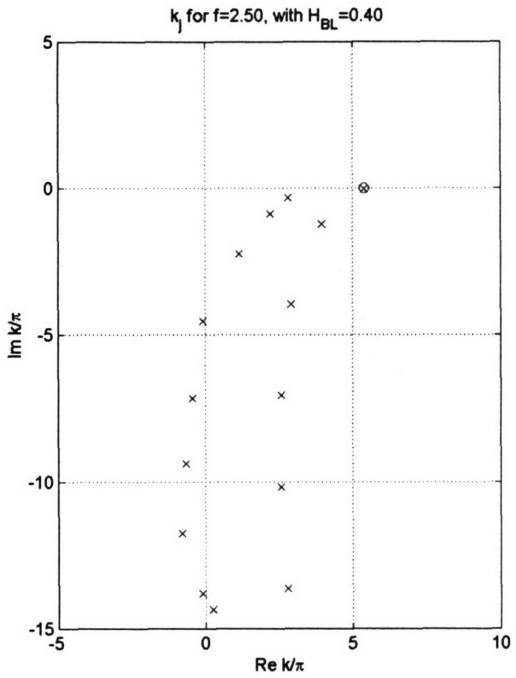

Figure 6.2.23a Eigenvalues k_j (×) obtained with TLM2 of N_λ=8 and R_P=0.50
for a homogeneous half-space (ρ=C_S=1, ν=0.3) for f_{ex}=2.5, (o: Exact Rayleigh pole k_R)

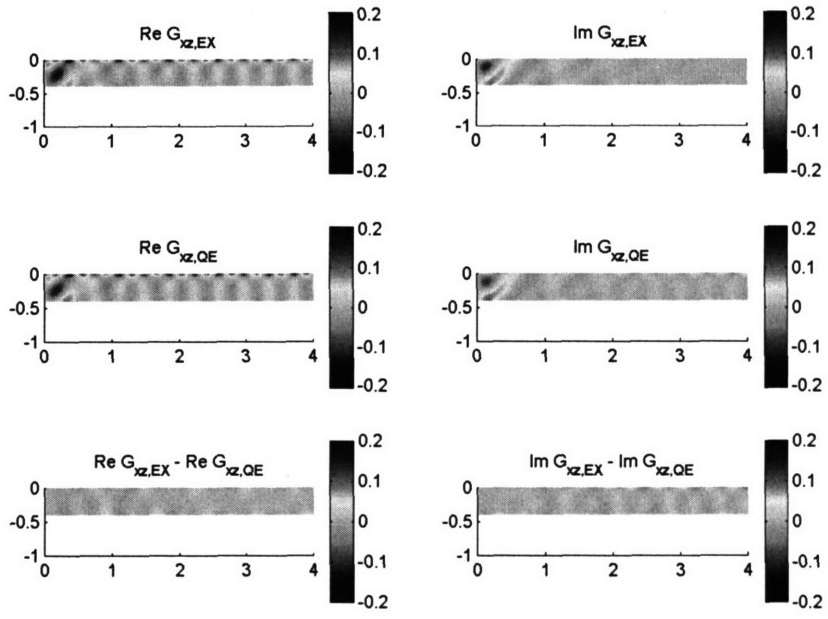

Figure 6.2.23b Displacements u_{xz}(=G_{xz}) obtained with TLM2 of N_λ=8 and R_P=0.50
in a homogeneous half-space (ρ=C_S=1, ν=0.3)
subjected to harmonic vertical line load of f_{ex}=2.5 applied at the top surface
($G_{xz\,QE}$: TLM2 of N_λ=8 and R_P=0.50; $G_{xz\,EX}$: Exact solution)

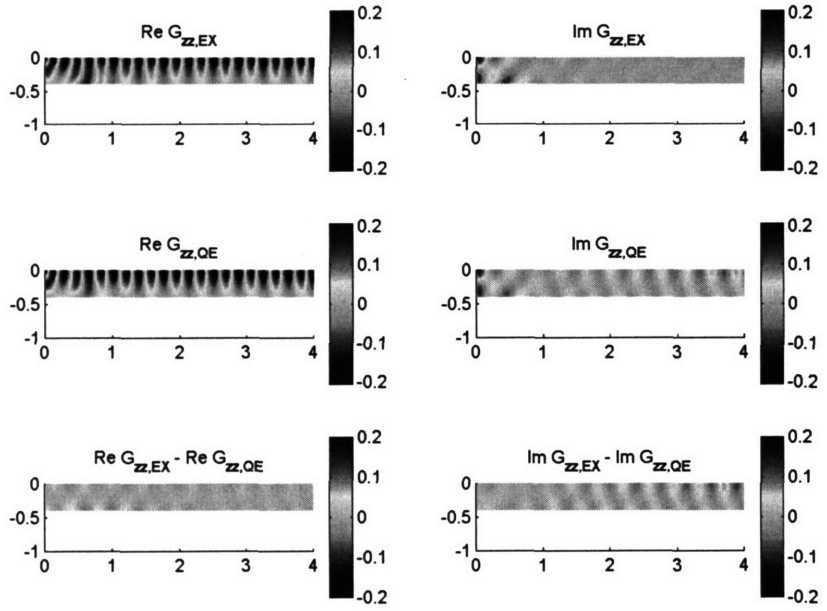

Figure 6.2.23c Displacements $u_{zz}(=G_{zz})$ obtained with TLM2 of N_λ=8 and R_P=0.50 in a homogeneous half-space (ρ=C_S=1, ν=0.3) subjected to harmonic vertical line load of f_{ex}=2.5 applied at the top surface ($G_{xz\,QE}$: TLM2 of N_λ=8 and R_P=0.50; $G_{xz\,EX}$: Exact solution)

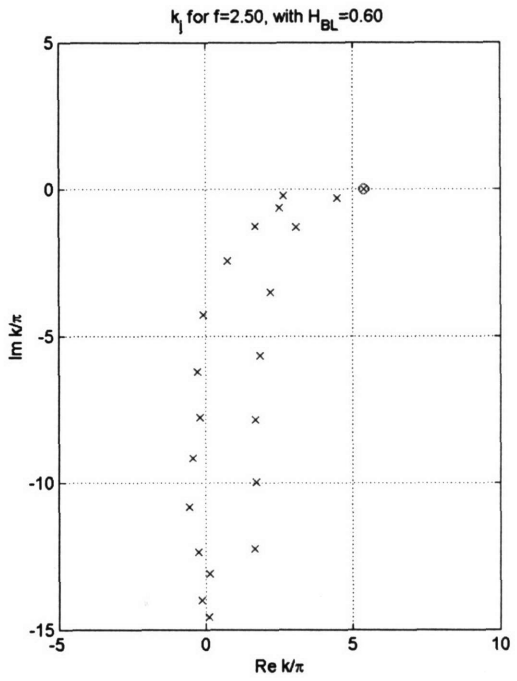

Figure 6.2.24a Eigenvalues k_j (×) obtained with TLM2 of N_λ=8 and R_P=0.75
for a homogeneous half-space (ρ=C_S=1, ν=0.3) for f_{ex}=2.5, (o: Exact Rayleigh pole k_R)

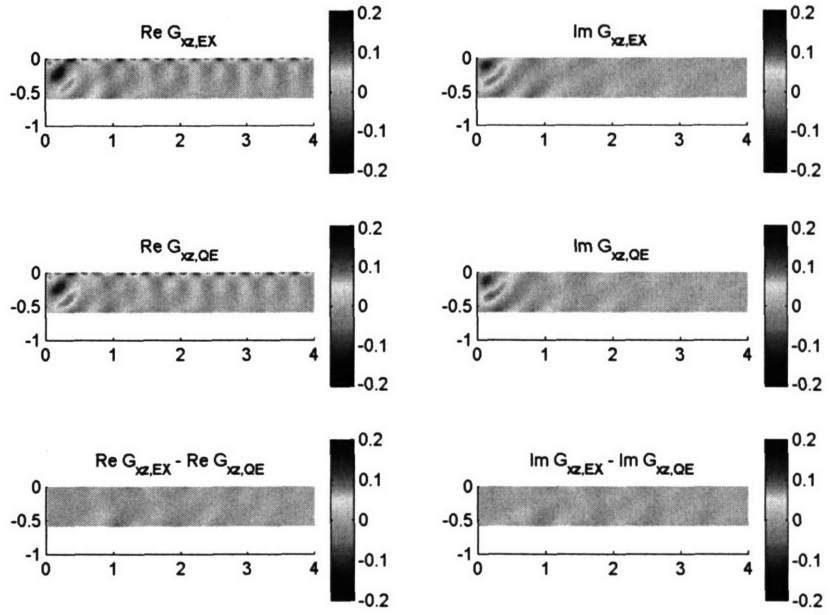

Figure 6.2.24b Displacements u_{xz}(=G_{xz}) obtained with TLM2 of N_λ=8 and R_P=0.75
in a homogeneous half-space (ρ=C_S=1, ν=0.3)
subjected to harmonic vertical line load of f_{ex}=2.5 applied at the top surface
($G_{xz\,QE}$: TLM2 of N_λ=8 and R_P=0.75; $G_{xz\,EX}$: Exact solution)

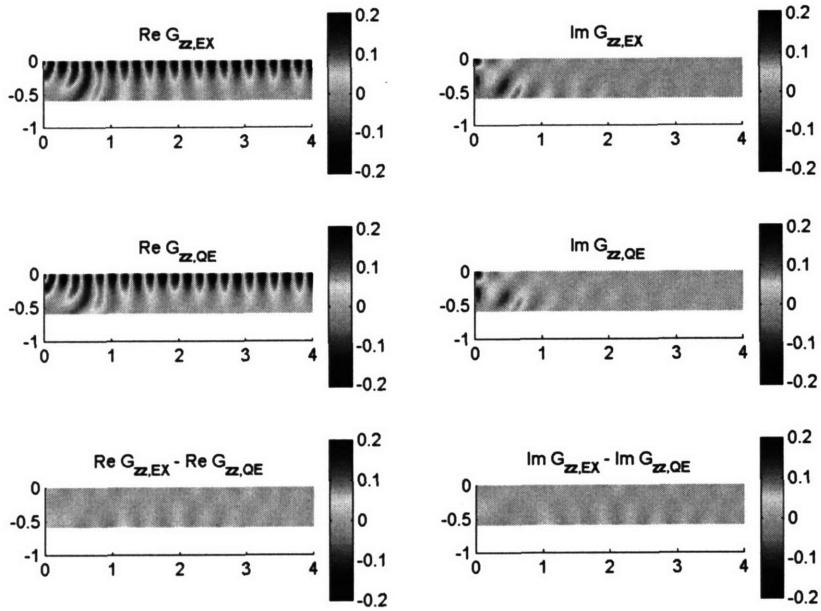

Figure 6.2.24c Displacements $u_{zz}(=G_{zz})$ obtained with TLM2 of N_λ=8 and R_P=0.75
in a homogeneous half-space (ρ=C_S=1, ν=0.3)
subjected to harmonic vertical line load of f_{ex}=2.5 applied at the top surface
($G_{xz\,QE}$: TLM2 of N_λ=8 and R_P=0.75; $G_{xz\,EX}$: Exact solution)

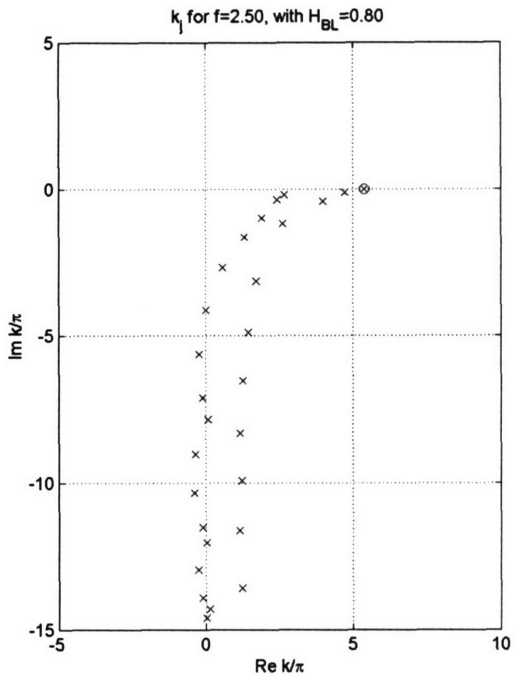

Figure 6.2.25a Eigenvalues k_j (×) obtained with TLM2 of N_λ=8 and R_P=1.0
for a homogeneous half-space (ρ=C_S=1, ν=0.3) for f_{ex}=2.5, (o: Exact Rayleigh pole k_R)

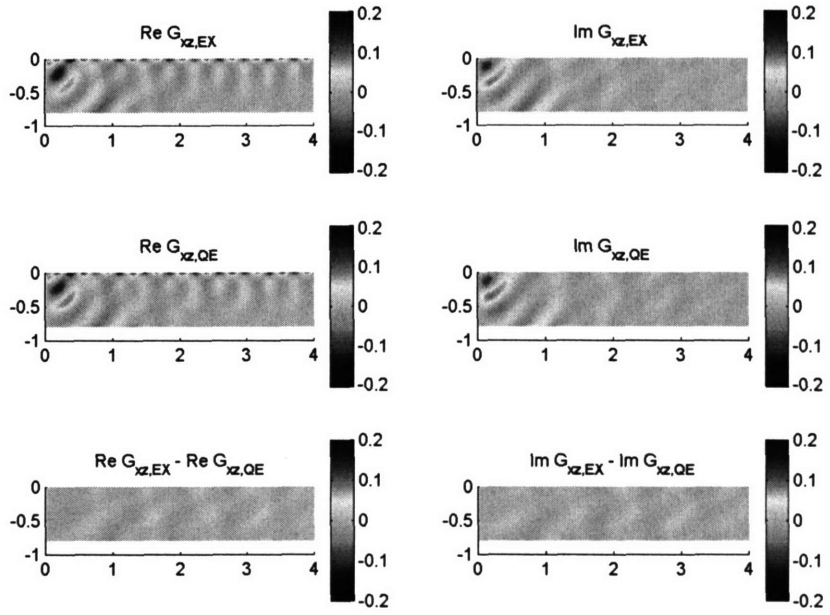

Figure 6.2.25b Displacements u_{xz}(=G_{xz}) obtained with TLM2 of N_λ=8 and R_P=1.0
in a homogeneous half-space (ρ=C_S=1, ν=0.3)
subjected to harmonic vertical line load of f_{ex}=2.5 applied at the top surface
($G_{xz\ QE}$: TLM2 of N_λ=8 and R_P=1.0; $G_{xz\ EX}$: Exact solution)

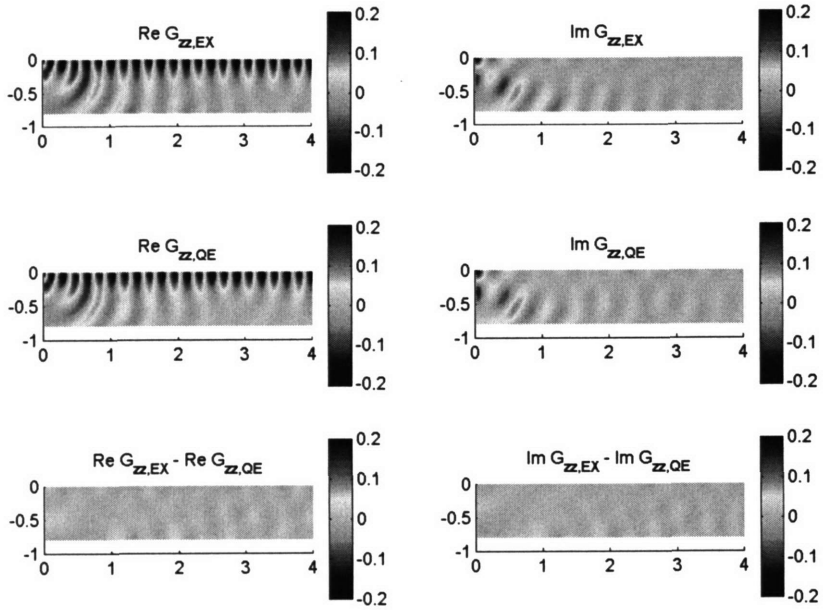

Figure 6.2.25c Displacements $u_{zz}(=G_{zz})$ obtained with TLM2 of N_λ=8 and R_P=1.0
in a homogeneous half-space (ρ=C_S=1, ν=0.3)
subjected to harmonic vertical line load of f_{ex}=2.5 applied at the top surface
($G_{xz\ QE}$: TLM2 of N_λ=8 and R_P=1.0; $G_{xz\ EX}$: Exact solution)

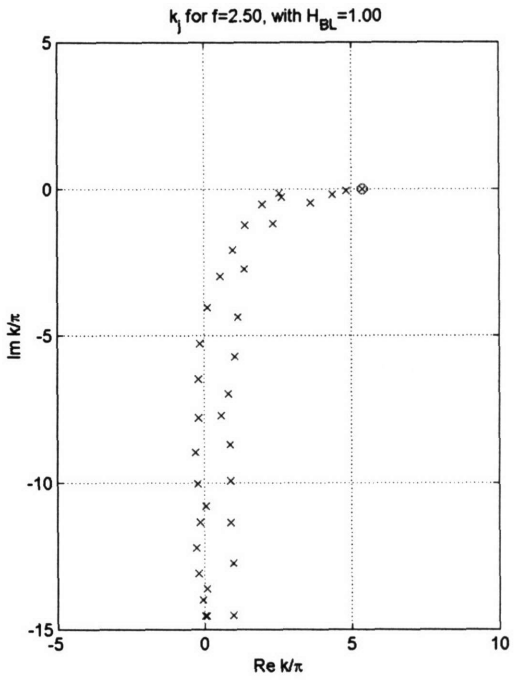

Figure 6.2.26a Eigenvalues k_j (×) obtained with TLM2 of N_λ=8 and R_P=1.25
for a homogeneous half-space (ρ=C_S=1, ν=0.3) for f_{ex}=2.5, (o: Exact Rayleigh pole k_R)

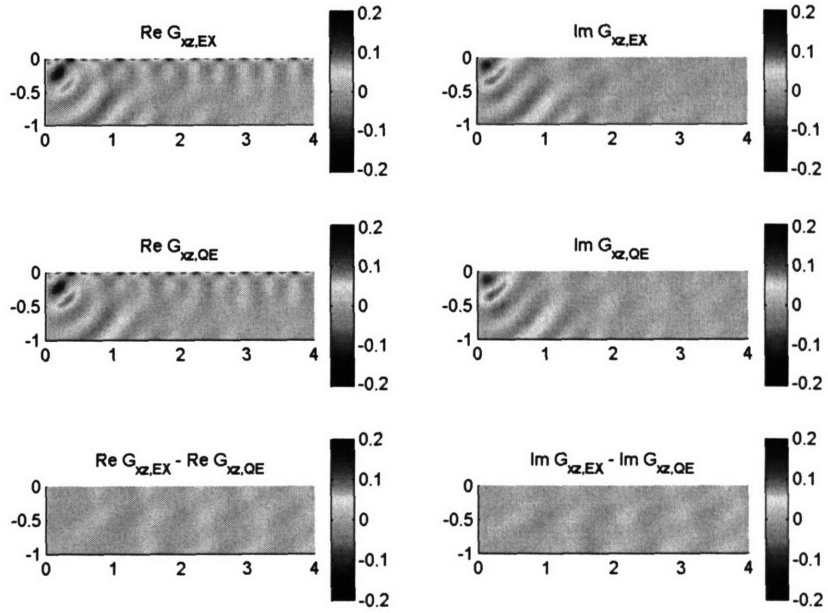

Figure 6.2.26b Displacements u_{xz}(=G_{xz}) obtained with TLM2 of N_λ=8 and R_P=1.25
in a homogeneous half-space (ρ=C_S=1, ν=0.3)
subjected to harmonic vertical line load of f_{ex}=2.5 applied at the top surface
($G_{xz\,QE}$: TLM2 of N_λ=8 and R_P=1.25; $G_{xz\,EX}$: Exact solution)

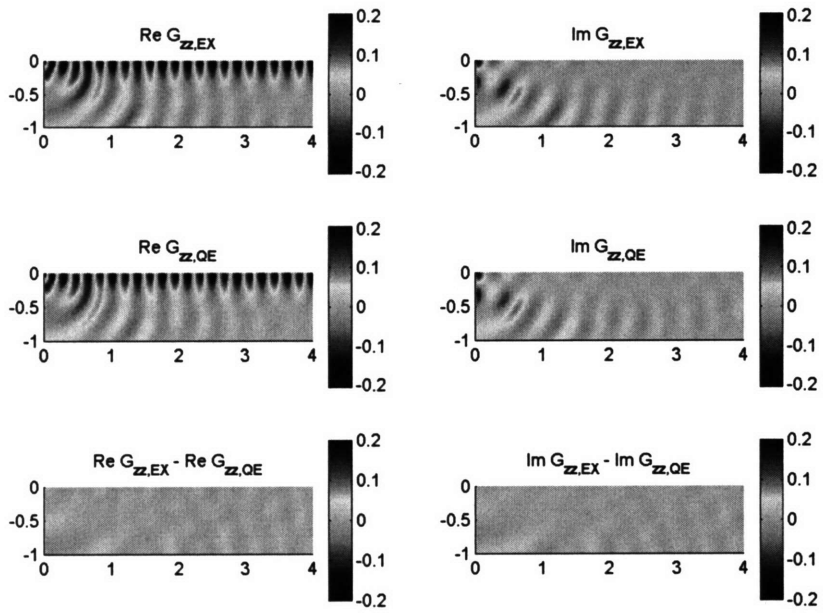

Figure 6.2.26c Displacements $u_{zz}(=G_{zz})$ obtained with TLM2 of N_λ=8 and R_P=1.25
in a homogeneous half-space (ρ=C_S=1, ν=0.3)
subjected to harmonic vertical line load of f_{ex}=2.5 applied at the top surface
($G_{xz\,QE}$: TLM2 of N_λ=8 and R_P=1.25; $G_{xz\,EX}$: Exact solution)

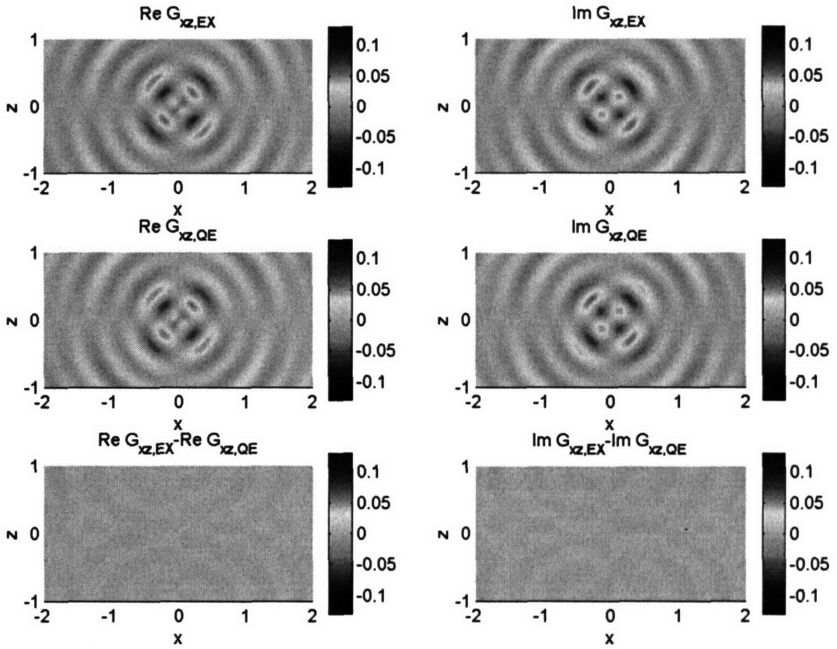

Figure 6.2.27a Displacements $u_{xz}(=G_{xz})$ in a homogeneous full-space (ρ=C_S=1, ν=0.25) subjected to harmonic vertical line load of f_{ex}=2.5 applied at the origin ($G_{xz\,QE}$: original $\mathbf{K}_{PB}$ of N_λ=8 and $H_{BL}(=R_P\lambda_P)$=1.0; $G_{xz\,EX}$: Exact solution)

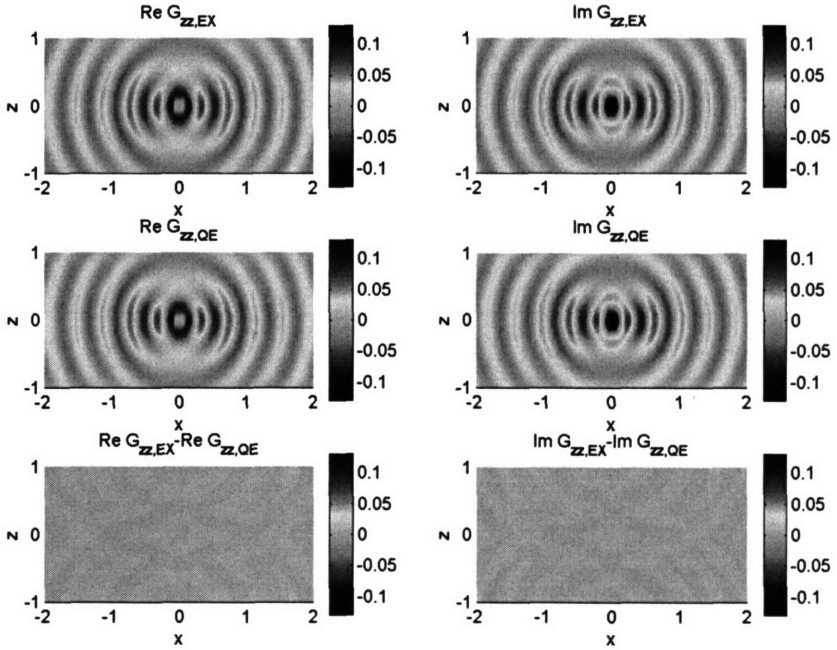

Figure 6.2.27b Displacements $u_{zz}(=G_{zz})$ in a homogeneous full-space (ρ=C_S=1, ν=0.25) subjected to harmonic vertical line load of f_{ex}=2.5 applied at the origin ($G_{zz\,QE}$: original $\mathbf{K}_{PB}$ of N_λ=8 and $H_{BL}(=R_P\lambda_P)$=1.0; $G_{zz\,EX}$: Exact solution)

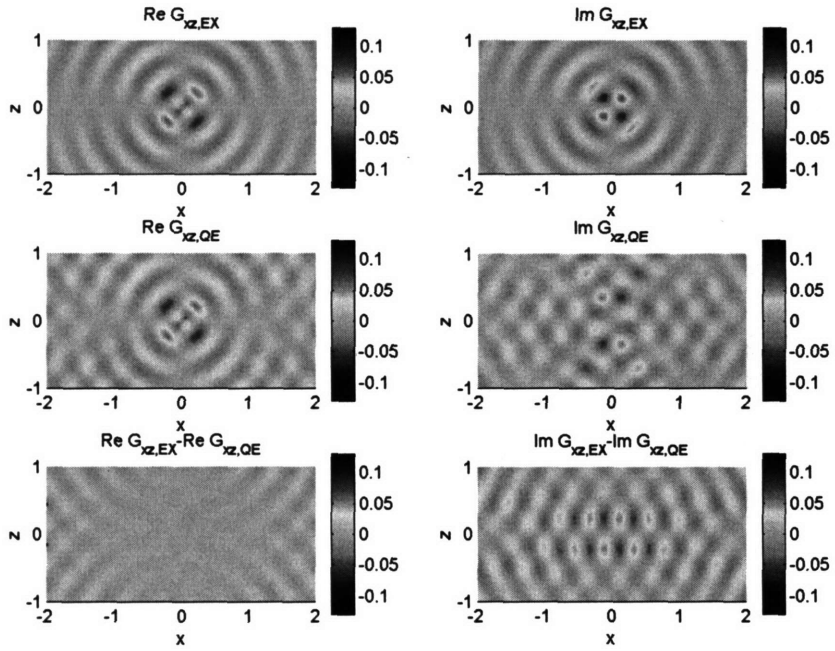

Figure 6.2.28a Displacements $u_{xz}(=G_{xz})$ in a homogeneous full-space (ρ=C_S=1, ν=0.45) subjected to harmonic vertical line load of f_{ex}=2.5 applied at the origin ($G_{xz\,QE}$: original $\mathbf{K}_{PB}$ of N_λ=8 and $H_{BL}(=R_P\lambda_P)$=1.0; $G_{xz\,EX}$: Exact solution)

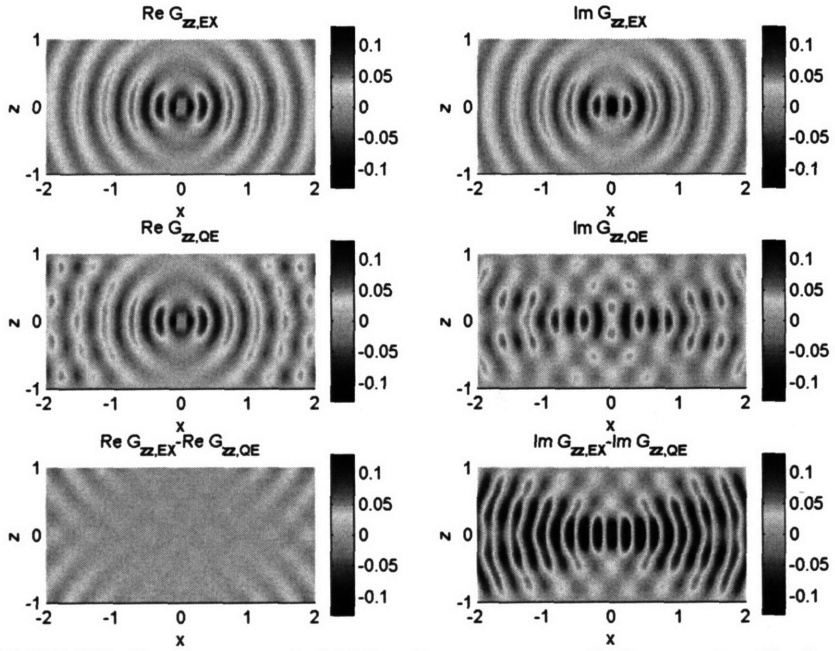

Figure 6.2.28b Displacements $u_{zz}(=G_{zz})$ in a homogeneous full-space (ρ=C_S=1, ν=0.45) subjected to harmonic vertical line load of f_{ex}=2.5 applied at the origin ($G_{zz\,QE}$: original $\mathbf{K}_{PB}$ of N_λ=8 and $H_{BL}(=R_P\lambda_P)$=1.0; $G_{zz\,EX}$: Exact solution)

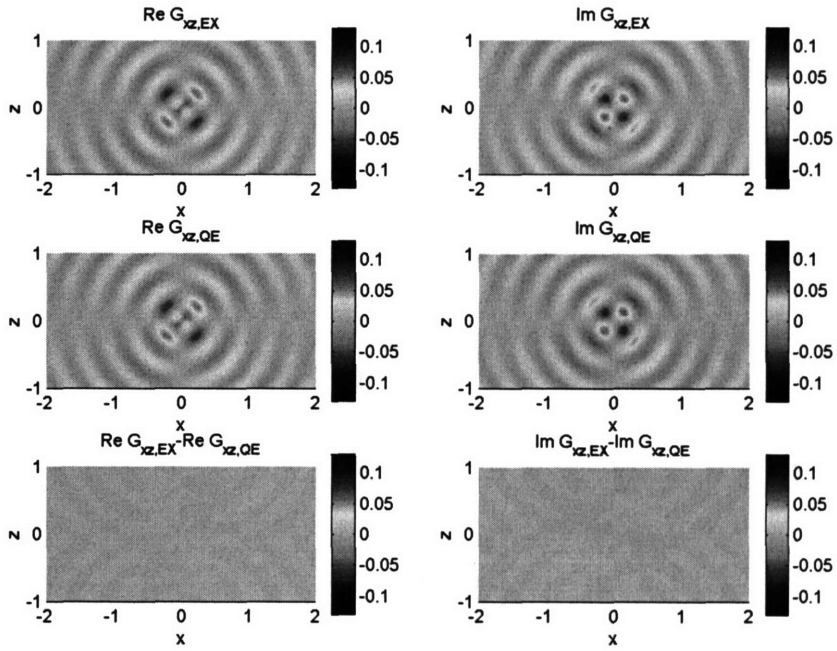

Figure 6.2.29a Displacements $u_{xz}(=G_{xz})$ in a homogeneous full-space (ρ=C_S=1, ν=0.45) subjected to harmonic vertical line load of f_{ex}=2.5 applied at the origin ($G_{xz\,QE}$: modified $\mathbf{K}_{PB}$ of N_λ=8 and $H_{BL}(=R_P\lambda_P)$=1.0; $G_{xz\,EX}$: Exact solution)

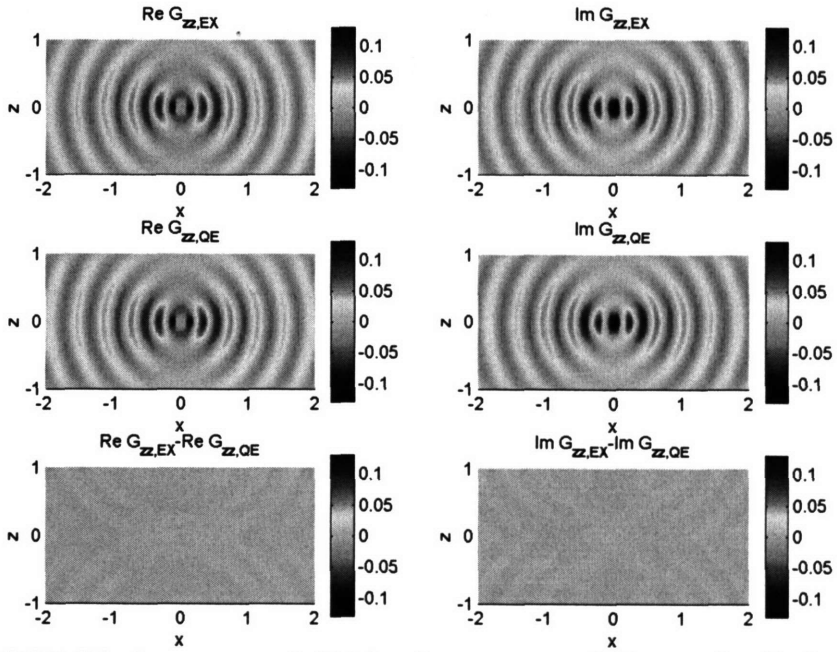

Figure 6.2.29b Displacements $u_{zz}(=G_{zz})$ in a homogeneous full-space (ρ=C_S=1, ν=0.45) subjected to harmonic vertical line load of f_{ex}=2.5 applied at the origin ($G_{zz\,QE}$: modified $\mathbf{K}_{PB}$ of N_λ=8 and $H_{BL}(=R_P\lambda_P)$=1.0; $G_{zz\,EX}$: Exact solution)

Figures for section 6.3

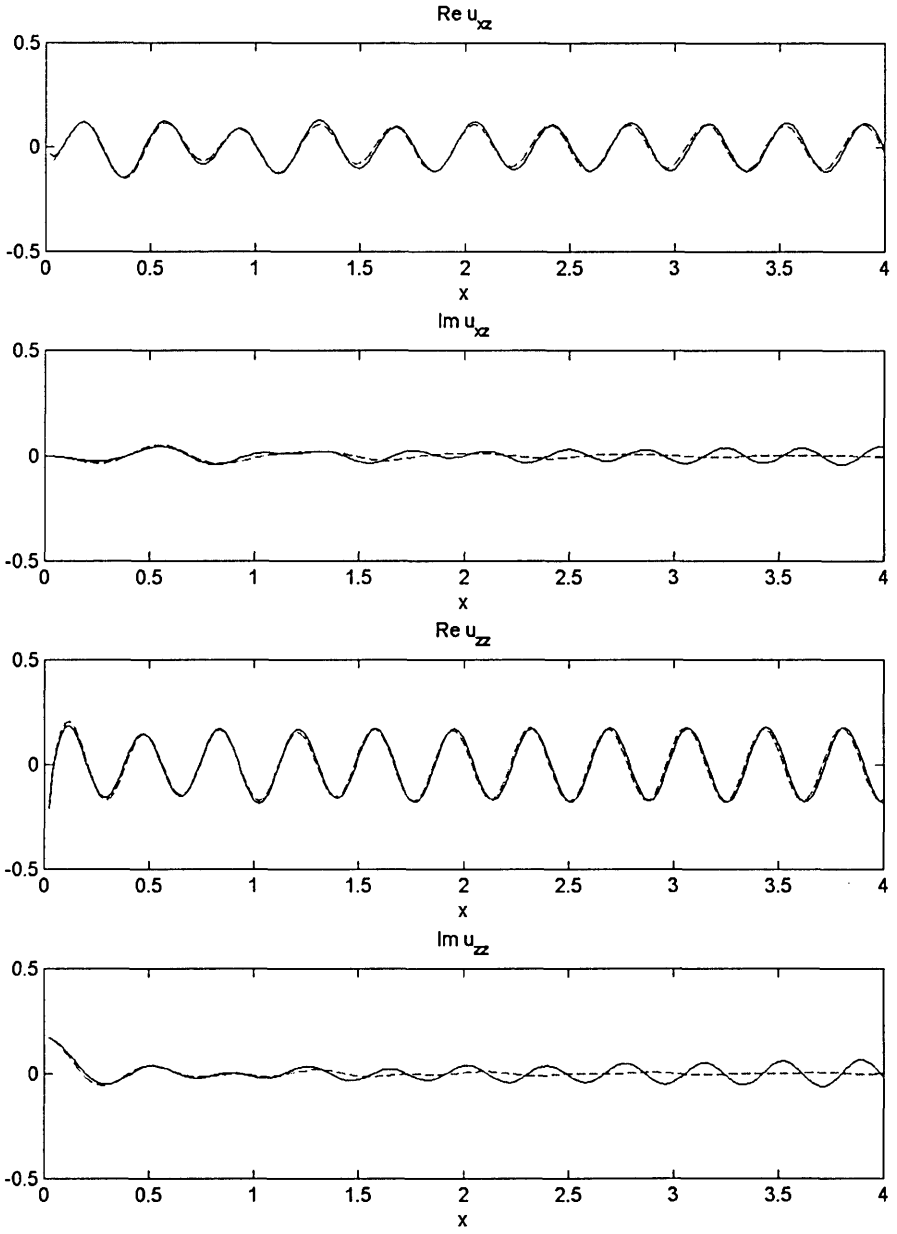

Figure 6.3.1a Surface u_{xz}, u_{zz} obtained with the conventional TLM2 of N_λ=4 combined with $\mathbf{K}_{PB}$ of H_{BL}=0.5(>λ_R=0.37), on a homogeneous half-space (ρ=C_S=1.0 and ν=0.30) subjected to a vertical line load of f_{ex}=2.5 applied at the top surface, (solid line: TLM2; dashed line: Exact solution)

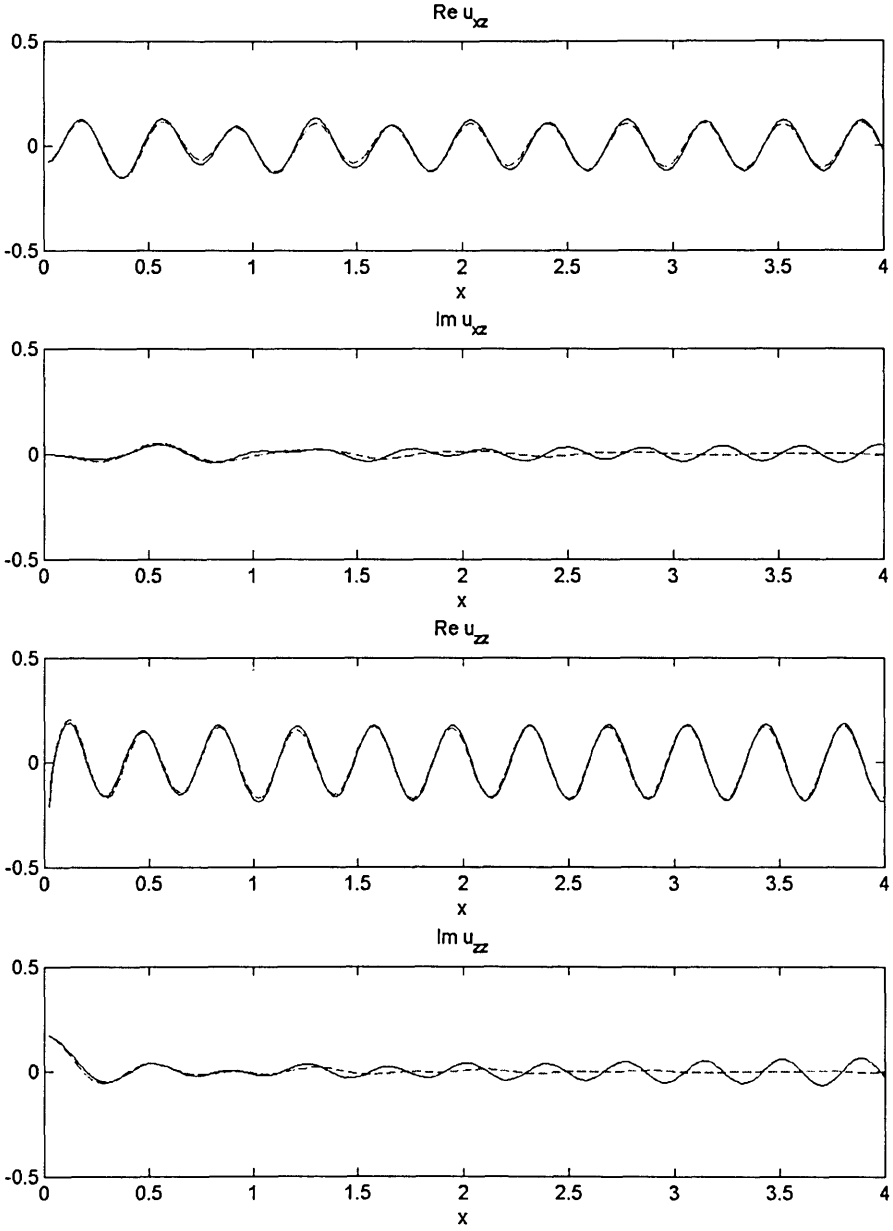

Figure 6.3.1b Surface u_{xz}, u_{zz} obtained with the conventional TLM2 of N_λ=8 combined with $\mathbf{K}_{PB}$ of H_{BL}=0.5(>λ_R=0.37), on a homogeneous half-space (ρ=C_S=1.0 and ν=0.30) subjected to a vertical line load of f_{ex}=2.5 applied at the top surface, (solid line: TLM2; dashed line: Exact solution)

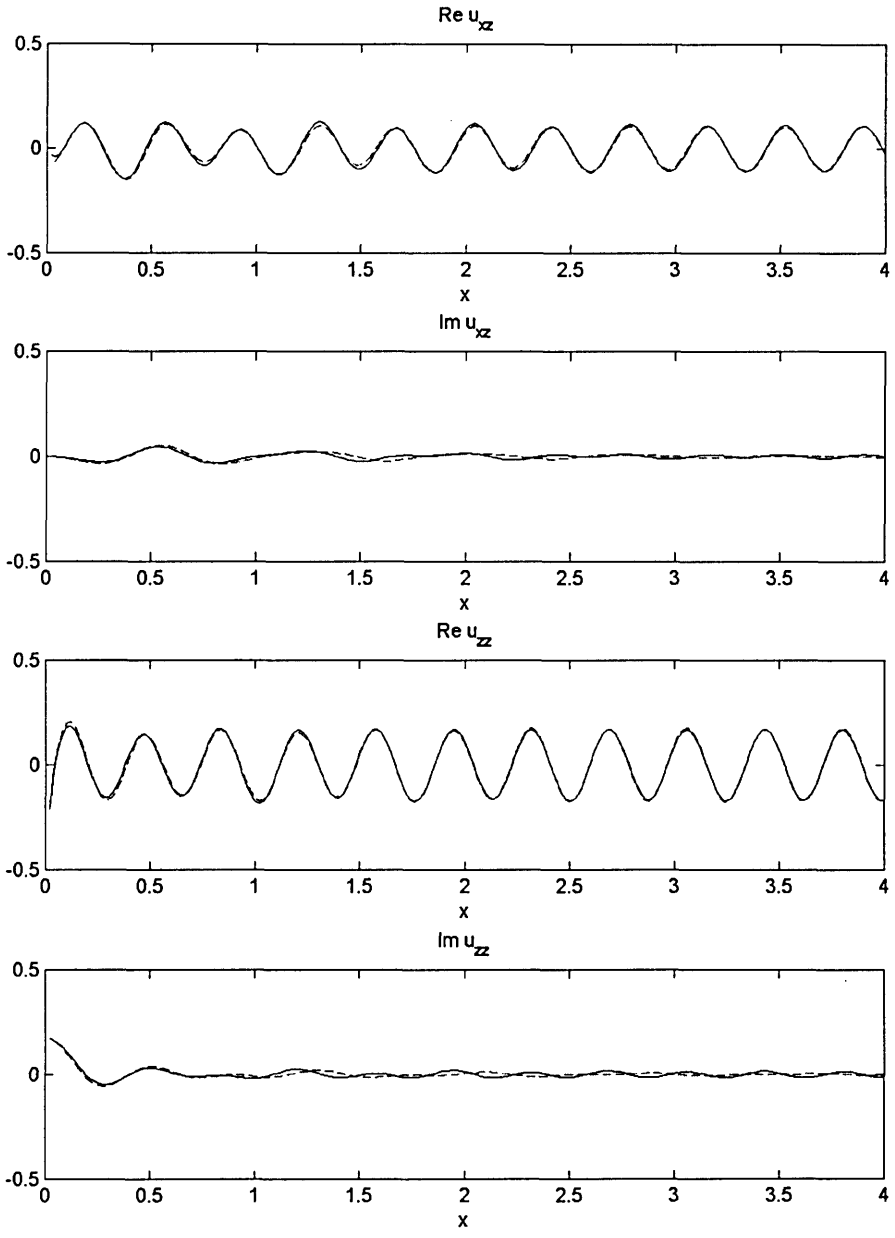

Figure 6.3.1c Surface u_{xz}, u_{zz} obtained with the hybrid TLM2 of N_λ=4 combined with $\mathbf{K}_{PB}$ of H_{BL}=0.5(>λ_R=0.37), on a homogeneous half-space (ρ=C_S=1.0 and ν=0.30) subjected to a vertical line load of f_{ex}=2.5 applied at the top surface, (solid line: TLM2; dashed line: Exact solution)

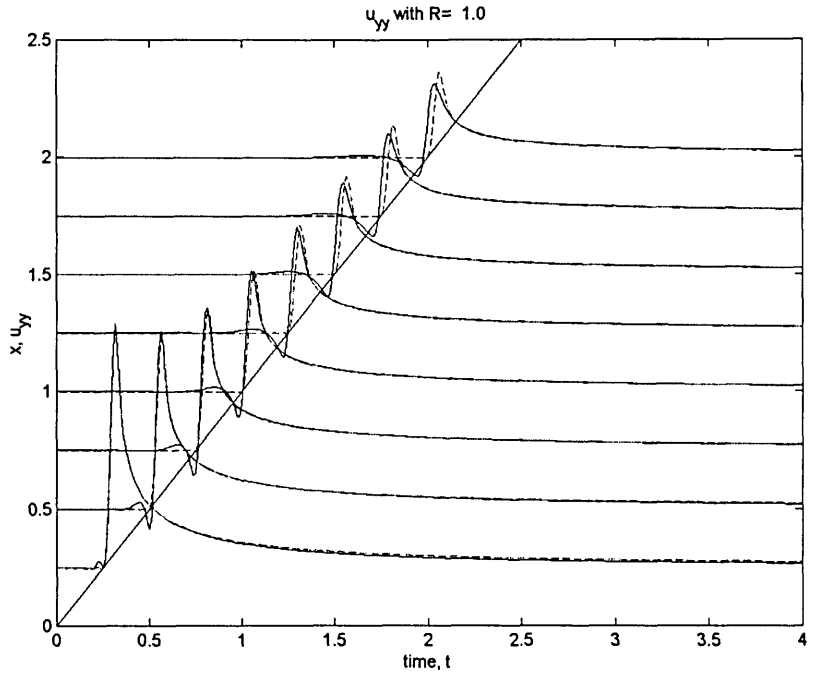

Figure 6.3.2 Seismograms of surface u_{yy} obtained with TLM2 of R=1.0 on a homogeneous half-space subjected to *SH* line load of t_d=0.2, (solid line: TLM2; dashed line: Exact solution)

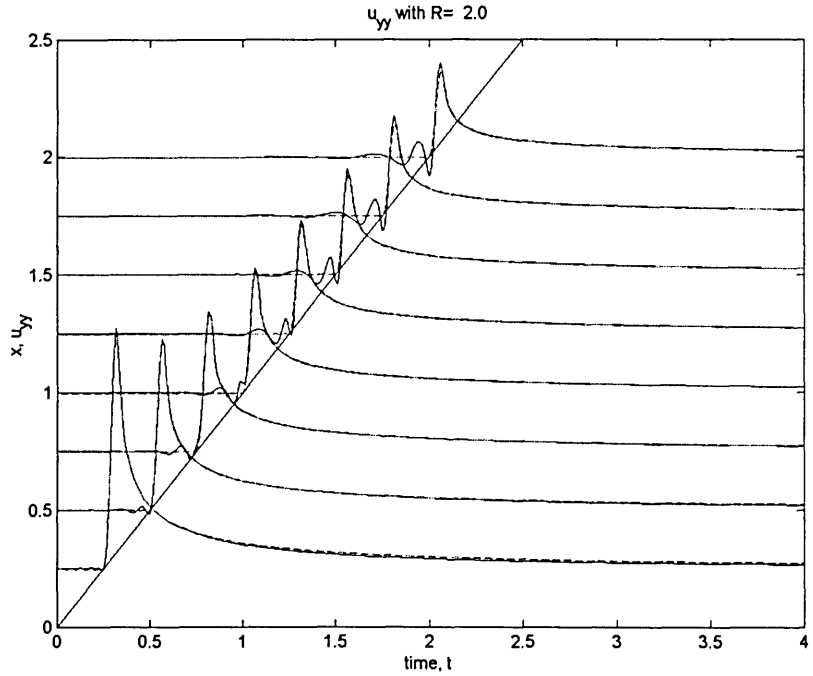

Figure 6.3.3 Seismograms of surface u_{yy} obtained with TLM2 of R=2.0 on a homogeneous half-space subjected to *SH* line load of t_d=0.2, (solid line: TLM2; dashed line: Exact solution)

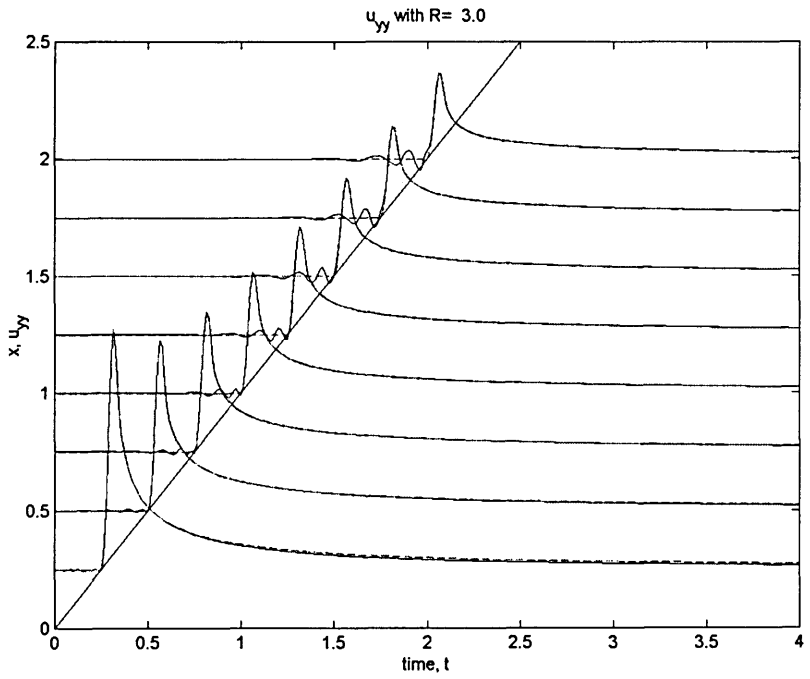

Figure 6.3.4 Seismograms of surface u_{yy} obtained with TLM2 of R=3.0 on a homogeneous half-space subjected to *SH* line load of t_d=0.2, (solid line: TLM2; dashed line: Exact solution)

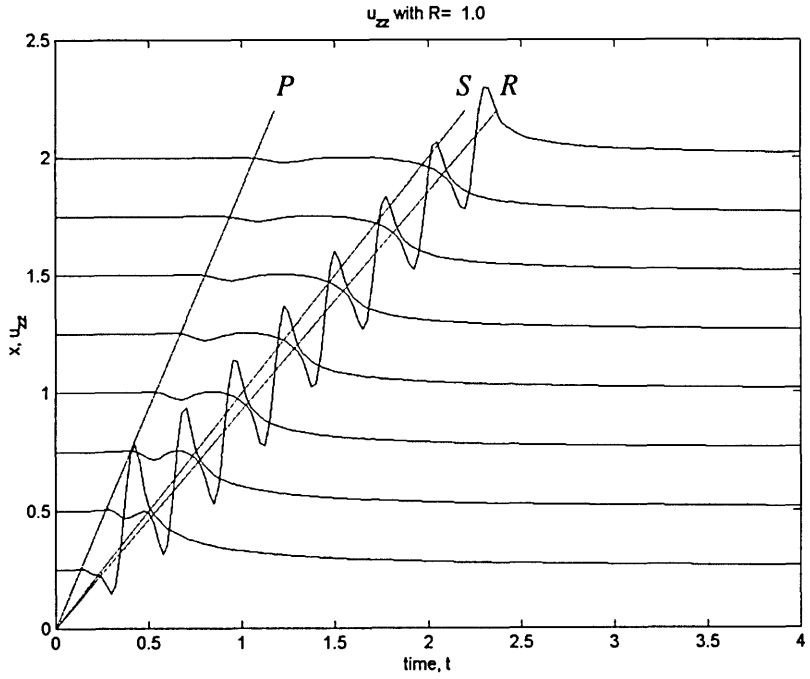

Figure 6.3.5 Seismograms of surface u_{zz} obtained with TLM2 of R=1.0 on a homogeneous half-space subjected to vertical line load of t_d=0.2

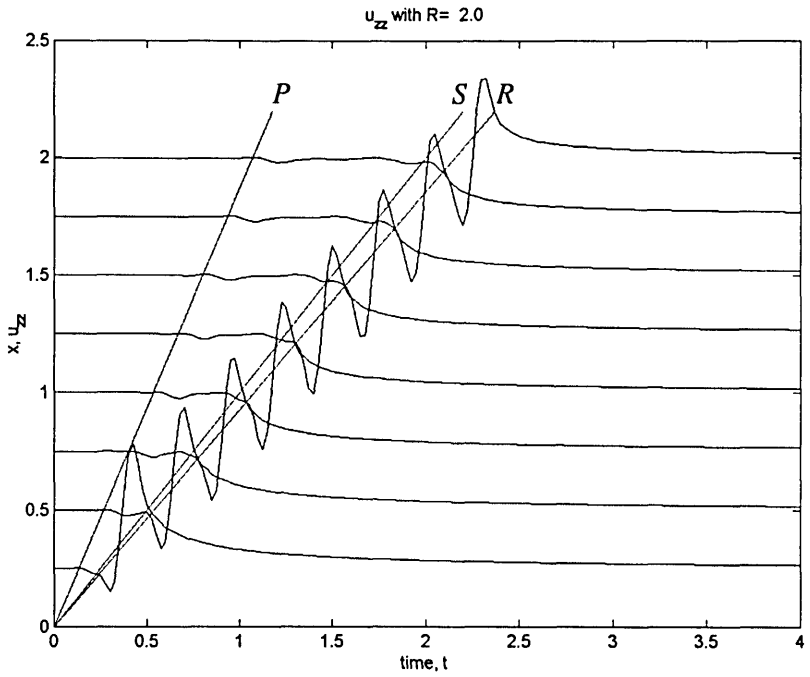

Figure 6.3.6 Seismograms of surface u_{zz} obtained with TLM2 of R=2.0 on a homogeneous half-space subjected to vertical line load of t_d=0.2

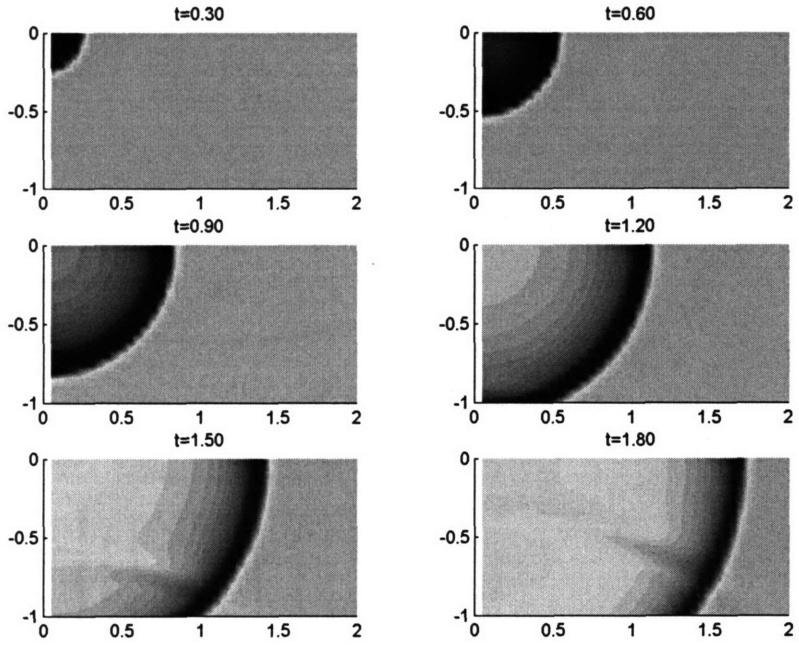

Figure 6.3.7 Snapshots of v obtained with TLM2 of N_λ=4, $N_{\lambda,\mathrm{BL}}$=4, and R_S=4.0 in a homogeneous half-space subjected to *SH* surface line load of t_d=0.2

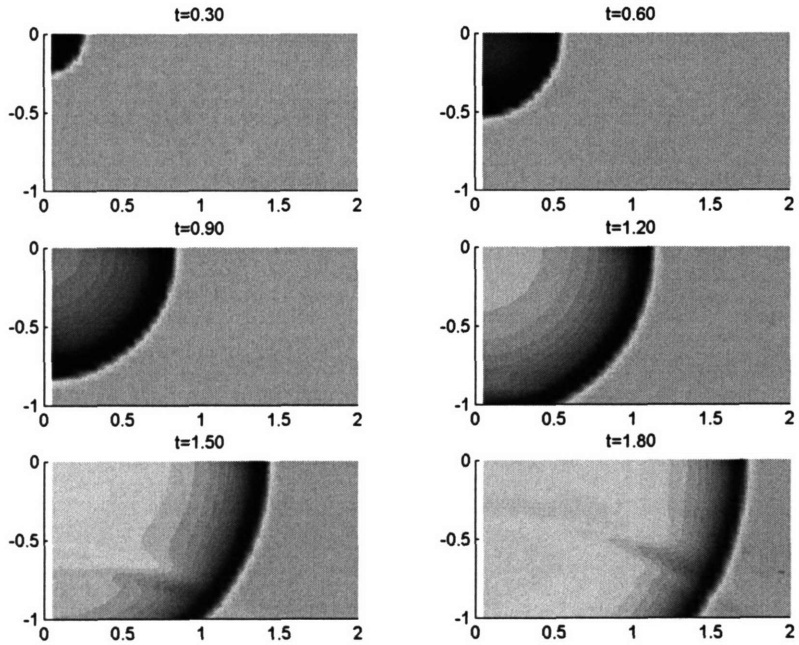

Figure 6.3.8 Snapshots of v obtained with TLM2 of N_λ=4, $N_{\lambda,\mathrm{BL}}$=8, and R_S=4.0 in a homogeneous half-space subjected to *SH* surface line load of t_d=0.2

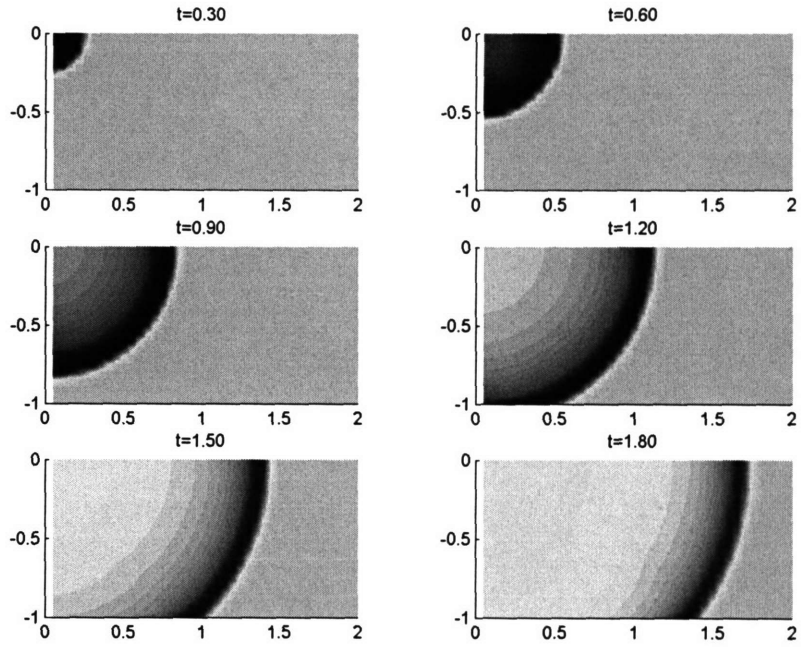

Figure 6.3.9 Snapshots of v obtained with TLM2 of N_λ=4, $N_{\lambda,\mathrm{BL}}$=12, and R_S=4.0 in a homogeneous half-space subjected to *SH* surface line load of t_d=0.2

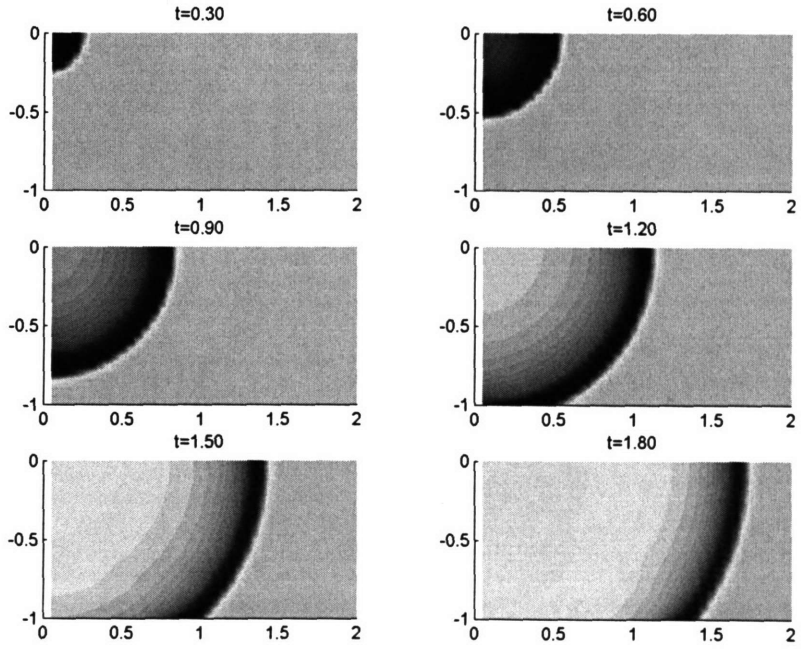

Figure 6.3.10 Snapshots of v obtained with TLM2 of N_λ=4, $N_{\lambda,\mathrm{BL}}$=16, and R_S=4.0 in a homogeneous half-space subjected to *SH* surface line load of t_d=0.2

Figures for section 6.4

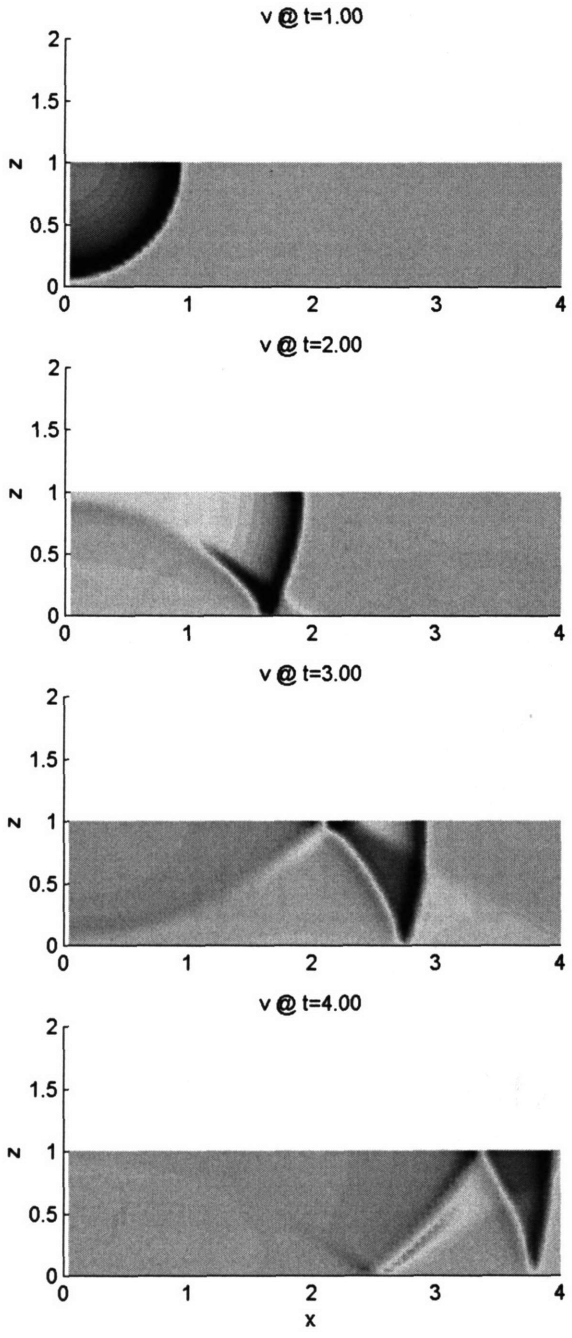

Figure 6.4.1 Snapshots of v for $0 \leq z \leq H$ in a one-layered half-space ($\rho_1=C_{S,1}=H=1.0$; $\rho_2=1.0$, $C_{S,2}=2.0$) subjected to SH surface line load of $t_d=0.2$

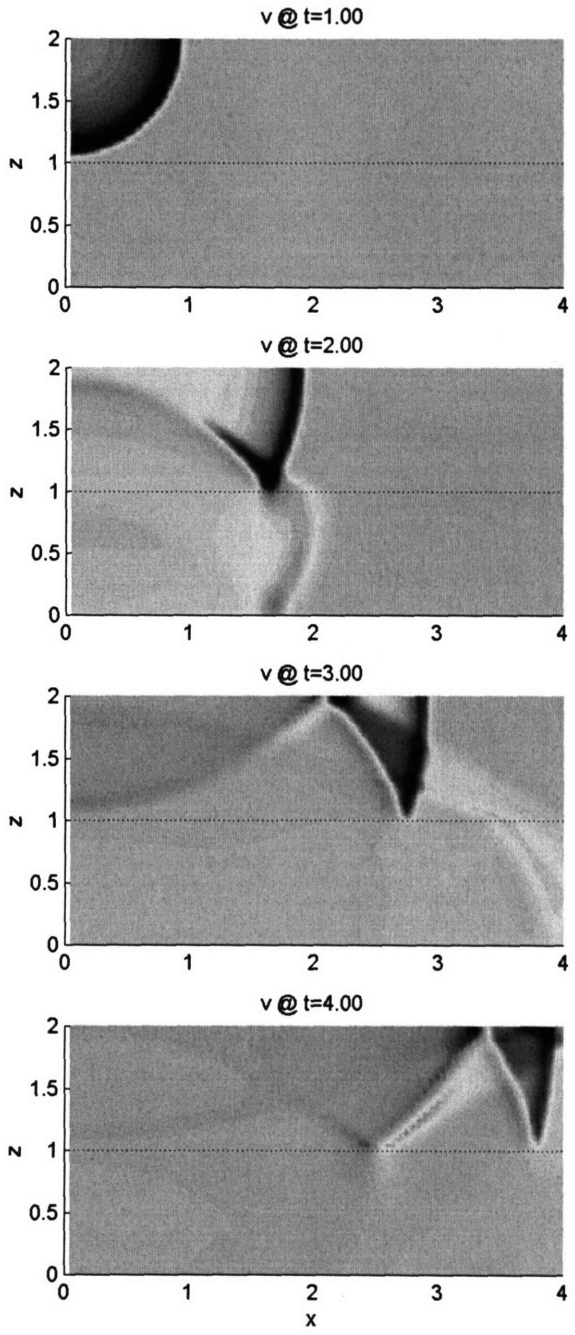

Figure 6.4.2 Snapshots of v for $0 \le z \le H(=H_1+H_2)$ in a two-layered half-space ($\rho_1=C_{S,1}=H_1=1.0$; $\rho_2=H_2=1.0$, $C_{S,2}=2.0$; $\rho_3=1.0$, $C_{S,3}=3.0$) subjected to *SH* surface line load of $t_d=0.2$

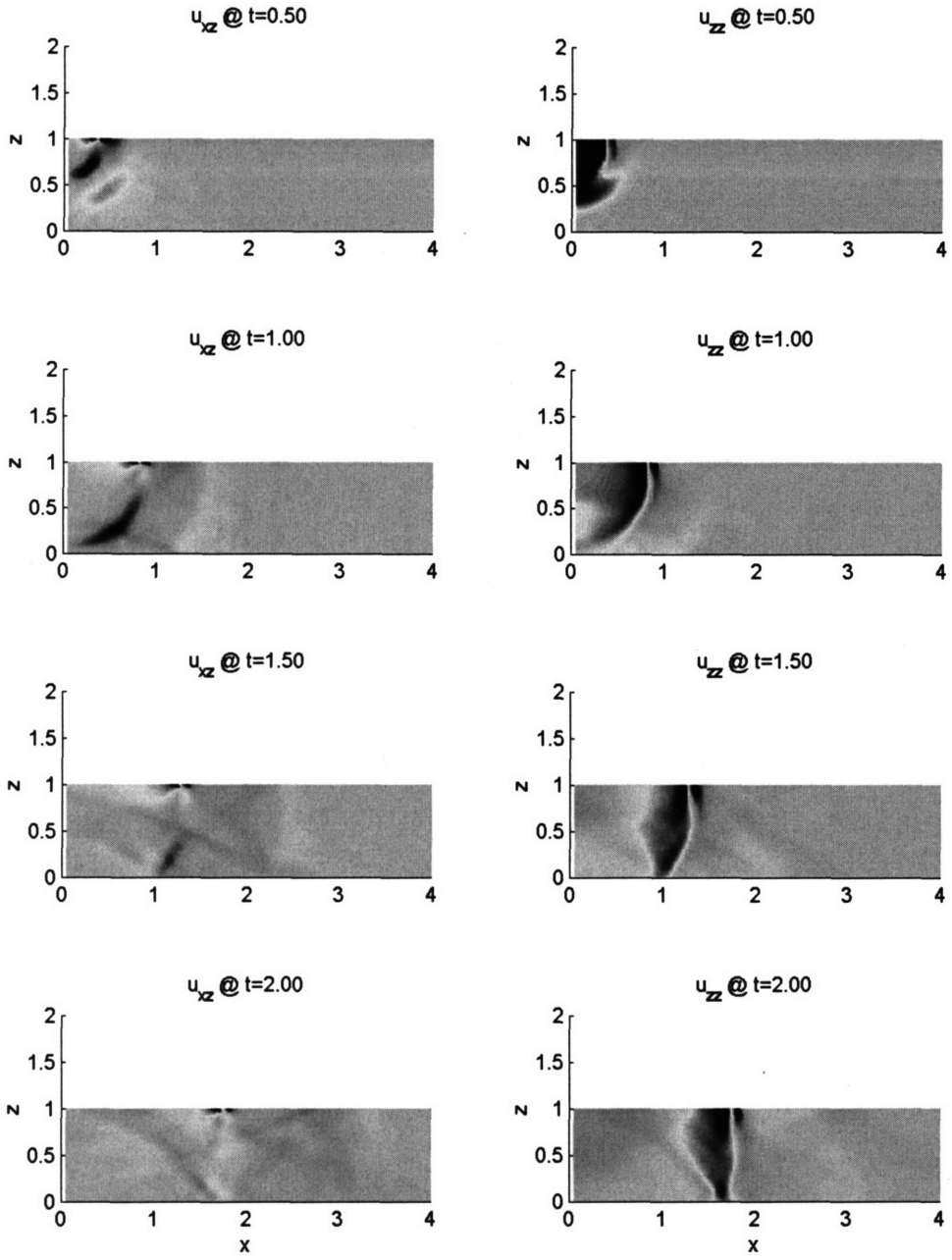

Figure 6.4.3 Snapshots of u_{xz}, u_{zz} for $0 \le z \le H$ in a one-layered half-space ($\rho_1=C_{S,1}=H=1.0$, $\nu_1=0.25$; $\rho_2=1.0$, $C_{S,2}=2.0$, $\nu_2=0.25$) subjected to vertical surface line load of $t_d=0.2$

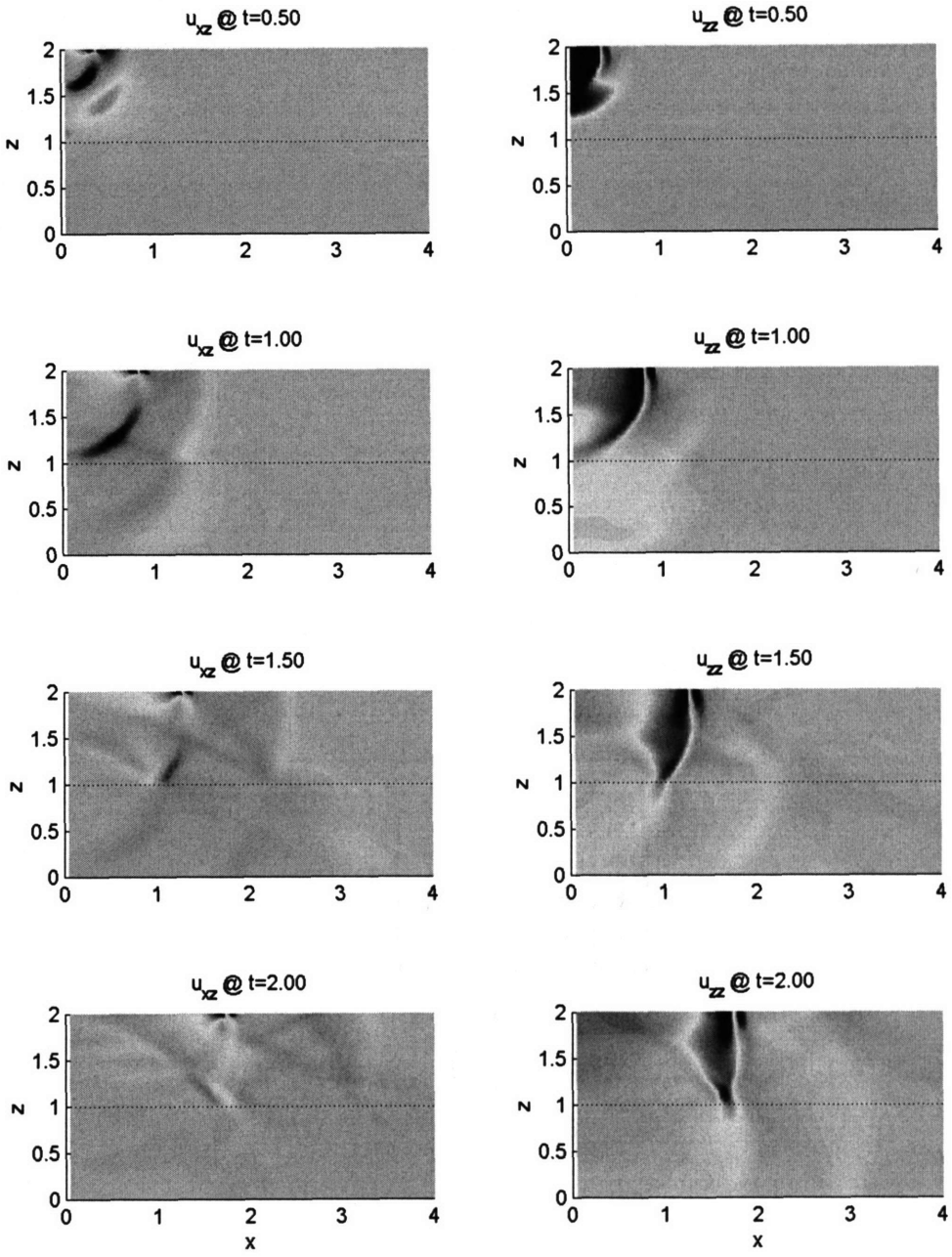

Figure 6.4.4 Snapshots of u_{xz}, u_{zz} $0 \le z \le H(=H_1+H_2)$ in a two-layered half-space ($\rho_1=C_{S,1}=H_1=1.0$, $\nu_1=0.25$; $\rho_2=H_2=1.0$, $C_{S,2}=2.0$, $\nu_2=0.25$; $\rho_3=1.0$, $C_{S,3}=3.0$, $\nu_3=0.25$) subjected to vertical surface line load of $t_d=0.2$

APPENDIX 6A: Contour Integral Solutions in x-ω domain

We present and derive the Green's functions in the space-frequency domain, or x-ω domain for short, associated with plane strain wave motions. Two types of semi-infinite media ($z \le 0$) are considered: 1) a layer on a half-space subjected to an *SH* surface line load (the *Love* wave problem), 2) a homogeneous half-space subjected to *SV-P* surface line loads. We apply the contour integration method over the complex wavenumber plane to obtain the Green functions in the x-ω domain.

6A.1 Green functions for *SH* surface line loads

Here, we consider a system of a layer of thickness H overlain by a homogeneous half-space that is subjected to an *SH* surface line load. Figure 6A.1 describes the problem of interest and the x-axis coincides with the interface between the upper layer and the half-space. The upper layer and the half-space are labeled as I and II, respectively, and ρ's and C's are the mass densities and the shear wave speeds, respectively. In a case of $C_I < C_{II}$, guided waves develop within the upper layer, which is known as the Love wave problem. We start by deriving the Green functions for this Love wave problem and then generalize the solutions for the other cases of $C_I = C_{II}$ and $C_I > C_{II}$.

The governing equations for the problem of interest are given in the x-t domain as

$$\rho_I \frac{\partial^2 v_I}{\partial t^2} - G_I \left[\frac{\partial^2 v_I}{\partial z^2} + \frac{\partial^2 v_I}{\partial z^2} \right] = \delta(x)\delta(z-H)\delta(t) = p_y \qquad \text{for } 0 \le z \le H \qquad \text{(6A.1a)}$$

$$\rho_{II} \frac{\partial^2 v_{II}}{\partial t^2} - G_{II} \left[\frac{\partial^2 v_{II}}{\partial z^2} + \frac{\partial^2 v_{II}}{\partial z^2} \right] = 0 \qquad \text{for } z \le 0 \qquad \text{(6A.1b)}$$

where v's are the displacements in the x-t domain and G's the shear moduli. Applying a double Fourier transformations with respect to x and t, we obtain the general solutions in the k-ω domain in the absence of the external load as

$$\bar{v}_I(k,z,\omega) = A\cos\beta z + B\sin\beta z \qquad \text{(6A.2a)}$$

$$\bar{v}_{II}(k,z,\omega) = Ce^{\gamma z} \qquad \text{(6A.2b)}$$

where $\beta = \sqrt{(\omega/C_I)^2 - k^2}$, $\gamma = \sqrt{k^2 - (\omega/C_{II})^2}$, and A, B, C are unknown constants. These are determined by satisfying the traction boundary condition at the top surface and the two continuity conditions for the displacement and internal stress at the interface z=0. Then, the Green functions $\bar{G}_{yy}$'s in the k-ω domain are obtained as

$$\bar{G}_{yy,I}(k,z,\omega) = \frac{1}{G_I\Delta}\left[-\cos\beta z - \mu\frac{\gamma}{\beta}\sin\beta z \right] = \frac{1}{G_I}\frac{N_I}{\Delta} = \frac{1}{G_I}K_I \qquad \text{for } 0 \le z \le H \qquad \text{(6A.3a)}$$

$$\bar{G}_{yy,II}(k,z,\omega) = \frac{1}{G_I\Delta}\left[-e^{\gamma z} \right] = \frac{1}{G_I}\frac{N_{II}}{\Delta} = \frac{1}{G_I}K_{II} \qquad \text{for } z \le 0 \qquad \text{(6A.3b)}$$

where

$$\Delta = [\beta\sin\beta H - \mu\gamma\cos\beta H], \qquad \text{(6A.4a)}$$

$$\mu = G_{II}/G_I, \qquad \text{(6A.4b)}$$

K's are the kernels, and N's the numerators of the kernels. The function Δ in equation (6A.4a) is the characteristic equation for Love waves, which in the case $\Delta = 0$ provides the dispersive

guided waves within the upper layer. Furthermore, it should be noticed that the kernels are all even functions of k and β, but odd functions of γ, which implies that the sign change and conjugate properties of the kernels are associated only with γ.

The Green functions in the x-ω domain are obtained by means of the inverse Fourier transform

$$\begin{aligned}\tilde{G}_{yy,l}(x,z,\omega) &= \frac{1}{2\pi}\int_{-\infty}^{\infty}\bar{G}_{yy,l}(k,z,\omega)e^{-ikx}dk \\ &= \frac{1}{2\pi G_{\mathrm{I}}}\int_{-\infty}^{\infty}\frac{N_l}{\Delta}e^{-ikx}dk = \frac{1}{2\pi G_{\mathrm{I}}}\int_{-\infty}^{\infty}K_l(k,\gamma,\beta,\Delta)e^{-ikx}dk \\ &= \frac{1}{2\pi G_{\mathrm{I}}}I_l\end{aligned} \tag{6A.5}$$

where I_l are the integrals to be calculated, and l=I or II. Since the Love wave equation produces the zeros of the denominators of the kernels at the poles, we can not integrate along the real k-axis. To overcome this obstacle, we deform the integral path into the complex k-plane, or ξ-plane, as shown in figure 6A.2. In figure 6A.2, $k_{\mathrm{I}} = \omega/C_{\mathrm{I}}$, $k_{\mathrm{II}} = \omega/C_{\mathrm{II}}$, and the set $-k_{\mathrm{M}},\ldots,-k_1,k_1,\ldots,k_{\mathrm{M}}$ represent the poles of the *Love* wave equation for a given frequency ω. It is noticed that all the poles are located along the real k-axis, assuming that the system of interest is undamped. Adding some amount of damping into the system, these poles move from the real k-axis to the complex ξ region. The contour integral path is then closed in the lower ξ-plane, because e^{-ikx} is used. The integrands in equation (6A.5) are odd functions of γ, and even functions of β. Therefore, there is a branch-point only around γ as shown in figure 6A.2. Then, the resulting contour integrals are given of the form

$$\begin{aligned}\oint dI_l &= I_l + \int_{C_{-\infty}} dI_l + \int_{-\mathrm{i}\infty}^{0} dI_l + \int_{0}^{k_{\mathrm{II}}} dI_l + \int_{k_{\mathrm{II}}}^{0} dI_l + \int_{0}^{-\mathrm{i}\infty} dI_l \\ &= -2\pi\mathrm{i}\sum_{m}^{M}(m\text{-th Residue})_l\end{aligned} \tag{6A.6}$$

where M is the total number of poles for a given frequency ω. Since the integrands vanish on $C_{-\infty}$, equation (6A.6) yields

$$I_l = -2\pi\mathrm{i}\sum_{m}(m\text{-th Residue})_l - \int_{Branch-cut} dI_l \tag{6A.7a}$$

$$\int_{Branch-cut} dI_l = \int_{-\mathrm{i}\infty}^{0} dI_l + \int_{0}^{k_{\mathrm{II}}} dI_l + \int_{k_{\mathrm{II}}}^{0} dI_l + \int_{0}^{-\mathrm{i}\infty} dI_l \tag{6A.7b}$$

Next, we need to identify the branch-cut so as to decide on the proper phases of γ and β. For this purpose, we shift up the real k-axis by $\mathrm{i}\bar{\eta}$ as shown in figure 6A.3. Then, γ^2 is given as

$$\begin{aligned}\gamma^2 &= (k_C + \mathrm{i}\bar{\eta})^2 - k_{\mathrm{II}}^2 \\ &= \left[k + \mathrm{i}(\eta + \bar{\eta})\right]^2 - k_{\mathrm{II}}^2 \\ &= k^2 - k_{\mathrm{II}}^2 - (\eta + \bar{\eta})^2 + 2\mathrm{i}k(\eta + \bar{\eta})\end{aligned} \tag{6A.8}$$

According to the signs of $\mathrm{Re}\gamma^2$ and $\mathrm{Im}\gamma^2$, we decide the (i,ii,iii,iv)-th quadrants for γ^2 as shown in figure 6A.3. Consequently, we can determine the (I,II,III,IV)-th quadrants for γ. Then, the branch-cut integrals are expressed as

$$\begin{aligned}\int_{Branch-cut} dI_l = &\int_{-\infty}^{0} K_l(\mathrm{i}\eta,-\mathrm{i}\bar{\gamma},\bar{\beta},\Delta_{\mathrm{II}}^{*})e^{-\mathrm{i}(\mathrm{i}\eta)x}d(\mathrm{i}\eta) + \int_{0}^{-\infty} K_l(\mathrm{i}\eta,\mathrm{i}\bar{\gamma},-\bar{\beta},\Delta_{\mathrm{II}})e^{-\mathrm{i}(\mathrm{i}\eta)x}d(\mathrm{i}\eta) \\ &+ \int_{0}^{k_{\mathrm{II}}} K_l(k,-\mathrm{i}\hat{\gamma},\beta,\Delta_{\mathrm{I}})e^{-ikx}dk + \int_{k_{\mathrm{II}}}^{0} K_l(k,\mathrm{i}\hat{\gamma},-\beta,\Delta_{\mathrm{I}}^{*})e^{-ikx}dk\end{aligned} \tag{6A.9}$$

where

$$\bar{\beta} = \sqrt{\eta^2 + k_{\rm I}^2} \tag{6A.10a}$$

$$\bar{\gamma} = \sqrt{\eta^2 + k_{\rm II}^2} \tag{6A.10b}$$

$$\hat{\gamma} = \sqrt{k_{\rm II}^2 - k^2} \tag{6A.10c}$$

$$\Delta_{\rm I} = \beta \sin \beta H + {\rm i}\mu\hat{\gamma} \cos \beta H, \quad \text{and} \quad \Delta_{\rm I}^* = conj(\Delta_{\rm I}) \tag{6A.10de}$$

$$\Delta_{\rm II} = \bar{\beta} \sin \bar{\beta} H - {\rm i}\mu\bar{\gamma} \cos \bar{\beta} H, \quad \text{and} \quad \Delta_{\rm II}^* = conj(\Delta_{\rm II}) \tag{6A.10fg}$$

Changing the direction of integration in the first and fourth integrals, we obtain

$$\begin{aligned}\int_{Branch-cut} dI_l = &- {\rm i}\int_0^{-\infty} K_l({\rm i}\eta, -{\rm i}\bar{\gamma}, \bar{\beta}, \Delta_{\rm II}^*) e^{-{\rm i}(i\eta)x} d\eta + {\rm i}\int_0^{-\infty} K_l({\rm i}\eta, {\rm i}\bar{\gamma}, -\bar{\beta}, \Delta_{\rm II}) e^{-{\rm i}(i\eta)x} d\eta \\ &+ \int_0^{k_{\rm II}} K_l(k, -{\rm i}\hat{\gamma}, \beta, \Delta_{\rm I}) e^{-{\rm i}kx} dk - \int_0^{k_{\rm II}} K_l(k, {\rm i}\hat{\gamma}, -\beta, \Delta_{\rm I}^*) e^{-{\rm i}kx} dk\end{aligned} \tag{6A.11}$$

The conjugate relationships between the kernels in each row in equation (6A.11) provides

$$\int_{Branch-cut} dI_l = -2\int_0^{-\infty} {\rm Im}\left[K_l({\rm i}\eta, {\rm i}\bar{\gamma}, -\bar{\beta}, \Delta_{\rm II})\right] e^{\eta x} d\eta + 2{\rm i}\int_0^{k_{\rm II}} {\rm Im}\left[K_l(k, -{\rm i}\hat{\gamma}, \beta, \Delta_{\rm I})\right] e^{-{\rm i}kx} dk \tag{6A.12}$$

Replacement of η by -η in the first term in equation (6A.12) yields

$$\int_{Branch-cut} dI_l = 2\int_0^{\infty} {\rm Im}\left[K_l(-{\rm i}\eta, {\rm i}\bar{\gamma}, -\bar{\beta}, \Delta_{\rm II})\right] e^{-\eta x} d\eta + 2{\rm i}\int_0^{k_{\rm II}} {\rm Im}\left[K_l(k, -{\rm i}\hat{\gamma}, \beta, \Delta_{\rm I})\right] e^{-{\rm i}kx} dk \tag{6A.13}$$

Next, we consider the residues in equation (6A.7a). The residues for each pole, k_m, are obtained by the limit

$$(m\text{-th Residue})_l = \lim_{k \to k_m} (k - k_m) \frac{N_l}{\Delta} e^{-{\rm i}kx} = \frac{N_l(k_m)}{\Delta'(k_m)} e^{-{\rm i}k_m x} \tag{6A.14}$$

where

$$\Delta' = \frac{d\Delta}{dk} = -\frac{k}{\beta}(1 + \mu\gamma H)\sin \beta H - (kH + \mu\frac{k}{\gamma})\cos \beta H \tag{6A.15}$$

Substitution of equations (6A.13) and (6A.14) into equation (6A.7a) produces

$$\begin{aligned} I_l = &-\pi{\rm i}\sum_{m=1}^{M}\left[-2{\rm i}\frac{N_l(k_m)}{\Delta'(k_m)}\sin kx\right] \\ &-2\left\{\int_0^{\infty} {\rm Im}\left[K_l(-{\rm i}\eta, {\rm i}\bar{\gamma}, -\bar{\beta}, \Delta_{\rm II})\right] e^{-\eta x} d\eta + {\rm i}\int_0^{k_{\rm II}} {\rm Im}\left[K_l(k, -{\rm i}\hat{\gamma}, \beta, \Delta_{\rm I})\right] e^{-{\rm i}kx} dk\right\}\end{aligned} \tag{6A.16a}$$

$$\begin{aligned} I_l = &-2\pi{\rm i}\sum_{m=1}^{M}\left[\frac{N_l(k_m)}{\Delta'(k_m)} e^{-{\rm i}k_m x}\right] \\ &-2\left\{\int_0^{\infty} {\rm Im}\left[K_l(-{\rm i}\eta, {\rm i}\bar{\gamma}, -\bar{\beta}, \Delta_{\rm II})\right] e^{-\eta x} d\eta + {\rm i}\int_0^{k_{\rm II}} {\rm Im}\left[K_l(k, -{\rm i}\hat{\gamma}, \beta, \Delta_{\rm I})\right] e^{-{\rm i}kx} dk\right\}\end{aligned} \tag{6A.16b}$$

where equations (6A.16a) and (6A.16b) are for the cases of the undamped and damped systems, respectively. Finally, the Green functions in the x-ω domain for the *Love* wave problem are of the form

$$\begin{aligned}\tilde{G}_{yy,l}(x, z, \omega) = &-\frac{1}{G_{\rm I}}\sum_{m=1}^{M}\left[\frac{N_l(k_m)}{\Delta'(k_m)}\sin kx\right] \\ &-\frac{1}{\pi G_{\rm I}}\left\{\int_0^{\infty} {\rm Im}\left[K_l(-{\rm i}\eta, {\rm i}\bar{\gamma}, -\bar{\beta}, \Delta_{\rm II})\right] e^{-\eta x} d\eta + {\rm i}\int_0^{k_{\rm II}} {\rm Im}\left[K_l(k, -{\rm i}\hat{\gamma}, \beta, \Delta_{\rm I})\right] e^{-{\rm i}kx} dk\right\}\end{aligned} \tag{6A.17a}$$

for the undamped system, and

$$\tilde{G}_{yy,I}(x,z,\omega)=-\frac{\mathrm{i}}{G_{\mathrm{I}}}\sum_{m=1}^{M}\frac{N_l(k_m)}{\Delta'(k_m)}e^{-\mathrm{i}k_m x}$$
$$-\frac{1}{\pi G_{\mathrm{I}}}\left\{\int_0^{\infty}\mathrm{Im}\left[K_l(-\mathrm{i}\eta,\mathrm{i}\overline{\gamma},-\overline{\beta},\Delta_{\mathrm{II}})\right]e^{-\eta x}d\eta+\mathrm{i}\int_0^{k_{\mathrm{II}}}\mathrm{Im}\left[K_l(k,-\mathrm{i}\hat{\gamma},\beta,\Delta_{\mathrm{I}})\right]e^{-\mathrm{i}kx}dk\right\} \tag{6A.17b}$$

for the damped system.

To complete our formulation, we present the Green's functions in more explicit form as
a) Undamped system:

$$\tilde{G}_{yy,\mathrm{I}}(x,z,\omega)=\frac{1}{G_{\mathrm{I}}}\sum_{m=1}^{M}\left[\frac{1}{\Delta'(k_m)}\left(\cos\beta_m z+\mu\frac{\gamma_m}{\beta_m}\sin\beta_m z\right)\sin k_m x\right]$$
$$+\frac{1}{\pi G_{\mathrm{I}}}\left\{\int_0^{\infty}\mathrm{Im}\left[\frac{1}{\Delta_{\mathrm{II}}}\left(\cos\overline{\beta}z+\mu\frac{\mathrm{i}\overline{\gamma}}{\overline{\beta}}\sin\overline{\beta}z\right)\right]e^{-\eta x}d\eta\right. \tag{6A.18a}$$
$$\left.+\mathrm{i}\int_0^{k_{\mathrm{II}}}\mathrm{Im}\left[\frac{1}{\Delta_{\mathrm{I}}}\left(\cos\beta z-\mu\frac{\mathrm{i}\hat{\gamma}}{\beta}\sin\beta z\right)\right]e^{-\mathrm{i}kx}dk\right\}$$

$$\tilde{G}_{yy,\mathrm{II}}(x,z,\omega)=\frac{1}{G_{\mathrm{I}}}\sum_{m=1}^{M}\left[\frac{e^{\gamma_m z}}{\Delta'(k_m)}\sin k_m x\right]$$
$$+\frac{1}{\pi G_{\mathrm{I}}}\left\{\int_0^{\infty}\mathrm{Im}\left[\frac{e^{\mathrm{i}\overline{\gamma}z}}{\Delta_{\mathrm{II}}}\right]e^{-\eta x}d\eta+\mathrm{i}\int_0^{k_{\mathrm{II}}}\mathrm{Im}\left[\frac{e^{-\mathrm{i}\hat{\gamma}z}}{\Delta_{\mathrm{I}}}\right]e^{-\mathrm{i}kx}dk\right\} \tag{6A.18b}$$

b) Damped system:

$$\tilde{G}_{yy,\mathrm{I}}(x,z,\omega)=\frac{\mathrm{i}}{G_{\mathrm{I}}}\sum_{m=1}^{M}\left[\frac{1}{\Delta'(k_m)}\left(\cos\beta_m z+\mu\frac{\gamma_m}{\beta_m}\sin\beta_m z\right)e^{-\mathrm{i}k_m x}\right]$$
$$+\frac{1}{\pi G_{\mathrm{I}}}\left\{\int_0^{\infty}\mathrm{Im}\left[\frac{1}{\Delta_{\mathrm{II}}}\left(\cos\overline{\beta}z+\mu\frac{\mathrm{i}\overline{\gamma}}{\overline{\beta}}\sin\overline{\beta}z\right)\right]e^{-\eta x}d\eta\right. \tag{6A.18c}$$
$$\left.+\mathrm{i}\int_0^{k_{\mathrm{II}}}\mathrm{Im}\left[\frac{1}{\Delta_{\mathrm{I}}}\left(\cos\beta z-\mu\frac{\mathrm{i}\hat{\gamma}}{\beta}\sin\beta z\right)\right]e^{-\mathrm{i}kx}dk\right\}$$

$$\tilde{G}_{yy,\mathrm{II}}(x,z,\omega)=\frac{\mathrm{i}}{G_{\mathrm{I}}}\sum_{m=1}^{M}\left[\frac{e^{\gamma_m z}}{\Delta'(k_m)}e^{-\mathrm{i}k_m x}\right]$$
$$+\frac{1}{\pi G_{\mathrm{I}}}\left\{\int_0^{\infty}\mathrm{Im}\left[\frac{e^{\mathrm{i}\overline{\gamma}z}}{\Delta_{\mathrm{II}}}\right]e^{-\eta x}d\eta+\mathrm{i}\int_0^{k_{\mathrm{II}}}\mathrm{Im}\left[\frac{e^{-\mathrm{i}\hat{\gamma}z}}{\Delta_{\mathrm{I}}}\right]e^{-\mathrm{i}kx}dk\right\} \tag{6A.18d}$$

where $\beta_m=\sqrt{k_{\mathrm{I}}^2-k_m^2}$, $\gamma_m=\sqrt{k_m^2-k_{\mathrm{II}}^2}$.

Now, we generalize the solutions for the two additional cases of $C_{\mathrm{I}}=C_{\mathrm{II}}$ and $C_{\mathrm{I}}>C_{\mathrm{II}}$. In both of these cases, there do not exist any poles. Therefore, the residue summations are canceled in equations (6A.17a and b). Then, the Green functions are modified to be of the form

$$\tilde{G}_{yy,I}(x,z,\omega)=-\frac{1}{\pi G_{\mathrm{I}}}\left\{\int_0^{\infty}\mathrm{Im}\left[K_l(-\mathrm{i}\eta,\mathrm{i}\overline{\gamma},-\overline{\beta},\Delta_{\mathrm{II}})\right]e^{-\eta x}d\eta+\mathrm{i}\int_0^{k_{\mathrm{II}}}\mathrm{Im}\left[K_l(k,-\mathrm{i}\hat{\gamma},\beta,\Delta_{\mathrm{I}})\right]e^{-\mathrm{i}kx}dk\right\} \tag{6A.19}$$

6A.2 Green functions for *SV-P* surface line loads

Next, we consider a homogeneous half-space ($z \le 0$) subjected to *SV-P* surface line loads, as shown in figure 6A.4. The governing equation is given in matrix form as

$$\rho \ddot{\mathbf{u}} - \mathbf{L}^T \mathbf{D} \mathbf{L} \mathbf{u} = \mathbf{p} \tag{6A.20}$$

where ρ is the mass density, the superscript dot represents the partial derivative with respect to time t,

$$\mathbf{u}(x,z,t) = \{u \quad w\}^T \qquad \text{(the displacement vector)} \tag{6A.21a}$$

$$\mathbf{p}(x,z,t) = \{p_x \quad p_z\}^T \qquad \text{(the applied line load vector)} \tag{6A.21b}$$

$$\mathbf{D} = \begin{Bmatrix} \lambda+2G & \lambda & \cdot \\ \lambda & \lambda+2G & \cdot \\ \cdot & \cdot & G \end{Bmatrix} \qquad \text{(the constitutive matrix)} \tag{6A.21c}$$

$$\mathbf{L} = \mathbf{L}_x \frac{\partial}{\partial x} + \mathbf{L}_z \frac{\partial}{\partial z} \qquad \text{(the differential operator)} \tag{6A.21d}$$

$$\mathbf{L}_x = \begin{Bmatrix} 1 & \cdot & \cdot \\ \cdot & \cdot & 1 \end{Bmatrix}^T, \text{ and } \mathbf{L}_z = \begin{Bmatrix} \cdot & \cdot & 1 \\ \cdot & 1 & \cdot \end{Bmatrix}^T. \tag{6A.21e,f}$$

In the constitutive matrix $\mathbf{D}$, the constants λ and G are called *Lamé*'s constants. Applying a double Fourier transformations to $\mathbf{u}(x,z,t)$ with respect to x and t, we obtain the general solution in the k-ω domain in the absence of the external force $\mathbf{p}$ as

$$\bar{\mathbf{u}}(k,z,\omega) = \begin{Bmatrix} \bar{u} \\ \bar{w} \end{Bmatrix} = \begin{bmatrix} e^{rz} & e^{sz} \\ \mathrm{i}\frac{r}{k}e^{rz} & \mathrm{i}\frac{k}{s}e^{sz} \end{bmatrix} \begin{Bmatrix} A \\ B \end{Bmatrix} \tag{6A.22}$$

where A and B are unknown constants, $r = \sqrt{k^2 - (\omega/C_P)^2}$, $s = \sqrt{k^2 - (\omega/C_S)^2}$, $C_P = \sqrt{(\lambda+2G)/\rho}$, and $C_S = \sqrt{G/\rho}$. Satisfying the traction boundary conditions at the top surface with equation (6A.21), we obtain the Green functions $\bar{G}_{ij}$ in the k-ω domain as

$$\bar{G}_{xx}(k,z,\omega) = \frac{1}{G\Delta}\left[2ke^{rz} - s\left(\frac{s}{k}+\frac{k}{s}\right)e^{sz}\right] = \frac{\mathrm{e}_{xx}}{G}\frac{N_{xx}}{\Delta} = \frac{\mathrm{e}_{xx}}{G}K_{xx} \tag{6A.23a}$$

$$\bar{G}_{zx}(k,z,\omega) = \frac{\mathrm{i}}{G\Delta}\left[2re^{rz} - k\left(\frac{s}{k}+\frac{k}{s}\right)e^{sz}\right] = \frac{\mathrm{e}_{zx}}{G}\frac{N_{zx}}{\Delta} = \frac{\mathrm{e}_{zx}}{G}K_{zx} \tag{6A.23b}$$

$$\bar{G}_{xz}(k,z,\omega) = \frac{\mathrm{i}}{G\Delta}\left[-k\left(\frac{s}{k}+\frac{k}{s}\right)e^{rz} + 2re^{sz}\right] = \frac{\mathrm{e}_{xz}}{G}\frac{N_{xz}}{\Delta} = \frac{\mathrm{e}_{xz}}{G}K_{xz} \tag{6A.23c}$$

$$\bar{G}_{zz}(k,z,\omega) = \frac{1}{G\Delta}\left[r\left(\frac{s}{k}+\frac{k}{s}\right)e^{rz} - 2r\frac{k}{s}e^{sz}\right] = \frac{\mathrm{e}_{zz}}{G}\frac{N_{zz}}{\Delta} = \frac{\mathrm{e}_{zz}}{G}K_{zz} \tag{6A.23d}$$

where $\mathrm{e}_{xx}=\mathrm{e}_{zz}=1$, $\mathrm{e}_{zx}=\mathrm{e}_{xz}=\mathrm{i}=\sqrt{-1}$, K_{ij} are the kernels in the integrals introduced later, and N_{ij} the numerators in each kernel K_{ij}. Furthermore, Δ is the *Rayleigh* surface wave equation defined as

$$\Delta = 4kr - ks\left(\frac{s}{k}+\frac{k}{s}\right)^2 \tag{6A.24}$$

The *Rayleigh* surface wave equation provides a non-dispersive *SV-P* propagation mode, i.e.

$$k_R = \omega / C_R \tag{6A.25a}$$

$$C_R = C_S(-0.0276\nu^3 - 0.056\nu^2 + 0.197\nu + 0.874) \tag{6A.25b}$$

where C_R is the phase velocity of Rayleigh waves, and ν is the Poisson's ratio of the half-space. It is also observed in equations (6A.23) that all the K_{ij} are odd functions of both s and r. Additionally, K_{zx} and K_{xz} are odd functions of k, which affects the phase of K_{ij}'s when k is replaced by $i\eta$ in the branch-cut integrals, as will be shown later.

We now perform an inverse Fourier transformations of $\bar{G}_{ij}$ so as to obtain the Green functions $\tilde{G}_{ij}$ in the x-ω domain as

$$\begin{aligned}\tilde{G}_{ij}(x,z,\omega) &= \frac{1}{2\pi}\int_{-\infty}^{\infty}\bar{G}_{ij}(k,z,\omega)e^{-ikx}dk \\ &= \frac{e_{ij}}{2\pi G}\int_{-\infty}^{\infty}\frac{N_{ij}}{\Delta}e^{-ikx}dk = \frac{e_{ij}}{2\pi G}\int_{-\infty}^{\infty}K_{ij}(k,s,r,\Delta)e^{-ikx}dk \\ &= \frac{e_{ij}}{2\pi G}I_{ij}\end{aligned} \tag{6A.26}$$

where $i,j = x,z$, and I_{ij} represent the integrals to be calculated. It is also noticed that the kernels K_{ij} are expressed as function of k, s, r, and Δ, which renders our future derivation much simpler. As shown in equation (6A.26), the kernels are singular when Δ=0, or equivalently $k=k_R$. Therefore, the integrals in equation (6A.26) can not be performed properly. To avoid this problem, we deform the integral paths into the complex wavenumber plane, or ξ-plane, as shown in figure 6A.5. We close the integral path by including the lower ξ-plane, because we use e^{-ikx} in equation (6A.26). Also, since all the kernels are odd functions of both s and r, the branch-cuts around both of the two branch points of $k_S = \omega / C_S$ and $k_P = \omega / C_P$ are placed along $\mathrm{Re}\, s = 0$ and $\mathrm{Re}\, r = 0$. Then, the result contour integrals are given as

$$\oint dI_{ij} = I_{ij} + \int_{C_{-\infty}} dI_{ij} + \int_{Branch-cut} dI_{ij} = -2\pi i \sum (\text{Residues})_{ij} \tag{6A.27a}$$

$$\begin{aligned}\int_{Branch-cut} dI_{ij} &= \int_{-i\infty}^{0} dI_{ij} + \int_{0}^{k_P} dI_{ij} + \int_{k_P}^{k_S} dI_{ij} \\ &+ \int_{k_S}^{k_P} dI_{ij} + \int_{k_P}^{0} dI_{ij} + \int_{0}^{-i\infty} dI_{ij}\end{aligned} \tag{6A.27b}$$

In the above equation, the integrals on $C_{-\infty}$ vanish, so equation (6A.27a) can be expresses as

$$I_{ij} = -2\pi i \sum (\text{Residues})_{ij} - \int_{Branch-cut} dI_{ij} \tag{6A.28}$$

In order to calculate the correct branch-cut integrals, we need to identify the branch-cuts and the phases of s and r. For this purpose, we make use of figure 6A.3 in the previous section just by replacing k_{II} by k_S or k_P in this section. Then, the branch-cut integrals in (6A.27b) are expressed in terms of s, r, Δ as

$$\begin{aligned}\int_{Branch-cut} dI_{ij} &= \int_{0}^{k_P} K_{ij}(k,-i\bar{s},-i\bar{r},\Delta_A^*)e^{-ikx}dk + \int_{k_P}^{0} K_{ij}(k,i\bar{s},i\bar{r},\Delta_A)e^{-ikx}dk \\ &+ \int_{k_P}^{k_S} K_{ij}(k,-i\bar{s},r,\Delta_B^*)e^{-ikx}dk + \int_{k_S}^{k_P} K_{ij}(k,i\bar{s},r,\Delta_B)e^{-ikx}dk \\ &+ \int_{0}^{\infty} K_{ij}(i\eta,-i\beta,-i\alpha,-\Delta_C)e^{-i(i\eta)x}d(i\eta) + \int_{-\infty}^{0} K_{ij}(i\eta,i\beta,i\alpha,\Delta_C)e^{-i(i\eta)x}d(i\eta)\end{aligned} \tag{6A.29}$$

where

$$\bar{s} = \sqrt{k_S^2 - k^2}, \qquad \bar{r} = \sqrt{k_P^2 - k^2},$$

$$\beta=\sqrt{\eta^2+k_S^2}\,, \qquad \alpha=\sqrt{\eta^2+k_P^2}\,,$$
$$\Delta_A=\Delta(k,\mathrm{i}\bar{s},\mathrm{i}\bar{r}), \qquad \Delta_A^*=\Delta(k,-\mathrm{i}\bar{s},-\mathrm{i}\bar{r})=conj(\Delta_A)$$
$$\Delta_B=\Delta(k,\mathrm{i}\bar{s},r), \qquad \Delta_B^*=\Delta(k,-\mathrm{i}\bar{s},r)=conj(\Delta_B)$$
$$\Delta_C=\Delta(\mathrm{i}\eta,\mathrm{i}\beta,\mathrm{i}\alpha) \tag{6A.30a-i}$$

Changing the integration directions, we obtain

$$\begin{aligned}\int_{Branch-cut} dI_{ij} &= \int_0^{k_P} K_{ij}(k,-\mathrm{i}\bar{s},-\mathrm{i}\bar{r},\Delta_A^*)e^{-\mathrm{i}kx}dk - \int_0^{k_P} K_{ij}(k,\mathrm{i}\bar{s},\mathrm{i}\bar{r},\Delta_A)e^{-\mathrm{i}kx}dk \\ &+ \int_{k_P}^{k_S} K_{ij}(k,-\mathrm{i}\bar{s},r,\Delta_B^*)e^{-\mathrm{i}kx}dk - \int_{k_P}^{k_S} K_{ij}(k,\mathrm{i}\bar{s},r,\Delta_B)e^{-\mathrm{i}kx}dk \\ &+ \int_0^{\infty} K_{ij}(\mathrm{i}\eta,-\mathrm{i}\beta,-\mathrm{i}\alpha,-\Delta_C)e^{-\mathrm{i}(\mathrm{i}\eta)x}d(\mathrm{i}\eta) - \int_0^{\infty} K_{ij}(\mathrm{i}\eta,\mathrm{i}\beta,\mathrm{i}\alpha,\Delta_C)e^{-\mathrm{i}(\mathrm{i}\eta)x}d(\mathrm{i}\eta)\end{aligned} \tag{6A.31}$$

Making use of the conjugate relationships between the kernels, not the whole integrands, we obtain the following.

$$\begin{aligned}\int_{Branch-cut} dI_{ij} = &- \int_0^{k_P} 2\mathrm{i}\,\mathrm{Im}\left[K_{ij}(k,\mathrm{i}\bar{s},\mathrm{i}\bar{r},\Delta_A)\right]e^{-\mathrm{i}kx}dk \\ &- \int_{k_P}^{k_S} 2\mathrm{i}\,\mathrm{Im}\left[K_{ij}(k,\mathrm{i}\bar{s},r,\Delta_B)\right]e^{-\mathrm{i}kx}dk \\ &+ \int_0^{\infty} 2\mathrm{e}_{ij}^{-1}\,\mathrm{Im}\left[\mathrm{e}_{ij}K_{ij}(\mathrm{i}\eta,\mathrm{i}\beta,\mathrm{i}\alpha,\Delta_C)\right]e^{\eta x}d\eta\end{aligned} \tag{6A.32}$$

The use of e_{ij} in the third term in equation (6A.32) is related to the fact that K_{zx} and K_{xz} are odd functions of k or $\mathrm{i}\eta$, as previously observed. Furthermore, we replace η by $-\eta$ and then obtain the branch-cut integrals in the form.

$$\begin{aligned}\int_{Branch-cut} dI_{ij} = &- \int_0^{k_P} 2\mathrm{i}\,\mathrm{Im}\left[K_{ij}(k,\mathrm{i}\bar{s},\mathrm{i}\bar{r},\Delta_A)\right]e^{-\mathrm{i}kx}dk \\ &- \int_{k_P}^{k_S} 2\mathrm{i}\,\mathrm{Im}\left[K_{ij}(k,\mathrm{i}\bar{s},r,\Delta_B)\right]e^{-\mathrm{i}kx}dk \\ &- \int_0^{\infty} 2\mathrm{e}_{ij}^{-1}\,\mathrm{Im}\left[\mathrm{e}_{ij}K_{ij}(-\mathrm{i}\eta,\mathrm{i}\beta,\mathrm{i}\alpha,\Delta_{C,-\eta})\right]e^{-\eta x}d\eta\end{aligned} \tag{6A.33}$$

where $\Delta_{C,-\eta}=\Delta(-\mathrm{i}\eta,\mathrm{i}\beta,\mathrm{i}\alpha)$.

We next continue to calculate the residues in equation (6A.28). The residues for the poles of $k=\pm k_R$ are

$$(\text{Residues})_{ij}=\lim_{k\to\pm k_R}(k\mp k_R)\frac{N_{ij}}{\Delta}e^{-\mathrm{i}kx}=\frac{N_{ij}(\pm k_R)}{\Delta'(\pm k_R)}e^{\mp\mathrm{i}k_Rx} \tag{6A.34}$$

where

$$\Delta'=\frac{d\Delta}{dk}=4r\left(1+\frac{k^2}{r^2}\right)-5s\left(1+\frac{k^2}{s^2}\right)+k\left(\frac{k^3}{s^3}+\frac{s^3}{k^3}\right) \tag{6A.35}$$

Then, the integrals I_{ij} are expressed as

$$\begin{aligned}I_{ij} = &-\pi\mathrm{i}\left[\frac{N_{ij}(-k_R)}{\Delta'(-k_R)}e^{\mathrm{i}k_Rx}+\frac{N_{ij}(k_R)}{\Delta'(k_R)}e^{-\mathrm{i}k_Rx}\right] \\ &+ \int_0^{k_P} 2\mathrm{i}\,\mathrm{Im}\left[K_{ij}(k,\mathrm{i}\bar{s},\mathrm{i}\bar{r},\Delta_A)\right]e^{-\mathrm{i}kx}dk \\ &+ \int_{k_P}^{k_S} 2\mathrm{i}\,\mathrm{Im}\left[K_{ij}(k,\mathrm{i}\bar{s},r,\Delta_B)\right]e^{-\mathrm{i}kx}dk \\ &+ \int_0^{\infty} 2\mathrm{e}_{ij}^{-1}\,\mathrm{Im}\left[\mathrm{e}_{ij}K_{ij}(-\mathrm{i}\eta,\mathrm{i}\beta,\mathrm{i}\alpha,\Delta_C)\right]e^{-\eta x}d\eta\end{aligned} \tag{6A.36a}$$

$$
\begin{aligned}
I_{ij} = &-2\pi \mathrm{i} \frac{N_{ij}(k_R)}{\Delta'(k_R)} e^{-\mathrm{i}k_R x} \\
&+ \int_0^{k_P} 2\mathrm{i}\,\mathrm{Im}\left[K_{ij}(k, \mathrm{i}\overline{s}, \mathrm{i}\overline{r}, \Delta_A)\right] e^{-\mathrm{i}kx} dk \\
&+ \int_{k_P}^{k_S} 2\mathrm{i}\,\mathrm{Im}\left[K_{ij}(k, \mathrm{i}\overline{s}, r, \Delta_B)\right] e^{-\mathrm{i}kx} dk \\
&+ \int_0^{\infty} 2\mathrm{e}_{ij}^{-1}\,\mathrm{Im}\left[\mathrm{e}_{ij} K_{ij}(-\mathrm{i}\eta, \mathrm{i}\beta, \mathrm{i}\alpha, \Delta_C)\right] e^{-\eta x} d\eta
\end{aligned}
\tag{6A.36b}
$$

where equations (6A.36a) and (6A.36b) are for the cases of the undamped and damped systems, respectively. The final expressions for the Green functions in the x-ω domain are then

$$
\begin{aligned}
\tilde{G}_{ij}(x, z, \omega) = &\frac{-\mathrm{i}\mathrm{e}_{ij}}{2G}\left[\frac{N_{ij}(-k_R)}{\Delta'(-k_R)} e^{\mathrm{i}k_R x} + \frac{N_{ij}(k_R)}{\Delta'(k_R)} e^{-\mathrm{i}k_R x}\right] \\
&+ \frac{\mathrm{e}_{ij}}{\pi G}\left\{\mathrm{i}\int_0^{k_P} \mathrm{Im}\left[K_{ij}(k, \mathrm{i}\overline{s}, \mathrm{i}\overline{r}, \Delta_A)\right] e^{-\mathrm{i}kx} dk\right. \\
&+ \mathrm{i}\int_{k_P}^{k_S} \mathrm{Im}\left[K_{ij}(k, \mathrm{i}\overline{s}, r, \Delta_B)\right] e^{-\mathrm{i}kx} dk \\
&\left.+ \int_0^{\infty} \mathrm{e}_{ij}^{-1}\,\mathrm{Im}\left[\mathrm{e}_{ij} K_{ij}(-\mathrm{i}\eta, \mathrm{i}\beta, \mathrm{i}\alpha, \Delta_C)\right] e^{-\eta x} d\eta\right\}
\end{aligned}
\tag{6A.37a}
$$

for the undamped system, and

$$
\begin{aligned}
\tilde{G}_{ij}(x, z, \omega) = &\frac{-\mathrm{i}\mathrm{e}_{ij}}{G} \frac{N_{ij}(k_R)}{\Delta'(k_R)} e^{-\mathrm{i}k_R x} \\
&+ \frac{\mathrm{e}_{ij}}{\pi G}\left\{\mathrm{i}\int_0^{k_P} \mathrm{Im}\left[K_{ij}(k, \mathrm{i}\overline{s}, \mathrm{i}\overline{r}, \Delta_A)\right] e^{-\mathrm{i}kx} dk\right. \\
&+ \mathrm{i}\int_{k_P}^{k_S} \mathrm{Im}\left[K_{ij}(k, \mathrm{i}\overline{s}, r, \Delta_B)\right] e^{-\mathrm{i}kx} dk \\
&\left.+ \int_0^{\infty} \mathrm{e}_{ij}^{-1}\,\mathrm{Im}\left[\mathrm{e}_{ij} K_{ij}(-\mathrm{i}\eta, \mathrm{i}\beta, \mathrm{i}\alpha, \Delta_C)\right] e^{-\eta x} d\eta\right\}
\end{aligned}
\tag{6A.37b}
$$

for the damped system.

Figures for appendix 6A

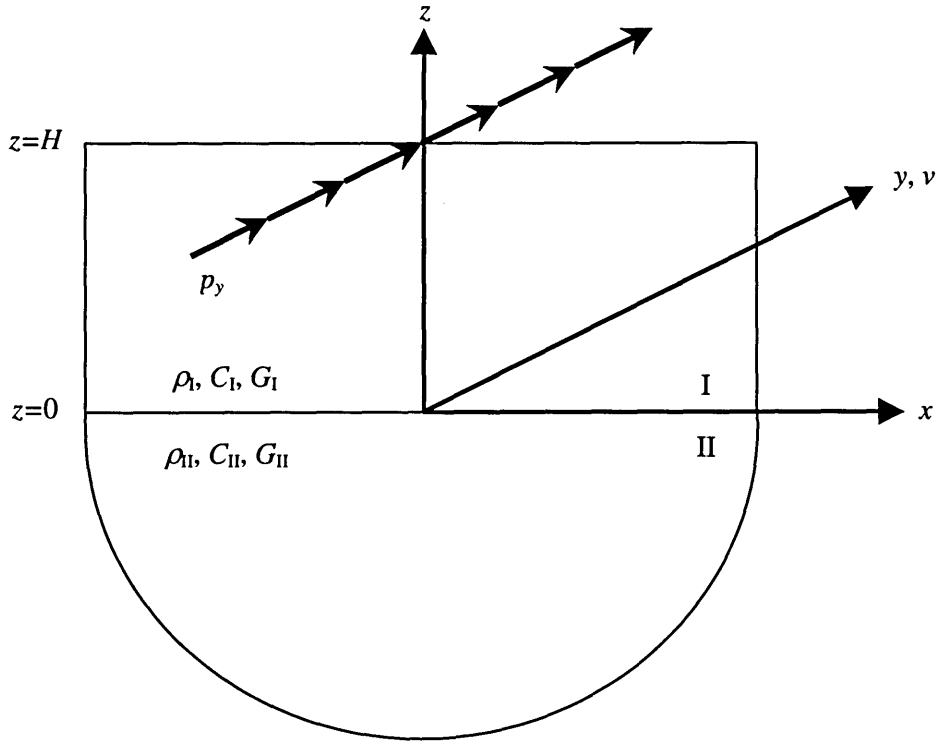

Figure 6A.1 Layered half-space subjected to an *SH* surface line load p_y

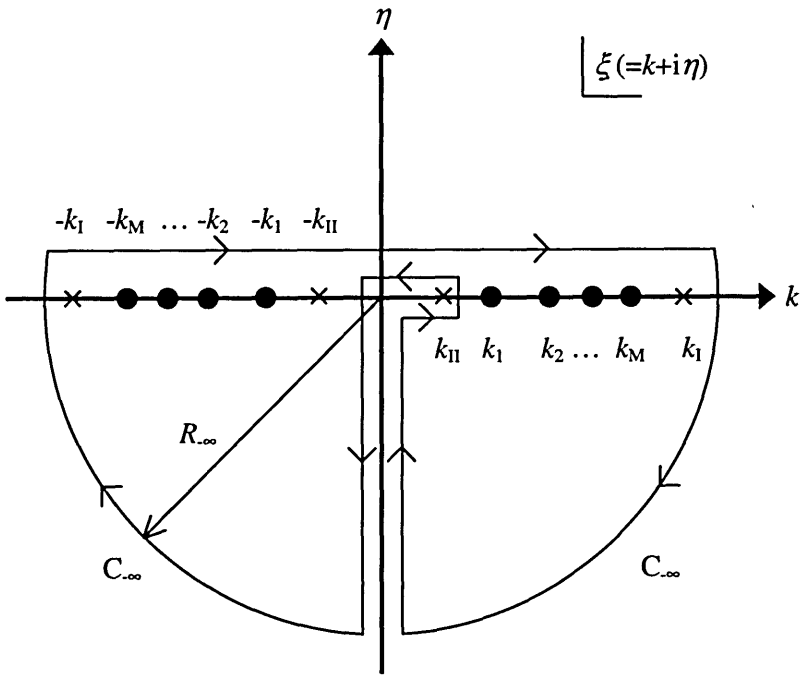

Figure 6A.2 Contour integral paths, branch-points (×), and poles (•): Love wave problem

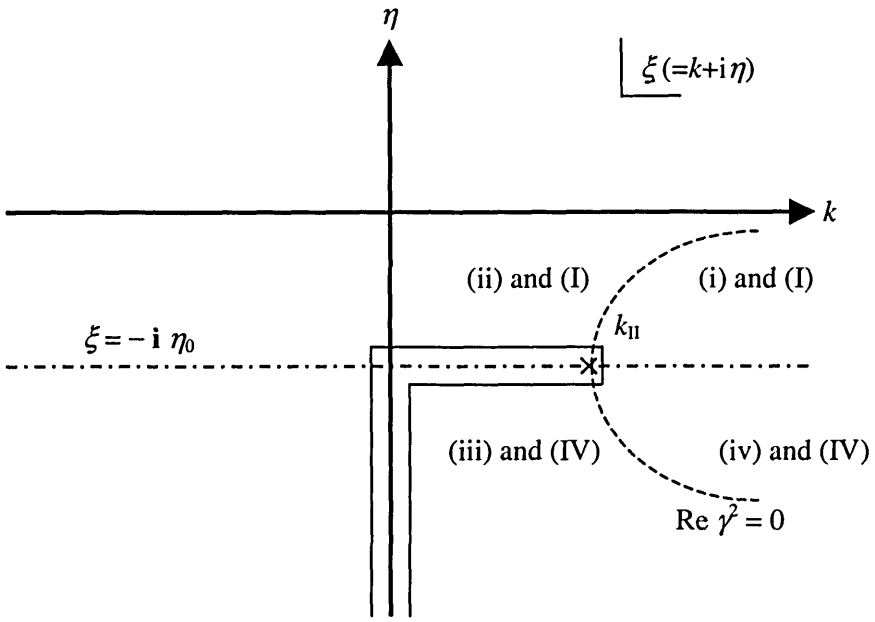

Figure 6A.3 Identification of the branch-cut and the quadrants for γ^2 (i-iv) and γ(I-IV)

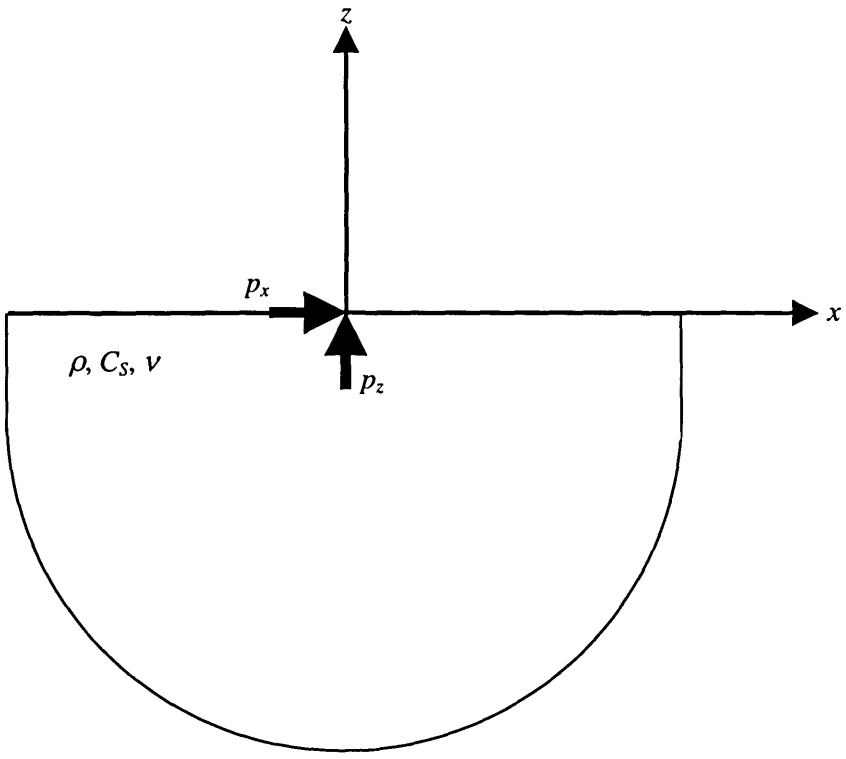

Figure 6A.4 Homogeneous half-space subjected to *SV-P* surface line loads

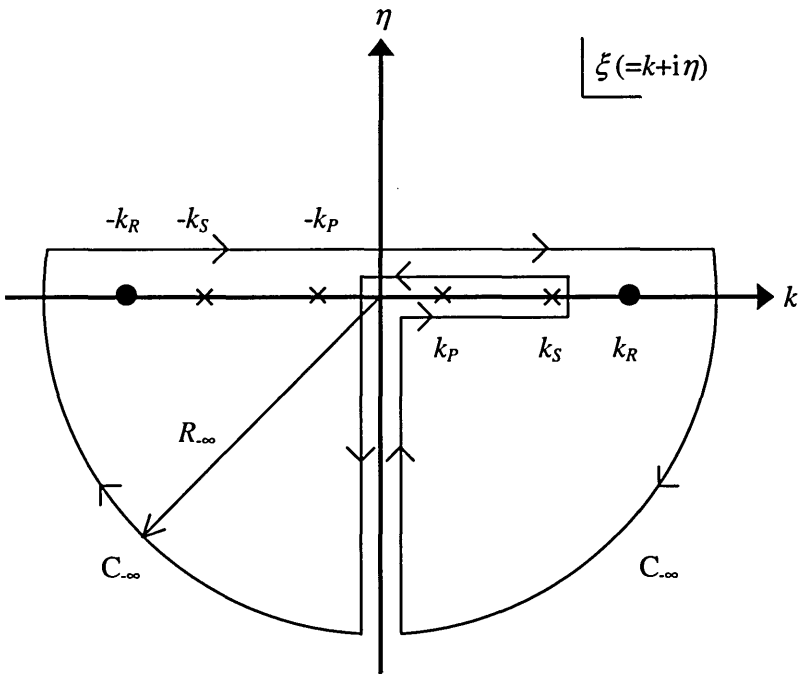

Figure 6A.5 Contour integral paths, branch-points (×), and poles (•): Rayleigh wave problem

Chapter 7 Cylindrical thin-layer method

7.1 Introduction

In this chapter, we introduce and formulate a new thin-layer method that is useful and efficient for the analysis of wave propagation in anisotropic, laminated cylindrical solids and shells. This new thin-layer method is herein called the cylindrical thin-layer method, or the CTLM for short. Basically, the CTLM is a new formulation TLM that is developed in the cylindrical coordinate system (r, θ, z), instead of in the Cartesian coordinate system (x, y, z) as the case of the TLM for flat layers. Also, discretization is performed along the radial (r–) direction in the sense of finite element. After developing the CTLM, we also verify its validation by means of an analytical comparison with the TLM for flat layers and two numerical examples for a homogeneous cylindrical solid and shell.

For the above purposes, we perform the following procedures. In section 7.2, we derive a general form of the wave equation for anisotropic material in the cylindrical coordinate system and also set up the boundary conditions that are necessary for formulating the CTLM. In section 7.3, we develop the CTLM by means of the principle of virtual work and the discretization of the wave equation along the radial (r–) direction. After all, we end up with the discrete wave equation for the systems of interest. For the verification of the formulated CTLM, we compare it with the TLM for flat layers, based on the fact that a hollow cylinder with a large radius relative to its thickness behaves like an infinite plate. In section 7.4, we solve the discrete wave equation by means of the Fourier transformations with respect to the spatial (θ, z) and temporal (t) variables and the associated eigenvalue problem in the frequency variable, which is a liner and real-valued problem. Thereafter, we apply the modal superposition to obtain the analytical response functions in the wavenumber-time domain. Finally, we perform the numerical transformations over wavenumbers to obtain the responses in the space-time domain due to dynamic excitations in the cylindrical solids and shells. In section 7.5, we formulate the analytical eigenvalue problem of the continuum that is associated with the propagation modes of isotropic homogeneous cylindrical solid and shell. In section 7.6, we compare the results of the eigenvalue problems obtained with the two of the CTLM and the analytical solution so as to verify the validations of the developed CTLM.

7.2 Wave equation in cylindrical coordinates

The wave equation and boundary conditions needed to describe and specify the behavior of an infinite cylindrical lamina are derived herein in the cylindrical coordinate system. The boundary conditions are prescribed on the inner and outer radial surfaces of each thin-layer. The material of interest is assumed to be anisotropic. At the end of this section, we obtain, using matrix methods, the wave equation for anisotropic media, and also for cross-anisotropic media so as to verify the proposed method.

7.2.1 Wave equation for cylindrically anisotropic media

Consider an infinitely long hollow cylinder (or cylindrical shell) of linear elastic, homogeneous, and anisotropy as shown in figure 7.2.1. The dynamic equilibrium equation, the stress-strain relation, and the strain-displacement relation at any point in the medium are expressed by

$$\mathbf{L}_\sigma^T \boldsymbol{\sigma} + \mathbf{b} = \rho \ddot{\mathbf{u}} \tag{7.2.1}$$

$$\boldsymbol{\sigma} = \mathbf{D}\boldsymbol{\varepsilon} \tag{7.2.2}$$

$$\boldsymbol{\varepsilon} = \mathbf{L}_\varepsilon \mathbf{u} \tag{7.2.3}$$

In the above equations, ρ is the mass density, and

$$\boldsymbol{\sigma} = \begin{bmatrix} \sigma_r & \sigma_\theta & \sigma_z & \tau_{\theta z} & \tau_{rz} & \tau_{r\theta} \end{bmatrix}^T \quad = \text{the stress tensor} \tag{7.2.4a}$$

$$\mathbf{b} = \begin{bmatrix} b_r & b_\theta & b_z \end{bmatrix}^T \quad = \text{the body load vector} \tag{7.2.4b}$$

$$\mathbf{u} = \begin{bmatrix} u_r & u_\theta & u_z \end{bmatrix}^T \quad = \text{the displacement vector} \tag{7.2.4c}$$

$$\boldsymbol{\varepsilon} = \begin{bmatrix} \varepsilon_r & \varepsilon_\theta & \varepsilon_z & \gamma_{\theta z} & \gamma_{rz} & \gamma_{r\theta} \end{bmatrix}^T \quad = \text{the strain tensor} \tag{7.2.4e}$$

$$\mathbf{D} = \begin{Bmatrix} d_{11} & d_{12} & d_{13} & d_{14} & d_{15} & d_{16} \\ d_{21} & d_{22} & d_{23} & d_{24} & d_{25} & d_{26} \\ d_{31} & d_{32} & d_{33} & d_{34} & d_{35} & d_{36} \\ d_{41} & d_{42} & d_{43} & d_{44} & d_{45} & d_{46} \\ d_{51} & d_{52} & d_{53} & d_{54} & d_{55} & d_{56} \\ d_{61} & d_{62} & d_{63} & d_{64} & d_{65} & d_{66} \end{Bmatrix} \quad = \text{constitutive matrix (symmetric!)} \tag{7.2.4f}$$

$$\mathbf{L}_\varepsilon^T = \begin{Bmatrix} \dfrac{\partial}{\partial r} & \dfrac{1}{r} & \cdot & \cdot & \dfrac{\partial}{\partial z} & \dfrac{1}{r}\dfrac{\partial}{\partial \theta} \\ \cdot & \dfrac{1}{r}\dfrac{\partial}{\partial \theta} & \cdot & \dfrac{\partial}{\partial z} & \cdot & \dfrac{\partial}{\partial r} - \dfrac{1}{r} \\ \cdot & \cdot & \dfrac{\partial}{\partial z} & \dfrac{1}{r}\dfrac{\partial}{\partial \theta} & \dfrac{\partial}{\partial r} & \cdot \end{Bmatrix} \quad = \text{diff. operator for strain} \tag{7.2.4g}$$

$$\mathbf{L}_\sigma^T = \begin{Bmatrix} \dfrac{\partial}{\partial r} + \dfrac{1}{r} & -\dfrac{1}{r} & \cdot & \cdot & \dfrac{\partial}{\partial z} & \dfrac{1}{r}\dfrac{\partial}{\partial \theta} \\ \cdot & \dfrac{1}{r}\dfrac{\partial}{\partial \theta} & \cdot & \dfrac{\partial}{\partial z} & \cdot & \dfrac{\partial}{\partial r} + \dfrac{2}{r} \\ \cdot & \cdot & \dfrac{\partial}{\partial z} & \dfrac{1}{r}\dfrac{\partial}{\partial \theta} & \dfrac{\partial}{\partial r} + \dfrac{1}{r} & \cdot \end{Bmatrix} \quad = \text{diff. operator for stress} \tag{7.2.4h}$$

The superscript T in the above equations denotes a transposed vector or matrix, and the double dot indicates the second partial derivative with respect to time t. Substituting equations (7.2.2 and 3) into equation (7.2.1), we obtain the wave equation in cylindrical coordinates:

$$\mathbf{L}_\sigma^T \mathbf{D} \mathbf{L}_\varepsilon^T \mathbf{u} + \mathbf{b} = \rho \ddot{\mathbf{u}} \tag{7.2.5}$$

On the other hand, the differential operators $\mathbf{L}_\varepsilon$ and $\mathbf{L}_\sigma$ can be written as

$$\mathbf{L}_\varepsilon = \mathbf{L}_r \frac{\partial}{\partial r} + \mathbf{L}_\theta \frac{1}{r}\frac{\partial}{\partial \theta} + \mathbf{L}_z \frac{\partial}{\partial z} + \mathbf{L}_1 \frac{1}{r} \tag{7.2.6a}$$

$$\mathbf{L}_\sigma = \mathbf{L}_r \frac{\partial}{\partial r} + \mathbf{L}_\theta \frac{1}{r}\frac{\partial}{\partial \theta} + \mathbf{L}_z \frac{\partial}{\partial z} + (\mathbf{L}_r - \mathbf{L}_1)\frac{1}{r} \tag{7.2.6b}$$

$$\mathbf{L}_r = \begin{bmatrix} 1 & \cdot & \cdot \\ \cdot & \cdot & \cdot \\ \cdot & \cdot & \cdot \\ \cdot & \cdot & \cdot \\ \cdot & \cdot & 1 \\ \cdot & 1 & \cdot \end{bmatrix}, \mathbf{L}_\theta = \begin{bmatrix} \cdot & \cdot & \cdot \\ \cdot & 1 & \cdot \\ \cdot & \cdot & \cdot \\ \cdot & \cdot & 1 \\ \cdot & \cdot & \cdot \\ 1 & \cdot & \cdot \end{bmatrix}, \mathbf{L}_z = \begin{bmatrix} \cdot & \cdot & \cdot \\ \cdot & \cdot & \cdot \\ \cdot & \cdot & 1 \\ \cdot & 1 & \cdot \\ 1 & \cdot & \cdot \\ \cdot & \cdot & \cdot \end{bmatrix}, \mathbf{L}_1 = \begin{bmatrix} \cdot & \cdot & \cdot \\ 1 & \cdot & \cdot \\ \cdot & \cdot & \cdot \\ \cdot & \cdot & \cdot \\ \cdot & \cdot & \cdot \\ \cdot & -1 & \cdot \end{bmatrix} \tag{7.2.6c-f}$$

It follows that the expansion of the product $\mathbf{L}_\sigma^T \mathbf{D} \mathbf{L}_\varepsilon$ is of the form

$$\mathbf{L}_\sigma^T \mathbf{D} \mathbf{L}_\varepsilon = \left(\mathbf{L}_r^T \frac{\partial}{\partial r} + \mathbf{L}_\theta^T \frac{1}{r}\frac{\partial}{\partial \theta} + \mathbf{L}_z^T \frac{\partial}{\partial z} + (\mathbf{L}_r^T - \mathbf{L}_1^T)\frac{1}{r} \right) \mathbf{D} \left(\mathbf{L}_r \frac{\partial}{\partial r} + \mathbf{L}_\theta \frac{1}{r}\frac{\partial}{\partial \theta} + \mathbf{L}_z \frac{\partial}{\partial z} + \mathbf{L}_1 \frac{1}{r} \right) \tag{7.2.7a}$$

which after more expansion yields

$$\begin{aligned} \mathbf{L}_\sigma^T \mathbf{D} \mathbf{L}_\varepsilon = {} & \mathbf{D}_{rr}\frac{\partial^2}{\partial r^2} + \mathbf{D}_{\theta\theta}\frac{1}{r^2}\frac{\partial^2}{\partial \theta^2} + \mathbf{D}_{zz}\frac{\partial^2}{\partial z^2} + \\ & + (\mathbf{D}_{r\theta} + \mathbf{D}_{\theta r})\frac{1}{r}\frac{\partial^2}{\partial r \partial \theta} + (\mathbf{D}_{rz} + \mathbf{D}_{zr})\frac{\partial^2}{\partial r \partial z} + (\mathbf{D}_{\theta z} + \mathbf{D}_{z\theta})\frac{1}{r}\frac{\partial^2}{\partial z \partial \theta} \\ & + (\mathbf{D}_{rr} + \mathbf{D}_{r1} - \mathbf{D}_{1r})\frac{1}{r}\frac{\partial}{\partial r} + (\mathbf{D}_{\theta 1} - \mathbf{D}_{1\theta})\frac{1}{r^2}\frac{\partial}{\partial \theta} \\ & + (\mathbf{D}_{rz} + \mathbf{D}_{z1} - \mathbf{D}_{1z})\frac{1}{r}\frac{\partial}{\partial z} - \mathbf{D}_{11}\frac{1}{r^2} \end{aligned} \tag{7.2.7b}$$

The material matrices $\mathbf{D}_{\alpha\beta}$ are defined by

$$\mathbf{D}_{\alpha\beta} = \mathbf{L}_\alpha^T \mathbf{D} \mathbf{L}_\beta, \qquad \text{with } \alpha, \beta = r, \theta, z, 1 \tag{7.2.8}$$

which are presented in Appendix 7A. These matrices depend only on the material properties, and can be readily evaluated for any anisotropic medium. It should be noted, however, that these equations assume that the constitutive properties are *not* a function of θ, so the material is assumed to have cylindrical symmetry. An example is the case of a wooden log. Substituting equations (7.2.7 and 8) into equation (7.2.5), we obtain the general wave equation for an anisotropic solid in cylindrical coordinates.

7.2.2 Boundary conditions

To assemble the discretized equations in the cylindrical thin-layer method in the next section, we need to specify the boundary conditions that relate the force equilibrium between the internal stresses and the external tractions at each cylindrical interface. Figure 7.2.2 shows the boundary conditions to be considered. The internal stresses in any cylindrical surface have three components and can be written in the vector form as

$$\mathbf{s} = \begin{bmatrix} \sigma_r & \tau_{r\theta} & \tau_{rz} \end{bmatrix}^T = \mathbf{L}_r^T \boldsymbol{\sigma} = \mathbf{L}_r^T \mathbf{D} \mathbf{L}_\varepsilon \mathbf{u} \tag{7.2.9a}$$

Application of equation (7.2.8) to equation (7.2.9a) yields then,

$$\mathbf{s} = \left[\mathbf{D}_{rr}\frac{\partial}{\partial r} + \mathbf{D}_{r\theta}\frac{1}{r}\frac{\partial}{\partial \theta} + \mathbf{D}_{rz}\frac{\partial}{\partial z} + \mathbf{D}_{r1}\frac{1}{r} \right] \mathbf{u} \tag{7.2.9b}$$

These matrices are given in Appendix 7A. Finally, the boundary conditions with prescribed external tractions $\mathbf{t}$ are of the form

$$\mathbf{t}-\mathbf{s}_v=\mathbf{0} \tag{7.2.10}$$

with $\mathbf{s}_v$ being the vector of internal stresses at the boundary with normal v. For an inner cylindrical boundary $\mathbf{s}_v=-\mathbf{s}$, while for an outer cylindrical boundary $\mathbf{s}_v=\mathbf{s}$, with $\mathbf{s}$ given in either case by equation (7.2.9a or b).

7.2.3 Wave equation for a cross-anisotropic medium

The elements of the constitutive matrix for a cross-anisotropic (transversely isotropic) material are given such that

$$\left.\begin{aligned} &d_{22}=d_{33}=\lambda+2G\\ &d_{23}=d_{32}=\lambda\\ &d_{44}=G \end{aligned}\right\}\ \text{in the isotropic plane } (\theta-z \text{ plane})$$

$$\left.\begin{aligned} &d_{11}=\lambda_t+2G_t\\ &d_{12}=d_{21}=d_{13}=d_{31}=\lambda_t\\ &d_{55}=d_{66}=G_t \end{aligned}\right\}\ \text{in the transverse direction (radial direction)} \tag{7.2.11}$$

All other elements d_{ij} are zero. Consequently, the wave equation in the cross-anisotropic medium is as follows:

$$\begin{aligned}
&\left[\begin{Bmatrix}\lambda_t+2G_t & \cdot & \cdot\\ \cdot & G_t & \cdot\\ \cdot & \cdot & G_t\end{Bmatrix}\frac{\partial^2}{\partial r^2}+\begin{Bmatrix}G_t & \cdot & \cdot\\ \cdot & \lambda+2G & \cdot\\ \cdot & \cdot & G\end{Bmatrix}\frac{1}{r^2}\frac{\partial^2}{\partial\theta^2}+\begin{Bmatrix}G_t & \cdot & \cdot\\ \cdot & G & \cdot\\ \cdot & \cdot & \lambda+2G\end{Bmatrix}\frac{\partial^2}{\partial z^2}\right.\\
&+\begin{Bmatrix}\cdot & \lambda_t+G_t & \cdot\\ \lambda_t+G_t & \cdot & \cdot\\ \cdot & \cdot & \cdot\end{Bmatrix}\frac{1}{r}\frac{\partial^2}{\partial r\partial\theta}+\begin{Bmatrix}\cdot & \cdot & \lambda_t+G_t\\ \cdot & \cdot & \cdot\\ \lambda_t+G_t & \cdot & \cdot\end{Bmatrix}\frac{\partial^2}{\partial r\partial z}+\begin{Bmatrix}\cdot & \cdot & \cdot\\ \cdot & \cdot & \lambda+G\\ \cdot & \lambda+G & \cdot\end{Bmatrix}\frac{1}{r}\frac{\partial^2}{\partial\theta\partial z}\\
&+\begin{Bmatrix}\lambda_t+2G_t & \cdot & \cdot\\ \cdot & G_t & \cdot\\ \cdot & \cdot & G_t\end{Bmatrix}\frac{1}{r}\frac{\partial}{\partial r}+\begin{Bmatrix}\cdot & -(\lambda+2G+G_t) & \cdot\\ \lambda+2G+G_t & \cdot & \cdot\\ \cdot & \cdot & \cdot\end{Bmatrix}\frac{1}{r^2}\frac{\partial}{\partial\theta}+\begin{Bmatrix}\cdot & \cdot & \lambda-\lambda_t\\ \cdot & \cdot & \cdot\\ \lambda+G_t & \cdot & \cdot\end{Bmatrix}\frac{1}{r}\frac{\partial}{\partial z}\\
&\left.-\begin{Bmatrix}\lambda+2G & \cdot & \cdot\\ \cdot & G_t & \cdot\\ \cdot & \cdot & \cdot\end{Bmatrix}\frac{1}{r^2}\right]\mathbf{u}+\mathbf{b}=\rho\ddot{\mathbf{u}}
\end{aligned} \tag{7.2.12}$$

By setting $\lambda_t=\lambda$ and $G_t=G$, we can obtain the case of isotropic materials.

7.3 Cylindrical thin-layer method

In this section, the cylindrical thin-layer method (CTLM) is formulated by means of the principle of virtual work and the discretization of the wave equation along the radial direction. In other words, the virtual work done by residual forces is considered, and both of linear and quadratic interpolations are employed to obtain the discretized equations. Finally, assembling all discretized wave equations, we obtain a system of partial differential equations. To verify this formulation,

all the coefficient matrices of a cylindrical thin-layer are compared with those for a flat thin-layer. This verification is based on the fact that a hollow cylinder whose radius is much larger than its thickness behaves as an infinite flat plate.

7.3.1 Formulation of the cylindrical thin-layer method

In the CTLM, physical cylindrical layers (or shells) are divided into thin-layers that are thin in the finite element sense. In addition, each thin-layer is divided into sub-layers. The number of sub-layers depends on the interpolation order m that is chosen for the cylindrical thin-layer formulation. Accordingly, the dimension of the total system of discretized equations also depends on the total number of thin-layers and the interpolation order m.

We cut out an individual cylindrical thin-layer from the whole system as shown in figure 7.3.1, and consider it as a free body in space. Depending on the interpolation order m, this thin-layer may contain in turn sub-layers which can be labeled with indices, l, l+1,..., l+m (from the inner layer to the outer surface). We also apply two external tractions $\mathbf{t}_l$ and $\mathbf{t}_{l+m}$ so as to preserve the dynamic equilibrium of this free body. We approximate the displacement field within a cylindrical thin-layer by means of an interpolation as follows.

$$\mathbf{u} = \mathbf{N}\mathbf{U} \tag{7.3.1}$$

where $\mathbf{N}$ is a matrix containing the interpolation polynomials, and $\mathbf{U}$ is a column vector composed of the interface displacement vectors

$$\mathbf{U} = \begin{bmatrix} \mathbf{u}_l^T & \mathbf{u}_{l+1}^T & \cdots & \mathbf{u}_{l+m}^T \end{bmatrix}^T \tag{7.3.2}$$

In the following, we will restrict our attention to only two interpolations of m=1 (*linear*) and 2 (*quadratic*). Then, the column vector $\mathbf{U}$ and the interpolation matrix $\mathbf{N}$ are of the form

$$\mathbf{U} = \begin{bmatrix} \mathbf{u}_l^T & \mathbf{u}_{l+1}^T \end{bmatrix}^T \tag{7.3.3a}$$

$$\mathbf{N} = \frac{1}{2}\begin{bmatrix} (1-\varsigma)\mathbf{I} & (1+\varsigma)\mathbf{I} \end{bmatrix} \qquad (-1 \le \varsigma \le 1) \tag{7.3.3b}$$

for linear expansion of m=1, and

$$\mathbf{U} = \begin{bmatrix} \mathbf{u}_l^T & \mathbf{u}_{l+1}^T & \mathbf{u}_{l+2}^T \end{bmatrix}^T \tag{7.3.4a}$$

$$\mathbf{N} = \frac{1}{2}\begin{bmatrix} \zeta(\zeta-1)\mathbf{I} & -2(\zeta-1)(\zeta+1)\mathbf{I} & \zeta(\zeta+1)\mathbf{I} \end{bmatrix} \qquad (-1 \le \varsigma \le 1) \tag{7.3.4b}$$

for quadratic expansion of m=2. In the above equations (7.3.3 and 4), $\mathbf{I}$ is the 3×3 identity matrix, $\varsigma = \frac{2}{h}(r - r_m)$, $h = r_{l+m} - r_l$ = thickness of a thin-layer, and $r_m = \frac{1}{2}(r_l + r_{l+m})$ = radius of the thin-layer's mid-surface. It follows that equation (7.3.1) can be rewritten in the following form

$$\mathbf{u} = \mathbf{N}\mathbf{U} = \frac{1}{2}\begin{bmatrix} (1-\varsigma)\mathbf{I} & (1+\varsigma)\mathbf{I} \end{bmatrix}\begin{bmatrix} \mathbf{u}_l \\ \mathbf{u}_{l+1} \end{bmatrix} \tag{7.3.5}$$

for linear expansion of m=1, and

$$\mathbf{u} = \mathbf{N}\mathbf{U} = \frac{1}{2}\begin{bmatrix} \zeta(\zeta-1)\mathbf{I} & -2(\zeta-1)(\zeta+1)\mathbf{I} & \zeta(\zeta+1)\mathbf{I} \end{bmatrix}\begin{bmatrix} \mathbf{u}_l \\ \mathbf{u}_{l+1} \\ \mathbf{u}_{l+2} \end{bmatrix} \tag{7.3.6}$$

for quadratic expansion of m=2, where

$$\mathbf{u}_l = \begin{bmatrix} u_r^l & u_\theta^l & u_z^l \end{bmatrix}^T,\ \mathbf{u}_{l+1} = \begin{bmatrix} u_r^{l+1} & u_\theta^{l+1} & u_z^{l+1} \end{bmatrix}^T,\ \text{and}\ \mathbf{u}_{l+2} = \begin{bmatrix} u_r^{l+2} & u_\theta^{l+2} & u_z^{l+2} \end{bmatrix}^T \tag{7.3.7abc}$$

Equations (7.3.5 and 6) represent a partial discretization of the displacement field, namely one in the layering direction, which in this case is the radial direction. This discretized displacement field is not an exact solution to the given wave equation. Thus when substituted into both the wave equation (7.2.5) and into the boundary conditions in equation (7.2.10), the displacement expansion in equation (7.3.1) does not identically satisfy equations (7.2.5) and (7.2.10). Therefore, in the sense of the finite element method, residual body forces $\mathbf{w}=\mathbf{w}(r,\theta,z,t)$ and the residual boundary tractions $\mathbf{q}=\mathbf{q}(r,\theta,z,t)$ are introduced as unbalanced forces:

$$\mathbf{L}_\sigma^T\mathbf{D}\mathbf{L}_\varepsilon\mathbf{u}+\mathbf{b}-\rho\ddot{\mathbf{u}}=\mathbf{w} \tag{7.3.8a}$$

$$\mathbf{t}-\mathbf{s}_v=\mathbf{q} \tag{7.3.8b}$$

Then, the method of weighted residuals requires that the virtual work done by the residual forces $\mathbf{w}$ and $\mathbf{q}$ as a result of the virtual displacement $\delta\mathbf{u}$ within the elementary volume $dV=r\,dr\,d\theta\,dz$ and on the boundary surface $dS=r\,d\theta\,dz$ of a cylindrical thin-layer be zero, i.e.,

$$\left[\delta\mathbf{u}_l^T\mathbf{q}_l r_l+\delta\mathbf{u}_{l+m}^T\mathbf{q}_{l+m}r_{l+m}+\int_{r_l}^{r_{l+m}}\delta\mathbf{u}^T\mathbf{w}r\,dr\right]d\theta\,dz=0 \tag{7.3.9}$$

In above equation (7.3.9), the first two terms represent the virtual work performed by the two residual tractions of $\mathbf{q}_l$ and $\mathbf{q}_{l+m}$ on the inner and outer boundaries of a cylindrical thin-layer, respectively. The integration term that follows corresponds to the virtual work done by the residual body forces $\mathbf{w}$. In equation (7.3.9), there is no term associated with internal stresses along the two boundaries that are parallel to the radial direction, i.e., $dS=r\,d\theta\,dr$ and $dS=dr\,dz$; the reason is that their virtual work cancels identically with the work of the equal and opposite stresses acting on neighboring elementary volumes. Substituting equations. (7.3.5, 6, and 8) into equation (7.3.9) and canceling out $d\theta\,dz$, we obtain

$$\begin{aligned}\delta\mathbf{u}_l^T\mathbf{t}_l r_l+\delta\mathbf{u}_{l+m}^T\mathbf{t}_{l+m}r_{l+m}+\delta\mathbf{U}^T\int_{r_l}^{r_{l+m}}\mathbf{N}^T\mathbf{b}r\,dr=\delta\mathbf{U}^T\left\{\int_{r_l}^{r_{l+m}}\mathbf{N}^T\mathbf{N}\rho r\,dr\right\}\ddot{\mathbf{U}}\\ -\delta\mathbf{U}^T\left\{\int_{r_l}^{r_{l+m}}\mathbf{N}^T\mathbf{L}_\sigma^T\mathbf{D}\mathbf{L}_\varepsilon\mathbf{N}r\,dr\right\}\mathbf{U}-\delta\mathbf{u}_l^T\mathbf{s}_l r_l+\delta\mathbf{u}_{l+m}^T\mathbf{s}_{l+m}r_{l+m}\end{aligned} \tag{7.3.10}$$

When we require this expression to be valid for arbitrary variations $\delta\mathbf{U}$, we obtain the dynamic equilibrium equation for a cylindrical thin-layer of the following form

$$\begin{bmatrix}\mathbf{p}_l\\ \mathbf{p}_{l+1}\\ \vdots\\ \mathbf{p}_{l+m}\end{bmatrix}=\left\{\int_{r_l}^{r_{l+m}}\mathbf{N}^T\mathbf{N}\rho r\,dr\right\}\begin{bmatrix}\ddot{\mathbf{u}}_l\\ \ddot{\mathbf{u}}_{l+1}\\ \vdots\\ \ddot{\mathbf{u}}_{l+m}\end{bmatrix}+\begin{bmatrix}-\mathbf{L}_r^T\mathbf{D}\mathbf{L}_\varepsilon r_l\mathbf{u}_l\\ \\ \\ \mathbf{L}_r^T\mathbf{D}\mathbf{L}_\varepsilon r_{l+m}\mathbf{u}_{l+m}\end{bmatrix}-\left\{\int_{r_l}^{r_{l+m}}\mathbf{N}^T\mathbf{L}_\sigma^T\mathbf{D}\mathbf{L}_\varepsilon\mathbf{N}r\,dr\right\}\begin{bmatrix}\mathbf{u}_l\\ \mathbf{u}_{l+1}\\ \vdots\\ \mathbf{u}_{l+m}\end{bmatrix} \tag{7.3.11}$$

The left hand side is the vector of the consistent external tractions $\mathbf{p}$ acting on the sub-layer interfaces which are the resultant of the interface tractions $\mathbf{t}$ and body loads $\mathbf{b}$. On the other hand, the right hand side contains the inertial loads as well as the elastic loads of deformation. Calculation of the above equation (7.3.11) with the chosen interpolation polynomials of order m and the material constitutive matrix yields

$$\mathbf{P}=\mathbf{M}\ddot{\mathbf{U}}-\mathbf{A}_{\theta\theta}\frac{\partial^2\mathbf{U}}{\partial\theta^2}-\mathbf{A}_{\theta z}\frac{\partial^2\mathbf{U}}{\partial\theta\,\partial z}-\mathbf{A}_{zz}\frac{\partial^2\mathbf{U}}{\partial z^2}-\mathbf{B}_\theta\frac{\partial\mathbf{U}}{\partial\theta}-\mathbf{B}_z\frac{\partial\mathbf{U}}{\partial z}+\mathbf{G}\mathbf{U} \tag{7.3.12}$$

where

$$\mathbf{P}=[\mathbf{p}_l\quad\mathbf{p}_{l+1}\quad\cdots\quad\mathbf{p}_{l+m}]^T \tag{7.3.13a}$$

$$\mathbf{M}=\int_{r_l}^{r_{l+m}}\rho r\mathbf{N}^T\mathbf{N}dr \tag{7.3.13b}$$

$$\mathbf{A}_{\theta\theta} = \int_{r_l}^{r_{l+m}} \frac{1}{r}\mathbf{N}^T\mathbf{D}_{\theta\theta}\mathbf{N}dr \tag{7.3.13c}$$

$$\mathbf{A}_{\theta z} = \int_{r_l}^{r_{l+m}} \mathbf{N}^T\left(\mathbf{D}_{\theta z} + \mathbf{D}_{z\theta}\right)\mathbf{N}dr \tag{7.3.13d}$$

$$\mathbf{A}_{zz} = \int_{r}^{r_{l+m}} r\mathbf{N}^T\mathbf{D}_{zz}\mathbf{N}dr \tag{7.3.13e}$$

$$\mathbf{B}_{\theta} = \int_{r_l}^{r_{l+m}} \mathbf{N}^T\mathbf{D}_{\theta r}\mathbf{N}'dr - \left\{\int_{r_l}^{r_{l+m}} \mathbf{N}^T\mathbf{D}_{\theta r}\mathbf{N}'dr\right\}^T + \int_{r_l}^{r_{l+m}} \frac{1}{r}\mathbf{N}^T\left(\mathbf{D}_{\theta 1} - \mathbf{D}_{1\theta}\right)\mathbf{N}dr \tag{7.3.13f}$$

$$\mathbf{B}_{z} = \int_{r_l}^{r_{l+m}} r\mathbf{N}^T\mathbf{D}_{zr}\mathbf{N}'dr - \left\{\int_{r_l}^{r_{l+m}} r\mathbf{N}^T\mathbf{D}_{zr}\mathbf{N}'dr\right\}^T + \int_{r_l}^{r_{l+m}} \mathbf{N}^T\left(\mathbf{D}_{z1} - \mathbf{D}_{1z}\right)\mathbf{N}dr \tag{7.3.13g}$$

$$\mathbf{G} = \int_{r_l}^{r_{l+m}} r\mathbf{N}'^T\mathbf{D}_{rr}\mathbf{N}'dr + \int_{r_l}^{r_{l+m}} \left[\mathbf{N}'^T\mathbf{D}_{r1}\mathbf{N} + \mathbf{N}^T\mathbf{D}_{1r}\mathbf{N}'\right]dr + \int_{r_l}^{r_{l+m}} \frac{1}{r}\mathbf{N}^T\mathbf{D}_{11}\mathbf{N}dr \tag{7.3.13h}$$

with $\mathbf{N}' = d\mathbf{N}/dr$. Notice that the $\mathbf{M}$, $\mathbf{A}_{\alpha\beta}$, and $\mathbf{G}$ matrices are symmetric, while the $\mathbf{B}_{\alpha}$ matrices are anti-symmetric. These matrices are given in full form in Appendices 7B and 7C, respectively, for the linear expansion of m=1 and for the quadratic expansion of m=2.

At this stage, the results for a single cylindrical thin-layer are overlapped with those of all other cylindrical thin-layers so as to generate the total system of equations in matrix form. To avoid the use of additional symbols, the same symbols as equation (7.3.12) are used to formulate the total system of equations for the multilayered cylindrical body.

$$\mathbf{P} = \mathbf{M}\ddot{\mathbf{U}} - \mathbf{A}_{\theta\theta}\frac{\partial^2\mathbf{U}}{\partial\theta^2} - \mathbf{A}_{\theta z}\frac{\partial^2\mathbf{U}}{\partial\theta\partial z} - \mathbf{A}_{zz}\frac{\partial^2\mathbf{U}}{\partial z^2} - \mathbf{B}_{\theta}\frac{\partial\mathbf{U}}{\partial\theta} - \mathbf{B}_{z}\frac{\partial\mathbf{U}}{\partial z} + \mathbf{G}\mathbf{U} \tag{7.3.14}$$

where

$$\mathbf{P} = \left[p_r^1 \quad p_\theta^1 \quad p_z^1 \quad p_r^2 \quad \cdots \quad p_z^N\right]^T \tag{7.3.15a}$$

$$\mathbf{U} = \left[u_r^1 \quad u_\theta^1 \quad u_z^1 \quad u_r^2 \quad \cdots \quad u_z^N\right]^T \tag{7.3.15b}$$

In above equations (7.3.15a and b), the superscripts indicate the interface or node to which they belong, and the subscripts denote the coordinate direction. The total system matrix is narrowly banded and has a total of $3N$ degrees of freedom, with N being the number of active interfaces, which depends on the number of layers, the expansion order (here, 1 or 2) and the boundary conditions at the top and bottom surfaces.

7.3.2 Comparison of the CTLM with the TLM

To verify the cylindrical thin-layer method formulated in section 7.3.1, we compare here the layer matrices of the CTKM with those of the TLM for flat layers. We base this comparison on the fact that a cylinder with large radius and small thickness behaves like a flat plate. For this purpose, we begin with defining a parameter of the form.

$$a = \frac{h}{2r_m} \tag{7.3.16}$$

in which h is the thickness of a cylindrical thin-layer, and r_m is the radius of the middle surface. When the radius of the cylinder is increased to infinity while holding the layer thickness h constant, r_m in each cylindrical thin-layer also increases without bound and the parameter a approaches zero.

Now, the system equation for a *single* cylindrical thin-layer is

$$\mathbf{M}\ddot{\mathbf{U}}-\mathbf{A}_{\theta\theta}\frac{\partial^2\mathbf{U}}{\partial\theta^2}-\mathbf{A}_{\theta z}\frac{\partial^2\mathbf{U}}{\partial\theta\partial z}-\mathbf{A}_{zz}\frac{\partial^2\mathbf{U}}{\partial z^2}-\mathbf{B}_{\theta}\frac{\partial\mathbf{U}}{\partial\theta}-\mathbf{B}_{z}\frac{\partial\mathbf{U}}{\partial z}+\mathbf{G}\mathbf{U}=\mathbf{0} \tag{7.3.17}$$

in which the layer matrices are as listed in Appendices 7B and 7C, respectively, for the linear and quadratic expansion. On the other hand, in Cartesian coordinates ($\bar{x}$, $\bar{y}$, $\bar{z}$), the system equation for flat layers is of the form

$$\bar{\mathbf{M}}\ddot{\mathbf{U}}-\bar{\mathbf{A}}_{xx}\frac{\partial^2\mathbf{U}}{\partial\bar{x}^2}-\bar{\mathbf{A}}_{xy}\frac{\partial^2\mathbf{U}}{\partial\bar{x}\partial\bar{y}}-\bar{\mathbf{A}}_{yy}\frac{\partial^2\mathbf{U}}{\partial\bar{y}^2}-\bar{\mathbf{B}}_{x}\frac{\partial\mathbf{U}}{\partial\bar{y}}-\bar{\mathbf{B}}_{y}\frac{\partial\mathbf{U}}{\partial\bar{y}}+\bar{\mathbf{G}}\mathbf{U}=\mathbf{0} \tag{7.3.18}$$

with layer matrices that will be identified in turn. In the equations above, a bar indicates that the matrices refer to those for flat layers. To make the comparison, we must now match the two coordinate systems:

$$r\rightarrow\bar{z}\,;\qquad\theta\rightarrow\bar{y}\,;\qquad z\rightarrow\bar{x} \tag{7.3.19a-c}$$

However, in equation (7.3.19b), the two coordinates θ and $\bar{y}$ are not dimensionally equal. Therefore, we divide the system equation by the mean radius r_m, and use it to define the characteristic arc length

$$\theta r_m = y \tag{7.3.20}$$

The system equation transforms then into

$$\tfrac{1}{r_m}\mathbf{M}\ddot{\mathbf{U}}-r_m\mathbf{A}_{\theta\theta}\frac{\partial^2\mathbf{U}}{\partial y^2}-\mathbf{A}_{\theta z}\frac{\partial^2\mathbf{U}}{\partial y\partial z}-\tfrac{1}{r_m}\mathbf{A}_{zz}\frac{\partial^2\mathbf{U}}{\partial z^2}-\mathbf{B}_{\theta}\frac{\partial\mathbf{U}}{\partial y}-\tfrac{1}{r_m}\mathbf{B}_{z}\frac{\partial\mathbf{U}}{\partial z}+\tfrac{1}{r_m}\mathbf{G}\mathbf{U}=\mathbf{0} \tag{7.3.21}$$

We will now show that the coefficient matrices of the cylindrical thin-layer method become the same as those for flat layers when r_m is made large enough i.e. as $r_m\rightarrow\infty$. When this is done, the parameter a tends to zero, that is

$$\lim_{r_m\rightarrow\infty} a=\lim_{r_m\rightarrow\infty}\frac{h}{2r_m}=0 \tag{7.3.22}$$

First, w consider the case of linear expansion CTLM of m=1. We begin with the mass matrices $\mathbf{M}$ and $\bar{\mathbf{M}}$:

$$\tfrac{1}{r_m}\mathbf{M}=\tfrac{1}{r_m}\lim_{a\rightarrow0}\frac{\rho h r_m}{6}\begin{Bmatrix}(2-a)\mathbf{I} & \mathbf{I}\\ \mathbf{I} & (2+a)\mathbf{I}\end{Bmatrix}=\frac{\rho h}{6}\begin{Bmatrix}2\mathbf{I} & \mathbf{I}\\ \mathbf{I} & 2\mathbf{I}\end{Bmatrix}\equiv\bar{\mathbf{M}} \tag{7.3.23}$$

Next, we examine the matrix $\mathbf{A}_{\theta\theta}$. For this purpose, we consider first the coefficients

$$c_1=\frac{1}{4a^2}\left[(1+a)^2\ln\frac{1+a}{1-a}-2a-4a^2\right]$$

$$c_2=-\frac{1}{4a^2}\left[(1-a^2)\ln\frac{1+a}{1-a}-2a\right]$$

$$c_3=\frac{1}{4a^2}\left[(1-a)^2\ln\frac{1+a}{1-a}-2a+4a^2\right] \tag{7.3.24a-c}$$

which appear in the definition of this matrix (see Appendix 7B). Expanding in Taylor series the logarithmic term

$$\ln\left(\frac{1+a}{1-a}\right)=2\left(a+\frac{1}{3}a^3+\frac{1}{5}a^5+\cdots\right) \tag{7.3.25}$$

and substituting this expansion into equations (7.3.24a-c), we obtain in the limit of large radius

$$\lim_{r_m\to\infty} c_1 = \frac{2}{3}a \qquad \lim_{r_m\to\infty} c_2 = \frac{1}{3}a \qquad \lim_{r_m\to\infty} c_3 = \frac{2}{3}a \tag{7.3.26a-c}$$

Substituting in turn these limiting expressions into the definition of $\mathbf{A}_{\theta\theta}$, we obtain

$$\begin{aligned}\lim_{r_m\to\infty} r_m\mathbf{A}_{\theta\theta} &= \lim_{r_m\to\infty}\frac{r_m a}{3}\begin{Bmatrix}2\mathbf{D}_{\theta\theta} & \mathbf{D}_{\theta\theta}\\ \mathbf{D}_{\theta\theta} & 2\mathbf{D}_{\theta\theta}\end{Bmatrix} = \frac{h}{6}\begin{Bmatrix}2\mathbf{D}_{\theta\theta} & \mathbf{D}_{\theta\theta}\\ \mathbf{D}_{\theta\theta} & 2\mathbf{D}_{\theta\theta}\end{Bmatrix}\\ &= \frac{h}{6}\begin{Bmatrix}2\mathbf{D}_{yy} & \mathbf{D}_{yy}\\ \mathbf{D}_{yy} & 2\mathbf{D}_{yy}\end{Bmatrix} \equiv \bar{\mathbf{A}}_{yy}\end{aligned} \tag{7.3.27}$$

For the matrices $\mathbf{A}_{\theta z}$ and $\bar{\mathbf{A}}_{xy}$ as well as the matrices $\mathbf{A}_{zz}$ and $\bar{\mathbf{A}}_{xx}$, we have immediately

$$\begin{aligned}\mathbf{A}_{\theta z} &= \frac{h}{6}\begin{Bmatrix}2(\mathbf{D}_{\theta z}+\mathbf{D}_{z\theta}) & \mathbf{D}_{\theta z}+\mathbf{D}_{z\theta}\\ \mathbf{D}_{\theta z}+\mathbf{D}_{z\theta} & 2(\mathbf{D}_{\theta z}+\mathbf{D}_{z\theta})\end{Bmatrix}\\ &= \frac{h}{6}\begin{Bmatrix}2(\mathbf{D}_{xy}+\mathbf{D}_{yx}) & \mathbf{D}_{xy}+\mathbf{D}_{yx}\\ \mathbf{D}_{xy}+\mathbf{D}_{yx} & 2(\mathbf{D}_{xy}+\mathbf{D}_{yx})\end{Bmatrix} \equiv \bar{\mathbf{A}}_{xy}\end{aligned} \tag{7.3.28}$$

and

$$\begin{aligned}\frac{1}{r_m}\mathbf{A}_{zz} &= \frac{h}{6}\begin{Bmatrix}2\mathbf{D}_{zz} & \mathbf{D}_{zz}\\ \mathbf{D}_{zz} & 2\mathbf{D}_{zz}\end{Bmatrix}\\ &= \frac{h}{6}\begin{Bmatrix}2\mathbf{D}_{xx} & \mathbf{D}_{xx}\\ \mathbf{D}_{xx} & 2\mathbf{D}_{xx}\end{Bmatrix} \equiv \bar{\mathbf{A}}_{xx}\end{aligned} \tag{7.3.29}$$

Next, we consider $\mathbf{B}_\theta$, which we take from Appendix 7B. As before, we expand the coefficients in the second term in Taylor series, and consider the limit as a goes to zero

$$\begin{aligned}\mathbf{B}_\theta &= \frac{1}{2}\begin{Bmatrix}\mathbf{D}_{r\theta}-\mathbf{D}_{\theta r} & \mathbf{D}_{r\theta}+\mathbf{D}_{\theta r}\\ -(\mathbf{D}_{r\theta}+\mathbf{D}_{\theta r}) & -(\mathbf{D}_{r\theta}-\mathbf{D}_{\theta r})\end{Bmatrix} + \frac{a}{3}\begin{Bmatrix}2(\mathbf{D}_{\theta 1}-\mathbf{D}_{1\theta}) & \mathbf{D}_{\theta 1}-\mathbf{D}_{1\theta}\\ \mathbf{D}_{\theta 1}-\mathbf{D}_{1\theta} & 2(\mathbf{D}_{\theta 1}-\mathbf{D}_{1\theta})\end{Bmatrix}\\ &= \frac{1}{2}\begin{Bmatrix}\mathbf{D}_{r\theta}-\mathbf{D}_{\theta r} & \mathbf{D}_{r\theta}+\mathbf{D}_{\theta r}\\ -(\mathbf{D}_{r\theta}+\mathbf{D}_{\theta r}) & -(\mathbf{D}_{r\theta}-\mathbf{D}_{\theta r})\end{Bmatrix}\\ &= -\frac{1}{2}\begin{Bmatrix}\mathbf{D}_{yz}-\mathbf{D}_{zy} & \mathbf{D}_{yz}+\mathbf{D}_{zy}\\ -(\mathbf{D}_{yz}+\mathbf{D}_{zy}) & -(\mathbf{D}_{yz}-\mathbf{D}_{zy})\end{Bmatrix} \equiv -\bar{\mathbf{B}}_y\end{aligned} \tag{7.3.30}$$

The negative sign in front of the matrix for plane layers is the results of the ordering of the layer interfaces. In the cylindrical case, we order the interfaces in the direction of growing r (i.e. from the inside to the outside), while for the flat layers, we order them in the direction opposite to the vertical coordinate (i.e. top layer first). This ordering indeed changes the signs, a fact that can be verified by exchanging in the expression above the diagonal and off-diagonal elements, respectively, and noticing that the same expression but with opposite signs is obtained.

As we shall see next, this same sign reversal will be observed in the $\mathbf{B}_z$ and $\bar{\mathbf{B}}_x$ matrices:

$$\begin{aligned}\frac{1}{r_m}\mathbf{B}_z &= \frac{1}{2}\begin{Bmatrix}\mathbf{D}_{rz}-\mathbf{D}_{zr} & \mathbf{D}_{rz}+\mathbf{D}_{zr}\\ -(\mathbf{D}_{rz}+\mathbf{D}_{zr}) & -(\mathbf{D}_{rz}-\mathbf{D}_{zr})\end{Bmatrix} - \frac{a}{6}\begin{Bmatrix}\mathbf{D}_{rz}-\mathbf{D}_{zr} & -(\mathbf{D}_{rz}-\mathbf{D}_{zr})\\ -(\mathbf{D}_{rz}-\mathbf{D}_{zr}) & \mathbf{D}_{rz}-\mathbf{D}_{zr}\end{Bmatrix}\\ &\quad + \frac{a}{3}\begin{Bmatrix}2(\mathbf{D}_{z1}-\mathbf{D}_{1z}) & \mathbf{D}_{z1}-\mathbf{D}_{1z}\\ \mathbf{D}_{z1}-\mathbf{D}_{1z} & 2(\mathbf{D}_{z1}-\mathbf{D}_{1z})\end{Bmatrix}\end{aligned} \tag{7.3.31}$$

and after discarding the last two matrices when $a\to 0$, we obtain

$$\frac{1}{r_m}\mathbf{B}_z = \frac{1}{2}\begin{Bmatrix} \mathbf{D}_{rz}-\mathbf{D}_{zr} & \mathbf{D}_{rz}+\mathbf{D}_{zr} \\ -(\mathbf{D}_{rz}+\mathbf{D}_{zr}) & -(\mathbf{D}_{rz}-\mathbf{D}_{zr}) \end{Bmatrix}$$
$$= -\frac{1}{2}\begin{Bmatrix} \mathbf{D}_{xz}-\mathbf{D}_{zx} & \mathbf{D}_{xz}+\mathbf{D}_{zx} \\ -(\mathbf{D}_{xz}+\mathbf{D}_{zx}) & -(\mathbf{D}_{xz}-\mathbf{D}_{zx}) \end{Bmatrix} \equiv -\bar{\mathbf{B}}_x \tag{7.3.32}$$

Finally, for the matrices $\mathbf{G}$ and $\bar{\mathbf{G}}$, we have

$$\frac{1}{r_m}\mathbf{G} = \frac{1}{h}\begin{Bmatrix} \mathbf{D}_{rr} & -\mathbf{D}_{rr} \\ -\mathbf{D}_{rr} & \mathbf{D}_{rr} \end{Bmatrix} + \frac{1}{2r_m}\begin{Bmatrix} -(\mathbf{D}_{1r}+\mathbf{D}_{r1}) & \mathbf{D}_{1r}-\mathbf{D}_{r1} \\ (\mathbf{D}_{1r}-\mathbf{D}_{r1})^T & \mathbf{D}_{1r}+\mathbf{D}_{r1} \end{Bmatrix}$$
$$+ \frac{a}{3r_m}\begin{Bmatrix} 2\mathbf{D}_{11} & \mathbf{D}_{11} \\ \mathbf{D}_{11} & 2\mathbf{D}_{11} \end{Bmatrix} \tag{7.3.33}$$

and after discarding the last two terms in the limit of large radius, we obtain

$$\frac{1}{r_m}\mathbf{G} = \frac{1}{h}\begin{Bmatrix} \mathbf{D}_{rr} & -\mathbf{D}_{rr} \\ -\mathbf{D}_{rr} & \mathbf{D}_{rr} \end{Bmatrix}$$
$$= \frac{1}{h}\begin{Bmatrix} \mathbf{D}_{zz} & -\mathbf{D}_{zz} \\ -\mathbf{D}_{zz} & \mathbf{D}_{zz} \end{Bmatrix} \equiv \bar{\mathbf{G}} \tag{7.3.34}$$

As having seen above, we have obtained the same results as for the flat layers. Hence, the formulation is consistent. Also, it is noted that we can conclude the same agreement with the case of the quadratic expansion CTLM, which is not discussed in the present study.

7.4 Solution of the discrete wave equation

The discrete system of equations in section 7.3 has been obtained by applying a finite element formulation in the radial direction, while maintaining the spatial (θ, z) and time (t) domains as continuous. To solve this system of equations, a Fourier transform is performed from the space-time domain to the wavenumber-frequency domain. This process yields an algebraic equation that contains the wavenumbers as parameters and the frequency as an eigenvalue, which corresponds to the TLM formulated in the time domain. Considering that the constitutive matrix is symmetric and positive-definite, it is possible to show that all eigenvalues in this problem will be real and non-negative. Using then these eigenvalues in the context of a modal superposition technique, we obtain in closed form the solution for the discrete equation of motion.

7.4.1 Transformation of the system of equations

The partial discretization of the wave equation in the layering direction eliminate the functional dependence on the radial coordinate r, and yield a system of partial differential equations only in the azimuthal, axial and time coordinates θ, z, t, respectively. From the preceding sections, this equation is obtained in the form.

$$\mathbf{P} = \mathbf{M}\ddot{\mathbf{U}} - \mathbf{A}_{\theta\theta}\frac{\partial^2\mathbf{U}}{\partial\theta^2} - \mathbf{A}_{\theta z}\frac{\partial^2\mathbf{U}}{\partial\theta\partial z} - \mathbf{A}_{zz}\frac{\partial^2\mathbf{U}}{\partial z^2} - \mathbf{B}_\theta\frac{\partial\mathbf{U}}{\partial\theta} - \mathbf{B}_z\frac{\partial\mathbf{U}}{\partial z} + \mathbf{G}\mathbf{U} \tag{7.4.1}$$

To solve this equation, we perform both spatial and temporal Fourier transforms in each coordinate. In the transformed domain, the discrete system displacement and traction fields can be written as $\bar{\mathbf{U}}$ and $\bar{\mathbf{P}}$, and their relationships with the actual domain variables are of the form

$$\mathbf{U} = \bar{\mathbf{U}} e^{\mathrm{i}(\omega t - n\theta - kz)} \tag{7.4.2a}$$

$$\mathbf{P} = \bar{\mathbf{P}} e^{\mathrm{i}(\omega t - n\theta - kz)} \tag{7.4.2b}$$

where ω is the angular frequency, and k, n are the axial and azimuthal wavenumbers, respectively, and

$$\bar{\mathbf{P}} = \left[\bar{p}_r^1 \quad \bar{p}_\theta^1 \quad \bar{p}_z^1 \quad \bar{p}_r^2 \quad \cdots \quad \bar{p}_z^N \right]^T \tag{7.4.3a}$$

$$\bar{\mathbf{U}} = \left[\bar{u}_r^1 \quad \bar{u}_\theta^1 \quad \bar{u}_z^1 \quad \bar{u}_r^2 \quad \cdots \quad \bar{u}_z^N \right]^T \tag{7.4.3b}$$

The partial derivatives implied by equations (7.4.2a and b) are then

$$\frac{\partial^2 \mathbf{U}}{\partial t^2} = -\omega^2 \mathbf{U} \qquad \frac{\partial \mathbf{U}}{\partial \theta} = -\mathrm{i} n \mathbf{U} \qquad \frac{\partial \mathbf{U}}{\partial z} = -\mathrm{i} k \mathbf{U}$$

$$\frac{\partial^2 \mathbf{U}}{\partial \theta \partial z} = -nk\mathbf{U} \qquad \frac{\partial^2 \mathbf{U}}{\partial \theta^2} = -n^2 \mathbf{U} \qquad \frac{\partial^2 \mathbf{U}}{\partial z^2} = -k^2 \mathbf{U} \tag{7.4.4a-f}$$

When these expressions are substituted into the system equation (7.4.1), we obtain the transformed system equation

$$\bar{\mathbf{P}} = \left(n^2 \mathbf{A}_{\theta\theta} + nk\,\mathbf{A}_{\theta z} + k^2 \mathbf{A}_{zz} + \mathrm{i} n \mathbf{B}_\theta + \mathrm{i} k \mathbf{B}_z + \mathbf{G} - \omega^2 \mathbf{M} \right) \bar{\mathbf{U}} \tag{7.4.5}$$

or more briefly

$$\bar{\mathbf{P}} = \bar{\mathbf{K}}\,\bar{\mathbf{U}} - \omega^2 \mathbf{M}\,\bar{\mathbf{U}} \tag{7.4.6}$$

7.4.2 Linear, real-valued eigenvalue problem

The analogy of equation (7.4.6) to a problem in structural dynamics suggests that it can be solved by a modal superposition involving the eigenvalue problem of the form.

$$\bar{\mathbf{K}}\,\Phi = \mathbf{M}\Phi\Omega^2 \tag{7.4.7}$$

where Φ is the matrix of eigenvectors and $\Omega = \mathrm{diag}\{\omega_j\}$ is the diagonal matrix of eigenvalues. While the eigenvalue problem of equation (7.4.7) can be solved easily, a more special class of problems will be considered so as to make the given eigenvalue problem both linear and real-valued. This process requires a new constitutive matrix corresponding to a medium that is somewhat more general than that of orthotropic materials. The new constitutive matrix for this medium is a symmetric, positive-definite constitutive matrix of the form

$$\mathbf{D} = \begin{Bmatrix} d_{11} & d_{12} & d_{13} & d_{14} & \cdot & \cdot \\ d_{21} & d_{22} & d_{23} & d_{24} & \cdot & \cdot \\ d_{31} & d_{32} & d_{33} & d_{34} & \cdot & \cdot \\ d_{41} & d_{42} & d_{43} & d_{44} & \cdot & \cdot \\ \cdot & \cdot & \cdot & \cdot & d_{55} & d_{56} \\ \cdot & \cdot & \cdot & \cdot & d_{65} & d_{66} \end{Bmatrix} \tag{7.4.8}$$

Now we proceed to investigate the nature of the equation (7.4.7) with this particular constitutive matrix. For this purpose, we rearrange equation (7.4.5) according to the degrees of freedom. In other word, we re-order the traction and displacement vectors $\bar{\mathbf{P}}$, $\bar{\mathbf{U}}$ as follows:

$$\bar{\mathbf{P}} = \left[\bar{\mathbf{p}}_r^T \quad \bar{\mathbf{p}}_\theta^T \quad \bar{\mathbf{p}}_z^T \right]^T = \left[\bar{p}_r^1 \quad \cdots \quad \bar{p}_r^N \quad \bar{p}_\theta^1 \quad \cdots \quad \bar{p}_\theta^N \quad \bar{p}_z^1 \quad \cdots \quad \bar{p}_z^N \right]^T \tag{7.4.9a}$$

$$\bar{\mathbf{U}} = \left[\bar{\mathbf{u}}_r^T \quad \bar{\mathbf{u}}_\theta^T \quad \bar{\mathbf{u}}_z^T\right]^T = \left[\bar{u}_r^1 \quad \cdots \quad \bar{u}_r^N \quad \bar{u}_\theta^1 \quad \cdots \quad \bar{u}_\theta^N \quad \bar{u}_z^1 \quad \cdots \quad \bar{u}_z^N\right]^T \tag{7.4.9b}$$

After this is done, the system equation (7.4.5) changes into an expression of the form

$$\begin{bmatrix}\bar{\mathbf{p}}_r\\ \bar{\mathbf{p}}_\theta\\ \bar{\mathbf{p}}_z\end{bmatrix} = \left\{\begin{bmatrix}\mathbf{A}_{\theta\theta}^{rr} & \mathbf{A}_{\theta\theta}^{r\theta} & \mathbf{A}_{\theta\theta}^{rz}\\ & \mathbf{A}_{\theta\theta}^{\theta\theta} & \mathbf{A}_{\theta\theta}^{\theta z}\\ sym. & & \mathbf{A}_{\theta\theta}^{zz}\end{bmatrix} n^2 + \begin{bmatrix}\mathbf{A}_{\theta z}^{rr} & \mathbf{A}_{\theta z}^{r\theta} & \mathbf{A}_{\theta z}^{rz}\\ & \mathbf{A}_{\theta z}^{\theta\theta} & \mathbf{A}_{\theta z}^{\theta z}\\ sym. & & \mathbf{A}_{\theta z}^{zz}\end{bmatrix} nk + \begin{bmatrix}\mathbf{A}_{zz}^{rr} & \mathbf{A}_{zz}^{r\theta} & \mathbf{A}_{zz}^{rz}\\ & \mathbf{A}_{zz}^{\theta\theta} & \mathbf{A}_{zz}^{\theta z}\\ sym. & & \mathbf{A}_{zz}^{zz}\end{bmatrix} k^2 \right.$$
$$+ \begin{bmatrix}\mathbf{B}_\theta^{rr} & \mathbf{B}_\theta^{r\theta} & \mathbf{B}_\theta^{rz}\\ -\mathbf{B}_\theta^{r\theta T} & \mathbf{B}_\theta^{\theta\theta} & \mathbf{B}_\theta^{\theta z}\\ -\mathbf{B}_\theta^{rz T} & -\mathbf{B}_\theta^{\theta z T} & \mathbf{B}_\theta^{zz}\end{bmatrix} \mathrm{i}n + \begin{bmatrix}\mathbf{B}_z^{rr} & \mathbf{B}_z^{r\theta} & \mathbf{B}_z^{rz}\\ -\mathbf{B}_z^{r\theta T} & \mathbf{B}_z^{\theta\theta} & \mathbf{B}_z^{\theta z}\\ -\mathbf{B}_z^{rz T} & -\mathbf{B}_z^{\theta z T} & \mathbf{B}_z^{zz}\end{bmatrix} \mathrm{i}k$$
$$\left. + \begin{bmatrix}\mathbf{G}^{rr} & \mathbf{G}^{r\theta} & \mathbf{G}^{rz}\\ & \mathbf{G}^{\theta\theta} & \mathbf{G}^{\theta z}\\ sym. & & \mathbf{G}^{zz}\end{bmatrix} - \omega^2 \begin{bmatrix}\mathbf{M}^{rr} & \cdot & \cdot\\ \cdot & \mathbf{M}^{\theta\theta} & \cdot\\ \cdot & \cdot & \mathbf{M}^{zz}\end{bmatrix} \right\} \begin{bmatrix}\bar{\mathbf{u}}_r\\ \bar{\mathbf{u}}_\theta\\ \bar{\mathbf{u}}_z\end{bmatrix} \tag{7.4.10}$$

where the subscripts have the same meaning as in equation (7.4.5), while the first and second superscripts denote the components of the traction and displacement fields, respectively. Substitution of the constitutive matrix given by equation (7.4.8) into equation (7.4.10) leads then to the much simpler equation

$$\begin{bmatrix}\bar{\mathbf{p}}_r\\ \bar{\mathbf{p}}_\theta\\ \bar{\mathbf{p}}_z\end{bmatrix} = \left\{\begin{bmatrix}\mathbf{A}_{\theta\theta}^{rr} & \cdot & \cdot\\ \cdot & \mathbf{A}_{\theta\theta}^{\theta\theta} & \mathbf{A}_{\theta\theta}^{\theta z}\\ \cdot & \mathbf{A}_{\theta\theta}^{\theta z} & \mathbf{A}_{\theta\theta}^{zz}\end{bmatrix} n^2 + \begin{bmatrix}\mathbf{A}_{\theta z}^{rr} & \cdot & \cdot\\ \cdot & \mathbf{A}_{\theta z}^{\theta\theta} & \mathbf{A}_{\theta z}^{\theta z}\\ \cdot & \mathbf{A}_{\theta z}^{\theta z} & \mathbf{A}_{\theta z}^{zz}\end{bmatrix} nk + \begin{bmatrix}\mathbf{A}_{zz}^{rr} & \cdot & \cdot\\ \cdot & \mathbf{A}_{zz}^{\theta\theta} & \mathbf{A}_{zz}^{\theta z}\\ \cdot & \mathbf{A}_{zz}^{\theta z} & \mathbf{A}_{zz}^{zz}\end{bmatrix} k^2 \right.$$
$$+ \begin{bmatrix}\cdot & \mathbf{B}_\theta^{r\theta} & \mathbf{B}_\theta^{rz}\\ -\mathbf{B}_\theta^{r\theta T} & \cdot & \cdot\\ -\mathbf{B}_\theta^{rz T} & \cdot & \cdot\end{bmatrix} \mathrm{i}n + \begin{bmatrix}\cdot & \mathbf{B}_z^{r\theta} & \mathbf{B}_z^{rz}\\ -\mathbf{B}_z^{r\theta T} & \cdot & \cdot\\ -\mathbf{B}_z^{rz T} & \cdot & \cdot\end{bmatrix} \mathrm{i}k$$
$$\left. + \begin{bmatrix}\mathbf{G}^{rr} & \cdot & \cdot\\ \cdot & \mathbf{G}^{\theta\theta} & \mathbf{G}^{\theta z}\\ \cdot & \mathbf{G}^{\theta z} & \mathbf{G}^{zz}\end{bmatrix} - \omega^2 \begin{bmatrix}\mathbf{M}^{rr} & \cdot & \cdot\\ \cdot & \mathbf{M}^{\theta\theta} & \cdot\\ \cdot & \cdot & \mathbf{M}^{zz}\end{bmatrix} \right\} \begin{bmatrix}\bar{\mathbf{u}}_r\\ \bar{\mathbf{u}}_\theta\\ \bar{\mathbf{u}}_z\end{bmatrix} \tag{7.4.11}$$

Additional manipulations of equation (7.4.11) with $\mathrm{i}(=\sqrt{-1})$ will yield a fully real and symmetric form system equation. This manipulation requires that we modify the vertical components of both load and displacement vectors by an i factor. This modification is accomplished by multiplying the first row by i and multiplying the first column by –i. Inspection of the structure of all matrices involved reveals that this transformation affects only the signs in the first rows of the fourth and fifth terms in equation (7.4.11). Finally, the following system equation is obtained

$$\begin{bmatrix}\mathrm{i}\bar{\mathbf{p}}_r\\ \bar{\mathbf{p}}_\theta\\ \bar{\mathbf{p}}_z\end{bmatrix} = \left\{\begin{bmatrix}\mathbf{A}_{\theta\theta}^{rr} & \cdot & \cdot\\ \cdot & \mathbf{A}_{\theta\theta}^{\theta\theta} & \mathbf{A}_{\theta\theta}^{\theta z}\\ \cdot & \mathbf{A}_{\theta\theta}^{\theta z} & \mathbf{A}_{\theta\theta}^{zz}\end{bmatrix} n^2 + \begin{bmatrix}\mathbf{A}_{\theta z}^{rr} & \cdot & \cdot\\ \cdot & \mathbf{A}_{\theta z}^{\theta\theta} & \mathbf{A}_{\theta z}^{\theta z}\\ \cdot & \mathbf{A}_{\theta z}^{\theta z} & \mathbf{A}_{\theta z}^{zz}\end{bmatrix} nk + \begin{bmatrix}\mathbf{A}_{zz}^{rr} & \cdot & \cdot\\ \cdot & \mathbf{A}_{zz}^{\theta\theta} & \mathbf{A}_{zz}^{\theta z}\\ \cdot & \mathbf{A}_{zz}^{\theta z} & \mathbf{A}_{zz}^{zz}\end{bmatrix} k^2 \right.$$
$$\left. + \begin{bmatrix}\cdot & -\mathbf{B}_\theta^{r\theta} & -\mathbf{B}_\theta^{rz}\\ -\mathbf{B}_\theta^{r\theta T} & \cdot & \cdot\\ -\mathbf{B}_\theta^{rz T} & \cdot & \cdot\end{bmatrix} n + \begin{bmatrix}\cdot & -\mathbf{B}_z^{r\theta} & -\mathbf{B}_z^{rz}\\ -\mathbf{B}_z^{r\theta T} & \cdot & \cdot\\ -\mathbf{B}_z^{rz T} & \cdot & \cdot\end{bmatrix} k \right\}$$

$$+\left\{\begin{bmatrix} \mathbf{G}^{rr} & \cdot & \cdot \\ \cdot & \mathbf{G}^{\theta\theta} & \mathbf{G}^{\theta z} \\ \cdot & \mathbf{G}^{\theta z} & \mathbf{G}^{zz} \end{bmatrix} - \omega^2 \begin{bmatrix} \mathbf{M}^{rr} & \cdot & \cdot \\ \cdot & \mathbf{M}^{\theta\theta} & \cdot \\ \cdot & \cdot & \mathbf{M}^{zz} \end{bmatrix}\right\} \begin{bmatrix} i\bar{\mathbf{u}}_r \\ \bar{\mathbf{u}}_\theta \\ \bar{\mathbf{u}}_z \end{bmatrix} \tag{7.4.12}$$

or more briefly

$$\hat{\mathbf{P}} = \hat{\mathbf{K}}\hat{\mathbf{U}} - \omega^2 \mathbf{M}\hat{\mathbf{U}} \tag{7.4.13}$$

where

$$\hat{\mathbf{P}} = \left[i\bar{p}_r^1 \ \cdots \ i\bar{p}_r^N \ \ \bar{p}_\theta^1 \ \cdots \ \bar{p}_\theta^N \ \ \bar{p}_z^1 \ \cdots \ \bar{p}_z^N \right]^T \tag{7.4.14a}$$

$$\hat{\mathbf{U}} = \left[i\bar{u}_r^1 \ \cdots \ i\bar{u}_r^N \ \ \bar{u}_\theta^1 \ \cdots \ \bar{u}_\theta^N \ \ \bar{u}_z^1 \ \cdots \ \bar{u}_z^N \right]^T \tag{7.4.14b}$$

Now it is seen that equation (7.4.13) is a general eigenvalue problem involving fully real and symmetric matrices. This eigenvalue problem is of the form

$$\hat{\mathbf{K}}\phi_j = \omega_j^2 \mathbf{M}\phi_j \tag{7.4.15}$$

where ϕ_j ($j = 1,2,...,3N$) is an eigenvector, and ω_j is the corresponding eigenvalue. The eigenvectors can be grouped into the modal matrix $\Phi = \{\phi_j\}$, and they satisfy the standard orthogonality conditions. Without loss of generality, they can be normalized with respect to the mass matrix, i.e.,

$$\Phi^T \mathbf{M} \Phi = \mathbf{I} \tag{7.4.16a}$$

$$\Phi^T \hat{\mathbf{K}} \Phi = \Omega^2 \tag{7.4.16b}$$

with

$$\Omega = diag\{\omega_j\} \qquad (j = 1,2,...,3N) \tag{7.4.17}$$

7.4.3 Modal superposition and responses in the space-time domain

A conventional modal superposition gives the solution to equation (7.4.13) in the wavenumber-time domain if $\hat{\mathbf{P}}$ in equation (7.4.13) is assumed to be of the separable form

$$\hat{\mathbf{P}} = \hat{\mathbf{P}}_0(n, k) f(t) \tag{7.4.18}$$

The solution is given as

$$\hat{\mathbf{U}} = \sum_{j=1}^{3N} \gamma_j h_j * f \phi_j \tag{7.4.19}$$

in which

$$\gamma_j = \phi_j^T \hat{\mathbf{P}}_0 \qquad = \text{modal participation factor} \tag{7.4.20a}$$

$$h_j = \frac{1}{\omega_{dj}} \exp(-\xi_j \omega_j t) \sin(\omega_{dj} t) \quad = \text{modal impulse response function} \tag{7.4.20b}$$

$$\omega_{dj} = \omega_j \sqrt{1 - \xi_j^2} \tag{7.4.20c}$$

In these expressions, the symbol $*$ indicates a convolution and ξ_j is the fraction of viscous modal damping. The use of equation (7.4.20b) with ω_{dj} gives the general solution so as to consider the effect of an arbitrary proportional viscous damping. It is noted that the modal mass implied by equation (7.4.20a) is unity because of the normalization of the eigenvectors in equation (7.4.16a).

Finally, we can obtain the responses in the space-time domain by means of the inverse Fourier transformation of the form.

$$\mathbf{U}(\theta,z,t)=\sum_{n=0}^{\infty}\left[\int_{-\infty}^{\infty}\hat{\mathbf{U}}(n,k,t)e^{-\mathrm{i}(n\theta+kz)}dk\right] \tag{7.4.21}$$

7.5 Analytical eigenvalue problem for a homogeneous solid and shell

We here formulate the analytical eigenvalue problem that is associated with the propagation modes of *isotropic* homogeneous cylindrical solids and shells. In the next section, we compare the eigenvalues of this analytical formulation with those of the CTLM so as to verify the validations of the latter.

In the absence of body forces, the wave equation for an isotropic medium is of the form.

$$\left[\mathbf{L}_{\sigma}^{T}\mathbf{D}\mathbf{L}_{\varepsilon}^{T}-\rho\frac{\partial^2}{\partial t^2}\right]\mathbf{u}=\mathbf{0} \tag{7.5.1}$$

where $\mathbf{u}=[u_r \quad u_\theta \quad u_z]^T$, the operators of $\mathbf{L}_\sigma$ and $\mathbf{L}_\varepsilon$ are the same as in sections 7.2, ρ is the mass density, and the material matrix $\mathbf{D}$ is

$$\mathbf{D}=\begin{Bmatrix}\lambda+2G & \lambda & \lambda & \cdot & \cdot & \cdot\\ \lambda & \lambda+2G & \lambda & \cdot & \cdot & \cdot\\ \lambda & \lambda & \lambda+2G & \cdot & \cdot & \cdot\\ \cdot & \cdot & \cdot & G & \cdot & \cdot\\ \cdot & \cdot & \cdot & \cdot & G & \cdot\\ \cdot & \cdot & \cdot & \cdot & \cdot & G\end{Bmatrix} \tag{7.5.2}$$

We assume a solution to equation (7.5.1) in the following form of separation of variables

$$\mathbf{u}=e^{\mathrm{i}\omega t}\mathbf{T}_n\mathbf{C}_n\mathbf{f}(z) \tag{7.5.3}$$

where

$$\mathbf{T}_n=\begin{Bmatrix}\cos n\theta & \cdot & \cdot\\ \cdot & -\sin n\theta & \cdot\\ \cdot & \cdot & \cos n\theta\end{Bmatrix}\ \text{or}\ \begin{Bmatrix}\sin n\theta & \cdot & \cdot\\ \cdot & \cos n\theta & \cdot\\ \cdot & \cdot & \sin n\theta\end{Bmatrix} \tag{7.5.4a}$$

$$\mathbf{C}_n=\begin{Bmatrix}C_n' & \dfrac{n}{\xi r}C_n & \cdot\\ \dfrac{n}{\xi r}C_n & C_n' & \cdot\\ \cdot & \cdot & -C_n\end{Bmatrix} \tag{7.5.4b}$$

$$\mathbf{f}(z)=[f_1 \quad f_2 \quad f_3]^T \tag{7.5.4c}$$

In equations (7.5.4), ω, n, and ξ are the frequency, azimuthal wavenumber, radial wavenumber, respectively, and $C_n=C_n(\xi r)$ is the cylindrical Bessel functions of order n that satisfy the following differential equation and recurrence relationships

$$\frac{d^2C_n}{dr^2}+\frac{1}{r}\frac{dC_n}{dr}+\left(\xi^2-\frac{n^2}{r^2}\right)C_n=0 \tag{7.5.5a}$$

$$C_n'=\frac{1}{2}(C_{n-1}-C_{n+1}) \tag{7.5.5b}$$

$$\frac{n}{\xi r}C_n=\frac{1}{2}(C_{n-1}+C_{n+1}) \tag{7.5.5c}$$

$$C_n'=\frac{dC_n}{d(\xi r)} \tag{7.5.5d}$$

Combining equations (7.5.1 and 3) and manipulating much algebra, we obtain

$$\left[\mathbf{L}_\sigma^T\mathbf{D}\mathbf{L}_\varepsilon^T-\rho\frac{\partial^2}{\partial t^2}\right]e^{i\omega t}\mathbf{T}_n\mathbf{C}_n\mathbf{f}=$$
$$e^{i\omega t}\mathbf{T}_n\mathbf{C}_n\left[-\xi^2\begin{Bmatrix}\lambda+2G & \cdot & \cdot\\ \cdot & G & \cdot\\ \cdot & \cdot & G\end{Bmatrix}-\xi\begin{Bmatrix}\cdot & \cdot & \lambda+G\\ \cdot & \cdot & \cdot\\ -(\lambda+G) & \cdot & \cdot\end{Bmatrix}\frac{d}{dz}\right.$$
$$\left.+\begin{Bmatrix}G & \cdot & \cdot\\ \cdot & G & \cdot\\ \cdot & \cdot & \lambda+2G\end{Bmatrix}\frac{d^2}{dz^2}+\rho\omega^2\begin{Bmatrix}1 & \cdot & \cdot\\ \cdot & 1 & \cdot\\ \cdot & \cdot & 1\end{Bmatrix}\right]\begin{Bmatrix}f_1\\ f_2\\ f_3\end{Bmatrix}=\mathbf{0} \tag{7.5.6}$$

Inspecting equation (7.5.6), we recognize that it can be uncoupled into two wave equations:
For *SH* waves,

$$Gf_2''+\left(\rho\omega^2-G\xi^2\right)f_2=0 \tag{7.5.7a}$$

For *SV-P* waves,

$$\begin{Bmatrix}G & \cdot\\ \cdot & \lambda+2G\end{Bmatrix}\begin{Bmatrix}f_1''\\ f_3''\end{Bmatrix}+\xi\begin{Bmatrix}\cdot & -(\lambda+G)\\ \lambda+G & \cdot\end{Bmatrix}\begin{Bmatrix}f_1'\\ f_3'\end{Bmatrix}$$
$$+\begin{Bmatrix}\rho\omega^2-\xi^2(\lambda+2G) & \cdot\\ \cdot & \rho\omega^2-\xi^2G\end{Bmatrix}\begin{Bmatrix}f_1\\ f_3\end{Bmatrix}=\begin{Bmatrix}0\\ 0\end{Bmatrix} \tag{7.5.7b}$$

where $f_j'=df_j/dz$ with j=1,2,3. Next, we assume $\mathbf{f}$ of the form

$$\mathbf{f}=e^{-ikz}\boldsymbol{\phi} \tag{7.5.8a}$$

$$\boldsymbol{\phi}=[\phi_1\quad\phi_2\quad\phi_3]^T \tag{7.5.8b}$$

Insert equation (7.5.8) into equations (7.5.7) to obtain the following eigenvalue problems:
For *SH* waves,

$$\left(-k^2G+\rho\omega^2-\xi^2G\right)\phi_2=0 \tag{7.5.9a}$$

whose eigenvalues are

$$\xi_S=\pm\sqrt{(\omega/C_S)^2-k^2} \tag{7.5.9b}$$

For *SV-P* waves,

$$\begin{Bmatrix}\rho\omega^2-\xi^2(\lambda+2G)-k^2G & ik\xi(\lambda+G)\\ -ik\xi(\lambda+G) & \rho\omega^2-\xi^2G-k^2(\lambda+2G)\end{Bmatrix}\begin{Bmatrix}\phi_1\\ \phi_3\end{Bmatrix}=\begin{Bmatrix}0\\ 0\end{Bmatrix} \tag{7.5.10a}$$

whose eigenvalues are

$$\xi_P=\pm\sqrt{(\omega/C_P)^2-k^2}\qquad\xi_S=\pm\sqrt{(\omega/C_S)^2-k^2} \tag{7.5.10bc}$$

where C_S is the S wave velocity and C_P is the P wave velocity. The mode shapes of this problem are then of the form

$$\Phi = \{\phi_j\} = \begin{Bmatrix} -i\xi_P & \cdot & k \\ \cdot & 1 & \cdot \\ k & \cdot & -i\xi_S \end{Bmatrix} \tag{7.5.11}$$

In equation (7.5.11), the first column vector ϕ_1 represents the P wave mode and the other two column vectors ϕ_2 and ϕ_3 represent the SH and SV wave modes. Finally, we obtain the general solution in the full form of separation of variables

$$\mathbf{u} = e^{i(\omega t - kz)}\mathbf{T}_n\left\{\mathbf{C}_{n,P}\phi_1 a + \mathbf{C}_{n,S}[\phi_2 b + \phi_3 c]\right\} = e^{i(\omega t - kz)}\mathbf{T}_n\mathbf{Z}_n\mathbf{a} \tag{7.5.12}$$

where a, b, c are the unknown constants to be determined, $\mathbf{C}_{n,P}$ and $\mathbf{C}_{n,S}$ are obtained with replacement of ξ in equation (7.5.4b) by ξ_P and ξ_S, respectively, and

$$\mathbf{Z}_n = \begin{Bmatrix} -i\xi_P Z'_{n,P} & \dfrac{n}{\xi_S r}Z_{n,S} & kZ'_{n,S} \\ -\dfrac{n}{r}iZ_{n,P} & Z'_{n,S} & k\dfrac{n}{\xi_S r}Z_{n,S} \\ -kZ_{n,P} & 0 & i\xi_S Z_{n,S} \end{Bmatrix} \tag{7.5.13a}$$

$$\mathbf{a} = [a \quad b \quad c]^T \tag{7.5.13b}$$

$$Z_{n,P} = J_n(\xi_P r) \text{ or } Y_n(\xi_P r) \tag{7.5.13c}$$

$$Z_{n,S} = J_n(\xi_S r) \text{ or } Y_n(\xi_S r) \tag{7.5.13d}$$

In equations (7.5.13cd), J_n and Y_n are the first and second kind Bessel functions of order n, respectively. In addition, when ξ_P and/or ξ_S are imaginary, we should replace J_n and Y_n by I_n and K_n, respectively, that are the first and second kind Modified Bessel functions of order n.
Also, we can alternatively express the general solution as

$$\mathbf{u} = e^{i(\omega t - kz)}\mathbf{T}_n[\mathbf{Z}_{n1}\mathbf{a}_1 + \mathbf{Z}_{n2}\mathbf{a}_2] \tag{7.5.14}$$

where

$$\mathbf{Z}_{n1} = \begin{Bmatrix} -i\xi_P J'_{n,P} & \dfrac{n}{\xi_S r}J_{n,S} & kJ'_{n,S} \\ -i\dfrac{n}{r}J_{n,P} & J'_{n,S} & k\dfrac{n}{\xi_S r}J_{n,S} \\ -kJ_{n,P} & 0 & i\xi_S J_{n,S} \end{Bmatrix} \tag{7.5.15a}$$

$$\mathbf{Z}_{n2} = \begin{Bmatrix} -i\xi_P Y'_{n,P} & \dfrac{n}{\xi_S r}Y_{n,S} & kY'_{n,S} \\ -i\dfrac{n}{r}Y_{n,P} & Y'_{n,S} & k\dfrac{n}{\xi_S r}Y_{n,S} \\ -kY_{n,P} & 0 & i\xi_S Y_{n,S} \end{Bmatrix} \tag{7.5.15b}$$

$$\mathbf{a}_1 = [a_1 \quad b_1 \quad c_1]^T \tag{7.5.15c}$$

$$\mathbf{a}_2 = [a_2 \quad b_2 \quad c_2]^T \tag{7.5.15d}$$

We consider the following boundary condition in the present problem.

$$\mathbf{s}=\begin{bmatrix}\sigma_r & \tau_{r\theta} & \tau_{rz}\end{bmatrix}^T=\mathbf{L}_r^T\mathbf{D}\mathbf{L}_\varepsilon\mathbf{u} \tag{7.5.16}$$

Apply equation (7.5.14) into equation (7.5.16) to obtain, again after huge algebraic manipulation,

$$\begin{Bmatrix}\sigma_r/(\lambda+2G)\\ \tau_{r\theta}/G\\ \tau_{rz}/G\end{Bmatrix}=e^{\mathrm{i}(\omega t-kz)}\mathbf{T}_n\left[\mathbf{A}_1(r)\mathbf{a}_1+\mathbf{A}_2(r)\mathbf{a}_2\right]=$$

$$=e^{\mathrm{i}(\omega t-kz)}\mathbf{T}_n\left[\begin{bmatrix}a_{11}^1 & a_{12}^1 & a_{13}^1\\ a_{21}^1 & a_{22}^1 & a_{23}^1\\ a_{31}^1 & a_{32}^1 & a_{33}^1\end{bmatrix}\begin{Bmatrix}a_1\\ b_1\\ c_1\end{Bmatrix}+\begin{bmatrix}a_{11}^2 & a_{12}^2 & a_{13}^2\\ a_{21}^2 & a_{22}^2 & a_{23}^2\\ a_{31}^2 & a_{32}^2 & a_{33}^2\end{bmatrix}\begin{Bmatrix}a_2\\ b_2\\ c_2\end{Bmatrix}\right] \tag{7.5.17}$$

where

$$a_{11}^1 \text{ or } a_{11}^2=\mathrm{i}\left\{\frac{\xi_P}{r}(1-\varepsilon)Z'_{n,P}+\left[\xi_P^2+\varepsilon k^2-\frac{n^2}{r^2}(1-\varepsilon)\right]Z_{n,P}\right\} \tag{7.5.18a}$$

$$a_{12}^1 \text{ or } a_{12}^2=\frac{n}{r}(1-\varepsilon)\left(Z'_{n,S}-\frac{1}{\xi_S r}Z_{n,S}\right) \tag{7.5.18b}$$

$$a_{13}^1 \text{ or } a_{13}^2=-k\frac{(1-\varepsilon)}{r}\left[Z'_{n,S}-\frac{n^2}{\xi_S r}Z_{n,S}+\xi_S rZ_{n,S}\right] \tag{7.5.18c}$$

$$a_{21}^1 \text{ or } a_{21}^2=\mathrm{i}\frac{2n}{r}\left(\frac{1}{r}Z_{n,P}-\xi_P Z'_{n,P}\right) \tag{7.5.18d}$$

$$a_{22}^1 \text{ or } a_{22}^2=-\frac{2}{r}Z'_{n,S}-\xi_S\left(1-\frac{2n^2}{\xi_S^2r^2}\right)Z_{n,S} \tag{7.5.18e}$$

$$a_{23}^1 \text{ or } a_{23}^2=\frac{2kn}{r}\left(Z'_{n,S}-\frac{1}{\xi_S r}Z_{n,S}\right) \tag{7.5.18f}$$

$$a_{31}^1 \text{ or } a_{31}^2=\mathrm{i}^2 2k\xi_P Z'_{n,P} \tag{7.5.18g}$$

$$a_{32}^1 \text{ or } a_{32}^2=-\mathrm{i}\frac{kn}{\xi_S r}Z_{n,S} \tag{7.5.18h}$$

$$a_{33}^1 \text{ or } a_{33}^2=\mathrm{i}\left(\xi_S^2-k^2\right)Z'_{n,S} \tag{7.5.18i}$$

$$\varepsilon=\frac{\lambda}{\lambda+2G}=\frac{\nu}{1-\nu} \tag{7.5.18j}$$

Next, we factor out the imaginary i in equation (7.5.17) from column 1 and multiply the last row by –i; also, for simplicity, we multiply all terms by r^2, and scale columns 2 and 3 by ξ_S and $\xi_S r$, respectively. The result is

$$\begin{Bmatrix}\mathrm{i}\sigma_r/(\lambda+2G)\\ \tau_{r\theta}/G\\ \tau_{rz}/G\end{Bmatrix}=e^{\mathrm{i}(\omega t-kz)}\mathbf{T}_n\left[\mathbf{B}_1(r)\mathbf{b}_1+\mathbf{B}_2(r)\mathbf{b}_2\right]$$

$$=e^{\mathrm{i}(\omega t-kz)}\mathbf{T}_n\left[\begin{bmatrix}b_{11}^1 & b_{12}^1 & b_{13}^1\\ b_{21}^1 & b_{22}^1 & b_{23}^1\\ b_{31}^1 & b_{32}^1 & b_{33}^1\end{bmatrix}\begin{Bmatrix}\mathrm{i}a_1\\ b_1\\ c_1\end{Bmatrix}+\begin{bmatrix}b_{11}^2 & b_{12}^2 & b_{13}^2\\ b_{21}^2 & b_{22}^2 & b_{23}^2\\ b_{31}^2 & b_{32}^2 & b_{33}^2\end{bmatrix}\begin{Bmatrix}\mathrm{i}a_2\\ b_2\\ c_2\end{Bmatrix}\right] \tag{7.5.19}$$

where

$$b_{11}^1 \text{ or } b_{11}^2 = \xi_P r(1-\varepsilon)Z'_{n,P} + \left[(\xi_P r)^2 + \varepsilon(kr)^2 - n^2(1-\varepsilon)\right]Z_{n,P} \tag{7.5.20a}$$

$$b_{12}^1 \text{ or } b_{12}^2 = n(1-\varepsilon)\left[(\xi_S r)Z'_{n,S} - Z_{n,S}\right] \tag{7.5.20b}$$

$$b_{13}^1 \text{ or } b_{13}^2 = -(kr)(1-\varepsilon)\left\{(\xi_S r)Z'_{n,S} + \left[(\xi_S r)^2 - n^2\right]Z_{n,S}\right\} \tag{7.5.20c}$$

$$b_{21}^1 \text{ or } b_{21}^2 = 2n\left[Z_{n,P} - (\xi_P r)Z'_{n,P}\right] \tag{7.5.20d}$$

$$b_{22}^1 \text{ or } b_{22}^2 = -2(\xi_S r)Z'_{n,S} - \left[(\xi_S r)^2 - 2n^2\right]Z_{n,S} \tag{7.5.20e}$$

$$b_{23}^1 \text{ or } b_{23}^2 = 2(k r)n\left[(\xi_S r)Z'_{n,S} - Z_{n,S}\right] \tag{7.5.20f}$$

$$b_{31}^1 \text{ or } b_{31}^2 = 2(k r)(\xi_P r)Z'_{n,P} \tag{7.5.20g}$$

$$b_{32}^1 \text{ or } b_{32}^2 = -(k r)n Z_{n,S} \tag{7.5.20h}$$

$$b_{33}^1 \text{ or } b_{33}^2 = (\xi_S r)\left[(\xi_S r)^2 - (k r)^2\right]Z'_{n,S} \tag{7.5.20i}$$

7.5.1 Cylindrical solid

First, we consider the propagation modes of a homogeneous cylindrical solid whose radius is r_o. From equation (7.5.19), we obtain the following stress-free condition at $r=r_o$ in the following form.

$$\mathbf{B}_1(r_o)\mathbf{b}_1 = \mathbf{0} \tag{7.5.21}$$

where we cancel the term $e^{i(\omega t - kz)}\mathbf{T}_n$. Then, the associated eigenvalue problem is of the form.

$$\det\left[\mathbf{B}_1(r_o)\right] = 0 \tag{7.5.22}$$

The roots (or zeros) of equation (7.5.22) provide the propagation modes of a homogeneous cylindrical solid for the continuum.

7.5.2 Cylindrical shell

We next consider the propagation modes of a homogeneous cylindrical shell whose inner and outer radii are r_i and r_o, respectively. From equation (7.5.19), we again obtain the following stress-free condition at $r=r_i$ and $r=r_o$

$$\begin{Bmatrix} \mathbf{B}_1(r_i) & \mathbf{B}_2(r_i) \\ \mathbf{B}_1(r_o) & \mathbf{B}_2(r_o) \end{Bmatrix} \begin{Bmatrix} \mathbf{b}_1 \\ \mathbf{b}_2 \end{Bmatrix} = \mathbf{0} \tag{7.5.23}$$

where we cancel the term $e^{i(\omega t - kz)}\mathbf{T}_n$. Finally, the associated eigenvalue problem is described as

$$\det\left[\begin{Bmatrix} \mathbf{B}_1(r_i) & \mathbf{B}_2(r_i) \\ \mathbf{B}_1(r_o) & \mathbf{B}_2(r_o) \end{Bmatrix}\right] = 0 \tag{7.5.24}$$

The roots (or zeros) of equation (7.5.24) represent the propagation modes of a homogeneous cylindrical shell for the continuum.

7.6 Comparison of numerical and analytical solutions

We compare the eigenvalues ω_j (frequencies) calculated with the CTLM against the exact analytical solutions so as to illustrate the validation of the formulated CTLM in this chapter. For

the practical purpose, we choose two simple structures and solve the associated eigenvalue problems. The two simple structures are (1) a homogenous cylindrical solid, (2) a homogeneous cylindrical shell. The exact analytical solutions for both are obtained in the previous section 7.5.

For the discrete models, we consider the both linear and quadratic expansion CTLM, or the CTLM1 and CTLM2 for short, respectively. We choose the total number of thin-layers N such as N=10 for the CTLM1 and N=5 for the CTLM2. In addition, to investigate the effect of the tuning factor μ of chapter 2 on the accuracy of eigenvalues calculated with the CTLM, we apply the lumped, tuned, and consistent mass matrices to the problem of interest. For the tuned mass matrix, we apply the optimal values of μ that are obtained for the TLM (formulated in the Cartesian coordinate system) in chapter 2, namely, μ=0.55 for the CTLM1 and μ=0.33 for the CTLM2 are used in this section.

7.6.1 Homogeneous cylindrical solid

First, we consider the propagation modes of a homogeneous cylindrical solid that is subjected to fully 3-dimensional wave motion, i.e. for the case of $n\geq 1$, with n being the wavenumber in θ direction. The geometry and material properties of the cylindrical solid are given such that the radius of the solid is r_o=1.0, the mass density and shear velocity are ρ=C_S=1.0, and the Poisson's ratio is ν=0.30. In particular, we are interested in its free vibration modes for n=1.

The dispersion curves of the propagation modes for n=1 are shown in figure 7.6.1 (for the lumped mass matrix), in figure 7.6.2 (for the tuned mass matrix), and in figure 7.6.3 (for the consistent mass matrix), in comparison with the exact analytical solution. Note in the three figures that the solid lines represent the propagation branches obtained with the CTLM, and the dashed lines represent the propagation branches obtained with the exact analytical solution. It is observed in all the three figures that the eigenvalues obtained with the CTLM are in good agreement with the exact analytical solutions. Also, notice that the accurate results are obtained only for the low modes, not for the high ones. Furthermore, it is shown that the CTLM2 with N=5 provides more accurate results than the CTLM1 with N=10, which again confirms that the quadratic expansion is not only more accurate, but also more efficient than the linear expansion, as shown in chapters 2–4 associated with the TLM.

Now, we consider the effect of the tuning factor μ on the accuracy of eigenvalues. Comparison of the three figures of 7.6.1, 7.6.2, and 7.6.3 verifies that the optimal values of μ=0.55 and μ=0.33 obtained for the TLM in chapter 2 provide much better agreement with the exact analytical solution than the other two values of μ=0 and 1 for the CTLM as well. Therefore, it is recommended to apply the optimal values of μ=0.55 and μ=0.33 to the CTLM as well as to the TLM.

7.6.2 Homogeneous cylindrical shell

Next, we consider the propagation modes of a homogeneous cylindrical shell subjected to fully 3-dimensional wave motion, i.e. for the case of $n\geq 1$. The geometry and material properties of the cylindrical solid are given such that the inner and outer radii are r_i=0.5 and r_o=1.5, the mass density and shear velocity are ρ=C_S=1.0, and the Poisson's ratio is ν=0.30. Again, we are interested in its free vibration modes for n=1.

The dispersion curves for n=1 of the homogeneous cylindrical shell are shown in figure 7.6.4 (for the lumped mass matrix), in figure 7.6.5 (for the tuned mass matrix), and in figure 7.6.6 (for the consistent mass matrix), in comparison with the exact analytical solution. In the three figures, the solid lines represent the propagation branches obtained with the CTLM, and the dashed lines represent the propagation branches obtained with the exact analytical solution. It is observed that the eigenvalues obtained with the CTLM show a good agreement with the exact analytical solutions. Also, notice that the accurate results are obtained only for the low modes. Furthermore, it is shown that the CTLM2 with N=5 provides more accurate results than the CTLM1 with N=10, which again confirms that the quadratic expansion is more accurate and more efficient than the linear expansion.

Now, we consider the effect of the tuning factor μ on the accuracy of eigenvalues. Comparison of the three figures of 7.6.4, 7.6.5, and 7.6.6 verifies that the optimal values of μ=0.55 and μ=0.33 provide much better agreement with the exact analytical solution than the other two values of μ=0 and 1 for the CTLM. Therefore, it is now strongly recommended to apply the optimal values of μ=0.55 and μ=0.33 to the CTLM.

Figures for chapter 7

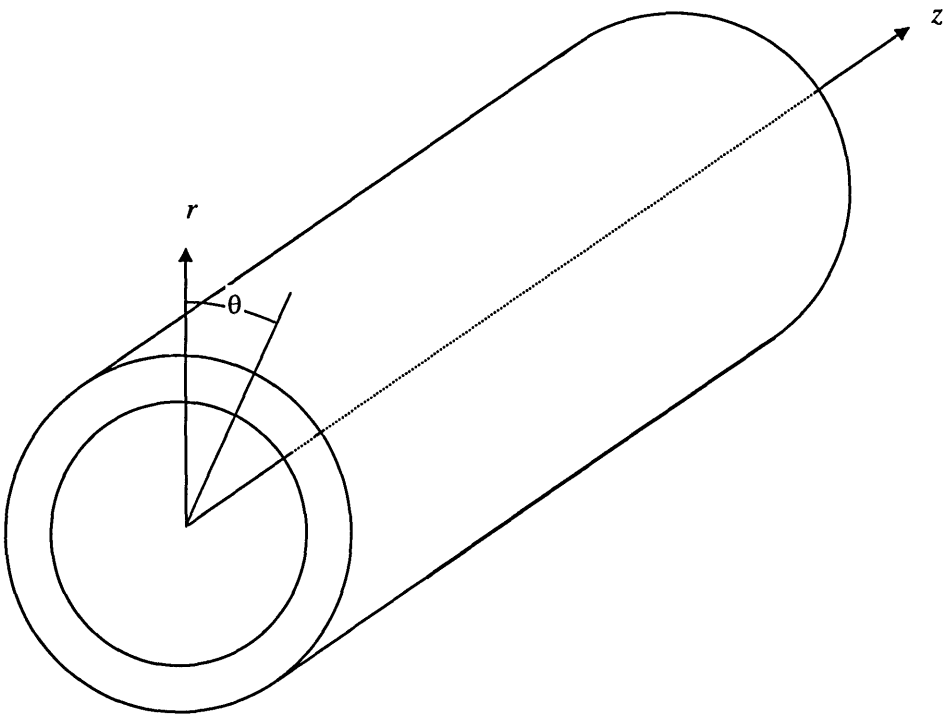

Figure 7.2.1 Infinitely long cylindrical shell
of linear elastic, homogeneous, and anisotropy and the cylindrical coordinate system used.

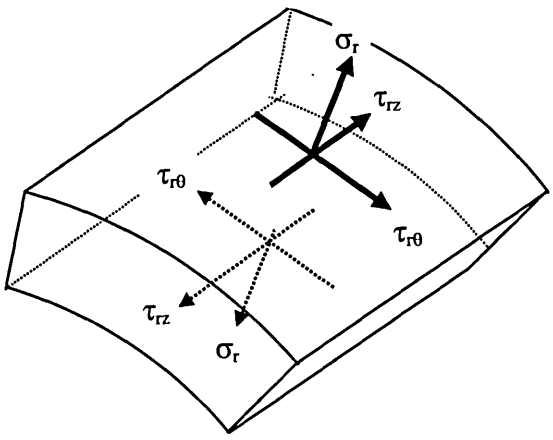

Figure 7.2.2 Boundary conditions on the inner and outer radial surfaces

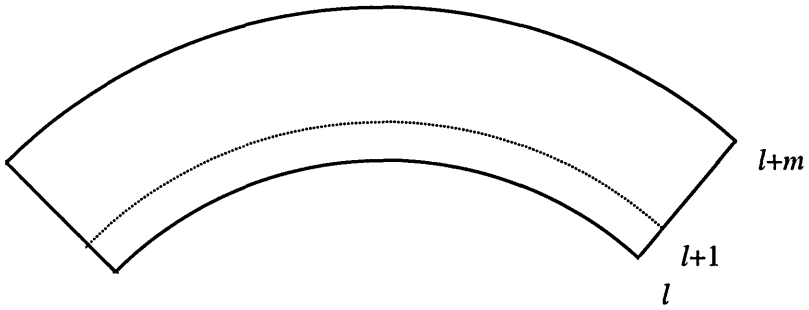

Figure 7.3.1 Individual cylindrical thin-layer

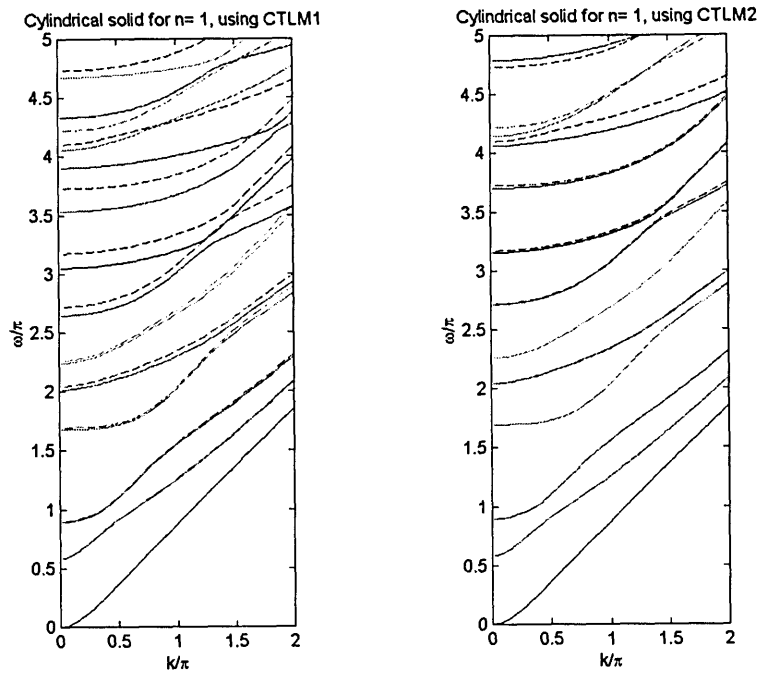

Figure 7.6.1 Propagation modes for n=1 in cylindrical solid using the lumped mass matrix (μ=0): solid line for CTLM; dashed line for Exact

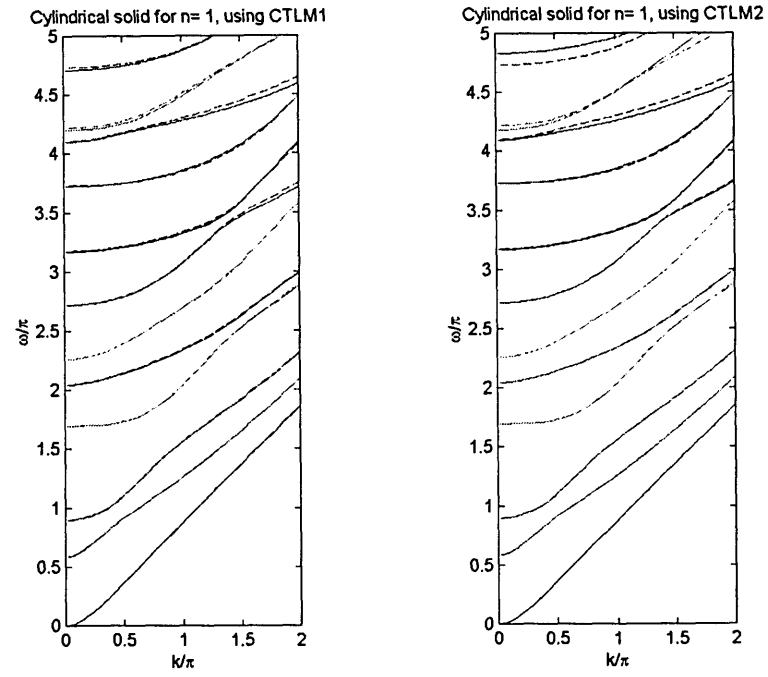

Figure 7.6.2 Propagation modes for n=1 in cylindrical solid using the tuned mass matrix : (μ=0.55 or 0.33): solid line for CTLM; dashed line for Exact

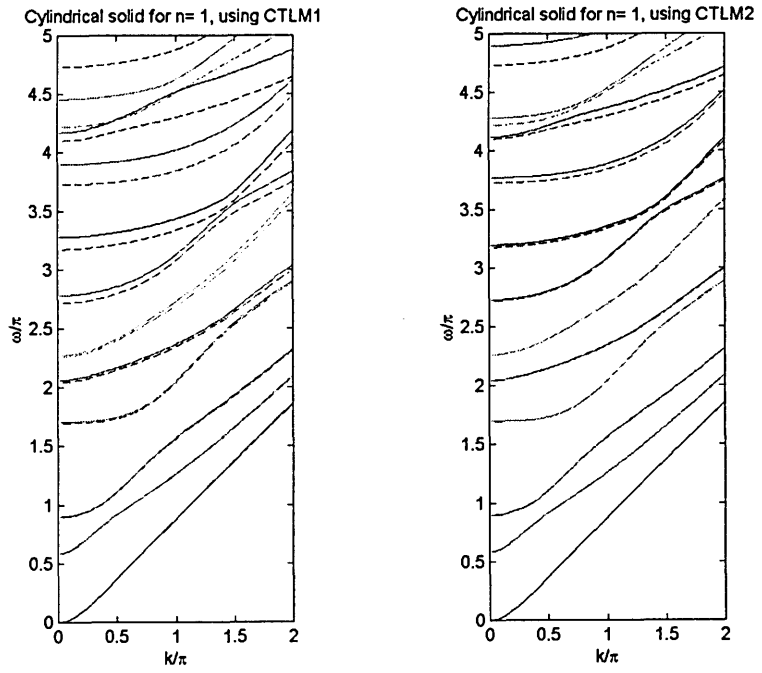

Figure 7.6.3 Propagation modes for n=1 in cylindrical solid using the consistent mass matrix (μ=1): solid line for CTLM; dashed line for Exact

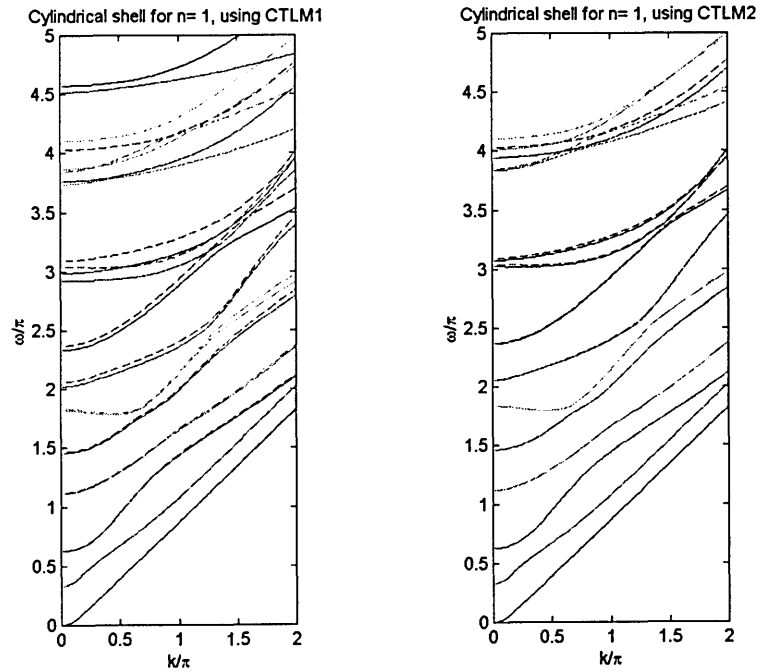

Figure 7.6.4 Propagation modes for n=1 in cylindrical shell using the lumped mass matrix (μ=0): solid line for CTLM; dashed line for Exact

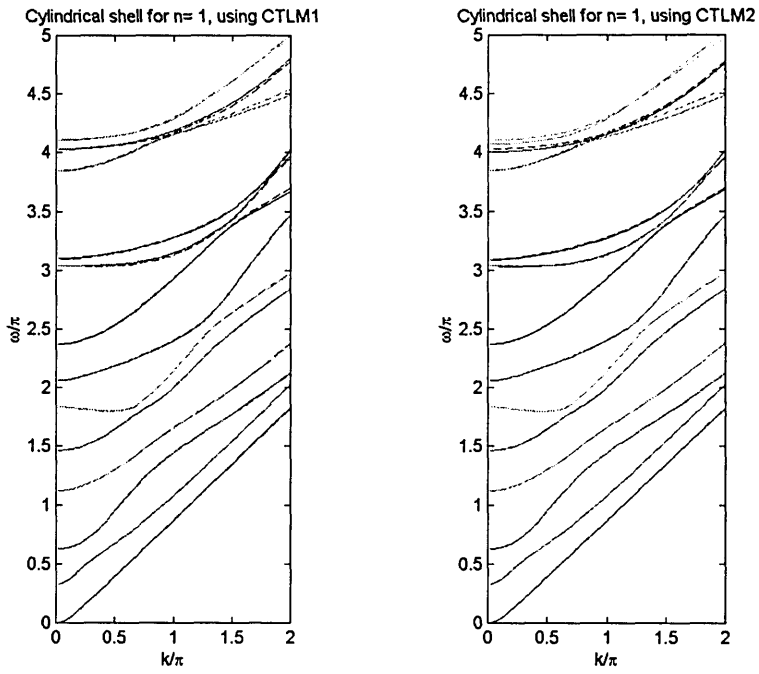

Figure 7.6.5 Propagation modes for n=1 in cylindrical shell using the tuned mass matrix (μ=0.55 or 0.33): solid line for CTLM; dashed line for Exact

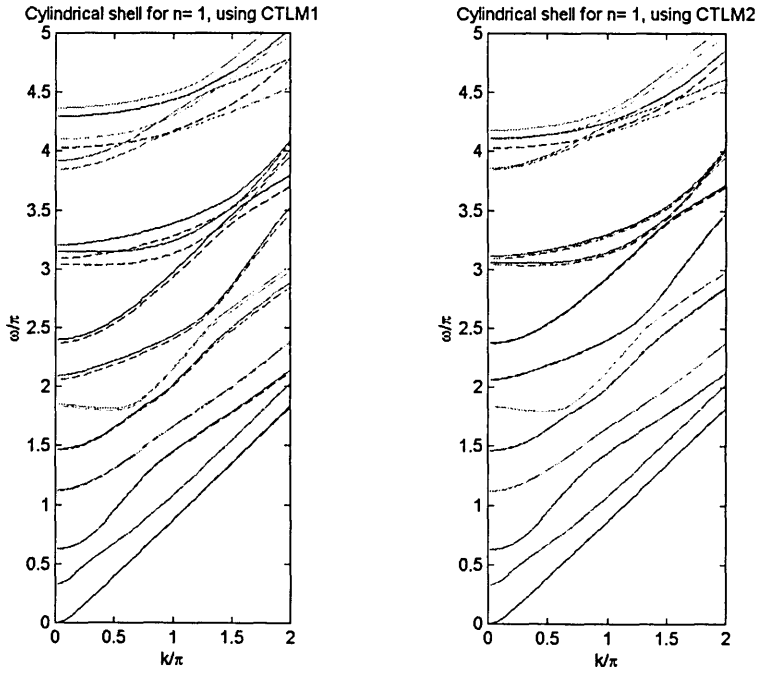

Figure 7.6.6 Propagation modes for n=1 in cylindrical shell using the consistent mass matrix (μ=1): solid line for CTLM; dashed line for Exact

APPENDIX 7A : Material matrices

$$\mathbf{D}_{rr}=\begin{Bmatrix} d_{11} & d_{16} & d_{15} \\ d_{16} & d_{66} & d_{56} \\ d_{15} & d_{56} & d_{55} \end{Bmatrix} \quad \mathbf{D}_{\theta\theta}=\begin{Bmatrix} d_{66} & d_{26} & d_{46} \\ d_{26} & d_{22} & d_{24} \\ d_{46} & d_{24} & d_{44} \end{Bmatrix} \quad \mathbf{D}_{zz}=\begin{Bmatrix} d_{55} & d_{45} & d_{35} \\ d_{45} & d_{44} & d_{34} \\ d_{35} & d_{34} & d_{33} \end{Bmatrix}$$

$$\mathbf{D}_{r\theta}=\mathbf{D}_{\theta r}^{T}=\begin{Bmatrix} d_{16} & d_{12} & d_{14} \\ d_{66} & d_{26} & d_{46} \\ d_{56} & d_{25} & d_{45} \end{Bmatrix} \qquad \mathbf{D}_{rz}=\mathbf{D}_{zr}^{T}=\begin{Bmatrix} d_{15} & d_{14} & d_{13} \\ d_{56} & d_{46} & d_{36} \\ d_{55} & d_{45} & d_{35} \end{Bmatrix}$$

$$\mathbf{D}_{\theta z}=\mathbf{D}_{z\theta}^{T}=\begin{Bmatrix} d_{56} & d_{46} & d_{36} \\ d_{25} & d_{24} & d_{23} \\ d_{45} & d_{44} & d_{34} \end{Bmatrix} \qquad \mathbf{D}_{r1}=\mathbf{D}_{1r}^{T}=\begin{Bmatrix} d_{12} & -d_{16} & \cdot \\ d_{26} & -d_{66} & \cdot \\ d_{25} & -d_{56} & \cdot \end{Bmatrix}$$

$$\mathbf{D}_{\theta 1}=\mathbf{D}_{1\theta}^{T}=\begin{Bmatrix} d_{26} & -d_{66} & \cdot \\ d_{22} & -d_{26} & \cdot \\ d_{24} & -d_{46} & \cdot \end{Bmatrix} \qquad \mathbf{D}_{z1}=\mathbf{D}_{1z}^{T}=\begin{Bmatrix} d_{25} & -d_{56} & \cdot \\ d_{24} & -d_{46} & \cdot \\ d_{23} & -d_{36} & \cdot \end{Bmatrix}$$

$$\mathbf{D}_{r\theta}+\mathbf{D}_{\theta r}=\begin{Bmatrix} 2d_{16} & d_{12}+d_{66} & d_{14}+d_{56} \\ d_{12}+d_{66} & 2d_{26} & d_{25}+d_{46} \\ d_{14}+d_{56} & d_{25}+d_{46} & 2d_{45} \end{Bmatrix}$$

$$\mathbf{D}_{r\theta}-\mathbf{D}_{\theta r}=\begin{Bmatrix} \cdot & d_{12}-d_{66} & d_{14}-d_{56} \\ -(d_{12}-d_{66}) & \cdot & d_{46}-d_{25} \\ -(d_{14}-d_{56}) & -(d_{46}-d_{25}) & \cdot \end{Bmatrix}$$

$$\mathbf{D}_{rz}+\mathbf{D}_{zr}=\begin{Bmatrix} 2d_{15} & d_{14}+d_{56} & d_{13}+d_{55} \\ d_{14}+d_{56} & 2d_{46} & d_{36}+d_{45} \\ d_{13}+d_{55} & d_{36}+d_{45} & 2d_{35} \end{Bmatrix}$$

$$\mathbf{D}_{rz}-\mathbf{D}_{zr}=\begin{Bmatrix} \cdot & d_{14}-d_{56} & d_{13}-d_{55} \\ -(d_{14}-d_{56}) & \cdot & d_{36}-d_{45} \\ -(d_{13}-d_{55}) & -(d_{36}-d_{45}) & \cdot \end{Bmatrix}$$

$$\mathbf{D}_{\theta z}+\mathbf{D}_{z\theta}=\begin{Bmatrix} 2d_{56} & d_{25}+d_{46} & d_{36}+d_{45} \\ d_{25}+d_{46} & 2d_{24} & d_{23}+d_{44} \\ d_{36}+d_{45} & d_{23}+d_{44} & 2d_{34} \end{Bmatrix}$$

$$\mathbf{D}_{rr}+\mathbf{D}_{r1}-\mathbf{D}_{1r}=\begin{Bmatrix} d_{11} & -d_{26} & d_{15}-d_{25} \\ 2d_{16}+d_{26} & d_{66} & 2d_{56} \\ d_{15}+d_{25} & \cdot & d_{55} \end{Bmatrix}$$

$$\mathbf{D}_{r1}+\mathbf{D}_{1r}=\begin{Bmatrix} 2d_{12} & -d_{16}+d_{26} & d_{25} \\ d_{26}-d_{16} & -2d_{66} & -d_{56} \\ d_{25} & -d_{56} & \cdot \end{Bmatrix}$$

$$\mathbf{D}_{r1}-\mathbf{D}_{1r}=\begin{Bmatrix} \cdot & -d_{16}-d_{26} & -d_{25} \\ d_{26}+d_{16} & \cdot & d_{56} \\ d_{25} & -d_{56} & \cdot \end{Bmatrix}$$

$$\mathbf{D}_{\theta 1}-\mathbf{D}_{1\theta}=\begin{Bmatrix} \cdot & -(d_{22}+d_{66}) & -d_{24} \\ (d_{22}+d_{66}) & \cdot & d_{46} \\ d_{24} & -d_{46} & \cdot \end{Bmatrix}$$

$$\mathbf{D}_{z1}-\mathbf{D}_{1z}=\begin{Bmatrix} \cdot & -d_{56}-d_{24} & -d_{23} \\ d_{24}+d_{56} & \cdot & d_{36} \\ d_{23} & -d_{36} & \cdot \end{Bmatrix}$$

$$\mathbf{D}_{rz}+\mathbf{D}_{z1}-\mathbf{D}_{1z}=\begin{Bmatrix} d_{15} & d_{14}-(d_{24}+d_{56}) & d_{13}-d_{23} \\ (d_{24}+2d_{56}) & d_{46} & 2d_{36} \\ d_{23}+d_{55} & -d_{36}+d_{45} & d_{35} \end{Bmatrix}$$

$$\mathbf{D}_{11}=\begin{Bmatrix} d_{22} & -d_{26} & \cdot \\ -d_{26} & d_{66} & \cdot \\ \cdot & \cdot & \cdot \end{Bmatrix}$$

For cross-anisotropic media, the material matrices are:

$$\mathbf{D}_{rr}=\begin{Bmatrix} \lambda_t+2G_t & \cdot & \cdot \\ \cdot & G_t & \cdot \\ \cdot & \cdot & G_t \end{Bmatrix} \quad \mathbf{D}_{\theta\theta}=\begin{Bmatrix} G_t & \cdot & \cdot \\ \cdot & \lambda+2G & \cdot \\ \cdot & \cdot & G \end{Bmatrix} \quad \mathbf{D}_{zz}=\begin{Bmatrix} G_t & \cdot & \cdot \\ \cdot & G & \cdot \\ \cdot & \cdot & \lambda+2G \end{Bmatrix}$$

$$\mathbf{D}_{r\theta}=\mathbf{D}_{\theta r}^{T}=\begin{Bmatrix} \cdot & \lambda_t & \cdot \\ G_t & \cdot & \cdot \\ \cdot & \cdot & \cdot \end{Bmatrix} \qquad \mathbf{D}_{rz}=\mathbf{D}_{zr}^{T}=\begin{Bmatrix} \cdot & \cdot & \lambda_t \\ \cdot & \cdot & \cdot \\ G_t & \cdot & \cdot \end{Bmatrix}$$

$$\mathbf{D}_{\theta z}=\mathbf{D}_{z\theta}^{T}=\begin{Bmatrix} \cdot & \cdot & \cdot \\ \cdot & \cdot & \lambda \\ \cdot & G & \cdot \end{Bmatrix} \qquad \mathbf{D}_{r1}=\mathbf{D}_{1r}^{T}=\begin{Bmatrix} \lambda_t & \cdot & \cdot \\ \cdot & -G_t & \cdot \\ \cdot & \cdot & \cdot \end{Bmatrix}$$

$$\mathbf{D}_{\theta 1}=\mathbf{D}_{1\theta}^{T}=\begin{Bmatrix} \cdot & -G_t & \cdot \\ \lambda+2G & \cdot & \cdot \\ \cdot & \cdot & \cdot \end{Bmatrix} \qquad \mathbf{D}_{z1}=\mathbf{D}_{1z}^{T}=\begin{Bmatrix} \cdot & \cdot & \cdot \\ \cdot & \cdot & \cdot \\ \lambda & \cdot & \cdot \end{Bmatrix}$$

$$\mathbf{D}_{r\theta}+\mathbf{D}_{\theta r}=\begin{Bmatrix} \cdot & \lambda_t+G_t & \cdot \\ \lambda_t+G_t & \cdot & \cdot \\ \cdot & \cdot & \cdot \end{Bmatrix}$$

$$\mathbf{D}_{r\theta}-\mathbf{D}_{\theta r}=\begin{Bmatrix} \cdot & \lambda_t-G_t & \cdot \\ -(\lambda_t-G_t) & \cdot & \cdot \\ \cdot & \cdot & \cdot \end{Bmatrix}$$

$$\mathbf{D}_{rz}+\mathbf{D}_{zr}=\begin{Bmatrix} \cdot & \cdot & \lambda_t+G_t \\ \cdot & \cdot & \cdot \\ \lambda_t+G_t & \cdot & \cdot \end{Bmatrix}$$

$$\mathbf{D}_{rz}-\mathbf{D}_{zr}=\begin{Bmatrix} \cdot & \cdot & \lambda_t-G_t \\ \cdot & \cdot & \cdot \\ -(\lambda_t-G_t) & \cdot & \cdot \end{Bmatrix}$$

$$\mathbf{D}_{\theta z}+\mathbf{D}_{z\theta}=\begin{Bmatrix} \cdot & \cdot & \cdot \\ \cdot & \cdot & \lambda+G \\ \cdot & \lambda+G & \cdot \end{Bmatrix}$$

$$\mathbf{D}_{rr}+\mathbf{D}_{r1}-\mathbf{D}_{1r}=\begin{Bmatrix} \lambda_t+2G_t & \cdot & \cdot \\ \cdot & G_t & \cdot \\ \cdot & \cdot & G_t \end{Bmatrix}$$

$$\mathbf{D}_{r1}+\mathbf{D}_{1r}=\begin{Bmatrix} 2\lambda_t & \cdot & \cdot \\ \cdot & -2G_t & \cdot \\ \cdot & \cdot & \cdot \end{Bmatrix}$$

$$\mathbf{D}_{r1}-\mathbf{D}_{1r}=\begin{Bmatrix} \cdot & \cdot & \cdot \\ \cdot & \cdot & \cdot \\ \cdot & \cdot & \cdot \end{Bmatrix}$$

$$\mathbf{D}_{\theta 1}-\mathbf{D}_{1\theta}=\begin{Bmatrix} \cdot & -(G_t+\lambda+2G) & \cdot \\ (G_t+\lambda+2G) & \cdot & \cdot \\ \cdot & \cdot & \cdot \end{Bmatrix}$$

$$\mathbf{D}_{z1}-\mathbf{D}_{1z}=\begin{Bmatrix} \cdot & \cdot & -\lambda \\ \cdot & \cdot & \cdot \\ \lambda & \cdot & \cdot \end{Bmatrix}$$

$$\mathbf{D}_{rz}+\mathbf{D}_{z1}-\mathbf{D}_{1z}=\begin{Bmatrix} \cdot & \cdot & \lambda_t-\lambda \\ \cdot & \cdot & \cdot \\ G_t+\lambda & \cdot & \cdot \end{Bmatrix}$$

$$\mathbf{D}_{11}=\begin{Bmatrix} \lambda+2G & \cdot & \cdot \\ \cdot & G_t & \cdot \\ \cdot & \cdot & \cdot \end{Bmatrix}$$

APPENDIX 7B : Layer Matrices for linear expansion

7B.1 Preliminary definitions

$$a=\frac{h}{2r_m} \qquad L=\frac{1}{4a^2}\left[\ln\frac{1+a}{1-a}-2a\right]$$

$$c_1=\frac{1}{4a^2}\left[(1+a)^2\ln\frac{1+a}{1-a}-2a-4a^2\right]=(1+a)^2L+\frac{a}{2}$$

$$c_2=-\frac{1}{4a^2}\left[(1-a^2)\ln\frac{1+a}{1-a}-2a\right]=-\left[(1-a^2)L-\frac{a}{2}\right]$$

$$c_3=\frac{1}{4a^2}\left[(1-a)^2\ln\frac{1+a}{1-a}-2a+4a^2\right]=(1-a)^2L+\frac{a}{2}$$

For a linear expansion, the layer matrices are then

$$\mathbf{M}=\frac{\rho h r_m}{6}\begin{Bmatrix}(2-a)\mathbf{I} & \mathbf{I}\\ \mathbf{I} & (2+a)\mathbf{I}\end{Bmatrix}$$

$$\mathbf{A}_{\theta\theta}=\begin{Bmatrix}c_1\mathbf{D}_{\theta\theta} & c_2\mathbf{D}_{\theta\theta}\\ c_2\mathbf{D}_{\theta\theta} & c_3\mathbf{D}_{\theta\theta}\end{Bmatrix}$$

$$\mathbf{A}_{\theta z}=\frac{h}{6}\begin{Bmatrix}2(\mathbf{D}_{\theta z}+\mathbf{D}_{z\theta}) & \mathbf{D}_{\theta z}+\mathbf{D}_{z\theta}\\ \mathbf{D}_{\theta z}+\mathbf{D}_{z\theta} & 2(\mathbf{D}_{\theta z}+\mathbf{D}_{z\theta})\end{Bmatrix}$$

$$\mathbf{A}_{zz}=\frac{hr_m}{6}\begin{Bmatrix}(2-a)\mathbf{D}_{zz} & \mathbf{D}_{zz}\\ \mathbf{D}_{zz} & (2+a)\mathbf{D}_{zz}\end{Bmatrix}$$

$$\mathbf{B}_{\theta}=\frac{1}{2}\begin{Bmatrix}\mathbf{D}_{r\theta}-\mathbf{D}_{\theta r} & \mathbf{D}_{r\theta}+\mathbf{D}_{\theta r}\\ -(\mathbf{D}_{r\theta}+\mathbf{D}_{\theta r}) & -(\mathbf{D}_{r\theta}-\mathbf{D}_{\theta r})\end{Bmatrix}+\begin{Bmatrix}c_1(\mathbf{D}_{\theta 1}-\mathbf{D}_{1\theta}) & c_2(\mathbf{D}_{\theta 1}-\mathbf{D}_{1\theta})\\ c_2(\mathbf{D}_{\theta 1}-\mathbf{D}_{1\theta}) & c_3(\mathbf{D}_{\theta 1}-\mathbf{D}_{1\theta})\end{Bmatrix}$$

$$\mathbf{B}_{z}=\frac{r_m}{2}\begin{Bmatrix}\mathbf{D}_{rz}-\mathbf{D}_{zr} & \mathbf{D}_{rz}+\mathbf{D}_{zr}\\ -(\mathbf{D}_{rz}+\mathbf{D}_{zr}) & -(\mathbf{D}_{rz}-\mathbf{D}_{zr})\end{Bmatrix}-\frac{ar_m}{6}\begin{Bmatrix}\mathbf{D}_{rz}-\mathbf{D}_{zr} & -(\mathbf{D}_{rz}-\mathbf{D}_{zr})\\ -(\mathbf{D}_{rz}-\mathbf{D}_{zr}) & \mathbf{D}_{rz}-\mathbf{D}_{zr}\end{Bmatrix}$$
$$+\frac{ar_m}{3}\begin{Bmatrix}2(\mathbf{D}_{z1}-\mathbf{D}_{1z}) & \mathbf{D}_{z1}-\mathbf{D}_{1z}\\ \mathbf{D}_{z1}-\mathbf{D}_{1z} & 2(\mathbf{D}_{z1}-\mathbf{D}_{1z})\end{Bmatrix}$$

$$\mathbf{G}=\frac{r_m}{h}\begin{Bmatrix}\mathbf{D}_{rr} & -\mathbf{D}_{rr}\\ -\mathbf{D}_{rr} & \mathbf{D}_{rr}\end{Bmatrix}+\frac{1}{2}\begin{Bmatrix}-(\mathbf{D}_{1r}+\mathbf{D}_{r1}) & \mathbf{D}_{1r}-\mathbf{D}_{r1}\\ (\mathbf{D}_{1r}-\mathbf{D}_{r1})^T & \mathbf{D}_{1r}+\mathbf{D}_{r1}\end{Bmatrix}$$
$$+\begin{Bmatrix}c_1\mathbf{D}_{11} & c_2\mathbf{D}_{11}\\ c_2\mathbf{D}_{11} & c_3\mathbf{D}_{11}\end{Bmatrix}$$

7B.2 Anisotropic case

In detail these matrices are

$$\mathbf{M}=\frac{\rho h r_m}{6}\begin{Bmatrix} 2-a & \cdot & \cdot & 1 & \cdot & \cdot \\ \cdot & 2-a & \cdot & \cdot & 1 & \cdot \\ \cdot & \cdot & 2-a & \cdot & \cdot & 1 \\ 1 & \cdot & \cdot & 2+a & \cdot & \cdot \\ \cdot & 1 & \cdot & \cdot & 2+a & \cdot \\ \cdot & \cdot & 1 & \cdot & \cdot & 2+a \end{Bmatrix}$$

$$\mathbf{A}_{\theta\theta}=\begin{Bmatrix} c_1d_{66} & c_1d_{26} & c_1d_{46} & c_2d_{66} & c_2d_{26} & c_2d_{46} \\ & c_1d_{22} & c_1d_{24} & c_2d_{26} & c_2d_{22} & c_2d_{24} \\ & & c_1d_{44} & c_2d_{46} & c_2d_{24} & c_2d_{44} \\ & & & c_3d_{66} & c_3d_{26} & c_3d_{46} \\ & & & & c_3d_{22} & c_3d_{24} \\ sym. & & & & & c_3d_{44} \end{Bmatrix}$$

$$\mathbf{A}_{\theta z}=\frac{h}{6}\begin{Bmatrix} 4d_{56} & 2(d_{25}+d_{46}) & 2(d_{36}+d_{45}) & 2d_{56} & d_{25}+d_{46} & d_{36}+d_{45} \\ & 4d_{24} & 2(d_{23}+d_{44}) & d_{25}+d_{46} & 2d_{24} & d_{23}+d_{44} \\ & & 4d_{34} & d_{36}+d_{45} & d_{23}+d_{44} & 2d_{34} \\ & & & 4d_{56} & 2(d_{25}+d_{46}) & 2(d_{36}+d_{45}) \\ & & & & 4d_{24} & 2(d_{23}+d_{44}) \\ sym. & & & & & 4d_{34} \end{Bmatrix}$$

$$\mathbf{A}_{zz}=\frac{hr_m}{6}\begin{Bmatrix} (2-a)d_{55} & (2-a)d_{45} & (2-a)d_{35} & d_{55} & d_{45} & d_{35} \\ & (2-a)d_{44} & (2-a)d_{34} & d_{45} & d_{44} & d_{34} \\ & & (2-a)d_{33} & d_{35} & d_{34} & d_{33} \\ & & & (2+a)d_{55} & (2+a)d_{45} & (2+a)d_{35} \\ & & & & (2+a)d_{44} & (2+a)d_{34} \\ sym. & & & & & (2+a)d_{33} \end{Bmatrix}$$

$$\mathbf{B}_\theta = \frac{1}{2}\begin{Bmatrix} \cdot & d_{12}-d_{66} & d_{14}-d_{56} & 2d_{16} & d_{12}+d_{66} & d_{14}+d_{56} \\ & \cdot & d_{46}-d_{25} & d_{12}+d_{66} & 2d_{26} & d_{25}+d_{46} \\ & & \cdot & d_{14}+d_{56} & d_{25}+d_{46} & 2d_{45} \\ & & & \cdot & d_{66}-d_{12} & d_{56}-d_{14} \\ & & & & \cdot & d_{25}-d_{46} \\ \textit{antisym.} & & & & & \cdot \end{Bmatrix}$$

$$+\begin{Bmatrix} \cdot & -c_1(d_{22}+d_{66}) & -c_1 d_{24} & \cdot & -c_2(d_{22}+d_{66}) & -c_2 d_{24} \\ & \cdot & c_1 d_{46} & c_2(d_{22}+d_{66}) & \cdot & c_2 d_{46} \\ & & \cdot & c_2 d_{24} & -c_2 d_{46} & \cdot \\ & & & \cdot & -c_3(d_{22}+d_{66}) & -c_3 d_{24} \\ & & & & \cdot & c_3 d_{46} \\ \textit{antisym.} & & & & & \cdot \end{Bmatrix}$$

$$\mathbf{B}_z = \frac{r_m}{2}\begin{Bmatrix} \cdot & d_{14}-d_{56} & d_{13}-d_{55} & 2d_{15} & d_{14}+d_{56} & d_{13}+d_{55} \\ & \cdot & d_{36}-d_{45} & d_{14}+d_{56} & 2d_{46} & d_{36}+d_{45} \\ & & \cdot & d_{13}+d_{55} & d_{36}+d_{45} & 2d_{35} \\ & & & \cdot & -(d_{14}-d_{56}) & -(d_{13}-d_{55}) \\ & & & & \cdot & -(d_{36}-d_{45}) \\ \textit{antisym.} & & & & & \cdot \end{Bmatrix}$$

$$+\frac{ar_m}{6}\begin{Bmatrix} \cdot & -d_{14}-4d_{24}-3d_{56} & d_{55}-d_{13}-4d_{23} & \cdot & d_{14}-2d_{24}-3d_{56} & d_{13}-2d_{23}-d_{55} \\ & \cdot & 3d_{36}+d_{45} & 2d_{24}+3d_{56}-d_{14} & \cdot & 3d_{36}-d_{45} \\ & & \cdot & 2d_{23}+d_{55}-d_{13} & d_{45}-3d_{36} & \cdot \\ & & & \cdot & -d_{14}-4d_{24}-3d_{56} & d_{55}-d_{13}-4d_{23} \\ & & & & \cdot & 3d_{36}+d_{45} \\ & \textit{antisym.} & & & & \cdot \end{Bmatrix}$$

$$\mathbf{G} = \frac{r_m}{h}\begin{Bmatrix} d_{11} & d_{16} & d_{15} & -d_{11} & -d_{16} & -d_{15} \\ & d_{66} & d_{56} & -d_{16} & -d_{66} & -d_{56} \\ & & d_{55} & -d_{15} & -d_{56} & -d_{55} \\ & & & d_{11} & d_{16} & d_{15} \\ & & & & d_{66} & d_{56} \\ sym. & & & & & d_{55} \end{Bmatrix}$$

$$+\frac{1}{2}\begin{Bmatrix} -2d_{12} & d_{16}-d_{26} & -d_{25} & . & d_{16}+d_{26} & d_{25} \\ & 2d_{66} & d_{56} & -(d_{16}+d_{26}) & . & -d_{56} \\ & & . & -d_{25} & d_{56} & . \\ & & & 2d_{12} & d_{26}-d_{16} & d_{25} \\ & & & & -2d_{66} & -d_{56} \\ sym. & & & & & . \end{Bmatrix}$$

$$+\begin{Bmatrix} c_1d_{22} & -c_1d_{26} & . & c_2d_{22} & -c_2d_{26} & . \\ & c_1d_{66} & . & -c_2d_{26} & c_2d_{66} & . \\ & & . & . & . & . \\ & & & c_3d_{22} & -c_3d_{26} & . \\ & & & & c_3d_{66} & . \\ sym. & & & & & . \end{Bmatrix}$$

7B.3 Transverse-isotropic case

The below equations are for the transverse isotropic case. If we change λ_t and G_t to λ and G, respectively, we obtain the expressions for the isotropic case.

$$\mathbf{A}_{\theta\theta} = \begin{Bmatrix} c_1G_t & . & . & c_2G_t & . & . \\ . & c_1(\lambda+2G) & . & . & c_2(\lambda+2G) & . \\ . & . & c_1G & . & . & c_2G \\ c_2G_t & . & . & c_3G_t & . & . \\ . & c_2(\lambda+2G) & . & . & c_3(\lambda+2G) & . \\ . & . & c_2G & . & . & c_3G \end{Bmatrix}$$

$$\mathbf{A}_{\theta z} = \frac{h}{6}\begin{Bmatrix} . & . & . & . & . & . \\ . & . & 2(\lambda+G) & . & . & \lambda+G \\ . & 2(\lambda+G) & . & . & \lambda+G & . \\ . & . & . & . & . & . \\ . & . & \lambda+G & . & . & 2(\lambda+G) \\ . & \lambda+G & . & . & 2(\lambda+G) & . \end{Bmatrix}$$

$$\mathbf{A}_{zz}=\frac{hr_m}{6}\begin{Bmatrix}(2-a)G_t & \cdot & \cdot & G_t & \cdot & \cdot \\ \cdot & (2-a)G & \cdot & \cdot & G & \cdot \\ \cdot & \cdot & (2-a)(\lambda+2G) & \cdot & \cdot & \lambda+2G \\ G_t & \cdot & \cdot & (2+a)G_t & \cdot & \cdot \\ \cdot & G & \cdot & \cdot & (2+a)G & \cdot \\ \cdot & \cdot & \lambda+2G & \cdot & \cdot & (2+a)(\lambda+2G)\end{Bmatrix}$$

$$\mathbf{B}_{\theta}=\frac{1}{2}\begin{Bmatrix}\cdot & \lambda_t-G_t & \cdot & \cdot & \lambda_t+G_t & \cdot \\ -(\lambda_t-G_t) & \cdot & \cdot & \lambda_t+G_t & \cdot & \cdot \\ \cdot & \cdot & \cdot & \cdot & \cdot & \cdot \\ \cdot & -(\lambda_t+G_t) & \cdot & \cdot & -(\lambda_t-G_t) & \cdot \\ -(\lambda_t+G_t) & \cdot & \cdot & \lambda_t-G_t & \cdot & \cdot \\ \cdot & \cdot & \cdot & \cdot & \cdot & \cdot\end{Bmatrix}$$

$$+\begin{Bmatrix}\cdot & -c_1(\lambda+2G+G_t) & \cdot & \cdot & -c_2(\lambda+2G+G_t) & \cdot \\ c_1(\lambda+2G+G_t) & \cdot & \cdot & c_2(\lambda+2G+G_t) & \cdot & \cdot \\ \cdot & \cdot & \cdot & \cdot & \cdot & \cdot \\ \cdot & -c_2(\lambda+2G+G_t) & \cdot & \cdot & -c_3(\lambda+2G+G_t) & \cdot \\ c_2(\lambda+2G+G_t) & \cdot & \cdot & c_3(\lambda+2G+G_t) & \cdot & \cdot \\ \cdot & \cdot & \cdot & \cdot & \cdot & \cdot\end{Bmatrix}$$

$$\mathbf{B}_{z}=\frac{r_m}{2}\begin{Bmatrix}\cdot & \cdot & \lambda_t-G_t & \cdot & \cdot & \lambda_t+G_t \\ \cdot & \cdot & \cdot & \cdot & \cdot & \cdot \\ -(\lambda_t-G_t) & \cdot & \cdot & \lambda_t+G_t & \cdot & \cdot \\ \cdot & \cdot & -(\lambda_t+G_t) & \cdot & \cdot & -(\lambda_t-G_t) \\ \cdot & \cdot & \cdot & \cdot & \cdot & \cdot \\ -(\lambda_t+G_t) & \cdot & \cdot & \lambda_t-G_t & \cdot & \cdot\end{Bmatrix}$$

$$+\frac{ar_m}{6}\begin{Bmatrix}\cdot & \cdot & -(\lambda_t-G_t+4\lambda) & \cdot & \cdot & \lambda_t-G_t-2\lambda \\ \cdot & \cdot & \cdot & \cdot & \cdot & \cdot \\ \lambda_t-G_t+4\lambda & \cdot & \cdot & -(\lambda_t-G_t-2\lambda) & \cdot & \cdot \\ \cdot & \cdot & \lambda_t-G_t-2\lambda & \cdot & \cdot & -(\lambda_t-G_t+4\lambda) \\ \cdot & \cdot & \cdot & \cdot & \cdot & \cdot \\ -(\lambda_t-G_t-2\lambda) & \cdot & \cdot & \lambda_t-G_t+4\lambda & \cdot & \cdot\end{Bmatrix}$$

$$\mathbf{G} = \frac{r_m}{h}\begin{Bmatrix} \lambda_t + 2G_t & . & . & -(\lambda_t + 2G_t) & . & . \\ & G_t & . & . & -G_t & . \\ & & G_t & . & . & -G_t \\ & & & \lambda_t + 2G_t & . & . \\ & & & & G_t & . \\ sym. & & & & & G_t \end{Bmatrix}$$

$$+\begin{Bmatrix} c_1(\lambda + 2G) - \lambda_t & . & . & c_2(\lambda + 2G) & . & . \\ & (c_1 + 1)G_t & . & . & c_2 G_t & . \\ & & . & . & . & . \\ & & & c_3(\lambda + 2G) + \lambda_t & . & . \\ & & & & (c_3 - 1)G_t & . \\ sym. & & & & & . \end{Bmatrix}$$

APPENDIX 7C : Layer Matrices for quadratic expansion

7C.1 Preliminary definitions

$$a=\frac{h}{2r_m}$$

$$c_{11}=\frac{1}{12a^4}\left\{3(1+a)^2\log\frac{1+a}{1-a}-4a^4-8a^3-12a^2-6a\right\}$$

$$c_{22}=\frac{1}{3a^4}\left\{3(1-a^2)^2\log\frac{1+a}{1-a}+10a^3-6a\right\}$$

$$c_{33}=\frac{1}{12a^4}\left\{3(1-a)^2\log\frac{1+a}{1-a}+4a^4-8a^3+12a^2-6a\right\}$$

$$c_{12}=c_{21}=-\frac{(1+a)}{6a^4}\left\{3(1-a^2)\log\frac{1+a}{1-a}+4a^3-6a\right\}$$

$$c_{23}=c_{32}=-\frac{(1-a)}{6a^4}\left\{3(1-a^2)\log\frac{1+a}{1-a}+4a^3-6a\right\}$$

$$c_{13}=c_{31}=\frac{1}{12a^4}\left\{3(1-a^2)\log\frac{1+a}{1-a}+4a^3-6a\right\}$$

For a quadratic expansion, the layer matrices are then

$$\mathbf{M}=\frac{\rho h r_m}{30}\begin{Bmatrix}(4-3a)\mathbf{I} & (2-2a)\mathbf{I} & -\mathbf{I}\\ (2-2a)\mathbf{I} & 16\mathbf{I} & (2+2a)\mathbf{I}\\ -\mathbf{I} & (2+2a)\mathbf{I} & (4+3a)\mathbf{I}\end{Bmatrix}$$

$$\mathbf{A}_{\theta\theta}=\begin{Bmatrix}c_{11}\mathbf{D}_{\theta\theta} & c_{12}\mathbf{D}_{\theta\theta} & c_{13}\mathbf{D}_{\theta\theta}\\ c_{21}\mathbf{D}_{\theta\theta} & c_{22}\mathbf{D}_{\theta\theta} & c_{23}\mathbf{D}_{\theta\theta}\\ c_{31}\mathbf{D}_{\theta\theta} & c_{32}\mathbf{D}_{\theta\theta} & c_{33}\mathbf{D}_{\theta\theta}\end{Bmatrix}$$

$$\mathbf{A}_{\theta z}=\frac{h}{30}\begin{Bmatrix}4(\mathbf{D}_{\theta z}+\mathbf{D}_{z\theta}) & 2(\mathbf{D}_{\theta z}+\mathbf{D}_{z\theta}) & -(\mathbf{D}_{\theta z}+\mathbf{D}_{z\theta})\\ 2(\mathbf{D}_{\theta z}+\mathbf{D}_{z\theta}) & 16(\mathbf{D}_{\theta z}+\mathbf{D}_{z\theta}) & 2(\mathbf{D}_{\theta z}+\mathbf{D}_{z\theta})\\ -(\mathbf{D}_{\theta z}+\mathbf{D}_{z\theta}) & 2(\mathbf{D}_{\theta z}+\mathbf{D}_{z\theta}) & 4(\mathbf{D}_{\theta z}+\mathbf{D}_{z\theta})\end{Bmatrix}$$

$$\mathbf{A}_{zz}=\frac{hr_m}{30}\begin{Bmatrix}(4-3a)\mathbf{D}_{zz} & (2-2a)\mathbf{D}_{zz} & -\mathbf{D}_{zz}\\ (2-2a)\mathbf{D}_{zz} & 16\mathbf{D}_{zz} & (2+2a)\mathbf{D}_{zz}\\ -\mathbf{D}_{zz} & (2+2a)\mathbf{D}_{zz} & (4+3a)\mathbf{D}_{zz}\end{Bmatrix}$$

$$\mathbf{B}_{\theta}=\frac{1}{6}\begin{Bmatrix}3(\mathbf{D}_{r\theta}-\mathbf{D}_{\theta r}) & 4(\mathbf{D}_{r\theta}+\mathbf{D}_{\theta r}) & -(\mathbf{D}_{r\theta}+\mathbf{D}_{\theta r})\\ -4(\mathbf{D}_{r\theta}+\mathbf{D}_{\theta r}) & & 4(\mathbf{D}_{r\theta}+\mathbf{D}_{\theta r})\\ (\mathbf{D}_{r\theta}+\mathbf{D}_{\theta r}) & -4(\mathbf{D}_{r\theta}+\mathbf{D}_{\theta r}) & -3(\mathbf{D}_{r\theta}-\mathbf{D}_{\theta r})\end{Bmatrix}$$

$$+\begin{Bmatrix}c_{11}(\mathbf{D}_{\theta 1}-\mathbf{D}_{1\theta}) & c_{12}(\mathbf{D}_{\theta 1}-\mathbf{D}_{1\theta}) & c_{13}(\mathbf{D}_{\theta 1}-\mathbf{D}_{1\theta})\\ c_{21}(\mathbf{D}_{\theta 1}-\mathbf{D}_{1\theta}) & c_{22}(\mathbf{D}_{\theta 1}-\mathbf{D}_{1\theta}) & c_{23}(\mathbf{D}_{\theta 1}-\mathbf{D}_{1\theta})\\ c_{31}(\mathbf{D}_{\theta 1}-\mathbf{D}_{1\theta}) & c_{32}(\mathbf{D}_{\theta 1}-\mathbf{D}_{1\theta}) & c_{33}(\mathbf{D}_{\theta 1}-\mathbf{D}_{1\theta})\end{Bmatrix}$$

$$\mathbf{B}_z = \frac{r_m}{6}\begin{Bmatrix} -3(\mathbf{D}_{zr}-\mathbf{D}_{rz}) & 4(\mathbf{D}_{zr}+\mathbf{D}_{rz}) & -1(\mathbf{D}_{zr}+\mathbf{D}_{rz}) \\ -4(\mathbf{D}_{zr}+\mathbf{D}_{rz}) & \cdot & 4(\mathbf{D}_{zr}+\mathbf{D}_{rz}) \\ 1(\mathbf{D}_{zr}+\mathbf{D}_{rz}) & -4(\mathbf{D}_{zr}+\mathbf{D}_{rz}) & 3(\mathbf{D}_{zr}-\mathbf{D}_{rz}) \end{Bmatrix}$$
$$+\frac{h}{60}\begin{Bmatrix} 11(\mathbf{D}_{zr}-\mathbf{D}_{rz}) & -12\mathbf{D}_{zr}-8\mathbf{D}_{rz} & \mathbf{D}_{zr}-\mathbf{D}_{rz} \\ 8\mathbf{D}_{zr}+12\mathbf{D}_{rz} & -16(\mathbf{D}_{zr}-\mathbf{D}_{rz}) & 8\mathbf{D}_{zr}+12\mathbf{D}_{rz} \\ \mathbf{D}_{zr}-\mathbf{D}_{rz} & -12\mathbf{D}_{zr}-8\mathbf{D}_{rz} & 11(\mathbf{D}_{zr}-\mathbf{D}_{rz}) \end{Bmatrix}$$
$$+\frac{h}{30}\begin{Bmatrix} 4(\mathbf{D}_{z1}-\mathbf{D}_{1z}) & 2(\mathbf{D}_{z1}-\mathbf{D}_{1z}) & -(\mathbf{D}_{z1}-\mathbf{D}_{1z}) \\ 2(\mathbf{D}_{z1}-\mathbf{D}_{1z}) & 16(\mathbf{D}_{z1}-\mathbf{D}_{1z}) & 2(\mathbf{D}_{z1}-\mathbf{D}_{1z}) \\ -(\mathbf{D}_{z1}-\mathbf{D}_{1z}) & 2(\mathbf{D}_{z1}-\mathbf{D}_{1z}) & 4(\mathbf{D}_{z1}-\mathbf{D}_{1z}) \end{Bmatrix}$$

$$\mathbf{G} = \frac{2}{3}\begin{Bmatrix} -\mathbf{D}_{rr} & \mathbf{D}_{rr} & \cdot \\ \mathbf{D}_{rr} & \cdot & -\mathbf{D}_{rr} \\ \cdot & -\mathbf{D}_{rr} & \mathbf{D}_{rr} \end{Bmatrix} + \frac{r_m}{3h}\begin{Bmatrix} 7\mathbf{D}_{rr} & -8\mathbf{D}_{rr} & \mathbf{D}_{rr} \\ -8\mathbf{D}_{rr} & 16\mathbf{D}_{rr} & -8\mathbf{D}_{rr} \\ \mathbf{D}_{rr} & -8\mathbf{D}_{rr} & 7\mathbf{D}_{rr} \end{Bmatrix}$$
$$+\frac{1}{6}\begin{Bmatrix} -3(\mathbf{D}_{r1}+\mathbf{D}_{1r}) & -4(\mathbf{D}_{r1}-\mathbf{D}_{1r}) & (\mathbf{D}_{r1}-\mathbf{D}_{1r}) \\ 4(\mathbf{D}_{r1}-\mathbf{D}_{1r}) & \cdot & -4(\mathbf{D}_{r1}-\mathbf{D}_{1r}) \\ -(\mathbf{D}_{r1}-\mathbf{D}_{1r}) & 4(\mathbf{D}_{r1}-\mathbf{D}_{1r}) & 3(\mathbf{D}_{r1}+\mathbf{D}_{1r}) \end{Bmatrix} + \begin{Bmatrix} c_{11}\mathbf{D}_{11} & c_{12}\mathbf{D}_{11} & c_{13}\mathbf{D}_{11} \\ c_{21}\mathbf{D}_{11} & c_{22}\mathbf{D}_{11} & c_{23}\mathbf{D}_{11} \\ c_{31}\mathbf{D}_{11} & c_{32}\mathbf{D}_{11} & c_{33}\mathbf{D}_{11} \end{Bmatrix}$$

7C.2 Anisotropic case

In detail these matrices are

$$\mathbf{M} = \frac{\rho h r_m}{30}\begin{Bmatrix} 4-3a & \cdot & \cdot & 2-2a & \cdot & \cdot & -1 & \cdot & \cdot \\ \cdot & 4-3a & \cdot & \cdot & 2-2a & \cdot & \cdot & -1 & \cdot \\ \cdot & \cdot & 4-3a & \cdot & \cdot & 2-2a & \cdot & \cdot & -1 \\ 2-2a & \cdot & \cdot & 16 & \cdot & \cdot & 2+2a & \cdot & \cdot \\ \cdot & 2-2a & \cdot & \cdot & 16 & \cdot & \cdot & 2+2a & \cdot \\ \cdot & \cdot & 2-2a & \cdot & \cdot & 16 & \cdot & \cdot & 2+2a \\ -1 & \cdot & \cdot & 2+2a & \cdot & \cdot & 4+3a & \cdot & \cdot \\ \cdot & -1 & \cdot & \cdot & 2+2a & \cdot & \cdot & 4+3a & \cdot \\ \cdot & \cdot & -1 & \cdot & \cdot & 2+2a & \cdot & \cdot & 4+3a \end{Bmatrix}$$

$$\mathbf{A}_{\theta\theta}=\begin{Bmatrix} c_{11}d_{66} & c_{11}d_{26} & c_{11}d_{46} & c_{12}d_{66} & c_{12}d_{26} & c_{12}d_{46} & c_{13}d_{66} & c_{13}d_{26} & c_{13}d_{46} \\ c_{11}d_{26} & c_{11}d_{22} & c_{11}d_{24} & c_{12}d_{26} & c_{12}d_{22} & c_{12}d_{24} & c_{13}d_{26} & c_{13}d_{22} & c_{13}d_{24} \\ c_{11}d_{46} & c_{11}d_{24} & c_{11}d_{44} & c_{12}d_{46} & c_{12}d_{24} & c_{12}d_{44} & c_{13}d_{46} & c_{13}d_{24} & c_{13}d_{44} \\ c_{21}d_{66} & c_{21}d_{26} & c_{21}d_{46} & c_{22}d_{66} & c_{22}d_{26} & c_{22}d_{46} & c_{23}d_{66} & c_{23}d_{26} & c_{23}d_{46} \\ c_{21}d_{26} & c_{21}d_{22} & c_{12}d_{24} & c_{22}d_{26} & c_{22}d_{22} & c_{22}d_{24} & c_{23}d_{26} & c_{23}d_{22} & c_{23}d_{24} \\ c_{21}d_{46} & c_{21}d_{24} & c_{12}d_{44} & c_{22}d_{46} & c_{22}d_{24} & c_{22}d_{44} & c_{23}d_{46} & c_{23}d_{24} & c_{23}d_{44} \\ c_{31}d_{66} & c_{31}d_{26} & c_{31}d_{46} & c_{32}d_{66} & c_{32}d_{26} & c_{32}d_{46} & c_{33}d_{66} & c_{33}d_{26} & c_{33}d_{46} \\ c_{31}d_{26} & c_{31}d_{22} & c_{31}d_{24} & c_{32}d_{26} & c_{32}d_{22} & c_{32}d_{24} & c_{33}d_{26} & c_{33}d_{22} & c_{33}d_{24} \\ c_{31}d_{46} & c_{31}d_{24} & c_{31}d_{44} & c_{32}d_{46} & c_{32}d_{24} & c_{32}d_{44} & c_{33}d_{46} & c_{33}d_{24} & c_{33}d_{44} \end{Bmatrix}$$

$$\mathbf{A}_{\theta z}=\frac{h}{30}\begin{Bmatrix} 4(2d_{56}) & 4(d_{25}+d_{46}) & 4(d_{36}+d_{45}) & 2(2d_{56}) & 2(d_{25}+d_{46}) & 2(d_{36}+d_{45}) \\ 4(d_{25}+d_{46}) & 4(2d_{24}) & 4(d_{23}+d_{44}) & 2(d_{25}+d_{46}) & 2(2d_{24}) & 2(d_{23}+d_{44}) \\ 4(d_{36}+d_{45}) & 4(d_{23}+d_{44}) & 4(2d_{34}) & 2(d_{36}+d_{45}) & 2(d_{23}+d_{44}) & 2(2d_{34}) \\ 2(2d_{56}) & 2(d_{25}+d_{46}) & 2(d_{36}+d_{45}) & 16(2d_{56}) & 16(d_{25}+d_{46}) & 16(d_{36}+d_{45}) \\ 2(d_{25}+d_{46}) & 2(2d_{24}) & 2(d_{23}+d_{44}) & 16(d_{25}+d_{46}) & 16(2d_{24}) & 16(d_{23}+d_{44}) \\ 2(d_{36}+d_{45}) & 2(d_{23}+d_{44}) & 2(2d_{34}) & 16(d_{36}+d_{45}) & 16(d_{23}+d_{44}) & 16(2d_{34}) \\ -(2d_{56}) & -(d_{25}+d_{46}) & -(d_{36}+d_{45}) & 2(2d_{56}) & 2(d_{25}+d_{46}) & 2(d_{36}+d_{45}) \\ -(d_{25}+d_{46}) & -(2d_{24}) & -(d_{23}+d_{44}) & 2(d_{25}+d_{46}) & 2(2d_{24}) & 2(d_{23}+d_{44}) \\ -(d_{36}+d_{45}) & -(d_{23}+d_{44}) & -(2d_{34}) & 2(d_{36}+d_{45}) & 2(d_{23}+d_{44}) & 2(2d_{34}) \end{Bmatrix}$$

$$\begin{Bmatrix} -(2d_{56}) & -(d_{25}+d_{46}) & -(d_{36}+d_{45}) \\ -(d_{25}+d_{46}) & -(2d_{24}) & -(d_{23}+d_{44}) \\ -(d_{36}+d_{45}) & -(d_{23}+d_{44}) & -(2d_{34}) \\ 2(2d_{56}) & 2(d_{25}+d_{46}) & 2(d_{36}+d_{45}) \\ 2(d_{25}+d_{46}) & 2(2d_{24}) & 2(d_{23}+d_{44}) \\ 2(d_{36}+d_{45}) & 2(d_{23}+d_{44}) & 2(2d_{34}) \\ 4(2d_{56}) & 4(d_{25}+d_{46}) & 4(d_{36}+d_{45}) \\ 4(d_{25}+d_{46}) & 4(2d_{24}) & 4(d_{23}+d_{44}) \\ 4(d_{36}+d_{45}) & 4(d_{23}+d_{44}) & 4(2d_{34}) \end{Bmatrix}$$

$$\mathbf{A}_{zz}=\frac{hr_m}{30}\begin{Bmatrix}
(4-3a)d_{55} & (4-3a)d_{45} & (4-3a)d_{35} & (2-2a)d_{55} & (2-2a)d_{45} & (2-2a)d_{35}\\
(4-3a)d_{45} & (4-3a)d_{44} & (4-3a)d_{34} & (2-2a)d_{45} & (2-2a)d_{44} & (2-2a)d_{34}\\
(4-3a)d_{35} & (4-3a)d_{34} & (4-3a)d_{33} & (2-2a)d_{35} & (2-2a)d_{34} & (2-2a)d_{33}\\
(2-2a)d_{55} & (2-2a)d_{45} & (2-2a)d_{35} & 16d_{55} & 16d_{45} & 16d_{35}\\
(2-2a)d_{45} & (2-2a)d_{44} & (2-2a)d_{34} & 16d_{45} & 16d_{44} & 16d_{34}\\
(2-2a)d_{35} & (2-2a)d_{34} & (2-2a)d_{33} & 16d_{35} & 16d_{34} & 16d_{33}\\
-d_{55} & -d_{45} & -d_{35} & (2+2a)d_{55} & (2+2a)d_{45} & (2+2a)d_{35}\\
-d_{45} & -d_{44} & -d_{34} & (2+2a)d_{45} & (2+2a)d_{44} & (2+2a)d_{34}\\
-d_{35} & -d_{34} & -d_{33} & (2+2a)d_{35} & (2+2a)d_{34} & (2+2a)d_{33}
\end{Bmatrix}$$

$$\begin{matrix}
-d_{55} & -d_{45} & -d_{35}\\
-d_{45} & -d_{44} & -d_{34}\\
-d_{35} & -d_{34} & -d_{33}\\
(2+2a)d_{55} & (2+2a)d_{45} & (2+2a)d_{35}\\
(2+2a)d_{45} & (2+2a)d_{44} & (2+2a)d_{34}\\
(2+2a)d_{35} & (2+2a)d_{34} & (2+2a)d_{33}\\
(4+3a)d_{55} & (4+3a)d_{45} & (4+3a)d_{35}\\
(4+3a)d_{45} & (4+3a)d_{44} & (4+3a)d_{34}\\
(4+3a)d_{35} & (4+3a)d_{34} & (4+3a)d_{33}
\end{matrix}\Bigg\}$$

$$\mathbf{B}_{\theta}=\frac{1}{6}\begin{Bmatrix}
\cdot & 3(d_{12}-d_{66}) & 3(d_{14}-d_{56}) & 4(2d_{16}) & 4(d_{12}+d_{66}) & 4(d_{14}+d_{56})\\
-3(d_{12}-d_{66}) & \cdot & 3(d_{46}-d_{25}) & 4(d_{12}+d_{66}) & 4(2d_{26}) & 4(d_{25}+d_{46})\\
-3(d_{14}-d_{56}) & -3(d_{46}-d_{25}) & \cdot & 4(d_{14}+d_{56}) & 4(d_{25}+d_{46}) & 4(2d_{45})\\
-4(2d_{16}) & -4(d_{12}+d_{66}) & -4(d_{14}+d_{56}) & \cdot & \cdot & \cdot\\
-4(d_{12}+d_{66}) & -4(2d_{26}) & -4(d_{25}+d_{46}) & \cdot & \cdot & \cdot\\
-4(d_{14}+d_{56}) & -4(d_{25}+d_{46}) & -4(2d_{45}) & \cdot & \cdot & \cdot\\
(2d_{16}) & (d_{12}+d_{66}) & (d_{14}+d_{56}) & -4(2d_{16}) & -4(d_{12}+d_{66}) & -4(d_{14}+d_{56})\\
(d_{12}+d_{66}) & (2d_{26}) & (d_{25}+d_{46}) & -4(d_{12}+d_{66}) & -4(2d_{26}) & -4(d_{25}+d_{46})\\
(d_{14}+d_{56}) & (d_{25}+d_{46}) & (2d_{45}) & -4(d_{14}+d_{56}) & -4(d_{25}+d_{46}) & -4(2d_{45})
\end{Bmatrix}$$

$$\begin{matrix}
-(2d_{16}) & -(d_{12}+d_{66}) & -(d_{14}+d_{56})\\
-(d_{12}+d_{66}) & -(2d_{26}) & -(d_{25}+d_{46})\\
-(d_{14}+d_{56}) & -(d_{25}+d_{46}) & -(2d_{45})\\
4(2d_{16}) & 4(d_{12}+d_{66}) & 4(d_{14}+d_{56})\\
4(d_{12}+d_{66}) & 4(2d_{26}) & 4(d_{25}+d_{46})\\
4(d_{14}+d_{56}) & 4(d_{25}+d_{46}) & 4(2d_{45})\\
\cdot & -3(d_{12}-d_{66}) & -3(d_{14}-d_{56})\\
3(d_{12}-d_{66}) & \cdot & -3(d_{46}-d_{25})\\
3(d_{14}-d_{56}) & 3(d_{46}-d_{25}) & \cdot
\end{matrix}\Bigg\}$$

$$
+\left\{\begin{array}{cccccc}
\cdot & -c_{11}(d_{22}+d_{66}) & -c_{11}d_{24} & \cdot & -c_{12}(d_{22}+d_{66}) & -c_{12}d_{24} \\
c_{11}(d_{22}+d_{66}) & \cdot & c_{11}d_{46} & c_{12}(d_{22}+d_{66}) & \cdot & c_{12}d_{46} \\
c_{11}d_{24} & -c_{11}d_{46} & \cdot & c_{12}d_{24} & -c_{12}d_{46} & \cdot \\
\cdot & -c_{21}(d_{22}+d_{66}) & -c_{21}d_{24} & \cdot & -c_{22}(d_{22}+d_{66}) & -c_{22}d_{24} \\
c_{21}(d_{22}+d_{66}) & \cdot & c_{21}d_{46} & c_{22}(d_{22}+d_{66}) & \cdot & c_{22}d_{46} \\
c_{21}d_{24} & -c_{21}d_{46} & \cdot & c_{22}d_{24} & -c_{22}d_{46} & \cdot \\
\cdot & -c_{31}(d_{22}+d_{66}) & -c_{31}d_{24} & \cdot & -c_{32}(d_{22}+d_{66}) & -c_{32}d_{24} \\
c_{31}(d_{22}+d_{66}) & \cdot & c_{31}d_{46} & c_{32}(d_{22}+d_{66}) & \cdot & c_{32}d_{46} \\
c_{31}d_{24} & -c_{31}d_{46} & \cdot & c_{32}d_{24} & -c_{32}d_{46} & \cdot
\end{array}\right.
$$

$$
\left.\begin{array}{ccc}
\cdot & -c_{13}(d_{22}+d_{66}) & -c_{13}d_{24} \\
c_{13}(d_{22}+d_{66}) & \cdot & c_{13}d_{46} \\
c_{13}d_{24} & -c_{13}d_{46} & \cdot \\
\cdot & -c_{23}(d_{22}+d_{66}) & -c_{23}d_{24} \\
c_{23}(d_{22}+d_{66}) & \cdot & c_{23}d_{46} \\
c_{23}d_{24} & -c_{23}d_{46} & \cdot \\
\cdot & -c_{33}(d_{22}+d_{66}) & -c_{33}d_{24} \\
c_{33}(d_{22}+d_{66}) & \cdot & c_{33}d_{46} \\
c_{33}d_{24} & -c_{33}d_{46} & \cdot
\end{array}\right\}
$$

$$
\mathbf{B}_z = \frac{r_m}{6}\left\{\begin{array}{cccccc}
\cdot & 3(d_{14}-d_{56}) & 3(d_{13}-d_{55}) & 4(2d_{15}) & 4(d_{14}+d_{56}) & 4(d_{13}+d_{55}) \\
-3(d_{14}-d_{56}) & \cdot & 3(d_{36}-d_{45}) & 4(d_{14}+d_{56}) & 4(2d_{46}) & 4(d_{36}+d_{45}) \\
-3(d_{13}-d_{55}) & -3(d_{36}-d_{45}) & \cdot & 4(d_{13}+d_{55}) & 4(d_{36}+d_{45}) & 4(2d_{35}) \\
-4(2d_{15}) & -4(d_{14}+d_{56}) & -4(d_{13}+d_{55}) & \cdot & \cdot & \cdot \\
-4(d_{14}+d_{56}) & -4(2d_{46}) & -4(d_{36}+d_{45}) & \cdot & \cdot & \cdot \\
-4(d_{13}+d_{55}) & -4(d_{36}+d_{45}) & -4(2d_{35}) & \cdot & \cdot & \cdot \\
2d_{15} & d_{14}+d_{56} & d_{13}+d_{55} & -4(2d_{15}) & -4(d_{14}+d_{56}) & -4(d_{13}+d_{55}) \\
d_{14}+d_{56} & 2d_{46} & d_{36}+d_{45} & -4(d_{14}+d_{56}) & -4(2d_{46}) & -4(d_{36}+d_{45}) \\
d_{13}+d_{55} & d_{36}+d_{45} & 2d_{35} & -4(d_{13}+d_{55}) & -4(d_{36}+d_{45}) & -4(2d_{35})
\end{array}\right.
$$

$$
\left.\begin{array}{ccc}
-(2d_{15}) & -(d_{14}+d_{56}) & -(d_{13}+d_{55}) \\
-(d_{14}+d_{56}) & -(2d_{46}) & -(d_{36}+d_{45}) \\
-(d_{13}+d_{55}) & -(d_{36}+d_{45}) & -(2d_{35}) \\
4(2d_{15}) & 4(d_{14}+d_{56}) & 4(d_{13}+d_{55}) \\
4(d_{14}+d_{56}) & 4(2d_{46}) & 4(d_{36}+d_{45}) \\
4(d_{13}+d_{55}) & 4(d_{36}+d_{45}) & 4(2d_{35}) \\
\cdot & -3(d_{14}-d_{56}) & -3(d_{13}-d_{55}) \\
3(d_{14}-d_{56}) & \cdot & -3(d_{36}-d_{45}) \\
3(d_{13}-d_{55}) & 3(d_{36}-d_{45}) & \cdot
\end{array}\right\}
$$

$$
+\frac{h}{60}\left\{\begin{array}{cccccc}
\cdot & -11(d_{14}-d_{56}) & -11(d_{13}-d_{55}) & -20d_{15} & -12d_{56}-8d_{14} & -12d_{55}-8d_{13} \\
11(d_{14}-d_{56}) & \cdot & -11(d_{36}-d_{45}) & -12d_{14}-8d_{56} & -20d_{46} & -12d_{45}-8d_{36} \\
11(d_{13}-d_{55}) & 11(d_{36}-d_{45}) & \cdot & -12d_{13}-8d_{55} & -12d_{36}-8d_{45} & -20d_{35} \\
20d_{15} & 8d_{56}+12d_{14} & 8d_{55}+12d_{13} & \cdot & 16(d_{14}-d_{56}) & 16(d_{13}-d_{55}) \\
8d_{14}+12d_{56} & 20d_{46} & 8d_{45}+12d_{36} & -16(d_{14}-d_{56}) & \cdot & 16(d_{36}-d_{45}) \\
8d_{13}+12d_{55} & 8d_{36}+12d_{45} & 20d_{35} & -16(d_{13}-d_{55}) & -16(d_{36}-d_{45}) & \cdot \\
\cdot & -(d_{14}-d_{56}) & -(d_{13}-d_{55}) & -20d_{15} & -12d_{56}-8d_{14} & -12d_{55}-8d_{13} \\
(d_{14}-d_{56}) & \cdot & -(d_{36}-d_{45}) & -12d_{14}-8d_{56} & -20d_{46} & -12d_{45}-8d_{36} \\
(d_{13}-d_{55}) & (d_{36}-d_{45}) & \cdot & -12d_{13}-8d_{55} & -12d_{36}-8d_{45} & -20d_{35}
\end{array}\right.
$$

$$
\left.\begin{array}{ccc}
\cdot & -(d_{14}-d_{56}) & -(d_{13}-d_{55}) \\
(d_{14}-d_{56}) & \cdot & -(d_{36}-d_{45}) \\
(d_{13}-d_{55}) & (d_{36}-d_{45}) & \cdot \\
20d_{15} & 8d_{56}+12d_{14} & 8d_{55}+12d_{13} \\
8d_{14}+12d_{56} & 20d_{46} & 8d_{45}+12d_{36} \\
8d_{13}+12d_{55} & 8d_{36}+12d_{45} & 20d_{35} \\
\cdot & -11(d_{14}-d_{56}) & -11(d_{13}-d_{55}) \\
11(d_{14}-d_{56}) & \cdot & -11(d_{36}-d_{45}) \\
11(d_{13}-d_{55}) & 11(d_{36}-d_{45}) & \cdot
\end{array}\right\}
$$

$$
+\frac{h}{30}\left\{\begin{array}{cccccc}
\cdot & -4(d_{56}+d_{24}) & -4d_{23} & \cdot & -2(d_{56}+d_{24}) & -2d_{23} \\
4(d_{56}+d_{24}) & \cdot & 4d_{36} & 2(d_{56}+d_{24}) & \cdot & 2d_{36} \\
4d_{23} & -4d_{36} & \cdot & 2d_{23} & -2d_{36} & \cdot \\
\cdot & -2(d_{56}+d_{24}) & -2d_{23} & \cdot & -16(d_{56}+d_{24}) & -16d_{23} \\
2(d_{56}+d_{24}) & \cdot & 2d_{36} & 16(d_{56}+d_{24}) & \cdot & 16d_{36} \\
2d_{23} & -2d_{36} & \cdot & 16d_{23} & -16d_{36} & \cdot \\
\cdot & (d_{56}+d_{24}) & d_{23} & \cdot & -2(d_{56}+d_{24}) & -2d_{23} \\
-(d_{56}+d_{24}) & \cdot & -d_{36} & 2(d_{56}+d_{24}) & \cdot & 2d_{36} \\
-d_{23} & d_{36} & \cdot & 2d_{23} & -2d_{36} & \cdot
\end{array}\right.
$$

$$
\left.\begin{array}{ccc}
\cdot & (d_{56}+d_{24}) & d_{23} \\
-(d_{56}+d_{24}) & \cdot & -d_{36} \\
-d_{23} & d_{36} & \cdot \\
\cdot & -2(d_{56}+d_{24}) & -2d_{23} \\
2(d_{56}+d_{24}) & \cdot & 2d_{36} \\
2d_{23} & -2d_{36} & \cdot \\
\cdot & -4(d_{56}+d_{24}) & -4d_{23} \\
4(d_{56}+d_{24}) & \cdot & 4d_{36} \\
4d_{23} & -4d_{36} & \cdot
\end{array}\right\}
$$

$$
\mathbf{G}=\frac{r_m}{3h}\begin{Bmatrix}
7d_{11} & 7d_{16} & 7d_{15} & -8d_{11} & -8d_{16} & -8d_{15} & d_{11} & d_{16} & d_{15}\\
7d_{16} & 7d_{66} & 7d_{56} & -8d_{16} & -8d_{66} & -8d_{56} & d_{16} & d_{66} & d_{56}\\
7d_{15} & 7d_{56} & 7d_{55} & -8d_{15} & -8d_{56} & -8d_{55} & d_{15} & d_{56} & d_{55}\\
-8d_{11} & -8d_{16} & -8d_{15} & 16d_{11} & 16d_{16} & 16d_{15} & -8d_{11} & -8d_{16} & -8d_{15}\\
-8d_{16} & -8d_{66} & -8d_{56} & 16d_{16} & 16d_{66} & 16d_{56} & -8d_{16} & -8d_{66} & -8d_{56}\\
-8d_{15} & -8d_{56} & -8d_{55} & 16d_{15} & 16d_{56} & 16d_{55} & -8d_{15} & -8d_{56} & -8d_{55}\\
d_{11} & d_{16} & d_{15} & -8d_{11} & -8d_{16} & -8d_{15} & 7d_{11} & 7d_{16} & 7d_{15}\\
d_{16} & d_{66} & d_{56} & -8d_{16} & -8d_{66} & -8d_{56} & 7d_{16} & 7d_{66} & 7d_{56}\\
d_{15} & d_{56} & d_{55} & -8d_{15} & -8d_{56} & -8d_{55} & 7d_{15} & 7d_{56} & 7d_{55}
\end{Bmatrix}
$$

$$
+\frac{2}{3}\begin{Bmatrix}
-d_{11} & -d_{16} & -d_{15} & d_{11} & d_{16} & d_{15} & \cdot & \cdot & \cdot\\
-d_{16} & -d_{66} & -d_{56} & d_{16} & d_{66} & d_{56} & \cdot & \cdot & \cdot\\
-d_{15} & -d_{56} & -d_{55} & d_{15} & d_{56} & d_{55} & \cdot & \cdot & \cdot\\
d_{11} & d_{16} & d_{15} & \cdot & \cdot & \cdot & -d_{11} & -d_{16} & -d_{15}\\
d_{16} & d_{66} & d_{56} & \cdot & \cdot & \cdot & -d_{16} & -d_{66} & -d_{56}\\
d_{15} & d_{56} & d_{55} & \cdot & \cdot & \cdot & -d_{15} & -d_{56} & -d_{55}\\
\cdot & \cdot & \cdot & -d_{11} & -d_{16} & -d_{15} & d_{11} & d_{16} & d_{15}\\
\cdot & \cdot & \cdot & -d_{16} & -d_{66} & -d_{56} & d_{16} & d_{66} & d_{56}\\
\cdot & \cdot & \cdot & -d_{15} & -d_{56} & -d_{55} & d_{15} & d_{56} & d_{55}
\end{Bmatrix}
$$

$$
+\frac{1}{6}\begin{Bmatrix}
-3(2d_{12}) & 3(d_{16}-d_{26}) & -3(d_{25}) & \cdot & 4(d_{16}+d_{26}) & 4d_{25}\\
3(d_{16}-d_{26}) & 3(2d_{66}) & 3(d_{56}) & -4(d_{16}+d_{26}) & \cdot & -4d_{56}\\
-3(d_{25}) & 3(d_{56}) & \cdot & -4d_{25} & 4d_{56} & \cdot\\
\cdot & -4(d_{16}+d_{26}) & -4d_{25} & \cdot & \cdot & \cdot\\
4(d_{16}+d_{26}) & \cdot & 4d_{56} & \cdot & \cdot & \cdot\\
4d_{25} & -4d_{56} & \cdot & \cdot & \cdot & \cdot\\
\cdot & (d_{16}+d_{26}) & d_{25} & \cdot & -4(d_{16}+d_{26}) & -4d_{25}\\
-(d_{16}+d_{26}) & \cdot & -d_{56} & 4(d_{16}+d_{26}) & \cdot & 4d_{56}\\
-d_{25} & d_{56} & \cdot & 4d_{25} & -4d_{56} & \cdot
\end{Bmatrix}
$$

$$
\begin{Bmatrix}
\cdot & -(d_{16}+d_{26}) & -d_{25}\\
(d_{16}+d_{26}) & \cdot & d_{56}\\
d_{25} & -d_{56} & \cdot\\
\cdot & 4(d_{16}+d_{26}) & 4d_{25}\\
-4(d_{16}+d_{26}) & \cdot & -4d_{56}\\
-4d_{25} & 4d_{56} & \cdot\\
3(2d_{12}) & -3(d_{16}-d_{26}) & 3(d_{25})\\
-3(d_{16}-d_{26}) & -3(2d_{66}) & -3(d_{56})\\
3(d_{25}) & -3(d_{56}) & \cdot
\end{Bmatrix}
$$

$$+\begin{Bmatrix} c_{11}d_{22} & -c_{11}d_{26} & \cdot & c_{12}d_{22} & -c_{12}d_{26} & \cdot & c_{13}d_{22} & -c_{13}d_{26} & \cdot \\ -c_{11}d_{26} & c_{11}d_{66} & \cdot & -c_{12}d_{26} & c_{12}d_{66} & \cdot & -c_{13}d_{26} & c_{13}d_{66} & \cdot \\ \cdot & \cdot & \cdot & \cdot & \cdot & \cdot & \cdot & \cdot & \cdot \\ c_{21}d_{22} & -c_{21}d_{26} & \cdot & c_{22}d_{22} & -c_{22}d_{26} & \cdot & c_{23}d_{22} & -c_{23}d_{26} & \cdot \\ -c_{21}d_{26} & c_{21}d_{66} & \cdot & -c_{22}d_{26} & c_{22}d_{66} & \cdot & -c_{23}d_{26} & c_{23}d_{66} & \cdot \\ \cdot & \cdot & \cdot & \cdot & \cdot & \cdot & \cdot & \cdot & \cdot \\ c_{31}d_{22} & -c_{31}d_{26} & \cdot & c_{32}d_{22} & -c_{32}d_{26} & \cdot & c_{33}d_{22} & -c_{33}d_{26} & \cdot \\ -c_{31}d_{26} & c_{31}d_{66} & \cdot & -c_{32}d_{26} & c_{32}d_{66} & \cdot & -c_{33}d_{26} & c_{33}d_{66} & \cdot \\ \cdot & \cdot & \cdot & \cdot & \cdot & \cdot & \cdot & \cdot & \cdot \end{Bmatrix}$$

7C.3 Transverse-isotropic case

The below equations are for the transverse isotropic case. If we change λ_t and G_t to λ and G, respectively, we obtain the expressions for the isotropic case.

$$\mathbf{A}_{\theta\theta} = \begin{Bmatrix} c_{11}G_t & \cdot & \cdot & c_{12}G_t & \cdot & \cdot & c_{13}G_t & \cdot & \cdot \\ \cdot & c_{11}(\lambda+2G) & \cdot & \cdot & c_{12}(\lambda+2G) & \cdot & \cdot & c_{13}(\lambda+2G) & \cdot \\ \cdot & \cdot & c_{11}G & \cdot & \cdot & c_{12}G & \cdot & \cdot & c_{13}G \\ c_{21}G_t & \cdot & \cdot & c_{22}G_t & \cdot & \cdot & c_{23}G_t & \cdot & \cdot \\ \cdot & c_{21}(\lambda+2G) & \cdot & \cdot & c_{22}(\lambda+2G) & \cdot & \cdot & c_{23}(\lambda+2G) & \cdot \\ \cdot & \cdot & c_{21}G & \cdot & \cdot & c_{22}G & \cdot & \cdot & c_{23}G \\ c_{31}G_t & \cdot & \cdot & c_{32}G_t & \cdot & \cdot & c_{33}G_t & \cdot & \cdot \\ \cdot & c_{31}(\lambda+2G) & \cdot & \cdot & c_{32}(\lambda+2G) & \cdot & \cdot & c_{33}(\lambda+2G) & \cdot \\ \cdot & \cdot & c_{31}G & \cdot & \cdot & c_{32}G & \cdot & \cdot & c_{33}G \end{Bmatrix}$$

$$\mathbf{A}_{\theta z} = \frac{h}{30}\begin{Bmatrix} \cdot & \cdot & \cdot & \cdot & \cdot & \cdot & \cdot & \cdot & \cdot \\ \cdot & \cdot & 4(\lambda+G) & \cdot & \cdot & 2(\lambda+G) & \cdot & \cdot & -(\lambda+G) \\ \cdot & 4(\lambda+G) & \cdot & \cdot & 2(\lambda+G) & \cdot & \cdot & -(\lambda+G) & \cdot \\ \cdot & \cdot & \cdot & \cdot & \cdot & \cdot & \cdot & \cdot & \cdot \\ \cdot & \cdot & 2(\lambda+G) & \cdot & \cdot & 16(\lambda+G) & \cdot & \cdot & 2(\lambda+G) \\ \cdot & 2(\lambda+G) & \cdot & \cdot & 16(\lambda+G) & \cdot & \cdot & 2(\lambda+G) & \cdot \\ \cdot & \cdot & \cdot & \cdot & \cdot & \cdot & \cdot & \cdot & \cdot \\ \cdot & \cdot & -(\lambda+G) & \cdot & \cdot & 2(\lambda+G) & \cdot & \cdot & 4(\lambda+G) \\ \cdot & -(\lambda+G) & \cdot & \cdot & 2(\lambda+G) & \cdot & \cdot & 4(\lambda+G) & \cdot \end{Bmatrix}$$

$$\mathbf{A}_{zz}=\frac{hr_m}{30}\begin{Bmatrix}(4-3a)G_t & \cdot & \cdot & (2-2a)G_t & \cdot & \cdot \\ \cdot & (4-3a)G & \cdot & \cdot & (2-2a)G & \cdot \\ \cdot & \cdot & (4-3a)(\lambda+2G) & \cdot & \cdot & (2-2a)(\lambda+2G) \\ (2-2a)G_t & \cdot & \cdot & 16G_t & \cdot & \cdot \\ \cdot & (2-2a)G & \cdot & \cdot & 16G & \cdot \\ \cdot & \cdot & (2-2a)(\lambda+2G) & \cdot & \cdot & 16(\lambda+2G) \\ -G_t & \cdot & \cdot & (2+2a)G_t & \cdot & \cdot \\ \cdot & -G & \cdot & \cdot & (2+2a)G & \cdot \\ \cdot & \cdot & -(\lambda+2G) & \cdot & \cdot & (2+2a)(\lambda+2G) \end{Bmatrix}$$

$$\begin{matrix}-G_t & \cdot & \cdot \\ \cdot & -G & \cdot \\ \cdot & \cdot & -(\lambda+2G) \\ (2+2a)G_t & \cdot & \cdot \\ \cdot & (2+2a)G & \cdot \\ \cdot & \cdot & (2+2a)(\lambda+2G) \\ (4+3a)G_t & \cdot & \cdot \\ \cdot & (4+3a)G & \cdot \\ \cdot & \cdot & (4+3a)(\lambda+2G) \end{matrix}\Bigg\}$$

$$\mathbf{B}_\theta=\frac{1}{6}\begin{Bmatrix}\cdot & 3(\lambda_t-G_t) & \cdot & \cdot & 4(\lambda_t+G_t) & \cdot & \cdot & -(\lambda_t+G_t) & \cdot \\ -3(\lambda_t-G_t) & \cdot & \cdot & 4(\lambda_t+G_t) & \cdot & \cdot & -(\lambda_t+G_t) & \cdot & \cdot \\ \cdot & \cdot & \cdot & \cdot & \cdot & \cdot & \cdot & \cdot & \cdot \\ \cdot & -4(\lambda_t+G_t) & \cdot & \cdot & \cdot & \cdot & \cdot & 4(\lambda_t+G_t) & \cdot \\ -4(\lambda_t+G_t) & \cdot & \cdot & \cdot & \cdot & \cdot & 4(\lambda_t+G_t) & \cdot & \cdot \\ \cdot & \cdot & \cdot & \cdot & \cdot & \cdot & \cdot & \cdot & \cdot \\ \cdot & (\lambda_t+G_t) & \cdot & \cdot & -4(\lambda_t+G_t) & \cdot & \cdot & -3(\lambda_t-G_t) & \cdot \\ (\lambda_t+G_t) & \cdot & \cdot & -4(\lambda_t+G_t) & \cdot & \cdot & 3(\lambda_t-G_t) & \cdot & \cdot \\ \cdot & \cdot & \cdot & \cdot & \cdot & \cdot & \cdot & \cdot & \cdot \end{Bmatrix}$$

$$+(G_t+\lambda+2G)\begin{Bmatrix}\cdot & -c_{11} & \cdot & \cdot & -c_{12} & \cdot & \cdot & -c_{13} & \cdot \\ c_{11} & \cdot & \cdot & c_{12} & \cdot & \cdot & c_{13} & \cdot & \cdot \\ \cdot & \cdot & \cdot & \cdot & \cdot & \cdot & \cdot & \cdot & \cdot \\ \cdot & -c_{21} & \cdot & \cdot & -c_{22} & \cdot & \cdot & -c_{23} & \cdot \\ c_{21} & \cdot & \cdot & c_{22} & \cdot & \cdot & c_{23} & \cdot & \cdot \\ \cdot & \cdot & \cdot & \cdot & \cdot & \cdot & \cdot & \cdot & \cdot \\ \cdot & -c_{31} & \cdot & \cdot & -c_{32} & \cdot & \cdot & -c_{33} & \cdot \\ c_{31} & \cdot & \cdot & c_{32} & \cdot & \cdot & c_{33} & \cdot & \cdot \\ \cdot & \cdot & \cdot & \cdot & \cdot & \cdot & \cdot & \cdot & \cdot \end{Bmatrix}$$

$$
\mathbf{B}_z = \frac{r_m}{6}\begin{Bmatrix}
\cdot & \cdot & 3(\lambda_t - G_t) & \cdot & \cdot & 4(\lambda_t + G_t) & \cdot & \cdot & -(\lambda_t + G_t) \\
\cdot & \cdot & \cdot & \cdot & \cdot & \cdot & \cdot & \cdot & \cdot \\
-3(\lambda_t - G_t) & \cdot & \cdot & 4(\lambda_t + G_t) & \cdot & \cdot & -(\lambda_t + G_t) & \cdot & \cdot \\
\cdot & \cdot & -4(\lambda_t + G_t) & \cdot & \cdot & \cdot & \cdot & \cdot & 4(\lambda_t + G_t) \\
\cdot & \cdot & \cdot & \cdot & \cdot & \cdot & \cdot & \cdot & \cdot \\
-4(\lambda_t + G_t) & \cdot & \cdot & \cdot & \cdot & \cdot & 4(\lambda_t + G_t) & \cdot & \cdot \\
\cdot & \cdot & \lambda_t + G_t & \cdot & \cdot & -4(\lambda_t + G_t) & \cdot & \cdot & -3(\lambda_t - G_t) \\
\cdot & \cdot & \cdot & \cdot & \cdot & \cdot & \cdot & \cdot & \cdot \\
\lambda_t + G_t & \cdot & \cdot & -4(\lambda_t + G_t) & \cdot & \cdot & 3(\lambda_t - G_t) & \cdot & \cdot
\end{Bmatrix}
$$

$$
+\frac{h}{60}\begin{Bmatrix}
\cdot & \cdot & -11(\lambda_t - G_t) & \cdot & \cdot & -8\lambda_t - 12G_t & \cdot & \cdot & -(\lambda_t - G_t) \\
\cdot & \cdot & \cdot & \cdot & \cdot & \cdot & \cdot & \cdot & \cdot \\
11(\lambda_t - G_t) & \cdot & \cdot & -12\lambda_t - 8G_t & \cdot & \cdot & (\lambda_t - G_t) & \cdot & \cdot \\
\cdot & \cdot & 12\lambda_t + 8G_t & \cdot & \cdot & 16(\lambda_t - G_t) & \cdot & \cdot & 12\lambda_t + 8G_t \\
\cdot & \cdot & \cdot & \cdot & \cdot & \cdot & \cdot & \cdot & \cdot \\
8\lambda_t + 12G_t & \cdot & \cdot & -16(\lambda_t - G_t) & \cdot & \cdot & 8\lambda_t + 12G_t & \cdot & \cdot \\
\cdot & \cdot & -(\lambda_t - G_t) & \cdot & \cdot & -8\lambda_t - 12G_t & \cdot & \cdot & -11(\lambda_t - G_t) \\
\cdot & \cdot & \cdot & \cdot & \cdot & \cdot & \cdot & \cdot & \cdot \\
(\lambda_t - G_t) & \cdot & \cdot & -12\lambda_t - 8G_t & \cdot & \cdot & 11(\lambda_t - G_t) & \cdot & \cdot
\end{Bmatrix}
$$

$$
+\frac{h}{30}\begin{Bmatrix}
\cdot & \cdot & -4\lambda & \cdot & \cdot & -2\lambda & \cdot & \cdot & \lambda \\
\cdot & \cdot & \cdot & \cdot & \cdot & \cdot & \cdot & \cdot & \cdot \\
4\lambda & \cdot & \cdot & 2\lambda & \cdot & \cdot & -\lambda & \cdot & \cdot \\
\cdot & \cdot & -2\lambda & \cdot & \cdot & -16\lambda & \cdot & \cdot & -2\lambda \\
\cdot & \cdot & \cdot & \cdot & \cdot & \cdot & \cdot & \cdot & \cdot \\
2\lambda & \cdot & \cdot & 16\lambda & \cdot & \cdot & 2\lambda & \cdot & \cdot \\
\cdot & \cdot & d_{23} & \cdot & \cdot & -2\lambda & \cdot & \cdot & -4\lambda \\
\cdot & \cdot & \cdot & \cdot & \cdot & \cdot & \cdot & \cdot & \cdot \\
-\lambda & \cdot & \cdot & 2\lambda & \cdot & \cdot & 4\lambda & \cdot & \cdot
\end{Bmatrix}
$$

$$
\mathbf{G}=\frac{r_m}{3h}\begin{Bmatrix}
7(\lambda_t+2G_t) & \cdot & \cdot & -8(\lambda_t+2G_t) & \cdot & \cdot & (\lambda_t+2G_t) & \cdot & \cdot \\
\cdot & 7G_t & \cdot & \cdot & -8G_t & \cdot & \cdot & G_t & \cdot \\
\cdot & \cdot & 7G_t & \cdot & \cdot & -8G_t & \cdot & \cdot & G_t \\
-8(\lambda_t+2G_t) & \cdot & \cdot & 16(\lambda_t+2G_t) & \cdot & \cdot & -8(\lambda_t+2G_t) & \cdot & \cdot \\
\cdot & -8G_t & \cdot & \cdot & 16G_t & \cdot & \cdot & -8G_t & \cdot \\
\cdot & \cdot & -8G_t & \cdot & \cdot & 16G_t & \cdot & \cdot & -8G_t \\
(\lambda_t+2G_t) & \cdot & \cdot & -8(\lambda_t+2G_t) & \cdot & \cdot & 7(\lambda_t+2G_t) & \cdot & \cdot \\
\cdot & G_t & \cdot & \cdot & -8G_t & \cdot & \cdot & 7G_t & \cdot \\
\cdot & \cdot & G_t & \cdot & \cdot & -8G_t & \cdot & \cdot & 7G_t
\end{Bmatrix}
$$

$$
+\frac{2}{3}\begin{Bmatrix}
-(\lambda_t+2G_t) & \cdot & \cdot & (\lambda_t+2G_t) & \cdot & \cdot & \cdot & \cdot & \cdot \\
\cdot & -G_t & \cdot & \cdot & G_t & \cdot & \cdot & \cdot & \cdot \\
\cdot & \cdot & -G_t & \cdot & \cdot & G_t & \cdot & \cdot & \cdot \\
(\lambda_t+2G_t) & \cdot & \cdot & \cdot & \cdot & \cdot & -(\lambda_t+2G_t) & \cdot & \cdot \\
\cdot & G_t & \cdot & \cdot & \cdot & \cdot & \cdot & -G_t & \cdot \\
\cdot & \cdot & G_t & \cdot & \cdot & \cdot & \cdot & \cdot & -G_t \\
\cdot & \cdot & \cdot & -(\lambda_t+2G_t) & \cdot & \cdot & (\lambda_t+2G_t) & \cdot & \cdot \\
\cdot & \cdot & \cdot & \cdot & -G_t & \cdot & \cdot & G_t & \cdot \\
\cdot & \cdot & \cdot & \cdot & \cdot & -G_t & \cdot & \cdot & G_t
\end{Bmatrix}
$$

$$
+\frac{1}{6}\begin{Bmatrix}
-6\lambda_t & \cdot & \cdot & \cdot & \cdot & \cdot & \cdot & \cdot & \cdot \\
\cdot & 6G_t & \cdot & \cdot & \cdot & \cdot & \cdot & \cdot & \cdot \\
\cdot & \cdot & \cdot & \cdot & \cdot & \cdot & \cdot & \cdot & \cdot \\
\cdot & \cdot & \cdot & \cdot & \cdot & \cdot & \cdot & \cdot & \cdot \\
\cdot & \cdot & \cdot & \cdot & \cdot & \cdot & \cdot & \cdot & \cdot \\
\cdot & \cdot & \cdot & \cdot & \cdot & \cdot & \cdot & \cdot & \cdot \\
\cdot & \cdot & \cdot & \cdot & \cdot & 6\lambda_t & \cdot & \cdot & \cdot \\
\cdot & \cdot & \cdot & \cdot & \cdot & \cdot & -6G_t & \cdot & \cdot \\
\cdot & \cdot & \cdot & \cdot & \cdot & \cdot & \cdot & \cdot & \cdot
\end{Bmatrix}
$$

$$
+\begin{Bmatrix}
c_{11}(\lambda+2G) & \cdot & \cdot & c_{12}(\lambda+2G) & \cdot & \cdot & c_{13}(\lambda+2G) & \cdot & \cdot \\
\cdot & c_{11}G_t & \cdot & \cdot & c_{12}G_t & \cdot & \cdot & c_{13}G_t & \cdot \\
\cdot & \cdot & \cdot & \cdot & \cdot & \cdot & \cdot & \cdot & \cdot \\
c_{21}(\lambda+2G) & \cdot & \cdot & c_{22}(\lambda+2G) & \cdot & \cdot & c_{23}(\lambda+2G) & \cdot & \cdot \\
\cdot & c_{21}G_t & \cdot & \cdot & c_{22}G_t & \cdot & \cdot & c_{23}G_t & \cdot \\
\cdot & \cdot & \cdot & \cdot & \cdot & \cdot & \cdot & \cdot & \cdot \\
c_{31}(\lambda+2G) & \cdot & \cdot & c_{32}(\lambda+2G) & \cdot & \cdot & c_{33}(\lambda+2G) & \cdot & \cdot \\
\cdot & c_{31}G_t & \cdot & \cdot & c_{32}G_t & \cdot & \cdot & c_{33}G_t & \cdot \\
\cdot & \cdot & \cdot & \cdot & \cdot & \cdot & \cdot & \cdot & \cdot
\end{Bmatrix}
$$

Chapter 8 Spherical thin-layer method

8.1 Introduction

In this chapter, we present and formulate another new thin-layer method that is a powerful technique for the analysis of wave propagation in anisotropic, laminated spherical solids and shells. We herein call the new method the spherical thin-layer method, or the STLM for short. Basically, the STLM is a new formulation TLM that is developed in the spherical coordinate system (r, ϕ, θ), instead of in the Cartesian coordinate system (x, y, z) as the case of the TLM for flat layers. Also, discretization is implemented along the radial (r–) direction in the sense of finite element, as the CTLM in chapter 7. After completing the formulation of the STLM, we verify its validation by means of an analytical comparison with the TLM for flat layers and two numerical examples for the propagation modes of a homogeneous spherical solid and shell.

For the above purposes, we perform the following procedures. In section 8.2, we derive a general form of the wave equation for anisotropic material in the spherical coordinate system and also set up the boundary conditions that are necessary for formulating the STLM. In section 8.3, we develop the STLM by means of the principle of virtual work and the discretization of the wave equation along the radial (r–) direction. After all, we obtain the discrete wave equation for the systems of interest. For the verification of the formulated STLM, we compare it with the TLM for flat layers, based on the fact that a spherical shell with a large radius relative to its thickness behaves like an infinite plate. In section 8.4, we solve the discrete wave equation by means of the Fourier-Legendre series with respect to the spatial variables of θ and ϕ, the Fourier transformation with respect to the temporal variable t, and the associated eigenvalue problem in the frequency variable. Thereafter, we apply the modal superposition to obtain the analytical response functions in the wavenumber-time domain. Finally, we perform the series summations over wavenumbers to obtain the responses in the space-time domain due to dynamic excitations in the spherical solids and shells. In section 8.5, we formulate the analytical eigenvalue problem of the continuum that is associated with the propagation modes of isotropic homogeneous spherical solid and shell. In section 8.6, we compare the results of the eigenvalue problems obtained with the two of the STLM and the analytical solution so as to verify the validations of the developed STLM.

8.2 Wave equation in spherical coordinates

The wave equation and boundary conditions needed to describe and specify the behavior of a spherical lamina are developed herein. The boundary conditions need to be prescribed on the inner and outer radial surfaces of each spherical thin-layer. The material is assumed to be anisotropic. At the end of this section, we obtain, using matrix methods, the wave equation for anisotropic media, and also for cross-anisotropic media so as to verify the proposed method.

8.2.1 Wave equation for spherical anisotropy media

Consider a spherical layer (or shell) of linear elastic, homogeneous anisotropy as shown in figure 8.2.1. The dynamic equilibrium equation, the stress-strain relation, and the strain-displacement relation at any point in the medium are expressed by

$$\mathbf{L}_\sigma^{\mathrm{T}}\boldsymbol{\sigma}+\mathbf{b}=\rho\ddot{\mathbf{u}} \tag{8.2.1}$$

$$\boldsymbol{\sigma}=\mathbf{D}\boldsymbol{\varepsilon} \tag{8.2.2}$$

$$\boldsymbol{\varepsilon}=\mathbf{L}_\varepsilon\mathbf{u} \tag{8.2.3}$$

In the above equations, ρ is the mass density, and

$$\boldsymbol{\sigma}=\left[\sigma_r \quad \sigma_\phi \quad \sigma_\theta \quad \tau_{\phi\theta} \quad \tau_{r\theta} \quad \tau_{r\phi}\right]^T \quad = \text{the stress tensor} \tag{8.2.4a}$$

$$\mathbf{b}=\left[b_r \quad b_\phi \quad b_\theta\right]^T \quad = \text{the body load vector} \tag{8.2.4b}$$

$$\mathbf{u}=\left[u_r \quad u_\phi \quad u_\theta\right]^T \quad = \text{the displacement vector} \tag{8.2.4c}$$

$$\boldsymbol{\varepsilon}=\left[\varepsilon_r \quad \varepsilon_\phi \quad \varepsilon_\theta \quad \gamma_{\phi\theta} \quad \gamma_{r\theta} \quad \gamma_{r\phi}\right]^T \quad = \text{the strain tensor} \tag{8.2.4e}$$

$$\mathbf{D}=\begin{Bmatrix} d_{11} & d_{12} & d_{13} & d_{14} & d_{15} & d_{16} \\ d_{21} & d_{22} & d_{23} & d_{24} & d_{25} & d_{26} \\ d_{31} & d_{32} & d_{33} & d_{34} & d_{35} & d_{36} \\ d_{41} & d_{42} & d_{43} & d_{44} & d_{45} & d_{46} \\ d_{51} & d_{52} & d_{53} & d_{54} & d_{55} & d_{56} \\ d_{61} & d_{62} & d_{63} & d_{64} & d_{65} & d_{66} \end{Bmatrix} = \text{constitutive matrix (symmetric!)} \tag{8.2.4f}$$

$$\mathbf{L}_\varepsilon^T=\begin{Bmatrix} \frac{\partial}{\partial r} & \frac{1}{r} & \frac{1}{r} & \cdot & \frac{1}{r\sin\phi}\frac{\partial}{\partial\theta} & \frac{1}{r}\frac{\partial}{\partial\phi} \\ \cdot & \frac{1}{r}\frac{\partial}{\partial\phi} & \frac{\cot\phi}{r} & \frac{1}{r\sin\phi}\frac{\partial}{\partial\theta} & \cdot & \frac{\partial}{\partial r}-\frac{1}{r} \\ \cdot & \cdot & \frac{1}{r\sin\phi}\frac{\partial}{\partial\theta} & \frac{1}{r}\frac{\partial}{\partial\phi}-\frac{\cot\phi}{r} & \frac{\partial}{\partial r}-\frac{1}{r} & \cdot \end{Bmatrix}$$

$$= \text{diff. operator for strain} \tag{8.2.4g}$$

$$\mathbf{L}_\sigma^T=\begin{Bmatrix} \frac{\partial}{\partial r}+\frac{2}{r} & -\frac{1}{r} & -\frac{1}{r} & \cdot & \frac{1}{r\sin\phi}\frac{\partial}{\partial\theta} & \frac{1}{r}\frac{\partial}{\partial\phi}+\frac{\cot\phi}{r} \\ \cdot & \frac{1}{r}\frac{\partial}{\partial\phi}+\frac{\cot\phi}{r} & -\frac{\cot\phi}{r} & \frac{1}{r\sin\phi}\frac{\partial}{\partial\theta} & \cdot & \frac{\partial}{\partial r}+\frac{3}{r} \\ \cdot & \cdot & \frac{1}{r\sin\phi}\frac{\partial}{\partial\theta} & \frac{1}{r}\frac{\partial}{\partial\phi}+\frac{2\cot\phi}{r} & \frac{\partial}{\partial r}+\frac{3}{r} & \cdot \end{Bmatrix}$$

$$= \text{diff. operator for stress} \tag{8.2.4h}$$

The superscript T in the above equations denotes a transposed vector or matrix, and the double dot indicates the second partial derivative with respect to time t. Substituting equations (8.2.2 and 3) into equation (8.2.1), we obtain the wave equation in spherical coordinates:

$$\mathbf{L}_\sigma^T\mathbf{D}\mathbf{L}_\varepsilon\mathbf{u}+\mathbf{b}=\rho\ddot{\mathbf{u}} \tag{8.2.5}$$

On the other hand, the differential operators $\mathbf{L}_\varepsilon$ and $\mathbf{L}_\sigma$ can be written as

$$\mathbf{L}_\varepsilon = \mathbf{L}_r \frac{\partial}{\partial r} + \mathbf{L}_\phi \frac{1}{r}\frac{\partial}{\partial \phi} + \mathbf{L}_\theta \frac{1}{r\sin\phi}\frac{\partial}{\partial \theta} + \mathbf{L}_1 \frac{1}{r} + \mathbf{L}_2 \frac{\cot\phi}{r} \tag{8.2.6a}$$

$$\mathbf{L}_\sigma = \mathbf{L}_r \frac{\partial}{\partial r} + \mathbf{L}_\phi \frac{1}{r}\frac{\partial}{\partial \phi} + \mathbf{L}_\theta \frac{1}{r\sin\phi}\frac{\partial}{\partial \theta} + (2\mathbf{L}_r - \mathbf{L}_1)\frac{1}{r} + (\mathbf{L}_\phi - \mathbf{L}_2)\frac{\cot\phi}{r} \tag{8.2.6b}$$

$$\mathbf{L}_r = \begin{Bmatrix} 1 & \cdot & \cdot \\ \cdot & \cdot & \cdot \\ \cdot & \cdot & \cdot \\ \cdot & \cdot & 1 \\ \cdot & 1 & \cdot \end{Bmatrix}, \mathbf{L}_\phi = \begin{Bmatrix} \cdot & \cdot & \cdot \\ \cdot & 1 & \cdot \\ \cdot & \cdot & \cdot \\ \cdot & \cdot & 1 \\ 1 & \cdot & \cdot \end{Bmatrix}, \mathbf{L}_\theta = \begin{Bmatrix} \cdot & \cdot & \cdot \\ \cdot & \cdot & \cdot \\ \cdot & \cdot & 1 \\ \cdot & 1 & \cdot \\ 1 & \cdot & \cdot \end{Bmatrix}, \mathbf{L}_1 = \begin{Bmatrix} \cdot & \cdot & \cdot \\ 1 & \cdot & \cdot \\ 1 & \cdot & \cdot \\ \cdot & \cdot & -1 \\ \cdot & -1 & \cdot \end{Bmatrix}, \mathbf{L}_2 = \begin{Bmatrix} \cdot & \cdot & \cdot \\ \cdot & \cdot & \cdot \\ \cdot & 1 & \cdot \\ \cdot & \cdot & -1 \\ \cdot & \cdot & \cdot \end{Bmatrix} \tag{8.2.6c-g}$$

It follows that the expansion of the product $\mathbf{L}_\sigma^T \mathbf{D} \mathbf{L}_\varepsilon$ is of the form

$$\mathbf{L}_\sigma^T \mathbf{D} \mathbf{L}_\varepsilon = \left(\mathbf{L}_r^T \frac{\partial}{\partial r} + \mathbf{L}_\phi^T \frac{1}{r}\frac{\partial}{\partial \phi} + \mathbf{L}_\theta^T \frac{1}{r\sin\phi}\frac{\partial}{\partial \theta} + (2\mathbf{L}_r - \mathbf{L}_1)^T \frac{1}{r} + (\mathbf{L}_\phi - \mathbf{L}_2)^T \frac{\cot\phi}{r} \right) \mathbf{D} \left(\mathbf{L}_r \frac{\partial}{\partial r} + \mathbf{L}_\phi \frac{1}{r}\frac{\partial}{\partial \phi} + \mathbf{L}_\theta \frac{1}{r\sin\phi}\frac{\partial}{\partial \theta} + \mathbf{L}_1 \frac{1}{r} + \mathbf{L}_2 \frac{\cot\phi}{r} \right) \tag{8.2.7a}$$

which after expansion yields

$$\begin{aligned}
\mathbf{L}_\sigma^T \mathbf{D} \mathbf{L}_\varepsilon = {} & \mathbf{D}_{rr}\frac{\partial^2}{\partial r^2} + \mathbf{D}_{\phi\phi}\frac{1}{r^2}\frac{\partial^2}{\partial \phi^2} + \mathbf{D}_{\theta\theta}\frac{1}{r^2\sin^2\phi}\frac{\partial^2}{\partial \theta^2} \\
& + (\mathbf{D}_{r\phi} + \mathbf{D}_{\phi r})\frac{1}{r}\frac{\partial^2}{\partial r \partial \phi} + (\mathbf{D}_{r\theta} + \mathbf{D}_{\theta r})\frac{1}{r\sin\phi}\frac{\partial^2}{\partial r \partial \theta} + (\mathbf{D}_{\phi\theta} + \mathbf{D}_{\theta\phi})\frac{1}{r^2\sin\phi}\frac{\partial^2}{\partial \phi \partial \theta} \\
& + (2\mathbf{D}_{rr} + \mathbf{D}_{r1} - \mathbf{D}_{1r})\frac{1}{r}\frac{\partial}{\partial r} + (\mathbf{D}_{\phi r} + \mathbf{D}_{r2} - \mathbf{D}_{2r})\frac{\cot\phi}{r}\frac{\partial}{\partial r} \\
& + (\mathbf{D}_{r\phi} + \mathbf{D}_{\phi 1} - \mathbf{D}_{1\phi})\frac{1}{r^2}\frac{\partial}{\partial \phi} + (\mathbf{D}_{\phi\phi} + \mathbf{D}_{\phi 2} - \mathbf{D}_{2\phi})\frac{\cot\phi}{r^2}\frac{\partial}{\partial \phi} \\
& + (\mathbf{D}_{r\theta} + \mathbf{D}_{\theta 1} - \mathbf{D}_{1\theta})\frac{1}{r^2\sin\phi}\frac{\partial}{\partial \theta} + (\mathbf{D}_{\theta 2} - \mathbf{D}_{2\theta})\frac{\cot\phi}{r^2\sin\phi}\frac{\partial}{\partial \theta} \\
& + (\mathbf{D}_{r1} - \mathbf{D}_{1r})\frac{1}{r^2} + (\mathbf{D}_{r2} + \mathbf{D}_{\phi 1} - \mathbf{D}_{12} - \mathbf{D}_{21})\frac{\cot\phi}{r^2} \\
& - \mathbf{D}_{\phi 2}\frac{1}{r^2\sin^2\phi} + (\mathbf{D}_{\phi 2} - \mathbf{D}_{22})\frac{\cot^2\phi}{r^2}
\end{aligned} \tag{8.2.7b}$$

The material matrices $\mathbf{D}_{\alpha\beta}$ are defined by

$$\mathbf{D}_{\alpha\beta} = \mathbf{L}_\alpha^T \mathbf{D} \mathbf{L}_\beta, \alpha, \beta = r, \phi, \theta, 1, 2 \tag{8.2.8}$$

which are presented in Appendix 8A. These matrices depend only on the material properties, and can be readily evaluated for any anisotropic medium. It should be noted, however, that these equations assume that the constitutive properties are *not* a function of ϕ and θ, so the material is assumed to have some kind of spherical symmetry. An example is the case of an onion-like body, such as the earth's crust. Substituting equations (8.2.7 and 8) into equation (8.2.5), we obtain the general wave equation for a spherically anisotropic solid.

8.2.2 Boundary conditions

To assemble the discretized equations in the thin-layer method, we need the boundary conditions that relate the force equilibrium between the internal stresses and the external tractions at each spherical interface. Figure 8.2.2 shows the boundary conditions. The internal stresses in any spherical surface have three components and can be written in the vector form as

$$\mathbf{s}=\begin{bmatrix}\sigma_r & \tau_{r\phi} & \tau_{r\theta}\end{bmatrix}^T=\mathbf{L}_r^T\boldsymbol{\sigma}=\mathbf{L}_r^T\mathbf{D}\mathbf{L}_\varepsilon\mathbf{u} \tag{8.2.9a}$$

Application of equation (8.2.8) to equation (8.2.9a) yields then,

$$\mathbf{s}=\left[\mathbf{D}_{rr}\frac{\partial}{\partial r}+\mathbf{D}_{r\phi}\frac{1}{r}\frac{\partial}{\partial\phi}+\mathbf{D}_{r\theta}\frac{1}{r\sin\phi}\frac{\partial}{\partial\theta}+\mathbf{D}_{r1}\frac{1}{r}+\mathbf{D}_{r2}\frac{\cot\phi}{r}\right]\mathbf{u} \tag{8.2.9b}$$

These matrices are given in Appendix 8A. Finally, the boundary conditions with prescribed external tractions $\mathbf{t}$ are of the form

$$\mathbf{t}-\mathbf{s}_\nu=\mathbf{0} \tag{8.2.10}$$

with $\mathbf{s}_\nu$ being the vector of internal stresses at the boundary with normal ν. For an inner spherical boundary $\mathbf{s}_\nu=-\mathbf{s}$, while for an outer spherical boundary $\mathbf{s}_\nu=\mathbf{s}$, with $\mathbf{s}$ given in either case by equations (8.2.9).

8.2.3 Wave equation for a cross-anisotropic medium

The elements of the constitutive matrix for a cross-anisotropic (transversely isotropic) material are

$$\left.\begin{aligned}&d_{22}=d_{33}=\lambda+2G\\&d_{23}=d_{32}=\lambda\\&d_{44}=G\end{aligned}\right\}\text{ in the isotropic plane (ϕ–θ plane)}$$

$$\left.\begin{aligned}&d_{11}=\lambda_t+2G_t\\&d_{12}=d_{21}=d_{13}=d_{31}=\lambda_t\\&d_{55}=d_{66}=G_t\end{aligned}\right\}\text{ in the transverse direction (radial direction)} \tag{8.2.11}$$

All other elements d_{ij} are zero. Consequently, the wave equation in the cross-anisotropic medium is as follows:

$$\left[\begin{Bmatrix}\lambda_t+2G_t & \cdot & \cdot\\ \cdot & G_t & \cdot\\ \cdot & \cdot & G_t\end{Bmatrix}\frac{\partial^2}{\partial r^2}+\begin{Bmatrix}G_t & \cdot & \cdot\\ \cdot & \lambda+2G & \cdot\\ \cdot & \cdot & G\end{Bmatrix}\frac{1}{r}\frac{\partial^2}{\partial\phi^2}+\begin{Bmatrix}G_t & \cdot & \cdot\\ \cdot & G & \cdot\\ \cdot & \cdot & \lambda+2G\end{Bmatrix}\frac{1}{r^2\sin^2\phi}\frac{\partial^2}{\partial\theta^2}\right.$$

$$+(\lambda_t+G_t)\begin{Bmatrix}\cdot & 1 & \cdot\\ 1 & \cdot & \cdot\\ \cdot & \cdot & \cdot\end{Bmatrix}\frac{1}{r}\frac{\partial^2}{\partial r\partial\phi}+(\lambda_t+G_t)\begin{Bmatrix}\cdot & \cdot & 1\\ \cdot & \cdot & \cdot\\ 1 & \cdot & \cdot\end{Bmatrix}\frac{1}{r\sin\phi}\frac{\partial^2}{\partial r\partial\theta}+(\lambda+G)\begin{Bmatrix}\cdot & \cdot & \cdot\\ \cdot & \cdot & 1\\ \cdot & 1 & \cdot\end{Bmatrix}\frac{1}{r^2\sin\phi}\frac{\partial^2}{\partial\phi\partial\theta}$$

$$\left.+2\begin{Bmatrix}\lambda_t+2G_t & \cdot & \cdot\\ \cdot & G_t & \cdot\\ \cdot & \cdot & G_t\end{Bmatrix}\frac{1}{r}\frac{\partial}{\partial r}+\begin{Bmatrix}\cdot & \lambda_t+G_t & \cdot\\ \cdot & \cdot & \cdot\\ \cdot & \cdot & \cdot\end{Bmatrix}\frac{\cot\phi}{r}\frac{\partial}{\partial r}+\right.$$

$$
+\begin{Bmatrix} \cdot & \lambda_t - G_t - 2(\lambda+G) & \cdot \\ 2(G_t+\lambda+G) & \cdot & \cdot \\ \cdot & \cdot & \cdot \end{Bmatrix} \frac{1}{r^2}\frac{\partial}{\partial\phi} + \begin{Bmatrix} G_t & \cdot & \cdot \\ \cdot & \lambda+2G & \cdot \\ \cdot & \cdot & G \end{Bmatrix} \frac{\cot\phi}{r^2}\frac{\partial}{\partial\phi}
$$

$$
+\begin{Bmatrix} \cdot & \cdot & \lambda - G_t - 2(\lambda+G) \\ \cdot & \cdot & \cdot \\ 2(G_t+\lambda+G) & \cdot & \cdot \end{Bmatrix} \frac{1}{r^2\sin\phi}\frac{\partial}{\partial\theta} + \begin{Bmatrix} \cdot & \cdot & \cdot \\ \cdot & \cdot & -(\lambda+3G) \\ \cdot & \lambda+3G & \cdot \end{Bmatrix} \frac{\cot\phi}{r^2\sin\phi}\frac{\partial}{\partial\theta}
$$

$$
+2\begin{Bmatrix} \lambda_t - 2(\lambda+G) & \cdot & \cdot \\ \cdot & -G_t & \cdot \\ \cdot & \cdot & -G_t \end{Bmatrix} \frac{1}{r^2} + \begin{Bmatrix} \cdot & \lambda_t - G_t - 2(\lambda+G) & \cdot \\ \cdot & \cdot & \cdot \\ \cdot & \cdot & \cdot \end{Bmatrix} \frac{\cot\phi}{r^2}
$$

$$
-\left[\begin{Bmatrix} \cdot & \cdot & \cdot \\ \cdot & \lambda & \cdot \\ \cdot & \cdot & G \end{Bmatrix} \frac{1}{r^2\sin^2\phi} - 2\begin{Bmatrix} \cdot & \cdot & \cdot \\ \cdot & G_t & \cdot \\ \cdot & \cdot & G_t \end{Bmatrix} \frac{\cot^2\phi}{r^2} \right] \mathbf{u} + \mathbf{b} = \rho\ddot{\mathbf{u}} \tag{8.2.12}
$$

By setting $\lambda_t=\lambda$ and $G_t=G$, we can obtain the case of isotropic materials.

8.3 Spherical thin-layer method

The spherical thin-layer method is formulated by means of discretization of the medium of interest along the radial (r–) direction, and applying the principle of virtual work to consider the work done by residual forces. Finally, assemblage of the discretized equations leads to a system of partial differential equations. To verify this formulation, all the coefficient matrices of a spherical thin-layer are compared with those of the TLM for flat thin-layers. This verification is based on the fact that a spherical shell whose radius is large when compared to its thickness behaves like an infinite, flat plate.

8.3.1 Formulation of the spherical thin-layer method

In the STLM, physical spherical layers (or shells) are divided into thin-layers that are thin in the finite element sense. In addition, each thin-layer is divided into sub-layers. The number of sub-layers depends on the interpolation order m that is chosen for the spherical thin-layer formulation. Accordingly, the dimension of the total system of discretized equations also depends on the total number of thin-layers and the interpolation order m.

We cut out an individual spherical thin-layer from the whole system as shown in fig. 8.3.1, and consider it as a free body in space. Depending on the order m of interpolation, this thin-layer may contain in turn sublayers which can be labeled with indices, l, l+1, $\cdots$, l+m (from the inner to outer surfaces). We also apply two external tractions $\mathbf{t}_l$ and $\mathbf{t}_{l+m}$ so as to preserve the dynamic equilibrium of this free body. We approximate the displacement field within a spherical thin-layer by means of an interpolation:

$$\mathbf{u} = \mathbf{N}\mathbf{U} \tag{8.3.1}$$

where $\mathbf{N}$ is a matrix containing the interpolation polynomials, and $\mathbf{U}$ is a column vector composed of the interface displacement vectors

$$\mathbf{U} = \left[\mathbf{u}_l^T \quad \mathbf{u}_{l+1}^T \quad \cdots \quad \mathbf{u}_{l+m}^T \right]^T \tag{8.3.2}$$

In the following, we will restrict our attention to only two interpolations of m=1 (*linear*) and 2 (*quadratic*). Therefore, the column vector $\mathbf{U}$ and the interpolation matrix $\mathbf{N}$ are of the form:
For linear expansion (m=1),

$$\mathbf{U}=\begin{bmatrix}\mathbf{u}_l^T & \mathbf{u}_{l+1}^T\end{bmatrix}^T \tag{8.3.3a}$$

$$\mathbf{N}=\frac{1}{2}[(1-\varsigma)\mathbf{I} \quad (1+\varsigma)\mathbf{I}] \qquad (-1\le\varsigma\le 1) \tag{8.3.3b}$$

For quadratic expansion (m=2),

$$\mathbf{U}=\begin{bmatrix}\mathbf{u}_l^T & \mathbf{u}_{l+1}^T & \mathbf{u}_{l+2}^T\end{bmatrix}^T \tag{8.3.4a}$$

$$\mathbf{N}=\frac{1}{2}[\zeta(\zeta-1)\mathbf{I} \quad -2(\zeta-1)(\zeta+1)\mathbf{I} \quad \zeta(\zeta+1)\mathbf{I}] \qquad (-1\le\varsigma\le 1) \tag{8.3.4b}$$

where $\mathbf{I}$ is the 3×3 identity matrix, $\varsigma=\frac{2}{h}(r-r_m)$, $h=r_{l+m}-r_l$ = thickness of a thin-layer, and $r_m=\frac{1}{2}(r_l+r_{l+m})$= radius of the thin-layer's mid-surface. Equation (8.3.1) can be rewritten in the following form:
For linear expansion (m=1),

$$\mathbf{u}=\mathbf{NU}=\frac{1}{2}[(1-\varsigma)\mathbf{I} \quad (1+\varsigma)\mathbf{I}]\begin{bmatrix}\mathbf{u}_l\\ \mathbf{u}_{l+1}\end{bmatrix} \tag{8.3.5}$$

For quadratic expansion (m=2),

$$\mathbf{u}=\mathbf{NU}=\frac{1}{2}[\zeta(\zeta-1)\mathbf{I} \quad -2(\zeta-1)(\zeta+1)\mathbf{I} \quad \zeta(\zeta+1)\mathbf{I}]\begin{bmatrix}\mathbf{u}_l\\ \mathbf{u}_{l+1}\\ \mathbf{u}_{l+2}\end{bmatrix} \tag{8.3.6}$$

where

$$\mathbf{u}_l=\begin{bmatrix}u_r^l & u_\theta^l & u_z^l\end{bmatrix}^T,\ \mathbf{u}_{l+1}=\begin{bmatrix}u_r^{l+1} & u_\theta^{l+1} & u_z^{l+1}\end{bmatrix}^T,\ \text{and}\ \mathbf{u}_{l+2}=\begin{bmatrix}u_r^{l+2} & u_\theta^{l+2} & u_z^{l+2}\end{bmatrix}^T \tag{8.3.7abc}$$

Equations (8.3.5 and 6) represent a partial discretization of the displacement field, namely one in the layering direction, which in this case is the radial direction. This discretized displacement field is not an exact solution to the given wave equation. Thus, when substituted into both the wave equation (8.2.5) and into the boundary conditions (8.2.10), the displacement expansion (8.3.1) does not identically satisfy equations (8.2.5 and 10). Therefore, in the sense of the finite element method, residual body forces $\mathbf{w}=\mathbf{w}(r,\phi,\theta,t)$ and the residual boundary tractions $\mathbf{q}=\mathbf{q}(r,\phi,\theta,t)$ are introduced as unbalanced forces:

$$\mathbf{L}_\sigma^T\mathbf{D}\mathbf{L}_\varepsilon\mathbf{u}+\mathbf{b}-\rho\ddot{\mathbf{u}}=\mathbf{w} \tag{8.3.8a}$$

$$\mathbf{t}-\mathbf{s}_v=\mathbf{q} \tag{8.3.8b}$$

The method of weighted residuals requires that the virtual work done by the residual forces $\mathbf{w}$ and $\mathbf{q}$ as a result of the virtual displacement $\delta\mathbf{u}$ within the elementary volume $dV=r^2dr\sin\phi\,d\phi\,d\theta$ and on the boundary surface $dS=r^2\sin\phi\,d\phi\,d\theta$ of a spherical thin-layer be zero, i.e.,

$$\left[\delta\mathbf{u}_l^T\mathbf{q}_l r_l^2+\delta\mathbf{u}_{l+m}^T\mathbf{q}_{l+m}r_{l+m}^2+\int_{r_l}^{r_{l+m}}\delta\mathbf{u}^T\mathbf{w}\,r^2dr\right]\sin\phi\,d\phi\,d\theta=0 \tag{8.3.9}$$

In above equation (8.3.9), the first two terms represent the virtual work performed by the residual tractions of $\mathbf{q}_l$ and $\mathbf{q}_{l+m}$ on the inner and outer boundaries, respectively, of a spherical thin-layer. The integration term that follows corresponds to the virtual work done by the residual body forces $\mathbf{w}$. In equation (8.3.9), there is no term associated with internal stresses along the two boundaries

that are parallel to the radial direction, i.e., $dS = r\,dr\sin\phi\,d\theta$ and $dS = r\,dr\,d\phi$; the reason is that their virtual work cancels identically with the work of the equal and opposite stresses acting on neighboring elementary volumes. Substituting equations (8.3.5 or 6) and (8.3.8) into equation (8.3.9) and canceling out $\sin\phi\,d\phi\,d\theta$, we obtain

$$\begin{aligned}&\delta\mathbf{u}_l^T\mathbf{t}_l\,r_l^2+\delta\mathbf{u}_{l+m}^T\mathbf{t}_{l+m}\,r_{l+m}^2+\delta\mathbf{U}^T\int_{r_l}^{r_{l+m}}\mathbf{N}^T\mathbf{b}\,r^2dr\\&=\delta\mathbf{U}^T\left\{\int_{r_l}^{r_{l+m}}\mathbf{N}^T\mathbf{N}\rho\,r^2dr\right\}\ddot{\mathbf{U}}-\delta\mathbf{U}^T\left\{\int_{r_l}^{r_{l+m}}\mathbf{N}^T\mathbf{L}_\sigma^T\mathbf{D}\mathbf{L}_\varepsilon\mathbf{N}\,r^2dr\right\}\mathbf{U}-\delta\mathbf{u}_l^T\mathbf{s}_l\,r_l^2+\delta\mathbf{u}_{l+m}^T\mathbf{s}_{l+m}\,r_{l+m}^2\end{aligned} \tag{8.3.10}$$

When we require this expression to be valid for arbitrary variations $\delta\mathbf{U}$, we obtain the dynamic equilibrium equation for a spherical thin-layer of the following form

$$\begin{bmatrix}\mathbf{p}_l\\\mathbf{p}_{l+1}\\\vdots\\\mathbf{p}_{l+m}\end{bmatrix}=\left\{\int_{r_l}^{r_{l+m}}\mathbf{N}^T\mathbf{N}\rho\,r^2dr\right\}\begin{bmatrix}\ddot{\mathbf{u}}_l\\\ddot{\mathbf{u}}_{l+1}\\\vdots\\\ddot{\mathbf{u}}_{l+m}\end{bmatrix}+\begin{bmatrix}-\mathbf{L}_r^T\mathbf{D}\mathbf{L}_\varepsilon r_l^2\mathbf{u}_l\\\\\\\mathbf{L}_r^T\mathbf{D}\mathbf{L}_\varepsilon r_{l+m}^2\mathbf{u}_{l+m}\end{bmatrix}-\left\{\int_{r_l}^{r_{l+m}}\mathbf{N}^T\mathbf{L}_\sigma^T\mathbf{D}\mathbf{L}_\varepsilon\mathbf{N}\,r^2dr\right\}\begin{bmatrix}\mathbf{u}_l\\\mathbf{u}_{l+1}\\\vdots\\\mathbf{u}_{l+m}\end{bmatrix} \tag{8.3.11}$$

The left hand side is the vector of the consistent external tractions $\mathbf{p}$ acting on the sub-layers interfaces which are the resultant of the interface tractions $\mathbf{t}$ and body loads $\mathbf{b}$. On the other hand, the right hand side contains the inertial loads as well as the elastic loads of deformation. Calculation of the above equation (8.3.11) with the chosen interpolation polynomials and the material constitutive matrix yields

$$\begin{aligned}\mathbf{P}=\mathbf{M}\ddot{\mathbf{U}}&-\mathbf{A}_{\phi\phi}\frac{\partial^2\mathbf{U}}{\partial\phi^2}-\mathbf{A}_{\phi\theta}\frac{1}{\sin\phi}\frac{\partial^2\mathbf{U}}{\partial\phi\partial\theta}-\mathbf{A}_{\theta\theta}\frac{1}{\sin^2\phi}\frac{\partial^2\mathbf{U}}{\partial\theta^2}\\&-\left(\mathbf{B}_{\phi1}+\cot\phi\,\mathbf{B}_{\phi2}\right)\frac{\partial\mathbf{U}}{\partial\phi}-\left(\mathbf{B}_{\theta1}+\cot\phi\,\mathbf{B}_{\theta2}\right)\frac{1}{\sin\phi}\frac{\partial\mathbf{U}}{\partial\theta}\\&+\left(\mathbf{G}_1+\cot\phi\,\mathbf{G}_2+\cot^2\phi\,\mathbf{G}_3\right)\mathbf{U}\end{aligned} \tag{8.3.12}$$

where

$$\mathbf{P}=\left[\mathbf{p}_l\quad\mathbf{p}_{l+1}\quad\cdots\quad\mathbf{p}_{l+m}\right]^T \tag{8.3.13}$$

$$\mathbf{M}=\int_{r_l}^{r_{l+m}}\mathbf{N}^T\mathbf{N}\rho\,r^2dr \tag{8.3.14}$$

$$\mathbf{A}_{\phi\phi}=\int_{r_l}^{r_{l+m}}\mathbf{N}^T\mathbf{D}_{\phi\phi}\mathbf{N}dr \tag{8.3.15a}$$

$$\mathbf{A}_{\phi\theta}=\int_{r_l}^{r_{l+m}}\mathbf{N}^T\left(\mathbf{D}_{\phi\theta}+\mathbf{D}_{\theta\phi}\right)\mathbf{N}dr \tag{8.3.15b}$$

$$\mathbf{A}_{\theta\theta}=\int_{r}^{r_{l+m}}\mathbf{N}^T\mathbf{D}_{\theta\theta}\mathbf{N}dr \tag{8.3.15c}$$

$$\mathbf{B}_{\phi1}=\int_{r_l}^{r_{l+m}}\mathbf{N}^T\mathbf{D}_{\phi r}\mathbf{N}'rdr-\left\{\int_{r_l}^{r_{l+m}}\mathbf{N}^T\mathbf{D}_{\phi r}\mathbf{N}'rdr\right\}^T+\int_{r_l}^{r_{l+m}}\mathbf{N}^T\left(\mathbf{D}_{\phi1}-\mathbf{D}_{1\phi}\right)\mathbf{N}dr \tag{8.3.15d}$$

$$\mathbf{B}_{\phi2}=\int_{r_l}^{r_{l+m}}\mathbf{N}^T\left(\mathbf{D}_{\phi\phi}+\mathbf{D}_{\phi2}-\mathbf{D}_{2\phi}\right)\mathbf{N}dr \tag{8.3.15e}$$

$$\mathbf{B}_{\theta1}=\int_{r_l}^{r_{l+m}}\mathbf{N}^T\mathbf{D}_{\theta r}\mathbf{N}'r\,dr-\left\{\int_{r_l}^{r_{l+m}}\mathbf{N}^T\mathbf{D}_{\theta r}\mathbf{N}'r\,dr\right\}^T+\int_{r_l}^{r_{l+m}}\mathbf{N}^T\left(\mathbf{D}_{\theta1}-\mathbf{D}_{1\theta}\right)\mathbf{N}dr \tag{8.3.15f}$$

$$\mathbf{B}_{\theta2}=\int_{r_l}^{r_{l+m}}\mathbf{N}^T\left(\mathbf{D}_{\theta2}-\mathbf{D}_{2\theta}\right)\mathbf{N}dr \tag{8.3.15g}$$

$$\mathbf{G}_1 = \int_{r_l}^{r_{l+m}} \mathbf{N}'^T \mathbf{D}_{rr} \mathbf{N}' r^2 \, dr + \left\{ \int_{r_l}^{r_{l+m}} \left[\mathbf{N}'^T \mathbf{D}_{1r} \mathbf{N} + \mathbf{N}^T \mathbf{D}_{1r} \mathbf{N}' \right] r dr \right\} + \int_{r_l}^{r_{l+m}} \mathbf{N}^T (\mathbf{D}_{11} + \mathbf{D}_{\phi 2}) \mathbf{N} \, dr \tag{8.3.15h}$$

$$\mathbf{G}_2 = -\int_{r_l}^{r_{l+m}} \mathbf{N}^T \mathbf{D}_{\phi r} \mathbf{N}' r \, dr + \int_{r_l}^{r_{l+m}} \left[\mathbf{N}'^T \mathbf{D}_{r2} \mathbf{N} + \mathbf{N}^T \mathbf{D}_{2r} \mathbf{N}' \right] r dr - \int_{r_l}^{r_{l+m}} \mathbf{N}^T (\mathbf{D}_{\phi 1} - \mathbf{D}_{12} - \mathbf{D}_{21}) \mathbf{N} \, dr \tag{8.3.15i}$$

$$\mathbf{G}_3 = \int_{r_l}^{r_{l+m}} \mathbf{N}^T \mathbf{D}_{22} \mathbf{N} \, dr \tag{8.3.15j}$$

with $\mathbf{N}' = d\mathbf{N}/dr$. These matrices are given in full form in Appendices 8B and 8C, respectively, for the linear and quadratic expansion.

At this stage, the results for a single spherical thin-layer are overlapped with those of all other spherical thin-layers so as to generate the system matrix. To avoid the use of additional symbols, the same symbols as equation (8.3.12) are used to formulate the system matrix equation for the N-layer spherical body.

$$\begin{aligned} \mathbf{P} = \mathbf{M}\ddot{\mathbf{U}} - \mathbf{A}_{\phi\phi} \frac{\partial^2 \mathbf{U}}{\partial \phi^2} - \mathbf{A}_{\phi\theta} \frac{1}{\sin\phi} \frac{\partial^2 \mathbf{U}}{\partial \phi \partial \theta} - \mathbf{A}_{\theta\theta} \frac{1}{\sin^2 \phi} \frac{\partial^2 \mathbf{U}}{\partial \theta^2} \\ - \left(\mathbf{B}_{\phi 1} + \cot\phi \mathbf{B}_{\phi 2} \right) \frac{\partial \mathbf{U}}{\partial \phi} - \left(\mathbf{B}_{\theta 1} + \cot\phi \mathbf{B}_{\theta 2} \right) \frac{1}{\sin\phi} \frac{\partial \mathbf{U}}{\partial \theta} \\ + \left(\mathbf{G}_1 + \cot\phi \mathbf{G}_2 + \cot^2 \phi \mathbf{G}_3 \right) \mathbf{U} \end{aligned} \tag{8.3.16}$$

where

$$\mathbf{P} = \left[p_r^1 \quad p_\phi^1 \quad p_\theta^1 \quad p_r^2 \quad \cdots \quad p_\theta^N \right]^T \tag{8.3.17a}$$

$$\mathbf{U} = \left[u_r^1 \quad u_\phi^1 \quad u_\theta^1 \quad u_r^2 \quad \cdots \quad u_\theta^N \right]^T \tag{8.3.17b}$$

In above equations (8.3.17a and b), the superscripts indicate the interface to which they belong, and the subscripts denote the coordinate direction. The system matrix is narrowly banded and has a total of $3N$ degrees of freedom, with N being the number of active interfaces, which depends on the number of thin-layers, the expansion order (here, 1 or 2) and the boundary conditions at the top and bottom surfaces.

8.3.2 Comparison of the STLM with the TLM

To verify the spherical thin-layer method formulated in section 8.3.1, we compare here the layer matrices involved against those of the TLM for flat layers. We base this comparison on the fact that a spherical shell with large radius and small thickness behaves like a flat plate. For this purpose, we explore the behavior of the parameter

$$a = \frac{h}{2r_m} \tag{8.3.18}$$

in which h is the thickness of a spherical thin-layer, and r_m is the radius of the middle surface. When the radius of the spherical shell is increased to infinity while holding the layer thickness constant, r_m in each spherical thin-layer also increases without bound and the parameter a approaches zero.

Now, the system equation for a *single* spherical thin-layer is

$$\mathbf{M}\ddot{\mathbf{U}}-\mathbf{A}_{\phi\phi}\frac{\partial^2\mathbf{U}}{\partial\phi^2}-\mathbf{A}_{\phi\theta}\frac{1}{\sin\phi}\frac{\partial^2\mathbf{U}}{\partial\phi\partial\theta}-\mathbf{A}_{\theta\theta}\frac{1}{\sin^2\phi}\frac{\partial^2\mathbf{U}}{\partial\theta^2}$$
$$-\left(\mathbf{B}_{\phi 1}+\cot\phi\,\mathbf{B}_{\phi 2}\right)\frac{\partial\mathbf{U}}{\partial\phi}-\left(\mathbf{B}_{\theta 1}+\cot\phi\,\mathbf{B}_{\theta 2}\right)\frac{1}{\sin\phi}\frac{\partial\mathbf{U}}{\partial\theta}+\left(\mathbf{G}_1+\cot\phi\,\mathbf{G}_2+\cot^2\phi\,\mathbf{G}_3\right)\mathbf{U}=\mathbf{0} \tag{8.3.19}$$

in which the layer matrices are as listed in Appendices 8B and 8C, respectively, for the linear and quadratic expansion. On the other hand, in Cartesian coordinates ($\bar{x}$, $\bar{y}$, $\bar{z}$), the system equation for flat layers is of the form

$$\bar{\mathbf{M}}\ddot{\mathbf{U}}-\bar{\mathbf{A}}_{xx}\frac{\partial^2\mathbf{U}}{\partial\bar{x}^2}-\bar{\mathbf{A}}_{xy}\frac{\partial^2\mathbf{U}}{\partial\bar{x}\partial\bar{y}}-\bar{\mathbf{A}}_{yy}\frac{\partial^2\mathbf{U}}{\partial\bar{y}^2}-\bar{\mathbf{B}}_x\frac{\partial\mathbf{U}}{\partial\bar{y}}-\bar{\mathbf{B}}_y\frac{\partial\mathbf{U}}{\partial\bar{y}}+\bar{\mathbf{G}}\mathbf{U}=\mathbf{0} \tag{8.3.20}$$

with layer matrices that will be identified in turn. In the equations above, a bar indicates that the matrices refer to those for flat layers. To make the comparison, we must now match the two coordinate systems:

$$r\to\bar{z}\,;\qquad \phi\to\bar{x}\,;\qquad \theta\to\bar{y} \tag{8.3.21a-c}$$

However, in equation (8.3.21b and c), the second and third pairs are dimensionally unequal. Therefore, we divide the system equation by the mean radius r_m^2, and use it to define the characteristic arc lengths

$$\phi r_m = x \tag{8.3.22-a}$$

$$\sin\phi\;\theta r_m = y \tag{8.3.22-b}$$

The system equation transforms then into

$$\tfrac{1}{r_m^2}\mathbf{M}\ddot{\mathbf{U}}-\mathbf{A}_{\phi\phi}\frac{\partial^2\mathbf{U}}{\partial x^2}-\mathbf{A}_{\phi\theta}\frac{\partial^2\mathbf{U}}{\partial x\partial y}-\mathbf{A}_{\theta\theta}\frac{\partial^2\mathbf{U}}{\partial y^2}$$
$$-\frac{1}{r_m}\left(\mathbf{B}_{\phi 1}+\cot\phi\,\mathbf{B}_{\phi 2}\right)\frac{\partial\mathbf{U}}{\partial x}-\frac{1}{r_m}\left(\mathbf{B}_{\theta 1}+\cot\phi\,\mathbf{B}_{\theta 2}\right)\frac{\partial\mathbf{U}}{\partial\theta}+\frac{1}{r_m^2}\left(\mathbf{G}_1+\cot\phi\,\mathbf{G}_2+\cot^2\phi\,\mathbf{G}_3\right)\mathbf{U}=\mathbf{0} \tag{8.3.23}$$

We will now show that the coefficient matrices of the spherical thin-layer method become the same as those for flat layers when r_m is made large enough, i.e., as $r_m\to\infty$. When this is done, the parameter a tends to zero, that is

$$\lim_{r_m\to\infty} a=\lim_{r_m\to\infty}\frac{h}{2r_m}=0 \tag{8.3.24}$$

First, w consider the case of linear expansion STLM of m=1. We begin with the mass matrices $\mathbf{M}$ and $\bar{\mathbf{M}}$:

$$\tfrac{1}{r_m^2}\mathbf{M}=\tfrac{1}{r_m^2}\lim_{a\to 0}\frac{\rho h r_m^2}{2}\begin{Bmatrix}(\frac{4}{15}a^2-\frac{2}{3}a+\frac{2}{3})\mathbf{I} & (\frac{1}{15}a^2+\frac{1}{3})\mathbf{I}\\ (\frac{1}{15}a^2+\frac{1}{3})\mathbf{I} & (\frac{4}{15}a^2+\frac{2}{3}a+\frac{2}{3})\mathbf{I}\end{Bmatrix}=\frac{\rho h}{6}\begin{Bmatrix}2\mathbf{I} & \mathbf{I}\\ \mathbf{I} & 2\mathbf{I}\end{Bmatrix}\equiv\bar{\mathbf{M}} \tag{8.3.25}$$

Next, we examine the matrix $\mathbf{A}_{\phi\phi}$.

$$\mathbf{A}_{\phi\phi}=\frac{h}{6}\begin{Bmatrix}2\mathbf{D}_{\phi\phi} & \mathbf{D}_{\phi\phi}\\ \mathbf{D}_{\phi\phi} & 2\mathbf{D}_{\phi\phi}\end{Bmatrix}=\frac{h}{6}\begin{Bmatrix}2\mathbf{D}_{yy} & \mathbf{D}_{yy}\\ \mathbf{D}_{yy} & 2\mathbf{D}_{yy}\end{Bmatrix}\equiv\bar{\mathbf{A}}_{xx} \tag{8.3.26}$$

For the matrices $\mathbf{A}_{\phi\theta}$ and $\bar{\mathbf{A}}_{xy}$ as well as the matrices $\mathbf{A}_{\theta\theta}$ and $\bar{\mathbf{A}}_{yy}$, we also have immediately

$$\mathbf{A}_{\phi\theta}=\frac{h}{6}\begin{Bmatrix}2(\mathbf{D}_{\phi\theta}+\mathbf{D}_{\theta\phi}) & \mathbf{D}_{\phi\theta}+\mathbf{D}_{\theta\phi}\\ \mathbf{D}_{\phi\theta}+\mathbf{D}_{\theta\phi} & 2(\mathbf{D}_{\phi\theta}+\mathbf{D}_{\theta\phi})\end{Bmatrix}=\frac{h}{6}\begin{Bmatrix}2(\mathbf{D}_{xy}+\mathbf{D}_{yx}) & \mathbf{D}_{xy}+\mathbf{D}_{yx}\\ \mathbf{D}_{xy}+\mathbf{D}_{yx} & 2(\mathbf{D}_{xy}+\mathbf{D}_{yx})\end{Bmatrix}\equiv\bar{\mathbf{A}}_{xy} \tag{8.3.27}$$

and

$$\mathbf{A}_{\theta\theta}=\frac{h}{6}\begin{Bmatrix}2\mathbf{D}_{\theta\theta} & \mathbf{D}_{\theta\theta}\\ \mathbf{D}_{\theta\theta} & 2\mathbf{D}_{\theta\theta}\end{Bmatrix}=\frac{h}{6}\begin{Bmatrix}2\mathbf{D}_{yy} & \mathbf{D}_{yy}\\ \mathbf{D}_{yy} & 2\mathbf{D}_{yy}\end{Bmatrix}\equiv\bar{\mathbf{A}}_{yy} \tag{8.3.28}$$

Next, we consider $\mathbf{B}_{\phi 1}+\cot\phi\,\mathbf{B}_{\phi 2}$.

$$\begin{aligned}
&\lim_{r_m\to\infty}\frac{1}{r_m}\left(\mathbf{B}_{\phi 1}+\cot\phi\,\mathbf{B}_{\phi 2}\right)\\
&=\lim_{r_m\to\infty}\frac{1}{r_m}\left[\frac{h}{12}\begin{Bmatrix}-(\mathbf{D}_{r\phi}-\mathbf{D}_{\phi r}) & \mathbf{D}_{r\phi}-\mathbf{D}_{\phi r}\\ \mathbf{D}_{r\phi}-\mathbf{D}_{\phi r} & -(\mathbf{D}_{r\phi}-\mathbf{D}_{\phi r})\end{Bmatrix}\right.\\
&\left.+\frac{h}{6}\begin{Bmatrix}2(\mathbf{D}_{\phi 1}-\mathbf{D}_{1\phi}) & \mathbf{D}_{\phi 1}-\mathbf{D}_{1\phi}\\ \mathbf{D}_{\phi 1}-\mathbf{D}_{1\phi} & 2(\mathbf{D}_{\phi 1}-\mathbf{D}_{1\phi})\end{Bmatrix}+\frac{r_m}{2}\begin{Bmatrix}\mathbf{D}_{r\phi}-\mathbf{D}_{\phi r} & \mathbf{D}_{r\phi}+\mathbf{D}_{\phi r}\\ -(\mathbf{D}_{r\phi}+\mathbf{D}_{\phi r}) & -(\mathbf{D}_{r\phi}-\mathbf{D}_{\phi r})\end{Bmatrix}\right]\\
&+\frac{1}{r_m}\cot\phi\frac{h}{6}\begin{Bmatrix}2(\mathbf{D}_{\phi\phi}+\mathbf{D}_{\phi 2}-\mathbf{D}_{2\phi}) & \mathbf{D}_{\phi\phi}+\mathbf{D}_{\phi 2}-\mathbf{D}_{2\phi}\\ \mathbf{D}_{\phi\phi}+\mathbf{D}_{\phi 2}-\mathbf{D}_{2\phi} & 2(\mathbf{D}_{\phi\phi}+\mathbf{D}_{\phi 2}-\mathbf{D}_{2\phi})\end{Bmatrix}\\
&=\frac{1}{2}\begin{Bmatrix}\mathbf{D}_{r\phi}-\mathbf{D}_{\phi r} & \mathbf{D}_{r\phi}+\mathbf{D}_{\phi r}\\ -(\mathbf{D}_{r\phi}+\mathbf{D}_{\phi r}) & -(\mathbf{D}_{r\phi}-\mathbf{D}_{\phi r})\end{Bmatrix}=-\frac{1}{2}\begin{Bmatrix}\mathbf{D}_{xz}-\mathbf{D}_{zx} & (\mathbf{D}_{xz}+\mathbf{D}_{zx})\\ -(\mathbf{D}_{xz}+\mathbf{D}_{zx}) & -(\mathbf{D}_{xz}-\mathbf{D}_{zx})\end{Bmatrix}\equiv-\bar{\mathbf{B}}_x
\end{aligned} \tag{8.3.29}$$

The negative sign in front of the matrix for plane layers is the result of the ordering of the layer interfaces. In the spherical case, we order the interfaces in the direction of growing r (i.e. from the inside to the outside), while for plane layers, we order them in the direction opposite to the vertical coordinate (i.e. top layer first). This ordering indeed changes the signs, a fact that can be verified by exchanging in the expression above the diagonal and off-diagonal elements, respectively, and noticing that the same expression but with opposite signs is obtained.

As we shall see next, this same sign reversal will be observed in the $\mathbf{B}_{\theta 1}+\cot\phi\,\mathbf{B}_{\theta 2}$ and $\bar{\mathbf{B}}_y$ matrices:

$$\begin{aligned}
&\lim_{r_m\to\infty}\frac{1}{r_m}\left(\mathbf{B}_{\theta 1}+\cot\phi\,\mathbf{B}_{\theta 2}\right)\\
&=\lim_{r_m\to\infty}\frac{1}{r_m}\left[\frac{h}{12}\begin{Bmatrix}-(\mathbf{D}_{r\theta}-\mathbf{D}_{\theta r}) & \mathbf{D}_{r\theta}-\mathbf{D}_{\theta r}\\ \mathbf{D}_{r\theta}-\mathbf{D}_{\theta r} & -(\mathbf{D}_{r\theta}-\mathbf{D}_{\theta r})\end{Bmatrix}\right.\\
&\left.+\frac{h}{6}\begin{Bmatrix}2(\mathbf{D}_{\theta 1}-\mathbf{D}_{1\theta}) & \mathbf{D}_{\theta 1}-\mathbf{D}_{1\theta}\\ \mathbf{D}_{\theta 1}-\mathbf{D}_{1\theta} & 2(\mathbf{D}_{\theta 1}-\mathbf{D}_{1\theta})\end{Bmatrix}+\frac{r_m}{2}\begin{Bmatrix}\mathbf{D}_{r\theta}-\mathbf{D}_{\theta r} & \mathbf{D}_{r\theta}+\mathbf{D}_{\theta r}\\ -(\mathbf{D}_{r\theta}+\mathbf{D}_{\theta r}) & -(\mathbf{D}_{r\theta}-\mathbf{D}_{\theta r})\end{Bmatrix}\right]\\
&+\frac{1}{r_m}\cot\phi\frac{h}{6}\begin{Bmatrix}2(\mathbf{D}_{\theta 2}-\mathbf{D}_{2\theta}) & \mathbf{D}_{\theta 2}-\mathbf{D}_{2\theta}\\ \mathbf{D}_{\theta 2}-\mathbf{D}_{2\theta} & 2(\mathbf{D}_{\theta 2}-\mathbf{D}_{2\theta})\end{Bmatrix}\\
&=\frac{1}{2}\begin{Bmatrix}\mathbf{D}_{r\theta}-\mathbf{D}_{\theta r} & \mathbf{D}_{r\theta}+\mathbf{D}_{\theta r}\\ -(\mathbf{D}_{r\theta}+\mathbf{D}_{\theta r}) & -(\mathbf{D}_{r\theta}-\mathbf{D}_{\theta r})\end{Bmatrix}=-\frac{1}{2}\begin{Bmatrix}\mathbf{D}_{yz}-\mathbf{D}_{zy} & (\mathbf{D}_{yz}+\mathbf{D}_{zy})\\ -(\mathbf{D}_{yz}+\mathbf{D}_{zy}) & -(\mathbf{D}_{yz}-\mathbf{D}_{zy})\end{Bmatrix}\equiv-\bar{\mathbf{B}}_y
\end{aligned} \tag{8.3.30}$$

Finally, for the matrices $\mathbf{G}$ and $\bar{\mathbf{G}}$, we have

$$\lim_{r_m\to\infty}\frac{1}{r_m^2}\mathbf{G}=\frac{1}{r_m^2}\left(\mathbf{G}_1+\cot\phi\,\mathbf{G}_2+\cot^2\phi\,\mathbf{G}_3\right)$$

$$=\lim_{r_m\to\infty}\frac{1}{r_m^2}\left[\frac{h}{12}\begin{Bmatrix}\mathbf{D}_{rr}+(\mathbf{D}_{r1}+\mathbf{D}_{1r}) & -\mathbf{D}_{rr}-(\mathbf{D}_{r1}+\mathbf{D}_{1r})\\ -\mathbf{D}_{rr}-(\mathbf{D}_{r1}+\mathbf{D}_{1r}) & \mathbf{D}_{rr}+(\mathbf{D}_{r1}+\mathbf{D}_{1r})\end{Bmatrix}\right.$$

$$+\frac{h}{6}\begin{bmatrix}2(\mathbf{D}_{11}+\mathbf{D}_{\phi 2}) & \mathbf{D}_{11}+\mathbf{D}_{\phi 2}\\ \mathbf{D}_{11}+\mathbf{D}_{\phi 2} & 2(\mathbf{D}_{11}+\mathbf{D}_{\phi 2})\end{bmatrix}+\frac{r_m}{2}\begin{bmatrix}-(\mathbf{D}_{r1}+\mathbf{D}_{1r}) & -(\mathbf{D}_{r1}-\mathbf{D}_{1r})\\ \mathbf{D}_{r1}-\mathbf{D}_{1r} & \mathbf{D}_{r1}+\mathbf{D}_{1r}\end{bmatrix}$$

$$\left.+\frac{r_m^2}{h}\begin{bmatrix}\mathbf{D}_{rr} & -\mathbf{D}_{rr}\\ -\mathbf{D}_{rr} & \mathbf{D}_{rr}\end{bmatrix}\right]$$

$$+\frac{1}{r_m^2}\cot\phi\left[\frac{h}{12}\begin{Bmatrix}-\mathbf{D}_{\phi r}+(\mathbf{D}_{r2}+\mathbf{D}_{2r}) & \mathbf{D}_{\phi r}-(\mathbf{D}_{r2}+\mathbf{D}_{2r})\\ \mathbf{D}_{\phi r}-(\mathbf{D}_{r2}+\mathbf{D}_{2r}) & -\mathbf{D}_{\phi r}+(\mathbf{D}_{r2}+\mathbf{D}_{2r})\end{Bmatrix}\right.$$

$$+\frac{h}{6}\begin{bmatrix}-2(\mathbf{D}_{\phi 1}-\mathbf{D}_{12}-\mathbf{D}_{21}) & -(\mathbf{D}_{\phi 1}-\mathbf{D}_{12}-\mathbf{D}_{21})\\ -(\mathbf{D}_{\phi 1}-\mathbf{D}_{12}-\mathbf{D}_{21}) & -2(\mathbf{D}_{\phi 1}-\mathbf{D}_{12}-\mathbf{D}_{21})\end{bmatrix}$$

$$\left.+\frac{r_m}{2}\begin{bmatrix}\mathbf{D}_{\phi r}-\mathbf{D}_{r2}-\mathbf{D}_{2r} & -\mathbf{D}_{\phi r}-\mathbf{D}_{r2}+\mathbf{D}_{2r}\\ \mathbf{D}_{\phi r}+\mathbf{D}_{r2}-\mathbf{D}_{2r} & -\mathbf{D}_{\phi r}+\mathbf{D}_{r2}+\mathbf{D}_{2r}\end{bmatrix}\right]+\frac{1}{r_m^2}\cot\phi\frac{h}{12}\begin{Bmatrix}4\mathbf{D}_{22} & 2\mathbf{D}_{22}\\ 2\mathbf{D}_{22} & 4\mathbf{D}_{22}\end{Bmatrix}$$

$$=\frac{1}{h}\begin{Bmatrix}\mathbf{D}_{rr} & -\mathbf{D}_{rr}\\ -\mathbf{D}_{rr} & \mathbf{D}_{rr}\end{Bmatrix}=\frac{1}{h}\begin{Bmatrix}\mathbf{D}_{zz} & -\mathbf{D}_{zz}\\ -\mathbf{D}_{zz} & \mathbf{D}_{zz}\end{Bmatrix}=\bar{\mathbf{G}} \tag{8.3.31}$$

As having seen above, we have obtained the same results as for flat layers. Hence, the formulation is consistent. Also, it is noted that we can conclude the same agreement with the case of quadratic expansion, which is not discussed in the present study.

8.4 Solution of the discrete wave equations

The discrete system equation in section 8.3 is obtained by applying a finite element formulation in the radial direction, while maintaining the spatial (ϕ, θ) and time (t) domains as continuous. To solve this system equation, Fourier and Legendre transformation are performed from the space-time domain to the wavenumber-frequency domain. This process yields an algebraic equation that contains the wavenumbers as parameters and the frequency as eigenvalues. Considering that the constitutive matrix is symmetric and positive-definite, it is possible to show that all eigenvalues in this problem will be real and non-negative. Using then these eigenvalues in the context of a modal superposition technique, we obtain the closed-form solution for the discrete equation of motion.

8.4.1 Transformation of the system of equations

The partial discretization of the wave equation in the layering direction eliminates the functional dependence on the radial coordinate r, and yields a system of partial differential equations in the

azimuthal, polar and time coordinates such as ϕ, θ, and t. From the preceding sections, this system of partial differential equations is

$$\begin{aligned}\mathbf{P} = \mathbf{M}\ddot{\mathbf{U}} - \mathbf{A}_{\phi\phi}\frac{\partial^2\mathbf{U}}{\partial\phi^2} - \mathbf{A}_{\phi\theta}\frac{1}{\sin\phi}\frac{\partial^2\mathbf{U}}{\partial\phi\partial\theta} - \mathbf{A}_{\theta\theta}\frac{1}{\sin^2\phi}\frac{\partial^2\mathbf{U}}{\partial\theta^2} \\ -\left(\mathbf{B}_{\phi 1} + \cot\phi\,\mathbf{B}_{\phi 2}\right)\frac{\partial\mathbf{U}}{\partial\phi} - \left(\mathbf{B}_{\theta 1} + \cot\phi\,\mathbf{B}_{\theta 2}\right)\frac{1}{\sin\phi}\frac{\partial\mathbf{U}}{\partial\theta} \\ +\left(\mathbf{G}_1 + \cot\phi\,\mathbf{G}_2 + \cot^2\phi\,\mathbf{G}_3\right)\mathbf{U}\end{aligned} \tag{8.4.1}$$

$$\mathbf{P} = \left[\, p_r^1 \;\; p_\phi^1 \;\; p_\theta^1 \;\; p_r^2 \;\; \cdots \;\; p_\theta^N \,\right]^T \tag{8.4.2a}$$

$$\mathbf{U} = \left[\, u_r^1 \;\; u_\phi^1 \;\; u_\theta^1 \;\; u_r^2 \;\; \cdots \;\; u_\theta^N \,\right]^T \tag{8.4.2b}$$

In particular, we assume the material matrix $\mathbf{D}$ to be of the form.

$$\mathbf{D} = \begin{Bmatrix} \lambda_t + 2G_t & \lambda_t & \lambda_t & \cdot & \cdot & \cdot \\ \lambda_t & \lambda + 2G & \lambda & \cdot & \cdot & \cdot \\ \lambda_t & \lambda & \lambda + 2G & \cdot & \cdot & \cdot \\ \cdot & \cdot & \cdot & G & \cdot & \cdot \\ \cdot & \cdot & \cdot & \cdot & G_t & \cdot \\ \cdot & \cdot & \cdot & \cdot & \cdot & G_t \end{Bmatrix} \tag{8.4.3}$$

To solve equation (8.4.1), we perform the Fourier transforms with respect to azimuthal coordinate θ and time t, and Legendre transforms with respect to polar coordinate ϕ. In the transformed domain, the discrete system displacement and traction fields can be written as $\bar{\mathbf{U}}$ and $\bar{\mathbf{P}}$, and their relationships with the actual domain variables are of the form

$$\mathbf{U} = e^{\mathrm{i}(\omega t - n\theta)}\,\mathbf{L}_m^n\,\bar{\mathbf{U}} \tag{8.4.4a}$$

$$\mathbf{P} = e^{\mathrm{i}(\omega t - n\theta)}\,\mathbf{L}_m^n\,\bar{\mathbf{P}} \tag{8.4.4b}$$

where

$$\mathbf{L}_m^n = \begin{Bmatrix} P_m^n & \cdot & \cdot \\ \cdot & P_m^{n\prime} & \dfrac{in}{\sin\phi}P_m^n \\ \cdot & -\dfrac{in}{\sin\phi}P_m^n & P_m^{n\prime} \end{Bmatrix} \tag{8.4.5a}$$

$$\bar{\mathbf{P}} = \left[\, \bar{p}_r^1 \;\; \bar{p}_S^1 \;\; \bar{p}_T^1 \;\; \bar{p}_r^2 \;\; \cdots \;\; \bar{p}_T^N \,\right]^T \tag{8.4.5b}$$

$$\bar{\mathbf{U}} = \left[\, \bar{u}_r^1 \;\; \bar{u}_S^1 \;\; \bar{u}_T^1 \;\; \bar{u}_r^2 \;\; \cdots \;\; \bar{u}_T^N \,\right]^T \tag{8.4.5c}$$

In equations (8.4.5a, b, and c), ($\bar{u}_r$, $\bar{p}_r$) are the displacement and traction components in the radial direction, ($\bar{u}_S$, $\bar{u}_T$) and ($\bar{p}_S$, $\bar{p}_T$) are *auxiliary* (non-physical) displacements and tractions components used to express the *actual* displacement components in ϕ and θ. In addition, ω is the angular frequency; n and m are the azimuthal and polar wavenumbers, respectively; and $P_m^{n\prime} = dP_m^n / d\phi$, with $P_m^n(\cos\phi)$ being the associated Legendre function that satisfies the Legendre equation about which we discuss in more detail in the next section 8.5. The partial derivatives in equation (8.4.1) are then

$$\frac{\partial^2 \mathbf{U}}{\partial t^2} = -\omega^2 \mathbf{L}_m^n \bar{\mathbf{U}} e^{i(\omega t - n\theta)} \qquad \frac{\partial \mathbf{U}}{\partial \theta} = -in\mathbf{L}_m^n \bar{\mathbf{U}} e^{i(\omega t - n\theta)} \qquad \frac{\partial \mathbf{U}}{\partial \phi} = \mathbf{L}_m^{n\prime} \bar{\mathbf{U}} e^{i(\omega t - n\theta)}$$

$$\frac{\partial^2 \mathbf{U}}{\partial \phi \partial \theta} = -in\mathbf{L}_m^{n\prime} \bar{\mathbf{U}} e^{i(\omega t - n\theta)} \qquad \frac{\partial^2 \mathbf{U}}{\partial \theta^2} = -n^2 \mathbf{L}_m^n \bar{\mathbf{U}} e^{i(\omega t - n\theta)} \qquad \frac{\partial^2 \mathbf{U}}{\partial \phi^2} = \mathbf{L}_m^{n\prime\prime} \bar{\mathbf{U}} e^{i(\omega t - n\theta)}$$

(8.4.6a-f)

where $\mathbf{L}_m^{n\prime}$ and $\mathbf{L}_m^{n\prime\prime}$ are the first and second derivatives of $\mathbf{L}_m^n$ operator with respect to ϕ.

Applying equations (8.4.4a and b) to the system equation (8.4.1) and performing huge algebraic manipulation, we obtain the transformed system equation as

$$e^{i(\omega t - n\theta)} \mathbf{L}_m^n \bar{\mathbf{P}} = e^{i(\omega t - n\theta)} \mathbf{L}_m^n (\hat{\mathbf{K}}\, \bar{\mathbf{U}} - \omega^2 \hat{\mathbf{M}} \bar{\mathbf{U}}) \tag{8.4.7}$$

Because of the structure of the matrices $\hat{\mathbf{K}}$ and $\hat{\mathbf{M}}$, equation (8.4.7) can be divided into two uncoupled modes, namely the *spheroidal* mode and the *torsional* mode. The spheroidal mode corresponds to the *SV-P* mode of flat plate problems, while the torsional mode corresponds to the *SH* mode. Therefore, we can separately express equation (8.4.7) in the form.

For the spheroidal mode,

$$\bar{\mathbf{P}}_S = \hat{\mathbf{K}}_S \bar{\mathbf{U}}_S - \omega_S^2 \hat{\mathbf{M}}_S \bar{\mathbf{U}}_S \tag{8.4.8a}$$

For the torsional mode,

$$\bar{\mathbf{P}}_T = \hat{\mathbf{K}}_T \bar{\mathbf{U}}_T - \omega_T^2 \hat{\mathbf{M}}_T \bar{\mathbf{U}}_T \tag{8.4.8b}$$

where the subscripts S and T identify the spheroidal and torsional modes, respectively, and

$$\bar{\mathbf{P}}_S = \left[\bar{p}_r^1 \quad \bar{p}_S^1 \quad \bar{p}_r^2 \quad \cdots \quad \bar{p}_S^N \right]^T \tag{8.4.9a}$$

$$\bar{\mathbf{U}}_S = \left[\bar{u}_r^1 \quad \bar{u}_S^1 \quad \bar{u}_r^2 \quad \cdots \quad \bar{u}_S^N \right]^T \tag{8.4.9b}$$

$$\bar{\mathbf{P}}_T = \left[\bar{p}_T^1 \quad \bar{p}_T^2 \quad \cdots \quad \bar{p}_T^N \right]^T \tag{8.4.9c}$$

$$\bar{\mathbf{U}}_T = \left[\bar{u}_T^1 \quad \bar{u}_T^2 \quad \cdots \quad \bar{u}_T^N \right]^T \tag{8.4.9d}$$

In addition, we display all the matrices $\hat{\mathbf{K}}_S$, $\hat{\mathbf{K}}_T$, $\hat{\mathbf{M}}_S$ and $\hat{\mathbf{M}}_T$ in Appendices 8B and 8C, respectively, for the linear and quadratic expansion.

8.3.2 Eigenvalue problems

The associated eigenvalue problem is then of the form

$$\hat{\mathbf{K}}_i \bar{\mathbf{U}}_i = \omega_i^2 \hat{\mathbf{M}}_i \bar{\mathbf{U}}_i \tag{8.4.10}$$

where i=S or T. The analogy of equation (8.4.10) to a problem in structural dynamics suggests that it can be solved by a modal superposition involving the following eigenvalue problem

$$\hat{\mathbf{K}}_i \Phi_i = \hat{\mathbf{M}}_i \Phi_i \Omega_i^2 \tag{8.4.11}$$

where $\Phi_i = \{\phi_{i,j}\}$ is the matrix of eigenvectors and $\Omega_i = diag\{\omega_{i,j}\}$ is the diagonal matrix of eigenvalues with j being the modal index. The eigenvector matrix Φ_i satisfies the following orthogonal conditions.

$$\Phi_i^T \hat{\mathbf{M}}_i \Phi_i = \mathbf{I} \tag{8.4.12a}$$

$$\Phi_i^T \hat{\mathbf{K}}_i \Phi_i = \Omega^2 \tag{8.4.12b}$$

8.4.3 Modal superposition and responses in the space-time domain

A conventional modal superposition gives the solution to equation (8.4.8) in the wavenumber-time domain if $\overline{\mathbf{P}}$ is assumed to be of the separable form

$$\overline{\mathbf{P}} = \overline{\mathbf{P}}_0(n,m)f(t) \tag{8.4.13}$$

The solution is then

$$\hat{\mathbf{U}}(n,m,t) = \sum_{j=1}^{2N \text{ or } N} \gamma_j h_j * f \, \phi_j \tag{8.4.14}$$

in which

$$\gamma_j = \phi_j^T \overline{\mathbf{P}}_0 \qquad = \text{modal participation factor} \tag{8.4.15a}$$

$$h_j = \frac{1}{\omega_{dj}} \exp(-\xi_j \omega_j t) \sin(\omega_{dj} t) \quad = \text{modal impulse response function} \tag{8.4.15b}$$

$$\omega_{dj} = \omega_j \sqrt{1-\xi_j^2} \tag{8.4.15c}$$

In these expressions, the symbol $*$ indicates a convolution, ξ_j is the fraction of viscous modal damping, and ω_{dj} is the damped natural frequency for the j^{th} mode. Notice that the modal mass implied by equation (8.4.15a) is unity because of the normalization in equation (8.4.12). Also, it is noted that equations (8.4.13-15) are available for both spheroidal and torsional modes.

Finally, we can express the response in the spatial and time domains as

$$\mathbf{U}(\phi,\theta,t) = \sum_{m=0}^{\infty} \sum_{n=0}^{m} e^{-in\theta} \mathbf{L}_m^n \hat{\mathbf{U}}_m^n(n,m,t) \tag{8.4.16}$$

where we use $\hat{\mathbf{U}}_m^n$ in stead of $\hat{\mathbf{U}}$ in order to clearly show the dependency of displacements on the wavenumbers m and n.

8.5 Analytical eigenvalue problem for a homogeneous solid and shell

We here formulate the analytical eigenvalue problem that is associated with the propagation modes of isotropic homogeneous spherical solids and shells. In the next section 8.6, we compare the eigenvalues of this analytical formulation with those of the STLM so as to verify the validations of the latter.

The wave equation in the space-time domain is given of the form

$$\left[\mathbf{L}_\sigma^T \mathbf{D} \mathbf{L}_\varepsilon - \rho \frac{\partial^2}{\partial t^2} \right] \mathbf{u} = \mathbf{0} \tag{8.5.1}$$

where $\mathbf{u} = \begin{bmatrix} u_r & u_\phi & u_\theta \end{bmatrix}^T$, the differential operators of $\mathbf{L}_\sigma$ and $\mathbf{L}_\varepsilon$ are the same as those in the previous sections, ρ is the mass density, and finally

$$\mathbf{D}=\begin{Bmatrix} \lambda+2G & \lambda & \lambda & \cdot & \cdot & \cdot \\ \lambda & \lambda+2G & \lambda & \cdot & \cdot & \cdot \\ \lambda & \lambda & \lambda+2G & \cdot & \cdot & \cdot \\ \cdot & \cdot & \cdot & G & \cdot & \cdot \\ \cdot & \cdot & \cdot & \cdot & G & \cdot \\ \cdot & \cdot & \cdot & \cdot & \cdot & G \end{Bmatrix} \tag{8.5.2}$$

We consider the solution in the next form of separation of variables.

$$\mathbf{u}(r,\phi,\theta,t)=e^{\mathrm{i}(\omega t-n\theta)}\mathbf{L}_m^n\bar{\mathbf{v}}(r) \tag{8.5.3}$$

where ω is the frequency, n the azimuthal wavenumber, and

$$\bar{\mathbf{v}}(r)=\left[\bar{v}_r(r) \quad \bar{v}_S(r) \quad \bar{v}_T(r)\right]^T \tag{8.5.4a}$$

$$\mathbf{L}_m^n=\begin{Bmatrix} P_m^n & \cdot & \cdot \\ \cdot & P_m^{n\prime} & \dfrac{in}{\sin\phi}P_m^n \\ \cdot & -\dfrac{in}{\sin\phi}P_m^n & P_m^{n\prime} \end{Bmatrix} \tag{8.5.4b}$$

$$P_m^n=P_m^n(\cos\phi) \ : \text{the associated Legendre function of the first kind} \tag{8.5.4c}$$

$$P_m^{n\prime}=\frac{dP_m^n}{d\phi} \tag{8.5.4d}$$

The first kind associated Legendre function P_m^n in equation (8.5.4c) satisfies the following differential equation and recurrence relations.

$$P_m^{n\prime\prime}+\cot\phi P_m^{n\prime}+\left[m(m+1)-\frac{n^2}{\sin^2\phi}\right]P_m^n=0 \tag{8.5.5a}$$

$$P_m^n(\cos\phi)=\frac{(1-\cos^2\phi)^{n/2}}{2^m m!}\frac{d^{n+m}(-\sin^2\phi)^m}{d(\cos\phi)^{n+m}} \tag{8.5.5b}$$

$$(2m+1)\cos\phi P_m^n=(m-n+1)P_{m+1}^n+(m+n)P_{m-1}^n \tag{8.5.5c}$$

$$P_m^{n\prime}=\frac{dP_m^n}{d\phi}=m\cot\phi P_m^n-\frac{m+n}{\sin\phi}P_{m-1}^n \tag{8.5.5d}$$

Substitution of equation (8.5.3) into equation (8.5.1) followed by much algebraic manipulation provides the next wave equation in the wavenumber-frequency domain

$$\left[\mathbf{L}_\sigma^T\mathbf{D}\mathbf{L}_\varepsilon-\rho\frac{\partial^2}{\partial t^2}\right]e^{\mathrm{i}(\omega t-n\theta)}\mathbf{L}_m^n\bar{\mathbf{v}}(r)=$$

$$e^{\mathrm{i}(\omega t-n\theta)}\mathbf{L}_m^n\left[\mathbf{C}_2\frac{d^2}{dr^2}+\mathbf{C}_1\frac{1}{r}\frac{d}{dr}+\mathbf{C}_0\frac{1}{r^2}+\omega^2\mathbf{M}\right]\bar{\mathbf{v}}(r)=\mathbf{0} \tag{8.5.6}$$

where

$$\mathbf{C}_0=\begin{Bmatrix} -2(\lambda+2G)-\bar{m}G & \bar{m}(\lambda+3G) & \cdot \\ 2(\lambda+2G) & -\bar{m}(\lambda+2G) & \cdot \\ \cdot & \cdot & -\bar{m}G \end{Bmatrix} \tag{8.5.7a}$$

$$\mathbf{C}_1 = \begin{Bmatrix} 2(\lambda+2G) & -\bar{m}(\lambda+G) & \cdot \\ \lambda+G & 2G & \cdot \\ \cdot & \cdot & 2G \end{Bmatrix} \tag{8.5.7b}$$

$$\mathbf{C}_2 = \begin{Bmatrix} \lambda+2G & \cdot & \cdot \\ \cdot & G & \cdot \\ \cdot & \cdot & G \end{Bmatrix} \tag{8.5.7c}$$

$$\mathbf{M} = \begin{Bmatrix} \rho & \cdot & \cdot \\ \cdot & \rho & \cdot \\ \cdot & \cdot & \rho \end{Bmatrix} \tag{8.5.7d}$$

$$\bar{m} = m(m+1) \tag{8.5.7e}$$

Next, we assume $\bar{\mathbf{v}}$ of the form

$$\bar{\mathbf{v}}(r) = \mathbf{z}_m \boldsymbol{\phi} \tag{8.5.8}$$

where

$$\mathbf{z}_m = \begin{Bmatrix} z_m' & \bar{m}\dfrac{z_m}{r} & \cdot \\ \dfrac{z_m}{r} & z_m' + \dfrac{z_m}{r} & \cdot \\ \cdot & \cdot & z_m \end{Bmatrix} \tag{8.5.9a}$$

$$z_m = z_m(\xi r) \qquad \text{: the spherical Bessel function of order } m \tag{8.5.9b}$$

$$z_m' = \frac{dz_m(\xi r)}{dr} = \xi \frac{dz_m(\xi r)}{d(\xi r)} \tag{8.5.9c}$$

$$\boldsymbol{\phi} = \{\phi_P \quad \phi_S \quad \phi_T\}^T \qquad \text{: mode shape} \tag{8.5.9d}$$

In equation (8.5.9b), ξ is the wavenumber in the radial direction, which will be the eigenvalue associated with the body waves in the spherical coordinate system. The spherical Bessel function z_m satisfies the following differential equation and is related to the cylindrical Bessel function C_m as

$$z_m'' + \frac{2}{r} z_m' + \left[\xi^2 - \frac{m(m+1)}{r^2}\right] z_m = 0 \tag{8.5.10a}$$

$$z_m(\xi r) = \sqrt{\frac{\pi}{2\xi r}} C_{m+1/2}(\xi r) \tag{8.5.10b}$$

In addition, the useful recurrence relations are

$$\frac{2m+1}{\xi r} z_m(\xi r) = z_{m-1}(\xi r) + z_{m+1}(\xi r) \tag{8.5.10c}$$

$$\frac{dz_m(\xi r)}{d(\xi r)} = \frac{m}{\xi r} z_m(\xi r) - z_{m+1}(\xi r) \tag{8.5.10d}$$

Again, substitution of equation (8.5.8) into equation (8.5.6) and much manipulation produce

$$\left[\mathbf{C}_2 \frac{d^2}{dr^2} + \mathbf{C}_1 \frac{1}{r}\frac{d}{dr} + \mathbf{C}_0 \frac{1}{r^2} + \omega^2 \mathbf{M}\right] \mathbf{z}_m \boldsymbol{\phi} =$$

$$\mathbf{z}_m \begin{Bmatrix} \rho\omega^2 - (\lambda+2G)\xi^2 & \cdot & \cdot \\ \cdot & \rho\omega^2 - G\xi^2 & \cdot \\ \cdot & \cdot & \rho\omega^2 - G\xi^2 \end{Bmatrix} \begin{Bmatrix} \phi_P \\ \phi_S \\ \phi_T \end{Bmatrix} = \mathbf{0} \qquad (8.5.11)$$

where we cancel the term $e^{i(\omega t - n\theta)}\mathbf{L}_m^n$. Finally, three fully uncoupled modes are obtained such as

(1) P mode: ϕ_P with $\xi_P = \omega / C_P$

(2) S mode: ϕ_S with $\xi_S = \omega / C_S$

(3) T mode: ϕ_T with $\xi_T = \omega / C_S$

where $C_P = \sqrt{(\lambda+2G)/\rho}$ and $C_S = \sqrt{G/\rho}$. It is noted that the P and S modes are related to the *spheroidal* mode, and T mode the *torsional* mode, which will be shown later in this section. Also, the mode shape is give as

$$\mathbf{\Phi} = \{\phi_P \quad \phi_S \quad \phi_T\} = \begin{Bmatrix} 1 & \cdot & \cdot \\ \cdot & 1 & \cdot \\ \cdot & \cdot & 1 \end{Bmatrix} \qquad (8.5.12)$$

Then, we can express $\bar{\mathbf{v}}(r)$ as

$$\bar{\mathbf{v}}(r) = \mathbf{z}_{m,P}\phi_P a + \mathbf{z}_{m,S}\phi_S b + \mathbf{z}_{m,T}\phi_T c = \mathbf{Z}_m \mathbf{a} \qquad (8.5.13)$$

where

$$\mathbf{Z}_m = \begin{Bmatrix} z_{m,P}' & \bar{m}\dfrac{z_{m,S}}{r} & \cdot \\ \dfrac{z_{m,P}}{r} & z_{m,S}' + \dfrac{z_{m,S}}{r} & \cdot \\ \cdot & \cdot & z_{m,T} \end{Bmatrix} \qquad (8.5.14a)$$

$$\mathbf{a} = [a \quad b \quad c]^T \qquad (8.5.14b)$$

$$\mathbf{z}_{m,i} = \mathbf{z}_m(\xi_i) \quad \text{with } i=P, S, \text{ or } T \qquad (8.5.14c)$$

$$z_{m,i} = z_m(\xi_i r) \quad \text{with } i=P, S, \text{ or } T \qquad (8.5.14d)$$

and a, b, c are unknown constants to be determined.

The alternative for the general solution in the wavenumber-frequency domain is

$$\bar{\mathbf{v}}(r) = \mathbf{Z}_{m1}\mathbf{a}_1 + \mathbf{Z}_{m2}\mathbf{a}_2 \qquad (8.5.15)$$

where

$$\mathbf{Z}_{m1} = \begin{Bmatrix} j_{m,P}' & \bar{m}\dfrac{j_{m,S}}{r} & \cdot \\ \dfrac{j_{m,P}}{r} & j_{m,S}' + \dfrac{j_{m,S}}{r} & \cdot \\ \cdot & \cdot & j_{m,T} \end{Bmatrix} \qquad (8.5.16a)$$

$$\mathbf{Z}_{m2}=\begin{Bmatrix} y_{m,P}' & \bar{m}\dfrac{y_{m,S}}{r} & \cdot \\ \dfrac{y_{m,P}}{r} & j_{m,S}'+\dfrac{y_{m,S}}{r} & \cdot \\ \cdot & \cdot & y_{m,T} \end{Bmatrix} \tag{8.5.16b}$$

$j_{m,i}=j_{m,i}(\xi_i r)$: the first kind spherical Bessel function of order m (8.5.16c)

$y_{m,i}=y_{m,i}(\xi_i r)$: the second kind spherical Bessel function of order m (8.5.16d)

$$\mathbf{a}_1=\begin{bmatrix} a_1 & b_1 & c_1 \end{bmatrix}^T \tag{8.5.16e}$$

$$\mathbf{a}_2=\begin{bmatrix} a_2 & b_2 & c_2 \end{bmatrix}^T \tag{8.5.16f}$$

The two vectors of $\mathbf{a}_1$ and $\mathbf{a}_2$ are the unknown constant vectors to be determined from given boundary conditions. The general solution in the space-time domain for harmonic waves is then determined in the form

$$\mathbf{u}(r,\phi,\theta,t)=e^{\mathrm{i}(\omega t-n\theta)}\mathbf{L}_m^n(\mathbf{Z}_{m1}\mathbf{a}_1+\mathbf{Z}_{m2}\mathbf{a}_2) \tag{8.5.17}$$

The boundary condition of interest is of the next form.

$$\mathbf{s}=\begin{bmatrix} \sigma_r & \tau_{r\phi} & \tau_{r\theta} \end{bmatrix}^T=\mathbf{L}_r^T\mathbf{D}\mathbf{L}_\varepsilon\mathbf{u} \tag{8.5.18}$$

Substituting equation (8.5.17) into equation (8.5.18), we finally end up with the following.

$$\mathbf{s}=\mathbf{L}_r^T\mathbf{D}\mathbf{L}_\varepsilon\left[e^{\mathrm{i}(\omega t-n\theta)}\mathbf{L}_m^n(\mathbf{Z}_{m1}\mathbf{a}_1+\mathbf{Z}_{m2}\mathbf{a}_2)\right]=e^{\mathrm{i}(\omega t-n\theta)}\mathbf{L}_m^n\left[\mathbf{A}_1(r)\mathbf{a}_1+\mathbf{A}_2(r)\mathbf{a}_2\right] \tag{8.5.19}$$

where

$$\mathbf{A}_1(r) \text{ or } \mathbf{A}_2(r)$$

$$=\begin{Bmatrix} \dfrac{2G}{r^2}\{[m^2-m-\xi_S^2r^2/2]z_{m,P}+2\xi_P r z_{m+1,P}\} & \dfrac{2G}{r^2}\bar{m}[(m-1)z_{m,S}-\xi_S r z_{m+1,S}] \\ \dfrac{2G}{r^2}[(m-1)z_{m,P}-\xi_P r z_{m+1,P}] & \dfrac{2G}{r^2}\{[m^2-1-\xi_S^2r^2/2]z_{m,S}+\xi_S r z_{m+1,S}\} \\ 0 & 0 \\ \dfrac{G}{r}[(m-1)z_{m,T}-\xi_T r z_{m+1,T}] & \end{Bmatrix} \tag{8.5.20}$$

In equation (8.5.20), z is j for $\mathbf{A}_1$ and y for $\mathbf{A}_2$ according to equations (8.5.15 and 16). As shown in equation (8.5.20), there are two uncoupled modes of spheroidal and torsional modes. Hence, we can separately express the two modes as

Spheroidal mode:

$$\mathbf{A}_{SP1}(r) \text{ or } \mathbf{A}_{SP2}(r)=$$

$$\begin{Bmatrix} \dfrac{2G}{r^2}\{[m^2-m-\xi_S^2r^2/2]z_{m,P}+2\xi_P r z_{m+1,P}\} & \dfrac{2G}{r^2}\bar{m}[(m-1)z_{m,S}-\xi_S r z_{m+1,S}] \\ \dfrac{2G}{r^2}[(m-1)z_{m,P}-\xi_P r z_{m+1,P}] & \dfrac{2G}{r^2}\{[m^2-1-\xi_S^2r^2/2]z_{m,S}+\xi_S r z_{m+1,S}\} \end{Bmatrix} \tag{8.5.21}$$

Torsional mode:

$$\mathbf{A}_{TR1}(r) \text{ or } \mathbf{A}_{TR2}(r) = \left\{ \frac{G}{r}[(m-1)z_{m,T} - \xi_T r z_{m+1,T}] \right\} \tag{8.5.22}$$

The associated constant vectors are also uncoupled as

Spheroidal mode:

$$\mathbf{a}_{SP1} = \begin{Bmatrix} a_1 \\ b_1 \end{Bmatrix} \text{ and } \mathbf{a}_{SP2} = \begin{Bmatrix} a_2 \\ b_2 \end{Bmatrix} \tag{8.5.23}$$

Torsional mode:

$$\mathbf{a}_{TR1} = \{c_1\} \text{ and } \mathbf{a}_{TR2} = \{c_2\} \tag{8.5.24}$$

8.5.1 Spherical solid

First, we are interested in the propagation modes of a homogeneous spherical solid with radius r_o. The two uncoupled eigenvalue problems are given from equation (8.5.19) as

Spheroidal mode:

$$\det \mathbf{A}_{SP1}(r_o) = 0 \tag{8.5.25}$$

Torsional mode:

$$\det \mathbf{A}_{TR1}(r_o) = 0 \tag{8.5.26}$$

The roots of equations (8.5.25 and 26) provide the propagation modes for the spheroidal and torsional modes, respectively, of the homogeneous spherical solid. In section 8.6, we consider only the spheroidal mode and compare them with the results obtained with the STLM.

8.5.2 Spherical shell

Next, we consider the propagation modes in a homogeneous spherical shell with r_i and r_o as the inner and outer radii, respectively. The eigenvalue problems to be considered are then

Spheroidal mode:

$$\det \begin{Bmatrix} \mathbf{A}_{SP1}(r_i) & \mathbf{A}_{SP2}(r_i) \\ \mathbf{A}_{SP1}(r_o) & \mathbf{A}_{SP2}(r_o) \end{Bmatrix} = 0 \tag{8.5.27}$$

Torsional mode:

$$\det \begin{Bmatrix} \mathbf{A}_{TR1}(r_i) & \mathbf{A}_{TR2}(r_i) \\ \mathbf{A}_{TR1}(r_o) & \mathbf{A}_{TR2}(r_o) \end{Bmatrix} = 0 \tag{8.5.28}$$

The roots of equations (8.5.27 and 28) provide the propagation modes for the spheroidal and torsional modes, respectively, of the homogeneous spherical shell. In section 8.6, we consider only the spheroidal mode and compare them with the results obtained with the STLM.

8.6 Comparison of numerical and analytical solutions

We compare the eigenvalues ω_j (frequencies) calculated with the STLM against the exact analytical solutions so as to illustrate the validation of the formulated STLM in this chapter 8. For the practical purpose, we choose two simple structures and solve the associated eigenvalue problems. The two simple structures are (1) a homogenous spherical solid, (2) a homogeneous spherical shell. The exact analytical solutions for both are obtained in the previous section 8.5.

For the discrete models, we consider the both linear and quadratic expansion STLM, or the STLM1 and STLM2 for short, respectively. We choose the total number of thin-layers N such as N=10 for the STLM1 and N=5 for the STLM2. In addition, to investigate the effect of the tuning factor μ of chapter 2 on the accuracy of eigenvalues calculated with the STLM, we apply the lumped, tuned, and consistent mass matrices to the problem of interest. For the tuned mass matrix, we apply the optimal values of μ that are obtained for the TLM (formulated in the Cartesian coordinate system) in chapter 2, namely, μ=0.55 for the STLM1 and μ=0.33 for the STLM2 are used in this section.

8.6.1 Homogeneous Spherical Solid

First, we consider the propagation modes of a homogeneous spherical solid subjected to only spheroidal wave motion. The geometry and material properties of the spherical solid are given such that the radius of the solid is r_o=1.0, the mass density and shear velocity are ρ=C_S=1.0, and the Poisson's ratio is ν=0.30.

The dispersion curves of the spheroidal modes are shown in figure 8.6.1 (for the lumped mass matrix), in figure 8.6.2 (for the tuned mass matrix), and in figure 8.6.3 (for the consistent mass matrix), in comparison with the exact analytical solution. Note in the three figures that the solid lines represent the propagation branches obtained with the STLM, and the dashed lines represent the propagation branches obtained with the exact analytical solution. It is observed in all the three figures that the eigenvalues of the spheroidal modes obtained with the STLM are in good agreement with the exact analytical solutions. Also, notice that the accurate results are obtained only for the low modes, not for the high ones. Furthermore, it is shown that the STLM2 with N=5 provides more accurate results than the STLM1 with N=10, which again confirms that the quadratic expansion is not only more accurate, but also more efficient than the linear expansion, as shown in chapters 2–4 associated with the TLM.

Now, we consider the effect of the tuning factor μ on the accuracy of eigenvalues. Comparison of the three figures of 8.6.1, 8.6.2, and 8.6.3 verifies that the optimal values of μ=0.55 and μ=0.33 obtained for the TLM in chapter 2 provide much better agreement with the exact analytical solution than the other two values of μ=0 and 1 for the STLM as well. Therefore, it is recommended to apply the optimal values of μ=0.55 and μ=0.33 to the STLM as well as to the TLM.

8.6.2 Homogeneous Spherical Shell

Next, we consider the propagation modes of a homogeneous spherical shell subjected to only spheroidal wave motion. The geometry and material properties of the spherical solid are given such that the inner and outer radii of the shell is r_i=0.5 and r_o=1.5, the mass density and shear velocity are ρ=C_S=1.0, and the Poisson's ratio is ν=0.30.

The dispersion curves of the spheroidal modes are shown in figure 8.6.4 (for the lumped mass matrix), in figure 8.6.5 (for the tuned mass matrix), and in figure 8.6.6 (for the consistent mass matrix), in comparison with the exact analytical solution. Note in the three figures that the solid lines represent the propagation branches obtained with the STLM, and the dashed lines represent

the propagation branches obtained with the exact analytical solution. It is observed in all the three figures that the eigenvalues of the spheroidal modes obtained with the STLM are in good agreement with the exact analytical solutions. Also, notice that the accurate results are obtained only for the low modes, not for the high ones. Furthermore, it is shown that the STLM2 with N=5 provides more accurate results than the STLM1 with N=10, which again confirms that the quadratic expansion is not only more accurate, but also more efficient than the linear expansion.

Now, we consider the effect of the tuning factor μ on the accuracy of eigenvalues. Comparison of the three figures of 8.6.4, 8.6.5, and 8.6.6 verifies that the optimal values of μ=0.55 and μ=0.33 obtained for the TLM in chapter 2 provide much better agreement with the exact analytical solution than the other two values of μ=0 and 1 for the STLM as well. Therefore, it is now strongly recommended to apply the optimal values of μ=0.55 and μ=0.33 to the STLM.

Figures for chapter 8

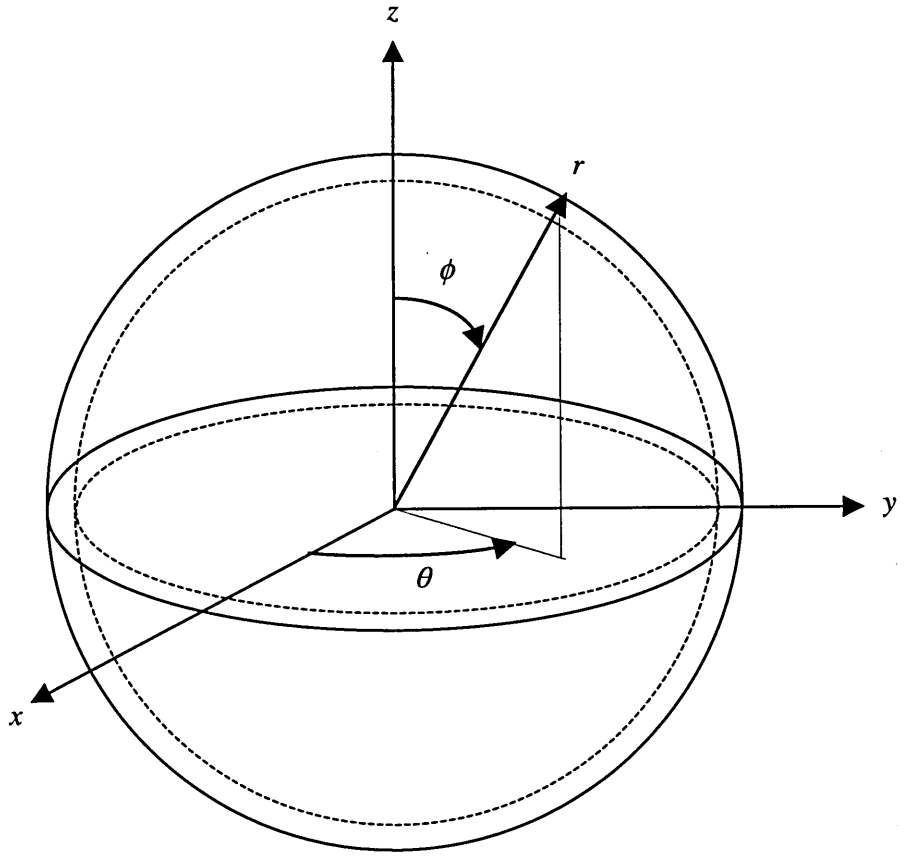

Figure 8.2.2 Spherical shell in spherical coordinate system

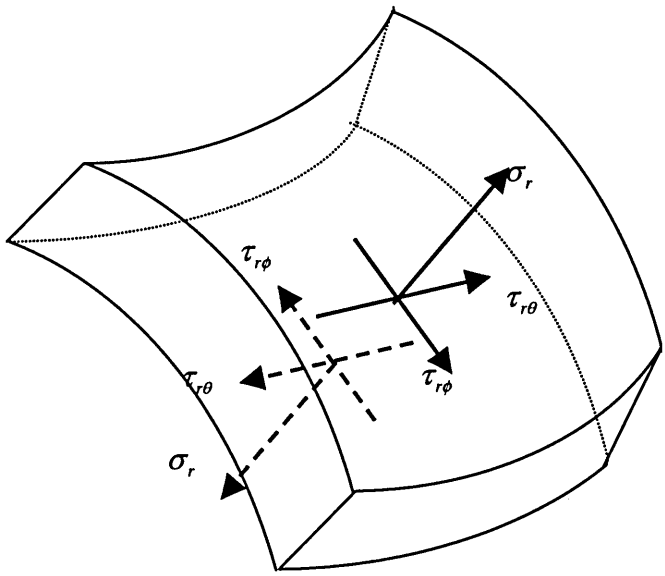

Figure 8.2.2 Boundary Conditions on spherical shell surfaces

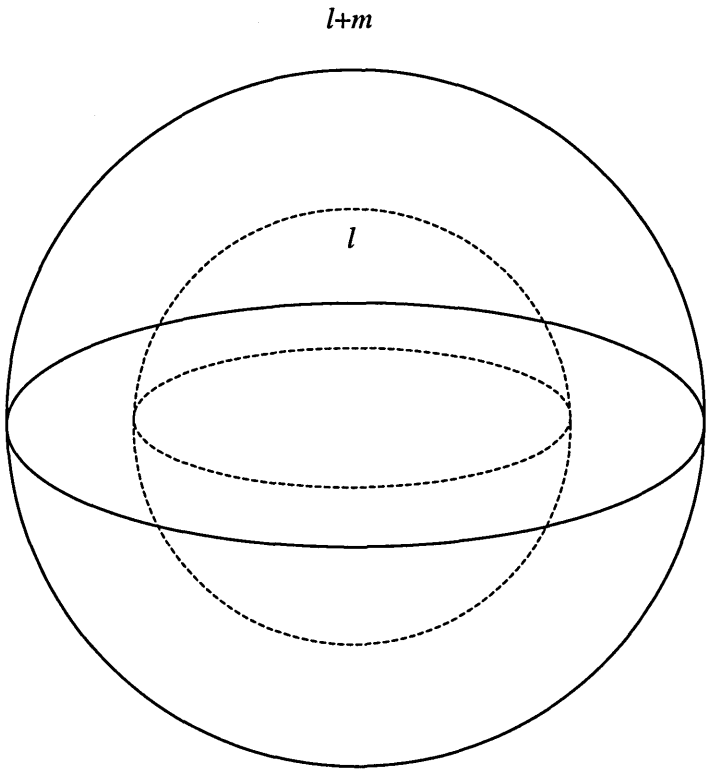

Figure 8.3.1 Individual spherical thin-layer

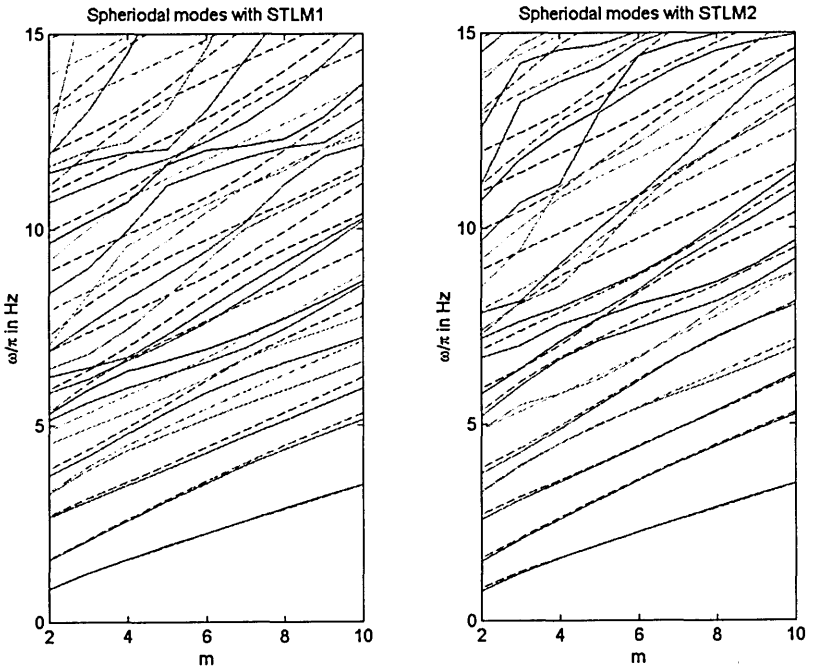

Figure 8.6.1 Spheroidal modes in spherical solid, using the lumped mass matrix (solid line: STLM; dashed line: Exact)

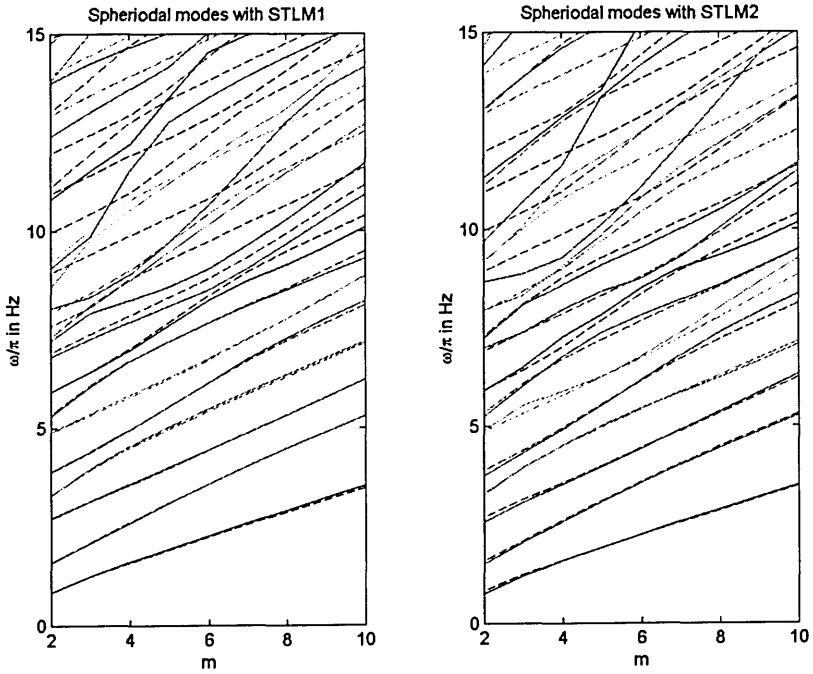

Figure 8.6.2 Spheroidal modes in spherical solid, using the tuned mass matrix (solid line: STLM; dashed line: Exact)

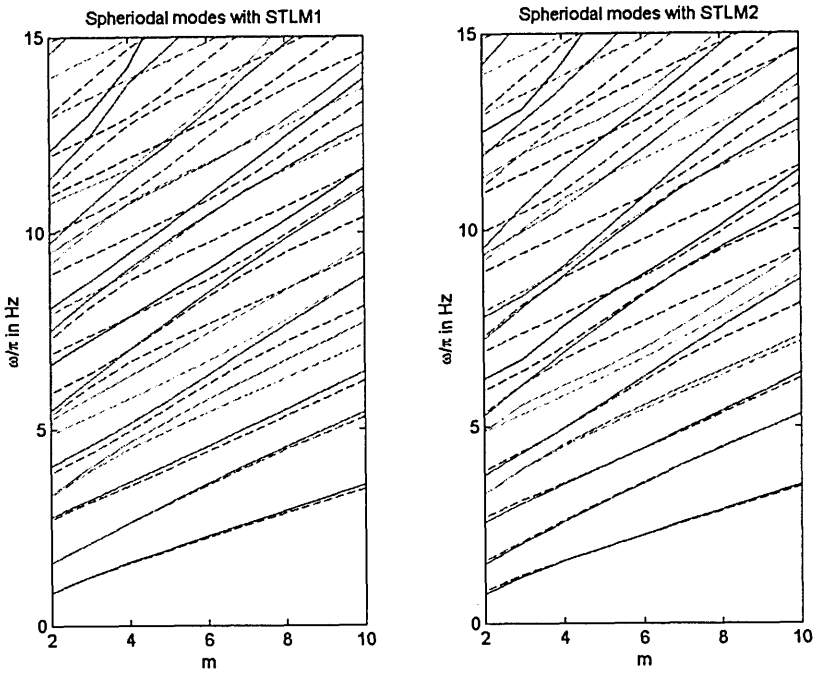

Figure 8.6.3 Spheroidal modes in spherical solid, using the consistent mass matrix (solid line: STLM; dashed line: Exact)

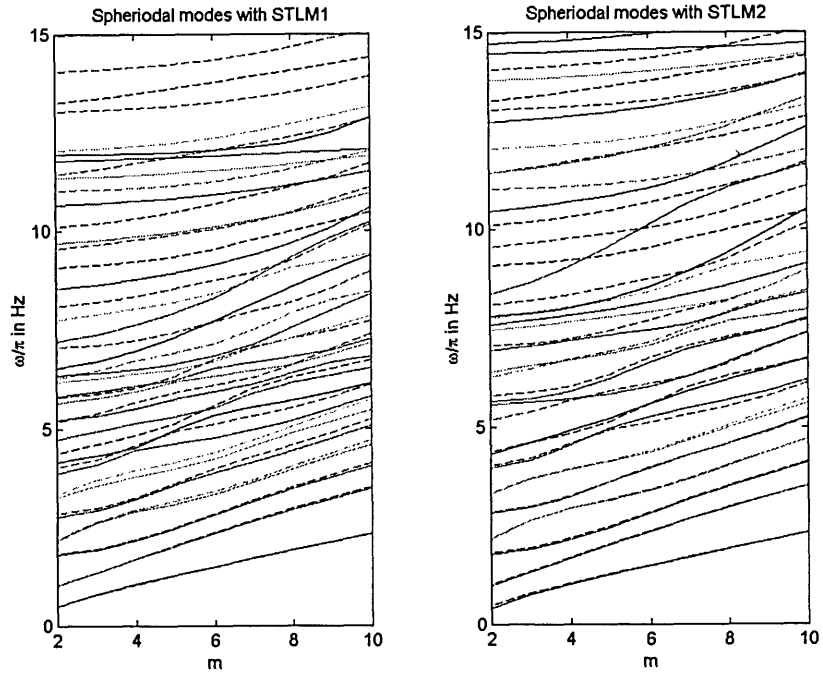

Figure 8.6.4 Spheroidal modes in spherical shell, using the lumped mass matrix (solid line: STLM; dashed line: Exact)

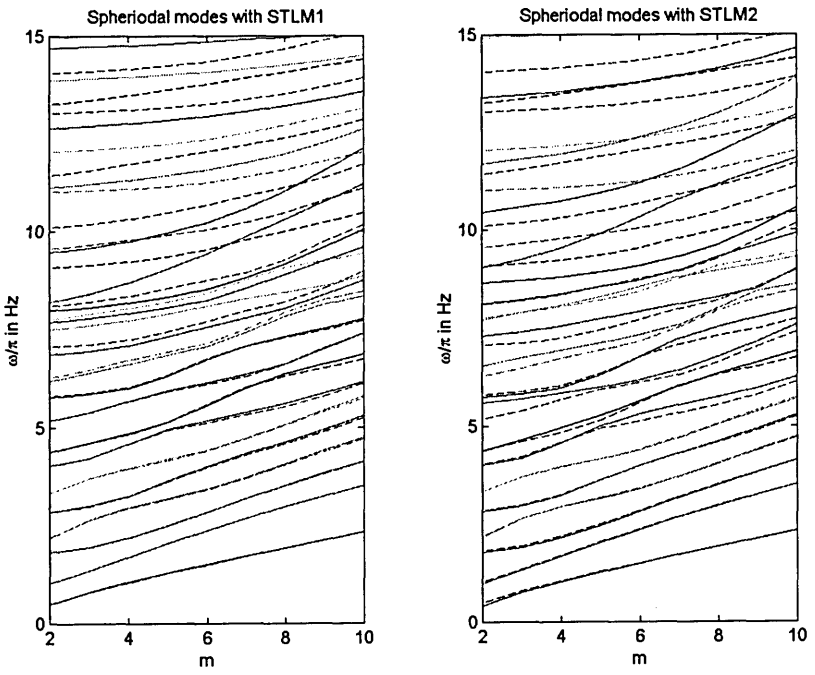

Figure 8.6.5 Spheroidal modes in spherical shell, using the tuned mass matrix (solid line: STLM; dashed line: Exact)

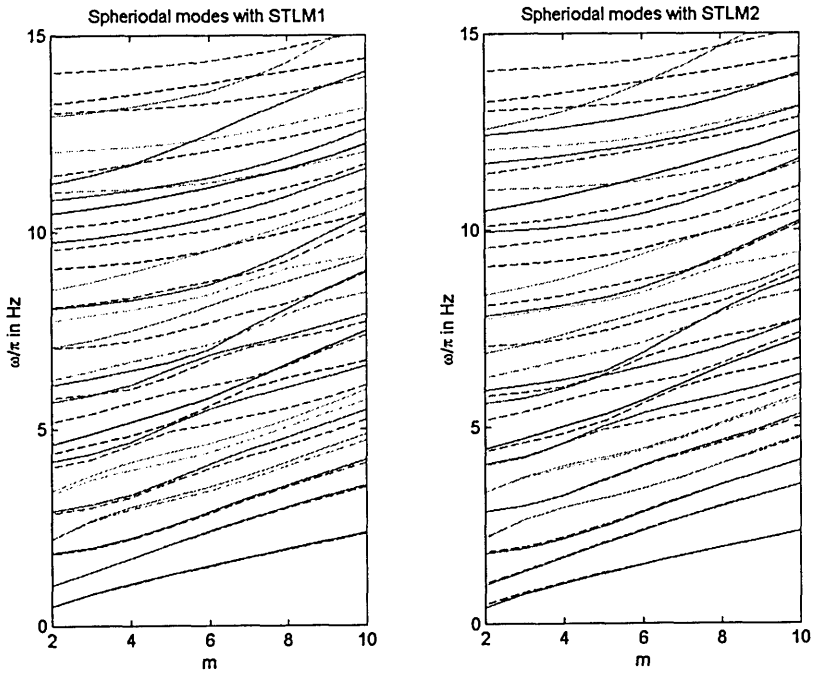

Figure 8.6.6 Spheroidal modes in spherical shell, using the consistent mass matrix (solid line: STLM; dashed line: Exact)

APPENDIX 8A : Material matrices

$$\mathbf{D}_{rr}=\begin{Bmatrix} d_{11} & d_{16} & d_{15} \\ d_{16} & d_{66} & d_{56} \\ d_{15} & d_{56} & d_{55} \end{Bmatrix} \quad \mathbf{D}_{\phi\phi}=\begin{Bmatrix} d_{66} & d_{26} & d_{46} \\ d_{26} & d_{22} & d_{24} \\ d_{46} & d_{24} & d_{44} \end{Bmatrix} \quad \mathbf{D}_{\theta\theta}=\begin{Bmatrix} d_{55} & d_{45} & d_{35} \\ d_{45} & d_{44} & d_{34} \\ d_{35} & d_{34} & d_{33} \end{Bmatrix}$$

$$\mathbf{D}_{r\phi}=\mathbf{D}_{\phi r}^{T}=\begin{Bmatrix} d_{16} & d_{12} & d_{14} \\ d_{66} & d_{26} & d_{46} \\ d_{56} & d_{25} & d_{45} \end{Bmatrix} \quad \mathbf{D}_{r\theta}=\mathbf{D}_{\theta r}^{T}=\begin{Bmatrix} d_{15} & d_{14} & d_{13} \\ d_{56} & d_{46} & d_{36} \\ d_{55} & d_{45} & d_{35} \end{Bmatrix}$$

$$\mathbf{D}_{\phi\theta}=\mathbf{D}_{\theta\phi}^{T}=\begin{Bmatrix} d_{56} & d_{46} & d_{36} \\ d_{25} & d_{24} & d_{23} \\ d_{45} & d_{44} & d_{34} \end{Bmatrix}$$

$$\mathbf{D}_{11}=\begin{Bmatrix} d_{22}+2d_{23}+d_{33} & -d_{26}-d_{36} & -d_{25}-d_{35} \\ -d_{26}-d_{36} & d_{66} & d_{56} \\ -d_{25}-d_{35} & d_{56} & d_{55} \end{Bmatrix} \qquad \mathbf{D}_{22}=\begin{Bmatrix} \cdot & \cdot & \cdot \\ \cdot & d_{33} & -d_{34} \\ \cdot & -d_{34} & d_{44} \end{Bmatrix}$$

$$\mathbf{D}_{12}=\mathbf{D}_{21}^{T}=\begin{Bmatrix} \cdot & d_{23}+d_{33} & -d_{24}-d_{34} \\ \cdot & -d_{36} & d_{46} \\ \cdot & -d_{35} & d_{45} \end{Bmatrix}$$

$$\mathbf{D}_{r1}=\mathbf{D}_{1r}^{T}=\begin{Bmatrix} d_{12}+d_{13} & -d_{16} & -d_{15} \\ d_{26}+d_{36} & -d_{66} & -d_{56} \\ d_{25}+d_{35} & -d_{56} & -d_{55} \end{Bmatrix} \quad \mathbf{D}_{r2}=\mathbf{D}_{2r}^{T}=\begin{Bmatrix} \cdot & d_{13} & -d_{14} \\ \cdot & d_{36} & -d_{46} \\ \cdot & d_{35} & -d_{45} \end{Bmatrix}$$

$$\mathbf{D}_{\phi 1}=\mathbf{D}_{1\phi}^{T}=\begin{Bmatrix} d_{26}+d_{36} & -d_{66} & -d_{56} \\ d_{22}+d_{23} & -d_{26} & -d_{25} \\ d_{24}+d_{34} & -d_{46} & -d_{45} \end{Bmatrix} \quad \mathbf{D}_{\phi 2}=\mathbf{D}_{2\phi}^{T}=\begin{Bmatrix} \cdot & d_{36} & -d_{46} \\ \cdot & d_{23} & -d_{24} \\ \cdot & d_{34} & -d_{44} \end{Bmatrix}$$

$$\mathbf{D}_{\theta 1}=\mathbf{D}_{1\theta}^{T}=\begin{Bmatrix} d_{25}+d_{35} & -d_{56} & -d_{55} \\ d_{24}+d_{34} & -d_{46} & -d_{45} \\ d_{23}+d_{33} & -d_{36} & -d_{35} \end{Bmatrix} \quad \mathbf{D}_{\theta 2}=\mathbf{D}_{2\theta}^{T}=\begin{Bmatrix} \cdot & d_{35} & -d_{45} \\ \cdot & d_{34} & -d_{44} \\ \cdot & d_{33} & -d_{34} \end{Bmatrix}$$

$$\mathbf{D}_{r\phi}+\mathbf{D}_{\phi r}=\begin{Bmatrix} 2d_{16} & d_{12}+d_{66} & d_{14}+d_{56} \\ d_{12}+d_{66} & 2d_{26} & d_{25}+d_{46} \\ d_{14}+d_{56} & d_{25}+d_{46} & 2d_{45} \end{Bmatrix}$$

$$\mathbf{D}_{r\phi}-\mathbf{D}_{\phi r}=\begin{Bmatrix} \cdot & d_{12}-d_{66} & d_{14}-d_{56} \\ -d_{12}+d_{66} & \cdot & -d_{25}+d_{46} \\ -d_{14}+d_{56} & d_{25}-d_{46} & \cdot \end{Bmatrix}$$

$$\mathbf{D}_{r\theta}+\mathbf{D}_{\theta r}=\begin{Bmatrix} 2d_{15} & d_{14}+d_{56} & d_{13}+d_{55} \\ d_{14}+d_{56} & 2d_{46} & d_{36}+d_{45} \\ d_{13}+d_{55} & d_{36}+d_{45} & 2d_{35} \end{Bmatrix}$$

$$\mathbf{D}_{r\theta}-\mathbf{D}_{\theta r}=\begin{Bmatrix} \cdot & d_{14}-d_{56} & d_{13}-d_{55} \\ -d_{14}+d_{56} & \cdot & d_{36}-d_{45} \\ -d_{13}+d_{55} & -d_{36}+d_{45} & \cdot \end{Bmatrix}$$

$$\mathbf{D}_{\phi\theta}+\mathbf{D}_{\theta\phi}=\begin{Bmatrix} 2d_{56} & d_{25}+d_{46} & d_{36}+d_{45} \\ d_{25}+d_{46} & 2d_{24} & d_{23}+d_{44} \\ d_{36}+d_{45} & d_{23}+d_{44} & 2d_{34} \end{Bmatrix}$$

$$2\mathbf{D}_{rr}+(\mathbf{D}_{r1}-\mathbf{D}_{1r})=\begin{Bmatrix} 2d_{11} & d_{16}-d_{26}-d_{36} & d_{15}-d_{25}-d_{35} \\ 3d_{16}+d_{26}+d_{36} & 2d_{66} & 2d_{56} \\ 3d_{15}+d_{25}+d_{35} & 2d_{56} & 2d_{55} \end{Bmatrix}$$

$$\mathbf{D}_{11}+\mathbf{D}_{\phi 2}=\begin{Bmatrix} d_{22}+2d_{23}+d_{33} & -d_{26} & -d_{25}-d_{35}-d_{46} \\ -d_{26}-d_{36} & d_{23}+d_{66} & -d_{24}+d_{56} \\ -d_{25}-d_{35} & d_{34}+d_{56} & -d_{44}+d_{55} \end{Bmatrix}$$

$$\mathbf{D}_{\phi r}+(\mathbf{D}_{r2}-\mathbf{D}_{2r})=\begin{Bmatrix} d_{16} & d_{13}+d_{66} & -d_{14}+d_{56} \\ d_{12}-d_{13} & d_{26} & d_{25}-d_{35}-d_{46} \\ 2d_{14} & d_{35}+2d_{46} & d_{45} \end{Bmatrix}$$

$$\mathbf{D}_{r\phi}+(\mathbf{D}_{\phi 1}-\mathbf{D}_{1\phi})=\begin{Bmatrix} d_{16} & d_{12}-d_{22}-d_{23}-d_{66} & d_{14}-d_{24}-d_{34}-d_{56} \\ d_{22}+d_{23}+2d_{66} & d_{26} & -d_{25}+2d_{46} \\ d_{24}+d_{34}+2d_{56} & 2d_{25}-d_{46} & d_{45} \end{Bmatrix}$$

$$\mathbf{D}_{\phi\phi}+(\mathbf{D}_{\phi 2}-\mathbf{D}_{2\phi})=\begin{Bmatrix} d_{66} & d_{26}+d_{36} & \cdot \\ d_{26}-d_{36} & d_{22} & -d_{34} \\ 2d_{46} & 2d_{24}+d_{34} & d_{44} \end{Bmatrix}$$

$$\mathbf{D}_{r\theta}+(\mathbf{D}_{\theta 1}-\mathbf{D}_{1\theta})=\begin{Bmatrix} d_{15} & d_{14}-d_{24}-d_{34}-d_{56} & d_{13}-d_{23}-d_{33}-d_{55} \\ d_{24}+d_{34}+2d_{56} & d_{46} & 2d_{36}-d_{45} \\ d_{23}+d_{33}+2d_{55} & -d_{36}+2d_{45} & d_{35} \end{Bmatrix}$$

$$\mathbf{D}_{\phi\theta}+(\mathbf{D}_{\theta 2}-\mathbf{D}_{2\theta})=\begin{Bmatrix} \cdot & d_{35} & -d_{45} \\ -d_{35} & \cdot & -d_{33}-d_{44} \\ d_{45} & d_{33}+d_{44} & \cdot \end{Bmatrix}$$

$$\mathbf{D}_{r1}-\mathbf{D}_{11}=\begin{Bmatrix} d_{12}+d_{13}-d_{22}-2d_{23}-d_{33} & -d_{16}+d_{26}+d_{36} & -d_{15}+d_{25}+d_{35} \\ 2d_{26}+2d_{36} & -2d_{66} & -2d_{56} \\ 2d_{25}+2d_{35} & -2d_{56} & -2d_{55} \end{Bmatrix}$$

$$\mathbf{D}_{r2}+\mathbf{D}_{\phi 1}-\mathbf{D}_{12}-\mathbf{D}_{21}=\begin{Bmatrix} d_{26}+d_{36} & d_{13}-d_{23}-d_{33}-d_{66} & -d_{14}+d_{24}+d_{34}-d_{56} \\ d_{22}-d_{33} & -d_{26}+3d_{36} & -d_{25}+d_{35}-2d_{46} \\ 2d_{24}+2d_{34} & 2d_{35}-2d_{46} & -4d_{45} \end{Bmatrix}$$

$$\mathbf{D}_{\phi 1}-\mathbf{D}_{1\phi}=\begin{Bmatrix} \cdot & -(d_{22}+d_{23}+d_{66}) & -(d_{24}+d_{34}+d_{56}) \\ (d_{22}+d_{23}+d_{66}) & \cdot & -(d_{25}-d_{46}) \\ (d_{24}+d_{34}+d_{56}) & d_{25}-d_{46} & \cdot \end{Bmatrix}$$

$$\mathbf{D}_{\theta 1}-\mathbf{D}_{1\theta}=\begin{Bmatrix} \cdot & -(d_{24}+d_{34}+d_{56}) & -(d_{23}+d_{33}+d_{55}) \\ (d_{24}+d_{34}+d_{56}) & \cdot & (d_{36}-d_{45}) \\ (d_{23}+d_{33}+d_{55}) & -(d_{36}-d_{45}) & \cdot \end{Bmatrix}$$

$$\mathbf{D}_{\theta 2}-\mathbf{D}_{2\theta}=\begin{Bmatrix} \cdot & d_{35} & -d_{45} \\ -d_{35} & \cdot & -(d_{33}+d_{44}) \\ d_{45} & (d_{33}+d_{44}) & \cdot \end{Bmatrix}$$

$$\mathbf{D}_{r1}+\mathbf{D}_{1r}=\begin{Bmatrix} 2d_{12}+2d_{13} & -d_{16}+d_{26}+d_{36} & d_{24}+d_{34}-d_{56} \\ -d_{16}+d_{26}+d_{36} & -2d_{66} & -2d_{56} \\ -d_{15}+d_{25}+d_{35} & -2d_{56} & -2d_{55} \end{Bmatrix}$$

$$\mathbf{D}_{r1}-\mathbf{D}_{1r}=\begin{Bmatrix} \cdot & -(d_{16}+d_{26}+d_{36}) & -(d_{15}+d_{25}+d_{35}) \\ (d_{16}+d_{26}+d_{36}) & \cdot & \cdot \\ (d_{15}+d_{25}+d_{35}) & \cdot & \cdot \end{Bmatrix}$$

$$\mathbf{D}_{\phi 1}-\mathbf{D}_{12}-\mathbf{D}_{21}=\begin{Bmatrix} d_{26}+d_{36} & -d_{23}-d_{33}-d_{66} & d_{24}+d_{34}-d_{56} \\ d_{22}-d_{33} & -d_{26}+2d_{36} & -d_{25}+d_{35}-d_{46} \\ 2d_{24}+2d_{34} & d_{35}-2d_{46} & -3d_{45} \end{Bmatrix}$$

For cross-anisotropic media, the material matrices are:

$$\mathbf{D}_{rr}=\begin{Bmatrix} \lambda_t+2G_t & \cdot & \cdot \\ \cdot & G_t & \cdot \\ \cdot & \cdot & G_t \end{Bmatrix} \qquad \mathbf{D}_{\phi\phi}=\begin{Bmatrix} G_t & \cdot & \cdot \\ \cdot & \lambda+2G & \cdot \\ \cdot & \cdot & G \end{Bmatrix} \qquad \mathbf{D}_{\theta\theta}=\begin{Bmatrix} G_t & \cdot & \cdot \\ \cdot & G & \cdot \\ \cdot & \cdot & \lambda+2G \end{Bmatrix}$$

$$\mathbf{D}_{r\phi}=\mathbf{D}_{\phi r}^{T}=\begin{Bmatrix} \cdot & \lambda_t & \cdot \\ G_t & \cdot & \cdot \\ \cdot & \cdot & \cdot \end{Bmatrix} \qquad \mathbf{D}_{r\theta}=\mathbf{D}_{\theta r}^{T}=\begin{Bmatrix} \cdot & \cdot & \lambda_t \\ \cdot & \cdot & \cdot \\ G_t & \cdot & \cdot \end{Bmatrix} \qquad \mathbf{D}_{\phi\theta}=\mathbf{D}_{\theta\phi}^{T}=\begin{Bmatrix} \cdot & \cdot & \cdot \\ \cdot & \cdot & \lambda \\ \cdot & G & \cdot \end{Bmatrix}$$

$$\mathbf{D}_{11}=\begin{Bmatrix} 4(\lambda+G) & \cdot & \cdot \\ \cdot & G_t & \cdot \\ \cdot & \cdot & G_t \end{Bmatrix} \qquad \mathbf{D}_{22}=\begin{Bmatrix} \cdot & \cdot & \cdot \\ \cdot & \lambda+2G & \cdot \\ \cdot & \cdot & G \end{Bmatrix} \qquad \mathbf{D}_{12}=\mathbf{D}_{21}^{T}=\begin{Bmatrix} \cdot & 2(\lambda+G) & \cdot \\ \cdot & \cdot & \cdot \\ \cdot & \cdot & \cdot \end{Bmatrix}$$

$$\mathbf{D}_{r1}=\mathbf{D}_{1r}^{T}=\begin{Bmatrix} 2\lambda_t & \cdot & \cdot \\ \cdot & -G_t & \cdot \\ \cdot & \cdot & -G_t \end{Bmatrix} \qquad \mathbf{D}_{r2}=\mathbf{D}_{2r}^{T}=\begin{Bmatrix} \cdot & \lambda_t & \cdot \\ \cdot & \cdot & \cdot \\ \cdot & \cdot & \cdot \end{Bmatrix}$$

$$\mathbf{D}_{\phi 1}=\mathbf{D}_{1\phi}^{T}=\begin{Bmatrix} \cdot & -G_t & \cdot \\ 2(\lambda+G) & \cdot & \cdot \\ \cdot & \cdot & \cdot \end{Bmatrix} \qquad \mathbf{D}_{\phi 2}=\mathbf{D}_{2\phi}^{T}=\begin{Bmatrix} \cdot & \cdot & \cdot \\ \cdot & \lambda & \cdot \\ \cdot & \cdot & -G \end{Bmatrix}$$

$$\mathbf{D}_{\theta 1}=\mathbf{D}_{1\theta}^{T}=\begin{Bmatrix} \cdot & \cdot & -G_t \\ \cdot & \cdot & \cdot \\ 2(\lambda+G) & \cdot & \cdot \end{Bmatrix} \qquad \mathbf{D}_{\theta 2}=\mathbf{D}_{2\theta}^{T}=\begin{Bmatrix} \cdot & \cdot & \cdot \\ \cdot & \cdot & -G \\ \cdot & \lambda+2G & \cdot \end{Bmatrix}$$

$$\mathbf{D}_{r\phi}+\mathbf{D}_{\phi r}=\begin{Bmatrix} \cdot & \lambda_t+G_t & \cdot \\ \lambda_t+G_t & \cdot & \cdot \\ \cdot & \cdot & \cdot \end{Bmatrix} \qquad \mathbf{D}_{r\phi}-\mathbf{D}_{\phi r}=\begin{Bmatrix} \cdot & \lambda_t-G_t & \cdot \\ -(\lambda_t-G_t) & \cdot & \cdot \\ \cdot & \cdot & \cdot \end{Bmatrix}$$

$$\mathbf{D}_{r\theta}+\mathbf{D}_{\theta r}=\begin{Bmatrix} \cdot & \cdot & \lambda_t+G_t \\ \cdot & \cdot & \cdot \\ \lambda_t+G_t & \cdot & \cdot \end{Bmatrix} \qquad \mathbf{D}_{r\theta}-\mathbf{D}_{\theta r}=\begin{Bmatrix} \cdot & \cdot & \lambda_t-G_t \\ \cdot & \cdot & \cdot \\ -(\lambda_t-G_t) & \cdot & \cdot \end{Bmatrix}$$

$$\mathbf{D}_{\phi\theta}+\mathbf{D}_{\theta\phi}=\begin{Bmatrix} \cdot & \cdot & \cdot \\ \cdot & \cdot & \lambda+G \\ \cdot & \lambda+G & \cdot \end{Bmatrix}$$

$$2\mathbf{D}_{rr}+(\mathbf{D}_{r1}-\mathbf{D}_{1r})=\begin{Bmatrix} 2(\lambda_t+2G_t) & \cdot & \cdot \\ \cdot & 2G_t & \cdot \\ \cdot & \cdot & 2G_t \end{Bmatrix}$$

$$\mathbf{D}_{11}+\mathbf{D}_{\phi 2}=\begin{Bmatrix} 4(\lambda+G) & \cdot & \cdot \\ \cdot & G_t+\lambda & \cdot \\ \cdot & \cdot & G_t-G \end{Bmatrix}$$

$$\mathbf{D}_{\phi r}+(\mathbf{D}_{r2}-\mathbf{D}_{2r})=\begin{Bmatrix} \cdot & \lambda_t+G_t & \cdot \\ \cdot & \cdot & \cdot \\ \cdot & \cdot & \cdot \end{Bmatrix}$$

$$\mathbf{D}_{r\phi}+(\mathbf{D}_{\phi 1}-\mathbf{D}_{1\phi})=\begin{Bmatrix} \cdot & \lambda_t-G_t-2(\lambda+G) & \cdot \\ 2(G_t+\lambda+G) & \cdot & \cdot \\ \cdot & \cdot & \cdot \end{Bmatrix}$$

$$\mathbf{D}_{\phi\phi}+(\mathbf{D}_{\phi 2}-\mathbf{D}_{2\phi})=\begin{Bmatrix} G_t & \cdot & \cdot \\ \cdot & \lambda+2G & \cdot \\ \cdot & \cdot & G \end{Bmatrix}$$

$$\mathbf{D}_{r\theta}+(\mathbf{D}_{\theta 1}-\mathbf{D}_{1\theta})=\begin{Bmatrix} \cdot & \cdot & \lambda_t-G_t-2(\lambda+G) \\ \cdot & \cdot & \cdot \\ 2(G_t+\lambda+G) & \cdot & \cdot \end{Bmatrix}$$

$$\mathbf{D}_{\phi\theta}+(\mathbf{D}_{\theta 2}-\mathbf{D}_{2\theta})=\begin{Bmatrix} \cdot & \cdot & \cdot \\ \cdot & \cdot & -(\lambda+3G) \\ \cdot & \lambda+3G & \cdot \end{Bmatrix}$$

$$\mathbf{D}_{r1}-\mathbf{D}_{11}=\begin{Bmatrix} 2[\lambda_t-\lambda-2(\lambda+2G)] & \cdot & \cdot \\ \cdot & -2G_t & \cdot \\ \cdot & \cdot & -2G_t \end{Bmatrix}$$

$$\mathbf{D}_{r2}+\mathbf{D}_{\phi 1}-\mathbf{D}_{12}-\mathbf{D}_{21}=\begin{Bmatrix} \cdot & \lambda_t-G_t-2(\lambda+G) & \cdot \\ \cdot & \cdot & \cdot \\ \cdot & \cdot & \cdot \end{Bmatrix}$$

$$\mathbf{D}_{\phi 1}-\mathbf{D}_{1\phi}=\begin{Bmatrix} \cdot & -(G_t+2\lambda+2G) & \cdot \\ (G_t+2\lambda+2G) & \cdot & \cdot \\ \cdot & \cdot & \cdot \end{Bmatrix}$$

$$\mathbf{D}_{\theta 1} - \mathbf{D}_{1\theta} = \begin{Bmatrix} \cdot & \cdot & -(G_t + 2\lambda + 2G) \\ \cdot & \cdot & \cdot \\ (G_t + 2\lambda + 2G) & \cdot & \cdot \end{Bmatrix}$$

$$\mathbf{D}_{\theta 2} - \mathbf{D}_{2\theta} = \begin{Bmatrix} \cdot & \cdot & \cdot \\ \cdot & \cdot & -(\lambda + 3G) \\ \cdot & (\lambda + 3G) & \cdot \end{Bmatrix}$$

$$\mathbf{D}_{r1} + \mathbf{D}_{1r} = \begin{Bmatrix} 4\lambda_t & \cdot & \cdot \\ \cdot & -2G_t & \cdot \\ \cdot & \cdot & -2G_t \end{Bmatrix}$$

$$\mathbf{D}_{r1} - \mathbf{D}_{1r} = \begin{Bmatrix} \cdot & \cdot & \cdot \\ \cdot & \cdot & \cdot \\ \cdot & \cdot & \cdot \end{Bmatrix}$$

$$\mathbf{D}_{\phi 1} - \mathbf{D}_{12} - \mathbf{D}_{21} = \begin{Bmatrix} \cdot & -G_t - 2(\lambda + G) & \cdot \\ \cdot & \cdot & \cdot \\ \cdot & \cdot & \cdot \end{Bmatrix}$$

APPENDIX 8B : Layer Matrices for linear expansion

8B.1 Layer matrices

For a linear expansion, the layer matrices are then

$$\mathbf{M}=\frac{\rho h r_m^2}{2}\begin{Bmatrix}\left(\frac{4}{15}a^2-\frac{2}{3}a+\frac{2}{3}\right)\mathbf{I} & \left(\frac{1}{15}a^2+\frac{1}{3}\right)\mathbf{I}\\ \left(\frac{1}{15}a^2+\frac{1}{3}\right)\mathbf{I} & \left(\frac{4}{15}a^2+\frac{2}{3}a+\frac{2}{3}\right)\mathbf{I}\end{Bmatrix}$$

$$\mathbf{A}_{\phi\phi}=\frac{h}{6}\begin{Bmatrix}2\mathbf{D}_{\phi\phi} & \mathbf{D}_{\phi\phi}\\ \mathbf{D}_{\phi\phi} & 2\mathbf{D}_{\phi\phi}\end{Bmatrix}$$

$$\mathbf{A}_{\phi\theta}=\frac{h}{6}\begin{Bmatrix}2(\mathbf{D}_{\phi\theta}+\mathbf{D}_{\theta\phi}) & \mathbf{D}_{\phi\theta}+\mathbf{D}_{\theta\phi}\\ \mathbf{D}_{\phi\theta}+\mathbf{D}_{\theta\phi} & 2(\mathbf{D}_{\phi\theta}+\mathbf{D}_{\theta\phi})\end{Bmatrix}$$

$$\mathbf{A}_{\theta\theta}=\frac{h}{6}\begin{Bmatrix}2\mathbf{D}_{\theta\theta} & \mathbf{D}_{\theta\theta}\\ \mathbf{D}_{\theta\theta} & 2\mathbf{D}_{\theta\theta}\end{Bmatrix}$$

$$\mathbf{B}_{\phi 1}=\frac{h}{12}\begin{Bmatrix}-(\mathbf{D}_{r\phi}-\mathbf{D}_{\phi r}) & \mathbf{D}_{r\phi}-\mathbf{D}_{\phi r}\\ \mathbf{D}_{r\phi}-\mathbf{D}_{\phi r} & -(\mathbf{D}_{r\phi}-\mathbf{D}_{\phi r})\end{Bmatrix}+\frac{h}{6}\begin{Bmatrix}2(\mathbf{D}_{\phi 1}-\mathbf{D}_{1\phi}) & \mathbf{D}_{\phi 1}-\mathbf{D}_{1\phi}\\ \mathbf{D}_{\phi 1}-\mathbf{D}_{1\phi} & 2(\mathbf{D}_{\phi 1}-\mathbf{D}_{1\phi})\end{Bmatrix}$$
$$+\frac{r_m}{2}\begin{Bmatrix}\mathbf{D}_{r\phi}-\mathbf{D}_{\phi r} & \mathbf{D}_{r\phi}+\mathbf{D}_{\phi r}\\ -(\mathbf{D}_{r\phi}+\mathbf{D}_{\phi r}) & -(\mathbf{D}_{r\phi}-\mathbf{D}_{\phi r})\end{Bmatrix}$$

$$\mathbf{B}_{\phi 2}=\frac{h}{6}\begin{Bmatrix}2(\mathbf{D}_{\phi\phi}+\mathbf{D}_{\phi 2}-\mathbf{D}_{2\phi}) & \mathbf{D}_{\phi\phi}+\mathbf{D}_{\phi 2}-\mathbf{D}_{2\phi}\\ \mathbf{D}_{\phi\phi}+\mathbf{D}_{\phi 2}-\mathbf{D}_{2\phi} & 2(\mathbf{D}_{\phi\phi}+\mathbf{D}_{\phi 2}-\mathbf{D}_{2\phi})\end{Bmatrix}$$

$$\mathbf{B}_{\theta 1}=\frac{h}{12}\begin{Bmatrix}-(\mathbf{D}_{r\theta}-\mathbf{D}_{\theta r}) & \mathbf{D}_{r\theta}-\mathbf{D}_{\theta r}\\ \mathbf{D}_{r\theta}-\mathbf{D}_{\theta r} & -(\mathbf{D}_{r\theta}-\mathbf{D}_{\theta r})\end{Bmatrix}+\frac{h}{6}\begin{Bmatrix}2(\mathbf{D}_{\theta 1}-\mathbf{D}_{1\theta}) & \mathbf{D}_{\theta 1}-\mathbf{D}_{1\theta}\\ \mathbf{D}_{\theta 1}-\mathbf{D}_{1\theta} & 2(\mathbf{D}_{\theta 1}-\mathbf{D}_{1\theta})\end{Bmatrix}$$
$$+\frac{r_m}{2}\begin{Bmatrix}\mathbf{D}_{r\theta}-\mathbf{D}_{\theta r} & \mathbf{D}_{r\theta}+\mathbf{D}_{\theta r}\\ -(\mathbf{D}_{r\theta}+\mathbf{D}_{\theta r}) & -(\mathbf{D}_{r\theta}-\mathbf{D}_{\theta r})\end{Bmatrix}$$

$$\mathbf{B}_{\theta 2}=\frac{h}{6}\begin{Bmatrix}2(\mathbf{D}_{\theta 2}-\mathbf{D}_{2\theta}) & \mathbf{D}_{\theta 2}-\mathbf{D}_{2\theta}\\ \mathbf{D}_{\theta 2}-\mathbf{D}_{2\theta} & 2(\mathbf{D}_{\theta 2}-\mathbf{D}_{2\theta})\end{Bmatrix}$$

$$\mathbf{G}_1=\frac{h}{12}\begin{Bmatrix}\mathbf{D}_{rr}+(\mathbf{D}_{r1}+\mathbf{D}_{1r}) & -\mathbf{D}_{rr}-(\mathbf{D}_{r1}+\mathbf{D}_{1r})\\ -\mathbf{D}_{rr}-(\mathbf{D}_{r1}+\mathbf{D}_{1r}) & \mathbf{D}_{rr}+(\mathbf{D}_{r1}+\mathbf{D}_{1r})\end{Bmatrix}+\frac{h}{6}\begin{Bmatrix}2(\mathbf{D}_{11}+\mathbf{D}_{\phi 2}) & \mathbf{D}_{11}+\mathbf{D}_{\phi 2}\\ \mathbf{D}_{11}+\mathbf{D}_{\phi 2} & 2(\mathbf{D}_{11}+\mathbf{D}_{\phi 2})\end{Bmatrix}$$
$$+\frac{r_m}{2}\begin{Bmatrix}-(\mathbf{D}_{r1}+\mathbf{D}_{1r}) & -(\mathbf{D}_{r1}-\mathbf{D}_{1r})\\ \mathbf{D}_{r1}-\mathbf{D}_{1r} & \mathbf{D}_{r1}+\mathbf{D}_{1r}\end{Bmatrix}+\frac{r_m^2}{h}\begin{Bmatrix}\mathbf{D}_{rr} & -\mathbf{D}_{rr}\\ -\mathbf{D}_{rr} & \mathbf{D}_{rr}\end{Bmatrix}$$

$$\mathbf{G}_2 = \frac{h}{12}\begin{Bmatrix} -\mathbf{D}_{\phi r} + (\mathbf{D}_{r2} + \mathbf{D}_{2r}) & \mathbf{D}_{\phi r} - (\mathbf{D}_{r2} + \mathbf{D}_{2r}) \\ \mathbf{D}_{\phi r} - (\mathbf{D}_{r2} + \mathbf{D}_{2r}) & -\mathbf{D}_{\phi r} + (\mathbf{D}_{r2} + \mathbf{D}_{2r}) \end{Bmatrix}$$
$$+ \frac{h}{6}\begin{Bmatrix} -2(\mathbf{D}_{\phi 1} - \mathbf{D}_{12} - \mathbf{D}_{21}) & -(\mathbf{D}_{\phi 1} - \mathbf{D}_{12} - \mathbf{D}_{21}) \\ -(\mathbf{D}_{\phi 1} - \mathbf{D}_{12} - \mathbf{D}_{21}) & -2(\mathbf{D}_{\phi 1} - \mathbf{D}_{12} - \mathbf{D}_{21}) \end{Bmatrix}$$
$$+ \frac{r_m}{2}\begin{Bmatrix} \mathbf{D}_{\phi r} - \mathbf{D}_{r2} - \mathbf{D}_{2r} & -\mathbf{D}_{\phi r} - \mathbf{D}_{r2} + \mathbf{D}_{2r} \\ \mathbf{D}_{\phi r} + \mathbf{D}_{r2} - \mathbf{D}_{2r} & -\mathbf{D}_{\phi r} + \mathbf{D}_{r2} + \mathbf{D}_{2r} \end{Bmatrix}$$
$$\mathbf{G}_3 = \frac{h}{12}\begin{Bmatrix} 4\mathbf{D}_{22} & 2\mathbf{D}_{22} \\ 2\mathbf{D}_{22} & 4\mathbf{D}_{22} \end{Bmatrix}$$

8B.2 Stiffness and mass matrices for the linear expansion

The stiffness and mass matrices for cross-anisotropic materials are given of the form.

8B.2.1 Spheroidal mode

$$\hat{\mathbf{K}}_S = \frac{h}{12}\begin{Bmatrix} 5\lambda_t + 2(1+2\bar{m})G_t + 16(\lambda+G) & -\bar{m}[\lambda_t + 3G_t + 8(\lambda+G)] \\ -[\lambda_t + 3G_t + 8(\lambda+G)] & 3G_t + 4\bar{m}\lambda + 8(\bar{m}-1)G \\ -5\lambda_t + 2(\bar{m}-1)G_t + 8(\lambda+G) & \bar{m}[\lambda_t - 3G_t - 4(\lambda+G)] \\ \lambda_t - 3G_t - 4(\lambda+G) & 3G_t + 2\bar{m}\lambda + 4(\bar{m}-1)G \end{Bmatrix}$$
$$\begin{matrix} -5\lambda_t + 2(\bar{m}-1)G_t + 8(\lambda+G) & \bar{m}[\lambda_t - 3G_t - 4(\lambda+G)] \\ \lambda_t - 3G_t - 4(\lambda+G) & 3G_t + 2\bar{m}\lambda + 4(\bar{m}-1)G \\ 5\lambda_t + 2(1+2\bar{m})G_t + 16(\lambda+G) & -\bar{m}[\lambda_t + 3G_t + 8(\lambda+G)] \\ -[\lambda_t + 3G_t + 8(\lambda+G)] & 3G_t + 4\bar{m}\lambda + 8(\bar{m}-1)G \end{matrix}\Bigg\}$$
$$+ \frac{r_m}{2}\begin{Bmatrix} -4\lambda_t & \bar{m}(\lambda_t - G_t) & \cdot & \bar{m}(\lambda_t + G_t) \\ (\lambda_t - G_t) & 2G_t & -(\lambda_t + G_t) & \cdot \\ \cdot & -\bar{m}(\lambda_t + G_t) & 4\lambda_t & -\bar{m}(\lambda_t - G_t) \\ (\lambda_t + G_t) & \cdot & -(\lambda_t - G_t) & -2G_t \end{Bmatrix}$$
$$+ \frac{r_m^2}{h}\begin{Bmatrix} \lambda_t + 2G_t & \cdot & -(\lambda_t + 2G_t) & \cdot \\ \cdot & G_t & \cdot & -G_t \\ -(\lambda_t + 2G_t) & \cdot & \lambda_t + 2G_t & \cdot \\ \cdot & -G_t & \cdot & G_t \end{Bmatrix}$$
$$= \bar{m}\frac{h}{12}\begin{Bmatrix} 4G_t & -[\lambda_t + 3G_t + 8(\lambda+G)] & 2G_t & [\lambda_t - 3G_t - 4(\lambda+G)] \\ \cdot & 4(\lambda+2G) & \cdot & 2(\lambda+2G) \\ 2G_t & [\lambda_t - 3G_t - 4(\lambda+G)] & 4G_t & -[\lambda_t + 3G_t + 8(\lambda+G)] \\ \cdot & 2(\lambda+2G) & \cdot & 4(\lambda+2G) \end{Bmatrix}$$

$$+\frac{h}{12}\begin{Bmatrix} 5\lambda_t+2G_t+16(\lambda+G) & \cdot & -5\lambda_t-2G_t+8(\lambda+G) & \cdot \\ -[\lambda_t+3G_t+8(\lambda+G)] & 3G_t-8G & \lambda_t-3G_t-4(\lambda+G) & 3G_t-4G \\ -5\lambda_t-2G_t+8(\lambda+G) & \cdot & 5\lambda_t+2G_t+16(\lambda+G) & \cdot \\ \lambda_t-3G_t-4(\lambda+G) & 3G_t-4G & -[\lambda_t+3G_t+8(\lambda+G)] & 3G_t-8G \end{Bmatrix}$$

$$+\bar{m}\frac{r_m}{2}\begin{Bmatrix} \cdot & (\lambda_t-G_t) & \cdot & (\lambda_t+G_t) \\ \cdot & \cdot & \cdot & \cdot \\ \cdot & -(\lambda_t+G_t) & \cdot & -(\lambda_t-G_t) \\ \cdot & \cdot & \cdot & \cdot \end{Bmatrix}+\frac{r_m}{2}\begin{Bmatrix} -4\lambda_t & \cdot & \cdot & \cdot \\ (\lambda_t-G_t) & 2G_t & -(\lambda_t+G_t) & \cdot \\ \cdot & \cdot & 4\lambda_t & \cdot \\ (\lambda_t+G_t) & \cdot & -(\lambda_t-G_t) & -2G_t \end{Bmatrix}$$

$$+\frac{r_m^2}{h}\begin{Bmatrix} \lambda_t+2G_t & \cdot & -(\lambda_t+2G_t) & \cdot \\ \cdot & G_t & \cdot & -G_t \\ -(\lambda_t+2G_t) & \cdot & \lambda_t+2G_t & \cdot \\ \cdot & -G_t & \cdot & G_t \end{Bmatrix}$$

$$\hat{\mathbf{M}}_S=\frac{\rho h r_m^2}{30}\begin{Bmatrix} 4a^2-10a+10 & \cdot & a^2+5 & \cdot \\ \cdot & 4a^2-10a+10 & \cdot & a^2+5 \\ a^2+5 & \cdot & 4a^2+10a+10 & \cdot \\ \cdot & a^2+5 & \cdot & 4a^2+10a+10 \end{Bmatrix}$$

8B.2.2 Torsional mode

$$\hat{\mathbf{K}}_T=\frac{h}{12}\begin{Bmatrix} 3G_t+4(\bar{m}-2)G & 3G_t+2(\bar{m}-2)G \\ 3G_t+2(\bar{m}-2)G & 3G_t+4(\bar{m}-2)G \end{Bmatrix}+\frac{r_m}{2}\begin{Bmatrix} 2G_t & \cdot \\ \cdot & -2G_t \end{Bmatrix}+\frac{r_m^2}{h}\begin{Bmatrix} G_t & -G_t \\ -G_t & G_t \end{Bmatrix}$$

$$=\bar{m}\frac{h}{6}\begin{Bmatrix} 2G & G \\ G & 2G \end{Bmatrix}+\frac{h}{12}\begin{Bmatrix} 3G_t-8G & 3G_t-4G \\ 3G_t-4G & 3G_t-8G \end{Bmatrix}+\frac{r_m}{2}\begin{Bmatrix} 2G_t & \cdot \\ \cdot & -2G_t \end{Bmatrix}+\frac{r_m^2}{h}\begin{Bmatrix} G_t & -G_t \\ -G_t & G_t \end{Bmatrix}$$

$$\hat{\mathbf{M}}_T=\frac{\rho h r_m^2}{30}\begin{Bmatrix} 4a^2-10a+10 & a^2+5 \\ a^2+5 & 4a^2+10a+10 \end{Bmatrix}$$

It is noted above that $\bar{m}=m(m+1)$.

APPENDIX 8C : Layer Matrices for quadratic expansion

8C.1 Layer matrices

For a quadratic expansion, the layer matrices are then

$$\mathbf{M}=\frac{\rho h r_m^2}{5}\begin{Bmatrix}\left(\frac{3}{7}a^2-a+\frac{2}{3}\right)\mathbf{I} & \left(\frac{1}{7}a^2-\frac{2}{3}a+\frac{1}{3}\right)\mathbf{I} & \left(-\frac{1}{14}a^2-\frac{1}{6}\right)\mathbf{I}\\ \left(\frac{1}{7}a^2-\frac{2}{3}a+\frac{1}{3}\right)\mathbf{I} & \left(\frac{8}{21}a^2+\frac{8}{3}\right)\mathbf{I} & \left(\frac{1}{7}a^2+\frac{2}{3}a+\frac{1}{3}\right)\mathbf{I}\\ \left(-\frac{1}{14}a^2-\frac{1}{6}\right)\mathbf{I} & \left(\frac{1}{7}a^2+\frac{2}{3}a+\frac{1}{3}\right)\mathbf{I} & \left(\frac{3}{7}a^2+a+\frac{2}{3}\right)\mathbf{I}\end{Bmatrix}$$

$$\mathbf{A}_{\phi\phi}=\frac{h}{30}\begin{Bmatrix}4\mathbf{D}_{\phi\phi} & 2\mathbf{D}_{\phi\phi} & -\mathbf{D}_{\phi\phi}\\ 2\mathbf{D}_{\phi\phi} & 16\mathbf{D}_{\phi\phi} & 2\mathbf{D}_{\phi\phi}\\ -\mathbf{D}_{\phi\phi} & 2\mathbf{D}_{\phi\phi} & 4\mathbf{D}_{\phi\phi}\end{Bmatrix}$$

$$\mathbf{A}_{\phi\theta}=\frac{h}{30}\begin{Bmatrix}4(\mathbf{D}_{\phi\theta}+\mathbf{D}_{\theta\phi}) & 2(\mathbf{D}_{\phi\theta}+\mathbf{D}_{\theta\phi}) & -(\mathbf{D}_{\phi\theta}+\mathbf{D}_{\theta\phi})\\ 2(\mathbf{D}_{\phi\theta}+\mathbf{D}_{\theta\phi}) & 16(\mathbf{D}_{\phi\theta}+\mathbf{D}_{\theta\phi}) & 2(\mathbf{D}_{\phi\theta}+\mathbf{D}_{\theta\phi})\\ -(\mathbf{D}_{\phi\theta}+\mathbf{D}_{\theta\phi}) & 2(\mathbf{D}_{\phi\theta}+\mathbf{D}_{\theta\phi}) & 4(\mathbf{D}_{\phi\theta}+\mathbf{D}_{\theta\phi})\end{Bmatrix}$$

$$\mathbf{A}_{\theta\theta}=\frac{h}{30}\begin{Bmatrix}4\mathbf{D}_{\theta\theta} & 2\mathbf{D}_{\theta\theta} & -\mathbf{D}_{\theta\theta}\\ 2\mathbf{D}_{\theta\theta} & 16\mathbf{D}_{\theta\theta} & 2\mathbf{D}_{\theta\theta}\\ -\mathbf{D}_{\theta\theta} & 2\mathbf{D}_{\theta\theta} & 4\mathbf{D}_{\theta\theta}\end{Bmatrix}$$

$$\mathbf{B}_{\phi 1}=\frac{h}{60}\begin{Bmatrix}11(\mathbf{D}_{\phi r}-\mathbf{D}_{r\phi}) & -12\mathbf{D}_{\phi r}-8\mathbf{D}_{r\phi} & \mathbf{D}_{\phi r}-\mathbf{D}_{r\phi}\\ 8\mathbf{D}_{\phi r}+12\mathbf{D}_{r\phi} & -16(\mathbf{D}_{\phi r}-\mathbf{D}_{r\phi}) & 8\mathbf{D}_{\phi r}+12\mathbf{D}_{r\phi}\\ \mathbf{D}_{\phi r}-\mathbf{D}_{r\phi} & -12\mathbf{D}_{\phi r}-8\mathbf{D}_{r\phi} & 11(\mathbf{D}_{\phi r}-\mathbf{D}_{r\phi})\end{Bmatrix}$$

$$+\frac{r_m}{6}\begin{Bmatrix}-3(\mathbf{D}_{\phi r}-\mathbf{D}_{r\phi}) & 4(\mathbf{D}_{\phi r}+\mathbf{D}_{r\phi}) & -(\mathbf{D}_{\phi r}+\mathbf{D}_{r\phi})\\ -4(\mathbf{D}_{\phi r}+\mathbf{D}_{r\phi}) & \cdot & 4(\mathbf{D}_{\phi r}+\mathbf{D}_{r\phi})\\ (\mathbf{D}_{\phi r}+\mathbf{D}_{r\phi}) & -4(\mathbf{D}_{\phi r}+\mathbf{D}_{r\phi}) & 3(\mathbf{D}_{\phi r}-\mathbf{D}_{r\phi})\end{Bmatrix}$$

$$+\frac{h}{30}\begin{Bmatrix}4(\mathbf{D}_{\phi 1}-\mathbf{D}_{1\phi}) & 2(\mathbf{D}_{\phi 1}-\mathbf{D}_{1\phi}) & -(\mathbf{D}_{\phi 1}-\mathbf{D}_{1\phi})\\ 2(\mathbf{D}_{\phi 1}-\mathbf{D}_{1\phi}) & 16(\mathbf{D}_{\phi 1}-\mathbf{D}_{1\phi}) & 2(\mathbf{D}_{\phi 1}-\mathbf{D}_{1\phi})\\ -(\mathbf{D}_{\phi 1}-\mathbf{D}_{1\phi}) & 2(\mathbf{D}_{\phi 1}-\mathbf{D}_{1\phi}) & 4(\mathbf{D}_{\phi 1}-\mathbf{D}_{1\phi})\end{Bmatrix}$$

$$\mathbf{B}_{\phi 2}=\frac{h}{30}\begin{Bmatrix}4(\mathbf{D}_{\phi\phi}+\mathbf{D}_{\phi 2}-\mathbf{D}_{2\phi}) & 2(\mathbf{D}_{\phi\phi}+\mathbf{D}_{\phi 2}-\mathbf{D}_{2\phi}) & -(\mathbf{D}_{\phi\phi}+\mathbf{D}_{\phi 2}-\mathbf{D}_{2\phi})\\ 2(\mathbf{D}_{\phi\phi}+\mathbf{D}_{\phi 2}-\mathbf{D}_{2\phi}) & 16(\mathbf{D}_{\phi\phi}+\mathbf{D}_{\phi 2}-\mathbf{D}_{2\phi}) & 2(\mathbf{D}_{\phi\phi}+\mathbf{D}_{\phi 2}-\mathbf{D}_{2\phi})\\ -(\mathbf{D}_{\phi\phi}+\mathbf{D}_{\phi 2}-\mathbf{D}_{2\phi}) & 2(\mathbf{D}_{\phi\phi}+\mathbf{D}_{\phi 2}-\mathbf{D}_{2\phi}) & 4(\mathbf{D}_{\phi\phi}+\mathbf{D}_{\phi 2}-\mathbf{D}_{2\phi})\end{Bmatrix}$$

$$\mathbf{B}_{\theta 1}=\frac{h}{60}\begin{Bmatrix}11(\mathbf{D}_{\theta r}-\mathbf{D}_{r\theta}) & -12\mathbf{D}_{\theta r}-8\mathbf{D}_{r\theta} & \mathbf{D}_{\theta r}-\mathbf{D}_{r\theta}\\ 8\mathbf{D}_{\theta r}+12\mathbf{D}_{r\theta} & -16(\mathbf{D}_{\theta r}-\mathbf{D}_{r\theta}) & 8\mathbf{D}_{\theta r}+12\mathbf{D}_{r\theta}\\ \mathbf{D}_{\theta r}-\mathbf{D}_{r\theta} & -12\mathbf{D}_{\theta r}-8\mathbf{D}_{r\theta} & 11(\mathbf{D}_{\theta r}-\mathbf{D}_{r\theta})\end{Bmatrix}$$

$$+\frac{r_m}{6}\begin{Bmatrix}-3(\mathbf{D}_{\theta r}-\mathbf{D}_{r\theta}) & 4(\mathbf{D}_{\theta r}+\mathbf{D}_{r\theta}) & -(\mathbf{D}_{\theta r}+\mathbf{D}_{r\theta})\\ -4(\mathbf{D}_{\theta r}+\mathbf{D}_{r\theta}) & \cdot & 4(\mathbf{D}_{\theta r}+\mathbf{D}_{r\theta})\\ (\mathbf{D}_{\theta r}+\mathbf{D}_{r\theta}) & -4(\mathbf{D}_{\theta r}+\mathbf{D}_{r\theta}) & 3(\mathbf{D}_{\theta r}-\mathbf{D}_{r\theta})\end{Bmatrix}$$

$$+\frac{h}{30}\begin{Bmatrix}4(\mathbf{D}_{\theta 1}-\mathbf{D}_{1\theta}) & 2(\mathbf{D}_{\theta 1}-\mathbf{D}_{1\theta}) & -(\mathbf{D}_{\theta 1}-\mathbf{D}_{1\theta})\\ 2(\mathbf{D}_{\theta 1}-\mathbf{D}_{1\theta}) & 16(\mathbf{D}_{\theta 1}-\mathbf{D}_{1\theta}) & 2(\mathbf{D}_{\theta 1}-\mathbf{D}_{1\theta})\\ -(\mathbf{D}_{\theta 1}-\mathbf{D}_{1\theta}) & 2(\mathbf{D}_{\theta 1}-\mathbf{D}_{1\theta}) & 4(\mathbf{D}_{\theta 1}-\mathbf{D}_{1\theta})\end{Bmatrix}$$

$$\mathbf{B}_{\theta 2}=\frac{h}{30}\begin{Bmatrix}4(\mathbf{D}_{\theta 2}-\mathbf{D}_{2\theta}) & 2(\mathbf{D}_{\theta 2}-\mathbf{D}_{2\theta}) & -(\mathbf{D}_{\theta 2}-\mathbf{D}_{2\theta})\\ 2(\mathbf{D}_{\theta 2}-\mathbf{D}_{2\theta}) & 16(\mathbf{D}_{\theta 2}-\mathbf{D}_{2\theta}) & 2(\mathbf{D}_{\theta 2}-\mathbf{D}_{2\theta})\\ -(\mathbf{D}_{\theta 2}-\mathbf{D}_{2\theta}) & 2(\mathbf{D}_{\theta 2}-\mathbf{D}_{2\theta}) & 4(\mathbf{D}_{\theta 2}-\mathbf{D}_{2\theta})\end{Bmatrix}$$

$$\mathbf{G}_1=\frac{h}{60}\begin{Bmatrix}\left(\frac{35}{a^2}-\frac{40}{a}+17\right)\mathbf{D}_{rr} & \left(-\frac{40}{a^2}+\frac{40}{a}-24\right)\mathbf{D}_{rr} & \left(\frac{5}{a^2}+7\right)\mathbf{D}_{rr}\\ \left(-\frac{40}{a^2}+\frac{40}{a}-24\right)\mathbf{D}_{rr} & \left(\frac{80}{a^2}+48\right)\mathbf{D}_{rr} & \left(-\frac{40}{a^2}-\frac{40}{a}-24\right)\mathbf{D}_{rr}\\ \left(\frac{5}{a^2}+7\right)\mathbf{D}_{rr} & \left(-\frac{40}{a^2}-\frac{40}{a}-24\right)\mathbf{D}_{rr} & \left(\frac{35}{a^2}+\frac{40}{a}+17\right)\mathbf{D}_{rr}\end{Bmatrix}$$

$$+\frac{h}{60}\begin{Bmatrix}11(\mathbf{D}_{r1}+\mathbf{D}_{1r}) & 8\mathbf{D}_{r1}-12\mathbf{D}_{1r} & (\mathbf{D}_{r1}+\mathbf{D}_{1r})\\ -12\mathbf{D}_{r1}+8\mathbf{D}_{1r} & -16(\mathbf{D}_{r1}+\mathbf{D}_{1r}) & -12\mathbf{D}_{r1}+8\mathbf{D}_{1r}\\ (\mathbf{D}_{r1}+\mathbf{D}_{1r}) & 8\mathbf{D}_{r1}-12\mathbf{D}_{1r} & 11(\mathbf{D}_{r1}+\mathbf{D}_{1r})\end{Bmatrix}$$

$$+\frac{r_m}{6}\begin{Bmatrix}-3(\mathbf{D}_{r1}+\mathbf{D}_{1r}) & -4(\mathbf{D}_{r1}-\mathbf{D}_{1r}) & (\mathbf{D}_{r1}-\mathbf{D}_{1r})\\ 4(\mathbf{D}_{r1}-\mathbf{D}_{1r}) & \cdot & -4(\mathbf{D}_{r1}-\mathbf{D}_{1r})\\ -(\mathbf{D}_{r1}-\mathbf{D}_{1r}) & 4(\mathbf{D}_{r1}-\mathbf{D}_{1r}) & 3(\mathbf{D}_{r1}+\mathbf{D}_{1r})\end{Bmatrix}$$

$$+\frac{h}{30}\begin{Bmatrix}4(\mathbf{D}_{\phi 2}+\mathbf{D}_{11}) & 2(\mathbf{D}_{\phi 2}+\mathbf{D}_{11}) & -(\mathbf{D}_{\phi 2}+\mathbf{D}_{11})\\ 2(\mathbf{D}_{\phi 2}+\mathbf{D}_{11}) & 16(\mathbf{D}_{\phi 2}+\mathbf{D}_{11}) & 2(\mathbf{D}_{\phi 2}+\mathbf{D}_{11})\\ -(\mathbf{D}_{\phi 2}+\mathbf{D}_{11}) & 2(\mathbf{D}_{\phi 2}+\mathbf{D}_{11}) & 4(\mathbf{D}_{\phi 2}+\mathbf{D}_{11})\end{Bmatrix}$$

$$\mathbf{G}_2=-\frac{h}{60}\begin{Bmatrix}11\mathbf{D}_{\phi r} & -12\mathbf{D}_{\phi r} & \mathbf{D}_{\phi r}\\ 8\mathbf{D}_{\phi r} & -16\mathbf{D}_{\phi r} & 8\mathbf{D}_{\phi r}\\ \mathbf{D}_{\phi r} & -12\mathbf{D}_{\phi r} & 11\mathbf{D}_{\phi r}\end{Bmatrix}+\frac{r_m}{6}\begin{Bmatrix}3\mathbf{D}_{\phi r} & -4\mathbf{D}_{\phi r} & \mathbf{D}_{\phi r}\\ 4\mathbf{D}_{\phi r} & \cdot & -4\mathbf{D}_{\phi r}\\ -\mathbf{D}_{\phi r} & 4\mathbf{D}_{\phi r} & -3\mathbf{D}_{\phi r}\end{Bmatrix}$$

$$+\frac{h}{60}\begin{Bmatrix}11(\mathbf{D}_{r2}+\mathbf{D}_{2r}) & 8\mathbf{D}_{r2}-12\mathbf{D}_{2r} & (\mathbf{D}_{r2}+\mathbf{D}_{2r})\\ -12\mathbf{D}_{r2}+8\mathbf{D}_{2r} & -16(\mathbf{D}_{r2}+\mathbf{D}_{2r}) & -12\mathbf{D}_{r2}+8\mathbf{D}_{2r}\\ (\mathbf{D}_{r2}+\mathbf{D}_{2r}) & 8\mathbf{D}_{r2}-12\mathbf{D}_{2r} & 11(\mathbf{D}_{r2}+\mathbf{D}_{2r})\end{Bmatrix}$$

$$+\frac{r_m}{6}\begin{Bmatrix}-3(\mathbf{D}_{r2}+\mathbf{D}_{2r}) & -4(\mathbf{D}_{r2}-\mathbf{D}_{2r}) & (\mathbf{D}_{r2}-\mathbf{D}_{2r})\\ 4(\mathbf{D}_{r2}-\mathbf{D}_{2r}) & \cdot & -4(\mathbf{D}_{r2}-\mathbf{D}_{2r})\\ -(\mathbf{D}_{r2}-\mathbf{D}_{2r}) & 4(\mathbf{D}_{r2}-\mathbf{D}_{2r}) & 3(\mathbf{D}_{r2}+\mathbf{D}_{2r})\end{Bmatrix}$$

$$-\frac{h}{30}\begin{Bmatrix}4(\mathbf{D}_{\phi 1}-\mathbf{D}_{12}-\mathbf{D}_{21}) & 2(\mathbf{D}_{\phi 1}-\mathbf{D}_{12}-\mathbf{D}_{21}) & -(\mathbf{D}_{\phi 1}-\mathbf{D}_{12}-\mathbf{D}_{21})\\ 2(\mathbf{D}_{\phi 1}-\mathbf{D}_{12}-\mathbf{D}_{21}) & 16(\mathbf{D}_{\phi 1}-\mathbf{D}_{12}-\mathbf{D}_{21}) & 2(\mathbf{D}_{\phi 1}-\mathbf{D}_{12}-\mathbf{D}_{21})\\ -(\mathbf{D}_{\phi 1}-\mathbf{D}_{12}-\mathbf{D}_{21}) & 2(\mathbf{D}_{\phi 1}-\mathbf{D}_{12}-\mathbf{D}_{21}) & 4(\mathbf{D}_{\phi 1}-\mathbf{D}_{12}-\mathbf{D}_{21})\end{Bmatrix}$$

$$\mathbf{G}_3 = \frac{h}{30}\begin{Bmatrix} 4\mathbf{D}_{22} & 2\mathbf{D}_{22} & -\mathbf{D}_{22} \\ 2\mathbf{D}_{22} & 16\mathbf{D}_{22} & 2\mathbf{D}_{22} \\ -\mathbf{D}_{22} & 2\mathbf{D}_{22} & 4\mathbf{D}_{22} \end{Bmatrix}$$

8C.2 Stiffness and mass matrices for the quadratic expansion

8C.2.1 Spheroidal mode

$$\mathbf{K}_S =$$

$$\frac{h}{60}\begin{Bmatrix} 61\lambda_t+(34+8\bar{m})G_t+32(\lambda+G) & \bar{m}[-11\lambda_t+3G_t-16(\lambda+G)] & -32\lambda_t+4(\bar{m}-12)G_t+16(\lambda+G) \\ -11\lambda_t+3G_t-16(\lambda+G) & 3G_t+8\bar{m}\lambda+16(\bar{m}-1)G & 12\lambda_t+4G_t-8(\lambda+G) \\ -32\lambda_t+4(\bar{m}-12)G_t+16(\lambda+G) & \bar{m}[12\lambda_t+4G_t-8(\lambda+G)] & 16[-\lambda_t+2(3+\bar{m})G_t+8(\lambda+G)] \\ -8(\lambda_t+2G_t)-8(\lambda+G) & -16G_t+4\bar{m}\lambda+8(\mu-1)G & 16[\lambda_t-3G_t-4(\lambda+G)] \\ 11\lambda_t+2(7-\bar{m})G_t-8(\lambda+G) & \bar{m}[-\lambda_t+3G_t+4(\lambda+G)] & -32\lambda_t+4(\bar{m}-12)G_t+16(\lambda+G) \\ -\lambda_t+3G_t+4(\lambda+G) & 3G_t-2\bar{m}\lambda-4(\bar{m}-1)G & 12\lambda_t+4G_t-8(\lambda+G) \end{Bmatrix}$$

$$\begin{Bmatrix} \bar{m}[-8(\lambda_t+2G_t)-8(\lambda+G)] & 11\lambda_t+2(7-\bar{m})G_t-8(\lambda+G) & \bar{m}[-\lambda_t+3G_t+4(\lambda+G)] \\ -16G_t+4\bar{m}\lambda+8(\bar{m}-1)G & -\lambda_t+3G_t+4(\lambda+G) & 3G_t-2\bar{m}\lambda-4(\bar{m}-1)G \\ 16\bar{m}[\lambda_t-3G_t-4(\lambda+G)] & -32\lambda_t+4(\bar{m}-12)G_t+16(\lambda+G) & \bar{m}[12\lambda_t+4G_t-8(\lambda+G)] \\ 16[7G_t+2\bar{m}\lambda+4(\bar{m}-1)G] & -8(\lambda_t+2G_t)-8(\lambda+G) & -16G_t+4\bar{m}\lambda+8(\bar{m}-1)G \\ \bar{m}[-8(\lambda_t+2G_t)-8(\lambda+G)] & 61\lambda_t+(34+8\bar{m})G_t+32(\lambda+G) & \bar{m}[-11\lambda_t+3G_t-16(\lambda+G)] \\ -16G_t+4\bar{m}\lambda+8(\bar{m}-1)G & -11\lambda_t+3G_t-16(\lambda+G) & 3G_t+8\bar{m}\lambda+16(\bar{m}-1)G \end{Bmatrix}$$

$$+\frac{r_m}{6}\begin{Bmatrix} -(20\lambda_t+16G_t) & 3\bar{m}(\lambda_t-G_t) & 8(\lambda_t+2G_t) & 4\bar{m}(\lambda_t+G_t) & \cdot & -\bar{m}(\lambda_t+G_t) \\ 3(\lambda_t-G_t) & -2G_t & -4(\lambda_t+G_t) & 8G_t & \lambda_t+G_t & \cdot \\ 8(\lambda_t+2G_t) & -4\bar{m}(\lambda_t+G_t) & \cdot & \cdot & -8(\lambda_t+2G_t) & 4\bar{m}(\lambda_t+G_t) \\ 4(\lambda_t+G_t) & 8G_t & \cdot & \cdot & -4(\lambda_t+G_t) & -8G_t \\ \cdot & \bar{m}(\lambda_t+G_t) & -8(\lambda_t+2G_t) & -4\bar{m}(\lambda_t+G_t) & 20\lambda_t+16G_t & -3\bar{m}(\lambda_t-G_t) \\ -(\lambda_t+G_t) & \cdot & 4(\lambda_t+G_t) & -8G_t & -3(\lambda_t-G_t) & 2G_t \end{Bmatrix}$$

$$+\frac{r_m^2}{3h}\begin{Bmatrix} 7(\lambda_t+2G_t) & \cdot & -8(\lambda_t+2G_t) & \cdot & (\lambda_t+2G_t) & \cdot \\ \cdot & 7G_t & \cdot & -8G_t & \cdot & G_t \\ -8(\lambda_t+2G_t) & \cdot & 16(\lambda_t+2G_t) & \cdot & -8(\lambda_t+2G_t) & \cdot \\ \cdot & -8G_t & \cdot & 16G_t & \cdot & -8G_t \\ (\lambda_t+2G_t) & \cdot & -8(\lambda_t+2G_t) & \cdot & 7(\lambda_t+2G_t) & \cdot \\ \cdot & G_t & \cdot & -8G_t & \cdot & 7G_t \end{Bmatrix}$$

$$
= \bar{m}\frac{h}{60}\begin{Bmatrix}
8G_t & [-11\lambda_t + 3G_t - 16(\lambda+G)] & 4G_t \\
\cdot & 8(\lambda+2G) & \cdot \\
4G_t & [12\lambda_t + 4G_t - 8(\lambda+G)] & 32G_t \\
\cdot & 4(\lambda+2G) & \cdot \\
-2G_t & [-\lambda_t + 3G_t + 4(\lambda+G)] & 4G_t \\
\cdot & -2(\lambda+2G) & \cdot
\end{Bmatrix}
$$

$$
\begin{Bmatrix}
[-8(\lambda_t+2G_t)-8(\lambda+G)] & -2G_t & [-\lambda_t+3G_t+4(\lambda+G)] \\
4(\lambda+2G) & \cdot & -2(\lambda+2G) \\
16[\lambda_t-3G_t-4(\lambda+G)] & 4G_t & [12\lambda_t+4G_t-8(\lambda+G)] \\
32[\lambda+2G] & \cdot & 4(\lambda+2G) \\
[-8(\lambda_t+2G_t)-8(\lambda+G)] & 8G_t & [-11\lambda_t+3G_t-16(\lambda+G)] \\
4(\lambda+2G) & \cdot & 8(\lambda+2G)
\end{Bmatrix}
$$

$$
+\frac{h}{60}\begin{Bmatrix}
61\lambda_t+34G_t+32(\lambda+G) & \cdot & -32\lambda_t-48G_t+16(\lambda+G) \\
-11\lambda_t+3G_t-16(\lambda+G) & 3G_t-16G & 12\lambda_t+4G_t-8(\lambda+G) \\
-32\lambda_t-48G_t+16(\lambda+G) & \cdot & 16[-\lambda_t+6G_t+8(\lambda+G)] \\
-8(\lambda_t+2G_t)-8(\lambda+G) & -8(2G_t+G) & 16[\lambda_t-3G_t-4(\lambda+G)] \\
11\lambda_t+14G_t-8(\lambda+G) & \cdot & -32\lambda_t-48G_t+16(\lambda+G) \\
-\lambda_t+3G_t+4(\lambda+G) & 3G_t+4G & 12\lambda_t+4G_t-8(\lambda+G)
\end{Bmatrix}
$$

$$
\begin{Bmatrix}
\cdot & 11\lambda_t+14G_t-8(\lambda+G) & \cdot \\
-8(2G_t+G) & -\lambda_t+3G_t+4(\lambda+G) & 3G_t+4G \\
\cdot & -32\lambda_t-48G_t+16(\lambda+G) & \cdot \\
16[7G_t-4G] & -8(\lambda_t+2G_t+\lambda+G) & -8(2G_t+G) \\
\cdot & 61\lambda_t+34G_t+32(\lambda+G) & \cdot \\
-8(2G_t+G) & -11\lambda_t+3G_t-16(\lambda+G) & 3G_t-16G
\end{Bmatrix}
$$

$$
+\bar{m}\frac{r_m}{6}\begin{Bmatrix}
\cdot & 3(\lambda_t-G_t) & \cdot & 4(\lambda_t+G_t) & \cdot & -(\lambda_t+G_t) \\
\cdot & \cdot & \cdot & \cdot & \cdot & \cdot \\
\cdot & -4(\lambda_t+G_t) & \cdot & \cdot & \cdot & 4(\lambda_t+G_t) \\
\cdot & \cdot & \cdot & \cdot & \cdot & \cdot \\
\cdot & (\lambda_t+G_t) & \cdot & -4(\lambda_t+G_t) & \cdot & -3(\lambda_t-G_t) \\
\cdot & \cdot & \cdot & \cdot & \cdot & \cdot
\end{Bmatrix}
$$

$$
+\frac{r_m}{6}\begin{Bmatrix}
-(20\lambda_t+16G_t) & \cdot & 8(\lambda_t+2G_t) & \cdot & \cdot & \cdot \\
3(\lambda_t-G_t) & -2G_t & -4(\lambda_t+G_t) & 8G_t & \lambda_t+G_t & \cdot \\
8(\lambda_t+2G_t) & \cdot & \cdot & \cdot & -8(\lambda_t+2G_t) & \cdot \\
4(\lambda_t+G_t) & 8G_t & \cdot & \cdot & -4(\lambda_t+G_t) & -8G_t \\
\cdot & \cdot & -8(\lambda_t+2G_t) & \cdot & 20\lambda_t+16G_t & \cdot \\
-(\lambda_t+G_t) & \cdot & 4(\lambda_t+G_t) & -8G_t & -3(\lambda_t-G_t) & 2G_t
\end{Bmatrix}
$$

$$+\frac{r_m^2}{3h}\begin{Bmatrix} 7(\lambda_t+2G_t) & \cdot & -8(\lambda_t+2G_t) & \cdot & (\lambda_t+2G_t) & \cdot \\ \cdot & 7G_t & \cdot & -8G_t & \cdot & G_t \\ -8(\lambda_t+2G_t) & \cdot & 16(\lambda_t+2G_t) & \cdot & -8(\lambda_t+2G_t) & \cdot \\ \cdot & -8G_t & \cdot & 16G_t & \cdot & -8G_t \\ (\lambda_t+2G_t) & \cdot & -8(\lambda_t+2G_t) & \cdot & 7(\lambda_t+2G_t) & \cdot \\ \cdot & G_t & \cdot & -8G_t & \cdot & 7G_t \end{Bmatrix}$$

$$\mathbf{M}_S=\frac{\rho h r_m^2}{5}$$

$$\begin{Bmatrix} \frac{3}{7}a^2-a+\frac{2}{3} & \cdot & \frac{1}{7}a^2-\frac{2}{3}a+\frac{1}{3} & \cdot & -\frac{1}{14}a^2-\frac{1}{6} & \cdot \\ \cdot & \frac{3}{7}a^2-a+\frac{2}{3} & \cdot & \frac{1}{7}a^2-\frac{2}{3}a+\frac{1}{3} & \cdot & -\frac{1}{14}a^2-\frac{1}{6} \\ \frac{1}{7}a^2-\frac{2}{3}a+\frac{1}{3} & \cdot & \frac{8}{21}a^2+\frac{8}{3} & \cdot & \frac{1}{7}a^2+\frac{2}{3}a+\frac{1}{3} & \cdot \\ \cdot & \frac{1}{7}a^2-\frac{2}{3}a+\frac{1}{3} & \cdot & \frac{8}{21}a^2+\frac{8}{3} & \cdot & \frac{1}{7}a^2+\frac{2}{3}a+\frac{1}{3} \\ -\frac{1}{14}a^2-\frac{1}{6} & \cdot & \frac{1}{7}a^2+\frac{2}{3}a+\frac{1}{3} & \cdot & \frac{3}{7}a^2+a+\frac{2}{3} & \cdot \\ \cdot & -\frac{1}{14}a^2-\frac{1}{6} & \cdot & \frac{1}{7}a^2+\frac{2}{3}a+\frac{1}{3} & \cdot & \frac{3}{7}a^2+a+\frac{2}{3} \end{Bmatrix}$$

8C.2.2 Torsional mode

$$\mathbf{K}_T=\bar{m}\frac{h}{60}\begin{Bmatrix} 8G & 4G & -2G \\ 4G & 32G & 4G \\ -2G & 4G & 8G \end{Bmatrix}+\frac{h}{60}\begin{Bmatrix} 3G_t-16G & -8(2G_t+G) & 3G_t+4G \\ -8(2G_t+G) & 16[7G_t-4G] & -8(2G_t+G) \\ 3G_t+4G & -8(2G_t+G) & 3G_t-16G \end{Bmatrix}$$

$$+\frac{r_m}{6}\begin{Bmatrix} -2G_t & 8G_t & \cdot \\ 8G_t & \cdot & -8G_t \\ \cdot & -8G_t & 2G_t \end{Bmatrix}+\frac{r_m^2}{3h}\begin{Bmatrix} 7G_t & -8G_t & G_t \\ -8G_t & 16G_t & -8G_t \\ G_t & -8G_t & 7G_t \end{Bmatrix}$$

$$\mathbf{M}_T=\frac{\rho h r_m^2}{5}\begin{Bmatrix} \frac{3}{7}a^2-a+\frac{2}{3} & \frac{1}{7}a^2-\frac{2}{3}a+\frac{1}{3} & -\frac{1}{14}a^2-\frac{1}{6} \\ \frac{1}{7}a^2-\frac{2}{3}a+\frac{1}{3} & \frac{8}{21}a^2+\frac{8}{3} & \frac{1}{7}a^2+\frac{2}{3}a+\frac{1}{3} \\ -\frac{1}{14}a^2-\frac{1}{6} & \frac{1}{7}a^2+\frac{2}{3}a+\frac{1}{3} & \frac{3}{7}a^2+a+\frac{2}{3} \end{Bmatrix}$$

It is noted above that $\bar{m}=m(m+1)$.

Chapter 9 Summary and Conclusions

In this dissertation, we have focused on three goals, namely

- Explore and improve the accuracy and convergence of the TLM by evaluating the numerical dispersion and through benchmark tests available for exact analytical solutions.
- Extend the applicability of the TLM to semi-infinite and infinite layered media.
- Develop two new TLM's for the analysis of wave motions in cylindrically and spherically laminated media.

In the first part, which is contained in chapters 2 and 3, we successfully and systematically derived the closed-form general solutions and spectrum equations for discrete full-spaces subjected to *SH* and *SV-P* plane waves, modeled with both the TLM1 and TLM2. Based on these, we comprehensively explored the numerical dispersion phenomena in the TLM discrete models from the point of view of wave motions. As a result, we provided a rule for the *least* number of thin-layers per wavelength required for accurate results, namely N_λ=4 for the TLM1 and N_λ=2 (or 5/2) for the TLM2. Then, by means of the error estimation over the significant range of vertical wavenumbers, we obtained the optimal tuning factors for the mix of consistent and lumped mass matrices, namely 0.55 for the TLM1 and 0.33 for the TLM2. The optimal tuning factors basically minimize the effect of the numerical dispersion on wave motions in the discrete models. We also derived the closed-form characteristic equations for several free-vibration problems such as anti-plane homogeneous discrete strata and plates, and in-plane homogeneous discrete plates with mixed boundary conditions. In addition, we formally obtained the propagation modes of discrete half-spaces such as a layer on a half-space subjected to anti-plane waves and a homogeneous half-space subjected to in-plane waves. Finally, we compared the eigenvalues for the above free-vibration problems modeled with discrete models against the associated exact analytical solutions, to which we applied different combinations of tuning factors. Finally, we established that the optimal tuning factors improve considerably the accuracy of the eigenvalues in the TLM. In addition, we determined that the TLM2 is more efficient and accurate than the TLM1. Thus, we recommend the use of the TLM2 rather than the TLM1 for more effective analyses.

In chapter 4, we assessed the accuracy and convergence of the TLM modal solutions by means of benchmark tests, and compared these with available exact analytical solutions for both displacements and stresses. For this purpose, we derived and presented the exact analytical solutions for some canonical examples in the appendices. We explored the TLM modal solutions from the point of view of spatial and temporal characteristics of sources and receivers, and also investigated the effect of numerical dispersion on the accuracy. From this exploration, we have assessed the potential for errors associated with the modal superposition in the TLM solutions, and provided criteria for the number of thin-layers per wavelength N_λ needed to calculate accurate responses fields. For the TLM in the frequency domain, $N_\lambda \geq 12$ is recommended for the TLM1 and $N_\lambda \geq 4$ for the TLM2. For the TLM in the time domain, $N_\lambda \geq 8$ is recommended for the TLM1 and $N_\lambda \geq 4$ for the TLM2. In addition, we found out that a hybrid of the exact and discrete solutions can improve considerably the accuracy and efficiency of the ω-TLM modal solutions. The hybrid method is basically a combination of the eigenvalues obtained with the continuous models and the mode shapes obtained with the ω-TLM.

The second part is described in chapters 5 and 6. In chapter 5, we successfully formulate the substructure method to analyze semi-infinite (or infinite) layered media by means of the t-TLM. For this purpose, we also derive new Green's functions in the wavenumber-time domain for a homogeneous half-space by means of the contour integration method. These Green's functions

are a key element in the substructure method formulated in this study. We present an efficient procedure to solve the required integral equations (convolutions) by means of discrete time series. Also, we propose the use of an artificial buffer layer to stabilize the solutions of the convolution equations, which is necessary, especially for the case in which the impedance contrast between the upper layered system and the half-space is very large or very small. Regarding the accuracy and stability of the formulated substructure method, we determine important criteria for the choice of four parameters as follows. First, the number of thin-layers per wavelength N_λ must satisfy the conditions of $N_\lambda \geq 12$ for the TLM1 and $N_\lambda \geq 6$ for the TLM2. Secondly, the maximum frequency-content in the modal solution f_M must be no less than twice the maximum frequency of the external source $f_{\max}$, i.e. $f_M \geq 2f_{\max}$. Thirdly, the time sampling for discrete time series Δt must be no greater than a quarter of the minimum period (or half of the *Nyquist* period), i.e. $\Delta t \leq 1/(4f_M)$. Finally, the thickness of the artificial buffer layer H_B must be no smaller than the smallest wavelength $\lambda_{\min}$ considered in analyses, i.e. $H_B \geq \lambda_{\min}$. Solving several numerical examples, we showed the validation of the developed substructure method and the above four criteria as well.

In chapter 6, we explore the characteristics of semi-infinite and infinite media modeled with the hybrid ω-TLM together with the paraxial approximation and the buffer layer. We first review some previous studies in the literature, and investigate some features of the hybrid system. From here, we find the accuracy of the response as function of the range x (i.e. distance to the receivers), which says that the response in the far-field deteriorates because of spurious reflection at the interface of the paraxial boundary with the buffer layer. In addition, we modify the paraxial approximation for *SV-P* wave problems to improve the stability of calculated responses when Poisson's ratio is $\nu \geq 0.30$. In addition, we propose the use of an adaptive buffer layer that is very efficient for seismogram calculation. Through numerical examples, we verify the efficiency of the adaptive buffer layer and determine the proper thickness and refinement of the adaptive buffer layer in the context of seismogram calculation.

The third part is expounded in chapters 7 and 8. In these two chapters, we introduce and formulate two new thin-layer methods, i.e. the cylindrical thin-layer method (CTLM) and the spherical thin-layer method (STLM). These are useful and efficient methods for the analysis of wave propagation in anisotropic, cylindrical and spherical laminas. We verify their validity by means of an analytical comparison with the TLM for flat layers and via two numerical examples for a homogeneous solid and shell. The analytical comparison is based on the fact that hollow cylinders and/or spheres with large radii relative to their thickness behave locally like an infinite plate. For the numerical comparison, we calculate the propagation modes of a homogeneous solid and shell and compare these with the exact analytical solutions. For this purpose, we present the exact analytical solutions for a homogeneous solid and shell. As it turns out, the CTLM and STLM show an excellent agreement with the associated exact analytical solutions. We also explore the effect of tuning factors on these new TLM's, and find that they are similar to those for flat layers.

REFERENCES

1. Ahmadian, H., M.I. Friswell, and J.E. Mottershead (1998). Minimization of the discretization error in mass and stiffness formulations by an inverse method, *International Journal for Numerical Methods in Engineering*, **41**, 371-387.

2. Alekseyev, A.S. and B.G. Mikhailenko (1976/1977). Solution of Lamb's problem for a vertically inhomogeneous half-space, *Akad. Nauk. Izu. Physics of the Solid Earth*, **12** (1), 748-755.

3. Arfken, G. (1985). *Mathematical Methods for Physicists*, 3rd Ed. Academic Press.

4. Belytschko, T. and R. Mullen (1977). On dispersive properties of finite element solutions, *International union of theoretical and applied mechanics*, 67-82, Symposium held at Northwest university, Evanston, IL, USA, September 12-15, 1977.

5. Bouillard, P. (1999). Influence of the pollution on the admissible field error estimation for FE solutions of the Helmhortz equation, *International Journal for Numerical Methods in Engineering*, **45**, 783-800.

6. Cagniard, L., (1962), *Reflection and refraction of progressive seismic waves*, E.A. Flinn and C.H. Dix (translated and revised), McGraw-Hill, New York.

7. Clayton, R. and Engquist, B. (1977), Absorbing boundary conditions for acoustic and elastic wave equations, *Bulletin of the Seismological Society of America*, **67**, 1529-1540.

8. Cummins, P.R., R.J. Geller, T. Hatori, and N. Takeuchi (1994). DSM complete synthetic seismograms: SH, spherically symmetric, case, *Geophysical Research Letters*, **21**, 15, 533-536.

9. Cummins, P.R. (1994). DSM complete synthetic seismograms: P-SV, spherically symmetric, case, *Geophysical Research Letters*, **21**, 15, 1663-1666.

10. Datta, S.K., A.H. Shah, R.L. Bratton, and T. Chakraborty (1988). Wave propagation in laminated composite plates, *Journal of Acoustic Society of America*, **83**, 6, 2020-2026, June.

11. Deraemaeker, A., I. Babuška, and P. Bouillard (1999). Dispersion and pollution of the FEM solution for the Helmhortz equation in one, two and three dimensions, *International Journal for Numerical Methods in Engineering*, **46**, 471-499.

12. Dominguez, J. and Abascal, R. (1984), On the fundamental solutions for the boundary integral equations in static and dynamic elasticity, *Engineering analysis*, CML Publications, Southampton, UK, Vol. 1, No. 3, pp. 128-134.

13. Dong, S.B. and R.B. Nelson (1972). On natural vibrations and waves in laminated orthotropic plates, *Journal of Applied Mechanics*, ASME, **39**, 739-745.

14. Dong, S.B. and K.E. Pauley (1978). Plane waves in anisotropic plates, *Journal of Engineering Mechanics*, ASCE, **104**, 4, 801-817, August.

15. Drake, L.A. (1972a). Love and Rayleigh waves in non-horizontally layered media, *Bulletin of the Seismological Society of America*, Vol. **62**, No. 5, 1241-1258, October.

16. Drake, L.A. (1972b). Rayleigh waves at a continental boundary by the finite element method, *Bulletin of the Seismological Society of America*, Vol. **62**, No. 5, 1259-1268, October.

17. Drake, L.A. (1980). Love and Rayleigh waves in irregular soil layers, *Bulletin of the Seismological Society of America*, **70**, 2, 571-582, April.

18. Engquist, B. and A. Majda (1977). Absorbing boundary conditions for the numerical simulation of waves, *Mathematics of Computation*, **31**, 139, 629-651, July.

19. Ewing, M., W. Jardetzky, and F. Press (1957). *Elastic waves in layered media*, McGraw-Hill, New York.

20. Galán, J.M. and R. Abascal (2002). Numerical simulation of Lamb wave scattering in semi-infinite plates, *International Journal for Numerical Methods in Engineering*, **53**, 1145-1173.

21. Geller, R.J. and T. Ohminato (1994). Computation of synthetic seismograms and their partial derivatives for heterogeneous media with arbitrary natural boundary conditions using the Direct Solution Method, *Geophys. J. Int.*, **116**, 421-446.

22. Geller, R.J. and T. Ohminato (1995). DSM synthetic seismograms using analytic trial functions: plane-layered, isotropic, case, *Geophys. J. Int.*, **120**, 163-172.

23. Ghibril, R. (1992). On the partial discretization of coupled plane stratified systems, *Ph.D. Thesis*, Department of Civil Engineering, MIT, February 1992.

24. Givoli, D. (1991). Non-reflecting boundary conditions, *Journal of Computational Physics*, **94**, 1-29.

25. Guan, F. and M. Novak (1994). Transient response of an elastic homogeneous half-space to suddenly applied rectangular loading, *Journal of Applied Mechanics*, ASME, **61**, 256-263.

26. Guan, F., I.D. Moore, and C.C. Spyrakos (1998). Two dimensional transient fundamental solution due to suddenly applied load in a half-space, *Soil Dynamics and Earthquake Engineeriing*, **17**, 269-277.

27. Han, X., G.R. Liu, and K.Y. Lim (2001a). Transient waves in plates of functionally graded materials, *International Journal for Numerical Methods in Engineering*, **52**, 851-865.

28. Han, X., G.R. Liu, and K.Y. Lim (2001b). Transient waves in a functionally graded cylinder, *International Journal of Solids and Structures*, **38**, 3021-3037.

29. Harkrider, D.G. (1964). Surface waves in multilayered elastic media I. Rayleigh and Love waves from buried sources in a multilayered elastic half-space, *Bulletin of the Seismological Society of America*, Vol. **54**, 2, 627-679, April.

30. Haskell, N.A. (1953). The dispersion of surface waves on multilayered media, *Bulletin of the Seismological Society of America*, Vol. **43**, 17-34.

31. Huang, K.H. and S.B. Dong (1984). Propagating waves and edge vibrations in anisotropic composite cylinders, *Journal of Sound and Vibration*, **96**(3), 363-379.

32. Kausel, E. (1974). Forced vibrations of circular foundations on layered media, *MIT Research Report R74-11*, Department of Civil Engineering, MIT, Cambridge, MA, 02139.

33. Kausel, E. and J.M. Roësset (1977). Semi-analytical hyperelement for layered strata, *Journal of Engineering Mechanics*, ASCE, **103**, 4, 569-588, August.

34. Kausel, E. (1981). An explicit solution for the Green's functions for dynamic loads in layered media, *MIT Research Report R81-13*, Department of Civil Engineering, MIT, Cambridge, MA, 02139.

35. Kausel, E. and J.M. Roësset (1981). Stiffness matrices for layered soils, *Bulletin of the Seismological Society of America*, **71**, 6, 1743-1761, December.

36. Kausel, E. and R. Peek (1982a). Dynamic loads in the interior of a layered stratum: An explicit solution, *Bulletin of the Seismological Society of America*, **72**, 5, 1459-1481, October.

37. Kausel, E. and R. Peek (1982b). Boundary integral method for stratified soils, *MIT Research Report R82-50*, Department of Civil Engineering, MIT, Cambridge, MA, 02139.

38. Kausel, E. (1986). Wave propagation in anisotropic layered media, *International Journal for Numerical Methods in Engineering*, **23**, 1567-1578.

39. Kausel, E. and S.H. Seale (1987). Static loads in layered halfspaces, *Journal of Applied Mechanics*, ASME, **54** (2), 403-408, June.

40. Kausel, E. (1988). Local transmitting boundaries, *Journal of Applied Mechanics*, ASME, **114** (6), 1011-1027, June.

41. Kausel, E. and S.H. Seale (1990). Dynamic and static impedances of cross-anisotropic halfspaces, *Soil Dynamics and Earthquake Engineering*, **9**, 4, 172-178.

42. Kausel, E. and J.M. Roësset (1992). Frequency domain analysis of undamped systems, *Journal of Engineering Mechanics*, ASCE, **118**, 4, 721-734, April.

43. Kausel, E. (1992). Physical interpretation and stability of paraxial boundary conditions, *Bulletin of the Seismological Society of America*, **82**, 2, 898-913, April.

44. Kausel, E. (1993). Discrete Green's function s for layered media: Time domain solution, Proceedings of the NSF workshop, *Geophysical Techniques for Site and Material Characterization*, held June 11-12, 1993 in Atlanta, Georgia.

45. Kausel, E. (1994). Thin-layer method: Formulation in the time domain, *International Journal for Numerical Methods in Engineering*, **37**, 927-941.

46. Kausel, E. (1998a). Blast loads v.s. point loads: the Missing factor, *Journal of Engineering Mechanics*, ASCE, **124**, 2, 243-244, February.

47. Kausel, E. (1998b). Dynamic point sources in laminated media via the thin-layer method, *Internal Journal of Solids and Structures*, **00**,000-000

48. Kundu, T. and A.K. Mal (1985). Elastic waves in a multilayered solid due to a dislocation source, *Wave motion*, **7**, 459-471, North-Holland.

49. Liu, G.R. and J.D. Achenbach (1994). A strip element method for stress analysis of anisotropic linearly elastic solids, *Journal of Applied Mechanics*, ASME, **61**, 270-277, June.

50. Liu, G.R. and J.D. Achenbach (1995). Strip element method to analyze wave scattering by cracks in anisotropic laminated plates, *Journal of Applied Mechanics*, ASME, **62**, 607-613, September.

51. Lysmer, J. (1970). Lumped mass method for Rayleigh waves, *Bulletin of the Seismological Society of America*, **60**, 1, 89-104, February.

52. Lysmer, J. and G. Waas (1972). Shear waves in plane infinite structures, *Journal of Engineering Mechanics*, ASCE, **98**, 85-105.

53. Maeda, T. and E. Kausel (1991). On the accuracy of some approximate antiplane half-space stiffness, *Bulletin of the Seismological Society of America*, Vol. **81**, No. 4, 1340-1258, August.

54. Mullen, R. (1982). Dispersion analysis of finite element semidiscretizations of the two-dimensional wave equation, *International Journal for Numerical Methods in Engineering*, **18**, 11-29.

55. Nelson, R.B., S.B. Dong and R.D. Kalra (1971). Vibrations and waves in laminated orthotropic circular cylinders, *Journal of Sound and Vibration*, **18**, 3, 429-444.

56. Nelson, R.B., and S.B. Dong (1973). High frequency vibrations and waves in laminated orthotropic plates, *Journal of Sound and Vibration*, **30**, 1, 33-44.

57. Olson, A.H., J.A. Orcutt, and G.A. Frazier (1984). The discrete wavenumber/finite element method for synthetic seismograms, *Geophys. J.R. astr. Soc.*, **77**, 421-460.

58. Park, J. (1998). Point sources in cylindrically laminated rods, *S.M. Thesis*, Department of Civil and Environmental Engineering, MIT, May 1998.

59. Prosper, D. (2001). Modeling and detection of delaminations in laminated plates, *Ph.D. Thesis*, Department of Civil and Environmental Engineering, MIT, May 2001.

60. Rattanawangcharoen, N., W. Zhuang, A.H. Shah, and S.K. Datta (1997). Axisymmetric guided waves in jointed laminated cylinders, *Journal of Engineering Mechanics*, ASCE, **123**(10), 1020-1026, October.

61. Richter, C. and G. Schmid (1999). A Green's function time-domain boundary element method for the elastodynamic half-plane, *International Journal for Numerical Methods in Engineering*, **46**, 627-648.

62. Rukos, E.A. (1978). Continuous elements in the finite element method, *International Journal for Numerical Methods in Engineering*, **12**, 11-33.

63. Schepers, W. (2001). Optimierungsmöglichkeiten bei der Anwendung der Methode der dünnen Schichten, Eingereicht als Diplomarbeit am Fachgebiet Grundbau und Bodenmechanik an der Technischen Universität Berlin, February 2001 (in Germany).

64. Seale, S.H. (1985). Dynamic loads in layered halfspaces, *Ph.D. Thesis*, Department of Civil Engineering, MIT, September 1985.

65. Seale, S.H. and E. Kausel (1989). Point loads in cross-anisotropic, layered halfspaces, *Journal of Engineering Mechanics*, ASCE, **115**, 3, 509-524, March.

66. Spiegel, M.R. (1968). *Mathematical Handbook of Formulas and Tables*, Schaum's outline series McGraw-Hill Inc.

67. Stacey, R. (1988). Improved transparent boundary formulations for the elastic-wave equation, *Bulletin of the Seismological Society of America*, **78**, 6, 2089-2097, December.

68. Tan, H.H. (1980). Displacement approach for generalized Rayleigh waves in layered solid-fluid media, *Bulletin of the Seismological Society of America*, **79**, 4, 1251-1263, August.

69. Tassoulas, J. (1981). Elements for the numerical analysis of wave motion in layered media, *MIT Research Report R81-2*, Department of Civil Engineering, MIT, Cambridge, MA, 02139.

70. Tassoulas, J. and E. Kausel (1983). Elements for the numerical analysis of wave motion in layered strata, *International Journal for Numerical Methods in Engineering*, **19**, 1005-1032.

71. Thomson, W.T. (1950). Transmission of elastic waves through a stratified soil medium, *Journal of Applied Physics*, **21**, 89-93, February.

72. Touhei, T. (1994). A discrete wavenumber and normal-mode superposition method for synthesis seismograms, *Bulletin of the Seismological Society of America*, **84**, 5, 1473-1483, October.

73. Waas, G. (1972). Linear two-dimensional analysis of soil dynamic problems in semi-infinite layer media, *Ph.D. Thesis*, University of California, Berkeley.

74. Woods, R.D. (1968). Screening of surface waves in soils, *Journal of Soil Mechanics and Foundation division*, ASCE, **94**, 4, 951-979, July.

75. Xi, Z.C., G.R. Liu, K.Y. Lam, and H.M. Shang (2000a). A strip-element method for analyzing wave scattering by a crack in an immersed axisymmetric laminated composite cylinder, *Journal of Acoustic Society of America*, **108**, 1, 175-183.

76. Xi, Z.C., G.R. Liu, K.Y. Lam, and H.M. Shang (2000b). Dispersion and characteristic surfaces of waves in laminated composite circular cylindrical shells, *Journal of Acoustic Society of America*, **108**, 5, 2179-2186.

77. Xu, P.-C. and A.K. Mal (1987). Calculation of the inplane Green's functions for a layered viscoelastic solid, *Bulletin of the Seismological Society of America*, **77**, 5, 1823-1837, October.